Pasquale Cavaliere

Water Electrolysis for Hydrogen Production

Water Electrolysis for Hydrogen Production

Pasquale Cavaliere

Water Electrolysis for Hydrogen Production

Springer

Pasquale Cavaliere
Department of Innovation Engineering
University of Salento
Lecce, Italy

Preface

Water electrolysis is an important technique for hydrogen production to face energy crisis. In past decades, great efforts and breakthroughs have been made in designing and optimizing bifunctional electrocatalysts.

Hydrogen can be used in its pure form as an energy carrier or as an industrial raw material.

It can also be combined with other inputs to produce what are referred to as hydrogen-based fuels and feedstocks. Hydrogen-based fuels and feedstocks can be produced using hydrogen from any source, whether electricity, biomass, or fossil fuels, and can readily be used in applications such as engines, turbines, and chemical processes. They include such derivative products such as synthetic methane, synthetic liquid fuels, and methanol, all of which require carbon alongside hydrogen. They also include ammonia, which can be used as a chemical feedstock or potentially as a fuel, and which is made by combining hydrogen with nitrogen.

In recent years, colors have been used to refer to different sources of hydrogen production. "Black," "grey," or "brown" refer to the production of hydrogen from coal, natural gas, and lignite, respectively. "Blue" is commonly used to produce hydrogen from fossil fuels with CO_2 emissions reduced by the use of CCUS. "Green" is a term applied to the production of hydrogen from renewable electricity. In general, there are no established colors for hydrogen from biomass, nuclear, or different varieties of grid electricity.

Hydrogen is regarded as the alternative energy carrier of the future due to higher energy density on a mass basis, less environmental problems, its abundant presence in different forms in the universe, and its convertibility into electricity or useful chemicals. It is the lightest element in the universe, which is without taste, color, odor, and non-toxic under normal conditions and has heating values of 2.4, 2.8 and 4 times higher than those of methane, gasoline and coal, respectively.

Hydrogen can be efficiently converted into electricity, and vice versa. It can be produced from renewable materials such as biomass and water, and most importantly, it is environmentally friendly at all processes utilizing hydrogen.

Water is the most abundant resource for hydrogen production which consists of hydrogen and oxygen. Hence, the water molecule can be split into hydrogen and oxygen if enough energy is provided. Water splitting process can be performed through different technologies. Water splitting for hydrogen production can be performed based on any of these sources and some hybrid types (combined two or many energy sources. Water-splitting hydrogen production methods can be categorized into five major types and a hybrid form where two or more types of energy are employed in a system for hydrogen production. Hydrogen from water by electricity based (electrolysis), mechanical based (from ultrasound through sono-chemical method), photonic based (photolysis or photo electrochemical water splitting), and thermal energy based (thermochemical cycles and thermolysis).

Electrolysis is one of the simplest ways to produce hydrogen from water. It can simply be summarized as the conversion of electric power to chemical energy in the form of hydrogen and oxygen as a byproduct with two reactions in each electrode: anode and cathode. There is a separator between anode and cathode electrodes which ensure products to remain isolated. The low-temperature electrolysis (LTE) occurs in temperatures of 70–90 °C, while the high-temperature electrolysis (HTE) takes place in 700–1000 °C with less electricity consumption. The advantage of HTE is that near-zero GHG emission can be achieved if an external clean heat source is employed.

Water-splitting thermochemical cycles are based on water decomposition through repetitive series of chemical reactions using intermediate reactions and substances which are all recycled during the process so that the overall reactions are equivalent to the dissociation of the water molecule into hydrogen and oxygen.

Thermochemical cycles are driven either by only thermal energy which are called pure thermochemical cycles, or by thermal and another form of energy (e.g., electrical, photonic) which are called hybrid thermochemical cycles.

Hydrogen could be produced from abundant sources of sea water along with solar energy, for countries where fresh water is scarce. The most promising way for the electrolysis of sea water in a H_2/O_2 cell is the use of oxygen-selective electrodes. Oxygen reaction depends rather upon the electrode material than the chlorine reaction does and at low overpotential with different electrode materials. Hot, coastal, hyper-arid regions with intense solar irradiation and strong on- and off-shore wind patterns are ideal locations to produce renewable electricity using wind turbines or photovoltaics. Given ample access to sea-water and scarce freshwater resources, such regions make the direct and selective electrolytic splitting of seawater into molecular hydrogen and oxygen a potentially attractive technology. Direct seawater electrolysis is an increasingly attractive electricity/hydrogen conversion and storage technology of the future. It will be most effective in regions with ample surplus renewable electricity, little access to freshwater, and yet sufficient access to ocean seawater. It also offers advantages for mobile maritime and offshore hydrogen-based power applications. Examples include powering underwater and unmanned maritime vehicles for maintenance of offshore installations. In combination with a hydrogen fuel cell, a reversible seawater electrolysis scheme is possible

that holds promise for the storage of surplus electricity in the form of molecular hydrogen, and more as a collateral process, purified water is formed during the fuel cell reaction. Based on the energy efficiency of reversible electrolyzer−fuel cell schemes, the resulting freshwater production may remain limited with respect to more conventional freshwater technologies.

Alkaline water electrolysis combined with renewable energy can be integrated into the distributed energy system by producing hydrogen for end use and as an energy storage media. Compared to the other major methods for hydrogen production, alkaline water electrolysis is simple but currently less efficient. The challenges for the widespread use of water electrolysis are also the durability and safety. Practical considerations of industrial electrochemical engineering and electrolyzr development led to the conclusion that the alkaline water electrolysis is still a better means for hydrogen production. Further R&D efforts to improve the efficiency are needed to widespread the application of the alkaline water electrolysis like developing electrocatalysts to significantly reduce electrochemical reaction resistance, electrolyte additives to facilitate the electron transfer and ionic transfer and to reduce electrode surface tension, electrode surface profile modifications and surface coatings, and more importantly, managing the gas bubble resistances.

Polymer electrolyte membrane (PEM) electrolysis occurs within an acidic electrolyte using a proton exchange membrane to transport protons (H+). PEM electrolysis operates at temperatures of 50–80 °C and pressures of less than 30 bar, achieving current densities of above 2 Acm^{-2} and energy efficiencies of 50–65%. PEM electrolysis is the most promising electrolytic method for producing green hydrogen due to its high-energy efficiencies comparable to AWS and SOE. PEM electrolysis allows for the generation of high purity hydrogen (up to 99.999 vol %) at high pressures, which reduces the requirement for post-production gas compression. Consequently, the generation of hydrogen via PEM electrolysis is the most attractive technology for commercial applications.

Hydrogen production by high-temperature steam electrolysis using the SOEC system is a promising environmentally friendly and energy-saving technology. Reducing operating temperatures and developing electrochemical and chemical stability/durability with minimal thermal stress/mismatch are key issues in the commercialization of the SOEC.

Photocatalysis is a water-splitting event to produce hydrogen from water that uses photonic energy. Most photocatalyst materials are made of semiconductor material because the semiconductor material has an energy gap that allows it to produce electron holes if it is charged with photonic energy from a source particular. In a solid-state or electrochemical PV cell as well as in a bulk photocatalytic cell, photogenerated minority carriers are propelled efficiently by the built-in field to the side where they are majority carriers that together with photogenerated majority carriers flow to the contacts or to a contact and the electrolyte. Consequently, the efficiency of collection of charge carriers generated in the depletion region and within a diffusion length of it is very high. Second, in bulk semiconductor–electrolyte devices and solid-state PV cells, reflection losses that can be substantial for the

high refractive indices of most semiconductors can be minimized by using AR coatings. Therefore, the overall efficiency of 24% and >40% has been achieved for single and multiple-junction solid-state PV cells.

Decoupled water splitting is a new and growing field focused on exploring how separating the electrochemical oxygen- and hydrogen-evolution reactions – either spatially, temporally, or both – can benefit electrolysis systems used for generating carbon-neutral hydrogen. Numerous types of decoupled electrolysis systems have been explored. These systems have allowed for earth-abundant catalysts to generate hydrogen at rates approaching that of precious metal catalysts in PEM electrolysis systems. Membrane separators have been replaced with cheaper alternatives or removed entirely, depending on the system. Membrane-free production of pressurized hydrogen has been achieved. Some mediators have energy- or hydrogen-storage densities that are approaching that of cryogenic hydrogen, albeit with an electrochemical penalty for accessing that hydrogen.

Both OER and HER catalytic processes are necessary to enhance water electrolysis efficiency, and they should be improved kinetically. At present, precious metals are considered the most prominent electrocatalysts. However, the main challenge is that the precious catalysts are rare on earth and, at a high cost, hindered the technology's extensive application. Research developments have been made to decrease the use of precious metals by adapting numerous techniques such as changing the material composition and structures via substitution of precious metals with non-precious metal-based catalysts.

Taken together, significant progress has been made in the design of electrocatalysts for water splitting for the production of hydrogen by advancing the atomic, molecular, and nanoscale materials engineering strategies. Despite the significant progress in understanding the electrocatalytic processes of the OER and HER, several challenges remain for the ultimate commercial large-scale production of hydrogen by water splitting electrolysis. First, the development of non-noble metal OER electrocatalysts with high activity and long-term stability performance in acidic media remains a challenging area of research and development. Recently, non-noble-metal-based carbides, phosphides, and chalcogenides have drawn great attention due to their high performance for OER in alkaline media. However, nanostructured electrocatalysts undergo composition and structural transformations during the reaction under OER conditions. Therefore, understanding the structural transformation is required to determine the real active phases and sites.

Nuclear energy can produce hydrogen in several ways: (1) nuclear heated steam reforming of natural gas, (2) electrolysis of water using nuclear power, (3) HTE using minor heat and major electricity from nuclear reactor, and (4) thermochemical splitting of water using major heat and minor electricity from the nuclear reactor. The existing light water reactor is only applicable to electrolysis of water and at <30% efficiency.

A variety of methods to separate and purify hydrogen exist. The processes in the removal of impurities from crude hydrogen to obtain a pure product can be roughly divided into three steps. The first step is pretreatment of the crude hydrogen for the removal of specific contaminants that are detrimental to subsequent separation

processes and for their conversion to easily separable species. The second step is the removal of both major and minor impurities to yield an acceptably pure hydrogen level. The prime separation technology here is the pressure swing adsorption (PSA) unit, which has several advantages over the other methods and is widely used in various fields of hydrogen separation. The third step is the final purification to a specified level. This is typically a cryogenic adsorption method at a liquid nitrogen temperature or the use of a palladium membrane. Both are capable of reducing impurities to below 1 ppm.

The development of hydrogen infrastructure and technologies is often considered in relation to broader economic development objectives, especially in the context of energy transitions. Hydrogen value chains touch upon many different types of technology and manufacturing sectors. Blending hydrogen into natural gas networks and infrastructure is foreseen for the transition phase. Networks are expected to be based on the conversion of existing natural gas pipelines for cross-border transport. At present, hydrogen is being transported using the existing gas grid or with modifications to the existing gas pipelines, or through dedicated pipelines. Transport cost data indicates that pipelines have a clear cost advantage compared to other transport means, reinforcing the need for regulation.

The infrastructure needed in an economy in which hydrogen is primarily used as a transport fuel is very different from one in which its primary value is as a heating fuel. Today no major hydrogen pipeline networks exist, and no liquified hydrogen ships are in commercial operation. Using existing storage and transport capacities, hydrogen, as the main pillar of energy transition, can reliably ensure security of supply during the change to renewable energy sources. In this way, energy transition – and sector integration specifically – can be promoted comparatively quickly and in-expensively along with the expansion of the power grids.

Today hydrogen is most commonly stored as a gas or liquid in tanks for small-scale mobile and stationary applications. However, the smooth operation of large-scale and intercontinental hydrogen value chains in the future will require a much broader variety of storage options. At an export terminal, for example, hydrogen storage may be required for a short period prior to shipping. Hours of hydrogen storage are needed at vehicle refuelling stations, while days to weeks of storage would help users protect against potential mismatches in hydrogen supply and demand. Much longer-term and larger storage options would be required if hydrogen were used to bridge major seasonal changes in electricity supply or heat demand, or to provide system resilience. The most appropriate storage medium depends on the volume to be stored, the duration of storage, the required speed of discharge, and the geographic avail-ability of different options.

Infrastructure such as pipeline and delivery networks is of particular importance for a new energy carrier such as hydrogen. While hydrogen can be produced locally, its storage and distribution benefit from economies of scale. When produced from fossil fuels in particular, its supply is cheaper when centralized. Hydrogen has low energy density, which makes it more challenging to store and transport than fossil fuels. However, it can be converted into hydrogen-based fuels and feedstocks, such as synthetic methane, synthetic liquid fuels, and ammonia, which can make use of

existing infrastructure for their transport, storage, and distribution. This can reduce the costs of reaching final users. Some of the synthetic hydrocarbons produced from hydrogen can be direct substitutes for their fossil equivalents. Ammonia is already used today as a feedstock in the chemical industry and could be a hydrogen carrier for the long-distance transport of hydrogen in the future, or itself be used as fuel in the shipping sector. Developing a new hydrogen value chain would be contingent upon successfully completing and connecting production, transmission, distribution, storage, and end-use infrastructure. This would require coordinated investment by many different market participants, which could be challenging for them to implement.

Hydrogen can support energy security in several ways. When hydrogen is deployed alongside electricity infrastructure, electricity can be converted to hydrogen and back, or further converted to other fuels, making end users less dependent on specific energy resources and increasing the resilience of energy supplies. If the right infrastructure is developed, it could be attractive in the future for countries to diversify their economies by exporting low-carbon energy in the form of hydrogen and hydrogen-based fuels, or importing hydrogen to benefit from competition that restrains prices. Countries with high-quality resources for hydrogen production are widely dispersed around the globe, and many current energy exporting countries are also endowed with renewable resources that could produce hydrogen. In an ambitious low-carbon context, such hydrogen trade would effectively enable trade and storage of wind and sunshine between different regions to overcome seasonal differences. Lastly, hydrogen could provide an additional way for countries to store reserves of energy strategically in a highly electrified low-carbon world.

Using hydrogen instead of carbon-containing fuels in energy end uses could also reduce local air pollution, improving environmental and health outcomes. Urban air pollution concerns and its related health impacts are now major drivers of energy policy decisions, and governments are keenly interested in ways of reducing air pollution and improving air quality. Because hydrogen can be stored or used in a variety of sectors, converting electricity to hydrogen can help with the matching of variable energy supply and demand, both temporally and geographically, alongside alternatives such as pumped-storage hydropower, batteries, and grid upgrades. If renewable power generation becomes sufficiently cheap and widespread, it can be used not only to provide low-carbon electricity but also to create low-carbon hydrogen that can displace fossil fuels in transport, heating and industrial raw materials, and indeed almost any application not susceptible to electrification. All this makes hydrogen one of a suite of technologies that work well together to support the growth of low-carbon energy at the level of the overall energy system.

Around the world, the state of existing regulations and standards currently limits hydrogen uptake. They deal with a range of technical but important questions such as how and where pressurized or liquefied hydrogen can be used, who can handle hydrogen, where hydrogen vehicles can go, tax regimes for conversion between energy carriers, whether CO_2 can be stored, and how much hydrogen can be present in natural gas pipelines. They need to be updated if hydrogen is to have the opportunity to fulfill its potential. Some important standards have yet to be agreed,

including standard dealing with hydrogen vehicle refuelling, gas composition for cross-border sales, safety measures, permitting, materials and how to measure lifecycle environmental impacts.

In addition to regulations and market design, the cost of production is a major barrier to the uptake of green hydrogen. Costs are falling – largely due to falling renewable power costs – but green hydrogen is still 2–3 times more expensive than blue hydrogen (produced from fossil fuels with carbon capture and storage) and further cost reductions are needed. A low cost of electricity is therefore a necessary condition for producing competitive green hydrogen. This creates an opportunity to produce hydrogen at locations around the world that have optimal renewable resources, in order to achieve competitiveness. Low electricity cost is not enough by itself for competitive green hydrogen production, however, and reductions in the cost of electrolysis facilities are also needed. This is the second largest cost component of green hydrogen production and is the focus of this report, which identifies key strategies to reduce investment costs for electrolysis plants from 40% in the short term to 80% in the long term.

All these issues are discussed a presented in the book, and we hope to give an instrument for focusing the open questions and for improving the scientific discussion on this fundamental subject.

Many thanks to all my family for the support in these months, many thanks to all my friends and colleagues.

My special thanks to all the Springer editorial office people for their professionalism. Finally, I would like to dedicate the work to my son Alessandro.

Lecce, Italy   Pasquale Cavaliere

Contents

Abbreviations

0D	Zero dimensions
1D	One dimension
2D	Two dimensions
3D	Three dimensions
A	Activated
AB	Ammonia borane
ABPE	Applied bias photon-to-current efficiency
AC	Alternating current
ACH	Air exchange per hour
AEL	Alkaline electrolysis
AEM	Anion exchange membrane
AFC	Alkaline fuel cell
AIDE	Adsorption-induced dislocation emission
AOPs	Advanced oxidation processes
APCE	Absorbed photon-to-current efficiency
APU	Auxiliary power unit
AR	Antireflection
ASME	American Society of Mechanical Engineers
AST	Accelerated stress test
ASTM	American Society for Testing and Materials
ATO	Antimony doped tin dioxide
ATR	Autothermal reforming
AWE	Alkaline water electrolysis
AWS	Alkaline water splitting
BAS	Biofilm airlift suspension
BCC	Body-centered cubic
BCL	Brown coal liquefaction
BCN	B-doped carbon nanotubes
BCZY	$BaxCe0.5Zr0.3Y0.2-yNiyO3-\delta$
BDD	Boron-doped diamond
BEV	Battery electric vehicles

BF	Blast furnace
BLEVE	Boiling liquid expanding vapor explosion
BOF	Basic oxygen furnace
BoP	Balance of plant
BP0	Initial burst pressure
BPM	Bipolar Membrane
BPP	Bipolar plates
BVE	Butler-Volmer equation
CAES	Compressed air energy storage
CAPEX	Capital expenditure
CB	Conduction band
CC	Carbon cloth
CCGT	Combined-cycle gas turbine
CCM	Catalyst-coated membrane
CCS	Carbon capture and storage
CCUS	Carbon capture, utilization, and storage
CCU	Carbon capture utilization
CD	Double-layer capacitance
CEA	Atomic Energy Commission
CER	Chlorine evolution reaction
CETS	Chemical energy transmission system
CFD	Computational fluid dynamics
CFP	Carbon fiber paper
CFY	Cr5FeY
CGA	Compressed Gas Association
CGO	Gadolinium-doped cerium oxide
CHP	Combined heat and power
CIGS	CuIn1–xGaxSe2
CL	Catalyst layer
CMSM	Carbon molecular sieve membranes
CNF	Carbon nanofibers
CNG	Compressed natural gas
CNRS	Centre national de la recherche scientifique
CNS	Carbon nanosheets
CNTs	Carbon nanotubes
COD	Chemical oxygen demand
Co-P@PC	Cobalt phosphides confined in porous P-doped carbon matrix
CQDs	Carbon quantum dots
CSA	Canadian standard association
CSC	Cathode-supported cell
CSR	Catalytic steam reforming
CTC	Coal to chemicals
CTL	Coal to liquids
CV	Cyclic voltammetric

CVD	Chemical vapor deposition
DBT	Dibenzyltoluene
DC	Direct current
DDT	Deflagration to detonation
DEA	Diethanolamine
DFT	Density functional theory
DGA	diglycolamine
DGH	Hydrogen adsorption
DI	Deionized
DIFFER	Dutch Institute for Fundamental Energy Research
DIPA	Diisopropanolamine
DMC	Methanol and dimethyl-carbonate
DMFC	Direct methanol fuel cell
DOE	Department of Energy
DOS	Surface-state-density
DR	Defect-rich
DRI	Direct reduced iron
DVB	Divinylbenzene
EAF	Electric arc furnace
ECERS	Enhanced cryogen exergy recovery system
ECPB	Electron-coupled-proton buffer
ECSA	Electrochemically active surface area
ED	Electrodialysis
EDI	Electrodeionization
EDL	Electrical double layer
EDTA	Ethylenediaminetetraacetic acid
EF	Fermi level
EGH	Partially exfoliated graphite
EHPM	Electrochemical hydrogen-pumping membranes
EIS	Electrochemical impedance spectroscopy
EL	Electrolysis
EMF	Electromotive force
EOI	Electrochemical oxidation index
EOR	Enhanced oil recovery
EPA	Environmental Protection Agency
ES	Nitrogen-rich emeraldine salt
ESC	Electrolyte-supported cell
ESR	Ethanol steam reforming
ETA	Event tree analysis
E-TAC	Electrochemical Thermally-Activated Chemical
FCC	Face-centered cubic
FCEV	Fuel cell electric vehicles
FCSHIP	Fuel cell technologies for ships
FDMPO	First d-block metal-based perovskite oxide

FEED	Frontend engineering and design
FFR	Fast frequency response
FeS2/CNTs	cobalt-doped iron disulphide CNTs
FRR	Fluorine release rate
FTO	Fluorine-doped tin oxide
G	Graphene
GA	Graphene aerogel
GCE	General current efficiency
g-C3N4	Graphitic carbon nitride
GDC	Gadolinium-doped ceria
GDL	Gas diffusion layer
GH2	Gaseous hydrogen
GHG	Greenhouse gases
GT-MHR	Gas turbine-modular helium reactor
GTL	Gas to liquid
GTR	Global technical regulation
HCP	Hexagonal close- packed
HD	Hydrogen deuteride
HDPE	High-density polyethylene
HE	Hydrogen embrittlement
HEDE	Hydrogen-enhanced decohesion
HEE	Hydrogen environment embrittlement
HELP	Hydrogen-enhanced localized plasticity
HER	Hydrogen evolution reaction
HESC	Hydrogen energy supply chain
HESIV	H-enhanced deformation-induced vacation
HET	Heterogeneous electron transfer
HFR	High-frequency resistance
HHV	High heating value
HI	Hydrogen iodide
HMF	Hydroxymethylfurfural
HOMO	Hole molecular orbital
HOR	Hydrogen oxidation reaction
HS	Hollow spheres
HSL	Health Safety Laboratory
HT	High temperature
HTE	High-temperature electrolysis
HTGR	High-temperature gas-cooled reactor
HTSE	High-temperature steam electrolysis
HTTR	High-temperature test reactor
HVC	High-value chemical
IA	HySAFE International Association for Hydrogen Safety
ICE	Internal combustion engine
ICMCB	Institut de Chimie de la Matière Condensée de Bordeaux

ICP-MS	Inductively coupled plasma-mass spectrometry
ICP-OES	Inductively coupled plasma-optical emission spectroscopy
IHE	Internal hydrogen embrittlement
IHP	Inner Helmholtz plane
IHL	Inner Helmholtz layer
IHX	Intermediate heat exchanger
IEA	International Energy Agency
IKTS	Institute for Ceramic Technologies and Systems
ILM	Ionic liquid membranes
IMO	International Maritime Organization
IPCE	Incident photon-to-current efficiency
IR	Infra red
IS	Iodine–sulfur
ISO	Organization for Standardization
IUPAC	International Union of Pure and Applied Chemistry
JAEA	Japan Atomic Energy Agency
KFX	Kameleon FireEx
KPIs	Key performance indicators
KSC	Kennedy Space Centre
LCaFN	$La0.6Ca0.4Fe0.8Ni0.2O3-\delta$
LCaNT	$LaxCayNi1-zTizO3$
LCaT-Fe	$La0.43Ca0.37Fe0.06Ti0.94O3$
LCeNT	$La0.8Ce0.1Ni0.4Ti0.6O3$
LCFS	Low-carbon fuel standard
LDHs	Layered double hydroxides
LFL	Lower flammability limit
LH2	Liquid hydrogen
LHV	Lower heating value
LEL	Lower explosion limit
LES	Large Eddy simulations
LFL	Lower flammability limit
LOHCs	Liquid organic hydrogen carriers
LUMO	Lowest unoccupied molecular orbital
Li-Ion	Lithium-ion battery
LL	Liquid liquid
LN_2	Liquid nitrogen
LNCO	$La_2NiO_{4+\delta}$
LNG	Liquefied natural gas
LNO	$La_2NiO_{4+\delta}$
LNO:PrDC	$La_2NiO_{4+\delta}$:Pr-doped ceria
LNT	$LaNiTiO_3$
LO2	Liquid oxygen
LOC	Loss of containment
LOER	Lattice oxygen evolution reaction

LOM	Lattice oxygen mediated mechanism
LOX	Liquid oxygen
LPG	Liquefied petroleum gas
LPNO	$La_2-xPrxNiO_{4+\delta}$
LSC	$La_{0.6}Sr_{0.4}CoO_{3-\delta}$
LSCF	$La_{0.6}Sr_{0.4}Co_{0.2}Fe_{0.8}O_3$
LSCM	$La_{0.75}Sr_{0.25}Cr_{0.5}Mn_{0.5}O_3$
LSGF	$La_{0.6}Sr_{0.4}Ga_{0.3}Fe_{0.7}O_3$
LSGM	Strontium-magnesium doped lanthanum gallate
LSM	Sr-doped lanthanum manganite
LSrNT	$La_{0.52}Sr_{0.28}Ni_{0.06}Ti_{0.94}O_3$
LSV	Linear sweep voltammetry
LTS	Low-temperature shift
LWIR	Long-wavelength infrared
M	Metal cations
MCFC	Molten carbonate fuel cell
MCH	Methylcyclohexane
MCFC	Molten carbonate fuel cell
MEA	Membrane electrode assembly
MEAs	Monoethanolamine
MED	Multiple effect distillation
MDEA	Methyl diethanolamine
MDES	Methyldiethoxysilane
MEA	Membrane electrolyte assembly
MF	Melamine foam
MHx	Metal hydrides
MIEC	Mixed ionic electronic conducting
MMD	Methamidophos
MMS	Mercury-mercury sulfate electrode
MNMCs	Multi-dimensional noble metal-based catalysts
MOF	Metal organic framework
MoS2/CNTs	Molybdenum disulphide supported carbon nanotubes
MSE	Mercury-mercurous sulfate electrode
MSF	Multi-stage flash distillation
MSX	Mid-course space experiment
MTBE	Methyl T-butyl ether
MTG	Methanol to gasoline
MVC	Mechanical vapor compression
MWCNT	Multi-wall carbon nanotubes
NAs	Nanotube array
NASA	National Aeronautics and Space Administration
NC	Nanocubes
NCNFs	N-doped carbon nanofibers
NETL	National Energy Technology Laboratory

NF	Ni foam
NFPA	National Fire Protection Association
NFPGNS	N and F dual-doped porous graphene nanosheets
NG	N-doped graphene
NGNP	Next-generation nuclear plant
NHE	Normal Hydrogen Electrode
Ni$_2$P/CNTs	Nickel phosphide supported CNTs
Ni@NC	Nitrogen-doped graphene
Ni NPs	Ni nanoparticles
NNO	Nd$_2$NiO$_{4+\delta}$
NPG	P-doped graphene
NPM	Non-precious metals
NSs	Nanosheet
NTP	Normal temperature and pressure
NW	Nanowires
NWP	Nominal working pressure
OC	Oxidation cocatalyst
OCV	Open circuit voltage
ODE	Ordinary differential equations
OFR	Oxygen flow rate
OHL	Outer Helmholtz layer
OHP	Outer Helmholtz plane
OER	Oxygen evolution reaction
OLEMS	Online electrochemical mass spectrometry
OPEX	Operating costs
ORR	Oxygen reduction reaction
PAFC	Phosphoric acid fuel cells
PBA	Prussian blue analogue
PBI	Acid-doped polybenzimidazole
PCT	Pressure-composition-temperature
PCGO	Praseodymium, cerium and gadolinium oxide
PCI	Pressure-composition-isotherm
PCT	Pressure-composition-temperature
PEC	Photoelectrochemical
PEFC	Polymer electrolyte fuel cell
PEGDA	Poly(ethylene glycol)diacrylate
PEGMEA	Poly(ethyleneglycol) methyl ether acrylate
PEM	Proton exchange membrane
PEMEL	Polymer exchange membrane electrolysis
PEM-FC	Proton exchange membrane fuel cell
PEMWE	Proton exchange membrane water electrolysis
PEN	Positive electrode-electrolyte negative electrode
PFCs	Perfluorinated compounds
PFSA	Perfluorinated sulfonic acid

PGM	Platinum group metal
PHES	Pumped-hydro energy storage
PILM	Polymerized ionic liquid membrane
PMBR	Pebble-bed modular reactor
PMMA	Polymethyl methacrylate
PMP	Polymer poly-4-methyl-2-pentyne
PNO	$Pr_2NiO_{4+\delta}$
POX	Partial oxidation
PRD	Pressure relief device
PS	Polystyrene
PSA	Pressure swing adsorption
PSS	polystyrene sulfonate
PtG	Power-to-gas
PTL	Porous transport layer
PV	Photovoltaic
PVD	Physical vapor deposition
PVP	Polysulfone-polyvinylpyrrolidone
PWM	Pulse width modulation
PZC	Point of zero charge
QCs	Quantum clusters
QD	Quantum dots
RANS	Reynolds averaged Navier-Stokes
RCS	Regulations, codes, and standards
RDS	Rate determining step
RFB	Redox-flow battery
rGO	Reduced graphene oxide
RH	Relative humidity
RHE	Reversible hydrogen electrode
RRDE	Rotating ring Disk Electrode
RO	Reverse osmosis
rSOEC	Reversible solid oxide electrolyzer cell
SAE	Society of Automotive Engineers International
SCE	Saturated calomel electrode
ScSZ	Scandia-stabilized zirconia
ScCeSZ	Cerium-doped ScSZ
SDC	Samarium-doped ceria
SHE	Standard hydrogen electrode
SMR	Steam methane reforming
SOEC	Solid-oxide electrolysis cell
SOFC	Solid-oxide fuel cell
STH	Solar to hydrogen
STEM	Scanning transmission electron microscopy
SWCNTs	Single-walled carbon nanotubes
SWRO	Seawater reverse osmosis

RDS	Rate determining step
SAGD	Steam assisted gravity drainage
SCN	Thiocyanate
SDC	$(CeO_2)0.8(SmO_{1.5})0.2$
SHE	Standard hydrogen electrode
SEM	Scanning electron microscope
SERP	Sorbent-enhanced reaction process
SLH2	Slush hydrogen
SILMs	Supported IL membranes
SMR	Steam methane reforming
SNG	Synthetic natural gas
SPE	Solid polymer electrolysis
SSF	Selective surface flow
STA	Silicotungstic acid
STP	Standard temperature and pressure
SWE	Sea water electrolysis
TEA	Triethanolamine
TEM	Transition electron microscopy
TEOS	Tetraethylorthosilicate
TFEC	Total final energy consumption
TJs	Tunnel junctions
TM	Transition metal
TMAs	Transition metal alloys
TMBs	Transition metal borides
TMCs	Transition metal carbides
TMD	Transition metal dichalcogenide
TMNs	Transition metal nitrides
TMP	Transition metal phosphide
TMS	Transitional metal sulphide
TNT	Trinitrotoluene
TOC	Total organic carbon
TOF	Turnover frequency
TPAOH	Tetrapropyl ammonium hydroxide
TPB	Three-phase boundary
TPCL	Triple-phase contact line
TPRD	Thermally activated pressure relief device
TRISO	Tri-isotropic
TSA	Temperature swing adsorption
TWSC	Thermochemical water-splitting cycle
UEL	Upper explosion limits
UF	Ultrafine
Ufb	Flat-band potential
UFL	Upper flammable limit
UGS	Underground gas storage

US	United States
UV	Ultraviolet
VB	Valence band
VCE	Vapour cloud explosion
VH	Volmer-Heyrovsky
VHTR	Very high temperature reactor
VIPs	Vacuum insulation panels
VLSFO	Very low sulfur fuel oil
VRHE	Versus the reversible hydrogen electrode
VRE	Variable renewable energy
VT	Volmer-Tafel
WAG	Works-arising gases
WGS	Water-gas-shift
WISE	Wide-field infrared survey explorer
WO_2/C	Tungsten dioxide supported carbon nanowires
XPS	X-ray photoelectron spectroscopy
XTL	Anything to liquid
YDC	Yttrium-doped ceria
YSZ	Yttria-stabilized zirconia
ZEMSHIPS	European fuel cell systems for zero emission ships
ZEV	Zero-emission vehicles

Fundamentals of Water Electrolysis

1 Introduction

In a general electrochemical cell, charge is transferred by the moving ions in a liquid or solid phase and by the movement of electrons in a solid phase. This allows for the acting electrochemical transformations of different species (Xu et al. 2023). The cell is built with two conductive electrodes placed into an ionically conductive electrolyte. Once voltage is applied at the electrodes, oxidative reactions take place at the anode while reducing reaction take place at the cathode (Fig. 1). Anode and cathode are linked by the current flow.

The global current flow is experienced as electrons in the electrodes and ions in the electrolyte. The first big classification of the electrochemical cells is between Galvanic cells and electrolysis cells. In the first ones, spontaneous reactions take place. Electrolysis cells require the electrical energy input. Galvanic cells are batteries or fuel cells. Here, the chemical reactions or transformations are coupled to suitable half-cell reactions to produce a negative free energy change for the overall cell process which can then result in power production via electricity generation. In electrolysis cells, a potential is required to drive the non-spontaneous electrochemical and chemical changes to occur at the electrodes. The rate of charge and ionic flux is directly related to the applied voltage.

Electrolytic processes or electrolyzers are used for a diverse range of applications including synthesis of chemicals and materials, extraction and production of metals, recycling, water purification and effluent treatment, metal and materials finishing and processing, energy storage and power generation and corrosion protection (Sun et al. 2021). Electrolysis is used for production of organic and, notably, inorganic chemicals.

Fig. 1 Electrochemical cell schematic
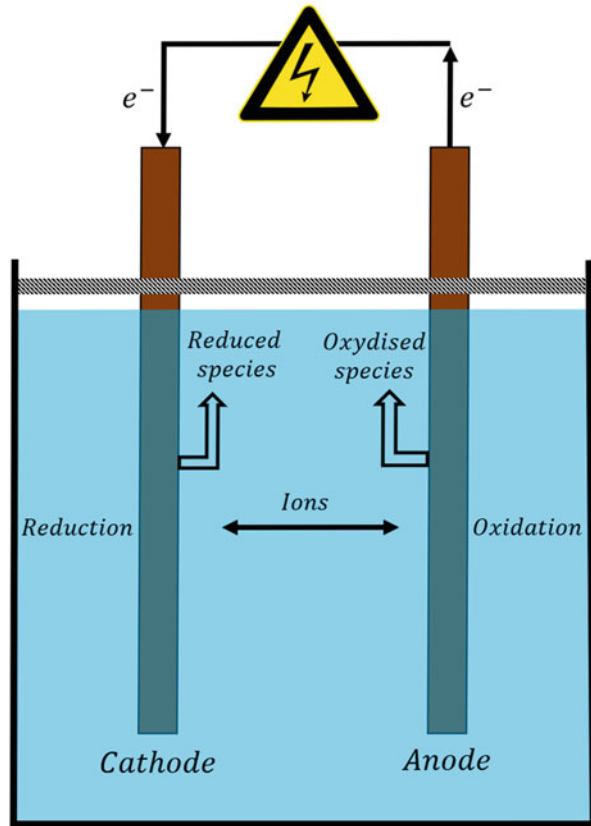
2 Hydrogen Production Through Electrolysis

Electrolysis is employed in many industries such as food, chemical, steel, pharmaceutical and so on to produce hydrogen. It is considered an exceptional way to produce fuel for the future. Water electrolysis is a green and safe system to produce hydrogen even if more than 75% of the costs of hydrogen generation are related to the electricity consumption (Zhao et al. 2023). If powered by renewable energy sources, it is considered the bast way to provide clean chemical energy.

2.1 Water Electrolysis History

Henry Cavendish was the first to identify hydrogen as an element in 1766. He discovered hydrogen by performing experiments with different metals in acidic media. The first apparatus Cavendish employed to collect hydrogen is shown in Fig. 2.
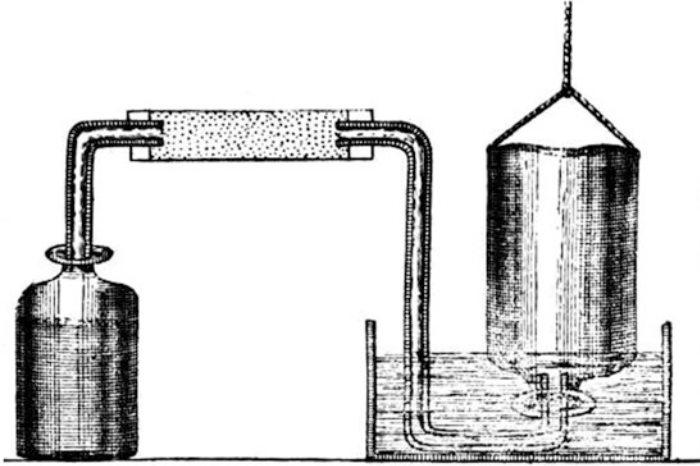
Fig. 2 Cavendish apparatus to collect hydrogen from metal-acid reactions

Water electrolysis was first discovered by the Dutch merchants Jan Rudolph Deiman and Adriaan Paets van Troostwijk in 1789. They employed an electrostatic generator to produce an electrostatic discharge between two gold electrodes immersed in water (Fig. 3).

Later, Johann Wilhelm Ritter developed a system to collect the product gases by employing a Volta's battery (Fig. 4).

The first industrial system to synthesize hydrogen and oxygen from water electrolysis was developed by Dmitry Lachinov in 1888 (Fig. 5).

All these electrolysis cells used to employ alkaline solutions up to the development of proton exchange membrane process by General Electric in the 60's of the last century.

2.2 Water Electrolysis Principles

A typical electrolytic cell consists of the following components: an external power supply; electrolyte solution; anode for the oxidation of water (anodic catalytic layer); and cathode for reduction of water (cathodic catalytic layer).

During water electrolysis, DC current passes through the electrodes when a voltage is applied (Fig. 6).

So water splits into hydrogen and oxygen:

$$H_2O + electric\ current \rightarrow H_2 + \frac{1}{2}O_2$$
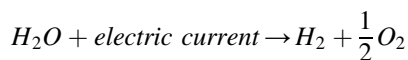
Fig. 3 Electrostatic generator employed for the first water electrolysis

Fig. 4 First system to collect the product gases from water electrolysis
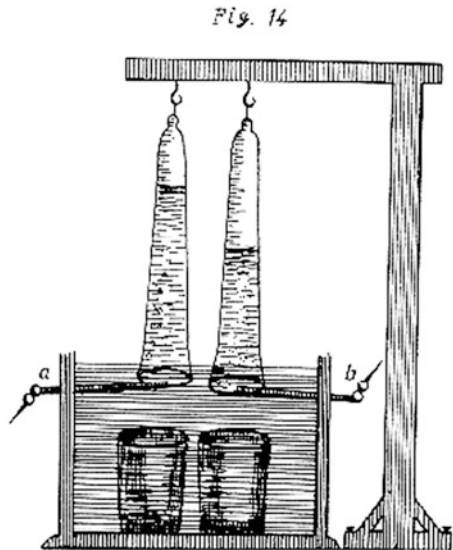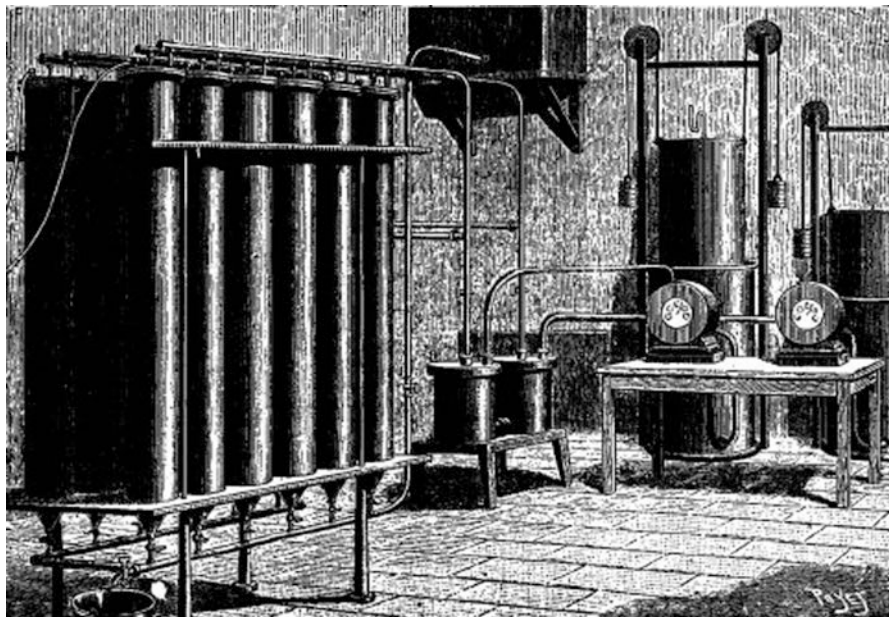
Fig. 5 First industrial water electrolysis cell

Fig. 6 Water electrolysis schematic
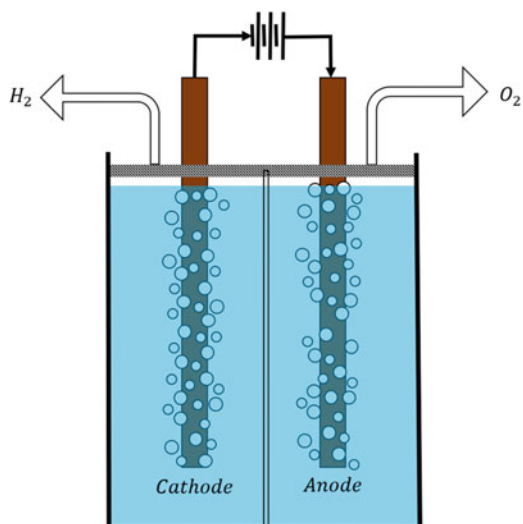
Fig. 7 Schematic pH profile for water electrolysis with neutral bulk electrolyte pH
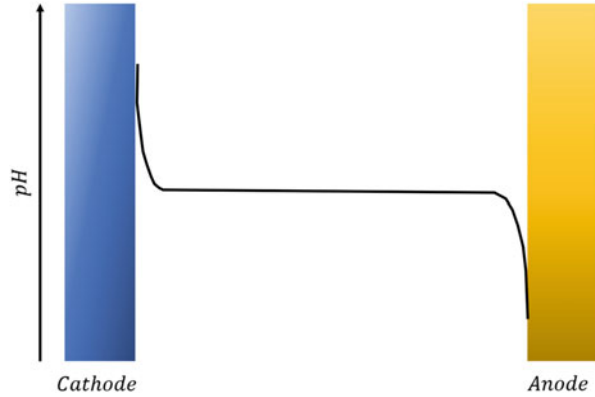
The employed electrolytes can be divided into acidic, alkaline, and neutral (Wei et al. 2023).

In processes where strongly alkaline or acidic conditions are not possible, there will be concentration overpotentials. HER will increase the pH close to the cathode while for example oxygen evolution will decrease the pH close to the anode (Fig. 7).

This will lead to increased concentration overpotentials (Seenivasan and Seo 2023).

The main industrial plants are based on alkaline water electrolysis operating with aqueous electrolytes containing compounds such as KOH at temperatures below 100 °C.

The cells have operating pressures around 30 bar so eliminating the needing for gas compression. During electrolysis also oxygen is produced, in alkaline media the single reactions at the anode and cathode are described by:

$$anode: 2OH^- \rightarrow \frac{1}{2}O_2 + H_2O + 2e^-$$

$$cathode: 2H_2O + 2e^- \rightarrow H_2 + 2OH^-$$
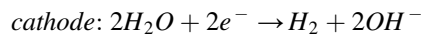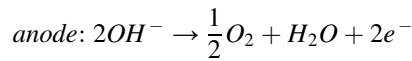
The cells employ a separator to avoid explosive mixtures between the developed gases.

In acidic media the reactions at anode and cathode are described by:

$$anode: H_2O \rightarrow \frac{1}{2}O_2 + 2H^+ + 2e^-$$

$$cathode: 2H^+ + 2e^- \rightarrow H_2.$$
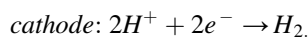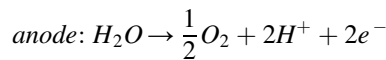
2.3 Electrode Potentials

The reduction potential of any half-cell reaction depends on the reactant chemical activities according to the Nernst equation, such that:

$$E_{red} = E_{red}^{\ominus} - \frac{RT}{zF} \ln \frac{a_{red}}{a_{ox}}$$

where $E_{red}^{\ominus}$ is the standard electrode potential, which is the reduction potential for a reversible electrode at standard conditions, R is the universal gas constant, T is temperature, z is the number of electrons transferred, F is the Faraday constant and a_{red}/a_{ox} is the quotient of the chemical activities of the reduced and oxidized form of the relative species.

Since it is impossible to measure a single electrode potential, $E_{red}^{\ominus}$ is given relative to the standard hydrogen electrode (SHE) reaction:

$$H^+ + e^- \leftrightarrow \frac{1}{2} H_{2(g)}$$
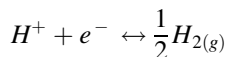
which is defined as 0 V. The SHE comprises a platinum electrode in a theoretical ideal solution of pH 0 with 1 atm. H_2 and where the hydrogen ions behave as an ideal gas with no interactions. Another, more practical standard hydrogen electrode, is the reversible hydrogen electrode (RHE), which also is a platinum electrode in 1 atm. H_2 but instead immersed in the same electrolyte as the WE, so that the pH is equal for both electrodes.

When the pH changes from the standard value, the SHE reverts to RHE. Therefore, the potential of the RHE is dependent on the pH and is a common and practical electrode to present data against, especially from pH dependent reactions such as water splitting. The redox potential of the RHE in 25 °C is defined as $E_{RHE} = 0–0.059pH$ according to Nernst equation, where the natural logarithm instead has been written as the base-10 logarithm.

However, in practice other reference electrodes such as Ag/AgCl are normally used and the measured potential is thereafter converted to the RHE. As an example, the pH dependence of the Ag/AgCl redox potential in 25 °C against RHE is shown in Fig. 8.
and is given by:

$$E_{Ag/AgCl vs.RHE} = 0.222 - 0.0257 \ln a_{Cl} - 0.59pH$$

where a_{ox} is set to unity in Nernst equation for the reactions. Throughout this thesis we have used Ag/AgCl electrodes immersed in 1 M KCl and therefore the second term is zero. The choice of reference electrode is important and do not come without issues, for example ionic leaching and potential drifts. For more accurate results, the RE should be experimentally calibrated against a physical RHE, that is a Pt electrode

Fig. 8 (**a**) Voltammogram showing typical current-voltage characteristics of the water splitting reactions. (**b**) Pourbaix diagram of water showing the reaction potentials at different pH and the potential of an Ag/AgCl electrode in 1 M KCl
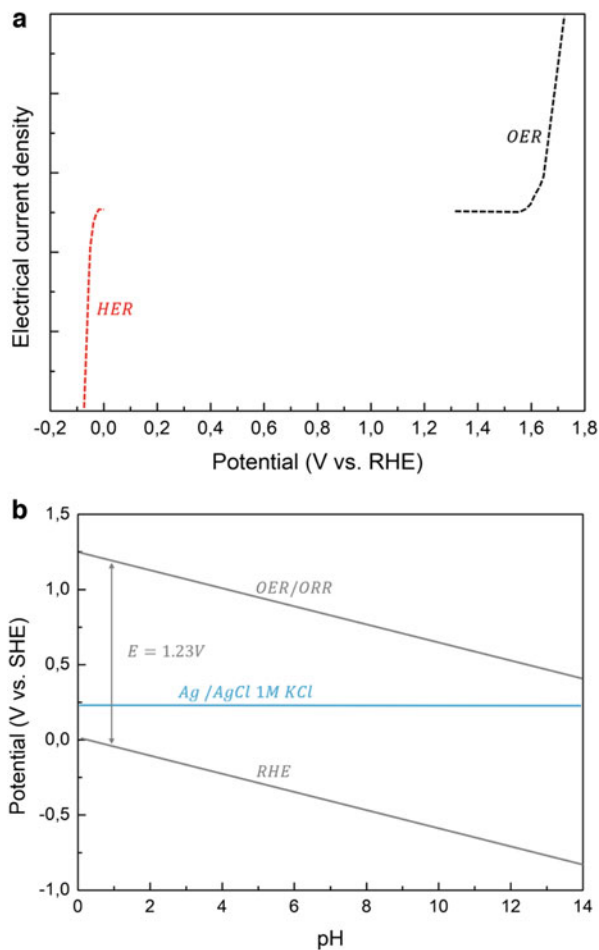
with continuous H_2 bubbling, to avoid any potential miscalculation or incorrectly calculated pH values. Even more optimally, an actual RHE should be used as RE directly since the risk of ionic leaching or potential drift of the RE is then avoided completely.

2.4 Hydrogen and Oxygen Evolution

When the electrodes are connected to an external power supply, they form an electric circuit. The anode electrode in the electrolytic cell device is connected with the positive electrode of the external power supply, and the cathode electrode is connected with the negative electrode of the external power supply. In the working

process, such as the water electrolysis to produce hydrogen and oxygen, the electron flow direction is the negative pole of the external power supply, to the cathode of the electrolytic cell, to the anode of the electrolytic cell, then to the positive pole of the external power supply, while the current flow direction is just the opposite. So the H+ reduction reaction (HER process) takes place on the cathode material of the electrolytic cell to produce H_2, and the O^{2-} oxidation reaction (OER) takes place on the anode material of the electrolytic cell to produce O_2. In order to ensure the working efficiency of the whole electrolytic cell, the electrode materials of the electrolytic cell have the following requirements: own good conductivity for electron transmission and can catalyze the corresponding redox reaction (Hoisang and Sakaushi 2022).

HER is the reaction acting at the cathode during the electrocatalytic decomposition of water. Tafel discovered it in 1905 resuming hydrogen evolution reaction on the metal surface in acidic media as follows:

$$M + H_3O^+ + e^- \rightarrow M - H_{ads} + H_2O \text{ (Volmer reaction)}$$

$$M - H_{ads} + H_3O^+ + e^- \rightarrow M + H_2 + H_2O \text{ (Heyrowsky reaction)}$$

$$M - H_{ads} + M - H_{ads} \rightarrow 2M + H_2 \text{(Tafel reaction)}$$

while in alkaline or neutral medium:

$$M + H_2O + e^- \rightarrow M - H_{ads} + OH^- \text{ (Volmer reaction)}$$

$$M - H_{ads} + H_2O + e^- \rightarrow M + H_2 + OH^- \text{ (Heyrowsky reaction)}$$

$$M - H_{ads} + M - H_{ads} \rightarrow 2M + H_2 \text{(Tafel reaction)}$$
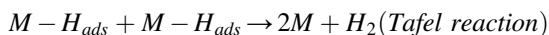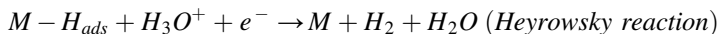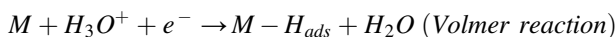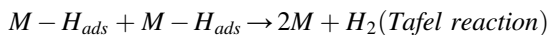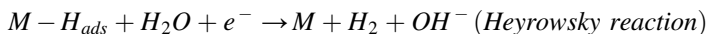
In the above reactions, M is the metallic material of the electrode, H_{ads} is the hydrogen that is adsorbed by the metal M. The Volmer reaction is called the adsorption step of hydrogen, the Heyrovsky reaction is called the electrochemical desorption step, and the Tafel reaction is called the chemical desorption step. The hydrogen evolution reaction is a typical catalytic two-electron transfer reaction of intermediates. Thanks to the drive of the applied potential, the electrode gains active H_{ads} from the electrolyte. Then, the adsorbed atoms combine to generate hydrogen through a desorption process. As observed by the analyses of the previous equations, different reaction mechanisms and paths take place in different electrolytic media, anyway HER evolves through three basic steps:

(a) Volmer reaction: the process is the electron transfer process, also known as the electrochemical process. Generally, in an acidic electrolyte, H^+ obtains an electron to H_{ads}. In alkaline electrolyte, H_2O can become an electronic OH^- and a H_{ads} process, it can be easily seen in acidic electrolyte; the Volmer reaction does not need to overcome the breakdown energy barrier of water molecules. Therefore, compared with the alkaline electrolyte, HER process are more likely to happen under the acidic condition.

(b) Heyrowsky reaction: known as the electrochemical desorption process. It is a process in which the protons generated by H^+ or H_2O electrolysis of H_{ads} and an electrolyte get an electron to form the H_2-molecule, and then desorption precipitation.

(c) Tafel reaction: known as the complex desorption process, is simply described as the conversion of $2H_{ads}$ to H_2 in both basic and acidic electrolytes.

A complete HER process includes an electrochemical process and one-step desorption process, so electrocatalysis of HER is often described as a Volmer-Heyrovsky or Volmer-Tafel mechanism. These three reaction steps may be the decisive process of a HER reaction, and the dynamic process of the reaction is generally determined by the Tafel slope of a HER polarization curve (Wan et al. 2022).

The slow discharge theory is based on the observation that the electrochemical reaction step (Volmer reaction) is the decisive step. Electrochemical desorption theory is based on the observation that the electrochemical desorption step (Heyrovsky reaction) is the decisive one. Following to a blending theory, the decisive step is the complex desorption step (Heyrovsky-Tafel reaction).

A deeper analysis leads to the conclusion that in the hydrogen evolution reaction, the reacting particles are first adsorbed on the catalyst surface by a certain force to form the reaction intermediate (M-H_{ads}), and then the bonds of M-H_{ads} are broken to form H_2. Therefore, the free energy ΔG_H of hydrogen adsorption is decisive for the overall rate of a hydrogen evolution reaction. Obviously, the adsorption capacity of the electrode is directly related to the action of the catalysts. In the case of weak adsorption, the Volmer reaction is inhibited, so, the rate controlling step is the Volmer itself. In the case of strong action of catalysts to break the M-H_{ads} bonds to form H_2, the desorption process of the reaction (Heyrovsky-Tafel) would become a decisive process. Therefore, for a hydrogen evolution catalyst, it is generally believed that the free energy $\Delta G_H \approx 0$ of hydrogen adsorption on the catalyst surface is the best.

Another important factor is represented by the current density driving the catalytic activity; as a matter of fact, the HER exchange current density as a function of the free energy of adsorbed hydrogen is shown in Fig. 9.

This diagram describes the catalytic activity of different metals known as Sabatier principle, that can be used to quantitatively describe the catalytic nature of catalysts, which is one of the important tools for the design and screening of HER catalysts.

OER is a process depending on many parameters such as the composition, the crystal structure, the surface properties and the shape of the employed material. It is accepted that the reaction mechanism is a four-electron transfer process, which requires a four-step redox reaction to produce O_2. For this reason, OER tends to be slower with respect to HER; so, it is the limiting aspect determining the overall performance of the electrolytic device. As a matter of fact, anode requires overpotential with respect to the cathode for the development of whole water electrolysis.

Fig. 9 Current density as a function of free energy for different catalysts during HER
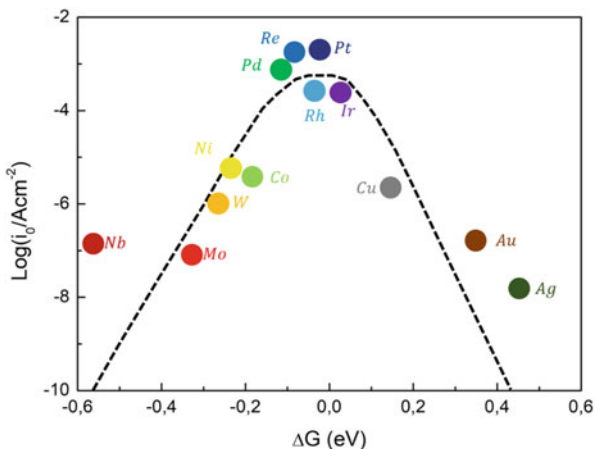
Given the four-electron behavior, OER is more complex with respect to HER. OER mechanisms are also different on different catalysts employed in the cell.

The main accepted oxygen evolution reactions in acidic media are:

$$M + H_2O \rightarrow M - OH_{ads} + H^+ + e^-$$

$$M - OH_{ads} \rightarrow M - O_{ads} + H^+ + e^-$$

$$M - OH_{ads} + M - OH_{ads} \rightarrow M - O_{ads} + M + H_2O$$

$$M - O_{ads} + M - O_{ads} \rightarrow 2M + O_2$$
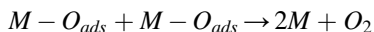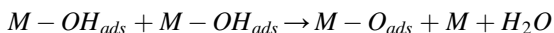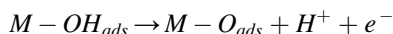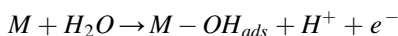
M is the catalytic activity site, the first two equations and the last one as well as the first equation and the last two act in parallel for the oxygen precipitation. In acidic media precious metals are employed as catalysts (Ir, Ru and their oxides) being other metals unsuitable because of rapid corrosion processes.

In alkaline or neutral media, the reactions evolution follows:

$$M + OH^- \rightarrow M - OH_{ads} + e^-$$

$$M - OH_{ads} + OH^- \rightarrow M - O_{ads} + H_2O + e^-$$

$$M - O_{ads} + M - O_{ads} \rightarrow 2M + O_2$$

$$M - OH_{ads} + 2OH^- \rightarrow M - OOH_{ads} + H_2O + e^-$$

$$M - OOH_{ads} + OH^- \rightarrow M + O_2 + H_2O + e^+$$
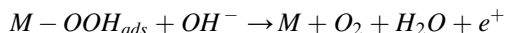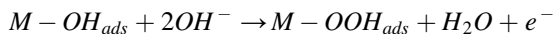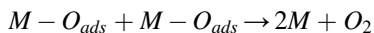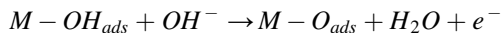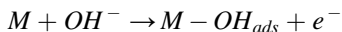
The main difference with respect to acidic media is represented by the adsorption of hydroxide ions. The OH group formed on the catalyst surface forms the adsorbed oxygen anion under the deprotonization of another OH^-, and further discharges to

form oxygen atoms. Alternatively, the last two equations show that the M-OH bond breaks with OH− to form peroxides, which then decompose to produce oxygen. The charge transfer step in the above reaction is the decisive velocity step, but the decisive velocity step is different for different materials and different reaction conditions, which can be identified according to the size of the Tafel slope. Scientists have developed a variety of high efficiency and stable OER electrocatalysts for the replacement of noble metal materials, such as transition metal oxides, perovskite materials, carbon-based non-metallic materials, etc. Among them, perovskite is a widely used OER electrocatalyst due to its complex and controllable electronic structure (Cavaliere 2022).

3   Theoretical Fundamentals

The Sabatier principle says that the interaction between a catalyst surface and reaction intermediates should be neither too strong nor too weak (Cai et al. 2023). If the interaction is too strong, the products will not desorb from the surface of the catalyst and consequently will prevent it from continuing to catalyze the reaction. In contrast, if the interaction is too weak, the reactants cannot be activated at the surface, and therefore, no reaction will occur. To fulfil these requirements, the binding energy between the catalytic surface sites and reactants/intermediates/products should be optimized.

The original Sabatier principle, which can be traced back to 1911, is a purely qualitative principle. Following nearly 50 years of development afterwards, a quantification through so-called 'volcano plots' has been established. A combination of the Sabatier principle and the Brønsted catalysis equation, demonstrating the relationship between thermodynamics and kinetics, permits the construction of these volcano plots (Gebremariam et al. 2022). The volcano plots were proposed by Balandin, among the others, in 1969 in a perspective review and successfully highlighted by Trasatti in 1972 for electrocatalysis. In these plots, a quantity, reflecting the reaction kinetics, is plotted against a property correlated with the stability of the intermediates. The former can be the potential, current or temperature at the beginning or during the reaction; the latter can be the heat of adsorption of a reactant or the formation energy of a product or reaction intermediates. The shape of these plots, resembling a volcano, is usually triangular with a single peak; and the optimally achievable binding energy is located at its apex.

As an example, Fig. 10 depicts a volcano plot for the HER on several metal surfaces.

In this plot, the theoretical binding energy of hydrogen on the metal surfaces (ΔE_H) is selected as the x-axis since, according to the reaction mechanism, the intermediates of HER, particularly in acidic electrolytes, are only hydrogen atoms adsorbed on the surface. In terms of the y-axis, the exchange current density of the HER is used. At low values of ΔE_H, the reaction is slow as it is hindered by the excessively strong binding of adsorbed hydrogen resulting in a low exchange current

Fig. 10 A 'volcano plot' describing the HER activity trends for different metal surfaces as a function of their theoretical binding energies to the hydrogen reaction intermediates. The catalysts located on the left-hand side exhibit relatively strong binding energies. The ones located on the right-hand side exhibit relatively weak binding energies
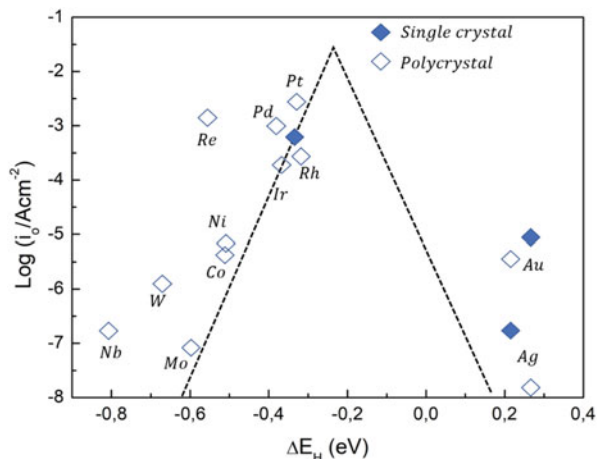
density. In contrast, at high values of $\Delta E H$, the reaction is restricted due to the slow rate of hydrogen adsorption. Therefore, a maximum HER activity should be found at an intermediate value of $\Delta E H$, with rapid rates of hydrogen desorption as well as hydrogen adsorption.

The Sabatier principle, together with its quantification using the 'volcano plots', has proven itself vital in predicting and explaining the catalytic properties as well as guiding new catalyst designs with the help of theoretical calculations such as density functional theory (DFT) calculations.

3.1 Basics of Catalyst Reactions

Electrocatalysis can be described as the study of catalysing reactions taking place at the interface between an electrode and an electrolyte (Hota et al. 2023). Already from this general and simple description it is evident that the field is highly inter-disciplinary and so one must be familiar with both surface science and physical chemistry. The goal of electrocatalysis is to optimize the rate of electrochemical reactions by a careful choice of electrode material. In water electrolysis, the electro-chemical generation of hydrogen and oxygen occurs at such electrodes and their catalytic properties directly affect the efficiency of the process. This chapter serves as an introduction to the catalysis of water electrolysis. Special attention will be given to the oxygen evolution reaction and the development of finding catalysts for that reaction until now.

Before describing the field of electrocatalysis, it is useful to have a definition of a catalyst. A catalyst increases the rate of a chemical reaction by providing a surface where the reactants can bind and react to form products with a lower energy barrier or activation energy. This phenomenon is illustrated in Fig. 11, where "red-black"
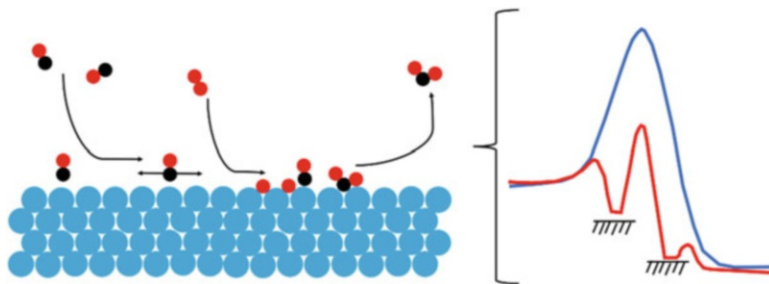
Fig. 11 A cartoon depicting how catalysis works. The blue surface works to facilitate binding of reactants and intermediates, which can then break and form bonds. The overall energy barrier for the reaction can be lowered using such catalytic surfaces. Notice that this simple explanatory figure is not appropriate for electrocatalysis, where the reactions can only proceed on electrode surfaces. However, the nature of the surface interaction is equally important

and "red-red" reacts to form "red-red-black". In gas or liquid phase, the reaction proceeds slowly due to a high energy barrier despite the fact that the product has a lower free energy. This is shown in the diagram to the right in Fig. 11 as the blue curve.

The slow rate is due to a short-lived transition state that has a low probability of being formed. If, however, the reactants bind to a suitable catalytic surface, intermediates are stabilized and can react with lower energy barriers, shown as the red curve.

As a result, the reaction can proceed at faster rates or the same rate can be achieved with less energy input. Thermal catalysis provides an intuitive example where the energy input is temperature (Wang et al. 2021). A new catalyst that decreases the operating temperature can make a chemical process much cheaper and a chemical plant (more) profitable. This simple explanation highlights the importance of catalysts and gives an impression of how they work. It is the binding of reactants, intermediates and products to the catalyst surface that lowers the energy barriers. However, any given surface that binds these species is not necessarily a good catalyst. In fact, it is crucial that the binding is balanced (Iqbal et al. 2023).

If the interaction is too weak reactants will not bind to the surface and no reaction takes place. If the interaction is too strong either reactants or products block the catalyst surface, causing little or no reaction to proceed. This concept has been demonstrated for many reactions with catalysts for electrochemical hydrogen evolution. Actually, the energy of hydrogen adsorption is used as descriptor and the activity has a clear optimum.

It is demonstrated that i_0, exchange current density used to indicate catalyst activity, should be maximized when the heat of formation for hydrogen on a catalyst surface is zero. The hydrogen adsorption energy is a reasonably good descriptor even though some of the surfaces in the study oxidize under reaction conditions. It also turns out that platinum is the best catalyst. Plots of catalyst activity as a function

of one or more descriptors are also called a volcano plots. In the field of catalysis volcano shaped activity plots are used extensively and identifying a suitable descriptor for a reaction can be seen as the first step towards solid understanding and design principles.

3.2 The Electrochemical Interface and the Electric Double Layer

The electric double layer appears at the surface of an electrode when the electrode is immersed into an electrolyte (Wang et al. 2022). The 'electric charges' in the electrode and the 'ionic charges' in the electrolyte rearrange close to the interface when a potential is applied. Specifically in the electrolyte, an excess of ionic charges will form in the vicinity of the electrode surface; and the structure formed by these oriented dipoles and charged species can be seen as two parallel layers, although the boundaries are rather loose, as shown in Fig. 12.
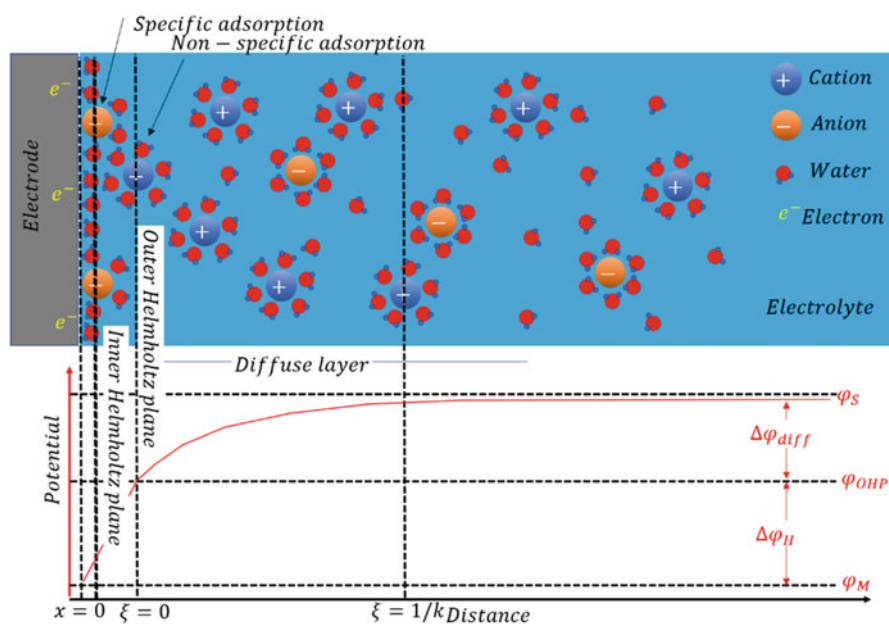
Fig. 12 Model of the electrical double layer. A negatively charged electrode in an aqueous electrolyte is used as an example. The plot reveals the corresponding potential distribution, in which $\Delta\varphi H$ and $\Delta\varphi diff$ are potential drops in the Helmholtz layer and the diffuse layer, respectively

The layer closest to the electrode, which is generally referred to as the Helmholtz layer or Stern layer, is comprised of solvent molecules and occasionally specifically adsorbed species.

The electric centers of the specifically adsorbed ions and the nearest non-specifically adsorbed ions are referred to as the 'inner Helmholtz plane' (IHP) and the 'outer Helmholtz plane' (OHP), respectively (Doan et al. 2021). The non-specifically adsorbed ions, driven only by long-range electrostatic forces, form the second layer, generally referred to as the diffuse layer, which extends from the OHP to the bulk electrolyte due to thermal agitation.

The current understanding of the electric double layer is based on the contributions of several generations of scientists. In 1853, Helmholtz58 initially proposed the electric double layer model, in which, one layer is the polarized electrode surface and the other one is the layer of counterions closely adhering to the charged electrode surface. This early model laid the foundations for understanding of the electrochemical interface, although it was not comprehensive as it did not consider the thermal motion that causes ions to leave the layer of counterions. In the first decade of the twentieth century, Gouy and Chapman considered the effect of thermal motion on the ions near the surface and introduced a diffuse model of the electrical double layer. In this model, they assumed excess ionic charges distributed as a function of the distance from the electrode surface, ignoring the inner Helmholtz layer. In 1924, Stern proposed the currently most recognized model, combining the Helmholtz electric double layer model with the diffuse model. In Stern's representation, some ions follow the proposition from Helmholtz and form an internal Stern layer adhering to the electrode while some form a diffuse layer, as Gouy-Chapman proposed. Since the 1950s, the model was further modified by Grahame, Bockris, Devanathan, and Müller.

At present, the well-recognized double layer model is comprised of three regions, namely the inner-Helmholtz plane, the outer-Helmholtz plane, and the diffuse layer . In the region of $0 \ll x \ll a/2$ (where x is the distance from the electrode surface and a is the diameter of the solvated counter-ion in the electrolyte), a water dipole layer with the so-called specifically adsorbed species, which lose to a certain aspect their solvation shells, is directly attached to the electrode surface and predominantly constitutes the inner-Helmholtz region. The outer-Helmholtz region is comprised of non-specifically adsorbed species which retain their full solvation shell. About $x \gg a/2$, the diffuse layer extends from the outer-Helmholtz plane to the bulk electrolyte.

In the region of $\mathbf{0 \ll x \ll a/2}$, namely the Helmholtz region, according to the Poisson equation, the relationship between the space-charge density and the potential can be written as (for a one-dimensional problem):

$$\frac{d^2 \varphi(x)}{dx^2} = -\frac{\rho}{\varepsilon_r \varepsilon_0}$$

where x is the direction vertical to the electrode surface, $\varphi(x)$ is the corresponding potential and ρ is the space-charge density.

Applying no potential and treating these ions as point charges, we can assume the charge density between the electrode and the Helmholtz plane to approach zero. Hence:

$$\frac{d^2\varphi(x)}{dx^2} = 0$$

Integrating this formula, we can get the following equation:

$$\frac{d\varphi(x)}{dx} = constant$$

With the boundary conditions, $x = 0$, $\varphi(0) = \varphi M$; $x = a/2$, $\varphi(a/2) = \varphi OHP$; the potential is written as:

$$\varphi(x) = \varphi_M - \frac{2[\varphi_M - \varphi_{OHP}]x}{a}$$

where φM is the potential of the electrode, φOHP the potential at the outer-Helmholtz plane.

The integral capacitance of the interface can be calculated from the following expression:

$$C = \frac{\varepsilon_r \varepsilon_0 A}{l}$$

where l is the distance separating the plates, A is the surface area of the plates, $\varepsilon 0$ is the vacuum permittivity, and εr is the relative permittivity. Based on experimental results, this capacitance should consist of two parts: the water dipole layer and the adsorbed ions. Thus, ignoring the surface area, the capacitance of the Helmholtz layer, CH, can be given by:

$$\frac{1}{C_H} = \frac{1}{C_{dipole}} + \frac{1}{C_{IHP} - C_{OHP}} = \frac{a_{H_2O}}{\varepsilon_{dipole}\varepsilon_0} + \frac{a_{ion}}{2\varepsilon_{IHP-OHP}\varepsilon_0}$$

where a_{H2O} and a_{ion} are the diameter of the water molecule and the largest solvated ion, respectively.

Moreover, the capacitance in the Helmholtz region is, in fact, primarily determined by the water molecules, as the effect of the ionic diameter is found to be rather limited.

It should be noted, however, that this formula does not clearly demonstrate the influence of the electrode materials and the structure of the electrode surface.

In the region of $x \gg a/2$, according to the Gouy-Chapman model, the diffuse region can be described by Boltzmann statistics. In this model, all ions in the

electrolyte are assumed to be point charges and influenced by both electric attraction and thermal motion. To simplify the following discussion, a new variable ξ is used to replace the distance x, where $\xi = x - a/2$. Then, the potential in the diffuse region can be rewritten as:

$$\varphi(x) = \varphi_S - \varphi(\xi)$$

where φs is the potential of the electrolyte and $\varphi(\xi)$ is the potential at the distance ξ.

According to the linearized Poisson-Boltzmann equation, the relationship between the space-charge density and the potential can be written as:

$$\frac{d^2\varphi(x)}{dx^2} = k^2[\varphi_S - \varphi(\xi)]$$

which solves to give:

$$\varphi_S - \varphi(\xi) = constant\ e^{-k\xi}$$

Combined with the boundary conditions, $\varphi_S - \varphi(\xi) = \varphi_S - \varphi_{OHP}$ when $\xi = 0$, thus becomes:

$$\varphi_S - \varphi(\xi) = [\varphi_S - \varphi_{OHP}]e^{-k\xi} = \Delta\varphi_{diff}e^{-k\xi}$$

where $\Delta\varphi_{diff}$ is the potential drop across the diffuse region, generally known as zeta-potential. When the distance from the outer Helmholtz layer, ξ, is equal to $k-1$, the potential drops to a value $1/e$ of $\Delta\varphi_{diff}$. This distance $k-1$ is normally taken as the length of the diffuse layer and referred to as Debye-length.

The capacitance of the diffuse layer can be given as:

$$C_{diff} = k\varepsilon_r\varepsilon_0$$

From this formula, the capacitance of the diffuse layer is closely associated with the electrolyte. The whole electric double layer, $\mathbf{0} \ll x \ll \mathbf{k-1}$, can be seen as the Helmholtz region and the diffuse layer connected in series.

The potential drop across the whole double layer region, $\Delta\varphi$, can be outlined as:

$$\Delta\varphi = [\varphi_{OHP} - \varphi_M] + [\varphi_S - \varphi_{OHP}]e^{-1} = \Delta\varphi_H + \frac{\Delta\varphi_{diff}}{e}$$

where $\Delta\varphi_H$ and $\Delta\varphi_{diff}/e$ are the potential drops in the Helmholtz region and the diffuse layer, respectively.

The capacitance of the whole double layer region, CD, can be summarized as:

$$\frac{1}{C_D} = \frac{1}{C_H} + \frac{1}{C_{diff}} = \frac{a_{H_2O}}{\varepsilon_{dipole}\varepsilon_0} + \frac{a_{ion}}{2\varepsilon_{IHP-OHP}\varepsilon_0} + \frac{1}{k\varepsilon_r\varepsilon_0}$$

where C_H and C_{diff} are the capacitances of the Helmholtz region and the diffuse layer, respectively.

In concentrated solutions, according to this expression, the capacitance C_D predominantly depends on C_H since C_{diff} is several orders of magnitude higher. In dilute solutions, on the other hand, the capacitance C_{diff} must be considered, as k decreases and C_{diff} becomes increasingly significant in this expression for CD.

The electric double layer plays an integral role in the functionality of numerous innovative energy systems, ranging from batteries to supercapacitors and from electrolyzers to fuel cells. However, further investigation is required as there are still various unsolved questions such as the question of the EDL structure in various systems.

3.3 Catalytic Active Sites

In electrocatalysis, active sites are an array of sites or a region in the catalyst surface that primarily determine the performance of the catalyst (Wang et al. 2023). According to the Sabatier principle, the interaction between reaction intermediates and catalysts should be optimal for the best performance. However, intermediates usually bind differently to various types of sites on the catalyst surface. Thus, the electrocatalytic performance of different surface sites can vary considerably. This inspired the principle of active sites. Langmuir was the first to affirm that, for authentic catalyst surfaces, the assumption that all sites are energetically identical and non-interacting was an unacceptable approximation. Consequently, he proposed the original model to describe the chemisorption of different surface sites. In this model, he assumed that an array of sites would control the activity, and the typical Langmuir adsorption isotherm was obtained. This model provided the first surface science approach in heterogeneous catalysis.

Subsequently, Taylor emphasized the heterogeneity of surface sites and the corresponding effects. Taylor recognized that '...there will be all extremes between the case in which all atoms in the surface are active and that in which relatively few are so active'; and non-equivalent sites can generate different activities due to the local environmental heterogeneity of surface atoms. This heterogeneity originates from both varied coordination numbers of surface atoms and different surface or bulk compositions. Terraces, edges, corners, ledges, vacancies, and kinks on the surface can all cause a variation of coordination numbers of surface atoms (Taylor 1925). In terms of catalysts with multiple components, it is apparent that the surface composition would differ from that of the bulk catalyst as well as between each crystal facet. This heterogeneity has a significant effect on the catalyst performance,

Fig. 13 The ORR activities of various stepped single crystalline surfaces and metal alloy catalysts. (**a**) Relative ORR activities of Pt and Pt alloy stepped single crystal electrodes at 0.9 VRHE in 0.1 M HClO4, as compared to Pt(111). Stepped single crystals with different atomic widths of the (111) terraces were characterised. (**b**) ORR activities of various Pt alloy catalysts at 0.9 VRHE relative to the corresponding Pt catalyst. The activities were plotted against the empirical radius of the solute metal
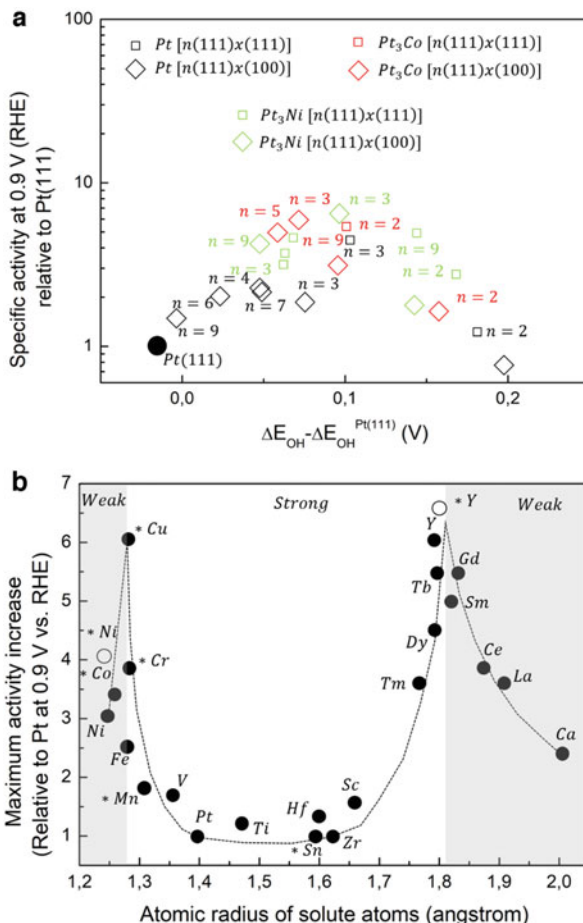
as has been confirmed by surface science studies on samples such as stepped single crystalline surfaces (Fig. 13a) and various metal alloy catalysts (Fig. 13b).

According to the statement of active sites in the Taylor's principle and experimental kinetic measurements, electrochemical reactions are divided into two categories depending on whether a specific surface structure is necessary to promote the reaction.

1. Structure-sensitive reactions. For these reactions, the adsorption of the intermediates/reactants and/or the following process predominantly occur on specific sites of the surface. Accordingly, it can be observed that there are always strong interactions between the reaction intermediates and the catalyst surface in this type of reactions.

2. Structure-insensitive reactions. In those reactions, all sites on the surface apparently exhibit similar activities. About some of these reactions, the surface even adapts itself to the reaction conditions, as Taylor stated: 'The amount of surface which is catalytically active is determined by the reaction catalyzed'. In this case, the interactions between intermediates and the catalyst surface are relatively weak.

The present study on active sites is important for deeper fundamental understanding of electrocatalysis and the design of new electrocatalysts. However, in-depth study requires more advanced research techniques, as identification of active centers requires in-situ experiments under the working conditions of catalytic systems.

3.4 Electrocatalytic Reactions in Energy Conversion and Storage

Water splitting, usually referred to as water electrolysis, is an electrochemical reaction that decomposes H_2O into O_2 and H_2. It is normally driven by a direct electric current (Tao et al. 2022). The corresponding reactions occurring at the cathode and anode are referred to as the hydrogen evolution reaction, HER, and oxygen evolution reaction, OER, respectively.

Generally, electrolytes are substances that conduct ions. When an electric field, E, is applied, the ions in the electrolyte experience electric field force, F_E:

$$F_E = ze_0E$$

where e_0 is the elementary charge, and z is the charge of the ion. The ions in the electrolyte move due to the electric field force, and this motion subsequently leads to an ionic electrical current flowing through the electrolyte.

Electrodes are electronic conductors used for exchanging electrons or ions with the non-metallic aspect, for example, a vacuum or air, an electrolyte or a semiconductor.

The electrodes can be metals or semiconductors. The electrodes responsible for transferring electrons from electrolyte species to external circuits are usually referred to as anodes, whilst those responsible for delivering electrons to the electrolyte species are usually referred to as cathodes.

Typical energy conversion or storage systems, such as electrolyzers and galvanic cells, are comprised of electrodes and electrolytes. For the electrolyzer system, when an electric field is applied, cations migrate towards the cathodes and anions towards the anodes; when the applied potential exceeds a specific value (namely the decomposition potential, φ_0), some cations will receive electrons from the cathodes and become reduced, and some anions will lose electrons at the anodes and become oxidized. This redox process, driven by a direct current, is referred to as electrolysis. With regard to the galvanic cell, the processes are similar but reversed in relation to the electrolyzer.

As stated, redox reactions in the electrolyzer can only occur when the applied potential, φ_c^{elec}, is higher than the decomposition potential, φ_0. At the potential φ_0, the corresponding free energy change, $\Delta_r G$, can be depicted as:

$$\Delta_r G = nF\varphi_0$$

where n is the number of electrons transferred during the reaction and F is the Faraday constant.

Therefore, the following equations will be established if the electrolyzer is functioning:

When:

$$\varphi_c^{elec} > \varphi_0$$

Then:

$$nF\varphi_c^{elec} - \Delta_r G > 0$$

In terms of a galvanic cell, if the cell is functioning (namely the cell is discharging), the driving voltage of the external system, φ_c^{galv}, is lower than the electromotive force of the cell, φ_0. Thus, the following equations should be established,

When:

$$\varphi_c^{galv} < \varphi_0$$

Then:

$$nF\varphi_c^{galv} - \Delta_r G < 0$$

Under standard conditions, i.e. when concentrations are 1 mol dm^{-3} and the pressure is 1 atm, this potential φ_0 is referred to as the standard electrode potential. About the electrolyzer system, φ_0 is referred to as the decomposition potential (*ED*). In terms of the galvanic cell, φ_0 is equal to the battery electromotive force (*E_0*)/ the electromotive force of the cell (emf).

However, due to the internal resistance of electrochemical systems, the measured decomposition potential is higher than its theoretical value; conversely, the observed electromotive force for galvanic cells is always significantly lower (Fig. 14).

Moreover, with increasing current, the cell potential increases in the electrolyzer system but decreases in the galvanic cell. If only taking the Ohmic drop into consideration, the corresponding relationships between the measured cell potential, *E*, and the current, *i*, can be simply indicated in:

$$E = E_D + iR_i$$

Fig. 14 Cell potential, E, plotted against load current, i. Red and black lines schematically depict the variation of the potentials for electrolyzer systems and galvanic cells, respectively. $E0$ is emf, ED – the decomposition potential, Ri- the internal resistance, Re- the external resistance. When the load current increases, the cell potential will increase in the electrolyzer system and decrease in the galvanic cell
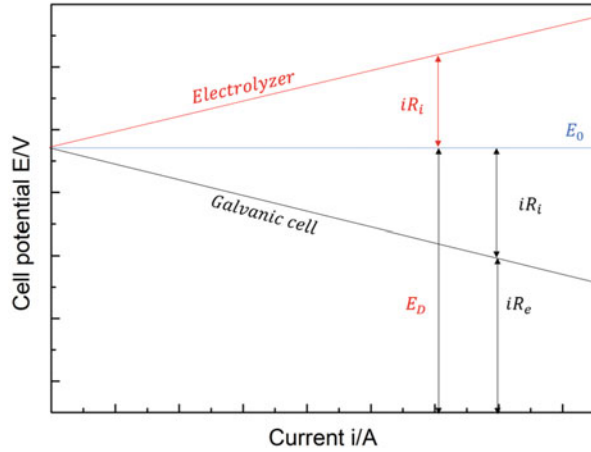
$$E = E_0 - iR_i = iR_e$$

for the electrolyzer system and the galvanic cell, respectively. Where R_i is the internal resistance of electrochemical systems, E_D- the decomposition potential, E_0 – the battery electromotive force, R_e- the external resistance in the electric circuit.

In fact, when a current flows through the cell, causing it to depart from equilibrium, not only will the Ohmic drop affect the cell voltage, but each electrode will display a characteristic current-voltage behavior; therefore, in general, the measured overall cell voltage will be a combination of both these effects.

3.5 Nernst Equation

An electrolyzer can only operate if the applied potential exceeds the decomposition potential. To investigate electrochemical systems, the first step should be to define this potential.

The chemical potential for a component i in a mixture, μ_i, is defined as:

$$\mu_i = \mu_i^{0\perp} + RT\ln a_i$$

where a_i is the activity of component i, $\mu_i^{0\perp}$ is the corresponding chemical potential at unit activity, T – temperature, R – universal gas constant.

Therefore, the total free energy of a mixture of all components can be written as:

$$G = \sum_i n_i \mu_i$$

If a reaction takes place in such a large volume that the fractions of both reactants and products are not considerably changed, the free energy change can be written as:

$$\Delta G_r = \sum_i v_i \mu_i$$

where v_i is the stoichiometric number of component i.

At equilibrium, the free energy change, ΔG_r, must be zero. Thus, the fundamental equation for a chemical reaction at equilibrium can be obtained according to:

$$\sum_i v_i \mu_i = 0$$

In electrochemical systems, materials of two different phases are brought in contact with each other, namely electrode and electrolyte, resulting in a potential difference, φ. If taking this potential difference φ between electrode and electrolyte into account, the free energy change becomes:

$$\Delta G_r = \sum_i v_i(\mu_i + z_i F \varphi) = \sum_i v_i \tilde{\mu}_i$$

The introduced $\tilde{\mu}_i$ is defined as the electrochemical potential, and the potential φ is always referred to as the Galvani potential. At the condition of electrochemical equilibrium, the fundamental reaction equilibrium expression becomes:

$$\sum_i v_i \tilde{\mu}_i = 0$$

Taking the simplest redox reaction as an example, we have:

$$S_{Red} \leftrightarrow S_{Ox} + ne^-$$
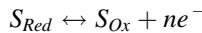
where S_{Red} and S_{Ox} are termed the reduced and oxidized components in the redox reaction, respectively. When this reaction is at equilibrium, namely that the double layer at the electrode interface and the Galvani potential difference stabilize, the following relationship can be achieved:

$$\tilde{\mu}_{Red} \leftrightarrow \tilde{\mu}_{Ox} + n\tilde{\mu}_{e^-}$$
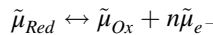
this equation becomes:

$$\mu_{Red}^{0\perp} = RT \ln a_{Red} + nF\varphi_M = \mu_{Ox}^{0\perp} + RT \ln a_{Ox} + nF\varphi_S + n\mu_{e^-}^0$$

Therefore, the Galvani potential difference, $\Delta\varphi$, can be written as:

$$\Delta\varphi = \varphi_M - \varphi_S = \frac{\mu_{Ox}^{0\perp} + n\mu_{e^-}^0 - \mu_{Red}^{0\perp}}{nF} + \frac{RT}{nF} \ln\left(\frac{a_{Ox}}{a_{Red}}\right)$$

$$\Delta\varphi = \Delta\varphi^0 + \frac{RT}{nF} \ln\left(\frac{a_{Ox}}{a_{Red}}\right)$$

where $\Delta\varphi^0$ is the standard Galvani potential difference. In the case that a_{Ox} and a_{Red} are equal, the standard Galvani potential difference is the Galvani potential difference between the electrolyte and the electrode.

For a normal redox reaction on the electrodes as shown in:

$$\sum_{Red} n_{Red} S_{Red} \leftrightarrow \sum_{OX} n_{Ox} S_{Ox} + ne^-$$
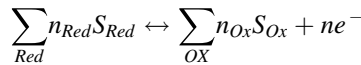
Then:

$$\sum_{Red} n_{Red}\left(\mu_{Red}^{0\perp} + RT \ln a_{Red}^{n_{Red}}\right) + nF\varphi_M = \sum_{Ox} n_{Ox}\left(\mu_{Ox}^{0\perp} + RT \ln a_{Ox}^{n_{Ox}}\right) + nF\varphi_S + n\mu_{e^-}^0$$

Therefore, the generalized Nernst equation can be obtained as:

$$E = E^0 + \frac{RT}{nF} \ln \frac{\prod Ox\, a_{Ox}^{n_{Ox}}}{\prod Red\, a_{Red}^{n_{Red}}}$$

Where:

$$\prod_t a_t^{n_t} = a_{S_1}^{n_1} \cdot a_{S_2}^{n_2} \cdot \ldots \cdot a_{S_i}^{n_i}$$

The Nernst equation relates the potential for an electrochemical reaction with the activities of the species participating in the reaction, the standard electrode potential and the temperature at the situation of electrochemical equilibrium (Lamy and Millet 2020).

Defining the absolute value of the potential appears to be impossible. In other words, $\Delta\varphi$ and $\Delta\varphi^0$ are not experimentally measurable. Therefore, an additional electrode with a constant Galvani potential difference is used as a reference point in the electrochemical systems. This electrode is referred to as the reference electrode, and the corresponding system is named the three-electrode system (with a working electrode, reference electrode and counter electrode). A widely accepted reference electrode is the standard hydrogen electrode (SHE) since this electrode can quickly and reproducibly establish its equilibrium potential and maintain this potential well over time. But in fact, the reversible hydrogen electrode (RHE) is the reference electrode used for experimental measurements because the SHE is closely associated

with the pH of the electrolyte and defined based on an 'ideal' solution. According to the Nernst equation, the relationship between the potentials versus the RHE and the SHE follows the equation:

$$E_{RHE} = E_{SHE} + \ln 10 \cdot \frac{RT}{2F} \log \left[\frac{a_{H_3O^+}^2}{p_{\frac{H_2}{p^0}}} \right]$$

Thus, at 25 °C and unit H_2 partial pressure ($p_{H2} = p^0$),

$$E_{RHE} = E_{SHE} + 0.0591 \cdot pH$$

As there are many reference electrodes to choose from, e.g., saturated calomel electrode (SCE), mercury-mercurous sulfate electrode (MSE) and mercury-mercury sulfate electrode (MMS), the MMS was chosen as the reference electrode for all the measurements in this research. The potential versus the MMS can be linked to that versus the RHE at room temperature through the following equation:

$$E_{RHE} = E_{MMs} + 0.6618 + 0.0591 \cdot pH$$

3.6 Butler-Volmer Equation

The Nernst equation describes the situation of the electrochemical system at equilibrium, but what about non-equilibrium states? In other words, based on the Nernst equation, the relationship between the potential of the reaction and activities of chemical species taking part in the reaction is established, but how does the potential influence the electrical current flowing through electrochemical systems when reactions occur on electrodes. Kinetic considerations are given by the Butler-Volmer equation.

According to the definition, the current density, j, for an electrochemical reaction is given by:

$$j = nFv$$

where v is the reaction rate, n is the number of electrons participating in the reaction, and F is the Faraday constant.

At the situation near the equilibrium, when the mass transfer-influence is so small that can be disregarded, the reaction rate v is given by:

$$v = k \cdot c = k^0 \exp\left(- \frac{\Delta G}{RT}\right) \cdot c$$

Fig. 15 Schematic of the free energy change in a redox reaction when one electron is transferred from the electrode. Only parts of the free energy change are reflected in the free energy change of the activated species
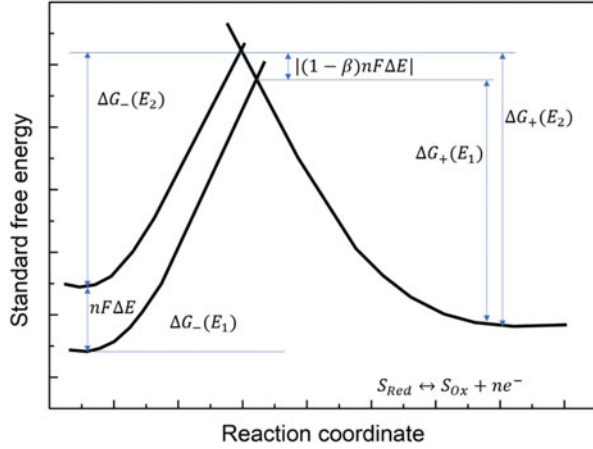
where k is the reaction rate constant, c is the concentration of reactants near the electrode surface. For this situation, the reaction rate constant, k, only depends on the free energy change; the concentration of reactants, c, is constant.

In the simplest case of redox reactions, and Fig. 15, the cathodic current density at the potential E_1, $j^-(E_1)$, is:

$$j^-(E_1) = -nFv_{Red} = -nF_{c_{Ox}}k_0'^- \exp\left[-\frac{\Delta G_-(E_1)}{RT}\right]$$

where c_{Ox} is the concentration of oxidized species. For the situation near the equilibrium, the transfer of the oxidized species from the bulk to the electrode surface is quick enough to keep the concentration c_{Ox} constant. Besides, the negative sign in this equation accounts for electrons flow from the electrode to the solution.

Only parts of the change in the free energy, caused by the potential change, are reflected in the free energy change of the activated species. When the electrode potential is changed from E_1 to E_2, there is no change in the free energies, $\Delta G_+(E)$, which means that not all free energy changes appear for the activated species.56 For simplicity, an asymmetry factor β is introduced, and the corresponding free energy changes on the cathode and anode are indicated in:

$$\Delta G_-(E_2) = \Delta G_-(E_1) + \beta nF \cdot \Delta E$$
$$\Delta G_+(E_2) = \Delta G_+(E_1) - (1-\beta)nF \cdot \Delta E$$

Therefore, on alteration of the electrode potential from $E1$ to $E2$, the current density on the cathode can be written as:

$$j^-(E_2) = -nF_{c_{Ox}}k_0'^- \exp\left[-\frac{\Delta G_-(E_1) + \beta nF \cdot \Delta E}{RT}\right]$$

A reference electrode is needed to measure the electrode potential. Thus, if taking the potential $E1$ as a reference point, i.e., the potential of the reference electrode, the potential change ΔE can be treated as the measured potential, E. Besides, as the reference electrode is independent of factors such as c_{Ox}, the part of $exp[-\Delta G_-(E_1)/RT]$ is constant and can be taken into the reaction rate constant, k_0^-.

The equation for the cathodic current density then becomes:

$$j^-(E) = -nF_{C_{Ox}}k_0'^- \exp\left[-\frac{\beta nF \cdot E}{RT}\right]$$

Like the cathodic current density, the anodic current density can be written as:

$$j^+(E) = +nF_{C_{Red}}k_0'^+ \exp\left[+\frac{(1-\beta)nF \cdot E}{RT}\right]$$

At the equilibrium potential, Er, the net current should be zero, which means:

$$j^-(E) = j^+(E) = j_0 \cdot j_0$$

is referred to as the exchange current density.

$$j^-(E) = j_0 = -nF_{C_{Ox}}k_0^- \exp\left[-\frac{\beta nF \cdot E_r}{RT}\right]$$

$$j^+(E) = j_0 = +nF_{c_{Red}}k_0^+ \exp\left[+\frac{(1-\beta)nF \cdot E_r}{RT}\right]$$

after the rearrangement, the following equation can be written:

$$E_r = \frac{RT}{nF} \ln\left(\frac{k_0^-}{k_0^+}\right) + \frac{RT}{nF} \ln\left(\frac{c_{Ox}}{c_{Red}}\right)0$$

If E_0 is used to replace the first summand, this equation becomes the Nernst equation. But it should be noted that this equation is obtained under the condition that the salt in the electrolytes is excessive. Thus, the activity coefficients of the oxidized or reduced species, a, are likely independent of the corresponding concentration, c.

Additionally, the exchange current density, j_0, can be calculated from:

$$-j_0 = nFk_0^- \left(c_{Red}^\beta c_{Ox}^{1-\beta}\right) \exp\left[-\frac{\beta nF \cdot E_0}{RT}\right]$$

$$+j_0 = nFk_0^+ \left(c_{Red}^\beta c_{Ox}^{1-\beta}\right) \exp\left[-\frac{(1-\beta)nF \cdot E_0}{RT}\right]$$

As the net current is zero, should be equal to:

$$nFk_0^- \exp\left[-\frac{\beta nF \cdot E_0}{RT}\right] = nFk_0^+ \exp\left[-\frac{(1-\beta)nF \cdot E_0}{RT}\right] = nFk_0$$

therefore,

$$j_0 = nFk_0 c_{Red}^{\beta} c_{Ox}^{1-\beta}$$

At the situation near the equilibrium, the actual electrode potential, E, should include not only the equilibrium potential, E_r, but also the overpotential, η. Thereby, the overpotential is the difference between the equilibrium potential and the applied potential required to initiate the electrode reactions. The net current is the algebraic sum of the cathodic and anodic current density:

$$j = j^+ + j^- = j_0\left\{\exp\left[\frac{(1-\beta)nF \cdot \eta}{RT}\right] - \exp\left[-\frac{\beta nF \cdot \eta}{RT}\right]\right\}$$

This is the famous Butler-Volmer equation. But note that this equation is under the condition of relatively low current density; i.e. there is no mass transfer effect. It also does not account for the adsorbate-adsorbate interactions.

At the situation far from the equilibrium, when the mass transfer influence has to be considered, the concentration of the activated species near the electrode surface will differ from the bulk concentration and change with time due to the mass transfer limitations. Therefore, the reaction rate, v, should be modified as:

$$v = k \cdot c(0,t) = k^0 \exp\left(-\frac{\Delta G}{RT}\right) \cdot c(0,t)$$

The more general expression of the Butler-Volmer equation, applicable to the mass transfer-influenced conditions, can be written as:

$$j = j_0\left\{\exp\left[\left(\frac{c_{Red(0,t)}}{c_{Red}}\right)\exp\left[\frac{(1-\beta)nF \cdot \eta}{RT}\right] - \left(\frac{c_{Ox}(0,t)}{c_{Ox}}\right)\exp\left[-\frac{\beta nF \cdot \eta}{RT}\right]\right.\right.$$

3.7 Tafel Equation, Overpotential and Limiting Current Density

Several fundamental concepts related to this work, i.e. Tafel equation, overpotential, and limiting current density, are introduced based on the Butler-Volmer equation.

When there is no mass transfer effect, the overpotential can be written based on Butler-Volmer equation.

Cathodic reactions:

$$\eta_{el} = \frac{RT}{\beta nF} \ln j_0 - \frac{RT}{\beta nF} \ln|j.|$$

Anodic reactions:

$$\eta_{el} = \frac{RT}{(1-\beta)nF} \ln j_0 + \frac{RT}{(1-\beta)nF} \ln |j.|$$

Therefore, the overpotential has the following form:

$$\eta = A + B \ln |j.|$$

This semi-logarithmic equation is the so-called Tafel equation, and B is the Tafel slope. This overpotential is mainly determined by the charge transfer, and thus termed as transfer overpotential, η_{el}.

Under the mass transfer-influenced conditions, the overpotential can be written based on the more general expression of the Butler-Volmer equation.

Cathodic reactions:

$$\eta_{diff} = -\frac{RT}{\beta nF} \ln\left(\frac{c_{Ox}^0}{c_{Ox}^S}\right)$$

Anodic reactions:

$$\eta_{diff} = +\frac{RT}{(1-\beta)nF} \ln\left(\frac{c_{Red}^0}{c_{Red}^S}\right)$$

This diffusion overpotential is clearly caused by the difference in species concentration between the near-electrode-surface and the bulk. The total overpotential, η_{tot}, is then:

$$\eta_{tot} = \eta_{el} + \eta_{diff}$$

If continuing to increase the overpotential (at very high current density), the current is not determined by the charge transfer but totally by diffusion. To simplify the discussion, the one-dimensional case is only considered. According to Fick's first law, the following equation can be written:

$$J_i = -D\left(\frac{\delta c_i}{\delta x}\right)$$

where J_i is the diffusion flux of electroactive species i, c_i is the concentration of electroactive species i, and D is the diffusion constant. The current density then can be written as:

$$j = \sum_i nFJ_i = \sum_i -nFD\left(\frac{\delta c_i}{\delta x}\right)_{x=0} = nFD\frac{c^0 - c^S}{\delta n}$$

where δN is referred to as Nernst diffusion layer thickness, c^0 is the concertation in bulk, and c^s is the concertation at the electrode surface. If assuming that the reaction on the electrode is fast enough to make c^s approach zero, the current density then becomes a limiting time-independent value, which is known as limiting current density, j_{lim}:

$$j_{lim} = nFD\frac{c^0}{\delta n}$$

The corresponding potential range is referred to as the limiting current range. The corresponding diffusion overpotential is also changed. The potential drop caused by the charge transfer is so small that ηel can be neglected. Thereby, η_{diff} can be seen as the potential drop from the bulk of electrolytes to the surface of electrodes at equilibrium. According to the Nernst equation, η_{diff} can be given as:

$$\eta_{diff} = \frac{RT}{nF} \ln \frac{c^S}{c^0}$$

So, the following equation will be obtained:

$$\frac{J}{j_{lim}} = 1 - \frac{c^S}{c^0}$$

And finally:

$$\eta_{diff} = \frac{RT}{nF} \ln\left(1 - \frac{J}{j_{lim}}\right)$$

In a word, at a low overpotential, the reaction kinetics are mainly controlled by the charge transfer; at a medium overpotential, the influence from both the charge transfer and the diffusion should be considered; at a very high overpotential, the reaction is presumably controlled by the diffusion.

3.8 Hydrogen Evolution Reaction

Water electrolysis is the process of decomposition of water into oxygen and hydrogen by applying an electric current. Oxygen and hydrogen can be separately collected at the anode and cathode, where the volume ratio of oxygen to hydrogen is 1:2.

The overall reaction of water electrolysis is:

$$2H_2O_{(l)} \rightarrow 2H_{(g)} + O_{2(g)}$$
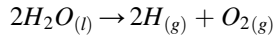
At standard atmospheric pressure and temperature, the equilibrium cell potential is 1.23 V. According to the Nernst equation, this theoretical cell potential is independent of the pH of the electrolyte. Although the theoretical value is just 1.23 V, the typical working potential of commercial electrolyzers is significantly higher, typically 1.8 V to 2 V, due to the unavoidable overpotential (Karthick et al. 2020).

Using proper catalysts is an effective way to reduce the overpotential in water electrolysis, as they can reduce the activation energy for the reaction. The choice of the catalyst determines the cell potential of electrolyzers and the conversion efficiency.

Nevertheless, due to the high energy density of hydrogen and its environmentally friendly characteristics, water electrolysis has already been applied in the industry for almost a century. At present, there are primarily two distinct types of industrial electrolyzers. One is an alkaline electrolyzer, in which anodes, cathodes, and electrolytes typically use Ni/Co/Fe composites, Ni-based materials, and highly concentrated KOH or NaOH solutions. The optimal temperature is from 60 to 80 °C, the typical current density is 0.2–0.4 A cm^{-2} and the hydrogen production is less than 760 N m^3 h^{-1}. The advantage of this electrolyzer is that the electrode materials, normally non-noble metal composites, are relatively cheap, but the low conversion efficiency severely limits its application. Another one is the polymer electrolyte membrane (PEM) electrolyzer. It typically uses Ir, Pt, and solid polymer electrolytes as anodes, cathodes, and electrolytes, respectively. The optimal temperature is from 50 to 80 °C, the operational current density is from 0.6 to 2 A cm^{-2} and the hydrogen production is less than 30 Nm^{3}h^{-1}. This electrolyzer has a good conversion efficiency, a high current density and a compact design, but the expensive electrode materials and membranes limit wider application of PEM-electrolyzers (Liu et al. 2022a).

During water electrolysis, hydrogen generates at the cathode side of the cell. The reaction taking place at this electrode is referred to as HER. The mechanism of this considerably simple reaction has been widely investigated in the literature.

In acidic media, the reaction equation at the cathode is:

$$2H^+ + 2e^- \rightarrow H_2$$
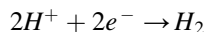
The corresponding mechanism involves a two-electron transfer and either follows so-called Volmer-Tafel step or the Volmer-Heyrovsky step, as shown in the following equations (* corresponds to an adsorption site):

Volmer step:

$$H^+ + e^- + {}^* \rightarrow {}^*H$$

Tafel step:

$$2^*H \rightarrow H_2 + 2^*$$

Heyrovsky step:

$$H^+ + e^- + {}^*H \rightarrow H_2 + {}^*$$
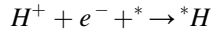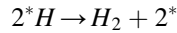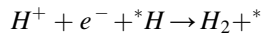
Recently, it has been observed that both types of electron transfer are present in acidic HER, especially at high overpotentials. The Tafel step is often recognized as the rate-determining step at least for the acidic HER on Pt-based electrodes (Liu et al. 2023). In alkaline media, the HER reaction follows the below scheme:

$$2H_2O + 2e^- \rightarrow 2OH^- + H_2$$
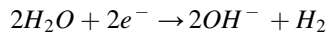
resembling that in acidic media, the mechanism is comprised of a two-electron transfer and follows either the Volmer-Tafel step or the Volmer-Heyrovsky step, as shown below. An additional water dissociation step is added to the Volmer step.

Volmer step:

$$H_2O + e^- + {}^* \rightarrow {}^*H + OH^-$$

Tafel step:

$$2^*H \rightarrow H_2 + 2^*$$

Heyrovsky step:

$$H_2O + e^- + {}^*H \rightarrow H_2 + OH^- + {}^*$$
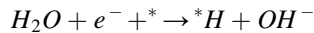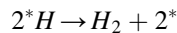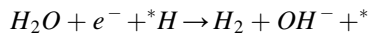
In contrast to the mechanism in acidic media, the Volmer step becomes the rate-determining step for Pt-based electrodes in alkaline electrolytes resulting in their lower overall HER performance (Wu et al. 2017).

According to the Sabatier principle, the highest activity should be observed on catalysts with an optimal hydrogen binding energy, as the adsorbed hydrogen is the only intermediate in both acidic and basic solutions. Relation of theoretical hydrogen binding energies with experimental HER activities of different materials leads to the

HER volcano plot shown in Fig. 15. To date, the highest HER performance in both acidic and alkaline solution has been achieved using Pt-based electrocatalysts.

Although the HER has undergone decades of investigation and solely involves one intermediate species, there are still several unsolved problems. For instance, improving the alkaline HER activity of Pt to a similar level as its performance in acidic media is crucial to improve the low conversion efficiency of alkaline electrolyzers (Zhang et al. 2023). Moreover, the design of new non-noble metal catalysts for the acidic HER would be highly beneficial to reduce the cost of the devices.

3.9   Oxygen Evolution Reaction

At the anode side of a water electrolyzer, oxygen is produced during so-called OER. Typically, it occurs on oxidized metal surfaces at relatively high overpotentials. In acidic media, the reaction equation is:

$$2H_2O \rightarrow O_2 + 4e^- + 4H^+$$
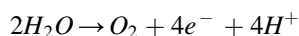
The corresponding mechanism is much more complex than that of the HER. It involves a four-electron transfer and has at least three reaction intermediates, being *OOH, *OH, *O. Though there are several possible reaction pathways, those shown in the following equations are widely accepted in the literature.

$$H_2O + ^* \rightarrow {}^*OH + H^+ + e^-$$

$$*O + H_2O \rightarrow *OOH + H^+ + e^-$$

$$*OOH \rightarrow O_2 + H^+ + * + e^-$$
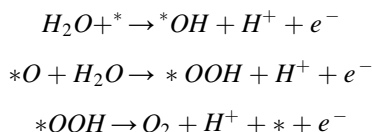
In alkaline solutions, the reaction equation is:

$$4OH^- \rightarrow 2H_2O + O_2 + 4e^-$$
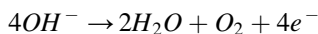
Like that in acidic media, the mechanism in alkaline solutions is also based on the four-electron transfer, which includes the same three different reaction intermediates (Chu et al. 2022).

The most recognized reaction pathway is shown as follows:

$$OH^- + ^* \rightarrow {}^*OH + e^-$$

$$*OH + OH^{-*} \rightarrow {}^*O + H_2O + e^-$$

$$*O + H_2O + [(OH)]^- \rightarrow *OOH + H_2O + e^-$$

$$*OOH + [(OH)]^- \rightarrow O_2 + H_2O + e^- + *$$
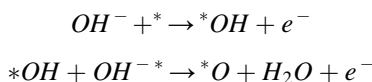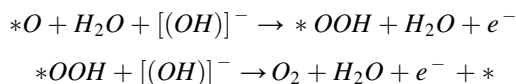
However, regardless of the electrolyte, the reaction rate of the OER is very low as compared to the HER. Although considerable efforts have been made to improve the OER performance, the poor stability of the oxide electrodes and the so-called 'scaling relations' are the critical bottlenecks of the OER, as explained below (Exner 2023). The surface structure of the electrode materials used for the OER changes over time due to an inevitable 'oxidation process' that occurs during the reaction. This process results in poor long-term stability and is difficult to study in-situ. Moreover, it is probable that some components of the oxide electrodes are directly involved in the OER. It was recently provided direct experimental evidence that lattice oxygen, i.e., oxygen incorporated in the bulk structure of the electrode material, is also involved in the OER.

Besides, based on thermodynamic calculations, the OER activity indeed depends on the binding energies of the reaction intermediates (i.e., *OOH, *OH, *O). Optimal adsorption energies of these critical intermediates should affirm a superior activity according to the Sabatier principle. It was discovered that the adsorption energies of *OOH, *OH, and *O are linearly related, also referred to as the 'scaling relations' (Fig. 16).
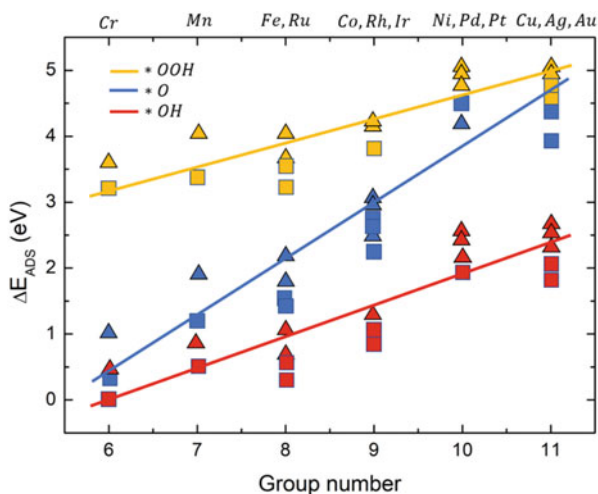
Fig. 16 Trends in adsorption energies of OER/ORR reaction intermediates. The values were calculated for doped graphite-based materials, in which the active sites are composed of transition metal and nitrogen atoms. The so-called 'scaling relations' indeed exist between the adsorption energies of *OH (red), *OOH (yellow) and *O (blue). There is a constant separation of ~ 3.10 eV between the adsorption levels of *OH and *OOH; *O is located in-between. The triangle and square symbols are values obtained from two different unit cells

4 Catalytic Activity

Finding and optimizing abundant electrocatalysts for electrolysis is essential to enable a sustainable hydrogen economy. An electrocatalyst is defined as a material that takes part in and facilitates an electrochemical reaction without being consumed or altered. Today, around 80% of all processes in chemical industries use some kind of catalyst. In water splitting, the performance of an electrocatalyst is mainly categorized by the amount of gas it can produce using as low overpotential as possible. This can be determined from potentiostatic measurements with LSV as shown in Fig. 17 where the current density corresponds to amount of gas produced (depending on the Faradaic efficiency). This specific figure shows three theoretical catalysts, with different hydrogen adsorption energies that are either too strong, weak, or optimal for HER.

The most common and reliable measure of a catalyst is the overpotential needed to produce a certain current density, usually at 10 mA/cm^2 because it is roughly the magnitude used in photo-electrochemical devices. In PEM or alkaline electrolyzers however, the operational current densities are much higher, but the overpotential at 10 mA/cm^2 allows suitable comparison of materials at lab scale. The reaction is often described to start at the "onset potential", which is a rather ambiguous measure and is not well defined. Usually, a straight line is drawn from the voltammogram where the current seems to start, commonly at around 5 mA/cm^2, and where it crosses the x-axis is said to be the onset potential. This is also dependent on the scale of the y-axis and electrochemical surface areas.

Two other parameters that can describe the activity are the exchange current density and Tafel slope and can be obtained from Tafel plots such as in Fig. 18.

These properties have physical meanings and are good measures. The exchange current density (jo) is the current when the net current for the reaction is zero, in other words, where the reaction proceeds in the forward and backwards direction with the

Fig. 17 Theoretical polarization of three different model systems with different free energy of hydrogen adsorption
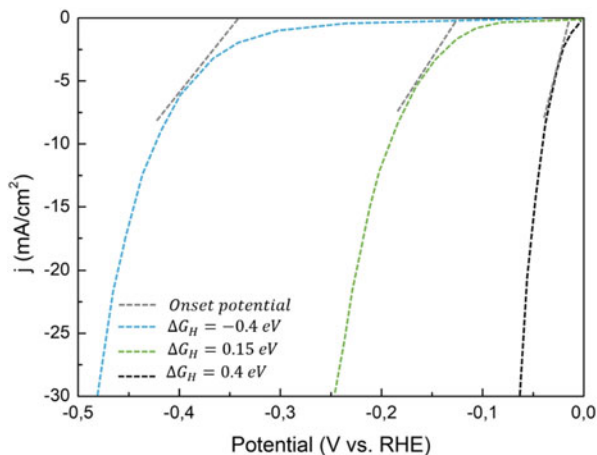
Fig. 18 Tafel plots of three
different model systems
with different free energy of
hydrogen adsorption
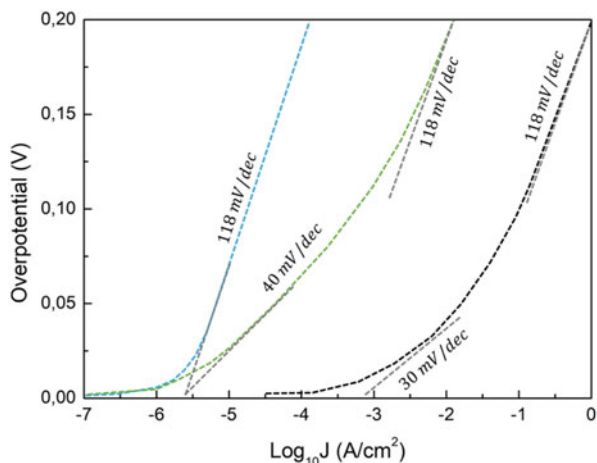
same rate. This value can be derived by extrapolating the Tafel slope to 0 V
overpotential. A high number of j_o means that the reaction kinetics are fast and
that the catalyst is efficient. However, it can be difficult to get accurate experimental
values for jo and even for similar metals measured in very pure conditions, the values
differ quite notably in the literature.

The Tafel slope is a measure of how much potential is needed for increasing the
current by one decade.

This slope can be used to describe the reaction mechanism and is also an
important factor for reaching high current densities with minimum amount of
overpotential.

The Tafel slope is obtained in linear sections of Tafel plots, which can be at
several regions if the reaction mechanism changes with potential.

CV plots can give information in wide potential ranges about the electrode/
electrolyte interface. A typical CV plot is shown in Fig. 19 and in this plot, (a-d)
is reduction and (e-f) are oxidation reactions of a gold-coated electrode in an alkaline
1 M KOH (pH = 14) electrolyte.

The water splitting reactions HER and OER are denoted by a and f while small
amounts of ORR could possibly occur at c from the oxygen evolved. In actual ORR
experiments, the electrolyte should be purged with O_2 prior to the measurement.
Moreover, there are two metal redox peaks at e and d, which we can see are not
reversible since the integrated area of e is much larger than the reduction peak d. The
peak at b could be assigned to metal-reduction or possibly be related to hydrogen
adsorption on the metal surface. However, the sources of these current responses are
just examples and to conclude their origin, theoretical models or further experiments
are often needed such as in-situ spectroscopic methods.

In Fig. 20, experimentally obtained LSV plots for OER are shown for several
Ni-Fe based catalysts with different atomic ratios of Ni and Fe. In this figure, the
onset potentials, overpotential at 10 mA/cm^2 and current/potential slopes can be

Fig. 19 CV plot of a gold electrode with reduction and oxidation peaks denoted
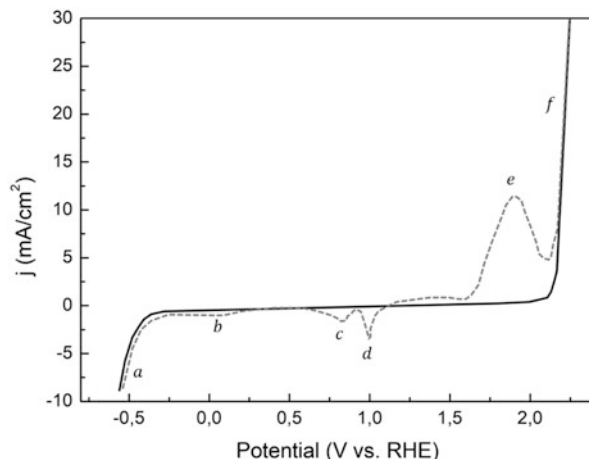
Fig. 20 Typical experimental LSV plots for OER, here for nickel and iron-based catalysts
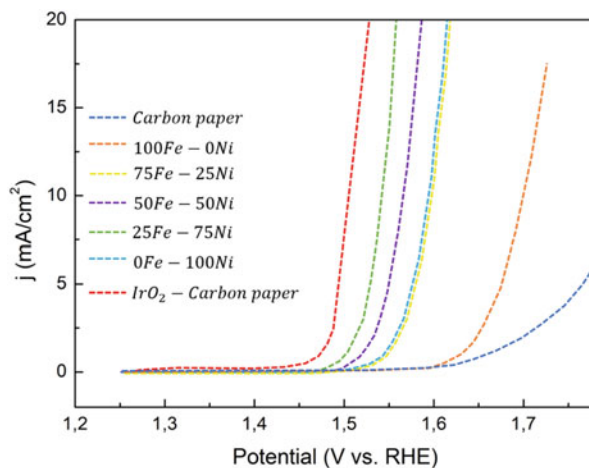
measured. Note that the thermodynamic potential for OER is 1.23 V and therefore the absolute potentials are much higher than for HER even though the overpotentials are around 0.25–0.5 V against OER for these catalysts.

4.1 Activity Definition

In electrochemistry, parameters that alone can estimate a materials catalytic activity are called activity descriptors (Kolle-Görgen et al. 2022). The ability to chemically bond to intermediate species have shown to be highly correlated to experimental activity. Since the reaction mechanisms for HER, OER and ORR differs, the

intermediate species vary for all these reactions, and consequently also the ideal catalysts. The HER is probably the most studied and simplest of these three reactions since adsorbed hydrogen atoms are the only intermediate species and therefore materials with optimal adsorption energies for hydrogen such as platinum excels. The adsorption free energy is calculated as:

$$\Delta G = \Delta H - T\Delta S$$

where ΔH and ΔS are the reaction enthalpy and entropy, respectively. Theoretically, ΔG can be calculated with ab-initio simulations such as density functional theory (DFT) with high precision. DFT is probably the most used theoretical tool for computational chemistry due to the high accuracy and efficiency with the ability to include hundreds of atoms in quantum mechanical modeling. However, finding new descriptors from the intrinsic properties in materials would be beneficial to overcome the need of time-consuming ab initio computational simulations, especially for large systems with many diverse adsorption sites. As an example, the trend in adsorption energies has shown to correlate to the energy of the d-band center relative to the Fermi energy, and therefore the electronic density of states could be such a descriptor. The density of states only needs one iteration in DFT calculations compared to numerous molecular dynamic optimizations needed for adsorption reactions. However, such descriptors often have problems to predict adsorption energies for disordered materials or when for example species bond to more atoms than one. Another descriptor for HER is the work function of the metal surface. It is however a macroscopic property and cannot predict diverse atomic sites Next to DFT, an interesting approach is by suing machine learning algorithms, which has been proven able to predict the d-band center and other intrinsic properties and are much faster than DFT calculations. By using machine learning, complicated relations involving many parameters could be used to estimate catalytic activities but needs large data sets and the relationships often lacks physical meaning. Furthermore, the errors in these models are still relatively large and need DFT calculations for training the models. Therefore, ab initio methods such as DFT are still considered essential. While the adsorption energies have proven very successful in describing the activity, they cannot alone explain the different behavior in varying pH or electrolytes and therefore further descriptors may be needed such as water or ionic interactions for more complete models.

For 4-electron multistep reactions like OER and ORR with several intermediates, the adsorption energy for each involved species must be considered and therefore, these reactions are usually harder to describe theoretically than HER.

The equilibrium potential of the full reaction is determined from the least thermodynamically favorable reaction step. Hence, ideal catalyst would have an equilibrium potential of 1.23 V for each of the individual electron transfer reaction steps involved. The free energy change for the four reaction steps in OER and ORR is given by:

$$\Delta G_1 = \Delta G(OOH_{ads}) - \Delta G(O_2) + eU$$
$$\Delta G_2 = \Delta G(O_{ads}) - \Delta G(OOH_{ads}) + eU$$

$$\Delta G_3 = \Delta G(OH_{ads}) - \Delta G(O_{ads}) + eU$$

$$\Delta G_4 = \Delta G(H_2O) - \Delta G(OH_{ads}) + eU$$

Where the reaction pathway for ORR is:

$$\Delta G_1 \rightarrow \Delta G_4$$

and for OER:

$$\Delta G_4 \rightarrow \Delta G_1$$

The free energy of an ($H^+ + e^-$) pair is equal to -eU at other potential than 0 V vs. SHE and the standard equilibrium potentials are given by the conditions where $\Delta G_i = 0$. From these thermodynamic relations, an optimal catalyst for either OER or ORR would bind the intermediate species with free energies according to:

$$\Delta G(OH_{ads}) = 1.23 eV$$

$$\Delta G(O_{ads}) = 2.46 \ eV$$

$$\Delta G(OOH_{ads}) = 3.69 \ eV$$

$$\Delta G(O_2) = 4.92 \ eV$$

by taking:

$$\Delta G(H_2O) = 0$$

Since it has been shown that these intermediates adsorption energies depend on each other, linear relations such as:

$$\Delta G(OOH_{ads}) = \Delta G(O_{ads}) + 1.23 \ eV$$

must be fulfilled for an optimal catalyst with zero overpotential. However, such materials have not yet been found.

As an example, the adsorption energy of OOH for metal-oxides has found to scale against the oxygen adsorption energy as:

$$\Delta G(OOH_{ads}) \approx 0.64 \Delta G(O_{ads}) + 2.4 \ eV$$

and for the graphene nanoribbons:

$$\Delta G(O_{ads}) \approx \Delta G(OH_{ads}) + 0.89 \ eV$$

Fig. 21 Equilibrium potential volcano plot of (**a**) HER (solid) and HOR (dashed)
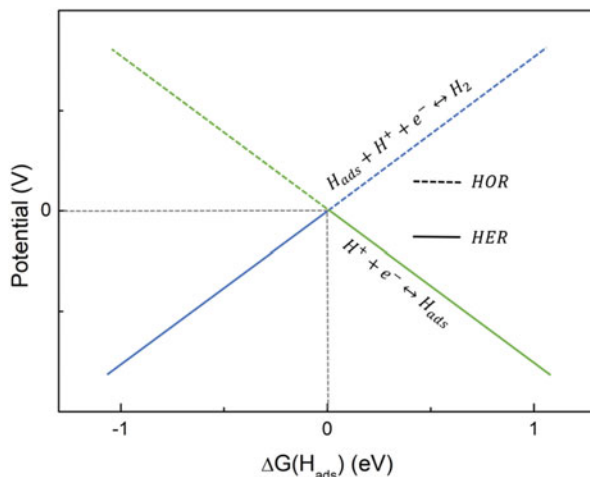
In Fig. 21, the equilibrium potentials are shown for HER/HOR as a function of $\Delta G(H_{ads})$ (Ekspong et al. 2020).

and in Fig. 22a,b for both ORR/OER as a function of $\Delta G(OH_{ads})$ and $\Delta G(O_{ads})$, respectively.

The volcanoes are turned ($\vee$) for oxidation reactions and all potentials below these are spontaneous, while for the reduction reactions (HER and ORR), all potentials above the volcano relations ($\wedge$) are spontaneous.

As an example, in Fig. 21 at $\Delta G(H_{ads}) = -1$ eV, the adsorption reaction is spontaneous for HER and the total equilibrium potential is restricted by the desorption reaction.

All volcanoes in Fig. 22 have the theoretical optimal limits shown with thick solid black lines at the intersections for clarity.

For HER and HOR, the ideal equilibrium potential is at 0 V for both reactions. Optimal catalysts would behave as the dashed lines in Fig. 22 where the OER/ORR reactions would start at 1.23 V.

4.2 Microkinetic Model

Electrochemical reactions can be described by microkinetic analysis, which is a powerful tool for examine the rate (activity) of catalytic reactions at atomic level.

The method relies on both experimental and theoretical observations to predict the rate for electrochemical reactions and in general, generates results such as concentration or reaction rates as a function of time, but in most cases, we are only interested in the steady-state solutions.

Fig. 22 (**a**) ORR/OER with linear relations of adsorption energies from a defective N-doped graphene nanoribbon and (**b**) ORR/OER with linear relations of adsorption energies from metal-oxides
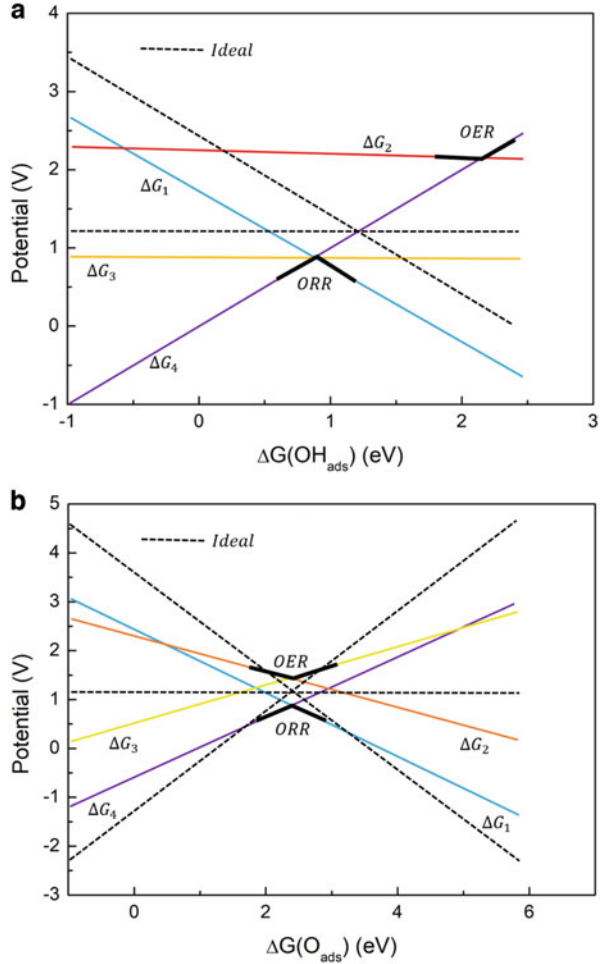
The reaction rates are determined by considering the free energy of adsorption on each adsorption site, and letting the rate follow an Arrhenius-type of relation such as:

$$k = Ae^{-\frac{\Delta G_0^1 + \alpha \phi z}{k_B T}}$$

where k is the rate constant, A is a pre-exponential factor, ΔG^1_0 is the standard free energy of activation at zero potential, α is the charge transfer coefficient, ϕ is the electro-chemical potential, z is number of involved electrons, and kB is the Boltzmann constant. The activation energies for each elementary reaction can be displayed by free energy curves, such as in Fig. 23.

Fig. 23 Free energy curves of HER through reaction R_1 and R_2 at (**a**) zero overpotential and at (**b**) non-zero overpotential. Three different catalyst are illustrated with different adsorption energies
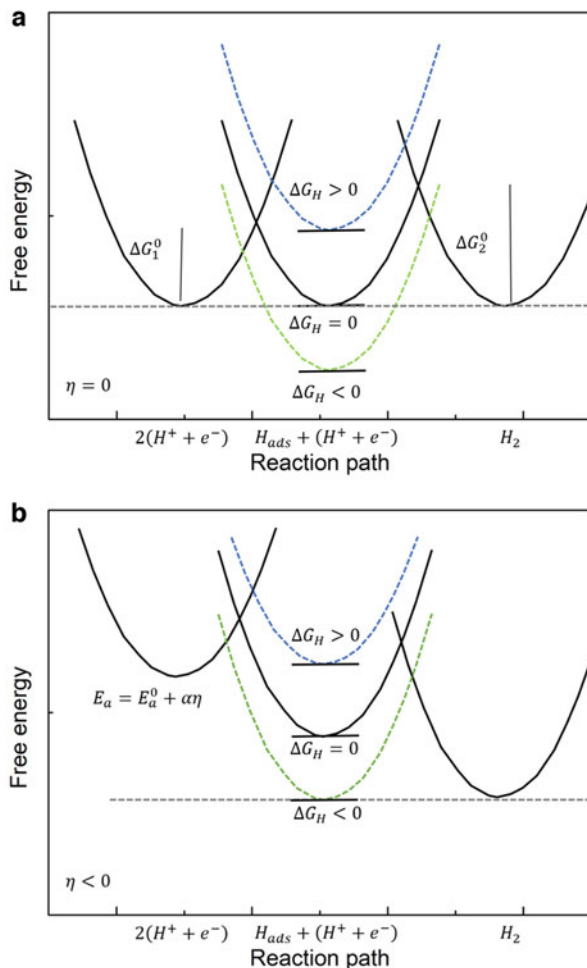
where the reaction R_1 and R_2 are shown at zero and non-zero overpotentials. In this figure, the reactions are catalyzed by three different materials with optimal $\Delta GH = 0$, weak $\Delta GH > 0$ and strong $\Delta GH < 0$ hydrogen adsorption energies. At zero overpotential, the reaction R1 is in equilibrium, non-spontaneous and spontaneous, respectively for the materials. The charge transfer coefficient α is the dependency of the free energy curve and activation energy, with respect to a change in potential, and is normally considered to be 0.5.

This coefficient is theoretically obtained from the slopes of the free energy curves at the point of intersection of the initial (x) and final (y) states as:

$$\alpha = \frac{x}{x+y}$$

It is experimentally possible to measure α from the Tafel slope when it is not dependent on any other variables such as H-coverage. The reaction rate for a typical adsorption reaction can further be determined as:

$$r = k(1 - \theta)C$$

where θ is the surface H-coverage, which is dimensionless and between [0,1] and C is the adsorption site concentration in the catalyst.

Non-equilibrium conditions can be studied by setting the electrochemical potential as:

$$\phi = \phi_* + \eta$$

where ϕ_* is the equilibrium potential and η is the applied overpotential. The equilibrium potential can be determined from rate equations by setting the reaction rates of the forward and backward directions equal and $\eta = 0$.

The equilibrium potential then depends on the equilibrium hydrogen coverage, which in turn, is found from $\Delta G(H_{ads})$ using a Langmuir adsorption isotherm. The $\Delta G(H_{ads})$ also depend on the macroscopic total hydrogen coverage of the material because of lateral interactions according to a Frumkin isotherm:

$$\Delta G(H_{ads}, \theta_{tot}) = \Delta G(H_{ads}, \theta_{tot} = 0) + r\theta_{tot}$$

and therefore, the total H-coverage used in DFT and from the Langmuir adsorption must equal at the equilibrium coverage. Finally, to calculate the complete reaction rate for multistep reactions, a master equation is used to calculate the steady state considering the forward and backward rates for each of the involved elementary steps.

Rather than using detailed microkinetic models, it is a common practice to use the Butler-Volmer equation (BVE) to describe the kinetics of electrochemical reactions. However, the BVE is only valid for simple one-step redox reactions and cannot accurately describe more complex reactions such as HER. Yet, the BVE gives accurate results when deriving kinetic properties such as the exchange current density and Tafel slopes.

The BVE can be related to the above-mentioned microkinetic rate equations such that:

$$k = Ae^{-\frac{\Delta G_0^1 + \alpha\phi z}{k_BT}} \propto i_0 e^{-\frac{\alpha\eta z}{k_BT}}$$

where i_0 contain all except the remaining exponential. The full rate in units of current density for a single step reaction (forward-backward) can then be written as:

$$i = i_0 e^{-\frac{\alpha\eta z}{k_BT}} + e^{\frac{(1-\alpha)\eta z}{k_BT}}$$

which is the BV equation. Evaluating the BVE at high overpotentials where one of the directions dominates, the Tafel slope:

$$\frac{dE}{dlog_{10}[I]}$$

can be derived from the Tafel equation:

$$\eta = Alog_{10}\left(\frac{i}{i_0}\right)$$

and as mentioned before, i_0 can be determined by extrapolating the equation to $\eta = 0$ V. Note that the Tafel slope, which is:

$$2.303\ k_B T / \alpha z$$

only depend on the charge transfer coefficient, α or the number of electrons involved for constant temperature. This often leads to misinterpretations since α is considered to be 0.5 for most reactions and that the number of electrons in a single reaction rarely is more than one. In reality, the Tafel slope also depend on coverage, and therefore the Tafel equation could only give accurate values of α if the coverage has stabilized. The need for selectively fitting α and z to explain the experimentally obtained Tafel slopes without any physical motivation shows one of the issues of using the simplified BVE expression when studying multi-step reactions.

In Fig. 24a, the equilibrium volcano plot for each reaction in HER is shown, and in Fig. 24b at non-equilibrium conditions with varying overpotential. Compared to the volcano plot in Fig. 24a, the y-axis instead shows the current density and there are three dashed lines, one for each of the elementary reaction, together with the overall volcano relation (solid black line).

The H-coverage goes towards zero at positive ΔGH and towards fully covered at negative ΔGH and vary according to the Langmuir isotherm.

If the volcano plot was independent of H-coverage (always full coverage), the current of reaction R_2 (blue line) would continue as a straight line following the relation on the left side of the volcano. This reaction is now limited by low coverages on the right side and therefore forming the volcano-like plot. Similarly, the rate of reaction R_1 is reduced by high H-coverage at negative ΔGH.

Following the evolution of the current density with overpotential in Fig. 24b, polarization plots and thereby Tafel slopes can be obtained. Any material that has negative ΔGH can only display Tafel slopes of 118 mV/dec since the H-coverage is basically constant at these energies. For materials with positive ΔGH, the Tafel slopes depend on the rate-determining step. If the Heyrovsky reaction (R_2) is rate-determining, the Tafel slope is 40 mV/dec and for the Tafel reaction (R_3), 30 mV/dec. For the Volmer reaction (R_1), 118 mV/dec is also obtained for positive values of ΔGH because the H-coverage either increases or is constant since R_1 is fastest. These Tafel slopes agrees with experimental and other theoretical values. Combination of

Fig. 24 (**a**) Volcano relation of the exchange current densities and adsorption free energy of hydrogen for the three elementary (green = R_1, blue = R_2, red = R_3) and the overall reaction of HER (black). (**b**) The evolution of the volcano plots (J vs. η) for HER. The black circle shows the results from Pt
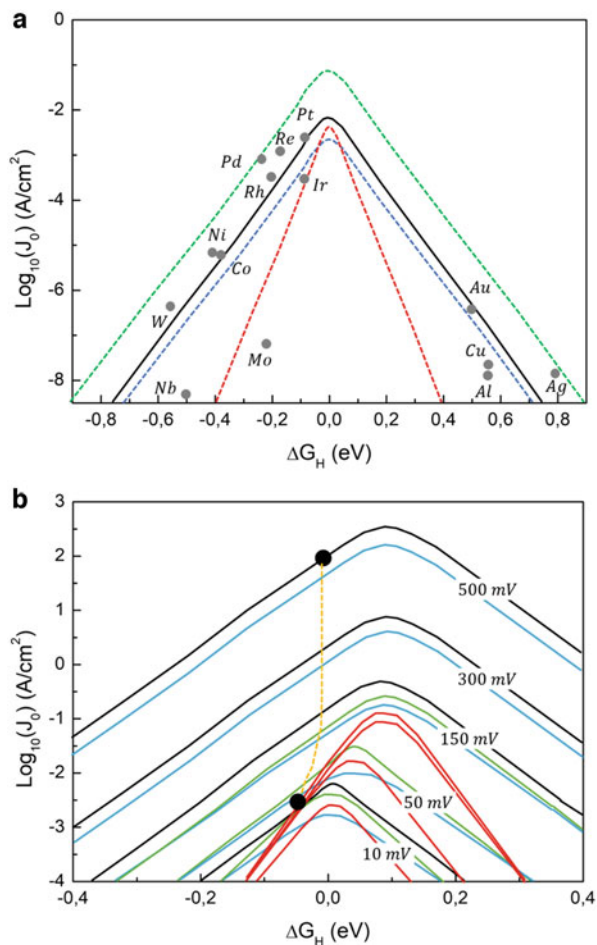
different sites in a material can result in mixed values of these slopes. The advantage of using our model, except more detailed analysis, is that all adsorption sites are included to show average characteristics of the material, which is beneficial for defective structures with various sites where quantification can be difficult. Finding ΔGH at the equilibrium H-coverage is also important. As an example, the exchange current density in Pt111 change by one order of magnitude considering zero and equilibrium H-coverages. Another example is that ΔGH on 1 T-MoS_2 is weakened by around 1 eV (depending on the system size) upon the second adsorbed H-atom because the first H-atom will trigger a phase transition from 1 T to 1 T'.

By following the current density in Figure for Pt, the Tafel plot is non-linear but later converge to 120 mV/dec. This does not agree with experimental Tafel slopes of Pt, which at low current densities is 30 mV/dec and at higher overpotentials increases to 120 mV/dec. The reason is that ΔGH is close to 0 eV for Pt. However,

the obtained equilibrium H-coverage of 0.8 monolayer matches with experimental results and therefore an alternative mechanism can probably explain the low Tafel slopes. To match the experimental Tafel slope of 30 mV/dec at low current densities for Pt, ΔGH must be slightly to the right of the top of the volcano:

$$\sim 0.05 < \Delta G_H < 0.2 \ eV$$

At these energies, the combination reaction (R_3) become rate-determining together with an increase of hydrogen coverage with overpotential.

Since the active mechanism of Pt-based materials is not yet fully understood, it is difficult to compare the results to experiments. It has been suggested by several reports that H-atoms preferers the fcc sites in Pt111 at equilibrium conditions, but at higher overpotentials the on top sites are activated with positive ΔGH and are responsible for the HER.

Still, more detailed studies for materials with free energies near the top of the volcano is needed to understand the exact reaction process. Even after 30 years of platinum metal single crystal studies, basic electrochemical reactions on these are not yet fully understood. Next to Pt, there are also other noble materials with similar activities such as Rh, Ir and Pd. The reason why Pt is often used is because the low Tafel slope, high reproductivity and inertness against the harsh conditions.

For catalysts with weak adsorption for on top sites, any adsorption sites further in the pathway such as fcc, hcp, bridge or four-fold sites will be discarded in the evaluation since the rate of desorption on the on top site is considered faster than adsorption for these sites. Weak adsorbing on top sites then acts like a surface diffusion barrier for other sites.

4.3 Nanomaterials

The main advantage of using nanomaterials as electrocatalysts is the huge surface area in relation to volume. This results in large activities per weight in the electrode since it is mostly the top atomic layers that participate in electrochemical reactions (Yoo et al. 2021).

At the electrode, the catalysts are usually combined with electrically conducting and high-surface area support materials for increasing the electrical contact, surface area and also for constructing a rigorous and stable electrode. Commonly used nanostructures are graphitic-like materials such as graphene and carbon nanotubes (CNTs). While the strength of these materials is gained by the polarized sp2-bonds, the delocalized electrons (above and under plane) in the pi-bonds makes them highly electrical conducting.

Ideal graphene has a unique electron density and is viewed as a metal with a zero bandgap while single-walled CNTs can either be semi-conducting or metallic depending on the chirality. On the other hand, multi-walled CNTs are generally always metallic. Structurally ordered and ideal graphitic materials are chemically

inert and stable in electrolytes and as a result from this, are useful as electrical support materials. A downside with the chemical inertness is that the adhesion to the catalyst material or electrode surface can be poor, leading to low electrical charge transfer at the interfaces. Inducing disorder or imperfections in the graphene lattice alters the chemical properties and is essential for many applications where graphene is used. This is similar for pristine CNTs that are chemically inert with low solubility and therefore functionalization of the surface is needed for catalyst adhesion (Al-Akraa and Asal 2018).

Inspired by semi-crystalline, high surface carbon materials like carbon black and reduced graphene oxide that are widely used in electrochemistry, we synthesized and applied nitrogen-doped multiwalled carbon nanotubes as a conducting, and chemically active support material.

By introducing nitrogen atoms in the carbon lattice, the structure is discorded and defect-rich, so that the nanotubes contain "hot spots" which are excellent for chemical bonding and have been shown to retain the high electrical conductivity of pristine carbon nanotubes. Some of these nitrogen-defects were also shown to be electrocatalytically active towards ORR in alkaline environments.

Introducing defects in nanomaterials have been a promising route for tuning the activity in nano-scale for otherwise inert materials. Defects can come in many variations such as vacancies, edge-defects, grain boundaries, substitutions, bond rotations, adatoms, interstitial atoms in layered 2D materials, among many others.

Any perturbation in otherwise crystalline materials are considered defects and will shift the adsorption energies of intermediates. There are several techniques to introduce defects in materials, such as plasma treatment, ball milling, doping, etching, annealing etc. However, producing specific defects are difficult and even to determine what defects are present can be challenging. In this section we go through some defective structures that were studied in this thesis and how they can be used for optimizing and finding new catalytic materials.

Transition metals such as Mo, Ni, Fe and Co has been extensively studied as electrocatalysts, either by themselves, as oxides, or by adding reactive elements such as S, Se or P (Ali et al. 2023; Ye et al. 2023). In recent years, 2D layered transition metal dichalcogenides and especially MoS2 has gained considerable interest as electrocatalysts and even as a photocatalysts. MoS_2 exists in several crystalline phases. The most stable phase is the trigonal 2H phase, while both the octahedral 1 T and disordered 1 T' are metastable phases that transforms to 2H at slightly elevated temperatures. In its most stable phase, MoS_2 is a semiconductor with an electronic bandgap that change significantly between bulk and monolayer structures and is studied far beyond the field of electrocatalysis such as in photonics and electronics. In contrast to 2H-MoS_2 the 1 T phases are highly conducting and therefore more useful for electrocatalysis.

Ever since the edge-atoms in MoS_2 was found highly active towards HER in theory, a lot of effort has been done to synthesize MoS_2 with high ratio of exposed edge-atoms, resulting in several inspiring reports (Liu et al. 2022b).
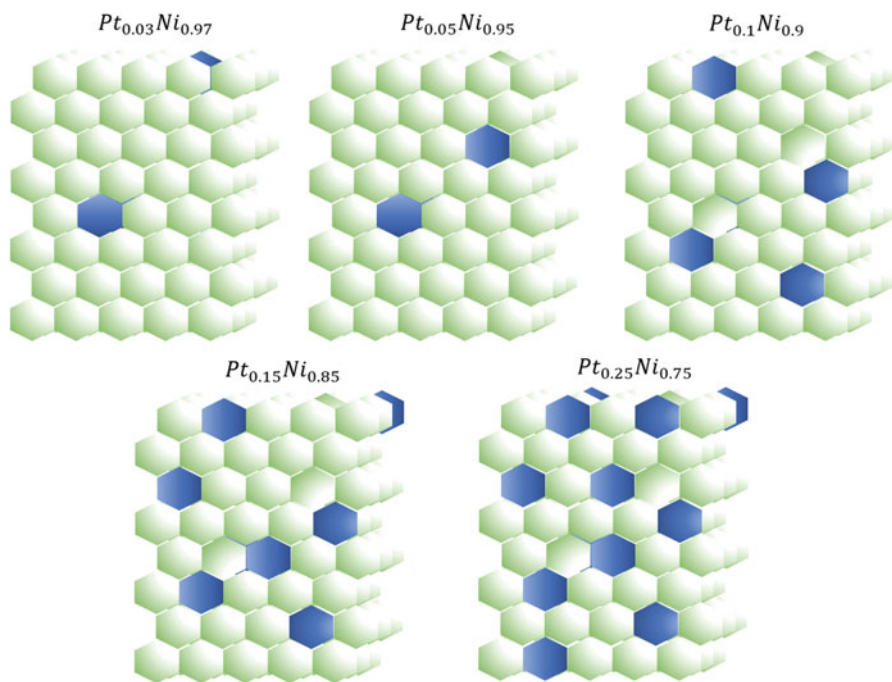
Fig. 25 Top view of different PtNi alloys

Another successful technique for replacing noble metals as catalysts, is by substituting some of the rare metal atoms with abundant elements. One of the most investigated systems is nickel/platinum alloys with Pt ranging from 0–25 atomic percentage (Fig. 25).

Homogenously dispersed PtxNi1-x alloy of x = 0.05 was optimal regarding catalytic activity displaying both high activity and stability compared to the other samples. All alloys displayed Tafel slopes of 30 mV/dec verifying that the reaction mechanisms were similar. According to the theoretical calculations, the surface of the nanoparticles needs to be Pt-rich (above 25% at.) for the material to display the high obtained experimental activity (Fig. 26).

Each Pt atom activates the three surrounding adsorption sites and hence a Pt concentration of 33% at. would be enough to activate the whole surface if they are homogeneously dispersed. Since the simulation could not explain the activity of the experimental samples, it is also possible that on top sites are activated at high H-coverages, similar as suggested for Pt catalysts, or that the experimental structures have higher Pt surface concentrations than 25%, even for the $Pt_{0.03}Ni_{0.97}$ sample.

If we instead focus on the OER, it is the noble metal oxides, Ir and Ru that show the best performance and stability. In acidic electrolytes no abundant material is yet found that is stable enough for this reaction. However, in alkaline electrolytes, especially nickel and iron alloys have shown as good, or even better performance in comparison to the noble metals.
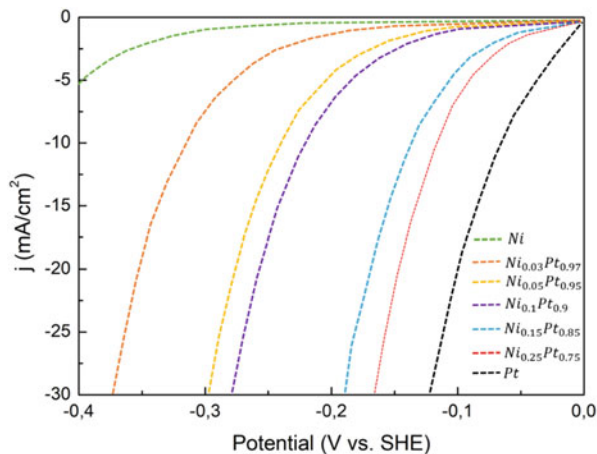
5 Pulsed Water Electrolysis

The application of pulses is a promising method to enhance the efficiency of water electrolysis (Rocha et al. 2021).

Pulsed electrolysis has been studied for more than seven decades. Yet, some new studies indicate that it is a method capable of improving the efficiency of hydrogen production by water splitting, with some of the reasons being the removal of gases from the electrode during the resting time and by the increase in the concentration of reacting ions at the electrode surface.

There are two types of pulsed operations: voltage pulses and current pulses. In the first, voltage is changed from a base value (called off-voltage) to a peak value (called on-voltage). The sum of on-time (ton) and off-time (toff) is the pulse period. The ratio between on-time and pulse period is defined as the duty cycle, and the frequency is the inverse of the pulse period. The pulse amplitude is the difference between off-voltage and on-voltage. The resulting current will be the sum of a faradaic current (if the peak current is in a potential range at which water electrolysis occurs) and a capacitive current for the charging/discharging of the double layer.

When a voltage pulse is imposed, the capacitive current can be estimated as the charge/discharge of an ideally polarized electrode:

$$i_c(t) = \frac{\Delta E}{R_s} \exp\left(-\frac{t}{R_s C_D}\right)$$

with ΔE the amplitude of the voltage pulse, Rs the solution resistance, CD the double layer capacitance, and t the time. Note that the capacitive current decays exponentially with time. The estimation of the faradaic current, on the other hand,

can be done considering a semi-infinite linear diffusion at a planar electrode. For a quasi-reversible, one-step, one-electron case (O + e- = R), the current time-behavior is given as:

$$i_f(t) = FA\left(k_f C_0^* - k_b C_R^*\right) \exp\left(H^2 t\right) erfc\left(H\sqrt{t}\right)$$

With:

$$k_f = k^0 \exp\left[-\alpha f(E - E_0)\right]$$

$$k_b = k^0 \exp\left[(1 - \alpha)f(E - E_0)\right]$$

$$f = \frac{F}{RT}$$

$$H = \frac{k_f}{\sqrt{D_0}} + \frac{k_b}{\sqrt{D_R}}$$

Where erfc is the error function complement of x, defined as:

$$erfc(x) = 1 - \frac{2}{\sqrt{\pi}} \int_0^x e^{-y^2} dy$$

where k_0 is the standard rate constant; α the transfer coefficient; F the Faraday constant; A the electrode area; k_f and k_b the rate constant for the forward (reduction) and backward (oxidation) reactions, respectively; C0* and CR* the concentration of the reactant O and the product R in the bulk, respectively; t is the time; R the gas constant; T the temperature; E voltage; E_0 the standard potential; D0 and DR the mass transfer coefficients for specimens O and R, respectively. The graphical representation of a voltage pulse with a peak voltage at which water electrolysis occurs and a base voltage at which no reaction is possible is shown in Fig. 27a.

The capacitive current was estimated using the previous equations. It can be seen that when a voltage pulse is applied, the total current starts mainly capacitive and after the complete charge of the electrical double layer – EDL, it becomes mainly faradaic. When the voltage returns to the base value, the EDL is discharged, giving a pure capacitive current.

In the case of current pulses, the voltage-time behavior at the beginning of a pulse can be estimated considering again the ideally polarized electrode:

$$E = i\left(R_s + \frac{t}{C_D}\right)$$

As the double layer is charged and the voltage reaches the reversible cell voltage, faradaic processes start to occur. Then, considering a quasireverible one-step one-electron reaction, the potential-time behavior is given by:

Fig. 27 Schematic
representation of (**a**) voltage
pulse with an on-voltage at
which a reaction occurs and
an off-voltage at which no
reaction occurs (**b**) current
pulse with a null total
current during off-time
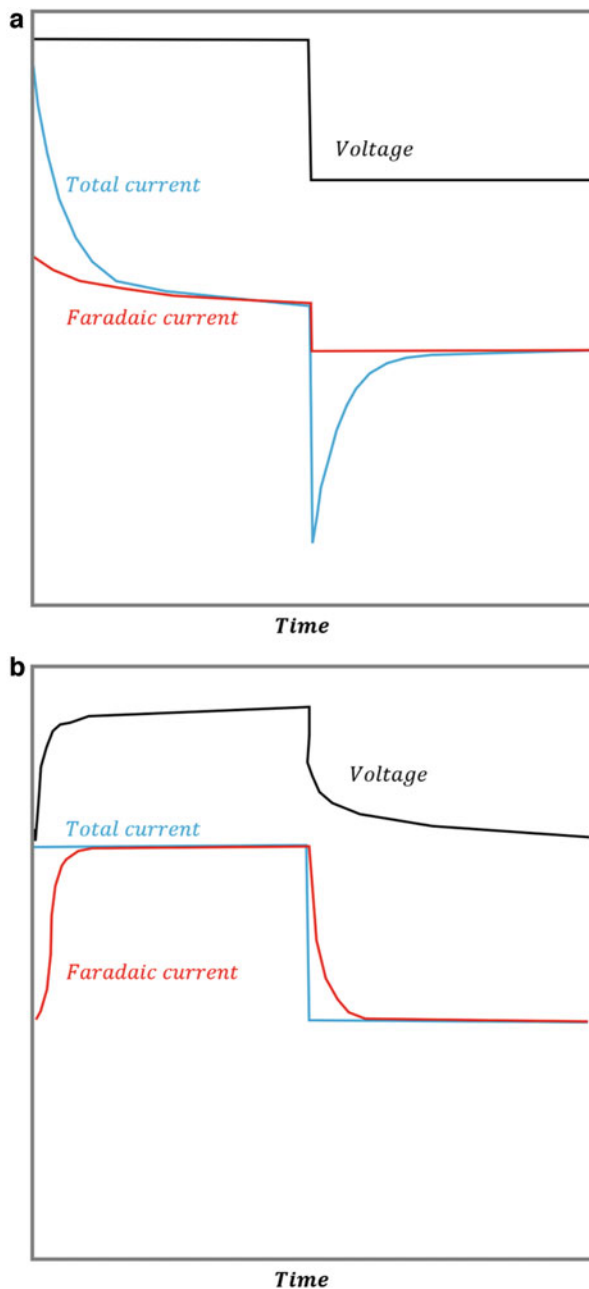
$$-\eta = \frac{RT}{F} i \left[\frac{2\sqrt{t}}{FA\sqrt{\pi}} \left(\frac{1}{C_0^*\sqrt{D_0}} + \frac{1}{C_R^*\sqrt{D_R}} \right) + \frac{i}{i_0} \right]$$

with η the overpotential and i_0 the exchange current. Additionally, when the current is off (0 A), the potential-time decay for a quasi-reversible reaction can be estimated as:

$$\eta(t) = \frac{\eta(t=0)}{\epsilon - \beta} \left[\epsilon \exp(\beta^2 t) erfc(\beta t) - \beta \exp(\epsilon^2 t) erfc(\epsilon t) \right]$$

With ϵ and β related to the relaxation times. Notice that the voltage relaxes to the reversible cell voltage. It was proposed a method to differentiate the capacitive current from the faradaic current when current pulses are applied to an electrochemical system. In this case, the ratio of the capacitive to total current density, h(y), is calculated as the numerical solution of the following equation:

$$\frac{1 - \exp\left[-\frac{1}{\psi} \int_0^x h(x)dx \right]}{1 - \exp\left[b - \frac{1}{\psi} \int_0^x h(x)dx \right]} = \sqrt{y} - \frac{1}{2} \int_0^x \left(\frac{h(x)dx}{\sqrt{y-x}} \sqrt{\frac{D_0}{D_R}} \right)$$

Where:

$$\exp(b) = \frac{C_0^*}{C_R^*}$$

$$\psi = \left(\frac{RT}{nF} \right) \left(\frac{4i_T C_D}{nFC_0^*\sqrt{\pi D_0}} \right)$$

The graphical representation of these equations for a current pulse with an off-current of 0 A is shown in Fig. 27b. In the beginning, the voltage increases linearly with time due to the charge of the EDL. Then, it increases with the square-root of time for the faradaic reaction. As in the voltage pulse case, the current starts mainly capacitive and then becomes faradaic. During the off period, the EDL is discharged by means of faradaic processes, which promotes a voltage decay.

There are different manners of comparing water electrolysis techniques. A simple way is to see at a constant voltage, what are the currents from each process. The one with the higher current is the most performing. Likewise, at constant current, the one with the lowest voltage is the best. Another way to compare different techniques is by the efficiency. At the same production rate, the one with the best efficiency is the greatest. Voltage efficiency is defined as:

$$\eta_{voltage} = \frac{E_{th}}{E_{cell}} = \frac{1.23V}{E_{cell}}$$

with Eth the theoretical voltage value (1.23 V for water electrolysis) and E_{cell} the cell voltage. Alternatively, efficiency can be calculated using the thermal neutral voltage:

$$\eta_{voltage,thermal} = \frac{1.48V}{E_{cell}}$$

Another way to define efficiency is by the energetic efficiency, defined as follows:

$$\eta_{energetic} = \frac{\dot{V}\Delta H}{P_{el}}$$

where V is the hydrogen production rate at standard conditions, ΔH is the heating value for hydrogen (lower or higher), and Pel is the consumed electric power. The lower heating value (LHV) is the energy released by the burn of hydrogen, considering water vapor as the only product and it is equal to 3.00 kW h/Nm^3. The higher heating value (HHV), on the other hand, considers liquid water as the only product and it is equal to 3.54 kWh/Nm. Using the Faraday law of electrolysis and the ideal gas law, one has an energetic efficiency equal to:

$$\eta_{energetic} = \frac{RT\Delta H}{zFP} \frac{i_{H_2}}{i_T} \frac{1}{E_{cell}}$$

with R the gas constant, T the standard temperature, z the stoichiometric electron coefficient (2 for hydrogen), F the Faraday constant, P the standard pressure, i_{H2} the current used for hydrogen production, i_T the total current, and E_{cell} the cell voltage. This first term is a constant. The second term is defined as Faraday efficiency and it is commonly 100% unless a parasitic reaction takes place. Considering no parasitic reaction, the energetic efficiency depends only on the cell voltage, as in the case of voltage efficiency.

Mass transport and capacitance effects in pulsed plating were evaluated. The authors claimed that after a circuit interruption, the current took some time to drop to zero because of the discharge of the EDL. Thus, if off-time was short enough that the current did not have time to decrease completely, the current would slightly fluctuate around an average value. In this case, pulsed electrolysis would be very similar to DC electrolysis. Assuming a linear concentration profile, the thickness of the pulsating diffusion layer can be expressed as:

$$\delta = \sqrt{2Dt_{on}\left(1 - \left(\frac{t_{on}}{t_{on} + t_{off}}\right)\right)}$$

with D the diffusion coefficient. It is independent of current density and of bulk concentration. Furthermore, the authors proposed that the time for the reactant concentration at the electrode surface to fall to zero is given by:

$$\tau = \frac{D(C_0 n F)^2}{2 i_p^2}$$

With i_p the pulse current. Finally, it was concluded that the depletion of reactants at the electrode surface can limit the rate of deposition and can cause powder formation. The previous two equations were obtained during plating, where there is the diffusion of metal ions in the electrolyte. In the case of water electrolysis, the effects of ion migration must be considered. Moreover, at the cathode during alkaline water electrolysis, it is difficult to talk about diffusion since the only reactant is the water solvent itself.

After other experiences, a model to calculate the current due to a triangular voltage pulse was proposed:

$$i_p(t) = i\_\mathrm{max} \exp(-kt)$$

where i_p is the actual pulse current, t the time, k a time constant, and the current peak value with:

$$i_{max} = \frac{E}{R_s}$$

And:

$$k = \frac{1}{R_s C_D}$$

If there is a succession of n pulses, the pulse current can be estimated as:

$$\frac{i_p}{i_{DC}} = 1 + \frac{i_{max}}{k \tau i_{DC}} [1 - \exp(-k\tau)]$$

with i_{DC} the DC current value and τ the pulse width. In their experiments, the pulsed current was two times greater than the DC current.

5.1   Inductive Pulses

The main idea of inductive pulsed water electrolysis is the application of a very high inductive voltage as compared to the equilibrium voltage, with the double layer storing and releasing energy during pulsed operation. This affects the bubble

behavior and changes the effective electrolyte resistance. With this method, the resulting current and voltage are not constant, but the power can be controlled by choosing the frequency and amplitude of the pulse in the first circuit. Consequently, this method can be classified as a power control method.

The time for the formation of the diffusion layer is estimated as:

$$t = \frac{1}{4D_0}\left(\frac{X}{X_{ad}}\right)^2 = \frac{\delta_{max}^2}{4D_0}$$

where D_0 is the diffusion coefficient, X_{ad} is the density of hydrogen ions on the cathode (cm^{-2}), X is the concentration of hydrogen ions in the bulk (cm^{-3}), and δ_{max} is the thickness of the diffusion layer. The time for the formation of a stable EDL was said to be several tens of milliseconds. The results have shown that at DC power, the increase in voltage also increases current and production rate but decreases the efficiency. Contrary to DC, in the pulsed power case, the production rate was decreased when the voltage at the secondary circuit was increased. In the case of relative low voltages (7.9 V and 9.7 V), the efficiency increased when increasing the pulse frequency (maintaining the pulse width at 300 ns). In the case of pulses with a voltage of 7.9 V and a frequency of 17 kHz, the efficiency and production rate were higher than DC at the same input power (2.6 V at 0.5 A).

5.2   Voltage Pulses

Pulse Width Modulation (PWM) in water electrolysis is based on a semiconductor switching element that promotes voltage pulses by cutting the circuit periodically. This is a way to control the amount of power delivered to an electrolysis cell. To illustrate this, an increase in the duty cycle increases the power delivered, even if the voltage is kept constant. This system is not ideal and presents some power dissipation. These losses can be due to switching or conduction losses. The latter is related to the nature of the switch, whilst the first has some other influencing variables such as control system, switching method, and power electronics circuitry. Among other things, it was stated that the equivalent circuit of a water electrolysis cell contains non-linear elements. Therefore, it was pointed out that the effect of applying other forms of voltage than DC may lead to a process improvement.

The way the average power consumption is calculated was as follows:

$$P = \sqrt{\frac{1}{T}\int_0^T V(t)^2} \cdot \sqrt{\frac{1}{T}\int_0^T i(t)^2 dt}$$

with V the cell voltage, i the current, and T the pulse period.
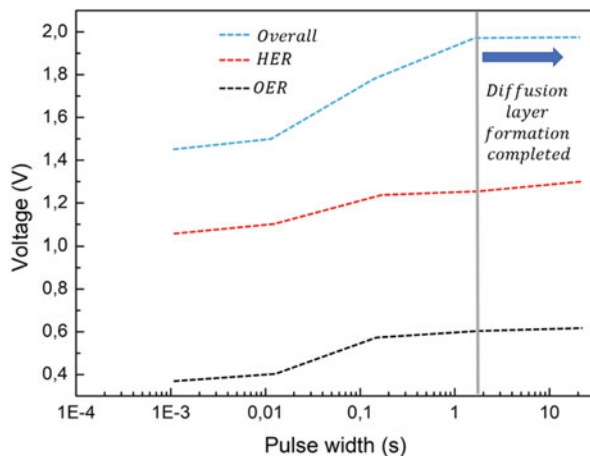
Fig. 28 Pulse width-cell voltage profile at a current density of 0.1 A.cm-2 for (black) oxygen evolution reaction at a nickel electrode and the reduction of the intermediate MnO electrode, thermodynamic cell voltage = 0.828 V; (red) hydrogen evolution reaction in metal hydride electrode and the oxidation of the MnO(OH) electrode, thermodynamic cell voltage = 0.402 V; (blue) and overall reaction i.g. sum of the two previous cell voltages, thermodynamic cell voltage = 1.229 V (blue)

5.3   Current Pulses

In pulsed electrolysis, the thickness of the diffusion layer is reduced, since it has not enough time to be completely formed and the reactants have time to diffuse back to the electrode surface, enhancing the efficiency of the process by a decrease in ohmic losses caused by mass transport. The higher the pulse frequency, the lower the thickness of the diffusion layer, explaining the observed increase in efficiency with frequency. The results can be seen in Fig. 28, which shows that for fixed currents, when on-time was lower than 2 s, the voltage was reduced. The authors explained that after this time, the diffusion layer was completely formed.

6   Conclusions

Water electrolysis is an important technique for hydrogen production to face energy crisis. In past decades, great efforts and breakthroughs have been made in designing and optimizing bifunctional electrocatalysts. The review summarizes the non-noble metal-based catalysts including metals, oxides, hydroxides, chalcogenides, phosphides, borides, nitrides, carbides and so on.

Some of them exhibit comparable and even superior water splitting performances to the benchmark noble metal based catalysts.

The optimizing strategies and the effects on the active sites and the intrinsic activities as well as on the performances are highlighted: (1) morphology engineering is utilized to expose more active sites; (2) conducting supports are used to improve the electrical conductivity and accelerate the transportation of electrons and ions; (3) multi-metal and defect engineering are implemented to fine tune the electronic configuration and states; (4) hetero-structures and/or interfaces are constructed to synergically boost water splitting performance. In practical applications, the combination of hybrid strategies is more effective in balancing OER and HER performances. Although gratifying developments have been made in electrocatalysts for overall water splitting, there is still some problems to be solved for potential applications in HER and OER.

Although DFT theory is a useful tool to give us understanding of the intermediates in reactions, the composites catalysts are becoming more complicated which become more difficult to identify the real active sites. There are generally two strategies to improve the catalytic activity of electrocatalysts: (1) increasing the number of active sites on a given electrode (e.g., through increased loading or improved catalyst structuring to expose more active sites per gram) or (2) increasing the intrinsic activity of each active site. Therefore, identification of the real active sites is one crucial thing for designing bifunctional catalysts. Advanced techniques such as scanning probe microscopy, ambient pressure X-ray photoelectron spectroscopy, soft X-ray absorption spectroscopy and other in situ techniques may provide potential to fathom the natural active sites.

Long-term stability. The overall water splitting is often conducted in alkaline or acidic aqueous medium, which may lead the surface polarization of catalysts. To achieve the extension from academic studies to industrial production, it is important to prevent catalysts from corrosion in the electrolyte in order to maintain the high activity and stability. Rational strategies could be useful for mitigating polarization of electrode.

To date, many high-performance HER, OER, and overall water splitting catalysts have been fabricated, but there is much room for improvement beyond laboratory environment. It is also vital to develop commercial electrocatalysts which offer both cost-effective and highly performance.

The strategies, such as, coating, encapsulating, anchoring, could be useful to mitigate the corrosion and structural collapse in the electrolyte during water splitting.

To date, non-noble transition metal-based water splitting mainly work well under alkaline and near neutral conditions due to their rapid dissolution in acidic solution. However, water splitting especially OER catalysts in acid have demonstrated critical advantages in the widespread application of overall water splitting devices. So far, the catalysts which perform better in the acidic condition are still noble metals or noble metal-based materials. High corrosion resistance in acidic condition is one of the basic requirements for designing catalysts. Different from the most transition metals and metal oxides, noble metals and metal sulfides/phosphides are usually corrosion-resistant in the acid. Their hybrid composites are most preferred. In addition, oxygen vacancies could also be adopted to improve the water splitting performances in acidic condition.

References

Al-Akraa IM, Asal YM, Khamis SD (2018) Assembling of NiOx/MWCNTs-GC anodic nanocatalyst for water electrolysis applications. Int J Electrochem Sci 13(10):9712–9720. https://doi.org/10.20964/2018.10.01

Ali A, Long F, Shen PK (2023) Innovative strategies for overall water splitting using nanostructured transition metal electrocatalysts. Electrochem Ener Rev 6(1):1. https://doi.org/10.1007/s41918-022-00136-8

Cai Z, Wang P, Zhang J (2023) Dual-purpose nickel-iron layered double hydroxides by controlled lanthanide and phosphide incorporation for promoting overall water splitting efficiency. J Alloys Compd 933:167743. https://doi.org/10.1016/j.jallcom.2022.167743

Cavaliere P (2022) Hydrogen assisted direct reduction of iron oxides. https://doi.org/10.1007/978-3-030-98056-6

Chu Y, Wang D, Shan X (2022) Activity engineering to transition metal phosphides as bifunctional electrocatalysts for efficient water-splitting. Int J Hydrog Energy 47(92):38983–39000. https://doi.org/10.1016/j.ijhydene.2022.09.070

Doan H, Kendrick I, Blanchard R (2021) Functionalized embedded monometallic nickel catalysts for enhanced hydrogen evolution: performance and stability. J Electrochem Soc 168(8):084501. https://doi.org/10.1149/1945-7111/ac11a1

Ekspong J, Gracia-Espino E, Wagberg T (2020) Hydrogen evolution reaction activity of heterogeneous materials: a theoretical model. J Phys Chem C 124(38):20911–20921. https://doi.org/10.1021/acs.jpcc.0c05243

Exner KS (2023) Implications of the M-OO··OO-M recombination mechanism on materials screening and the oxygen evolution reaction. J Phys Energy 5(1):014008. https://doi.org/10.1088/2515-7655/aca82a

Gebremariam GK, Jovanović AZ, Dobrota AS (2022) Hydrogen evolution volcano(es)—from acidic to neutral and alkaline solutions. Catalysts 12(12):1541. https://doi.org/10.3390/catal12121541

Hoisang W, Sakaushi K (2022) Key criteria for next-generation dimensionally stable electrodes towards large-scale green hydrogen production by water electrolysis. Curr Opin Electrochem 36:101136. https://doi.org/10.1016/j.coelec.2022.101136

Hota P, Das A, Maiti DK (2023) A short review on generation of green fuel hydrogen through water splitting. Int J Hydrog Energy 48(2):523–541. https://doi.org/10.1016/j.ijhydene.2022.09.264

Iqbal S, Ahmed K, Ayub K (2023) Transition metals incorporated on phosphorene sheet as cost-effective single atom catalysts for hydrogen evolution reaction: a DFT study. Comput Theor Chem 1220:113998. https://doi.org/10.1016/j.comptc.2022.113998

Karthick K, Mansoor Basha AB, Sivakumaran A (2020) Enhancement of HER kinetics with RhNiFe for high-rate water electrolysis. Catal Sci Technol 10(11):3681–3693. https://doi.org/10.1039/D0CY00310G

Kolle-Görgen E, Fortunato G, Ledendecker M (2022) Catalyst stability in aqueous electrochemistry. Chem Mater 34(23):10223–10236. https://doi.org/10.1021/acs.chemmater.2c02443

Lamy C, Millet P (2020) A critical review on the definitions used to calculate the energy efficiency coefficients of water electrolysis cells working under near ambient temperature conditions. J Power Sources 447:227350. https://doi.org/10.1016/j.jpowsour.2019.227350

Liu Q, Ranocchiari M, Van Bokhoven JA (2022a) Catalyst overcoating engineering towards high-performance electrocatalysis. Chem Soc Rev 51(1):188–236. https://doi.org/10.1039/D1CS00270H

Liu H, Wang P, Jiang J (2022b) Construction of stable Mox Sy /CeO2heterostructures for the electrocatalytic hydrogen evolution reaction. Phys Chem Chem Phys 24(8):4891–4898. https://doi.org/10.1039/D1CP05466J

Liu F, Gao Y, Yu D (2023) Ni-ZIF-8@ZIF-67-derived bimetallic doped Pt-based carbon catalyst for hydrogen evolution reaction. J Electrochem Ener Conv Stor 20(2):021006. https://doi.org/10.1115/1.4054647

Rocha F, de Radiguès Q, Thunis G, Proost J (2021) Pulsed water electrolysis: a review. Electrochim Acta 377:138052. https://doi.org/10.1016/j.electacta.2021.138052

Seenivasan S, Seo J (2023) Inverting destructive electrochemical reconstruction of niobium nitride catalyst to construct highly efficient HER/OER catalyst. Chem Eng J 454:140558. https://doi.org/10.1016/j.cej.2022.140558

Sun L, Luo Q, Dai Z et al (2021) Material libraries for electrocatalytic overall water splitting. Coord Chem Rev 444:214049. https://doi.org/10.1016/j.ccr.2021.214049

Tao M, Azzolini JA, Stechel EB et al (2022) Review – engineering challenges in green hydrogen production systems. J Electrochem Soc 169(5):054503. https://doi.org/10.1149/1945-7111/ac6983

Taylor HS (1925) A Theory of the cathalitic surface. https://doi.org/10.1098/rspa.1925.0061

Wan H, Long G, Yang S (2022) Real-time monitoring of hydrogen production by water electrolysis using a tapered polarization-maintaining optical fiber Mach–Zehnder Interferometer. Ener Technol 10(10):2200349. https://doi.org/10.1002/ente.202200349

Wang X, Zhou M, Zhang F (2021) Redox targeting of energy materials. Curr Opin Elctrochem 29:100743. https://doi.org/10.1016/j.coelec.2021.100743

Wang R, Ohashi M, Ishida M (2022) Water transport analysis during cathode dry operation of anion exchange membrane water electrolysis. Int J Hydrog Energy 47(97):40835–40848. https://doi.org/10.1016/j.ijhydene.2022.09.181

Wang C, Humayun M, Debecker DP (2023) Electrocatalytic water oxidation with layered double hydroxides confining single atoms. Coord Chem Rev 478:214973. https://doi.org/10.1016/j.ccr.2022.214973

Wei S, Xing P, Tang Z (2023) Spindle-shaped cobalt-doped iron phosphide anchored on three-dimensional graphene electrocatalysis for hydrogen evolution reactions in both acidic and alkaline media. J Power Sources 555:232414. https://doi.org/10.1016/j.jpowsour.2022.232414

Wu C, Fang Q, Liu Q (2017) Engineering interfacial charge-transfer by phase transition realizing enhanced photocatalytic hydrogen evolution activity. Inorg Chem Front 4(4):663–667. https://doi.org/10.1039/C6QI00596A

Xu S, Wu Q, Lu B-A (2023) Recent advances and future prospects on industrial catalysts for green hydrogen production in alkaline media. Wuli Huaxue Xuebao/Acta Phys-Chim Sin 39(2):2209001

Ye F, Ma X, Cao Y (2023) Heterogeneous layered multiple transition metal composite electrocatalysts with controlled composition for hydrogen production. Int J Hydrog Energy 48(5):1733–1746. https://doi.org/10.1016/j.ijhydene.2022.10.065

Yoo S, Kim Y, Yoon Y (2021) Encapsulation of Pt nanocatalyst with N-containing carbon layer for improving catalytic activity and stability in the hydrogen evolution reaction. In. J Hydrog Energy 46(41):21454–21461. https://doi.org/10.1016/j.ijhydene.2021.03.225

Zhang J, Dang J, Zhu X (2023) Ultra-low Pt-loaded catalyst based on nickel mesh for boosting alkaline water electrolysis. Appl Catalys B Env 325:122296. https://doi.org/10.1016/j.apcatb.2022.122296

Zhao M-J, He Q, Xiang T (2023) Automatic operation of decoupled water electrolysis based on bipolar electrode. Renew Energy 203:583–591. https://doi.org/10.1016/j.renene.2022.12.083

Hydrogen and Energy Transition

1 Introduction

CO_2 emissions continue to grow despite the efforts to reduce greenhouse emissions to reduce the global warming. This is mainly due to the continuous increase in gas and oil consumption in all the human civil and industrial activities. The global CO_2 emissions increased from 36,153 in 2017 to 37,016 Mt in 2019 (Fig. 1). This corresponds to an increase of 1.1% per year, while the increase related to the energy production increased by over 1.7% in the same period. In addition, we should consider that the world population increased by almost 5 times from 1900 to 2021 and the global CO_2 emissions increased by 2.5 times in the last 30 years. This is mainly due to the energy consumption that grows by 2% from the 60's to 2018 and by 2.2% in the last year (Fig. 2).

In Fig. 3 they are shown the levels of CO_2 emissions from gas, oil and coal utilization in 2018.

An extensive shift in the global energy system is necessary and all the energy sectors should find ways to reduce CO_2 emissions. The industrial sector accounts for the largest share of global Total Final Energy Consumption (TFEC) among all sectors (almost 40%). Consequently, the mitigation of industrial CO_2 emissions has a crucial role in meeting climate targets. Given a continuously increasing demand for industrial products, the key for industrial decarbonization is decoupling its production from the produced CO_2 emissions. For achieving this goal it's necessary energy and material efficiency strategies, such as adoption of best available technologies and improved scrap collection and reprocessing rates (Luh et al. 2020).

Other relevant measures are switching to lower-carbon fuels and feedstocks, such as natural gas as substitution for coal, and future adoption of Carbon Capture and Storage (CCS) in industrial processes. In addition, more recent literature suggests increased industrial electrification as a suitable option for decarbonization.
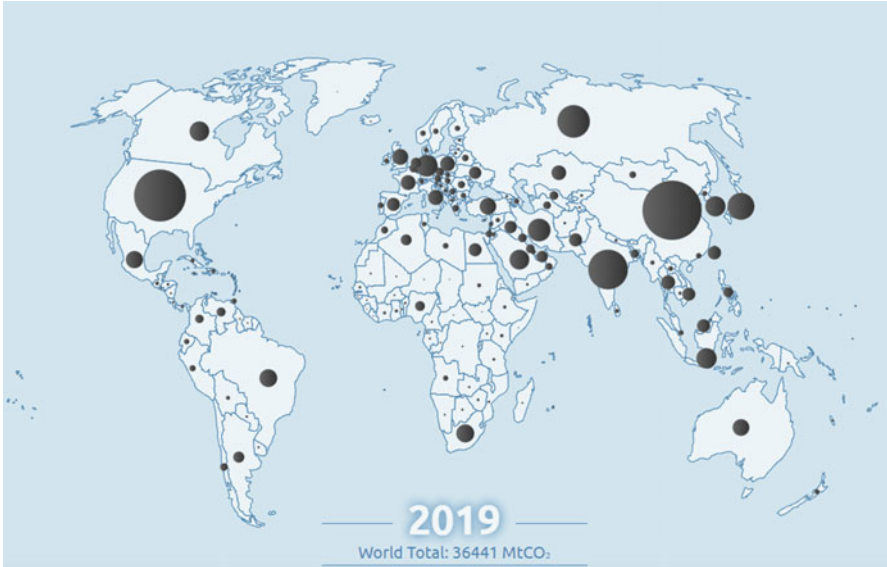
Fig. 1 Carbon dioxide global emissions (http://www.globalcarbonatlas.org/)

Fig. 2 Energy consumption over the time
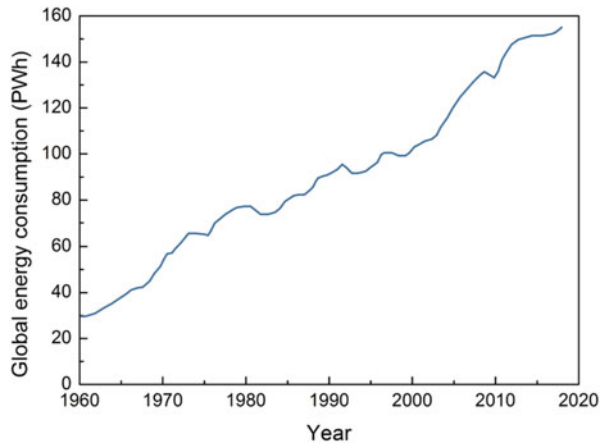
This option has received increasing attention due to the possibility of generating electricity from low-carbon energy sources, such as renewables, nuclear energy, and fossil fuels with integrated CCS.

In this scenario, the renewable energy sources growth in each world region in shown in Fig. 4 with a net increase of 7% from 2017 to 2018.

The renewable source by technology is shown in Fig. 5.

Anyway, this growth is not sufficient to reduce the overall greenhouse emissions in order to reduce the global warming. As a matter of fact, Fig. 6 shows the historical expansion of electricity generation technologies.

Fig. 3 Carbon dioxide emissions from fossil fuels in 2018
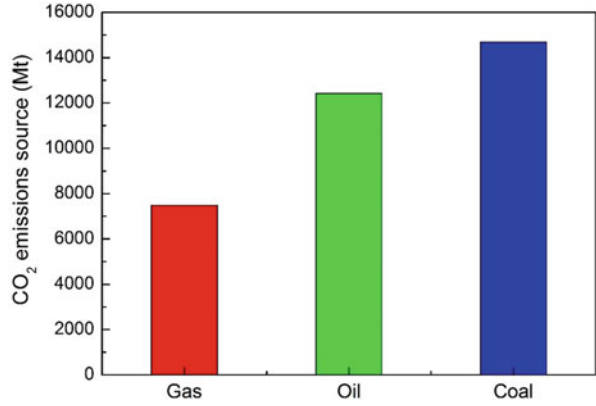
Fig. 4 Renewables by region in 2018
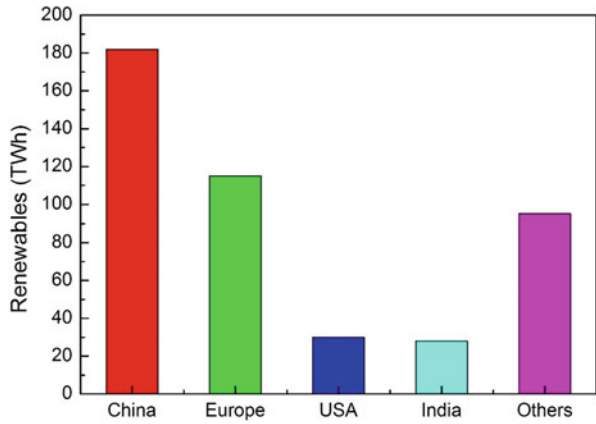
Fig. 5 Renewables by source in 2018
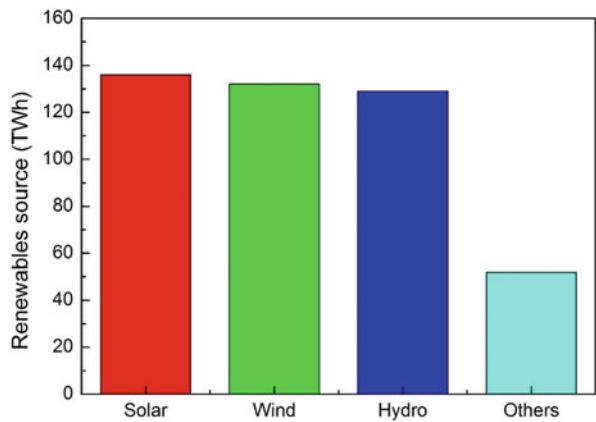
Fig. 6 Global electricity
generation per year
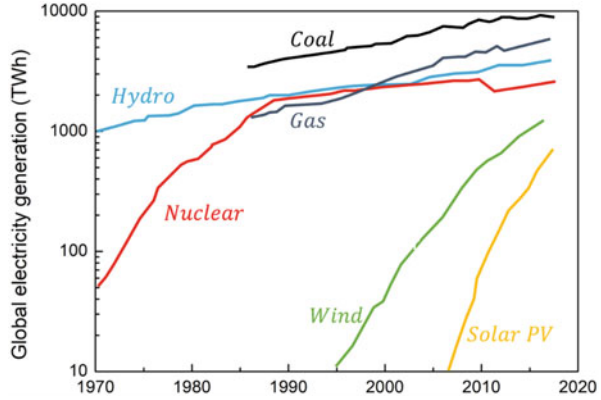
Fig. 7 Wind and solar
electricity production
forecasts by 2050
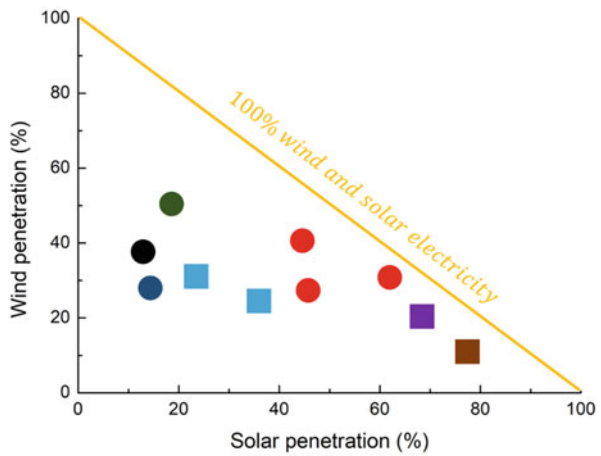
Global electricity generation from solar PV is an order of magnitude lower than
conventional technologies but it shows a very rapid progression. The small unit size
and low unit investment have enabled a much faster scaling through replication
compared with other technologies. Today, solar source provides the cheapest elec-
tricity in many parts of the world and the milestone of attaining a cumulative
capacity higher than 1 TW is expected before 2023 (Victoria et al. 2021).

Partial-equilibrium models using annual resolution also tend to result in low solar
contributions. For example, the model, which supports the analyses of policy options
for the European Commission, estimates that solar PV supplies less than 20% of
electricity demand in all the cost-optimal 1.5 and 2 °C scenarios for 2050. This is
well below the cost-optimal solar penetration obtained by other energy models
including hourly resolution (Fig. 7).

A major transformation and redesign of the global energy system is required
towards decarbonization and to achieve the Paris Agreement targets. This Grand
Transition is a complex pressing issue where global joint efforts and system solu-
tions are essential and hydrogen is one of them.

Fig. 8 Hydrogen chemical element
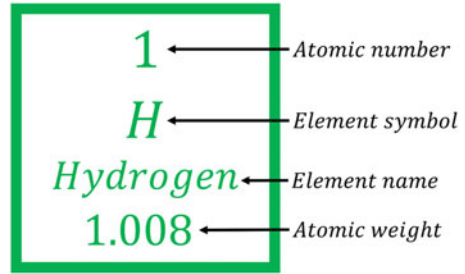
Hydrogen has the potential to be a powerful effective accelerator towards a low-carbon energy system, capable of addressing multiple energy challenges: from facilitating the massive integration of renewables and decarbonization of energy production, to energy transportation in a zero-carbon energy economy, to electrification of end uses (World Energy Council 2018).

Hydrogen is believed to be the energy vector and the fuel of the future (Fig. 8).

Hydrogen discovery append at the beginning of 1500 when Paracelsus let to react iron with sulfuric acid. Two hundred years later, Myelin reported this gas explosive power. Boyle was the first, in the eighteenth century, to synthesize the gas from the reaction of iron with various acids. Finally, in 1776, Cavendish identified hydrogen as a unique element presenting it to the Royal Society of London. Then Lavoisier named it as hydrogen in 1783. The first example of hydrogen production from electrolysis is due to Nicholson and Carlisle in 1800. It was liquified in 1898 by Dewar. Its famous important use was due to Zeppelin in 1900 to sustain his airship.

Hydrogen is considered a very effective instrument to vehicle the low-carbon energy system because of its capabilities to address many energy challenges from facilitating the massive integration of renewables and decarbonization of energy production, to energy transportation in a zero-carbon energy economy, to electrification of end uses. This is due to the fundamental capability to burn without dangerous emissions.

Hydrogen produced from renewable electricity through Power-to-Hydrogen can facilitate the integration of high levels of variable renewable electricity into the energy system.

An electrolyser is a device that splits water into hydrogen and oxygen using electricity (Fig. 9).

When electricity is produced from renewable energy sources, electrolytic hydrogen can be considered to be green. At the same time, electrolyzer can help integrate renewable electricity into power systems, as their electricity consumption can be adjusted to follow wind and solar power generation. Green hydrogen then also becomes a carrier for renewable electricity (Proost 2020).

The versatility of hydrogen synthesis (Fig. 10) makes it available for many industrial applications.

Given the different available technologies, 95% of the hydrogen used today is produced from fossil fuels while only the remaining 5% is from other alternative

Fig. 9 Hydrogen and oxygen bubbles formation
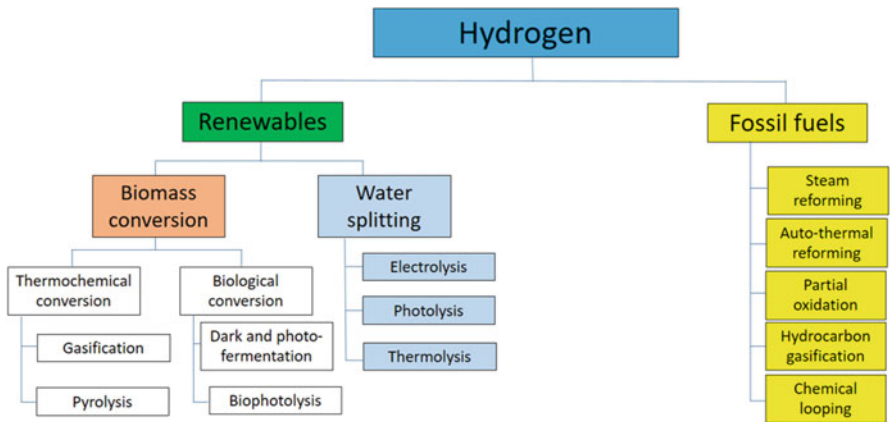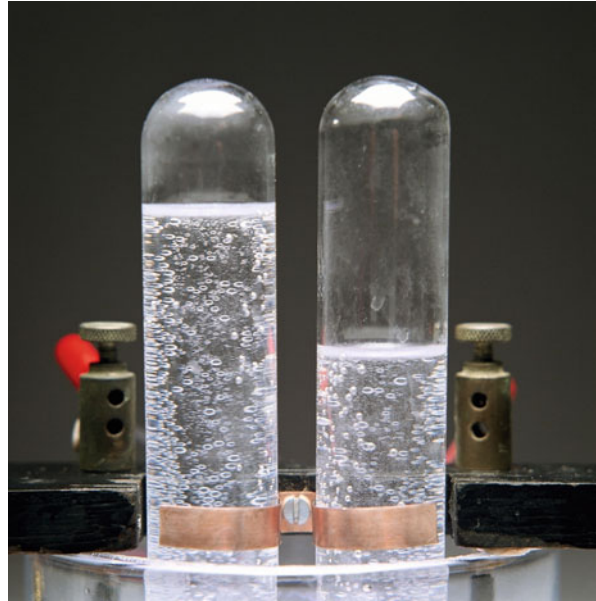
Fig. 10 Available technologies for hydrogen production

sources including biomass. Steam reforming of gases is employed to produce 60% of hydrogen worldwide, this is accompanied with the emission of 30 million tons of CO_2. So even if the direct use of hydrogen is carbon-free, its synthesis can be accompanied with huge greenhouse gases emissions (Okolie et al. 2021).

As a matter of fact, Hydrogen ironmaking is based on the fundamental substitution of carbon with hydrogen to reduce iron ores (Sun et al. 2020). This is considered the most promising frontier in the development of a sustainable future steel production (Tang et al. 2020).

In 2020 Hydrogen has been the protagonist of a considerable development. It is fast becoming the center of the energy transition through the climate neutral society in 2050 from innovative niche technology.

It will become a crucial energy vector and the other leg of the energy transition – alongside renewable electricity – by replacing coal, oil and gas across different segments of the economy (Fig. 11).

The increasing role of renewables in the power sector has raised the need of complementary technologies to balance the grid, and, understanding that electricity cannot be stored easily, allows an opportunity for hydrogen technologies.

The situation of hydrogen production in Europe is shown in Fig. 12.

Hydrogen technologies can play a significant role in distributing energy in a low carbon energy world.

Critical to the cost, energy use and emissions is the delivery. The choice of hydrogen delivery mode, such as road transport or pipelines, depends upon specific geographic and market characteristics.

Hydrogen can be converted back to electricity to provide constant power when the renewable source is unavailable, helping stabilize the electrical grid and, in addition, the excess can be sold for a variety of other purposes. Hydrogen is a strategically important commodity, both as a primary feedstock to the refining, fertilizer, and chemical industries and as a by-product of other industrial processes. Hydrogen can be injected into the natural gas grid to support the distribution of a clean gas at the same time as reducing emissions and stranded assets.

To stabilize electric grids is required to control electric flow to the output of renewable energy power generators.

Controlling flow of electricity on electricity output from renewable energy power generators is required to stabilize electric grids. To make effective use of renewable energy to avoid output control, however, electricity storage facilities are required (Abdalla et al. 2018), in this view storage batteries may play a key role in the immediate future. As renewable energy expands with the necessity of output controls as large-scale and long-term power-to-gas systems using hydrogen will increase.

To achieve the decarbonization of the transport sector a social change, and technological modifications are needed. Zero-emission vehicles (ZEV), fuel cell electric vehicles (FCEV) and battery electric vehicles (BEV) are being progressively introduced for this purpose. Today, several studies recognize an important contribution of hydrogen mobility to decarbonize the transport sector and to create extra environmental benefits and number of countries adopt FCEV technology.

Hydrogen shows more energy density per unit weight and unit cubic volume than lithium-ion and other storage batteries. Therefore, fuel cell vehicles are preferred to other zero emission vehicles in large vehicles for long-range transportation. The improvement of fuel cell efficiency and output density will increase the maximum driving distance and allows to make smaller fuel cell.
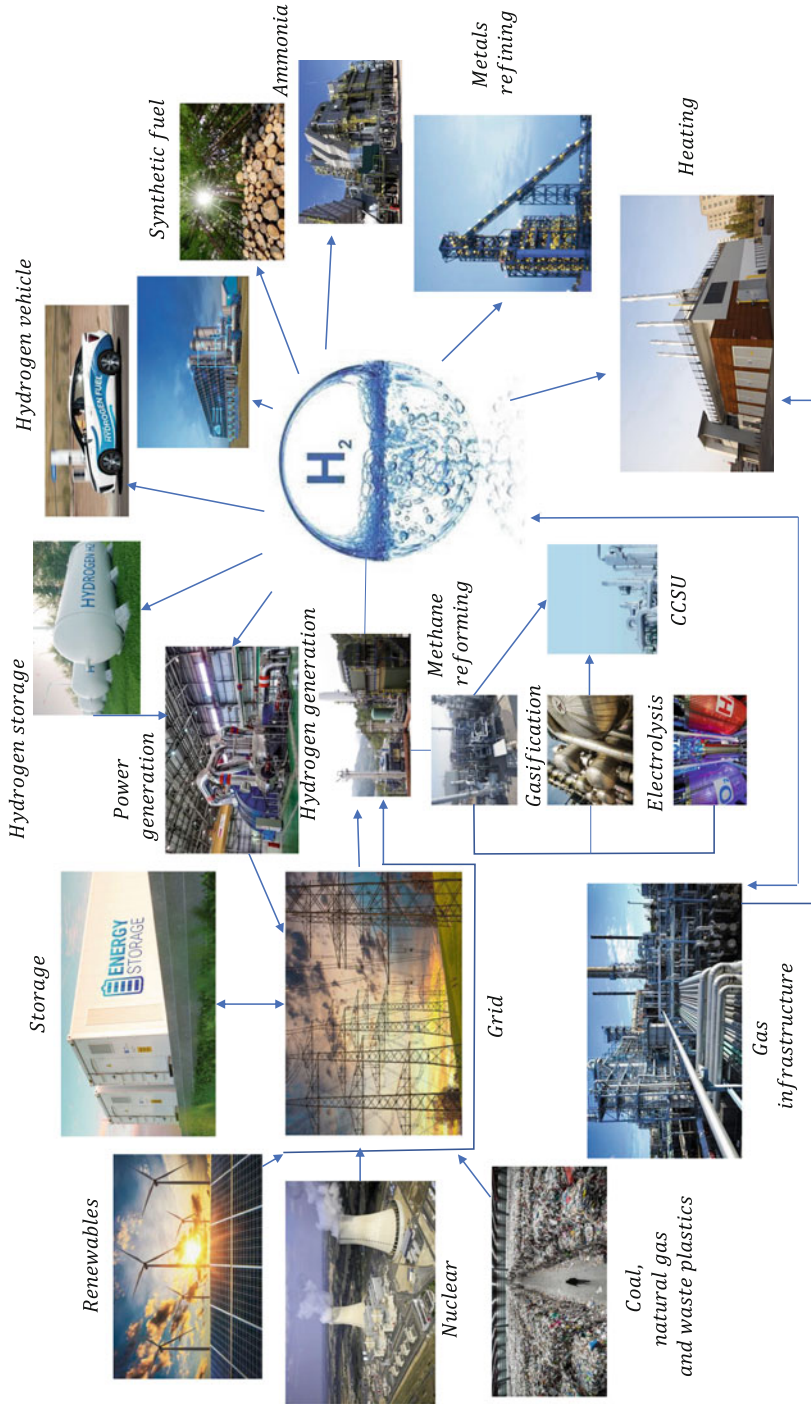
Fig. 11 Hydrogen production and utilization

Fig. 12 Geographic distribution of identified industrial hydrogen production facilities

Battery electric vehicles (BEVs) with lithium-ion batteries are easier to produce but show inferior maximum driving distance and charging time compared to FCVs. With the introduction and enhancement of environmental regulations BEVs are expected to spread rapidly.

Hydrogen as an energy carrier could offer a climate-friendly solution to decarbonizing industry (Birat 2020). It is used in the production of carbon steels, special metals and semiconductors in the steel and electronics industries. Hydrogen is used to process crude oil into refined fuels and that's why hydrogen demand is increasing.

Renewable hydrogen can simplify the value chain for many industries and can be used as a feedstock for production of methane, clean chemicals, and fertilizers. Synthetic methane can be produced through a power-to-methane process that can be injected into the natural gas grid. In addition, hydrogen is widely used as a feedstock for production of numerous chemicals that are widely used in the industry such as ammonia.

Ammonia (NH_3): (1) shows an higher hydrogen density than other carriers (1.5 times as high as liquefied hydrogen) and is available through smaller-scale and cheaper infrastructure development, (2) is produced from natural gas and relatively cheaper, and (3) is available for existing commercial supply chains. Ammonia can be directly used for power generation without any dehydrogenation process and emits no CO_2 during combustion.

To achieve the decarbonization target hydrogen can be used for the heating of the building as fuel or in specific technology, or a combination of both, offering high efficiency in heat and power generation.

Like natural gas, hydrogen can be handled as fuel. Fuel cell technologies that efficiently generate electricity and heat from hydrogen can be used to reduce carbon in various areas including power generation, transportation, industrial processes, and heat use.

Supply and adjustment capacity of natural gas power generation is indispensable for renewable energy power generation expansion. However, hydrogen power generation can work in the same way as natural gas power generation and may become a leading option to reduce carbon in fossil power generation in a view of reducing costs in the future.

Hydrogen can be combined with CO_2 to produce methane in the so-called methanation process. Methane has great potential as an energy carrier for (1) the effective utilization of existing energy supply infrastructure (including city gas pipes and LNG power plants) and (2) low-carbon heat use.

Conditions for utilizing methane from CO_2-free hydrogen include the procurement of massive amounts of CO_2-free hydrogen at low cost, the presence of large-scale CO_2-emitting sources and the availability of existing LNG infrastructure.

Hydrogen power generation, such as natural gas power generation, is expected to provide to regulate power supply source and to increase generation capacity not only for electricity production. Therefore, hydrogen power generation will become the principal actor in reducing carbon emissions over the medium to long term while working as a regulated power supply and backup power source required for expanding renewable energy. Hydrogen-based power generation is the most important application that should be promoted in conjunction with international supply chain development because of the massive amount of hydrogen that the application consumes.

Hydrogen can be used in conjunction with natural gas for power generation and will initially be used mainly for existing natural gas power plants and for small cogeneration systems to promote hydrogen diffusion.

Long-term electricity storage will be important for using massive renewable energy oversupply without output control. For this reason, hydrogen will be effective for storing energy on a large-scale, long-term basis over multiple seasons.

In this way, hydrogen as along with renewable energy is expected to play a key role in reducing carbon in the electricity system.

Hydrogen has long been used across several industries, including the oil & gas industry where hydrogen is used in a process called hydrocracking, used to convert crude heavy petroleum extracts into lighter, usable forms of fuel. However, the developments leading to use of hydrogen as a transportation fuel, large-scale energy storage medium or in so-called power-to-gas applications to provide a clean and viable energy source to power vehicles or to provide power and heat for households and larger buildings is the potential game-changing solution. Hydrogen derived from water is heralded as an enabler of the Grand Transition into cleaner future (Olabi et al. 2021).

2   The Energy Carrier of the Future

Hydrogen will be the leading actor in the climate neutral economy, in the role of crucial energy vector and the other leg of the energy transition alongside renewable electricity replacing coal, oil, gas and conventional hydrogen in various economy segments. Renewables soon will dominate the system, in this scenario, hydrogen will be a contribute to enable sectoral integration. As a direct product from renewable energy production, hydrogen can enable the transition to renewable sources by providing a mechanism to flexibly transfer energy across sectors, time, and place in a more circular energy system. In addition, hydrogen is a versatile energy carrier (Fig. 13) and strategic value chain that is key to the decarbonization of heavy industries.

Furthermore, hydrogen can be seasonally stored and transported cost-effectively over long distances, largely using the existing natural gas infrastructure. Beyond the potential of hydrogen production from renewable and low carbon sources there is the ability to store renewable energy as hydrogen during peak of production. That help the reduction of renewable electricity, bringing flexibility to the power sector, etc., under demand-response schemes, and efficiency to the functioning of the future energy system.

Hydrogen is an energy carrier, which means that its role is like that of electricity (Reddy et al. 2020). Both hydrogen and electricity can be produced by various energy sources and technologies. Both are versatile and can be used in many different applications. From the use of either hydrogen or electricity there is no production of greenhouse gases, particulates, sulphur oxides or ground level ozone. If the hydrogen is used in a fuel cell, it emits only water as product with energy. However, both hydrogen and electricity can have a high CO_2 intensity upstream if produced from fossil fuels such as coal, oil or natural gas.

Fig. 13 Hydrogen energy
carrier
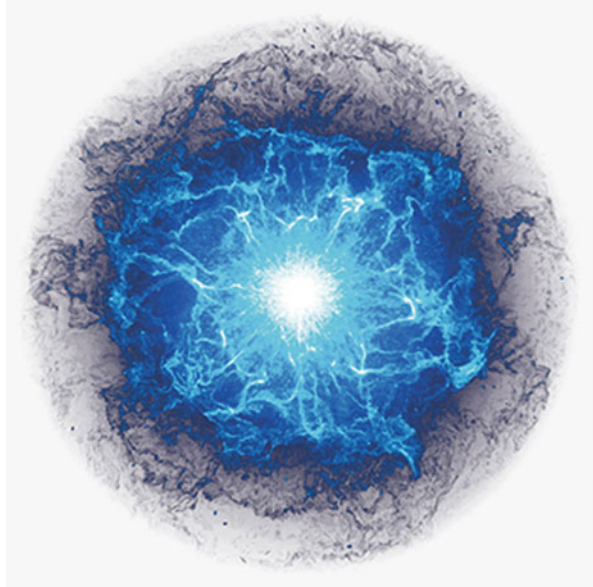
The crucial difference between hydrogen and electricity is that hydrogen is a chemical energy carrier, composed of molecules and not only electrons. This distinction upholds all the reasons why hydrogen might overtake electricity in some situations (and vice versa).

One of the strengths of chemical energy is that it can be stored and transported in a stable way, like nowadays is done with coal, oil, natural gas and biomass.

Molecules can be stored for a long period and thanks to the molecular nature of the hydrogen, it can be combined with other elements, like carbon and nitrogen, to form hydrogen-based fuels easy to handle and it can be used as feedstock to reduce emission in industry; hydrogen can be transported across the sea in ships, burned to produce high temperatures and used in existing infrastructure and business models design around fossil fuels.

The combustion products of any type of fuels are generally: water, CO_2 and nitrogen. The hydrogen combustion product is only water. The hydrogen cycle is analogous to the natural carbon cycle, but no carbon is involved. In contrast to biomass, no living matter is required; the disadvantage is that in ambient conditions hydrogen is a gas (Fig. 14).

When an energy carrier, including fossil fuels, is produced, converted or used it incurs an efficiency loss. In the case of hydrogen, these losses can be accumulated in the value chain. Converting electricity to hydrogen, shipping it, storing it and then converting it into electricity again in a fuel cell cost 30% of the initial electricity input. This makes hydrogen more expensive than electricity, or the natural gas used to produce it. It is also desirable to reduce the conversions number between energy carriers in any value chain. Considering zero energy supply constraints and evaluating fixed CO_2 emissions, efficiency can be considered ad an economic issue in the
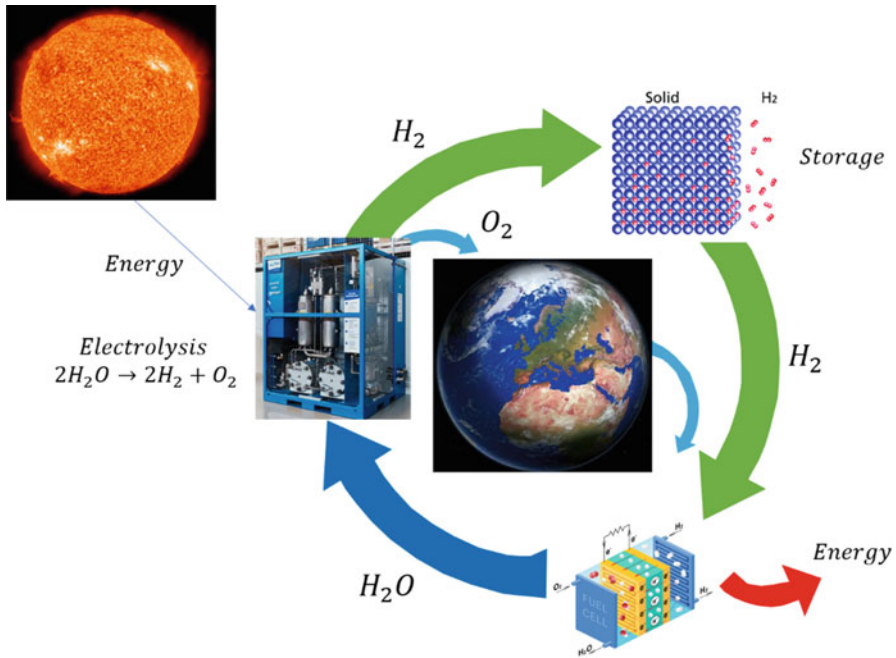
Fig. 14 Hydrogen cycle

entire value chain. This is important because hydrogen can be used with higher efficiency in certain applications, and it could be produced without greenhouse emissions.

Hydrogen can be used in its pure form as an energy carrier or as an industrial raw material. It can also be combined with other elements to create hydrogen-based fuels and feedstocks, both of them produced using hydrogen from any source (electricity, biomass, fossil fuels) and can be used in any applications, as engines, turbines and chemical processes, for example: production of derivative molecules such as methane, synthetic liquid fuels and methanol, all of these require carbon alongside hydrogen; also ammonia, which can be used as a chemical feedstock or as a fuel, and it is made combining hydrogen and nitrogen.

Power-to-X is a term used for the conversion of electricity to other energy carriers or chemicals, through hydrogen produced by electrolysis of water. The "X" stands for any resulting fuels, chemicals, power, or heat. For example: power-to-gas refers to the production of electrolytic hydrogen itself or also to synthetic methane produced from electrolytic hydrogen combined with CO_2. Sometimes hydrogen-based fuels that integrate electrolytic hydrogen are referred as "electro-fuels", or "solar fuels" if the power come from solar energy.

3   Physical and Chemical Properties

Hydrogen is the first element in the periodic table with the atomic number 1. It is the lightest and most abundant element in the universe representing 75 mass% or 90 vol % of all matter. On Earth, hydrogen is found in compound with almost every other element (just think about water: the hydrogen content is in the 1014 t order in the total water supply of the world). Hydrogen exists also as a free element in the atmosphere, but less than 1 ppm (by volume).

Free ionic hydrogen is more reactive than molecular hydrogen, the non-polar-covalent compound of two hydrogen atoms. In 1776, Henry Cavendish identified hydrogen as a distinct species. It was given the name 'water maker' by Lavoisier 7 years later, who proved that water was composed of hydrogen and oxygen.

Hydrogen, with a standard atomic mass of 1.0078225 u, has three naturally occurring isotopes. The most common hydrogen isotope is the stable protium (1H, H) with an abundance in nature of more than 99.98%. The second isotope is the stable deuterium (2H, D) or heavy hydrogen discovered in 1932 by Urey. Deuterium has a natural fraction of 0.014% with physical and chemical properties slightly different from 1H. Nearly all D in natural hydrogen is in combination with hydrogen atoms, the diatomic HD with a fraction of 0.032% in natural hydrogen; the existence of molecular D is highly improbable. The third hydrogen isotope is the radioactive tritium (3H, T) with a half-life of 12.3 a, discovered in 1934 by Rutherford. But also, the short lived isotopes 4H, 5H, and 7H have been synthesized in the meantime.

In these years, to refer to different type of source of hydrogen colors was used: "black" for hydrogen produced from coal, "grey" from natural gas and "brown" from lignite; "blue" is used for hydrogen produced from fossil fuels with reduced CO_2 emission, using CCU (Carbon Capture Utilization); "green" is referred to hydrogen produced from renewable energies. No color were associated to biomass, nuclear or other varieties of grid electricity because of the variability on the environmental impacts depends on energy source, region and type of CCU applied.

Hydrogen contains more energy per unit of mass than natural gas or gasoline, making it attractive as a transport fuel (Table 1). However, hydrogen has low energy

Table 1 Physical properties of hydrogen (IEA 2019)

Property	Hydrogen	Comparison
Density (gas)	0.089 (kg/m^3)	1/10 of NG
Density (liquid)	70.79 (kg/m^3)	1/6 of NG
Boiling point	−252.76 °C	90 °C below NG
Energy per unit of mass (LHV)	120.1 MJ/kg	3× gasoline
Energy density	0.01 MJ/L	1/3 of NG
Specific energy	8.5 MJ/L	1/3 of NG
Flame velocity	346 cm/s	8× CH$_4$
Ignition range	4–77% by volume	6× CH$_4$
Autoignition temperature	585 °C	220° for gasoline
Ignition energy	0.02 MJ	1/10 of CH$_4$

density per unit volume because of its lightness, indeed hydrogen is the lightest element. This means that compared with other fuels, to have the same energy of other fuel larger volumes must be used. This can be achieved, for example, using larger or faster-flowing pipelines and larger storage tanks. Hydrogen can be compressed, liquefied, or transformed into hydrogen-based fuels that have a higher energy density, but this (and any subsequent re-conversion) led to losses in term of efficiency.

In a wide temperature range and even at high pressure (up to about 10 MPa) hydrogen can be considered an ideal gas. At standard temperature and pressure conditions, it is a colourless, odourless, tasteless, non-toxic, non-corrosive, non-metallic diatomic gas, which is in principle physiologically not dangerous. Due to its low-density hydrogen must be compressed or liquefy.

Hydrogen rapidly mixes with the ambient air when release. The diffusion velocity is proportional to the diffusion coefficient and varies with temperature according to the product Tn, where n is in the range 1.72–1.8. Hydrogen diffusivity in air is 4 times larger than air diffusivity in air. The rising velocity depends on the density difference between hydrogen and air as well as on drag and friction forces, shape and size of the rising gas volume, and atmospheric turbulence, so it can't be directly determined only under the influence of buoyant forces, that is a favorable safety effect in unconfined areas, but it can cause a hazardous situation in confined spaces where hydrogen can accumulate. Buoyancy and diffusion mixed determine the rate at which the gas mixes with the ambient air. The rapid mixing of hydrogen with air led to a safety concern because it's easy to have flammable mixtures, but then quickly dilute to the non-flammable range.

Hydrogen can be a problem for its grater rate of release than other gases, due to its small size, small molecular weight, and its low viscosity. Small amount of diffusion is possible through intact materials also, and it can lead to gas accumulation in confined spaces. Compared to water hydrogen's leakage rate is 50 times higher and compared to nitrogen is 10 times higher. To detect the leaks colorant can be added, but it can't be done in every situation or for liquefied hydrogen.

Hydrogen dissolved in liquids can permeate into adjoining vessel materials. At high temperatures and pressures, hydrogen causes decarburization and embrittlement in mild steels. This is a serious concern in any situation involving storage or transfer of hydrogen gas under pressure. Is required properly material selection to prevent embrittlement.

Hydrogen exists in two different forms depends on the temperature: ortho (nuclear spin aligned) and para (spins anti-aligned) hydrogen. At room temperature, hydrogen is 75% ortho and 25% para. Above 80 K para hydrogen is the steadier form. At 20 K the thermal equilibrium is at concentration of 99.821% para and 0.179% ortho. Over 3–4 days period the transition takes place until a new equilibrium state is reached. Magnetic impurities and small oxygen concentrations can catalyze ortho-para conversions increasing the rate by various magnitude orders to the order of hours. Any concentration of the spin state can be created with help of catalysts at any temperature. The properties of the two spin states are not so different, but the larger difference is in the energy between the two varieties, that brings

difference about specific heat and thermal conductivity. Free hydrogen atoms and ions are generating by the presence of a radiation fields, and they act like catalysts before recombining. The recombination produces excess of ortho hydrogen.

Above 193 K hydrogen exhibits a positive Thompson-Joule effect: the temperature of hydrogen gas increase upon depressurization, that can lead to ignition, but it's a small possibility of a spontaneous ignition just by this effect, an explosion has more chances to start because of electrostatic charging of dust particles during depressurization or auto-ignition at high temperatures.

Liquid hydrogen (LH_2) needs one third of its heat of combustion to liquify but has the advantage of extreme purity and has the more economic type for storage and distribution under conditions. To maintain the temperature tank the boiloff loss is unavoidable. When the ortho hydrogen is stored the evaporation rate is enhanced. The ortho-para conversion at 20 k liberate 670 kJ/kg, it is huge compared to 446 kJ/kg of the latent heat of vaporization at the same temperature. It's means that is needed a design of the hydrogen loop that can remove the heat of conversion in a safe way.

Cold hydrogen gas is less volatile than ambient gas, so when there are open pools of LH_2 it needs to be considered that there is more possibility of flammable mixture formation. LH_2 rapidly contaminates itself because of the condensation and solidification of air constituents, that brings a lot of oxygen in particular areas and the formation of shock-explosive mixtures. An additional hazard is given by the volume increase by a factor 845 in confined areas when LH_2 is heated up to ambient conditions. In enclosed space the final pressure can rise to 172 MPa, that over-pressurizes systems to explosion.

A temperature decrease below the boiling point can results in liquid and solid hydrogen mixtures or slush hydrogen, SLH_2. Slush offers the advantages of a higher density and a prolongation of the storage time of the cryogen as the solid melts and absorbs heat. When vapor pressure decreases below the atmospheric pressure, a system against the air ingress must be considered. When solid is formed, the heat released led to the ortho-para hydrogen conversion.

At the temperature of 13.8 K and pressure 7.2 kPa all the three phases can exist in equilibrium: the triple point (Fig. 15).

If hydrogen is maintained above its critical temperature and pressure a single phase is formed: supercritical fluid. It is gas-like because it's compressible and liquid-like because of the comparable density, and there is transitory state in between characterized by strong structural fluctuations causing the unusual behavior of fluid properties near their critical point. It exhibits higher flow rate compared with liquids. In the supercritical state cryogenic hydrogen thermophysical properties strongly depend on temperature and pressure, and near the critical region they vary a lot. At the pseudo-critical temperature Cp has a maximum: thermal spike phenomenon. Because of its dependence of viscosity on temperature supercritical hydrogen might undergo a turbulent-to-laminar transition. Heat transfer coefficients are unpredictable in the transition regime and are much lower in the laminar regime.

Hydrogen at pressure of $2–3 \times 105$ MPa and temperature of about 4400 K will make a transition phase to metallic hydrogen, that may be superconductive at room
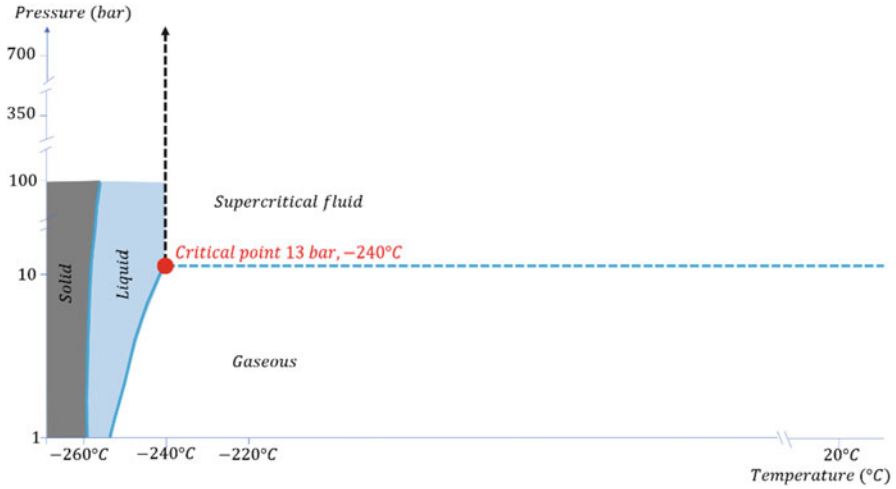
Fig. 15 Hydrogen state diagram
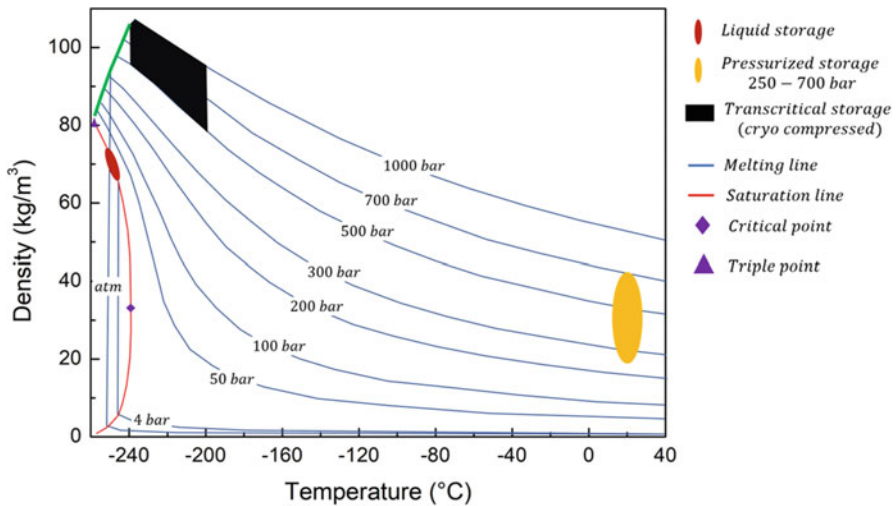
Fig. 16 Density of hydrogen under different temperature and pressure conditions

temperature. This effect, predicted in 1935, was eventually proven in a shock compression test in 1996. Metallic hydrogen is accepted as existing in the interior of Saturn and Jupiter but has no practical application on Earth so far.

Both gaseous and liquid hydrogen are insulator, but above the critical "breakdown" voltage it becomes an electrical conductor due to ionization.

The hydrogen density as a function of temperature and pressure is shown in Fig. 16.

Under normal conditions, hydrogen is a colorless, odorless and non-toxic gas. The density of hydrogen in its gaseous state at NTP is only 0.089 g/l. Below its boiling point of −252.76 °C (1 atm) hydrogen exists as liquid. In the liquid state hydrogen has a density of 70.79 g/l (at the boiling point at 1 atm). Liquefaction increases the density of hydrogen by a factor of ~800.

A hydrogen marked attribute is its negative Joule-Thompson coefficient. Due to that hydrogen heat up when choking from higher to lower pressure since its inversion temperature is reached (71 °C), from that temperature hydrogen shows a normal Joule-Thompson coefficient. Typically, the liquefaction of gases makes use of the Joule-Thomson effect.

Hydrogen, as other energy carriers, manifest risks in term of safety and health when it is used on a large scale. It requires special equipment and procedure to handle it, also because of its molecules size and lightness; in fact, hydrogen is so small that it can diffuse into some materials, and it may increase their chance of failure or it may escape through sealings and pipes. Hydrogen is non-toxic gas, but it is flammable, due to its wide ignition range and low ignition energy, but thanks to its buoyancy and diffusivity, that led to a quickly dissipation, it can be mitigate. It has a flame that is colorless and odorless, making it harder for people to detect fires and leaks.

3.1 Metal Hydrides

The chemistry of hydrogen is very versatile, it creates various chemical interactions and bonds leading to many compounds with different elements of the periodic table (Hirscher et al. 2020). Detailed analysis of intermetallic hydrides reveals their crystal chemistry and electronic, magnetic and hydrogen storage related properties.

Hydrogen shows high energy densities once it is stored in the solid state. Complex metal-hydrides are employed in this direction to obtain both high gravimetric and volumetric energy densities (Fig. 17).

By storing in the solid state, the general reaction is described by:

$$M_{(s)} + H_{2(g)} \rightarrow MH_{2(s)}$$
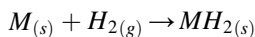
the thermodynamic considerations on a general metal hydride system like this, found a correlation between the temperature of hydrogen release and uptake at a given equilibrium pressure and the enthalpy change for the reaction through the van't Hoff equation:

$$\ln\left(\frac{P(H_2)}{P^{\Theta}}\right) = \frac{\Delta H_r}{RT} - \frac{\Delta S_r}{R}$$
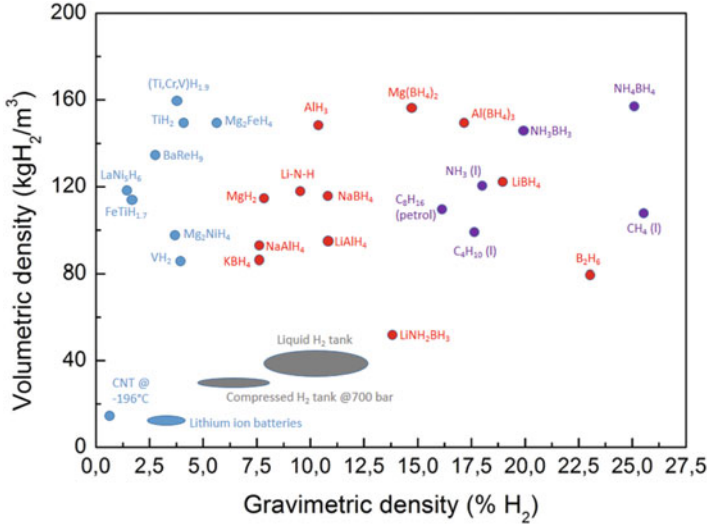
Fig. 17 Volumetric and gravimetric energy density for various materials (Moller et al. 2017)

Where $P(H_2)$ and $P^{\ominus}$ are equilibrium pressure and a reference pressure of 1 bar, R is the gas constant, and T is the temperature. ΔH_r and ΔS_r are the enthalpy and entropy of the reaction.

A material's hydrogen release temperature is usually described as T(1 bar) given for an equilibrium pressure of $P_{eq}(H_2) = 1.0$ bar. In this case, the van't Hoff equation is reduced to:

$$T(1\ bar) = \frac{\Delta H_r}{\Delta S_r}$$

Most metal hydride systems have $S_r \approx 130$ J/(K mol) since the major contribution to the reaction entropy change ΔS_r is from the change in state from molecular hydrogen gas, $S^{\ominus}(H_2(g)) = 130.7$ J/ (K mol), to the solid state in which the entropy is assumed to be close to zero, $S^{\ominus}(H_2(s)) \approx 0$ J/(K mol). To reach an equilibrium pressure of P $(H_2) = 1$ bar at a moderate temperature of 25 °C the decomposition enthalpy should be $\Delta H_r \sim 40$ kJ/mol.

A pressure-composition-temperature (PCT) plot is created to determine the reaction enthalpy and entropy in experimental way performing pressure-composition-isotherm (PCI) experiments. At first, it is formed the α-phase: a solid solution between the metal and hydrogen before the β- phase: initiate of nucleation and growth of the metal hydride. See Fig. 18, left.

An equilibrium pressure dependent on temperature will be reach due to the coexisting of the two phases. As hydrogen content in the β-phase increases, it will be at same point saturated, and pressure will increase. Performing various PCIs experiments at different temperatures allows the construction of a PCT plot which
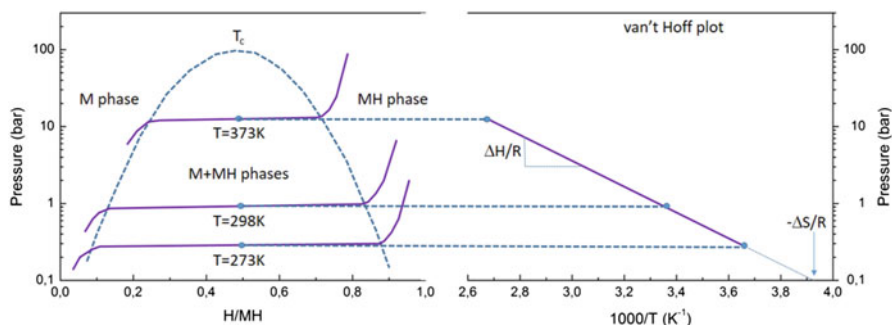
Fig. 18 Pressure-composition-temperature plot for a generic metal-hydride
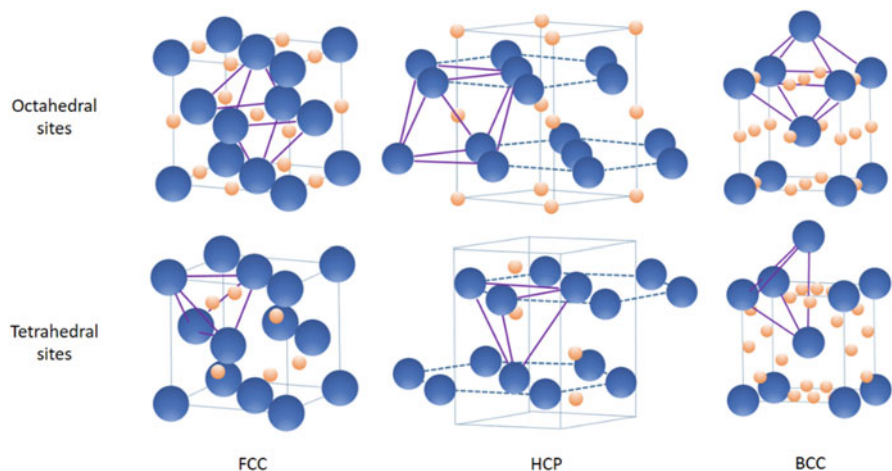
Fig. 19 Metal-hydrides crystal structures

can determine the equilibrium pressure as a function of temperature. This leads to creation of the van't Hoff plot from which ΔH and ΔS can be extracted from the slope and the intersection of the line, respectively, see Fig. 18, right.

Higher volumetric and gravimetric hydrogen densities can be reached using metal hydrates, with improvement of performance consequently. Alloys with up to five metals employment can led to a performance breakthrough due to its higher entropy that influence the hydrogen release.

Metallic hydrides are interstitial hydrides, in which hydrogen occupies the octahedral and/or tetrahedral sites in the metal structure, as shown in Fig. 19.

Metallic hydrides formation led to a metal lattice expansion by up to 20–30 vol%. To improve hydrogen storage capacity and thermodynamic and kinetic properties various type of metallic hydrides have been developed.

Metals and alloys with body-centered cubic (BCC) structure have less close-packed structures as compared to those of face-centered cubic (FCC) and hexagonal close-packed (HCP) structures. Among the known metallic hydrides, BCC alloys reach the largest reversible hydrogen capacity, i.e. up to ~3 wt% at room temperature.

The capacity to form stable and efficient bonds over thousands of cycles is another basic requisite. Improved kinetics of hydrogen release with large potentials is shown when magnesium-based alloys are used. Hydrogen forms covalent bonds to other elements (e.g. boron, aluminum and nitrogen) and that allows to novel materials with stunning structures, compositions and physical and chemical properties, known as complex hydrides. Usually, these materials have high gravimetric and volumetric hydrogen density, but it's hard to reach the reversible hydrogen release and uptake.

Aluminum and boron build complex hydrides of the type M^{+x} $[AlH^-_4]_x$ and M^{+x} $[BH^-_4]_x$. One electron is almost completely transferred from the cation to each $[AlH^-_4]$ and $[BH^-_4]$ anion, while the hydrogen is covalently bound to the aluminum or boron. The alkali, alkali earth and many of the transition metal with boron and aluminum form a large variety of lightweight metal–hydrogen complexes, that show a gravimetric hydrogen density greater up to an order of magnitude than metal hydrides. In the complex hydrides hydrogen is in the corners of a tetrahedron that have boron or aluminum in the center. The negative charge of the anion, $[BH_4]^-$ and $[AlH_4]^-$, is compensated by a cation, e.g. Li or Na.

Interesting storage properties are shown by the hydride complexes of borane, the tetrahydroborates (boranate) $M[BH_4]$, and of alane, the tetrahydroaluminate (alanate) $M[AlH_4]$, they are stable materials and decompose only at high temperature, usually above the complex's melting point. $Li[BH_4]$ (18 mass%), compared with $Be[BH_4]_2$ (28.9 mass%), is the compound with the highest gravimetric hydrogen density at room temperature (Zuttel et al. 2010).

3.2 Liquid Organic Hydrogen Carriers

Liquid organic hydrogen carriers (LOHCs) are liquids that can be reversibly hydrogenated and dehydrogenated. In the dehydrogenation phase hydrogen is the only product and the carrier liquid returned to its original state to be hydrogenated again. Figure 20 illustrates the basic principles of the LOHC concept.

Hydrogenation step is exothermic (meaning that heat is released in the reaction) and it is typically carried out at elevated temperatures (100–240 °C) and pressures (10–50 bar) with the presence of catalysts. In the endothermic dehydrogenation step to release hydrogen is required the same amount of heat. Catalytic dehydrogenation is generally carried out at 150–400 °C and pressures down to 10 bar.
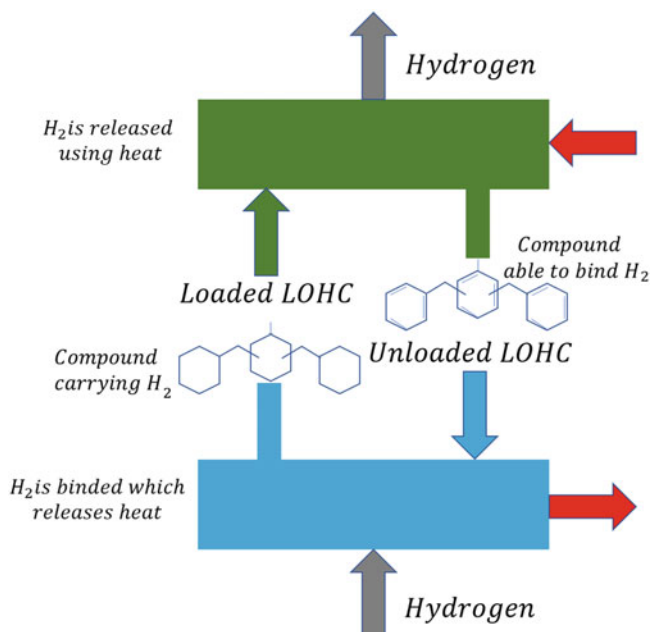
Fig. 20 LOHC basic

The LOHC is compatible with existing fuel infrastructure and it's one of the advantages of its concept. Additionally, there is no hydrogen loss in long-term storage or transport at normal conditions in contrast with liquid H_2 delivery chains that have a lot of boil-off losses.

There are various LOHC compounds under research: aromatic hydrocarbons or heterocyclic compounds (carbazoles, pyridines or pyrroles).

Ideal LOHC would have high hydrogen storage density, low reaction enthalpy, low degradation and it would be non-toxic, cheap and have high enough melting point to stay in liquid form also in cold conditions. Furthermore, the conversion reactions would take place at moderate conditions using low-cost catalysts. Lately most attention has been paid to dibenzyltoluene–perhydro-dibenzyltoluene (H0-DBT–H18-DBT), toluene–methylcyclohexane (TOL–MCH) and N-ethylcarbazole–dodecahydro-N-ethylcarbazole (NEC–H12-NEC) systems.

The high reaction enthalpies that occur in the LOHC concept is demonstration of the significant amount of heat required to release hydrogen. The heat transfer losses must be considered: if heat should be provided by hydrogen about 25–30% of released hydrogen would have to be burned. Additionally, as the required temperature level is quite high, it is not possible to use low-value waste-heat sources in most cases. Although the same amount of heat is released during hydrogenation but at a lower temperature level. The energy spent in dehydrogenation can be in part compensated by using this heat.

The dehydrogenation step needs low pressure in the LOHC concept and it's a disadvantage because in the high-pressure hydrogen application (e.g. bottle filling stations or mobility applications) an energy penalty to gas compression add to the other. Electrolyzers can produce up to some 30–50 bar with only a minor additional energy penalty compared to atmospheric operation.

Dibenzyltoluene (DBT) was seen as the most promising due to high storage density, availability at reasonable price and its low melting point.

Hydrogen released from LOHCs has a relatively high purity. For DBT-based systems purity 4.0 (99.99 vol%) is achievable just by cooling the gas/vapor stream in a dephlegmator which condenses the part of the LOHC that left the reactor as vapor. The remaining impurities are mainly water and hydrocarbons, which form as decomposition products of the LOHC. The most relevant remaining impurities are methane, toluene and benzyltoluene.

4   Chemical Properties

Hydrogen reacts with a lot of materials to form ionic or covalent hydrides, it bonds with non-metals, which have high electro-negativity and metals, which have low electro-negativity. The electro-negativity is a measure for the attraction of electrons to nucleus. The electro-negativity of the hydrogen is 2.20 on the Pauling scale.

Hydrogen is highly flammable when bonds with oxygen in a wide range of concentrations. The hydrogen energy density is high related to the mass: 1 kg of hydrogen contains 141.86 MJ (gross heat of combustion), which is about 2.5 times than is contained in 1 kg of natural gas.

The LHV energy content of hydrogen is 242 kJ/mol; the HHV energy content is 286 kJ/mol; there is a 15.6% of difference between LHV and HHV, a large amount compared to other gases, it's due to heat liberated of the water vapor (that can be captured in a turbine).

A stoichiometric hydrogen-air mixture, in which all fuel is consumed during the reaction (where maximum combustion energy is released) contains 29.5 vol% of hydrogen. Water vapor is the only product of hydrogen combustion. It burns in a non-luminous, almost invisible pale blue, hot flame to water vapor, liberating the chemically bound energy as heat (gross heat of combustion). The flame temperature of a burning premixed and stoichiometric hydrogen–air mixture is a maximum of 2403 K.

There is a wide flammability range for hydrogen (at room temperature) between 4 and 75 vol% in air and up to 95 vol% in oxygen. The LFL, as the minimum amount of fuel that supports combustion, is the limit since a continuous leakage will be reached. With higher temperature the flammability range increases. The influence of the temperature is expressed in the modified Burgess-Wheeler equation for the LFL, at ambient pressure:

$$c_{LFL} = c_{LFL}(300\ K) - \frac{3.14}{\Delta H_c}(T - 300) = 4 - 0.013(T - 300)$$

Where:

ΔH_c is the net heat of combustion;
T is the temperature, K.

The respective equation for the upper flammability limit (UFL) is:

$$c_{UFL} = 74 + 0.026(T - 300)$$

valid for the temperature range 150–300 K. Measurements of upward flame propagation at higher temperatures have shown a further increase of the UFL with initial temperature reaching 87.6% at 673 K. There are still no experimental data available on the influence of moisture on the flammability limits. For the determination of the LFL and UFL of mixtures of fuels, the Le Chatelier rule is the most applied method:

$$\frac{1}{L_m} = \sum \frac{y_i}{L_i}$$

where

y_i is the volume fraction of fuel i;
L_i is the flammability limit of fuel i.

Le Chatelier's rule was found to be in accurate agreement with experimental data for the system H_2–CO.

The potential for an explosion of a flammable hydrogen–air mixture is very high. The hydrogen auto-ignition temperature, which is the minimum temperature of a hot surface that can ignite a flammable mixture, is in the range of 800–1000 K dependent on the experimental conditions. It is relatively high but can be lowered by catalytic surfaces. Hydrogen gas don't show a flash point (minimum temperature at which a liquid gives off vapor at sufficient concentration to form a flammable mixture with air near the liquid surface) because hydrogen is a gas in ambient conditions. This means that cryogenic hydrogen will flash at all temperature above its boiling point (20 K).

The minimum ignition energy (the spark energy required to ignite the most easily ignitable hydrogen concentration in air) is at 0.02 mJ, much lower than hydrocarbon-air mixtures. That means that a weak spark or the electrostatic discharge from a flow of pressurized H_2 gas or from a person (about 10 mJ) would be sufficient to ignition; but there is no difference from other burnable gases. With the increasing of the temperature, pressure, or oxygen content the minimum ignition energy decrease. The hydrogen hot air jet ignition temperature is lower than other hydrocarbons and decreases with increasing jet diameter. It is also dependent on jet velocity and mixture composition.

Fig. 21 Burning velocities in hydrogen–air mixtures as measured by various authors
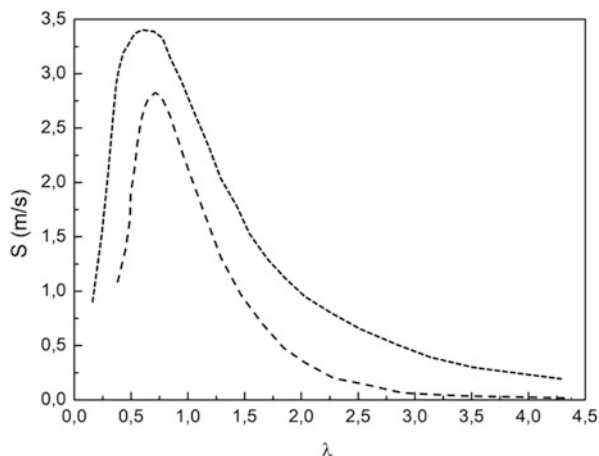
The quenching gap in air is the distance between two flat plates at which flammable mixture ignition is suppressed: it's the smallest diameter of a tube through which a flame can propagate. Faster burning gases have smaller quenching gaps. Hydrogen has a quenching gap of 0.64 mm. The maximum experimental safe gap is the maximum distance between two flat plates which still allows flame propagation through the gap; for hydrogen is 0.08 mm. Because of the high explosion pressures, the maximum experimental safe gap is always smaller than the quenching gap.

The burning velocity in a flammable gas mixture is the speed of a combustion wave advance into a stationary flammable mixture and is a property of the gas depending on temperature, pressure, and concentration. The burning velocity of hydrogen is shown in Fig. 21: in air at stoichiometric ambient condition is 2.55 m/s, reaching a maximum of 3.2 m/s at a concentration of 40.1% and can also increase to 11.75 m/s in pure oxygen. It's higher than other hydrocarbon fuel-air mixtures due to fast chemical kinetics and high diffusivity of hydrogen. The higher the burning velocity, the greater is the chance for a transition from deflagration to detonation (DDT). In contrast, the flame speed, which is related to a fixed observer, is much greater than the burning velocity due to the expansion of the combustion products, instabilities, and turbulent deformation of the flame. The maximum possible speed of a deflagration burning flame is given by the speed of sound in the combustion products gas mixture, which is 975 m/s for a stoichiometric H_2–air mixture.

Usually, the detonatability range is in the 18–59 vol% of hydrogen concentration, but it depends on the system size.

A detonation range of 13–70% of H_2 is given for a 43 cm tube. In the Russian Federation's detonation test facility RUT, the largest of its kind, a lower detonatability limit of as low as 12.5 vol% has been observed. In pure oxygen, the detonation range is extended to 15–90%.

The detonation velocity in air reaches values in the range of 2000 m/s; in pure oxygen, it is up to 3500 m/s.

Fig. 22 Detonation cell size
of hydrogen and other fuels
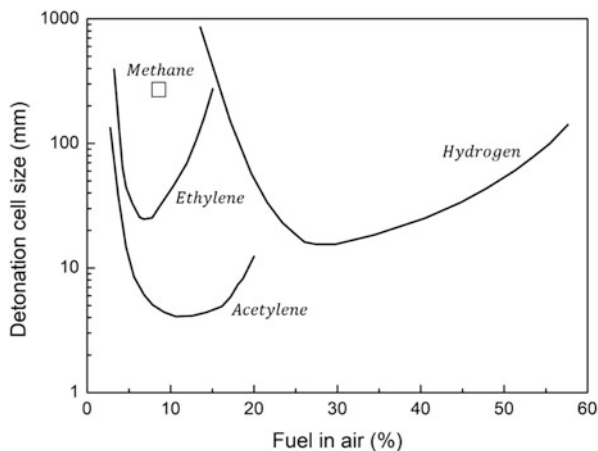
The size of the detonation cell is a measure of the reactivity; the smaller the cell, the more reactive is the mixture (Fig. 22).

It is an indicator for DDT and can be measured experimentally. A stoichiometric hydrogen-air mixture has a cell size of 15 mm and it makes hydrogen-air mixture highly reactive, in contrast, a stoichiometric methane-air mixture has a cell size of about 330 mm and it makes the mixture the last sensitive of the common fuels. Cell sizes increase with increasing deviation from stoichiometry. In the late 1970s a measurement of the detonation cell size, λ, was achieved.

The first step was finding a correlation between cell size and critical tube diameter $(d = 13 \times \lambda)$. This is an empirical law that bring to a simple surface energy model and to the derivation of a critical initiation charge weight for various hydrocarbon-air mixtures in quite good agreement with experimental data.

The critical tube diameter is the minimum diameter required for a detonation wave to emerge from a tube and become a detonation in an unconfined cloud. It is a measure of minimum dimensions of an unconfined detonable cloud. The detonation initiation energy given in mass of high explosive (TNT or tetryl) is the minimum energy necessary to initiate a spherical detonation wave; the energy content of tetryl corresponds to 4.3 MJ/kg.

The distance in which the flame front at the ignition point turns to a detonation depends on certain parameters: temperature, pressure, mixture composition, geometry (obstacles) and ignition source strength. A typical ratio of tube length to diameter to detonate a stoichiometric hydrogen–air mixture is approximately 100.

From experience the hydrogen-air cloud developed from the accidental release of hydrogen at failure of a storage tank or pipeline can liberate a small portion of its thermal energy content un the case of explosion, in the range of 0.1–10% and in most cases below 1%. But the explosion of a hydrogen-air mixture cloud forms different pressure wave dependent on the combustion mode, ad is shown in Fig. 23.

Fig. 23 Pressure signals from different hydrogen combustion modes
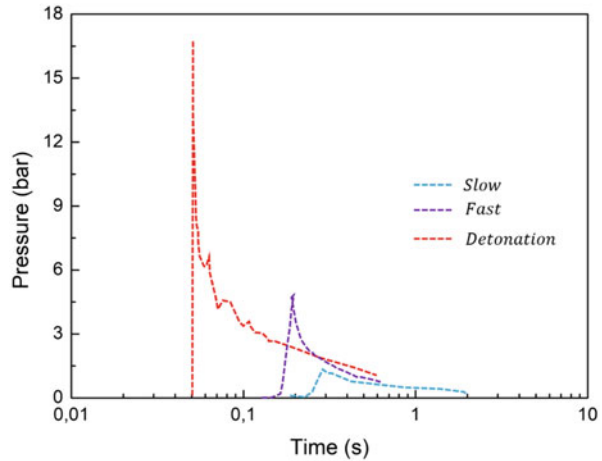
In the deflagration of a free hydrogen–air gas cloud, the maximum overpressure is in the order of 10 kPa. An overpressure of 7 kPa is still thought not dangerous; at 7 kPa, people would fall to the ground; at 35 kPa, damage of ear drums is expected; 240 kPa is considered a threshold value above which fatalities must be taken into account.

The flame thermal energy corresponds to the HHV, but it can be reduced by the absorption of the atmosphere moisture (emissivity $\varepsilon < 0.1$) contrary to hydrocarbon flames ($\varepsilon \approx 1$). Ergo, despite its high flame temperature, the burning hazard is small. The major problem is the non-visibility of the flame and the consequent difficulty of recognizing and localizing it, but an advantage is that there is no smoke generation, and it is important in confined areas.

5 Hydrogen Production

Hydrogen can be produced from a various resource: natural gas, nuclear power, biogas and renewable power (solar and wind). Electricity (from the grid or renewable sources is used yet to produce hydrogen). In the long period, solar energy and biomass can be used more directly to produce hydrogen as new technologies cost competitive.

Based on how it is produced there is different environmental impact and energy efficiency. Several projects are underway to decrease costs associated with hydrogen production.

Hydrogen is required for essential chemical processes since a lot, so its production is at the center of any industrialized society.

From 2020, the production of hydrogen is 95% from fossil fuels by steam reforming of natural gas and other light hydrocarbons, partial oxidation of heavier hydrocarbons, and coal gasification. Other methods include biomass gasification, zero-CO_2-emission methane pyrolysis and electrolysis of water.

There are many ways hydrogen is produced or obtained from different sources as the availability of the hydrogen is variably high. But we must separate the hydrogen from different molecules and there are several methods to do such type of separation.

Further, hydrogen is be labelled as black/brown, grey, green, blue hydrogen based on from which material or molecule it is extracted or produced.

- Black/brown, Coal using gasification
- Grey, Natural gases using steam-methane reforming
- Green, Electrolysis of water
- Blue, Fossil fuels.

However, the factors affecting the production can be limitations to the production such as:

- Cost and time
- Efficiency of the processes
- Environmental impact
- Effectiveness
- Quality of hydrogen
- Waste and by-products

Hydrogen Production methods can be categorized in 4 ways:

1. THERMAL METHODS
2. PHOTOCATALYTIC METHODS
3. BIOLOGICAL & PHOTONIC METHODS
4. ELECTRICAL & ELECTROLYZER TECHNOLOGIES METHODS

Thermal methods use thermochemical reaction to separate the hydrogen from the organic compounds. It can be further categorized into classes based on endothermic and exothermic reaction used for separation process. Currently most of the hydrogen is produced using the thermal methods.

Hydrogen can be produced using a range of energy sources and technologies. Global hydrogen production today is dominated by the fossil fuels. Electrolytic hydrogen – that is, hydrogen produced from water and electricity – plays only a minor role. With declining costs for renewable power (solar PV and wind), interest is now growing in water electrolysis for hydrogen production and in the scope for further conversion of that hydrogen into hydrogen-based fuels or feedstocks, such as synthetic hydrocarbons and ammonia, which are more compatible than hydrogen with existing infrastructure.

Hydrogen can be extracted from fossil fuels and biomass, or from water, or from a mix of both. Around 275 Mtoe of energy are used to produce hydrogen today (2% of global total primary energy demand). The primary source for hydrogen production is natural gas; in the methanol industries and in refineries hydrogen is produced by

steam methane reformers using natural gas. Natural gas accounts for around three-quarters of the annual global dedicated hydrogen production of around 70 million tons of hydrogen (MtH_2), using around 205 billion cubic meters (bcm) of natural gas (6% of global natural gas use). Coal comes next, due to its dominant role in China: it accounts for an estimated 23% of global dedicated hydrogen production and uses 107 Mt of coal (2% of global coal use). Oil and electricity account for the remainder of the dedicated production.

This means that hydrogen production generates notable CO_2 emissions: 10 tons of carbon dioxide per ton of hydrogen (tCO_2/tH_2) from natural gas, 6 12 tCO_2/tH_2 from oil products, and 19 tCO_2/tH_2 from coal. This results in total CO_2 formation of about 830 $MtCO_2/yr$, corresponding to the combined CO_2 emissions of Indonesia and the United Kingdom. Most of this CO_2 is emitted to the atmosphere, although in ammonia/urea plants the concentrated CO_2 streams from steam methane reforming (SMR) (around 130 $MtCO_2$ each year) are captured and used in the production of urea fertilizer.

Reforming is the most widespread method for producing hydrogen from natural gas. There are three methods: steam reforming (using water as an oxidant and a source of hydrogen), partial oxidation (using oxygen in the air as the oxidant), or a combination of both called autothermal reforming (ATR).

Steam reforming is used to extract hydrogen from natural gas and – much less frequently – from liquefied petroleum gas and naphtha. Partial oxidation is used to extract hydrogen from heavy fuel oil and coal. In all cases, a synthesis gas mostly made of carbon monoxide and hydrogen is formed, then converted to hydrogen and CO_2 if pure hydrogen is the main product. Other processes include gasification (where the raw material, such as coal or biomass, is converted into a synthesis gas that is then transformed into hydrogen and CO_2) and electrolysis (where hydrogen is produced by splitting water into hydrogen and oxygen). Though known for a long time, electrolysis plays only a minor role in total hydrogen production today, mostly in the chlor-alkali industry where hydrogen is a by-product.

5.1 Steam Reforming

The steam reforming is an endothermic equilibrium reaction, in which hydrogen is obtained through a catalyzed reaction between a hydrocarbon and steam:

$$C_nH_m + nH_2O \leftrightarrow nCO + \left(n + \frac{1}{2}m\right)H_2$$
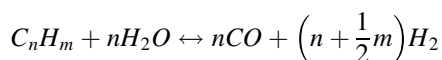
The methane steam reforming is the most prominent steam reforming method. Methane is the simplest hydrocarbon molecule, have an energy density of 55.5 $MJKg^{-1}$, in reforming it reacts with steam at 700–1000 °C and pressure range of 3–25 bars.
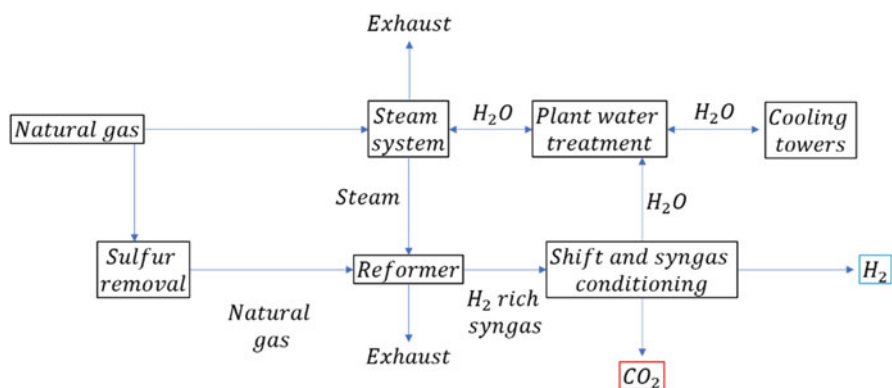
Fig. 24 NG reforming schematic

Natural gas or other methane containing hydrocarbons: ethane, propane, butane, pentane, or light and heavy naphta. First they are sent to a steam system to combust, heating steam, or a sulphur removing device, sulphur can poison the catalysts in the reformer (Fig. 24).

Then steam from the steam system and clean methane (CH_4) go to a reformer, where a catalyst activates the endothermic reaction:

$$CH_4 + H_2O \rightarrow CO + 3H_2$$
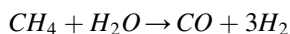
One of the most important challenges in MSR processes is the high reaction temperatures managing. At the center of the catalytic bed there is a temperature of 700–800 °C, it means that is needed an external reactor wall temperature of 1200 °C.

Autothermal Reforming (ATR) is a process which uses the heat from exothermic Reaction (Partial oxidation) for sustaining the endothermic reaction by feeding air, steam, and the reacting feedstock (methane, methanol & ethanol) to produce H_2-rich stream. The main characteristics of ATR are:

- Requires low energy –by selection of proper O_2/fuel ratio
- No external heat needed
- Availability of O_2 promotes gasification reaction.

Ni-based catalyst is mostly used in methane auto-thermal reaction because of low cost.

Promoter or bimetallic catalytic systems can improve the performance of these catalysts such as: – $10Ni_{-0.9}Re/Ce_{0.5} Zr_{0.5} O_2/Al_2O_3$. Catalysts has shown high resistance to oxidation and sintering of the Ni active component as well as the resistance to coking.

The catalyst preparation method improves the catalytic performance by enhancing the physicochemical properties of catalyst.

These techniques modify the metal-support interaction, thus changing the kinetics of the catalyst which can result in enhanced productivity, reduced cost, and optimized energy requirements.

The results showed that the 40% Cu-loaded catalyst had the highest catalytic activity: the presence of $Ca_2Fe_2O_5$ tunes the redox activity and mobility of the lattice oxygen, obtaining a H_2 production rate of 37.6 $\mu mol.H_2.g_{COC}^{-1}.s^{-1}$ at 240 °C.

Pt-based catalysts showed the highest ethanol conversion, hydrogen yield and the lowest carbon formation rate.

The bimetallic catalysts showed the best catalytic activity, due to the formation of PtZn and NiZn alloys.

5.2 Hydrogen from Coal

Hydrogen production from coal using gasification is a well-established technology, used for many decades by the chemical and fertilizer industries to produce ammonia (especially in China). Globally around 130 coal gasification plants in operation, more than 80% of which are in China. Hydrogen production using coal produces CO_2 emissions of about 19 tCO_2/tH_2, which is twice as much as natural gas.

When there is a high CO_2 emission there also is necessary a carbon capture technology. The CCU brings some point of challenge: coal produces hydrogen with a low hydrogen-to-carbon ratio (from coal is 0.1:1; from methane is 4:1) and left a lot of impurities in the feedstock (sulphur, nitrogen, and minerals).

The synthesis gas obtained from the gasification of coal could be used to fuel a combined cycle power plant and if the coal gasification plant was equipped with CCU the generated electricity would count as low carbon.

If an additional water-gas-shift (WGS) unit could be added, the synthesis gas could also be used to produce more hydrogen, in this way the coal gasification plant can shift between the production of electricity and hydrogen according to which is more profitable.

Most of the hydrogen production from coal nowadays takes place in China using coal gasification, generally for ammonia production. China is exploring the role of hydrogen in its economy, and the cheapest way of producing it in coal, with costs amounting to RMB 0.6–0.7/m^3 (about USD 1/kgH_2).

CHN Energy, China's largest power company, is also the world's largest hydrogen production company, with its 80 coal gasifiers can produce around 8 MtH_2/yr, which is equivalent to 12% of global dedicated hydrogen production. Using coal with CCU currently looks likely to be the lowest-cost way of producing cleaner hydrogen in China, but current technologies enable a CO_2 intensity only as low as 2 kilograms of carbon dioxide per kilogram of hydrogen (kgCO_2/kgH_2) while advanced technologies may permit this to reach as low as 0.4 kgCO_2/kgH_2.

In Australia the Hydrogen Energy Supply Chain (HESC) Latrobe Valley project is trying to produce hydrogen from lignite using high-pressure partial oxidation. The related CarbonNet Carbon Capture and Storage Project presents a potential solution

for mitigating CO_2 separated from the hydrogen production process in the commercial phase. The hydrogen produced would be liquefied and exported to Japan. The first step is a one-year pilot project to treat 160 tons of lignite to produce 3 tH_2.

5.3 Hydrogen from Biomass

Hydrogen can be produced from biomass in numerous ways. In biochemical microorganisms produce biogas (anaerobic digestion), acids, alcohols, and gases (fermentation) from organic materials. Thermochemical gasification of biomass process convert biomass to a mix of carbon monoxide, CO_2, hydrogen and methane. Among these processes, anaerobic digestion to produce biogas is the most technically mature even if it can be work on sewage agricultural sludge, food processing and household waste, and some energy crops. Fermentation can process the non-edible cellulosic part of some plants. Gasification could potentially convert all organic matter, and in particular the lignin component of biomass, but the technology is not yet completely developed, and there is the problem of catalysts poisoning by the tars formation in the process (Ericsson 2017). The produced gas need to be processed to extract hydrogen.

The biomass process is obviously complex, is also a low-carbon hydrogen production more expensive than solar-based or wind-based electrolysis.

The production of hydrogen from biomass limit is also represented by the availability of economical biomass. For example, satisfying a theoretical hydrogen demand of 60 MtH_2 in the US market –corresponding to four times the United States' current hydrogen demand – would require almost 100% of its technical biomass potential, but only 6% of its wind power, and less than 1% of its solar power potential (Ruth et al. 2017). Combining hydrogen production from biomass with carbon capture and storage could be an option to create so-called "negative emissions", that may have a future.

Bio-oil molecules has larger energy density than biomass, composed by a mixture of organics including alcohols, carboxylic acids, aldehydes, ketones, furans, phenolic, etc.

The molecular structures of organic molecules (methanol, formic acid, ethanol, acetic acid, acetaldehyde, acetone, and furfural) derived from bio-oil can influence the reactivity and tendency to coking during steam reforming.

The steam reforming of ethanol, acetic acid, acetaldehyde, or acetone required much higher temperature, and generated remarkable amounts of coke deposits, especially acetone and acetaldehyde.

The catalyst is important in the coke formation mechanisms: relative studies demonstrate that alumina support influences the catalytic stability in methanol, acetic acid, and acetone steam reforming.

Furthermore, an important problem is the availability and renewability of the feedstock; bio-alcohols such as methanol, ethanol and glycerol can be easily obtained from renewable sources, therefore they seem to be a valuable alternative to natural gas.

The steam reforming of the methanol (SRM) reaction yields hydrogen as its main product and carbon dioxide and carbon monoxide in small amounts along with unreacted H_2O and CH_4.

Cu based catalyst like $CuFeO_2$-CeO_2 nano-powder catalyst, with a heterogeneous delafossite structure, prepared by the self-combustion glycine nitrate process show good activity of H_2 production as lower temperature at generation rate of 2582.25 STP $cm^3.min^{-1}.g_{cat}^{-1}$ at flow rate of 30 sccm at 400 °C.

$ZnCeZr_9Ox$ catalyst exhibited a full methanol conversion and an H_2 production rate of 0.31 $molh^{-1}.g_{cat}^{-1}$ at 400 °C and when it is incorporated with Zn^{2+} into $CeZr_9OX$ matrix, it modify the surface O_{Latt}/O_{Ads} ratio, and produce a Zn-O-Zr interfacial structure, corresponding to the lattice/bridge oxygen thus by increasing the CO_2 selectivity.

Zn-modified Pt/MoC catalyst exhibited superior hydrogen production activity, with exceptionally low CO selectivity at low temperatures (120–200 °C), due to the formation of _-MoC1-x phase and to the enhanced Pt dispersion.

$InxPdy/In_2O_3$ aerogels exhibited excellent CO_2 selectivity of 99% at 300 °C.

Ethanol production The production of ethanol passes first from the fermentation of saccharides and then from distillation processes, obtaining bioethanol, that can be used for ethanol steam reforming (ESR).

Nickel based catalyst is mostly used for ESR because of low cost.

The greatest disadvantage of ESR processes is the carbon formation. To avoid this problem a lot of strategies are studied, for example: using a promoter and controlling the metal particle sizes.

Potassium is the most prominent promoter for Co/Al_2O_3–CaO catalysts, due to their higher hydrogen yield and lower methane selectivity than the unpromoted catalysts, because of the methanation reaction suppression.

Catalyst (Pt-Cu@$mSiO_2$) for ESR at low temperature show better result by using encapsulation strategy with Pt-Cu alloy Nanoparticles. The mesoporous SiO_2 shell prevents leaching and aggregation of active sites and spatially suppresses the carbon deposition on the active surface.

Graphene–encapsulated Ni nanoparticles (Ni@Gr), fabricated with in-situ growth method, shows good results and efficiency IN ESR at 550 °C.

Glycerol is produced as by product of bio-diesel production, using it can produce 7 moles of hydrogen per $C_3H_8O_3$ mole. In glycerol steam reforming, using noble metal-based catalyst especially Pt-based one, it shows excellent performances.

Furthermore, presence of promoters suppresses the coke formation.

The catalytic behavior of Ni catalyst supported on CaO-modified attapulgite in glycerol steam reforming, has shown that the addition of CaO promotes the dispersion of the active component, promoting the water gas shift reaction, thus leading to improved hydrogen yields. Also, while addition of CaO enhances the inhibition of carbon deposition, extends the stability of the catalyst.
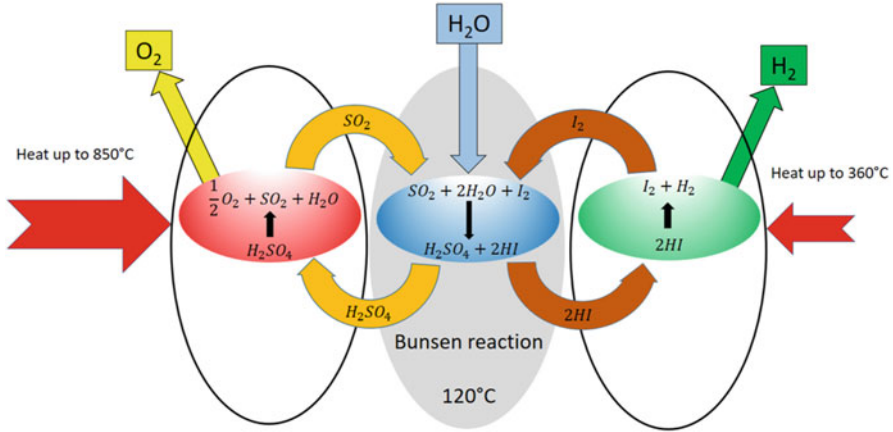
Fig. 25 Sulphur-iodine process schematic

5.4 Hydrogen Through Nuclear

A great impact to the hydrogen production will be given by the nuclear plants belonging to the generation IV. Different generation IV plants are under development, among them the most promising ones are sodium fast, lead fast, very high temperatures gas cooled fast, supercritical water cooled and molten salts cooled reactors. The main technologies under development for the hydrogen production are:

– Sulphur-Iodine (Fig. 25).

The sulfur-iodine cycle consists of three chemical reactions, in addition to the dissociation of water. The first one is the exothermic Bunsen reaction:

$$I_2 + SO_2 + 2H_2 \leftrightarrow 2HI + H_2SO_4$$
$$\Delta H = -75 \pm 15 \; kJ/mol$$
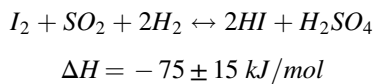
It is spontaneous react at 20–100 °C. At reactant concentrations, implicating an excess of iodine, a phase separation occurs between the two acid products leading to a H_2SO_4 phase principally devoid of HI.

   The second reaction:

$$2H_2SO_4 \leftrightarrow 2H_2O + 2SO_2 + O_2$$
$$\Delta H = 186 \; kJ/mol$$
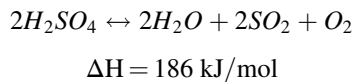
is the endothermic sulfuric acid decomposition step between 600 and 900 °C, which can be assumed to two reactions:

$$H_2SO_4 \leftrightarrow SO_3 + H_2O$$

$$2SO_3 \leftrightarrow 2SO_2 + O_2$$
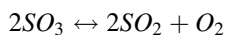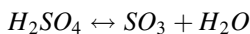
The first stage occurs at a temperature of 300–400 °C, in contrast the second stage occurs at 600–900 °C with some solid catalyst.

The third reaction:

$$2HI \leftrightarrow H_2 + I_2$$
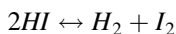
$$\Delta H = 12 \; kJ/mol$$

is the hydriodic acid decomposition reaction. This is a quite endothermic reaction at the temperature 300–450 °C, and it can be conducted in the liquid or gas phase.

Section I is for the Bunsen reaction, which produce and separate H_2SO_4 and HI for Sections II and III, and the O_2 is also separated in this step. Recycled I_2 from Section III reacts with water and SO_2 which comes from Section II in a countercurrent reactor. They spontaneous reacted at 20–100 °C. It results in the formation of a solution of two acids, H_2SO_4 and HI. This solution contains two phases with different density. The lower density phase contains all the H_2SO_4 acid at a concentration of about 50% by weight with traces of I_2 and SO_2. And the higher density phase contains all the HI with amounts of I_2 in an H_2O solution and small amount of SO_2. Both phases are separated. The concentration of H_2SO_4 is increased to be about 57% by weight by reacting the H_2SO_4 phase with molten iodine and SO_2. Then sulfuric acid with some water is transferred to Section II for concentration and decomposition. The lower phase containing HI, H_2O, I_2 and SO_2 goes through a degassing step, which removes practically all the SO_2 and is then transferred to Section III for purification and HI separation. And for the oxygen separate. It was mixed with SO_2, coming directly from the SO_3 decomposition reaction of Section II, then it passes through the reactor, the SO_2 is removed by reaction with I_2 and H_2O, and the gas leaving the top of the main solution reactor is practically the pure oxygen, but there is a small amount of iodine with them. A scrub column is used for removing iodine. Then the pure oxygen leaves the system as a product.

Section II is the H_2SO_4 concentration and decomposition step. The concentration is an important part before decomposition. The 57% by weight sulfuric acid is concentrated in a series of flash evaporators and separators. It is then decomposed to H_2O and SO_3, and the SO_3 is decomposed to SO_2 and O_2 at 850 °C. The nuclear energy is used in this reactor. The gaseous mixture of SO_2 and O_2 is then separated from the H_2O and unreacted H_2SO_4 before it is sent to Section I. Most heat needed in this section, as it reacts at high temperature about 850 °C.

In Section III there are also two steps: the HI separation step and the HI decomposition step. In the HI separation step: the HI is trying to be separated from the HI-I_2-H_2O solution which comes from Section I. It is complex step as there are three compounds should be separated from HI. In this step a concentrated phosphoric acid is used to separate 95% of the I_2 away from the solution. The solution

containing HI, H_2O, H_2SO_4 and some I_2 is transferred to an extractive distillation column, where most of the H_2O remains with the phosphoric acid, and HI, I_2 and a very small amount of H_2O are removed as overhead vapor. The vapor is then cooled to condense and separate. The purified liquid HI at 5 MPa from HI separation step is pumped into a decomposition reactor. Then it catalytically decomposed at about 300 °C in it. After the reaction another separation should be taken to get the pure hydrogen production. The hydrogen product is separated from most of the I_2 and some HI in a liquid gas separator. Then the gaseous H_2 product is scrubbed with H_2O. Finally, the pure hydrogen is the resulting product in this step and flow out from there. And the I_2 is returned into Section I.

A major advantage of the S-I cycle for hydrogen production is that there are not any harmful by products or emissions from the process. All the chemical reactions have been demonstrated. The only outlet is hydrogen and oxygen. If it can be heated with a nuclear source, it could prove to be an ideal environmental solution to hydrogen production. And one more important advantage is that it offers the higher efficiency than any other hydrogen production process.

However, there are some disadvantages in this cycle. There are sulfuric acid and hydroiodic acid contained in this cycle, both are very corrosive, it is harmful and must be contained properly. The material of the reactors and all the units in this cycle should be avoided to acid.

– Copper-Chlorine (Fig. 26).
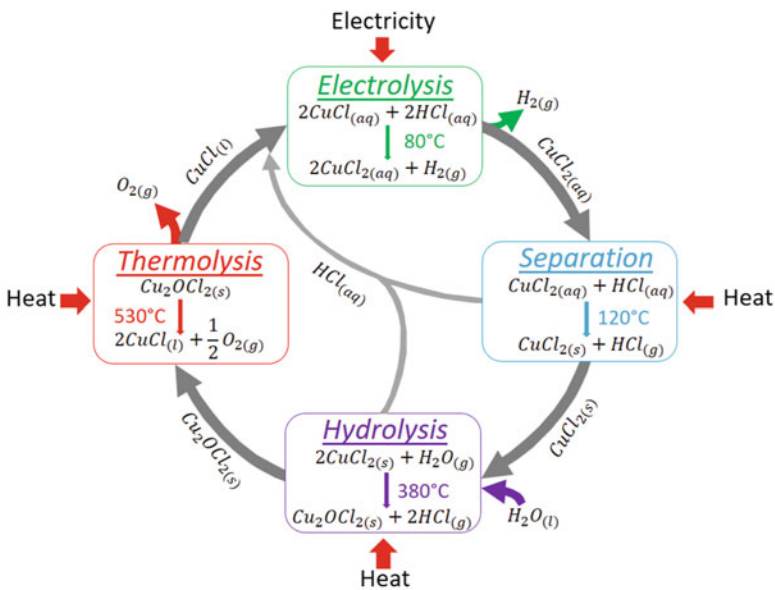
Fig. 26 Copper-chlorine process schematic

The Cu-Cl cycle consists of a closed loop of thermally driven chemical reactions, where water is decomposed into hydrogen and oxygen, and all other intermediate compounds are recycled with no emissions to the environment (Naterer et al. 2014). The four reactions of the Cu-Cl cycle are:

$$2CuCl_{(aq)} + 2HCl_{(aq)} \rightarrow 2CuCl_{2(aq)} + H_{2(g)}$$

$$2CuCl_{2(aq)} + HCl_{(aq)} \rightarrow 2CuC_{(s)} + HCl_{(g)}$$

$$2CuCl_{2(s)} + H_2O_{(g)} \rightarrow Cu_{2OCl_{2(s)}} + 2HCl_{(g)}$$

$$2CuCl_{2(s)} \rightarrow 2CuCl_{(l)} + \frac{1}{2}O_{2(g)}$$
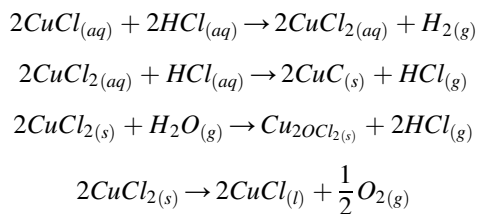
In the oxygen production step of the Cu-Cl cycle, an intermediate compound, solid copper oxychloride (Cu_2OCl_2), is decomposed into oxygen gas and molten cuprous chloride (CuCl). The solid feed of Cu_2OCl_2 is supplied to the oxygen production reactor from the $CuCl_2$ hydrolysis reaction that operates at a temperature of 350e450 °C. Gas species leaving the oxygen reactor include oxygen gas and potentially impurities of products from side reactions, such as CuCl vapor, chlorine gas, HCl gas (trace amount) and H_2O vapor (trace amount). The substances exiting the reactor are molten CuCl, potentially solid $CuCl_2$ from the upstream hydrolysis reaction, due to the incomplete decomposition of $CuCl_2$ at a temperature lower than 550 °C, as well as reactant particles entrained by the flow of molten CuCl.

In comparison to other thermochemical cycles, the Cu-Cl cycle has the advantage of an ability to utilize low-grade waste or process heat to achieve higher thermal efficiency and lower cost of hydrogen production than other technologies. The Cu-Cl cycle has a reduced electrical power requirement, compared to typical water electrolysis, for its CuCl/HCl electrolysis. The $CuCl_2$ hydrolysis reaction and Cu_2OCl_2 thermolysis reaction form a closed loop with the CuCl/HCl electrolyzer to produce hydrogen in the cycle. In the hydrolysis reactor, the chemical conversion effectiveness decreases as reactants are consumed.

Testing of the one 300 cm^2 cell showed a current density of 0.55 A/cm^2 at 0.7 V. A two 300 cm^2 cell stack was then fabricated and tested to ensure that the mass flow distribution was even and that there were no shunt currents. At 0.7 V, the current density was 0.36 A/cm^2 and H_2 production was 98% of the theoretical value. Conversion of Cu(I) to Cu(II) was 65% when the flow rate was 210 mL/min.

– High temperature steam electrolysis (Fig. 27)

High Temperature Steam Electrolysis (HTSE), based on reversed solid oxide fuel cell technology, appears as a relevant process to produce CO_2-free hydrogen and oxygen. The dissociation of steam into H_2 and O_2 requires less energy than in the case of the electrolysis of liquid water. In addition, when the temperature increases, a part of the energy required for the steam dissociation can be brought by heat instead of only electricity. It can be high temperature waste heat and surplus energy from power plants during off-pick hours. These elements make the HTSE technology

$$90\% H_2O + 10\% H_2 \qquad\qquad 10\% H_2O + 90\% H_2$$

$4e^- \rightarrow$ | Porous cathode

$$2H_2O + 4e^- \rightarrow 2H_2 + 2O^{--}$$

Gastight electrolyte

$$2O^{--} \rightarrow O_2 + 4e^-$$

Porous anode

O_2
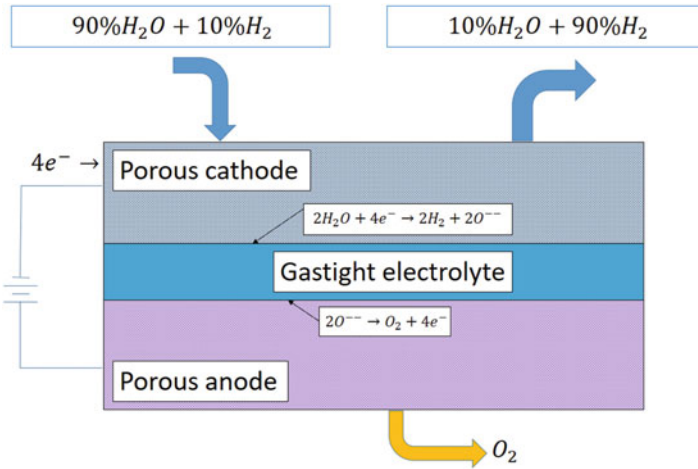
Fig. 27 High temperature steam electrolysis process schematic

O_2 storage H_2 storage

Heat
800–1200 °C

H_2O

SO_2

$$H_2SO_4 \leftrightarrow \frac{1}{2}O_2 + H_2O + SO_2 \qquad\qquad SO_2 + 2H_2O \leftrightarrow H_2SO_4 + H_2$$

$$H_2SO_4$$
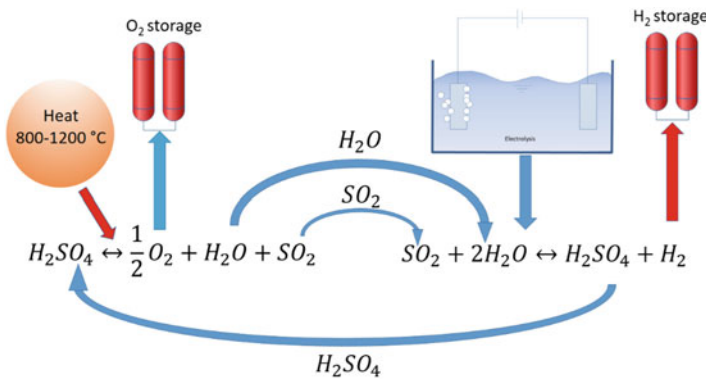
Fig. 28 Hybrid-sulphur process schematic

promising in terms of global efficiency. The highest could be the temperature, the best would be the efficiency, more that electrochemical kinetics are favored by the increase of the temperature.

However, limitations due to materials and costs occur and the targeted operating temperature is around 800 °C or even below, down to 700 °C. To become competitive with other hydrogen technologies, HTSE must exhibit high durability (25,000 hours) and high performances (high hydrogen production rates, i.e., ~40 mgH$_2$/cm^2/h or ~ -1 A/cm^2 but also good gas tightness to recover as much as possible the hydrogen produced). In addition, cost-effective stack and system components must be considered.

– Hybrid-sulphur (Fig. 28)

The HyS cycle (also known as Westinghouse cycle) is a combination of electro-chemical and thermochemical processes. Compared to the S-I cycle, this cycle id advantageous in that it only consists of two main stages. The first stage involves the electrolysis of water and SO_2, as follows:

$$SO_2 + 2H_2O \rightarrow H_2SO_4 + H_2$$
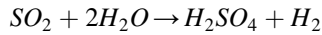
This reaction takes place at 87 °C and yields hydrogen and sulphuric acid. In the second stage, H_2SO_4 is decomposed to form water, oxygen and SO_2, as follows:

$$H_2SO_4 \rightarrow H_2O + SO_2 + \frac{1}{2}O_2$$
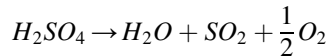
This is however an intermediate decomposition step, sulphuric acid decomposing first to Sulphur thioxide and steam and then further to SO_2 and oxygen. The decomposition reaction at around 800 °C is common to the S-I and HyS cycles, metal oxides are used as catalytic materials.

To allow more efficient electricity generation and thermal conditions suitable for most thermochemical processes, a new type of reactor called the Very High Temperature Reactor (VHTR) has been proposed (Jaszczur et al. 2015). This type of reactor is a helium-cooled reactor with a gas outlet temperature at least of 950 °C; the reactor is graphite-moderated and has a ceramic core.

All cycles considered exhibit an increase in efficiency if the reactor outlet temperature is raised. Increasing the reactor outlet temperature leads to an increase in plant power output rate as well as an increase in efficiency. High or very high temperature reactors used for electricity and hydrogen production have significant future potential to improve efficiency by raising the reactor outlet temperature or steam temperature. Small unit size, safety, low operation and maintenance costs, modular construction and high temperature may offer benefits for various applications beyond electricity generation (e.g., district heating, heating for refinery, metallurgical, petrochemical operations, and other high and low temperature process heating). In addition to the benefit of high efficiency energy conversion, hydrogen production or other thermal processes that require large amounts high temperature heat can be accommodated with such nuclear reactors.

5.5 Biological and Photonic Methods

In Biological methods hydrogen is produced from renewable resources such as bio-waste, biomass, solar energy, anaerobic bacteria, and different types of algae.

In general, the photo-production of O_2 & H_2 is catalyzed by microorganisms at ambient temperature and pressure.

The biological methods have a low environmental impact and appreciable hydrogen production efficiency.

In dark fermentation method, the hydrogen is produced without the light of the sun using anaerobic organisms from organic materials such as sugars, amino acids, waste materials and waste waters.

It is considered as one of the low production cost methods.

Typically Clostridium bacteria, the spore-forming obligate anaerobic microorganisms, are considered the most efficient bacteria in hydrogen production.

There are 2 types of fermentation:

Acetate,

$$C_6H_{12}O_6 \rightarrow 2CH_3COOH + 4H_2 + 2CO_2$$

Butyrate,

$$C_6H_{12}O_6 \rightarrow CH_3CH_2CH_2COOH + H_2 + 2CO_2$$

The process depends on factors: pH, temperature, pressure, hydraulic retention time, type of organism, the composition of the substrate and the presence of metals.

Clostridiales and Enterobacteriales are considered best for the highest yield of the H_2 production.

The addition of iron and nickel nanoparticles improves the fermentation process by enhancing H_2 production with clostridium butyricum.

One of the main problems with this process is Homoacetogenesis.

The rate and yield of the dark fermentation process is higher than the others, but the problem associated with this process is a low hydrogen concentration (40–60%; v/v).

The low hydrogen production capacity compared with high unit capital investment has been investigated and remains the major challenge of the dark fermentation method.

Photofermentation is a process in which hydrogen is produced from organic compounds through a nitrogenase catalyzed reaction, in the presence of light energy, by photosynthetic or anaerobic bacteria, such as Rhodobium, Rhodobacter, Rhodospirillum, and Rhodopseudomonas.

These bacteria use sunlight to convert small organic molecules into biomass releasing carbon dioxide and hydrogen under anaerobic conditions.

The common reaction of photofermentation is as follows:

$$CH_3COOH + 2H_2O + light \leftrightarrow 4H_2 + 2CO_2$$

Factors such as intensity and wavelength of light influence the production of hydrogen in the bacterial system. Light intensity has a direct relationship with the hydrogen production rate until it attains a saturation point, which further depends on the substrates and the microorganisms used.

Lighting and mixing significantly affect the hydrogen production performance from agricultural waste mixing enhance the mass transfer and shorten the lag phase, however the higher is the mixing speed the higher is the light intensity requirement.

Intermittent stirring has shown to increase the hydrogen production rate of 65.05% compared to continuous stirring, in corn Stover hydro-lysate photo-fermentation.

Hydrogen production is strongly dependent on the pH and inoculation volume ratio as the decrease in pH due to metabolic acid production is limiting factor in H_2 production during the photofermentation of glucose.

Photofermentation can be coupled with dark fermentation or used as a wastewater treatment technique. Wastewater treatment using photosynthetic bacteria has given satisfactory results.

A combination of ultra-sonication and biosorption using banana peels waste pretreatment, for mixed effluents of 70% restaurant and 30% brewery, enhance the photofermentative hydrogen production processes.

The addition of iron, molybdenum, and EDTA to the photofermentation of a blend of pre-treated brewery (30%) and restaurant (70%) effluents was found beneficial for the hydrogen production and bacterial growth by Rhodobacter sphaeroides.

In this method, the carbon monoxide is reacted with water in the presence of photosynthetic bacteria to produce hydrogen.

The overall reaction is:

$$CO + H_2O \leftrightarrow CO_2 + H_2$$

$$\Delta G^0 = -201 \ kJ/mol$$
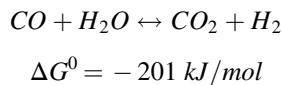
This method is not prominent for production because of homoacetogenesis.

Several experiments have been carried out as it show the highest hydrogen production was obtained at pH = 5 with a CO loading of 2000 cm^3.d^{-1} as hydrogen consumption increased with the pH from 5 to 8.

Biophotolysis is a dissociation of water molecules into hydrogen and oxygen molecules in biological organism under solar radiation.

It can be also defined as "photonic-driven hydrogen production" process as water is splitted with the help of cyanobacteria and blue-green algae.

The maximum hydrogen accumulation can be obtained with wild type, filamentous, non-heterocystous cyanobacterium desertifilum sp. IPPAS B-1220 with the yield of 0.229 mol.mg chlorophyll^{-1} h^{-1} under the light for 166 h.

It can be further categorised into direct and indirect bio-photolysis:

1. Direct bio-photolysis:

It is an attractive way to produce hydrogen as it uses water and sunlight as an energy source.

In direct biophotolysis, photosynthetic process occurs with microalgae under sunlight:

$$2H_2O + light \rightarrow 2H_2 + O_2$$
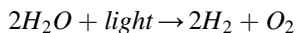
Microorganisms performing this activity are species of different green algae (photoautotrophic organism) and cyanobacteria.

Chlamydomonas reinhardtii is the most used microalgae.

Hydrogen production from microalgae is an attractive and eco-friendly process as it produces hydrogen from water, which is easily available and sunlight as an energy source with no accumulation of carbon dioxide and a solar energy efficiency of >80%.

2. Indirect bio-photolysis:

Indirect photolysis involves several steps, biomass production, concentration, and dark aerobic fermentation.

Generally, Indirect bio-photolysis is a two-step process:

1. Photosynthesis:

$$12H_2O + 6CO_2 + solar\ energy \rightarrow 6O_2 + C_6H_{12}O_6$$
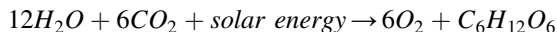
2. Hydrogen and carbon dioxide is generated:

$$C_6H_{12}O_6 + 12H_2O + solar\ energy \rightarrow 6CO_2 + 12H_2$$
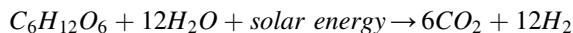
Hydrogenase and nitrogenase enzymes are responsible for the hydrogen production.

The maximum light conversion efficiency of this process is 16.3%. At low light illumination, better light conversion efficiency is achieved, and it decreases with the increasing light illumination. But the conversion efficiency is 1–2%.

6 Conclusions

Hydrogen can be used in its pure form as an energy carrier or as an industrial raw material.

It can also be combined with other inputs to produce what are referred to as hydrogen-based fuels and feedstocks. Hydrogen-based fuels and feedstocks can be produced using hydrogen from any source, whether electricity, biomass, or fossil fuels, and can readily be used in applications such as engines, turbines and chemical processes. They include such derivative products as synthetic methane, synthetic liquid fuels and methanol, all of which require carbon alongside hydrogen. They also include ammonia, which can be used as a chemical feedstock or potentially as a fuel, and which is made by combining hydrogen with nitrogen.

Power-to-X is a commonly used term for the conversion of electricity to other energy carriers or chemicals, generally through hydrogen produced by the electrolysis of water. The "X" can stand for any resulting fuel, chemical, power or heat. For example, power-to-gas refers to the production of electrolytic hydrogen itself or synthetic methane produced from electrolytic hydrogen combined with CO_2. Likewise, power-to-liquids refers to the production of hydrogen-based liquid fuels. Together, hydrogen-based fuels that integrate electrolytic hydrogen are sometimes referred to as "electro-fuels" or, in the very specific case of power from solar energy, solar fuels.

In recent years, colors have been used to refer to different sources of hydrogen production. "Black", "grey" or "brown" refer to the production of hydrogen from coal, natural gas and lignite respectively. "Blue" is commonly used to produce hydrogen from fossil fuels with CO_2 emissions reduced using CCUS. "Green" is a term applied to production of hydrogen from renewable electricity. In general, there are no established colors for hydrogen from biomass, nuclear or different varieties of grid electricity.

References

Abdalla AM, Hossain S, Nisfindy OB et al (2018) Hydrogen production, storage, transportation and key challenges with applications: a review. Energy Convers Manag 165:602–627. https://doi.org/10.1016/j.enconman.2018.03.088

Birat JP (2020) Society, materials, and the environment: the case of steel. Metals 10(3):331. https://doi.org/10.3390/met10030331

Ericsson K (2017) Biogenic carbon dioxide as feedstock for production of chemicals and fuels: a techno economic assessment with a European perspective. Environmental and energy system studies. Lund University

Hirscher M et al (2020) Materials for hydrogen-based energy storage e past, recent progress and future outlook. J Alloys Compd 827:153548. https://doi.org/10.1016/j.jallcom.2019.153548

http://www.globalcarbonatlas.org/

IEA (2019) The future of hydrogen

Jaszczur M, Rosen MA, Sliwa T, Dudek M, Pieńkowski L (2015) Hydrogen production using high temperature nuclear reactors: efficiency analysis of a combined cycle. In: 6th International conference on hydrogen production, May 3–6, 2015 UOIT—Oshawa, Ontario, Canada

Luh S, Budinis S, Giarola S et al (2020) Long-term development of the industrial sec-tor – case study about electrification, fuel switching, and CCS in the USA. Comput Chem Eng 133: 106602. https://doi.org/10.1016/j.compchemeng.2019.106602

Moller KT, Jensen TR, Akiba E, Li H-W (2017) Hydrogen - A sustainable energy carrier, Prog Nat Sci: Mater Int 27(1):33–40. https://doi.org/10.1016/j.pnsc.2016.12.014

Naterer GF, Suppiah S, Stolberg L et al (2014) Progress of international program on hydrogen production with the copper-chlorine cycle. Int J Hydrogen Energy 39:2431–2445. https://doi.org/10.1016/j.ijhydene.2013.11.073

Okolie JA, Patra BR, Mukherjee A, Nanda S, Dalai AK, Kozinski JA (2021) Futuristic applications of hydrogen in energy, biorefining, aerospace, pharmaceuticals and metallurgy. Int J Hydrogen Energy 46:8885–8905. https://doi.org/10.1016/j.ijhydene.2021.01.014

Olabi AG, Bahri AS, Abdelghafar AA, Baroutaji A, Sayed ET, Alami AH, Rezk H, Abdelkareem MA (2021) Large-vscale hydrogen production and storage technologies: current status and

future directions. Int J Hydrog Energy 46:23498–23528. https://doi.org/10.1016/j.ijhydene.2020.10.110

Proost J (2020) Critical assessment of the production scale required for fossil parity of green electrolytic hydrogen. Int J Hydrogen Energy 45:17067–17075. https://doi.org/10.1016/j.ijhydene.2020.04.259

Reddy SN, Nanda S, Vo DVN, Nguyen TD, Nguyen VH, Abdullah B, Nguyen-Tri P (2020) Hydrogen: fuel of the near future. In: Nanda S, Vo DVN, Nguyen-Tri P (eds) New dimensions in production and utilization of hydrogen. Elsevier, Cambridge, MA, pp 1–20. https://doi.org/10.1016/B978-0-12-819553-6.00001-5

Ruth MF, Jadun P, Pivovar B (2017) H2@Scale: technical and economic potential of hydrogen as an energy intermediate. In: Presentation at the fuel cell seminar and energy exposition, Long Beach, CA, 9 November. https://doi.org/10.5065/D6M32STK

Sun W, Wang Q, Zhiu Y et al (2020) Material and energy flows of the iron and steel industry: status quo, challenges and perspectives. Appl Energy 268:114946. https://doi.org/10.1016/j.apenergy.2020.114946

Tang J, Chu M-S, Li F, Feng C, Liu Z-G, Zhou Y-S (2020) Development and progress on hydrogen metallurgy. Int J Miner Metall Mater 27(6):713–723. https://doi.org/10.1007/s12613-020-2021-4

Victoria M, Haegel N, Peters IM et al (2021) Solar photovoltaics is ready to power a sustainable future. Joule 5:1–16. https://doi.org/10.1016/j.joule.2021.03.005

World Energy Council (2018) Hydrogen an enabler of the Grand Transition

Zuttel A, Remhof A, Borgschulte A et al (2010) Hydrogen: the future energy carrier. Philos Trans R Soc A368:3329–3342. https://doi.org/10.1098/rsta.2010.0113

Thermochemical Water Splitting Cycles

1 Introduction

Water electrolysis is not thermodynamically favorable because of its requirement of an energy input to drive the whole process (Turner 2004).

During water electrolysis, the splitting into hydrogen and oxygen acts thanks to the application of a potential between the anode and the cathode of the electrochemical cell. Given the Gibbs free energy relationship:

$$\Delta G^0 = \Delta H^0 - T\Delta S^0$$

knowing the standard enthalpy of formation (386.03 kJ/mol) and the ideal gas entropy (0.163 kJ/mol/K) of gas water, the Gibbs energy of water at 298 K can be calculated:

$$\Delta G^0 = 286.04 - (298 * 0.163) = 237.46 \, kJ/mol$$

Given this energy value, it is possible to calculate the required voltage to split water electrolytically:

$$V_{rev} = -\frac{\Delta G^0}{nF} = -\frac{237460}{2 * 96485} = -1.23V$$

being n the number of electrons required to obtain a hydrogen molecule (2) and F the Faraday's constant (Funk 2001).

The voltage value of 1.23 V requires that all the products go in the gaseous state. In low temperature electrolyzers where water is at atmospheric pressure and at temperatures below 90 °C, additional energy is required:

$$V_{tn} = -\frac{\Delta H^0}{nF} = -\frac{286030}{2*96485} = -1.48V$$

Once electrolysis is conducted at higher pressures and higher temperatures, V_{tn} tends to approach V_{rev}.

Another important aspect is related to the overall efficiency of the process. Electrolysis takes place at the potential of 1.48 V, but it is very slow. So, additional potential is necessary to accelerate the various reactions (Zeng and Zhang 2010). This is known as overpotential and its potential reduction is related to the efficiency of the electrolytic apparatus. Physically, overpotential is necessary due to the extremely low conductivity of water and the contemporary high activation energy required to split into hydrogen and oxygen. For this reason, first of all, salts, basics or acids are added to the water to increase the conductivity. Then, catalysts are employed to improve the activation of the reactions at the electrodes (Holladay et al. 2009).

In efficiency way to see the process, Faradaic efficiency must be considered; it is the ratio of the number of moles of hydrogen produced versus the charge passed. If the process has a 100% Faradaic efficiency, then every electron produced by the oxidation of water is transferred to a corresponding proton to produce hydrogen (Anantharaj et al. 2018). Now, Faradaic efficiency can be close to 100% but it will be to consider an efficient decrease due to component degradation of the electrochemical cell and the crossover of hydrogen to the oxygen-producing side of the cell. The other efficiency is related to an energy balance between the produced hydrogen in terms of its high heating value (HHV) and the energy required to produce it. So, efficiency can be calculated as:

$$\eta_{eff} = \frac{moles\ of\ hydrogen \cdot HHV_{H_2}}{I \cdot V \cdot t} \cdot 100$$

being I the cell current, V the applied voltage, and t the time interval during which the reactions evolve.

2   Principles of Water Splitting

The equation of the German chemist Walther Nernst can be obtained from thermodynamics. The variation of Gibbs free energy is a function of the concentrations of the species participating in a chemical reaction

$$aA + bB + \ldots \rightarrow mM + nN + \ldots$$
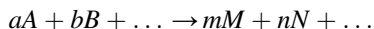
and is given by:

$$\Delta G = \Delta G^0 + RT \cdot \ln\left(\frac{a_M^m \cdot a_N^n \cdot \ldots}{a_A^a \cdot a_B^b \cdot \ldots}\right)$$

where:

$$a_A^a, a_B^b, \ldots, a_M^m, a_N^n, \ldots$$

are the activities of the species.

Some species involved in the electrode reaction are solids or pure liquids. For these pure substances, the activity is constant, and its value is considered unitary. The activity of the gases is usually taken to be the partial pressure of the gases expressed in the atmosphere, and the activity of the ions in dilute solution is generally considered to be their molar concentration (Sapountzi et al. 2017).

By substituting in the Gibbs free energy equation and dividing each member of the equation by -nF, we obtain the Nernst equation. Nernst's equation expresses the relationship between the potential of an electrochemical cell and the concentrations of its constituents at equilibrium. In the specific case of an electrochemical cell, it is written:

$$\Delta E = \left(E_{cathode}^0 - E_{anode}^0\right) - \frac{RT}{nF} \ln\left(\frac{a_M^m \cdot a_N^n \cdot \ldots}{a_A^a \cdot a_B^b \cdot \ldots}\right)$$

In 1832, Michael Faraday stated his two laws of electrolysis:

1. The weights of substances formed at an electrode during electrolysis are directly proportional to the quantity of electricity that passes through the electrolyte.
2. The weights of different substances formed by the passage of the same quantity of electricity are proportional to the equivalent weight of each substance.

The quantity of material (m) produced is:

$$m = k \cdot \int_0^t I \cdot dt$$

where k is a proportionality constant and I is the instantaneous current flowing through the cell. In a cell with circulation of continuous current, most of this current is connected to chemical reactions (faradic current) and a small part, generally negligible can be used for other purposes (non-Faradic current).

Thus, the amount of material that forms or disappears at the electrodes is proportional to the intensity of the current and the duration of the electrolysis t. Knowing the number of moles is (m/M), which corresponds to a quantity of electricity:

$$Q = \frac{m}{M} \cdot N \cdot F = I \cdot t$$

m is the mass of substances formed (g); M is the molar mass of substances formed (g/mol.); n is number of exchanged electrons, I is the current in amperes (A),

$$Q = I \cdot t$$

is the quantity of electricity in coulomb (C), t is the time (s).

The potential difference for a cell of an electrolyzer, which is always:

$$\Delta E = 1.8 - 2.0V$$

at the current density of:

$$j = 1000 - 300 \, Am^2$$

in industry water electrolysis, is an addition of four terms:

$$\Delta E = \Delta E_{the} + \eta_a + \eta_c + RI$$

with: η_a (V) is the anodic overvoltage; η_c (V) is the cathodic overvoltage; R (Ω) is the global resistance and I (A) is the current.

Figure 1 shows the relationship between the electrolyzer cell potential and operating temperature.

The cell potential-temperature plane is divided into three zones by the so-called equilibrium voltage line and thermo-neutral voltage line. The equilibrium voltage is the theoretical minimum potential required to dissociate water by electrolysis, below that value the electrolysis of water cannot proceed. The equilibrium voltage

Fig. 1 Cell potential for hydrogen production by water electrolysis as a function of temperature
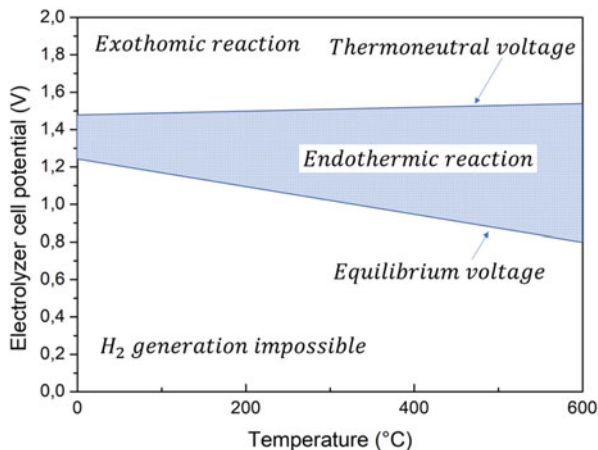
decreases with increasing temperature. The thermo-neutral voltage is the actual minimum voltage that must be applied to the electrolysis cell, below that value the electrolysis is endothermic and above that value, exothermic. The thermoneutral voltage naturally includes the overpotentials of the electrodes, which are only weakly dependent on temperature. Hence, the thermo-neutral voltage only exhibits a slight increase with temperature. If water electrolysis takes place in the shaded area in Fig. 1, the reaction will be endothermic.

As these electrochemical reactions are heterogeneous surface processes, it is convenient to relate the reaction rate to the electrode area, A, as:

$$\frac{dm}{A \cdot dt} = \frac{I}{A \cdot n \cdot F}$$

Therefore, the expression for current density is:

$$j = \frac{I}{A}$$

may be rewritten as:

$$j = \frac{nF}{A} \cdot \frac{dm}{dt}$$

For a general electrochemical reaction:

$$O + ne^- \leftrightarrow R$$
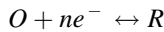
Under nonequilibrium potential conditions, the equation that best describes the current density versus potential is the Butler-Volmer expression:

$$j = \overrightarrow{j}_a + \overleftarrow{j}_c = nF\overleftarrow{k}_0 C_R(0,t)e^{\frac{\alpha_a nF\left(E-E^0\right)}{RT}} - nF\overrightarrow{k}_0 C_R(0,t)e^{\frac{\alpha_c nF\left(E-E^0\right)}{RT}}$$

where:

$\overrightarrow{j}_a$ *and* $\overleftarrow{j}_c$ are, respectively, the anodic and cathodic current density; and $\overrightarrow{k}_0$ and $\overrightarrow{k}_0$ are, respectively, the rates constants of the anodic and cathodic reaction; α_a and α_c are, respectively, the anodic and cathodic exchanges coefficients; E^0 is the standard potential.

Under the control of electron transfer rate, (the concentration of the electrodes' surface is equal to the concentration in the bulk), this equation can be expressed as current density versus overpotential ($\eta = E-E_{eq}$):

$$j = j_0 j\left(e^{\frac{\alpha_a nF\eta}{RT}} - e^{\frac{\alpha_c nF\eta}{RT}}\right)$$

The anodic and cathodic exchanges coefficients (α_a, and α_c) are related ($\alpha_a + \alpha_c = 1$), and generally:

$$\alpha \approx \alpha_a \approx \alpha_c \approx \frac{1}{2}$$

For a given single-step reaction at a constant temperature, the j versus η characteristics will depend on j_0, α_a, and α_c.

For large η values, the Butler-Volmer equations can be simplified to give the Tafel equation:

$$|\eta| = a \cdot \log|j| + b$$

so:

$$For \ll 0, \log(j) = -\log(j_0) - \left(\frac{\alpha_c nF}{2.3RT}\right) \cdot \eta$$

$$For \gg 0, \log(j) = -\log(j_0) - \left(\frac{\alpha_a nF}{2.3RT}\right) \cdot \eta$$

For the hydrogen evolution reaction (HER), the Volmer-Tafel and Volmer-Heyrovský mechanisms are often proposed and well known. The first step involves the formation of adsorbed hydrogen (Volmer step):

$$H_2O + e^- \leftrightarrow H_{ads} + OH^-$$
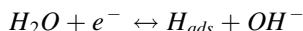
which is then followed by either chemical desorption (Tafel step):

$$2H_{ads} \leftrightarrow H_2$$
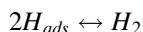
or electrochemical desorption (Heyrovský step):

$$H_{ads} + H_2O + e^- \leftrightarrow H_2 + OH^-$$
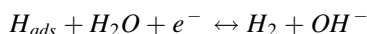
For the hydrogen evolution reaction (HER), the overpotential, η_{H2}, is generally calculated by the Tafel equation (Anantharaj et al. 2016). Hydrogen formation is intrinsically determined by the strength of the bond between hydrogen and the electrode surface. Pd has the lowest heat of adsorption of hydrogen:

$$\Delta H_{ads,Pd,298}(H_2) = 83 \ kJmol^{-1}$$

for Ni, the heat of adsorption is:

$$\Delta H_{ads,Ni,298}(H_2) = 105 kJmol^{-1}$$

Electrode properties, type and concentration of the electrolyte, and temperature.

are parameters that also influence hydrogen formation. If hydrogen adsorption is the rate-determining step, electrode materials with more edges and cavities in their surface structure will favor electron transfer and create more centers for hydrogen adsorption (Jiang et al. 2020). If hydrogen desorption is the rate-determining step, physical properties such as surface roughness or perforation will prevent bubbles from growing and increase electron transfer by adding reaction area, as a result increasing the rate of electrolysis. When the overpotential is low, electron transfer is not as fast as desorption and hydrogen adsorption will be the rate-determining step. At the opposite, when the potential is high enough, hydrogen desorption will be the rate-determining step (Mandin et al. 2014). The hydrogen adsorption energy is a good parameter to identify the most promising materials for the HER.

The mechanism of the oxygen evolution reaction (OER) is more complex than that suggested for HER. The most generally accepted mechanism for the OER is:

$$OH^- \leftrightarrow OH_{ads} + e^-$$

$$OH^- + OH_{ads} \leftrightarrow O_{ads} + H_2O + e^-$$

$$O_{ads} + Oads \leftrightarrow O_2$$
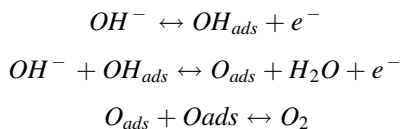
The mechanism is controlled by the charge transfer at low temperatures. On the other hand, at high temperatures, the recombination step controls the reaction on Ni electrode. Usually, acid solutions or PEMs are used as electrolytes in water electrolyzers due to the high ionic conductivity of their acid media and are free from carbonate formation, as compared with alkaline electrolytes (Carmo et al. 2013). So, noble metals are used as electrocatalysts for OER in acidic media. Bifunctional electrocatalysts, which can work for both oxygen evolution and oxygen reduction, have also been proposed for water electrolysis.

The electrical resistance in a water electrolysis system has three main components: (1) the resistance in the system circuits; (2) the mass transport phenomena including ions transfer in the electrolyte; (3) the gas bubbles covering the electrode surfaces and the diaphragm.

The nature and the dimensions of the materials used in the electrodes and the connections and the electric circuit, the methods of their preparations are responsible for the electrical resistance of the system (Siracusano et al. 2011). It can be expressed as follows:

$$R = \sum_i \frac{l_i}{A_i \cdot \chi_i}$$

where χ_i (Ω^{-1} m^{-1}) is the electrical conductivity for each component of the circuit, including wires, connectors, and electrodes. This part of the resistance can be

reduced by reducing the length of the wire, increasing the cross-section area, and adopting more conductive wire material.

The ionic solution conductivity χ is a function of concentration and temperature (Jiang et al. 2021). For an ionic solution containing ions (i), charged $+z_i$ or $-z_i$ and at the concentration Ci in mol·m^{-3}, the conductivity of the solution, noted χ (Ω^{-1} m^{-1}), is:

$$\chi = \sum_i \lambda_i \, z_i \, C_i$$

with: λ_i is the equivalent conductivity of the ion (i) in, S·m^2·mol^{-1}.

The presence of bubbles in the electrolyte solution and on the electrode surfaces causes additional resistances to the ionic transfer and surface electrochemical reactions (Ateya and El-Anadouli 1991). One of the accepted theoretical equations to study the bubble effect in the electrolyte is given as follows:

$$\kappa_g = \kappa(1 - 1.5f)$$

where κ is the specific conductivity of the gas-free electrolyte solution; f is the volume fraction of gas in the solution.

Convective mass transfer plays an important role in the ionic transfer, heat dissipation and distribution, and gas bubble behavior in the electrolyte. The viscosity and flow field of the electrolyte determines the mass (ionic) transfer, temperature distribution and bubble sizes, bubble detachment and rising velocity, and in turn influence the current and potential distributions in the electrolysis cell. As the water electrolysis progresses the concentration of the electrolyte increases, resulting in an increase in the viscosity. Water is usually continuously added to the system to maintain a constant electrolyte concentration and thus the viscosity (Özdemir and Taymaz 2022).

The physics of gas evolution proceeds through three phases: nucleation, growth and detachment. Bubbles start nucleating at electrode surface from solution once the solution becomes highly supersaturated with produced gas. Subsequently, bubbles grow by dissolved gas diffusion to their surface or by coalescence with others, and finally detach from the electrode when the forces pulling them away overcome the surface forces binding them. There are a lot of phenomena of gas evolution in every stage, the effect on process parameters have been studied experimentally and theoretically, but there are a lot of them that must be investigated. Just as growth of bubbles is complicated, so are the effects of gas bubbles which include electrolyte solution mixing and obstruction of electric current. Impeding the current, bubbles decrease electrolyte conductivity and so add to ohmic losses in the cell. Mixing the electrolyte there is bubbles creation that enhances heat transfer from the electrode and mass transfer to the electrode surface.

Bubbles may nucleate when the electrolyte near the electrode is supersaturated with gas as in the electrolytic production of H_2, for example. A flux of H_2 based on a current of a few mA/cm^2 is sufficient to supersaturate the liquid since H_2 is sparingly

soluble. When the dissolved gas concentration reaches a critical value, bubbles nucleate and grow. The critical dissolved H_2 concentration leading to nucleation can be theoretically obtained from classical nucleation theory; but the effectiveness of this theory for electrolytic gas evolution needs further examination.

Nucleation theory born in the 1920s when investigators considered the thermodynamics and kinetics of single-component phase transitions. From this work evolved classical nucleation theory in which density fluctuations engender vapor nuclei that may grow or decay depending on whether the bubble nucleus is higher or smaller than a certain size, determined by so-called critical radius. At this stage, the bubble is in metastable chemical and mechanical equilibrium with its surroundings. The frequency of formation of critical nuclei is inversely proportional to the exponential of the isothermal minimum work required to form such nuclei divided by kT, being k the Boltzmann constant and T the temperature. Thus, the essential features of nucleation theory are the expression defining the size of the critical bubble nucleus and the formulation of the rate expression as an exponential function of the work associated with the production of a nucleus having this dimension.

Electrolytically evolved gas bubbles nucleate from solutions of gas dissolved in a host liquid; for this reason, theory for multiple components is required for this case. An expression for the critical radius for multi-component systems is given by:

$$R_c = \frac{2\sigma}{\frac{\eta P\infty}{v_1} + \frac{P'C'}{v_2 C_0} - P'}$$

where $P\infty$ is the vapor pressure of solvent at the temperature of the liquid, P' is the external pressure in the liquid, v_1, v_2 are the vapor phase activity coefficients of the solvent and solute, C' is the concentration of the gas in the solution surrounding the bubble, expressed as moles of solute per mole of solvent, $\underline{C}_0$ is the equilibrium concentration of the gas in the solvent when a flat surface of the solvent is exposed to the gas only at T' and P', expressed as moles of solute per mole of solvent, σ is the surface tension of the liquid-gas interface often assumed equal to the surface tension of the liquid vapor interface, and η is defined as:

$$\eta = \exp\left(\frac{V_1(P' - P\infty)}{kT} - C'\right)$$

where V_1 is the specific volume of the pure solvent. The solute gas decreases the critical radius from that of the pure solvent at the same temperature and pressure; therefore, the rate of nucleation correspondingly increases.

The rate equation derived for the pure solvent:

$$J = Z exp\left(- \frac{16\pi\sigma^3}{3kT(P'' - P')^2} \right)$$

Where J is the frequency of nucleation $(scm^3)^{-1}$, Z is the frequency factor, a very weak function of T and P, and P'' is the pressure inside the critical size bubble) also applies to multi-component solutions; however, P'' has two contributions in this case. The dissolved gas exerts a vapor pressure in addition to the vapor pressure of the pure solvent. The increase of P'' lowers the critical radius and therefore decreases the maximum sustainable supersaturation.

The prediction of the maximum attainable limit of supersaturation is given by:

$$P'' = \frac{P'}{v_2 C_0} + \frac{P\infty}{v_1}\left[exp\left(\frac{V1(P' - P\infty)}{kT} - C' \right) \right]$$

The growth stage of gas evolution includes the diffusion of dissolved gas to the gas/liquid interface and the coalescence of bubbles. This mechanism starts with nucleation, followed by growth by diffusion, coalescence of small bubbles, radial movement of small bubbles and their coalescence with stationary medium-size bubbles, and scavenging coalescence of the medium bubbles by large ones moving along the electrode. This is the process by which large O_2 bubbles are built in basic medium.

Detachment as the final phase in the physics of gas evolution has also been subject of both theoretical and experimental studies. The bubbles are found to detach once the surface adhesive forces, related to bubble contact angles, can no longer restrain them. In contrast to these equilibrium measurements, studies of the dynamics of gas evolution showed that the bubble formed by the coalescence of two large bubbles would jump off the electrode and sometimes even return. It was also reported that bubble coalescence often precedes their detachment from the electrode surface. It was concluded that the expanding boundaries of the new bubble mechanically forced it off the electrode. It was further speculated that bubbles' movement towards the electrode could be affected by electrostatic forces on a moving bubble or by surface forces varying with concentration.

Related to the detachment of bubbles is their mobility on electrode surfaces. Investigation of the forces holding a drop on an inclined plane led to conclusion that drops holding onto these surfaces are a result of the contact angle hysteresis, the adherence between bubbles' advancing and retreating contact angles. The main cause of hysteresis is roughness of the surface. Figure 2 illustrates the relation between the hysteresis angle, the contact angle, and the volume of the largest bubble that sticks to a surface facing downward and inclined by γ degrees to the horizontal and how they determine the minimal and maximal size of electrolytically produced bubbles in aqueous media. With increasing the contact angle and keeping the other parameters constant, increase of bubble size can be observed.

Bubble growth and consequently its final size are determined by several parameters including electrode material, current density and different additives (Bakker
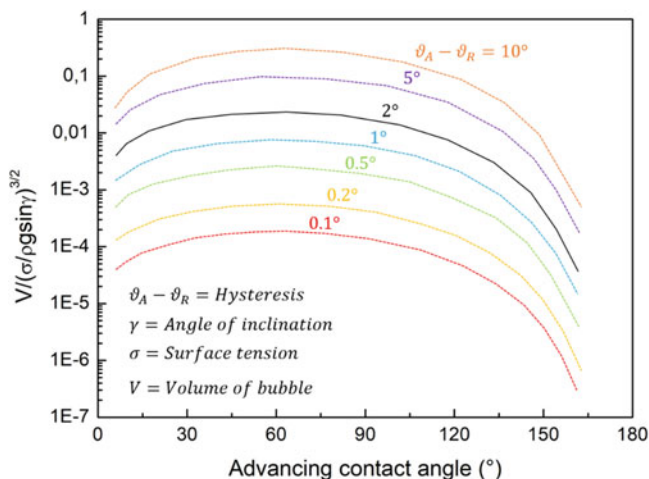
Fig. 2 Cell potential for hydrogen production by water electrolysis as a function of temperature

and Vermaas 2019). In addition, it has been established that current density affects bubble size, but there are still some disagreements in the literature about its exact effect. The size of H_2 bubbles produced in alkaline medium is not influenced by current density and they are the smallest ones. On the other hand, O_2 bubbles evolved in the same medium rapidly grew for current density values higher than 30 mA/cm^2 (Fig. 3).

Besides the electrode material and current density, additives are another parameter believed to influence bubble behavior and size. Studies showed that presence of additives such as gelatin, glycerin and β-naphthochinolin in the electrolyte solutions results in evolution of smaller bubbles in most cases with formation of frothy mixture being observed. It is believed that additives reduced the ratio of the bubble diameter to the contact diameter by half and increased the electrode wettability. This resulted in the presence of a thick film of electrolyte between the gas and the electrode that is less adhesive than thin films. Still, the forces holding the bubbles to the electrode were most likely weakened proportionally to the decrease of both the perimeter of the contact area and the contact angle. Moreover, it is speculated that the inhibitors stabilize the bubble interfaces and avert their coalescence on the electrode.

In addition to electrode material, current density value and presence of additives in the electrolyte, other process parameters have been reported to influence bubble size and behavior. It was found that the bubble size decreased with increasing flow rate in the interelectrode area with significantly higher current densities being achieved in comparison to those in stagnant electrolyte. Furthermore, electrode orientation and configuration are also expected to affect bubble size.

Electrolytically evolved bubbles enhance heat and mass transfer to gas evolving electrodes because the growing and detaching of gas bubbles mix the electrolyte near the surface with electrolyte in the bulk. Evolving gas bubbles can accelerate mass transfer to rates achieved by only intense mechanical stirring or flow and is thus very
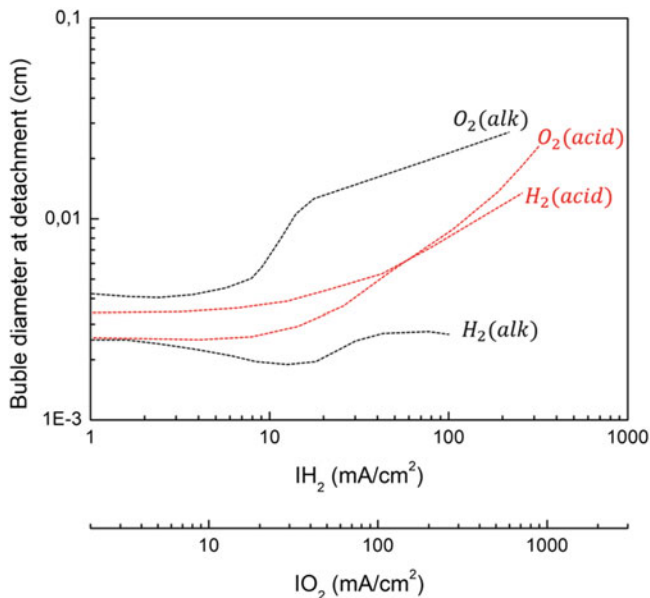
Fig. 3 Bubbles evolution in alkaline and acidic media

effective where circumstances allow its use. Phenomena of gas evolution discussed at the outset are responsible for mixing at the electrode. The growing bubbles produce convection as their boundaries expand by diffusion and coalescence. When a bubble detaches, electrolyte must flow to fill the vacancy. The effective density of a heterogeneous mixture of gas and electrolyte is lower than that of bulk electrolyte; so there is macro-stirring of the electrolyte by the rising gas bubbles (gas lift). Severely, these are complicated phenomena to describe and it seems impossible to mathematically analyze the flows; therefore, engineers have constructed theories which explain and correlate the experimental results and patterns.

Investigators of mass transfer enhancement at gas-evolving electrodes have generally reported Nernst mass transfer boundary layer thickness, as a function of gas evolution rate (cm^3/cm^2s) or current density. The Nernst boundary layer thickness is given by:

$$\delta_N = \frac{nFDC}{i}$$

where n stands for the equivalents per mole, D is the diffusivity and F is Faraday's constant. The Nerst boundary layer is essentially the reciprocal of a mass transfer coefficient divided by the molecular diffusivity.

Figure 4 is a plot of the results on mass transfer enhancement in acid solutions. It may be observed that the boundary layer thickness decreases with the increase of the gas evolution rate (Vincent et al. 2018). At the highest gas evolution rates,

Fig. 4 Boundary layer
thickness as a function of
current density in acidic
media
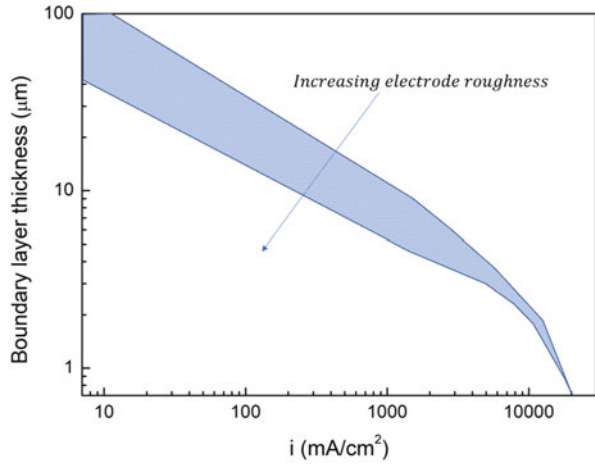
corresponding to 10 A/cm^2, the boundary layer thickness is of the order of 1 μm
which is fairly thin.

The Nernst boundary layer thickness is a simple characteristic of the mass transfer
rate and is usually expressed by:

$$\delta_N = ai^b$$

considering fluid viscosity, kinematic viscosity and the diffusion coefficient, the
exponent b is the center of differences between the schools of thought, taking on
values from −0.25 to −0.87. The comparison between acidic and alkaline media is
shown in Fig. 5.

The slope change, around 30 mA/cm^2, corresponds to a change in bubble size for
the O_2 bubbles evolved in basic solution. This was considered an indication of the
onset of coalescence between bubbles on the electrode.

3   Low Temperature Electrolysis

Gibbs free energy (ΔG) is defined as the net internal energy available to work,
therefore less work is done by changes in temperature and pressure (Ayers et al.
2019). Enthalpy (ΔH) is an intrinsic property of a material that is a function of
temperature and pressure.

In electrolysis, the energy is supplied to the cell by heat (Q) and electrical energy
(W_{elec}). The relationship between enthalpy, energy input and Gibbs free energy is
shown in:

Fig. 5 Boundary layer
thickness as a function of
current density in acidic and
alkaline media

Fig. 5 Boundary layer thickness as a function of current density in acidic and alkaline media
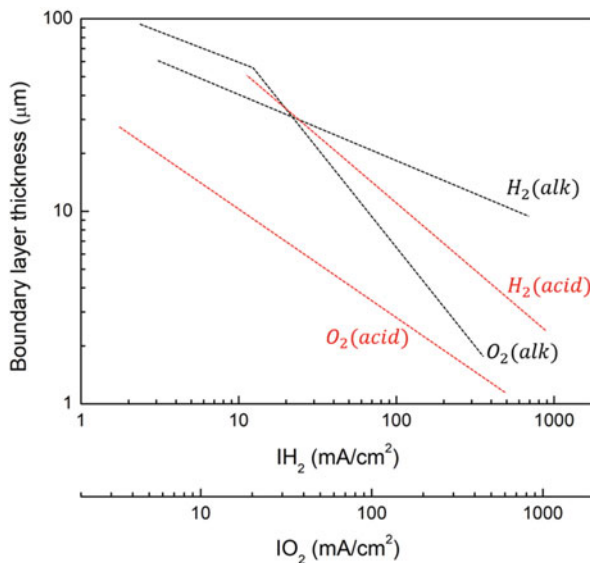
$$\Delta H = \Delta G + T\Delta S = W_{elec} + Q$$

where T is temperature and ΔS is change in entropy. By considering the change in the functions above, the overall change in Gibbs free energy and the operating potential can be calculated (Marangio et al. 2009).

At standard temperature and pressure (S.T.P., 298 K, 1 atm), Gibbs free energy of formation represents the thermo-neutral voltage and is where hydrogen and oxygen are produced with 100% thermal efficiency. To enable electrolysis mode the voltage must be greater than the open circuit voltage (OCV: voltage corresponding to zero current). It is determined by the variation in Gibbs free energy of formation between reactants and products. As previously mentioned, Gibbs free energy varies with temperature and state (gas or liquid). This is shown by:

$$E_0 = -\frac{\Delta G_0}{zF}$$

where E_o is the theoretical minimum reversible potential of an electrolysis cell, z is the number of electrons transferred in the reaction and F is the Faraday constant (96,485 Coulomb mol^{-1}).

At S.T.P., the Gibbs free energy of formation of water is +237.2 kJ mol^{-1}; therefore E_o = 1.23 V and it represents the minimum voltage required to split water. Ignoring heat transfer in the system, the total enthalpy required must be provided by the inputted electrical energy. But we are not in an ideal world, so heat transfer does exist and the thermo-neutral potential (1.48 V) is required to enable the electrochemical reaction.

The real potential (E_{cell}) needed to split water at a reasonable rate will require E_{cell} to be greater than E_o. The difference between the two is known as overpotential, losses or polarization. The Nernst potential (V_n) accounts for the changes in the activity of the reaction and is shown in:

$$V_n = E_0 + \frac{RT}{2F} \ln \left(\frac{P_{H_2} P_{O_2}^{\frac{1}{2}}}{P_{H_2O}} \right)$$

where P_{H2}, P_{O2} and P_{H2O}, are the partial pressures of hydrogen, oxygen and water respectively. This equation enables the calculation from experimental data, since the temperature of water entering the electrolyzer varies:

$$P_{H_2O} = 610.78 \exp \left[\frac{T_c}{T_c + 238.3} (17.2694) \right]$$

where T_c is the temperature (°C) of water entering the electrolysis cell. The partial pressures of hydrogen and oxygen are calculated using measurements from the electrolysis cathode and anode:

$$P_{H_2} = P_c - P_{H_2O}$$
$$P_{O_2} = P_a - P_{H_2O.}$$

where P_c and P_a are the partial pressures (atm) measured at the cathode and anode of the electrolysis cell respectively.

However, hydrogen evolution does not occur at the reversible potential (1.23 V). This is the result of resistances (overpotential) in the electrolysis system. These resistances in the process mean a higher potential is required to split water to overcome these barriers.

An electrical circuit analogy can be used to illustrate the various resistances encountered during the electrolysis process (Fig. 6).

$$R_{cell} = R_1 + R_1' + R_{bubble,O_2} + R_{bubble,H_2} + R_{ions} + R_{membrane} + R_{anode} + R_{cathode}$$
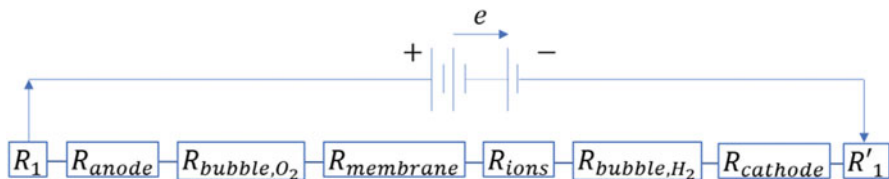
Fig. 6 Electrical circuit analogy of water electrolysis

The three main types of resistance in the electrolysis cell are electrical, transport and electrochemical reaction resistances (Darband et al. 2019). Electrical resistances (R_1 and R'_1) directly result in heat generation which points to waste electrical energy in the form of heat according to Ohm's law. In water electrolysis the resistances in electrical circuits. The resistances of the electrodes and connecting circuits are determined by the material types and dimensions, preparation methods, and the conductivities of each component. It can be expressed as follows:

$$R = \sum \frac{1}{A \kappa_g}$$

where κ is the electrical conductivity ($\Omega^{-1}\ m^{-1}$), subscript g represents each component of the circuit, which includes wires, connectors and electrodes. These items can be improved by decreasing the length of wire, using a higher surface area of electrode and using a material with higher electrical conductivity.

The ion transfer in the electrolyte is dependent on the electrolyte concentration (if liquid), membrane (if solid), and distance separating the cathode and anode (Grdeń et al. 2008). The molar conductivity, which is different from the conductance rate in the metallic conductor, is used instead of conductivity. It is illustrated in:

$$\Lambda = \frac{\kappa}{C}$$

where Λ is the molar conductivity ($m^2\ \Omega^{-1}\ mol^{-1}$) and C is the electrolyte concentration. Molar conductivity is also a function of the mass transfer of ions and concentration.

The presence of bubbles on the electrode surfaces creates resistances to the ionic transfer and thus the electrochemical reaction. The study of the bubble effect in electrolytes is a wide area of research and is most accepted:

$$\kappa_g = \kappa(1 - 1.5f)$$

where κ is the specific conductivity of the electrolyte (gas-free) and f is the volume fraction of gas in the electrolyte solution. If bubble coverage (θ) is taken into:

$$\rho = \rho_0 (1 - \theta)^{-\frac{3}{2}}$$

where ρ_0 is the specific resistivity of the electrolyte (gas-free). Electrical resistances can also be calculated by Ohm's Law:

$$R = \frac{V}{I}$$

in which, when potential V is applied only at R_1 or R'_1, current I is measured. Alternatively, resistance can be calculated using R = L/(kA), where L is the length, k

is the specific conductivity, and A the cross-sectional area of the conductor. Transport resistances ($R_{bubble,O2}$, $R_{bubble,H2}$, R_{ions} and $R_{membrane}$) are physical resistances such as gas bubbles covering the electrode surface, resistances to ionic transfer of species in the electrolyte, and due to resistance of ion flow in the membrane. These losses are known as ohmic loss (Schalenbach et al. 2013).

Mass transfer, temperature distribution and bubble sizes, are determined by the viscosity and the flow field of the electrolyte. Other parameters affected include bubble detachment and rising velocity, of which all functions are transport related resistances. It is important to note, that during electrolysis the concentration of electrolyte increases (since water is being consumed), and therefore the solution will become increasingly viscous; hence, resulting in a rise in transport related resistances.

Current research in water electrolysis is focused to increase mass transfer on the electrode surfaces, but this could disadvantage the production rate of hydrogen. Aiding mass transfer on the electrode surfaces will enable higher bubble formation, which would reduce the contact surface area between the electrode and the electrolyte, and consequently limit the availability of sites for nucleation. Circulating the electrolyte through the electrolyzer via pumps can mechanically remove gas bubbles from the surface quicker, and subsequently reduce bubble overpotential in the electrolyzer (Liang et al. 2020).

Electrochemical reaction resistances (R_{anode} and $R_{cathode}$), also known as activation losses, are overpotentials required to overcome the activation energies on the cathode and anode surface for the formation of hydrogen and oxygen respectively. These are inherent energy barriers of the reactions and determine the reaction kinetics of the electrochemical reaction (Fig. 7).

When equilibrium occurs at OCV, there are dynamic currents at both electrodes and are symbolic of electrode behavior. These dynamic currents at the cathode and anode are known as the exchange current density, that is defined as the rate of reduction at the cathode and oxidation at the anode and represent the electrode's

Fig. 7 Potential losses contributions from water electrolysis
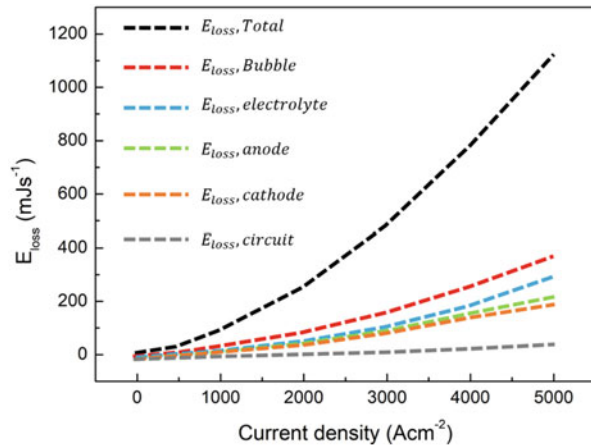
Fig. 8 Overpotential
variation with current
density
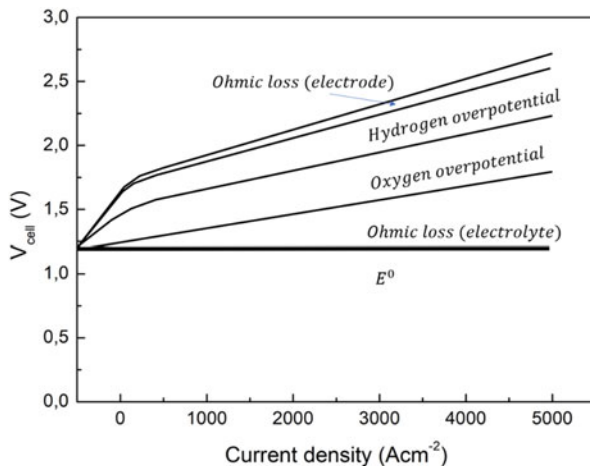
ability to transfer electrons and happens equally in both directions, culminating in zero change in electrode composition. A small exchange current density shows slow reaction kinetics and slow rate of electron transfer. A large exchange current density exhibits the opposite behavior.

Overpotential is also a function of current density not only temperature (Zhou et al. 2018).

Figure 8 shows with increasing current density, the different types and overall cell overpotential increase.

The initiation of an electrochemical reaction on an electrodes surface requires the overcoming of an energy barrier (Hu et al. 2019). This energy barrier is more commonly known as activation energy and is the extra energy required to overcome energy barrier of the rate determining step of the electrochemical reaction to a value at which the reaction will proceed at a suitable rate. It is known as an activation overpotential in the electrochemical reaction. The following equation shows the Butler-Volmer equation, used for calculating activation overpotential:

$$I = A \cdot j_0 \left\{ \exp\left[\frac{\alpha_c nF}{RT}\left(E - E_{eq}\right)\right] - \exp\left[-\frac{\alpha_c nF}{RT}\left(E - E_{eq}\right)\right] \right\}$$

Where I is the electrode current, A is the electrode active surface area, jo is the exchange current density, E is the electrode potential, E_{eq} is the equilibrium potential, T is the absolute temperature, n is the number of electrons in reaction, F is the Faraday constant, R is the universal gas constant, αc is the cathodic charge transfer coefficient, α_a is the anodic charge transfer coefficient.

These activation losses can also be calculated for the anode, η_a, and cathode, η_c and are presented in the Tafel Equations:

$$\eta_a = \frac{RT}{\alpha_a zF} \ln\left(\frac{i}{1_{a,0}}\right)$$

$$\eta_c = \frac{RT}{\alpha_c zF} \ln\left(\frac{i}{1_{c,0}}\right)$$

where α_a and α_c, are the electron transfer coefficients of the anode and cathode respectively, $i_{a,o}$ and $i_{c,o}$ are the exchange current densities (A cm^{-2}) for the anode and cathode respectively, and I is the current density (A cm^{-2}) of the electrolysis cell.

Resistances in the electrolysis reaction that are ohmic losses, are the resistance to the flow of ions in the solution and membrane and the resistance to flow of electrons in the electrode materials. As previously mentioned, these resistances can be calculated by Ohm's law. The ohmic overpotential, η_o, can be calculated using the electrolysis cell's current density, i, membrane thickness (cm), φ, and the conductivity (Siemen cm^{-1}) of the cell, ω. This is shown in:

$$\eta_0 = \frac{\varphi}{\omega} i$$

where ω considers the sum of membrane resistance, ion transfer resistance and electrical resistances of electrodes and interconnects if the cell is part of a stack.

Other forms of overpotential include bubble overpotential, which arises from resistance caused by bubble evolution on the electrode surface, and thus limits the contact area of the electrode available for electrochemical reactions to occur. This decreases the current density on the electrode. The extra potential required to overcome this resistance is usually considered negligible.

Another form of resistance in the electrolysis reaction is concentration overpotential. This occurs due to the depletion of charge carriers at the electrode surface. It is linked to bubble overpotential, in that bubble evolution at the electrode surface, prevents charge carriers contacting the electrode surface for the triple phase boundary reaction to occur.

The efficiency of an electrolysis cell is inversely proportional to the cell voltage, which is dictated by the current density (Anantharaj et al. 2018). The current density is also directly correlates to the hydrogen productivity per unit electrode surface area.

It is commonly seen that higher potentials result in higher rates of hydrogen production; but this results in low efficiencies. Consequentially, commercial electrolysers usually operate around 2 V, which maximizes the electrolyser efficiency, where hydrogen output is not as important as the overall electrolysis efficiency.

The system efficiency can be calculated from the electrolysis cell energy and the ancillary losses. The system efficiency uses the higher heating value (HHV) of hydrogen (39 kWh/kg), the energy used by the cell (kWh), the DC power supply efficiency, and the ancillary loads e.g. pumps, values etc. (kWh):

$$System\ efficiency = \frac{HHV}{\left(\dfrac{\frac{cell\ input\ energy}{power\ supply\ efficiency} + ancillaty\ losses}{hydrogen\ produced}\right)}$$

where HHV is measured in kWh/kg, cell input energy and ancillary losses are in kWh, and hydrogen produced is measured in kg. To calculate the cell efficiency, the Nernst equation can be used to calculate the theoretical cell potential and then the cell efficiency can be calculated from:

$$Cell\ efficiency = \frac{Theoretical\ cell\ potential}{Actual\ cell\ potential}$$

Voltage efficiency allows the measurement of effective voltage to split water in the total voltage applied to the whole electrolysis cell. This is shown in:

$$Voltage\ efficiency = \frac{E_a - E_c}{E_{cell}}$$

where Ea and Ec are the potential of the anode and cathode respectively.

Two other types of efficiency measurement of electrolysis reactions based on energy changes in the system are the Faraday Efficiency and the Thermal Efficiency. They used Gibbs free energy and enthalpy of the water splitting reaction respectively. Both use the theoretical open-circuit energy requirement plus ancillary losses as the energy input:

$$Faraday\ efficiency = \frac{\Delta G}{\Delta G + losses} = \frac{E_{\Delta G}}{E_{cell}}$$

$$Thermal\ efficiency = \frac{\Delta H}{\Delta G + losses} = \frac{E_{\Delta H}}{E_{cell}}$$

At S.T.P. (25oC, 1 atm), these equations can be simplified further:

$$Faraday\ efficiency\ (25\,^\circ C) = \frac{1.23V}{E_{cell}}$$

$$Thermal\ efficiency = \frac{1.48V}{E_{cell}}$$

where $E_{\Delta H}$ and $E_{\Delta G}$ are the thermo-neutral and open-circuit potentials respectively, and E_{cell} is the cell potential.

The Faraday efficiency is the percentage of theoretical energy needed for water to decompose in the actual cell potential. The thermal efficiency, instead, defines the additional cell potential that is required, above the open-circuit voltage, to maintain the thermal balance throughout the reaction. Theoretically, this means that if the

reaction is occurring endothermically, then the thermal efficiency may exceed 100% (heat being consumed from the environment).

The Faraday efficiency will always be less than 1, because there are always resistances (losses) in an electrochemical system. Thermal efficiency can be higher than 1 if the cell potential is between the open-circuit voltage and the thermo-neutral voltage.

Another type of efficiency calculation is the measurement of hydrogen gas output from the electrolysis cell in terms of the total electrical energy applied to the system.

These are with respect to the HHV of hydrogen and the hydrogen production rate:

$$Efficiency\ of\ H_2\ production\ rate = \frac{Productivity\ per\ unit\ volume}{\Delta E} = \frac{V}{Uit}$$

where ΔE is the cell energy input (kJ), V is the hydrogen productivity per unit volume (m^3/m^3 h), U is the cell potential (V), i is the current (A), and t is the time (s). Alternatively, the yield of hydrogen produced can be measured in terms of electrical energy input:

$$Hydrogen\ yield = \frac{Usable\ energy}{\Delta E} = \frac{283.8}{Uit}$$

where 283.8 kJ is the HHV of one mole of hydrogen and time t, corresponds to the time required to produce one gram of hydrogen.

Lastly, energy efficiency can also be calculated by subtracting the energy losses from the energy input. This is shown in:

$$Net\ efficiency = 1 - \frac{E_{losses}}{E_{input}}$$

This allows the identification of high resistance locations in the electrolysis cell, that need to be improved. A method for increasing efficiency is to lower these resistances which contribute a significant amount to the overall resistance of the electrolysis cell. This can include electrode materials with a lower activation overpotential, and the movement of electrodes together to reduce ohmic resistance.

Another way is to thermodynamically reduce the energy needed for water splitting, whilst maintaining a high hydrogen yield (Safari and Dincer 2020). This can be achieved by increasing the temperature and/or pressure. The temperature of reaction, electrolyte type and properties, as well as electrode materials, has huge implications on the performance of the electrolysis reaction (Fig. 9).

The reactions within electrolysis occur at the electrodes. The electron flow through the contact between the electrode and the electrolyte enables the formation of hydrogen and oxygen gas to occur. The rate of the electrode reaction is determined by the current density, and this depends on various parameters.

Firstly, the material and any pre-treatment of the electrode surface affect the rate of reaction. Secondly, the electrode potential impacts the flow of electrons through

Fig. 9 Effect of temperature on the overpotential of the cathode and anode
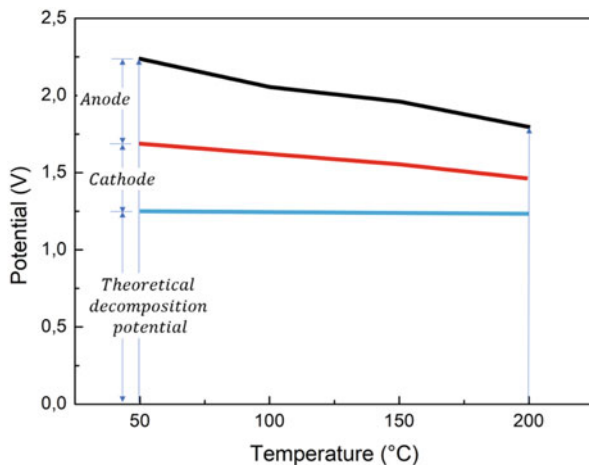
the electrolysis cell i.e. higher potential results in a faster rates of reaction on the electrode surface and hence a higher current density.

Finally, the rate of reaction on the surface of the electrode is dependent on the composition of the electrolyte solution next to the electrodes (Miller et al. 2020). When under operation, these ions adjacent to the electrode undergo migration in the solution to form layers near the electrode surface. This is known as the electrical double layer (Fig. 10).

When a current is forced to flow between two electrodes through an electrolyte, charge separation is created at each solid/liquid interface and two electrochemical capacitors are formed. In these capacitors at the electrode/electrolyte interface, dissolved ions in the bulk electrolyte are attracted to the electrode surface by an equal and opposite charge. It is considered that the behavior at the interface is described in terms of a capacitor. It is a consequence of the "free charge" approach that when a continuous current flow is applied through the interface a strict distinction should be made between Faraday and non-Faraday currents. Faraday currents are responsible for charging of the double-layer capacitor, while non-Faraday currents are the charge flow connected with the charge transfer processes occurring at the interface. An interface at constant pressure and temperature can be changed by varying the concentration of the components in the bulk phases.

The accumulation of ions near the electrode forms two mobile layers (Doan et al. 2021). The layer closest to the electrode is called the inner Helmholtz layer (IHL), where the ions are well ordered and aligned with one another. The other layer is termed the outer Helmholtz layer (OHL), which consists of non-uniform ions adjacent to the IHL. The ionic charges of the ions adjacent to the electrode surface are balanced by oppositely charged ions in the electrode itself. The potential between the electrode and ions can be plotted against the distance from the electrode surface. This is shown in Fig. 11.

IHL   OHL
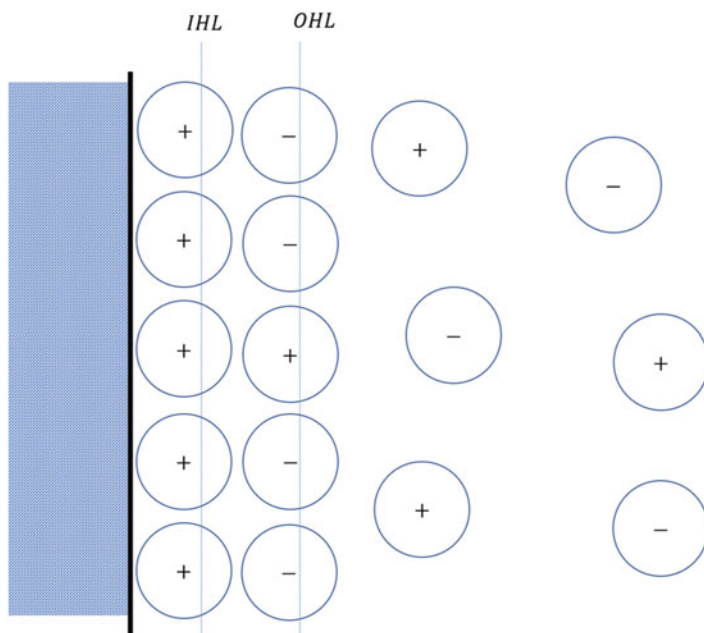
Fig. 10 Schematic of electrical double layer
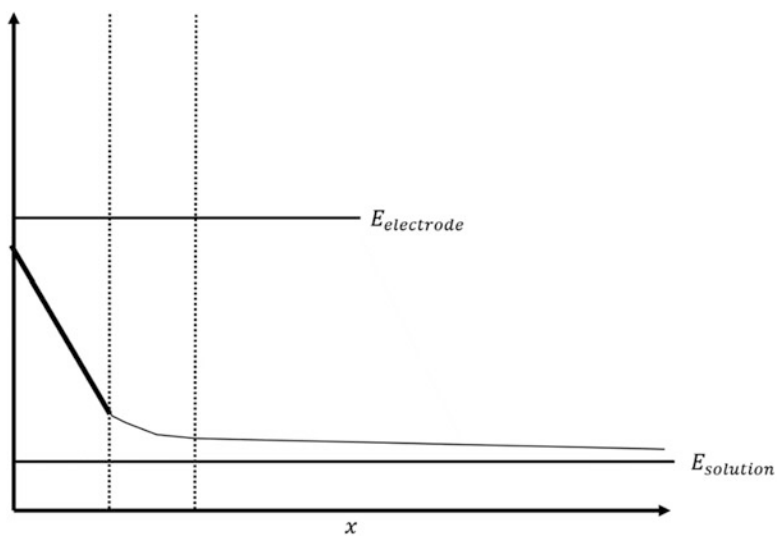
Fig. 11 Effect of distance on the potential between the electrode and ions

The figure shows that voltage exists between the electrode and electrolyte solution. This is a direct result of the double layer. The addition of inert electrolyte to the electrolysis process compresses (reduces the thickness of) the double layer and consequently the distance that the potential decays to zero is much shorter.

The electrical double layer phenomenon leads to capacitive behavior of the electrode reaction. This principle of the electrical double layer acting as capacitor needs to be take into account with electrode kinetics (Rozain and Millet 2014).

Faraday's laws are based quantitative relationships of electrode reactions during the process of electrolysis. Faraday's law states:

$$m = \frac{Q}{F}\frac{M}{z}$$

where m is the mass (g) of a substance liberated at the electrode, Q is the total electrical charge (C) passed through the substance, F is the Faraday constant (96,485 C/mol), M is the molar mass of the substance, and z is the valency number of electrons transferred per ion. This equation can be rearranged to form:

$$N = \frac{Q}{zF}$$

where N is the number of moles of electrolyzed species. From this the rate of electrolysis can be defined as:

$$Rate = \frac{dN}{dt}$$

and dQ/dt can be expressed as electrical current (since $Q = It$). When considering electrode kinetics, the surface area is vital parameter for the electrochemical reaction kinetics, and hence should not be excluded from thought. The rate of electrolysis can be rewritten as:

$$Rate = \frac{I}{nFA} = \frac{j}{nF}$$

where j is the current density (A/cm^2). To calculate the reaction rate constant, the Arrhenius equation is used:

$$k = Ae^{\frac{E_a}{RT}}$$

where E_a is the activation energy (kJ/mol), A is the pre-exponential factor, R is the gas constant (8.314 J/K mol), and T is the reaction temperature.

The Butler-Volmer equation determines the link between the reaction rate and current flow, the corresponding reliance of current density on the electrode surface

Fig. 12 Effect of potential change on Gibbs energy for (**a**) the relationship between energy change and state of reaction and (**b**) magnified picture of shaded area (**a**)
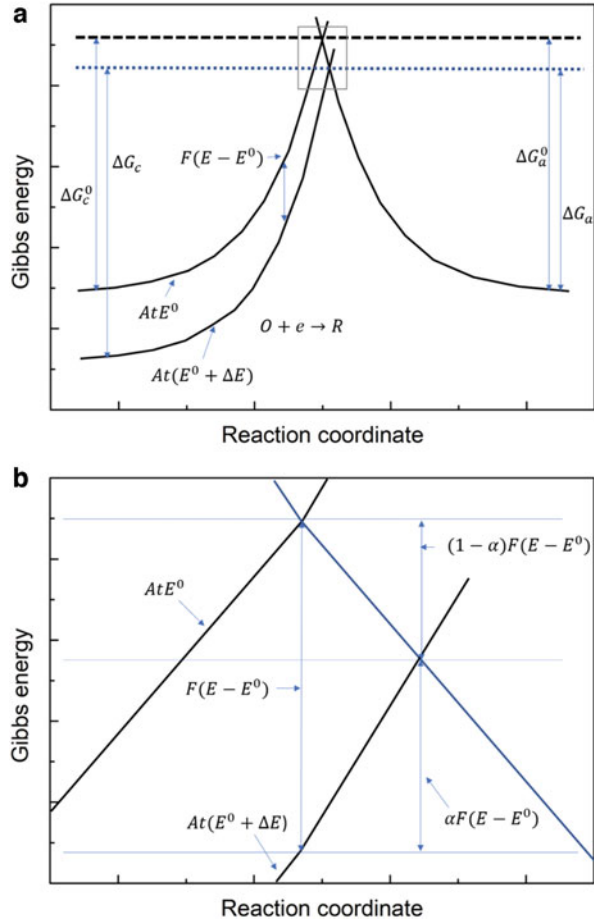
potential, and the composition of the electrolyte solution adjacent to the electrode surface. The equation is adapted from the transition-state theory and presented in:

$$I = I_{cathode} - I_{anode} = FAk^0 \left(C_0(0,t)e^{-\alpha f(E-E_0)} - C_R(0,t)e^{-f(1-\alpha)(E-E_0)} \right)$$

where A is the electrode surface area in contact with the electrolyte solution, k_0 is the standard rate constant, $C_0(0,t)$ is the concentration of reaction species at the cathode/anode in the oxidized state i.e. for the cathode; the hydrogen ions (H+). The (0,t) represents the distance from the electrode, and the specific time at which the current occurs, α is the transfer coefficient (value $0 < \alpha < 1$), f is the F/RT ratio, which is a constant. CR(0,t) is the concentration of reaction product at the cathode/anode in the reduced state i.e. for the cathode; the hydrogen gas (0.5H2).

Fig. 13 Expression of
exchange current density for
hydrogen and oxygen
overpotential
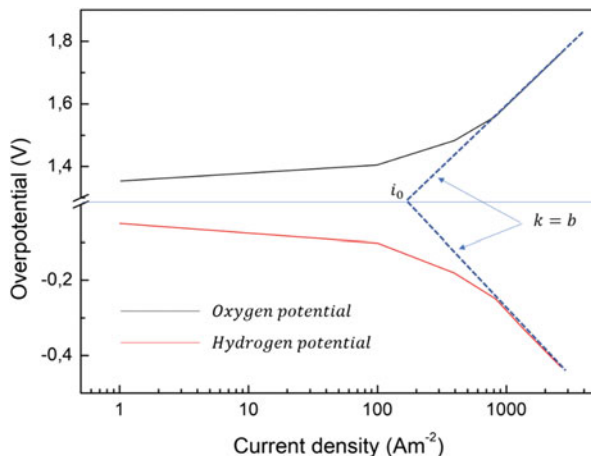
The transition-state theory, illustrated in Fig. 12, shows the reaction path for the electrochemical reactions in terms of the Gibbs free energy of the reactions, and the position of coordinates in the reaction path.

When the potential is increased by ΔE, as shown in Fig. 12a, the decrease in Gibbs free energy is $F(E-E_o)$. As a result there is a reduction in Gibbs free energy of hydrogen ions in the HER by $(1-\alpha)(E-E_o)$, and the increase in Gibbs free energy of hydrogen gas by $\alpha(E - E_o)$.

This proves that Butler-Volmer equation can be derived from the rate equations previously mentioned, if there is no limitation to mass transfer during the electrochemical reactions at the electrodes. Using Fig. 12b the Butler-Volmer Equation can be simplified to:

$$i = i_0 \left(e^{-\alpha f \eta} - e^{(1-\alpha)f\eta} \right)$$

whereas previously mentioned, i_0 is the exchange current density. From this equation we can derive overpotential for both electrodes. This is the Tafel equation:

$$\eta = a + b \log i$$

where $a = (2.3RT)/(\alpha F)\log io$ and $b = (-2.3RT)/(\alpha F)$.

The proportional relationship between the overpotential and the logarithm of current density is determined by exchange current density, i_0, and the slope b; known as the Tafel slope. Both parameters are used to measure the reaction kinetics of electrodes for electrochemistry.

This analysis (Fig. 13) shows that the rate of electrolysis can be expressed by the current density. The current density can be mirrored by the exchange current density, which represents the current associated with the open-circuit potential, on the surface of the electrodes. It is also dependent on the overpotential.

4 Thermodynamic at High Pressure

At Standard Temperature and Pressure conditions, (STP defined by the IUPAC, International Union of Pure and Applied Chemistry, is an absolute pressure of 1 bar and a temperature of 273.15 K), the splitting of water is a non-spontaneous reaction which means that the change in Gibbs energy is positive.

For an electrochemical process operating at constant pressure and temperature the maximum possible useful work (i.e., the reversible work) is equal to the change in Gibbs energy. Since work is viewed from the point of view of the chemical reaction system, the electrical work is positive for an electrolyser and negative for a fuel cell.

The change in enthalpy for the electrochemical decomposition of water is

$$\Delta H_{T,p} = \Delta G_{T,p} + T \Delta S_{T,p}$$

$\Delta H_{T,\ p}$ (J.mol^{-1}) is the enthalpy change at T and p, $\Delta G_{T,\ p}$ (J.mol^{-1}) is the Gibbs free energy, $\Delta S_{T,\ p}$ (J.mol^{-1} K^{-1}) entropy change, T temperature (K), p the pressure (atm).

Two essential voltages, considering the energy needed for the hydrogen production, are defined:

The enthalpy voltage at T and p:

$$V_{T,p} = \frac{\Delta H_{T,p}}{nF}$$

The water electrolysis voltage at T and p:

$$E_{T,p} = \frac{\Delta G_{T,p}}{nF}$$

n: Number of electrons transferred per formula conversion, F: The Faraday constant equal to 96500 Cmol^{-1}.

The voltage associated with $\Delta H_{T,\ p}$ is commonly called the thermo-neutral cell voltage; it is the voltage at which a perfectly efficient cell would operate if electricity provided the entire energy requirement. Under these conditions, the cell does not generate any waste heat, nor does it require any heat input; the cell has no net heat exchange; hence it is then said to be 'thermo-neutral' (Uosaki et al. 2016).

Since the enthalpy voltage and the water electrolysis voltage depend on the enthalpy and the Gibbs energy of the formation reaction of water, we can predict the temperature changes by means of a well-known thermodynamics relationships. The calculation approach is since the enthalpy and Gibbs energy are properties that depend on the initial and final states of compounds (reactants and products); they may be calculated for any convenient path connecting these two states. The first part of our calculation is to propose a hypothetical path that leads from liquid water at

Fig. 14 Possible thermodynamic path leading to hydrogen at defined temperature from water at 25 °C
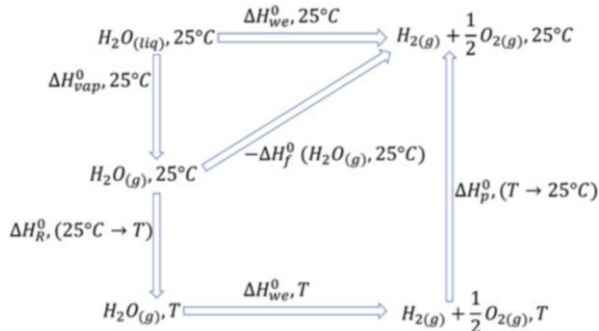
25 °C to gaseous hydrogen and oxygen at temperature above 100 °C and up, under atmospheric pressure. This path is illustrated on Fig. 14.

The entities used are defined as follows:

$\Delta H^0_{vap}, 25\degree C$	Heat of vaporization of water at 25 °C atm constant pressure (1 atm)
$\Delta H^0_R, 25\degree C \rightarrow T$	Total enthalpy change of reactants (water) at a constant pressure (1 atm) from 25 °C to T
$\Delta H^0_{we}, T$	Enthalpy of water electrolysis at constant pressure (1 atm) at T
$\Delta H^0_{we}, 25\degree C$	Enthalpy of water electrolysis at constant pressure (1 atm) at 25 °C
$\Delta H^0_p, (T \rightarrow 25\degree C)$	Total enthalpy change of products (hydrogen and oxygen) at a constant pressure (1 atm) from T to 25 °C
$\Delta H^0_f (H_2O_{(g)}, 25\degree C)$	Standard heat formation of water at 25 °C

The reason for choosing this possible schematic is based on the fact that the entire entities (enthalpies) can be calculated, and data of water are available.

The enthalpy of water electrolysis at any temperature and pressure is expressed as follows:

$$\Delta H_{T,p} - \Delta H_{25\degree C,1atm} = \left[\Delta H_{T,p} - \Delta H_{T,1\ atm}\right] - \left[\Delta H_{T,1\ atm} - \Delta H_{25\degree C,1\ atm}\right]$$

$$\Delta H_{T,p} - \Delta H_{T,1atm} = \left[\Delta H_{T,p} - \Delta H_{T,1\ atm}\right]_{H_2} - \left[\Delta H_{T,p} - \Delta H_{T,1\ atm}\right]_{O_2}$$
$$- \left[\Delta H_{T,p} - \Delta H_{T,1\ atm}\right]_{H_2O}$$

$$\Delta H_{T,1\ atm} - \Delta H_{25\degree C,1\ atm} = \left[H_{T,1\ atm} - H_{25\degree C,1\ atm}\right]_{H_2}$$
$$+ 0.5\left[H_{T,1\ atm} - H_{25\degree C,1\ atm}\right]_{O_2} - \left[H_{T,1\ atm} - H_{25\degree C,1\ atm}\right]_{H_2O}$$

The same expression can be developed for the entropy and Gibbs free energy for water electrolysis. The only limitation is that the species involved are considered at ideal gas state, thus the enthalpies of reactants and products are expressed as a function of temperature by equation of the form:

$$\Delta H^0(T, final) = \Delta H^0(T, initial) + \sum_{species} \int_{T,initial}^{T,final} C_{p,species}^0(T) dT$$

(T, initial): initial temperature, [K]; (T, final): final temperature, [K]; C_p^0: heat capacity of the p species, function of temperature, [J.mol^{-1} K^{-1}]. The entropy change is expressed by considering the following thermodynamic relationship of ideal gas state:

$$\Delta S^0(T, final) = \Delta S^0(T, initial) + \sum_{species} \int_{T,initial}^{T,final} C_{p,species}^0(T) dT$$

So, we obtain the temperature effect of enthalpy voltage as follows:

$$V_{T,1atm} = 1.4850 - 1.490 \ 10^{-4}(T - 273.15) - 9.84 \ 10^{-8}(T - 273.15)^2$$

and the Gibbs free energy for the corresponding temperature and then the reversible voltage as:

$$E_{T,1atm} = 1.5184 - 1.5421 \ 10^{-3}T - 9.523 \ 10^{-5}T \ln T + 9.84 \ 10^{-8}T^2$$

Since data have been extrapolated from steam table of water, the last equations are covering the temperature range from 25 °C to 327 °C.

The effect of pressure on both E and V is given by the following well know thermodynamics relationship:

$$H_{T,p_2} - H_{T,p_1} = \int_{p_1}^{p_2} \left(v - T\left(\frac{\delta v}{\delta T}\right) \right) dp$$

v (m^3) is the volume of the components and R is the universal gas constant, R = 82.058 (atm cm^3 mol^{-1} K^{-1}).

The integral can be handled under different consideration; we choose the virial equation of state to be performed with an eye to unifying the works of many authors into a comprehensive understanding of the method.

The remain calculation consists in the evaluation of the enthalpy departure for water; the task has been greatly simplified as the data for the thermodynamics properties of water are available and can be handled as data sheet or as embedded computer subroutine. We use the published computer program of steam table from The International Association for the Properties of Water and Steam. The range of data is for temperatures and pressures:

$$273.15K < T < 1073.15K$$

Fig. 15 Variation of
electrolysis and enthalpy
voltage with temperature at
1 atm
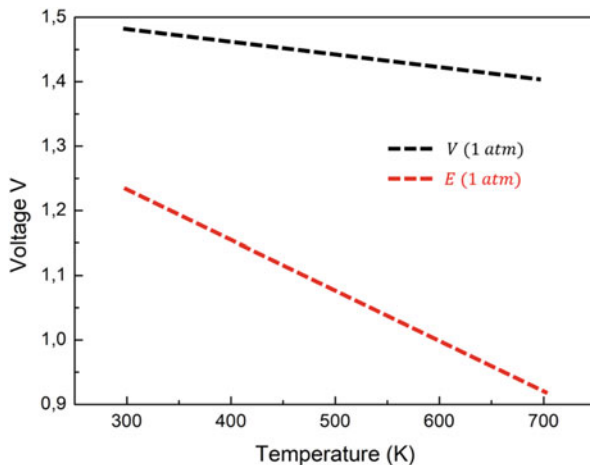
$$0 < p < 1000\ bar$$

The enthalpy voltage is calculated for the value from 1 bar to 1000 bars using the expression:

$$V_{T,p} = V_{T,1\ atm} + \Delta H_{T,p} - \frac{\Delta H_{T,1\ atm}}{nF}$$

and the water electrolysis voltage:

$$E_{T,p} = E_{T,1atm} + \Delta G_{T,p} - \frac{\Delta G_{T,1\ atm}}{nF}$$

The temperature change at 1 atm is shown on Fig. 15 and the pressure change is shown on Fig. 16.

We observe that V(1 atm) and E(1 atm) decreases as the temperature is rising, elevating temperature promote the splitting water significantly.

We observe as enthalpy voltage, V, decreases, reversible voltage, E, increases with rising pressure at 298 K. For E the curve increases rapidly from 1 atm to 50 atm then rise steadily. In fact, according to Le Chatelier principle, the water electrolysis considered as an equilibrium equation, increasing pressure will lead to encourage water formation then more energy would be necessary to overcome the reverse reaction.

In the next section we present the variation of enthalpy and electrolysis voltage versus the variation of temperature and pressure in Figs. 17 and 18.

Increasing pressure will increase the energy consummation and then more energy is required to perform hydrogen production.

Fig. 16 Variation of electrolysis and enthalpy voltage with pressure at 298 K
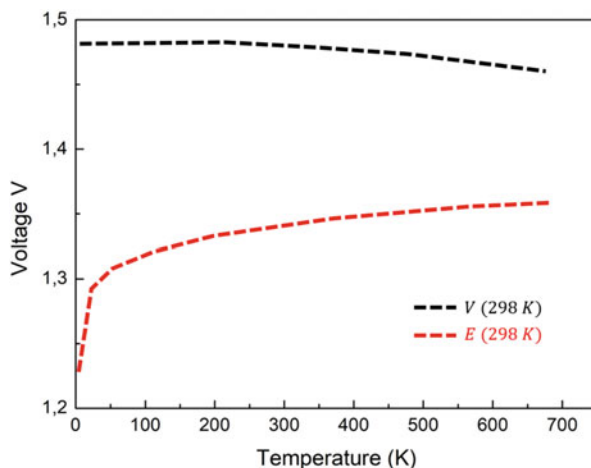
Fig. 17 Enthalpy voltage against pressure and temperature variations
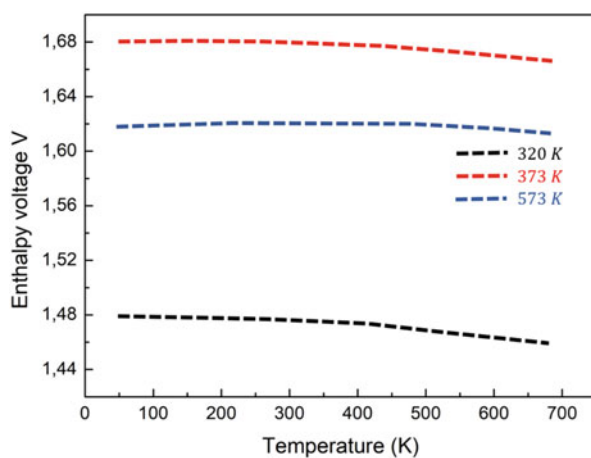
We observe that temperature plays an advantageous factor for reducing the enthalpy and electrolysis voltage, since the energy of molecules agitation (water) introduced by temperature, tends to promote electrolysis, thus reducing electrical potential.

5 Thermodynamic of Catalytic Activity

In electrocatalysis, the primary energy input is the potential difference over two electrodes, ΔU. Electrochemical reactions include the transfer of electrons between the electrode and reactants and the rate of this transfer can be tuned with ΔU. The electrodes are immersed in an electrolyte which provides ionic conductivity, due to a

Fig. 18 Electrolysis
voltage against pressure and
temperature variations
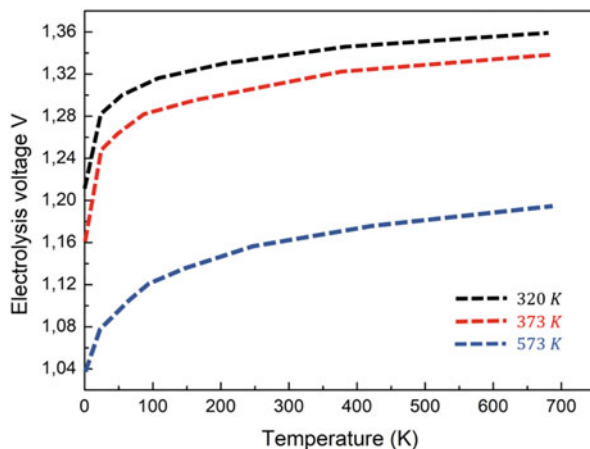
high concentration of protons or hydroxide ions. Furthermore, electrochemical reactions are reduction-oxidation, redox, reactions.

They can always be divided into two half reactions, each proceeding at their respective electrode. The electrode at which oxidation of a reactant occurs is called the anode, whereas the electrode where a reduction occurs is called the cathode. The change in Gibbs free energy of formation for a reaction, ΔG_f, determines the equilibrium potential, U_{cell}, for a given electrochemical cell, consisting of two electronically connected electrodes immersed in an electrolyte.

This is formulated in equation:

$$U_{cell} = -\frac{\Delta G_f}{nF}$$

where U_{cell} is the equilibrium potential also called reversible open circuit potential of the cell, F is the Faraday constant (96485 C/mol) and n the number of electrons transferred in the reaction. While this equation holds at standard conditions, the change in Gibbs free energy for a reaction vary with temperature and pressure. This variation can be calculated by the general relationship:

$$jJ + kK \rightarrow mM$$

as:
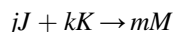
$$\Delta G_f = \Delta G_f^0 - RTln\left(\frac{a_J^j - a_K^k}{a_M^m}\right)$$

where ΔG^0_f is the change in Gibbs free energy at standard conditions, R the gas constant, T the temperature and a denotes reactant activity; $a = P/P_0$. P is partial pressure and P_0 the standard pressure, 1 atm.

The previous equations gives the Nernst equation which relates the reversible open circuit potential to temperature and pressure:

$$U_{cell} = U_{cell}^0 - \frac{RT}{nF} \ln\left(\frac{a_J^j - a_K^k}{a_M^m}\right)$$

With these equations it is possible to evaluate the minimum potential difference needed to run a non-spontaneous reaction in an electrochemical cell, or similarly the maximum potential difference generated by a spontaneous reaction. However, the actual operating potentials, ΔU of such cells are typically significantly different from U_{cell}. The components of the operating voltage are the following:

$$\Delta U = U_{cell} \pm \eta \pm \Delta U_\Omega \pm \Delta U_t$$

In the previous equation "$\pm$" should be "+" for power consuming cells where non-spontaneous reactions are driven, whereas "$-$" should be used for power generating cells. η denotes the overpotential needed to drive the reaction when current is flowing due to non-ideal kinetics at the electrode interface. $\Delta U\Omega$ is the loss of potential difference due to resistance losses in the system and finally $\Delta U t$ is the potential increase or decrease over time. Electrocatalysis deals with decreasing η by finding the best suited electrode material. The theoretical relation between overpotential η and current j is described in the Butler-Volmer equation:

$$j = j_0 \left[\exp \frac{(1-\alpha)nF\eta}{RT} - \exp \frac{\alpha nF\eta}{RT} \right]$$

j_0 is the exchange current density and α is a symmetry factor. The exchange current density is a quantity that defines the current flowing in both directions when a reaction is in equilibrium. From the previous equation it is evident that a high i_0 results in higher currents for a given η. It is also noteworthy that the current is exponentially dependent on overpotential, η.

At high overpotentials one of the two exponentials becomes negligible and a simpler version can be formulated (Mo et al. 2019). In semilogarithmic form this version is known as Tafel lines. In short, Tafel slopes indicate the change in potential for a ten-fold increase in current. From this definition it is obvious that lower Tafel slopes are desirable. Traditionally, electrochemical experiments have been conducted with the aim of determining the Tafel slope of reactions on specific electrode materials. It is commonplace in the literature to use Tafel slopes to phenomenologically deduce a reaction mechanism. However, this requires several loaded assumptions, including the value of a symmetry factor, an adsorption isotherm, etc.

Electrolysis is a general term describing the process of driving a non-spontaneous electrochemical reaction by applying a potential over two electrodes. This contrasts with a potential difference generated from a spontaneous electrochemical reaction

like in the case of fuel cells. In water electrolysis hydrogen and oxygen gasses are generated from water:

$$2H_2O_{(l)} \rightarrow 2H_{2(g)} + O_{2(g)}$$

This is an energy demanding reaction with a change in Gibbs free energy of 237.2 kJ/mol at standard conditions. If this is done in an electrochemical cell, an electrolyzer, a potential difference of 1.23 V is required at room temperature and standard pressure. As discussed above, for any significant current a higher potential must be applied in terms of overpotential and resistance losses. The efficiency of such a process is typically defined from the change in enthalpy of the reaction. The enthalpy can be taken for either water as a liquid (higher heating value, HHV, equivalent of 1.48 V) or as a gas (lower heating value, LHV, equivalent of 1.25 V):

$$efficiency = \frac{1.48V}{V_c}$$

where V_c is the cell voltage. Note that for electrolyzers using the HHV results
   in higher efficiencies while for fuels cells in lower. The overall reaction can be split into half reactions:

$$4H^+ + 4e^- \rightarrow 2H_{2(g)} \quad Hydrogen\ evolution$$

$$2H_2O_{(l)} \rightarrow O_{2(g)} + 4H^+ + 4e^- \quad Oxygen\ evolution$$
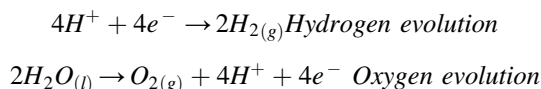
These two half reactions will be treated more carefully in the following.
   The electrolytic evolution of hydrogen gas is one of the most, if not the most, studied electrochemical reactions throughout the history of electrochemistry as a research field. In fact, fundamental studies on hydrogen evolution have helped shape the modern understanding of electrochemical processes. It is a simple two electron transfer process where protons are reduced to form molecular hydrogen. The overall reaction in acid can be written as:

$$2H^+ + 2e^- \rightarrow H_{2(g)}$$
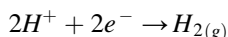
The equilibrium potential of this reaction is 0 V using the conventional electrochemical potential scale. In acidic environment, the reaction can be further split up into the following reaction steps:

$$H^+_{(aq)} + e^- + * \rightarrow H^* \quad (Volmer)$$

$$2H^* \rightarrow H_{2(g)} + 2 * \quad (Tafel)$$

$$H^* + e^- + H^+ \rightarrow H_{2(g)} + *(Heyrovsky)$$
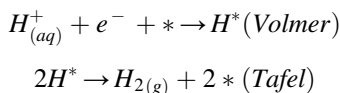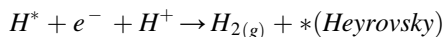
While it is commonly accepted that the first step is the Volmer process, it has proven difficult to understand whether the Tafel or Heyrovsky mechanism dominates. The Tafel step takes place on Pt(110) and Heyrovsky on Pt(100). However, for polycrystalline surfaces it is difficult to assess experimentally through kinetic measurements alone. Despite this ambiguity in the understanding of hydrogen evolution there is only one intermediate, which is adsorbed hydrogen, H∗.

The binding between a surface and this intermediate has turned out to be an exceptionally good descriptor for identifying active catalysts. The best-known catalyst for the reaction is platinum which can catalyze the reaction at negligible overpotentials. It should also be noted that hydrogen evolution is significantly faster in acid compared to alkaline. In alkaline the overpotential needed to reach around 1.5 A/cm^2 is at least 100 mV higher than the same reaction in acid. An overview of the range of active catalysts available for HER can be found in Fig. 19 for both acid and alkaline electrolytes.

Fig. 19 An overview of catalyst materials for HER. The logarithmic of the current density is plotted as function of overpotential. (**a**) Catalysts tested in acidic solutions. (**b**) Catalysts tested in alkaline solutions
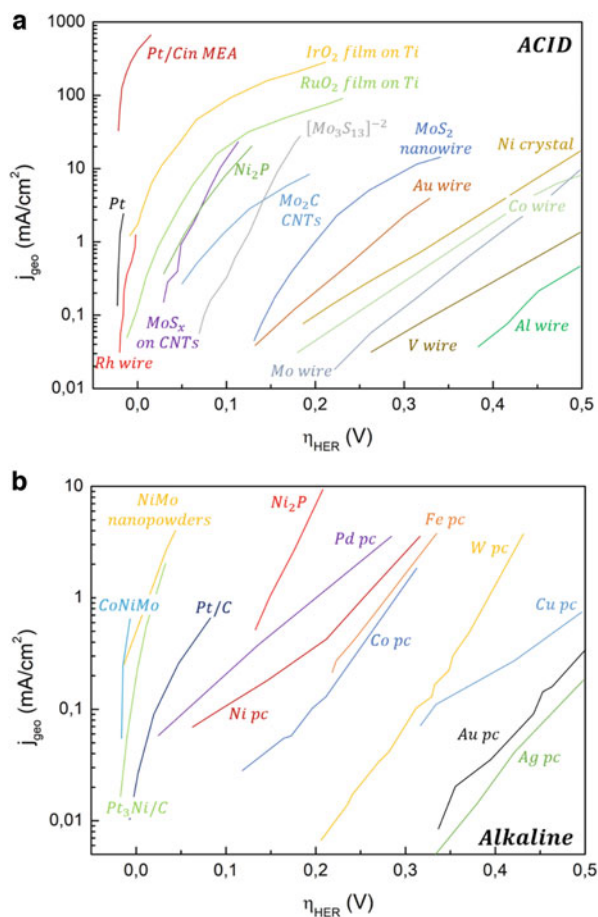
Fig. 20 Comparison of
overpotentials needed to
drive 10 mA/cm^2 dependent
on the choice of electrode
material
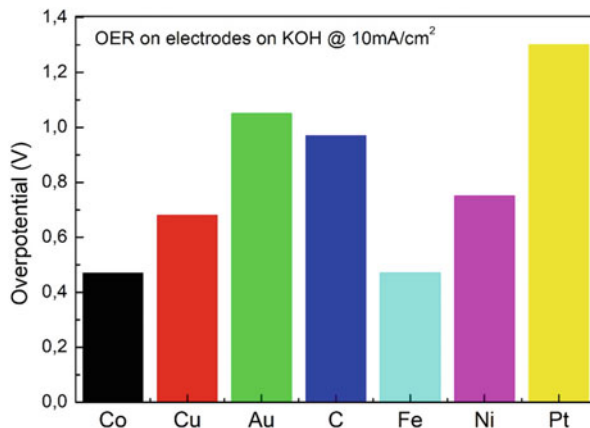
Compared to HER the oxygen evolution reaction, OER, is more complex and involves several intermediates. As discussed in the previous section, the hydrogen electrode in an electrolyzer can run at appreciable current densities with lower than 50 mV overpotential using a very low amount of platinum. This is far from the situation at the oxygen electrode which imposes a large overpotential, more than 300 mV, at significant currents with a high loading of even the best catalysts. While 1.23 VRHE is already highly oxidizing, the substantial overpotential makes matters worse so that the selection of stable materials available for this electrode is rather narrow. For these reasons it has long been recognized as a great challenge in electrochemistry to find new active and stable catalysts for this reaction.

The first attempts at understanding OER were made in the 1940's and 50's with experiments with various electrode materials. The conclusions describe the difficulties in comparing the activities of different materials due to large variance in Tafel slope dependent on current density and measurement procedure. These issues are still haunting researchers today where the comparison of electrode materials from different groups is complicated by different preparation and experimental methods. They were tested twelve metals as anodes and for all of them substantial overpotentials were needed to drive the reaction. Some of these results can be seen in Fig. 20, where the overpotentials needed to reach 10 mA/cm^2 for seven electrode materials are shown.

It wasn't until 1980 that the knowledge of oxides was successfully combined with measurements of OER activity. This approach was famously constructed a volcano shaped activity plot based on the heat of transition from lower to higher oxide. The impact of this report lies in the fact that oxide and not metallic properties are related to activity, which better reflect the electrode interface at the reaction conditions. At the same time the volcano plot suggests that an optimum at a specific formation energy exists so that experimentalists are provided with a design principle (Fig. 21).

A few descriptors were investigated such as number of d-band electrons, heat of formation for the corresponding metal hydroxide, magnetic moment and stability limits.

Fig. 21 Volcano plot showing the overpotential for reaching approximately 1 mA/cm^2 for OER as a function of the heat of oxide transition $\Delta H0t$
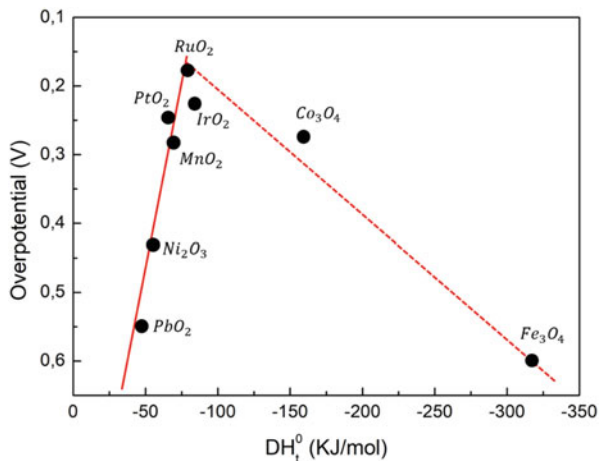
In parallel with the scientific communities' efforts to understand the concepts behind OER activity, an important discovery had been made in one of the industrial research laboratories. The active components of the oxides were Ru and Ir and they were mixed with Sn, Ta and Ti for better stability and selectivity. These electrodes were, as their name suggests, more stable under reaction conditions compared to the graphite anodes originally used for chlorine evolution.

At this point it is useful to investigate the reaction mechanism of OER. Several reaction mechanisms have been proposed but here we will consider one of the most common, which is also the one used in the free energy models. In acidic solution it can be written in the following way. First a water molecule is dissociated into an adsorbed hydroxide and a solvated proton:

$$H_2 + * \rightarrow HO * + H^+ + e^-$$

The hydroxide is further oxidized to adsorbed atomic oxygen:

$$HO * + H^+ + \dot{ei} - \rightarrow O * + 2(H^+ + e^-)$$
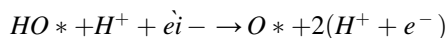
From the adsorbed oxygen atom and a water molecule a superoxide, *OOH, can be formed:

$$H_2O + O * + 2(H^+ + e^-) \rightarrow HOO * + 3(H^+ + e^-)$$
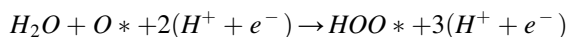
Finally, molecular oxygen is formed and leaves the surface:

$$HOO * \rightarrow O_{2(g)} + (H^+ + e^-) + *$$
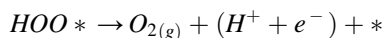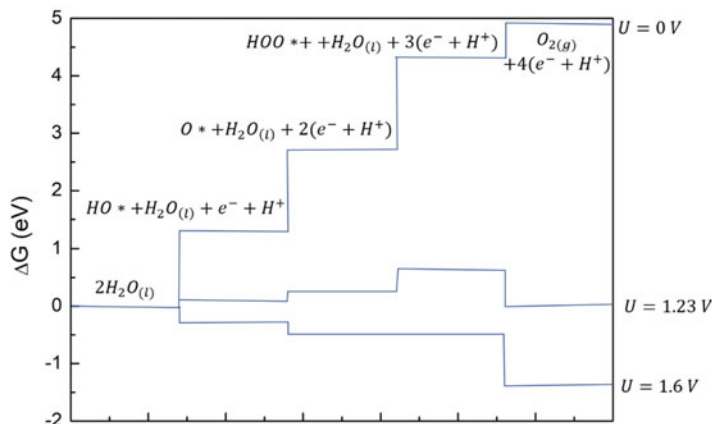
Fig. 22 Free energy diagram for the oxygen evolution reaction based on the binding of interme-diates to a rutile RuO2 surface, shown for 0, 1.23 and 1.6 V. At the equilibrium potential, 1.23 V the first three steps are still not energetically favorable, which means that an extra overpotential is needed for the reaction to proceed at significant rates

In these equations $*$ denotes an active surface site. In alkaline environment the reaction mechanism looks slightly different, but the intermediates are the same:

$$4OH^- \rightarrow OH* + 3OH^- + e^-$$

$$OH* + 3OH^- + e^- \rightarrow O* + H_2O + 2OH^- + 2e^-$$

$$O* + H_2O + 2OH^- \cong +2e^- \rightarrow HOO* + H_2O + OH^- + 3e^-$$

$$HOO* + H_2O + OH^- + 3e^- \rightarrow O_2 + 2H_2O + 4e^-$$
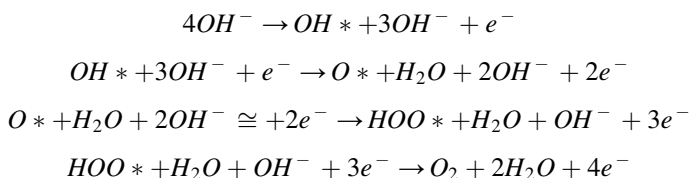
The binding energies of the intermediates, O$*$, OH$*$ and OOH$*$ are central to the model. Using the quantum mechanical method Density Functional Theory, DFT, it is possible to calculate these energies on various surfaces such as metals and metal oxides. From the binding energies each step in the reaction mechanism can be evaluated and for a reaction step to be thermodynamically allowed the change in free energy should be zero or negative. When all steps are zero or downhill in energy the reaction can run at "significant" rates. The calculations are summarized in free energy diagrams as shown in Fig. 22, where a rutile (110) RuO$_2$ surface is used as catalytic surface.

The free energy profile of the reaction taking place at U $= 0$ V has all steps going uphill in energy and the final step is 4.92 V higher than the beginning.

This value fits with the total energy needed to split water, which has so far been stated as 1.23 V per electron. When the potential is increased to 1.23 V it turns out that the energy profile is not flat, but instead three out of four steps are still uphill in energy. In fact, to get all steps flat or downhill it requires 1.60 V. For the ideal catalyst all steps would require 1.23 V to become flat. The last step that becomes flat

for RuO_2 is the third which includes the formation of ∗OOH. For RuO_2 it was therefore concluded that the third step is potential determining since the binding to ∗OOH is slightly too weak. It should be noted that energy barriers for each step are not directly considered.

The thermodynamic analysis was also extended to predicting a volcano shaped activity plot based on a single descriptor, the binding to oxygen. This was justified based on the apparent correlation between binding energies for similar intermediates. Later it has been found that Brøndsted-Evans-Polanyi relations exists for the oxygen intermediates of OER on several surfaces, such as metals and oxides. These relations correlate the energy of formation for transition states to the overall thermodynamic change in free energy of a reaction step. In other words, the energy barriers associated with a reaction can be described as a linear function of the change in free energy. With the DFT method and thermodynamic analysis in place a natural step forward was to extend the calculations to a large variety of materials. From such calculations universal scaling relations emerged.

Scaling relations provide a simple correlation between the binding energy of similar adsorbates independently from the surface. In this way the binding energies of ∗OH or ∗OOH is correlated to the binding energy of ∗O. By averaging over many oxides it was found that the adsorption energy of ∗OOH, ΔE*OOH, could be described as a function of ΔE*OH in the following equation:

$$\Delta E_{*OOH} = \Delta E_{*OH} + 3.2\ eV$$

Independently of the nature of the oxides there is a constant offset of 3.2 eV between step 1 and step 3 in the reaction mechanism. For the ideal catalyst this difference is 2.46 eV, since two electrons and protons are transferred from step 1 to 3. The discrepancy between the ideal catalyst and the best possible catalyst following these scaling relations is 0.74 eV or 0.37 eV per step which is close to the predicted overpotential of RuO_2. Notice that even though the offset is the same for all the oxides it doesn't mean that they are all as good as RuO_2. The predicted overpotential of 0.37 V only results from optimal splitting of the 3.2 eV offset into two steps and therefore the 0.37 V is a minimum overpotential. For OER catalysis it is therefore seemingly impossible to find a simple surface with the ideal binding energies to all intermediates.

This limitation is shown in Fig. 23, where the theoretically predicted overpotential is shown for various oxides as a function of a single descriptor.

The descriptor in this case is the difference in Gibbs free energy for ∗O and ∗OH adsorption. While these theoretically predicted overpotentials relate to a thermodynamic allowance of the reaction, the comparison to experimental current densities is not straightforward. However, the trends found from such analyses are in good agreement with experiments and, in fact, the overpotential needed to drive 10 mA/cm2 on flat surfaces match to the theory within 100–200 mV for most materials.

With theory and experiments in good agreement, it is evident that RuO_2 is a unique catalyst for OER, which has been shown in several studies. Unfortunately, as it has been mentioned earlier, ruthenium is a scarce element produced as a

Fig. 23 Volcano shaped activity plot for oxygen evolution on various oxide surfaces. The activity is shown as overpotential needed for all reaction steps to be downhill in energy, which is then plotted as function of the difference in free energy for step 1 and 3, $\Delta G0\ O* - \Delta G0HO*$. The points are calculated values for the indicated surfaces, while the solid lines are derived from scaling relations between the OER intermediates
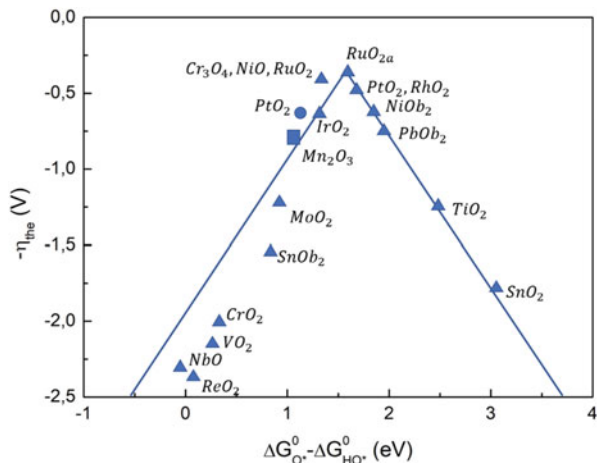
by-product in platinum extraction. It is therefore problematic to use for technologies that are to be scaled up to the terawatt level. At the same time the stability of RuOx based electrodes have turned out to be unsatisfactory for long lifetime of electrolyzers and many commercial anodes for electrolysis instead use iridium or mixtures of the two. Iridium is even more scarce and therefore a search for alternative catalysts has long been the focus in the research field. The experimental progress can be divided into efforts aimed at acidic electrolytes and efforts aimed at alkaline electrolytes.

In acidic electrolyte, relevant for PEM cells, most experimental studies are focused on understanding and improving the noble metal oxides, RuOx and IrOx. In a study, Ir and Pt electrodes were studied for activity towards OER. They paid special attention to the electrochemical active surface area which was determined by CO adsorption prior to activity measurement. Here it should be noted that addressing the electrochemical surface area for oxides is not well established due to a lack of accurate methods. However, for metallic surfaces it can be done with high precision; to a first degree the electrochemically formed oxide area should not vary much from the initial metallic. On this basis Ru outperformed Ir and Pt. At the same time, it was also evident that Ru nanoparticles were too unstable under the reaction conditions. This can be seen in Fig. 24 where the activity is normalized to the amount of CO adsorbed.

Since the activity of RuOx based catalysts is high compared to other oxides, it is interesting to investigate whether further activity enhancements are possible. It has indeed been shown to be the case in various studies, where especially mixtures with Ni or Co stand out. A theoretical model explaining these enhancements has recently been proposed based on an extended analysis. In this model the adsorption of *OOH, which was shown to be a limiting factor, can be stabilized by introducing a hydrogen acceptor close to the catalytic site. If this acceptor can retrieve the hydrogen atom from *OOH (and regenerate) at potentials close to OER, the overpotential could be

Fig. 24 Comparison of results for anodic polarisation of Ru, Ir and Pt polycrystalline disks (bulk) and nanoparticles. Ru is shown in black, Ir in red and Pt in blue. Bulk measurements are indicated with dashed lines while nanoparticles are in solid lines. The current is normalised with the amount of CO adsorbed on the surface, based on electrochemical CO stripping
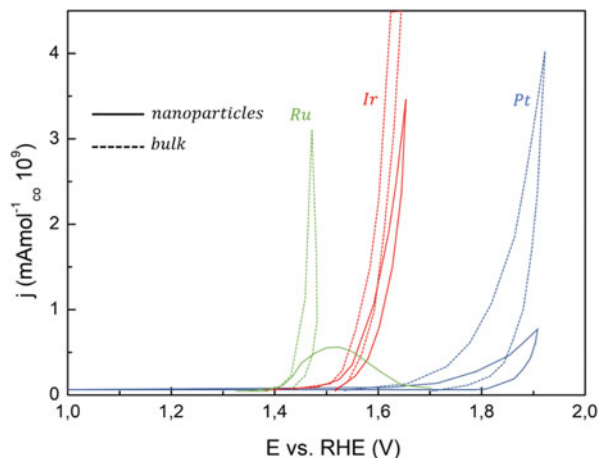
decreased for surfaces that are limited by a too weak adsorption of ∗OOH compared to ∗OH. Essentially, a selective stabilization of OOH by immediate splitting into adsorbed H and O2 is proposed to occur on active Ru sites with an oxidized Ni or Co site as neighbor.

Just as it can be complicated to compare Tafel slopes from different materials prepared differently, it can be quite di-cult to document activity enhancements from mixed oxides appropriately. First, it is important that the pure oxide is performing as good as possible, which is why proper benchmarking is critical. Second, the reason for improvements can be manifold. Depending on preparation method a big contributor is increase in surface area, which changes the current measured directly. Other examples are increase in conductivity and change in electrode-electrolyte interface.

To understand the influence of surface structure on catalytic activity single crystal studies are useful for investigations of the oxygen reduction reaction. However, this is not trivial for OER due to difficulties in preparation of oxide single crystals and reconstruction taking place under reaction conditions. From a report, early works on geometric effects are analyzed and it was argued that polycrystalline and single crystal studies often suffer from poor characterization of the surface structure during reaction conditions. From their own electrochemical experiments, the (110) surface of rutile RuO_2 exhibited a change in Tafel slope as a function of the overpotential and a roughening of the surface during testing. Unfortunately, that study did not include any surface science methods to confirm the expected crystalline orientation. The overall goal of these early studies was to map out Tafel slopes as a function of the surface structure. This phenomenological approach, although theoretically valid, have achieved little success in OER due to difficulties in reproducibility for similar materials across different research groups.

In practical devices the catalyst must be nanostructured to maximize the surface area and minimize catalyst loading. For Ru and Ir based catalysts therefore compelling to investigate the activity of well-defined nanoparticles.

Fig. 25 Overview plot of
recent studies on OER
catalysts tested in acidic
media
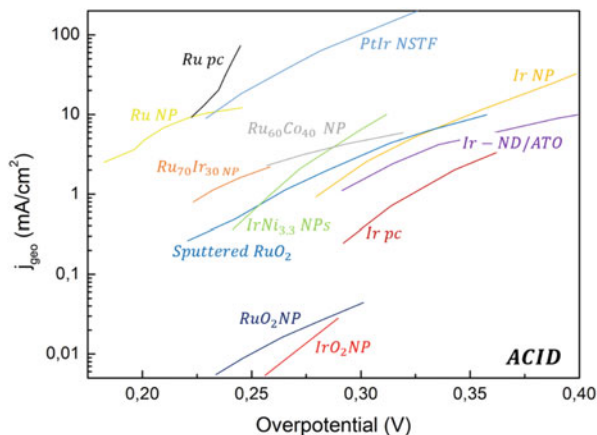
Compared to the opposite reaction ORR where there is a large amount of work in this area, there are only few studies available for OER.

From those experiments it was suggested that changing the size from 45 to 15 nm led to increased current densities for OER. Investigations of particle size effects are related to which facets or sites that are active, and a decrease in particle size generally leads to a higher fraction of undercoordinated sites vs. flat terrace sites. According to DFT calculations the binding to intermediates on flat terrace sites results in activity trends that match experimental values.

The binding on undercoordinated sites is instead expected to be radically different and would not be expected to play a dominant role in the reaction.

From such considerations it is expected that smaller particles exhibit lower specific activity, but possibly higher mass activity. Another related research effort is focused on substituting the noble metal core with a more abundant element, while keeping the activity constant. This has been done successfully for IrNi nanoparticles. $IrNi_3$ particles exhibited a mass activity 10 times higher than rutile IrO_2 particles. The recent efforts for finding better OER catalysts in acid is summarized in Fig. 25, where the current is normalized to geometric surface area. It is clear from this plot that only noble metal oxides are considered and currently no other materials are being reported as alternatives.

A far larger group of materials can withstand the reaction conditions in alkaline electrolytes. This is quickly realized by scanning through the Pourbaix diagrams of the elements, where most stable compounds are shown as function of pH and electrochemical potential. A renewed interest in perovskite materials has been taken, who tested a set of oxides with the aim of finding design principles for activity towards OER. It was attempted to identify a suitable bulk property that could relate to the OER activity of a group of perovskites. They successfully constructed a volcano shaped activity plot based on the filling of the eg band and identified Ba0.5Sr0.5Co0.8Fe0.2O$_{3-x}$ as a highly active catalyst. The eg band filling was argued to be a suitable descriptor for OER due to strong overlap of this particular

Fig. 26 Volcano shaped activity plot for a range of perovskites. The activity is shown as the potential needed to reach 0.5 mA/cm² as function of the computed O p-band center. In the left side of the figure there are stable perovskite materials, which improve in activity as the O p-band center incrases. For high O p-bands some perovskite have been observed to become amorphous
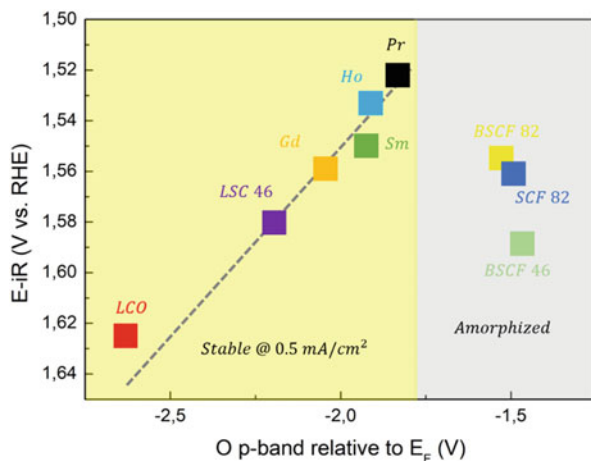
orbital with the oxygen adsorbate orbital. So, the eg band filling should have a direct implication in the charge transfer from electrode to adsorbate and influence the binding strength. An optimum eg band filling of 1 was proposed. Due to difficulties in measuring and calculating the eg band filling, it was later reported a similar finding where the O p-band center was used to describe the OER activity of double perovskites such as $Pr0.5Ba0.5CoO_{3-\delta}$. This descriptor could be found from DFT calculations and compared to oxidation state found with chemical titration techniques. In Fig. 26 the results of this work can be seen as a volcano shaped plot, indicating an optimum O p-band center of -1.7 eV relative to the Fermi level, EF. With a higher O p-band center the oxides tend to become amorphous during OER testing, which was the case for $Ba0.5Sr0.5Co0.8Fe0.2O_{3-x}$.

Parallel to these efforts of relating bulk oxide properties to OER activity, other groups have focused on nickel or cobalt based catalysts where especially Ni hydroxides mixed with iron have proven relevant. It was measured a range of electrodeposited transition metal oxides and found 2 nm thick $Ni0.9Fe0.1O_x$ able to reach 10 mA/cm² at only 340 mV overpotential. The advantage of measuring such thin films is that almost all the material can be considered active, and roughness will not play a large role. A disadvantage is that it is challenging to characterize such thin layers and there could be a large dependence on interaction with the substrate. Nevertheless, similar activities were reported. Interestingly, it was reported that pure NiO_x is not very active on its own but, due to inherent iron contamination from alkaline solutions and glassware, most Ni electrodes are in fact doped with iron. This has spurred further investigations into mixed nickel-iron oxides.

These studies mark an interesting new era in electrocatalysis, where new understanding arises from combinations of methods, rather than phenomenologically relying on pure electrochemical parameters such as Tafel slope and exchange current density. An additional focus point in the field of OER is the benchmarking of a large range of materials to allow for better comparison. It should be noted that even though almost all known catalysts are tested, only Ru, Ir and Pt are active in acidic

Fig. 27 Overview plot of
recent experiments with
OER catalysts tested in
alkaline media
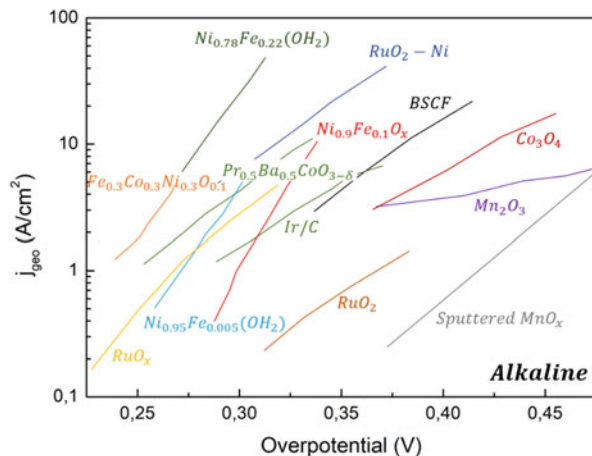
environment. To sum up this section of the most active catalysts for OER in alkaline environment a unified Tafel is shown in Fig. 27.

Manganese-based catalysts for OER represent another interesting case, which in many studies has been inspired by nature. This is due to the manganese-calcium complex responsible for the turnover of molecular oxygen in photosystem II. Manganese is also an extremely abundant element, among the most available transition metals, and it is considered environmentally friendly. Finally, it is one of the few transition metal oxides with a stable solid phase in the OER relevant potential region in acidic conditions that is also catalytically active.

Some of the first manganese-based OER catalysts to be reported were made with thermal decomposition. It was concluded that both β-MnO_2 and α-Mn_2O_3, on either Ti or Pt, and their mixtures could be used as anodes for oxygen evolution, even though they were inferior to RuO_2-based electrodes. The electrodes were tested in both acid and alkaline electrolytes. Ti substrates yielded better adhesion for the catalyst, while using a Pt substrate resulted in better conductivity. It was further speculated that oxygen vacancies in the catalyst layer provide the necessary conductivity, which decreases upon prolonged oxidation of the electrode due to an increase of oxygen content. This effect could be responsible for a slow deactivation of the catalyst activity when measured at high current density or potential over time. The existence of various Mn oxides (MnO, Mn_3O_4, Mn_2O_3, MnO_2 and several different crystalline phases) has also led to studies on the influence of the initial oxide on the OER activity, so-called structure-activity relations.

In some reports Mn in a +3 state was concluded superior in terms of activity. This view is supported by characterizations of Mn oxides before and in some instances after electrochemical testing. The DFT calculations suggested that at OER relevant potentials the MnO_2 phase was most stable, which is consistent with the bulk stability regions found in the Pourbaix diagram. It is therefore unlikely that a +3 state of Mn would persist at the electrode surface at highly anodic potentials. On the contrary, it is likely that the preparation method and the resulting roughness or

Fig. 28 Overview plot of
recent experiments with Mn
based OER catalysts tested
in various electrolytes
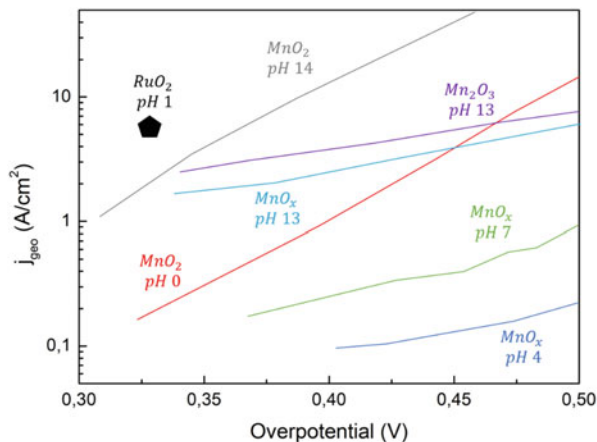
conductivity of the catalyst play a large role in determining an activity hierarchy. However, to elucidate the dependence on oxidation state in-situ techniques must be used so that the surface can be characterized under reaction conditions. Such studies are currently not available for Mn-based OER catalysts. A selection of active Mn-based OER catalysts is shown in Fig. 28 as a Tafel plot. From that plot it is evident that even with one type of material, e.g. Mn oxides, the range of measured activities is rather large.

In the previous sections it has been briefly mentioned that the OER catalysts must survive in extremely harsh and oxidizing conditions. It is therefore of utmost importance that new and active catalysts are stable in those conditions for an extended amount of time. However, while searching for new materials long term testing is not often a focus point and instead many groups turn to shorter electrochemical tests (2–24 hours) at either constant potential or constant current density. The question is whether these tests reveal any stability that can be extrapolated to the long term. A pure electrochemical test at constant current density have traditionally been the standard.

This type of test is justified by the operation mode such a catalyst would typically work under in an actual device. A certain amount of hydrogen is needed, or a certain amount of energy is used and the electrolyzer is therefore likely to operate under constant current density. If the catalyst deactivates over time it leads to an increase in the applied potential to reach the constant current density.

However, since the current is exponentially dependent on the overpotential small changes in potential lead to huge changes in current. So, when measuring the potential at constant current the changes are normally within 50 mV, which may be judged acceptable from the researcher's point of view. This type of test does not inform the researcher about any specific changes in the catalyst structure, purity, or electrode thickness. More importantly it does not reveal when a complete loss of the catalyst material will occur.

Recently, stability tests have received increased attention in the field of OER, likely inspired by the importance that stability plays in the evaluation of ORR catalysts. For Pt based ORR catalysts a typical accelerated stability test consists of 10000 cycles in a relevant potential range after which the loss of activity is reported. The ORR proceeds at potentials where Pt is thermodynamically stable but the start-stop conditions in fuel cells can cause surface oxidation followed by reduction, resulting in loss of platinum. Conversely, for OER catalysts many materials are prepared in a state that is not thermodynamically stable at potentials higher than 1.6 VRHE. For prolonged operation at high current densities the surface is bound to change structure, and this can lead to a loss of catalyst material. Such effects have been elegantly shown for a selection of noble metal oxides. In those studies, an online Inductively Coupled Plasma-Mass Spectrometry (ICP-MS) system is used to measure corrosion products while the catalysts are under potential control.

The results can be seen in Fig. 29 for Ru, Ir, Pt and Au, where dissolution rates and voltametric profiles are shown. The potential is slowly scanned between 0 and 1.5 VRHE, while the dissolved species are measured with the ICP-MS.

Notice that for Ru the dissolution occurs solely at the peak potential whereas it is stable at all other potentials. This contrasts with the other three metals, which all dissolve upon reduction, although at a much lower rate compared to Ru.

With such a dissolution prole it is unlikely that Ru can be used in electrolyzers. Instead Ir appears as the best compromise between activity and stability. In fact, through annealing procedures it has been shown that IrOx can be even more stable, reaching a mass loss rate of only 1 pg/cm^2/s at approximately 1.75 VRHE. For a realistic catalyst loading of 0.15 mg/cm^2 this corrosion rate corresponds to just below 5 years of constant operation. However, since IrOx dissolves primarily at potentiodynamic conditions it is likely that the mode of operation will have a large impact on the lifetime, where less start-stops lead to a longer lifetime.

The dissolution products can in some cases be detected electrochemically with a separate electrode during a catalyst test. This is the case for ruthenium dissolving as RuO_4, which can be reduced at 1.1 VRHE. In practice, this type of test is carried out with a Rotating Ring Disk Electrode, RRDE, setup where the catalyst is loaded as a standard rotating disk and the separate electrode is positioned as a ring around the disk. This geometry allows for an accurate determination of the efficiency with which the ring picks up products from a reaction at the disk. A few groups have characterized Ru dissolution with this method and the Faradaic efficiency for RuO_4 formation is between 6 and 15%. It should be noted that this technique is also frequently used for the determination of Faradaic efficiency towards oxygen evolution. A combination of RRDE and ICP-MS measurements were used to elucidate trends of stability among the metals that can catalyze OER, see Fig. 30.

They found that the more unstable metals were also more active catalysts. However, the trend found which can be seen in Fig. 31, appears to contrast with the simple inverse stability-activity relationship.

From the two Figs. 30 and 31, the activity trends are the same, but in 31 the stability results are not consistent with an inverse relationship. It should be noted that in both of these analyses the metal stabilities are evaluated at a constant current and
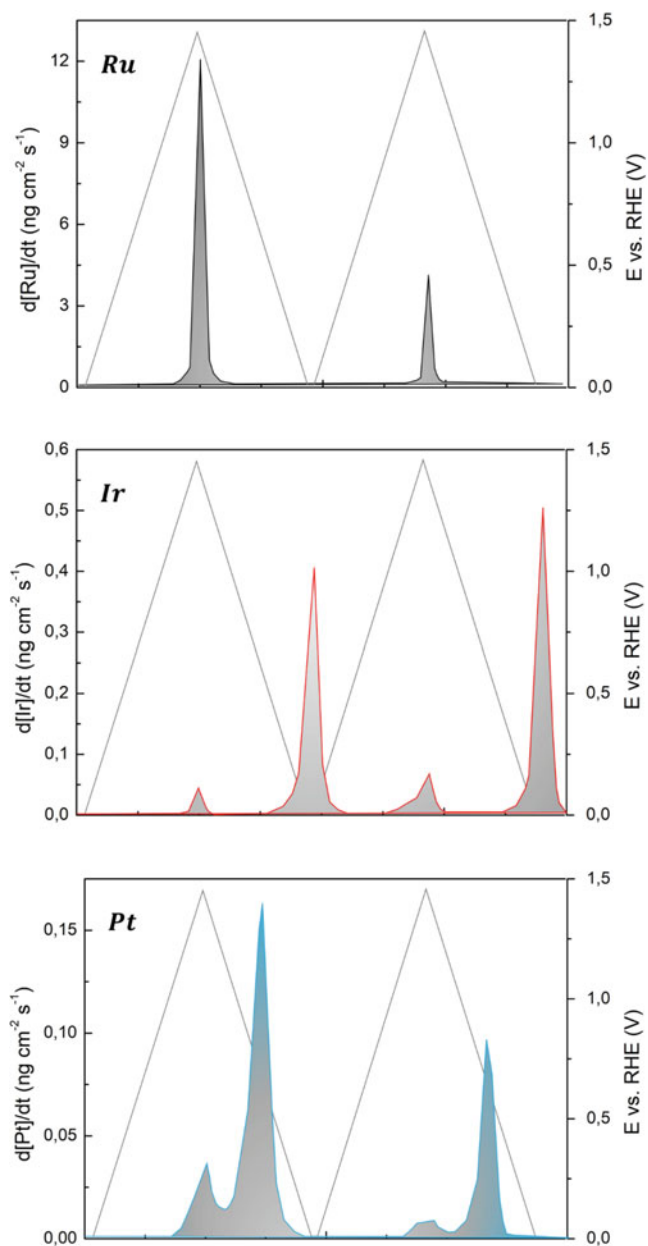
Fig. 29 Figure showing the stability of Ru, Ir, Pt and Au under OER reaction conditions, from top to bottom respectively. The mass losses are measured with online Inductively Coupled Plasma-Mass Spectrometry systems and are plotted as function of time. The potential is indicated with the lines and second axes on the right. In this way, it is possible to directly correlate the amount of mass lost to the potential applied to the electrodes
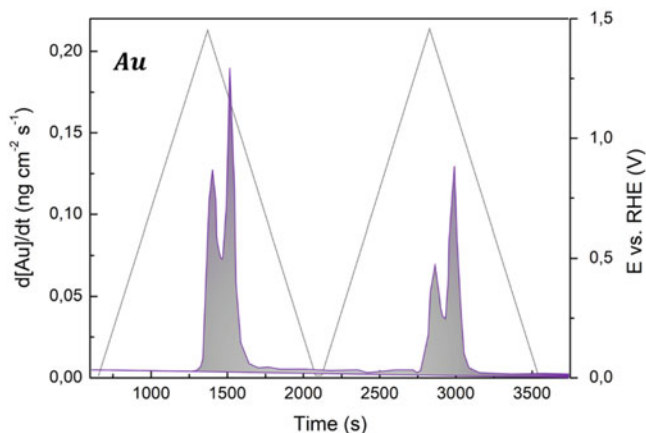
Fig. 29 (continued)
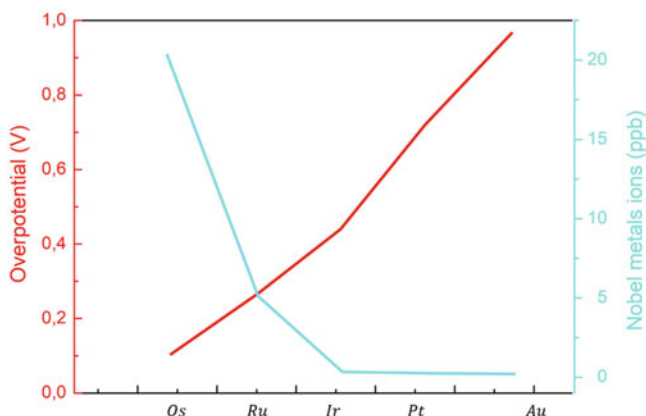
Fig. 30 Stability and activity trends for Os, Ru, Ir, Pt and Au under a constant current density of 5 mA/cm^2. The stability is measured as concentration of metals in solution after test (ppb). The activity is shown as the overpotential needed to reach 5 mA/cm^{-2}

therefore at different potentials. For instance Au is evaluated at potentials around 2 VRHE whereas Ru is evaluated at 1.5 VRHE. These contradicting results suggest that a more in-depth understanding of the dissolution phenomena is needed before an established model can be reached. In terms of stability analyses for non-noble metal oxides there are less studies available at this time. However, one of most active catalysts based on non-precious metals, Ba0.5Sr0.5Co0.8Fe0.2O$_{3-x}$, or in short BSCF, has been subjected to Transition Electron Microscopy, TEM, analysis before and after electrochemical tests, that consisted of cyclic voltammetry and from the TEM images it was evident that the BSCF particles change from a crystalline phase to an amorphous one. At the same time the catalytic activity increases, which is
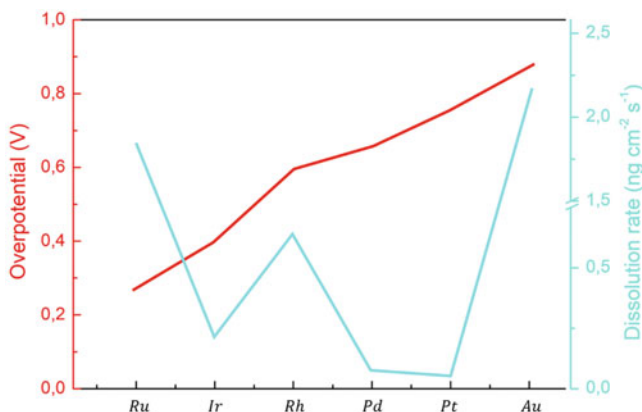
Fig. 31 Trends of activity and stability for Ru, Ir, Rh, Pd, Pt and Au under a constant current density of 0.8 mA/cm^2. The dissolution rate, in ng.cm^{-2}.s^{-1} is found with online ICP-MS at a constant current density of 0.8 mA/cm^{-2}. Note the scale break in the dissolution rate. The activity is shown as the overpotential needed to reach 0.8 mA/cm^{-2}

likely due to a roughening of the surface causing more active sites to be available. The authors therefore argued that the leaching of Ba^{2+} and Sr^{2+} ions was related to the position of the O p-band center. BSCF has an O p-band center positioned relatively high compared to other catalyst materials, like La0.4Sr0.6CoO$_3$ $_-$ $_\delta$, LaCoO$_3$ and LaMnO$_3$, all of which retain crystallinity after electrochemical testing.

Important progress has been made in terms of understanding the reaction and finding suitable descriptors that can aid in designing better catalysts. From theoretical analyses, scaling relations have been used to predict and describe trends in activity for a large group of oxides. Unfortunately, the scaling relations between intermediates also mean that it is complicated to surpass the performance of existing RuO$_2$ catalysts. Nevertheless, a large amount of work has been dedicated to optimizing Ni, Fe and Co based catalysts for use in alkaline solution and new materials are being reported frequently. The stability of new and active catalysts are not often reported in a very transparent way. Furthermore, there is a lack of progress for identifying non-noble metal based catalysts that can work in acidic solution. The new catalysts reported in acidic solutions are instead based on Ru and Ir.

6   Membranes for Water Splitting

Different types of electrolytes can be deployed in an EL cell: an alkaline electrolysis (AEL) cell works with a basic liquid electrolyte. In a proton exchange membrane (PEM) EL cell, an acidic ionomer—a process often called solid polymer electrolysis (SPE)—is used, and a high-temperature (HT) EL cell has a solid oxide as the electrolyte.

There are few ways of synthesizing the ion exchange or polymer membranes including sulfonation, polymer blending, acid or base doping, addition of inorganic fillers, pores filling, in-situ polymerization, and electrospinning. High-performance membranes must have the following characteristics (Henkensmeier et al. 2021):

- High proton conductivity
- Good electrical insulation
- High mechanical and thermal stability
- Good oxidative and hydrolytic stability
- Cost-effectiveness
- Low tolerance to ion crossover/good barrier property
- Low swelling stress
- Capability for fabrication of membrane electrode assemblies

One of the most important characteristics of the exchange membranes is water uptake that influences the electrochemical activity and hydromechanical stability of the membrane. Certainly, water is the fundamental element for transfer mechanism from the anode to the cathode in an electrochemical cell including an operation using non-sulfonated membranes in almost anhydrous condition and especially at high temperatures. However, the mechanical strength for a membrane with a higher water uptake reduces due to exorbitant swelling of the membrane.

7   Conclusions

Hydrogen is regarded as the alternative energy carrier of the future due to the higher energy density on a mass basis, less environmental problems, its abundant presence in different forms in the universe, and its convertibility into electricity or useful chemicals. It is the lightest element in the universe, which is without taste, color, odor, and non-toxic under normal conditions and has heating values of 2.4, 2.8 and 4 times higher than those of methane, gasoline and coal, respectively.

Hydrogen can be efficiently converted into electricity, and vice versa. It can be produced from renewable materials such as biomass and water, and most importantly, it is environmentally friendly at all processes utilizing hydrogen.

Development and scaling up hydrogen production technologies such as thermochemical water splitting cycles (TWSCs) in an integrated and sustainable manner for large-scale hydrogen production can foster hydrogen economy and sustainable energy development.

Water is the most abundant resource for hydrogen production which consists of hydrogen and oxygen. Hence, the water molecule can be split into hydrogen and oxygen if enough energy is provided. Water splitting process can be performed through different technologies. Water splitting for hydrogen production can be performed based on any of these sources and some hybrid types (combined two or many energy sources. Water splitting hydrogen production methods can be categorized into five major types and a hybrid form where two or more types of energy are

employed in a system for hydrogen production. Hydrogen from water by electricity based (electrolysis), mechanical based (from ultrasound through sonochemical method), photonic based (photolysis or photo electrochemical water splitting), thermal energy based (thermochemical cycles and thermolysis).

Electrolysis is one of the simplest ways to produce hydrogen from water. It can simply be summarized as conversion of electric power to chemical energy in the form of hydrogen and oxygen as a by-product with two reactions in each electrode: anode and cathode. There is a separator between anode and cathode electrodes which ensure products to remain isolated. The low-temperature electrolysis (LTE) occurs in temperatures of 70–90 °C while the high temperature electrolysis (HTE) takes place in 700–1000 °C with less electricity consumption. The advantage of HTE is that near zero GHG emission can be achieved if an external clean heat source is employed.

Water-splitting thermochemical cycles are based on water decomposition through repetitive series of chemical reactions using intermediate reactions and substances which are all recycled during the process so that the overall reactions are equivalent to the dissociation of the water molecule into hydrogen and oxygen. Theoretically, thermal energy is the only requirement for this process. Thermochemical water splitting cycle (TWSCs) are for hydrogen production using thermal energy and recycling of materials for reuse. TWSCs are not very catalyst dependent and the only consumed substance in the cycle is water, which is the source of hydrogen, and all other materials can be recycled.

The thermochemical cycles are driven either by only thermal energy which are called pure thermochemical cycles, or by thermal and another form of energy (e.g. electrical, photonic) which are called hybrid thermochemical cycles. In hybrid TWSCs, water, high temperature heat from concentrated solar plants or nuclear reactors, and electricity or photonic energy are the inputs while hydrogen and oxygen are the outputs. Water can be decomposed to H_2 and O_2 just in one step. However, due to the undesirable thermodynamics and the very high temperature required for the single-step, thermochemical cycles are proposed as a repeating set of reactions in which water is split using thermal energy at the temperatures below 2000 °C and usually in two or multi steps.

References

Anantharaj S, Ede SR, Sakthikumar K (2016) Recent trends and perspectives in electrochemical water splitting with an emphasis on sulfide, selenide, and phosphide catalysts of Fe, Co, and Ni: a review. ACS Catal 6(12):8069–8097. https://doi.org/10.1021/acscatal.6b02479

Anantharaj S, Ede SR, Karthick K (2018) Precision and correctness in the evaluation of electrocatalytic water splitting: revisiting activity parameters with a critical assessment. Energy Environ Sci 11(4):744–771. https://doi.org/10.1039/C7EE03457A

Ateya BG, El-Anadouli BE (1991) Effects of gas bubbles on the polarization behavior of porous flow through electrodes. J Electrochem Soc 138(5):1331–1336. https://doi.org/10.1149/1.2085781

Ayers K, Danilovic N, Ouimet R et al (2019) Perspectives on low-temperature electrolysis and potential for renewable hydrogen at scale. Ann Rev Chem Biomol Eng 10:219–239. https://doi.org/10.1146/annurev-chembioeng-060718-030241

Bakker MM, Vermaas DA (2019) Gas bubble removal in alkaline water electrolysis with utilization of pressure swings. Electrochim Acta 319:148–157. https://doi.org/10.1016/j.electacta.2019.06.049

Carmo M, Fritz DL, Mergel J et al (2013) A comprehensive review on PEM water electrolysis. Int J Hydrogen Energy 38(12):4901–4934. https://doi.org/10.1016/j.ijhydene.2013.01.151

Darband GB, Aliofkhazraei M, Shanmugam S (2019) Recent advances in methods and technologies for enhancing bubble detachment during electrochemical water splitting. Renew Sustain Energy Rev 114:109300. https://doi.org/10.1016/j.rser.2019.109300

Doan H, Kendrick I, Blanchard R et al (2021) Functionalized embedded monometallic nickel catalysts for enhanced hydrogen evolution: performance and stability. J Electrochem Soc 168(8):084501. https://doi.org/10.1149/1945-7111/ac11a1

Funk JE (2001) Thermochemical hydrogen production: past and present. Int J Hydrogen Energy 26(3):185–190. https://doi.org/10.1016/S0360-3199(00)00062-8

Grdeń M, Łukaszewski M, Jerkiewicz G et al (2008) Electrochemical behaviour of palladium electrode: oxidation, electrodissolution and ionic adsorption. Electrochim Acta 53(26):7583–7598. https://doi.org/10.1016/j.electacta.2008.05.046

Henkensmeier D, Najibah M, Harms C (2021) Overview: state-of-the art commercial membranes for anion exchange membrane water electrolysis. J Electrochem Energy Convers Storage 18(2):024001. https://doi.org/10.1115/1.4047963

Holladay JD, Hu J, King DL (2009) An overview of hydrogen production technologies. Catal Today 139(4):244–260. https://doi.org/10.1016/j.cattod.2008.08.039

Hu C, Zhang L, Gong J (2019) Recent progress made in the mechanism comprehension and design of electrocatalysts for alkaline water splitting. Energy Environ Sci 12(9):2620–2645. https://doi.org/10.1039/C9EE01202H

Jiang W-J, Tang T, Tang T (2020) Synergistic modulation of non-precious-metal Electrocatalysts for advanced water splitting. Acc Chem Res 53(6):1111–1123. https://doi.org/10.1021/acs.accounts.0c00127

Jiang S, Sun H, Wang H et al (2021) A comprehensive review on the synthesis and applications of ion exchange membranes. Chemosphere 282:130817. https://doi.org/10.1016/j.chemosphere.2021.130817

Liang C, Zou P, Nairan A et al (2020) Exceptional performance of hierarchical Ni-Fe oxyhydroxide@NiFe alloy nanowire array electrocatalysts for large current density water splitting. Int J Hydrogen Energy 13(1):86–95. https://doi.org/10.1039/C9EE02388G

Mandin P, Derhoumi Z, Roustan H et al (2014) Bubble over-potential during two-phase alkaline water electrolysis. Electrochim Acta 128:248–258. https://doi.org/10.1016/j.electacta.2013.11.068

Marangio F, Santarelli M, Calì M (2009) Theoretical model and experimental analysis of a high pressure PEM water electrolyser for hydrogen production. Int J Hydrogen Energy 34(3):1143–1158. https://doi.org/10.1016/j.ijhydene.2008.11.083

Miller HA, Bouzek K, Hnat J et al (2020) Green hydrogen from anion exchange membrane water electrolysis: a review of recent developments in critical materials and operating conditions. Sustain Energy Fuel 4(5):2114–2133. https://doi.org/10.1039/C9SE01240K

Mo J, Stefanov BI, Lau THM et al (2019) Superior performance of ag over Pt for hydrogen evolution reaction in water electrolysis under high overpotentials. ACS Appl Energy Mater 2(2):1221–1228. https://doi.org/10.1021/acsaem.8b01777

Özdemir SN, Taymaz I (2022) Three-dimensional modeling of gas–liquid flow in the anode bipolar plate of a PEM electrolyzer. J Braz Soc Mech Sci Eng 44(8):354. https://doi.org/10.1007/s40430-022-03664-y

Rozain C, Millet P (2014) Electrochemical characterization of polymer electrolyte membrane water electrolysis cells. Electrochim Acta 131:160–167. https://doi.org/10.1016/j.electacta.2014.01.099

Safari F, Dincer I (2020) A review and comparative evaluation of thermochemical water splitting cycles for hydrogen production. Energy Convers Manag 205:112182. https://doi.org/10.1016/j.enconman.2019.112182

Sapountzi FM, Gracia JM, Weststrate CJK-J (2017) Electrocatalysts for the generation of hydrogen, oxygen and synthesis gas. Prog Energy Comb Sci 58:1–35. https://doi.org/10.1016/j.pecs.2016.09.001

Schalenbach M, Carmo M, Fritz DL (2013) Pressurized PEM water electrolysis: efficiency and gas crossover. Int J Hydrogen Energy 38(35):14921–14933. https://doi.org/10.1016/j.ijhydene.2013.09.013

Siracusano S, Di Blasi A, Baglio V et al (2011) Optimization of components and assembling in a PEM electrolyzer stack. Int J Hydrogen Energy 36(5):3333–3339. https://doi.org/10.1016/j.ijhydene.2010.12.044

Turner JA (2004) Sustainable hydrogen production. Science 305(5686):972–974. https://doi.org/10.1126/science.1103197

Uosaki K, Elumalai G, Dinh H et al (2016) Highly efficient electrochemical hydrogen evolution reaction at insulating boron nitride nanosheet on inert gold substrate. Sci Rep 6:32217. https://doi.org/10.1038/srep32217

Vincent I, Choi B, Nakoji M (2018) Pulsed current water splitting electrochemical cycle for hydrogen production. Int J Hydrogen Energy 43(22):10240–10248. https://doi.org/10.1016/j.ijhydene.2018.04.087

Zeng K, Zhang D (2010) Recent progress in alkaline water electrolysis for hydrogen production and applications. Prog Energy Comb Sci 36(3):307–326. https://doi.org/10.1016/j.pecs.2009.11.002

Zhou H, Yu F, Zhu Q (2018) Water splitting by electrolysis at high current densities under 1.6 volts. Energy Environ Sci 11(10):2858–2864. https://doi.org/10.1039/C8EE00927A

Water Purification and Desalinization

1 Introduction

Electrochemical water splitting is generally used to produce molecular hydrogen via alkaline and solid oxide electrolysis that have nowadays a hydrogen production efficiency up to 67% (Wei and Xu 2018). The major cost of the hydrogen production is the electricity consumption and in part operational costs for chemicals, also potassium hydroxide or other solid electrolytes.

In the next 10 years, the US department of energy goal is to reduce the total cost of hydrogen production by 50%. To reduce the electricity and chemical reagent consumption in molecular hydrogen production a new strategy to find an alternative electrolyte is required. A wastewater electrolysis cell can provide a practicable method to self-sustainable on-site wastewater treatment with simultaneous decentralized H_2 production (Huang et al. 2016).

Electrochemical systems are generally used for the treatment of high salinity wastewater as dye wastewater (textile), landfill leachate, olive mill wastewater, tannery wastewater, livestock industry wastewater, and reverse osmosis concentrates, among many other usages. Non-biodegradable degradations or recalcitrant environmental pollutants in electrochemical cell are also studied using laboratory-generated electrolyte (substrates of interest in background electrolyte).

The cathodic current efficiency and energy efficiency of H_2 production changes a lot depending on the electrolyte composition (NaCl or Na_2SO_4 background, electrical conductivity, concentration of electron donating substrates other than water), cell configuration (distance between anode and cathode, geometric area), and operating condition (applied cell voltage). The reported values ranged from 40% to 80% for current efficiency and from 15% to 60% for energy efficiency. The major scavenging reactions for H_2 production include reduction of RCS (to chloride ion) in NaCl background and reduction of oxygen (to superoxide radical and its dissociation products). The H_2 production efficiency was usually higher in the $NaSO_4$ background than in the NaCl background. In the NaCl background solution, the current

and energy efficiency are enhanced by the presence of electron donating substrates. For example, batch injections of small amounts of organics including urea, phenol, and other oxidizable organics sharply enhanced the production of H_2. The RCS can be made unable to accept electrons by the organics to improvement the H_2 production favoring water. Electrical conductivity decreasing or applied cell voltage increasing led to H_2 production energy efficiency decrease, due to the increase in ohmic energy losses.

It would be advantage to electrolyze saline water in a cell behaves as a H_2/O_2 one. Under normal conditions of sea water electrolysis, however, mass transfer limitations and reaction kinetics combine to make the cell products H_2/Cl_2 (Yu et al. 2019).

The production of hydrogen from seawater electrolysis it can be made by two different processes.

The first option is to subject the water to total desalination to remove all dissolved salts and produce essentially distilled water, that can then be subjected to electrolysis, alkaline- electrolyte and electrolysis is cells.

The disadvantages of this approach are additional capital cost of water treatment and desalination system, and the environmental problems arising from the need to dispose the residual salts removed during desalination. The advantages are the ability to use developed technology for the direct electrolysis of fresh water.

The second option is to design an electrolyze system capable of utilizing sea water for direct electrolysis (Tong et al. 2020). It is probable that these systems would operate at a low power density and electrolyze only a small portion of the water in contact with electrodes. The disadvantages are: new technology must be developed to solve the probable corrosion and contamination problems and the evolution of undesirable electrochemical products such as chlorine. The advantages are possible lower capital cost and natural elimination of the waste brine which is only slightly enriched with salts. It may also be possible to recover economically significant quantities of the metals present in sea water, in particular magnesium in a form of magnesium hydroxide.

Transport control of chlorides in saline solutions, otherwise Cl evolution, is a function of the current density. Electrolysis of sea water at low current density (less than 1 mA/cm^2) favors oxygen evaluation. Accordingly, increasing the current density will increase Cl_2 evolution until a value of limitation in chloride mass transport is reached. The current density at this stage is called limiting C.D., corresponding to a value of 100–1000 mA/cm^2.Once this value is exceeded, Cl_2 evolution is suppressed, while O_2 is favored (Khan et al. 2021).

In the last few decades, the energy requirement of SWRO desalination plants has decreased from 9–10 to <3 kWh m^{-3} currently. This has led to a decrease in levelized cost of SWRO desalinated water from 42.2 to o0.6 $ per m^3 and resulted in a 6.5-fold increase in global desalination capacity. As of 2020, total production capacity reached 4100 million m^3 per day, 70% of which is based on RO. The increase in production capacity is expected to follow the same trend in the next decades, as per planned and under construction plants.

Despite the resources and efforts that have gone into developing this technology, direct seawater splitting remains in its infancy and distant from commercialization (Zheng et al. 2021).

2 Water Purification

The production process brings a H_2-rich mixture of gases; this mixture has to be purified to reach ultra-high purity levels required by fuel cells (99.97%).

The H_2 production methods based on SMR and gasification involve a final H_2 purification step in which CO_2 and other impurities are removed from the hydrogen gas. This final H_2 purification step is the most important for the hydrogen economy implementation because polymer electrolyte membrane (PEM) fuel cells require ultra-high-purity hydrogen (mole fraction $\geq$ 99.97% and CO $\leq$ 0.2 ppm) and, furthermore, the majority of other hydrogen applications such as general industrial applications, hydrogenation and water chemistry also need high levels of hydrogen purity ($\geq$99.95).

The interest in the production of ultra-high-purity hydrogen has strongly increased in recent years and this has placed pressure on the development of alternative methods of hydrogen purification (Kumar and Himabindu 2019).

At the moment, the most used technologies for hydrogen purification are pressure swing adsorption (PSA), cryogenic distillation and amine-based absorption for CO_2 removal from H_2.

Membrane separation technology appears as an emerging and very promising industrial process that will be able to compete and eventually replace the traditional separation techniques, due to its many associated advantages (Paidar et al. 2016).

A membrane is a physical solid barrier between two phases (gaseous or liquid), with a certain perm-selectivity towards one or more components of a mixture. In gas separation applications, the force that normally drives the different species to permeate a membrane is the partial pressure difference between both sides of the membrane.

Membrane technology offers many advantages: simpler operation; higher adaptability; compactness and lightweight; modular design with simpler up-scaling and down-scaling; lower labor intensity; lower capital, operating and maintenance costs; higher energy efficiency and a much lower environmental impact, among other advantages.

H_2 perm-selective membranes in membrane reactors, i.e. Innovative integrated systems in which both reaction and separation are carried out in the same equipment, improve fuel conversion owing to the shifting of reaction equilibrium conditions.

These membrane technologies are:

1. Carbon molecular sieve membranes (CMSM)
2. Ionic liquid membranes (ILM)

3. Metal based membranes
4. Electrochemical hydrogen pumping membranes (EHPM).

CMSM are produced through the carbonization of polymeric precursors at high temperatures and under a controlled atmosphere.

The characteristics of this membrane are: high corrosion resistance, high thermal stability and excellent permeability and perm-selectivity, when compared to polymeric membranes.

The CMSM structure is turbostratic and described as "slit-like" with a bimodal pore size distribution with micropores connecting ultramicropores.

Micropores provide sorption sites while ultra-micropores (called constrictions) are the responsible for the molecular sieving mechanism of gas permeation observed in this type of membranes.

One important advantage of CMSM is their particularly ability to separate H_2 (kinetic diameter = 2.89 Å) from gas molecules with much larger kinetic diameters such as N_2 (3.64 Å), CH_4 (3.80 Å) and C_3H_8 (4.30 Å).

The permeability of CMSM to H_2 are most often in the range 100–1000 Barrer, although values >5000 Barrer have been reported.

There are different mechanisms developed on molecular sieving: gate sieving and tubular sieving.

Advantages: resistant to CO and sulphur poisoning, they are suitable at low temperatures.

Disadvantages: brittle, small permeation fluxes, poor performance for the separation of H_2/CO_2 mixtures, stability, aging effect.

Ionic liquids are negligible to vapor pressure, non-flammability, and solubility of CO_2 is higher as compared to H_2 which makes it perfect for the separation of H_2 from CO_2/H_2.

Ionic liquid-based membranes are used for CO_2 from gas streams separation (CO_2/N_2, CO_2/CH_4, and CO_2/H_2).

Different types of membranes containing ILs are:

1. Supported IL membranes (SILMs)
2. Polymer-IL composites membranes
3. Polymer-IL gel membranes
4. Polymerized ionic liquid membrane (PILM)
5. Composite membranes (PILM-ILs)

The sorption-diffusion mechanism in ionic liquid-based membranes can be facilitated by a CO_2-selective transport mechanism. This so-called CO_2-selective facilitated transport utilizes reactions between CO_2 and CO_2 carriers to enhance the transport of CO_2 through the membrane, resulting in a significantly improved permeability and selectivity of the membrane to CO_2.

The permeability to CO_2 in ionic liquid-based membranes is usually higher than the permeability to H_2, these are CO_2-selective membranes that can permeate CO_2, and retain H_2 and other impurities (CH_4, CO), producing high-pressure H_2 (retentive side) and low-pressure CO_2 (permeate side).

ILs are still mostly used and produced at the lab scale which is very far from the industrial scale in terms of costs.

The CO_2/H_2 separation performances of PILM are better according to the industrial requirements. By synthesizing new PILM and blending in free ILs with high permeability and selectivity, PILM-IL composites have the potential to achieve excellent separation performances.

The mechanism of hydrogen transport through dense metal membranes occurs via a sorption-diffusion mechanism. The steps involved in hydrogen permeation from high to a low partial pressure gas region are following:

1. Dissociative adsorption of H_2 on the gas-metal interface
2. Sorption of the atomic hydrogen into the bulk metal
3. Diffusion of atomic hydrogen through the bulk metal membrane
4. Re-combination of atomic hydrogen to form
5. Hydrogen molecules at the interface metal/gas permeate
6. Desorption of molecular hydrogen.

Metals like niobium (Nb), vanadium (V), and tantalum (Ta), have higher hydrogen permeation flux then palladium (Pd) in the temperature range of 0–700 °C.

However, palladium has superior catalytic activity to dissociation of molecular hydrogen and high permeability to atomic H_2.

Pd-based membranes virtually infinite selectivity and allow the production of ultra-pure hydrogen at 99.99999% purity.

Depending on their structure, palladium-based membranes can be classified either as unsupported (free-standing) membranes or as supported membranes.

Palladium-based membranes besides offering excellent hydrogen selectivity, can be used in membrane reactors, providing the possibility to combine both the chemical reaction for hydrogen production and the purification step in a unique system (Al-Mufachi et al. 2015).

Due to the lack of palladium resources in the planet, it is a very expensive metal and the large-scale industrial purification of H_2 using palladium membranes seems to be unfeasible.

Contrary to fuel cells and electrolysis, the chemical reaction involved in EHP does deliver neither energy, nor new products: simply hydrogen goes in, and hydrogen goes out and is suitable for hydrogen purifications even when present at low concentrations.

The basic working principle of an EHP is that a multicomponent stream containing H_2 is directed into the anodic compartment of an electrochemical cell, where the hydrogen molecules are oxidized in the catalyst layer of a porous electrode.

Due to the applied potential difference, the resultant protons are then selectively "pumped" across a proton-conducting membrane, while the electrons go to the cathode through the external circuit.

Finally, the protons and electrons recombine at the cathode producing molecular hydrogen:

$$Anode : H_2 \rightarrow 2H^+ + 2e^-$$

$$Cathode : 2H^+ + 2e^- \rightarrow H_2$$
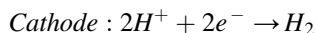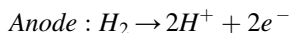
Multiple proton-conducting membranes for EHP applications like perfluorinated sulfonic acid (PFSA) polymers for low temperature, phosphoric acid-doped polybenzimidazole (PBI) for intermediate temperatures and solid oxide membrane for higher temperatures.

The advantages of EHPM are: a high selectivity, high hydrogen permeation and relatively low energy consumption. Due to the use of precious metals (Pt) as electro-catalyst and use of expensive proton-conductor membranes the technology remains expensive.

EHPs do not require a driving pressure differential, electricity is the driving force that can produce pure H_2 at a higher pressure than the incoming feedstock gas.

2.1   Electrolysis of Sea Water

The water for electrolysis has to be highly pure feeds with a minimum requirement of American Society for Testing and Materials (ASTM) Type II deionized (DI) water (resistivity 41 MΩ cm) while ASTM Type I DI water (410 MΩ cm) is preferred. ASTM defines Type II water, as required in commercial electrolyzers, as having a resistivity of 41 MΩ cm, sodium, and chloride content <5μg L^{-1} and <50 ppb of total organic carbon (TOC).

Seawater represents 96.5% of earth's water resources, so the focus is on the direct electrolysis of seawater to produce hydrogen considering the additional capital and operating costs associated to water purification. A technology for direct seawater splitting could potentially be used in coastal arid zones that have limited access to freshwater, yet plenty of access to seawater and renewable electricity from solar, wind and geothermal.

Seawater electrolysis could be done to either produce chlorine via chloride oxidation or oxygen via water oxidation. Although chlorine is a valuable industrial chemical, the quantities produced for the growing hydrogen market would far exceed global demand for chlorine (Khan et al. 2021). Therefore, one of the major challenges has been the development of active and stable anode catalysts for selective oxygen evolution over chlorine.

The competing chlorine evolution reaction (CER) is thermodynamically unfavorable compared to the oxygen evolution reaction (OER) (480 mV higher in alkaline media), but it is a two-electron reaction, in contrast to OER which involves four electrons. This difference in the numbers of electrons involved makes OER kinetically unfavorable. While some progress has been made on the development of selective catalysts for OER from alkaline simulated seawater, reaching stable and industrially relevant current densities (4300 mA cm^{-2}) has been a major challenge from seawater (pH = 8). Even though carbonate and borate ions are present in

seawater, their average concentration is too low to sustain high current densities. Majority of reports at industrially relevant current densities use seawater with a borate buffer or additives such as KOH. Furthermore, seawater is essentially a non-buffered electrolyte, which causes a change in pH near the electrode surface during electrolysis (as high as 5–9 pH units), leading to salt precipitation as well as catalyst and electrode degradation. Other challenges include the presence of other ions, bacteria, microbes, as well as small particulates, which limit the long-term stability of catalysts and membranes.

In the last few decades, the energy requirement of SWRO desalination plants has decreased from 9–10 to <3 kWh m^{-3} currently.

A schematic of the desalinization technology is shown in Fig. 1.

The PEM electrolysis plant consists of the electrolyzer stacks and the mechanical and electrical balance of plant (BoP) components. The electrical BoP consists of the AC to DC rectifier for converting grid electricity while the mechanical BoP consists of other auxiliary components such as pumps, heat exchangers, temperature swing adsorption (TSA) subsystem and most importantly a deionizer (DI) system.

The SWRO plant contains the RO unit which uses a membrane barrier and pumping energy to separate salts from saline water. Water is forced through semi-permeable membranes using high-pressure pumps, this led to a dense separation layer (thin film composite membrane) allowing the passage of pure water molecules while rejecting dissolved salts and other impurities. To control RO membrane (bio)fouling and scaling, the SWRO system necessitates physical and chemical pretreatment steps depending on the feedstock.

Physical treatment: dual media, sediment and carbon filters or low-pressure membranes, such as ultrafiltration; chemical one: coagulant polymer, antiscalant, acid, chlorination/dechlorination. A combination of these filters provides a wide spectrum of reduction.

There are several RO pretreatments designs that could be adopted depending on the quality of water needed. The desalination unit consists of a double-pass RO system designed to attain the high purity of water required by the PEM electrolyzer. The SWRO-PEM coupled system could be in coastal regions with intense solar irradiation and/or wind energy available to produce renewable electricity via photovoltaic cells, wind turbines or even offshore structures, that can be used for hydrogen supply for shipping for example (Cavaliere 2022).

2.2 Wastewater Treatment

Sources of wastewater can generally be divided into three groups: domestic wastewater which mainly includes organic waste such as sewage, household chemicals and stormwater, etc.; agricultural and horticultural wastewater such as pesticide and fertilizer runoff, animal effluent; industrial wastewater which usually concentrated and specific to the each industry such as dairy, pharmaceuticals, paints and dyes, petrochemicals, detergents, plastics, steel industries, paper and pulp industries, etc. (Lu et al. 2020).
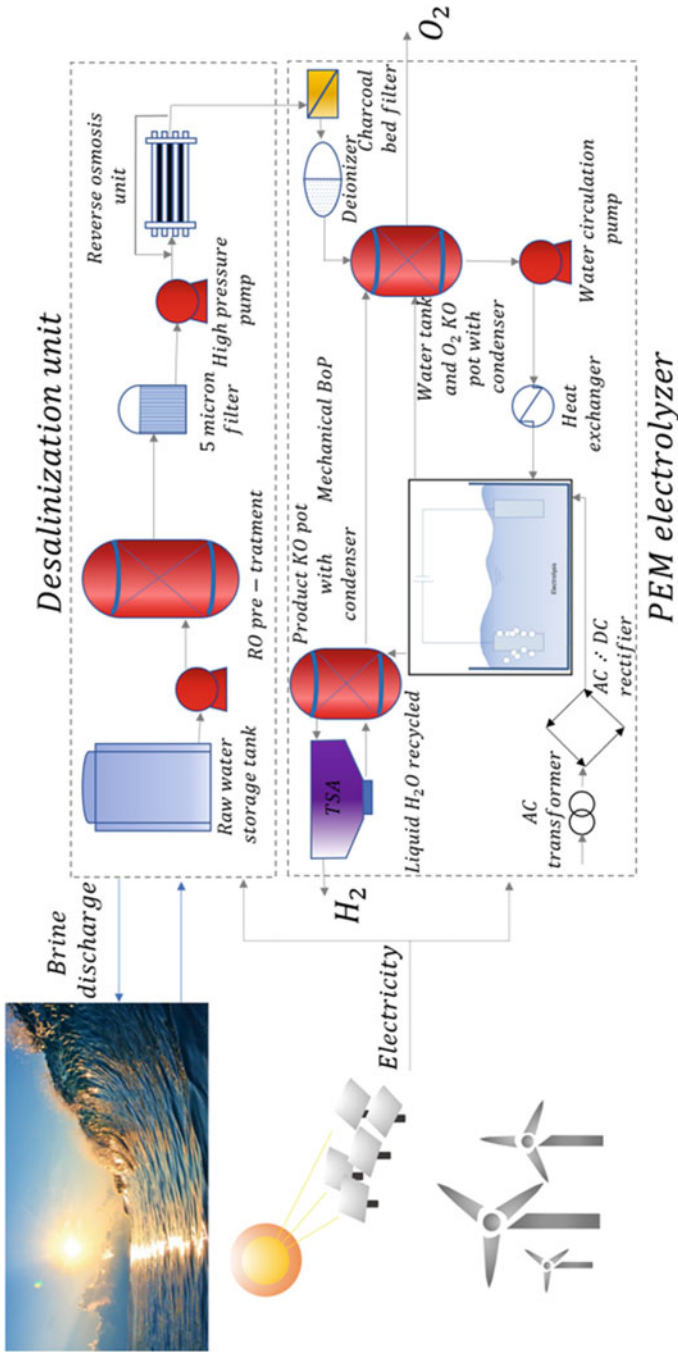
Fig. 1 Seawater desalinization for hydrogen production

The treatment processes for wastewater can be one of these three methods: physical, biological and advanced oxidation processes (AOPs).

Physical treatment includes processes where physically substances are removed from the wastewater using physical barriers or natural forces such as gravity and electromagnetic force. Physical methods include screening, filtering, floatation, and adsorption can only partially treat the waste streams and quite often use with the other technique to complete the treatment. The good example of the ineffectiveness of this method is when the wastewater includes dissolved organic or microbiological substances that cannot be easily separated from the wastewater.

Biological treatment is considered as the leading technique to treat most of the wastewater due to it is low capital and operating costs. These biological processes can be either aerobic or anaerobic depending on the type of wastewater to be treated, and thus, the type of microorganisms used. While these methods are applicable to a wide range of waste streams, they are ineffective against bio-toxic or bio-refractory substances present in the waste stream.

Chemical and advanced oxidation processes are alternatives to the biological treatment processes when these are not capable of degradation of refractory organic and toxic compounds. These methods typically involve in the generation or use of strong oxidizing species or highly active radicals. Examples of these species include ozone, hydrogen peroxide and hydroxyl radicals. These active species oxidize organic compounds and oxidize them into carbon dioxide, water and other smaller molecules (which can be oxidized further by the biological process). Some examples of chemical oxidation processes include the use of hydrogen peroxide, ozone, wet air oxidation and chlorine whereas advanced oxidation processes (AOPs) include the electrochemical oxidation, Fenton process, photocatalysis, O3/UV radiation, and cavitation. Even if these methods are very robust and effective, they also have some major shortcomings: low processing capacity, require the storage of dangerous reactants and environmental problem due to accumulation of large number of oxidants, require a pre-treatment in some cases and require high capital and operating costs. In general, these methods are used if either dangerous or toxic compounds are present in the waste stream or the final use is drinking water (Murgolo et al. 2019).

Therefore, it is necessary to select more efficient methods than those selected for conventional treatment processes.

Electrochemical oxidation is a promising method for the complete elimination of the organic pollutants and remediation of wastewater (Fig. 2). This method can be applied for the wastewater containing chemical oxygen demand (COD) less than 5 g L^{-1}. The main characteristics associated with electrochemical wastewater are:

- versatility; it can treat a wide range of effluent volumes and contamination concentrations and compounds which are normally difficult to treat with conventional methods.
- environmentally compatible; it uses electrical energy and electron to operate which is clean, and very effective reagent.

Fig. 2 Conceptual diagram of an electrochemical cell for oxidation of wastewater
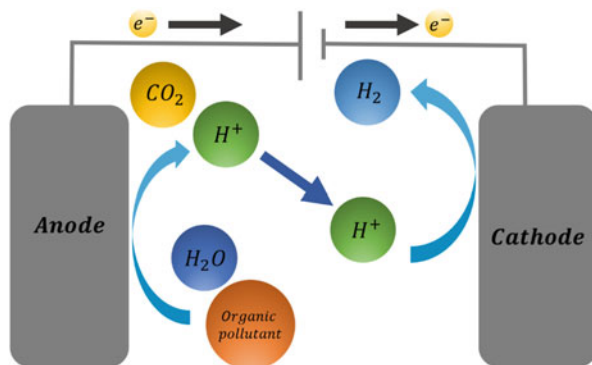
- ease of operation; automation and control of process is easy and can be quickly started-up and shut-down.

However, despite the low capital and maintenance costs, the operating costs can be high due to the low current efficiency of the process (i.e. the proportion of the current used for organic oxidation). In most cases, it is the oxygen evolution reaction which occurs in parallel to the organic oxidation reaction, which lowers the current efficiency of electrochemical wastewater treatment processes.

Over the past few decades, the focus was on the improvement of the electrochemical stability and electrocatalytic activity of the electrode materials. The studies were based on efficiency of various anodes materials on wide range wastewater determination, and on the factors that influence performances of the process including developing models of the mechanism and kinetics of electrochemical wastewater treatment. Electrochemical oxidation of pollutants is commonly divided into two oxidation mechanisms depending on the place where the overall oxidation occurs. When the oxidation occurs at or on the electrode surface the process is known as direct oxidation, indirect oxidation occurs when the electrode produces a reactant which then reacts with the wastewater within the aqueous solution away from the electrode surface.

Direct oxidation, which also known as anodic oxidation, pollutants are oxidized directly after adsorption on the anode surface, which indicate a significant role of the anode materials in the efficiency and selectivity of the oxidation process (Fig. 3).

Pollutants have to reach the electrode surface before reacting, so mass transfer is a rule for this process.

Depends on the anode materials, anodic oxidation takes place in two different pathways:

- Electrochemical conversion. If the anode materials are "active" or have low oxygen evolution overpotential, organic pollutants are partially oxidized. In the case of the "active" anode, first a chemisorbed hydroxyl radical is generated on the electrode surface, then oxidation process completed through higher oxide by a direct transfer of electrons from the electrode surface. This leads to the production
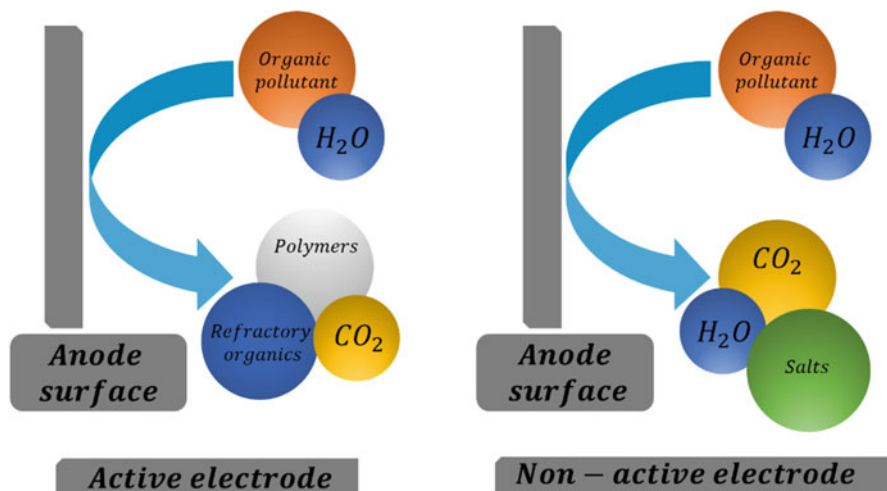
Fig. 3 Schemes for direct oxidation of organic pollutants

Table 1 Potential for oxygen evolution reaction on various anodes

Anode material	Anode category	Oxidation potential (V vs. SHE)
RuO_2	Active	1.47
IrO_2	Active	1.52
Pt	Active	1.6
Graphite	Active	1.7
SnO_2	Non-active	1.9
PbO_2	Non-active	1.9
Ti/BDD	Non-active	2.7

of polymers and many refractory organics as final products of the oxidation process. Thus, biological treatment is required as secondary treatment.

- Electrochemical combustion. If the anode materials are "non-active" or consider as high oxygen evolution overpotential, the complete oxidation of the organic pollutant occurs, which leads to the formation of water, carbon dioxide. In the case of "non-active" anode materials, the weak interaction between the electrode surface and hydroxyl radicals -physiosorbed-, result in complete oxidation of organic compounds (Table 1).

The generalized scheme of the electrochemical oxidation of organic pollutants on the metal oxide anode (MO_x) is illustrated in Fig. 4.

The first step of the reaction is the discharge of H_2O molecules at the anode to form an adsorbed hydroxyl radical:

Fig. 4 Generalised scheme
of the electrochemical
conversion and combustion
of organics with
simultaneous oxygen
evolution at the lattice of the
oxide anode

$$MO_x + H_2O \rightarrow M_x(*OH) + H^+ + e^-$$
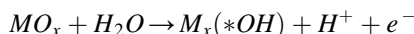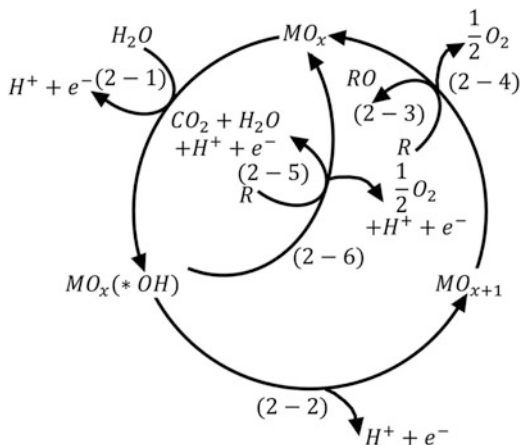
The following steps based on the anode materials can be distinguished into two
mechanism pathways; In the case of the "active" anode, the adsorbed hydroxyl
radicals further oxidize on the anode, forming the so-called" higher oxide" (MO_{x+1}):

$$M_x(*OH)MO_{x+1} + H^+ + e^-$$
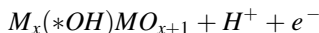
The higher oxide (MO_{x+1}) acts as a mediator in the oxidation process of organic
compounds:

$$R + MO_{x+1} \rightarrow RO + MO_x$$
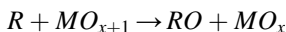
The side reaction of oxygen evolution:

$$MO_{x+1} \rightarrow MO_x + \frac{1}{2}O_2$$
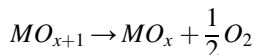
is in competition with the conversion of the organic compounds.

In the case of the "non-active" anode, oxidation of organics is mediated by
hydroxyl radicals directly, which leads to complete combustion of organic
compounds:

$$R + MO_x(*OH) \rightarrow H_2O + CO_2 + H^+ + e^- + MO_x$$
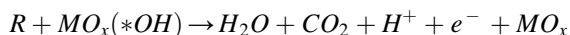
This reaction competes with the side reaction of hydroxyl radicals to oxygen
evolution without any interaction with the "non-active" anode surface:

Fig. 5 Extension of the reaction pattern proposed for the electrochemical incineration of organics, to the case of active chlorine mediated electrochemical incineration

$$MO_x(*OH) \rightarrow MO_x + \frac{1}{2}O_2 + H^+ + e^-$$
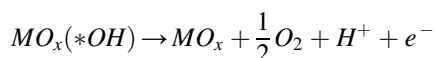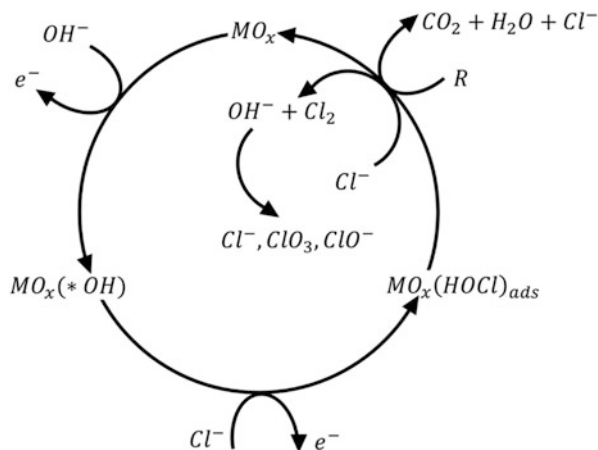
The most common reaction occurs at the cathode during the oxidation is hydrogen evolution:

$$2H^+ + 2e^- \rightarrow H_2$$
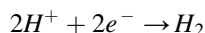
During indirect oxidation, the oxidation of wastewater of species occurs in the bulk solution via the electrochemical generation of a mediator such as peroxide, chlorine, Fenton's reagent, hypochlorite, peroxydisulfate and ozone (Fig. 5).

These oxidants can be produced either in the anodic or cathodic process, which can lead to the complete combustion to carbon dioxide, water. The most used electrochemical oxidants are chlorine and hydrogen peroxide, due to their effectiveness in dealing with the organic pollutants (Fig. 6).

To obtaining high removal efficiency of wastewater in indirect electrolytic processes are the following:

- High generation rate of intermediate
- Low overpotential
- The reaction rate of the pollutant and intermediate species must be higher than the rate of any competing reactions.
- Zero or minimum absorption of organic pollutants.

2.3 Electrochemical Wastewater Treatment

The pioneering studies on the electrochemical oxidation of wastewater have carried out by Dabrowski in the '70s, Kirk, Stucki, Kotz, Chettiar and Watkinson in the
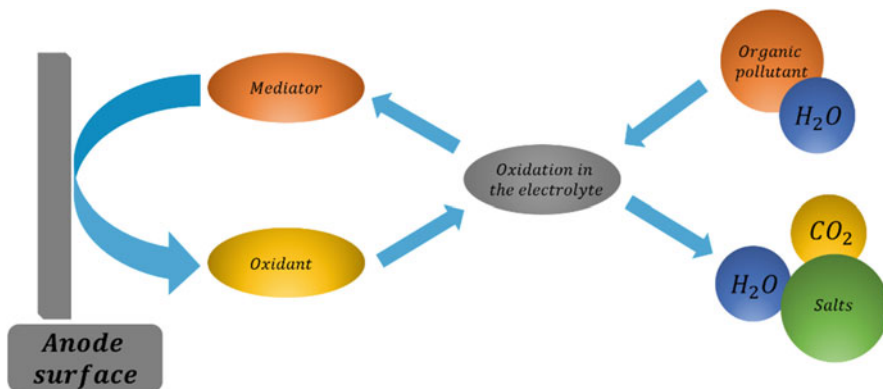
Fig. 6 Scheme for indirect oxidation of organic pollutants

Fig. 7 Example of azodic dyes, Methyl orange
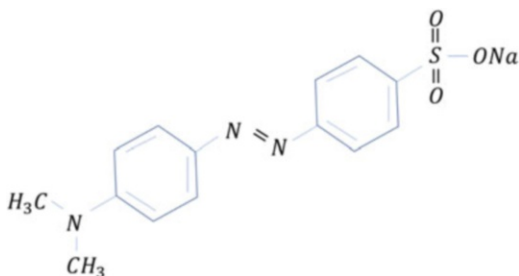
'80s, and later in the early '90s by Comninellis. In these studies, to reach the optimal condition, some suggested the oxidation of organic pollutants at two-dimensional electrodes or planar electrodes and for more complexed pollutants the use of three-dimensional multi-phase electrode or nonplanar electrodes. Also, various compounds have been investigated, including phenolic groups, herbicides and pharmaceutical drugs, Textile Dyes etc. (Chen 2004).

The discharge of the natural or synthetic dyes in the environment lead to serious health problems and endanger the aquatic species (Fig. 7). The azoic dyes are found to be carcinogenic and highly poisonous to the ecosystem.

To investigate the effect of BDD anode on the oxidation of Eriochrome Black T, Methyl orange, and Congo red experiments were conducted. The results revealed that complete chemical oxygen demand (COD) and color removal was attained for all azoic dyes.

The efficiency of the process seems to be unaffected by the dye molecule, but it depends on the dye concentration range. The energy requirement initially increases linearly up to 80% removal, followed by exponential increment, which makes this technique suitable for pre-treatment of the waste, but not for the complete removal due to the energy cost.

Fig. 8 Example of naphthalene sulfonate compounds, 2-Naphthalenesulfonic acid
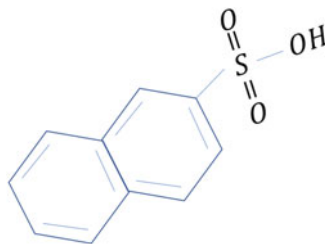
It was investigated the alizarin red S dye oxidation using an activated carbon fiber electrode. The results indicated that an activated carbon fiber anode is more able to remove color than the carbon fiber anode. Increasing the activated carbon fiber anodes specific surface area and absorption capacity a higher electrochemical degradation of dye is possible. The chemical oxygen demand (COD) shows that removal efficiency of aqueous dye solution in a neutral or alkaline medium is higher than in acidic medium by 74% after 1 h of electrolysis. Maximum color and COD removals were about 98% and 76.5%, respectively.

The petroleum effluents consist of serious environmental pollution, which contains a wide range of toxic compounds with high chemical oxygen demand (COD). The inorganic substances inside the petroleum effluents give rise to aromatic petroleum hydrocarbons, and phenolic compounds which are the main contributor to high COD (Yao et al. 2019). Some researcher studied the electro-oxidation of petroleum refinery wastewater, in particular, it was studied the removal of organic and inorganic pollutants from the petroleum refinery wastewater by using two-dimensional system, three-dimensional system (only Fe particle assisted) and three-dimensional multi-phase (both Fe particle and air assisted) system with graphite used as anode and cathode. The result showed the introduction of iron particles as a third electrode assisted with air lead to achieve highest COD removal efficiency of 92.8% and low salinity of 84 μScm^{-1}. The applied conditions of this experiment, such as pH and cell voltage were 6.5 and 12 V, respectively, while fine iron particles were in use. This electrochemical system is a promising way to treat refinery wastewater.

The naphthalene sulfonate compounds have low toxicity in the environment, but due to their high solubility in water and slow rate or non-biodegradability are considered as a potential risk for the ecosystem (Fig. 8).

The main usage of naphthalene sulfonate compounds in the industry is to produce dispersants, detergents, and azo dye. It was investigated the electrochemical oxidation feasibility of an industrial wastewater containing mixture of naphthalene sulfonates and some other refractory organic pollutants. A biofilm airlift suspension (BAS) reactor employed along with an undivided electrochemical cell equipped with a BDD anode.

The overall degradation efficiency of the biological process occurring in the BAS reactor was at 70% maximum based on the COD measurement. The biological process was less effective on the naphthalene sulfonates. However, these organics were completely mineralized by the secondary process of electrochemical oxidation. The results indicated that the energy consumption and time required could be

reduced from 80 kWhm^{-3} and 4 h to 61 kWhm^{-3} and 3 h for complete minerali-
zation of raw and biologically pre-treated, respectively.

The pulp and paper industries discharge significant effluent with high chemical
oxygen demand, toxicity and color. Electrochemical oxidation can potentially be a
solution to this problem. Others investigated the possibility of treating the pulp and
paper wastewater; in particular, the effect of the two-dimensional electrode of Ti/Co/
SnO$_2$ on paper mill wastewater and found low degradation efficiency. The usages of
active carbon particles as packed bed particle electrodes with Ti/Co/SnO$_2$ anode led
to achieving high degradation efficacy, 75% color removal and decrease in dimen-
sionless COD to 0.137 after 1 h.

2.4   Electrochemical Treatment of Persistent Wastewater

The herbicides and pharmaceutical drugs are another pollutant that can be found in
sewage effluents, surface water (Fig. 9).

Some examples of these pollutants in the environments are paracetamol, antibi-
otics ofloxacin and lincomycin and methamidophos. It was investigated the effect of
electrochemical oxidation on herbicides and pharmaceutical drugs at BDD anode
(Fig. 10).

The results showed that the electrochemical oxidation in a batch flow reactor
under the steady condition is very effective for complete mineralization of this kind
of pollutants. The efficiency of the process increased with increased drug concen-
tration, temperature, current density, and liquid flow, although it is unaffected by pH

Fig. 9 Example of herbicide, 4-Chloro-2-tolyloxyacetic acid
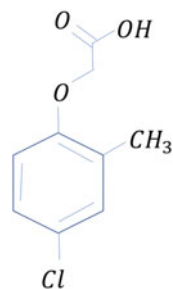
Fig. 10 Example of pharmaceutical, ofloxacin
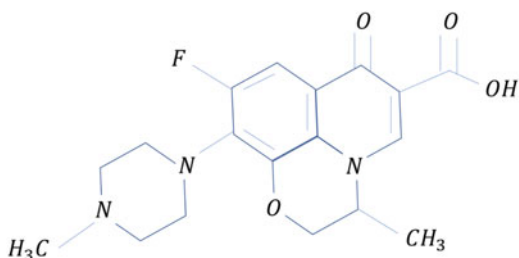
Fig. 11 Example of
pesticide, methamidophos

$$H_3CO - \overset{\overset{\displaystyle O}{\|}}{\underset{\underset{\displaystyle SCH_3}{|}}{P}} - NH_2$$
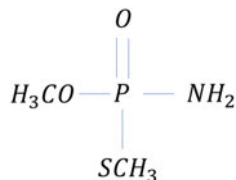
Fig. 12 Example of
surfactant,
Perfluorooctanoic acid

$$CF_3(CF_2)_5CF_2 \overset{\overset{\displaystyle O}{\|}}{\diagup} OH$$
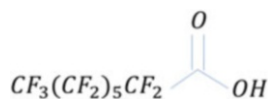
in aqueous solution. They also indicated that the degradation kinetics follow a
pseudo first order reaction.

It was investigated the mechanism and effectiveness of electro-oxidation of three
different anodes of Ti/Pt, graphite and 3D activated carbon electrode on the antibi-
otics ofloxacin and lincomycin. The result showed that ofloxacin is oxidized effi-
ciently in all anodes whereas, lincomycin was hardly oxidized mainly due to difficult
induction of the molecules deprotonation. The COD removal of 90% achieved at
Ti/Pt, graphite and 3D activated carbonin 374, 793, and 102 min respectively. The
best electrode for a continuous industrial process is 3D activated carbon electrode,
but its high corrosion rate at high applied potential makes it difficult to use in
applications.

It was investigated the oxidation of methamidophos (MMD), a highly toxic
pesticide, in a sodium sulphate aqueous solution on the three different anodes
(Pb/PbO2, Ti/SnO2, and Si/BDD) (Fig. 11).

The results showed that under the galvanostatic conditions, the performance of
the anode is influenced by pH and current density. The complete combustion of
MMD occurred only at a Si/BDD anode with the applied current density of
50 mAcm^{-2}. The current efficiency of the fabricated electrode for MMD removal
follows the order: Si/BDD > Pb/PbO$_2$ > Ti/SnO$_2$.

The wide usage of surfactant such as perfluorinated compounds (PFCs) in fire
retardants, surfactants and protective coating for the carpets and clothing is respon-
sible for widespread contamination of this pollutants in wastewater, surface water,
animal, and human body (Fig. 12).

Others investigated the possibility of treating the surfactant compounds waste-
water; in particular the electrolysis of persistent organic pollutant of perfluorooctane
sulfonate (PFOS) at Ti/PbO$_2$, Ti/TiO$_2$-NTs/PbO$_2$ and Ti/TiO$_2$-NTs/Ag$_2$O/PbO$_2$
electrode with supporting electrolyte of 1.4 gL^{-1} NaClO$_4$. The results showed the
highest removal efficiency of perfluorooctane sulfonate with the ratio of 74.87% are
obtained at the Ti/TiO$_2$-NTs/Ag$_2$O/PbO$_2$ anode after 3 h of electrolysis at a constant
current density of 30 mAcm^{-2} with a pseudo-first-order kinetic constant of
0.0165 min^{-1}. In general, the anode stability and electrocatalytic activity towards
removal of the PFOS followed the sequence: Ti/TiO$_2$-NTs/Ag$_2$O/PbO$_2$ > Ti/TiO$_2$-
NTs/PbO$_2$ > Ti/PbO$_2$.
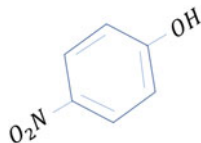
The phenolic compounds are increasingly often found in industrial effluents,
urban and agricultural wastes. The high stability, solubility and toxicity of these
compounds induce a dramatic problem for the drinking-water reservoir as well as the
environment, and it has been classified as high priority pollutants by the United
States EPA (Fig. 13).

It was studied the oxidation of 2-nitrophenol, 3-nitrophenol, and 4-nitrophenol on
four different SnO_2-based electrodes in 0.5 M Na_2SO_4 supported electrolyte adjusted
to pH. The degradation of the nitrophenols revealed that the rate constant for the
electrochemical oxidation of the nitrophenols decreases in the order: 2-NP > 4-
NP > 3-NP. The lifetime tests exhibited that doping different metal oxide into SnO_2-
based electrode, increase the service life significantly. In particular, the lifetime of
Ti/SnO_2-Sb_2O_5 electrode under 160 mAcm^{-2} current density was 12 h while
Ti/SnO_2-Sb_2O_5-IrO_2 electrode with the same condition had a very long lifetime of
155 days. The results indicated that the degradation of 4-NP at the four SnO_2-base
electrodes explained by pseudo-first-order kinetics and follows in the order:
Ti/SnO_2-Sb_2O_5 > Ti/SnO_2-Sb_2O_5-PtOx > Ti/SnO_2-Sb_2O_5-IrO_2 > Ti/SnO_2-
Sb_2O_5-RuO_2. Even though the first two electrodes showed higher activity towards
4-NP elimination, but due to their short service lifetimes, it is not a good option for
the oxidation process. However, Ti/SnO_2-Sb_2O_5-IrO_2 anode has best performance
with long lifetime service and high activity towards oxidation.

It was studied the oxidation of phenolic compounds, triazine, diuron and
3,4-dichloroaniline at BDD anodes. The result identified that the critical factor in
obtaining high current efficiency during wastewater oxidation is the rate of mass
transfer between an electrode surface and wastewater species. To achieve high mass
transfer coefficient ($\sim$10–4 ms^{-1}), an impinging cell was used. The results showed
that if the applied current density is low enough, the process can be carried out at the
current efficiency close to 100%, resulting in the nearly complete oxidation of the
organic pollutant.

In other work, it was examined phenol oxidation on Ti/PbO_2 and Pt electrodes
and compared the results with DSA RuO_2-based anodes. The performance of phenol
oxidation on the three electrodes containing RuO_2 follows the sequence: Ti/Sb-Sn-
RuO_2-Gd > Ti/Sb-Sn-RuO_2 > Ti/RuO_2. Comparing this result with Ti/PbO_2 and Pt
electrodes showed that Ti/PbO_2 and Pt electrodes they are still more efficient. In case
of RuO_2 anodes, phenol partially oxidized and aromatic intermediates formed, such
as benzoquinone, hydroquinone, maleic acid, succinic acid, and oxalic acid, and thus
wastewater still contained considerable total organic carbon (TOC). The complete
removal of TOC occurred only at the Ti/PbO_2 anode after 400 °C of charge
consumed.

Fig. 14 Example of
phenolic compounds with
chlorine atoms, 2,6-
dichlorophenol
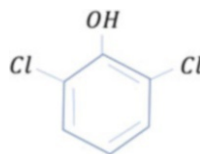
It was investigated reticulated glassy carbon anodes for oxidation of phenol in a
flow-by electrochemical cell. They showed that the electrode surface could be
blocked with mostly insoluble polymeric products at low anodic potentials and
high phenol concentration (over the range of 5–20 mmolL^{-1}), led to a rapid decrease
in the reaction rate. On the other hand, complete organic oxidation is possible at
higher temperatures of 50 °C and applied potentials (1.9 V vs SCE). These condi-
tions led to faster electrode corrosion and reduced current efficiency because of the
electrode resistance increasing.

It was discussed phenol oxidation at Pt anodes in a two-compartment cell,
supported by 150 gL^{-1} Na$_2$SO$_4$ adjusted to pH 12.3 or 3. The oxidation process
occurs in two parallel steps: in the first step, aromatic intermediates such as hydro-
quinone, catechol and benzoquinone are formed, followed by aromatic ring opening,
with the formation of aliphatic acids that are stable to further oxidation. Due to the
formation of these intermediates, only partial TOC removal can be attained, and
current efficiency decreased during electrolysis. The electrochemical oxidation
index (EOI) was uninfluenced by current density and temperature, while it depended
on the pH and phenol concentration.

It was studied the electrolysis of 2-chlorophenol and 2,6- dichlorophenol using a
porous carbon felt anode, a fixed bed of carbon pellets and a dimensionally stable
anode Ti/RuO$_2$ in a flow cell (Fig. 14).

The result showed the efficient removal of chlorophenol and their oxidation
intermediate at both carbon-based anodes. The flow rate through the cell did not
affect the reaction kinetics but decreasing the initial concentration of chlorophenols
led to a decrease in the reaction rate. Increasing the current densities led to lower
current efficiency. In case of DSA electrode, if a divided electrochemical cell was
used, the chlorophenols can be rapidly removed, but the need of a membrane in this
cell design results in a more complex and expensive setup.

2.5   *Efficiency and Energy Parameters in Electrochemical*
Oxidation

Instantaneous current efficiency is defined as the ratio of the electrochemical equiv-
alent current density for the oxidation of specific compound to the total applied
current density during electrolysis:

$$ICE = \frac{current\ density\ consumed\ by\ specific\ compound}{total\ applied\ current\ density}$$

Instantaneous current efficiency also can be determined based on the oxygen flow rate (OFR) method and the chemical oxygen demand (COD) method. Chemical oxygen demand is a standard parameter in wastewater treatment terminology, which measures the amount of oxygen required to oxidize organic pollutants in aqueous solution. This parameter then provides the number of electrons needed to be removed from the solution to obtain full mineralization. The oxygen flow method uses:

$$ICE = \frac{\dot{V}_0 - (\dot{V}_t)_{org}}{\dot{V}_0}$$

where V_0 is the oxygen flow rate determined in the anodic compartment at t $=$ 0 when there are no organic pollutants present in the reaction (cm^3min^{-1}) and V_t is the oxygen flow rate at desire time of t in the presence of organic pollutants (cm^3min^{-1}); or with the COD method:

$$ICE = \frac{(COD_t - COD_{t+\Delta t})}{8I\Delta t} FV$$

Where $(COD)_t$ and $(COD)_{t+\Delta t}$ are the chemical oxygen demands at time t and $t + \Delta t$ (gL^{-1}), I is the current (A), F is Faraday's constant (96,485 $Cmol^{-1}$), V is the electrolyte volume (L), and 8 is the oxygen equivalent mass (geq^{-1}).

The general current efficiency (GCE) is the average value of the instantaneous current efficiency during overall oxidation and is determined based on ICE:

$$GCE = \int_0^t ICE\ dt$$

The specific energy consumption (*Es*p), is typically expressed as the energy consumed in Whg^{-1} for removal of a unit mass of COD from wastewater:

$$E_{sp} = \frac{tUI}{COD_t - COD_{(t+\Delta t)}} \frac{1}{V}$$

Where U is the average cell potential (V), I is current density (A), V is the volume of the electrolyte (L), $(COD)_t$ and $(COD)_{t+\Delta t}$ are the chemical oxygen demands at time t and $t + \Delta t$ (gL^{-1}).

The simple electrode reaction of:
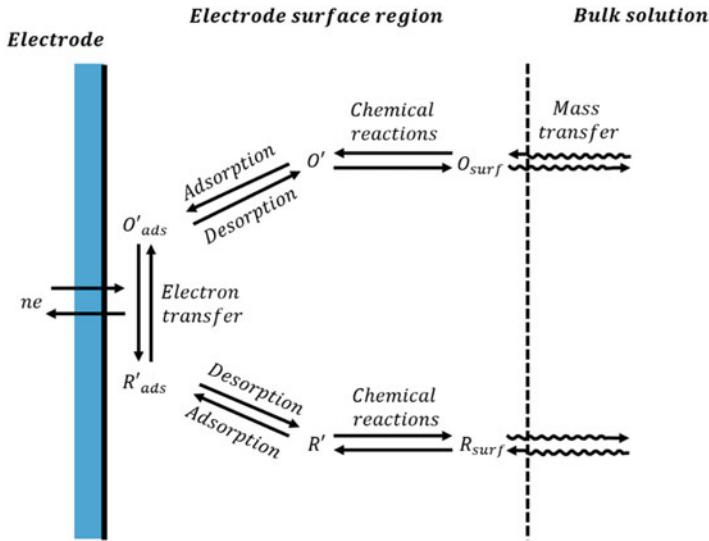
Fig. 15 Pathway of a general electrode reaction

$$O + ne^- \leftrightarrow R$$
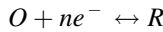
consists of two stable and soluble species of O and R in the electrolysis medium that interconvert at the surface of electrode. In general, the limiting mechanisms are as follow:

1. Electron transfer
2. Mass transfer
3. Coupled chemical reactions
4. Other surface reaction such as adsorption and phase formation

When the mass transfer of species from the bulk to the surface of electrode is very fast which means efficient stirring and low current applied, the oxidation reaction is controlled by kinetics of reaction and the concentration of species at the surface of electrode is equal to the concentration of species in the bulk solution (Fig. 15).

In this case, the rates constant of reaction is potential dependent and can be expressed through Butler-Volmer equation e.g.:

$$k_f = k_f^0 \exp^{\frac{\beta F}{RT}(E - E_{rev})}$$

$$k_b = k_b^0 \exp^{\left(-\frac{(1-\beta)F}{RT}\right)(E - E_{rev})}$$

where R, T, β, F, kf and kb are the gas constant, temperature, symmetry factor, faraday constant, forward and backward rate constants respectively and E and E_{rev} are the anode and reversible potential. The parameter β –symmetry factor- usually

has a value of approximately 0.5 for metal. The difference between the rate of the forward and backward reactions at the electrode surface is proportional to the current of the kinetic control and defined as:

$$i = nFA\left[k_f C_0 - k_b C_R\right]$$

Where, A, C_O and C_R are the electrode area, surface concertation of O and R respectively.

When kinetics of the electrode reaction is sufficiently fast or sufficiently high current is applied, the concentration of reactant on the surface of electrode become equal to zero because of the mass transfer of the reactant from the bulk solution to the surface of electrode become insufficient.

Mass transfer can occur by:

1. Migration. Movement of charge species due to the gradient of electrical potential.
2. Convection. Movement of species due to the density gradient and forced convection with bulk movement.
3. Diffusion. Movement of the species due to the concentration gradient.

The migration effects can be neglected by choosing the condition such as presence of high concentration (>0.1 M) of inert or supporting electrolyte and concertation of 10^{-3} M of electroactive species. In this condition charge can easily transfer across the electrolyte without any solution resistance. The convection effects also can be eliminated by using forced convection such as stirrer or agitator or using the continuous flow cell. Considering above condition, through this work we consider the case of only diffusion control governing the oxidation process when it is under the mass transport condition.

The maximum production rate of the electrochemical cell under mass transfer control can be estimated via limiting current density i_{lim}:

$$i_{lim} = nFk_m C_{org}$$

Where i_{lim} is the limiting current density for the electrochemical oxidation of an organic compound under specific hydrodynamic conditions (Am^{-2}), n is the number of electrons involved in the reaction, F is the Faraday constant (96,485 $Cmol^{-1}$), k_m is the mass transport coefficient (ms^{-1}) and C_{org} is the concentration of organic pollutants in the electrolyte ($molm^{-3}$). To limit the current density equation are necessary specific hydrodynamic condition such as: the adsorption of the organic compounds at the electrode surface is negligible, the global rate of electrochemical oxidation of organic compounds is a fast reaction, and it is controlled by mass transport of organic to the diffusion layer of the anode surface, which indicates that hydrodynamic parameters of the electrochemical cell are independent of the chemical nature of the organic compound present in the electrolyte.

The limiting current density can be defined based on the chemical oxygen demand (COD), which can be used when a mixture of organic compounds or the actual wastewater is treated):

$$i_{lim} = 4Fk_mCOD$$

Where 4 is the number of exchanged electrons per mole of oxygen, F is the Faraday constant (96,485 $Cmol^{-1}$), (COD) is the chemical oxygen demands (mol m^{-3}), km is the mass transport coefficient (ms^{-1}).

2.6 Kinetics and Mechanism of Organic Oxidation

In recent years there has been expanding attention for ecological damage by industrial contamination, and as a result much research and development into new technologies for wastewater treatment is underway. Because of the variability of wastewater, which is discharged by industrial activities, new advanced oxidation processes should be capable of treating toxic and non-biodegradable compounds.

Electrochemical wastewater treatment, where organic species are oxidized at anodes is a promising alternative to traditional processes. However, electrochemical oxidation has had limited penetration into industrial processes due to the high energy requirements for this process. The presence of the oxygen evolution reaction (OER) which occurs in parallel to the oxidation of organic compounds is the main cause for high energy consumption during electrochemical wastewater treatment as this lowers the current efficiency of the process (Kapałka et al. 2008). Thus, anodes with high overpotentials for the OER (known as non-active anodes) are commonly used to increase current efficiency of organic reaction, but this in turn increases the cell potential which again leads to high energy consumption. To improve the current efficiency of the organic oxidation reaction, various metal oxides have been examined. For example, SnO_2 and Sb-doped SnO_2 have been shown to be a good anode for electrochemical wastewater treatment due to its high overpotential for the oxygen evolution reaction and are inexpensive relative to anodes which incorporate noble metal oxide coatings. SnO_2-based anodes are normally considered to be non-active anodes, where the organic oxidation mechanism involves the generation of hydroxyl radicals which subsequently oxidize the organics at electrode interface and within the bulk of the electrolyte. This usually leads to the complete oxidation of organic compounds due to the high activity and low selectivity of the hydroxyl radical for organic oxidation. While SnO_2 or Sb-doped SnO_2 anodes exhibit good electrochemical wastewater treatment performance, by adding a small amount of IrO_2 or RuO_2 to Sb_2O_5-SnO_2 anodes, the service life and catalytic activity of the anodes can be increased dramatically. However, given that both IrO_2 and RuO_2 are excellent electrocatalysts for the OER, it is unclear if these additions to SnO_2-based anodes will suppress the formation of the hydroxyl radicals in favor of oxygen gas.

As the mechanism for organic oxidation is normally suggested to involve intermediates of oxygen evolution, it seems inevitable that oxygen evolution will occur in parallel with organic oxidation. The relative magnitude of these reactions will depend on both the inherent kinetics of the two reactions and the rate of mass transfer of the organic species into the reaction zone. The latter case means even anodes with extremely poor OER kinetics, will evolve oxygen under conditions where the applied current is larger than the rate at which organics can be transported from the bulk electrolyte into the reaction zone. For boron-doped diamond (non-active) anodes it is possible to balance the organic mass transfer rate with rate of the organic oxidation reaction to achieve an efficiency of 100% with almost complete oxidation of the organic species. For non-active electrodes, this balance can be achieved as the inherent reaction rate between the generated hydroxyl radicals is both fast and independent of electrode potential. This balance however is much more difficult for active anodes. Even at applied currents above the theoretical mass transfer limited organic oxidation rate, the fraction of current which goes to the OER will be dependent of the relative kinetics of the OER and the organic oxidation reactions.

Clearly as the organic oxidation is mediated via the higher-oxide surface species (e.g. IrO_3) for active anodes, and as the surface coverage of these species is potential dependent, balancing reaction rate and mass transfer to achieve high current efficiencies is much more challenging.

Certainly, it possible that the current efficiency can be close to zero if the rate constant of organic oxidation is much smaller than that for the OER. Even though an assumption that organic oxidation reaction is much faster than the oxygen evolution reaction has been successfully applied in models and validated by experiment even at electrodes which are known to be very active for oxygen evolution.

As the mass transport behavior within the electrochemical flow cell has a strong influence on the current efficiency of oxidation, the diffusion layer thickness (δ) at the anode can be calculated from:

$$\delta = \frac{nFDC_{bulk}}{i_{lim}}$$

Where i_{lim} is the limiting current density (Acm^{-2}), n is the number of electrons transferred, F the Faraday constant ($96,485\ Cmol^{-1}$), D is the diffusion coefficient (cm^2s^{-1}), C_{bulk} is the concentration of the diffusing specie in the bulk of the electrolyte ($molcm^{-3}$).

While the anodic oxidation of organic molecules at electrodes has complex reaction mechanisms, some useful insights can be gained by considering simple cases. The two most important general mechanisms for the oxidation of organics at anodes are based on both "active" or "non-active" anodes. For active anodes, the oxidation of the organic is mediated by the higher-oxide (S-O, e.g. IrO_3) formed on the anode surface at potentials above the thermodynamic OER potential, whereas on non-active anodes the organic is oxidized by hydroxyl radicals generated by anode. Given that the potential for hydroxyl radical generation is 2.74 V vs NHE, if the

anode operates at potentials much lower than this, it seems reasonable to assume that hydroxyl generation will be negligible. This is certainly consistent with IrO_2 anodes which are known to operate at low anodic potentials (IrO_2 is an excellent electrocatalyst for the OER) and have been shown not to generate significant quantities of hydroxyl radicals. In addition, either boron-doped diamond and SnO_2 anodes are known to generate hydroxyl radicals and are typically found to have very high overpotentials for the OER.

To ensure that the mechanism is consistent with proposed mechanisms for the OER, the higher oxide is formed via the electrochemical oxide path:

$$S + H_2O \leftrightarrow S - OH + H^+ + e^-$$

$$S - OH \leftrightarrow S - O + H^+ + e^-$$

$$S - O \leftrightarrow S + \frac{1}{2}O_2$$
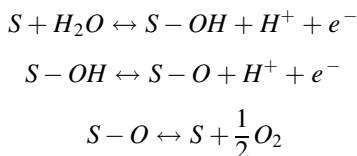
Where S is a free-surface site. The higher oxide formed in step two of the OER mechanism can form oxygen gas via reaction the last reaction or oxidize an organic molecule (R) via reaction:

$$S - O + R \leftrightarrow S + RO$$
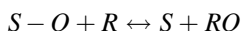
Thus, it should be expected that oxygen gas evolution will compete with the oxidation of organics within an electrochemical wastewater treatment process when the anode potential is above 1.23 V vs RHE. But, as the thermodynamic requirements for organic oxidation are often lower than that for oxygen evolution, it is possible that oxidation of organic compounds can occur below 1.23 V vs RHE.

2.7 Pulsed Electrochemical Wastewater Oxidation

To facilitate the mass transportation and to improve the energy consumption non-steady-state techniques are studied, as pulsed voltage, pulsed current, or reverse polarity (Wang et al. 2020).

The pulsed electrolysis technique are used in various industries such as metal deposition, electro dissolution, electrochemical machining, battery and hydrogen production etc. Some of this research was conducted specifically to find out the effect of pulse on the mass transfer and current efficiency of the system. As an example, hydrogen production is one of the industries that uses pulse power to improve production efficiency. In similar study on effect of pulsed electrolysis on hydrogen production, the result show that using this method enhances the mass transport of oxygen and hydrogen bubbles due to the pumping effect. This provides less contact with oxygen bubbles to improve corrosion resistance of anode

electrodes. Moreover, decreasing mass transfer losses on the electrode surface resulted in a 20–25% lower energy consumption to produce 1 mol of hydrogen in the cell.

During pulsed electrolysis, a short period of high overpotential is applied, leading to a very steep concentration gradient of the reactant at the electrode surface. This steep concentration gradient results in a very high current for a short period at rates which are much higher than the equivalent mass transport limited current under normal potentiostatic conditions. Before the concentration gradient grows further into the electrolyte (leading to the mass transfer limiting current), the overpotential is stepped to a low value where the electron transfer rate is very low. In this low overpotential pulse period, the concentration gradient reverts to a flat gradient at the bulk electrolyte concentrations due to diffusion (Fig. 16).

The electrochemical oxidation of organics at the anode follows a complex reaction process. To study this mechanism is better to consider a simple model. Considering the "non-active" electrode mechanism used for oxidation of organic compounds, in which the oxidation of organics species is mediated by hydroxide radicals physiosorbed on the anode surface during the water discharge step (step 1).

$$S + H_2O \leftrightarrow S(OH) + H^+ + e^- \quad Step\ 1$$

$$S(OH) \leftrightarrow S + \frac{1}{2}O_2 + H^+ + e^- \quad Step\ 2$$

$$S(OH) + R \leftrightarrow S + RO + H^+ + e^- \quad Step\ 3$$
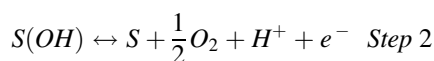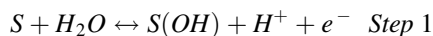
Where S here represents a free surface site. In this mechanism, the oxidation of organic species (step 3) competes with the generation of oxygen gas (step 2). There are more complex reaction mechanisms for 'non-active' electrodes by others.

The critical factor for this study which controls the current efficiency of the overall process is the relative rate of steps 2 and 3 while competing for the same intermediate, $S(OH)$. This mechanism differs from the mechanism proposed for 'active' anodes such as Iridium oxide and platinum, where the oxidation of organic spices is mediated by the higher oxide (S-O) which chemisorbed on the anode surface at high potentials. For this simplifier model, the adsorption process of the organic molecule has been ignored. Another assumption is that all steps leading the OER are considered chemically reversible, while organic oxidation process is chemically irreversible. The reaction rate for each step is given by:

$$r_1 = k_1 c_{H_2O}(1 - \theta) - k_{-1} c_H + \theta$$
$$r_2 = k_2 \theta - k_{-2} c_{O_2}^{\frac{1}{2}} c_H + (1 - \theta)$$
$$r_3 = k_3 \theta c_{R,surf}$$

Where k_1 and k_{-1} are forward and backward rate constants, c are concentrations, θ is the surface coverage of $OH.$ with the fraction of free sites given by $(1 - \theta)$. The units of all rate equations are $\text{mols}^{-1}\ \text{cm}^{-2}$. Note that in this model, the surface
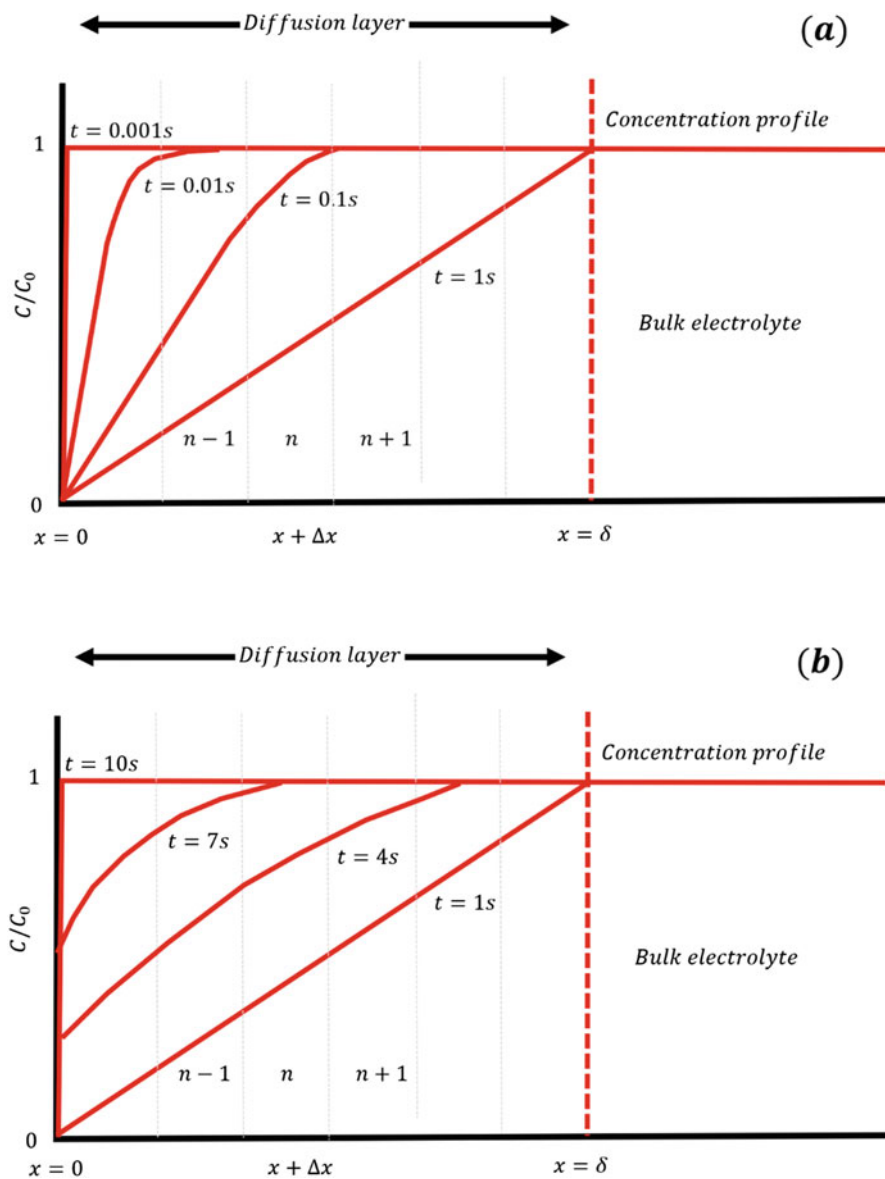
Fig. 16 Concentration gradient in diffusion layer (**a**) high overpotential pulse (mass transport region) (**b**) low overpotential pulse (electron transfer limited region)

concentration of organic species used to implement the mass transport consideration into the rate equation for the organic oxidation.

The assumption for these reactions is that their rate constant is potential dependent so that Butler-Volmer kinetics can be used. For example:

$$k_i = k_i^0 \exp^{\frac{\beta F}{RT(E - E_{rev})}}$$

$$k_{-i} = k_{-i}^0 \exp^{-\frac{(1-\beta)F}{RT}(E - E_{rev})}$$

where R, T, β and F are the gas constant, temperature, symmetry factor and Faraday constant respectively and E and E_{rev} are the anode and reversible potential for the OER respectively. The parameter symmetry factor (β) usually has a value of approximately 0.5, although this value can differ, especially for reactions involving adsorbed species such as OER.

The current density (i) is calculated by summing the rates of all involved reactions in organic oxidation:

$$i = F(r_1 + r_2 + r_3)$$

Instantaneous current efficiency is another important parameter that reflects the fraction of the current that goes towards organic oxidation and can be calculated from the reaction rates:

$$ICE = \frac{r_1}{r_1 + r_2 + r_3}$$

In the above model, multiple parameters must be known or estimated before simulating the reaction. The overall OER (sum of step 1 and 2) is:

$$H_2O \leftrightarrow \frac{1}{2}O_2 + 2H^+ + 2e^-$$
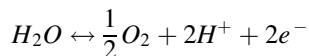
The reaction has the reversible thermodynamic potential of $E_{rev} = 1.23\ V$ vs RHE. At this potential ($\eta = E - E_{rev} = 0$) the system must be an equilibrium and thus the overall equilibrium constant is defined as:

$$K = \frac{(c_{O_2})^{\frac{1}{2}}(c_{H^+})^2}{c_{H_2O}}$$

As thermodynamics must be satisfied at $\eta = E - E_{rev} = 0$, this reduces the number of freely definable rate constants through:

$$K = K_1 K_2 = \left(\frac{k_1}{k_{-1}}\right)\left(\frac{k_2}{k_{-2}}\right)$$

where K is the overall equilibrium constant, and K_1 and K_2 are the equilibrium constants for step 1 and 2 in the reaction. In this case, only 3 of the 4 kinetics parameters for steps 1 and 2 are independent and freely definable.

The dynamic potential model contains loops of two steps; a short period at high overpotential and a short period at low overpotential, which each step individually

acts as a constant potential. The initial conditions for the first step are the same as the constant potential model and the initial conditions for the second step is the last value of concentration, surface coverage and time obtained from ODE solver of the same step. Similarly, for the following loops, the last value obtained from the ODE solver of each step is used for the initial condition of the next pulse step.

The surface coverage must be known to determine the current density passing through the anodes. This is described by ODE built from reaction steps 1–3:

$$\frac{d\theta}{dt} = \frac{\left[k_1 c_{H_2O}(1-\theta) - k_{-1} c_{H^+}\theta - k_2\theta + k_{-2} c_{O_2}^{\frac{1}{2}} c_{H^+}(1-\theta) - k_3\theta c_{R,surf}\right]}{N_{tot}}$$

Where N_{tot} is the number of surface sites per unit electrode area ($mol\,cm^{-2}$). Finally, the concentration of organic species across the system must be determined. Here, the assumption of a planar diffusion across the boundary layer of the electrode is made to account for the mass transport of organic species to the electrode surface. Then according to the Fick's second law, the concentration of organic species as a function of time can be determined at any given nod, n, across the boundary layer by using the method of lines:

$$\frac{dc_{R,n}}{dt} = D_R \frac{(c_{R,n+1} + c_{R,n-1} - c_{R,n})}{\Delta x^2}$$

where D_R is the diffusion coefficient of the organic species and Δx is the width of the segment the distance between two nodes within the boundary layer. The boundary conditions with the concentration within the bulk electrolyte found by:

$$\frac{dc_{R,bulk}}{dt} = D_R \left(\frac{A}{V_{bulk}}\right) \frac{c_{R,n=\left(\frac{\delta}{\Delta x}\right)} - c_{R,bulk}}{\Delta x}$$

With the concentration in the segment immediately adjacent to the electrode surface $c_{R,surf}$ found by:

$$\frac{dc_{R,surf}}{dt} = D_R \frac{c_{R,n=2} - c_{R,surf}}{\Delta x} - \frac{k_3\theta c_{R,surf}}{\Delta x}$$

The simulated kinetic parameters of the steady-state polarization curve for "non-active" anode were assigned to be applied in the constant and dynamic potential organic oxidation (Fig. 17).

Based on the OER mechanism, the surface coverage of S-OH approaches 1 at high overpotentials. This simulation model 0.1 can describe the OER of any "non-active" anode that follows similar behavior. The kinetics of the organic oxidation at surface coverage equal to 1, is independent of overpotential but dependent on surface concentration ($c_{R,surf}$) and organic rate constant (k_3). Normally when the

Fig. 17 The simulated
surface coverage of
S-OH vs. overpotential
during the oxygen evolution
reaction at pH = 2
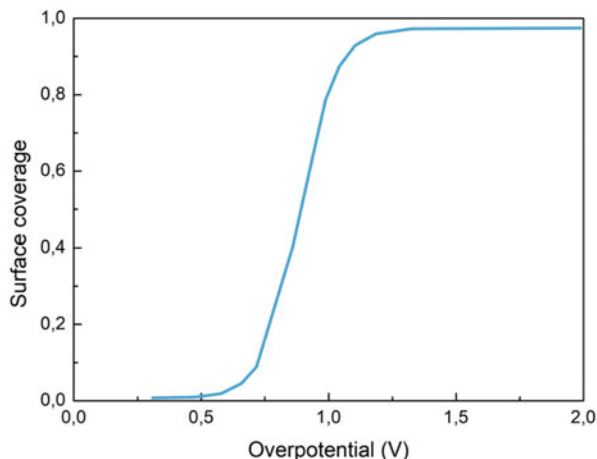
Fig. 18 The surface
concentration behavior vs
time over various constant
potential
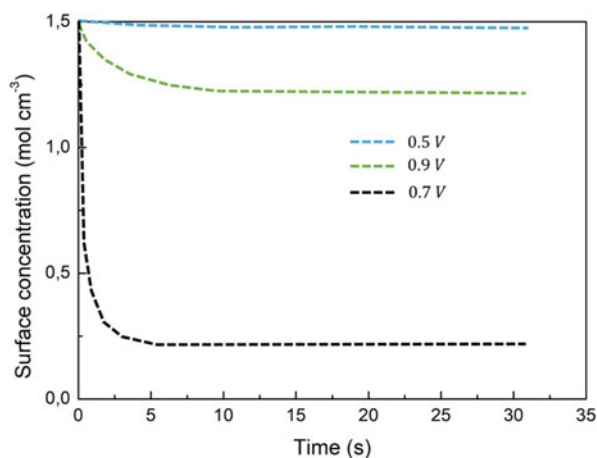
organic oxidation rate is independent with overpotential, mass transport is considered to limit the overall oxidation rate.

The model was used to simulate and study the kinetics of the electro-oxidation of an organic compound at "non active" anode. The constant potential electrolysis was simulated at various potential, and the effect of potentials at surface concentration is investigated. The potential range was chosen to cover kinetic and mass transport limitation. The model shows that an increase in the applied anode potential leads to decrease in organic concentration at the anode surface and reaches zero at overpotentials where surface coverage of S-OH is equal to 1 (Fig. 18).

The investigation of electrochemical wastewater oxidation involves measuring the change in organic concentration throughout electrolysis and can be simulated using the model described. The simulation of the bulk concentration of organic species revealed that the organic oxidation follows first-order kinetics (Fig. 19),

Fig. 19 Plot of $ln(c_{R,bulk}/c_{(R,bulk,0)})$ as a function of time, $c_{R,bulk} = 1.5 \times 10^{-7}$ $mol\ cm^{-3}$
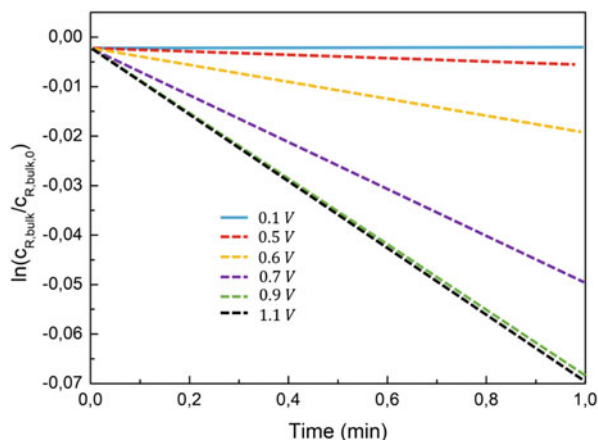
which agrees with experimental reports by others. While increasing the overpotential, initially oxidation process is limited by kinetics of organic species and low coverage of hydroxyl radicals on the anode surface, but most of the current is consumed by organic oxidation reaction. So, high current efficiency is expected. When operating potential exceeds the equivalent limiting current density, the rate of organic oxidation becomes independent of overpotential. At this condition, electrolysis is fast, but current efficiency decreases because the excess current is wasted to the parallel reaction of oxygen evolution.

The determination of apparent first-order rate constant over the overpotential range also helps us to identify the kinetic and mass transport region, in which potential higher than equivalent limiting current density can be avoided to achieve higher current efficiency. Others discussed that to avoid fouling electrodes with polymeric adhesive products during the aromatic compound electrolysis, the high applied potential of $E > 2.0$ V vs. SHE (overpotential >0.77 V) should be applied (Fig. 20).

The simulated apparent first-order reaction can satisfy this criterion, in which the rate of oxidation of organic compounds at around 0.8 V overpotential is fast enough (mass transport limited) that electrode fouling can be avoided.

The primary purpose of using pulsed potential is to optimize the electrolysis condition where mass transfer rate of organic compounds from the bulk solution to the surface of electrode improved by imposing a short period of high overpotential. This high overpotential oxidizes the organics species immediately next to the electrode surface rapidly, leading to a very steep concentration gradient (essentially instantly after the high overpotential is applied). This sharp concentration gradient means that the diffusional flux of the organic species is also very high, allowing the oxidation rate of the organic species to be much higher than what would be possible under potentiostatic conditions. This high oxidation rate will only last for a short period as the concentration profile will extend further into the electrolyte causing the diffusion rate to decrease towards the expected "steady-state" mass transfer limiting

Fig. 20 The simulated
overpotential dependence of
the apparent first-order rate
constant (k_{app})
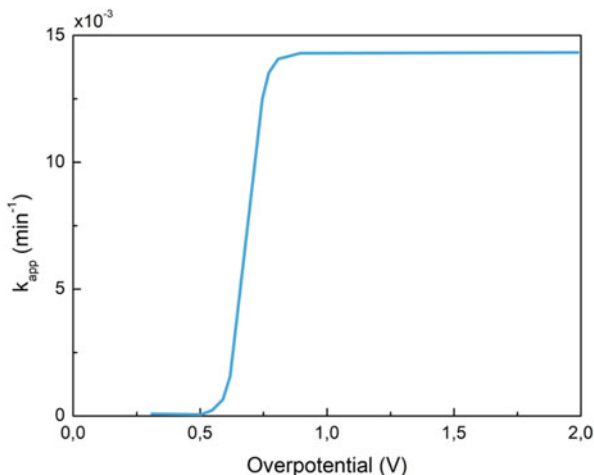
rate. Before this happens the high overpotential is switched to a low overpotential
(one where the reaction rate is very low) which allows the concentration gradient of
reactant species to replenish near the electrode surface (Fig. 21).

Operating under pulsed potential conditions results in a higher instantaneous
current density, in which the possible influences on the kinetics of different reaction
can lead to change in their relative proportion of current and possibly achieving
higher current efficiency. In other industry such as electroplating industry employ
the pulsed electrolysis to achieve higher current efficiency.

The electric double layer at the electrode-solution interface can have high capac-
itance, and some charge requires to raise its potential to the value needed for the
water discharge step at the rate corresponding to the applied pulsed potential. In
published literature for steady-state conditions (constant potential condition), usually
the effect of an electric double layer (EDL) or capacitance is neglected primarily due
to activation period before running the electrolysis. In this model, the effect of
electric double layer is not included (Fig. 22).

The performance of pulsed electrolysis against the constant potential electrolysis
can be investigated by plotting the degradation of organic concentration vs charge
consumed during the electrolysis. The result revealed that during the electrolysis the
lowest charge consumed to achieve same level of organic concentration is when
either electrolysis, under constant potential of 0.4 V or when pulsed potential
condition at high step of 1.6 V at 8 ms and low step of 0.4 V at 1 s are applied.
Further analysis on charge consumed during electrolysis for organic oxidation step
(step 3) and OER step (step 2) showed that at constant potential of 0.4 V, majority of
charge consumed during the electrolysis process goes towards organic oxidation.
This agrees with previous report in literature stated that higher current efficiency is
achievable when electrolysis operated under kinetics limitation. Although under this
condition higher current efficiency is achievable but general oxidation rate is very
slow due to generation of tiny current at this low potential (Fig. 23).

Fig. 21 Pulsed potential electrolysis (a) surface coverage (b) current density over electrolysis time
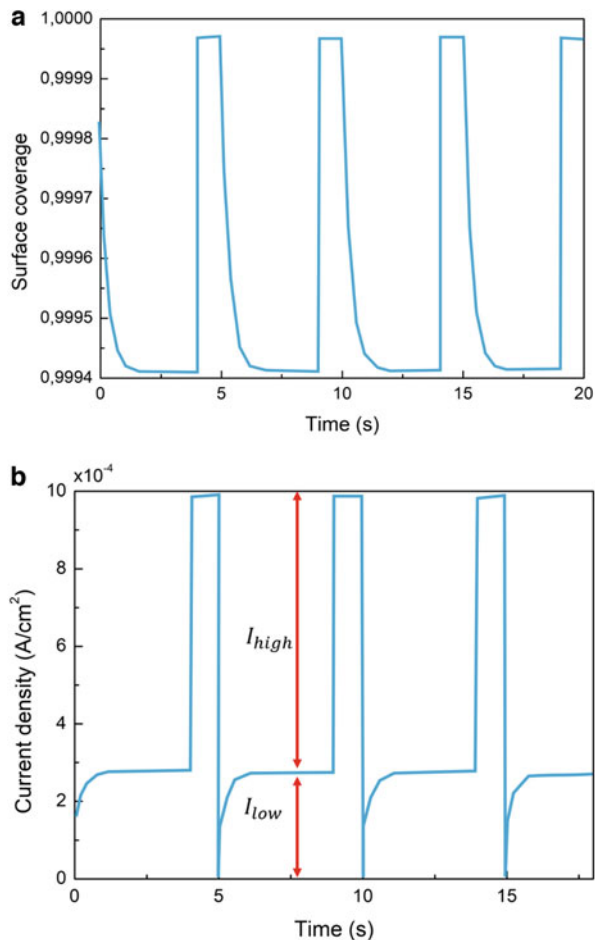
The Fig. 24 shows that an applied high potential at very short time of 8 ms, leads to majority of charge goes towards organic oxidation step leading to achieve higher current efficiency and just before the concentration gradient grows further into electrolyte, leading to the mass transfer limiting current, the overpotential is stepped to a low value where the electron transfer rate is very low.

Further investigation on change in concentration gradient of organic model over the electrolysis time for constant potential at 0.4 V and the pulsed electrolysis at high step of 1.6 V for 8 ms and low step of 0.4 V for 1 s revealed that although for both of these processes same amount of charge consumed but the electrolysis time is much faster, about 8 min, when pulsed potential electrolysis is used (Fig. 25).

Finally, pulsed electrolysis facilitates a higher flux of organic species during the short periods. The anode after this period is high enough to drive the desired oxidation reaction, so achieving higher current efficiency. The best performance, which means lowest charge consumed for same level of organic degradation is when
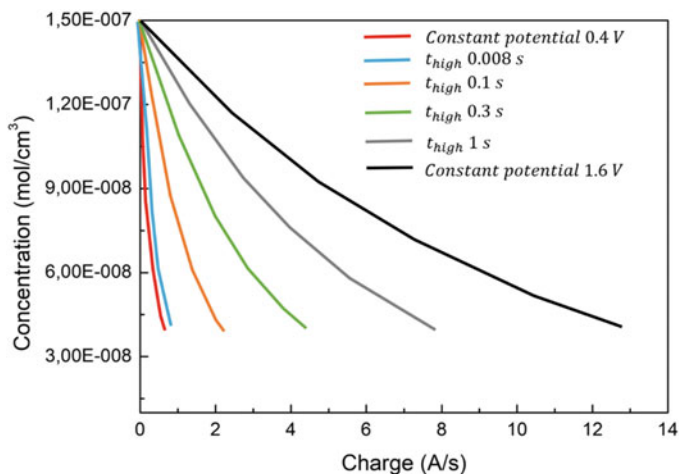
Fig. 22 The bulk concentration as a function of charge at high pulsed overpotential of 1.6 V and low pulsed overpotential of 0.7 V for 30 min electrolysis

Fig. 23 Charge consumed during the constant electrolysis at 0.4 V for OER step (black line) and Organic oxidation step (red line)
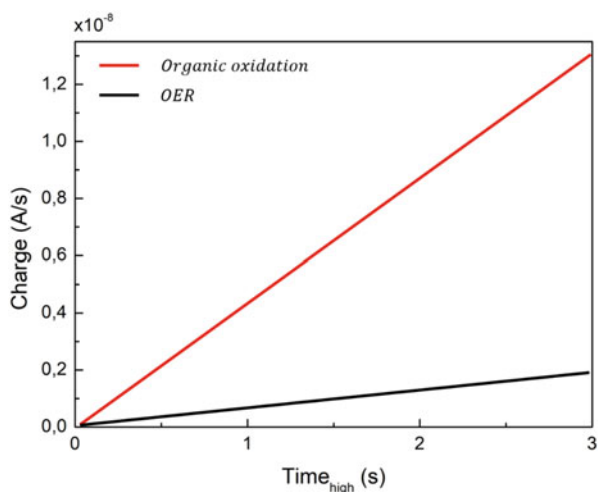
pulsed potential condition at high step of 1.6 V at 8 ms and low step of 0.4 V at 1 s are applied. Further analysis on charge consumed during electrolysis for organic oxidation step (step 3) and OER step (step 2) showed that at both cases, majority of charge consumed during the electrolysis process goes towards organic oxidation but in case of constant potential of 0.4 V due to generation of tiny current at this low potential, general oxidation rate is very slow and for the same amount of charge electrolysis time of 25 days is required, whereas in case of an applied high potential step electrolysis time of 8 min is sufficient. It was also found that the potential dependence of the apparent first-order oxidation rate constant is explained by this model.

Fig. 24 Charge consumed during the pulsed electrolysis at high step at 1.6 V for 8 ms and low step of 0.4 V for 1 s, for OER step (black line) and Organic oxidation step

Fig. 25 Change in concentration over the electrolysis time for constant potential of 0.4 V (black line) and pulsed electrolysis at high step of 1.6 V for 8 ms and low step of 0.4 V for 1 s (red line)

The current efficiency of pulse potential organic oxidation is improved considerably over a range of potentials compare to constant potential electrolysis. Taking into consideration of the best step combination, the proposed pulsed electrolysis can be a breakthrough in the electrochemical wastewater treatment and in general can be implied in any other electrochemical process which follows a similar process.

3   Direct Sea Water Electrolysis

Due to its content in anions that would interfere and compete with the water-splitting electrocatalysis seawater is not suitable feed for electrolyzer technologies, even if is widely available (Farras et al. 2021).

Although the composition of seawater varies from region to region, the average overall salt concentration of all ions ranges at about 3.5 wt % with pH $\sim$ 8.9–12 Considering all ions with their corresponding standard redox potentials, the oxidation of bromide and chloride would compete with the oxidation of water. However, the low concentration of Br^- means its competing oxidation is typically neglected as a first approximation and in comparison, with chloride oxidation in seawater electrolyzer studies. Clearly, the dominant ions are Na^+ and Cl^-, which is an aqueous 0.5 M NaCl solution considered a reasonable surrogate of natural seawater. Early work on selective electrolysis of seawater into hydrogen and oxygen was conducted. Interested in a selective working electrolyzer anode, he conducted electrolysis in unbuffered seawater and showed a predominance of the chlorine evolution reaction (CER: $2\,Cl^- \rightarrow Cl_2 + 2e^-$) at realistic larger current densities. The desired OER (OER: $2H_2O \rightarrow O_2 + 4H^+ + 4e^-$) was dominant only at current densities below 1 mAcm^{-2} or at very high current densities in which CER mass-transfer limitations become noticeable which, in turn, favor the OER. This is shown in Fig. 26.

In addition to the interest in an OER selective water electrolyzer anode, the chlorine industry was generating great interest, and the community started to investigate the anodic behavior in theory and experimentally. A parallel activity scaling for both OER and HER reactions in either alkaline or acidic solutions independent of the electrode material is shown in Fig. 27.

A Pourbaix diagram including the chloride and the oxygen chemistry is shown in Fig. 28. Based on this, the chlorine evolution reaction (CER) at low pH and the hypochlorite formation in high pH solution are the main OER competing reactions.

Fig. 26 Theoretical evolution of seawater anode chemistry knowledge and concepts. Log current vs voltage for chlorine and oxygen in seawater
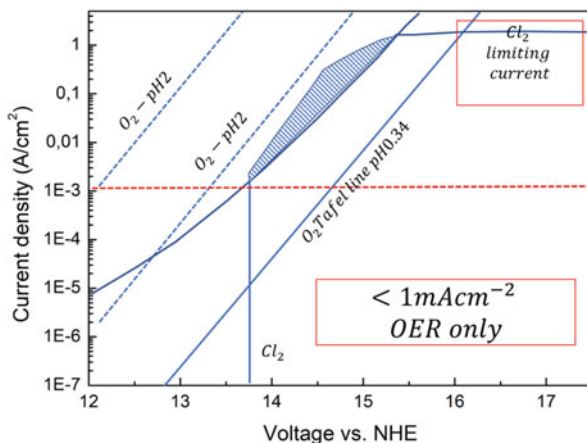
Fig. 27 Theoretical evolution of seawater anode chemistry knowledge and concepts. Potential of ClER vs OER at the same current density for several oxides and alkaline acidic electrolytes
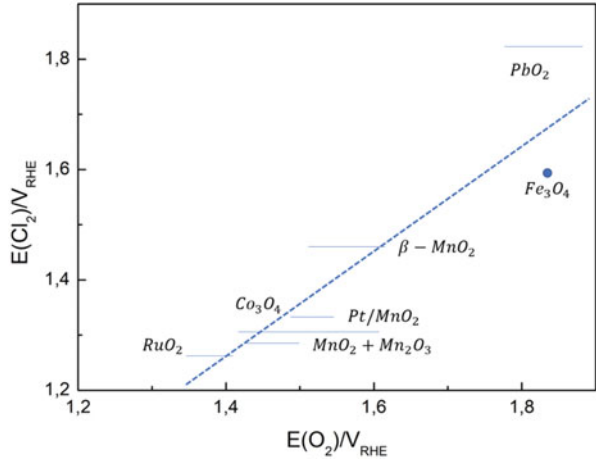
Fig. 28 Theoretical evolution of seawater anode chemistry knowledge and concepts. Pourbaix diagram of oxygen evolution reaction and chloride chemistry
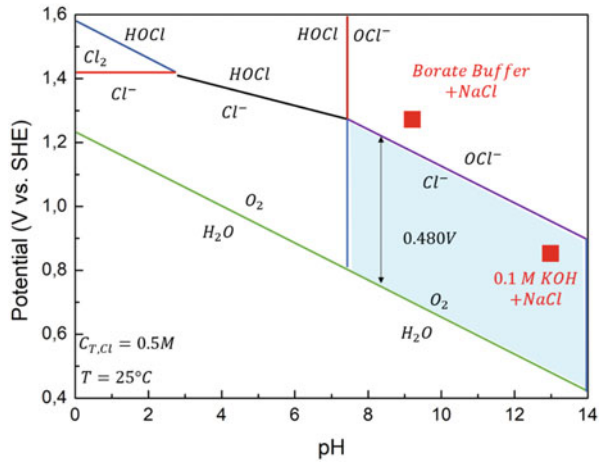
The following equations show the corresponding chloride chemistry reactions at low and at high pH, respectively:
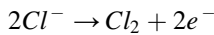
$$CIER:$$
$$2Cl^- \rightarrow Cl_2 + 2e^-$$
$$E^0 = 1.26 \ V \ vs.SHE, pH = 0$$
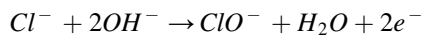
$$Hypoclorite:$$
$$Cl^- + 2OH^- \rightarrow ClO^- + H_2O + 2e^-$$
$$E^0 = 0.89 \ V \ vs.SHE, pH = 14$$

More recently, a more detailed CER mechanism was presented proposing a Volmer−Heyrovsky mechanism on RuO_2 surfaces. Involved in the mechanism, it describes an on-top oxygen (Oot) that caps all undercoordinated ruthenium sites (Rucus) of a $RuO_2(110)$ surface:

$$Volmer:$$
$$O_{ot} + 2Cl^- \rightarrow O_{ot} - Cl + e^- + Cl^-$$
$$Heyrovsky:$$
$$O_{ot} - Cl + Cl^- \rightarrow O_{ot} + Cl_2 + e^-$$
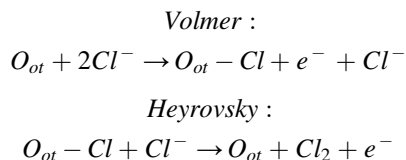
The mechanism consists of a Cl^- adsorption on the Oot combined with a discharge of the anion. This adsorption is followed by a direct recombination of the adsorbed chlorine species O Cl ot$^-$ with a Cl^- anion from the electrolyte to finally evolve Cl_2. In contrast to the sluggish $4e^-$ transfer reaction of the OER, the chloride chemistry involves only $2e^-$. Even though the thermodynamics favors the OER, the kinetics are much faster for the chloride reactions, which leads to smaller overpotentials. Consequently, maximizing the thermodynamic potential difference of both reactions will result in a convenient high potential window for selective OER. This is given for pH > 7.5, where the maximum potential difference is maximized $\Delta E = 480$ mV. Based on this, high pH values facilitate the selective splitting of seawater.

Reaching high current densities in typical liquid-based electrolyzer cells leads to a dramatic pH decrease at the anode even if the ideal solution of a direct seawater electrolyzer don't take in account this. Even though carbonate and borate ions are present in seawater, their average concentration is too low to sustain proton handling at high currents. Hence, seawater cannot be used without a buffer or additives with current seawater electrolyzer technology, but other solutions like membranes or different cell designs might be possible to overcome this local pH change.

To overcome the membrane-based difficulties, novel approaches for alternative hydrogen production routes from seawater are reported (Dresp et al. 2019). One approach is photocatalytic splitting.

While the previous investigations focused primarily on seeking high-performance OER selective catalyst for the anode, the catalyst material and the chemistry at the cathode seems more straightforward, because the thermodynamic potentials for electrochemical deposition or competing reactions are not as close as for the OER and CER. However, the catalytic activity in natural seawater with its interfering ions and the near-neutral pH seems also challenging.

An interesting aspect of direct seawater electrolysis consists of the production of freshwater when back converting the produced hydrogen and oxygen into electricity and water, as indicated in the inset in Fig. 29.

These results can be achieved in one single device, termed a reversible seawater electrolyzer, or in two separated subsequent combined fuel cell and electrolyzer devices.

Considering realistic electrolyzer/fuel cell efficiencies and calculating the required energy to produce 1 Nm^3H_2O, a reversible seawater electrolyzer would
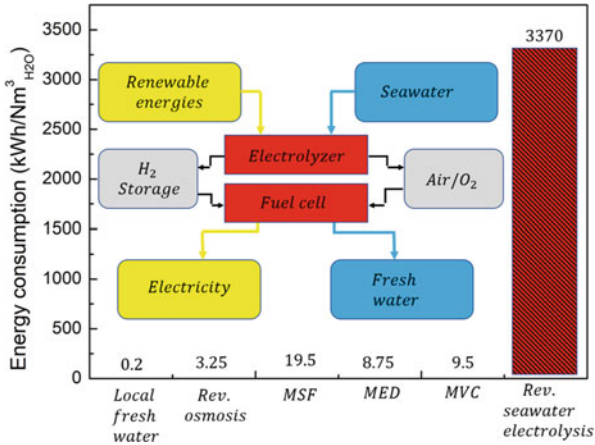
Fig. 29 Energy consumption of various desalination technologies and the local water treatment supplier per Nm^3. MSF multistage flash distillation, MED multi-effect distillation, MVC mechanical vapor compression. The reversible seawater electrolysis is based on realistic conditions assuming 79% electrolyzer and 50% fuel cell efficiencies. Inset: Sketch for reversible seawater electrolysis based on renewable energy

require an energy input of roughly 3370 kWh for every Nm^3H_2O water produced. Compared to other established technologies, such as reverse osmosis, multistage flash distillation, multi-effect distillation, and mechanical vapor compression, the energy consumption of a reversible seawater electrolyzer to desalinate 1 Nm^3H_2O is several orders of magnitude higher.

Although the water produced in the fuel cell process is perfectly purified water, reverse osmosis is currently by far the most efficient technology to produce freshwater.

However, reverse osmosis entails several drawbacks, like the frequent maintenance of the membrane and the exhaust saltwater feed's harm to the environment. Only the water treatment of the local freshwater supplier consumes less energy per Nm^3H_2O.

Reversible seawater electrolysis should be perceived more as an energy storage technology than a freshwater production technology when transforming the hydrogen back into electricity and water by using the fuel cell.

One possible process scheme providing constant and sustainable freshwater production through a combination of photovoltaics with reverse osmosis, a direct seawater electrolyzer and a fuel cell, is shown in Fig. 30.

During the day, the photovoltaic device supplies the electricity for both water purification by reverse osmosis and the stationary power demand (city). Thus, the reverse osmosis desalinates seawater and provides potable freshwater, while the power demand is met by photovoltaics. Excess solar electricity drives the direct seawater electrolyzer, producing solar hydrogen, which is stored locally. At night, in the absence of solar electricity, the hydrogen fuel cell system supplies electrical stationary power and produces freshwater directly by the fuel cell and indirectly by powering the reverse osmosis.

Fig. 30 Process scheme of
freshwater production based
on seawater electrolysis
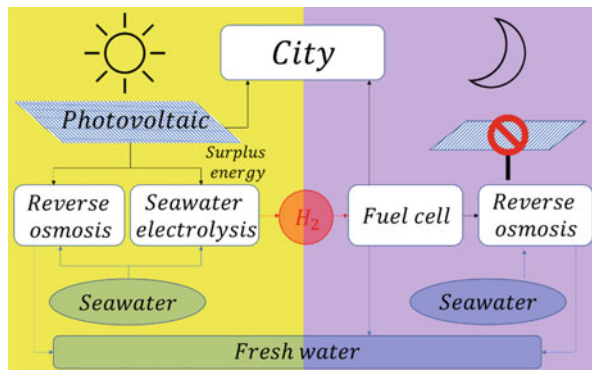
In conclusion, in specific environments and under certain conditions, reversible seawater electrolysis offers advantages for the storage of surplus electricity in the form of molecular hydrogen and for the collateral purification of seawater in combination with a fuel cell device.

Splitting seawater by using today's established technologies requires careful water pre-purification. After basic filtering, seawater is purified in a first step by reverse osmosis (RO). The purification of 9 kg of H_2O via RO requires about 0.03 kWh.

Consequently, even assuming an input power excess with a factor of 10, the resulting energy consumption of RO to produce 1 kg of H_2 amounts to a mere 0.3 kWh, which appears negligible against the typical energy input per kilogram of $H_2(\sim 47-66 \text{ kWhkg}^{-1}H_2)$.

The conventional electrolysis scheme offers slight advantages in terms of energy consumption. However, in many cases, the resulting purity of RO water still does not reach the required purity level of membrane-based freshwater electrolysis.

Therefore, an additional purification step will be required. PEM membranes require, in parts, ion exchanged ultra-purified (18 MΩcm) water for sustained operation. Hence, seawater-splitting schemes using those conventional membrane electrolyzers do require additional energy, space, and investment.

Catalysts and separators of liquid alkaline electrolyzers, on the other hand, tend to be more tolerant for electrolyte impurities than membrane-based electrolyzers. However, they require ample amounts of concentrated KOH solutions.

More importantly, under the highly alkaline conditions at common electrolyzer potentials (1.8–2.4 V), traces of chloride ions would be electro-oxidized to hypo-chlorite ions, harming the catalyst and limiting the long-term stability of the system.

Even though the conventional PEM and liquid alkaline electrolyzer schemes display slight energetic advantages over direct seawater electrolyzers, under certain conditions, the latter may still prove superior on the system level for hydrogen production applications in spatially constrained offshore or mobile maritime applications. Thus, even though the conventional PEM and liquid alkaline electrolyzer schemes display slight energetic advantages over direct seawater electrolyzers, under

certain conditions, the latter may still prove superior on the system level for hydrogen production applications in spatially constrained offshore or mobile maritime applications.

4 Conclusions

Hydrogen could be produced from abundant sources of sea water along with solar energy, for countries where fresh water is scarce. Ecological requirements, more specifically the absence of sufficient chlorine evolution in sea water electrolysis (SWE), make it a must to change the H_2/Cl_2 cell to a H_2/O_2 instead.

Chlorine produced by electrolysis dissolves in solution. Once the liquid phase approaches saturation, chlorine will appear in the gas phase. Thus, both the C.D. and quantity of electricity used will influence the evolution of Cl_2 in the gas phase. Cells with almost Cl_2-free anode gas for sea water electrolysis are possible depending on the quantity of electricity consumed as well as the cell design to ensure thorough mixing, hence more absorption of the gas in the liquid phase.

The most promising way for the electrolysis of sea water in a H_2/O_2 cell is the use of oxygen-selective electrodes. Oxygen reaction depends rather upon the electrode material than the chlorine reaction does and at low overpotential with different electrode materials.

Chlorine evolution at the anode replaces oxygen even for chloride concentrations lower than those of sea water. This shows how mass transfer and kinetics combine to make chlorine evolution the dominant anodic reaction product.

Using desalinated water for electrolysis has the added advantage of being able to treat water from a wide variety of sources, such as brackish groundwater, surface water, seawater, and domestic and industrial wastewater. To make it more affordable and accessible, research efforts should be directed towards improving desalination processes, devising more effective and durable membranes, for example, to produce more water per unit of energy.

Given the fact that current RO systems are operating nearly at an ideal energy consumption of 2 $kWhm^{-3}$, further improvement in membrane efficiency will only result in limited reductions in energy and cost. However, there are potential opportunities for improving pre-treatment and brine post-treatment technologies to reduce the cost and environmental impact of RO. Specifically, if one can eliminate or reduce pretreatment demands via the development of fouling resistant membranes, reducing usage of chemicals, or by using membrane modules with improved hydrodynamic mixing, this could further reduce the energy consumption and total water cost.

Hot, coastal, hyper-arid regions with intense solar irradiation and strong on- and off-shore wind patterns are ideal locations to produce renewable electricity using wind turbines or photovoltaics. Given ample access to seawater and scarce freshwater resources, such regions make the direct and selective electrolytic splitting of seawater into molecular hydrogen and oxygen a potentially attractive technology. The key catalytic challenge consists of the competition between anodic chlorine

chemistry and the oxygen evolution reaction (OER). This Perspective addresses some aspects related to direct seawater electrolyzers equipped with selective OER and hydrogen evolution reaction (HER) electrocatalysts.

Direct seawater electrolysis is an increasingly attractive electricity/hydrogen conversion and storage technology of the future. It will be most effective in regions with ample surplus renewable electricity, little access to freshwater, and yet sufficient access to ocean seawater. It also offers advantages for mobile maritime and offshore hydrogen-based power applications. Examples include powering underwater, unmanned maritime vehicles for maintenance of offshore installations. Range and refueling time of hydrogen-powered vehicles greatly outperform those of comparable battery-based vehicles. Because of the compact design, direct seawater electrolyzers are expected to pose fewer system engineering challenges compared to multistep schemes. The key chemical challenge is the design of robust and selective electrodes to suppress undesired electrochemical processes that are associated with the contaminants, primarily chloride chemistry.

Several active and selective catalysts have been identified as selective and active anode and cathode materials. However, advanced membranes and novel separator concepts appear critical to increase stability of direct seawater electrolyzer devices. Even though standard RO purification of seawater requires limited amounts of energy, it may be insufficient to reach the necessary levels of water purity. The necessary multiple consecutive purification steps are likely to reduce the overall robustness of the seawater electrolyzer system because all additional devices, such as reverse osmosis systems, require frequent and additional maintenance compared with a single direct seawater-splitting device.

In combination with a hydrogen fuel cell, a reversible seawater electrolysis scheme is possible that holds promise for the storage of surplus electricity in the form of molecular hydrogen, and more as a collateral process, purified water is formed during the fuel cell reaction. Based on the energy efficiency of reversible electrolyzer−fuel cell schemes, the resulting freshwater production may remain limited with respect to more conventional freshwater technologies. Here, a new process concept for a sustained freshwater supply based on the combination of RO water purification and direct seawater electrolysis was developed and suggested. Offshore wind parks and solar energy-rich coastal desert regions would benefit the most from this combined process technology, where molecular hydrogen is transformed back into electricity and water.

References

Al-Mufachi NA, Rees NV, Steinberger-Wilkens R (2015) Hydrogen selective membranes: a review of palladium-based dense metal membranes. Renew Sustain Energy Rev 47:540–551. https://doi.org/10.1016/j.rser.2015.03.026

Cavaliere P (2022) Hydrogen from electrolysis. In: Hydrogen assisted direct reduction of iron oxides. Springer, Cham. https://doi.org/10.1007/978-3-030-98056-6_6

Chen G (2004) Electrochemical technologies in wastewater treatment. Sep Purif Technol 38(1): 11–41. https://doi.org/10.1016/j.seppur.2003.10.006

Dresp S, Dionigi F et al (2019) Direct electrolytic splitting of seawater: opportunities and challenges. ACS Energy Lett 4:933–943. https://doi.org/10.1021/acsenergylett.9b00220

Farras P, Strasser P, Cowan AJ (2021) Water electrolysis: Direct from the sea or not to be? Joule 5(8):1921–1923. https://doi.org/10.1016/j.joule.2021.07.014

Huang X, Qu Y, Cid CA (2016) Electrochemical disinfection of toilet wastewater using wastewater electrolysis cell. Water Res 92:164–172. https://doi.org/10.1016/j.watres.2016.01.040

Kapałka A, Fóti G, Comninellis C (2008) Kinetic modelling of the electrochemical mineralization of organic pollutants for wastewater treatment. J Appl Electrochem 38:7–16. https://doi.org/10.1007/s10800-007-9365-6

Khan MA, Al-Attas T et al (2021) Seawater electrolysis for hydrogen production: a solution looking for a problem? Energy Environ Sci 14:4831–4839. https://doi.org/10.1039/d1ee00870f

Kumar SS, Himabindu V (2019) Hydrogen production by PEM water electrolysis – a review. Mater Sci Energy Technol 2(3):442–454. https://doi.org/10.1016/j.mset.2019.03.002

Lu S, Zhao B, Chen M (2020) Electrolysis of waste water containing aniline to produce polyaniline and hydrogen with low energy consumption. Int J Hydrogen Energy 45(43):22419–22426. https://doi.org/10.1016/j.ijhydene.2020.06.116

Murgolo S, Franz S, Arab H et al (2019) Degradation of emerging organic pollutants in wastewater effluents by electrochemical photocatalysis on nanostructured TiO_2 meshes. Water Res 164: 114920. https://doi.org/10.1016/j.watres.2019.114920

Paidar M, Fateev V, Bouzek K (2016) Membrane electrolysis—history, current status and perspective. Electrochim Acta 209:737–756. https://doi.org/10.1016/j.electacta.2016.05.209

Tong W, Forster M, Dionigi F et al (2020) Electrolysis of low-grade and saline surface water. Nat Energy 5:367–377. https://doi.org/10.1038/s41560-020-0550-8

Wang J, Yao J, Wang L et al (2020) Multivariate optimization of the pulse electrochemical oxidation for treating recalcitrant dye wastewater. Sep Purif Technol 230:115851. https://doi.org/10.1016/j.seppur.2019.115851

Wei C, Xu ZJ (2018) The comprehensive understanding of 10 mA cmgeo -2 as an evaluation parameter for electrochemical water splitting. Small Methods 2:1800168. https://doi.org/10.1002/smtd.201800168

Yao J, Pan B, Shen R (2019) Differential control of anode/cathode potentials of paired electrolysis for simultaneous removal of chemical oxygen demand and total nitrogen. Sci Total Environ 687: 198–205. https://doi.org/10.1016/j.scitotenv.2019.06.106

Yu L, Zhu Q, Song S et al (2019) Non-noble metal-nitride based electrocatalysts for high-performance alkaline seawater electrolysis. Nat Commun 10:5106. https://doi.org/10.1038/s41467-019-13092-7

Zheng W, Lee LYS, Wong KY (2021) Improving the performance stability of direct seawater electrolysis: from catalyst design to electrode engineering. Nanoscale 13:15177–15187. https://doi.org/10.1039/D1NR03294A

Alkaline Liquid Electrolyte Water Electrolysis

1 Introduction

The exiting steel technologies are based on fossil fuels, i.e., mostly on carbon, natural gas, mix of carbon and hydrogen, and electric arc furnaces. For CO_2-lean process routes, three major ways of solutions have been identified: decarbonizing whereby coal would be replaced by hydrogen or electricity in hydrogen reduction or electrolysis of iron ore processes, CCS technology introduction, and the use of sustainable biomass. Among all these solutions the main routes are evolving toward the use of Hydrogen as main energy carrier (Fig. 1).

This triangle matrix explains how reducing agents and fuels can be selected from three possibilities such as carbon, hydrogen, and electrons. The diagram represents all existing energy sources where coal is near to carbon on the carbon-hydrogen line, natural gas is near to hydrogen, hydrogen from electrolysis of water is on the hydrogen-electricity line, etc.

Most of the hydrogen employed in the energy and industrial sectors is produced from fossil fuels (over 90%). The main employed processes are the coal gasification or the natural gas reforming. Nowadays, only a small percentage of hydrogen is produced via electrolysis (Fig. 2). In addition, just a quarter of electrolysis is due to water, the main quantity is produced via chloralkaline electrolysis process (Moussallem et al. 2008).

Obviously, the decarbonization of human activities needs that hydrogen will be produced through sustainable routes. Electrolysis of water from renewable energy source is one of the most promising processes. Renewable hydrogen is essential to produce carbon-neutral fuels for transportation, raw materials for the chemical and steel industry, and seasonal energy storages. So the goal is to transform the current fossil-based hydrogen production to fossil-free-based resources. Water electrolyzers split water into hydrogen and oxygen using electricity, and the supplied electrical energy is converted into chemical energy carried by hydrogen. Water electrolysis is feasible for large-scale and fossil-free hydrogen production and can play a vital role
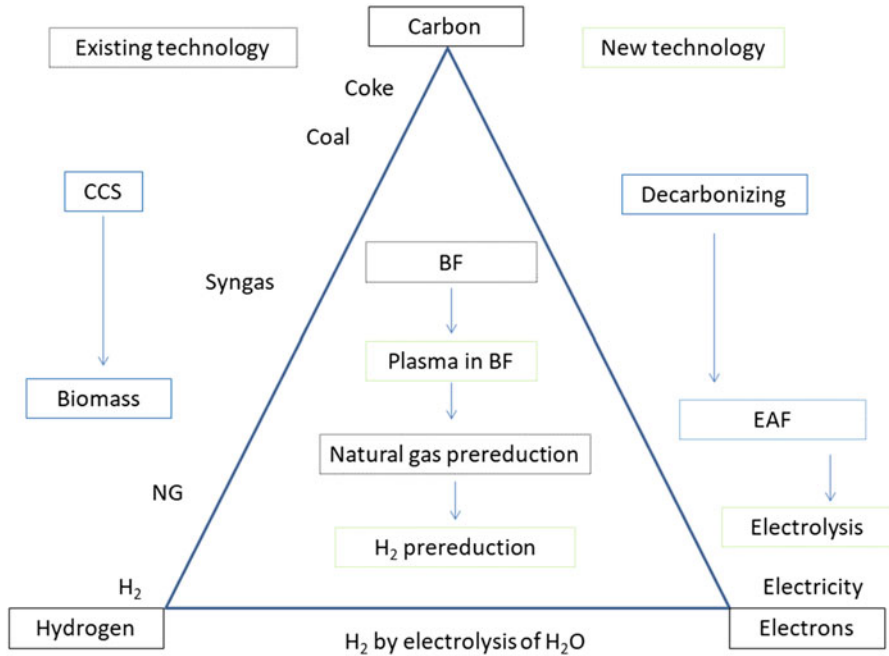
Fig. 1 Pathways of technologies for GHG emissions abatement

Fig. 2 Global hydrogen production sources. Over a total world production around 60 * 106 t
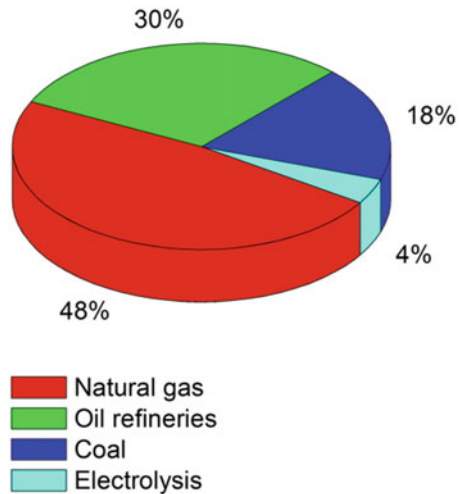
in the whole energy system reconstruction. The installed water electrolyzer have capacity in order of terawatts. A major role in saving electrical energy consumption and price of electrolytic hydrogen and oxygen can be played by power electronics, required in the DC power supply to water electrolysis processes.

2   Alkaline Water Electrolysis

Electrolysis of water is considered the cleanest technology to produce hydrogen with high purity. Obviously, half cell reactions are strongly dependent on the pH of the employed electrolyte.

Given the overall water splitting into hydrogen and oxygen described in Chap. 1, the half-cell reactions in alkaline media are:

$$2H_2O + 2e^- \rightarrow H_{2(g)} + 2OH^- \quad [Cathode\ (-)]$$

$$2OH^- \rightarrow H_2O + \frac{1}{2}O_{2(g)} + 2e^- \quad [Anode\ (+)]$$
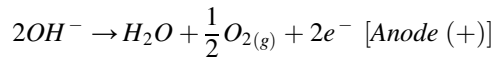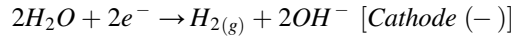
The working principles of alkaline water electrolysis cell is schematized in Fig. 3.

Basing on the Nernst equation, the potential of anode and cathode can be calculated by:

$$E^+ = E^{\ominus}_{H_2O/O_2} + \frac{R_{PG}T}{nF} \ln \frac{(a_{H_2O})\left(f^{\frac{1}{2}}_{O_2}\right)}{a^2_{OH^-}}$$
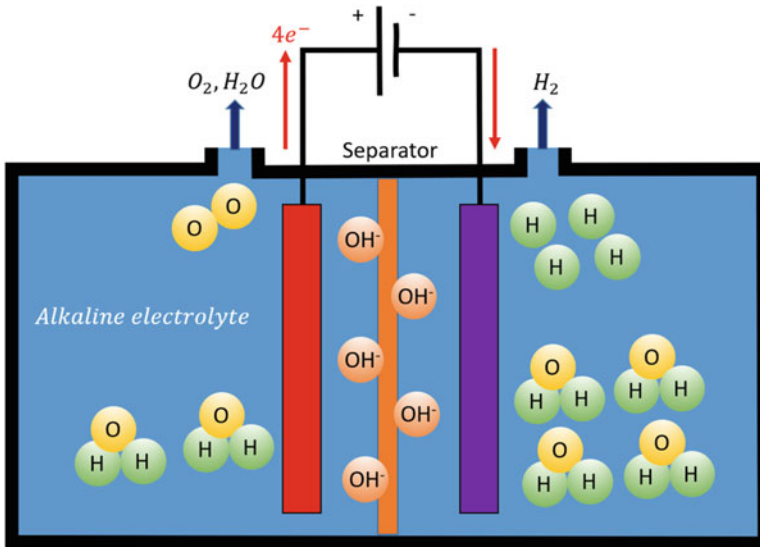
Fig. 3   Schematic of alkaline water electrolysis cell

$$E^- = E^{\ominus}_{H_2O/O_2} + \frac{R_{PG}T}{nF} \ln \frac{a^2_{H_2O}}{(a_{H_2O})\left(f^{\frac{1}{2}}_{O_2}\right)}$$

If oxygen can be considered as an ideal gas, at room temperature we can simplify by obtaining:

$$E^+ \approx 1.23 + pk_e - 0.06 \text{ pH}$$

In the same way, by considering hydrogen an ideal gas, at room temperature:

$$E^- \approx pk_e - 0.06 \text{ pH}$$

So, the overall electric voltage necessary to split water into hydrogen and oxygen will be:

$$E_{cell} = E^+ - E^- = 1.23 \text{ V}$$

It is demonstrated that the free energy electrolysis voltage of the water splitting reactions is not dependent on the pH. The corresponding potential of each electrode, which is shifted along the potential axis, would be changed to follow the function of the electrolyte pH.

   Anyway, as described in Chap. 1, overpotential is necessary to drive the overall process. The potential excess is due to the resistance losses in the cell (η_Ω), to the kinetic barriers of half-reactions on the anode (η_a) and on the cathode (η_c):

$$E_{op} = 1.23 \text{ V} + \eta_\Omega + \eta_a + \eta_c$$

The previous equation suggests that the overpotential can be reduced by optimal design of the cell and by the reduction of losses at the electrodes by employing appropriate catalysts. Obviously, the electrocatalysts act in different ways during HER or OER due to the different mechanisms taking place at the anode and at the cathode.

   As already mentioned, the hydrogen production rate (mol/s) is linearly proportional to the current of the cell:

$$\dot{n}_{H_2} = \eta_F \frac{(i_{cell}A_{cell})}{zF} = \eta_F \frac{I_{cell}}{zF}$$

Where $\dot{n}_{H_2}$ is the hydrogen production rate (mol/s), η_F is the Faraday efficiency, also known as the current efficiency, i_{cell} is the current density (A/cm^2), A_{cell} is the effective cell area (cm^2), z is the number of moles of electrons transferred in the reaction (for hydrogen, z = 2), F is the Faraday constant (9.6485×10^4 C/mol), and I_{cell} is the stack current (A).

As a general behavior, the anodic and cathodic reactions in acidic media is given by:

$$Anode: 2H_2O \rightarrow 4H^+ + O_2 + 4e^-$$
$$Cathode: 2H^+ + 2e^- \rightarrow H_2$$

While in alkaline media:

$$Anode: 4OH^- \rightarrow O_2 + 2H_2O + 4e^-$$
$$Cathode: 2H_2O + 2e^- \rightarrow 2OH^- + H_2$$
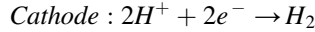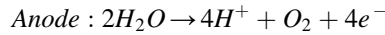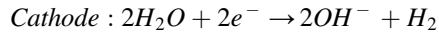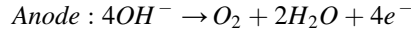
The involving of proton and hydroxide ions in the anodic and cathodic reactions is determined by the pH of electrolyte. To enable high ionic conductivity between the electrodes, a high amount of the charge carriers in the form of protons or hydroxide ions must be provided, which means that either strong acids or bases are typically used as the electrolytes for technical water electrolyzers. When the same electrolyte is used at the anode and cathode, the thermodynamics of water electrolysis (which is basically determined by the difference between the anodic and cathodic equilibrium potentials) is pH independent.

The energy required for the water decomposition is the enthalpy change of the process, that also is the enthalpy of formation of water, ΔH. The water electrolysis process is endothermic ($\Delta H > 0$). The free energy of the water splitting reaction, called Gibbs free energy change ΔG, must be supplied to the electrodes as electrical energy. The remainder is the thermal energy Q, which is the product of the process temperature T and the entropy change ΔS. These thermodynamic quantities can be written as:

$$\Delta H = \Delta G + Q = \Delta G + T\Delta S$$

In constant standard ambient conditions (298.15 K, 1 atm pressure), the required electrical work ΔG is equal to 237.2 kJ/mol (non-spontaneous reaction), and the amount of heat required Q is equal to 48.6 kJ/mol. Thus, the chemical reaction for water electrolysis can be expressed as:

$$H_2O_{(l)} + 237.2 \text{ kJ}_{el.} * \text{mol}^{-1} + 48.6 \text{ kJ}_{Heat} * \text{mol}^{-1} \rightarrow H_{2(g)} + \frac{1}{2}O_{2(g)} \Delta H_0$$
$$= 285.8 \text{ kJ} * \text{mol}^{-1}$$
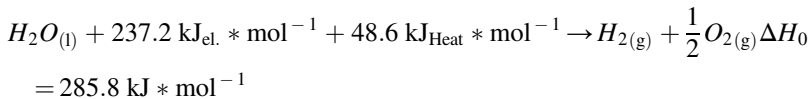
The lowest voltage to have the water splitting is called the reversible voltage U_{rev}, which is directly proportional to the Gibbs free energy change:

Fig. 4 Reversible and thermoneutral voltages as a function of cell temperature
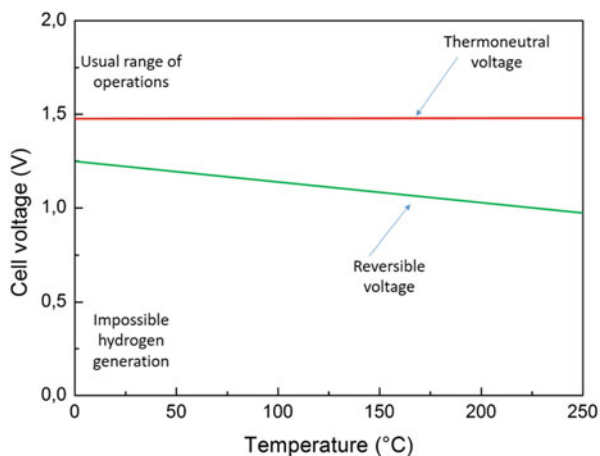
$$U_{rev} = \frac{\Delta G}{zF}$$

Without the input of thermal energy, the minimum voltage required becomes the thermoneutral voltage U_{tn}:

$$U_{tn} = \frac{\Delta H}{zF}$$

The reversible voltage and the thermoneutral voltage in standard ambient conditions are 1.23 V and 1.48 V, respectively. For commercial water electrolyzers, all energy for the water electrolysis process is provided as electrical energy. Both the reversible voltage and the thermoneutral voltage are thermodynamic state functions dependent on the cell temperature and pressure, even if the thermoneutral voltage changes only slightly as a function of temperature and pressure (Ulleberg 2003). The reversible voltage and the thermoneutral voltage are illustrated in Fig. 4 as a function of cell temperature at atmospheric pressure.

The effect of pressure on reversible voltage is exemplified in Fig. 5.

A temperature increase will slightly reduce the overall energy demand ΔH of an ideal liquid water electrolysis process as the demand for electrical energy ΔG is more notably reduced than the demand for thermal energy $T\Delta S$ is increased (Ursua et al. 2012). Operation at higher temperatures is favorable as heat losses caused by overvoltages, and it can be used to reduce the reversible voltage of water splitting. Thus, the utilization of thermal energy is an essential aspect in energy efficient water electrolysis processes. The overall energy requirement ΔH will stay practically constant as a function of pressure in an ideal liquid water electrolysis process. However, a change in pressure will increase the demand for electrical energy ΔG; for instance, an increase from 0.1 to 10 MPa at a cell temperature of 75 °C will increase the reversible voltage by 9%, but the demand for thermal energy $T\Delta S$ is correspondingly reduced.

Fig. 5 Reversible voltage as a function of pressure for different cell temperatures
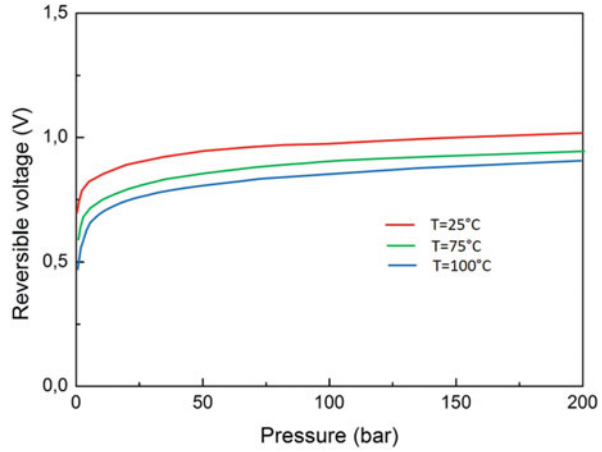
Now, the voltage of the electrolytic cell is the sum of the reversible voltage and all the overpotentials developing in the cell through the following equation:

$$U_{cell} = U_{rev} + U_{ohm} + U_{act} + U_{con}$$

where U_{cell} is the cell voltage, U_{rev} is the open-circuit, the reversible voltage as a function of temperature and pressure, U_{ohm} is the overvoltage caused by Ohmic losses in the cell elements, U_{act} is the activation overvoltage, and U_{con} is the concentration overvoltage. The current–voltage characteristics of an electrolytic cell can be described by a polarization curve. An example of a polarization curve for AEL and PEMEL water electrolyzer cells is illustrated in Fig. 6.

In the AEL water electrolysis, the Ohmic losses are mainly affected by: the ionic conductivity of the liquid electrolyte, the thickness of the electrolyte layer, and the thickness and conductivity of the electrodes (Milewski et al. 2014). In the PEMEL water electrolysis, the ionic resistance of the polymeric membrane and the electrical resistance of the separator plates and current collectors are the main contributors to the Ohmic losses (Schalenbach et al. 2014).

The activation overpotential is caused by the anode and cathode reaction kinetics. The concentration overpotential is caused by mass transfer limitations at high current densities, where the supply of the reactant (water) is not sufficient to support the reaction rate of the production of hydrogen and oxygen gases at the electrode surfaces. The concentration losses are typically negligible for commercial water electrolyzers—especially for AEL electrolyzers—because of the relatively low current densities in the cells (Haverkort and Rajaei 2021). Another non-linear region will appear in the cell polarization curve above the limiting (high) current density if mass transport losses occur. Other evidence on the effect of temperature on the AEL performances underline that with consideration of the bubble effect, the anode activation overvoltage, cathode overvoltage, Ohmic overvoltage, and supplied cell voltage are higher than those without consideration of bubble effect (Swiegers et al.

Fig. 6 Overpotentials in
AEL and PEMEL cells
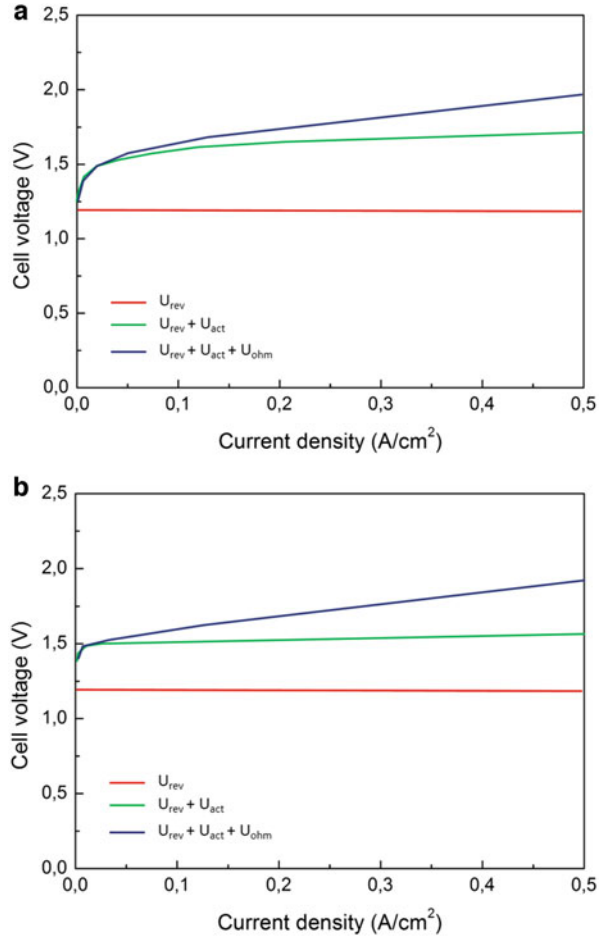
2021). The difference in Ohmic overvoltage with and without consideration of the
bubble effect linearly increases because the bubble number is proportional to the
current density variation. The bubble effect due to the temperature increase on the
performance of the stack is not higher than that due to the current density increase.
The amount of power consumed by the heater is exponentially increased at low
current density and is gradually decreased as the current density is increased. As the
operating temperature is decreased, the heater power consumption is decrease (Jang
et al. 2021).

The ideal cell behavior is shown in Fig. 7.

At room temperature and pressure, water decomposition starts at the
thermoneutral voltage of 1.48 V. As the cell current increases, the hydrogen pro-
duction increases. The Faraday efficiency is typically circa 1 as current density is
increased towards the nominal current density of the electrolyzer, bat the Faraday
efficiency may considerably drop if low current density occurs.
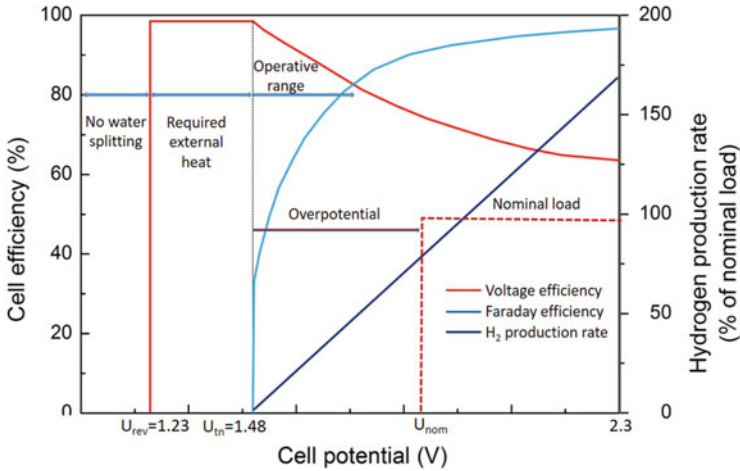
Fig. 7 Ideal cell behavior as a function of the potential

The voltage efficiency η_v of a water electrolyzer is given by:

$$\eta_v = \frac{U_{tn}}{U_{cell}}$$

The voltage efficiency is often used as an indicator of the energy efficiency of water electrolyzers. However, even if the voltage efficiency represents the electrical losses in the cell or cell stack, it does not consider the possible stray current flow or gas crossovers over the anode and cathode compartments. The Faraday efficiency, or current efficiency, η_F is experimentally quantified as the ratio of the ideal hydrogen production rate to the actual hydrogen output from the electrolytic cell (or stack). To include both the voltage and Faraday efficiencies in a single quantity, the definition-specific energy consumption should be used to assess the energy efficiency of a water electrolysis process:

$$E_s = \frac{\int_0^{t_1} I_{stack} U_{stack} dt)}{\int_0^{t_1} \dot{m}_{H_2} dt}$$

where E_s is the specific energy consumption, I_{stack} is the stack current, U_{stack} is the stack voltage, $\dot{m}_{H2}$ is the hydrogen gas mass flow rate, and t_1 is the inspected time span. The specific energy consumption describes the amount of energy consumed to produce a mass unit of hydrogen gas. The energy efficiency of a water electrolysis process can be calculated from:

$$\eta_e = \frac{HHV_{H_2}}{E_s}$$

where HHV_{H_2} is the higher heating value of hydrogen (39.4 kWh/kg or 3.54 kWh/Nm^3).

Alternatively, the lower heating value of hydrogen (LHV) can be used as a reference (33.3 kWh/kg or 3.00 kWh/Nm^3). The difference between the LHV and HHV is the latent heat of condensation. Typically, the HHV value is used as the reference for water electrolysis processes because liquid water is usually supplied to the process, in the case of alkaline and PEMEL water electrolyzers and the energy required for evaporation of water must be considered. The specific energy consumption of the water electrolysis process is further affected by the Faraday efficiency, which is non-linear with respect to the current density.

The selection between the currently commercially widely available alkaline and PEMEL technologies will set requirements for the required system components; alkaline technology needs a supply of liquid electrolyte, its controlled circulation, and separation from product gases. Furthermore, alkaline electrolyzer stacks are typically limited in their construction because of the liquid electrolyte supply and gas-liquid transport, which has made 200–300 V the typical stack voltage for industrial electrolyzers. The PEMEL technology avoids the construction limitations of the alkaline stacks, but the requirement for high electric currents (to produce more gases) and the exclusively bipolar construction of PEMEL stacks still sets the stack DC currents relatively high compared with the stack DC voltage.

PEMEL water electrolyzers achieve voltage efficiencies comparable to that at higher current densities, in other words, they have lower cell impedances. Therefore, smaller variations in the instantaneous supply voltage cause greater fluctuations in the supplied current for PEMEL cells. Instantaneous high current density variation may have an adverse impact on cell degradation, for this reason it could be necessary to limit the current slew rate. Cell degradation increases the cell voltage over time, and the increased electrolyzer voltage resulting from degradation should be considered in the system design and operation (Siracusano et al. 2018).

Operating conditions, mainly cell temperature and pressure, affect the reversible voltage and impedance of the electrolytic cell, and have an impact on the system efficiency. Increasing the cell temperature is generally beneficial to the cell voltage efficiency, but selected materials will limit the temperature. The cell reversible voltage is also affected by anode and cathode compartment pressures. The resulting change in voltage efficiency from an increase in pressure is comparable with the ideal isothermal compression of hydrogen gas. However, if the surrounding system, such as post-electrolysis synthesis processes or gaseous storage of hydrogen gas, requires elevated pressures, PEMEL electrolyzers may opt to operate at a differential pressure and output only hydrogen gas at an elevated pressure, while alkaline electrolyzers are limited to balanced pressure operation. In the PEMEL water electrolysis, the change in hydrogen outlet pressure from 20 to 40 bar may result in unchanged electrical energy consumption (Koponen et al. 2017). However, an increase in pressure may compromise the control range of the electrolyzer and its

Table 1 Electrolysis cells properties

Technology	AEC	PEMEL	SOEC
Electrolyte	KOH	NAFION	YSZ
Cathode	Ni, Ni-Mo alloys	Pt, Pt-Pd	Ni, YSZ
Anode	Ni, Ni-Co alloys	RuO_2, IrO_2	LSM/YZS
Current density (A/cm^2)	0.2–0.4	0.6–2	0.3–2
Cell voltage (V)	1.8–2.4	1.8–2.2	0.7–1.5
Voltage efficiency (%)	62–82	67–82	~100
Cell area (m^2)	<4	<0.3	<0.01
Operating temperature (°C)	60–80	50–80	650–1000
Operating pressure (bar)	<30	<200	<25
Production rate (m^3/h)	<760	<40	<40
Stack energy (kWh/m^3)	4.2–5.9	4.2–5.5	>3.2
Lifetime (h)	<90,000	<60,000	<10,000
Maturity	Mature	Commercial	Demonstration
Capital cost (euro/kW)	<1200	<2300	>2000

specific energy consumption as the gas crossover rate is increased. Furthermore, operating the water electrolyzer in non-optimal conditions may risk the lifetime of the electrolytic cells.

As a matter of fact, the summarized properties of the described systems are listed in Table 1 (Schmidt et al. 2017).

Water supply and water purification are required to guarantee the normal operation of the water electrolysis process and to preserve the lifetime of the electrolytic cells. In the alkaline water electrolysis, water is consumed from the liquid electrolyte solution, whose concentration must be maintained by an inlet of deionized water. Meanwhile, the PEMEL water electrolysis is electrolysis of deionized water. The conductivity of the inlet water affects the operation of the electrolytic cell, its energy efficiency and ageing, and the presence of alkaline electrolyte decreases the gas solubility, which has an impact on the gas crossover (Haug et al. 2017).

Under alkaline conditions, the HER becomes more complex with respect to acidic media because it is directly dependent on the oxygen evolution reaction (OER) at the anode, which affects HER dynamics by supplying protons to the cathode through the deprotonization of hydroxide ions (OH^-). The HER pathways in alkaline media have been described in Chap. 1.

The HER mechanism in neutral and alkaline solution as shown in Fig. 8.

HER's primary reaction step is the Volmer reaction or the release reaction in which the beginning of electron transfer is carried out. At first, the H+ (H_3O+) combines with an electron to form H* deposited/adsorbed on the electrode surface. The adsorbed H* is then removed/desorbed by two paths to form H_2. The first desorption step follows the Heyrovsky mechanism reaction in which the H* atom in an adsorbed state merges with a free H+/e− couple form H_2. The second desorption step follows the Tafel reaction mechanism in which two adsorbed H* combine to produce H_2.

Fig. 8 HER mechanism in
alkaline media
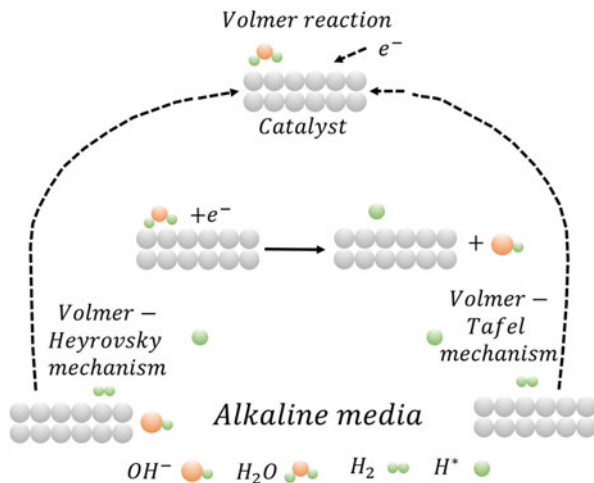
High Tafel slopes indicate the Volmer reaction as the rate-determining step, which includes the adsorption of hydrogen on catalyst surface under low H coverage. It can also be seen that HER electrode kinetics changes in distinctive solution in which different solution can lead to follow a distinctive process of electron transfer, which successively forms catalytic mechanism differently. Consequently, a catalytic mechanism should be discussed concerning a specific solution.

Oxygen evolution reaction (OER) is the second half-reaction in the electrochemical water splitting process that occurs at the anode and requires four-electron transfer. Generally, OER processes involve incredibly high overpotential compared to HER. OER is recognized as the primary congestion in recovering the overall energy efficiency of the water electrolysis process. There are three intermediate products (O*, OH*, OOH*) in the OER reaction mechanism. Therefore, the production of oxygen followed two different routes in acidic or alkaline solution. The OER reaction mechanism is quite similar in other pH solutions. The change is that OH- is absent in acidic solution. Thus, M reacts with H_2O to produce MOH. Afterwards, MOH constantly encounter electron transfer to form MO. The MO and O_2 can be made by two different processes in which the first approach led to combine two MO to form O_2 directly, and the second approach is to let O_2 continuously react with MO to produce MOOH, and later it reacts with MOOH to form O_2. At different pH of the solution showed similar OER mechanism and the distinction is that OH− is not present in acidic solution. Therefore, M reacts with H_2O to produce MOH. Consequently, the MOH continues to experience the transfer of electrons to form MO. After the formation of MO, O_2 can be formed in the solution by two different paths. One approach is the decomposition of MO to form O_2 directly, and the second approach is to let H_2O or OH- further react with MO to produce MOOH. MOOH decomposes to form O_2, as shown in Fig. 9.
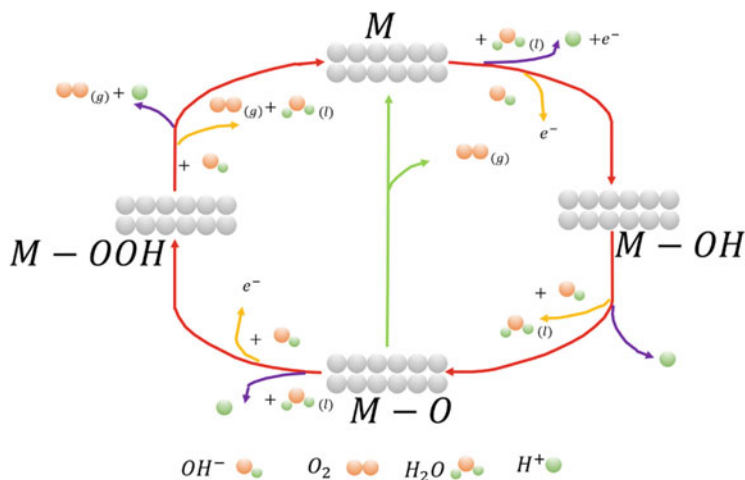
Fig. 9 The oxygen evolution reaction (OER) mechanism in acidic solution (purple line) and alkaline solution in (yellow line)

According to the Sabatier principle, the adsorption is excessively weaker to have adsorption. However, adsorption is strong to cause desorption, and only a catalyst with moderate binding capability is suitable. As a result of this process, it can be presumed that when the adsorption bonding on O and the catalysts is excessively weak, the formation of OH* does not readily form OOH*. The catalyst's performance can only reach the peak when the combined bonding capacity of O with the catalysts is un under moderate conditions.

In electrolysis, the direct current power supply is utilized by sustainable energy sources such as wind, solar and biomass energy. However, only 4% hydrogen has been achieved from the water electrolysis method due to economic challenges and expensive constituents (electrocatalysts) of the overall process. Soon, it is expected to increase these expenses due to more renewable resource usage. The decomposition reaction has a specific energy requirement in the context of temperature and pressure of the water. The minimum requirement of water decomposition voltage as a function of temperature and pressure is defined by Gibbs free energy:

$$\Delta G = \Delta H - T\Delta S$$

where ΔG is the Gibbs free energy for water formation, ΔH is the enthalpy change for water formation and ΔS is the entropy changes for water formation.

The equilibrium cell voltage E_{eq} is determined by the Gibbs free energy as shown in:

$$\Delta G = -nFE_{eq}$$

where, n is the number of moles of electron transferred, F is Faraday's constant, and E_{eq} is the equilibrium voltage. Considering water dissociation, n, the number of moles of electron transfer in the reaction is $2e^-$, and the value of F is 96,485 C/mol. At the standard temperature (25 °C) and pressure (1 atm) condition, ΔG is 274.2 kJ/mol and $E_{eq} = 1.23$ V and the current efficiency is 100%. However, the slow kinetics of HER and OER at the cathode and anode, respectively, of the electrolytic cell required high overpotentials to produce significant current densities. As a result, the energy consumption of commercial water electrolysis is 1.5–2.5 times higher than the theoretical energy consumption. Besides that, inadequate energy efficiency, conventional water electrolysis also has the consequence of the generation of explosive O_2/H_2 gas mixture. Moreover, the challenges to using noble metal-based electrocatalysts required to catalyze the HER and OER in standard water electrolysis process. It resulted in huge cost for hydrogen production and hindered the commercial production at a large scale.

After water slitting, the two gases go through a series of conditioning stages as shown in Fig. 10.

For the hydrogen gas, it must be eliminated all the traces of electrolyte, water and oxygen.
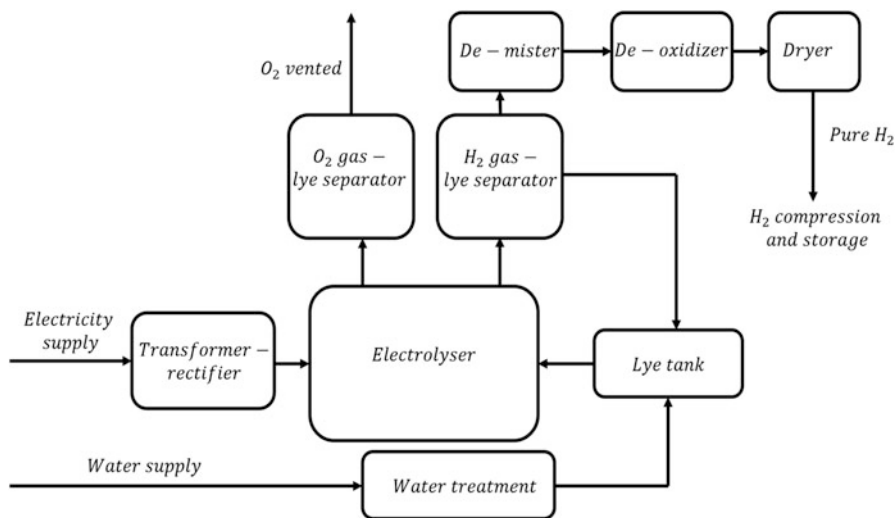
Fig. 10 AEM schematic flow

3   Catalytic Reactions

3.1   HER Catalysts

The main problem related to water splitting is the high electricity consumption due to polarization taking place at the electrodes surface leading to increased electrolysis voltage (Wang et al. 2021). Hence, the development of low-cost, highly efficient, and stable HER electrocatalysts for large-scale and eco-friendly production of hydrogen is fundamental.

Both OER and HER catalytic processes are necessary to enhance water electrolysis efficiency, and they should be improved kinetically. Currently, precious metals are considered the most prominent electrocatalysts. However, the main challenge is that the precious catalysts are rare on earth and shown high cost hindered the technology's extensive application. The advancement in water electrolysis catalysts is insufficient. However, a research development has been made to decrease the use of precious metals by adapting numerous techniques such as changing the material composition and structures via substitution of precious metals with non-precious metal-based catalysts.

Several transition metals compounds have been used in alkaline water electrolysis (AWE) such as Fe, Mn, Co and Ni-based, including their oxides have been comprehensively explored in the past several years to replace precious metals electrocatalysts for HER and OER half-cell reactions in electrochemical water electrolysis process. Several processes have been carried out to enhance OER and HER catalytic performance, such as escalating electrical conductivity, improved stability and bimetallic compounds conductivity, and synergetic effect using hybrid compounds using combined inherently combined carbon with chemically sensitive metal compounds (Zhang et al. 2021).

As described in Chap. 1, HER can divided into two main parts: the formation of H* (Volmer step) and the generation of H_2 (Heyrovsky step or Tafel step). So, given the overall reaction:

$$2H_2O + 2e^- \rightarrow H_2 + OH^-$$
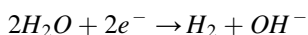
the various steps are described by:

$$H_2O + e^- \rightarrow H^* + OH^- \quad (Volmer)$$
$$H_2O + e^- + H^* \rightarrow H_2 + OH^- \quad (Heyrowsky)$$
$$H^* + H^* \rightarrow H_2 \quad (Tafel)$$
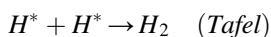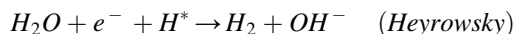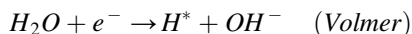
That in alkaline media requires an additional step of water pre-dissociation, which would probably introduce an energy barrier that may affect the reaction rate, with the formation of H* on the catalyst surface, there are two possibilities: one possibility is the Heyrovsky reaction, in which the adsorbed hydrogen atom combines with an

Fig. 11 Volmer-Heyrowsky and Volmer-Tafel route on platinum
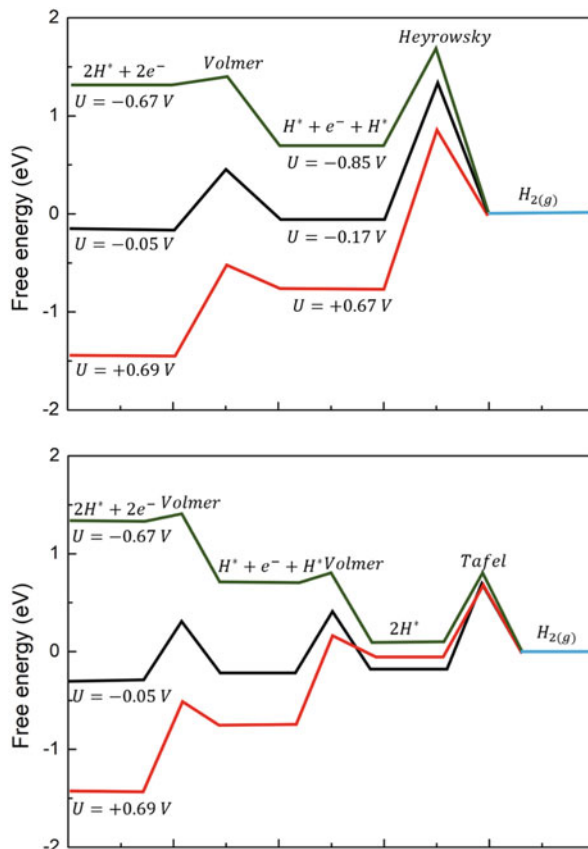
electron transferred from the electrode surface and a proton from the electrolyte to form a hydrogen molecule; the other is the Tafel reaction, in which two (adjacent) adsorbed hydrogen atoms combine to form a hydrogen molecule. The possible rate controlling step(s) can be determined simply by the Tafel slope value of the polarization curves.

Now, in alkaline solution, HER is high sluggish because of high water dissociation energy barriers and strong metal-OH$_{ads}$ interactions.

Pt is the most efficient electrocatalyst thanks to its high adsorption properties. As a summary, the Pt activity for Volmer-Heyrowsky and for Volmer-Tafel routes is shown in Fig. 11.

Ru is cheaper than Pt, for this reason, Pt-Ru alloys are employed in alkaline water electrolysis. Also, the crystal structure can influence the catalytic behavior. As a matter of fact, in the case of Pt-Ru, an improvement in the apparent activity is recorded by employing a core shell structure due to the weak binding of hydrogen and optimal interaction with the hydroxyl species during the reaction. So, further developments led to the design of nanoparticles immersed in cheaper matrixes. An

extreme solution is represented by single atom dispersion leading to the maximum efficiency. As a matter of fact, atomic layer deposition allows to increase by more that 30 times the catalytic activity of platinum. It is clear how other precious metals can be employed as catalysts even if their stability represents a core problem.

Carbon-based structures are very electrolytically active in many conversion reactions such as HER, OER and ORR (Dai 2017). As a main difference with respect to metals we should underline carbon resistance to corrosion attacks in all the employed media. The main employed structures are in activated nanotubes, graphene and fullerene. Heteroatom doping is demonstrated to be the most efficient way to increase the catalytic activity of carbon. For alkaline electrolysis, N, S, P and B are considered the best dopant materials. With heteroatoms incorporated into the carbon lattice, the surface-state-density (DOS) peak of the adjacent C atoms would shift toward the Fermi level, resulting in promoted bonding between the valence band of the hybrid orbital of adjacent C atoms and the orbital of H, and thus reduce the free energy of the reaction process. In general, co-doping with more than one specie results more efficient. As a matter of fact, the doped N and P species could coactivate the adjacent C atom in the graphene matrix by affecting its valence orbital energy levels to synergistically induce enhanced reactivity toward the HER. As a result, the dual-doped graphene shows higher electrocatalytic HER activity than the single-doped ones. As a summary, a lot of research works are focused on the improvement of the electrocatalytic performance of metal-free carbon-based materials (Hu and Dai 2016). However, although the heteroatom-doped carbon or defected carbon exhibits higher activity than the conventional carbon materials, most of the reported ones are inferior to the metal-based ones due to the relatively low catalytic activity of carbon. Therefore, to take full advantage of the heteroatom-doped carbon materials, the development of stable non-precious metal/carbon-based composite electrocatalysts should be a rewarding research direction for achieving efficient HER.

Transition metals as well as their oxides, carbides and sulfides are very effective to substitute precious metals as catalysts due to low cost and high availability. The chemical basic is represented by the fact that metal sulfide clusters with five permanent ligands in a distorted octahedral ligation shell have been proven to be the active sites for the HER. The integration of metal sulfides with conductive substrates is a promising method to obtain HER electrocatalysts with high activity and excellent conductivity, that could ensure mass as well as electron transfer at the same time during the HER process. A relevant tendency is represented by the constructions of hybrid electrocatalysts coupling the action of carbon doped materials and transition metals compounds. Furthermore, it is demonstrated that the introduction of more than one type of transition metals compounds has much better electrochemical performance than of the pure ones, possibly due to synergistic effects.
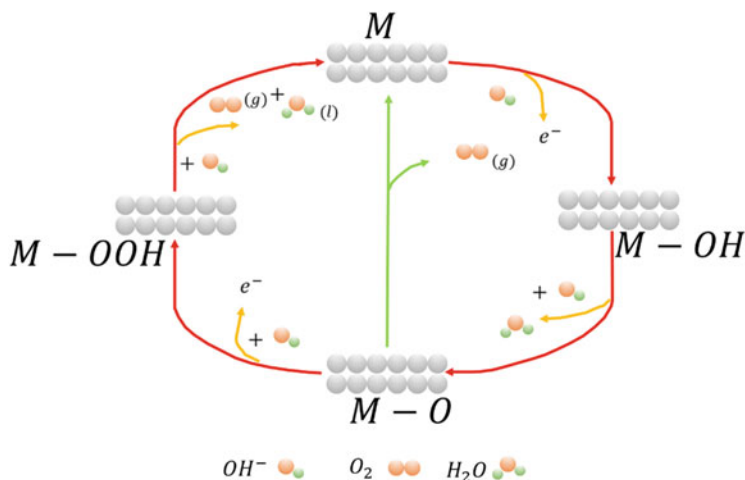
Fig. 12 General OER mechanism in alkaline media

3.2   OER Catalysts

As the main difference with HER, much higher overpotentials are required to drive the OER because of the sluggish four electron-proton-coupled path which leads to greater energy loss. To obtain a high-performance OER catalyst, great efforts have been devoted to evaluating the OER activity of various kinds of materials, including metal oxides (e.g., noble metal oxides, perovskite oxides, spinel oxides), metal hydroxides, metal chalcogenides (sulfides, selenides, or tellurides), metal pnictides (phosphides and nitrides), organometallics (metal coordination complexes), and non-metal materials. And also in this case, transition metals employment is shown up as an efficient and cheap solution for anode electrocatalysts design.

On the other hand, metal sulfides, phosphides, selenides, and nitrides also have been demonstrated as promising electrocatalytic materials for the OER in terms of high activity and long-term durability. However, when these materials are applied in the OER, there could be phase transformations.

Due to the complexity of the $4e^-$ OER process and the gradual evolution of active sites, it is difficult to propose an explicit mechanism. Nonetheless, based on research works, a general OER mechanism has been proposed as displayed in Fig. 12.

First, a hydroxyl radical is adsorbed on the active center (M) to generate M–OH through $1e^-$ oxidation. Then, the coupling of proton and electron between M–OH and hydroxyl anion (OH^-) gives the M–O intermediate. There are two possibilities that could follow: one is the combination of two M–O to produce O_2 directly; the other is M–O being attacked by OH^-, and with $1e^-$ oxidation, there is the formation of M–OOH that reacts with OH^- to give O_2 and the regeneration of the active center. Although there is no consensus on the OER mechanism, it is reckoned that the bonding between the M–O and the active center has substantial effect on the activity of catalysts.

Fig. 13 Perovskite structure
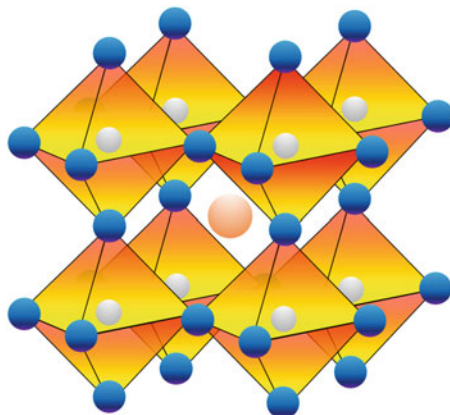
Iridium and Rutile oxides are usually considered as state-of-the-art OER electrocatalysts because of their high initial activity, but the deactivation and high cost severely hinder actual commercial application. Therefore, some smart strategies, such as alloying treatment, surface structure regulation, and stress strain engineering, are deployed to enhance their intrinsic activity and durability. When an Ir crystal lattice is doped with a transition metal such as Cu, Fe, Co, or Ni, the electronic structure of Ir may be distorted, leading to the optimization of bonding strength between the intermediate(s) and the alloy catalyst.

Perovskite oxides have a general formula of ABO_3. The transition metal (b) occupies the center of the octahedron, and the adjacent octahedrons connect with one another by sharing the corner, and the alkaline metal and/or rare-earth metal (a) gains access to the free space to complete the whole framework (Fig. 13).

OER activity of perovskite materials is related to the strength of B-OH bonding, which is regulated by the electron population of σ^* band. The research results led to suggestions made for the design of high-performance electrocatalysts: eg electrons should have access to unity, i.e., a near-unity occupancy of the eg orbital of surface transition metal ions and robust covalent interaction between transition metals and O atoms is beneficial for the OER.

$A'B'_2O_4$ is the generalized formula of spinel oxides whose structure is illustrated in Fig. 14.

There are two kinds of units in the spinel framework, namely, octahedral (Oh) and tetrahedral (Td), that define the $(A_2 + Td)(B_3 + Oh)_2O_4$ and $(A_2 + Oh)(B_3 + Td)$ $(B_3 + Oh)O_4$ configurations. Looking into the perovskites, there is a different d-band splitting model (Td: egt2g; Oh: t2geg) because of the two different coordination environments in the spinel oxides. With low-cost, moderate conductivity, and stability in electrolytes, spinel oxides are considered as promising catalysts for the OER.

Unique layered and electronic structure of metal hydroxides has important impact in the OER field. However, the inferior intrinsic activity of active sites and the poor conductivity induce a sluggish OER process.
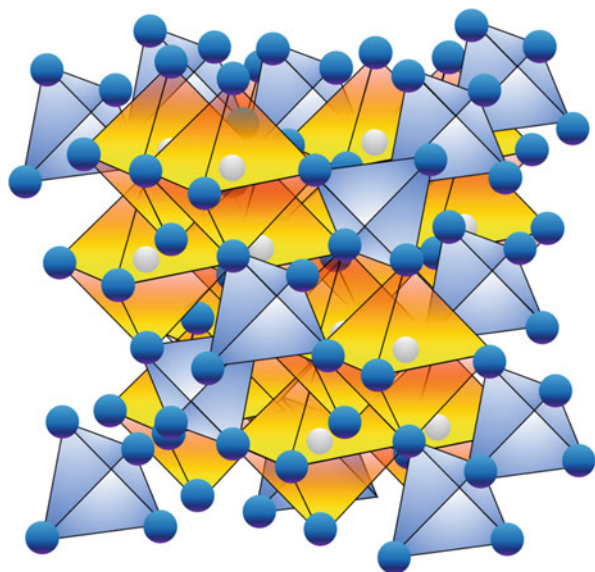
Metal chalcogenides and pnictides are emerging OER catalysts which have attracted vast attention. Usually there is transformation from the initial phase to metal oxyhydroxide on the surfaces of these materials upon the OER. These materials (metal sulfides, phosphides, selenides, and nitrides) also show excellent HER activity, indicating they are promising bifunctional electrocatalysts to catalyze overall water splitting. It has been verified that the properties of an electrocatalyst can be improved by combining the electrocatalytically active material with a conductive substrate.

The organometallics with defined geometric and electronic structures are usually identified as ideal molecular compounds to investigate the active sites and mechanisms of the OER.

As low-cost OER catalysts, non-metal materials have received considerable attention. Carbon-based materials with good electroconductivity and chemical stability in acid and alkaline electrolytes have also been identified as promising OER electrocatalysts. As a matter of fact, the oxidized carbon nanotubes showed the OER activity comparable to those of certain metal-based materials.

3.3 Cell Components

A cell for alkaline water electrolysis is composed of an external power source, an anode, a cathode, a conductor (current collector), a separator, and an electrolyte. The energy required for the overall process is provide by an external power source. The conductor, also called current collector, is used to support the catalyst and to ensure
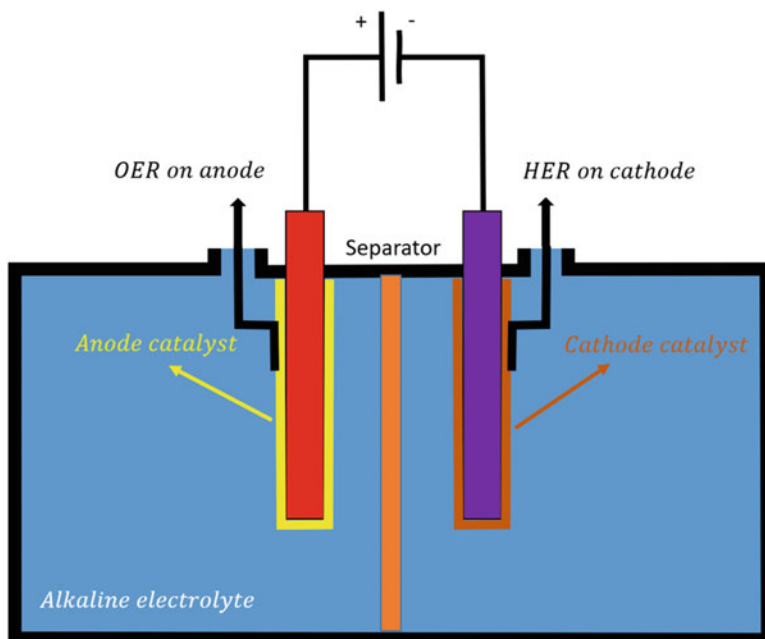
Fig. 15 Alkaline water electrolysis cell schematic

electrical contact of the supported catalysts to the electrodes and to compensate their weak in-plane conductivity. Various porous and electron conducting materials, such as carbon or metal foams, fleeces, or sintered bodies can be used as current collectors. The prime requirement for a current collector is conductivity (Fig. 15).

Typically, the electric conductivities of metals are above 10^4 Scm^{-1}, which are more than four orders of magnitude higher than the ionic conductivities of electrolytes. In other words, the Ohmic drops in the current collectors have minor contributions to the overall Ohmic drop in electrolysis cells. The electrolyte provides the ionic conductivity between the electrodes as well as within the porous structures of the electrodes. The main function of the separator is to separate the generated oxygen and hydrogen evolved in the anodic and cathodic compartments. Besides the anode/cathode catalysts, electrolytes and separators are also critical components for water splitting. Ionic conductivity between the electrodes and within the porous structures of catalysts is provided by the electrolytes. Hence, the criteria of a suitable electrolyte are high ionic conductivity and non-corrosive to electrodes. In this regard, alkali (potassium or sodium hydroxide) solutions are the common commercial electrolytes for alkaline water electrolysis systems because they are more conductive than the other alkali metal bases (with respect to equal molarities) and unreactive to electrodes, hence, avoiding large corrosion loss.

During the process, hydrogen ions are forced toward the cathode and here reduced to molecular hydrogen. On the other hand, hydroxide ions move toward the anode and here oxidized to molecular oxygen. The porous separator is employed to avoid H_2-O_2 mixing. The adopted porous separator should be filled with the liquid electrolyte to enable ionic conduction between the electrodes, simultaneously providing ionic conductivity and ensuring the separation of the gases. The main properties of the alkaline water electrolysis separators are: high porosity and wettability; small dimensions of the pores in order to avoid the bubbles penetration that leads to a permeability reduction; high pores volume in order to improve ionic conductivity; high electrical resistance in order to avoid parasitic currents between the electrodes; thin dimensions in order to reduce the Ohmic losses; good ductility and good mechanical stability; electrical stability and corrosion resistance in the alkaline solution.

Now Zirfon is the most prominent material for separators (Lavorante et al. 2015). It is a composite material of zirconia and polysulfone. Endowed with the flexibility of the polymer together with the stiffness and wettability of ceramic zirconia, Zirfon is high performing and stable for alkaline water electrolysis. So, the separator made of Zirfon is highly stable in concentrated KOH solutions even at elevated temperatures.

As before mentioned, overpotential significantly affects the output performance of a water electrolysis cell system. To obtain high-energy conversion efficiency, one of the most critical issues is to effectively reduce the overpotential.

To increase the cell efficiency, some crucial factors must be taken into account like the working voltage, that is directly related to the energy consumption. As the voltage increases at the same current level, hydrogen production efficiency increases; the current density, that is directly related to the hydrogen production rate. High current density means higher production efficiency even if an increase in bubbles production contributes to overpotential. So, a compromise between hydrogen production rate and bubbles formation must be reached (Zhou et al. 2018).

The temperature for alkaline water electrolysis is below 90 °C. High temperature leads to fast water consumption even if is accompanied by faster separator damaging.

The pressure increasing leads to a reduction of bubbles dimensions with the result of reduction of Ohmic losses.

The type and concentration of the electrolyte is fundamental because it is directly related to the cell resistance. The conductivity can be improved with appropriate additives.

4   Ni-Based Alloys Catalytic Performances

As mentioned above, in alkaline media the HER can evolve through the Volmer step water dissociation:

$$H_2O + M + e^- \leftrightarrow M - H_{ad} + OH^-$$
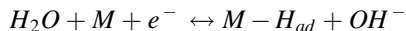
followed by either the formation of the reactive intermediate Had, Heyrovsky step:

$$H_2O + M + e^- \leftrightarrow MH_{ads} + OH^-$$

$$H_2O + MH_{ads} + e^- \leftrightarrow H_2 + M + OH^-$$
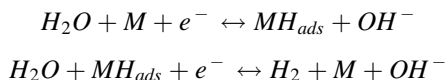
or the Tafel recombination step:

$$H_2O + M + e^- \leftrightarrow MH_{ads} + OH^-$$

$$MH - ads + MH_{ads} \leftrightarrow H_2 + 2M$$
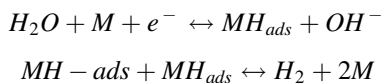
Ni-based materials show high catalytic performances in alkaline media (Zeng and Zhang 2014). Obviously, many combinations such as $NiCo_2O_4$ have been explored to improve the electrodes reactivity. Basically, with high cobalt contents (over 40%) the Volmer reaction is the controlling step of the hydrogen evolution reaction, promoting the Ni-H_{ads} species formation. Co-Ni-Fe electrodes show that the controlling reaction mechanism is via Volmer and then Tafel paths, where a Heyrosky stages was favored. The electrocatalytic activity depends on operating temperature and on the iron percentage. NiCoZn alloys show excellent corrosion resistance, but the formation of a passive layer leads to a decrease in the catalytic activity for the hydrogen evolution reaction. This problem can be solved by adding small quantities of noble metals during the electrodes production (mainly via electrodeposition).

The stability of electrodes is improved in the case of Ni-Mo alloys. This stability is due to the formation of an intermetallic compound (Ni_4Mo).

Ni-Ti alloys show that the catalytic activity increases as the titanium content increases. For this system, it was found that the HER takes place via the Volmer-Heyrowsky mechanism.

Ni-Cu alloys present good stability, good oxidation resistance and good electrical conductivity.

The formation of amorphous alloys contributes to develop larger specific area materials compared to nickel alloys. For example, Ni-S-Mn based alloy showed an improved performance and better stability for the Hydrogen evolution reaction. The catalytic activity of Ni-S compound decays due to leaching induced by the presence of sulfur.

5 Influence of Process Conditions on Gas Purity in Alkaline Water Electrolysis

Gas purity is an important criterion of alkaline water electrolysis (Jang et al. 2021). The produced hydrogen typically has a purity higher than 99.9 vol.% (without additional purification), at the contrary the gas purity of oxygen is in the range of 99.0–99.5 vol.%. As both product gases can form explosive mixtures in the range of approximately 4–96 vol.% of foreign gas contamination, technical safety limits for an emergency shutdown of the whole electrolyzer system are at a level of 2 vol.%. Therefore, the product gas impurity needs to be below this limit during operation to ensure continuous production. The current densities are in the range from 0.05 to 0.7 Acm^{-2} and the system pressures range from 1 to 20 bar.

While the gas impurities with separated electrolyte cycles are below 0.7 vol.% for all tested current densities and pressure levels, mixing of the electrolyte cycles increases the gas impurity significantly. In addition, two similarities can be seen: the gas impurity lowers with increasing current density and increases at higher pressure levels. Both effects are physically explainable: while the contamination flux stays constant with varying current densities, the amount of produced gas becomes lower in a linear relationship. Hence, at a higher current density, the contamination is more diluted than at a lower current density. Therefore, the operation in the part-load range is more critical due to the higher gas impurity.

The amount of dissolved product gas increases with pressure; thus, high concentration gradients for the diffusion through the separator material are available, and more dissolved foreign gas reaches the other half-cell when mixing. However, operation at slightly elevated pressures is favorable, as the costly first mechanical compression level can be avoided by the direct compression inside the electrolyzer system. With mixed electrolyte cycles, the gas impurity reaches critical values even at higher current densities during pressurized operation. While at atmospheric pressure, the gas impurity is only at a current density of 0.05 Acm^{-2}, slightly above the safety limit of 2 vol.% H_2 in O_2, this limit is already reached at 0.5 Acm^{-2} for a system pressure of 10 bar. At 20 bar, no sufficient gas purity could be measured, as even a current density of 0.7 Acm^{-2} results in a gas impurity of 2.5 vol.%.

Precise knowledge of the resulting gas purity is important to prevent safety shutdown when the electrolyzer is dynamically operated using a renewable energy source. Not only the cell voltage of an electrolyzer but also the purity of the gaseous products is of major interest as limits of operation range of the plant. In literature the acceptable part-load operation of an industrial alkaline water electrolyzer is typically given with 10–40% of the nominal load.

Below this working range the oxygen quality is significantly reduced through contamination of hydrogen and vice versa. One source of this contamination is the diffusion of the product gases through the separator. This led to a gas quality degradation, but also to an electrolyzer's electrical efficiency decrease due to the reaction between oxygen and hydrogen (at the cathode) forming back the water. The

second source of contamination is the dissolution of gas in the electrolyte. After saturation with corresponding gas, dissolved gas is able to outgas in the opposite gas separator because the anolyte and catholyte cycle are continuously mixed to compensate the difference in electrolyte concentration caused by the electrode reactions.

This operation mode may lead to safety issues as the lower (LEL) and upper explosion limits (UEL) of H_2/O_2 mixtures are given with 3.8 mol % and 95.4 mol % H_2 at atmospheric pressure and 80 °C. Consequently, industrial electrolyzers must be shut down as soon as a content of 2 vol% foreign gas is measured in the exhaust, which is about 50% of LEL or UEL. The contamination of the product gases is important when the electrolyzer is operated at low current densities and therefore low gas production rates because the mentioned phenomena are mostly independent of the electrolyzer load. When the electrolyzer is part of a power-to-gas plant and coupled with a renewable energy source an operation in the part-load region is conceivable.

It was reported that the daily operation of an alkaline electrolyzer powered with solar energy was mainly restricted by the oxygen purity at low global insolation and the resulting low current density. To reduce the anodic hydrogen content a possibility is represented by a Pt-catalyzed combustion of hydrogen and oxygen back to water by a gas recombiner. Another option is an optimized lye circulation control to keep the gas impurities low. Unfortunately, only the qualitative description of this effect was described; the quantitative influence of the electrolyte flow rate on the gas purity was not published. Further work was done to measure the anodic hydrogen content at specific electrolyte temperatures and flow rates with different separators.

The gas crossover in alkaline water electrolysis is mainly caused by two phenomena: gas dissolution in the electrolyte and diffusion through the separator.

The solubility of gases in electrolyte solutions needs to be known for gas-liquid transfer estimations. Unfortunately, data for the solubility of hydrogen and oxygen in concentrated potassium hydroxide solution under electrolysis conditions is scarce. Most published papers only provide values for the solubility at room temperature or slightly above.

To estimate the amounts of dissolved gases under electrolysis conditions we propose a method for calculation. It is well known that gas solubility mostly decreases with increasing salt concentration. This behavior can be described by applying the Setchenov relation, which is suitable for electrolyte concentrations of about cs = 2 mol L^{-1} − 5 mol L^{-1}. At even higher salt concentrations the gas solubility may be underestimated:

$$\log\left(\frac{c_{i,0}}{c_{i,s}}\right) = Kc_s$$

The variables $c_{i,0}$, $c_{i,s}$ and c_s describe the gas solubility in pure water, in the salt solution and the molar concentration of the salt solution, respectively. The parameter K is the so called Setchenov constant. It is specific to the dissolved gas and the salt and slightly dependent on temperature:

Table 2 Model parameters. The hT,i value for H2 and O2 is valid from 273 to 353 K, while the value for N2 is valid from 278 to 345 K

Ion	h_i (m^3kmol^{-1})	Gas	$h_{G,i,0}$ (m^3kmol^{-1})	$h_{T,i}$ (m^3kmol^{-1})
Na^+	0.1143	H_2	−0.0218	−0.000299
K^+	0.0922	O_2	0	−0.000334
OH^-	0.0838	N_2	−0.001	−0.000605

Table 3 Model parameters for Henry coefficients of H2, O2 and N2 in pure H2O

Gas	A	B	C	D	E
H_2	−0.1233	−0.1366	0.02155	−0.2368	0.8249
O_2	−0.0005943	−0.1470	−0.0512	−0.1076	0.8447
N_2	−0.1021	−0.1482	−0.019	−0.03741	0.8510

$$K = \sum (h_i + h_{G,i})n_i$$

The parameter h_i is a salt specific constant; $h_{G,i}$ takes into account the dissolved gas; n_i denotes the index of the ion in the formula of the salt, which is simply multiplied with the sum of the salt and gas specific constant. For K^+ and OH^- n_i is unity for both ions. The temperature dependence of the gas-specific constant $h_{G,i}$ is assumed to be a linear function of the temperature in the range from 273 to 363 K:

$$h_{G,i} = h_{G,i,0} + h_{T,i}(T - 298.15K)$$

The necessary parameter values for the calculation of O_2, H_2 and N_2 solubility in concentrated NaOH or KOH are given in Table 2.

For calculation of the solubility in pure water $c_{i,0}$ the empirical relationship by is proposed, which relates the Henry coefficient of the gases H_i (in atm) with the temperature T (in K) of the solvent. Its validity is given in the temperature range from 273 to 647 K:

$$A\left(log\,\overline{H}_1\right)^2 + B\left(\frac{1}{T}\right)^2 + C\left(log\,\overline{H}_1\right)\left(\frac{1}{T}\right) + D\left(log\left(\overline{H}_1\right)\right)E + \left(\frac{1}{T}\right) - 1 = 0$$

This equation is only applicable if H_i is inserted as $H_i = H_i \cdot 10^{-4}$ and $1/T = 1/T \cdot 10^3$. The needed constants are given in Table 3

The calculation of the gas solubility in pure water is then performed with the following equation which considers the solvent density ρ, the molar mass M and the partial pressure of the gas p_i above the solvent:

$$c_{i,0} = \frac{\rho}{M} \frac{p_i}{101325\ PaH_i}$$

Fig. 16 Comparison of measured and modelled hydrogen and oxygen solubility as a function of the KOH concentration at a gas partial pressure of 101,325 Pa
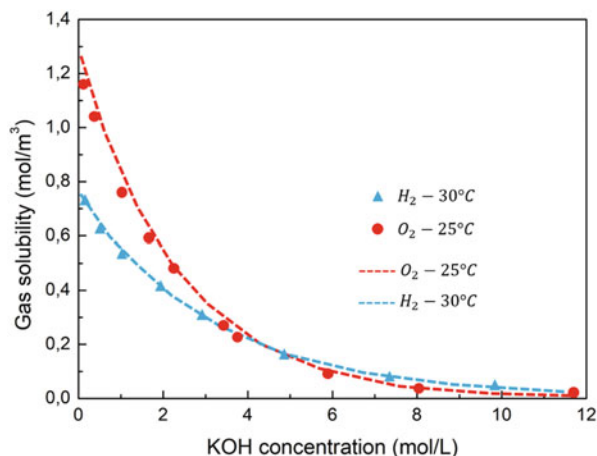
The usually applied electrolyte in alkaline water electrolysis is a 30 wt% KOH solution, which corresponds to a molar concentration of about 6.9 mol L^{-1}. If a typical electrolysis temperature of about 80 °C and atmospheric pressure $p_{abs} = p_{H2} = 101,325$ Pa is assumed we provide a H2 concentration of $c_{H2,0} = 0.753$ mol m^{-3} in pure water and $c_{H2,KOH} = 0.155$ mol m^{-3} in 6.9 mol L^{-1} KOH, respectively.

Figure 16 shows a comparison of measured and modelled gas solubilities as a function of the potassium hydroxide concentration.

As already mentioned, the hydrogen concentration is overestimated by the model and reveals a solubility increase with growing temperature although a decreasing saturation concentration was measured. The oxygen concentration is underestimated in the low temperature region but can be predicted with good accuracy, especially at higher temperature.

The separator in an electrochemical cell has two main functions: it is necessary to prevent any short circuits between the electrodes and to avoid the mixing of hydrogen and oxygen. Therefore, the separator needs to be stable in the highly alkaline conditions of an alkaline electrolyzer. Furthermore, the separator should be very conductive for the transport of OH^- ions between anode and cathode, so that low voltage drops are caused.

The conductivity of a separator depends on its porosity and tortuosity as the current passes through the liquid electrolyte present in the pores. The gases dissolved in the electrolyte can diffuse through the pores of the separator and contaminate the evolved gas of the opposite half-cell. A small reduction of the diffusion through the separator can be achieved by higher electrolyte flow rates, which increase the nucleation growth rate of the gas bubbles. It's largely demonstrated that the electrolyte is supersaturated with either oxygen or hydrogen in the vicinity of the electrode.

In case of a zero-gap cell setup this supersaturation should be responsible for the concentration gradient for gas diffusion across the separator. The gas crossover through separator is commonly described using Fick's law:

$$J_{i,cross} = \frac{D_{i,j,eff}}{d_{Sep}} \left(c_i^{cat} - c_i^{ano} \right)$$

If the assumption is made that only dissolved gas can crossover and no pressure gradient is present, $J_{i,cross}$ describes the overall molar flux density through the separator. In Equation c_i denotes the cathodic and anodic concentration of dissolved gas i, whereas d_{Sep} is the separator thickness and $D_{i,j,eff}$ the effective gas diffusion coefficient in the separator. As the separator is filled with electrolyte the diffusion coefficients $D_{i,j}$ of the gases in the lye need to be known for the calculation of the effective diffusion coefficient.

These diffusion coefficients make it possible to estimate the effective diffusion coefficient in the separator in analogy to the diffusion in porous media or membranes. The formula is commonly given as:

$$D_{i,j,eff} = \frac{\varepsilon D_{i,j}}{\tau}$$

Here, ε and τ describe the separator porosity and tortuosity, respectively.

6   Conclusions

Alkaline water electrolysis combined with renewable energy can be integrated into the distributed energy system by producing hydrogen for end use and as an energy storage media. Compared to the other major methods for hydrogen production, alkaline water electrolysis is simple but currently less efficient. The challenges for widespread use of water electrolysis are also the durability and safety.

These disadvantages require further research and development effort.

This chapter has examined the fundamentals of the water electrolysis and compared the performance of various water electrolysis designs as well as introduced several emergent water electrolysis technologies.

Based on the thermodynamic and kinetic analyses of the alkaline water electrolysis, several resistances hindering the efficiency of the alkaline water electrolysis process have been identified. These include resistances due to bubbles, reaction activation energy, ionic transfer, and electrical resistances in the circuit. The bubble resistance is suggested to be reduced by electrode modification and electrolyte additives. Reaction overpotential can be optimized by electrode material selection and preparation. Also, transport-related resistances such as bubble resistance and electrolyte resistance can be reduced by improving mass transport such as bubble elimination by electrolyte circulation. By identifying the resistances causing extra energy losses, this study opens the opportunities to minimize the energy input especially at high current density.

Practical considerations of industrial electrochemical engineering and electrolyser development led to the conclusion that the alkaline water electrolysis is still a better means for hydrogen production. Further R&D efforts to improve the efficiency are needed to widespread the application of the alkaline water electrolysis like developing electrocatalysts to significantly reduce electrochemical reaction resistance, electrolyte additives to facilitate the electron transfer and ionic transfer and to reduce electrode surface tension, electrode surface profile modifications and surface coatings, and more importantly, managing the gas bubble resistances.

References

Dai L (2017) Carbon-based catalysts for metal-free electrocatalysis. Curr Opin Electrochem 4(1): 18–25. https://doi.org/10.1016/j.coelec.2017.06.004

Haug P, Koj M, Turek T (2017) Influence of process conditions on gas purity in alkaline water electrolysis. Int J Hydrog Energy 42(15):9406–9418. https://doi.org/10.1016/j.ijhydene.2016.12.111

Haverkort JW, Rajaei H (2021) Voltage losses in zero-gap alkaline water electrolysis. J Power Sources 497:229864. https://doi.org/10.1016/j.jpowsour.2021.229864

Hu C, Dai L (2016) Carbon-based metal-free catalysts for electrocatalysis beyond the ORR. Angew Chem Int Ed 55:11736–11758. https://doi.org/10.1002/anie.201509982

Jang D, Choi W, Cho H-S et al (2021) Numerical modeling and analysis of the temperature effect on the performance of an alkaline water electrolysis system. J Power Sources 506:230106. https://doi.org/10.1016/j.jpowsour.2021.230106

Koponen J, Kosonen A, Ruuskanen V, Huoman K, Niemelä M, Ahola J (2017) Control and energy efficiency of PEM water electrolyzers in renewable energy systems. Int J Hydrog Energy 42(50):29648–29660. https://doi.org/10.1016/j.ijhydene.2017.10.056

Lavorante MJ, Reynoso CY, Franco JI (2015) Water electrolysis with Zirfon® as separator and NaOH as electrolyte. Desalin Water Treat 56(13):3647–3653. https://doi.org/10.1080/19443994.2014.974214

Milewski J, Guandalini G, Campanari S (2014) Modeling an alkaline electrolysis cell through reduced-order and loss-estimate approaches. J Power Sources 269:203–211. https://doi.org/10.1016/j.jpowsour.2014.06.138

Moussallem I, Jörissen J, Kunz U et al (2008) Chlor-alkali electrolysis with oxygen depolarized cathodes: history, present status and future prospects. J Appl Electrochem 38:1177–1194. https://doi.org/10.1007/s10800-008-9556-9

Schalenbach M, Carmo M, Fritz DL (2014) Pressurized PEM water electrolysis: efficiency and gas crossover. Int J Hydrog Energy 38(35):14921–14933. https://doi.org/10.1016/j.ijhydene.2013.09.013

Schmidt O, Gambhir A, Staffell I, Hawkes A, Nelson J, Few S (2017) Future cost and performance of water electrolysis: an expert elicitation study. Int J Hydrog Energy 42(52):30470–30492. https://doi.org/10.1016/j.ijhydene.2017.10.045

Siracusano S, Van Dijk N, Merlo L et al (2018) Degradation issues of PEM electrolysis MEAs. Renew Energ 123:52–57. https://doi.org/10.1016/j.renene.2018.02.024

Swiegers GF, Hoang AL, Hodges A (2021) Current status of membraneless water electrolysis cells. Curr Opin Electrochem 32:100881. https://doi.org/10.1016/j.coelec.2021.100881

Ulleberg Ø (2003) Modeling of advanced alkaline electrolyzers: a system simulation approach. Int J Hydrog Energy 28(1):21–33. https://doi.org/10.1016/S0360-3199(02)00033-2

Ursua A, Gandía LM, Sanchis P (2012) Hydrogen production from water electrolysis: current status and future trends. Proc IEEE 100(2):410–426. https://doi.org/10.1109/JPROC.2011.2156750

Wang S, Lu A, Zhong CJ (2021) Hydrogen production from water electrolysis: role of catalysts. Nano Converg 8:4. https://doi.org/10.1186/s40580-021-00254-x

Zeng K, Zhang D (2014) Evaluating the effect of surface modifications on Ni based electrodes for alkaline water electrolysis. Fuel 116:692–698. https://doi.org/10.1016/j.fuel.2013.08.070

Zhang F, Yu L, Wu L et al (2021) Rational design of oxygen evolution reaction catalysts for seawater electrolysis. Trends Chem 3(6):485–498. https://doi.org/10.1016/j.trechm.2021.03.003

Zhou H, Yu F, Zhu Q (2018) Water splitting by electrolysis at high current densities under 1.6 volts. Energy Environ Sci 11:2858–2864. https://doi.org/10.1039/C8EE00927A

Proton Exchange Membrane Water Electrolysis

1 Introduction

The polymer electrolyte membrane, also known as proton exchange membrane or solid polymer electrolyte (SPE) membrane electrolysis uses a perfluoro-sulfonic acid polymer which selectively allows the conduction of protons through it, while separating the produced gasses and electrically insulating the electrodes (Bessarabov et al. 2015).

The reactant liquid water is fed to the anode catalyst with an applied voltage over the cell. The supplied water is oxidized to oxygen, protons and electrons. This anode half reaction is called the oxygen evolution reaction (OER).

The protons are transported through the proton exchange membrane to the cathode side, while the electrons are transported through the external circuit to the cathode, where they recombine with the protons to produce gaseous hydrogen (Millet et al. 2011).

The PEM electrolysis process is a low temperature technology as it operates best at temperature between 20 °C and below the boiling point of water, typically at 80 °C. The kinetics of the electrode reaction is enhanced by increasing the temperature, but at temperatures close to the boiling point of water, the components of the PEM electrolysis cell become unstable (Grigoriev et al. 2010). Nafion® which is commonly used as the polymer electrolyte for example starts to lose its mechanical stability at such temperatures and the metal components become susceptible to electrochemical corrosion. State-of-the-art PEM electrolysis cells operate typically at current densities of 0.5–2.5 Acm^{-2}, achieving corresponding cell voltage of 1.7–2.1 V.

Typical operating pressures range from atmospheric up to 5 MPa, with dry hydrogen production efficiency of up to 99.99%. Higher pressure operating systems up to 20 MPa are however, being considered to reduce the balance of plant cost, especially in applications where the hydrogen is stored under pressure (Grigoriev et al. 2011).

   Although the alkaline water electrolysis is the more established technology, PEM water electrolysis has some distinct advantages over its older counterpart, such as:

- PEM electrolysis cells can operate at much higher current densities, thereby, reducing
- the hydrogen production costs.
- The cell design is much simpler and compact, since only pure water is fed into the cell.
- Because of its low thermal mass, PEM electrolysis cells can respond much quickly to power in-put, which makes it more suitable for use with a wide range of power sources.
- The thin polymer electrolyte membrane allows for shorter pathway for proton transport, thus lowering the ohmic losses.
- Gas purity from the PEM electrolysis is much higher because of low gas crossover and no mixture of gasses with liquid electrolyte, as is with the alkaline cell.
- The compactness of the PEM cell makes it suitable for high pressure operations, to reduce system and hydrogen production costs.

Despite these advantages, there are as well certain drawbacks facing PEM water electrolysis, compared with other water electrolysis technologies.

   The membrane electrode assembly (MEA) consisting of the membrane and electrodes is at the center of the cell, symmetrically separating it into two equal compartments; the anode (oxygen production) and the cathode (hydrogen production) compartments (Ito et al. 2011).

   The MEA is made up of the proton conducting membrane, PEM, sandwiched between the anode and the cathode electrodes. The membrane is only proton conducting while the electrodes are electron conducting. The MEA has three major functions:

1. enable the transfer of protons from the anode to the cathode side;
2. prevent the crossover of produced gasses from one compartment to the other, hence ensuring the production of high purity gases;
3. provide electrical isolation.

Typically, Perfluoro-sulfonic acid (PFSA) such as Nafion® from DuPont is the proton conducting membrane used in PEM water electrolysis. A good membrane must have high proton conductivity and low gas permeability.

   The electrodes consist of a mixture of porous catalysts and ionomer of the membrane and it is where the electrochemical reactions occur. Precious metals are typically used as catalysts to give to electrodes the ability to conduct both electrons and protons. In state-of-the-art MEAs, the electrodes are directly coated on the membrane and they have catalyst loading of 1–2 mg/cm^2 on the anode and ~1 mg/cm^2 on the cathode (Burdzik et al. 2018).

   In a PEM water electrolysis cell or stack, the bipolar plate is an electrically conducting sheet that physically separates adjacent cells while at the same time electrically connecting them. It is called a "bipolar" plate because it serves as the

anode in the one cell and as the cathode of the adjacent cell (Langemann et al. 2015). Hence, the use of the term "bipolar plate" becomes ambiguous in a single cell since its bipolar function becomes redundant. In a single cell the plate serves only the function of water distribution and gas removal, so it is usually referred to as the end plate (not to be confused with the component, end plate described below which in this case is traditionally called the pressure plate). To reliably serve the functions for which it is designed, the bipolar plates have to demonstrate high electrical conductivity, high mechanical and electrochemical stability and impermeability to gasses. For this reason, the use of stable metals such as titanium is common in PEM water electrolysis (Bystron et al. 2018).

The end plate is one of the main components of a PEM electrolyzer. Conventionally, stack (cell) components are assembled between two end plates, which serve as a supporting structure for the unit cells. Therefore, the end plate bears the entire mechanical load applied on the stack (cell) through clamping bolts and provides passage for reactant water and product gasses in and out of the stack (cell) respectively. The major role of the end plate is to provide a uniform and optimal pressure distribution between various components of the stack (cell). Through the distribution of pressure between sealing rings and relevant stack (cell) components (external stack), water and gas tightness of the stack is achieved. By the distribution of contact pressure between the bipolar plates and current collectors, as well as between the current collectors and the MEA (internal stack), contact resistance between them can be reduced, and as a result improved performance and efficiency of the electrolyser stack (cell).

Non-uniformly distributed contact pressure in the internal stack (cell) may result in a non-uniform current density and heat distribution which may cause hot spots formation and ultimately lead to the failure of the MEA. Therefore, the end plate design also has a direct effect on the lifetime of an electrolysis stack (cell). While large mechanical pressure through the end plates is necessary for tightness and contact resistance minimization of the stack, over-compressing of the stack may result in the damage of stack components. Excess compression affects the porosity and permeability of the porous transport layer (PTL), and consequently, mass transport in the PTL and the catalyst layer (Nouri-Khorasani et al. 2017). Excess compression may also lead to failure of the sealing rings or fracture of other stack components if their design tolerances were not tightly chosen. As a result, the clamping pressure applied on the end plates and the design of the end plate must be optimized to achieve the requirement for low contact resistance while avoiding mass transport limitation and failure or fracture of some major components.

The porous transport layer is also sometimes referred to as current collector. In the PEM electrolysis cell, it is placed between the bipolar (end) plate and the MEA in both the anode and the cathode half cells. The function of the porous transport layer is two-fold:

1. To transport electrical current from the bipolar (end) plate and uniformly distribute it to the active layer (electrode surface) where the water splitting reaction occurs;

2. Transport of produced gasses from the electrodes to the flow channels of the bipolar (end plates) to be evacuated from the cell at the manifolds.

It is therefore, primordial that the PTL has a high electrical conductivity and gas permeability, high mechanical and electrochemical stability (corrosion), good surface smoothness, as well as optimal porosity and microstructure to be able to perform its functions. Although large pores will facilitate the transport of water to and removal of gases away from the active area, this will also lead to an increase in the resistance of electrical current transport through the PTL and compromise the interfacial contact between the PTL and the electrode and the PTL and the bipolar plate. An optimization of the surface property, porosity, and microstructure of the PTL is therefore critical.

Despite the many advantages that the PEM water electrolysis technology enjoys over other water electrolysis technologies, it still has to overcome certain challenges in order for the technology to be commercially viable. The current trend in research and development efforts in PEM water electrolysis is geared towards attaining targets that are set to address these challenges.

The lifetime issues of a PEM water electrolyzer can be categorized under durability and reliability concerns. Durability issues may lead to: reduction in cell performance, which can be caused by many factors such as, increase in ohmic resistance when cations released from a corroded metal component blocks the electrochemical active area; low purity of produced gasses which can be a result of gas crossover due to membrane thinning. These two effects reduce the energetic and faradaic efficiency of PEM water electrolysis. While these durability issues may not immediately cause the shut-down of the electrolyzer, continuous degradation may eventually lead to reliability concerns (Frensch et al. 2019).

Unlike durability issues, reliability issues of a PEM electrolyzer are those that will lead to the immediate shut down of the plant, such as safety and component failure. Safety issues typically arise when the gas-cross permeation is so high that the hydrogen content in the anode half-cell surpasses the tolerable 5% threshold to form explosive hydrogen – oxygen gas mixture.

Component failures are mostly mechanical and the cell component most vulnerable to failure is the thin MEA, as it can easily get punctured. The metal components such as the bipolar plate and the PTLs (current collectors) are also susceptible to mechanical failure due to embrittlement when exposed to hydrogen for long periods and at high pressures.

The voltage efficiency is the ratio of the thermo-neutral voltage to the actual cell polarization at given operating conditions. Hence, the efficiency is compromised because of the buildup of irreversible degradation effects within the cell, viz; activation and ohmic overvoltage, as well as overpotentials due to mass transport. Therefore, to improve the voltage efficiency, research trend is focused on:

1. Highly reactive electrocatalysts with high exchange current densities;
2. Thinner membranes with high proton conductivities;

3. Metallic bipolar plates and PTLs with low resistivity (sometimes, coated with inert metals);
4. Mitigating the mass transport overpotential by optimizing the PTL (Schmidt et al. 2020).

2 Proton Exchange Membrane Water Electrolysis

PEMEL water electrolyzers are categorized into acidic PEMELs and alkaline PEMELs, but only the acidic PEM variant is widely commercially available (Schalenbach et al. 2016). From this point on, the designation 'PEMEL water electrolysis' refers to the commercial, traditional acidic PEMEL variant, and the alkaline PEMEL is referred to as anion exchange membrane (AEM) water electrolysis.

Given the overall water electrolysis reaction:

$$2H_2O \rightarrow 2H_2 + O_2$$
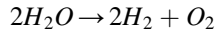
The reactions at the two electrodes in acidic media are:

$$2H^+ + 2e^- \rightarrow H_2 \quad @cathode$$

$$H_2O \rightarrow 2H^+ + \frac{1}{2}O_2 + 2e^- \quad @anode$$

while in alkaline or neutral media:

$$2H_2O + 2e^- \rightarrow H_2 + 2OH^- \quad @cathode$$

$$2OH^- \rightarrow H_2O + \frac{1}{2}O_2 + 2e^- \quad @anode$$
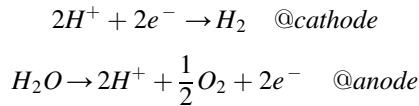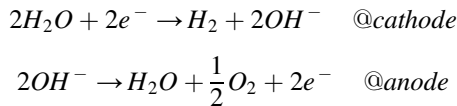
The PEMEL water electrolysis employs a solid polymer (sulphonated fluoropolymers) electrolyte that is a thin (250 μm thickness) proton-exchange membrane. The schematic of the process is given in Fig. 1

Water is supplied to the anode, where water is first decomposed with a sufficient electric potential to oxygen gas. H^+ protons pass through the polymer membrane, and at the cathode combine with electrons to form hydrogen gas. Iridium and platinum are employed as catalyst at anode and cathode respectively. The current collector is made of titanium to increase the lifetime of the cell (Carmo et al. 2013).

Even though the thermodynamic potential for water electrolysis is 1.23 V, the kinetics of the reaction restricts the reaction to happen at this potential. An extra potential called over potential must be applied for the reaction to occur (Fig. 2).
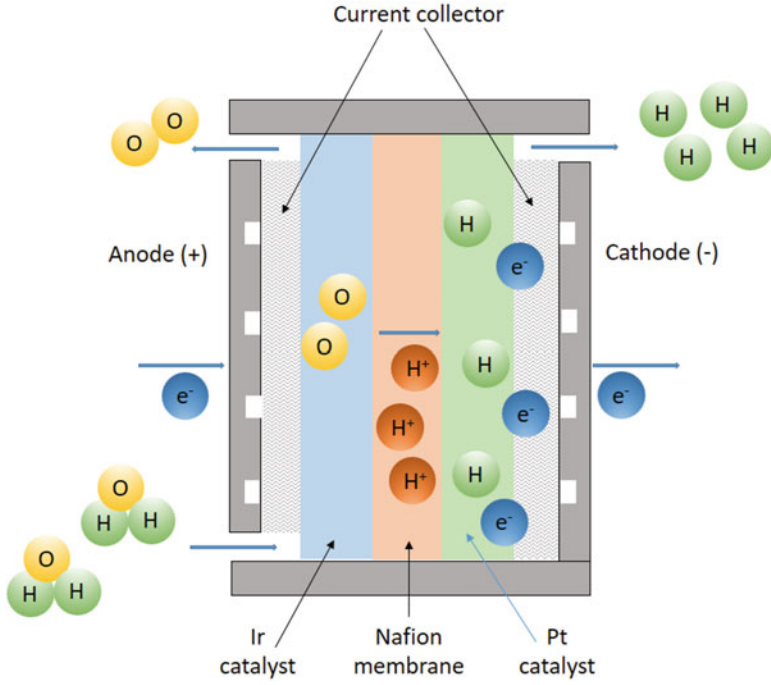
Fig. 1 PEMEL schematic
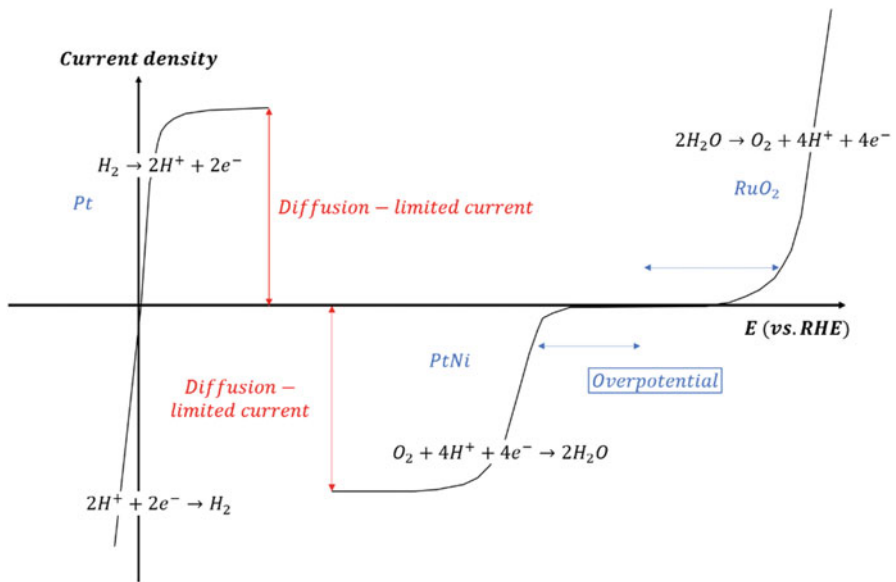
Fig. 2 Schematic of redox reaction of water

The over potential depends on the catalytic material used. i.e. electrocatalyst has to be chosen in such a way to give low over potential. Both hydrogen evolution reaction (HER) and oxygen evolution reaction (OER) requires catalyst for the respective reaction to occur.

Since HER is faster than OER, most of the over-potential loss in PEM electrolyzer occurs on the anode side.

2.1 Hydrogen Evolution Reaction

Hydrogen evolution/oxidation is one of the most studied electrochemical reactions.

Hydrogen evolution reaction is kinetically feasible reaction compared to OER. The suitable catalyst for HER is also derived based on the bond strength between the catalyst and chemisorbed H (S-H).

HER takes place at the cathode, in acidic media the evolution follows the equations:

$$H^+ + * + e^- \rightarrow H_{ads} \quad (Volmer\ reaction)$$

$$H^+ + H_{ads} + e^- \rightarrow H_2 + * \quad (Heyrovsky\ reaction)$$

$$2H_{ads} \rightarrow H_2 \quad (Tafel\ reaction)$$
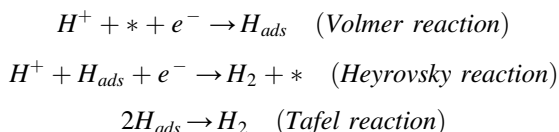
Here, H_{ads} designates the hydrogen atoms adsorbed on the electrode surface; H^+: the hydrated proton; H_2: the hydrogen molecule; e^-: the electron.

HER is a classical two electrons process and can evolve through the Volmer-Heyrovsky or the Volmer-Tafel path. The HER reaction only has one catalytic intermediate H* (where H* denotes a hydrogen atom adsorbed at the electrode surface). Consequently, the rate of the overall reaction is largely determined by the free energy of hydrogen adsorption. Volmer reaction is the limiting step in the case of weak hydrogen binding on the surface. In the case of strong binding, Heyrovsky-Tafel reaction is the limiting step. As a matter of fact, there is an optimum in the hydrogen adsorption energy. It is possible to calculate the three reactions rates as a function of the electrode potential E_{SHE}:

$$v_1 = k_1^0 [H^+](1 - \theta_H) \exp\left(\frac{-\alpha F E_{SHE} - \beta \Delta G_H}{RT}\right)$$

$$v_{-1} = k_{-1}^0 (\theta_H) \exp \frac{(1 - \alpha) F E_{SHE} + (1 - \beta) \Delta G_H}{RT}$$

$$v_2 = k_2^0 [H^+](\theta_H) \exp\left(\frac{\alpha F E_{SHE} + (1 - \beta) \Delta G_H}{RT}\right)$$

$$v_{-2} = k_{-2}^0 p_{H_2} (1 - \theta_H) \exp\left(\frac{(1 - \alpha) F E_{SHE} - \beta \Delta G_H}{RT}\right)$$

$$v_3 = k_3^0 (\theta_H^2) \exp\left(\frac{2(1-\beta)\Delta G_H}{RT}\right)$$

$$v_{-3} = k_{-3}^0 (1-\theta_H)^2 p_{H_2} \exp\left(-\frac{2\beta\Delta G_H}{RT}\right)$$

where θ_H is the coverage of the adsorbed hydrogen; ΔG_H is the free energy of adsorbed hydrogen atoms.

k_1^0, k_{-1}^0, k_2^0, k_{-2}^0 the positive and inverse rate constants of the equilibrium potentials for reactions 1 and 2; F: Faraday constant; R: Boltzmann constant; T: temperature; α: the corresponding transfer coefficient of a Butler-Voltter-type kinetic for the electrochemical steps and β: variations in the rate constant of the Brønsted-Evans-Polanyi coefficient.

The total current density of a Volmer-Heyrovsky (VH) mechanism can be calculated as:

$$j = \frac{-2Fk_2^0[H^+]\exp\left(\frac{-\alpha FE_{SHE}+(1-\beta)\Delta G_H}{RT}\right)}{1 + \left(\frac{k_{-1}^0}{k_1^0[H^+]}\right)\exp\left(\frac{FE_{SHE}+\Delta G_H}{RT}\right) + \frac{k_2^0}{k_1^0}\exp\left(\frac{\Delta G_H}{RT}\right)}$$

and Volmer-Tafel (VT) mechanism is calculated as:

$$j = -2Fk_3^0\left(\frac{\exp\left(\frac{(1-\beta)\Delta G_H}{RT}\right)}{1 + \frac{k_{-1}^0}{k_1^0[H^+]}\exp\left(\frac{FE_{SHE}+\Delta G_H}{RT}\right)}\right)^2$$

When the rates for these reactions are expressed as a function of the reversible hydrogen electrode (E_{RHE}), the following shows the expression for the VH mechanism and VT mechanism:

$$j = -\frac{2Fk_2^0[H^+]^{1-\alpha}\exp\left(\frac{-\alpha FE_{RHE}+(1-\beta)\Delta G_H}{RT}\right)}{1 + k_{-1}^0\exp\left(\frac{FE_{RHE}+\Delta G_H}{RT}\right) + \frac{k_2^0}{k_1^0}\exp\left(\frac{\Delta G_H}{RT}\right)}$$

$$j = -2Fk_3^0\left(\frac{\exp\left(\frac{(1-\beta)\Delta G_H}{RT}\right)}{1 + \frac{k_{-1}^0}{k_1^0}\exp\left(\frac{FE_{RHE}+\Delta G_H}{RT}\right)}\right)^2$$

These relationships describe a volcano behavior of the current as a function of the binding energy of hydrogen (Fig. 3).

If ΔG_H is too positive, the H_{ads} bonds strongly with the electrode surface, making the initial Volmer step easy, but the subsequent Tafel/Heyrovsky reaction cannot proceed. In reverse, if ΔG_H is too negative, H_{ads} has a weak interaction with the electrode surface, resulting in an inhibited Volmer reaction. The expressions for the

Fig. 3 Activity volcano for the VH and VT routes
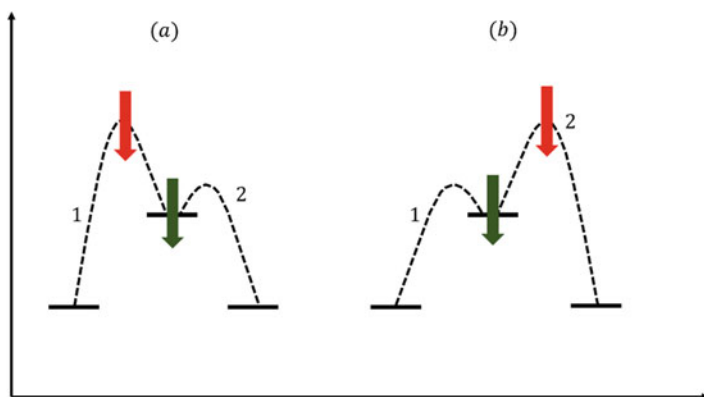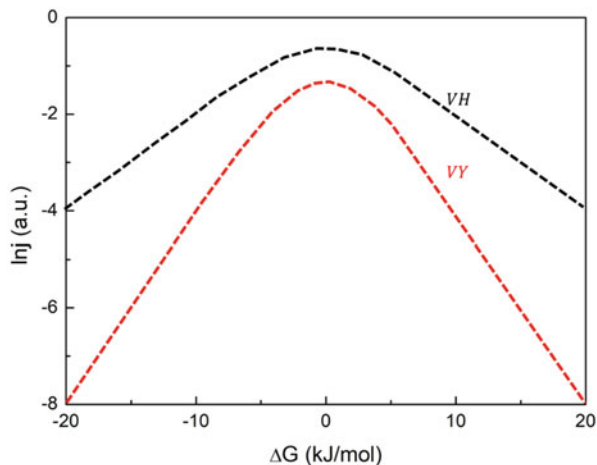
Fig. 4 Potential free energy surfaces for the two-step reactions

VT mechanism and VH mechanism show that: the rate-determining step is independent on ΔG_H; ΔG_H is a constant independent of coverage; and the acid/base feature (the charged nature) of the intermediates featuring in so many pathways relevant to molecular catalysts is what makes these pathways so sensitive to solution pH (Liu et al. 2022).

So, it is necessary to optimize the free energy to increase the catalysis potential; anyway, this issue is complex because of the different steps through which the reaction can evolve.

By considering Fig. 4, this is the case in which $\Delta G_H > 0$.

In all the cases, the rate-determining step (RDS) needs to overcome the highest reaction energy. Considering the VH mechanism, we have two energy landscapes: (a) $k_2 \gg k_1$ and (b) $k_1 \gg k_2$. So, v_1 is as the rate-determining step in the former

case, and v_2 is the RDS in the latter. Following the classical chemical kinetics, it is necessary to work on step one for the latter and on step 2 for the former. Anyway, the best way is to decrease the energy of the intermediate state (green arrow); but, this is thermodynamically unfavorable and is known as "thermodynamic bottleneck." The rate-determining step is the "kinetic bottleneck".

The "model" can be simplified when the strategy is applied to decrease the thermodynamic bottleneck rather than the kinetic bottleneck. The classic way is to obtain the equilibrium potentials or, equivalently, the equilibrium constants, corresponding to each reaction step. For the Volmer-Heyrovsky mechanism, the suitably defined "standard" equilibrium potentials are showed in:

$$E_1^{eq} = -\frac{\Delta G_H}{F}$$

$$E_2^{eq} = \frac{\Delta G_H}{F}$$

If the free energy is positive, reaction 1 is thermodynamically unfavorable. So, a minimum potential corresponding to E_1^{eq} must be applied to allow the occurring of the reaction.

Now, to estimate the HER catalytic performance, it is fundamental to evaluate the total electrode activity. A general formula to evaluate the catalytic current density is given by:

$$j(\eta) = \frac{i(\eta)}{A}\left[\sum_{x=1}^{S} TOF_x(\eta)\right]\cdot\frac{\eta F}{AN_A} = S\cdot\overline{TOF}(\eta)\cdot\frac{nF}{AN_A}$$

Where j is the catalytic current density $\left[\frac{A}{cm_{electrode}^2}\right]$; I is the catalytic current [A]; η is the overpotential [V]; A is the electrode active area $cm_{electrode}^2$; S is the number of active surface sites; n is the number of transferred electrons (2); F: Faraday constant; N_A is Avogadro's number; TOF_x in the turnover frequency of the sites; $\overline{TOF}$ is the average turnover frequency of all sites.

2.2 Oxygen Evolution Reaction

The oxygen evolution reaction (OER) is a counter electrode reaction occurring in electrolyzers (Mayousse et al. 2011). The OER is more challenging because the OER is a four electron-proton reaction way, while the HER is a two electron-transfer reaction, and, consequently, the OER requires a higher energy (higher overpotential) to overcome the kinetic barrier of the OER to occur. In the OER reaction process, it requires the distribution of four redox processes over a narrow potential range, the coupling of multiple protons and electron transfers, and the formation of two oxygen-oxygen bonds.

Electrocatalytic kinetics are fundamentally related to the charge transfer during the reactions, in a general way:

$$O + ne^- \leftrightarrow R$$
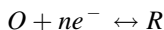
So, the reactions kinetics are favored by catalysts that easily allow the adsorption of reactant on the electrode surface. Generally, the OER activity of the catalysts are measured through overpotential, exchange current density, and Tafel slope. Their analysis provides information about the mechanisms of electrochemical reactions (Kaya and Demir 2017).

First of all, the overpotential is the crucial factor describing the OER performances of the electrocatalysts. As previously mentioned, the overpotential is higher with respect to the equilibrium one because of the electrode kinetic barrier, so, following the Nerst equation:

$$E = E^{0/} + \frac{RT}{nF} In \frac{C_o}{C_R}$$

E is the applied potential for driving a reaction carried out, $E^{0/}$ is the formal potential of the overall reaction, T refers to absolute temperature, R is the universal gas constant, F is the Faraday constant, n is the number of transferred electrons in the reaction, and C_O and C_R are the concentrations of oxidized and reduced reagents. The overpotential will be:

$$\eta = E - E_{eq}$$

The other crucial factor is represented by the current density, for an electrocatalytic reaction the total current is the sum of the anodic current:

$$j_a = nFk_a[C_R] \exp\left(\frac{\alpha_a nFE}{RT}\right)$$

where k_a and α_a represent the rate constant of the anodic-half reaction and anodic transfer coefficient and the cathodic current:

$$j_c = nFk_C[C_c] \exp\left(\frac{\alpha_a nFE}{RT}\right)$$

where k_c and α_c represents the rate constant of the cathodic-half reaction and cathodic transfer coefficient. At equilibrium:

$$\eta = 0 \rightarrow E = E_{eq}$$

the two currents are equal. The corresponding current is the exchange current (j_0) at an overpotential of 0 V. Then the exchange current density can be obtained by the area of the electrode (A) and the exchange current:

$$\frac{j_0}{A} = i_0$$

j_0 exactly represents the intrinsic activity/charge transferring interactions between the electrocatalyst and reactant. A high exchange current density is usually a good parameter of being a good electrocatalyst for the OER reaction.

The main properties to be gained by catalysts are stability and good conductivity. The electrical conductivity can be calculated as:

$$\sigma = \frac{l}{AR}$$

where l is the catalyst layer thickness, R is the catalyst electrical resistance and A is the surface area of the electrode covered with catalyst. Now, OER is a four-electron transformation, so, many intermediate species can form during the oxygen evolution. In acidic media, given M as the active site, the first step will be:

$$M + H_2O \rightarrow M - OH_{ads} + H^+ + e^-$$
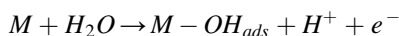
The second step acts through a second electron transfer:

$$M - OH \rightarrow M - O_{ads} + H^+ + e^-$$
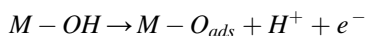
Then it is followed by a recombination step:

$$M - OH + M - OH \rightarrow MO + M + H_2O$$
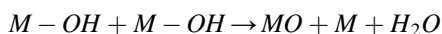
Then, the formation of oxygen on two active sites takes place:

$$2M - O_{ads} \rightarrow 2M + O_2$$
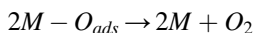
Depending on the employed catalyst and the electrical conditions, step one can evolve through two sub-reactions:

$$M + H_2O \rightarrow M - OH^*_{ads} + H^+ + e^-$$
$$M - OH^*_{ads} \rightarrow M - OH_{ads}$$
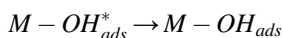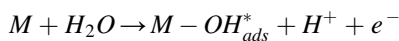
M-OH$_{ads}$* and M-OH$_{ads}$ have the same chemical structure but different energy states. This kind of evolution depends on the strength of adsorption of the intermediates and on the composition of the oxide layer.

Fig. 5 Elements employed as HER catalysts

2.3   Cell Components

The elements normally employed as electrocatalysts are underlined in Fig. 5.

Mainly catalysts can be divided into two main groups: those based on precious metals, those based on non-noble elements (Ayers 2021). The main problems related to the employment of non-noble metals compounds is the lower activity and stability. The best performances are achieved through Pt-based electrocatalysts. One way to reduce the Pt usage is its embedding in a matrix with nanoparticles shapes. This reduces the Pt volume in the electrode and increases the activity of the catalyst. Recently, an evolution of this design led to the employment of Pt-Ru nanoparticles. Sometimes nanoparticles are doped with non-noble elements such as Cu. In other solutions, Pt single atoms are embedded in different structures with other elements to improve the overall activity (Fig. 6).

Iridium and Ruthenium are catalysts considered among the noble metals. They have some advantages such as overpotential and reduced costs. By coupling with other elements such as Si and by nano structuring, high hydrogen production efficiency can be obtained. The schematic of HER in this solution is schematized in Fig. 7.

Transition metal dichalcogenides (TMDs) with delamination properties have extremely strong catalytic properties for electrochemical HER when diluted into a separate sheet structure (Li et al. 2018). The layer is built with a transition metal atom plus two chalcogens atoms. By varying the metal and the chalcogens, different catalytic activities can be obtained.
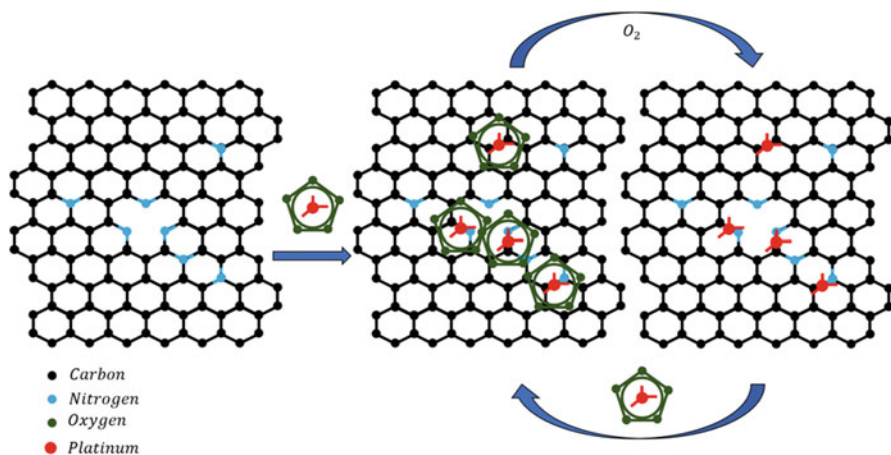
Fig. 6 Schematic of Pt catalyst on graphene
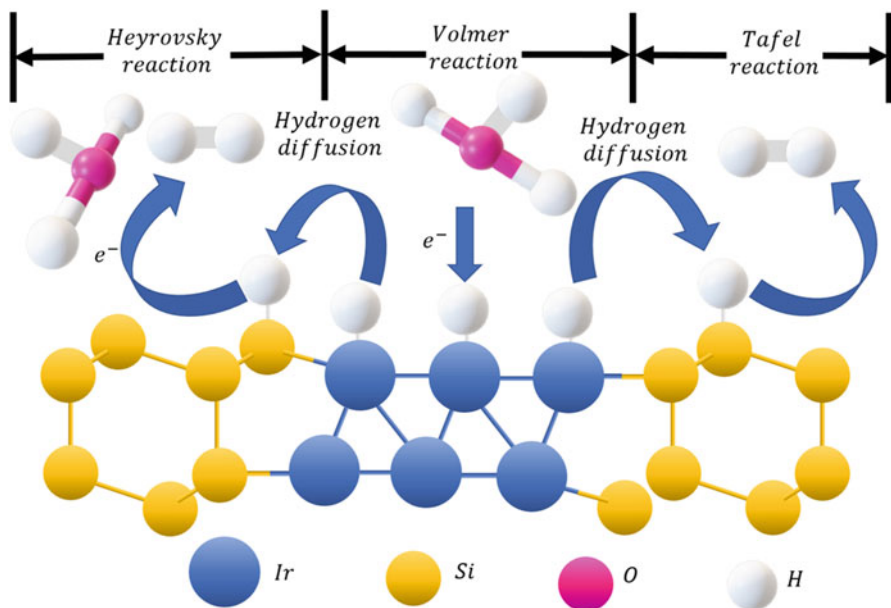
Fig. 7 HER evolution on Ir-Si catalyst

The transition metal phosphide (TMP) has proven to be effective for the hydro-electric analysis of hydrogen and is a catalyst with high activity, high stability, and near 100% Faraday efficiency for use in strong acids, strong bases, and neutral electrolytes. Transition metal phosphide can be considered to dope P atoms into the

crystal lattice of the transition metal. So far, only six different transition metals (Fe, Co, Ni, Cu, Mo, W) have been found to be useful for the electrochemical hydrogen evolution of TMP.

Metal carbides have platinum-like catalytic properties, which have greatly encouraged researchers (Karimi and Peppley 2017). The catalytic performance of metal carbides for the hydroelectric analysis of hydrogen depends on its surface composition, which is directly related to the synthesis of the catalyst. Transition metal nitrides have excellent physic-chemical properties. On the one hand, the introduction of N atoms can modify the d-band of the metal and cause the d-band shrinkage of the metal, which makes the transition metal nitride have a Pd-like, Pt-like electronic structure; on the other hand, the atomic radius of the N atom is small. It can be attached to the lattice gap, so that the metal atoms in the metal nitride can be closely packed, which makes the metal nitride have excellent electronic conductivity. The above good characteristics and high corrosion resistance make metal nitride materials have wider application prospects than metals or metal alloys (Bi et al. 2021).

About the oxygen evolution reaction, the precious metals are the most active catalysts with an activity following this behavior:

$$Ru > Ir > Pd > Rh > Pt > Au$$
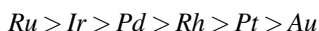
Since RuO_2 is not stable enough in acidic OER, it tends to cause a decrease in activity, while IrO_2 has high stability in an acidic medium. Ir-Ru oxides show better stability with respect to the simple oxides. Catalytic performance can be improved by adding Ta, Mo, Nb, and Ti.

At present, the research on Cu metal alloys is also extensive, the addition of Cu not only reduces the amount of noble metal, but also enhances the catalytic activity by forming a uniform distribution of the nanocage structure and electronic structure.

The most used support materials are metal oxides, and most reported in the SnO_2 groups and TiO_2-based compounds. The oxides doping leads to improvements in the conductivity. The combined morphology and porous structure together enhance the OER performance of the catalyst. In addition to metal oxides, metal carbides have also been reported as the OER carriers due to their high electrical conductivity and stability.

Unlike conventional alkaline electrolyte water electrolysis, proton electrolyte membrane (PEM) water electrolysis systems using high strength perfluoro-sulfonic acid membranes as the electrolyte have greater energy efficiency, no pollution, higher hydrogen production rate, and simpler design (Siracusano et al. 2017).

The water uptake by a Nafion membrane is exhibited in terms of weight percent of water (ω) and water content (λ). The water uptake delivered as ω is obtained via the weight of the wet sample ω_{wet} and dry sample ω_{dry}:

$$\omega[\%] = \frac{\omega_{wet} - \omega_{dry}}{\omega_{dry}}$$

The amount of water molecules per sulfonic acid site can be represented by λ. The relationship between λ and ω is expressed as:

$$\lambda = \omega \cdot \frac{EW}{M_{H_2O}}$$

where EW is the equivalent weight and M_{H2O} is the molar weight of water.

There are typically two proton conduction mechanisms in PEM: the vehicle mechanism and the Grotthuss-type mechanism, which is also known as tectonic diffusion. The foundation of the vehicle mechanism is the production of ionic compounds consisting of the diffusion of protons and carrier molecules. Many reports have shown that it occurs in acidic aqueous solutions and acidic polymer environments. The mechanism of Grotthuss is that protons are transported from one site to another in an environment without carriers; the activation energy of which depends on the hydrogen bond discrete energy and the spacing between the sites. These two proton conduction mechanisms are not independent and occur to some extent at the same time. An experimental relationship allows for the calculation of proton conductivity (κ):

$$\kappa \left[\frac{S}{cm} \right] = (0.005139\lambda - 0.00326) \exp \left[1268 \left(\frac{1}{303} - \frac{1}{T} \right) \right]$$

The relationship between the proton conductivity and temperature of Nafion membranes is presented below:

$$\kappa = \kappa_0 \exp \left(-\frac{E_\kappa}{RT} \right)$$

The membrane pre-treatment on the water absorption (λ) and conductivity (κ) of the membrane is important for the application of fuel cells and electrolytes. The membrane electrode assembly (MEA) of the PEM electrolyzers can be constructed in a variety of forms.

Under an applied electric field, a proton and water molecules may traverse across a PEM, and this can be called electro-osmosis. The number of water molecules dragged by per H^+ is defined as the electro-osmotic drag coefficient, marked as n_{drag}, which depends on the water content in the membrane. When the membrane is fully hydrated, the membrane temperature will become the only limiting condition for n_{drag} during its preparation process of chemical plating. The correlation can be expressed as follows:

$$n_{drag} = 0.0134 \cdot T + 0.03$$

The MEA is key device for proton exchange membrane water electrolysis (PEMWE), which is of a sandwich structure containing a solid electrolyte membrane, catalyst layer (CL), and gas diffusion layer (GDL). As the place that the
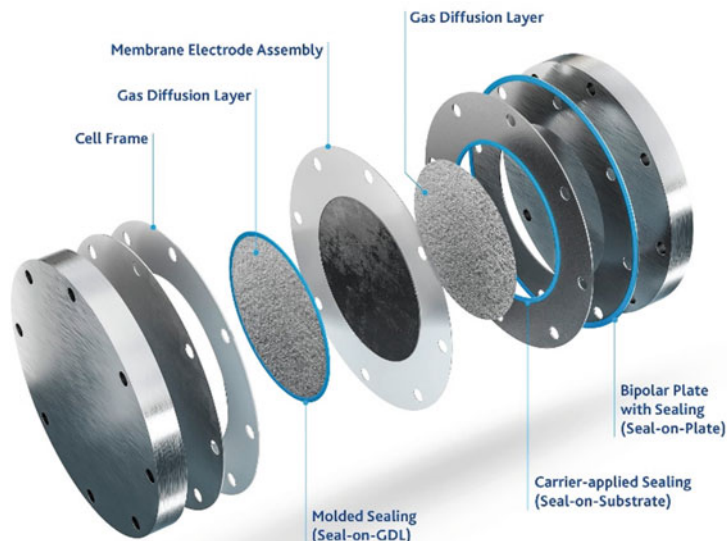
Fig. 8 PEM assembly schematic

electrode reaction occurs, the structure of CL and GDL strongly affects reactant and product transfer (gas-water two-phase flow), resistance, motion of proton and electron, as well as other relative processes involved in the electrode reaction. Consequently, optimizing the structure of the MEA is always a key issue in enhancing the performance of the MEA.

A single cell of PEMWE commonly consists of a MEA, GDL, current collector (in some cases, GDL is also used as the current collector), sealant, bipolar plate, endplate as well as other accessories, such as an insulator, compression plate, and so on (Fig. 8).

Numerous materials are employed for manufacturing those sub-elements. For example, carbon paper, titanium mesh, porous titanium, as well as porous nickel are usually employed as the GDL and current collector. Graphite, stainless steel, and titanium are used as the bipolar plate. Aluminum, stainless steel, titanium, and Delrin are usually used as the endplate. The geometry of flow field strongly affects the hydrodynamics inside the stack and insures distribution of water in each individual cell. Homogeneous water distribution is important to obtain an equal lifetime of each cell and stack performance. The stack must be compressed with an appropriate pressure to make sure the cell sealed and to avoid gas leak, or MEA crack resulted by lower or higher torque, as well as Ohmic losses due contact resistance decreases the stack efficiency. The performance of the PEMWE is not only determined by the

cell structure, but also depends on operating conditions. Many efforts confirmed that efficiency increases with temperature mainly because of an enhanced electrochemical reaction at higher temperature. In fact, the water flow rate does not play a significant role in the performance of the PEMWE. However, if the flow rate of water is too low, the stack temperature rises uncontrollably, and the appropriate water flow rate is chosen for cooling purposes at an operating current density. A high-pressure operation is potentially interesting for the direct storage of hydrogen in pressurized vessels. Some applications require storage pressures up to several hundred bars.

3   Gas Crossover

For both electrolysis technologies several possibilities exist, which cause hydrogen crossover (Klose et al. 2020).

In general, these permeation routes can be divided into diffusive and convective mass transfer mechanisms.

One of the possible crossover mechanisms is the diffusion of electrolysis products across the membrane or separator into the opposite half-cell compartment for both technologies. Usually, the products may diffuse through the solid and aqueous phase of the separating unit. However, it is reported that diffusion through the solid phase of a fully hydrated Nafion membrane is roughly one order of magnitude smaller compared to its liquid phase. Similar information can be found for Zirfon™ as the diffusion through the separator's solid phase is also assumed to be negligible. Additionally, the separator is further presumed to be impermeable for gas bubbles at atmospheric pressure. Thus, it is comprehensible for both technologies that only species that are dissolved in water or KOH solution are considered for diffusion across the separating unit. This is done by application of Fick's law in PEM and alkaline water electrolysis:

$$N_{H_2}^{diff} = D_{H_2}^{eff} \frac{\Delta c_{H_2}}{\delta_{\text{sep}}}$$

Here, Δc_{H2} represents the dissolved hydrogen concentration gradient across the separating unit with the thickness δ_{sep}, whereas D_{H2}^{eff} denotes the effective diffusion coefficient of hydrogen in the membrane or separator. The estimation of the effective diffusion coefficient in polymer electrolyte membranes or porous media is typically done by correction of the molecular diffusion coefficient in the aqueous solvent D_{H2} with the porosity ε and tortuosity τ of the separating unit:

$$D_{H_2}^{eff} = \frac{\varepsilon}{\tau} D_{H_2}$$

In PEM electrolysis the concentration gradient across the membrane Δc_{H2} can be estimated with the cathodic concentration of dissolved hydrogen $c_{H_2}^{cat}$ as the anodic hydrogen concentration $c_{H_2}^{ano}$ is approximately zero. However, this assumption becomes also applicable for AEL if the electrolyzer is operated with separated electrolyte cycles:

$$\Delta c_{H_2} \approx c_{H_2}^{cat} - c_{H_2}^{ano}$$

Henry's law states that a species' dissolved concentration is directly proportional to its partial pressure in the gas phase. Therefore, this approach can be applied for the calculation of the cathodic dissolved hydrogen concentration. Within the following Equation S_{H2} denotes the hydrogen solubility in the solvent, whereas the cathodic hydrogen partial pressure is represented by $p_{H_2}^{cat}$:

$$c_{H_2}^{cat} = S_{H_2} p_{H_2}^{cat}$$

Data of the hydrogen solubility in pure water was published for atmospheric pressure conditions. Further data for pressures ranging from 25 to 1000 atm can be found. However, literature for the hydrogen solubility in concentrated potassium hydroxide solution is scarce.

The cathodic hydrogen partial pressure can be obtained if it is assumed that the cathodic oxygen partial pressure is negligible and that the hydrogen is saturated with water vapor. Then the following Equation applies, where p^{cat} denotes the total cathodic pressure:

$$p_{H_2}^{cat} = p^{cat} - p_{H_2O}^{cat}$$

The calculation of the water vapor pressure may be performed by application of the Antoine equation with parameters for pure water.

Finally, the diffusional hydrogen flux across the separating unit can be described with the following Equation:

$$N_{H_2}^{diff} = D_{H_2}^{eff} S_{H_2} \frac{p_{H_2}^{cat}}{\delta_{sep}}$$

The product of the effective diffusion and solubility coefficient $D_{H_2}^{eff} S_{H_2}$ is frequently provided in form of the permeability coefficient K_{H2}, which is a classical material property for separating units.

Convection represents another general cause of crossover, which can be divided into several further mechanisms. Generally, convective mass transport is mathematically expressed by the following equation. There, v_{solv} describes the velocity of solvent (PEM: water, AEL: KOH solution) moving perpendicular to the separating unit, whereas cH2 denotes the concentration of dissolved gas within the solvent:

$$N_{H_2}^{conv} = v_{solv} c_{H_2}$$

One possible reason for convective permeation is the transport of electrolyte and dissolved species across the separating unit due to the presence of total pressure gradients. For the mathematical description of this transport mechanism commonly Darcy's law is applied:

$$N_{H_2}^{dp} = \frac{K_{sep}}{\eta} S_{H_2} p_{H_2}^{cat} \frac{\Delta p}{\delta_{sep}}$$

Here, K_{sep} denotes the permeability of the separating unit, η is the dynamic viscosity of the solvent, whereas Δp describes the absolute pressure difference between the cathodic and anodic compartment. The concentration of dissolved hydrogen is again estimated by the insertion of Henry's law. The hydraulic permeability K_{sep} of porous media such as membranes can be estimated by the Hagen-Poiseuille or Kozeny-Carman equations:

$$K_{sep} = \frac{\varepsilon d^2}{32\tau}$$

$$K_{sep} = \frac{\varepsilon^3}{K_{koz} a^2 (1 - \varepsilon)^2}$$

Here, ε represents the porosity, d the pore diameter, τ the tortuosity and a the specific surface area of the separating unit, while K_{koz} denotes the Kozeny constant, which depends on the porous media. For a rough estimation of the hydraulic permeability K_{sep} in this work the Hagen-Poiseuille equation is used. The necessary porosities and pore diameters of both applied separating units are given within the setup section.

To make a worst case estimate the tortuosity is chosen to be $\tau = 1.5$ for both systems. Considering that the permeability for the Nafion membrane and Zirfon™ separator are approximated to be $5 \cdot 10^{-20}$ m^2 and $2 \cdot 10^{-16}$ m^2, respectively. These estimates match literature data of both separating units quite well. For that reason, AEL with a porous separator is theoretically more prone to convective permeation. But it has to be noted that it is also more convenient to mix the electrolyte cycles at identical pressure levels, which is also an important reason for balanced pressure operation. However, if it is assumed that commonly applied back pressure control valves can control the anodic and cathodic pressures with an accuracy of roughly 1%, it becomes comprehensible that a differential pressure across the separator may be formed. Thus, it is conceivable that either dissolved hydrogen or oxygen could convectively be transported into the opposite half-cell.

Despite that, literature suggests that no pressure-driven permeation is evident for Nafion membranes. This allows the operation of PEM electrolyzers under asymmetrical pressure conditions. Here, the cathode is typically pressurized, whereas the anodic cycle stays at atmospheric pressure, which can be favorable in terms of

energy demand. However, if alternative membrane materials are applied, this operation mode may also promote a permeation flux as the resulting pressure-driven water flow carries dissolved hydrogen into the anodic compartment.

A further possibility to cause convective permeation is the electro-osmotic drag. Due to the electric field and the associated movement of ions, the electroneutral solvent can be dragged with them across the separating unit. Hence, dissolved gas may also be transported through it. Thus, in PEM electrolysis dissolved oxygen may be dragged along with the transport of protons from the anodic into the cathodic half-cell. On the contrary, the electro-osmotic drag could also be capable of reducing hydrogen permeation as it may transport dissolved hydrogen back to the cathode. In contrast, OH– ions are responsible for the charge transport in AEL. According to the half-cell reactions these hydroxide ions are transported from the cathodic to the anodic compartment, which therefore may enhance hydrogen and reduce oxygen crossover.

However, no publication was found that could confirm or quantify this mechanism. A rough estimation of the electro-osmotic crossover flux can be carried out with the following Equation:

$$N_{H_2}^{drag} = \frac{\left(S_{H_2} p_{H_2}^{cat} \right)}{c_{solv}} \frac{n_{drag} i}{F}$$

Here, c_{solv} is the concentration of solvent within the separating unit and n_{drag} is the electroosmotic drag coefficient, which describes the ratio between the flux of dragged solvent molecules to that of the charged ions. Jacobson et al. (2014) (Fig. 9) compared drag coefficients of proton-conducting Nafion membranes to that of a hydroxide-conducting Tokuyama A201 membrane for the application in acid and alkaline fuel cells. Their results showed a smaller value for the anion-conducting membrane, which may be attributed to the different charge carrier or

Fig. 9 Electro-osmotic drag coefficients of water in proton exchange poly (perfluoro-sulfonic acid) membranes, A210 hydroxide anion exchange membrane
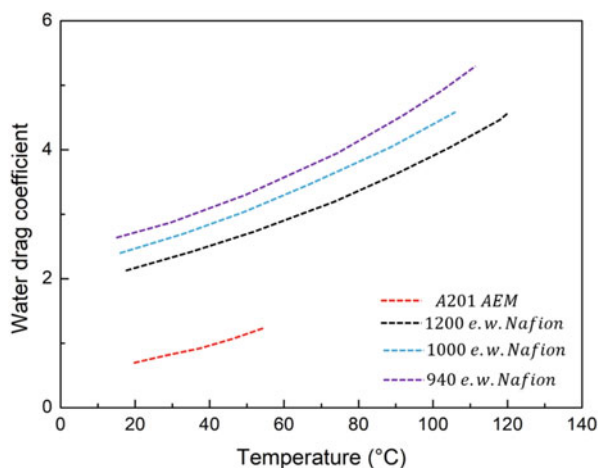
water domain. A temperature-dependent correlation for the estimation of the drag coefficient in a Nafion membrane used for PEM electrolysis can be found in the publication by Onda et al. (2002).

The electrochemical reactions in AEL cause a change in electrolyte concentration since water is consumed at the cathode, whereas it is produced in the anodic half-cell. Therefore, the anodic and cathodic electrolyte cycles are usually mixed to balance this concentration gradient. However, this process management leads to a decrease of the resulting product gas purity as the electrolyte is saturated with dissolved electrolysis products. For that reason, the electrolysis cell is continuously fed with dissolved hydrogen and oxygen from the gas separators, where they are then able to outgas. To prevent this crossover mechanism, it is necessary to separate the electrolyte cycles. But due to the shift in the anodic and cathodic electrolyte concentrations the cell efficiency may decrease, as the electrolyte conductivity is reduced with prolonged time (Trinke et al. 2018).

It is generally assumed for gas evolving electrodes that the electrolysis products are produced in dissolved form before gas bubbles grow at active nucleation sites (Lee et al. 2017). Nucleation sites are small electrode surface irregularities, which depend on the material and its roughness. For the nucleation sites to become active a sufficient deviation from equilibrium concentration of the generated product is mandatory. Consequently, the electrolyte becomes supersaturated, which describes a higher concentration of dissolved hydrogen within the electrode boundary or catalyst layer than it would be expected through Henry's law. The existence of this supersaturated concentration of dissolved species could already be proven experimentally. Hence, the subsequent mass transfer of dissolved hydrogen is mainly controlled by two competing mechanisms. Dissolved hydrogen is either transported to the electrolyte bulk in dissolved form or to the gas-liquid interface of gas bubbles present in the electrode boundary layer. However, dissolved hydrogen may also be transported through the separating unit of the electrolysis cell.

As theory of the diffusive and convective crossover mechanisms only supposed hydrogen equilibrium concentration (Henry's law), supersaturation enhances these crossover mechanisms in PEM and zero-gap alkaline electrolysis. However, the influence of supersaturation on crossover can only be accounted, if the previously mentioned equations are expressed in their concentration forms instead of the gas pressure expressions.

The following Equation can be used for the calculation of the dissolved gas concentration within the catalyst layer in PEM electrolysis:

$$c_{H_2}^{cat} = \frac{\frac{i}{2F} + k_L S_{H_2} p_{H_2}^{cat}}{k_L + \frac{D_{H_2}^{eff}}{\delta_{sep}}}$$

Here k_L denotes the mass transfer coefficient, which includes several transport and transfer steps: beginning with the desorption of the electrolysis product from the catalyst particles up to the transfer into the gas phase within the pore space. For the

PEM catalyst layers it is suggested that this mass transfer coefficient is significantly affected by the diffusion of the dissolved gas from the catalyst particles to the pore space through the ionomer. Already small limitations can lead to a significant increase of the dissolved gas concentration. Additionally, the last equation reveals that supersaturation also increases towards higher current densities. So, it is necessary to consider that the concentration of dissolved gas is not solely a function of gas solubility, system pressure and the electrode specific mass transfer coefficient, but also of current density: $c_{H_2}^{cat} = f\left(p_{H_2}^{cat}, S_{H_2}, k_L, i\right)$.

4 Voltage Losses

The measured cell voltage, E_{cell} can be defined by adding the contributions of various voltage losses to the reversible cell voltage, E_{rev}, (note that current, potentials, and overpotentials are taken as positive values) (Immerz et al. 2018):

$$E_{cell} = E_{rev} + i \cdot (R_{memb} + E_{el}) + |\eta_{HER}| + \eta_{OER} + i \cdot \left(R_{H^+,cath}^{eff} + R_{H^+,an}^{eff}\right) + \eta_{mt}$$

where i is the electrolyzer current. R_{memb} and R_{el} are the ohmic resistance of the membrane and the electrical resistance respectively.

η_{HER} and η_{OER} are the kinetic overpotentials of the HER and OER, while $R_{H^+,cat}^{eff}$ and $R_{H^+,an}^{eff}$ represent the proton transport resistance in the respective catalyst layers. H_{mt} describes additional losses related to mass transport phenomena. The voltage losses for an MEA based on a Nafion^R 212 membrane operated at 80 °C and ambient pressure are shown exemplarily in Fig. 10 (anode: IrO_2/TiO_2, 2 mgIrcm^{-2}; cathode: Pt/C, 0.35 mgPtcm^{-2}).

According to thermodynamics, the reaction enthalpy, ΔH, defines the total energy needed for the electrochemical splitting of water:

$$\Delta H = \Delta G + T \Delta S$$

where ΔG is the Gibbs free energy of the reaction, T is the temperature, and ΔS is the change in entropy of the system. At standard conditions (298 K, 1 bar), the Gibbs free energy $\Delta G0$ is 237 kJ/mol. This represents the minimum electrical work needed for splitting water at the corresponding theoretical cell potential:

$$E_{rev}^0 = \left|\frac{\Delta G^0}{nF}\right| = 1.23 \text{ V}$$

where n is the number of transferred electrons in the reaction (n = 2) and F is the Faraday constant (96,485 As mol^{-1}). The thermoneutral potential, E_{tn}^0, is defined as the potential at which water electrolysis can be conducted without the production or
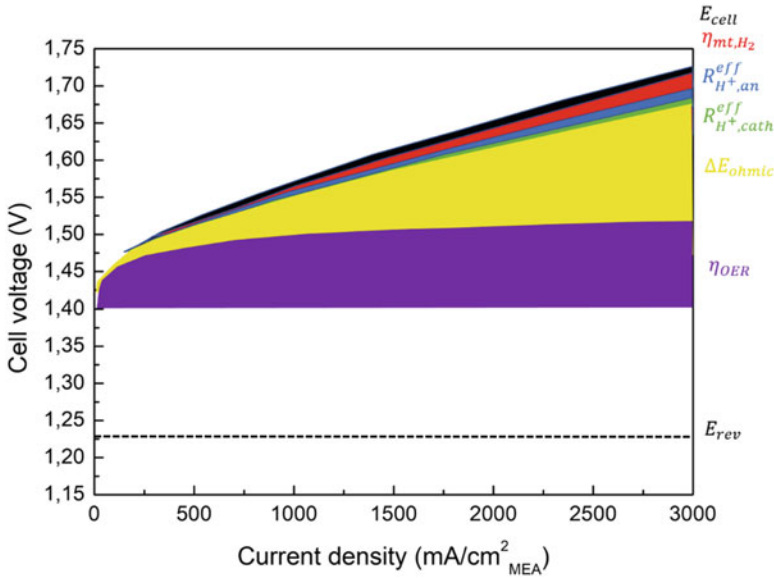
Fig. 10 Contributions of various voltage losses to overall cell voltage

consumption of heat, i.e., where a thermally insulated electrolyzer would operate at constant temperature:

$$E^0_{tn} = \left| \frac{\Delta H^0}{nF} \right| = 1.48 \text{ V}$$

Here, ΔH^0 is the reaction enthalpy at standard conditions ($\Delta H^0 = 286 \text{ kJ mol}^{-1}$).

The reversible cell voltage, E_{rev}, is a function of temperature and activity of the species involved in the reaction and can be calculated:

$$E_{rev} = E^0_{rev} + \frac{RT}{2F} \ln \left(\frac{a_{H_2} \cdot (a_{O_2})^{\frac{1}{2}}}{a_{H_2O}} \right)$$

where the temperature dependence of the standard reversible potential, E^0_{rev}, can be calculated as:

$$E^0_{rev} = 1.2291 \text{ V} - 0.0008456 \text{ V} \cdot (T - 298.15 \text{ K})$$

For liquid water, the activity of water, a_{H_2O}, is one, while the activities of the gaseous species, a_{H_2} and a_{O_2}, are represented by the ratio of their partial pressures to the standard pressure of 1 bar. Consequently, E_{rev} can be expressed as:

$$E_{rev} = E_{rev}^0 + \frac{RT}{2F} \ln\left[\left(\frac{p_{H_2}}{1\ bar}\right) \cdot \left(\frac{p_{O_2}}{1\ bar}\right)^{\frac{1}{2}}\right]$$

where p_{H2} and p_{O2} are the partial pressure of H_2 and O_2, respectively. At the typical measurement conditions of 80 °C and ambient pressure used in most of this work, the saturation pressure of H_2O is 0.47 bara, resulting in $p_{H2} = p_{O2} = 0.53$ bara. This yields a reversible cell voltage $E_{rev} = 1.17$ V.

In a real system, the cell voltage is of course higher because of the contributions of different overpotentials. To determine the voltage efficiency, η_v, of an electrolyzer, the theoretically required amount of energy for the reaction, i.e., the reaction enthalpy ΔH^0, has to be divided by the actual electrical energy input determined from the operating cell potential E_{cell}:

$$\eta_v = \left|\frac{\Delta H^0}{2FE_{cell}}\right|$$

The voltage efficiency can be calculated based on the higher heating value (HHV) of H_2 or on the lower heating value (LHV) of H_2. The HHV corresponds to the reaction enthalpy from liquid water to gaseous hydrogen and is commonly used to calculate the efficiency (η_{HHV}) if H_2 is utilized chemically or if one aims to consider the heat balance of the electrolyzer. The efficiency based on the LHV (η_{LHV}), on the other hand, is used when the product H_2 is used energetically (e.g., transformation to electrical energy with a fuel cell) in an application which does not benefit from the condensing enthalpy of water ($\Delta H_{vap}^0 = 44$ kJ mol^{-1}). A way to characterize the efficiency of an electrolyzer independent of the further utilization of the produced H_2 is to state the amount of electrical energy required to produce a certain amount of hydrogen in kWh kg^{-1}(H_2) or kWh Nm^{-3}(H_2) (at atmospheric pressure and 0 °C).

To determine the overall efficiency of an electrolyzer, not only the voltage efficiency, η_v, has to be considered but also losses due to permeation of H_2 and O_2 through the membrane (Ayers et al. 2012). This is expressed by the faradaic efficiency, η_F, which depends on the used materials (membrane material and thickness), the operating conditions (pressure, temperature), and the current density at which the electrolyzer is operated. In this work, the term efficiency usually refers to the efficiency of an electrolyzer single cell or stack. To determine the overall efficiency of an electrolyzer system, also balance of plant (BoP) components such as pumps, heaters, and power electronics need to be considered.

The measured cell potential, E_{cell}, is comprised of the reversible cell voltage, E_{rev}. Ohmic losses in an electrolyzer can be divided into ionic losses due to the proton transport resistance of the membrane, R_{memb}, and losses due the electrical resistance contributions within the cell, R_{el}. The total ohmic resistance of a single cell is typically quantified by the high frequency resistance, R_{HFR}, which can be accessed via electrochemical impedance spectroscopy (EIS):

$$R_{HFR} = R_{memb} + R_{el}$$
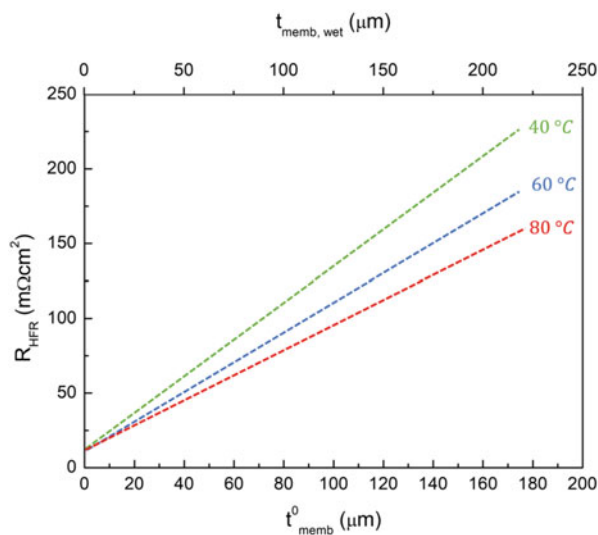
Fig. 11 High frequency resistance, RHFR, as a function of the membrane thickness determined at operating temperatures of 40 °C (green triangles), 60 °C (blue circles) and 80 °C (red squares). The lower x-axis shows the nominal membrane thickness at 25 °C and 50% relative humidity, t0memb, while the upper x-axis represents the actual membrane thickness in the electrolyzer, $t_{memb,wet}$. R_{HFR} was determined from the x-axis intercept in a Nyquist plot for an electrochemical impedance measurement performed at a DC current density of 1 A cm^{-2} and a perturbation current of 0.04 A cm^{-2} in a frequency range of 100 kHz to 1 Hz

To deconvolute the contributions of R_{memb} and R_{el} to the total ohmic resistance, R_{HFR} can be measured for MEAs with membranes of different thickness, as shown in Fig. 11.

Since Rel is independent of membrane thickness, while R_{memb} is expected to scale linearly with the actual membrane thickness, the contributions of both can be determined by a linear regression of the data points:

$$R_{HFR} = \frac{1}{k_{memb}} \cdot t_{memb,wet} + R_{el}$$

To determine the correct values for the ionic conductivity of the membrane, κ_{memb}, in S cm^{-1}, the actual thickness of the membrane in the electrolyzer, $t_{memb,wet}$, needs to be used instead of the nominal membrane thickness, t^0_{memb}, at 25 °C and 50% relative humidity (RH). The difference between the two arises from the swelling of the membrane in the electrolyzer, i.e., in the presence of liquid water at elevated temperatures. In general, it is expected that the membrane swells in the in-plane as well as in the through-plane direction. However, since the edges of the membrane are compressed between the gaskets of the cell hardware, a significant expansion in the in-plane direction is not expected and it is assumed that swelling only occurs in the through-plane direction (Carmo et al. 2015).

Consequently, the increase in membrane thickness, Δt_{memb}, equals the total volume increase, ΔV_{memb} and the thickness of the membrane in equilibrium with liquid water, $t_{memb,wet}$, can be expressed according to equation:

$$t_{memb,wet} = t_{memb,dry} \left(1 + \frac{M_{H_2O} \cdot \rho_{memb,dry} \cdot \lambda}{\rho_{H_2O} \cdot EW} \right)$$

where M_{H2O} is the molecular weight of water, $\rho_{memb,dry}$ is the density of the dry membrane (≈ 2 g cm^{-3} for Nafion^R), ρ_{H2O} is the density of water, λ is the water content and EW is the equivalent weight.

The kinetic overpotential or activation overpotential is the result of irreversible processes within an electrochemical reaction. It is commonly described by the Butler-Volmer equation:

$$i_{+/-} = i_0 \cdot rf \cdot \left[\exp\left(\frac{\alpha_a F}{RT}\, \eta \right) - \exp\left(- \frac{\alpha_c F}{RT}\, \eta \right) \right]$$

where $i_{+/-}$ is the current of a half-cell reaction and η is the overpotential, which has a positive sign for an anodic and a negative sign for a cathodic reaction. i_0 is the exchange current density, a kinetic reaction rate constant, which depends on the specific electrocatalyst, and rf is the electrode roughness factor, which relates the real surface area of the catalyst to the geometric area of the electrode (in units of cm$^2_{surface}$/cm$^2_{electrode}$). α_a and α_c are the transfer coefficients of the anodic and the cathodic reaction, describing the symmetry of the energy barrier and the number of exchanged electrons in the rate determining step. F is the Faraday constant; T is the temperature and R is the gas constant.

Due to the fast reaction kinetics of the HER on Pt and the small resulting overpotential, the Butler-Volmer equation can be linearized and η_{HER} can be expressed as:

$$\eta_{HER} = i_{HER} R_{K,HER}$$

where i_{HER} is the current of the HER (cathodic current: $i_{HER} < 0$) and:

$$R_{K,HER} = \frac{RT}{(\alpha_a + \alpha_c) \cdot F \cdot rf \cdot i_{0,HER}}$$

Here, α_a and α_c are the transfer coefficients and $i_{0,HER}$ is the exchange current density of the HER at the respective operating temperature. The roughness factor, rf, can be determined from the Pt loading, L_{Pt}, and the electrochemically active surface area, $A_{Pt,el}$:

$$rf = L_{pt} \cdot A_{Pt,el}$$

The kinetics of the OER in a PEM are much slower compared to the HER, causing a significant activation overpotential, η_{OER}. For large overpotentials, the Butler-Volmer equation can be simplified to the so-called Tafel equation:

$$i_{OER} = i_0 \cdot rf \cdot \exp\left(\frac{\alpha_a F}{RT}\,\eta_{OER}\right)$$

In this case, the kinetic overpotential of the OER can be expressed as:

$$\eta_{OER} = \frac{2.303\,RT}{\alpha_a F}\,\log\left(\frac{i_{OER}}{i_{0,OER}rf}\right) = b\log\left(\frac{i_{OER}}{i_{0,OER}rf}\right)$$

where b is referred to as the Tafel slope, representing the overpotential increase required for a 10× increase in current. The Tafel slope can be extracted from experimental data by a linear regression of the iR-free cell voltage when plotted on a logarithmic current scale.

Voltage losses related to transport phenomena, E_{tr}, can be expressed by subtracting ohmic and kinetic losses from the measured cell voltage:

$$E_{tr} = E_{cell} - E_{rev} - i(R_{memb} + R_{el}) - |\eta_{HER}| - \eta_{OER} = i\left(R^{eff}_{H^+.cath} + R^{eff}_{H^+.an}\right) + \eta_{mt}$$

The remaining losses can be divided into overpotentials due to the proton transport resistance in the catalyst layers and an overpotential due to mass transport phenomena, which can include water transport to the active sites as well as transport of the evolved gases from the active sites to the gas outlet of the cell.

Due to the fast kinetics, the HER will occur preferably very near the electrode/membrane interface, and losses due to proton transport within the electrode will be small. The effective proton transport resistance of the cathode, $R^{eff}_{H^+,cath}$, can be calculated based on the charge transfer resistance, $R_{K,HER}$, and the sheet resistance for proton transport, $R_{H^+,cath}$, according to:

$$\frac{R_{H^+.cath}}{R^{eff}_{H^+.cath}} = \frac{\beta}{\frac{e^\beta + e^{-\beta}}{e^\beta - e^{-\beta}} - \frac{1}{\beta}}$$

where β is given by:

$$\beta = \left(\frac{R_{H^+.cath}}{R_{K,HER}}\right)^{\frac{1}{2}}$$

The sheet resistance for proton transport, $R_{H^+,cath}$, can be determined by EIS using a one-dimensional transmission-line model. $R_{H^+,cath}$ can be calculated:

$$R_{H^+,cath} = \rho_{H^+,cath} t_{cath}$$

where t_{cath} is the electrode thickness of the cathode.

The effective proton transport resistance of the anode, $R_{H^+,an}^{eff}$, can be calculated from the sheet resistance for proton transport, $R_{H^+,an}$ as:

$$R_{H^+,an}^{eff} = \frac{R_{H^+,an}}{3 + \zeta}$$

where ζ is a correction factor which accounts for the effect of a reduced catalyst utilization in the anode. ζ is a function of the ratio of the sheet resistance for proton transport to the kinetic resistance:

$$i \frac{R_{H^+,an}}{b}$$

where i is the current density, $R_{H+,an}$ the sheet resistance for proton transport and b the Tafel slope. For small values of $i \cdot R_{H+,an}/b$, the catalyst utilization approaches 100% and the correction factor, ζ, goes to zero. The sheet resistance for proton transport in the Ir-based anode, $R_{H+,an}$, could in principle be determined by EIS analogous to the transmission line analysis used for PEM fuel cell cathodes. $R_{H+,an}$ can be estimated with the correlation:

$$R_{H^+,an} = \frac{t_{an}}{k \cdot \left(\frac{V_{ion,wet}}{\tau} \right)}$$

Here, tan is the electrode thickness, κ is the conductivity of the ionomer, $V_{ion,wet}$ is the volume fraction of ionomer in the electrode equilibrated with liquid water, and τ is the tortuosity of the ionomer phase in the electrode.

5   Operating Conditions

Apart from improving materials and components, optimization of operating conditions is crucial to ensure a high efficiency and lifetime of a PEM (Fallisch et al. 2017).

Typical operating temperatures of state-of-the-art PEM-WEs are in a range of 50–80 °C.

Generally, higher temperatures lead to an improved performance due to a higher ionic conductivity of the membrane and faster reaction kinetics resulting in lower ohmic and kinetic overpotentials. Figure 12 shows polarization curves along with the HFR obtained for an MEA with a Nafion[R] 117 membrane (≈175 μm) and catalyst loadings of 1.2 $mg_{Ir}cm^{-2}$ and 0.3 $mg_{Pt}cm^{-2}$, respectively. Measurements were performed at temperatures of 40 °C, 60 °C, to 80 °C.

Fig. 12 (**a**) Ambient pressure polarization curves measured for an MEA with a NafionR 117 membrane and catalyst loadings of 1.2 mgIr cm^{-2} (IrO$_2$/TiO$_2$) and 0.3 mgPt cm^{-2} (Pt/C) at operating temperatures of 40 °C (green), 60 °C (blue), and 80 °C (red). Full lines represent the measured cell voltage, while dashed lines give the cell voltage corrected by HFR. (**b**) Corresponding HFR
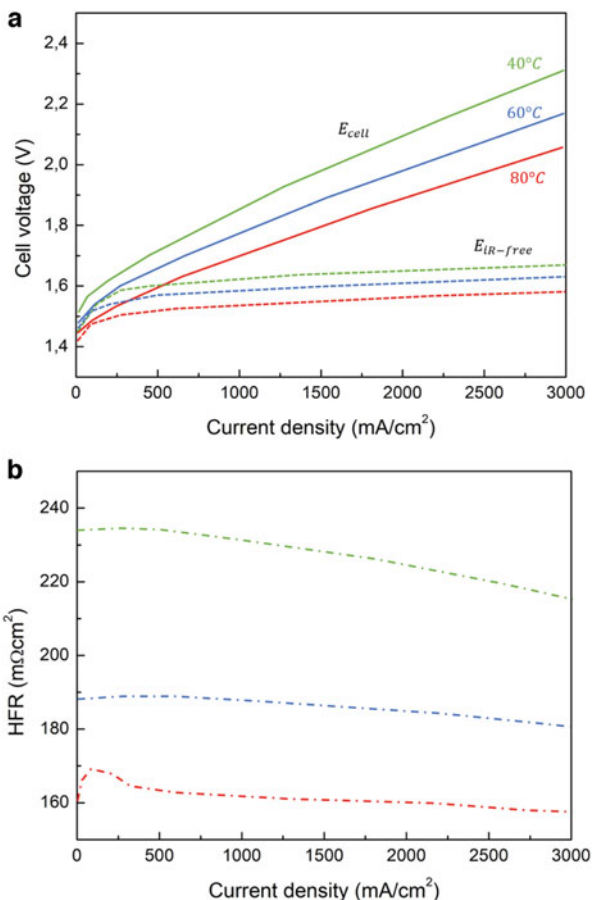
The difference in cell voltage between 40 and 80 °C is ≈160 mV at a current density of 1 Acm^{-2} and increases to more than 250 mV at 3 Acm^{-2}. This difference is the result of a 50% increase of membrane conductivity from 40 and 80 °C, resulting in a reduction of the HFR by ≈70 mΩcm^2 at 1 Acm^{-2}. For higher current densities, the HFR values slightly decrease, which can be explained by an increase of the temperature in the MEA due to the produced waste heat and, hence, a lower ionic resistance. This effect is most pronounced for the lowest temperature of 40 °C because of a higher total membrane resistance. Apart from the reduced ohmic resistance at higher temperature, a reduced kinetic overpotential is responsible for a difference of ≈90 mV when increasing the operating temperature from 40 to 80 °C (estimated from the difference in iR-free cell voltage at the lowest measured current density of 10 mAcm^{-2}). Reduced proton transport resistances in the electrodes as well as changes in mass transport resistance might also have an effect at higher current densities, but their influence on the overall performance is expected to be comparably small. This analysis shows that increasing the operating temperature of a PEM can significantly improve the performance.

However, high temperatures lead to an increase of the gas permeability and a decrease of the mechanical stability of the membrane and might result in an accelerated degradation rate (Ferrero et al. 2013). Along with stability issues with ion-exchange resins at temperature up to 60 °C, which are used to maintain the purity of the process water, these are the reasons why in today's commercial PEM-WE systems the temperature usually does not exceed 60–70 °C. Nevertheless, alternative membrane materials with good mechanical and gas barrier properties at elevated temperatures, such as short sidechain PFSA membranes, could enable operation at higher temperatures in the future.

Typical operating pressures of commercial PEM-WEs are in a range of 20–50 bar, but also higher pressures up to 350 bar have been demonstrated. Pressurized electrolysis is beneficial compared to ambient pressure operation because it could allow direct storage of H_2 without subsequent mechanical compression and it also reduces the effort for gas drying due to the lower water content at higher pressure. However, high-pressure operation leads to more demanding material requirements, imposes additional safety precautions, and reduces the faradaic efficiency due to a higher gas permeation through the membrane, especially critical at small current densities. Pressurized PEMs can be operated at balanced pressure (similar pressure on hydrogen and oxygen sides) or differential pressure (only hydrogen being pressurized). While balanced pressure reduces mechanical stress on the components compared to differential pressure, it requires a high-pressure water pump, handling of high pressure O_2, and leads to a reduced purity of H_2 due to an increased O_2 permeation rate (Olesen et al. 2019).

Several studies investigated the influence of operating pressure and mode (balanced vs. differential) on the overall system efficiency. Depending on the desired delivery pressure of H_2, an optimum was found for a pressure of 30–45 bar with differential pressure operation being more efficient than balanced pressure operation. Newer studies suggest that by reducing the energy demand for the gas drying process, the optimum operating pressure is shifted to values below 20 bar.

Figure 13 shows polarization curves along with the HFR recorded at ambient pressure ($p_{cath} = p_{an} = 1$ bar), differential pressure of 29 bar ($p_{cath} = 30$ bar, $p_{an} = 1$ bar), and balanced pressure of 30 bar ($p_{cath} = p_{an} = 30$ bar).

It can be observed that the cell voltage increases for high pressure operation compared to ambient pressure. The HFR is similar for all measurements with slightly lower values at high current densities and balanced pressure of 30 bar. An increase of cell voltage with pressure is expected due to the pressure dependency of the reversible cell voltage. At the applied operating temperature of 80 °C, the saturation pressure of water is 0.47 bar. Consequently, the partial pressure of H_2 and O_2 can be obtained by subtracting 0.47 bar from the total pressure in the cathode/anode compartment.

For the given cathode pressures of 1 and 30 bar this yields H_2 partial pressures of 0.53 and 29.53 bar, which results in a Nernstian voltage shift of 61 mV at 80 °C. Assuming that all other voltage losses are independent of the cathode pressure, the expected iR-free cell voltage at a differential pressure of 30 bar can be calculated by adding the Nernstian shift to the measured data at ambient pressure.

Fig. 13 (**a**) Polarization curves at 80 °C measured for an MEA with a NafionR117 membrane and catalyst loadings of 1.2 mgIr cm^{-2} (IrO$_2$/TiO$_2$) and 0.3 mgPt cm^{-2} (Pt/C) at ambient pressure (red), differential pressure of 29 bar (blue), and balanced pressure of 30 bar (green). Full lines represent the measured cell voltage, while dashed lines give the cell voltage corrected by HFR. (**b**) Corresponding HFR
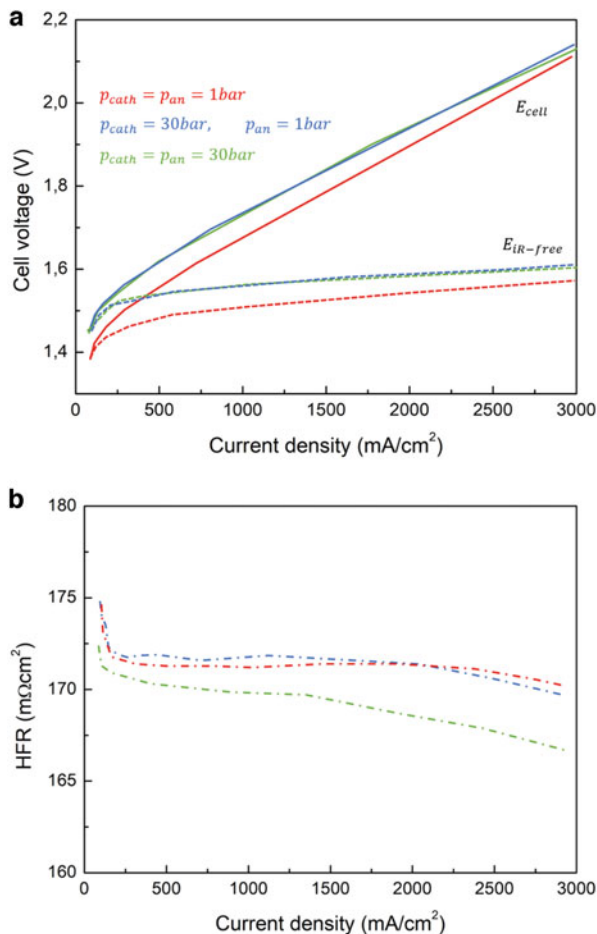
6   Degradation Phenomena

Sufficient lifetime is a key factor for commercialization of PEM with a DOE target for component replacement as high as 10 years. A lifetime of 60,000 h has been demonstrated for a commercial stack design by Proton OnSite with a relatively low degradation rate of 4 μVh^{-1}, while an improved system showed no measurable performance decay over more than 40,000 h. Even longer lifetimes of >100,000 have been demonstrated for PEM-WEs used for naval O$_2$ generation. However, these systems were operated at (quasi-)stationary conditions and relatively low temperatures and current densities (e.g., 50 °C and 1.3 Acm^{-2} for Proton OnSite test).

Furthermore, thick membranes (NafionR N1110, thickness of 254 μm, EW = 1100) and high catalyst loadings (10 mg cm^{-2} total PGM loading) were used. Application of PEMs for means of energy storage in a future energy scenario mainly based on renewable sources might result in frequent load cycles (accompanied by variations of temperature and pressure) and possible start-stop events, which could accelerate degradation processes. Additionally, cost reduction will result in thinner membranes, lower catalyst loadings, and operation at elevated current density and pressure, which could further increase degradation rates (Suermann et al. 2019).

Membrane and ionomer can degrade due to thermal, mechanical, and/or chemical stress. Chemical degradation of PFSA ionomers occurs due to radical induced attack leading to a gradual decomposition of the polymer. O_2 permeating through the membrane to the cathode reacts with atomic hydrogen chemisorbed on the surface of the platinum catalyst to form hydrogen peroxide (H_2O_2) and peroxyl radicals ($HO_2\bullet$), which can decompose into highly reactive nucleophilic radicals ($HO\bullet$). The chemical degradation then occurs generally by an attack of non-fluorinated end groups by the $HO\bullet$ radical. At dry operating conditions, also the R-CF$_2$-SO$_3$H-group can be attacked and decomposed to R-CF$_2\bullet$ from where the chain unzipping continues in a similar manner.

In PEM-WEs, the formation of H_2O_2 and the resulting membrane degradation is expected to occur predominantly at the cathode, since the Ir-based anode catalyst is in the oxide form during operation, suppressing the recombination of H_2 and O_2. Degradation of the membrane and ionomer can be quantified by measuring the fluorine release rate (FRR) and/or the membrane thickness. While membrane thinning due to chemical attack will first result in a performance increase due to a lower ohmic resistance, it will lead to increased gas permeation and, ultimately, cell failure due to formation of pin holes. Chemical degradation of the membrane and ionomer can be accelerated by introduction of cationic contaminations from the feed water or parts of the cell hardware. Transition metal cations such as Fe^{3+} and Cu^{2+} can promote the chemical decomposition of hydrogen peroxide to radicals, which accelerates membrane thinning.

Furthermore, cations can exchange with protons in the PFSA material resulting in a decreased proton conductivity. The performance loss due to this cation poisoning is reversible as shown by Sun et al. (2019), who could restore the initial performance of a contaminated MEA by treating the membrane with sulfuric acid. Stability of the membrane to mechanical stress is of great importance as well, especially for operation at elevated pressure. Creep failure under the cell stack loads at high operating pressure is a problem, especially for thin membranes. Ayers et al. (2021) showed a significant improvement in lifetime for thin reinforced PFSA membranes compared to standard PFSA membranes due to their better mechanical stability. Operating conditions can have a significant influence on membrane degradation as well. High gas pressure can lead to an increased FRR and a higher risk of mechanical failure. Increasing the temperature will lead to faster chemical degradation with FRRs increasing approximately by two orders of magnitude with a temperature increase from 55 to 150 °C.

Additionally, softening of the membrane material at high temperatures makes it more vulnerable to mechanical stress (Lee et al. 2013).

Degradation of the catalyst layer can occur due to dissolution or agglomeration of the catalyst as well as by catalyst surface blocking by metal ions. Dissolution of the Ir-based catalyst on the anode of a PEM-WE depends on the oxidation state of Ir, and a possible degradation mechanism was proposed. Furthermore, dissolution of Ir seems to be accelerated by high current densities (i.e., high potentials) or during load cycling. It was observed diffusion of dissolved iridium into the membrane during operation at high current density and they were showed spherical agglomerates of Ir nanoparticles in the membrane after load cycling between 1.4 and 2.0 V.

Dissolution of the Ir catalyst should in general lead to a lower OER activity due to a reduced electrochemically active surface area (ECSA). This effect is often masked by the high catalyst loadings used in PEM but would lead to a more significant performance decay for low Ir-loadings.

Agglomeration of catalyst particles was observed on the Pt cathode along with a migration and detachment from the carbon support. The contribution of this effect to the cell degradation was, however, found to be insignificant, which is consistent with the above discussed high HER activity of Pt.

Finally, cationic contaminations originating from the feed water or cell components can occupy ion exchange sites of the ionomer in the catalyst layer, resulting in an increase of the charge transfer resistance.

At anodic potentials in a PEM-WE, the surface of titanium based BPPs and PTLs is passivated by a thin oxide film. For prolonged operation at high potentials, this passivation can lead to a significant increase of the contact resistance between PTL and BPP. Noble metal coatings are frequently used to prevent passivation but add significant cost to the system. Corrosion of titanium at typical anode potentials is in general not expected but could occur due to the presence of fluoride ions originating from membrane/ionomer decomposition.

On the cathode, H_2 embrittlement could lead to cracking and mechanical failure of titanium based BPPs, however, it has been shown that H_2 uptake can be eliminated by applying a nitride coating.

In summary, many different degradation processes can take place in PEMs.

However, quantification of these effects is challenging due to long lifetimes for state of-the art materials ($>$10,000 h) under standard operating conditions (constant load).

Furthermore, comparison of literature results regarding degradation is difficult due to varying operating conditions and test protocols. Consequently, standardized AST protocols need to be developed to trigger specific degradation mechanisms to study durability of new materials in a reasonable time frame. ASTs can further be used to investigate the influence of different operating conditions, such as increased temperature, pressure, and intermittent operation on PEM lifetime.

7 Catalysts Activity

Any additional energy input over +1.23 V that is required to induce water splitting is known as the overpotential (η) and represents the intrinsic thermodynamic inefficiency of a particular system. The HER has a negligible activation energy whilst the OER has a large kinetic inhibition (large η) originating from a 4-electron proton coupled mechanism. Hence, the development of effective OER electrocatalysts is critical given that the OER is the limiting factor to an electrolyzer's efficiency. Given the aim of reducing the cost of hydrogen production via PEM electrolysis, researchers have attempted to produce NPM catalysts capable of efficient water splitting. For NPMs to have the potential of replacing precious metal catalysts, within a commercial electrolyzer, they need to exhibit low overpotentials towards the HER or the OER and achieve high current densities in acidic conditions. Enhancing the lifetime of the PEM cell and stack is critical to commercial implementation; therefore, the catalyst materials must also show excellent stability and corrosion resistance in acidic media. This paper will provide a detailed overview of the currently available literature regarding NPM catalysts for use as the cathodic and anodic materials within PEM electrolyzers (Hughes et al. 2021; Gao et al. 2021).

Presently, platinum (Pt) or Pt based electrocatalysts exhibit optimal electrochemical activity towards the hydrogen evolution reaction (HER), however long-term application within commercial electrolyzers is limited by high cost and low earth abundance.

The potential for scalability within NPM catalysts is dependent on the loading of the catalyst material, where a higher mass loading may reach a plateau with precious metal catalysts about activity but would result in inflated overhead and material costs. The activity per unit mass (or mass activity) is therefore a critical metric to assessing a NPM catalysts feasibility for use within commercial PEM electrolysis. Typical loading of commercial Pt/C on the cathode of a PEM electrolyzer is 0.5–1.0 $mgPt\,cm^{-2}$, where the mass activity of Pt/C is ca. 0.27 Amg^{-1} at 50 mV (vs. RHE). The stability of each HER catalyst in acidic conditions will be discussed and referenced to the benchmark stability of Pt/C, which remains stable for 50 h during chronopotentiometry measurements at $-10\ mA\ cm^{-2}$. Note, that a commercial PEM electrolyzer has been quoted to exhibit a lifetime of up to 60,000 h with no decay in cell voltage. The outlook regarding the decline in PEM electrolyzer performance is currently focused on catalyst degradation at the anode, however these degradation mechanisms are poorly understood. It was demonstrated that changes in the electrochemically active surface area (ECSA) and degradation of the Pt cathode results from power cycling in a PEM electrolyzer, which is thought to have a more significant effect on the performance of a PEM electrolyzer than initially thought. Thus, it is critical that studies of HER catalysts include extensive stability reports. Within this study we are addressing ways in which laboratory scale electrochemical techniques can assess the suitability of a catalyst for commercial PEM electrolysis.
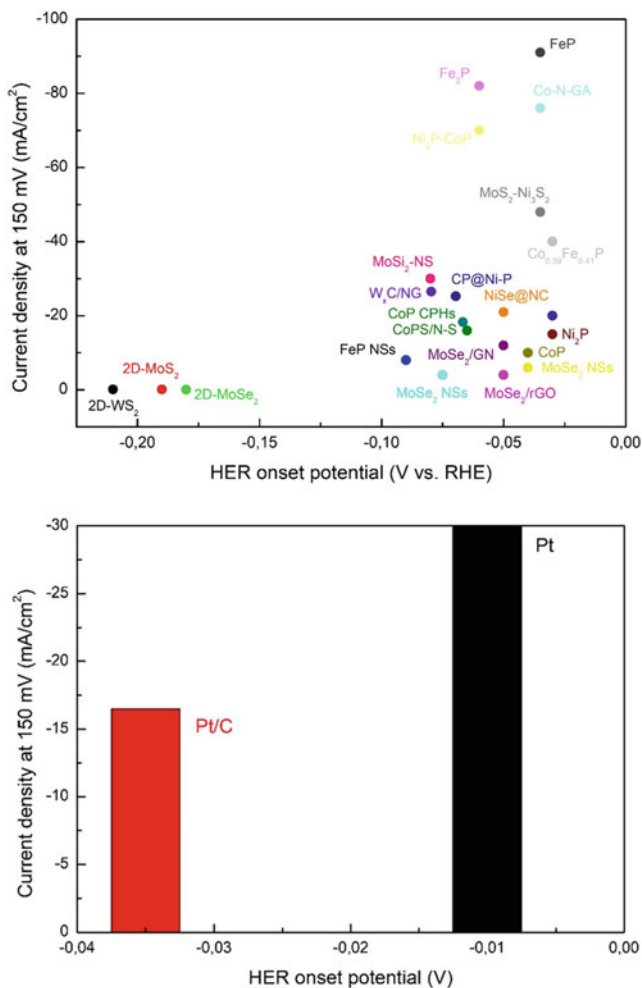
Fig. 14 Graphical overview of optimal performing catalysts towards the hydrogen evolution reaction (HER) in acidic media; HER onset potential (V vs. RHE) against the current density $(mAcm^{-2})$

Figure 14 shows the HER onset potential (V vs. RHE) vs. current density at -150 mV $(mAcm^{-2})$ for the catalysts. The HER onset is determined as the potential at which the Faradaic current commences, which is signified by the observed current deviating from the background current by the value of -25 μAcm^{-2}.

7.1 Transition Metal Dichalcogenides (TMD's)

In recent years, transition metal dichalcogenides (TMD's) such as MoS_2, $MoSe_2$, WS_2 and WSe_2 have been shown to be promising cathodic materials to act as HER catalysts (Pan 2014). A TMD nanosheet consists of two layers of chalcogens surrounding a single plane of a transition metal, where multiple layers are bonded by out-of-plane Van Der Waals interactions. TMD's contain two anisotropic planes: the relatively inert basal planes, and the highly active edge planes, which exhibit a fast rate of heterogeneous electron transfer (HET). An example of the use of a TMD towards the HER is a study that electrochemically tuned $2H–MoS_2$ with Li via a lithiation reaction, with sulfonated MoS_2 ($S–MoS_2$) conducting Li electrochemical intercalation. This resulted in a layer exfoliation and 2H to + 1 T phase conversion (semi conducting to metallic). $Li–MoS_2$ was chemically deposited onto carbon fiber paper and exhibited a HER onset potential of ca. -0.10 V (vs. RHE). For comparison, the optimal polycrystalline Pt electrode exhibits a HER onset potential of -0.01 V (vs. RHE). The 1 T phase of MoS_2 possesses a larger number of active sites compared to the 2H phase, which results in a higher charge transfer rate. Due to the metallic character in the partially filled d-band the 1 T phase is 107 times more conductive than the 2H phase. Increasing the ECSA of the electrode by reducing the size of the deposited nanoparticles also enhances conductivity and allows for stronger interactions. The 1 T phase of $Li–MoS_2$ exhibits high achievable current densities of -200 mA cm^{-2} at $\eta = 200$ mV; and exhibits a mass activity of 0.20 A mg^{-1} at 0.1 V (vs. RHE), which is nearing the mass activity of commercial Pt/C (0.27 A mg^{-1} at 0.05 V (vs. RHE)). However, there is insufficient stability data to conclude the suitability of the material within a PEM electrolyzer. A small potential window between +0.1 to -0.2 V (vs. RHE) was used to assess the variance in HER onset potential over 7000 cycles. This is not representative of the measured cell voltage of an operating PEM cell using benchmark Pt/C and Ir catalyst materials, which can be between +1.4 and +2.0 V. When assessing catalysts, the complete potential range of a PEM electrolyzer must be taken into account. This is due to the process of passivity, where corrosion of the catalyst layers during periods of electrolyzer inactivity, or during cell operation, can lead to oxidative conditions within the cathodic catalyst layer. They were carried out potentiostatic measurements at a $\eta = 118$ mV (vs. RHE) which reflected little variation in the current density (ca. -10 mAcm^{-2}) over a 2 h duration. The duration of this stability measurement is too short when compared against the benchmark stability of the Pt/C catalyst, which remains stable for more than 50 h within the same conditions. Additionally, PEM electrolyzers quote a stack lifetime of between 20,000 and 60,000 h, therefore more information must be provided regarding the stability of this HER catalyst.

The HER catalysis of TMD's can also be optimized by hybridization with a graphitic material such as graphene and carbon nanotubes, these graphitic additives increase the number of electronic conductive pathways and therefore the conductivity of a material. Doping TMD's with transition metals increases electron density at

the electrocatalytic active sites and allows electron transfer at the edge planes. It was enhanced the catalysis and conductivity of MoS_2 with Vanadium and Nitrogen dopants and reduced graphene oxide (rGO), respectively: V, N–MoS_2/rGO. The V, N–MoS_2/rGO composite was synthesized via a solvothermal method, which increased the number of defect sites on the basal and edge planes. A HER onset potential of -0.03 V (vs. RHE) was reported by the V, N–MoS_2/rGO suggesting excellent HER kinetics. The V, N–MoS_2/rGO also displays a high achievable current density of -100 $mAcm^{-2}$ at an overpotential of ca. 160 mV, however there is no statement of mass activity, hence there is no defining activity metric to assess whether the V, N–MoS_2/rGO is a feasible cathodic alternative to commercial Pt/C within a PEM electrolyzer. Note that previous reports have stated the mass activity of MoS_2/rGO to be 0.085 Amg^{-1} at 0.1 V (vs. RHE). Chronoamperometric measurements at $\eta = 90$ mV (vs. RHE) for 20 h exhibits no variation in a current density of -20 $mAcm^{-2}$. The absence of any long-term stability data involving TMD's is likely a result of their instability within aqueous solutions, over a large pH range. The suitability of any MoS_2 containing materials for PEM electrolysis is highly unlikely given the formation of oxidative defects, in the form of MoO_3, on the surface of MoS_2 nanosheets when in the presence of water.

It is also common to hybridize $MoSe_2$ with graphene additives. Certain studies have highlighted that $MoSe_2$ expresses the smallest band gap of all TMD's and therefore exhibits the best conductivity, where direct bandgaps of 1.88, 1.57, 2.03 and 1.67 eV relate to MoS_2, $MoSe_2$, WS_2 and WSe_2. They were hydrothermally prepared $MoSe_2$ nanosheets and $MoSe_2$/rGO which exhibited HER onset potentials of -0.15 and -0.05 V (vs. RHE), respectively. The HER onset potential exhibited by the $MoSe_2$/rGO hybrid is stated as an improvement on its MoS_2 counterpart, where a comparative study displays a HER onset potential of -0.08 V (vs. RHE) for its MoS_2/rGO hybrid. Additionally, the previously reported values of 0.085 and 0.14 Ag^{-1} for the mass activity of MoS_2/rGO and $MoSe_2$/rGO at 0.1 V (vs. RHE) demonstrates that $MoSe_2$ exhibits superior HER catalysis (Note: the mass activity of $MoSe_2$ is still not competitive with commercial Pt/C). This is explained by density functional theory (DFT) calculations for Gibbs free energy for hydrogen absorption (ΔG_H^0) at different H+ surface coverages on each TMD nanosheet. A proficient HER catalyst such as Pt will exhibit a ΔG_H^0 value close to the thermoneutral value ($\Delta G_H^0 = 0$). Values of -0.14 and -0.23 eV, are expressed by $MoSe_2$ at 75% H+ surface coverage and MoS_2 at 50% H+ surface coverage, respectively. Note that the values of ΔG_H^0 for $MoSe_2$ and MoS_2 stated within this study were those that were closest to the thermoneutral value. Tang and coworkers probed the stability of their $MoSe_2$/rGO catalyst deposited on fluorine doped tin oxide (FTO) using chronoamperometry measurements at 200 mV, where a slight degradation in current density from ca. 13.0 to ca. 12.5 $mAcm^{-2}$ was observed over a 2 h duration. It should be noted that displaying a catalyst stability study for a duration of 2 h is not sufficient to conclude that a catalyst displays efficient HER catalysis. Therefore, it is not appropriate to conclude that the $MoSe_2$/rGO catalyst utilized within this study is applicable to commercial PEM electrolysis given that the benchmark Pt/C catalyst remains stable for up to 50 h.

7.2 *Metal Organic Framework Derivatives*

Metal organic frameworks (MOF's) are typically organic/inorganic porous materials composed of grouped or ungrouped metal centers bound to organic ligands to exhibit a crystalline morphology (Xu et al. 2021). The HER catalysis displayed by MOF's is determined by several factors. The highly porous nature of MOF's results in surface roughness and therefore a high number of exposed active sites and enhanced heterogeneous electron transfer (HET). The HET process occurs at the triple phase boundary, which comprises of the electrolyte, catalyst phases and gaseous species within a PEM electrolyzer. Porosity also results in a large ECSA, which allows for the significant interface between the electrolyte and catalyst surface. Surface porosity plays a significant role in hydrogen adsorption and desorption, where stronger proton adsorption leads to a faster supply of protons but can also lead to slow release of hydrogen from active sites, hence poor HER kinetics. The porosity of MOF's may be tuned to achieve balanced adsorption/desorption behaviors. The nature of adsorption and desorption is dependent on the interaction between unfilled d orbitals of the transition metal and s orbitals of hydrogen. MOF's possess compositional flexibility, where the transition metal d orbitals can be tuned to increase electron density and enhance the HER activity. Pristine MOFs often suffer from poor conductivity and high charge transfer resistance. This can be mitigated by anchoring MOFs to carbon supports, which can significantly improve catalytic activity by increasing the number of electron conductive pathways. It was developed a cobalt embedded nitrogen graphene aerogel (Co–N-GA) whilst they controlled the porosity by confining the growth of MOFs within the graphene aerogel. The Co–N-GA exhibits excellent catalysis towards the HER with a HER onset potential of ca. -0.03 (vs. RHE), nearly matching the activity of Pt/C. The graphene aerogel and pristine MOF exhibit negligible HER activity, suggesting that the excellent performance of Co–N-GA is a result of the Co embedded in the few layered N-doped carbon aerogel. The optimized porosity of the Co–N-GA achieved by etching and hydrothermal treatment also contributed to the excellent HER catalysis. The Co–N-GA displays good achievable current density, reaching -100 mA cm^{-2} at $\eta = 183$ mV. The suitability of Co–N-GA within PEM electrolyzers relies on its mass activity and stability within acidic media. The mass activity of the Co–N-GA is not reported within the study and there is no data within the literature regarding a comparable HER catalyst within acidic media. This metric should be considered in future studies utilizing this catalyst. Promising stability data is offered within the study where chronoamperometry at -0.11 V (vs. RHE) does not alter the current density at -45 mAcm^{-2}. However, there is no evidence of the Co–N-GA's corrosion resistance over a longer duration than 5000 s. Given that the HER activity of this catalyst is benchmarked against Pt/C, the stability must also be referenced to Pt/C. The absence of long-term stability data is likely a result of the instability of the GA component in acidic conditions, as literature suggests that graphene degrades with prolonged exposure to water, and low pH conditions.

Isolated metal atoms (Ni, Fe and Co) have previously demonstrated proficient electrochemical activity towards the HER, due to their low coordination and unsaturated atoms functioning as active sites. It was developed an activated-Ni-carbon (A-Ni-C) catalyst, by carbonising an Ni-MOF precursor at 700 °C to obtain Ni-C, where HCl leaching was repeated to dissolve exposed Ni metal. A constant potential was applied to activate the catalysts. The A-Ni-C catalyst displays a HER onset potential of -0.03 V (vs. RHE) and achieves a current density of -100 mAcm^{-2} at $\eta = 112$ mV. There is no data on the mass activity of the A-Ni-C, however it was anchored zero valence single Ni atoms on graphdiyne which exhibited a mass activity of 16.6 Amg^{-1} at 0.2 V (vs. RHE), which is 7.19 times higher than Pt/C (2.31 Amg^{-1}). The excellent catalysis and conductivity of the A-Ni-C is attributed to the synergistic electrical charge transfer between catalytic active sites and the underlying graphitic carbon. Chronoamperometric measurements at $\eta = 45$ mV revealed fluctuating current deviation during 25 h measurements. The current density undergoes an increase at 11 h to ca. -14 mAcm^{-2}, which is due to catalyst activation. For that reason, the stability of the active catalyst is only tested for 14 h. The absence of a long-term stability study is likely a result of the instability of metallic Ni in acidic conditions. Ni undergoes very fast dissolution in weakly acidic solutions when exposed to normal operating temperatures of a PEM cell. In the temperature range 65–75 °C, full nickel dissolution is likely achieved in less than 200 min. The thermal and acidic instability of single atom Ni make it unsuitable for cathodic application within a PEM electrolyzer. Similarly, Co and Fe dissolve in 0.5 M H$_2$SO$_4$ under thermal and potential control, however, corrosion of these metal atoms may be inhibited by alloying with metal ions such as Zn^{2+} and Mn^{2+}. The dissolution of metal ions in acidic conditions is inhibited by the strong adsorption of Zn^{2+} and Mn^{2+} onto the primary metal surface, the primary metals being Ni, Co or Fe. When Zn^{2+} and Mn^{2+} are deposited onto the surface of the primary metal, they increase the potential at which dissolution occurs, because they exhibit less electronegative HER onset potentials compared to Ni, Co or Fe. This method is called under potential deposition, and has beneficial effects on the stability of a catalyst, however, leads to the increase in onset potential of the HER and OER.

7.3 Transition Metal Phosphides (TMP's)

The study of transition metal phosphides (TMP's) as active and stable cathodic materials has led to interesting discoveries about the nature of catalysis within transition metals and the electro kinetic contribution of phosphide ions. First row transition metals typically follow the trend of Mn < Fe < Co < Ni in regard to their electrochemical performance towards the HER; however, the trend is reversed when we consider the stability of the monometallic ion in acidic media (Brito et al. 2022). The phase space of TMP's has brought attention to their performance as catalysts for the HER, given that variation of phase and crystal structure of the transition metal results in different properties. For example, iron phosphides, FeP, Fe$_2$P and Fe$_3$P all
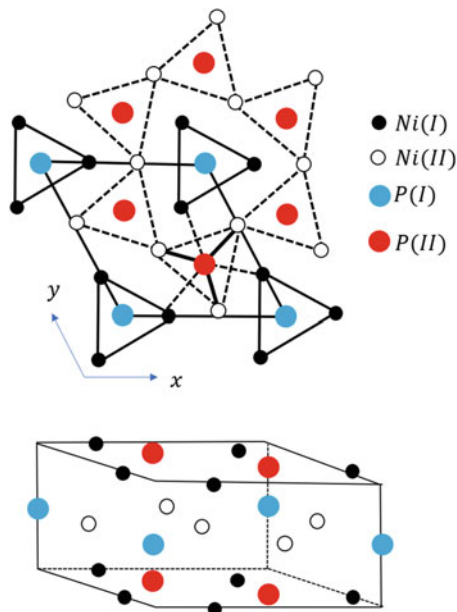
exhibit different catalytic activity and stability in acidic media. The crystal systems of FeP, Fe_2P and Fe_3P are orthorhombic, hexagonal, and tetragonal, respectively. Fe_3P is made up of the weakest covalent bonds in the ferric species but exhibits the strongest ionic interactions, largest metallicity and contains the largest number of Fe–Fe interactions. Exposed stepped surfaces of three-fold Fe and Fe–Fe bridge sites are thought to exhibit affinity for H+ ions, where Fe–P sites result in weaker adsorption of H+ ions. Similarly, to the iron phosphides, Ni–Ni interactions are responsible for strong hydrogen absorption, whereas Ni–P interactions exhibit weaker H+ affinity. An increase in the transition metal content leads to pronounced d-band character across the fermi level, which results in advantageous adsorption/ desorption behaviors, larger areas of electron density and a higher number of active sites within the compound. It was demonstrated that the Ni_2P crystal is made up of two types of Ni and P site, denoted in Fig. 15 as Ni (I), Ni (II), P (I) and P (II).

Figure 16 exhibits two types of supercell models.

The first model displays exposed Ni_3P_2 upon the (0 0 1) surface and the second exposed Ni_3P upon the (0 0 2) surface. The density of state (DOS) for the supercell models of Ni_2P informs us how developed the d-band is across the fermi level, where a higher DOS relates to significant adsorbent interaction, hence a lower activation barrier for the HER. The Ni_2P synthesized by the ligand stabilization method exhibits excellent electrochemical performance towards the HER with a HER onset potential of −0.03 V (vs. RHE), which is comparable to the HER onset potential of the optimal Pt/C electrocatalyst. The HER activity of Ni_2P remains unchanged after 500 cycles. The onset potentials of catalysts are typically assessed by CV up to 10,000 cycles; therefore, 500 C V cycles is not sufficient to assess the

longevity of a catalyst onset potential. The corrosion resistance and stability of the Ni_2P catalyst is not displayed within the study with no chronopotentiometric data to assess long-term durability. Transition metals alloyed with P show reduced metal dissolution in acidic media, as it is less thermodynamically favored. Ni_2P with a phosphorus content of ~30% P exhibits excellent corrosion resistance, making it more suitable as a cathodic catalyst layer within a PEM electrolyzer; whereas phosphorus content of ~15% P in a TMP is unsuitable, as stability and PEM cell lifetime would be reduced. However, higher P content can also lead to the restriction of electron delocalization in the transition metal, hence reducing the conductivity and the HER catalysis.

8 OER Catalysts Activity

Electrolytic water splitting is limited by the slow kinetics of the 4-electron coupled mechanism of the OER and therefore requires an efficient catalyst, which typically comprises of Ir and Ru oxides. In recent years, there has been a lot of research highlighting the excellent performance of OER catalysts in alkaline conditions, however these catalysts tend to be highly unstable in an acidic environment. The anchoring of OER catalysts to carbonaceous supports, as is common within HER studies, is not applicable for research of anodic catalysts within PEM electrolyzers, where high oxidation potentials lead to the formation of oxide films at the anode and corrosion of carbon materials.

Figure 17 is a plot exhibiting the OER onset potential (V vs. RHE) against the over potential required to reach +10 $mAcm^{-2}$. The OER onset is determined as the potential at which the Faradaic current commences, which is signified by the observed current deviating from the background current by the value of +25 μAcm^{-2}.
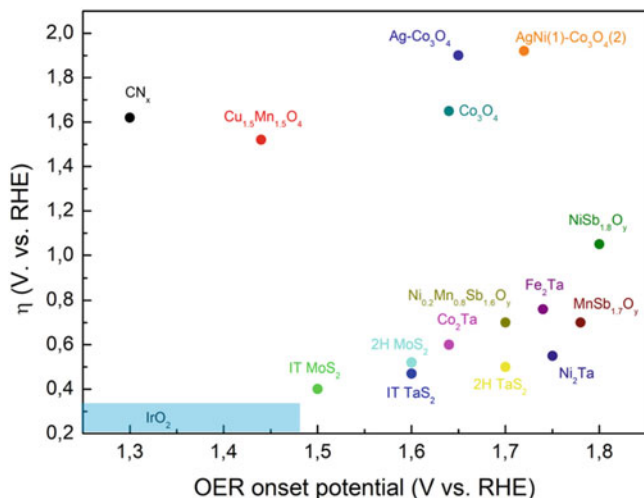
Fig. 17 Graphical overview of optimal performing catalysts towards the oxygen evolution reaction (OER) within acidic media; OER onset potential (V vs. RHE) against the over potential or ⬚ (V) required to reach +10 mA cm^{-2}. Optimal OER activity region occupied by IrO2 shown for comparison

8.1 Unary Metal Oxides

Unary metal oxides such as MnO_x, FeO_x, CoO_x and NiO_x have received considerable attention due to them being materials that show corrosion-resistant properties and good OER activity in acidic conditions. The stability of these oxides increases across the first row of transition metals (Ni to Mn), due an increase in the metal-oxygen bond strength, defining MnO_x as a highly stable material within low pH electrolytes. However, the stability observed for MnO_x comes at the cost of reduced OER activity, being that four adjacent Mn_{III} sites are required to produce two Mn_{IV} sites (the phase required for oxygen bonding). The small probability of coordinating four grouped Mn_{III} sites results in a material that exhibits poor OER activity in acidic media. Conversely, OER activity increases moving across the first row of the transition metals (Mn to Ni), owing to a weakening of the metal-oxygen interactions, which also results in reduced corrosion resistance. This activity trend is best described by the Sabatier principle, where the surface metal cations (M) are the active sites for the OER. The principle states that catalysts with optimal $M - O$ bond strength exhibit the best OER catalysis, whereas 'too strong' or 'too weak' $M - O$ interactions lead to reduced OER activity. The OER proceeds with the following $M - O$ bond intermediates: $M - OH$, $M - O$, M-OOH and M-OO. It was benchmarked the performance of mixed metal oxides and unary metal oxides in 1 M H_2SO_4 based on OER activity, stability, ECSA and Faradaic efficiency. IrO_x, NiO_x, CoO_x, CoO_x*, $NiCuO_x$, $NiCoO_x$, $NiFeO_x$ and $CoFeO_x$ were electrodeposited in varying mass

incorporations separately upon glassy carbon (GC) electrodes and then explored towards the OER. All materials exhibited similar catalytic activity in acidic media, where the lowest over-potentials to reach +10 mAcm^{-2} were exhibited by CoO$_x$* and CoFeO$_x$ ($\eta = {\sim}700$ mV (vs. SCE)). The mass activities of the unary metal oxides are not reported within this study. However, literature mass activity values of 0.11, 0.04, 0.03 and 0.12 Ag^{-1} correspond to CoO$_x$, NiO$_x$, FeO$_x$ and CoFeO$_x$, respectively. These values coincide with the findings by McCrory and co-workers given that CoO$_x$ and CoFeO$_x$ exhibit mass activities closest to that of IrO$_2$ (ca. 0.30 Ag^{-1}). The mass activity values exhibited by the metal oxides are not competitive with IrO$_2$, however financial incentives to implement these catalysts within the anode of PEM electrolyzers could arise from the low cost of raw Co, Fe and Ni metal (<£0.05 g^{-1}) compared to the high cost of pure Ir metal (ca. £58.00 g^{-1}). Only IrO$_x$ exhibited stability in acidic conditions. The instability of each electrodeposited non-noble catalyst was outlined by cycling for 2 h under oxidative conditions, given that all materials exhibited similar catalytic performance to the GC support. The observed instability arises when basic metal oxides meet strong acids, protonation occurs throughout the metal oxide framework, resulting in weak $M - O$ interactions. The strongly acidic 1 M H$_2$SO$_4$ electrolyte is rarely used in catalysis studies and is likely not representative of the pH conditions within a PEM electrolyzer. However, various studies have highlighted the instability of unary metal oxides in higher pH ranges of 2–3, in which certain mixed metal oxides exhibit stability.

It was designed several electrochemically active and acid-stable earth catalysts supported on FTO. Figure 18 depicts how it was used the chemistry of unary metal oxides to synthesize composites that used MnO$_x$ and PbO$_x$ as stabilizing elemental influences on highly active Co centers.

Tafel analysis in 100 mM Phosphate & 1 M KNO$_3$ (pH 2.5) for the unary metal oxides CoO$_x$, FeO$_x$, MnO$_x$, PbO$_x$ and IrO$_x$ yielded values of 82, 51, 650, 121 and 32 mV dec^{-1}, respectively. It is important to observe the stabilizing effects of unary metal oxides within mixed metal oxide films as a control. Mixed CoMnO$_x$ films electrodeposited at three different potentials exhibit Tafel values like that of CoO$_x$ at ${\sim}83$ mVdec^{-1}, displaying no variation in OER activity. Pb was substituted for Mn as the structural element within the mixed metal oxides, where a Tafel value of ${\sim}72$

Fig. 18 Content overview outlining how properties such as activity and stability of the abundant non-precious metals Co, Mn, Pb and Fe can be combined to result in a proficient OER catalyst
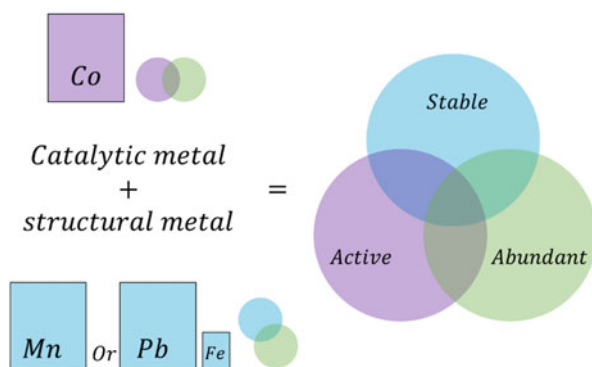
mVdec^{-1} was observed for CoPbO$_x$. The presence of Mn and Pb in the composites provides a structural framework that prevents the reduction of the catalytic active sites through the elimination of O$_2$, which would lead to M − O bond weakening. Instead, the elements that provide structural frameworks are oxidized to more stable forms i.e. PbO$_x$ = PbO$_2$, hence providing a more corrosion resistant composite. Chronopotentiometry was used to evaluate the long-term acid stability of the materials. For the OER at 0.1 mAcm^{-2}, CoMnO$_x$ electrodeposited at +0.90 V exhibited an OER potential of +1.5 V (vs. NHE) remaining undissolved after 12 h, compared to +2.0 V (vs. NHE) for MnO$_x$, remaining stable after 12 h. Chronopotentiometry at +1.0 mAcm^{-2} was used to further assess the stability of the mixed metal oxides, where CoMnO$_x$ electrodeposited at +0.90 V dissolved after 30 min. However, PbO$_x$ demonstrated long term acidic stability at +2.9 V (vs. NHE) for over 12 h. The stabilizing role of unary metal oxides such as PbO$_x$ and MnO$_x$ within mixed metal oxides is evident and present a promising method for enhancing the stability of active transition metals.

8.2 Mixed Metal Oxides

Structural unary metal oxides enhance the stability of Co containing mixed metal oxide films. It was demonstrated that the addition of structural oxides PbO$_x$ and MnO$_x$ into active Co centers did not result in reduced OER catalysis. Huynh and co-workers deposited Pb ions in unison with CoFeO$_x$ films to result in a CoFePbO$_x$ composite that exhibited the optimal Tafel value of ~70 mV dec^{-1}. Chronopotentiometry at +1.0 mAcm^{-2} was used to assess the stability of the CoFePbO$_x$ mixed film, which remained uncorroded at ca. + 1.8 V (vs. NHE) for over 50 h of constant cycling. Mixed metal oxides are typically uncommon compositions of metal oxide-based constituents, where most studies do not state values of mass activity (Zhang et al. 2022). However, it is expected that the mass activity of a mixed metal oxide will decrease with the addition of less active structural oxides such as PbO$_x$ and MnO$_x$.

Mn and Pb are often utilized as structural frameworks to improve corrosion resistance within active metal oxides, however, unary MnO$_x$s are limited by poor OER catalysis. Adjustment of the transition metal d-band position relative to the fermi level is thought to increase the number of optimal interactions of reactant and product species at the catalytic active sites. An increase in the number of optimal reactant-product interactions facilitates efficient adsorption and desorption processes. As a result, the OER onset potential is lowered. It was tuned the d-band in amorphous MnO$_2$ with Cu and F to match the fermi level of IrO$_2$ (−1.33 eV). Cu$_{1.5}$Mn$_{1.5}$O$_4$ and Cu$_{1.5}$Mn$_{1.5}$O$_4$:F were synthesized by a facile procedure and supported on porous Ti foil, where F was incorporated in %wt variations to achieve the correct linear shift of the d-band towards that of IrO$_2$. The Cu$_{1.5}$Mn$_{1.5}$O$_4$ and Cu$_{1.5}$Mn$_{1.5}$O$_4$:F composites both exhibited OER onset potentials of +1.43 V (vs. RHE), which matches the catalysis of IrO$_2$. The optimum incorporation of

10 %wt F into the $Cu_{1.5}Mn_{1.5}O_4$ composite, showed improvements in the current density at +1.55 V (vs. RHE) where current densities of +9.15, +6.36 and +7.74 $mAcm^{-2}$ were displayed by the F-doped and non-doped composites, as well as IrO_2, respectively. The following results suggest that F doping enhances electrical conductivity of the composite at 10 wt% incorporation. Surrounding literature also suggests that F doping has a positive influence on the stability of transition metal catalysts within acidic conditions. This is due to an increase in the number of polar metal-F interactions with high binding energies. They were carried out electrochemical stability studies that showed minimal deviation in OER performance over the course of 6000 cycles, with chronoamperometric measurements at +1.55 V (vs. RHE), over a 24 h duration also exhibiting no deviation in current density. However, there is a lack of long-term stability data to assess the suitability of fluorine doped metal oxides for anodic application within PEM electrolyzers, where chronopotentiometric measurements for up to 200 h and CV cycling for a minimum of 50,000 cycles should be exhibited to compare against the benchmark IrO_2 catalyst. It is possible to impart greater stability and activity to mixed metal oxides with the addition of Sb, which is thermally stable. It was sputter coated $Ni_xMn_{1-x}Sb_{1.6-1.8}O_y$ species-based catalysts onto conductive films of antimony-doped tin oxide (ATO) and evaluated catalytic activity in 1.0 M H_2SO_4 by cyclic voltammetry and chronopotentiometry. In general, films containing both Ni and Mn exhibited the lowest overpotentials, where the lowest over potential of 672 mV (vs. RHE) was displayed by $Ni_{0.5}Mn_{0.5}Sb_{1.7}O_y$. Chronopotentiometry under galvanostatic control at 10 $mAcm^{-2}$ and cyclic voltammetry outlined that $Ni_{0.5}Mn_{0.5}Sb_{1.7}O_y$ was stable for more than 150 h, with negligible increases in over potential. At several points during chronopotentiometric measurements, ICP-MS was used to determine the concentration of dissolved solids within the acidic electrolyte, where 56, 17 and 11% of the Mn, Ni and Sb, respectively, had leached from the $Ni_{0.5}Mn_{0.5}Sb_{1.7}O_y$ electrode after 144 h. The leaching of Mn within the composite provides a stable structural framework around the active surface of Ni leading to enhanced OER catalysis. Further stability of the composite is explained by the formation of the crystalline MSb_2O_6 rutile-type phase. The remarkable observations within this study outline the most stable phase of mixed metal oxides through the doping of the composite with antimony. Incorporation of $Ni_{0.5}Mn_{0.5}Sb_{1.7}O_y$ into the catalyst layer of the anodic side of a PEM electrolyzer would exhibit a 57% Faradaic efficiency.

8.3   Beyond Metal Oxides

TMD's typically exhibit good OER activity, however, suffer from dissolution in acidic conditions and poor stability in a highly oxidative environment, which hampers their application within PEM electrolyzers. They were exfoliated MoS_2 and TaS_2 nanosheets using liquid phase and lithium intercalation and assessed the catalysis of the trigonal prismatic (2H) versus the octahedral (1 T) phases in 0.5 M

H_2SO_4. The overpotentials to reach +10 mAcm^{-2} of 420, 450, 480 and 540 mV (vs. RHE) for 1 T-MoS_2, 1 T-TaS_2, 2H–MoS_2 and 2H–TaS_2 are comparable to that of IrO_2 (390 mV vs. RHE). Density functional theory (DFT) calculations outline that the catalysis exhibited by the TMD's is a result of the HET at the edge sites. Energy profiles of the IT and 2H phases of MoS_2 and TaS_2 show that the lowest activation barriers are exhibited by the 1 T phase. The stability of each material in acidic media is poor. Chronopotentiometric curves using 1 T-MoS_2 were recorded at +10 mAcm^{-2} after 2000 cycles between +1.2 and +2.0 V (vs. RHE). There was a marked increase in onset potential from +1.6–1.7 V (vs. RHE) after 2 h, suggesting poor stability in acidic and oxidative conditions.

Intermetallic alloys can consist of highly active transition metals, that are typically prone to dissolution in acidic media (Ni, Co and Fe), with corrosion resistant early transition metals (V, Nb and Ta). This combination can create stable catalysts that are potentially suitable as the anodic catalyst layers within PEM electrolyzers. They were synthesized first row transition metal alloys with Ta via high temperature and metallurgical routes. These alloys exhibit stable properties in acidic media relative to the single element components Ni, Fe and Co.

The crystal structure of the intermetallic alloys is shown in Fig. 19 using Ni2Ta as an example, which is the most catalytically active and stable anode material in acidic conditions.

Ni_2Ta rods were arc melted and their OER activity was assessed in 0.5 M H_2SO_4 with polycrystalline powders of Ni_2Ta, Co_2Ta and Fe_2Ta. Overpotentials of 980, 570, 600 and 770 mV (vs. RHE) were observed at +10 mAcm^{-2}, respectively.

Fig. 19 Crystal structure of Ni2Ta showing the positions of the Ni and Ta atoms

Ni

Ta
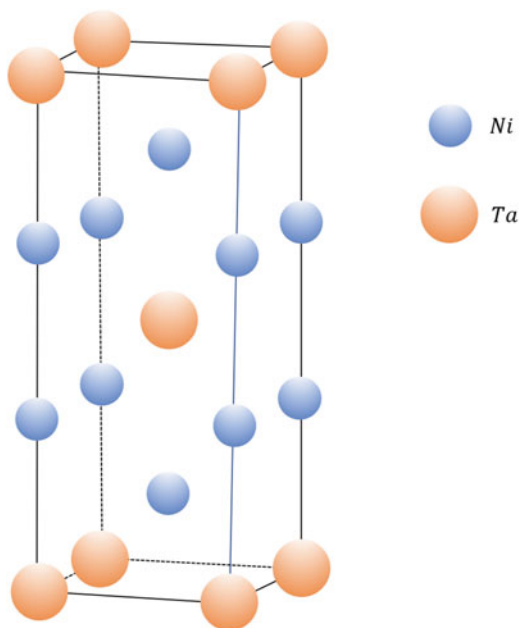
The Ni_2Ta rods exhibited no deviation in OER performance during galvanostatic measurements at 10 mAcm^{-2} for 3 days. Corrosion resistance of the Ni_2Ta rods was assessed by ICP-OES, which was used to measure time dependent dissolution of Ni and Ta from the Ni_2Ta rods. A pure Ni control rod leached 43.6 μg min^{-1} of Ni, whereas the Ni_2Ta rods exhibited Ni dissolution of only 0.393 μg min^{-1}. This is superior to the corrosion data obtained for IrO_2 and RuO_2 within 0.5 M H_2SO_4. The rate of Ta dissolution was 0.15 ngmin^{-1}, hence highlighting the formation of TaO_x upon dissolution of Ni, where TaO_x is known to be highly stable in acidic media. Like Mn and Pb, Ta has the potential to be incorporated into the structures of active OER materials to enhance stability and corrosion resistance. This should be considered in future studies. Note that Wu, Mondschein and co-workers did not state values of mass activity for their catalysts and representative comparisons may not be stated.

8.4 Anodic Conductive Supports

The suitability of a catalyst material for use within PEM electrolysis is not only based on the active material. Promising catalysts are anchored upon supporting materials for several reasons: reducing the cost of the catalyst-coated membrane (CCM) by reducing catalyst loading; enhancing electrical conductivity of the catalyst layer; increasing lifetime of the CCM; and providing a large surface area for catalyst deposition (Rozain et al. 2016).

Excellent electrical conductivity and high surface area for catalyst dispersion are properties that shape carbon-based materials as effective catalyst supports within fuel cells and the cathodic side of PEM electrolyzers. Anchoring cathodic catalyst materials to carbon-based supports has many benefits: carbon supports provide electronic conduction pathways between the electrode and the catalyst; carbon supports allow catalytic materials to be deposited on a nanoparticle level; and carbon materials are also durable in acidic media. Catalyst supports are therefore key to the current output of the electrolyzer and its longevity. However, carbon-based supports are not suitable for application within the anodic side of electrolyzers given that they suffer fast corrosion under high oxidative potentials.

Effective support materials can enhance the electro kinetics of the anodic catalyst layer. Increasing the electroactive surface area allows for the optimal surface dispersion of highly active particles that lower the OER onset potential. This increase in surface area also enables the low loading of active catalyst materials thus reducing the costing associated with the MEA. Degradation of the catalyst layers can result in reduced system and stack lifetimes within PEM electrolyzer cells. Therefore, research of corrosion resistant materials provides a pathway to increasing the lifetime of PEM electrolyzer technologies. Titanium is typically used as the anodic support material within PEM electrolyzers. Titanium (TiO_2) and tin oxides (SnO_2) have been studied as alternative OER supports given their high resistance to anodic oxidative conditions, however, are mainly utilized as supports for IrO_2 or RuO_2 within the literature and are limited by their poor electronic conductivity (~10^{-6} Scm^{-1}).

One study utilizing a TiO_2 support for a noble metal free OER catalyst embedded iron oxide within titania nanowires (Fe_2O_3/TiO_2 NWs). The Fe_2O_3/TiO_2 NWs and Fe_2O_3 supported on Ti foam exhibited OER onset potentials of +1.46 and +1.63 V (vs. RHE). Given that Fe_2O_3 is unstable in acidic media within anodic oxidative conditions, it is important to assess the stabilizing effect of the titania nanowires. Chronopotentiometry at +1.9 V (vs. SCE) for 20 h in 0.5 M H_2SO_4 displayed current density decays of 30.3 and 66.7% for the Fe_2O_3/TiO_2 NWs and Fe_2O_3 supported on Ti foam, respectively. Fe_2O_3 embedded within titania nanowires experiences less current degradation than its counterpart without a titania support. Antimony doped tin oxide (ATO) is a support material highlighted for its high conductivity (0.57 Scm^{-1}), thermal stability (>250 °C) and acid stability in oxidative conditions. They were supported Cobalt hexacyanoferrate nanoparticles upon ATO (ATO@CoHFe), where the ATO@17% CoHFe (39.7 mg ATO and 8 mg CoHFe) exhibited optimal OER catalysis with an onset potential of 1.80 V (vs. RHE), compared to the negligible OER catalysis exhibited by the unmodified ATO support. The stability of the ATO@17% CoHFe was probed within a PEM electrolyzer cell at a fixed voltage of +2.0 V for 22 h, where a 10% degradation in current density was observed. The cell potential was ramped to +2.2 V, where a significant degradation in current density was observed, which was attributed to leaching within the ATO support. Quantification of the dissolved ATO support was carried out by ICP-MS, where at a cell voltage of +2.0 V elemental losses for Sn and Sb were 0.16 and 8.5%, respectively. When the potential was ramped to +2.2 V, elemental losses of 22.6 and 52.7% were recorded for Sn and Sb, respectively. These findings are unprecedented given that ATO has only been reported to be stable at cell voltages up to +1.8 V. The above studies challenge the application of titania or ATO as anodic catalyst support systems within PEM electrolyzer cells, particularly at high oxidative potentials (>+ 1.8 V) where significant current degradation and elemental dissolution is observed. It is evident that more research needs to be carried out regarding nonprecious metals supported on highly stable conductive substrates. The studies within this area are sparse and typically focus on precious metal catalysts such as IrO_2 or RuO_2.

9 Conclusions

Plenty of HER studies report on catalysts that exhibit excellent HER catalysis and compare that to the near zero overpotential of the benchmark Pt/C catalyst; as a result, there is a plethora of proficient HER catalysts within literature. However, most of these studies evaluating HER specific catalysts contain limited information on the long-term durability of their catalysts, thus a definitive conclusion on their suitability within PEM electrolysis is challenging. It would be natural to assume that if the HER activity of each catalyst were benchmarked against Pt/C, then their stability should also be benchmarked against Pt/C. This is a critical measurement

given that the partial degradation of a PEM electrolyzers performance may be attributed to the Pt based cathode. However, of all the HER studies reviewed herein, only two catalysts are tested using chronopotentiometry for a duration longer than 20 h, where Pt/C is known to remain stable for more than 50 h.

None of these HER studies coincide their stability measurements with ICP-MS measurements, thus there is a lack of information pertaining to leaching within HER specific catalysts. There is progress within the synthesis of HER catalysts, where alloying active metals such as Ni, Fe or Co with highly stable metals such as Pb, Zn, Sb, Ta or Mn creates a structural framework that exhibits promising stability in acidic conditions. This is also observed when active metal centers are doped with optimal quantities of phosphorus, such as CP@Ni–P which remains stable after 150 h of chronopotentiometry at -10 mAcm^{-2} in acidic conditions.

It is often the case that more comprehensive stability examinations take place in studies regarding OER specific catalysts. This is likely due to the high oxidative potentials at the surface of the anode as the Faradaic process of the OER proceeds. Because of this, many studies deposit OER specific catalysts on non-carbon-based supports such as ATO or FTO. Studies that support their OER specific catalysts on carbonaceous materials are uninstructive on the basis that data obtained by this method is not translational to commercial PEM electrolysis.

However, most studies that take this factor into account carry out more extensive stability studies, involving chronopotentiometric measurements for 50 h or more, coupled with ICP-MS analysis. The same principles for catalyst synthesis used in HER catalysis apply to OER catalysts too, where stable elements provide a structural framework for active metals and therefore high stability. OER catalysts such as: Ni_2Ta, $MnSb_{1.7}O_y$, $NiSb_{1.8}O_y$ and $Ni_{0.5}Mn_{0.5}Sb_{1.7}O_y$ synthesized using these principals achieve catalyst durability from 70 to 200 h, where the benchmark OER catalyst IrO_2, is known to remain stable for up to 200 h during chronopotentiometric measurements.

Another key consideration for the application of NPM catalysts at the anode or cathode of a PEM electrolyzer is mass activity (current output per unit mass). This activity metric merges catalyst loading and current output to differentiate between excellent catalysis because of ultra-high catalyst loading, and relative catalysis with low catalyst loading.

If the mass activities of NPM HER and OER catalysts are benchmarked against the mass activities of the precious metal catalysts currently utilized in commercial PEM electrolysis, the economic viability of these catalysts for use within PEM electrolyzsers can be calculated based on required quantities and cost of raw materials. However, mass activity is not reported in the majority of studies utilizing NPM HER and OER catalysts but is regularly provided in studies regarding precious metal based catalysts. It is common within the literature for mass activities to be reported at a range of different potential values, making comparisons between the mass activities of different catalysts impractical.

References

Ayers K (2021) High efficiency PEM water electrolysis: enabled by advanced catalysts, membranes, and processes. Curr Opin Chem Eng 33:100719. https://doi.org/10.1016/j.coche.2021.100719

Ayers KE, Capuano C, Anderson EB et al (2012) Recent advances in cell cost and efficiency for PEM-based water electrolysis. ECS Trans 41:15. https://doi.org/10.1149/1.3684798

Ayers K, Danilovic N, Harrison K, Xu H (2021) PEM Electrolysis, a Forerunner for Clean Hydrogen. Electrochem. Soc. Interface 30:67. https://doi.org/10.1149/2.F16214IF

Bessarabov B, Wang H, Li H, Zhao N (2015) PEM electrolysis for hydrogen production. https://doi.org/10.1201/b19096

Bi J, Yang J, Liu X et al (2021) Development and evaluation of nitride coated titanium bipolar plates for PEM fuel cells. Int J Hydrog Energy 46(1):1144–1154. https://doi.org/10.1016/j.ijhydene.2020.09.217

Brito J, Restivo J, Sousa JPS et al (2022) Implementation of transition metal phosphides as Pt-free catalysts for PEM water electrolysis. Energies 15(5):1821. https://doi.org/10.3390/en15051821

Burdzik A, Stähler M, Friedrich I et al (2018) Homogeneity analysis of square meter-sized electrodes for PEM electrolysis and PEM fuel cells. J Coat Technol Res 15:1423–1432. https://doi.org/10.1007/s11998-018-0074-3

Bystron T, Vesely M, Paidar M et al (2018) Enhancing PEM water electrolysis efficiency by reducing the extent of Ti gas diffusion layer passivation. J Appl Electrochem 48:713–723. https://doi.org/10.1007/s10800-018-1174-6

Carmo M, Fritz DL et al (2013) A comprehensive review on PEM water electrolysis. Int J Hydrog Energy 38(12):4901–4934. https://doi.org/10.1016/j.ijhydene.2013.01.151

Carmo M, Henkensmeier D, Lüke W et al (2015) Inhibiting the swelling behavior of nafion membranes for PEM water electrolysis. Meet Abstr MA2015-02:1515. https://doi.org/10.1149/MA2015-02/37/1515

Fallisch A, Schellhase L, Fresko J et al (2017) Investigation on PEM water electrolysis cell design and components for a HyCon solar hydrogen generator. 42(19):13544–13553. https://doi.org/10.1016/j.ijhydene.2017.01.166

Ferrero D, Lanzini A, Santarelli M et al (2013) A comparative assessment on hydrogen production from low- and high-temperature electrolysis. Int J Hydrog Energy 38(9):3523–3536. https://doi.org/10.1016/j.ijhydene.2013.01.065

Frensch SH, Fouda-Onana F, Serre G et al (2019) Influence of the operation mode on PEM water electrolysis degradation. Int J Hydrog Energy 44(57):29889–29898. https://doi.org/10.1016/j.ijhydene.2019.09.169

Gao J, Tao H, Liu B (2021) Progress of nonprecious-metal-based electrocatalysts for oxygen evolution in acidic media. Adv Mater 33:2003786. https://doi.org/10.1002/adma.202003786

Grigoriev SA, Kalinnikov AA, Millet P et al (2010) Mathematical modeling of high-pressure PEM water electrolysis. J Appl Electrochem 40:921–932. https://doi.org/10.1007/s10800-009-0031-z

Grigoriev SA, Porembskiy VI, Korobtsev SV (2011) High-pressure PEM water electrolysis and corresponding safety issues. Int J Hydrog Energy 36(3):2721–2728. https://doi.org/10.1016/j.ijhydene.2010.03.058

Hughes JP, Clipsham J, Chavushoglu H, Rowley-Neale SJ, Banks CE (2021) Polymer electrolyte electrolysis: a review of the activity and stability of non-precious metal hydrogen evolution reaction and oxygen evolution reaction catalysts. Renew Sustain Energy Rev 139:110709. https://doi.org/10.1016/j.rser.2021.110709

Immerz C, Bensmann B, Trinke P et al (2018) Local current density and electrochemical impedance measurements within 50 cm single-channel PEM electrolysis cell. J Electrochem Soc 165:F1292. https://doi.org/10.1149/2.0411816jes

Ito H, Maeda T, Nakano A (2011) Properties of Nafion membranes under PEM water electrolysis conditions. Int J Hydrog Energy 36(17):10527–10540. https://doi.org/10.1016/j.ijhydene.2011.05.127

Jacobson LC, Ren X, Molinero V (2014) Assessing the effects of crowding, pore size, and interactions on electro-osmotic drag coefficients. J Phys Chem C 118(4):2093–2103. https://doi.org/10.1021/jp410910r

Karimi F, Peppley BA (2017) Metal carbide and oxide supports for iridium-based oxygen evolution reaction electrocatalysts for polymer-electrolyte-membrane water electrolysis. Electrochim Acta 246:654–670. https://doi.org/10.1016/j.electacta.2017.06.048

Kaya MF, Demir N (2017) Numerical investigation of PEM water electrolysis performance for different oxygen evolution electrocatalysts. Fuel Cells 17(1):37–47. https://doi.org/10.1002/fuce.201600216

Klose C, Saatkamp T, Münchinger A et al (2020) All-hydrocarbon MEA for PEM water electrolysis combining low hydrogen crossover and high efficiency. Adv Energy Mater 10:1903995. https://doi.org/10.1002/aenm.201903995

Langemann M, Fritz DL, Müller M (2015) Validation and characterization of suitable materials for bipolar plates in PEM water electrolysis. Int J Hydrog Energy 40(35):11385–11391. https://doi.org/10.1016/j.ijhydene.2015.04.155

Lee B, Park K, Kim HM et al (2013) Dynamic simulation of PEM water electrolysis and comparison with experiments. Int J Electrochem Sci 8:235–248

Lee CH, Banerjee R, Arbabi F et al (2017) Porous transport layer related mass transport losses in polymer electrolyte membrane electrolysis: a review. In: International conference on nanochannels, microchannels, and minichannels (ICNMM). https://doi.org/10.1115/ICNMM2016-7974

Li A, Sun Y, Yao T et al (2018) Earth-abundant transition-metal-based electrocatalysts for water electrolysis to produce renewable hydrogen. Chem Eur J 24:18334–18355. https://doi.org/10.1002/chem.201803749

Liu Y, Huang S, Peng S et al (2022) Novel Au nanoparticles-inlaid titanium paper for PEM water electrolysis with enhanced interfacial electrical conductivity. Int J Miner Metall Mater 29:1090–1098. https://doi.org/10.1007/s12613-022-2452-1

Mayousse E, Maillard F, Fouda-Onana F (2011) Synthesis and characterization of electrocatalysts for the oxygen evolution in PEM water electrolysis. Int J Hydrog Energy 36(17):10474–10481. https://doi.org/10.1016/j.ijhydene.2011.05.139

Millet P, Mbemba N, Grigorie SA (2011) Electrochemical performances of PEM water electrolysis cells and perspectives. Int J Hydrog Energy 36(6):4134–4142. https://doi.org/10.1016/j.ijhydene.2010.06.105

Nouri-Khorasani A, Ojong ET, Smolinka T (2017) Model of oxygen bubbles and performance impact in the porous transport layer of PEM water electrolysis cells. Int J Hydrog Energy 42(48):28665–28680. https://doi.org/10.1016/j.ijhydene.2017.09.167

Olesen AC, Frensch SH, Kær SK et al (2019) Towards uniformly distributed heat, mass and charge: a flow field design study for high pressure and high current density operation of PEM electrolysis cells. Electrochim Acta 293:476–495. https://doi.org/10.1016/j.electacta.2018.10.008

Onda K, Murakami T, Hikosaka T et al (2002) Performance analysis of polymer-electrolyte water electrolysis cell at a small-unit test cell and performance prediction of large stacked cell. J Electrochem Soc 149(8):1069–1078. https://doi.org/10.1149/1.1492287

Pan H (2014) Metal dichalcogenides monolayers: novel catalysts for electrochemical hydrogen production. Sci Rep 4:5348. https://doi.org/10.1038/srep05348

Rozain C, Mayousse E, Guillet N et al (2016) Influence of iridium oxide loadings on the performance of PEM water electrolysis cells: part II–advanced oxygen electrodes. Appl Catal B: Environ 182:122–131. https://doi.org/10.1016/j.apcatb.2015.09.011

Schalenbach M, Tjarks G, Carmo M, Lueke W, Mueller M, Stolten D (2016) Acidic or Alkaline? Towards a New Perspective on the Efficiency of Water Electrolysis. J. Electrochem. Soc. 163:F3197. https://doi.org/10.1149/2.0271611jes

Schmidt G, Suermann M, Bensmann B et al (2020) Modeling overpotentials related to mass transport through porous transport layers of PEM water electrolysis cells. J Electrochem Soc 167:114511. https://doi.org/10.1149/1945-7111/aba5d4

Siracusano S, Baglio V, Van Dijk N et al (2017) Enhanced performance and durability of low catalyst loading PEM water electrolyser based on a short-side chain perfluorosulfonic ionomer. Appl Energy 192:477–489. https://doi.org/10.1016/j.apenergy.2016.09.011

Suermann M, Bensmann B, Hanke-Rauschenbach R (2019) Degradation of proton exchange membrane (PEM) water electrolysis cells: looking beyond the cell voltage increase. J Electrochem Soc 166:F645. https://doi.org/10.1149/2.1451910jes

Sun X, Simonsen SC, Norby T et al (2019) Composite membranes for high temperature PEM fuel cells and electrolysers: a critical review. Membranes 9(7):83. https://doi.org/10.3390/membranes9070083

Trinke P, Haug P, Brauns J et al (2018) Hydrogen crossover in PEM and alkaline water electrolysis: mechanisms, direct comparison and mitigation strategies. J Electrochem Soc 165:F502. https://doi.org/10.1149/2.0541807jes

Xu X, Sun H, Jiang SP et al (2021) Modulating metal–organic frameworks for catalyzing acidic oxygen evolution for proton exchange membrane water electrolysis. SusMat 1:460–481. https://doi.org/10.1002/sus2.34

Zhang S, Ma X, He Y et al (2022) Amorphous mixed Ir–Mn oxide catalysts for the oxygen evolution reaction in PEM water electrolysis for H2 production. Int J Hydrog Energy. https://doi.org/10.1016/j.ijhydene.2022.11.316

Anion Exchange Membrane Water Electrolysis

1 Introduction

AEM water electrolysis cells consist of a hydrocarbon anion exchange membrane and two transition metal catalyst-based electrodes. The distilled water or a low concentration alkaline solution can be utilized as the electrolyte in the AEM, rather than concentrated KOH solution. The AEM approach combines the merits of PEM and alkaline electrolysis. Polymeric anion exchange membranes have recently been developed by researchers from organizations and universities, although interest has predominantly been focused on catalyst design towards half-cell test rather than the further application of AEM electrolysis (Li and Baek 2021).

AEM electrolysis technology is still under early development and requires further investigation. Coordinated research of AEM electrolysis is currently needed to improve power efficiency, membrane stability and ionic conductivity, to reduce the total stack cost, and to integrate catalysts into AEM systems. Some works that have been conducted at laboratory scale provide valuable guidance for understanding the operating mechanism, and developing the main electrocatalyst, membrane and ionomer components.

One of the predominant benefits of AEM electrolysis is the ability to use platinum group metal (PGM)-free electrocatalysts towards the hydrogen evolution reaction (HER) and oxygen evolution reaction (OER) in separate reaction chambers. This reduces the capital cost of AEM water electrolysis. Current challenges in AEM catalyst development are the optimization of chemical composition, stability and overall activity when integrated in the AEM system. PGM-free electrocatalysts usually have relatively low mass-specific activity compared with noble metal-based catalysts, which leads to large catalyst loading on the membrane electrode assembly (MEA) and large Ohmic resistance losses.

Noble metal Ruthenium and Iridium (Pt, Ru and Ir) based HER catalysts have demonstrated excellent HER activity in a pH-universal environment. PGM-free HER electrocatalysts lack this property because HER kinetics are sluggish under

alkaline conditions, due to the further proton dissociation step from water molecules and the formation of hydrogen intermediates (H_{ad}) on comparing with catalyst working in acid condition.

H_2O dissociation and subsequent H_{ad} adsorption on the catalyst surface is quite slow and the consequent formation of initial hydrogen intermediates becomes the rate determining step (RDS) of the entire HER mechanism. This makes the alkaline HER more complex than HER in acidic conditions because some important species/ steps (H_{ad}, hydroxyl adsorption and water dissociation) must be optimized for superior performance. Specifically, in AEM HER electrolysis more energy is required to break the robust H-O covalent bonds of water and is regarded a crucial step that determines HER activity. Within this context, rational design of PGM-free HER electrocatalysts on AEM system is of superb importance to bring out the distinguished advantages over the PEM for up-coming hydrogen society. Some studies have also reported the superior performance of AEM eletrolyzer using PGM-free HER catalyst over the PGM-based materials in either PEM or AEM system. Their application further proves the reliable hydrogen acquisition in the AEM approach. Here, the development of those inexpensive HER materials evaluated in AEM electrolysis is emphasized in this section.

Ni-based hybrids are frequently adopted as HER catalysts in AEM electrolysis. In most studies, they are reported to have activity inferior to PGM materials. Ni nanopowders with a catalyst loading of $2\,mgcm^{-2}$ can be used as a hydrogen evolution catalyst in AEM electrolysis systems and have achieved a current density of $100\,mAcm^{-2}$ at an applied voltage of 1.99 V at a temperature of 44 °C. Particle-type electrodes were also developed with ultra-low Ni/Pt particle loading ($13.2\,\mu gcm^{-2}$), coated on carbon paper. The as-prepared MEA using Pt-Ni/CP-2 as the cathode electrocatalyst exhibited pronounced performance with an available current density of $250\,mAcm^{-2}$ at $1.9\,V_{cell}$ (60 °C). This performance surpassed or approached the top activity in previous reports using a much higher catalyst loading range of 3.1–$80\,mgcm^{-2}$. Despite this, Ni metal still has relatively poor activity and stability, and for enhanced performance needs to be combined with other materials, such as transition metals-based oxides, chalcogenide selenides, nitrides, and phosphides.

Using commercially available materials such as ACTA 3030 ($Ni/(CeO_2$-$La_2O_3)/$ C) as the HER electrocatalyst, the performance of these mixed Ni-based oxides was tested in a diluted $K_2CO_3/KHCO_3$ electrolyte solution (pH 10–11) separated by an A-201 anion exchange membrane (Tokuyama Corporation). The catalyst loading on the cathode was thought to have a huge influence on the performance of the AEM system when the $CuCoO_x$ mixed oxides was fixed at the loading of $36\,mgcm^{-2}$ on anode. By varying the $Ni/(CeO_2$-$La_2O_3)/C$ loading from 0.6 to $7.4\,mgcm^{-2}$, an exported cell potential between 2.01 and 1.89 V was obtained at $470\,mAcm^{-2}$ at 43 °C. The cathode catalyst loading also affected the alternating-current (AC/1 kHz) resistance at different current density values, although the reaction mechanism remains controversial considering complexity of the system. It is also worth noting that stability of the as-prepared system was remarkable, with no cell potential degradation in 800 h under a constant differential pressure of 3 MPa. This suggests its potential value for durable and efficient hydrogen production.

Employing alloys is also a viable approach to improve HER activity on Ni. A NiMo alloy cathode and NiFe alloy anode were assembled and impregnated with a self-crosslinking quaternary ammonia polysulfone (xQAPS) membrane as the MEA. The anode and cathode had a high catalyst loading of $40\,\mathrm{mgcm^{-2}}$, which led to an AEM cell performance of $400\,\mathrm{mAcm^{-2}}$ at a cell voltage of 1.8–1.85 V under 70 °C pure water electrolyte. In another work, $Ni_{0.9}Mo_{0.1}$ nanosheets were synthesized and tested to have a cathode performance comparable to Pt nanoparticles in a AEM cell. The sponge-like structure of the NiMo alloy was believed to expose a much higher specific surface area. The NiMo/X72 achieved $1\,\mathrm{Acm^{-2}}$ at 1.9 V in 1 M KOH, while the Pt particle reached the same current density value at 1.8 V, suggesting a small performance gap between the NiMo alloy and Pt-PGM catalyst.

The multiple four-electron reaction on OER indicates a more complex mechanism and inherently sluggish character compared with HER. It requires efficient catalyst participation to adsorb the reactants and to transfer them as intermediates to the surface of the catalyst for subsequent steps. In an AEM system, cell performance has a close relationship with, and largely depends on, OER (Vincent and Bessarabov 2018).

In contrast with the few works on cathode HER catalysts, many PGM-free electrocatalysts have been explored and tested in integrated AEM cells with excellent performance. Nickel/iron (NiFe)-based materials have been validated with predominant OER activity for multiple applications. Their activities are also being evaluated in AEM cells. In a control experiment with atomic ratios (Fe/Ni), a $NiFeO_x$ hybrid was synthesized, and converted from a less crystalline feature to the spinel phase with higher Fe content. When assessed in a single AEM cell, the Ni1Fe1 oxide anode showed a large current density of $650\,\mathrm{mAcm^{-2}}$ at 2 V below a temperature of 50 °C. However, it had poor durability in a 500 h potential cycling test, losing more than $150\,\mathrm{mAcm^{-2}}$ during the initial 400 h.

NiFe-based layered double hydroxides (LDHs), known to be excellent OER catalysts and to accelerate the reaction, have also been studied (Park et al. 2022). A particle lowering strategy was proposed to improve the performance of NiFe-LDH based on a reverse relationship between lateral size and effective surface area. The increase in the latter parameter was speculated to greatly enhance hydroxyl ions in the feed. Another merit was the reduction in the catalyst layer film thickness, which lowered ohmic losses on the MEA. A one-spot spontaneous gelation-deflocculation method was introduced to prepare ultra-fine NiFe-LDH particles with a small lateral size of less than 10 nm. The as-prepared NiFe-LDH possessed both pronounced OER activity in half- and single cells over IrOx and required a low overpotential of 247 mV to reach $10\,\mathrm{mAcm^{-2}}$, compared with 281 mV in IrOx @ $10\,\mathrm{mAcm^{-2}}$. In a full AEM cell, the MEA employing ultra-fine NiFe-LDH as the anode electrocatalyst demonstrated superior performance, reaching 74.7% conversion efficiency and a cell voltage of 1.59 V under working conditions of $1.0\,\mathrm{Acm^{-2}}$ at 80 °C. This performance was acknowledged to be the highest among PGM-free catalyst decorated MEAs by far.

To further investigate the OER half-cell test and full AEM electrolyzer performance, various transition metal (Ni, Co and Fe)-based oxides/hydroxides were prepared using a surfactant-free hydrothermal method. Interestingly, the NiFeOxHy oxyhydroxides exhibited the best OER performance in the half-cell, but the worst activity in the AEM stack. This may be due to the fact that NiFeOxHy has poor electrical conductivity, and no liquid electrolyte permeates to its surface. Therefore, only a portion of the total surface-active sites participated in the reaction. Using dry electrical conductivity as a reliable indicator, the effect of those oxides/hydroxides on the three-electrode system and AEM system performance can be better understood. Conductivity has a positive role by tuning the OER performance of those oxide/hydroxide materials. Intentionally anchoring Fe-species on the surface of the $NiCoO_x$ results in substantially improved activity on the $Fe/NiCoO_x$ because of the enhanced electrical conductivity. Thus, this finding may help establish the correlation between catalyst performance in the traditional three-electrode system and practical AEM system through the positive interaction on oxide/hydroxide catalyst interface. It also underlines the essential factor on the earth abundant OER catalyst selection towards AEM utilization goal (Xu et al. 2018).

Although Ni/Fe-based materials have been widely investigated as OER catalysts, they are rarely studied for AEM electrolysis because of their poor stability. Further efforts should focus on composition, architecture, and facile synthesis methods to enhance overall performance in practical devices.

The anion exchange membrane (AEM) is one of the core components in AEM electrolysis systems. They transfer hydroxyl ions from the cathode chamber to the anode chamber and prohibit gas crossover and electron transmission during practical electrochemical operation. AEMs are composed of a hydrocarbon polymer backbone as the main chain, and a side chain of anion exchange functional groups. The polymeric backbone typically uses polysulfone (PSF) or polystyrene (PS) to connect divinylbenzene (DVB), and typical ion exchange groups are those containing ammonium ($–NH3+$, $-RNH2+$, $-RN+$, $=R2N+$) or phosphonium ($-R3P+$) groups. Good ion exchange membranes should be qualified with the following properties, high perm-selectivity, good ionic conductivity, robust thermal and mechanical stability, and superior chemical stability.

Synthesizing viable anion exchange membranes for practical application remains challenging. It is particularly hard to balance the knotty issues of good mechanical stability and high ionic conductivity. While forming abundant ion exchange groups on the polymer backbone will increase ionic conductivity, it may also reduce the mechanical strength of the polymer main chain, by increasing excess water uptake. The chemical stability of the AEM cannot always be guaranteed because of hydroxide attacks on the fixed ions. Another crucial factor that hinders AEM development is the degradation of ammonium groups, which can proceed in two different ways, via Hofmann elimination and nucleophilic substitution.

2 Anion Exchange Membrane Water Electrolysis

Compared with the proton exchange membrane electrolyzer and solid oxide electrolyzer, AEM water electrolysis is almost the only electrolysis technology that is producing hydrogen on an industrial scale and is well established in many countries. The main advantage of this technology lies in the fact that the electrode can be made of abundant and cheap materials (e.g., iron or nickel steel-based electrodes for hydrogen production and nickel used for oxygen production).

a typical AEM water electrolysis cell consists of an anode, a cathode, a power supply, a diaphragm, and the electrolyte, where the two electrodes are immersed in an electrolyte, such as aqueous potassium hydroxide (KOH) or sodium hydroxide (NaOH). The cell working temperature is usually lower than 80 °C (Fig. 1).

When a voltage is applied to the anion membrane cell, electrons flow from the anode to the cathode, which are accompanied by the water oxidation and reduction reactions on the two electrodes, respectively:

$$H_2O \rightarrow H_2 + \frac{1}{2}O_2$$
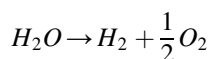
At the anode, hydroxyl ions (OH$^-$) of the electrolyte are oxidized into oxygen gas (O$_2$), by the oxygen evolution reaction:
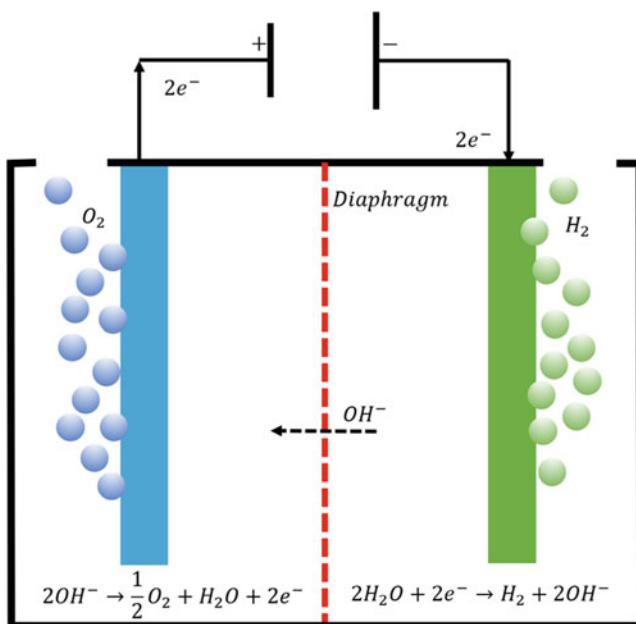
Fig. 1 AEM schematic

$$2OH^- \rightarrow \frac{1}{2}O_2 + H_2O + 2e^-$$
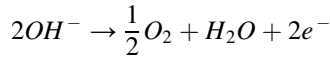
At the cathode, the hydrogen production takes place by reducing the water into hydrogen gas (H_2) and OH^- ions, by the hydrogen evolution reaction:

$$2H_2O + 2e^- \rightarrow H_2 + 2OH^-$$
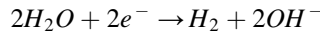
2.1   Thermodynamic of Water Splitting

Water splitting is not thermodynamically spontaneous, the thermodynamic reaction is described by:

$$\Delta_r H = \Delta_r G - T\Delta_r S$$

where, $\Delta_r G$ (in $Jmol^{-1}$) is the Gibbs free energy change of reaction, representing the minimum electrical energy required for water splitting reactions, which is normally provided by the electric supplier units. While $\Delta_r S$ (in $Jmol^{-1}$ K^{-1}) is entropy change, T is the temperature (in Kelvin), thus the $T\Delta_r S$ (in $Jmol^{-1}$) represents the minimum heat required to split 1 mole of water, this will be supplied by the working temperature conditions.

According to the first principle of thermodynamics, two thermodynamic voltages can be well defined to describe water electrolysis: the free energy electrolysis voltage E (in volts), also called the reversible voltage or thermodynamic voltage and the enthalpy voltage V (in volts), commonly called thermo-neutral voltage, representing the total energy required for the reaction to occur. They are defined as below:

$$E = \frac{\Delta_r G}{nF}$$

$$V = \frac{\Delta_r H}{nF}$$

where: n is the number of electrons transferred during splitting of one water molecule (n = 2) and F is the Faraday constant ($\approx 96{,}485$ $Cmol^{-1}$).

The values of $\Delta_r G$ and $\Delta_r H$ depend on the applied pressure and the temperature on the reaction system. In the case of standard conditions (T = 298 K and p = 105 Pa), water is a liquid while oxygen and hydrogen are gases. The standard free energy, enthalpy values are:

$$\Delta_r G^0 = 237.22 \frac{kJ}{mol} \rightarrow E^0 = \frac{\Delta_r G^0}{2F} = 1.23V$$

$$\Delta_r H^0 = 285.84 \frac{kJ}{mol} \rightarrow V^0 = \frac{\Delta_r H^0}{2F} = 1.48V.$$

E^0 here represents the minimum electrical energy required to produce hydrogen, whereas V^0 represents the minimum total energy required to start the reaction. In addition, according to the entropy $\Delta_r S$ (163.15 $Jmol^{-1}$ K^{-1}), a voltage value of 0.25 V can be achieved, which represents the minimum supplementary overvoltage with respect to the E^0 required for the water decomposition to occur. It should be noted that all thermodynamic values ($\Delta_r G$, $\Delta_r H$, $\Delta_r S$, E, and V) are dependent on the temperature, which change as a function of the temperature at constant standard pressure. With the increasing temperature, the required electricity and the reversible voltage decrease, which thus leads to the increasing of the heat demand. Overall, the thermodynamic state functions resulted in reversible voltage (E) and thermoneutral voltage (V) for a water splitting reaction that gives three relations against the electrolysis cell voltage (E_{cell}):

$$E_{cell} < E \rightarrow the\ reaction\ does\ not\ occur$$

$$E < E_{cell} > V \rightarrow extra\ heat\ is\ required\ to\ drive\ the\ reaction$$

$$V < E_{cell} \rightarrow the\ reaction\ occurs\ and\ extra\ heat\ develops$$

The reversible potentials of anode (E_{anode}) and cathode ($E_{cathode}$) can be described by the Nernst equation, the values depend on the standard potential, the reaction temperature, and the activity of the reactants:

$$E_{anode} = E_{\frac{O_2}{H_2O}} = E^0_{\frac{O_2}{H_2O}} + \frac{RT}{nF} \ln\left(\frac{(a_{H_2O}) * (a_{O_2})^{\frac{1}{2}}}{(a_{OH^-})^2}\right)$$

$$E_{cathode} = E_{\frac{H_2O}{H_2}} = E^0_{\frac{H_2O}{H_2}} + \frac{RT}{nF} \ln\left(\frac{(a_{H_2O})^2}{(a_{OH^-})^2 * (a_{H_2})}\right)$$

where: R represents the ideal gas constant (8.314 $Jmol^{-1}$ K^{-1}) and a_x is the activities of the chemical species.

Therefore, when no external electrical energy is applied to the electrolyzer, the thermodynamic voltage for the overall reaction can be calculated by the potential difference (ΔE) between the anode and the cathode, which is also called the equilibrium cell voltage (E^0_{cell}). The value can be expressed as below:

$$E^0_{cell} = \Delta E = E_{anode} - E_{cathode} = E^0_{\left(\frac{O_2}{H_2O}\right)} - E^0_{\left(\frac{H_2O}{H_2}\right)} + \frac{RT}{nF} \ln\left(\frac{(a_{H_2}) * (a_{O_2})^{\frac{1}{2}}}{(a_{H_2O})}\right)$$

The thermodynamic studies help to determine the related cell voltage required for an electrolysis cell. But the aspects of reaction kinetics at the electrodes are not taken into consideration. In practice, due to the existence of an activation energy barrier, limited reaction rate, and the bubble formation, the electrode reactions are inherently slow even when the equilibrium potential is reached, thus an overpotential (η) above the equilibrium cell voltage is demanded for starting both reactions. In addition, to overcome the resistance from the diaphragm and the electrical circuit, as well as the ionic migration process, additional energy is also needed. This extra energy in turn causes the Ohmic drop (iR_{cell}) within the cell. Hence, the practical E_{cell} can be written as:

$$E_{cell} = E_{anode} - E_{cathode} + \sum \eta + iR_{cell}$$

$$\sum \eta = |\eta_{anode}| + |\eta_{cathode}|$$

where: i is the current that the electrolysis cell operates and R_{cell} is the total resistance of the cell, which depends on the electrolyte conditions, the electrodes, and cell design.

The polarization curve of a water electrolyzer in standard conditions (25 °C and 1 bar) is shown in Fig. 2.

The overpotentials and the Ohmic drop of the cell change with the applied current.
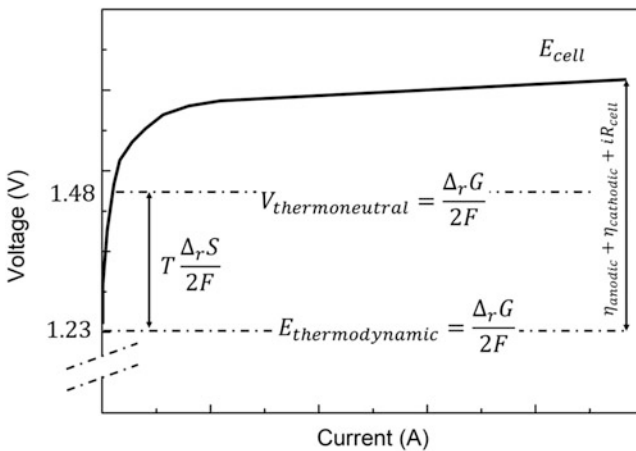
Fig. 2 Polarization curve of a water electrolyzer

In electrochemistry, the kinetics of charge transfer processes at any electrode/electrolyte interface follow a Butler-Volmer relationship, then, in a first approximation (no mass transport limitations), the theoretical current density (normalized by the electrode surface) for the water splitting reaction can be written as:

$$j = j_0 \exp\left(\frac{\alpha n F}{RT} * \eta_{anode}\right) - \exp\left(\frac{\beta n F}{RT} * \eta_{cathode}\right)$$

where: j_0 is the exchange current density and α and β are the charge transfer coefficients of anode and cathode, respectively, and $\beta = 1 - \alpha$.

In the situation of a second approximation and suppose that the anodic overvoltage is large enough, the cathodic overvoltage will become negligible, and then the above relationship can be simplified to the following:

$$j = j_0 \exp\left(\frac{\alpha n F}{RT} * \eta_{anode}\right)$$

While if anodic overvoltage is large enough and the cathodic one can be negligible, the relationship becomes:

$$j = j_0 \exp\left(\frac{\beta n F}{RT} * \eta_{cathode}\right)$$

From the above two simplified equations, the overvoltage can be further expressed as a function of the current density, which are called Tafel equations:

$$\eta_{anode} = a + b \log j$$

$$a = -2.3 \frac{RT}{\alpha n F} \log j_0$$

$$b = 2.3 \frac{RT}{\alpha n F}$$

$$\eta_{cathode} = a' + b' \log j$$

$$a' = -2.3 \frac{RT}{\beta n F} \log j_0$$

$$b' = 2.3 \frac{RT}{\beta n F}$$

Therefore, the exchange current densities (j_0), the Tafel slopes (a and a'), and the transfer coefficients (α and β) can be determined from the tested polarization curves (Fig. 3).

These kinetic data are strongly influenced by the electrode materials and allows to analyze the rate limiting step of the reactions, which are commonly employed to compare the catalytic activities of the used catalysts.
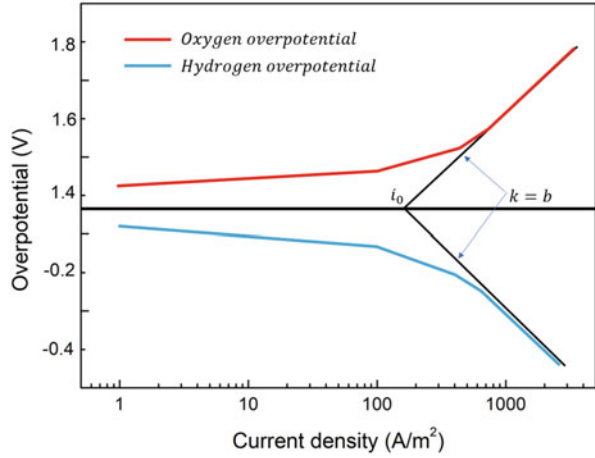
As mentioned earlier, the actual cell voltage (E_{cell}) is higher than the equilibrium potential (E^0_{cell}) due to the overpotentials from both electrode and the cell resistance. When the energy consumed in the auxiliary equipment is not considered, the overall energy efficiency ε_{cell} can be expressed as:

$$\varepsilon_{cell} = \frac{\Delta_r H^0}{\left(\Delta_r G^0 + T\Delta_r S^0 + nF\left(|\eta_{anode}| + |\eta_{cathode}| + jR_{cell}\right)\right)}$$

where $\Delta_r H^0$, $\Delta_r G^0$, and $T\Delta_r S^0$ represent the enthalpy, the Gibbs free energy, and the entropy at the equilibrium ($j = 0$), respectively.

For:

$$E_{cell} = E^0_{cell} + |\eta_{anode}| + |\eta_{cathode}| + jR_{cell}$$

then the overall energy efficiency:

$$\varepsilon_{cell} = \frac{\Delta_r H^0}{\left(\Delta_r G^0 + T\Delta_r S^0 + nF\left(|\eta_{anode}| + |\eta_{cathode}| + jR_{cell}\right)\right)}$$

$$= \frac{\left(\frac{E^0_{cell} + T\Delta_r S^0}{nF}\right)}{\left(\frac{E_{cell} + T\Delta_r S^0}{nF}\right)}$$

$$= \frac{E^0_{cell}}{E_{cell}} * \left\{ \frac{\frac{1+T\Delta_r S^0}{\Delta_r G^0}}{\left(\frac{1+T\Delta_r S^0}{\left(\Delta_r G^0 + nF(|\eta_{anode}| + |\eta_{cathode}| + jR_{cell})\right)} \right)} \right\}$$

In the case of low temperature water electrolysis, heat input is small in comparison to the total energy provided to drive the reactions, this condition is expressed by:

$$\frac{T\Delta_s S^0}{\Delta_r G^0} \ll 1$$

then, the simplified expression of the cell efficiency will be given by:

$$\varepsilon_{cell} = \frac{E^0_{cell}}{E_{cell}} = \frac{E_{anode} - E_{cathode}}{E_{cell}}$$

AEM electrolyzers can be divided into two main groups: monopolar and bipolar. In the monopolar device, several individual cells are parallel to each other, in which the electrodes are alternatively connected to the opposite terminals of the power supply (Fig. 4).

Thus, the overall voltage applied to the electrolysis cell is equal to the voltage applied to each unit cell voltage in the cell. The major attractions of monopolar electrolyzers are relatively few components, which are cheap and individual cells may be isolated for repair or replacement, which allows maintenance to be carried out more rapidly and effectively with a minimum of downtime for the plant. However, despite the relative simplicity of monopolar electrolyzer systems and cheaper manufacture than the bipolar type, most commercial anion electrolyzers are bipolar (Fig. 5).
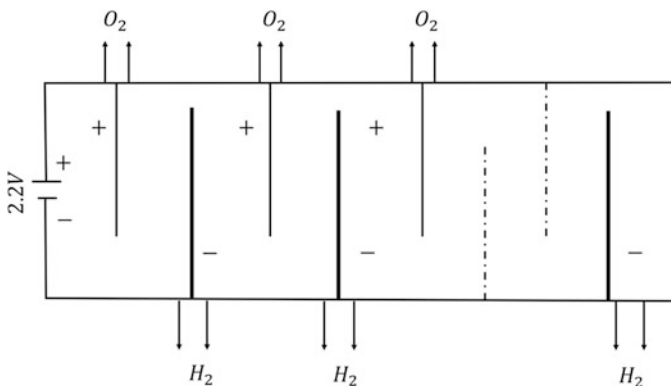
Fig. 4 Monopolar electrolysis cell schematic
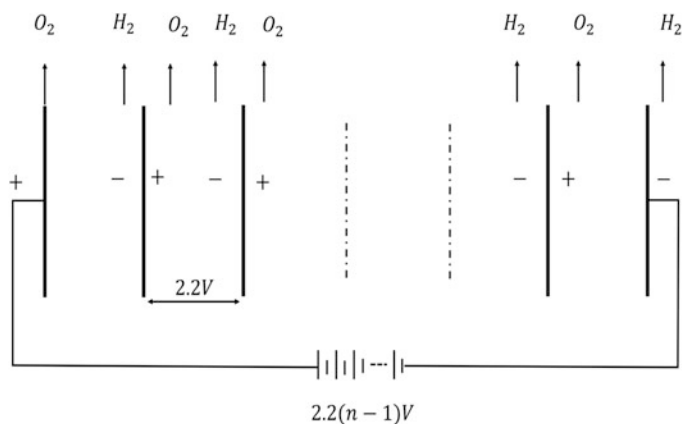
Fig. 5 Bipolar electrolysis cell schematic

For the bipolar configuration, a series of compact parallel electrodes are assembled, each of which is cathodic on one side and anodic on the other. The overall cell voltage is the sum of the individual pairs of voltages. In industrial processes, the typical cell voltage for the monopolar configuration is normally 2.2 V and the value for the bipolar configuration is 2.2 × (n − 1) V (n represents the number of electrodes). Therefore, in comparison to the monopolar water electrolyzer, the bipolar arrangement decreases the Ohmic losses on the aspect of the electrical circuit but requires much effort in design and manufacturing to avoid the leakage of the electrolyte and gas between the individual cells.

3 Cell Components

3.1 Electrodes

Overall, an electrolysis cell consists of electrodes (both anode and cathode) and the corresponding electrocatalysts, a membrane for the transfer of hydroxyl ions (OH⁻) termed as AEM (Faid et al. 2020).

Platinum-group metals are the most active and stable catalysts for the HER, but their high cost and low reservation limit their applications in industry. Thus, searching for highly efficient electrocatalysts to replace Pt is vital to further advance the electrolysis technology. Considerably, non-precious catalytic materials, such as Fe-, Ni-, or Co-based electrocatalysts have widely been investigated, but their single metal compounds are often prone to be corroded and deactivated under alkaline reaction conditions.

Ni and its alloys or composites are the one of the most investigated catalysts for the HER electrodes owing to their excellent corrosion resistance in high pH alkaline solutions. However, the main issue for Ni metal alone when employed as a cathode is

the low catalytic activity. Therefore, Ni is often designed as an alloy form to improve its catalytic activity, and a related study showed that Ni-alloyed transition metal (e.g., Mo, Zn, Co, W, Fe, Cr) exhibit the HER electrocatalytic activity in the order of:

$$NiMo > NiZn > NiCo > NiW > NiCr > Ni$$

Obviously, a combination of more than two metals allows for an improvement in the catalytic activity. Fe alone or combined with Mo is also one of the most investigated materials for developing highly efficient HER electrocatalysts. Among various Ni alloys, the binary Ni-Mo-based material electrodes are the most popular catalysts for the HER owing to their good stability, high conductivity, and excellent activity, as a matter of fact:
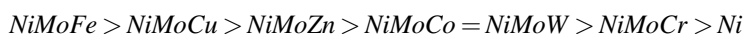
$$NiMoFe > NiMoCu > NiMoZn > NiMoCo = NiMoW > NiMoCr > Ni$$

Alkaline electrolysis systems are mainly hindered by the sluggish anodic reaction. The best catalysts for the OER are usually these Ir- and Ru-based materials. Many scientifical evidence reported that the OER activity of these catalysts decrease with the order of:

$$Ru > Ir > RuO_2 > IrO_2$$

Great attention has been paid to develop non-precious materials based on transition metals, for these catalysts exhibit comparable and even better catalytic activity than those noble metals, as well as good chemical and mechanical stability. Currently, the most used anode materials for the AEM water electrolysis cell are based on nickel and cobalt.

Nickel (hydro) oxides are found to be the most efficient nickel-based electrocatalysts to catalyze the OER.

To further enhance the water oxidation activity of Ni-based catalysts, combining them with transition metals is a feasible route.

Cobalt-based materials are another important category of the OER electrocatalysts owing to their exceptional 3d electronic configurations. The metallic Co alone seems a potential catalyst selection for the OER, but at high anodic potentials, the metal Co shows limited stability, even for these highly stable metallic Co nanoparticles.

Carbon nanotubes and graphene-based novel carbon materials demonstrate better resistance to chemical and electrochemical corrosion, they have been widely employed to design 3D nano- or micro-structures for the OER electrodes.

Metal-organic complex-based OER catalysts, including molecular catalysts, polyoxometalates, and metal-organic frameworks are also frequently studied catalysts toward the OER. By far, several metal-organic complexes have been designed for the OER by choosing active metal nodes and conductive organic linkers or by introducing catalytic active species into the complexes.

3.2 Anion Exchange Membrane

For the AEM water electrolysis systems, the electrolyte is usually the aqueous solution of KOH or NaOH for their highest specific conductivity. And the ionic conductivity increases with temperature (Pushkareva et al. 2020).

The electrolyte volume stored in the electrolysis cells is determined by the two-electrode distance (gap), and the distance usually varies in the range of a millimeter to several centimeters. The Ohmic losses of the electrolyte rise because of the increase of the two-electrode distance. If the amount of the electrolyte is too small, the concentrations of the reactive species change rapidly during operation, which will influence the stability of the cell. Therefore, the volume of the electrolyte must be adjusted continuously to replenish losses according to the product gases.

Importantly, to separate the hydrogen and oxygen gases formed at the two electrodes, the use of diaphragms is often required in such alkaline systems from the perspective of safety. Another major function of a diaphragm is the separation of the two electrodes to prevent any short circuits. Generally, a diaphragm features a porous structure, the average pore size is usually less than 1 μm. Besides the separation of gases, the diaphragm also allows the transport of water and OH− between two-electrode compartments.

Composites made from stable hydrophobic polymer binders and hydrophilic ceramics or polymers were proposed by providing high chemical stability, good mechanical strength, and excellent electrolyte pore filling capabilities.

In a water electrolysis cell, the role of an AEM is to conduct hydroxyl ions from the cathode to the anode at a very high speed. The OER and HER occur at the anode and cathode, respectively. These electrodes and the AEM are the heart of a water electrolysis cell. For an electrolysis cell to be feasible for practical application, it must have highly selective and efficient ion transport through the AEM (Yuzer et al. 2020).

The transport of hydroxyl ions through the AEM can be well explained by the Grotthuss mechanism, diffusion, migration, and convection (Fig. 6).

The Grotthuss mechanism, diffusion, migration, and convection are the dominant transport mechanisms for hydroxide transport through AEMs. The assumption that the majority of the OH− is transported through the AEM by the Grotthuss mechanism is because OH− exhibit Grotthuss behavior in aqueous solutions, comparable to protons. According to this mechanism, hydroxide diffuses through the hydrogen-bonded network of water molecules through the formation/cleavage of covalent bonds. It has been proposed that the movement of the hydrated hydroxyl ion is accompanied by a hyper-coordinating water molecule (Fig. 7).

The arrival of another electron-donating water molecule leads to hydrogen bond rearrangements, re-orientations and hydrogen ion transfer, and the formation of a fully tetrahedrally coordinated water molecule.

Basically, the hydroxide is transported through the membrane along a chain of water molecules through hydrogen bond formation and cleavage of the hydrogen bond. Next to the Grotthuss mechanism, diffusion and convection are supposed to be
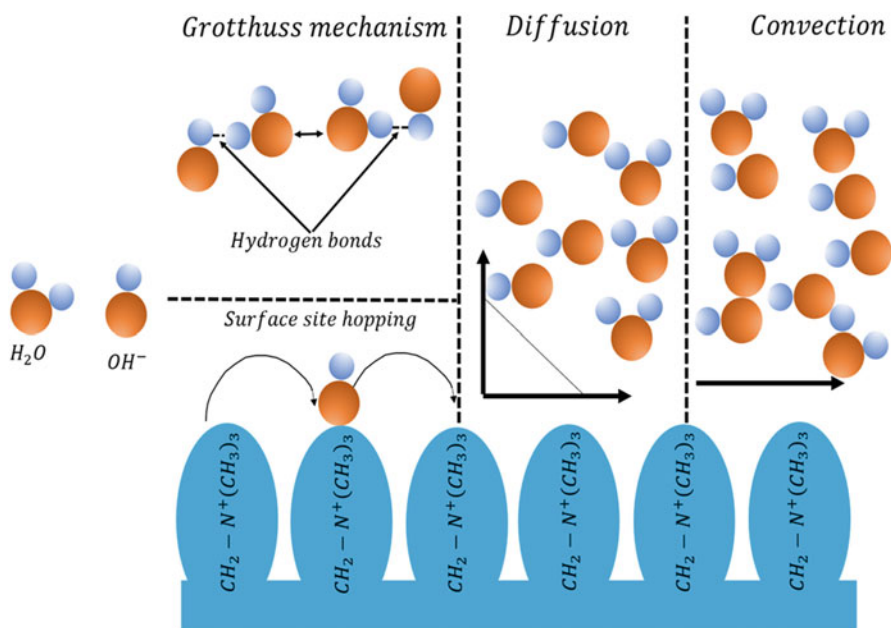
Fig. 6 Grotthuss mechanism-diffusion-convection schematic
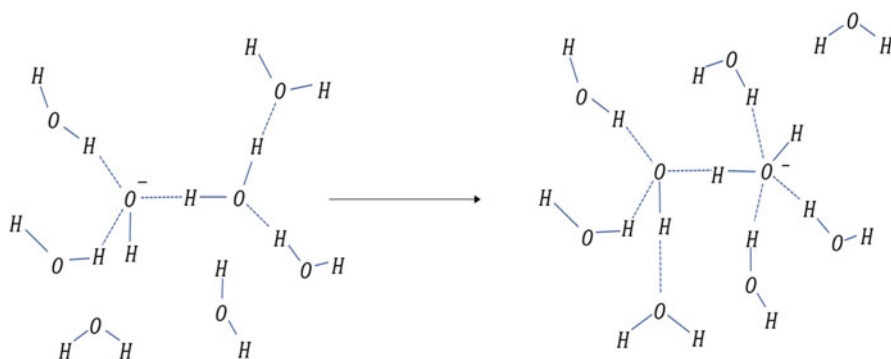
Fig. 7 Transport mechanism of hydrated hydroxide ions in aqueous solution

important. Diffusive transport occurs in the presence of a concentration and/or electrical potential gradient. Convective transport across the membrane appears for since hydroxides moving through the membrane, drag water molecules with them through the membrane, thus generating a convective flow of water molecules within the membrane. Surface site hopping of hydroxyl anions occurs on quaternary ammonium groups present on the membrane. This type of transport is thought to be of secondary transport across the membrane because the water present in the system acts as a permanent dipole and interacts with the fixed charges of the

membrane. This strong coordination of water molecules around the ammonium groups imparts a reduction of the possibility of the ionic species to interact with the ammonium groups on the membrane.

After the Grotthuss mechanism, diffusion and convection are important. The presence of an electrical potential gradient leads to diffusion. A convective flow of water molecules within the membrane is generated by the hydroxyl ions by dragging water molecules with themselves through the membrane. Surface site hopping is a secondary mode of ionic transport because the water present in the system is a permanent dipole which can interact with the fixed charges of the membrane. This interaction reduces the possibility of water molecules for interaction with ammonium ions.

Platinum-group metals are the most active and stable catalysts for the HER, but their high cost and low reservation are the main limit to the industrial applications. Thus, searching for highly efficient electrocatalysts to replace Pt is vital to further advance the electrolysis technology. Considerably, non-precious catalytic materials, such as Fe-, Ni, or Co-based electrocatalysts have widely been investigated, but their single metal compounds are often ready to be corroded and deactivated under alkaline reactions conditions. A great deal of effort has been devoted to optimizing the activity of these metals through improving their resistance to corrosion by alloying or doping.

Ni and its alloys or composites are the one of the most investigated catalysts for the HER electrodes owing to their excellent corrosion resistance in high pH alkaline solutions. However, the main issue for Ni metal alone when employed as a cathode is the low catalytic activity. Therefore, Ni is often designed as an alloy form to improve its catalytic activity, and a related study showed that Ni-alloyed transition metals (Mo, Zn, Co, W, Fe, Cr) exhibit the HER electrocatalytic activity in the order of:

$$NiMo > NiZn > NiCo > NiW > NiFe > NiCr > Ni$$

When deposited on steel substrates. Among various Ni alloys, the binary Ni-Mo based materials are the most popular catalysts for the OER owing to their stability, high conductivity and excellent activity. In addition, some ternary Ni-based alloys are deposited on steel substrates as catalytic electrodes for the HER, the obtained electrodes showed an activity order of:

$$NiMoFe > NiMoCu > NiMoZn = NiMoW > NiMoCr > Ni$$

on steel.

Fe alone or combined with Mo is also one of the most investigated materials for developing highly efficient HER electrocatalysts. The Fe-Mo alloys demonstrate a high hydrogen evolution rate for the large real surfaces areas. And it is found that the corrosion resistance of Fe-Mo can be further improved by Ni doping. Other Fe-based alloys such as amorphous $Fe_{82}B_{18}$, $Fe_{80}Si_{10}B_{10}$, $Fe_{60}Co_{20}Si_{10}B_{10}$, alloys are also investigated for HER. After doping with B and Si, the overpotential of FeCo alloy is decreased due to enhanced surface area (Fig. 8).
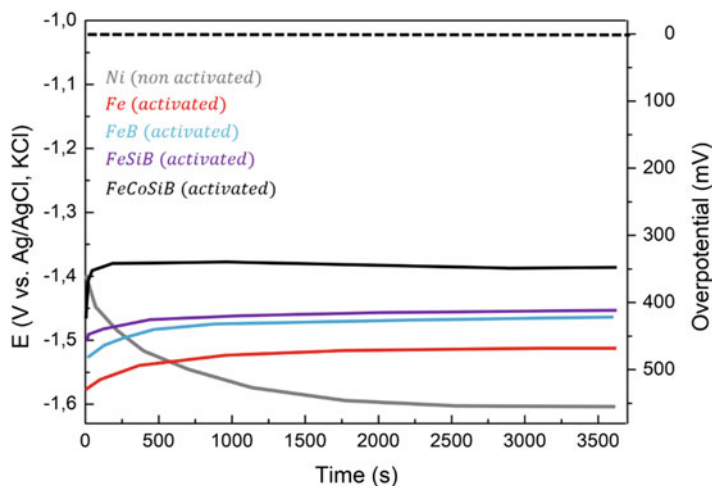
Fig. 8 Galvanostatic results of Fe-based catalysts with or without B/Si dopants
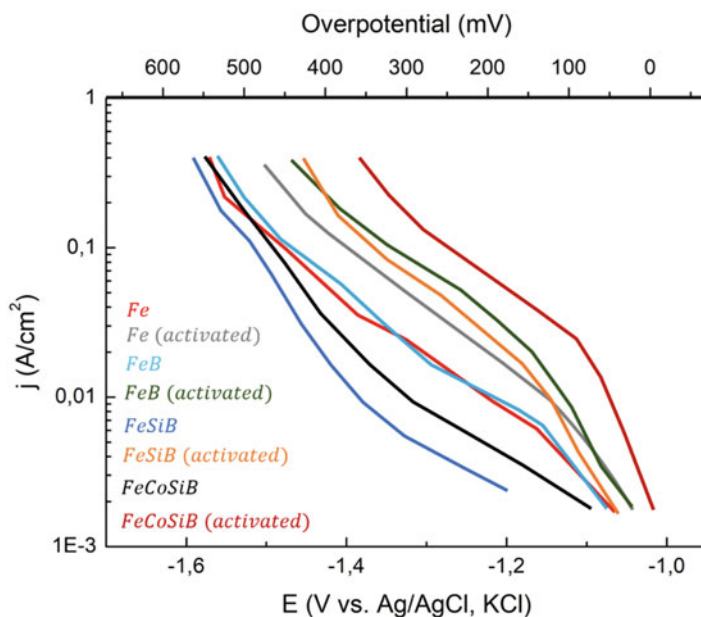
Fig. 9 Tafel plots results of Fe-based catalysts with or without B/Si dopants

The corresponding Tafel plots also indicate the optimized activity of the doped and pre-treated samples (Fig. 9).

In addition, other Fe-based crystalline alloys, such as $Fe_{90}R_{10}$ (R = Ce, Sm, Y, and Mm-mischmetal) and Fe-Zn-R (R = rate earth metals; La, Y, Gd and

mischmetal) are also investigated. The results show that the synergic effect of multi-phase made a great contribution to enhance HER efficiency.

Studies for Co-based HER electrocatalysts mainly focus on Co-Mo alloys for their high corrosion resistance and good hydrogen evolution performance. It is also confirmed that increasing the Mo content in a Co-Mo alloy can enhance the electrocatalytic HER activity of the resulted composites. Additionally, nanocrystal-line alloys of $Ni_{30}Mo_{70}$, $Co_{30}Mo_{70}$, $Co_{30}Ni_{70}$, $Co_{10}Ni_{20}Mo_{70}$ were also prepared and investigated for catalyzing the HER. The $Co_{30}Ni_{70}$ showed the best performance, which was attributed to the small grain size that resulted in high specific surface areas.

It is known that Mo doping of various alloy composites is one of the most important routes to optimize the HER performance. In addition, phosphorous (P) doping of alloys is another effective method for preparing the HER electrocatalyst. As the existence of phosphorous in a crystal lattice leads to structure distortion, the formed catalytic materials usually are amorphous. A variety of P-doped alloys have been reported, such as Mi-Mo-P, Co-Mo-P, Fe-Ni-P and so on.

The anodic OER has more remarkable overpotential than the cathodic HER due to sluggish four electron oxidation process. Therefore, alkaline electrolysis systems are mainly hindered by the sluggish anodic reaction. The best catalysts for OER are usually the Ir- and Ru-based materials. The OER activity of these catalysts decrease with the order of:

$$Ru > Ir > RuO_2 > IrO_2$$

but the severe dissolution of the catalysts in alkaline media limit their widespread application. Some efforts have been devoted to developing the OER catalysts by reducing the amount of Ir (Ru) via doping these catalysts with non-precious metals. In fact, more attention has been paid to develop non-precious materials based on transition metals, for these catalysts exhibit comparable and even better catalytic activity than the cobalt. As shown in Fig. 10, many relative activity data for Co- and Ni-based oxides is investigated, and the beneficial synergic effect between metal ions can be extremely highlighted.

Ni-based electrocatalysts are the most potential candidates for the OER owing to the merits of their low cost and rich reserves. Among them, nickel (hydro) oxides are found to be the most efficient nickel-based electrocatalysts to catalyze the OER. Moreover, nickel hydroxides can be easily synthesized cy chemical or electrochem-ical methods, whereas nickel oxides can be prepared by the hydrothermal method or annealing the as-synthesized nickel hydroxides under controlled atmosphere. Recently, nickel phosphide, sulfides, and selenides also attracted great attention because of their good OER performance. However, many studies have shown that these phosphides, sulfides and selenides suffered from "in situ transformation" during the OER process and the resultant metal oxides and hydroxides on the bulk surface are really active species for the OER. To further enhance the water oxidation activity of Ni-based catalysts, combining them with transition metals is a feasible route. To date, a great deal of research has indicated that Fe is the most effective and

Cobalt – based oxides | 0.4 / Co

	Mg	Al	Ca	Ti	V	Cr	Mn	Fe	Ni	Cu	Zn	Ga	Sr	Mo	Ba	Co	W	Bi	
	0.6[a]	0.8	1.0	0.4	0.6	1.0	0.6	0.8	1.6	0.6	0.6	0.6	1.0	0.6	1.0	0.8	0.8	1.2	
		0.2[b]	0.0	0.0	0.2	0.8	0.4	2.0	2.0	0.2	0.4	0.0	0.0	0.0	0.8	1.4	0.8	1.0	Mg
			2.2	0.0	0.4	0.2	0.6	0.6	2.6	2.4	0.4	0.6	1.0	0.8	1.6	1.8	0.8	3.4	Al
Al	1.2[d]			0.2	1.0	1.0	0.4	1.6	3.2	0.6	2.4	1.4	1.4	0.6	0.8	1.8	1.8	2.8	Ca
Ca	2.4	3.4			0.0	0.0	0.0	0.0	0.0	0.0	0.0	0.6	0.0	1.2	0.0	0.0	1.2	0.0	Ti
Ti	0.0	0.8	0.0			0.6	0.0	1.6	1.2	0.8	0.6	0.8	1.2	0.0	0.4	0.4	1.0	0.6	V
V	0.8	1.2	1.0	0.8			0.2	2.0	2.4	1.4	0.6	0.6	1.4	0.0	2.2	0.0	2.8	1.2	Cr
Cr	2.4	3.2	3.0	3.4	2.0			2.0	1.6	0.0	0.2	0.0	1.0	0.4	0.0	0.0	0.8	0.6	Mn
Mn	0.0	2.0	0.8	0.6	1.6	1.0			2.4	1.6	1.2	0.8	2.6	2.0	3.0	2.6	1.8	0.6	Fe
Fe	3.2	3.8	4.8	0.6	2.0	4.0	2.4			0.2	3.4	2.2	3.4	1.4	3.2	1.6	1.8	1.4	Ni
Co	2.0	1.6	3.2	0.0	1.2	2.4	1.6	2.4			0.8	1.4	0.4	0.4	0.8	0.2	1.4	0.8	Cu
Cu	0.2	1.8	0.4	0.0	0.0	1.0	0.0	0.8	0.2			0.4	0.8	0.8	2.0	0.4	0.0	1.8	Zn
Zn	1.4	2.8	3.0	0.0	1.0	3.4	0.2	1.8	3.4	1.0			1.6	0.8	2.8	1.4	2.4	2.4	Ga
Ga	2.2	2.0	2.8	2.6	1.6	2.4	1.4	3.8	2.2	1.4	1.0			1.0	2.0	1.2	1.4	1.6	Sr
Sr	1.4	3.0	3.4	0.6	1.4	1.8	0.8	4.4	3.4	0.4	1.2	2.4			1.0	0.4	0.0	0.6	Mo
Mo	1.0	1.4	2.4	1.6	1.2	1.2	1.6	2.4	1.4	0.0	2.0	2.2	1.8			1.2	1.4	0.6	Ba
Ba	2.0	2.6	3.6	1.8	1.0	2.6	1.0	4.2	3.2	0.0	1.8	2.4	2.4	1.2			1.2	0.0	Ce
Ce	1.0	2.2	1.8	0.8	1.6	2.2	1.0	3.2	1.8	0.0	0.0	3.0	0.6	0.8	1.2			1.2	W
W	1.4	1.8	1.0	1.2	1.4	1.8	1.4	3.6	1.8	2.8	1.2	1.4	1.6	2.6	1.4	1.6			
Bi	1.8	1.6	3.0	0.4	0.0	2.6	0.8	1.6	1.4	0.2	1.0	1.0	2.2	1.6	2.0	1.0	0.0		
	Mg	Al	Ca	Ti	V	Cr	Mn	Fe	Ni	Cu	Zn	Ga	Sr	Mo	Ba	Co	W	Bi	
	0.2[b]	2.4	2.0	1.0	1.0	2.4	1.0	2.4	1.6	1.0	1.4	1.8	1.8	1.6	1.8	1.6	1.0	1.0	

Ni / 1.0 **Nickel – based oxides**

Fig. 10 Maximal average activity of cobalt and nickel-containing compounds

compatible element. After combining with Ni-based catalysts, their OER activities are obviously enhanced. By far, several Ni-Fe bimetallic-based electrocatalysts have been widely and deeply investigated as the OER electrocatalysts, such as NiFe oxides, Ni-Fe hydroxides and NiFe oxyhydroxides. Besides engineering the morphology of NiFe compounds, the amount of Fe content plays a significant role in the OER activity, for example, it was reported that Ni-Fe oxyhydroxides containing 40% Fe exhibited much higher activity for the OER than other materials. In particular, the state of Fe in the Ni-Fe oxides highly depends on its content. When the Fe content is less than 25%, Ni is replaced by Fe cations to form γ-Ni1-xFexOOH, when the content was greater than 25%, crystal γ-FeOOH could form. Theoretically, the OER overpotentials of Fe sites in pure or doped Ni-/Fe-oxyhydroxides were much smaller than that of Ni sites. This is consistent with the Discrete Fourier Transform (DFT) calculations, in which they found Fe sites were much more active than the Ni sites in $Ni_{1-x}FeXOOH$ for OER.

Co-based materials are another important category of the OER electrocatalysts owing to their exceptional 3d electronic configurations. The metallic Co alone seems a potential catalyst selection for the OER, but a high anodic potential, the metal Co shows limited stability, even for these highly stable metallic Co nanoparticles. As much, a great number of Co-based oxides, including hydri(oxy) oxides, perovskites, sulfides, nitrides, and phosphates have been studied. As for these CoS_x, CoN_x and CoP_x, similar to other discussed catalysts, nickel-based ones have also attracted a

huge amount of attention for catalyzing the OER, but they were also the catalysts precursor, and the real catalytic active species were formed subsequently. Furthermore, with the aid of nanotechnology, Co-based oxides with various nanostructures have developed and great achievements have been made, especially for the Co_3O_4-based OER catalyst. However, the conductivity of Co_3O_4 electrode materials is normally low, which need to be doped with Ni, Cu, Li and La to improve their conductivity. In addition, designing Co-based hybrid materials or coupling Co-based catalysts with other conductive substrates is another effective route to enhance the catalytic performance. For example, various catalytic materials, such as Co_2MnO_4, $NiCo_2O_4$, $Co_xFe_{3-x}O_4$, SnO_2 and NiO_2, have been widely used to enhance the performance of Co_3O_4 or build a £D heterostructure. It is noted that although metal electrodes based on Ni, Cu and Fe exhibit higher corrosion resistance under an increased pH electrolyte, severe corrosion and contamination still take place on these metals during electrochemical measurements, as well as on many traditional carbon materials. In contrast, carbon nanotubes and graphene-based novel carbon materials demonstrate better resistance to chemical and electrochemical corrosion, they have been widely employed to design 3D nano- or micro-structures for the OER electrodes.

Layered double hydroxides (LDHs), a kind of hydrotalcite-like compound, are a large category of 2D anionic clay materials. To date, a broad collection of LHDs such as binary ZnCo, CoCo, CoFe, NiCo, NiFe and LiFe and ternary FeNiCo and NiFeMn have been developed for water oxidation electrocatalysts. LDH materials containing Fe usually exhibited much higher activity for the OER.

Metal-organic-complex- based OER catalysts, including molecular catalysts, polyoxometalates, and metal-organic frameworks are also frequently studied catalysts toward the OER. By far, several metal-organic complexes have been designed for the OER by choosing active metal nodes and conductive organic linkers or by introducing catalytic active species into complexes. With their porous structure, they can facilitate the diffusion of reactive species and accelerate charge transfer.

4   Conclusions

Hydrogen produced by PEM and AEM electrolysis is expected to become a larger share of the global hydrogen market, because they offer notable environmental advantages over the conventional hydrocarbon extraction method. An AEM electrolyzer can be integrated with intermittent energy resources and this would greatly lower the total cost of the cell/stack. Moreover, the system also offers great flexibility, including the ability to use compressed hydrogen storage cylinders for facile hydrogen utilization, or not. The produced high-purity hydrogen can be directly used in many fields, such as fuel cells and chemical hydrogenation.

However, at this stage in development, research and development should include an integration of technology development on these critical components to achieve significant deployment and market penetration at megawatt scale. Especially,

improving durability and lifetime of AEM is critically important to fit industrial operating conditions. The swelling issue of AEMs in alkaline electrolyte should be resolved to improve stability against reactive oxygen species. Also, a standard accelerated stress test needs to be proposed from both academic research society and industry. It is crucial for the determination of targeted lifetime ($>10,000$ h) on AEMs.

References

Faid AY, Xie L, Barnett AO et al (2020) Effect of anion exchange ionomer content on electrode performance in AEM water electrolysis. Int J Hydrogen Ener 45(53):28272–28284. https://doi.org/10.1016/j.ijhydene.2020.07.202

Li C, Baek J-B (2021) The promise of hydrogen production from alkaline anion exchange membrane electrolyzers. Nano Energy 87:106162. https://doi.org/10.1016/j.nanoen.2021.106162

Park YS, Jeong JY, Jang MJ et al (2022) Ternary layered double hydroxide oxygen evolution reaction electrocatalyst for anion exchange membrane alkaline seawater electrolysis. J Ener Chem 75:127–134. https://doi.org/10.1016/j.jechem.2022.08.011

Pushkareva IV, Pushkarev AS, Grigoriev SA et al (2020) Comparative study of anion exchange membranes for low-cost water electrolysis. Int J Hydrogen Ener 45(49):26070–26079. https://doi.org/10.1016/j.ijhydene.2019.11.011

Vincent I, Bessarabov D (2018) Low cost hydrogen production by anion exchange membrane electrolysis: a review. Renew Sustain Energy Rev 81(2):1690–1704. https://doi.org/10.1016/j.rser.2017.05.258

Xu D, Stevens MB, Cosby MR et al (2018) Earth-abundant oxygen Electrocatalysts for alkaline anion-exchange-membrane water electrolysis: effects of catalyst conductivity and comparison with performance in three-electrode cells. ACS Catal 9(1):7–15. https://doi.org/10.1021/acscatal.8b04001

Yuzer B, Selcuk H, Chehade G et al (2020) Evaluation of hydrogen production via electrolysis with ion exchange membranes. Energy 190:116420. https://doi.org/10.1016/j.energy.2019.116420

Solid Oxide Water Electrolysis

1 Introduction

The solid oxide electrolysis cell (SOEC) technique with high-temperature water electrolysis to produce hydrogen has the following advantages:

(i) reducing the cost of the process;
(ii) requirement of less electrical energy;
(iii) operating at high current densities produce a large quantity of high pure hydrogen.

Furthermore, the required thermal energy for SOEC operation can be supplied from external sources like industrial waste heat, wind energy, and solar energy. Therefore, developing SOEC water electrolysis technologies for hydrogen production is of great urgency and significance (Song et al. 2019).

2 Solid Oxide Electrolysis

The working principle of SOEC is schematized in Fig. 1.

The overall water electrolysis reaction consists of two electrochemical half-reactions, at the hydrogen electrode:

$$H_2O + 2e^- \rightarrow H_2 + O^{2-}$$
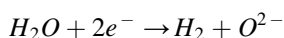
at the oxygen electrode:

$$2O^{2-} \rightarrow O_2 + 4e^-$$
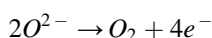
The specific reaction process on the two electrodes is shown in Fig. 2:
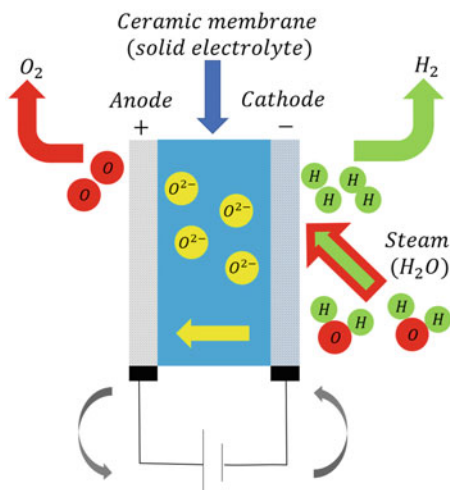
After galvanization, the water molecules on the hydrogen electrode side diffuse to the "hydrogen electrode-electrolyte-hydrogen water vapor mixture" three-phase boundary (TPB) to decompose, producing an adsorbed state of hydrogen and oxygen (Su et al. 2019). The combination of H and H form H_2, and then the diffusion of the hydrogen electrode is collected. However, O captures two electrons to form O^{2-}, diffuses through the oxygen ion conductor electrolyte to the anode and electrolyte interface, and O_{2-} ions are oxidized at the interface. The two electrons flow completes the current loop to the external circuit, and the oxygen that loses electrons combines into O_2, and diffuses out of the oxygen electrode.

3   Cell Components

The SOEC belongs to the classic sandwich structure. The main composition of the electrolytic cell consists of a dense electrolyte layer in the middle and a porous cathode and anode on both sides (Fig. 3).

The solid oxide electrolyte is mainly used to conduct oxygen ions or proton between the electrodes, block the electronic conductance, and separate the oxidizing gas from the reducing gas. Thus, the electrolyte is required to be completely dense in structure and requires high ionic conductivity and negligible electronic conductance. The electrode materials are generally porous in structure to facilitate gas diffusion and transport. In addition, the flat SOEC devices require a sealing material. Since the SOEC operates at higher temperatures, the sealing material acts to prevent oxidation and reduce gas leakage, has a thermal expansion coefficient that matches the rest of the battery, and has good physical and chemical stability at high temperatures (Tucker 2020). Most of the sealing materials are made of cassia glass composite materials, and the glass phase softens at high temperatures to prevent leakage.
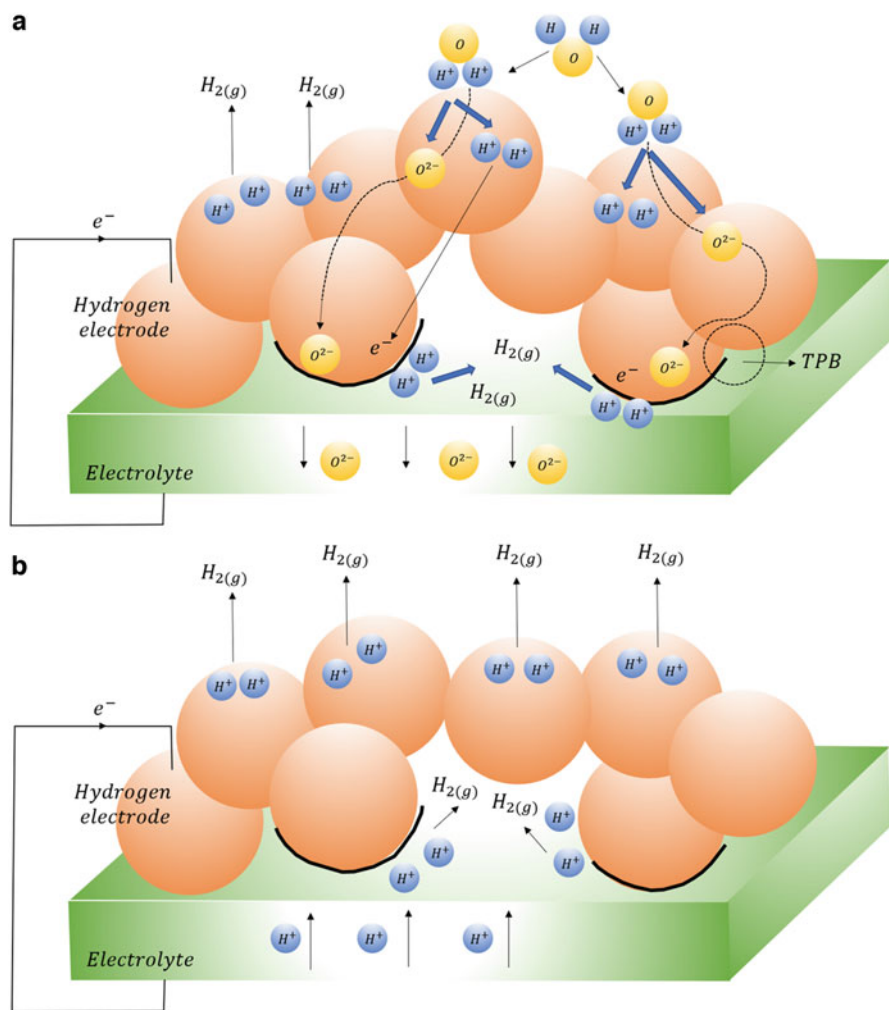
Fig. 2 Schematic representation of the transport of electron and oxide ion in hydrogen electrode (**a**), electron and proton in hydrogen electrode (**b**), electron and proton in oxygen electrode (**c**), and electron and oxide ion in oxygen electrode (**d**)
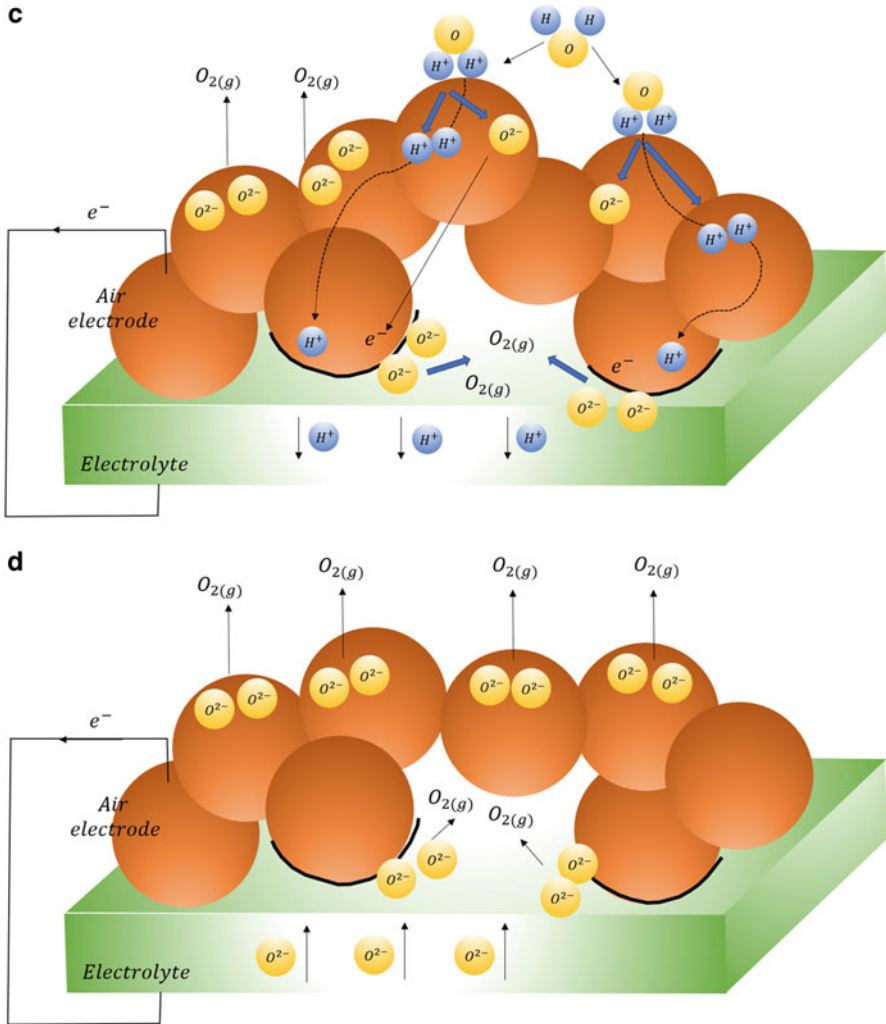
Fig. 2 (continued)

Moreover, the monomer cell also requires a connector material to form the stack. The normal SOEC works at high temperatures, thus, there are many significant limitations on selecting electrodes, electrolytes, and interconnect materials. Therefore, the SOEC material requirements of high conductivity, a compatible thermal expansion coefficient, excellent dimensional, mechanical, chemical, and thermal stability and battery integration, are strict: dense electrolytes have poor electronic conductivity, good ionic conductivity, and good chemical stability under severely reduced or oxidizing atmospheres; the dense electrolyte should be as thin as possible to reduce the Ohmic overpotential, but should also have a hermetic structure that completely separates the syngas and O_2; pore size and porosity are designed not only
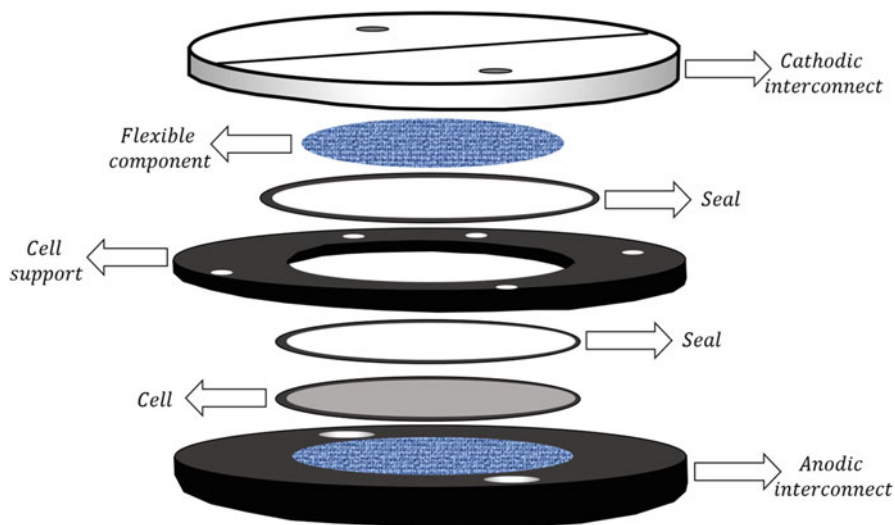
Fig. 3 Cell schematic

to support gas transport, but also to provide sufficient three-phase boundaries (TPB, electrolyte/electrode/gas interface); electrodes and electrolytes should have compatible coefficients of thermal expansion to prevent material failure; interconnect materials should be chemically stable in reducing and oxidizing environments. This is especially important because they are in contact with both $CO_{(g)}$, $H_2O_{(g)}$, $CO_{2(g)}$, and $O_{2(g)}$; manufacturing costs and raw materials should be as cheap as possible.

3.1 Hydrogen Electrode

The morphology and composition of the hydrogen electrode play an important role in the efficiency of water electrolysis, and the electrode serves as the hydrogen evolution reaction active site (Kim et al. 2018).

The porous hydrogen electrode allows decomposition of H_2O in the SOEC, where the supplied electrons travel from the interconnectors to the electrolyte/electrode interface, allowing oxygen ion reactants to be transported through the electrolyte, then the product hydrogen is removed from the active site of the oxygen ion conducting SOEC system. On the other hand, in a proton conducting SOEC system, H_2O electrolysis occurs on the hydrogen electrode, and the fully utilized product of pure hydrogen is collected from the hydrogen electrode. The two different ion-conducting systems schematic is shown in Fig. 4.
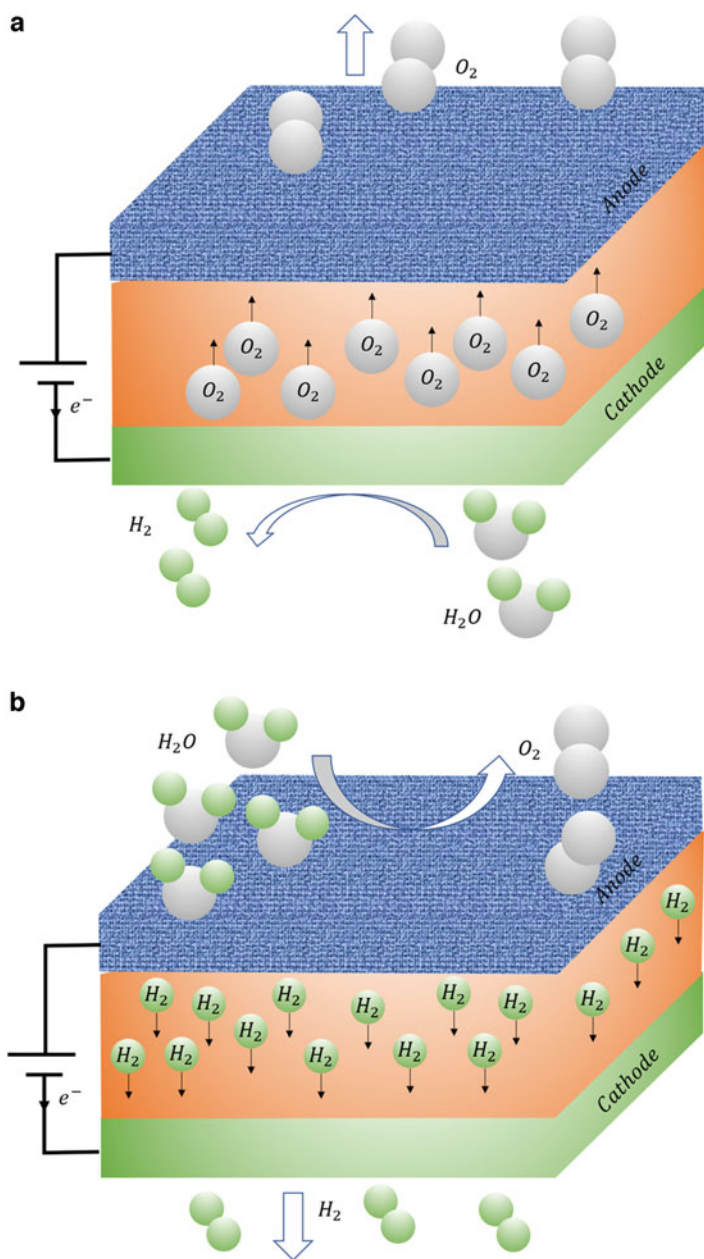
Fig. 4 Two different ion-conducting systems of the SOECs, schematic proton-conducting SOEC (**a**) and oxygen ion-conducting SOEC (**b**)

As we all know, the Ni-based composite materials with yttria stabilized zirconia (YSZ) and yttrium-doped barium cerate zirconate are excellent oxygen ion and proton conductors. Thus, Ni-YSZ and Ni-yttrium-doped barium cerate zirconate materials are extensively used as hydrogen electrodes due to their lower cost compared to noble metal, relatively reasonable properties of electrochemical activity, chemical stability, and matching thermo-mechanical expansion coefficient with the other components. The perovskite-based mixed ionic and electronic conductors is another class of hydrogen electrodes.

So far, although a variety of hydrogen electrode materials have been proposed and developed, there is no single composite or composite material that can meet all the requirements of the SOEC operation stability, mobility, flexibility, and low cost. The Ni-based composite materials tend to agglomerate and degrade the performance under long-term SOEC operation conditions.

3.2 Oxygen Electrode

The oxygen electrode is an important part of the SOEC system. Increasing the OER activity at the oxygen electrode is one of the significant parameters for improving the electrochemical catalytic performance of the SOEC (Xia et al. 2022). Thus, the main properties of the SOEC oxygen electrode should include high electronic/ionic conductivity and catalytic activity for the OER, chemical compatibility, and stability with electrolytes materials. The oxygen electrodes in the SOEC are mainly divided into three large classes:

(1) the metal electrodes: both nickel and platinum can be used as hydrogen electrodes, but only noble metals such as platinum or gold can be used as oxygen electrodes in the SOECs.
(2) ceramic electrode materials.
(3) composite electrode, that is developed with the aim to enhance the reaction zone, thereby increasing electrode activity and even stability. In addition, the composite electrode can be generally classified into two types: ceramic-metal composite electrodes (such as Ni-YSZ, Ni-SDC [samaria-doped ceria], LSCM-Cu, etc.) and ceramic-ceramic electrodes (such as LSC-YSZ, LSM-YSZ, LSM-GDC, etc.). In addition to enhancing activity, the composite electrode also achieves a tighter overall thermal expansion match with the electrolyte (Fu et al. 2022).

3.3 Solid Oxide Electrolyte

The solid electrolyte is the core part of the SOEC system, and its properties (including conductivity, stability, thermal expansion coefficient, and sintering temperature) not only directly affect the performance of the electrolytic cell, but also determine the matching electrode materials and preparation techniques (Laguna-Bercero 2012). The primary role of electrolytes is to conduct oxygen ions or protons

$$H_2O + 2e^- \rightarrow H_2 + O^{2-}$$

$$O^{2-} \rightarrow O + 2e^-$$
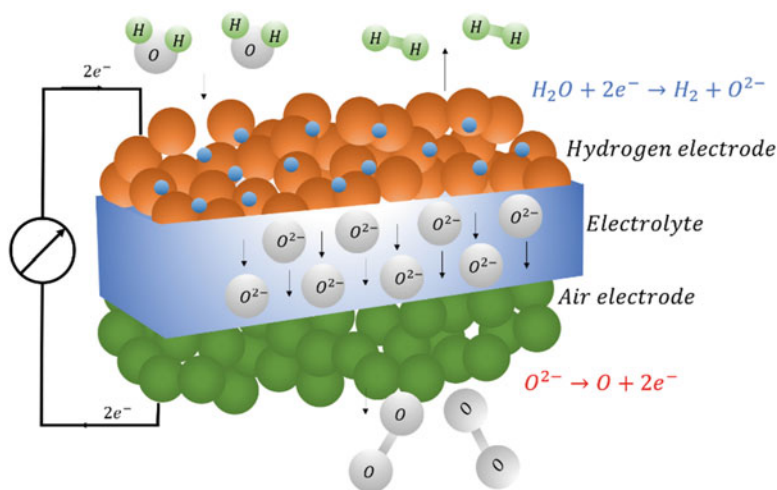
Fig. 5 Working principle diagram of oxygen ion-conducting electrolyte in the SOEC system

between the electrodes, block electron conductance and separate oxidation, thus reducing gases. Therefore, electrolytes require sufficiently high ionic conductivity and negligible electronic conductivity. It is structurally completely dense and maintains chemical properties in an oxidizing and reducing atmosphere. The crystal structure and the dimensional stability are stable enough. Furthermore, the electrolyte requirements should be compatible with the electrode material in mechanical and chemical properties from room temperature to operating temperature and manufacturing temperature.

At present, solid oxide electrolyte materials are mainly divided into three categories: the first one is an oxygen ion-conducting type, the second one is a proton-conducting type, and the third one is a mixed-conducting type.

The first category of solid oxide electrolyte is a typical oxygen ion-conducting model (Fig. 5).

The conduction mechanism of such solid oxide electrolytes is through oxygen vacancy transitions in the material structure or movement of oxygen in the self-interstitials. Thus, increasing the number of oxygen vacancy defects or oxygen interstitials would increase the oxygen ionic conductivity.

The main oxygen ion-conducting electrolytes in the SOECs system include Zirconia (ZrO_2)- and ceria (CeO_2)-based materials and their derivatives such as YSZ, since these materials can stabilize the cubic phase, thus, YSZ is a promising oxygen ion-conducting electrolyte operating at a high-temperature range (800–1000 °C). Ceria-based electrolytes are another oxygen ion-conducting electrolyte, which provide higher ionic conductivity than a YSZ-based at an intermediate temperature (500–800 °C). The main effective strategies to further improve the performance are doping rare earth elements (Sm, Ga), introducing an intermediate buffer layer (YSZ), and preparing a composite oxygen ion-conducting electrolyte.
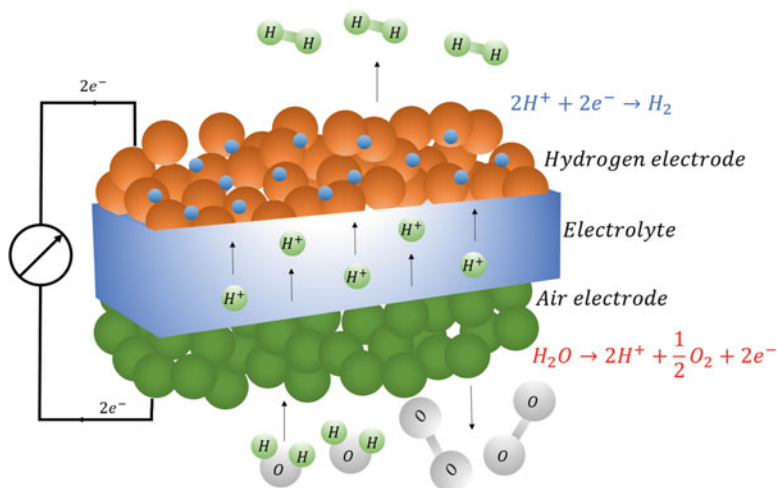
Fig. 6 Working principle diagram of proton-conducting electrolyte in the SOEC system

The second category of solid oxide electrolyte is a proton-conducting electrolyte (Fig. 6).

Under high temperature, the proton transports in proton-conducting materials, such as perovskites oxides, through the following three major steps: dissociative adsorption, the Grotthuss mechanism, and rotational diffusion. Currently, the primary challenges of proton-conducting materials are to fabricate or develop a high proton conductivity material, with excellent electrochemical/chemical stability, and a suitable thermal expand coefficient.

Among these proton-conducting materials, the perovskite oxides ceramic materials show the more comprehensive performance properties. The barium cerate ($BaCeO_3$)-based and zirconate ($BaZrO_3$)-based electrolytes are widely investigated as the proton-conducting electrolyte materials for the SOEC system.

4   High Temperature Steam Electrolysis

High temperature electrolysis can be performed with Solid Oxide Cells, that are solid oxide fuel cell operated in reverse mode. The cell is based on a solid oxide electrolyte that must be operated at high temperature in order to reach sufficient ionic conductivity (Reytier et al. 2015).

Water electrolysis, showed in the following Equation, is the reaction in which the water molecule is split into its constituents, hydrogen and oxygen. The reaction is endothermic and needs both thermal and electrical energy to be performed:

$$H_2O + Energy \rightarrow H_2 + \frac{1}{2}O_2$$
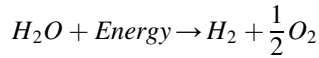
In solid oxide cells the ion that is conducted by the electrolyte is O^{2-}, the ions are transferred from the steam-hydrogen electrode (cathode) to the oxygen-air electrode (anode). The two half reactions are reported in:

$$H_2O + 2e^- \rightarrow H_2 + O^{2-} \quad Cathode$$

$$O^{2-} \rightarrow \frac{1}{2}O_2 + 2e^- \quad Anode.$$
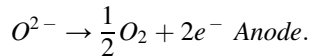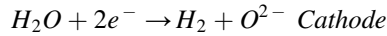
The overall energy demand for water electrolysis ΔH is described by the following Equation:

$$\Delta H = \Delta G + T\Delta S$$

and it is composed by two terms: ΔG is the Gibbs free energy change of the reaction and is the part of the energy demand that has to be supplied in form of electrical energy while $T \cdot \Delta S$ represents the thermal energy demand. The dependence of these terms on the temperature is showed in Fig. 7.

The main fact that can be noticed in Fig. 7 is that high temperature steam electrolysis intrinsically needs less energy than water electrolysis to be performed if the energy demand for vaporization is not taken into account. This thermodynamic advantage leads to good opportunity for heat integration with low temperature sources for steam generation. At cell level, where steam electrolysis is performed, while the overall energy demand ΔH slightly increases from ambient temperature to
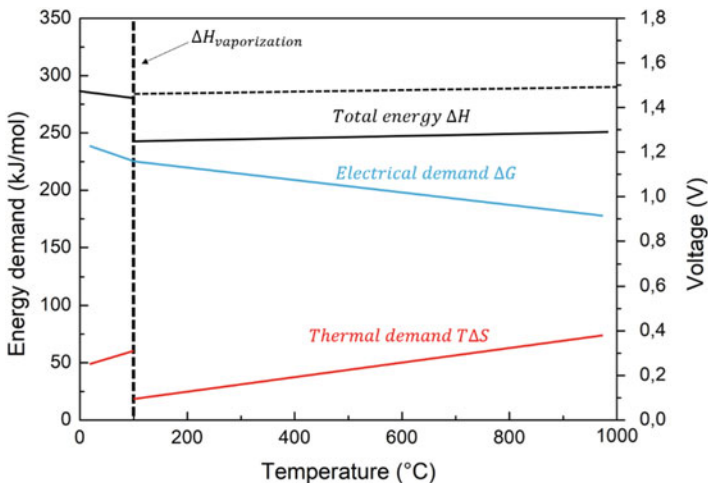
Fig. 7 Energy demand for water electrolysis as function of temperature

the operating temperature range of solid oxide electrolysis (700–900 °C), the electrical demand decreases from being 93% of energy demand at 100 °C to 77% at 750 °C.

The reversible voltage is the minimum cell voltage that would be required to perform steam electrolysis and is dependent on the Gibbs free energy change as in Equation:

$$V_{rev} = \frac{\Delta G}{zF}$$

Where z is the number of electrons involved in every reaction (z = 2) and F is the Faraday constant equal to 96,485 C/mol.

The thermoneutral voltage, defined in Equation:

$$V_{TN} = \frac{\Delta H}{zF}$$

is the cell operating voltage at which the heat generated by cell internal irreversibility is enough to provide the heat demand of the electrolysis reaction, resulting in the fact that an ideal cell can be operated in thermal equilibrium at this voltage. In this way, only electrical energy has to be supplied to the cell in order to perform steam electrolysis. The cell thermoneutral voltage is equal to 1.285 V at 750 °C considering only the energy demand for steam electrolysis, meaning that this is the voltage at which the cell operates at thermal equilibrium, i.e. the cell temperature is uniform, and the inlet and outlet temperature of the reactants are the same. If also the energy for steam generation has to be taken into account, the cell operating voltage necessary to cover the tire energy demand would be around 1.5 V.

The thermoneutral voltage at cell and stack level is important because an electrolysis cell operated at voltage lower than thermoneutral is endothermic and heat needs to be provided to the cell in order to sustain the reaction and keep the cell in the operating temperature range (Chen et al. 2017). If a cell is operated at voltages higher than the thermoneutral voltage the cell is exothermic, and the heat generated by irreversibility, mainly by Joule effect, must be removed from the cell in order to avoid excessive cell overheating.

4.1 Cell Physical Model

Normally, a physical model of this kind of cells represents a Single Repeating Unit (SRU) whose inputs and outputs are multiplied to reach the desired stack size. The cell is modelled in five layers: Cathode side interconnector plate, Steam side (Cathode) flow channels, Positive Electrode-Electrolyte Negative Electrode (PEN) assembly, Air side (Anode) flow channels and Anode side interconnector plate (Luo et al. 2014). Each layer is discretized in control volumes in which the equations for

energy and species conservation are implemented. The spatial resolution can be increased increasing the number of nodes.

Each gaseous node control volume is assumed to be a perfectly stirred reactor, temperatures and species concentrations are averaged between inlet and outlet and assumed constant in the node for heat exchange and Nernstian voltage calculations.

Energy conservation equations for each control volume of the cathode channels, PEN layer, anode channels and interconnector plates are presented in Equations:

$$\rho_{cath} \cdot c_{p_{cath}} \cdot V_{cath} \cdot \frac{dT_{cath}}{dt} = \dot{Q}_T + \dot{H}_{in} - \dot{H}_{out} + \dot{Q}_{ion} - \dot{Q}_{react}$$

$$\rho_{PEN} \cdot c_{PEN} \cdot V_{PEN} \cdot \frac{dT_{PEN}}{dt} = \dot{Q}_T + \dot{Q}_{GEN}$$

$$\rho_{an} \cdot c_{p_{an}} \cdot V_{an} \cdot \frac{dT_{an}}{dt} = \dot{Q}_T + \dot{H}_{IN} - \dot{H}_{OUT} - \dot{Q}_{ion}$$

$$\rho_{plate} \cdot c_{p_{plate}} \cdot V_{plate} \cdot \frac{dT_{plate}}{dt} = \dot{Q}_T$$

where H_{in}, and H_{out} are the total enthalpy terms at the inlet and outlet condition of the gaseous nodes, ρ is the density, V is the volume and c, c_p are the specific heat capacity. Q_{ion}, is the term related to the sensible enthalpy of the oxygen ions crossing the electrolyte from the cathode to the anode side, evaluated at PEN temperature according to Equation:

$$\dot{Q}_{ion} = \frac{I}{4F} \cdot h_{O2}$$

Q_{GEN} is the term related to the heat generated or absorbed by the cell depending on the electrolysis thermodynamic behavior, evaluated according to Equation:

$$\dot{Q}_{GEN} = \dot{Q}_{react} - VI$$

Where Q_{react} is the heat of the reaction evaluated at PEN temperature, V is the cell voltage and I is the current of the node:

$$\dot{Q}_{react} = \frac{I}{2F} \left(h_{H2} + \frac{1}{2} h_{O2} - h_{H_2O} \right)$$

Q_T is the term related to convective and conductive heat transfer between solid-solid, solid-gaseous and gaseous-gaseous interfaces:

$$\dot{Q}_T = \dot{Q}_{cond} + \dot{Q}_{conv}$$

The convective heat transfer is calculated assuming fully developed flow resulting in a constant Nusselt number, equal to 4, allowing the evaluation of a constant convective heat transfer coefficient with the following equation:

$$N_u = \frac{h_{conv} \cdot D_h}{k}$$

where h_{conv}, is the convective heat transfer coefficient, k is the thermal conductivity of the involved gas and D_h the hydraulic diameter of the cell channel.

Cathode and anode flow also present species conservation balances needed to take into account the different species concentration along the flow channels. On the cathode side the species are H_2 and H_2O and the species conservation are expressed in Equations:

$$\frac{p_{cath} \cdot V_{cath}}{RT_{cath}} \cdot \frac{d\chi_{H_2}}{dt} = \left(\dot{n}_{cath}\chi_{H_2}\right)_{in} - \left(\dot{n}_{cath}\chi_{H_2}\right)_{out} - \frac{I}{2F}$$

$$\frac{p_{cath} \cdot V_{cath}}{RT_{cath}} \cdot \frac{d\chi_{H_2O}}{dt} = \left(\dot{n}_{cath}\chi_{H_2O}\right)_{in} - \left(\dot{n}_{cath}\chi_{H_2O}\right)_{out} + \frac{I}{2F}$$

while on the anode side the considered species are O_2 and N_2 according to Equations:

$$\frac{p_{an} \cdot V_{an}}{RT_{an}} \cdot \frac{d\chi_{O_2}}{dt} = \left(\dot{n}_{an}\chi_{O_2}\right)_{in} - \left(\dot{n}_{an}\chi_{O_2}\right)_{out} - \frac{I}{4F}$$

$$\frac{p_{an} \cdot V_{an}}{RT_{an}} \cdot \frac{d\chi_{N_2}}{dt} = \left(\dot{n}_{an}\chi_{N_2}\right)_{in} - \left(\dot{n}_{an}\chi_{N_2}\right)_{out}$$

where n is the total molar flow rate in the anode or cathode channel and χ is the species molar fraction, p, V and T are the pressure, volume and temperature of the respective channel position and R is the universal gas constant. The current is negative, so hydrogen and oxygen are yielded at the cathode and anode side respectively while water steam is depleted at the cathode side.

The cell voltage is determined starting from the species concentration in each node with the evaluation of the local Nernst potential according to Equations:

$$U_{Nerst} = U_0 + \left(\frac{RT_{PEN}}{2F}\right) \ln\left(\sqrt{p_{an}}\left(\frac{\chi_{H_2}\sqrt{\chi_{O_2}}}{\chi_{H_2O}}\right)\right)$$

$$U_0 = -\frac{\Delta g_f}{2F}$$

where U_0 is the reversible voltage, Δ_{gf} is the molar Gibbs free energy of formation at the PEN nodal temperature T_{PEN} and χ is the species molar fraction.

The equation for the ohmic resistance of the cell can been derived with an exponential fitting of ASR(T) values:

$$ASR_{cell} = A e^{\frac{B}{e^{T_{cell}}}}$$

The local ohmic overpotentials and cell voltage can be evaluated node by node with the following equations:

$$U_{ohmic} = i ASR_{cell}(T_{PEN}) + i ASR_{interconnect}$$

$$V_{cell} = U_{Nerst} + U_{ohmic}$$

The electrolysis system is controlled by the electric power supplied to the stack. At every time step the current that can be imposed to each cell is computed as follow:

$$I = \frac{P_{stack}}{V_{cell} n_{cell}}$$

where P_{stack} is the electric power supplied to the stack, V_{cell} is the voltage of the cells and n_{cell} the number of cells in the stack. The water feed necessary to the system is determined and consequently modulated as inlet stream to the system model via the Faraday's Law of electrolysis:

$$\dot{N}_{H_2O} = \frac{I}{2F} \frac{n_{cell}}{SU}$$

where SU is the steam utilization factor defined as the ratio between the stoichiometric steam flow necessary to perform the electrolysis process at a given current and the inlet steam flow supplied to the system.

Cell temperature control is one of the key issues involved in the dynamic operation of high temperature solid oxide systems. In this work the temperature control is performed via the manipulation of the air flow at the anode side, in this way the air flow has two functions: removing the oxygen produced by the electrolysis process and provide active cooling or heating to the stack.

5   Materials for Solid Oxide Electrolysis

An electrolysis cell, with a typical thickness of 200–300 μm, is constituted of an oxygen electrode (anode) and a hydrogen electrode (cathode) separated by a dense ionic conducting electrolyte. In the case of a solid oxide electrolysis cell (SOEC), water supplied at the cathode side is reduced into H_2 and O^{2-} ions. The latter cross the electrolyte to eventually form O_2 by oxidation at the anode side (Nechache and Hody 2021).

The two main SOEC architectures considered so far are the electrolyte-supported cell (ESC) and the cathode-supported cell (CSC) architectures. These two technologies are distinguished by the main, thicker layer that provides mechanical support to the cell. Therefore an ESC has a thick electrolyte, on which thin cathode and anode are deposited. On the other hand, a CSC has a thick cathode (hydrogen electrode), on which a thin electrolyte and anode are deposited. This thickness discrepancy leads to operating temperature and performance differences. In this paper, the main focus is on alternative/innovative CSC materials.

SOEC appears to be a possible game-changer technology for several markets in the mid/long term (2025–2030), identified as: (i) large scale H_2 production thanks to its high-power efficiency when external heat is available, (ii) Power-to-X by coupling SOEC with chemical reactors to produce several fuels/liquids such as ammonia, methanol and formic acid, (iii) Power-to-Power thanks to its reversible SOFC/SOEC operation ability. In addition, SOEC shows very interesting flexibility since it can be considered for both decentralized hydrogen production close to the end user and centralized mass production in countries with high renewable potential. Further flexibility lies in the ability to produce multiple gases (syngas by $H_2O + CO_2$ co-electrolysis, CO by CO_2 electrolysis, etc. . . .).

5.1 State of the Art Materials

A solid oxide electrolysis cell (SOEC) is typically constituted of four layers: the hydrogen (or steam) electrode, the electrolyte, the oxygen (or air) electrode, and the intermediate layer between the oxygen electrode and the electrolyte (also called barrier layer). The interconnector is also an important element that can be considered as a layer in a stack of cells (>2 cells).

The electrolyte is the central layer of the SOEC that determines the composition of the surrounding layers (hydrogen electrode, oxygen electrode and intermediate layer). The electrolyte must be highly conductive for ions (O^{2-} oxygen ions in the case of a SOEC) to allow good performance, electrically insulating to prevent electronic conduction, and sufficiently dense to avoid gas transport between the two electrode atmospheres. On the other hand, the mechanical strength as well as the thermal and chemical stabilities of the material are critical to ensure sufficient durability. The state-of-the-art material is the yttria-stabilized zirconia (YSZ), and especially the 8 mol% yttria-doped (8YSZ), a dense zirconium oxide-based ceramic (cubic crystal structure stabilized by the addition of yttria). 8YSZ shows good and stable performance over time in the typical SOEC temperature range 700–850 °C thanks to a high ionic conductivity ($10^{-2} - 10^{-1}$ Scm^{-1}) associated with good thermal and chemical stabilities. Gadolinium-doped ceria (CGO or GDC) is also more and more used as electrolyte material thanks to its high ionic conductivity but its high sintering temperature (~1500 °C) remains challenging as it restricts co-sintering possibilities (Tan et al. 2022).

The oxygen electrode (O_2 electrode) is where O^{2-} ions are oxidized to oxygen, mostly in the first microns closest to the electrode/electrolyte interface. A good material must include a high mixed ionic-electronic conductivity along with excellent electrocatalytic activity as well as suitable chemical and thermal compatibilities towards the electrolyte over time. This last point is particularly difficult to achieve. This explains why an intermediate layer between the oxygen electrode and the electrolyte is generally required. Co-based and Sr-doped perovskites are often used as O_2 electrode materials for their higher electrocatalytic performance. The state-of-the-art are perovskites $(La,Sr)(Co,Fe)O_3$-based and $La_{0.8}Sr_{0.2}MnO_{3-\delta}$-based materials with optimized microstructures (particle size and volumetric content in single layers) to reduce polarization resistance and enhance durability. LSCF is a mixed ionic and electronic conductive (MIEC) material that presents a high electrical and ionic conductivity (10^2 and 10^{-2} S cm^{-1} at 800 °C, respectively) along with high oxygen diffusion properties (oxygen diffusion and oxygen surface exchange coefficients), achieving superior electrocatalytic activity. LSM is considered as a reference material thanks to its chemical and thermal stabilities in addition to acceptable performance

The hydrogen electrode (H_2 electrode) is where steam is electrochemically reduced into hydrogen. This reaction takes place close to the electrolyte/electrode interface (~5–10 μm) at sites where the electrical phase (electron conductive), the ionic phase (O^{2-} conductive) and the gaseous phase (steam supply and hydrogen release) meet, called the triple phase boundaries (TPBs). Hence, the hydrogen electrode material has to be a porous electronic-ionic conductor. The state-of-the art material is a ceramic-metal (cermet) material composed of the reference electrolyte YSZ and nickel, a non-precious metal catalyst with high electronic conductivity. It is typically referred as Ni-YSZ. Ni-CGO is the electrode material, mostly used with CGO electrolyte.

As mentioned above, it is particularly challenging to find compatible oxygen electrode and electrolyte materials. Indeed, Co-based O_2 electrodes show higher thermal expansion coefficient (TEC) compared to YSZ electrolyte, meaning significant thermal mismatching that can weaken both mass transfer process and charge exchange, leading to a larger ohmic resistance. Besides, Co is a relatively high-cost element that can be volatile during higher temperature sintering processes. On the other hand, the Sr element can easily segregate during operation, leading to significant performance decrease and degradation. Hence, to mitigate this overhead, an intermediate layer (or barrier layer) is usually added between the O_2 electrode and the electrolyte, acting as a transition layer to allow good thermal compatibility and avoid chemical interactions (element migration) while ensuring a good ionic conductivity. Gadolinium-doped cerium oxide (CGO or GDC) and yttrium-doped cerium (YDC) are common reference materials. Furthermore, another typical approach is to use a composite material as O_2 electrode that includes the electrolyte material, e.g., LSM-YSZ, thus avoiding the use of an intermediate layer. This latter approach is possible for O_2 electrode materials that are chemically stable regarding the electrolyte material, which is not the case between LSCF and YSZ due to Sr segregation issues as extensively reported in the literature.

The interconnector is an element that plays a key role in the stacking of SOECs. Indeed, this metallic layer connects the single cells in a stack. This element acts not only as a current collector, completing the circuit of the electrochemical system, but also as a physical barrier separating the H_2 electrode and the O_2 electrode gas atmospheres between two adjacent cells. Furthermore, an interconnector must fulfill the following technical requirements: high electrical and thermal conductivity, stability at high temperatures (typically in the range 600–900 °C), formation of a dense low resistive oxide layer in both oxidizing and reducing atmospheres. The most commonly used interconnector materials are usually based on either high-chromium containing stainless steels or powder metallurgical manufactured Cr-alloys. Crofer 22 APU or 22H, Ducralloy, CFY and CrFe5 are noteworthy examples. For both kind of materials, chromium oxides are formed when operated at high temperatures, preventing the well-known breakaway oxidation. Chromium evaporation also happens typically under SOFC/SOEC operations with potentially detrimental effects on the performance and the durability of the stack (Zhang et al. 2013).

Most of the research efforts related to interconnector materials are dedicated to SOFC operations. Indeed, most of the performance and durability issues related to the interconnector are similar to both SOFC and SOEC operations. One can mention degradation issues (coking, cracks, delamination) due to chemical interaction with reductive/oxidative gas atmospheres and electrode materials, and also mechanical strength issues. However, it seems quite surprising that only little research work exists on interconnector materials, specifically focused on SOEC.

5.2 Innovative Materials

The emergence of innovative electrolyte materials is strategic as it will directly influence both composition of all the other layers constituting the cell and the operation conditions, i.e., the temperature and the current, two parameters that are key to determine the final economic viability of the technology. Ideally, a cell based on an electrolyte that can operate at lower temperature (700 °C or even lower) and higher current densities (>1 Acm^{-2}), while maintaining high ionic conductivity and sufficient mechanical strength, can lead to a system that will allow a lower production cost of hydrogen. Nevertheless, there have been few recent developments regarding innovative electrolyte materials. This section briefly mentions a couple of alternative materials that has been developed in the last 5–10 years.

Scandia-stabilized zirconia (ScSZ) is a material that presents higher ionic conductivity than YSZ – the 10%mol composition being the highest – which results in superior current densities under operation. However, ScSZ mechanical strength is lower than YSZ, which explains its use only for electrolyte-supported cell technology where the electrolyte thickness is typically >50 μm, versus 5–10 μm for the cathode-supported cell technology. Cerium-doped ScSZ (ScCeSZ) material is also considered as addition of Ce provides higher ionic conductivity while maintaining mechanical strength.

ScSZ-type electrolyte material has drawn much attention over the past several years. Indeed, it has been thoroughly studied and developed by the IKTS research institute as well as the Kerafol company. The latter has even integrated it in its manufactured cell technology, a core component of the stacks and systems developed by SUNFIRE, one of the current industrial leaders in SOEC-based technologies.

Strontium-magnesium doped lanthanum gallate (LSGM) is a perovskite material considered as a candidate electrolyte material thanks to its high ionic conductivity. LSGM, however, presents several drawbacks: difficulty in processing and interaction with many perovskite H2 electrode materials, including Ni-YSZ.

ICMCB (CNRS laboratory) has recently considered gadolinium-doped ceria (GDC), and especially GDC10 (10%-doped, $Ce_{0.9}Gd_{0.1}O_{2-\delta}$), as a potential electrolyte material because it offers the possibility to significantly reduce the operating temperature to 500–600 °C while maintaining high ionic conductivity. This is of particular interest as operating at a lower temperature significantly reduces degradation issues and possibly the production cost of hydrogen, especially in the case of massive/large-scale production. Only preliminary work has been reported so far which should be followed by first measurements under SOEC operating conditions.

The current state-of-the-art material, Ni-YSZ, still presents several degradation issues during long time operations under high current densities (>1 Acm^{-2}), typically nickel agglomeration and nickel depletion. These limitations critically affect the SOEC performance and must be addressed to allow long-term operations (>20 kh) which is mandatory to make SOEC economically viable. Hence, several materials have recently emerged.

The "metal-catalyst" exsolution approach consists in emerging the metal-catalyst from the backbone structure of the perovskite material onto its surface by applying a voltage (or current) under a reductive H_2 atmosphere near the working temperature of the cell (Yan et al. 2020). Hence, depending on the processing conditions (T, atmosphere, voltage/current) and the initial material composition (nature of the metal-catalyst, its doping level, composition of other elements) different microstructures can be obtained, as well as size, shape and distribution of the metal-catalyst at the material surface. This flexibility is of particular interest as it potentially offers the possibility to manufacture a cell adapted to a specific application with optimized characteristics (high performance but limited durability or lower performance with long durability). The main advantages of this approach are improvement of the catalyst activity (especially for nanoparticles) as well as thermal and coking resistance, leading to very high performances (up to >2 Acm^{-2}). However, stabilization of the microstructure as well as distribution, size and shape of the catalyst over time remain the main challenges, leading to significant performance and degradation issues.

St Andrews University, and more particularly Irvine's group, has been studying the "metal-catalyst exsolution" approach for almost 20 years, mainly in SOFC first, and more recently in SOEC (Zhang et al. 2020). The group has developed exsoluted nanoparticles that have remarkable stability, do not agglomerate, and have low tendency to create carbon nanofibers, thanks to their firm anchoring to the ceramic

surface. The method used is faster, cheaper and gives better access to hardly reachable locations than conventional impregnation methods, at the same time maintaining better control over the amount and distribution of deposited particles. However, the materials developed through this method dedicated mainly to SOFC must be further adapted for SOEC operation (microstructure, composition, etc. …). The most advanced H_2 electrode material currently developed is $LaxCayNi_{1-z}TizO_3$ (LCaNT). Irvine's group has recently compared exsolution of Ni nanoparticles from $LaNiTiO_3$ (LNT) based materials under reducing atmosphere conditions and under varying potentials using a combination of XRD, SEM, TEM and STEM. Three potential H_2 electrode materials have been tested, namely $La_{0.52}Ca_{0.28}Ni_{0.06}Ti_{0.94}O_3$ (LCaNT), $La_{0.52}Sr_{0.28}Ni_{0.06}Ti_{0.94}O_3$ (LSrNT) and $La_{0.8}Ce_{0.1}Ni_{0.4}Ti_{0.6}O_3$ (LCeNT), leading to the following observations: (i) LCaNT and LCeNT both exsolve large numbers of Ni nanoparticles during reduction whereas LSrNT does not; (ii) all the materials exsolve Ni nanoparticles after electrochemical poling at 2.0 V, with a larger number of nanoparticles for LCaNT; (iii) much more Ni exsoluted nanoparticles have been produced in the reducing atmosphere for LCaNT and LCeNT. This group also investigated Ni exsolution from $BaxCe_{0.5}Zr_{0.3}Y_{0.2-y}Ni_yO_{3-\delta}$ (BCZY), a potential H_2 electrode material for proton conducting electrolysis.

The Dutch Institute For Fundamental Energy Research (DIFFER) and Newcastle University examined the co-electrolysis behavior of LCaT-Fe/YSZ/LSM-YSZ/LSM cell, with $La_{0.43}Ca_{0.37}Fe_{0.06}Ti_{0.94}O_3$ (LCaT-Fe) that contains Fe-exsoluted nanoparticles which enhance the electro-catalytic activity. In terms of performance, -0.45 A cm^{-2} at 1.5 V has been achieved under 15% CO_2 + 15% H_2O + 70% N_2 at 850 °C, and up to -0.55 Acm^{-2} at 1.6 V. Moreover, the cell exhibits stable behavior without any significant voltage increase during the transient galvanostatic experiment.

Inha University (Korea) has investigated the exsolution of Ni from $Ni_{0.4}Mg_{0.6}O$ powder. SEM observations suggest that the size and dispersion state of Ni nanoparticles depend on reduction temperature and crystallographic orientation of $Ni_{0.4}Mg_{0.6}O$ powder. Ni nanoparticles have been reversibly exsoluted and oxidized in response to an atmosphere.

Recently, Kyushu University has considered Cu-exsolution for steam electrolysis and co-electrolysis, showing preliminary performances of up to -1.08 Acm^{-2} at 1.6 V on an electrolyte-supported button cell (0.2 cm^2).

In recent years, gadolinium-doped ceria (GDC) has brought attention as a rising H2 electrode material to combine with Ni. This has been achieved thanks to a better ionic conductivity compared to YSZ, its mixed ionic-electronic conduction properties and its compatibility with YSZ electrolyte (no need of an intermediate layer meaning potentially reducing cell manufacturing cost). Most of the studies carried out so far on Ni-GDC are for SOFC, with only a few studies investigating SOEC.

DLR has recently reported a study on a long-term test of a SOEC stack using Ni-GDC as H_2 electrode. This stack is provided by SUNFIRE and composed of 30 electrolyte-supported cells Ni-GDC/YSZ/GDC/LSCF. Tests are performed in both SOEC and reversible SOFC/SOEC modes for 3370 h and 2000 h, respectively,

with 70% steam conversion (SOEC) and 70% fuel utilization (SOFC). The SOEC test leads to a low degradation of 0.5%/1000 h for i = -0.52 A cm^{-2}. The reversible SOFC/SOEC test consists in applying 0.18 A cm^{-2} in SOFC and up to -0.52 A cm^{-2} in SOEC, leading to degradations of 3.0%/1000 h and 1.2%/1000 h, respectively. Therefore, Ni-GDC is a good candidate and stands as an alternative to Ni-YSZ as H2 electrode material for SOEC based on electrolyte-supported cells.

La$_{0.6}$Sr$_{0.4}$Ga$_{0.3}$Fe$_{0.7}$O$_3$ (LSGF) is a mixed conducting perovskite characterized by a good conductivity coupled with a remarkable stability. In particular, LSGF is suitable for use along with LSGM electrolyte presented before since these materials present similar composition and structure. This material could be a serious alternative H2 electrode in case of LSGM further emergence as electrolyte.

Padova University, in collaboration with St. Andrews University (Irvine's group) and Mines St Etienne, considered several LSGF-based materials as H$_2$ electrode in reversible symmetrical solid oxide cells. Preliminary tests on reversible cells are carried out with LSGF electrodes impregnated with Pd/CGO, including in electrolysis mode under 10% H$_2$O + 90%N$_2$ at 850 °C, showing a quite low performance of -0.1 A cm^{-2} at 1.25 V. Deeper investigations are necessary to further evaluate the potential of LSGF material.

An original material has been recently elaborated and tested by University of Yamanashi (Japan) for reversible operations. This material, Ni–Co-SDC/Ni-YSZ, is a composite double layer H$_2$ electrode consisting of: (i) (CeO$_2$)$_{0.8}$(SmO$_{1.5}$)$_{0.2}$ (SDC) scaffold with highly dispersed Ni–Co nanoparticles as the catalyst layer where the electrochemical reactions take place, and on top of it (ii) a thin current collecting layer of Ni–YSZ cermet. SDC shows good mixed ionic-electronic conduction under reducing H$_2$ atmosphere, while Ni–Co nanoparticles ensure a decent electrocatalytic activity. Preliminary works demonstrate highly reversible performance at 800 °C via control of the microstructure.

The most recent work demonstrates long-term operation capability for this H$_2$ electrode material in both SOEC and reversible SOFC/SOEC modes. Indeed, the complete button cell (0.28 cm^2) composed of Ni–Co-SDC/Ni-YSZ//YSZ//SDC//LSCF-SDC is operated at 800 °C by applying -0.5 A cm^{-2} in SOEC mode and cycles of 0.5 A cm^{-2} and -0.5 A cm^{-2} in reversible SOFC/SOEC mode. Both tests last over 600 h. Significant degradation of the cell, and especially of Ni–Co-SDC/Ni-YSZ, is noticed during SOEC mode test. This degradation is drastically mitigated by operating the cell in reversible SOFC/SOEC mode, showing further improvement of the cell durability. Therefore, Ni–Co-SDC/Ni-YSZ is an attractive material that needs to demonstrate increased cell performance under reversible operation, while maintaining low degradation. In the meantime, scaling-up efforts are also necessary.

Long time operation under high current densities (>1 A cm^{-2}) is a main source of degradation for the oxygen electrode, including the state-of-the-art LSCF-based and LSM-based materials. Degradation includes (i) migration of elements such as Sr and Co that fragilize the electrode structure, (ii) delamination at the electrolyte/electrode interface consecutive to formation of holes due to locally high PO$_2$, and (iii) appearance of cracks. All these issues have detrimental consequences on cell performance and durability and need to be addressed. Optimization of state-of-the-

art materials has been explored. Very promising results on a button cell (0.8 cm^2) are obtained by Jülich (in collaboration with ICMCB specialized on nickelate-based O$_2$ electrode materials, see below) using LSCF infiltrated with ~8 wt%-LSC as the O$_2$ electrode. The obtained performance is -2 A cm^{-2} at 1.5 V under 50% H$_2$O + 50% H$_2$ at 800 °C. The degradation study is under progress. A similar approach is adopted by University of Tehran to improve the reversible performance of LSM by infiltration of LaNi$_{0.5}$Co$_{0.5}$O$_3$ nickelate nanoparticles. DTU (Denmark) demonstrates that this approach is not sufficient to permit the use of CGO as O$_2$ electrode material since the infiltration of CGO-backbone with LSC has a negative effect on both performance and degradation.

Nevertheless, optimization of O$_2$ electrode materials is still needed to reach performance and durability levels compatible with commercialization of SOEC systems, leaving the research opportunities open to alternative candidates.

Nickelate-based materials have been considered for more than 10 years as good O$_2$ electrode candidate. Ln$_2$NiO$_{4 + \delta}$ nickelates (Ln = La, Nd, Pr) and their derivatives have been demonstrated to combine redox stability (except undoped Pr$_2$NiO$_{4 + \delta}$) with significant oxygen content changes allowing better electrocatalytic activity and mixed ionic-electronic transport, as well as moderate thermal expansion and negligible chemical expansion. These materials have been showing operating abilities as O$_2$ electrode in SOFC, SOEC and reversible SOFC/SOEC modes. However, depending on their composition, nickelate-based materials still suffer from (i) chemical and/or thermal instability, (ii) instability under higher oxygen atmosphere, (iii) limited performance, and (iv) degradation issues over long-term operation.

The Jülich Research Center has studied two nickelate-based materials: Co-doped La$_2$NiO$_{4 + \delta}$ (LNCO) with Aachen University and 50:50 La$_2$NiO$_{4 + \delta}$: Pr-doped ceria (LNO:PrDC) with ICMCB. This approach aims at improving the electrocatalytic activity of LNO. Both materials are integrated as O$_2$ electrode in a commercial button cell (1.024 cm^2) and tested under 50% H$_2$O + 50% H$_2$ at 800 °C, showing similar performance at 1.5 V: -1.6 A cm^{-2} for LNCO and -1.53 A cm^{-2} for LNO: PrDC. A first durability test is also performed for LNCO by applying -1 A cm^{-2} for 250 h, showing less degradation than LNO (value not reported). University of Aveiro has also shown that surface modification of LNO electrode with PrO$_x$ submicron particles results in noticeable improvement of the electrochemical activity. Since one of the main drawbacks of Ln$_2$NiO$_{4 + \delta}$-based materials are their reactivity with reference electrolytes YSZ and CGO, University of Zaragoza has employed two strategies to avoid this unwanted phenomenon: direct formation of Ln$_2$NiO$_{4 + \delta}$ phase into YSZ scaffolds by infiltration and the development of a barrier layer. The infiltration approach is performed with Nd$_2$NiO$_{4 + \delta}$ phase in YSZ scaffolds, showing 0.76 W cm^{-2} at 0.8 V and 800 °C. For the second approach, a mixed praseodymium, cerium and gadolinium oxide (PCGO) layer is formed at the PNO-CGO electrode-electrolyte interface, leading to satisfactory performance and stability of the tested cell with -0.98 Acm^{-2} at 1.2 V and 800 °C under 50% H$_2$O + 50% H$_2$. Further developments of these different promising approaches are

needed to ensure good stability and performance of $Ln_2NiO_{4 + \delta}$-based materials over long-term operations. Scaling-up capability of the associated processes is also a critical aspect to be carefully considered, especially for the infiltration approach.

Through their long-time experience on nickelates, ICMCB has developed several nickelate-based materials for SOFC and SOEC operations, including: (i) $La_2NiO_{4 + \delta}$ (LNO) that shows high chemical stability but poor electrochemical activity, (ii) $Pr_2NiO_{4 + \delta}$ (PNO) which is less stable chemically but significantly more active electrochemically, and (iii) $Nd_2NiO_{4 + \delta}$ (NNO) that presents interesting conductivity properties but too unstable. Thus, ICMCB tries to combine advantages of LNO and PNO while minimizing their drawbacks by exploring $La_{2-x}Pr_xNiO_{4 + \delta}$ (LPNO). Several LPNO compositions are synthesized and characterized. The use of LPNO as O_2 electrode material is particularly relevant when considering its physic-chemical properties compatible with SOFC/SOEC operations, which includes surface exchange and oxygen diffusion coefficients, TECs and electrical conductivity. Moreover, the O_2 electrode reaction is more efficient with Pr-rich composites than La-rich ones, but less stable chemically. Overall, $La_{1.5}Pr_{0.5}NiO_{4 + \delta}$ appears to be the best compromise. A durability test of $La_{1.5}Pr_{0.5}NiO_{4 + \delta}$ is performed under both SOFC and SOEC modes in symmetrical button cell configuration ($\sim$1 cm^2) LPNO/GDC/YSZ/GDC/LPNO by applying 0.3 A cm^{-2} for 1800 h (Fig. 7), showing a much better stability under SOEC conditions, confirming the good potential of $La_{1.5}Pr_{0.5}NiO_{4 + \delta}$ as O_2 electrode for SOEC operation. Scalability of this material must be demonstrated though.

University of Aveiro (Portugal) has characterized $Nd_{0.8}Sr_{1.2}Ni_{0.8}M_{0.2}O_{4-\delta}$ (M = Ni, Co, Fe) nickelates as prospective O_2 electrode, emphasizing on structural stability, ionic-electronic conductivity, and thermomechanical compatibility with the electrolyte. Adding Sr element allows enhancing both ionic and electronic conductivities, with a positive effect on electrocatalytic properties. However, as already mentioned earlier, Sr segregation can lead to significant degradation issues, even more for long-term operations. It is shown that (i) the average thermal expansion coefficients of $Nd_{0.8}Sr_{1.2}Ni_{0.8}M_{0.2}O_{4-\delta}$ are close to that of the reference intermediate layer material CGO, (ii) Co and Fe have a negative effect on the electronic-ionic material conductivity, and (iii) the electrochemical activity under open circuit voltage (OCV, zero-current) is similar for all three compositions of $Nd_{0.8}Sr_{1.2}Ni_{0.8}M_{0.2}O_{4-\delta}$, and substantially improved by surface modification with PrOx. This first characterization must be followed by further examination of this material, especially when M = Ni, including thorough performance and durability tests under standard SOEC conditions.

Along with Ni–Co-SDC/Ni-YSZ H_2 electrode material, University of Yamanashi also focuses on the elaboration and the development of an alternative O_2 electrode material for reversible operations, e.g., LSCF-SDC. This material combines the properties of the reference material LSCF with the highly effective O^{2-} conductive behavior of SDC under oxygen atmosphere. Moreover, infiltration of SDC in LSCF scaffold enhances the performance of the cell in both SOEC and SOFC modes. Therefore, in the same work presented above, enhancement of both performance and durability of the material are demonstrated after infiltration of SDC in LSCF, for

tests in symmetrical and complete cell configurations, clearly revealing the potential of this alternative material. Results in complete cell configuration are especially impressive: except for the initial operation time (first 100 h), a very low degradation is observed on the O_2 electrode side for 400 h, and almost disappears when the SOFC/SOEC cycling process is applied. Even if the current applied are still quite low (-0.5 A cm^{-2}), these results confirm the special attention that should be given to the innovative cell developed by University of Yamanashi.

$La_{0.6}Ca_{0.4}Fe_{0.8}Ni_{0.2}O_{3-\delta}$ (LCaFN) is an interesting perovskite-type material as it avoids the use of both Co and Sr elements that present several issues, as aforementioned. This material is elaborated by Huazhong University (China), integrated to the button cell (0.5 cm^2) Ni-YSZ/YSZ/GDC/LCaFN-GDC and investigated in reversible SOFC/SOEC mode, reaching -1.2 Acm^{-2} for 1.4 V at 800 °C. A short stability test under operation is realized by applying -0.2 Acm^{-2} for 12 h. This is a preliminary test to validate the possible use of this material. Complete and deeper evaluation of this material is needed to better appreciate the potential of LCaFN as O_2 electrode material.

The intermediate layer can play a crucial role to avoid the degradation issues of the oxygen electrode mentioned above. One has to keep in mind that its development is conditioned by the development of innovative electrolyte and oxygen electrode materials. Thus, for all the alternative O_2 electrode materials presented above and tested with YSZ as the electrolyte, GDC (or CGO) is used as the intermediate layer. A specific literature research for alternative/innovative intermediate layer under SOEC operation reveals that GDC-based material is almost systematically used. Yttrium-doped ceria (YDC) is also used in some case studies. The only alternative material recently reported is related to the complete cell developed by University of Yamanashi, namely $(CeO_2)_{0.8}(SmO_{1.5})_{0.2}$ (SDC), to ensure a good compatibility under operation between LSCF-SDC O_2 electrode and YSZ electrolyte.

Graz University of Technology has performed a characterization and performance study of several commercial SOC stacks operated under realistic conditions in both SOFC and SOEC modes to evaluate their system integration ability. Part of the study consists in comparing the influence of the interconnector materials on the performance and durability of the stacks. The studied stacks are composed of either Crofer 22 APU or CFY, two reference interconnector materials. The study shows that lightweight stacks composed of thin Crofer 22 APU plates are more fragile and more sensitive to thermal distortion and stresses. Inhomogeneity in cell's performance is also observed for one of these stacks, maybe attributed to extensive clamping force applied for stack sealing. In the meantime, two heavier stacks composed either of CFY interconnects or solid interconnects made of Crofer 22 APU reveal no negative effect on stack performance.

Crofer 22H ferritic steel is considered by Jülich as a potential SOEC stack interconnect material in the realistic operating conditions of a SOEC system for CO2/H2O co-electrolysis. Moreover, at the H2 electrode side, a nickel wire mesh is commonly used for the contacting between Ni-YSZ electrode and interconnector. This motivates the focus of this study on the joints between Crofer 22H and Ni- and CuNi contact materials, since most research works on this specific aspect are carried

out in SOFC mode. To simulate the conditions at the inlet and outlet of the stack, the interconnector and wires are exposed to CO_2/H_2O^- and CO/H_2-rich gases, respectively, for 1000 h between 600 and 800 °C. Regardless of the considered test conditions, several protective oxide scales are formed at the interconnector surface, all mainly constituted of chromic oxide and/or Cr/Mn spinel. On the other hand, no carbon transfer (a major degradation issue in co-electrolysis mode) is observed from the gas atmosphere into the interconnector, including the high carbon activity of CO/H_2-rich gas typically present at the stack outlet. However, at the joints between the interconnect and the wires, this carbon-rich gas atmosphere leads to the appearance of a carburized area with important precipitation of $M_{23}C_6$ and/or M_7C_3. This is the consequence of significant carbon transfer from the gas to the interconnector, through either CuNi-wires or Ni-wires, with the effect being heightened for the Ni-wires. Only minor carbon transfer is observed at the stack inlet, only for 600 °C. Furthermore, a partial contact loss is noticed between the interconnector and the wire in the case of CuNi-wire.

6   Conclusions

Hydrogen production by high-temperature steam electrolysis using the SOEC system is a promising environmentally friendly and energy saving technology. Reducing operating temperatures and developing electrochemical and chemical stability/durability with minimal thermal stress/mismatch are key issues in the commercialization of the SOEC. Recent studies have shown that compared with traditional oxygen ion conducting SOECs, proton electrolytes have the advantages of high pure hydrogen content, low nickel oxidation, high current efficiency, relatively low operating temperature, etc., and have improved proton conductivity of electrolytes. Whether improving the chemical stability of the ceramic-based electrolyte or increasing the proton conductivity of the zirconium-based electrolyte, the SOEC efficiency can be improved. Testing and understanding structural and electrochemical modifications under in situ conditions can provide a perspective for reducing material degradation and thus improve their durability. This chapter overviews the working principle, the component materials of the SOEC, the development of electrolytes, hydrogen electrodes, and oxygen electrode materials, and presents the design scheme, preparation method, and performance optimization of the SOEC. It is believed that advanced manufacturing/characterizing techniques should emerge to improve the durability and activity of the SOEC materials soon.

References

Chen M, Sun X, Chatzichristodoulou C et al (2017) Thermoneutral operation of solid oxide electrolysis cells in potentiostatic mode. ECS Trans 78:3077. https://doi.org/10.1149/07801.3077ecst

Fu Z, Wang Z, Li Y et al (2022) Effects of composite electrode structure on performance of intermediate-temperature solid oxide electrolysis cell. Energies 15(19):7173. https://doi.org/10.3390/en15197173

Kim J, Jun A, Gwon O et al (2018) Hybrid-solid oxide electrolysis cell: a new strategy for efficient hydrogen production. Nano Energy 44:121–126. https://doi.org/10.1016/j.nanoen.2017.11.074

Laguna-Bercero MA (2012) Recent advances in high temperature electrolysis using solid oxide fuel cells: a review. J Power Sources 203:4–16. https://doi.org/10.1016/j.jpowsour.2011.12.019

Luo Y, Shi Y, Li W et al (2014) Comprehensive modeling of tubular solid oxide electrolysis cell for co-electrolysis of steam and carbon dioxide. Energy 70:420–434. https://doi.org/10.1016/j.energy.2014.04.019

Nechache A, Hody S (2021) Alternative and innovative solid oxide electrolysis cell materials: a short review. Renew Sustain Energy Rev 149:111322. https://doi.org/10.1016/j.rser.2021.111322

Reytier M, Di Iorio S, Chatroux A et al (2015) Stack performances in high temperature steam electrolysis and co-electrolysis. Int J Hydrog Energy 40(35):11370–11377. https://doi.org/10.1016/j.ijhydene.2015.04.085

Song Y, Zhang X, Xie K et al (2019) High-temperature CO2 electrolysis in solid oxide electrolysis cells: developments, challenges, and prospects. Adv Mater 31:1902033. https://doi.org/10.1002/adma.201902033

Su C, Lü Z, Wang C et al (2019) Effects of a YSZ porous layer between electrolyte and oxygen electrode in solid oxide electrolysis cells on the electrochemical performance and stability. Int J Hydrog Energy 44(29):14493–14499. https://doi.org/10.1016/j.ijhydene.2019.04.092

Tan K, Yan X, Zhu Z et al (2022) Solid oxide cells with cermet of silver and gadolinium-doped-ceria symmetrical electrodes for high-performance power generation and water electrolysis. Int J Hydrog Energy 47(60):25090–25103. https://doi.org/10.1016/j.ijhydene.2022.05.291

Tucker MC (2020) Progress in metal-supported solid oxide electrolysis cells: a review. Int J Hydrog Energy 45(46):24203–24218. https://doi.org/10.1016/j.ijhydene.2020.06.300

Xia Z, Deng Z, Jiang C et al (2022) Modeling and analysis of cross-flow solid oxide electrolysis cell with oxygen electrode/electrolyte interface oxygen pressure characteristics for hydrogen production. J Power Sources 529:231248. https://doi.org/10.1016/j.jpowsour.2022.231248

Yan Z, Hitt JL, Turner JA et al (2020) Renewable electricity storage using electrolysis. PNAS 117(23):12558–12563. https://doi.org/10.1073/pnas.1821686116

Zhang X, O'Brien JE, O'Brien RC et al (2013) Improved durability of SOEC stacks for high temperature electrolysis. Int J Hydrog Energy 38(11):20–28. https://doi.org/10.1016/j.ijhydene.2012.09.176

Zhang J, Gao MR, Luo JL (2020) In situ exsolved metal nanoparticles: a smart approach for optimization of catalysts. Chem Mater 32(13):5424–5441. https://doi.org/10.1021/acs.chemmater.0c00721

Photoelectrochemical Water Electrolysis

1 Introduction

Hydrogen is an ideal, clean, carbon-free carrier of energy that produces only water vapor as a waste product and has potential applications in automobiles, airplanes, and in home-heating. The total annual global consumption of energy in 1998 was estimated to be 112.5 terakilowatt hour (TkWh), that is, 384 quads (quadrillion British thermal unit [Btu]) equivalent to mean power generation during the year of 12.8 terawatt (TW), of which the United States consumed 29 TkWh, that is, 99 quads equivalent to mean power generation during the year of ~3.3 TW. The projected mean power generation for the years 2050 and 2100 has been estimated to be 28 and 46 TW, respectively. By far, sunlight provides the largest of all carbon-neutral energy sources. In fact, 123.05 TkWh, that is, 448 quads equivalent to mean power generation during the year of 14 TW of solar energy falls on the earth every hour. Thus, more energy from sunlight strikes the earth in 1 h than all the energy consumed on the planet in a year. The most successful technologies taking advantage of this resource are photovoltaics (PVs; solar electricity), a $10 billion industry that is currently growing at a rate of 35–40% each year. Continued growth of the PV sector at a rate of ~25% would increase the production level from 1.7 GW in 2005 to 380 GW in 2030, and thus would satisfy a significant fraction of the world energy demand. Moreover, among the renewable sources, PVs have the highest potential to reduce the costs compared to biomass, geothermal, wind, and solar thermal. According to the World Petroleum Life-Cycle prediction, world oil production may already have peaked in 2006, whereas the Organization of Petroleum Exporting Countries (OPEC) oil production will exceed non-OPEC production beginning in 2007. Of course, as recognized by them, the peak year may shift a little. Because the oil and natural gas prices are fluctuating in the range $55–110/bbl and $7.5/million Btu, respectively, electricity generation is shifting increasingly toward coal. It is therefore essential to accelerate the development of techniques to produce hydrogen from an abundant source of energy, the sun, to slow down the threat of global

warming. Photo-electrolysis of water and especially the use of semiconductor–electrolyte interfaces illuminated with sunlight for the production of hydrogen from water and other suitable solvents have been reviewed in several excellent publications (Martín de Vidales et al. 2016). At present, only about 5% of the commercial hydrogen production is primarily via water electrolysis, whereas the other 95% is mainly derived from fossil fuels. This does not represent in- house consumption of hydrogen such as oil refineries and ammonia plants where the bulk of hydrogen is consumed.

Fundamental studies of the semiconductor–electrolyte interface could only be initiated with the availability of well-defined single crystals of germanium and silicon around 1960, and of II-VI and III-V compounds, stable oxide semiconductors, and metal chalcogenides (layered compounds) afterward. Studies of micro-heterogeneous systems such as suspensions and colloidal solutions of semiconductor particles were initiated in 1976–1978. The semiconductors absorb light very effectively; the absorption coefficients of semiconductors range between 10^{-3} cm^{-1} for indirect bandgap semiconductors and 10^{-5}–10^{-6} cm^{-1} for direct bandgap semiconductors.

There are two principal methods for the electrolysis of water to generate hydrogen viz. active, that is, photo-assisted and passive or dark and non-photo-assisted. The active method consists of utilization of photogenerated charge carriers in the electrolysis of water and other products. In the passive method, the electrolysis is carried out in the dark at low (80 °C) temperatures using an alkaline electrolyte such as NaOH or proton exchange membrane cells involving polymeric sulfonic acids, at intermediate (200–500 °C) temperatures for which suitable electrolytes are still being sought, and at high (>800 °C) temperatures using oxide electrolytes such as yttria-stabilized zirconia. Photovoltaic technology including the electrochemical photovoltaic cells could be useful in this method as a source of electricity.

2   Photoelectrochemical Water Electrolysis

Thermodynamically, PEC water splitting is an energetically uphill reaction with a stand Gibbs free energy change of 237.2 kJ mol^{-1}, or a potential of 1.23 eV per electron (Minggu et al. 2010). t is composed of two half reactions including the hydrogen evolution reaction (HER) and the oxygen evolution reaction (OER):

$$Water\ oxydation: 2H_2O + 4h^+ \rightarrow O_2 + 4H^+$$

$$Water\ reduction: 2H_2O + 4H^+ \rightarrow O_2 + 4H^+$$

$$Overall\ water\ splitting: 2H_2O \rightarrow 2H_2 + O_2$$
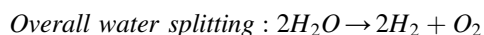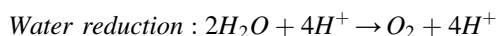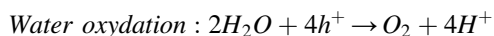
Generally, there are three major physiochemical processes involved in a complete PEC water splitting reaction (Fig. 1).
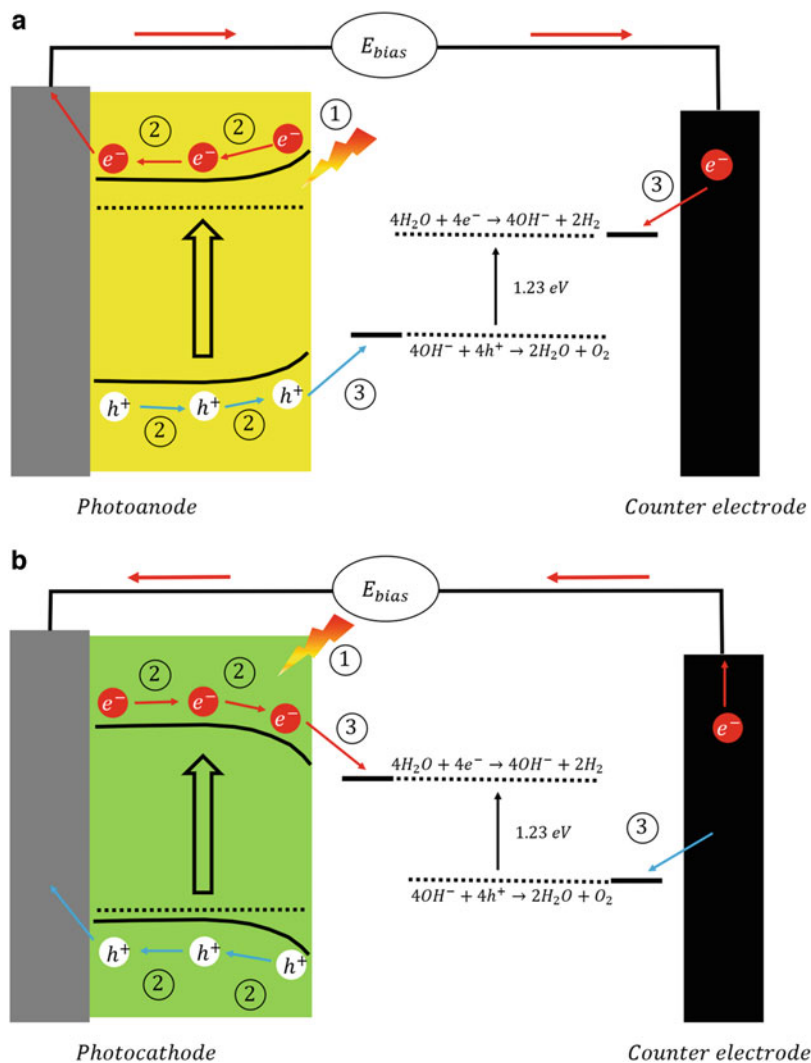
Fig. 1 Schematic representation of PEC water splitting process consisting of (**a**) a photoanode and a metal counterpart and (**b**) a photocathode and a metal counterpart

The first process is the absorption of solar light irradiation by the photoelectrode materials, followed by the generation of charge carrier pairs, where the electrons are excited to the conduction band (CB) and the corresponding holes are left in the valence band (VB), upon the energy of incoming photons being greater than the bandgap energy (E_g) of semiconductor (Yang et al. 2019). The second process is the separation and transport of charge carriers through the semiconductor to the surface of corresponding electrodes in opposite directions. The last process is the redox reactions of water that occurred at the interface of electrode/electrolyte.

As illustrated in Fig. 1a, in a PEC device based on an n-type semiconductor as the photoanode and metal (e.g., Pt) as the counter electrode, the photogenerated holes accumulate on the surface of the photoanode and oxidize the water to O_2. Meanwhile, the electrons reached on the surface of the counter electrode drive the HER process to produce H_2. Whereas in the case of a p-type semiconductor as the photocathode (Fig. 1b), the water is reduced to H_2 on the surface of the photocathode and O_2 is concurrently produced on the counter electrode.

From the view of thermodynamics, the photoelectrode semiconductors must be able to absorb sunlight photon energy that is larger than 1.23 eV to ensure the process of overall PEC water splitting (Zhang et al. 2020). Additionally, the top of the VB of the photoanode semiconductor must be more positive than the oxygen evolution potential for oxidizing water to O_2. Analogously, the CB bottom edge of the photocathode semiconductor should be more negative than the hydrogen evolution potential to reduce H^+ to H_2. However, in practice, even if the CB and VB of a semiconductor can satisfy the above conditions, PEC water splitting cannot always occur automatically due to the Ohmic losses and kinetic overpotentials required for driving the half reactions. Thus, semiconductors with the Eg of 1.6–2.4 eV are preferred for a practical photoelectrode to sustain the overall PEC water splitting.

3 PEC Water Splitting

Based on the concept of PEC water splitting, the simplest PEC device contains a single semiconductor (as either photoanode or photocathode to perform water oxidation or reduction) and a standard metallic counter electrode (e.g., Pt).

In this configuration, to overcome the thermodynamic barrier of overall water splitting and the potential loss caused by charge recombination processes, the bandgap of a single photoelectrode should be larger than 1.6 eV. However, the wide bandgap also means that the visible light absorption efficiency will be low and the photons with long wavelengths cannot be absorbed. Additionally, in most cases, to effectively drive the separation of the photogenerated electrons and holes, an external bias is usually required for the single photoelectrode system to function (Samuel et al. 2020).

To overcome the above drawbacks of single photoelectrode systems, alternative approaches including PEC tandem systems and PEC/photovoltaic cell coupled devices (PEC/PV systems) have been developed to achieve efficient PEC water splitting without an external bias (Fig. 2).

Tandem cell configuration is a promising approach to address the issues of a single photoelectrode system for unassisted PEC water splitting (Kim et al. 2016). Different from the single photoelectrode systems, in this configuration, an n-type and a p-type semiconductor are simultaneously used as photoanode (producing oxygen) and photocathode (producing hydrogen), respectively. The self-bias produced from the mismatching of Fermi levels of the n- and p-type semiconductors can act as an extra driving force for the separation and transportation of the photogenerated charge
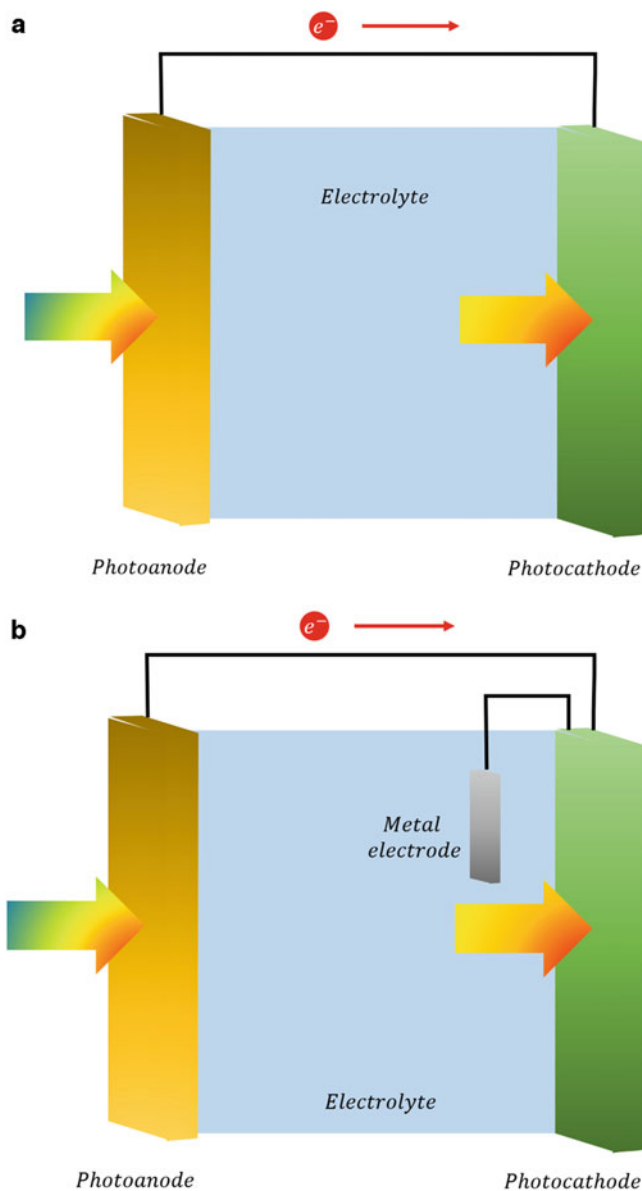
Fig. 2 Simplified illustration of the (**a**) PEC tandem cell and (**b**) PEC/PV configuration (taking the photoanode/PV as an example)

carriers to oxidize and reduce water. In a tandem PEC cell, the photocathode and the photoanode are connected in a series and the sunlight must firstly pass through the photoanode and then photocathode. In this case, photons with shorter wavelengths in the solar spectrum are absorbed first by the photoanode, while the remaining longer-

wavelength photons are transmitted and captured by the photocathode. Therefore, after two or more steps of sunlight absorption, more solar photons are absorbed and utilized by more suitable semiconductors and an improved overall PEC water splitting efficiency is consequently achieved in a tandem cell.

A PEC/PV system is another attractive approach for the unassisted solar water splitting, which is constructed by integrating a PEC device with a PV cell in a tandem configuration (Jiang et al. 2017). It is also considered as the most viable strategy for the practical applications among various clean hydrogen production methods. In a PEC/PV system, the solar light is the only energy input for the whole system, which is the same as the PEC tandem device. On the other hand, the bandgap alignment of photoelectrodes in this configuration is not related with the water redox process because the PV cells can directly act as the bias supply. Therefore, there is no limitation on choosing the photoelectrode materials regarding the bandgap.

3.1 Photoelectrodes Performances

In terms of evaluating the performance of photoelectrode materials, the comparison of onset potential and photocurrent density at 1.23 V versus reversible hydrogen electrode (RHE) for photoanode and 0 V vs. RHE for photocathode is commonly adopted. Also, four primary efficiency metrics based on energy input and product conversion are of equal significance, which can be divided into the following two categories:

1. Benchmark efficiency (suitable for general reporting of stand-alone PEC water splitting capability), STH;
2. Diagnostic efficiencies (suitable to measure and understand the PEC performance of the photoelectrode materials), Applied bias photon-to-current efficiency (ABPE), Incident photon-to-current efficiency (IPCE)/external quantum efficiency, Absorbed photon-to-current efficiency (APCE)/internal quantum efficiency.

Among these efficiency metrics, STH efficiency is the most important one as it is an ultimate performance indicator of a PEC water splitting cell, which can be used to describe the conversion efficiency of the overall water splitting under zero-bias conditions (Miller 2015). Zero-bias means that there is no applied voltage between the working electrode and counter electrode, and all the energy in the water splitting process is supplied by sunlight. For the measurement of STH efficiency, the working electrode and counter electrode must be operated in an electrolyte solution of the same pH under short-circuit conditions. Additionally, the electrolyte should not contain any sacrificial donors or acceptors.

For the calculation of STH efficiency, it can be expressed as the ratio between the total energy generated and the total energy input from sunlight irradiation:

$$STH = \frac{Total\ energy\ generated}{Total\ energy\ input} = \frac{\Delta G_{rH2}}{P_{sum}S}$$

where ΔG is the change in the Gibbs free energy through the reaction from H_2O to O_2 and H_2 (237.2 kJ mol^{-1}), r_{H2} is the rate of hydrogen production in moles per second, P_{sum} is the incident light intensity (100 mW cm^{-2}), S is the illuminated area of the photoelectrode (cm^2). Alternatively, STH efficiency of a PEC device can also be calculated from the relation that power is the product of voltage (1.23 V vs. RHE), short-circuit current density, and the Faradaic efficiency for hydrogen evolution (η_F):

$$STH = \frac{|j_{SC}|1.23\eta_F}{P_{sum}}$$

where j_{SC} (mAcm^{-2}) is the short-circuit photocurrent density normalized to the illuminated electrode area.

The STH efficiency is generally used to evaluate the performance of unassisted overall PEC water splitting. When an external bias is applied between the working and counter electrodes in a single photoelectrode cell, the ABPE is also frequently used because the STH does not reflect a true PEC water splitting process:

$$ABPE = \frac{P_{out} - P_{in}}{P_{light}} = \frac{j_{ph}(1.23 - V_{bias})}{P_{light}}$$

where j_{ph} is the photocurrent density obtained under an applied bias V_{bias}.

Like STH, there are also several common pitfalls in the ABPE characterization. Thus, for the correct measurement of ABPE, the following factors should be considered: (1) the value of V_{bias} should be measured between the working and counter electrodes (not the bias with respect to the reference electrode); (2) the electrolyte solution should not contain any sacrificial donors or acceptors; and (3) the electrolytes in two compartment cells must have the same pH (Peter 2015).

IPCE is another important diagnostic efficiency merit of the PEC device. Strictly speaking, it is identical to the external quantum efficiency. IPCE is extensively used to specify the photo-response of a photoelectrode as a function of the wavelength of incident photons (Ye et al. 2019). It is defined as the number of photogenerated charge carriers contributing to the photocurrent per incident photon, which can be expressed by the following equation:

$$IPCE = \frac{Total\ energy\ converted\ electrons}{Total\ energy\ of\ incident\ electrons} = \frac{\left(\frac{j_{photo}}{e}\right) * \left(\frac{hc}{\lambda}\right)}{P(\lambda)} \cdot 100$$

where j_{photo} is the photocurrent density at the specific wavelength of the incident light (mA cm^{-2}), e is the charge of an electron (1.602 × 10^{-19} C), h is Planck's constant (6.626 × 10^{-34} J s), c is the speed of light (3.0 × 10^8 m s^{-1}), λ is the

wavelength of the incident light (nm), P(λ) is the incident light intensity at the specific wavelength (mW cm^{-2}).

During the calculation of IPCE, optical losses such as photon reflection and transmission are disregarded. To correct these optical losses to truly understand the inherent performance of a photoelectrode, the APCE is often used to determine the quantum efficiency. The APCE is defined as the number of photogenerated charge carriers contributing to the photocurrent per absorbed photon, which is termed the internal quantum efficiency. It is measured as the ratio of photocurrent collected per incident photons absorbed, as shown in the following equation:

$$APCE = \frac{IPCE(\lambda)}{A(\lambda)} = \frac{IPCE(\lambda)}{1 - R - T} \cdot 100$$

where A, R, and T are the optical absorption, reflection, and transmission, respectively.

4 Cell Design

Generally, a PEC water splitting cell is composed of four components: (i) a reactor, (ii) electrodes, (iii) an electrolyte, and (iv) a membrane or separator (Fig. 3).

PEC measurements are commonly performed in a single- or double-compartment reactor which is transparent to solar light or equipped with an optical quartz window that allows the light to reach the surface of the photoelectrode. Especially, in the double-compartment reactor, a membrane is additionally required to separate the anode and cathode compartments to avoid the mixing of the evolved oxygen and hydrogen gases.

The electrode is a key component of a PEC water splitting cell, which can be classified into a two-electrode system including working electrode and counter electrode, and a three-electrode system involving working electrode, counter electrode, and reference electrode (Peter 2021). Commonly, a two-electrode system is used to assess STH efficiency of a whole cell and a three-electrode system is for the performance of a working electrode as a half cell. In a two-electrode system, the working and counter electrodes are immersed in an aqueous electrolyte and one or both is photoactive. The dark- and photocurrents are recorded as a function of applied bias against a counter electrode based on an ideal hypothesis that the potential of the counter electrode is the same as the potential of the redox reaction. However, in practice, the potential of the counter electrode is not at the equilibrium potential of the redox reaction because of the reaction overpotential, which in turn depends on the current density. It also means that the potential of the working electrode cannot be measured exactly in a simple two-electrode configuration. Consequently, in a laboratory test situation, a three-electrode PEC system containing a reference electrode (such as Ag/AgCl electrode and saturated calomel electrode) is

Fig. 3 PEC cell in a (**a**) single and (**b**) double compartment configuration
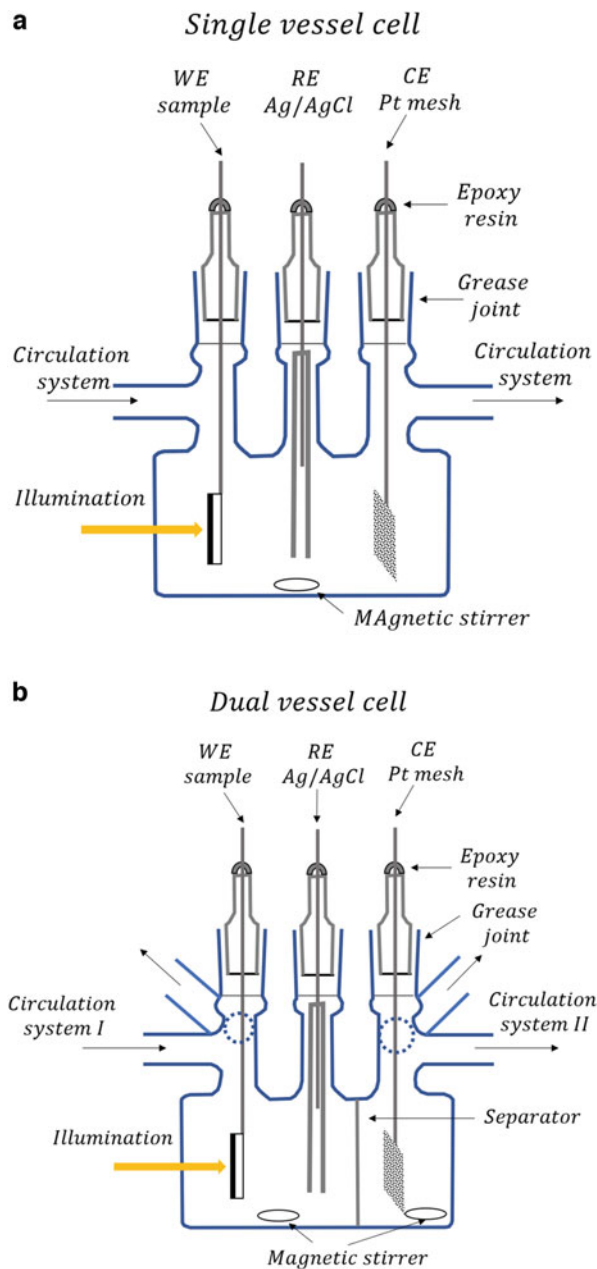
widely employed to study the half reactions of PEC water splitting and evaluate the performance of the working electrode.

4.1 Photoelectrodes Materials

Photocathodes are responsible for water reduction and employ p-type semiconductors. Usually, in an ideal PEC cell, the photocathode material should have a suitable band structure including a small bandgap (1–1.5 eV) with excellent optical/electrical properties, and the potential of the CB should also be more negative than the hydrogen reduction potential to generate the required cathodic current for water reduction. Figure 4 shows the overview of the energy positions of the CB and VB for several p-type semiconductors that are commonly employed as photocathodes for water reduction.

Additionally, an optimum photocathode material should have a non-corrosive nature, e.g., stable in an aqueous electrolyte under light illumination. The last requirement for a promising photocathode is its earth abundancy and low cost to guarantee the feasibility of large-scale application.

Si is one of the most widely used photocathode materials for PEC water splitting because of its narrow bandgap (1.1 eV), earth abundance, environmental friendliness, and large-scale production capability. However, the practical application of the Si photocathode in the PEC water splitting field is mainly hindered by two factors: the instability in the electrolyte solution and the lack of effective surface cocatalysts (Roger et al. 2017).

As one of the most widely investigated photocathodes for solar water splitting, Cu_2O has a direct bandgap of 1.9–2.2 eV that makes it able to absorb the visible light of the solar spectrum, and consequently achieve a theoretical STH efficiency of 18%.

Besides the Cu_2O, several p-type Cu- and Fe-based ternary oxide semiconductors, such as $CuFeO_2$ (1.5 eV), $CaFe_2O_4$ (1.9 eV), $CuNb_3O_8$ (1.5 eV), and $LaFeO_3$ (2.1 eV) have also been investigated as photocathodes in recent studies.

As one representative category of efficient sunlight-absorbing materials, I–III–VI_2 chalcogenides (I = Ag, Cu; III = In, Ga; VI = S, Se) have emerged as a leading class of thin film photovoltaic materials due to their tunable bandgap (ca. 1.0–2.4 eV), high photo-absorption coefficients (ca. 105 cm^{-1}), and usability in the polycrystalline state.

Gallium phosphide (GaP) is a typical III–V semiconductor that has a bandgap (2.2–2.3 eV) and a more negative CB edge than the water reduction potential. Moreover, previous studies have reported that the p-type GaP has a higher photostability for longer periods in electrolytes under cathodic conditions than that of its n-type form. All of these reasons make GaP a suitable photocathode for PEC water splitting. As another typical III–V semiconductor, indium phosphide has also been considered as a promising PEC photocathode because of its narrow bandgap of 1.35 eV that well matches the solar spectrum. Recently, III–V nitride semiconductors, for instance GaN and InGaN, have also emerged as a new generation of
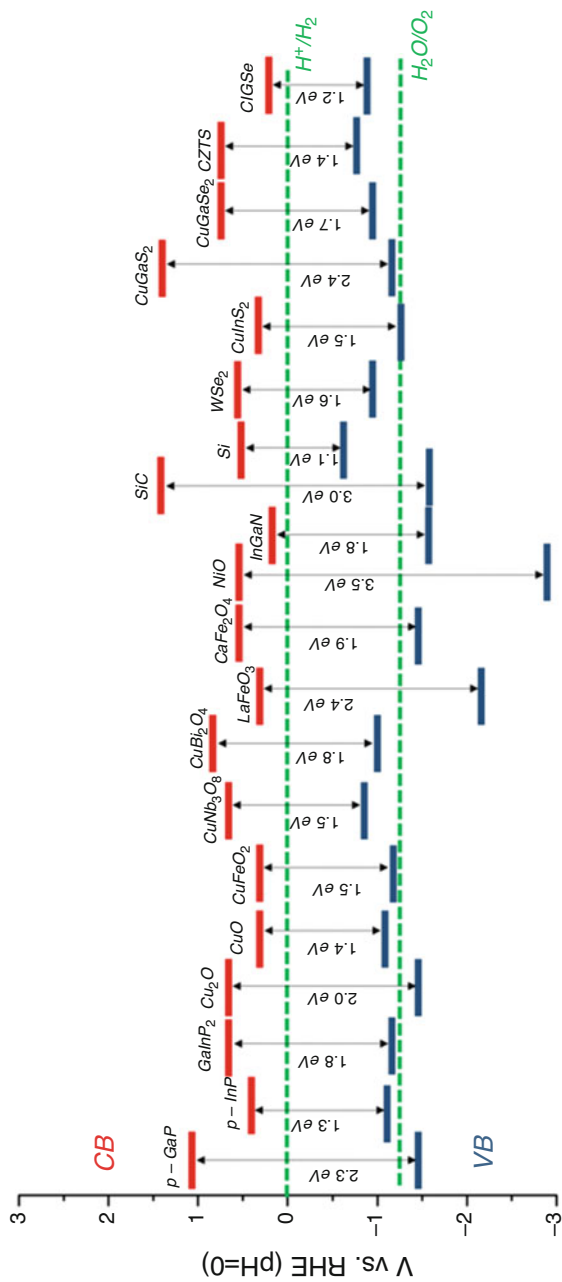
Fig. 4 Band alignment of selected p-type semiconductors that have been used for the construction of H₂-evolving photocathodes

photocathode materials for PEC water splitting. Different from the poor PEC stabilities of conventional III–V compounds originating from their covalent chemical bonds, the III-nitrides exhibit extremely high stability in an aqueous electrolyte owing to their ionic bonding characteristic (Peter and Upul Wijayantha 2014).

In some recent studies, transition metal dichalcogenides (TMDs), such as MoS_2, $MoSe_2$, WS_2, and WSe_2, have also been proven as promising photocathodes for PEC water splitting due to their distinct advantages including suitable bandgap (1–2 eV) and high light absorption coefficients (105–106 cm^{-1}).

In terms of improving the performance of photocathodes, the HER electrocatalysts are often loaded to the photocathode surface as cocatalysts to reduce the HER overpotential (activation energy) and suppress surface charge recombination by acting as electron or hole acceptors. Among many noble metals, Pt, with the largest work function, is regarded as the best HER electrocatalyst candidate for accepting electrons (Ali et al. 2021).

A photoanode is an n-type semiconductor, being responsible for the water oxidation in a PEC cell. The requirements of a promising effective photoanode include a favorable bandgap to absorb a wide range of solar spectrum, efficient charge separation and transportation, and fast OER activity. More importantly, the VB edge of a photoanode material should be more positive than that of the oxygen evolution potential to drive the water oxidation. Also, an optimal photoanode should have high stability in aqueous solution, low cost, and environmental friendliness. To date, many n-type semiconductors have been investigated as photoanodes for solar water splitting. Examples of promising photoanodes include monometallic oxides (TiO_2, ZnO, WO_3, and α-Fe_2O_3), bimetallic oxides ($BiVO_4$), and metal (oxy)nitrides (Ta_3N_5 and $TaON$). Simultaneously, Co, Ni, and Fe-based OER electrocatalysts have also been widely used as cocatalysts to improve the oxygen evolution and water splitting performance of various photoanodes (Qiu et al. 2019).

As one of the most promising PEC photoanodes, TiO_2, with a bandgap of ~3.2 eV, was the first one reported that ignited the photocatalysis field. Since then, it has been intensively investigated as a photoanode owing to many favorable properties, such as the suitable band edge positions straddling the water redox potentials, excellent photostability in aqueous solution, and high earth abundance.

Like TiO_2, ZnO also has a broad bandgap of ~3.2 eV, but with a higher carrier mobility. Moreover, ZnO is an environmentally friendly and inexpensive semiconductor, making it suitable for use as a photoanode for PEC water splitting.

Compared to other metal oxides, WO_3 has many important merits, such as the long minority carrier diffusion length (150 nm) and carrier lifetime, and excellent chemical stability in acidic conditions. Additionally, it has a bandgap of 2.5–2.8 eV that can harvest ~12% of the solar spectrum.

As one of the most stable forms of iron oxides, α-Fe_2O_3 has attracted tremendous attention recently owing to its high abundance, low cost, non-toxicity, superior chemical stability, and favorable bandgap (2.0–2.2 eV) that allows it to absorb all the UV and a significant portion of visible light. Theoretically, the maximum STH conversion efficiency of hematite photoanode can reach 16.8%. Considerable efforts have been made in the past decades. For example, nano-structuring of hematite to

shorten the charge diffusion pathway, elemental doping (e.g., Ti, Sn, P, and oxygen vacancies) to improve the bulk electronic conductivity, heterojunction construction (such as Fe_2O_3/TiO_2, $Fe_2O_3/MgFe_2O_4$, $Fe_2O_3/ZnFe_2O_4$, and Fe_2O_3/Fe_2TiO_5) to promote the charge separation, and surface treatment to facilitate the charge transfer from hematite into electrolyte and accelerate the OER kinetics (Nellist et al. 2016).

As an n-type semiconductor composed of relatively inexpensive and non-toxic elements, $BiVO_4$ has recently gained significant attention because it has a relatively narrow bandgap (2.4 eV) for theoretically absorbing almost 10% of the solar energy, an appropriate VB position that permits a high photovoltage around 1 V for the water oxidation reaction, and an excellent stability. The theoretical maximum photocurrent density and STH efficiency of a $BiVO_4$ photoanode are 7.4 mAcm^{-2} at 1.23 V vs. an RHE and 9.1%, respectively. To obtain a more efficient $BiVO_4$ photoanode, diverse modification strategies have been developed. For example, the short electron diffusion length of a $BiVO_4$ photoanode can be significantly increased by adopting elemental doping (e.g., W- and Mo-doping) and/or nanostructure engineering. On the other hand, constructing a heterojunction, such as $BiVO_4/WO_3$, has also been widely used to promote the charge separation. For the slow OER kinetics, these can be greatly improved by loading the oxygen evolution cocatalysts such as Co-Pi and FeOOH/NiOOH onto the surface of the photoanode.

Owing to the smaller electronic negativity of N than O, the VB of metal (oxy)-nitrides consisting of N 2p orbitals are more negative than that of the metal oxides with O 2p orbitals, while the CB composed of metal atomic orbitals remains unchanged, resulting in the largely decreased bandgap and increase visible light absorption of metal (oxy)nitride.

As mentioned above, compared with the HER process on the photocathode surface, the kinetics of the OER at the surface active sites of photoanodes are more sluggish because it is a multi-step, four-electron and four-proton, process, which severely limits the performance of photoanode materials. Therefore, loading the water oxidation electrocatalysts onto the surface of photoanodes as cocatalysts has been widely employed to promote its OER kinetics. As shown in Fig. 5, the presence of the OER electrocatalysts on the photoanode cannot only significantly increase the photocurrent density, but also results in an obviously lowered onset potential.

The negative shift of the onset potential corresponds to the lowered overpotential required to realize the water redox reaction during the PEC water splitting process.

Ion exchange membranes are commonly employed to separate the anodic and cathodic electrolytes in a double-compartment PEC reactor to avoid mixing the produced hydrogen and oxygen and the back reactions (i.e., cathodic O_2 reduction), thus causing low productivity of the PEC water splitting. Three types of ion exchange membranes have been explored in the PEC systems, including proton exchange membranes, anion exchange membranes, and bipolar membranes (Vargas-Barbosa et al. 2014).

The most used PEM in PEC water splitting is Nafion®, a perfluoro-sulfonic acid membrane with polytetrafluoroethylene as support, though it is known for the high cost. In fact, as one of the best proton conductive membranes (H+ conductivity of

a

b
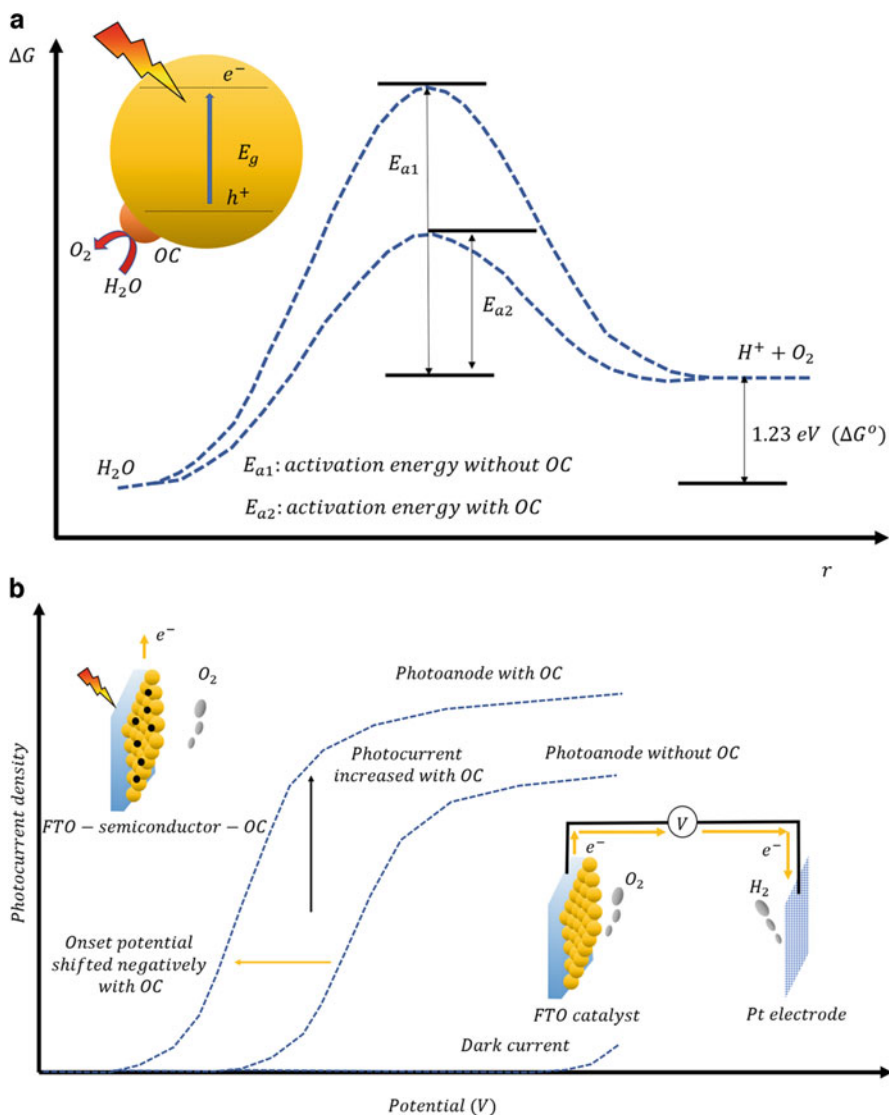
Fig. 5 Schematic description of the role of oxidation cocatalysts in (**a**) photocatalytic water oxidation and (**b**) PEC water oxidation

about 0.1 S/cm at room temperature), Nafion has some other advantages, such as the low gas permeability and exceptional mechanical and chemical stability. Therefore, Nafion has been widely used in traditional fuel cells and electrolyzers.

Different from PEMs, AEMs only allow the transport of anions, such as OH^-. Recently, AEMs have also been investigated for PEC water splitting cells as an alternative for PEMs. Among various AEMs, Selemion is a popular commercial one

that is prepared from styrene, Chloromethyl styrene, and divinylbenzene containing quaternary ammonium groups, which has a high efficiency in alkaline media.

Nowadays, the application of BPMs in PEC water splitting has emerged owing to their additional advantages in guaranteeing the reactions in each chamber to proceed under different electrolyte conditions that best fit their exigencies. BPMs can dissociate water into H+ and OH− and block the anion transport from the cathode compartment to the anode compartment through the cation-exchange layer and the cation transport from the anode compartment to the cathode compartment through the anion-exchange layer, which allows maintaining a different pH at either side of the membrane. Therefore, the employment of a BPM can significantly expand the possibilities for practical PEC cell designs.

The electrolyte solution containing charged ions is an essential component of a PEC water splitting cell for mediating the charge transfer between the working and counter electrodes, which also plays an important role in determining the performance and stability of photoelectrodes. Therefore, the type of electrolyte solution (acidic, neutral, or basic) for PEC water splitting should be carefully selected. Usually, the considerations need to be accounted for in the selection including the stability of ionic species, the ionic conductivity, and the diffusion of each ion through a potential membrane. In addition to these, the electrolyte solution should not have absorption bands in the spectral window of the photoelectrode materials and should be favorable for the long-term stability of photoelectrodes, and the concentration of electrolyte solution should be sufficiently ionically conductive ($\sim$0.1 M or above) to ensure minimum solution resistance.

5 Solar Energy to Hydrogen

A semiconductor–electrolyte junction is formed when a semiconductor is immersed in an appropriate electrolyte (Mayer 2017). The chemical potential of a semiconductor is given by the Fermi level, whereas the chemical potential of a liquid electrolyte is determined by its redox potential. It is instructive to compare the references for the energy scales for the two systems. In electrochemistry, the redox potentials are measured against the standard redox potential of the hydronium ion/hydrogen gas couple, or normal hydrogen electrode (NHE) also termed standard hydrogen electrode (SHE). (Two other standards viz. saturated calomel [HgCl$_2$] electrode [SCE] or silver chloride [Ag/AgCl] are also used.) However, the potential of vacuum is taken as the zero potential in solid-state physics. Conversions can be carried out easily by remembering that the standard H+/H redox potential with respect to vacuum is +4.5 eV. (The potentials of standard calomel and Ag/AgCl electrodes with respect to the standard H+/H redox potential are 0.234 and 0.197 V, respectively.) If the initial Fermi level of an n-type semiconductor is above (more negative with respect to) the initial electrolyte redox potential, electrons will flow from the n-type semiconductor to the electrolyte. The charge transfer leaves behind a depletion region in the semiconductor and a potential barrier. The charge in the
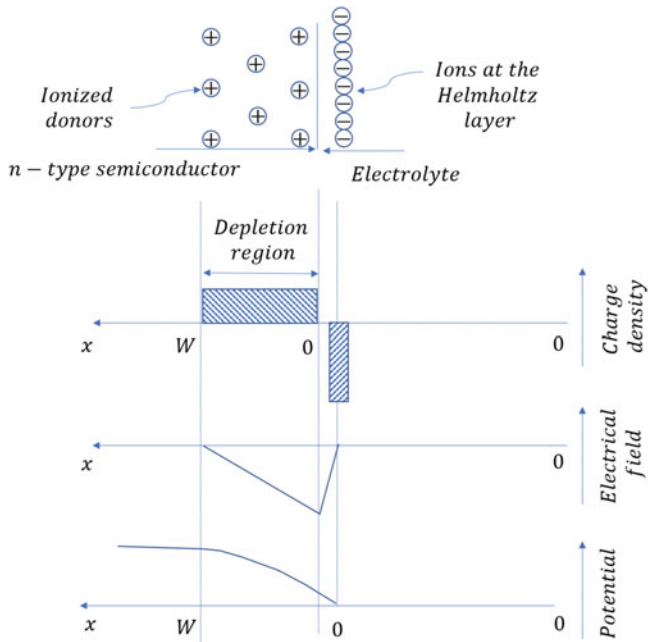
Fig. 6 Depletion and Helmholtz layers, field and potential across a semiconductor–electrolyte interface

depletion layer is compensated by a charge of the opposite sign that is induced in the electrolyte within a localized ~1 nm thick layer, known as the Helmholtz layer. It is composed of oriented water molecule dipoles and electrolyte ions adsorbed at the electrode surface. The potential drop, VH, across the Helmholtz layer (also known as the Helmholtz barrier) is determined by the nature of the aqueous environment of the electrolyte and the properties of the photoelectrode surface. The performance characteristics of photoelectrochemical (PEC) cells depend, to a large extent, on the potential drop, VH, across the Helmholtz layer. The junction has characteristics similar to those of a Schottky barrier formed between a semiconductor and a metal.

The semiconductor has a net space charge of immobile, positively charged donor ions uncompensated by the mobile electron cloud. Figure 6 shows the formation of the depletion and Helmholtz layers, field, and potential across a semiconductor–electrolyte interface (Gao et al. 2023).

The formation of the double layer leads to conduction and valence band bending and development of a field that opposes further charge transfer (Fig. 6). Finally, equilibrium is reached when there is no net transfer of charge across the junction. The equilibrium potential barrier is formed with a built-in voltage VB because of the band bending. The energy level diagram of a semiconductor–electrolyte junction and solid-state and electrochemical energy scales are depicted in Fig. 7.

The depletion layer width in a semiconductor diode of silicon having doping densities on p- and n-sides of 1.4×1015 and $1.4 \times 1018 \, \text{cm}^{-3}$ is ~0.86 μm, the width
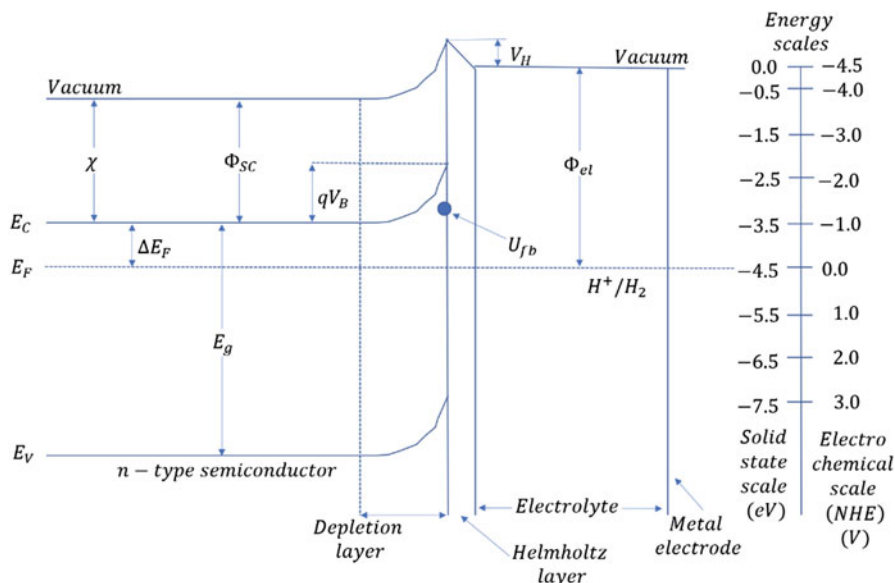
Fig. 7 Energy level diagram of a semiconductor–electrolyte junction and solid-state and electrochemical energy scales

being higher at lower doping densities. In contrast, in concentrated (>0.5 M) electrolytes, the charged Helmholtz layer is mostly localized. The flat- band potential Ufb is an important parameter that is related to the properties of both the semiconductor and the electrolyte.

It is the potential, which if applied to the semiconductor would flatten the conduction and valence bands. It is given by:

$$U_{fb} = (\chi + \Delta E_F + V_H) - 4.5 = (\Phi_{SC} + V_H) - 4.5$$

where χ is the electron affinity; ΔE_F the difference between the Fermi level EF and the majority carrier band edge of the semiconductor (conduction band in the present case); φ_{sc} and φ_{el} are work functions of the semiconductor and the electrolyte, respectively, and measure the Fermi level potential with respect to vacuum; and 4.5 is the scaling factor.

Because of the adsorption equilibrium for H+ and OH− ions between the surface of semiconductors and an aqueous (aq) solution, the semiconductor surface attains the point of zero charge (PZC). The flat-band potential Ufb of most semiconductors including all oxides and other compounds such as n- and p-type GaAs, p-type GaP, and n- and p-type InP in an aqueous solution is determined solely by pH and shifts proportionately with pH with a slope of −59 mV/decade, that is, pH, for example:

Fig. 8 AM 1.5 global solar spectrum

$$S_S - OH + H_{aq}^+ = S_S + OH_2^+$$
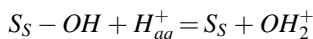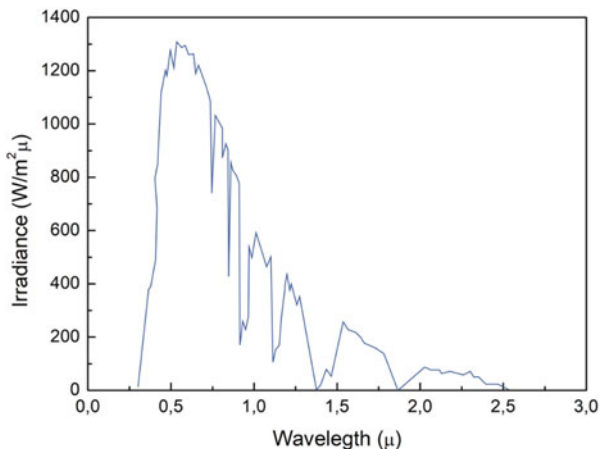
where S_s – OH refers to the OH group present at the semiconductor surface. The flat-band potential Ufb remains nearly constant for n- and p-type Si and metal chalcogenides such as n-CdSe and CdTe at pH below 6, and n-CdS for pH about 10, most probably because the semiconductor surface has no OH group in these pH ranges. Moreover, for metal chalcogenides the flat-band potential Ufb becomes more negative in the presence of S^{2-} and Se^{2-} ions in the solution, whereas it becomes more positive in the presence of Cd^{2+} ions in the solution.

Light can be completely absorbed in a thin layer of a solid electrode. Only semiconductors are useful in photoelectrochemical cells because the lifetimes of excited states in metals are very short. Electron–hole pairs are generated when the semiconductor is illuminated with photons of energy $h\nu > E_g$, where E_g is the semiconductor bandgap. Electrons and holes excited to energy levels far away from the band edges are thermalized very quickly within 10^{-12}–10^{-13} s. Hence, all light quanta with larger energy than E_g contribute only the bandgap energy to the photoconversion. The sunlight that has a typical spectrum at the earth's surface is termed air mass 1.5 global (AM 1.5 global) as shown in Fig. 8.

Here air mass (number) defines the number of times sunlight traversed the thickness of the earth's air atmosphere; global defines the total radiation from direct and diffuse radiation. Therefore, semiconductors with bandgaps in the range 1–2 eV are more useful than those of higher or lower bandgaps for the conversion of solar energy. The minority charge carriers, viz. holes that are generated within a diffusion length of the depletion region and diffuse into it, together with those generated in the depletion region itself are separated by the built-in field and are swept to the semiconductor surface, and can produce anodic oxidation by recombining with the electrons provided by the negatively charged ions reaching the semiconductor–electrolyte interface. The majority charge carriers, viz. electrons that are carried to the semiconductor bulk, flow through the external circuit and can participate in a

cathodic reduction reaction on being injected into the electrolyte at the counter-electrode. The semiconductor potential is driven toward the flat-band potential by illumination.

In the liquid junction PV cells, there is only one redox couple in the electrolyte. There is no chemical change; hence Gibb's free energy also does not change. The physics behind the operation of liquid junction solar cells is analogous to solid-state Schottky barrier cells. The carriers generated within the space-charge region and within a diffusion length of it are carried to the side where they become majority carriers. The carriers collected at the external contacts are available for work on an external load. The maximum possible open-circuit voltage V_{oc} is the difference between flat-band and redox potential of the predominant redox couple. The photo-current depends on the bandgap of the semiconductor. The lower the bandgap the higher is the photocurrent. However, the open-circuit voltage decreases with decreasing bandgap. There is an optimum of the bandgap in the range 1.3–1.4 eV, where the photocurrent and photovoltage are optimum and the resultant PV conver-sion efficiency using sunlight at the earth's level attains the maximum value. The practical upper limit for the Schottky barrier–type PV solar cells is 10–12% because of the band bending, that is, the height of the potential barrier at the semiconductor/metal junctions are lower than the semiconductor bandgap. In cells prepared with n-GaAs, surface recombination velocities have been reduced by a chemisorbed Ru^{3+} monolayer. It can be exceeded in the liquid junction electrochemical solar cells because of the possibility of increasing the band bending by adjusting the redox potential of the electrolyte. Liquid junction cells are easy to fabricate. Polycrystalline materials usually present problems of reduced efficiency because of the imperfect contact between two solid phases. This problem can be overcome by an intimate contact between the electrolyte and the crystalline grains in a polycrystalline semiconductor.

It is essential to adjust the redox potentials carefully to avoid photo-corrosion while providing enough band bending to collect the charge carriers efficiently. Hence, concentrations of redox components are kept high enough to scavenge carriers while preventing depletion near the electrode. It is necessary to carefully consider the constitution of the redox electrolyte. The electrolyte must be conductive and should absorb the incident solar radiation as little as possible. Thin cell structures are preferred for this purpose.

In the photo-electro-synthetic cells, there are two effective redox couples in the electrolyte so that there is a net chemical change. When the net free energy change is positive, it is termed photo-electrolysis. However, when the net free energy change is negative, it is termed photocatalysis.

Splitting of water to generate hydrogen and oxygen is an endothermic reaction, and is accompanied by a large increase in Gibbs free energy $\Delta G°$ that can be provided by energetic photons and is expressed as:

$$H_2O \rightarrow H_2 + \frac{1}{2}O_2$$

$$\Delta G^0 = 237.1 \frac{kJ}{mol} \ equivalent \ to \ 2.458 \frac{eV}{molecule}$$
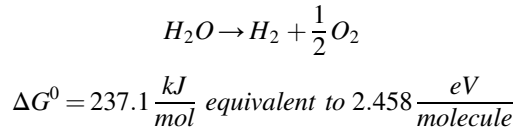
Hydrogen generation from water is a two-electron process. However, for oxygen generation each atom releases two electrons, so that water splitting to generate a molecule of oxygen is a four-electron process. The average energy of the electron process is 118.5 kJ/mol, equivalent to $\Delta E_0 H_2O = 1.229$ eV/electron (lower hydrogen heating value reaction energy) based on liquid water conversion at 25 °C.

In photo-electrolysis, the anodic reaction has a more positive redox potential than the cathodic reaction (Leenheer and Atwater 2010). An example is the photo-assisted electrolysis of water to produce hydrogen and oxygen. In a typical photo-electrolysis cell, one electrode is a semiconductor, whereas the other is a metal. On illumination of the n-type semiconductor–electrolyte interface, the Fermi level in the semiconductor rises toward the flat-band potential. The maximum possible rise in the Fermi level with the electrodes shorted together is given by the flat-band potential Ufb. For direct water photo-electrolysis to occur on illumination, the flat-band potential Ufb must lie above (more negative compared to) the H^+/H_2 potential, whereas the O_2/H_2O potential should lie above the valence band of the n-type semiconductor. Usually, the valence band of the n-type semiconductor would lie below the O_2/H_2O potential. However, only a few semiconductors have Ufb above the H^+/H_2 potential, viz. n-SrTiO$_3$, Nb$_2$O$_3$, n-ZrO$_2$, n-Ta$_2$O$_5$, n-BaTiO$_3$, n-KTaO$_3$, n-InP, p-GaAs, n-CdS, n-SiC, and n-TiO$_2$ (in alkaline electrolyte), hence direct hydrogen and oxygen could be generated in a Schottky barrier–type liquid junction cell (Ros et al. 2020).

Neglecting the difference between the Fermi level and the majority carrier band edge of the semiconductor ΔEF, the flat-band potential Ufb is the potential of the majority carrier band edge of the semiconductor with respect to the H^+/H_2 potential. Often the band-edge positions are provided at different pH values. Since it is known that the positions of band edges of oxides and mixed oxides become 59 meV more negative when the pH is increased by 1, majority carrier band edges of the oxide semiconductors can be calculated at any pH value.

An energy level diagram for an n-type semiconductor/metal photo-electrolysis cell in which the flat-band potential Ufb lies above the H^+/H_2 potential, whereas the O_2/H_2O potential lies above the valence band of the n-type semiconductor is shown in Fig. 9.

Here, the available photovoltage is more than the thermodynamic potential difference for water splitting (1.229 V at 25 °C). It also overcomes the intrinsic energy level mismatches η_c and η_a, where η_c is the mismatch of the counterelectrode metal Fermi level EF above the H^+/H_2 potential required to sustain the current flow and η_a the mismatch due to the difference between O_2/H_2O potential and the valence band edge at the interface. The intrinsic energy level mismatch η_a is determined only by the bandgap and is independent of the current. Holes that are generated in the n-type semiconductor within a diffusion length of the depletion region and diffuse
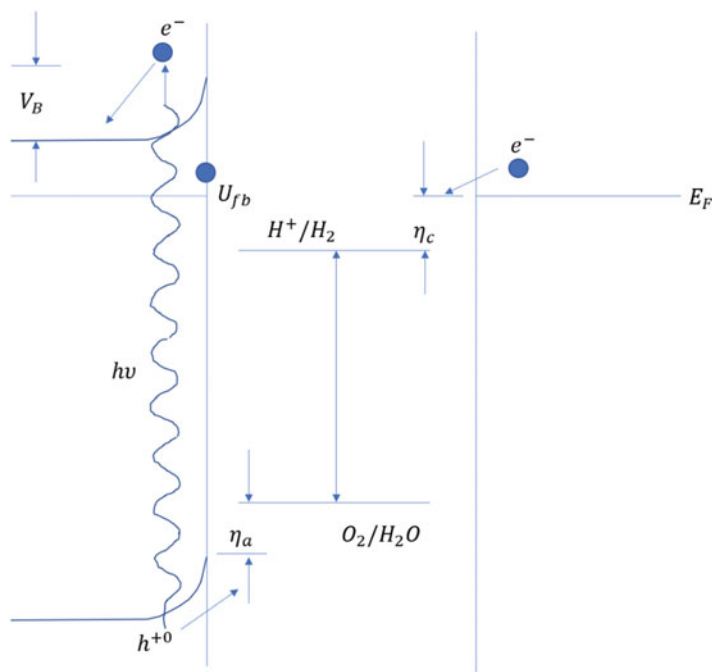
Fig. 9 Energy level diagram for an n-type semiconductor–metal photo-electrolysis cell in which the flat-band potential Ufb lies above the H⁺/H₂ potential, whereas the O₂/H₂O potential lies above the valence band of the n-type semiconductor

into it, together with those generated in the depletion region itself are separated and swept to the semiconductor surface by the built-in field. Because of the favorable band-edge positions and the available necessary overpotentials, they can produce anodic oxidation of water molecules and generate oxygen. However, the photogenerated electrons flow through the n-type semiconductor bulk to the back contact and from there to the metal counterelectrode where they are donated to reduce hydronium ion and to generate hydrogen. The excess photovoltage remaining after fulfilling the preceding minimum requirements is used to overcome the kinetic, diffusion, and ohmic overpotential losses which are collectively termed polarization loss. Often the intrinsic energy level mismatches η_c and η_a are considered as a part of the kinetic overpotential loss. The polarization loss determines the rate of generation of hydrogen and oxygen. In fact, collectively these losses could be significant when gas evolution occurs. As mentioned earlier, only a few semiconductors can provide such a photovoltage. Although $SrTiO_3$, Nb_2O_3, and ZrO_2 are suitable for direct water splitting to generate hydrogen and oxygen, their bandgaps are too high in the range 3.4–3.5 eV. Therefore, these wide bandgap semiconductors are illuminated by UV radiation that is hardly available in the solar spectrum and are not practical for use in solar hydrogen generation. CdS and SiC have favorable conduction and valence

band positions. However, they have problems with photo-corrosion (Chen et al. 2020).

in the case of most n-type semiconductors, the flat-band potential lies below the H^+/H_2 potential at neutral pH, and therefore hydrogen and oxygen evolution would not occur. In these cases, it is essential to apply an external anodic bias to raise the Fermi level to generate H_2 and O_2. The bias can be applied with either an external voltage or by immersing the anode in a basic solution and the cathode in an acid, and the two compartments being separated by a membrane. Energy is saved in hydrogen generation because the photovoltage on the semiconductor supplements the external bias.

The charge carriers may reduce or oxidize the semiconductor itself leading to decomposition. This poses a serious problem for practical photoelectrochemical devices. Absolute thermodynamic stability can be achieved if the redox potential of oxidative decomposition reaction lies below the valence band and the redox potential of the reductive decomposition reaction lies above the conduction band. In most cases, usually one or both redox potentials lie within the bandgap. Then the stability depends on the competition between thermodynamically possible reactions. When the redox potentials of electrode decomposition reactions are thermodynamically more favored than electrolyte redox reactions, the result is electrode instability, for example, ZnO, Cu_2O, and CdS in an aqueous electrolyte.

Most semiconductors are prone to anodic photo-decomposition because holes have a very high oxidizing power, especially in aqueous electrolytes. Therefore, it is easier to achieve semiconductor electrode stability using p-type semiconductors for which the minority carriers are electrons. In general, semiconductors are less vulnerable to cathodic corrosion than anodic. When the minority carriers (i.e., electrons) in p-type semiconductors are donated to the electrolyte for carrying out the reduction reaction, they also provide cathodic protection to the semiconductor surface.

Typical decomposition reactions are shown in the following where (aq) means a solvated species:

$$Si + 4h^+ + 2H_2O \rightarrow SiO_{2aq} + 4H^+_{aq}$$

$$GaAs + 6h^+ + 3H_2O \rightarrow Ga^{3+}_{aq} + AsO^{3-}_{3(aq)} + 6H^+_{aq}$$

$$CdS + 2h^+ \rightarrow Cd^{2+}_{aq} + S$$

$$ZnO + 2h^+ \rightarrow Zn^{2+}_{aq} + \frac{1}{2}O_2$$

$$Cu_2O + 2h^+ + H_2O \rightarrow 2CuO + 2H^+_{aq}$$

$$MoS_2 + 14h^+ + 9H_2O \rightarrow MoO_{3(aq)} + 2SO^{2-}_{3(aq)} + 18H^+_{aq}$$

$$GaSe + 7h^+ + 3H_2O \rightarrow Ga^{3+}_{aq} + 2SeO^{2-}_{3(aq)} + 6H^+_{aq}$$
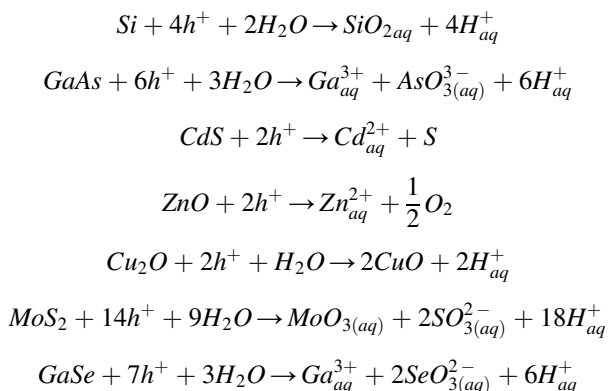
Cathodic processes (n-type specimen or photodecomposition of p-type semiconductors) in aqueous electrolytes:

$$Si + 4e^- + 4H_2O \rightarrow SiH_4 + 4OH^-$$

$$CdS + 2e^- \rightarrow Cd + S^{2-}_{aq}$$

$$ZnO + 2e^- + H_2O \rightarrow Zn + 2OH^-_{aq}$$

$$Cu_2O + 2e^- \rightarrow 2Cu + 2OH^-_{aq}$$

$$GaSe + 2e^- \rightarrow Ga + Se^{2-}_{aq}$$
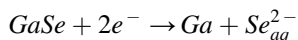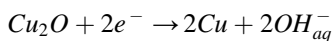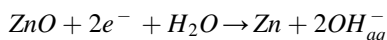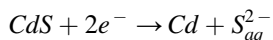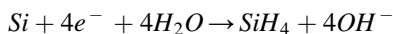
The reactions that are more favored thermodynamically tend to be also favored kinetically. Semiconductor electrodes can be stabilized by using this effect. For this purpose, redox couples in the electrolyte are established with the redox potential more negative than the oxidative decomposition potential, or more positive than reductive decomposition potential in such a manner that the electrolyte redox reaction occurs preferentially compared to the electrode decomposition reaction.

Kinetic stability has been observed in n-type semiconducting compounds of transition metals having layered structures due to the d–d nature of the indirect electronic transition and the inertness of van der Waals surface to chemical attack in these materials. Here, the valence band states are weakly bound (i.e., have little bonding character), whereas there is little weakening of bonds in the conduction band states. Overall, the electronic excitation does not affect the bond strength significantly. Thus, although the overall reaction affinity for corrosion is thermodynamically large in these systems, a high activation barrier for decomposition exists. Kinetic stability can also be achieved by a competing redox reaction that consumes the electronic charge carriers at the interface quickly enough to prevent the decomposition reactions. For example, photooxidation of CdS electrode in contact with the redox system is prevented by a competing reaction with polysulfide ion:

$$S^{2-}_n + S^{2-} + 2h^+ \rightarrow S^{2-}_{n+1}$$
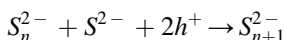
The lifetime of the electrode is a critical parameter for device applications. For practical applications, it is necessary that there should be no significant decline in the output, under load, during a time period that is at least 1000 times the time taken to totally decompose the moles of product in the electrode.

Although several of the conventional semiconductors present reasonable stability, they are far from meeting this rigorous criterion.

Chalcogenides of transition metals of group VIa, such as WSe_2, $MoSe_2$, and $MoTe_2$, show very interesting results in terms of stability. Molybdenite exists as large natural crystals (Mo et al. 2022). The cells made with these have shown reasonable conversion efficiency. WSe_2 with a bandgap of 1.16 eV comes closest to fulfilling the criterion of stability with an equivalent lifetime of 3 years, whereas the desired lifetime is >20 years. It has several limitations besides the lack of
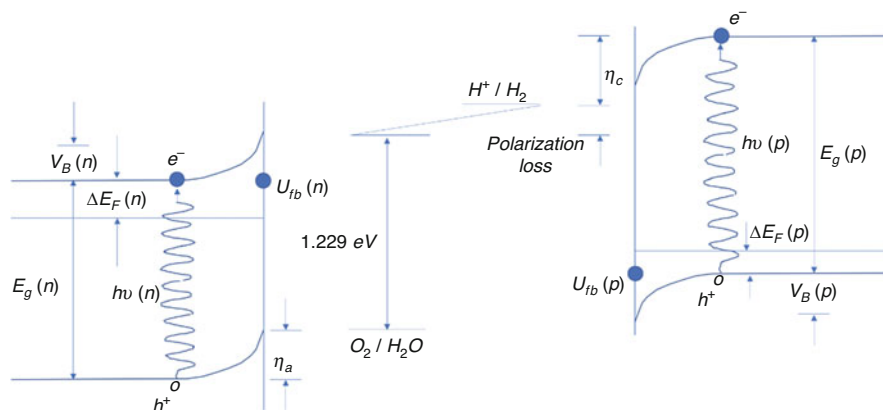
Fig. 10 Direct splitting of water with illuminated and interconnected photoanode and photocathode

technological and industrial base. p-WSe$_2$ has an indirect bandgap and low minority carrier diffusion length. Moreover, the surface recombination velocities for this layered compound are excessive for all except the van der Waals planes that unfortunately act as mirrors for a part of the sunlight.

Besides the requirements of the formation of high energy barriers, low surface recombination velocity, high stability, being benign to the environment, and low cost, ideal semiconductor electrodes must possess high interfacial electron transfer rates or high catalytic activity of the semiconductor surface. However, a metal or metal complex catalyst deposited on the semiconductor surface can also act as a surface recombination center as well as a barrier. This can be overcome by depositing well-scattered nanodots of catalyst metal.

The following semiconductors that have more appropriate bandgaps in the range 1–2 eV for solar energy conversion and that have been used for photo-electrolysis cells to generate hydrogen and oxygen by water splitting have been listed among the more interesting and efficient: p-InP(Ru), n-Fe$_2$O$_3$ and p-Fe$_2$O$_3$, and n- Ru$_x$Fe$_{1-x}$S$_2$. Catalyzed p-type InP has been found to possess several interesting properties such as appropriate bandgap for efficient sunlight conversion, p-type conductivity, and chemical passivation from corrosion based on coverage by a hydrated and compact indium oxide layer, and nonleaking high barrier at the catalyst–semiconductor interface.

Direct splitting of water can be accomplished by illuminating two interconnected photoelectrodes, a photoanode, and a photocathode as shown in Fig. 10.

Here, E$_g$(n) and E$_g$(p) are, respectively, the bandgaps of the n- and p-type semiconductors and ΔEF(n) and ΔEF(p) are, respectively, the differences between the Fermi energies and the conduction band-minimum of the n-type semiconductor bulk and valence band-maximum of the p-type semiconductor bulk. Ufb(p) and Ufb (n) are, respectively, the flat-band potentials of the p- and n-type semiconductors with the electrolyte. In this case, the sum of the potentials of the electron–hole pairs generated in the two photoelectrodes can be approximated by the following expression:

$$U_{fb} + \Delta E_F(p) - \Delta E_F(n) = U_{fb}(p) - U_{fb}(n) + \Delta E_F(p) - \Delta E_F(n) = \frac{\Delta G}{nF} + \eta_a(n)$$
$$+ \eta_c(p) + iR$$

All the terms in the preceding equation have the unit of energy per unit charge or electropotential. Ufb is the total flat-band potential which is the sum of band bending Ufb(p) in the p-type semiconductor and Ufb(n) in the n-type semiconductor. (The sign for Ufb(n) is negative because it is typically a negative number for the depletion layer junctions of interest.) The input energy of an absorbed photon must be greater than or equal to the semiconductor bandgap E_g. ΔG, n, and F are the Gibbs free energy in Joules per mole, the number equivalents of electrons per mole of material in equivalents per mole, and Faraday's constant in coulombs per equivalent, respectively. $\Delta G/nF$ in Joules per coulomb, that is, volts, is the portion of this potential energy per unit charge recovered as free energy of the net endoergic reaction in the electrolyte. In the case of the generation of hydrogen and oxygen by splitting water, the energy difference between the levels of H^+/H_2 and O_2/H_2O is 1.229 eV. The reduction of water to hydrogen occurs on the photocathode, which is the illuminated p-type semiconductor that provides an electron for this reduction. The oxidation of water to oxygen occurs on the photoanode, which is the illuminated n-type semiconductor that accepts an electron for this oxidation. $\eta_a(n)$ and $\eta_c(p)$ are the intrinsic, current-independent energy level mismatches of the n- and p-type semiconductor electrodes, respectively, and polarization loss is the total overpotential due to kinetic, diffusion, and ohmic losses consumed in the electrolyte for the flow of ions. The energy level mismatches, $\eta_a(n)$, $\eta_c(p)$, and polarization loss are the irreversible, entropy-producing terms that represent the lost potential energy per unit charge.

Thus, the potential can be maximized by matching the band edges to the respective redox levels and by minimizing the polarization loss. Moreover, the efficiency can be increased by employing two different segments of the solar spectrum to illuminate the two photoelectrodes. In this case, an optimum efficiency is reached when one semiconductor has a bandgap of ~1.8 eV and the other has a bandgap of ~1 eV. If such a tandem arrangement is employed, then the energetic photons having energy greater than 1.8 eV are absorbed by the higher bandgap semiconductor, whereas the lower energy photons pass through the higher bandgap semiconductor and the electrolyte and are incident on the lower bandgap semiconductor electrode, which absorbs the photons having energy greater than 1 eV. For efficient energy conversion, the photocurrents of the two electrodes must be equal. The maximum theoretical efficiency for dual photoelectrodes at AM 1.0 has been predicted to be 25% for the generation of hydrogen and oxygen by splitting water.

Considerable increase in cell performance has resulted from the following developments: advances in the design of metamorphic sub-cells to reduce carrier recombination and to increase voltage, wide bandgap tunnel junctions (TJs) that can function at high concentrations, metamorphic buffers for transitioning from substrate lattice to active sub-cell lattice, antireflection (AR) coatings for concentrator cells, and integration into current- matched triple-junction cells for terrestrial spectrum.

Many researchers have prepared nano-sized semiconductors with very large reactive surface area to enhance surface adsorption and photocatalytic reduction and oxidation reactions for the generation of H_2 and O_2 by water splitting. There is neither a separate cathode for reduction of water to hydrogen nor a separate anode for oxidation of water to oxygen when particulate suspensions of suitable semiconductor materials such as TiO_2, $SrTiO_2$, CdS, and $MoSe_2$ in an electrolyte are employed to carry out photocatalytic activity for water splitting (Hisatomi et al. 2014).

When a molecule in a solution absorbs light, an electron in the highest occupied molecular orbital (HOMO) is excited to the lowest unoccupied molecular orbital (LUMO) creating an electron vacancy, that is, a hole in the HOMO. The electron may be provided to a molecule in the solution to reduce it, whereas the hole in the HOMO may be provided to a molecule in the solution to oxidize it. This is like the reduction–oxidation process in the bulk semiconductor/electrolyte photo-electrolytic cell described earlier.

Optical properties of large (≥ 15 nm) semiconductor particles in suspension and colloidal solution are like those of extended (bulk) crystals. Quantization of energy levels occurs in small particles when the electrons and holes are limited by the potential walls of particles having size of the order of the De Broglie wavelength of the charge carriers.

Although the De Broglie wavelength of free electrons is ~0.1 nm, the value of an electron in a small crystallite can be much larger because the effective mass of electrons in a small particle is considerably smaller. Energy levels evolve from HOMO and LUMO to those of clusters, Q-sized particles, and finally bulk semiconductor.

Electrons and holes generated by energetic illumination in a small semiconductor particle can easily reach the surface and can carry out reduction and oxidation processes of adsorbed species, respectively, by providing and accepting electrons before they have a chance to recombine. Therefore, the quantum yield can be high.

It is instructive to calculate the efficiency of generation of hydrogen and oxygen by splitting water using a simple PV cell and an electrolysis setup in the dark in which case the energy input is from sunlight incident on the PV cells and the output is the amount of hydrogen and oxygen generated by the setup. The energy return in the form of generated hydrogen is usually calculated by considering the thermodynamic potential difference of 1.229 V at 25 °C for water splitting. As mentioned earlier, the losses are the material-dependent energy level mismatches η_c and η_a and the polarization loss that collectively represents the overpotentials due to kinetic, diffusion, and ohmic voltage losses for sustaining the current. Water splitting is an endothermic reaction. If it is carried out in a thermally isolated system in which the losses have been minimized, water will become progressively cooler and eventually freeze. The reaction can be carried out indefinitely by operating at the thermoneutral voltage for water splitting of 1.48 V, where the generated heat will sustain the endothermic reaction. In practice, if the system obtains the requisite heat energy from the ambient to which it is exposed, and the cooling thus provided may even be welcome and therefore is not counted. The overall efficiency of the PV electrolysis system is then the product of efficiencies of the PV cells and the electrolysis setup at

the operating voltage. Ideally, the operating voltage should be the optimum power point Vp of the PV cells at which their efficiency is maximum and hence is specified as the efficiency. For PV cells of total area, A, incident AM 1.5 solar radiation of 100 mW/cm², optimum current Ip at the optimum power point Vp, the PV conversion efficiency η is given by:

$$PV_{efficiency}, \eta\% = \frac{V_p \chi I_p}{100 \frac{mW}{cm^2} xA} \cdot 100$$

For the operating voltage at the optimum power point Vp and the Faradaic current for water splitting of Ip, the overall solar to hydrogen generation PV electrolysis efficiency is given by:

$$PV_{electrolysis\ efficiency}\% = \frac{P_{out}}{P_{in}} \cdot 100 = \frac{I_p}{P_{in}} E_0^{H_2O} \cdot 100 = \frac{I_p mA}{\frac{100mW}{cm^2} xA} \cdot 1.229 \cdot 100$$

$$= \frac{1.229\eta}{V_p}$$

Thus the PV electrolysis efficiency will be high if losses are minimized to operate the PV electrolysis setup at a voltage as low as possible compared to the thermodynamic potential difference of 1.229 V for water splitting at 25 °C. In practice, the electrolyzer cost is reduced by increasing the rates of generation of hydrogen and oxygen, that is, by increasing the operating voltage to 2 V, thus resulting in higher polarization loss. Also, in the case of some tandem solar cells, the optimum voltages are high. The operating voltages can be reduced to as low as 1.35 V by employing optimized electrodes and working with low currents obtained at low solar irradiances. Lastly, the operating voltages can be reduced to 1.28 V by providing additional excitation. For these three cases of operating voltages of 2, 1.35, and 1.28 V, the respective PEC efficiencies will be 61.5%, 91%, and 96% of the PV cell efficiency. It may often be noted that stirring is employed to improve PEC efficiency. A strict calculation should provide the efficiency including the energy input required for stirring.

Several researchers have tried to emulate the PV electrolysis design by utilizing multi-junction cells or multiple PV cells in combination with electrolysis systems. When the electrical field is generated in an illuminated solid-state device, it is not essential for the semiconductor to remain in direct contact with the electrolyte. Consequently, the various, often conflicting, requirements of formation of a semiconductor–electrolyte junction efficiently generating a photovoltage using the solar spectrum, stability of the semiconductor against corrosion by highly reactive electrolytic solution, and high catalytic activity at the semiconductor surface are eliminated.

The PV/electrolysis setup for the GaInP₂/GaAs dual-junction solar cell is shown in Fig. 11.

Fig. 11 PV/electrolysis
setup using the GaInP2/
GaAs dual-junction
solar cell
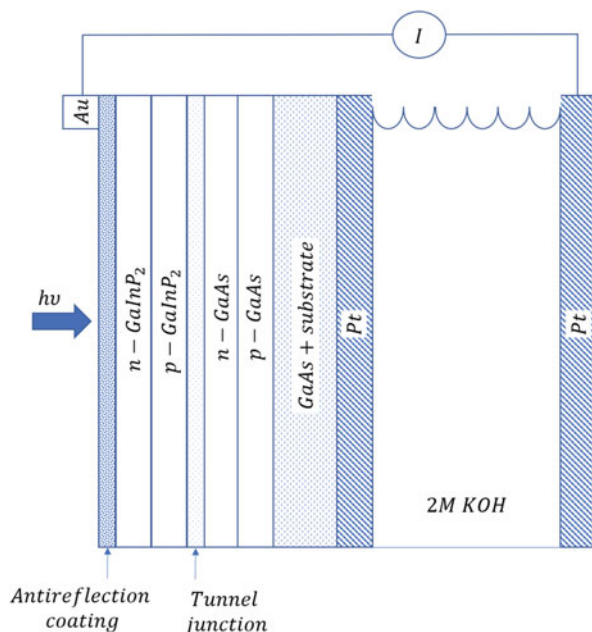
The top p–n GaInP$_2$ junction with a bandgap of 1.83 eV was designed to absorb the visible portion of the solar spectrum and the bottom p–n GaAs junction with a band-gap of 1.42 eV absorbed the near-IR portion of the spectrum that was transmitted through the top junction. The GaInP$_2$/GaAs tandem junction solar cell was mounted with the platinum back-contact layer forming an anode in an electrolyte consisting of 2 M KOH prepared using analytical grade reagents dissolved in fresh deionized distilled water. The platinum foil counterelectrode was connected to the gold or silver contact grid with a copper wire through an external circuit. Illumination from a 75 W Xe arc lamp was made incident onto the AR coating and front grid of the GaInP$_2$ top cell. Electrons from electron– hole pairs photogenerated within a diffusion length from the p–n junction by high-energy photons with energy hν greater than the GaInP$_2$ bandgap energy of 1.83 eV can diffuse into the p–n junction, and together with those generated in the depletion layer are transported to the n-type GaInP$_2$ layer by the built-in field of the top GaInP$_2$ junction. The electrons flow through the n-type GaInP$_2$ to the front contact grid and through the external circuit to the platinum cathode. However, the photogenerated holes flow through the p-type GaInP$_2$ toward the TJ. The photons with energy below the bandgap of GaInP$_2$ are transmitted to the bottom GaAs junction. Electrons from electron–hole pairs photogenerated by the photons with energy hν greater than the GaAs bandgap energy of 1.42 eV are separated by the built-in field of the bottom GaAs junction, flow toward the TJ, and recombine with the holes that have flowed there from the top GaInP$_2$ junction.

The electrons flow through the n-type GaInP$_2$ to the front contact grid and through the external circuit to the platinum cathode. However, the photogenerated holes flow through the p-type GaInP$_2$ toward the TJ. The photons with energy below the bandgap of GaInP$_2$ are transmitted to the bottom GaAs junction. Electrons from electron–hole pairs photogenerated by the photons with energy hν greater than the GaAs bandgap energy of 1.42 eV are separated by the built-in field of the bottom GaAs junction, flow toward the TJ, and recombine with the holes that have flowed there from the top GaInP$_2$ junction. The holes from the photogenerated electron–hole pairs flow through the p-type GaAs toward the GaAs substrate. This low bandgap p-type GaAs layer makes an indirect contact with the electrolyte through the substrate and a thin platinum metal layer ohmic back contact and anode. The total voltage generated across the tandem GaInP$_2$/GaAs cell V$_{ph}$ is the sum of the voltages across the two junctions, V$_{ph1}$ and V$_{ph2}$. If the total voltage produced by the GaInP$_2$/GaAs tandem cell is sufficient to drive the water redox reactions, and to provide any additional voltage needed to overcome the overvoltage losses resulting from the hydrogen and oxygen evolution reactions, then the hydrogen and oxygen can be generated by split- ting water. In such a case, the electrons generated in the top GaInP$_2$ cell flowing through the external circuit to the platinum cathode will reduce water to generate hydrogen. Two photons are, therefore, required to put one electron into the external circuit. A total of four electrons generated using four photons are needed to provide two electrons for generating a hydrogen molecule.

The electrons received by the bottom contact from the anode for oxidizing the water to oxygen recombine with the holes generated in the GaAs bottom cell at the interface with the metal contact. Again, eight holes generated using eight photons will be needed to provide four holes to form an oxygen molecule at the anode. Thus a total of eight photons, four of higher energy h$\nu > 1.83$ eV and four of intermediate energy $1.83 > $ h$\nu > 1.42$ eV, are needed to generate eight electron–hole pairs—four of the electrons flowing through the external circuit to complete the water splitting and reaching the back contact to recombine with the four holes reaching there. The remaining four electrons, after flowing through the bottom n-type GaAs layer and the n+ GaAs layer of the TJ recombine with the four holes flowing through the p-type layer of the top GaInP cell and p+ GaInP$_2$ layer of the TJ. Thus, eight photons are required to produce two molecules of H$_2$ and one molecule of O$_2$ by splitting two molecules of water.

The total output photovoltage must exceed the thermodynamic potential difference for water splitting (1.229 V at 25 °C), the energy level mismatches for the anodic and cathodic processes, and the polarization loss or overvoltages due to kinetic, diffusion, and IR potential losses in the bulk of electrolyte.

PV current–voltage and power–voltage characteristics of a standard GaInP$_2$/GaAs tandem cell were measured under 100 mW/cm^2 illumination. The PV parameters under illumination were an open-circuit voltage V$_{oc}$ = 2.32 V, a short-circuit current density J$_{sc}$ = 13.4 mA/cm^2, a fill factor FF = 0.88, and a PV conversion efficiency of 28.5%. Under the same illumination, the standard triple-junction a-Si:H solar cell exhibited an open-circuit voltage V$_{oc}$ = 2.16 V, a short-circuit current density J$_{sc}$ = 6.6 mA/cm^2, a fill factor FF = 0.62, and a PV conversion efficiency of

9%. Outdoor photocurrent measurements were monitored using an analog/digital data acquisition system, whereas the solar radiation was measured by the Solar Energy Research Facility Group of the National Renewable Energy Laboratory (NREL). Illumination for indoor experiments was provided by a 75 W Xe arc lamp. Photocurrent was measured with a potential-controlled potentiostat using a conventional two-electrode cell configuration.

The photocurrent was measured at various bias voltages for both the GaInP$_2$/GaAs dual-junction solar cell and triple n–i–p junction a-Si:H cell setups, with the back-contact Pt layer anode, Pt foil cathode, and 2 M KOH electrolyte under 100 mW/cm^2 illumination. The hydrogen production was found to be proportional to the current density through Faradaic correlation. For the GaInP$_2$/GaAs tandem junction cell setup, the light-limited current density was reached at the negative bias of approximately -0.57 V. Thus, the cell generated hydrogen, oxygen, and electrical power while operating at that potential.

The efficiency for hydrogen production was calculated using the equation: efficiency = (power out)/(power in). The only input power was the incident light. Photocurrent electrolysis efficiency of 100% was assumed, that is, the entire flow of electrons in the external circuit and the electrolyte was assumed to be utilized for the production of hydrogen and oxygen. Thus, the output power was estimated by multiplying all the hydrogen production photo- current by 1.23 V, the theoretical fuel cell limit at 25 °C, to calculate the hydrogen production efficiency of 16.5% for the PV GaInP$_2$/GaAs tandem cell electrolysis setup. Although this was the highest measured efficiency for group III-V tandem junction PV cell electrolysis setup, it was only 57.9% of the PV conversion efficiency of the 28.5% GaInP/GaAs tandem cell under AM 1.5 illumination. This was because electrical power generated when the cell is operating at -0.57 V was not considered. It was deemed impractical to configure such a system for producing hydrogen, oxygen, and electricity. Hence, it was suggested that the excess available power be allocated as a cushion against the loss of solar-to-hydrogen conversion efficiency under low solar irradiance or to compensate for the decrease in cur- rent density of the system due to reduction of dissolved oxygen rather than water at the cathode. While estimating the efficiency of a PEC setup that uses PV cells, it may be noted that the maximum efficiency of the PV cell is derived when it is operating at the optimum power point and that the PEC efficiency improves when the PEC cell is operated close to 1.23 V. First, PEC efficiency close to PV cell efficiency could be obtained by using a low-loss DC-to-DC voltage converter.

Second, if PV electricity is supplied to a commercial electro- lyzer with a typical efficiency of ~70%, the solar-to-hydrogen efficiency using an array of 28.5% efficient PV cells would be ~20%. Thus, the integrated system would actually give ~83% of the optimum.

The measured short-circuit current was found to follow the solar irradiance during the day. Moreover, copious amounts of gas were observed to evolve from the electrodes during the entire period. The integrated ratio of input-to-output power efficiency of hydrogen production by solar irradiance during this experiment was

calculated to be 16.4% at an average solar irradiance of 659 mWh/cm^2. This result was found to be in good agreement with indoor measurements under similar conditions that showed hydrogen generation throughout the experiment.

It would be possible to reduce the mismatch between the voltage at optimum power and the voltage needed for the efficient generation of hydrogen and oxygen by splitting water in PEC cells if the optimum power point voltage of 2.755 V from the recently developed 40.1% efficient, lattice-matched concentrator cell illuminated with 135× concentrated sun- light is used to provide the voltage to two PEC cells connected in series. Although the efficiency of metamorphic triple-junction solar cells at 240 suns is higher (40.7%), it may not be possible to reduce the energy level mismatch and polarization losses of the two PEC cells low enough for operation with the present optimum power point voltage of 2.589 V. It would be preferable to use the triple-junction cells without concentration. For this purpose, it would be essential to develop these cells further to improve the present optimum power voltages for the lattice-matched and metamorphic solar cells of 2.3 and 2.06 V to ~2.7 V.

For the amorphous hydrogenated silicon, a-Si:H, three n-type, intrinsic i, and p-type region junction (n–i–p triple junction) PV cell electrolysis setup, the light-limited current was reached approximately at zero bias, that is, at short-circuit. Thus, the a-Si:H PV cell electrolysis setup produced only the chemicals hydrogen and oxygen without any electrical power. This represents the ideal condition of operation for the PV electrolysis system. The hydrogen production efficiency for the triple-junction a-Si:H PV cell electrolysis setup under incident irradiance of 100 mW/cm^2 was calculated to be 7.8%. Thus, the PV electrolysis efficiency was 86.7% of the PV conversion efficiency of 9% of the a-Si:H PV cell. This significantly high fraction of the total incident energy could be achieved because an effective electrolysis voltage of only 1.42 V was required to sustain the low- current density. Thus, there was a better match between the maximum operating voltage of the a-Si:H PV cell and the voltage required for electrolysis. Here again this is not the correct comparison and the comments made earlier must be applied also to this case while comparing the efficiencies.

The operating voltage of highly efficient, individual single-junction PV cells cannot sup- ply the total voltage required for water splitting. They have been carried out research on the development of multiple bandgap tandem photo-electro-chemical cell. It uses a pair of polycrystalline thin-film solar cells that transmit IR photons unused in the PV conversion. The transmitted IR photons are made incident on a photoanode to reduce the overvoltage required for oxygen evolution (Fig. 12).

The chosen PV cells are amenable to economic mass production. More importantly, in this case, the photocatalyst need not be grown directly over the PV cell. As seen earlier, multiple-bandgap, solid-state tandem III-V compound semiconductor and a-Si:H PV cells have been used successfully for hydrogen generation by PV electrolysis. As discussed earlier, the best PV conversion efficiencies of 19.5% and 16.5% have been achieved with small-area, polycrystalline $CuIn_{1–x}Ga_xSe_2$ (CIGS) and CdTe thin-film solar cells. Since tandem polycrystalline thin-film cells are more difficult to fabricate, it is essential to use a pair of cells to obtain the necessary voltage required for water splitting. Interconnected two or more cells can be

Fig. 12 PEC cell that uses polycrystalline thin-film solar cells with a photoanode
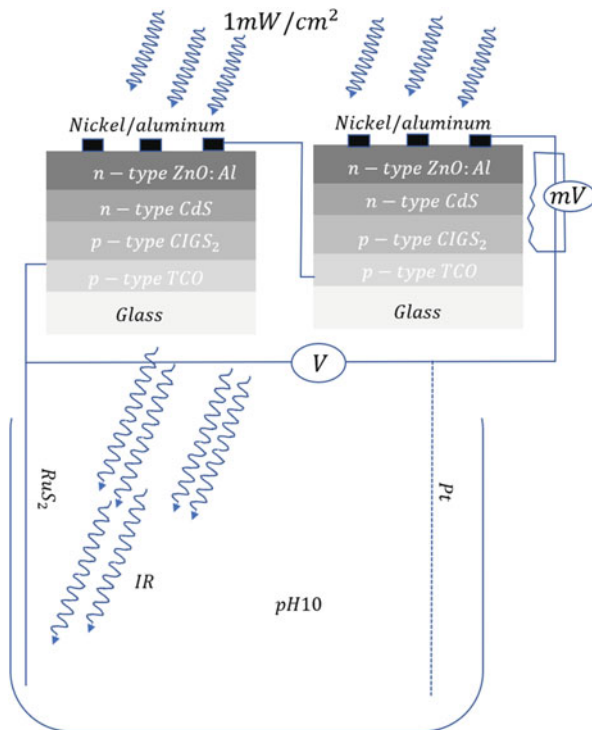
compared to tandem junction solar cells because integrally interconnected a-Si:H, CdTe, and CIGS thin-film PV modules are already being manufactured in multimegawatt quantities annually. When the thin-film solar cells transmit the unused IR photons, the voltage needed for splitting water can be reduced significantly by illuminating an appropriate photoanode with the transmitted IR photons. Here, only the photo- anode and cathode are in contact with the electrolyte. Moreover, this setup effectively integrates the PV cells and photoelectrolysis by using different parts of the solar spectrum for efficient water splitting.

6 Conclusions

Photocatalysis is a water splitting event to produce hydrogen from water that uses photonic energy. Most photocatalyst materials are made of semiconductor material because the semiconductor material has an energy gap that allows it to produce electron holes if it is charged with photonic energy from a source. This electron-hole pair will later cause a water splitting event. So far, the most widely used semiconductor material as photocatalyst is TiO_2. Interest in TiO_2 to be used as photocatalyst compared to other semiconductor materials, TiO_2 is known to have various

important advantages, for applications of hydrogen production from water (fractionation of water), including having high stability, corrosion resistance, abundant availability in nature and relatively inexpensive prices.

It is instructive to compare bulk and particulate photoelectrochemical and solid-state devices. Considerable efforts are made to increase the surface area in particulate photo- electrochemical devices because of the beneficial effects of larger surface area on catalytic processes. However, it may be remembered that although a large surface area is beneficial in catalysis, it can be detrimental in photoelectrochemical cells because of the high recombination rates. In a solid-state or electrochemical PV cell as well as in a bulk photo- catalytic cell, the photogenerated minority carriers are propelled efficiently by the built-in field to the side where they are majority carriers that together with the photogenerated majority carriers flow to the contacts or to a contact and the electrolyte. Consequently, the efficiency of collection of charge carriers generated in the depletion region and within a diffusion length of it is very high. Second, in bulk semiconductor–electrolyte devices and solid-state PV cells, reflection losses that can be substantial for the high refractive indices of most semiconductors can be minimized by using AR coatings. Therefore, the overall efficiency of 24% and >40% have been achieved for single and multiple-junction solid-state PV cells. Reflection losses cannot be minimized in particulate suspension-type photocatalytic cells. Moreover, in bulk photocatalytic cells, hydrogen, and oxygen generation by splitting water and accumulation can take place at separate locations and thus the reverse reaction of generated hydrogen and oxygen to water can be mostly avoided. This again is not possible in particulate suspension-type photocatalytic cells that can suffer from high reverse reaction rates besides high recombination rates of photogenerated carriers.

Considerable progress has been made in the field of photoelectrolysis cells for hydrogen generation using sunlight. Particulate NiO_x/TiO_2 photocatalyst has already been used for stoichiometric production of hydrogen and oxygen on a sunny day and a cloudy day with the quantum efficiency of >1.79%. Layered compounds with Ni/NiO cocatalyst have also shown good conversion at 330 nm. Doping with other anions and ion implantation would assist in improving the PEC conversion efficiencies in combination with other processes.

Generation of hydrogen from H_2S using cadmium sulfide with waste products as sacrificial agents to avoid photo-corrosion of the semiconductor is expected to grow as a niche application.

.

References

Ali M, Pervaiz E, Noor T (2021) Recent advancements in MOF-based catalysts for applications in electrochemical and photoelectrochemical water splitting: a review. Int J Energy Res 45(2): 1190–1226. https://doi.org/10.1002/er.5807

Chen S, Huang D, Xu P et al (2020) Semiconductor-based photocatalysts for photocatalytic and photoelectrochemical water splitting: will we stop with photocorrosion? J Mater Chem A 8: 2286–2322. https://doi.org/10.1039/C9TA12799B

Gao RT, Nguyen NT, Nakajima T et al (2023) Dynamic semiconductor-electrolyte interface for sustainable solar water splitting over 600 hours under neutral conditions. Sci Adv 9(1): eade4589. https://doi.org/10.1126/sciadv.ade4589

Hisatomi T, Kubota J, Domen K (2014) Recent advances in semiconductors for photocatalytic and photoelectrochemical water splitting. Chem Soc Rev 43:7520–7535. https://doi.org/10.1039/C3CS60378D

Jiang C, Moniz SJA, Wang A et al (2017) Photoelectrochemical devices for solar water splitting– materials and challenges. Chem Soc Rev 46:4645–4660. https://doi.org/10.1039/C6CS00306K

Kim JH, Kaneko H, Minegishi T et al (2016) Overall photoelectrochemical water splitting using tandem cell under simulated sunlight. Chem Sus Chem 9(1):61–66. https://doi.org/10.1002/cssc.201501401

Leenheer AJ, Atwater HA (2010) Water-splitting photoelectrolysis reaction rate via microscopic imaging of evolved oxygen bubbles. J Electrochem Soc 157(9):B1290. https://doi.org/10.1149/1.3462997

Martín de Vidales MJ, Cotillas S, Perez-Serrano JF et al (2016) Scale-up of electrolytic and photoelectrolytic processes for water reclaiming: a preliminary study. Environ Sci Pollut Res 23:19713–19722. https://doi.org/10.1007/s11356-016-7189-9

Mayer MT (2017) Photovoltage at semiconductor–electrolyte junctions. Curr Opin Electrochem 2(1):104.110. https://doi.org/10.1016/j.coelec.2017.03.006

Miller EL (2015) Photoelectrochemical water splitting. Ener. Environ Sci 8:2809–2810. https://doi.org/10.1039/C5EE90047F

Minggu LJ, Daud WRW, Kassim MB (2010) An overview of photocells and photoreactors for photoelectrochemical water splitting. Int J Hydrogen Energy 35(11):5233–5244. https://doi.org/10.1016/j.ijhydene.2010.02.133

Mo QL, Hou S, Wei ZQ et al (2022) Fine tuning of charge motion over homogeneous transient metal chalcogenides heterostructured photoanodes for photoelectrochemical water splitting. Chem Eng J 433(3):133641. https://doi.org/10.1016/j.cej.2021.133641

Nellist MR, Laskowski FAL, Lin F et al (2016) Semiconductor–electrocatalyst interfaces: theory, experiment, and applications in photoelectrochemical water splitting. Acc Chem Res 49(4): 733–740. https://doi.org/10.1021/acs.accounts.6b00001

Peter LM, Upul Wijayantha KG (2014) Photoelectrochemical water splitting at semiconductor electrodes: fundamental problems and new perspectives. Chem Phys Chem 15(10):1983–1995. https://doi.org/10.1002/cphc.201402024

Peter LM (2015) Photoelectrochemical water splitting. A status assessment. Electroanalysis 27(4): 864–871. https://doi.org/10.1002/elan.201400587

Peter L (2021) Fundamental aspects of photoelectrochemical water splitting at semiconductor electrodes. Curr Opin Green Sustain Chem 31:100505. https://doi.org/10.1016/j.cogsc.2021.100505

Qiu Y, Pan Z, Chen H et al (2019) Current progress in developing metal oxide nanoarrays-based photoanodes for photoelectrochemical water splitting. Sci Bullet 64(18):1348–1380. https://doi.org/10.1016/j.scib.2019.07.017

Roger I, Shipman MA, Symes MD (2017) Earth-abundant catalysts for electrochemical and photoelectrochemical water splitting. Nat Rev Chem 1:0003. https://doi.org/10.1038/s41570-016-0003

Ros C, Andreu T, Morante JR (2020) Photoelectrochemical water splitting: a road from stable metal oxides to protected thin film solar cells. J Mater Chem A 8:10625–10669. https://doi.org/10.1039/D0TA02755C

Samuel E, Joshi B, Kim MW et al (2020) Morphology engineering of photoelectrodes for efficient photoelectrochemical water splitting. Nano Energy 72:104648. https://doi.org/10.1016/j.nanoen.2020.104648

Vargas-Barbosa NM, Geise GM, Hickner MA et al (2014) Assessing the utility of bipolar membranes for use in photoelectrochemical water-splitting cells. Chem Sus Chem 7(11): 3017–3020. https://doi.org/10.1002/cssc.201402535

Yang W, Prabhakar RR, Tan J et al (2019) Strategies for enhancing the photocurrent, photovoltage, and stability of photoelectrodes for photoelectrochemical water splitting. Chem Soc Rev 48: 4979–5015. https://doi.org/10.1039/C8CS00997J

Ye KH, Li H, Huang D et al (2019) Enhancing photoelectrochemical water splitting by combining work function tuning and heterojunction engineering. Nat Commun 10:3687. https://doi.org/10.1038/s41467-019-11586-y

Zhang H, Wang H, Xuan J (2020) Rational design of photoelectrochemical cells towards bias-free water splitting: thermodynamic and kinetic insights. J Power Sour 462:228113. https://doi.org/10.1016/j.jpowsour.2020.228113

Decoupled Water Splitting

1 Introduction

An unavoidable consequence of electrolysis in a conventional electrolyzer is that the production of oxygen and hydrogen takes place in the same device separated only by a membrane. This in turn defines a number of limitations on the operation of a conventional system; namely, (1) extremely high levels of gas purity (>99.999%), specifically for electronic applications, cannot be directly obtained from the electrolyzer without requiring further purification; (2) operation at low loads and at frequently changing loads reduces the lifetime of the membrane and further increases the potential for gas crossover; and (3) production of hydrogen at high pressure requires high differential pressure across the membrane. To maintain the integrity of the membrane a thicker membrane is used in these circumstances resulting in higher cell resistance and consequently lower efficiency. In this respect, it is interesting to see if water electrolysis could be done in a fundamentally different way, perhaps mirroring the activation of water in photosynthesis which has two sets of coupled processes, that is, a light reaction which results in oxygen evolution and a dark reaction which harnesses the proton gradient and electrons for organic activation.

Recent work has demonstrated that a new route to water splitting is possible and the limitations described earlier can be circumvented by decoupling the hydrogen and oxygen production via the introduction of a redox mediator (McHugh et al. 2020). This mediator effectively intercepts the electrons formed by water oxidation, being itself reduced, and the consequent increase in negative charge is balanced by the protons formed which are associated with the reduced mediator Fig. 1).

The hydrogen evolution reaction can then be carried out in a separate device (Fig. 2).

By separating the production of hydrogen from oxygen, such devices have the potential to overcome the low load, high-pressure/efficiency, and purity limitations of conventional electrolyzers.

Fig. 1 Mediated oxygen generation
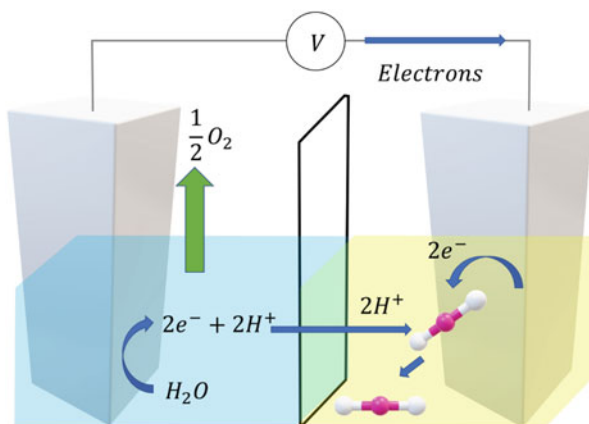
Fig. 2 Mediated hydrogen generation
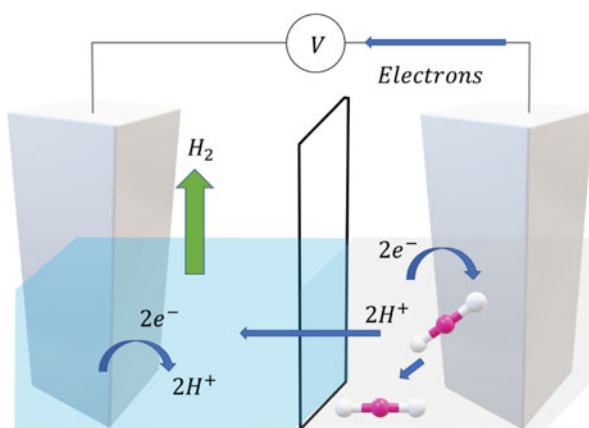
2   Decoupled Electrochemical Water Splitting Fundamentals

In decoupled electrochemical water splitting, the HER is coupled to an oxidation half-reaction of a redox mediator (M^-), while the OER is coupled to a reduction half-reaction of M:

$$Cathode : 2H^+ + 2e^- \rightarrow H_2$$

$$Anode : 2M^- \rightarrow 2M + 2e^-$$

$$Overall : 2H^+ + 2M^- \rightarrow H_2 + 2M$$

$$Cathode : 2M + 2e^- \rightarrow 2M^-$$

$$Anode: H_2O \rightarrow 2H^+ + 2e^- + \frac{1}{2}O_2$$

$$Overall: 2M + H_2O \rightarrow 2M^- + 2H^+ + \frac{1}{2}O_2$$
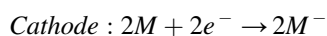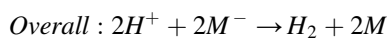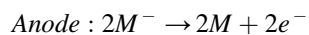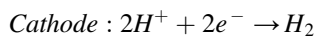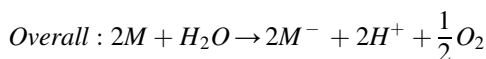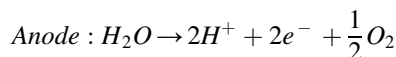
The net reaction is equivalent to the water-splitting reaction, and H_2 and O_2 are collected as outputs. The mediator is cycled back and forth through oxidation states in a manner akin to either a redox-flow battery (RFB) or a solid-state battery, depending on whether the mediator is in a liquid or solid phase (Rausch et al. 2014).

In both electrochemical water splitting and decoupled electrochemical water splitting, the only system inputs are water and electrical power, and the only outputs are H_2 and O_2 (Ifkovits et al. 2021). However, since pH is on a log scale and can be determined largely by the electrolyte, the actual pH change during independent operation of the decoupled cells depends on both the initial pH of the electrolyte and the current passed during decoupled operation.

The previous equations can be modified slightly for mediators that also uptake and release protons during operation:

$$Cathode: 2H^+ + 2e^- \rightarrow H_2$$

$$Anode: 2MH_2 \rightarrow 2M^* + 2H^+ + 2e^-$$

$$Overall: 2MH_2 \rightarrow H_2 + 2M^*$$

$$Cathode: 2M^* + 2H^+ + 2e^- \rightarrow 2MH_2$$

$$Anode: H_2O \rightarrow 2H^+ + 2e^- + \frac{1}{2}O_2$$

$$Overall: 2M^* + H_2O \rightarrow 2MH_2 + \frac{1}{2}O_2$$
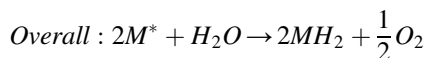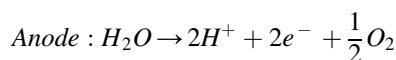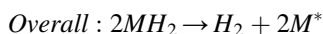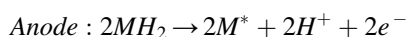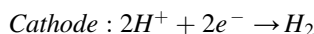
The net reaction is still equivalent to the water-splitting reaction, but the system remains in proton balance. Mediators operated in alkaline environments undergo similar reactions but are balanced with hydroxide ions rather than protons.

Coupling to M allows separation of the HER and OER in time, space, or both. Purported benefits of such arrangements include: (1) the removal or substitution of costly electrolyzer components, such as ion-exchange membranes and precious metal catalysts; (2) facile coupling with intermittent renewable energy sources; (3) membrane-free generation of pressurized hydrogen; (4) mitigation of the risk of explosion that accompanies simultaneous production of H_2 and O_2 during water splitting.

M can be either a soluble redox couple, such as V^{3+}/V^{2+} or $[Fe(CN)_6]^{3-/4-}$, or a solid, such as $NiOOH/Ni(OH)_2$. The phase of M affects the physical components as well as the operation of the system. Systems with a soluble redox mediator can operate under either static or flow conditions because M can be pumped between chambers. In systems with solid-state mediators, M typically is integrated with an
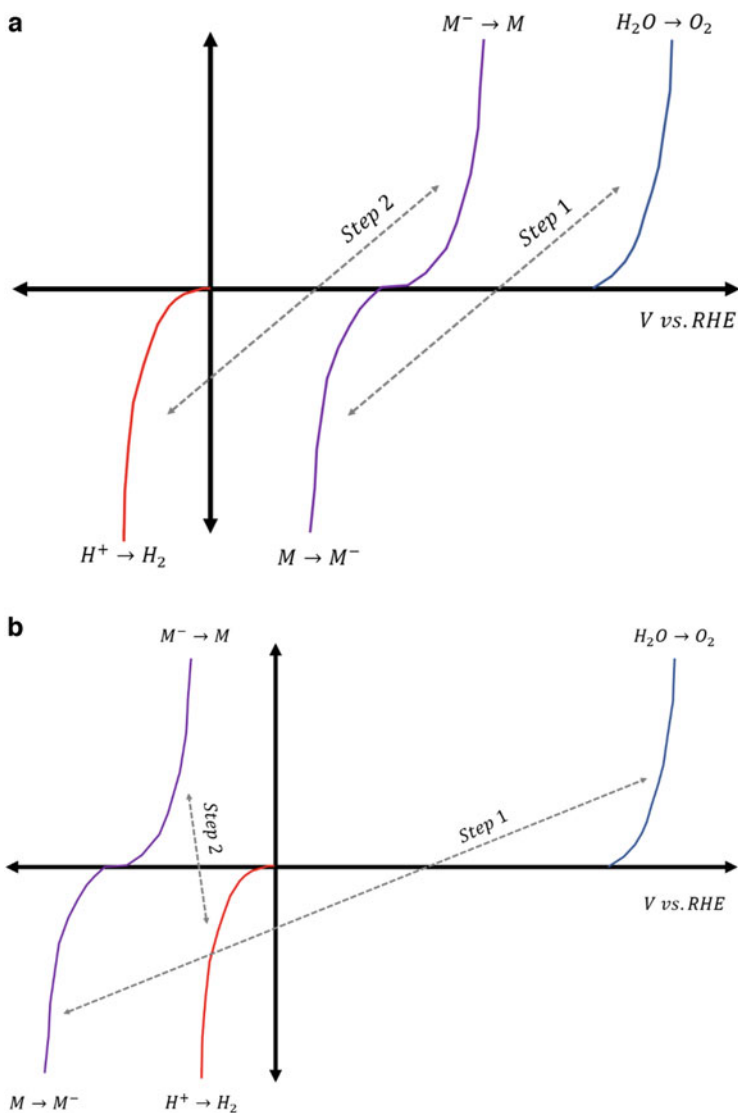
Fig. 3 Notional current–voltage behavior for decoupled water-splitting systems. (**a**) E0(M0/−) falls between E0(H^+/H_2) and E0(O_2/H_2O), dividing the thermodynamically required voltage for water splitting into two non-spontaneous steps. (**b**) E0(M0/−) falls outside of the range from E0(H^+/H_2) to E0(O_2/H_2O). In this case, the voltage required for step 1 is greater than that required for water splitting, but step 2 proceeds spontaneously

electrode that can be moved between cells to be partnered with the HER or OER. Depending on the choice of M, the standard potential $E^0(M^{0/-})$ may fall either inside or outside of the potential range bracketed by $E^0(H^+/H_2)$ and $E^0(O_2/H_2O)$. Notional current–voltage data for these two situations are shown in Fig. 3.

The position of $E^0(M^{0/-})$ relative to $E^0(H^+/H_2)$ and $E^0(O_2/H_2O)$ affects how the system is configured physically in addition to how it operates in practice. If $E^0(M^{0/-})$ falls between $E^0(H^+/H_2)$ and $E^0(O_2/H_2O)$, then coupling to M can reduce the maximum instantaneous power required by the system by dividing the thermodynamically required voltage for water splitting into multiple non-spontaneous steps. If $E^0(M^{0/-})$ falls outside of the range from $E^0(H^+/H_2)$ to $E^0(O_2/H_2O)$, then coupling to M can increase the thermodynamically required voltage for the first step, but the second step can proceed spontaneously without any external circuit or electrochemical cell.

3 Decoupled Water Splitting Cells

Decoupled electrochemical water-splitting systems therefore can be sorted into four classes, based on the phase of M and whether one or both steps require input power (Fig. 4).

For liquid-mediated systems with two non-spontaneous steps (Type 1), the cell for each of the two steps is composed of an RFB half-cell and an electrolysis half-cell. The electrolyte containing the mediator that was reduced in Step 1 can be pumped to a second cell where the mediator is re-oxidized; alternatively, the electrode for the electrolysis half-cell could be exchanged and the cell could be run with polarity opposite to that used in Step 1. Liquid-mediated systems require a separator to keep the mediator and electrolysis products contained within their proper half-cells. Liquid-mediated systems with a spontaneous second step (Type 2) generally resemble a cell composed of an RFB half-cell and an electrolysis half-cell, paired with a catalyst bed. Systems of this type do not require the HER to occur over an electrode surface, because external power input is not required to drive that step (Ifkovits et al. 2021).

Solid-mediated systems with two non-spontaneous steps (Type 3) typically use a single decoupling electrode that is paired alternately with the proper electrode for either the HER or OER. In general, the cell for each of the two steps in these systems is composed of an electrolysis half-cell and a battery half-cell. Solid-mediated systems with a spontaneous second step (Type 4) generally are configured similarly to their nonspontaneous counterparts. Specifically, the cell for each of the two steps is composed of an electrolysis half-cell and a battery half-cell; however, the second cell does not require an external power source.

All four types of decoupled electrolysis systems allow some components, such as electrodes and cells, to be shared among Step 1 and Step 2.

Decoupled water splitting is a new and growing field focused on exploring how separating the electrochemical oxygen- and hydrogen-evolution reactions – either spatially, temporally, or both – can benefit electrolysis systems used for generating carbon-neutral hydrogen. From the field's inception in 2013, a vast range of mediators, catalysts, separators, electrochemical environments, light absorbers, and
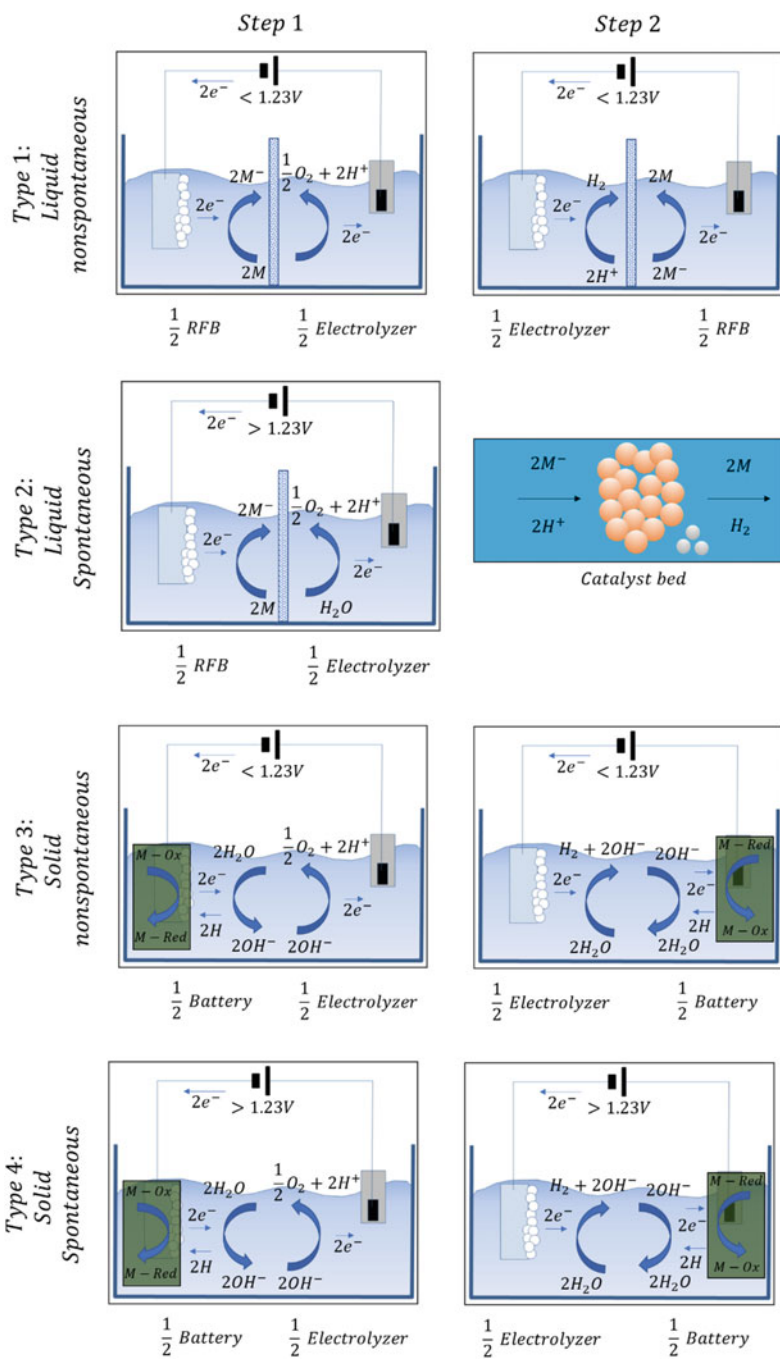
Fig. 4 Four types of decoupled water-splitting systems

Fig. 5 Comparison of fluoride concentration in solution measured as a function of time for a conventional electrolyzer and an STA-mediated electrolyzer. Fluoride is a product of Nafion breakdown
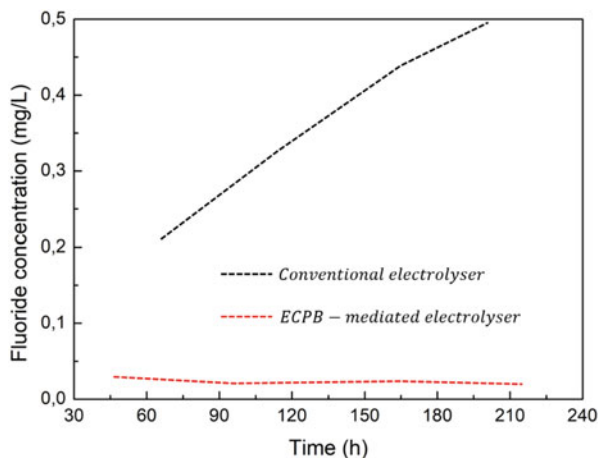
engineering optimizations have been implemented, creating a diverse group of systems for consideration (Huang and Wang 2020).

These systems have allowed for earth-abundant catalysts to generate hydrogen at rates approaching that of precious metal catalysts in PEM electrolysis systems. Membrane separators have been replaced with cheaper alternatives or removed entirely, depending on the system. Membrane-free production of pressurized hydrogen has been achieved. Some mediators have energy- or hydrogen-storage densities that are approaching that of cryogenic hydrogen, albeit with an electrochemical penalty for accessing that hydrogen. Oxygen evolution has been replaced with other value-added oxidation reactions, with mediators further implemented in completely modular electrochemical synthesis schemes. The intrinsic safety and operational flexibility of electrolysis have been substantially improved as well (Symes and Cronin 2013).

Elements of decoupled water-splitting systems may also be exploited beneficially in unassisted photoelectrochemical water-splitting systems. PECs operate at low current density compared to conventional electrolyzers, and decoupled systems have shown the most improvement to membrane stability and gas crossover when the current density is low. Furthermore, the collection of gaseous hydrogen over a vast array of PEC devices is a difficult engineering feat, which may be alleviated by redox-mediated generation of hydrogen in a central facility. In either case, the modularity and flexibility of decoupled electrolysis systems can enable the rearrangement of electrochemical reactions and facilitate changes in the aqueous environment in PECs, which may decrease reaction overpotentials or increase semiconductor stability (Peñas et al. 2019).

In many experiments, it was demonstrated how t the decoupled system had an order of-magnitude less membrane degradation than its coupled counterpart (Fig. 5).

The spatial decoupling of the HER from the OER has been hypothesized to produce a lower concentration of reactive oxygen species, which are known to degrade ion-exchange membranes.

Decoupled water-splitting systems contain more process components than conventional electrolyzers, including RFBs, catalyst beds, and auxiliary electrodes, as well as mass flow equipment such as piping, pumps, and solid-conveying systems. The systems sometimes utilize expensive and low-durability mediator materials.

It is not known whether the stated potential benefits of decoupled water-splitting systems – such as flexibility and modularity – can outweigh costs associated with increased system complexity. For these systems, the cost-benefit analysis is a moving target, as innovation will continually – and perhaps unevenly – drive down costs of both conventional electrolysis and decoupled water splitting systems.

4   E-TAC

Very recently, a hydrogen production route very similar to electrolysis has been proposed (Dotan et al. 2019). This method is known as E-TAC, it uses electricity to split water into hydrogen and oxygen. However, unlike conventional electrolysis, hydrogen and oxygen are generated separately in different steps – an Electrochemical (E) step and a Thermally-Activated Chemical (TAC) step (Fig. 6).

Alkaline electrolysis is based on the contemporary oxygen and hydrogen evolution reactions taking place at high temperature. In this solution, the membrane does not allow the O_2/H_2 crossover. In the case of E-TAC, the water splitting process takes place into two separate steps. The first electrochemical step, acting at 25 °C, proceeds following the reactions:

$$4H_2O + 4e^- \rightarrow 4OH^- + 2H_2$$
$$\left(Ni(OH)_2 + OH^- \rightarrow NiOOH + H_2O + e^-\right) * 4$$
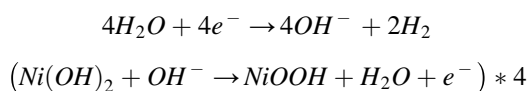
During this step, only hydrogen bubbles are observed without oxygen production at the anode (in the supplementary material in Dotan et al. 2019, very interesting movies, describing the process, can be observed).

The second chemical step, acting at 90 °C, proceeds following the reaction:

$$4NiOOH + 2H_2O \rightarrow 4Ni(OH)_2 + O_2$$
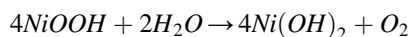
The results belonging to pilot plants show an efficiency close to 95%. The potential for industrial scale-up is envisioned through a multi-cell design. In this design, cold and hot electrolyte are moved from one cell to another in order to regenerate the anode and let gases to flow (Fig. 7).

The main advantage of this system is believed to be a membrane-free cell capable of producing hydrogen and oxygen into separate steps. This eliminates all the problems and costs related to the membrane-based cells. The lack of a membrane enables high-pressure hydrogen production, potentially exceeding 100 bars. The
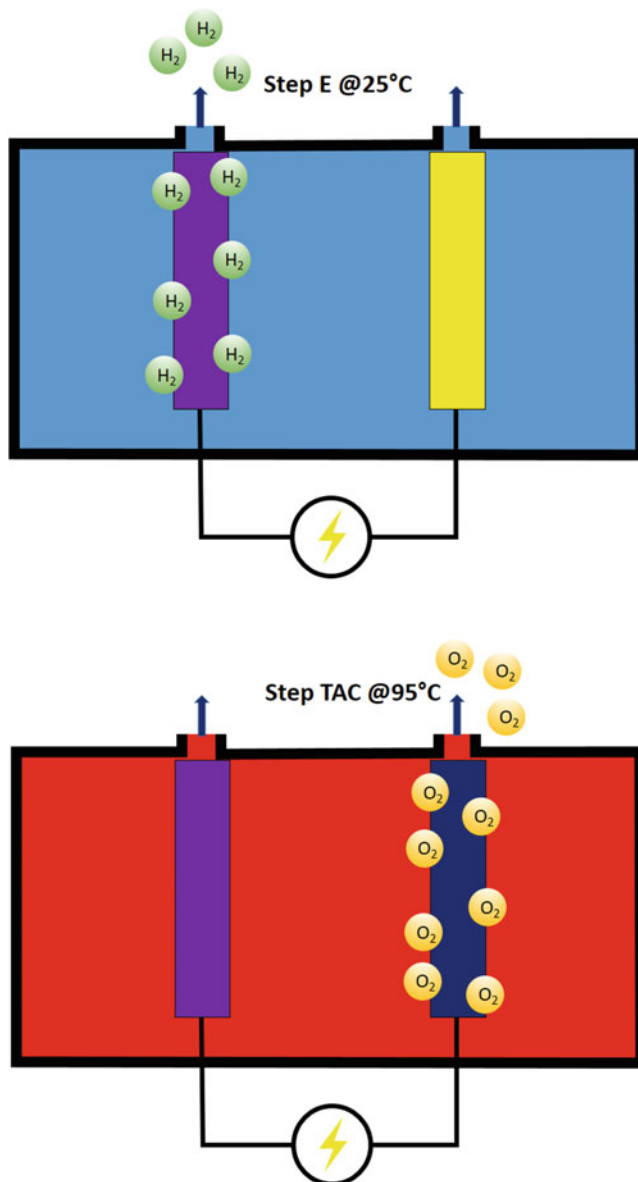
Fig. 6 E-TAC hydrogen and oxygen production schematic

possibility of operating with low anode potential leads this system to be very competitive in terms of energy balance.
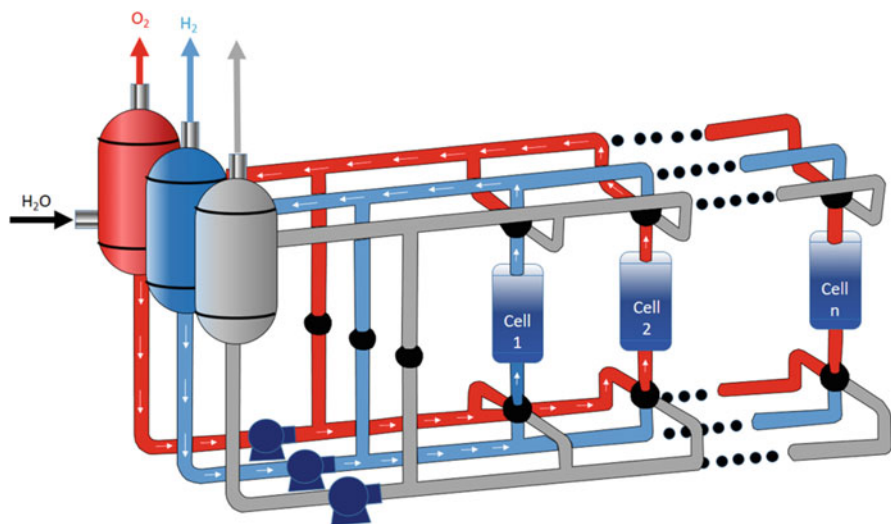
Fig. 7 E-TAC multi-cell design

5 Conclusions

Decoupled water splitting is a new and growing field focused on exploring how separating the electrochemical oxygen- and hydrogen-evolution reactions – either spatially, temporally, or both– can benefit electrolysis systems used for generating carbon-neutral hydrogen. From the field's inception in 2013, a vast range of mediators, catalysts, separators, electrochemical environments, light absorbers, and engineering optimizations have been implemented, creating a diverse group of systems for consideration.

Research in decoupled water splitting has benefited from methods that have been known for decades in related fields, such as (photo)electrochemistry and heterogeneous catalysis. Similar research challenges are found across these fields, such as high OER overpotentials and the longevity of device components.

Numerous types of decoupled electrolysis systems have been explored. These systems have allowed for earth-abundant catalysts to generate hydrogen at rates approaching that of precious metal catalysts in PEM electrolysis systems. Membrane separators have been replaced with cheaper alternatives or removed entirely, depending on the system. Membrane-free production of pressurized hydrogen has been achieved. Some mediators have energy- or hydrogen-storage densities that are approaching that of cryogenic hydrogen, albeit with an electrochemical penalty for accessing that hydrogen. Oxygen evolution has been replaced with other value added oxidation reactions, with mediators further implemented in completely modular electrochemical synthesis schemes. The intrinsic safety and operational flexibility of electrolysis have been substantially improved as well.

Elements of decoupled water-splitting systems may also be exploited beneficially in unassisted photoelectrochemical water splitting systems. PECs operate at low current density compared to conventional electrolyzers, and decoupled systems have shown the most improvement to membrane stability and gas crossover when the current density is low. Furthermore, the collection of gaseous hydrogen over a vast array of PEC devices is a difficult engineering feat, which may be alleviated by redox-mediated generation of hydrogen in a central facility. In either case, the modularity and flexibility of decoupled electrolysis systems can enable the rearrangement of electrochemical reactions and facilitate changes in the aqueous environment in PECs, which may decrease reaction overpotentials or increase semiconductor stability.

Technical hurdles and knowledge gaps for the implementation of decoupled electrolysis devices still exist. As is the case with photoelectrochemical electrolysis research, quantifying the long term performance of a device is non-trivial. Generally device performance has been evaluated for dozens of cycles over the time scale of days at most, which is far from the decades-long timescale that is needed for grid-scale electrolyzers. Use of earth-abundant catalyst beds in Type 2 systems has been primarily investigated in proof-of-concept systems that have focused on demonstration and determination of the initial rate of hydrogen production, with rigorous kinetic studies only being introduced relatively recently.

Values for turnover numbers gleaned from the available data have shown TON <10 for several earth-abundant catalysts, leaving in question the long-term performance of such materials.

However, these studies were not focused on improving the TON, so these values should be considered as a lower bound.

Many decoupled electrolysis systems require the movement of charged liquid or solid mediators, both of which introduce logistical and thus cost concerns. The impact of corrosive mediators has been mentioned briefly, but the economic impact on the longevity of hardware or the requirement of using more expensive components has not been analyzed.

These and other unanswered questions, of both a fundamental scientific and practical engineering nature, stand between full utilization of decoupled water splitting systems in clean, industrial hydrogen generation.

References

Dotan H, Landman A, Sheehan SW et al (2019) Decoupled hydrogen and oxygen evolution by a two-step electrochemical–chemical cycle for efficient overall water splitting. Nat Energy 4:786–795. https://doi.org/10.1038/s41560-019-0462-7

Huang J, Wang Y (2020) Efficient renewable-to-hydrogen conversion via decoupled electrochemical water splitting. Cell Rep Phys Sci 1(8):100138. https://doi.org/10.1016/j.xcrp.2020.100138

Ifkovits ZP, Evans JM, Meier MC et al (2021) Decoupled electrochemical water-splitting systems: a review and perspective. Energy Environ Sci 14:4740. https://doi.org/10.1039/D1EE01226F

McHugh PJ, Stergiou AD, Symes MD (2020) Decoupled electrochemical water splitting: from fundamentals to applications. Adv Energy Mater 10:2002453. https://doi.org/10.1002/aenm.202002453

Peñas P, van der Linde P, Vijselaar W et al (2019) Decoupling gas evolution from water-splitting electrodes. J Electrochem Soc 166(15):H769. https://doi.org/10.1149/2.1381914jes

Rausch B, Symes MD, Chisholm G et al (2014) Decoupled catalytic hydrogen evolution from a molecular metal oxide redox mediator in water splitting. Science 345(6202):1326–1330. https://doi.org/10.1126/science.1257443

Symes MD, Cronin L (2013) Decoupling hydrogen and oxygen evolution during electrolytic water splitting using an electron-coupled-proton buffer. Nat Chem 5:403–409. https://doi.org/10.1038/nchem.1621

Electrocatalysts for Water Splitting

1 Introduction

Among many aspects of the progress in the development of the sustainable power package of the future, catalysis, or electrocatalysis, has played a major role in overcoming the kinetic energy barriers for electrochemical reactions of water, oxygen, and hydrogen in water-splitting cells and fuel cells (Wang et al. 2021).

Usually, the overall reaction of water electrolysis can be divided into two half-cell reactions: hydrogen evolution reaction (HER) and oxygen evolution reaction (OER). HER is the reaction where water is reduced at the cathode to produce H_2, and OER is the reaction where water is oxidized at the anode to produce O_2. One of the critical barriers that keep water splitting from being of practical use is the sluggish reaction kinetics of OER and HER due to high overpotentials, a measure of the kinetic energy barriers. Therefore, catalysis plays a major role in both OER and HER. Highly effective catalysts are required to minimize the overpotentials for OER and HER towards efficient H_2 and O_2 production (Anwar et al. 2021).

The design of catalysts or electrocatalysts depends on the operating conditions of the water electrolysis cell. Currently, there are three main types of electrolysis technologies: (1) proton exchange membrane (PEM) electrolysis (2) alkaline electrolysis (3) high-temperature solid oxide water electrolysis. The solid oxide water electrolysis requires high energy consumption because of the high temperature. For the PEM based electrolysis cell, the water splitting is performed under acidic condition and using PEM. This condition has some advantages over other conditions such as lower gas permeability and high proton conductivity. It features high energy efficiency and fast hydrogen production rate. However, the requirement of acidic media limits the OER electrocatalysts to noble metal and noble metal oxide catalysts, which are the state-of-the-art OER electrocatalysts in the acidic media. This requirement leads to a high cost for the cell. For the alkaline electrolysis cell, water splitting is performed under alkaline condition. In comparison with cells using acidic media, water splitting in alkaline media broadens the selection of the electrocatalysts to non-

noble metals or metal oxides. However, the activity of HER in alkaline media is usually 2–3 orders of magnitude lower than the activity of HER in acidic media (Schalenbach et al. 2018).

Therefore, the design of optimal electrocatalysts suitable for the different media with low-cost, high catalytic activity, and good durability for electrolytic water splitting is very challenging.

There are several challenging areas for the development of active, stable, and low-cost electrocatalysts (Khan et al. 2018). First, while most of the efficient OER catalysts such as Ir and Ru based electrocatalysts exhibit a high dissolution resistance in acidic condition, most of the non-noble metal-based electrocatalysts cannot survive under such condition (Shit et al. 2021). Thus, the challenge is to develop stable and robust non-noble metal OER electrocatalysts with high activity and long-term stability performance in acidic media. Second, while non-noble-metal-based electrocatalysts such as carbides, phosphides, and chalcogenides have drawn great attention due to their high performance for OER in alkaline media, the catalysts undergo composition and structural transformation during OER condition. Thus, the identification of the real active sites remains elusive, and it is challenging to develop techniques to detect the real active sites to guide the design and preparation of optimal catalysts. Third, the knowledge on the catalytic mechanisms of many electrocatalysts, especially transition metal-based catalysts for HER in alkaline condition, is rather limited in comparison with HER in acidic condition. Thus, an important challenge is to determine the factors that govern the catalytic mechanism of HER in alkaline media.

Taken together, significant progress has been made in the design of electrocatalysts for water splitting to produce hydrogen by advancing the atomic, molecular, and nanoscale materials engineering strategies (Yin et al. 2020). Hydrogen is a promising substitute for fossil fuel as its highest gravimetric energy density and zero pollution emission, which provides a clean and renewable energy as an alternative to fossil fuels. The development of water splitting cells as an efficient energy conversion and storage system play an important role in hydrogen production. However, the energy efficiencies of water electrolysis are hindered by the sluggish reaction kinetics of OER and HER due to high overpotentials which lead to only 4% of the word's hydrogen generation from water splitting at present. To facilitate the practical use of water splitting in industries, the design of efficient catalysts plays a major role in both OER and HER to minimize the overpotential and improve the energy efficiencies (Yu et al. 2018). In this chapter, we highlighted some of the significant advances in the development of nanostructured noble-metal-based and non-noble-metal-based electrocatalysts for HER and OER, which show high performance approaching benchmark catalysts Pt and IrO_2/RuO_2 for the HER and OER with low cost. Fundamental insights have been gained into the mechanistic details of the synergistic structure, morphology, and composition of the catalysts for HER and OER in different media. The current understanding of the reaction mechanisms for HER and OER, especially the emerging LOM for OER, could lead to new advances in overcoming the limitation of the traditional AEM by providing a new avenue for the design of better OER electrocatalysts (Chen and Hu 2020).

Despite the significant progress in understanding the electrocatalytic processes of the OER and HER, several challenges remain for the ultimate commercial large-scale production of hydrogen by water splitting electrolysis. First, the development of non-noble metal OER electrocatalysts with high activity and long-term stability performance in acidic media remains a challenging area of research and development. This challenge stems from the increasing use of proton exchange membrane (PEM) electrolysis are promising water electrolysis because of PEM's high energy efficiency and fast hydrogen production rate. PEM electrolysis for water splitting is operated under acidic conditions. For HER, there is various efficient non-noble metal electrocatalyst available in acid media. However, for OER, most of the efficient OER catalyst is Ir- and Ru-based electrocatalysts which have higher dissolution resistance in acidic condition. For non-noble metal-based electrocatalysts, most of them, cannot survive under such conditions. Thus, there is a clear need for the development of stable and robust non-noble metal OER electrocatalysts (Yang et al. 2021a). Recently, it was demonstrated a rational approach for designing non-noble metal based electrocatalysts that exhibit high activity and stability in acidic media by treating activity and stability as a decoupled elements of mixed metal oxides.

For example, manganese is used as a stabilizing structural element which is coupled to the catalytically active Co center in $CoMnO_x$ film. Secondly, there is a limited knowledge of the detailed catalytic mechanisms especially for transition-metal-based HER and OER electrocatalysts. The intrinsic active site of electrocatalysts cannot be completely determined based on the descriptor of TOF.

Recently, non-noble-metal-based carbides, phosphides, and chalcogenides have drawn great attention due to their high performance for OER in alkaline media (Huang et al. 2020). However, the nanostructured electrocatalysts undergo composition and structural transformations during the reaction under OER conditions. Therefore, understanding the structural transformation is required to determine the real active phases and sites. Gaining insight into the detailed mechanism, structural transformation, real active sites is critical for the rational design of the optimal performance catalysts. Integration of in situ characterization techniques and theoretical modeling is an advanced approach to gain insights into the structural transformation, reaction intermediates, and reaction pathways of the catalysts. Thirdly, it is difficult to directly compare various nano-structured catalyst materials based on the performance descriptors due to the different mass loadings of the catalysts on the electrode and the different materials of substrate which may affect the electron transfer rate by different electrochemical measurement methods. More effective electrocatalysts screening strategies are needed to establish the standard evaluation protocol for effective comparisons of the performances of catalysts from different research groups. Nevertheless, the surge of recent interests in nano-structure and lattice oxygen engineering of catalysts is expected to lead to new advances in the design of active, stable, and low-cost OER and HER electrocatalysts for the mass commercialization of water-splitting based hydrogen production (Wu et al. 2021).

In recent years, various low-cost materials have been demonstrated with great potential as efficient and stable electrocatalysts. For instance, transition metal sulfides, selenides, carbides, borides, nitrides, phosphides and nanocomposites are

utilized in HER; transition metal oxides, hydroxides, phosphates and polymeric carbon nitride are employed in OER. Although these materials have performed excellent HER or OER properties in their respective alkaline or acidic media, the water-splitting performance is usually unsatisfactory when organized the materials in the same electrolyte (Anantharaj and Aravindan 2020). Namely, the HER catalysts produce mass hydrogen but poor OER efficiency in acidic media; the OER catalysts present ideal OER performance but less hydrogen production in alkaline media. How to integrate outstanding HER and OER performance of a catalyst in one cell has been an important problem for determining whether it can be a qualified bifunctional catalyst.

The bifunctional catalysts are commonly required to balance electron donating-accepting characteristics and thus facilitating both HER and OER processes (Jin et al. 2019). Hence, an eligible bifunctional electrocatalyst is defined to integrate and simplify the water-splitting system to overwhelm the above problem and lower the manufacturing cost of hydrogen.

2   Design Principles

In recent years, non-noble metal-based hydrogen evolution catalysts, including cost-effective transition metal (TM) carbides, nitrides, sulfides, phosphides, and borides with various nano-structures have been intensively researched by institutions at home and abroad (Zhang et al. 2021a). Reducing the overpotential of cathodic hydrogen evolution reaction and realizing large current hydrogen production at low potential, to reduce electric energy consumption is the key to water electrolysis hydrogen production technology. To date, the research work of high-performance transition metal-based electrochemical hydrogen evolution catalyst can be mainly cataloged as the following three factions according to its activation mechanism:

– Promoting the active site density;
– Improving the conductive properties;
– Modulating the electronic structure.

Since the active site is an important place for the catalytic reaction to occur, increasing the coverage of the active sites per unit area is the most straightforward and effective solution for improving the activity of the catalyst (Yang et al. 2021b).

Increasing the intrinsic conductive properties of the catalyst to facilitate the charge transfer is a feasible route to improve the electrocatalytic activity (Raja Sulaiman et al. 2022). Combining the electrocatalyst with a highly conductive matrix is another effective strategy to improve the performance of the electrocatalysts. Studies have shown that the coated carbon layer can effectively prevent the Mo_2C nanoparticles from aggregating and oxidizing as well as impart them rapid electron transfer ability. The presence of heteroatom dopants, such as N and P, made the catalyst a great many of active sites exposed (Yu et al. 2022). Besides, the RGO substrates further enhanced the overall conductivity of the catalyst and improved the dispersion of Mo_2C nanoparticles.

Moderate proton adsorption on electrocatalysts is a prerequisite for decent hydrogen evolution reaction, which could be realized via modifying the d-orbitals features as well as tailor the Fermi level and in turn favors a more thermo-neutral hydrogen-binding energy G to accomplish a desirable electrochemical activity. It was confirmed by theoretical simulation and spectroscopic characterizations that N and P co-doped carbon could alter the surface electron states of the catalyst, and effectively reduce the adsorption strength of these phosphides to hydrogen and yield a ΔGH^* value close to zero.

So, electrocatalysts with increased active site density, improved electron transport properties and/or tailored electronic configuration were achieved, exhibiting not only prominent electrocatalytic HER activity, but also rapid kinetic metrics as well as superior stability, which may shed a new light on designing of great catalytic active and robust electrocatalysts towards efficient water splitting (Eftekhari 2017). Consequently, from which the following conclusions can be drawn: (i) exposing maximally the catalytic active sites of electrocatalysts is a prerequisite for decent HER; (ii) the charge transfer ability and electron configuration of the electrocatalyst also play decisive roles on the HER catalytic activity; (iii) the employed defect engineering, heterojunction designing, phase engineering, lattice strain, heteroatomic doping and constructing hierarchical structure on the basis of interfacial engineering strategies have profound amplification effect on both the activity and stability of HER electrocatalysts functioned via the arbitrary combination and integration of the three elementary factors described in above items (i) and (ii).

Based on the essential design concept, the further research on HER electrocatalysts in terms of structure, morphology, phase, and composition may be conducted from the following attempts:

 (i) Developing late-model atomically dispersed catalysts or neighboring single heteroatomic pairs. Since the atomic utilization rate of the single atomic catalysts is as high as 100%, the single atom possesses large specific surface areas, ensuring the maximum exposure of the active center. Moreover, there should exist a fascinating synergistic interaction between the neighboring single heteroatomic pairs.
 (ii) Exploring new types of metal/semiconductor Mott–Schottky conjunctions. The synergy between metal and semiconductor Schottky contact interface may impart the catalysts attractive charge transfer ability and desirable electron regulation, yielding outstanding electrochemical performances.
(iii) Anion and cation dual-substituting strategies may also provide a new concept to boost performance of precious metal-free electrocatalysts.

May these careful designing enables HER electrocatalysts with lower overpotential, high catalytic activity and stability, thus making transition metal compounds satisfy the requirements as much as possible of the industrialization of the electrocatalytic water splitting technology in the aspects of both cost and performance.

3   HER Electrocatalysts

Of many methods for H_2 production, making H_2 via electrochemical hydrogen evolution reaction (HER) and water splitting is a cutting-edge research area, but the method uses expensive noble metals and organometallic complexes for efficient electrocatalysis (Fig. 1).

Platinum group metals including Pt, Pd, Ru, Ir and Rh can provide free energy for hydrogen adsorption close to zero, which makes them highly active as HER electrocatalysts (Li and Baek 2019). As explained by the Sabatier principle, the moderate Pt–H bonding strength of Pt-based electrocatalysts can allow for optimized hydrogen adsorption and desorption on surfaces, which will lead to high catalytic efficiency in corresponding HER electrocatalysts. Pd, which is more abundant than Pt in the Earth's crust and ~ five times cheaper than Pt, is also a viable alternative because of a similar atomic size to Pt with a lattice mismatch of only 0.77%. Pd can also be used to adsorb large amounts of hydrogen not only on its surface but also in its bulk. As an even cheaper alternative to Pt, Ru also displays a moderate Ru–H bond strength [~65 kcal mol^{-1}(1 kcal = 4186 J)] that can provide low barriers for hydrogen desorption. To date, platinum group metals remain the most effective and practical HER electrocatalysts because of low overpotentials and fast HER kinetics (Hu et al. 2019). However, associated high costs and limited supplies hinder widespread commercial application. These metals (e.g., Pt and Ru) are scarce on earth, precious, and get dissolved easily during electrochemical processes. Thus, some cheap and stable alternatives are needed to reduce the use of noble metals.

Fig. 1 Elements for HER catalysis

Metal-organic frameworks (MOFs) are emerging as promising material owing to excellent properties of regular channels, high specific area, and abundant active sites. During the last decade, MOFs have been employed for chemical hydrogen storage, gaseous fuel storage, photochemical and electro-chemical energy storage, and conversion and overall water splitting for HER and oxygen evolution reaction (OER). Tremendous research is being done for hydrogen evolution by electrocatalysis, photocatalysis and chemo-catalysis. Different desired functional groups can be easily anchored over the surface of MOFs owing to their adjustable and designable channel size, channel structure and channel environment. Although MOFs show low conductivity and stability in alkaline and acidic media as pristine and composites, their derivatives are stable (Cai et al. 2022). Thus, it is better to use MOFs as precursors for synthesis of electroactive metal nanoparticles, their compounds, and other porous materials after undergoing several heating treatments. The resulting compounds have shown excellent catalytic performance for water splitting and oxygen reduction reactions. However, in heating treatment at very high temperatures, the ordered composition of active sites and MOF can be completely lost. MOFs possess designable structure, large channels, high surface area and very clear chemistry. Basically, MOFs are constituted by metal nodes and organic linkers, and these are the active sites for the catalytic process. Broadly, MOFs can be categorized into three types: pristine MOFs, composites of MOFs and MOF-derived materials. There is a good opportunity to introduce more catalytically active species in the metal nodes and linkers such as metals, porphyrin and bipyridine based ligands. Functionalization of ligands with electron-donating and electron-withdrawing groups have also been reported. Besides, MOFs provide good permeability and can act as templates for introducing active species with controllable geometry, constitution, and location. For HER, electrochemically active and conductive MOFs should be synthesized. In other ways, MOFs can be supported on conductive substrates, or a hybrid of MOFs can be developed for enhanced HER. In recent years many interesting reviews have been published in this emerging field. Several reviews are available in 2017, but after that several excellent results have been observed and none of the review is available on combined study for pristine composite and derivatives of MOFs for HER and overall water splitting. Presently, MOF-based electro-catalysts are being developed by substantial progress and interesting findings are reported continuously. In this view, for the development of efficient MOF-based electrocatalysts for hydrogen evolution reaction and overall water splitting, a summary of recent advantageous work in this field is of great significance.

Water splitting reactions during the electrocatalysis involve two half reactions that are hydrogen evolution reactions (HER) and oxygen evolution reaction (OER). OER is a complex process involving four electrons and several surface adsorbed intermediates. For HER, there should be a chemical bond between catalyst surface and hydrogen atom to facilitate the electron-proton transfer process, and the bond should be sufficiently weak for easy desorption of hydrogen from the catalyst surface. Evaluation of change in Gibbs free energy ($\Delta G*H$) is done through the HER free energy diagram, which is required for a study of hydrogen adsorption and

evolution from the catalytic surface (Zhang et al. 2019). HER reaches maximum when the value of ΔG^*H is zero. "Volcano curve" correlation is also very important, which is plotted in between HER activity (HER exchange current density) and ΔG^*H for different catalyst surfaces.

HER is one of the half reactions in the electrochemical water splitting process. The reaction is the same in different acid-base solutions. The HER electrocatalysts research is escalating for hydrogen production and only certain elements in the periodic table are favorable for this application. Two fundamental mechanisms are commonly observed in the HER catalysis, the Volmer-Heyrovsky mechanism and the Volmer-Tafel mechanism. Different reaction pathways involving in either of these mechanisms (Xu et al. 2020). In general, the HER mechanism involves two major reactions in acidic solution. HER's primary reaction step is the Volmer reaction or the release reaction in which the beginning of electron transfer is carried out. At first, the H^+ (H_3O^+) combines with an electron to form H^* deposited/adsorbed on the electrode surface. The adsorbed H^* is then removed/desorbed by two paths to form H_2. The first desorption step follows the Heyrovsky mechanism reaction in which the H^* atom in an adsorbed state merges with a free H^+/e^- couple form H_2. The second desorption step follows the Tafel reaction mechanism in which two adsorbed H^* combine to produce H_2.

It is experimentally observed, and high Tafel slopes indicate the Volmer reaction as the rate-determining step, which includes the adsorption of hydrogen on catalyst surface under low H coverage. HER electrode kinetics changes in distinctive solution in which different solution can lead to follow a distinctive process of electron transfer, which successively forms catalytic mechanism differently. Consequently, a catalytic mechanism should be discussed concerning a specific solution.

Commonly, noble metals such as Pt, Pd, Ir, Ru and Rh are used for this process because they can provide high active sites for hydrogen adsorption. However, these catalysts are considerably expensive to utilize in commercial applications. The use of these catalysts is insufficient and almost obstructed due to their high cost. To address this challenge, research were conducted on dispersing Pt-based electrocatalysts onto the surface of numerous materials utilizing specific atomic or sub-nanometric bands. Carbon nanotubes have been investigated in support of platinum. They showed promising results, platinum-based nanoparticles through additional treatment such as nitrogen doping which can activate π-electron in conjugated carbon (Meng et al. 2019).

The investigations associated with HER in PEME emphasizes the progress of electrocatalysts for the cathode. In most previous literature, platinum and palladium-based material have been used as an effective catalyst for the HER. The platinum provides superior HER activity and shows excellent stability in acidic conditions. Though, widely dispersed carbon-supported platinum-based materials are standard catalysts for HER in PEME. However, these platinum-based electrocatalysts are the costliest. Therefore, most studies focused on reducing catalysts and operational costs by enhancing the catalysts' specified production and durability. The insufficiency and high price of precious metal (platinum and palladium) used in the hydrogen evolution reaction of PEME are inappropriate for commercial application.

Therefore, three distinct approaches have been selected to reduce the cost of operation in PEME, such as declining use of precious metals, utilizing inexpensive precious metals, emerging inexpensive non-precious substitute catalysts (Anwar et al. 2021).

The Pt and Pt/C precious metal compounds are extensively used for the HER in the SOE process because they showed high electrocatalytic activity. The significant disadvantages of platinum catalysts in SOE are expensive and prone to Pt poisoning. Therefore, the alternative option is palladium (Pd) catalysts discovered by various researchers. The emphasis has been given to iridium oxide (IrO_2) and ruthenium oxide (RuO_2) for their superior electrocatalytic properties. Furthermore, more investigation has been conducted on carbon to improve precious metal catalysts and carbon as supporting material. There are several advantages to use carbon as supporting material on Pd, such as enhancing triple-phase boundaries for electrochemical half-cell reactions, the easiest way to release hydrogen gas due to porous metal catalysts and increased metal electrical conductivity.

The most promising transitional metals used in HER catalysts are Fe, Ni, Cu, Mo and W (Sun et al. 2020).

The qualitative procedure to predict heterogeneous electrocatalytic activity has been proposed by Paul Sabatier and stated that the catalytic efficiency is dependent on the absorption of heat on the electrode surface. In the present case of HER activity that it is observed to follow a volcano-type connection in the binding free energy of hydrogen should be adjoining to that of advanced platinum catalysts (Gibbs free energy tends to zero). Therefore, another metal to nickel (smaller Gibbs free energy than other non-precious metals) to form nickel alloys such as Ni–Mo, Ni–Co, Ni–Cu and ternary metals Ni–Mo–Zn is a favorable process to produce a higher performance of HER catalysts (Abuin et al. 2019). If two transition metal metals blended to give enhanced electrical conductivity, creating Ni–Co alloys an effective catalyst due to better inherent electrocatalytic activities and anti-corrosion performance in alkaline solution.

Another significant compound used for HER catalysts is transitional metal phosphides in alkaline media. These phosphides acquired higher electrocatalytic activity, considerable stability, and bifunctional characteristics for both HER and OER electrocatalysis. Transitional metal phosphides have superior electrical conductivities compared with resultant transitional metal oxides. Consequently, because of this property, nickel-based phosphides getting enormous importance as HER catalysts.

Cobalt oxides can be used as an HER electrocatalyst in which the catalytic properties showed the most negligible electrical conductivity. To improve the electrical conductivity of the catalysts, the growth of electrocatalysts should be directed on the conductive samples such as carbon nanotubes, graphene, metal foam and carbon cloth.

More weight percentage of phosphide (P) in cobalt phosphide exposed more active locations on the catalyst's surface. Therefore, increase the rate of P can drastically improve cobalt phosphide catalytic activity.

They were developed transitional metal sulphide (TMS) and transitional metal phosphorous (TMP) compounds with similar function for the HER electrocatalytic process (Premnath et al. 2022). They proposed that the sulphur atom's electronegativity is superior to the phosphorous atom, larger bond strength is produced between sulphur and hydrogen. Therefore, overpotential is significantly increased, leading to a reduction in HER electrocatalytic efficiency. Cobalt sulphide is hardly used as a semiconductor as an HER catalyst, while it has exceptional properties such as thermodynamic stability in acidic media.

Cobalt selenides ($CoSe_2$) are a favorable catalyst due to their optimum electronic arrangement within cobalt-based electrocatalysts. All materials attained superior electronegativity and are easier at pull towards positively charged protons to support HER electrolytic process. A similar on-site oxidation reaction formed a cobalt-based oxide that coincides with the catalyst proceed OER process. Whereas the strength of the Se–H bond is lower than the P–H bond and S–H bond, the cobalt selenide (Co–Se) generates a better hydrogen discharge rate than those of cobalt phosphide (Co–P) and cobalt sulphide (Co–S) at the HER electrocatalytic process (Zhang et al 2020).

Transition metal carbides have been studied and investigated as a potential substitute for precious metal electrocatalysts in PEME electrolysis due to their low cost, high availability, high surface, high-surface-area, and high electronic conductivity. As a result, transitional metal carbides are used to obtained comparable electrocatalytic properties as platinum metal. Moreover, the transitional metals explored for these applications are Ti, V, Mo, Ta and W, and these are significantly abundant in nature and inexpensive. However, they cannot be used independently because they exhibited a higher overpotential of 0.300 V vs. RHE (V) than pure platinum metal. However, they are used as supporting material for precious metals in which platinum loading reduces PEME electrocatalytic operating cost.

The carbon-supported electrocatalysts, particularly earth-rich, inexpensive nanomaterials encapsulated in nickel doped graphene, are comprehensively studied in possible HER electrocatalysts for substitutive to platinum. These materials are molybdenum disulphide supported carbon nanotubes (MoS_2/CNTs), nickel phosphide supported CNTs (Ni_2P/CNTs), cobalt doped iron disulphide CNTs (FeS_2/CNTs), tungsten dioxide supported carbon nanowires (WO_2/C) and Co–Fe nanoalloys (Li et al. 2023). However, these platinum-free carbon-supported HER catalysts have been investigated for PEME application but rarely reported. Among these electrocatalysts, MoSx and palladium-based nano carbons appeared to be the most efficient and active electrocatalysts in the context of HER electrocatalysis.

The SOE cell mechanism is opposite of the solid-oxide fuel cell; thus, the anode/cathode of a fuel cell can be used as the cathode/anode for the electrolysis cell, e.g., nickel-yttria-stabilized zirconia (Ni-YSZ) is generally used as an anode in fuel cell and also a common cathode in the SOE electrolysis cell for hydrogen production. However, Ni-YSZ showed low stability and required high hydrogen concentration to protect nickel from oxidation. This is the reason for nickel agglomeration during the long-lasting high temperature of the hydrogen process. This problem can be addressed by using redox perovskite oxides as the electrode in the hydrogen production process.

The most optimal HER electrocatalysts can reduce energy and cost compelled for electrochemical water splitting through the decreased overpotential. Therefore, research development to produce efficient non-precious electrocatalysts for HER is critically important and challenging. Recently, cobalt and nickel-based electrocatalysts have been extensively used as an HER electrocatalysts in the water electrolysis process. This research provides a comprehensive understanding of the latest Ni and Co-based electrocatalysts, including nickel-based alloys, nickel-based phosphides, cobalt oxides, cobalt phosphides, cobalt sulphides, cobalt selenides, and some are other transitional metal-supported nanomaterials such as molybdenum disulphide supported carbon nanotubes (MoS_2/CNTs), nickel phosphide supported CNTs (Ni_2P/CNTs), cobalt doped iron disulphide CNTs (FeS_2/CNTs), tungsten dioxide supported carbon nanowires (WO_2/C), Co–Fe nanoalloys, and nickel-yttria-stabilized zirconia (Ni-YSZ). They are the most effective and active electrocatalysts for HER electrocatalysis.

4   Metals and Alloys

The catalytic activity of non-precious metals is in the order of:

$$Ni > Mo > Co > W > Fe > Cu > Mn$$

However, poor stability in strong acid or alkaline electrolytes is regarded as a major issue of pure non-precious metal catalysts. In addition, less advantages can be observed for transition metals in the conventional forms of bulk or aggregated particles. The introduction of supports or substrates can not only disperse and protect metallic core from corrosion in the harsh environment, but also speed the catalytic reaction.

Coupling transition metals with various nitrogen doped carbonaceous materials is a common method to promote the water splitting performances (Chang et al. 2021). For example, Ni nanoparticles catalyst on the nitrogen doped carbon to conduct the overall water splitting. It is suggested that carbon support can help Ni particles disperse and reduce the contact resistance between them and the surface nitrogen sites, adjust the electronic states of the catalytic centers to enhance the catalytic activity. Among numerous carbonaceous materials, graphene is another kind of typical and excellent selections. They were fabricated Ni nanoparticles (Ni NPs) encapsulated in few-layer nitrogen-doped graphene (Ni@NC) (Fig. 2).

The synergistic effects between the Ni NPs and the N-doped thin graphene shell resulted in highly efficient and ultra-stable overall water splitting performance in alkaline media with an operation voltage of 1.60 V to achieve the current density of 10 mA cm^{-2}. To enhance the performances, many different forms and dimensions of carbon materials were also gathered in one system. Meanwhile, coupling these carbon materials with defective metals could further optimize the intrinsic activity of active sites and Gibbs free energy of adsorption.
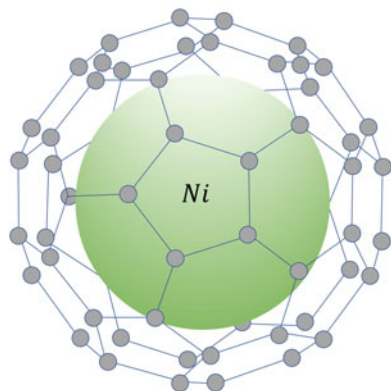
Constructing multi-metal system is a promising way to look beyond the single metals, since the alloying could tune the d-band electron filling and impact the affinity of the alloy electrocatalyst toward the adsorbate species of interest.

For decades, nickel-based and cobalt-based alloys have been widely studied due to their low-cost and competitive activity. Among nickel-based binary alloys, the electrocatalytic performances towards to HER were concluded in the following order:

$$Ni - Mo > Ni - Co > Ni - W > Ni - Fe > Ni - Cr$$
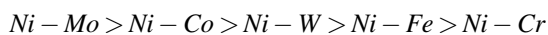
Diverse morphologies, such as nanoparticles, microspheres, hollow nanorods, nanowires, etc., have been fabricated to increase the active sites and boost the overall water splitting performances. In addition, the structure of supports or substrates is also an important factor in designing alloys electrocatalysts. They were prepared bimetallic nickel–iron alloy nanoparticles encapsulated and dispersed in nitrogen-doped bamboo-like carbon nanotubes. The NiFe/NC‖NiFe/NC two-electrode system only needed 1.58 V to drive the overall water splitting at 10 mA cm^{-2} without obvious degradation in 24 h. Besides those commonly used conductive materials, other materials with unique morphology could also be good choices of supports. Reported a MoNi4 electrocatalyst anchored on MoO_2 cuboids arrays exhibiting a very small overpotential of 15 mV at 10 mA cm^{-2} and a low Tafel slope of 30 mV dec^{-1} in 1 M KOH for HER. The Density Functional Theory (DFT) calculations indicated that the Volmer step was fully speeded up with the introduction of MoNi$_4$ electrocatalyst (Fig. 3).

Poor stability in acid electrolyte is regarded as a major problem for metal-based catalysts especially for OER. Similarly, most of metals enhance their oxidative corrosion and OER efficiency by means of carbon protection and contribution, respectively. Some precious metal, such as Ir, is an ideal and stable catalyst for OER in acidic condition. Introducing non-noble metal, such as Ni, Co and Fe, into Ir is another way to reduce usage and optimize catalytic performance. A monodisperse IrM (M = Ni, Co, Fe) nanoclusters (1.5–2 nm) on carbon substrate have shown a low
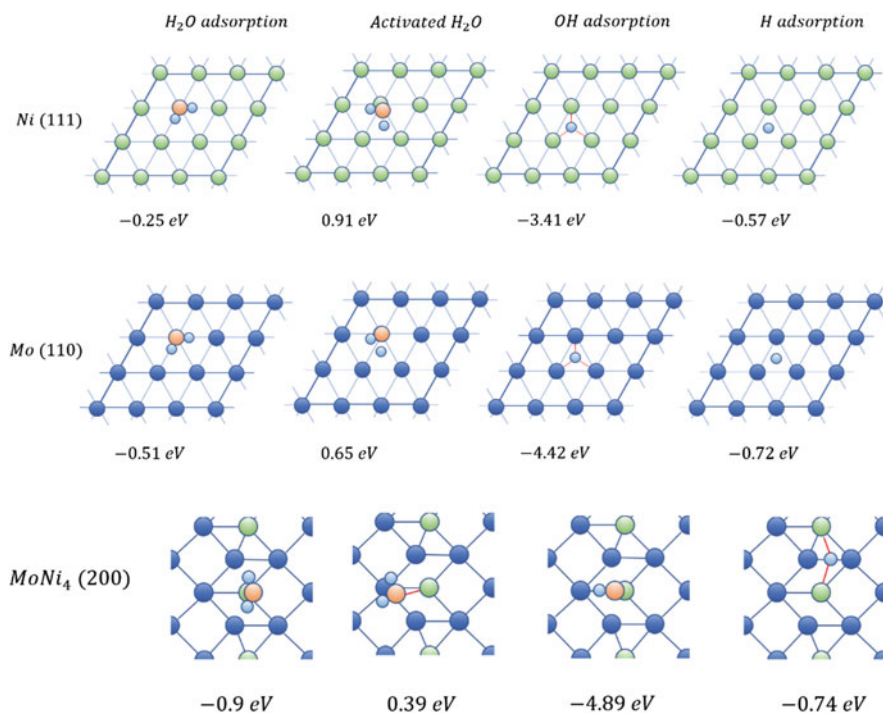
Fig. 3 Calculated free energies of H2O adsorption, activated H2O adsorption, OH adsorption and H adsorption

cell voltage of ~1.58 V at 10 mA cm^{-2} in acid solution. These research works open a new area of designing and synthesizing acidic stable bifunctional electrocatalysts for overall water splitting.

The functionalized supports and substrates could enhance the catalytic performances from the following aspects: (1) increasing the density of accessible active sites; (2) boosting charge transfer from conductive supports to catalyst surfaces; (3) constructing catalyst-support interaction to adjust the electronic states of the active sites or direct participation in the reaction. Meanwhile, non-metal element doping is another remarkable strategy to enhance intrinsic activity of catalysts.

Incorporating the third or more metal into a binary alloy could enhance the OER performances and be good for HER, especially if the content of dopants could be precisely regulated.

5 Transition Metals Oxides and Hydroxides

As is well-known, metal oxides and hydroxides are poorly stable and begin to dissolve when they are exposed to highly acidic solution at highly oxidized overpotentials unless precious RuO_2 and IrO_2. Hence, metal oxides and hydroxides have not been applied to water splitting for a long time until it was demonstrated an impressive water photolysis efficiency of 12.3% by using efficient NiFe layer double hydroxide bifunctional catalyst. Only 1.7 V voltage (iR uncorrected) is required at 10 mA cm^{-2} overall water splitting current in alkaline solution. This immediately evoked great focus on metal oxides and hydroxides served as bifunctional materials with low overpotential and long-term stability (Xu 2020).

About single metal hydroxides, the electrocatalytic performance could be achieved by increasing the number of active sites through the design of morphology and electrode structure. Direct growth of single metal hydroxides on conductive agents becomes a highly effective way to make active and durable electrode for water splitting. In addition, metallic foam or foil is another good choice for growing single-metal hydroxides.

Although single-metal hydroxides electrocatalysts have made progress in water splitting, the introduction of other metals could modulate 3d electronic structures to further boost the performances. In recent years, several double-metal hydroxides such as Ni-Fe, Co-Fe, Ni-Co, Mn-Co, and so on have been served as catalysts in water splitting (Loh et al. 2020).

In addition, some conductive materials with varied morphology are adopted.

Introducing defects into double-metal hydroxides is another viable strategy to enhance the intrinsic activity. Incorporation nonmetallic dopants with double-metal hydroxides is also effective for improving intrinsic activity. For example, nitrogen atom could change the electronic structure of metal hydroxides and impart them with the suitable water separation energy.

In addition, introducing two or more cations could better adjust the electronic structure and atomic arrangement to produce more active center. Ni, Fe, Co are common dopants for improving electrocatalytic properties. In addition, doping high-valence metal ions could effectively draw electrons to the valence band of neighboring 3d metal ions for accelerating the catalytic process.

Support engineering has also been widely investigated in metal oxides in influencing the electronic properties, which, in turn, affect on catalytic activities. Similarly, the multiple metals could fine tune the adsorption energy of related intermediates in multiple metals oxides. In general, OER activity continuously increases with increasing Ni contents, while HER activity shows an opposite trend with preferably higher Co contents.

As another representative multi-metal oxide, perovskite oxides, have been adopted as a new category of efficient electrocatalysts for OER and ORR in alkaline solutions owing to their physical, chemical, and catalytic properties.

No matter single-metal or multi-metal oxides, other strategies focused on increasing active sites and intrinsic activities have been investigated to boost the water splitting performances. Morphology design is always one valid way to expose more active sites.

Engineering defect sites is also a positive way on modifying the electronic structure of metal oxides and enhancing the intrinsic electrocatalytic activities. Rich defects and grain boundaries can provide abundant active sites, leading to an improved OER activity as well as appreciable activity for the HER.

Inspired by studies in batteries, electrochemical intercalation/extraction method is a promising strategy to tune the composition and strain of different existing catalysts continuously and controllably and thus possibly improve their catalytic activities dramatically.

Utilizing metal oxides as one block of composites is another favorable strategy for accelerating the HER and OER kinetics by optimizing the chemisorption of precursor molecules or/and reaction intermediates. The interfaces between components in the composite could produce higher activity than single component. For example, the introducing of metal hydroxides made the catalytic metal sites more active and most importantly strong synergistic effects existed at the interfaces. Compared to metal hydroxides, assembling single metal or alloys could tune the electrical conductivity, intrinsic HER activity and stability through modifying intermediate bonds and electronic structure of metal oxides.

Like NiO, cobalt oxides have also received enormous attention in building efficient electrocatalyst. Metallic Co could preferentially absorb H atom due to its lower binding energy of H atom in the Co@CoO system, while CoO would speed the adsorption of OH^- due to the positively charged Co^{2+} species. Furthermore, CoOx plays an important role in Co-based oxides due to the mixed valence states of $Co^{2+/3+/4+}$. In addition, the coupling effects of single metal and single metal oxides could be extended to alloy and multi-metal oxides.

In general, Ni atoms are recognized as excellent water dissociation centers, while Mo atoms own superior hydrogen adsorption properties. Therefore, NiMo-based catalysts can serve as more promising candidates than NiCo-based catalysts for water splitting. Likewise, the synergistic effect between nanoalloys and defective oxides resulted in abundant active sites exposed, high electrical conductivity, and low charge-transfer resistance, thus leading to particularly excellent HER and OER activities.

6 Transition Metals Chalcogenides

Recently, 2D MoS_2 nanosheets with rich edge sites have been studied as a promising electrocatalyst for HER. Inspired by this, many researchers have spent intensive attention to explore suitable metal chalcogenides as efficient electrocatalysts applied in whole water splitting (Jo et al. 2021). Heterogeneous doping can effectively improve the electronic conductibility of carbon materials, and thereby enhance both HER and OER catalytic activities.

In general, binary transition metal sulfides show higher intrinsic HER and OER activities than single metal one. Because the valence electron orbit of 3d metal can be tuned to modify the electron donating and accepting characteristics, and to enhance the charge transfer and reduce the kinetic energy barrier. Comparing with metal dopants, anion decoration could regulate the electronic structure but with little influence on the crystal structure and catalytic active sites, preferentially optimizing the adsorption energy of reactive species to greatly increase the electrocatalytic activity. Based on cation and anion doping strategies, the mutual substitutions on metal sulfides may preferably tune the hydrogen adsorption free energy to improve water splitting performance.

The strong interfacial coupling effects between transition metal sulfides are crucial to optimize their bifunctional electrocatalytic performances. Taking nickel sulfides (e.g., Ni_3S_2, NiS_2, NiS, etc.) as examples, they performed a limited activity for overall water splitting, that is, highly active for OER but unsatisfactory activity for HER (Ding et al. 2019). Heterogeneous nanostructures not only bring highly active OER properties, but also produces numerous active sites and electron-reconfigured interfaces. The interfaces were beneficial for the chemisorption of hydrogen and oxygen-containing intermediates, thus accelerating the overall water splitting. As mentioned above, bimetallic sulfides may afford richer redox active sites than the single metal sulfides.

Furthermore, coupling transition metal sulfides with metal oxides or hydroxides is valid to construct interfaces and further enhance the performance. To summarize, engineering of heterostructures interface with metal oxides or hydroxide could be a prospective strategy for efficient overall water splitting.

The radius of Se is larger than that of S, the metallic property of Se is more obvious than S, the ionization energy for Se is smaller than that of S. As a result, some special attributes associated with metal selenides make them more appealing in water splitting compared with metal sulfides. Different from traditional conductive current collectors and carbon materials, the metal–organic framework (MOF)-derived porous carbon not only provides vast channels to accelerate electron/ion transfer, but also reacts with metal species through an in-situ carbonization.

Doping non-metal elements is remarkable to modify the physical and chemical properties of selenides. Theoretical calculation revealed: i) The phosphorus dopants immensely optimized the adsorption free energy of H atoms on the active sites; ii) The synergistic effect between Se vacancies and P displacements around the vacancies accelerated the charge transfer speed and the proton kinetics. When integrating the material as both anode and cathode, a low voltage of 1.64 V was applied to achieve a current density of 10 mA cm^{-2}.

Currently, some mixed transitional metal selenides have been reported showing high electrocatalytic performance owing to the high donation of Jahn-Teller effect. The significant mismatch in the Jahn-Teller distortion degree of Ni and Co led to a subtle atomic arrangement and offers more active sites. The incorporation of heterogeneous spin states of Co atoms into nickel selenide could trigger Jahn-Teller effects and offer more active sites and promote the catalytic activities.

Constructing hybrid materials could efficiently boost the catalytic performance by the coupling effects between different components.

7   Transition Metals Phosphides

Transition metal phosphides (TMPs) are known with favorable mechanical strength, good electrical conductivity, and high electrochemical activity for HER and OER (Kim et al. 2021). During OER process in alkaline condition, the transition metal on TMPs could be readily oxidized into high valence oxo/hydroxo-species, which can serve as the active sites for catalysis. And the electrically conductivity of TMP facilitates the charge transfer and thus markedly accelerates the OER kinetics. In case of the HER, P atoms can participate in the reaction and form a moderate bond with intermediates and products, thus facilitating the proton reduction. 3D CFP electrode with vertically aligned Ni-P nanosheets exhibited excellent HER and OER performance with a low cell voltage of 1.5 V in the water electrolyzer and a superior long-term durability, even comparable to the state of art Pt/C (20% Pt) and RuO_2. Moreover, similar research including Ni-P foam, Cu_3P supported on Ni foam, core–shell CoP nanoparticle-embedded N-doped carbon nanotube, and Co-P film on copper foil etc., have also been extensively investigated.

The morphological structures of the electrocatalysts play a major role in accelerating the chemical reaction rate. Hollow structures have been accepted as a beneficial way to enhance the electrocatalytic performance, due to a large active area and high density of active sites exposed, and abundant interior space for smart mass diffusion pathways.

Substituting a second or more metals into monometallic phosphides could effectively alter the electronic structure of the parent compounds to tune the hydrogen (or water) adsorption energy and enhance the catalytic activity. The NiCoP catalyst demonstrated more excellent electrocatalytic properties than NiP and can be used as both cathode and anode for overall water splitting with high efficiency and excellent long-term durability. DFT calculations confirmed that Co substitution affected the electronic structure of Ni2P and the surface adsorption energy of the reactants, thereby leading to the high HER activity of NiCoP. Moreover, the NiCoP-derived oxides provided the real active sites for OER.

Furthermore, the different morphologies such as, NiCoP hollow nano-bricks, hierarchical nano-cone arrays, yolk-shell spheres, MOF derived nanotubes on Ni foam, have also been designed to expose more active sites. These regular morphologies indeed exposed more active sites and produced fast and facile transport of electrons and gases.

Actually, a great number of research works have also been done to study the other bimetallic phosphides, such as, NiFeP, FeCoP, CuCoP, NiMoP. Ni might modify the electronic states of Fe and P and lower the charge-transfer resistance (Feng et al. 2022). The porous Ni-Fe-P nanostructures showed faster electron transport and accelerated kinetics during the water electrolysis. Fe-tuned Ni_2P electrocatalysts

with controllable morphology and structure were also synthesized via simple hydro-thermal method and subsequent in situ phosphorization. It revealed an ultrasensitive iron species-triggered electrochemical behavior. The optimal of Ni and Fe endowed the sample with stronger binding force, more accessible active sites to electrolyte ions and enlarged space for gas release.

Mn and Cu as naturally abundant elements are also doped into TMPs. Cu doping led to more free electrons, less Co-P covalent bonds and thus improved electrical conductivity. Cu doping can also alter the ΔGH^* value being closer to thermos-neutrality in both CoP and Co_2P systems, facilitating the reaction kinetics. Among the binary metal dopants, Ni-Mo-based phosphides showed attractive performances owing to the high electrical conductivity of Mo and high electrochemical activity of Ni. Some researchers even added two or more metals into phosphides, owing to the synergic effects between the cation dopants.

In the case of non-metal-atom doping, the incorporation of like N, S, O etc. into TMPs can also enrich charge density and modify the electrocatalytic performance. Benefited from the introduction of N, electronegative P atoms was achieved to grab electrons from Fe centers and serve as the base to trap protons, creating more active sites for effective HER activity. Regarding to OER process, N atoms can properly modify the bond strength between FeP and oxygen (O), thus endow the expedited oxygen evolution for excellent OER performance of N-FeP catalyst. Additionally, S doped NiCoP nanosheet arrays with rich P vacancies (A-NiCoP|S) were developed and showed the improved electronic structure as well as the optimized free energy of hydrogen adsorption, leading to the promoted catalytic performances. The low overpotentials of 88 mV for HER and 264 mV for OER at 10 mA cm^{-2} was achieved for A-NiCoP|S as bifunctional electrocatalysts.

The ratio of cation and anion is decisive to the electrocatalytic activity. It was demonstrated that O doping can not only elongate $M - P$ (M = Mo, Co) bonds but also enhance the intrinsic conductivities of TMPs because of much higher DOS across the Fermi level and facilitated electron transfer.

To sum up, the introduction of O- into the TMPs resulted in more easily occupied 3d orbit of cations, giving rise to frequent electron transfer between different metals and their strengthening oxophilicity (e.g., $M - OH$ bond strength) to facilitate the OER initialization.

8 TMPs Based Composites

The multi-component hybrids were proved to effectively improve electrocatalytic performances. Given that semiconducting metal phosphides and metals are hybrid-ized, Mott-Schottky interface emerges and promotes the electron transfer, thus improves the HER activity for metal and OER performance for metal phosphides. So the Mott-Schottky hybrids is a proof-of-concept strategy. For example, Mott-Schottky typed Co/CoP electrocatalysts based on Janus nanoparticles exhibited high activity for HER and OER, complete water splitting, and long-term stability in the

electrolyte solution over a wide pH range of 0–14. The activity enhancement can be ascribed to the redistribution of electrons at the Co/CoP interface and the lowered valence band of CoP, so that the electrons can flow through the Co/CoP interface smoothly.

The electron transfer of the conductive carbon framework can boost the electronic conductivity, and the confinement effect of carbon matrix also inhibits the aggregation of nanoparticles and improves the dispersion of TMPs. Heterogeneous co-doping in carbon materials can significantly improve electrocatalytic performances owing to the synergistic effects between the doped dopants. Cobalt phosphides confined in porous P-doped carbon matrix (Co-P@PC) exhibited outstanding electrochemical performance and excellent long-term stability. These high efficiencies can be ascribed to the synergistic effect between the intrinsically active Co-P, porous P-doped carbon matrix, and thin carbon layer.

High temperature pyrolysis of metal–organic frameworks (MOFs) and then phosphidation is a facile approach to produce porous TMPs and carbon coating simultaneously.

Under alkaline conditions, anodic polarization was convenient to produce oxidation or hydroxide as the active center. Therefore, the combination of TMPs with transition metal oxides might synergistically promote the HER and OER processes (Theerthagiri et al. 2021). In addition, nanocomposite structure can create active sites at phase boundaries, which would promote H atom adsorption and desorption on catalyst through adjusting the charge distribution among different components.

The electrocatalytic properties of TMPs nanomaterials can also be well improved through interface engineering. FeOx/FeP hybrid nanorods are efficient electrocatalyst in wide pH range. The abundant interfaces between FeOx and FeP can not only facilitate the water adsorption and dissociation but also optimize the Gibbs free energy for hydrogen adsorption.

Phosphorylation can increase phosphate groups and absorb energy to reconstruct high energy bonds. The catalytic performance can be greatly improved by phosphorylation modification, owing to the efficiently tuned chemical composition and surface electronic state.

9 Other Compounds

Transition metal borides (TMBs) are also endowed with some special characteristics for water splitting, which have attracted soaring attention (Wang et al. 2020). In some amorphous TMBs systems, reverse electron transferred from boron to metal will cause electrons accumulated at metal sites, facilitating the electrochemical reactions. The inevitable surface oxidation of TMBs results in the active species like borates, boron oxides, TM oxides, and so on. This will greatly affect the catalytic reactions, and their HER and OER activity were indeed investigated as early as the 80′s in the last century. TMBs displayed great potential to be applied as electrocatalysts in a wide pH range. The boride content is crucial to the catalytic

properties. In theory, the boron-rich active sites promote the charge density redistribution and thus facilitate the balance of chemisorption and desorption of reaction intermediates, so that the ΔGH^* is closer to zero to favor the HER process. Anchoring TMBs on conductive carbon nanomaterials can also yield high catalytic activity and good stability.

Transition metal nitrides (TMNs) have recently received increasing attentions (Lin et al. 2022). They are interstitial compound containing the parent metals and N atoms inserted into the interstitial sites. Bimetallic nitrides with a rich class of fascinating compounds are better than monometallic nitrides in the electrocatalytic performance.

Transition metal carbides (TMCs) possess good corrosion resistance, strong stability and mechanical strength, high catalytic activity, and selectivity. Since the discovery of Pt-like catalytic behaviors of tungsten carbide in 1973, metal carbides have immediately attracted great interests and attentions. Simultaneously, many strategies mentioned above have also been adopted to improve the water splitting performances of TMCs. Nickel carbides (NiCx) is also an ideal prototype to fabricate high-performance electrocatalysts owing to the low cost and superior electric conductivity. Some strategies including heteroatom doping or combination with carbon substrates, were also utilized on metal carbides catalysts for higher catalytic activities. High-index facets have a high density of atomic steps and kinks and can act as active sites.

In recent years, non-metallic nano-catalysts, particularly the heteroatom-doped carbon nanomaterials become a new horizon in the field of catalysis. It takes unique advantages, e.g. environmental friendliness, low cost, high electrocatalytic activity, stable chemical structure and strong tolerance to acidic/alkaline environments. Furthermore, their OER and HER can be distinctly altered through changing the local charge density and asymmetrically spinning the density of carbon lattice. N doping in multi-walled CNTs demonstrated that pyridinic N moieties were active sites for HER and OER due to their unique electron-withdrawing effect. Moreover, considering the coupling effect from co- or tri- heteroatoms doping in carbon materials, N and F dual doped porous graphene nanosheets (NFPGNS) were prepared as efficient bifunctional metal-free electrocatalysts. The co-doping could effectively modify the electron acceptor–donor properties and electronic states around C, leading to strong adsorption and lowered $|\Delta GH^*|$ value.

To date, the optimizing strategies and the effects on the active sites and the intrinsic activities as well as on the performances are: (1) morphology engineering is utilized to expose more active sites; (2) conducting supports are used to improve the electrical conductivity and accelerate the transportation of electrons and ions; (3) multi-metal and defect engineering are implemented to fine tune the electronic configuration and states; (4) hetero-structures and/or interfaces are constructed to synergically boost water splitting performance. In practical applications, the combination of hybrid strategies is more effective in balancing OER and HER performances. Although gratifying developments have been made in electrocatalysts for overall water splitting, there is still some problems to be solved for potential applications in HER and OER (Fig. 4).

Fig. 4 Illustration of future perspectives for enhancing the performance of electrocatalytic water splitting
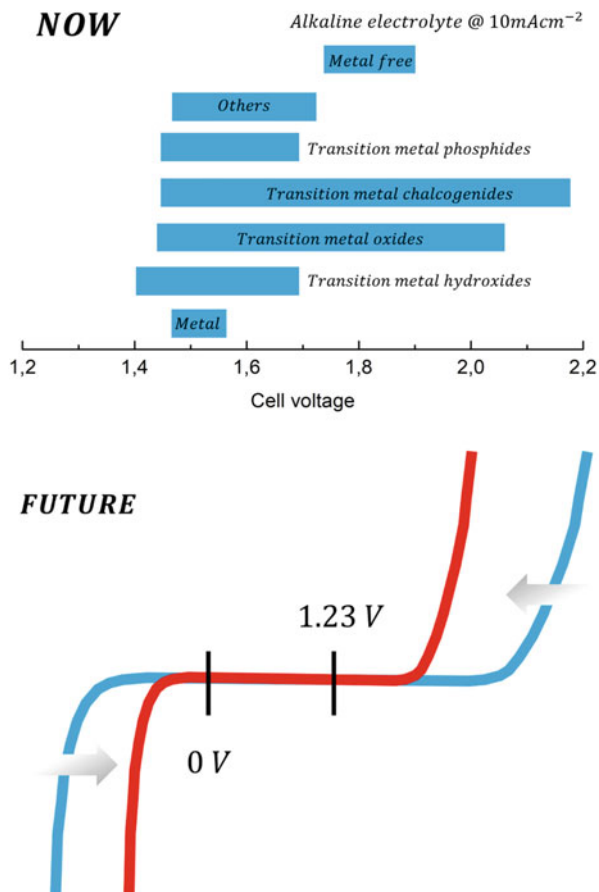
10   OER Catalysts

From the mechanistic point of view, the most popular proposed reaction schemes involve the coupling of electron and proton transfer in every step. If this coupling was always present in the oxygen evolution reaction pathway, it would put severe limitations on the optimization of the catalysts (Stelmachowski et al. 2021). In such a case, the energy barrier for each of the electron transfer steps would be different, and thus at least one would be higher than 1.23 V and the thermodynamic potential of the overall reaction could not be attained (Fig. 5).

However, highly active OER catalysts can be designed as multi-component materials, where the proposed linear correlation of the binding energies of intermediates (scaling relations) are valid no more, and other mechanisms may come into play. Nonetheless, high catalytic activity is only one of the requirements for a practical application of an OER catalyst in water splitting devices since the catalytic materials are also required to exhibit long-term stability.

Fig. 5 Energetics of OER over RuO2. Red, solid lines depict the Gibbs free energies of the reaction intermediates at three different external potentials $U = 0$ V, $U = 1.23$ V, and $U = 1.60$ V. Only at 1.60 V are all the reaction steps thermodynamically favorable. Green, dashed line depicts the ideal 1.23 V barrier for all of the reaction steps
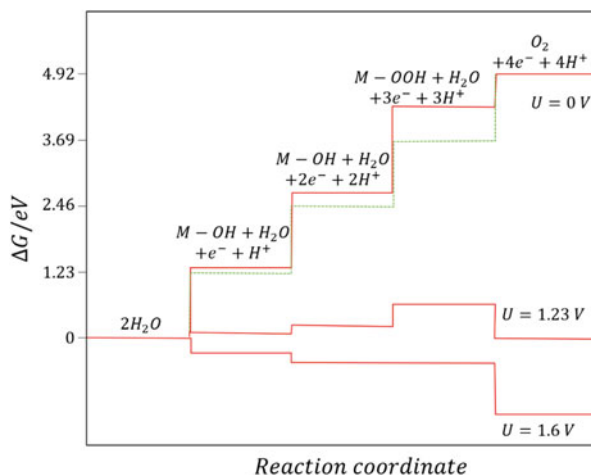
Oxygen evolution reaction (OER) is the second half-reaction in the electrochemical water splitting process that occurs at the anode and requires four-electron transfer. Generally, OER processes involve incredibly high overpotential compared to HER. OER is recognized as the primary congestion in recovering the overall energy efficiency of the water electrolysis process. Therefore, it is necessary to obtain highly efficient OER catalysts that can successfully decrease the kinetic barrier (Xu et al. 2021).

There are three intermediate products (O∗, OH∗, OOH∗) in the OER reaction mechanism. Therefore, the production of oxygen followed two different routes in acidic or alkaline solution. The OER reaction mechanism is quite similar in other pH solutions. The change is that OH− is absent in acidic solution. Thus, M reacts with H2O to produce MOH. Afterwards, MOH constantly encounter electron transfer to form MO. The MO and O_2 can be made by two different processes in which the first approach led to combine two MO to form O_2 directly, and the second approach is to let O_2 continuously react with MO to produce MOOH, and later it reacts with MOOH to form O_2.

At different pH of the solution showed similar OER mechanism and the distinction is that OH− is not present in acidic solution. Therefore, M reacts with H_2O to produce MOH. Consequently, the MOH continues to experience the transfer of electrons to form MO. After the formation of MO, O_2 can be formed in the solution by two different paths. One approach is the decomposition of MO to form O_2 directly, and the second approach is to let H_2O or OH− further react with MO to produce MOOH. MOOH decomposes to form O_2. According to the Sabatier principle, the adsorption is excessively weaker to have adsorption. However, adsorption is strong to cause desorption, and only a catalyst with moderate binding capability is suitable. As a result of this process, it can be presumed that when the adsorption bonding on O and the catalysts is excessively weak, the formation of OH∗ does not readily form OOH∗. The catalyst's performance can only reach the peak when the combined bonding capacity of O with the catalysts is un under moderate conditions.

The primarily used precious catalysts metals are Ir and Ru due to their superior stability, lower Tafel slopes and less overpotential. However, Pt and Pd have also been used, but their energy efficiency is lower than the Ir and Ru. The oxides of Ir and Ru, such as IrO_2 and RuO_2, are active and stable than their pure metal because metal is extra soluble than oxides in prime electrolytes. The metal oxides decreased stability and potential for commercial applications.

In electrochemistry, high-porous textured materials with a large surface area can provide various advantages. For example, precious metal catalysts with porous structures exhibited high catalytic activities for OERs dur to their high surface area. The most common route to synthesize porous metal catalysts is polymeric or inorganic pellets such as polystyrene (PS) and polymethyl methacrylate (PMMA) or silica beads.

Consequently, producing a large scale of hydrogen energy needs various noble catalysts that lead to an increase in the cost to produce hydrogen at the commercial level. As a result, a practical approach is to employ nanoparticles metal such as Au, Ag, Pt, Ru, RuO_2, Ir, IrO_2, and NiRuP to deposit on the carbon surface. The electrocatalytic properties of nanoparticles are significantly superior to the pure metallic system. Moreover, performance can be further enhanced by using bimetallic nanoparticles electrodeposition of carbon surface. The catalytic performance advancement can be allocated to the formation of nanoparticles active sites for quick detachment and superior electron transfer.

The strategic process to enhance the OER catalyst energy efficiency is to alloy Ru or Ir with other transition metals such as metal oxides, hydroxides, sulfides, phosphides, nitrides, and selenides showed superior electrocatalytic properties.

The PEME technique has been continuously available for more than ten years for commercial purposes. However, costly materials are usually necessary to attain higher energy efficiencies and lengthier processes than alkaline water electrolysis. This PEME technology retains numerous advantages such as superior current density, a pure rank of hydrogen, safe operation because of a solid polymer electrolytic separator. Therefore, the PEME technique has an evolving rate of future interest, including the development of fabricated materials and different components. Commonly used OER electrocatalysts include Ir and Ru oxides, in which Ru oxide shows better performance than Ir oxides due to improved electrocatalytic performance.

The SOE electrochemical process is the reversal mode of a solid oxide fuel cell (SOF). SOE oxygen evolution reaction occurs at the anode, which is the limiting element of SOE. Typically, anodic OER performance needs to be enhanced, and one critical process is the incorporation of precious metals such as platinum (Pt), palladium (Pd), and silver (Ag) used as an anode. Conversely, the catalytic effect of precious incorporated metal has not been extensively investigated and studied, and less inapplicable literature is available.

Efforts have been made to develop efficient noble-free OER electrocatalysts. Several research and strategies enhance active metal sites by monitoring composite texture, composition, morphology, and the intermediate product's binding energy through material doping. Additionally, analyzing and incorporating hybrid structure

into the precious metal composites to increase the energy efficiency of OER electrocatalyst. One recent approach to address this problem is to analyze the transition metal and their composites compound, to replace the noble metals electrocatalysts. The transitional metal compounds such as Fe, Co, and Ni being substantially available, inexpensive, corrosion-resistant, and highly effective in an alkaline solution to employed as an OER electrocatalyst.

The primary benefit of using nickel oxide for the OER is their superior corrosion-resistant properties in the alkaline electrolytic solution. Moreover, changing the particle size, surface area, texture of the nickel oxide led to enhanced electrocatalytic properties and OER activities.

Ni-based catalysts have commonly been used in HER electrocatalysis in alkaline water electrolysis; however, they are gaining popularity in OER electrocatalysis due to their promising OER activities.

Currently, Ni-based DLHs also explored the suitable opportunity for the application of electrochemical water splitting OER electrocatalyst. Even though it has low electrical conductivity, Ni-based DLHs hold specific textures that enhance OER performances. Compared to various DLHs catalysts, Ni–Fe-DLH exhibit higher catalytic performance.

The other transitional metals alloying with nickel can increase the OER performance, and the numerous alloys studied regarding electrocatalyst application with nickel are Co and Fe. The reason to increase the combination of two transitional metals is to provide better catalytic properties compared to a single metal synergistically.

This is concluded that comprehensive research has been conducted on mono-oxides, bimetallic oxides, ternary oxides, and composites and Ni hybrids have been evident to be effective materials for OERs in an alkaline electrolytic solution.

Cobalt hydroxides ($Co(OH)_2$) has been comprehensively examined as an effective and persistent electrocatalyst for OER water electrolysis. Commonly, the formal synthesis of cobalt hydroxide is powder coprecipitated with cobalt salts in an alkaline solution. The regular implemented process is facile, and the chemical composition and texture of the final catalyst are under control.

The cobalt oxides (CoOx) have been extensively studied as an electrocatalyst in applying the electrochemical water electrolysis method. The most widely used process is to prepare cobalt oxides is by the annealing treatment.

The cobalt sulphides (CoxSy) are conventionally synthesized by the wet chemical method. Commonly used sulphur sources to produce cobalt sulphides are carbon disulphide, thioacetamide, sodium sulphide and thiourea (Gu et al. 2022).

Apart from nickel and cobalt-based oxide compounds, manganese oxides (MnO_2) have recently increased consideration as essential electrocatalysts for OER activities. The electrochemical and physiochemical properties are supported by the morphology and crystallography of the catalysts.

The precious OER catalysts in PEME, such as Ir and Ru, acquired the least overpotentials, in which Ir-based catalysts possess improved stability than Ru-based catalysts. There are numerous studies that have been conducted to improve the stability and catalytic properties of IrO_2 and RuO_2 through doping with other oxides

such as a tin oxide (SnO_2), tantalum pentoxide (Ta_2O_5), cobalt II, III oxide (Co_3O_4), and manganese oxide (MnO_2). However, enhancing the molar concentration of these economic oxides can reduce the active surface area and electrical conductivity of the electrocatalyst.

The noble OER catalysts in SOE technology are platinum (Pt), palladium (Pd) and silver (Ag) which is commonly used as an anode. Mostly these metals are costly and rarely available in nature. However, to decrease the cost of electrocatalysts, various methods have been used, including enhancing the catalytic activity and strength of the non-precious metal catalyst. Barium-strontium-cobalt-ferrite perovskite catalysts have been reported to possess superior electrocatalytic activities for SOE cathodes. Moreover, these perovskites are also used for the anodic application in this process.

The top priority of extensible hydrogen production has significantly driven the development of inexpensive and robust catalysts for electrochemical water electrolysis. To replace noble metals and their derivatives, transitional metals such as Fe, Co, Ni, Mo, Cu etc., selenides have demonstrated a promising catalyst on both HER and OER processes.

Cobalt-based selenide has been showing as outstanding electrocatalysts in the past years for the electrochemical water splitting process.

Nickel-based selenide has been an extremely efficient catalyst for electrochemical water electrolysis and exhibits superior durability in acidic and alkaline media.

Metal borides/borates are promising to provide inexpensive electrocatalysts for the commercialization of electrochemical water splitting. The synthesis for metal boride/borates is less energy-intensive and nontoxic when compared to those needed for the synthesis of other nonprecious electrocatalysts, making them a preferable approach. The catalysts (Ni–B) deposited by the electroless process yield better performance when compared to the same catalysts prepared using the standard reduction method.

The multimetal oxyhydroxides perform better than noble metal catalysts for the OER process in the alkaline medium.

To enhance the efficiency of water electrolysis, researchers chose biomass electrooxidation to replace traditional OER electrocatalysis, such as 5-hydroxymethylfurfural (HMF) electrooxidation urea electrooxidation.

MOFs are materials that can be fabricated by linking metal ions with organic linkers, showing open crystalline structures, unique porosity, structural flexibility, and tunable capability. Conductive materials can be interlinked with the channels of MOFs or provide support for the growth of MOFs. Several composites/derivatives have been extensively used to synthesize MOFs-based electrocatalysts, such as cobalt-based MOFs, iron-based MOFs, and nickel-based MOFs derivates. Iron is abundantly available on earth and has been widely explored as an iron-based MOF derivative of electrocatalysts for the electrochemical water splitting process.

10.1 Carbon Free Materials

Tafel slope is an indication of the reaction mechanism since it is related to the rate-determining step. In the oxygen evolution, the reaction mechanism in alkaline medium can be described as a series of steps assuming a single-site mechanism (* denotes an active site), as follows:

$$* + OH^- \leftrightarrow *OH + e^- \ \textit{Tafel slope} = 120\frac{mV}{dec}$$

$$OH + OH^- \leftrightarrow *O + H_2O + e^- \ \textit{Tafel slope} = 30\frac{mV}{dec}$$

$$*O + OH^- \leftrightarrow *OOH + e^- \ \textit{Tafel slope} = 40\frac{mV}{dec}$$

$$*OOH + OH^- \leftrightarrow *OO^- + H_2O \ \textit{Tafel slope} = 30\frac{mV}{dec}$$

$$*OO^- \leftrightarrow * + O_2 + e^- \ \textit{Tafel slope} = 22 \ or \ 40 \ mV/dec.$$
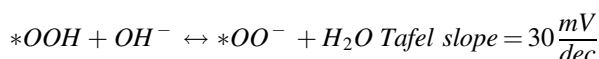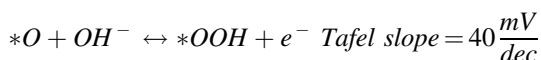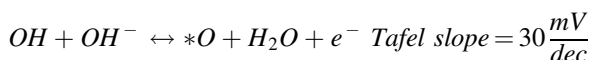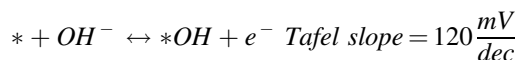
The Tafel slope depends on the reaction determining the overall rate (i.e., the rate-determining step), which is a factor relying on the catalyst formulation and the overpotential.

An ideal catalyst should provide a catalytic pathway with the rate-determining step being associated with the lowest Tafel slope and towards four electrons for efficient oxygen formation. It is important to point out that a catalyst formulation may present active sites with different natures (presence of defects, different facets, etc.), which can lead to intermediate values of Tafel slopes because of the contribution from single active sites to the overall activity.

Identification of the active phase in the OER in the case of crystalline metal hydroxides, which is crucial for understanding the reaction mechanism, and a rational design of catalysts are often impeded by the presence of at least two polymorphs, α-phase and β-phase, as in the case of $Ni(OH)_2$ and $Co(OH)_2$. On the other hand, mixed-metal hydroxide phases have the advantage of a more flexible electron configuration. The addition of a different metallic element to a chosen hydroxide phase allows for the tuning of the electronic structure of the material and hence influences the adsorption energy of the reaction intermediates. Thus, it is one of the most common ways to enhance the reactivity of hydroxide-based materials.

Oxyhydroxides composed of Ni-Fe and Co-Fe are reported as the most active electrocatalyst for OER in the liquid alkaline electrolytes. It is postulated that the iron dispersed in the matrix of NiOOH or CoOOH forms the actual active sites. Since FeOOH could not serve as a standalone catalytic material due to its electrical insulating properties, the nickel and cobalt oxyhydroxides provide electrical conductivity and chemical stability. Recently, by comparison of Co-rich and Ni-rich (oxy)hydroxide nanosheets, it was found that the increased strength of M–O bonds and porosity at the nanoscale substantially enhance the electrocatalyst stability during the electrochemical reaction.

Similarly, to hydroxide electrocatalysts, first-row transition metal oxides (especially of Ni, Co, and Fe) are the most popular metal oxide materials researched for oxygen evolution reaction in alkaline electrolytes. Spinel- and perovskite-type oxide materials have been extensively studied. For example, in Co_3O_4 the generation of oxygen vacancies enhances conductivity, and interactions with the support of or by doping with heteroatoms stabilizes Co^{4+}, which leads to the enhancement of electrocatalytic activity. In general, stabilization of high oxidation states, as well as Fe^{4+} and Ni^{4+} in oxide matrices (spinel, perovskite), leads to better OER reactivity. It must be noted that the structural evolution taking place during electrochemical anodic reaction undergoes a remarkable structural transformation of the metal oxide catalysts under very high potential yields and results in the formation of the oxyhydroxide phase overlayer at the catalyst surface.

Similarly, to metal hydroxides and oxides, in the case of transition metal chalcogenides (TMCs) the most promising catalysts are Fe, Co, and Ni-based materials, including metal sulfides, selenides, and tellurides. While TMCs have been broadly investigated in the electrocatalytic hydrogen evolution reaction, there is still room for their optimization towards OER.

The high electrical conductivity of metal nitrides renders them ideal candidates for electrocatalytic materials, including oxygen evolution reaction. Similarly, to oxide and oxyhydroxide electrocatalysts, mixed metal nitrides (bi- or trimetallic) exhibit a great potential due to the possibility of tuning their electronic properties.

Although phosphides may exhibit semiconducting or even insulating properties, for a particular atomic ratio of phosphorus and transition metal and suitable electronegativity difference the phosphides may exhibit metallic character, and for some metal-rich compounds superconductivity has been observed. Exceptional conductivity of some bi- and trimetallic phosphides is reflected in the similar electronic structure to respective purely metallic materials. FeP/Ni_2P hybrid electrocatalyst supported 3D Ni foam proved ex aequo the best OER reactivity in alkaline conditions. Moreover, it presented very high HER activity, allowing it to act as a bifunctional catalyst for overall water splitting in the same alkaline electrolyte. Thermodynamically, under oxidizing conditions, metal sulfides are less stable than their respective metal oxides, while metal nitrides and phosphides are less stable than sulfides and phosphides, respectively. During strongly oxidative conditions of OER in water, it may be anticipated that metal nitrides and phosphides (and sulfides, selenides) can easily undergo surface oxidation to the corresponding metal hydroxides or oxides. Importantly, oxidation of electrocatalysts, such as cobalt and nickel phosphides in an alkaline environment can be used as an activation process for the oxygen evolution reaction in a neutral solution.

10.2   Carbon-Based Materials

Compared with traditional carbon materials, nanocarbons always exhibit higher electrical conductivity, larger surface area, tunable structural hierarchy, ultra-thin graphitic layer, and low dimensional properties. These unique features endow nanocarbons with multifunctionalities to strongly couple with other catalytically active components, resulting in significantly enhanced performances.

In recent years, transition metal/carbon (TM/C) composites have surfaced as a new class of effective catalysts for electrochemical oxygen and hydrogen evolution reactions. These composites usually exhibit the reactivity characteristics of their components (metal compound or carbon); however, the synergetic and interfacial effects are sought for and designed to endorse the material with enhanced electrocatalytic activities. A combination of cheap components, i.e., carbon and Fe-, Co-, Ni-phases and promising reactivities render them perfect candidates for the replacement of precious metal-based electrodes. Thus, new material formulations of the TM/C type, such as hierarchically porous carbon-supported TMs, carbon network supported TMs or carbon encapsulated TMs, are being developed to explore the possibility of deriving new functionalities. Parallel to developing new carbon morphologies, carbon doping, especially with S and N, is used to obtain enhanced properties of the hybrid materials.

The oxygen evolution reactivities of spinel compounds, which are amongst the most active phases in the OER, are reported to be enhanced by dispersed deposition of spinel oxide phase onto structured carbon substrates such as graphene, single-walled carbon nanotubes (SWCNTs), and carbon nanosheets (CNS). Such a case was reported for the $CoCr_2O_4$, deposited onto carbon nanosheets or Co_3O_4 deposited onto carbon porous nanowire array, which displayed excellent OER activities, even outperforming the benchmark RuO_2.

Another highly active phase in the OER, NiFe hydroxide, was deposited in the form of nanoplates onto different nanocarbon-type materials to improve their electrical conductivity. Various classes of carbon materials were studied, ranging from graphene with different oxidation degrees to amorphous carbons nanoparticles (i.e., Vulcan XC-72R or Ketjen Black) to carbon nanotubes and carbon quantum dots. The composite materials formed with carbon black or carbon nanomaterials usually exhibit higher OER activity than single material type catalysts.

The transition metal alloys (TMAs) encapsulated in N-doped graphene are promising hybrid electrocatalysts for water splitting. The enhanced electron transfer at the interface of the TM core and the graphene shell is the main advantage for improved OER reactivity.

Moreover, by changing the chemical composition of the transition metal core or thickness of the graphene shell, the electrocatalytic activity may be further tuned to improve the water-splitting activity. Transition metal sulfide (TMS) nanoparticles and nanosheets could be downsized to expose more highly active sulfur edges by a nano-confinement effect of carbon nanomaterials, resulting in the enhanced reactivity of TMSs. Such materials combined into TMS/carbon hybrids can be further

enhanced by the rational introduction of another heteroatom, such as nitrogen, or defects into the composite materials. It is anticipated that the TMS/carbon composite materials may be good alternatives to precious metals, even for oxygen evolution reaction in acidic media. In the case of transition metal phosphides (TMPs), TMP/carbon composites are proven to be very effective for water splitting. Like other composite materials, the heterointerfaces with carbon are crucial in providing their high OER reactivity. The enhancement of active site exposition and acceleration of mass transport can be obtained in all cases by constructing composite structures based on hierarchically porous carbons, which may allow further improvement of the performance of all TM-phase carbon composites for water splitting.

A combination of two types of nanostructured carbon building blocks into nanocomposite structures has also been reported for electrochemical applications in lithium-ion batteries, metal–air batteries as oxygen reduction catalysts and bifunctional catalysts (OER and ORR), and as hydrogen evolving catalysts. The carbon components are usually 1D structures (e.g., nanotubes) interconnecting 2D or 3D carbons doped with nitrogen to improve their electronic conductivity. In such materials, the carbon/carbon structure acts as a support for well-dispersed, non-noble, metal-based nanoparticles. The enhanced electrocatalytic activity of these materials is ascribed to the optimized surface chemical composition and distribution of the active phase, large specific surface area, and hierarchically porous microstructure resulting in improved electron and mass transport abilities.

The utilization of nanocarbons for high-efficiency hybrid electrocatalysts is based on the following effects: acceleration of the electron and mass transport; modification of the morphologies and properties of active components during the composite/hybrid fabrication; manipulation of the electronic structure through the interfacial charge transfer; generation of confinement effects resulting in (1) spatial restriction to hamper the sintering of nanoparticles, (2) significant electronic interaction to modify the property and activity of carbon shells, and (3) physical isolation of embedded nanoparticles from hostile operating conditions; and supporting electrocatalysts into 3D free-standing electrodes.

Recently, novel synthesis routes for the fabrication of new carbon structures have been extensively explored. The obtained materials can be additionally pre-treated before using as catalysts or supports to enhance their electrochemical performance during the OER process. Pre-treatment of carbons is instrumental in increasing specific surface area, introducing heteroatoms, tuning the electronic structure, improving conductivity, and developing porosity.

The great abundance of the hydroxide/oxide carbon materials results from the relative ease of the preparation of the structured catalysts. The synthesis procedures usually do not require high temperature treatments and a variety of precursors can be used. Among the reported synthesis methods, by far the most popular is the hydrothermal treatment of pretreated carbon with metal salt in the Teflon-lined autoclave placed in a conventional oven/dryer.

Although from a thermodynamic point of view, metal sulfides are less stable than metal oxides under oxidizing potentials and metal nitrides and phosphides are less stable than sulfides and so on, an abundance of such electrocatalytic systems has

been reported in recent years also for the OER. It can thus be anticipated that metal chalcogenides, nitrides, and phosphides would be readily oxidized, at least on the surface, to the respective metal oxides/hydroxides in the strongly oxidative environments of OER. Therefore, care must be taken when characterizing such systems and particular attention should be paid to the spent catalysts.

One of the ongoing issues concerning the production of the highly active and stable catalysts for water splitting is the cost of the metal active phase. Among metal-free alternatives, carbon-based electrodes have recently attracted great attention due to their relatively low price and robustness (mechanical strength, electrical conductivity) which is of paramount importance while designing OER electrocatalysts for large-scale application. A broad family of carbon-based nanomaterials can be fabricated offering various structures and dimensionalities: 0D (fullerenes, carbon dots), 1D (nanotubes, nanofibers), 2D (graphene and graphemic materials, such as few-layer graphenes, graphene nanoribbons), or 3D (capsules, spheres, nanoporous structures). Such structural diversity has an immediate impact on the physicochemical properties of the materials and hence OER activity.

The susceptibility of carbon materials to chemical reactions is linked to topological and edge defects. Nevertheless, to boost intrinsic OER activity, pristine materials usually require surface and/or structural modifications that at present are often realized by the introduction of heteroatoms, such as O, N, S, F, B, and the formation of stable surface-specific functional groups. Furthermore, doping leads to changes in the charge distribution and electronic properties as well as the formation of additional defects, besides the intrinsic ones, enhancing the electrocatalytic performance of carbons. The extent of possible modifications depends on the electronegativity and size of the doping atoms.

An important aspect of doped catalysts is their stability in harsh reaction conditions (high OER potential and corrosive environment), since the oxidation of carbon, or heteroatom, is thermodynamically favorable. From a practical point of view, stability is even more important than the initial reactivity of the novel heteroatom-doped carbon material.

Finally, the purity of the heteroatom-doped concerning trace metals should be carefully evaluated. The functionalization procedures may lead to the unintentional introduction of traces of metals that may be responsible for the significant improvement of the electrocatalytic performance.

Besides co-doping, one important strategy to enhance the electrocatalytic kinetics is microstructure engineering of the non-metal carbonaceous catalysts. In the case of 2D graphenic-based catalysts, the electron transfer can be diminished due to the susceptibility of these materials to stacking together that results in shielding of the active sites. Thus, 3D carbons materials, such as carbon hydrogels, foams, and hierarchical porous carbons are commonly used as electrode materials or supports for energy storage and conversion devices. The porous structure allows for the increase in the utilization efficiency of the catalytically active centers, providing access to the sites to the electrolyte and reactants.

One of the materials that has recently attracted significant attention in electrocatalytic applications is graphitic carbon nitride (g-C_3N_4), mostly due to its tailorable structure and high nitrogen content (pyridinic and pyrrolic N) in the carbon framework.

Nevertheless, the catalytic activity of bulk g-C_3N_4 suffers from low surface area and insufficient electronic conductivity. Doping with heteroatoms, designing nanostructures, and composite materials seem to be promising solutions for improving the electrocatalytic performance of carbon nitride.

Metal oxide–hydroxide composites with carbons are being increasingly used to improve the electrocatalytic performance of the transition metal active phase. Such a combination promotes electron transport to the current collector by decreasing the thickness of the poorly conductive oxyhydroxide phase. In addition, the application of the porous carbons offers the benefits of enhanced access of the liquid phase reactants to the surface of the solid electrocatalyst. The formation of such composite materials enables an efficient way to reach the state-of-the-art OER activities.

Mixed Ni–Fe hydroxides were obtained through preferential templating on graphene edges where the edge-rich vertical graphene support provided the unoccupied density of states on the graphene edges, which can preferentially template specific valence orbital alignment of the Fe–O entities. This specific interaction of the graphene edge–metal component resulted in the formation of beneficial undersaturated and strained Fe-sites with high valence states, and at the same time, it boosted the formation of redox-activated Ni species. These two effects resulted in an improved OER reactivity. For the Ni@Pt core–shell nanoplates and Ni/rGO composites, the overpotential of Ni/rGO is lower than pure Ni and the enhanced performance of Ni/rGO was ascribed to the possible effect of the rGO coatings. The GO was added in the synthesis of the Ni-Al LDH precursor and with the addition of hydrazine hydrate as a reducing agent in the reduction reaction, GO and Ni-Al LDH are simultaneously reduced. The morphology of obtained product is maintained as hexagonal nanoplates, which further improves the catalytic performance. According to the results of electrochemical impedance spectroscopy, the excellent conductivity of rGO plays a major role in reducing the influence of Ni oxidation in the process of water splitting, and it can effectively improve the electrical conductivity of the anode, facilitating electron extraction and shortening ion transport pathways during OER.

Transition metal chalcogenides (TMCs—sulfides, selenides, tellurides, where TM usually is Co, Ni, Fe), due to their multivalent oxidation states, abundant defects sites, and structural diversity, exhibit excellent abilities for electrocatalytic water splitting. Such materials are much cheaper than noble metals and exhibit noble-metal-like catalytic properties at the same time. Further, the electronic properties of TMCs can be tunable due to the ion-exchange process and the metal-chalcogen ratio variation in the electrocatalysts.

However, TMCs nanomaterials suffer from low stability, easy aggregation of particles, low electronic conductivity, and limited surface area, which can result in poor electrochemical activity. One of the strategies to overcome these obstacles aims at the fabrication of TMC/carbon composites and taking synergistic advantages of

both materials. Combining TMCs with carbon materials significantly improves the intrinsic conductivity, facilitates charge transfer of the hybrids, as well as promotes the electroactivity of catalysts.

Recently, great efforts have been taken to develop hybrid structures of carbons and transition metal sulfides, particularly cobalt-based ones.

Other promising electrode materials for water splitting include transition-metal nitrides, in which the electrocatalytic activity, stability, and the number of active sites can be improved by controlling the composition, shape, and morphology of nanoparticles. The presence of nitrogen atoms positively affects the electronic structure of the catalyst, leading to high electron density near the Fermi level and enhanced charge transfer. The strong interaction between g-C3N4 support and CoN may form a region of charge excess and enable electron transport from the cobalt active site to the neighboring Co–N bond. Then, the electrons from the OER process could be accepted by the excess regions and accordingly improve the OER activity of the mixed material.

Furthermore, the intrinsic conductivity and OER activity of transition-metal nitrides can be modulated by merging the metal active phase with conductive supports such as carbons. Designing composite catalysts, namely transition-metal nitrides/carbon matrix, can also result in better accessibility of active sites and improved stability during electrochemical reactions due to avoiding the aggregation of nanoparticles and improving the corrosion resistance under strongly acidic and basic conditions. To get superior electrocatalytic activity and stability, the optimization of the carbon:TM is required. One of the approaches focuses on encapsulation of metal nanoparticles into an N-doped carbon shell, which may prevent the corrosion and agglomeration of metal NPs in an alkaline electrolyte.

Recently, it has been revealed that the incorporation of foreign metal atoms into the crystal lattice of TM-based catalysts changes the local coordination environment and electronic configuration and hence improves the electrocatalytic performance.

Most recently, growing interest in terms of carbon-supported OER catalysts is related to transition-metal phosphides (TMPs), mostly due to their relatively low price and earth-abundance reserves. The metal phosphides are thermodynamically less stable than corresponding metal hydroxides/oxides under oxidation potentials. Thus, gradually formed metal hydroxide/oxide phases on the TMPs surface during electrochemical reactions are considered to provide the actual active centers for oxygen evolution reaction, while the inner TMPs core acts as the conductive scaffold. Since the morphology and/or structure of metal phosphides may undergo reconstruction upon a redox process, the TMPs do fall entirely under the conventional definition of the term catalyst. Moreover, the transformations of composition and structure of the original catalysts into the final active species are difficult to predict since they may proceed along various paths. Therefore, different electrocatalysts should be extensively studied by experimental and theoretical methods to deeply understand their reaction mechanisms.

The graphical summary of the best electrocatalysts reported in this discussion is presented in Fig. 6.

Fig. 6 Graphical summary of the best reported electrocatalysts for oxygen evolution reaction divided into different classes of carbon-based composite materials; presented data are for OER process in 1 M (full symbol) and 0.1 M (half-empty symbol) alkaline solution
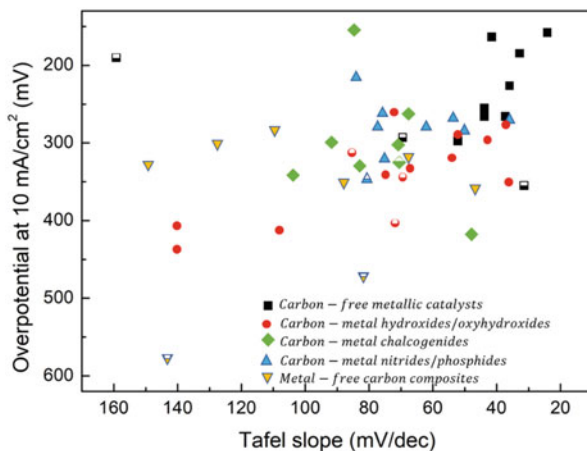
To date, the lowest OER overpotential and lowest Tafel slope are achieved with carbon-free metal catalysts, with Fe and Ni oxyhydroxides and phosphides presenting the most promising activity within noble metal-free catalysts in an alkaline environment.

One of the main problems arising with these materials is that the electrical conductivity of oxide phases could not be improved sufficiently, which causes ohmic resistance and hinders electron transfer within the catalyst layer for practical electrodes, which are usually different from lab-scale ideal conditions.

The main interface encountered with the OER electrocatalysts is the solid–liquid–gas one, where the material meets the electrolyte and the reaction product, oxygen. Other interfaces include phase boundaries between components of the composite material and phase boundaries created between outermost layers of materials (e.g., oxides, phosphides) and the oxidized/hydroxylated surfaces directly responsible for the catalytic action. The optimization and rational design of three-phase interfaces are of paramount importance in electrocatalytic applications and include the exposure of the active sites, mass diffusion enhancement, and boosting of electron transfer. Improvement in one direction may hinder the overall performance due to a decreased efficiency of another.

At the interfaces between two active components, reconstructed active centers exhibit different chemical properties due to modified bonding and electronic interactions with the neighboring atoms. Moreover, in the vicinity of the interface, materials exhibit structural disorder, increased defects concentration, additional phases, and various molecular components. Therefore, the new active centers located at or in the vicinity of the interfaces can be responsible for the actual catalytic activity and stability rather than the original components. Typical interfaces present in the electrocatalysts include hydroxide-oxide composites, such as $Ni(OH)_2$–CeO_2, where the improved catalytic activity can be assigned to the strong electronic coupling of the oxide and hydroxide phases, which favorably modulates the interaction between the reaction intermediate and catalyst.

Another type involves an in situ formation of the active phase overlayer, especially from materials unstable under reaction conditions, as in β-NiO(OH)/Ni$_2$P@NiO catalyst supported on Mg$_2$O(OH)$_2$-like phase, which is formed during the oxygen evolution reaction, where the Ni2P nanoparticles are immediately oxidized forming a core–shell structure.

The enhanced performance of the core–shell material is hypothesized to result from the reactivity modulation due to the development of a lattice strain in the interfacial area, and the high surface area of the supported electrocatalyst.

Nanocomposites with enhanced electrical conductivities can be created by combining two or more different types of carbon materials. For example, developed for energy storage application, a composite of carbon nanofibers (CNF) with natural graphite microspheres was found to form a continuous conductive network resulting in improved cycling performance. Moreover, improved penetration of the composite surface by the electrolyte resulted in a faster electrode reaction kinetics and the CNF/graphite network provided mechanical stabilization for the electroactive system by accommodating volume changes and thus preventing its mechanical degradation by cracking.

An accurate design, synthesis, modification and detailed characterization of well-defined carbon–carbon or carbon–non carbon materials' interfaces are the basis for the engineering of nanocomposites with tailored properties targeted for specific applications.

Every step of the composite preparation will influence the final electrocatalytic activity, notably, heteroatom doping of carbon materials, precursor types of active components, and applied synthetic procedures. The approaches to study composited materials usually lie between two borderline cases. On one hand, a deep understanding of the complex interfacial structures and the interaction of the comprising materials is studied. On the other hand, the preparation of model composites with regulated and optimized interface structure is pursued to gain more fundamental knowledge. Eventually, both approaches mix and should lead to the same goal, which is an improvement in the performance of the electrocatalytic materials.

Interface engineering in carbon-based nanocomposites employs two main types of chemical interactions: covalent and non-covalent. Both types can result in the desired interfacial interactions, however, different synthesis strategies are used for the preparation of the materials. Covalent interactions (chemical bonding) are most often obtained through techniques such as chemical vapor deposition, condensation reaction, radical polymerization, and hydrothermal techniques. Non-covalent interactions, typically achieved by self-assembly mixing and in situ polymerization approaches, usually involve π–π interactions, hydrogen bonding, and van der Waals forces.

For the Ni$_2$P/Fe$_2$P–O system, an occurrence of synergistic effects of Ni$_2$P(O)/Fe$_2$P(O) interfaces, formed by active surface layers and metallic phosphide bulk, is proposed. On the surface, phosphates possibly act as a proton-coupled electron transfer mediator, while doped oxyhydroxides could accelerate the formation of O–O bonds and lower the activation barrier for OER. The underlying Ni$_2$P/Fe$_2$P could retain its conductive properties and promote the electron transfer process. A

heterojunction within hierarchical CoP-nanowire–FeP-nanorod branched heterostructures endows it with intimate interfacial contact between CoP and FeP, thus inducing a built-in electric field at the interface, which is said to promote the charge transfer and enhancement of the electrocatalytic activity. In the hierarchical $Co(OH)_2$/Ag/FeP hybrid structure, where the Ag nanoparticles were uniformly distributed on the surface of FeP nanorod arrays, and the latter decorated $Co(OH)_2$ nanosheets, which provided an increased catalytically active area, resulted in a changed electron structure due to the formation of interfaces involved in $Co(OH)_2$/Ag/FeP hybrid, which is considered to be beneficial to generate low-charge state Fe^{2+} and highly-oxidized $Co^{3+/4+}$. A heterostructure resulting from a direct combination of CoP and CeO_2 mainly benefits from the abundant interfaces between CoP nanosheets and CeO_2 nanoparticles that generate a high concentration of oxygen vacancies and catalytically active sites, as well as tuning the surface electronic states. Another direct combination of phosphorus-rich and oxygen-rich phases, cobalt hydroxide–black phosphorus nanosheets, resulted in an interface that exhibits small interlayer distance, large interlayer binding energy, and significant charge transfer between $Co(OH)_2$ and black phosphorus, indicating a strong interlayer interaction and metallic interface, resulting in an improved conductivity and fast electron transfer.

Sulfide active phases are often investigated for both OER and HER, with potential application as bifunctional catalysts. Introducing $Ni(OH)_2$ to the Ni_3S_2 yielded an electrocatalyst with low ionic and electronic resistances enabled by modulation of the surface atomic configuration of the sulfide phase. This led not only to high OER activity but also accelerated the Volmer step and OH– adsorption during the HER. Moreover, the obtained loose and interconnected nanoforest-like architecture facilitated the full exposure of active sites with enhanced electrolyte infiltration and bubble escape. Strongly coupled NiS nanoparticles/Bi_2WO_6 nanosheets formed a 0D/2D heterojunction catalyst with interfacial synergistic effect and a strongly coupled electronic effect. The NiS nanoparticles were evenly distributed on the surface of Bi_2WO_6 nanosheets allowing for maximum atom utilization. The re-coordinated nickel and oxygen species act as bridges at the interface, resulting in a novel valence-bond environment of the O–Ni–S bond structure to enhance the charge and mass transfer for the surface reactions. Cu_2S–CoOx/Cu foam profited from the synergistic effect between Cu_2S and CoOx, and electronic coupling between the two components. The catalyst benefits also from the distribution of CoOx on Cu_2S nanowires, which possess good electronic conductivity.

The formation of an intimate hydroxide–oxide interface is similarly beneficial for OER. In particular, the addition of CeO_2 to hydroxide phases appears to result in strong electronic interaction formed by the intimate hydroxide–CeO_2 interfaces, which might favorably modulate the interaction between intermediate and catalyst.

The CeO_2 addition effect results probably from the enrichment of the electronic distribution near the Fermi level, boosting the electron transfer efficiency from local active centers to adsorbates. Other combinations are also reported, such as dual-interface structure in NiV-LDH@FeOOH on Ni foam, which brings about improved electrical conductivity and optimized electronic structure.

In carbon-based composites, the carbon component provides a high surface area to deposit the active phase or support and active phase. A combination of Ni_2P nanoparticles and $Mg_2O(OH)^{2-}$ like support grown on carbon paper results in immediate oxidation of the Ni_2P nanoparticles during OER, through the core–shell structuring, eventually forming active and stable β-$NiO(OH)/Ni_2P@NiO$ catalyst supported on a $Mg_2O(OH)^{2-}$ like phase. The authors suggest that the high performance of the catalyst results from the development of a substantial degree of lattice strain in the core–shell nanoparticles and the realization of the supported catalyst with a high surface area. Formation of carbon-supported OER catalyst by decomposition of precursors based on the metal–organic framework compounds, like FeHP-ZIF-67, may lead to a durable connection between the carbon and phosphide components, which persists after the oxidation of the phosphide to oxyhydroxide species. These kinds of materials demonstrate increased resistance to aggregation of Co_2P nanoparticles, while the formation of active interfaces by partially connecting the Fe_2P microspheres is also observed, which facilitates a rapid charge transfer. N-$NiMoO_4/NiS_2$ catalyst on carbon fiber cloth exhibits enhanced electron transfer from N-$NiMoO_4$ to NiS_2 through abundant epitaxial heterogeneous interfaces at the atomic level. Moreover, this superaerophobic binder-free 3D open electrode with 2D nanosheets provides a large specific surface area that favors gas release from the surface (H_2 and O2).

11   Noble Metals Electrocatalysts

Noble metal catalysts (Pt, Pd, Ir, Ru, and Rh) have been known as the state-of-art catalysts. Nevertheless, the low natural abundance, fancy price, as well as poor anti-poisoning ability have impeded their further application in electrocatalysis. To obtain high-performance catalysts and improve the utilization of noble metals, the common-used approach is alloying with other earth-abundant metals to form noble metal-based catalysts (Gao et al. 2021).

Recently, multi-dimensional noble metal-based catalysts (MNMCs) are receiving more intensive attention for their high atomic utilizations and promoted catalytic behaviors. MNMCs mainly including zero-dimensional (0D) structures (single-atom/nanoclusters/nanodots), one-dimensional (1D) nanowires (NWs)/nanorods/nanotubes/nanofibers/nanobelts, and two-dimensional (2D) nanosheets (NSs)/nanoplates/nanoflakes, and three-dimensional (3D) nanonetworks/nanoaero gels/nanobranches/hollow nanospheres.

The metallic nanomaterials with well-defined structures showed superior physicochemical property. For example, the 1D NWs and 2D NSs exhibited high electron mobile mobility performance, more surface active sites and areas compared to the bulk materials.

Those merits of MNMCs endow them with great potential in surface-related electrocatalysis. Faced with numerous catalysts with diverse dimensions and nanostructures, designing universal yet precise methods to achieve uniform and large-scale synthesis is of great importance yet challenging.

Developing universal strategies to synthesize MNMCs, which could not only improve the utilization of precious metals to reduce the cost to realize the mass production of MNMCs, but also provide valuable references on the synthesis of other noble metal-based nanomaterials for further application. On this basis, some

of the general methods to MNMCs also overcome the drawback of classic synthetic methods and then effectively optimize the nanostructures of MNMCs, which is favorable to exhibited enhanced catalytic properties. To be specific, the advanced universal strategies with robust active sites increasement and electronic interaction optimization benefit the positive manipulation of surface active sites and electronic structures, the rational phase and facet control introduced by the general methods could modify the synergistic effect and construct the high-performance high-index facets, through those optimizations, the electrocatalytic activities and stabilities would be effectively improved.

Up till now, lots of universal methods have been reported to obtain MNMCs, while the specific universality in methods still exist drawbacks and difficulties. First, some general approaches have been adopted to synthesize two or three kinds of catalysts, for example, Fan et al. prepared a kind of Au@M (M = Pt, Pd) nanoplates via a facile and universal strategy, which lack the wider universality for other metals (except Pt and Pd). It is highly desirable to develop extensive general method for maximum utilization and mass productions, which could offer valuable solutions for practical application. Second, studies on universal methods for preparing Pt-based and Pd-based multidimensional catalysts are in the majority, such as the successful construction PtM (M = Fe, Co, Ni) NWs and PdM (M = Zn, Cd, and ZnCd) NSs. However, less studies on other noble metal-based (such as Ir, Rh, Ru) catalysts were reported.

Monometallic Ir nanosheets, Rh nanoplates have been synthesized, which also showed great potential in electrocatalytic field. Herein, the universality of methods for preparing multi-metallic Ir-/Rh-/Ru-based catalysts are still deserved. Third, the electrocatalytic applications of MNMCs via universal method often focus on some specific aspects. If the as-obtained catalysts could serve as multi-functional catalysts, the universal synthetic method could give full play to its effect. A representative case is the synthesis of bi-functional PtM (M = Co, Ni) nanotubes for robust ORR and methanol electrooxidation.

The electrochemical property of obtained nanomaterials play a significant role in electrocatalytic applications. Although great efforts have been devoted to enhance the catalytic behaviors by increasing numbers of active sites, boosting inherent activity, modifying electronic structure, and etc., yet still difficult to improve the catalytic performance of the whole series of catalysts.

It is well known that it is important to tailor well-defined morphologies for further performance improvement. Herein, developing effective strategy with precise design and manipulation on the elaborated structures of MNMCs to further reach the high catalytic activity and stability is desirable, such as constructing catalysts with defect-rich and high-performance phase, regulated electronic structure, and optimized synergistic effect, and etc. In addition, another approach to the performance enhancement is the exploration of advanced noble metal–metal-based catalysts, such as single atomic catalysts.

As a conclusion of the present chapter we would like to underline that electrocatalytic materials produced via electrodeposition find large attention in the very recent literature. Finding inexpensive electrocatalysts and electrodes is considered a major challenge for the hydrogen evolution reaction (HER). Several lines of research have shown that nickel-molybdenum alloys are the best catalysts after platinum in terms of activity and function for the HER. Coating nickel-molybdenum alloy on nickel

foam increases the electrochemically active surface area, which makes the resulting electrode a promising candidate for use as the cathode of alkaline water electrolyzers. Experimental data have shown that nickel-molybdenum deposition in the sulfate-nickel bath on graphene oxide surface with enhanced active surface contact between substrate and composite promotes the HER. In addition, previous reports have shown that nickel-molybdenum composite coating has more electrochemical activity than nickel molybdenum alloy. Thus, the composite coating may be useful in the HER applications. Due to the high activity of nickel for HER and its high stability in alkaline media, this element is considered as one of the most important materials used in alkaline electrolyzers. However, inactivation of the nickel surface due to the formation of nickel hydride and saturation at high concentrations is the main problem of using Ni electrodes. Surface modification and adding molybdenum to increase surface area are some of the modification methods to overcome the inactivity problem (Zhiani et al. 2023).

To improve the performance of alkaline water electrolysers, many research papers have described the progress of electrocatalyst development for both OER and HER in acidic and alkaline conditions. This is the consequence of the urgent need for low-cost, stable and highly active electrocatalysts for efficient hydrogen production. OER is considered the most difficult reaction, as it is more kinetically unfavourable than HER. As such, much current effort has focused on developing OER electrocatalysts. Coating electrocatalysts on cheap, robust substrates such as stainless steel has several advantages, since it can provide low-cost, stable and durable electrodes for the OER. However, it is important to bear in mind that catalyst performance is signifcantly dependent on the physical and chemical properties of these systems. For coatings, this includes quality and uniformity when they were deposited as a thin layer on substrates, for which the selection of coating technique plays a really important role when fabricating high-performance electrodes. There are a number of successful coating techniques reported in the literature for OER catalysts (Wang et al. 2023). Coatings can improve reaction kinetics for the OER, and the goal is to develop methods to coat substrates that can be afordable, easily scalable and uniform, to enable large-scale manufacturing of low-cost electrolysers.

Electrodeposition is a fast, environmentally friendly, and cheap approach that can be done at room temperature. Moreover, in this method, the catalyst loading adheres to the substrate without any binder. Polymeric binders that are usually used in many other synthesizing methods are known as a factor that deteriorates electrical conductivity, and they also decrease the long-term stability of catalysts. As an example, using the electrodeposition method to synthesize Ni-Co-B alloy makes it possible to decrease the fabrication costs and enhance the electrocatalytic performance, and eventually, make the industrial usage of this alloy more feasible (Jokar et al. 2021).

Compared with other synthesis methods, electrodeposition is simple and environmentally friendly, which can avoid phosphidation at high temperature and use of toxic phosphorous sources. Furthermore, TMPs' catalysts can be electrodeposited directly on conductivity substrate to form anode or cathode for water electrolysis and the fabrication of electrode would be simplified. Strictly speaking, the resulting materials from this method are usually not pure TMPs, which include corresponding phosphates, metal, or alloys. Moreover, the composition of the obtained materials could be changeable with synthesis conditions such as electrochemical method, potential, conductivity, electrolyte, deposition time, and conductive substrate (Zhang et al. 2021b).

In recent times, certain successes in the development of cheaper electrocatalysts, in particular, those based on transition metal chalcogenides, have been achieved. These materials possess quite good chemical resistance in alkaline solutions and, therefore, can be used for modification of both cathodes and anodes. Of specific scientific and practical interest is the applicability of these catalytic materials to increase the performance characteristics of electrodes made of porous metals, in particular, nickel foam. These modern materials possess high chemical resistance, considerable surface area, open pores, and high electron conductivity throughout the 3D structure. Such porous materials are modified mainly by electrodeposition or hydrothermal synthesis (Fominski et al. 2020).

12   Conclusions

Electrochemical water electrolysis is an emerging field of research that enables the generation of pure hydrogen and oxygen from water. It is an efficient process to store convert hydrogen gas into hydrogen energy. Currently, the PEME method is regarded as the most advanced technology, whereas SOE has remained in the experimental state. Both OER and HER catalytic processes are necessary to enhance water electrolysis efficiency, and they should be improved kinetically. At present, precious metals are considered the most prominent electrocatalysts. However, the main challenge is that the precious catalysts are rare on earth and, at a high cost, hindered the technology's extensive application.

The advancement in water electrolysis catalysts is insufficient. However, a research development has been made to decrease the use of precious metals by adapting numerous techniques such as changing the material composition and structures via substitution of precious metals with non-precious metal-based catalysts.

Several transition metals compounds have been used in alkaline water electrolysis (AWE) such as Fe, Mn, Co and Ni-based, including their oxides have been comprehensively explored in the past several years to replace precious metals electrocatalysts for HER and OER half-cell reactions in electrochemical water electrolysis process. Numerous processes have been carried out to enhance OER and HER catalytic performance, such as escalating electrical conductivity, improved

stability and bimetallic compounds conductivity, and synergetic effect using hybrid compounds using combined inherently combined carbon with chemically sensitive metal compounds.

Primarily, the electrocatalysts used in the SOE process at high temperatures are unstable. There are three critical aspects of SOE such as ionic conductivity, electronic conductivity, and catalytic conductivity. The active surface area of the OER and HER electrodes should be expanded. One crucial observation extracted from this process is that solid oxide electrolysis cells and fuel cells are the opposite. Therefore, the fuel cell's anodic material can be utilized as the cathodic material of the electrolysis cell. The main problem in the SOE process is the cost-effective catalysts for commercial application; the cost may be decreased due to utilizing different non-precious electrocatalysts in the process. Further decrease in overpotential and stability is required.

A lack of investigation has been done on the non-precious catalysts in PEME. It can provide efficient OER and HER performance in commercial water electrolysis applications.

There are insufficient non-precious catalysts that are stable in acidic electrolytes, where PEME operate. However, pure non-precious metals are not efficient for OER applications, thus, they can act as supporting roles for precious metals. The transitional metal oxides and carbides such as NbC, SnO_2, Ta_2O_5, TiO_2, WC and TiC can be utilized as OER and HER electrode materials to decrease the use of precious metals and operational costs. Although, these supporting materials fails to demonstrate any activity for OER in the PEME process.

Therefore, precious metals are required for PEME electrolysis with the substitution of precious metals with non-precious metal electrocatalysts for oxygen evolution reactions still impracticable.

MOF electrocatalysts for OER and HER reaction need more research because organic catalysts on anode and cathode are under development. It exhibited useful properties such as large surface area, unique physiochemical properties, and porous structure catalysts.

The non-precious metals electrocatalysts for OER and HER half-cell reactions are comprehensively reviewed in the last several years to decrease or replace precious metals usage due to their high cost and commercialization. However, numerous challenges are continued in the hydrogen production for inexpensive non-precious catalysts are following:

- Insufficient knowledge of non-precious catalytic mechanism in alkaline solution
- Major problem of corrosion for both OER and HER carbon intensive catalysts in alkaline and acidic solution
- Instability of ceramic catalysts for OER and HER in SOE at high temperature
- PEME electrolysis contained non-active characteristics of transitional metal oxide.
- A reduction in potential due to non-precious metals overload at the anode
- The synthesis procedure is complicated for bifunctional catalyst.
- Synthesis process can affect the catalysis structure and its performance.

- Transition metals low electrical conductivity
- The challenge is to prepare non-precious catalysts that can exceed the precious metal properties.
- Determine and resolve the strengths, shortcomings, and hazard of low carbon hydrogen systems.
- There are numerous innovative research opportunities for investigators and scientists to develop modern highly effective catalysts for OER and HER process. The future research recommendations are as follows:
- Novel and facile synthetic methods to produce non-precious metal-based catalysts for OER and HER with high electrocatalytic activity.
- Optimize life expectancy, reduce deterioration, and design extrapolation process.
- Establish the commercial practicability of hydrogen systems, complete chain of source-to-end.
- Plan, design, establish, and experimentally testing of large-scale hydrogen system of storing.
- Comprehensive understanding and designing of OER and HER electrocatalytic mechanism.
- A further investigation in non-precious catalysts for OER and HER in the PEME process.
- The research advancement in the non-precious catalyst for OER and HER in the SOE process
- The future development and application of MOF-based composite catalysts for OER and HER in water electrolysis process
- The catalysts with industrially promising current density (generally >0.5 A/cm^2) are still required. In addition, the development of membrane electrode assembly (MEA) is highly urgent.

References

Abuin G, Coppola R, Diaz L (2019) Ni-Mo alloy electrodeposited over Ni substrate for HER on water electrolysis. Electrocatalysis 10:17–28. https://doi.org/10.1007/s12678-018-0490-2

Anantharaj S, Aravindan V (2020) Developments and perspectives in 3D transition-metal-based electrocatalysts for neutral and near-neutral water electrolysis. Adv Energy Mater 10(1): 1902666. https://doi.org/10.1002/aenm.201902666

Anwar S, Khan F, Zhang Y et al (2021) Recent development in electrocatalysts for hydrogen production through water electrolysis. Int J Hydrog Energy 46:32284–32317. https://doi.org/10.1016/j.ijhydene.2021.06.191

Cai W, Liu X, Wang L et al (2022) Design and synthesis of noble metal–based electrocatalysts using metal–organic frameworks and derivatives. Mater Today Nano 17:100144. https://doi.org/10.1016/j.mtnano.2021.100144

Chang J, Zang S, Li J et al (2021) Nitrogen-doped porous carbon encapsulated nickel iron alloy nanoparticles, one-step conversion synthesis for application as bifunctional catalyst for water electrolysis. Electrochim Acta 389:138785. https://doi.org/10.1016/j.electacta.2021.138785

Chen P, Hu X (2020) High-efficiency anion exchange membrane water electrolysis employing non-Noble metal catalysts. Adv Energy Mater 10(39):2002285. https://doi.org/10.1002/aenm. 202002285

Ding J, Ji S, Wang H et al (2019) Mesoporous nickel-sulfide/nickel/N-doped carbon as HER and OER bifunctional electrocatalyst for water electrolysis. Int J Hydrog Energy 44(5):2832–2840. https://doi.org/10.1016/j.ijhydene.2018.12.031

Eftekhari A (2017) Electrocatalysts for hydrogen evolution reaction. Int J Hydrog Energy 42(16): 11053–11077. https://doi.org/10.1016/j.ijhydene.2017.02.125

Feng S, Yu Y, Li J et al (2022) Recent progress in seawater electrolysis for hydrogen evolution by transition metal phosphides. Cat Com 162:106382. https://doi.org/10.1016/j.catcom.2021. 106382

Fominski DV, Nevolin VN, Romanov RI et al (2020) Surface physicochemical treatment of nickel foam for increasing its electrocatalytic activity in overall water splitting. Inorg Mater Appl Res 11:458–466. https://doi.org/10.1134/S2075113320020124

Gao F, Zhang Y, Wu Z et al (2021) Universal strategies to multi-dimensional noble-metal-based catalysts for electrocatalysis. Coord Chem Rev 436:213825. https://doi.org/10.1016/j.ccr.2021. 213825

Gu Z, Zhang Y, Wei X et al (2022) Unveiling the accelerated water electrolysis kinetics of Heterostructural iron-cobalt-nickel Sulfides by probing into crystalline/amorphous interfaces in stepwise catalytic reactions. Adv Sci 9(30):2201903. https://doi.org/10.1002/advs. 202201903

Hu C, Zhang L, Gong J (2019) Recent progress made in the mechanism comprehension and design of electrocatalysts for alkaline water splitting. Energy Environ Sci 12:2620–2645. https://doi. org/10.1039/C9EE01202H

Huang J, Jiang Y, An T et al (2020) Increasing the active sites and intrinsic activity of transition metal chalcogenide electrocatalysts for enhanced water splitting. J Mater Chem A 8:25465–25498. https://doi.org/10.1039/D0TA08802A

Jin H, Joo J, Chaudhari NK et al (2019) Recent progress in bifunctional electrocatalysts for overall water splitting under acidic conditions. Chem Electro Chem 6(13):3244–3253. https://doi.org/ 10.1002/celc.201900507

Jo S, Lee KB, Sohn JI (2021) Direct electrosynthesis of selective transition-metal chalcogenides as functional catalysts with a tunable activity for efficient water electrolysis. ACS Sustain Chem Eng 9(44):14911–14917. https://doi.org/10.1021/acssuschemeng.1c05130

Jokar A, Toghraei A, Maleki M, Barati Darband G (2021) Facile electrochemical synthesis of Ni-Co-B film on Cu sheet for dual-electrocatalysis of hydrogen and oxygen evolution reactions. Electrochim Acta 389:138691. https://doi.org/10.1016/j.electacta.2021.138691

Khan MA, Zhao H, Zou W et al (2018) Recent progresses in electrocatalysts for water electrolysis. Electrochem Energ Rev 1:483–530. https://doi.org/10.1007/s41918-018-0014-z

Kim IS, Cho HS, Kim MJ et al (2021) Sacrificial species approach to designing robust transition metal phosphide cathodes for alkaline water electrolysis in discontinuous operation. J Mater Chem A 9:16713–16724. https://doi.org/10.1039/D1TA01181B

Li C, Baek JB (2019) Recent advances in noble metal (Pt, Ru, and Ir)-based electrocatalysts for efficient hydrogen evolution reaction. ACS Omega 1:31–40. https://doi.org/10.1021/acsomega. 9b03550

Li GL, Miao YY, Qiao XY et al (2023) Engineering edge sites based on NiS2/MoS2/CNTs heterojunction catalyst for overall water splitting. Apll Surf Sci 615:156309. https://doi.org/ 10.1016/j.apsusc.2022.156309

Lin L, Piao S, Choi Y et al (2022) Nanostructured transition metal nitrides as emerging electrocatalysts for water electrolysis: status and challenges. Energy Chem 4(2):100072. https://doi.org/10.1016/j.enchem.2022.100072

Loh A, Li X, Taiwo OO et al (2020) Development of Ni–Fe based ternary metal hydroxides as highly efficient oxygen evolution catalysts in AEM water electrolysis for hydrogen production. Int J Hydrog Energy 45(46):24232–24247. https://doi.org/10.1016/j.ijhydene.2020.06.253

Meng Y, Huang X, Lin H et al (2019) Carbon-based nanomaterials as sustainable noble-metal-free electrocatalysts. Front Chem 7:759. https://doi.org/10.3389/fchem.2019.00759

Premnath K, Madhavan J, Prasad S (2022) Ultra-efficient, low-cost and carbon-supported transition metal sulphide as a platinum free electrocatalyst towards hydrogen evolution reaction at alkaline medium. Int J Hydrog Energy 47(100):41974–41983. https://doi.org/10.1016/j.ijhydene.2021.09.120

Raja Sulaiman RR, Wong WY, Loh KS (2022) Recent developments on transition metal–based electrocatalysts for application in anion exchange membrane water electrolysis. Int J Energy Res 46(3):2241–2276. https://doi.org/10.1002/er.7380

Schalenbach M, Zeradjanin AR, Kasian O et al (2018) A perspective on low-temperature water electrolysis–challenges in alkaline and acidic technology. Int J Electrochem Sci 13:1173–1226. https://doi.org/10.20964/2018.02.26

Shit S, Bolar S, Murmu NC (2021) An account of the strategies to enhance the water splitting efficiency of noble-metal-free electrocatalysts. J Ener Chem 59:160–190. https://doi.org/10.1016/j.jechem.2020.10.022

Stelmachowski P, Duch J, Sebastian D et al (2021) Carbon-based composites as electrocatalysts for oxygen evolution reaction in alkaline media. Materials 14:4984. https://doi.org/10.3390/ma14174984

Sun H, Yan Z, Liu F et al (2020) Self-supported transition-metal-based electrocatalysts for hydrogen and oxygen evolution. Adv Mater 32(3):1806326. https://doi.org/10.1002/adma.201806326

Theerthagiri J, Murthy AP, Lee SJ et al (2021) Recent progress on synthetic strategies and applications of transition metal phosphides in energy storage and conversion. Ceram Int 47(4):4404–4425. https://doi.org/10.1016/j.ceramint.2020.10.098

Wang D, Song Y, Zhang H et al (2020) Recent advances in transition metal borides for electrocatalytic oxygen evolution reaction. J Electroanal Chem 861:113953. https://doi.org/10.1016/j.jelechem.2020.113953

Wang S, Lu A, Zhong C-J (2021) Hydrogen production from water electrolysis: role of catalysts. Nano Converg 8:4. https://doi.org/10.1186/s40580-021-00254-x

Wang Y, Williamson N, Dawson R et al (2023) Electrodeposition of nickel–iron on stainless steel as an efficient electrocatalyst coating for the oxygen evolution reaction in alkaline conditions. J Appl Electrochem 53:877–892. https://doi.org/10.1007/s10800-022-01817-4

Wu H, Feng C, Zhang L et al (2021) Non-noble metal electrocatalysts for the hydrogen evolution reaction in water electrolysis. Electrochem Energy Rev 4:473–507. https://doi.org/10.1007/s41918-020-00086-z

Xu ZJ (2020) Transition metal oxides for water oxidation: all about oxyhydroxides? Sci China Mater 63:3–7. https://doi.org/10.1007/s40843-019-9588-5

Xu H, Shang H, Wang C et al (2020) Surface and interface engineering of noble-metal-free electrocatalysts for efficient overall water splitting. Coord Chem Rev 418:213374. https://doi.org/10.1016/j.ccr.2020.213374

Xu Y, Wang C, Huang Y et al (2021) Recent advances in electrocatalysts for neutral and large-current-density water electrolysis. Nano Energy 80:105545. https://doi.org/10.1016/j.nanoen.2020.105545

Yang J, Jang MJ, Zeng X et al (2021a) Non-precious electrocatalysts for oxygen evolution reaction in anion exchange membrane water electrolysis: a mini review. Electrochem Commun 131:107118. https://doi.org/10.1016/j.elecom.2021.107118

Yang H, Driess M, Menezes PW (2021b) Self-supported electrocatalysts for practical water electrolysis. Adv Energy Mater 11(39):2102074. https://doi.org/10.1002/aenm.202102074

Yin X, Yang L, Gao Q (2020) Core–shell nanostructured electrocatalysts for water splitting. Nanoscale 12:15944–15969. https://doi.org/10.1039/D0NR03719B

Yu F, Yu L, Mishra IK et al (2018) Recent developments in earth-abundant and non-noble electrocatalysts for water electrolysis. Mater Today Phys 7:121–138. https://doi.org/10.1016/j.mtphys.2018.11.007

Yu Y, Chen Q, Li J et al (2022) Progress in the development of heteroatom-doped nickel phosphates for electrocatalytic water splitting. J Colloid Interf Sci 607(2):1091–1102. https://doi.org/10.1016/j.jcis.2021.09.032

Zhang J, Zhang Q, Feng X (2019) Support and interface effects in water-splitting electrocatalysts. Adv Mater 31(31):1808167. https://doi.org/10.1002/adma.201808167

Zhang W, Cui L, Liu J et al (2020) Recent advances in cobalt-based electrocatalysts for hydrogen and oxygen evolution reactions. J Alloys Compd 821:153542. https://doi.org/10.1016/j.jallcom.2019.153542

Zhang XY, Yu WL, Zhao J et al (2021a) Recent development on self-supported transition metal-based catalysts for water electrolysis at large current density. Appl Mater Today 22:100913. https://doi.org/10.1016/j.apmt.2020.100913

Zhang A, Xiao Y, Cao Y et al (2021b) Electrodeposition, formation mechanism, and electrocatalytic performance of Co-Ni-P ternary catalysts coated on carbon fiber paper. J Solid State Electrochem 25:1503–1512. https://doi.org/10.1007/s10008-021-04929-7

Zhiani M, Taghiabadi MM, Bagherabadi MH (2023) Optimization of Ni-Mo-coated stainless steel as a high-performance cathode in alkaline water electrolysis. Electrocatalysis 14:473–483. https://doi.org/10.1007/s1211.678-023-00810-5

Thermodynamic and Kinetic Analysis of Hydrogen Production Processes

1 Introduction

The basic mechanisms of electrolysis are based on the kinetic parameters controlling the atomistic reaction process of metal electrode that is polarized in an electrolyte solution.

2 Role of Catalysts

Some of the grand challenges facing scientists today is lowering the energy barrier to split water, store the hydrogen, reduce the cost of specialty materials to achieve this process, scale up production, and overall fundamental research insights at each step. This paragraph will attempt to address the first challenge of lowering the energy requirement to split water by the use of an electrocatalyst.

In water electrolysis, the oxygen evolution reaction (OER) is as follows:

$$4OH^- \leftrightarrow 2H_2O + O_2 + 4e^-$$
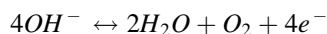
Within the electrolyzer, the OER takes place at the anode where oxygen is produced. Cost, availability, and activity are all factors equally important in electrocatalyst design. Initial studies into active electrocatalysts yielded optimal results when using rare, costly metal oxides IrO_2 and RuO_2 in acidic media (Jiang et al. 2023). According to recent published studies on OER electrocatalysts, transition metal oxides have shown encouraging results (Moradi et al. 2022). These transition metals included Fe, Ni, Co, Mn, Mo, and W and were in alkaline media.

Fig. 1 Adsorption energy of OOH vs. adsorption energy of OH based on density functional theory (DFT) calculations. The red star indicates the adsorption energies of an ideal OER catalyst
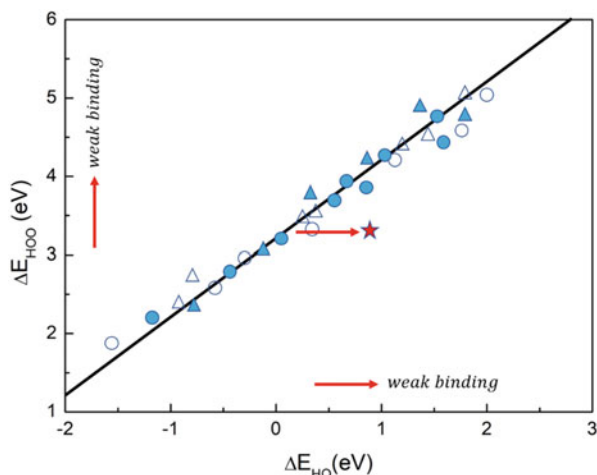
The OER is the half reaction that limits the overall water splitting efficiency, due to the complexity of the four-proton/four electron transfer. While there is no definitive mechanism for the OER, the most accepted mechanism in alkaline media is shown in the following equations:

$$S + OH^- \leftrightarrow S - OH + e^-$$

$$S - OH + OH^- \leftrightarrow S - O + H_2O + e^-$$

$$S - O + OH^- \leftrightarrow S - OOH + e^-$$

$$S - OOH + OH^- \leftrightarrow S + O_2 + H_2O + e^-$$
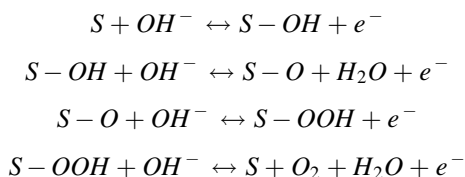
Currently no catalyst can perform the OER at thermodynamic potentials. This is due to the linear-scaling relationship between adsorbed OH ($\cdot$ OH) and adsorbed OOH ($\cdot$ OOH). Rossmeisl and co-workers performed density functional theory (DFT) calculations on a wide range of OER catalysts and found that as the binding strength of $\cdot$ OH weakens, the binding strength of $\cdot$ OOH weakens linearly.

Figure 1 shows the linear scaling relationship between the adsorption energy of $\cdot$ OOH, ΔEOOH, and the adsorption energy of $\cdot$ OH, ΔEOH, for several types of catalysts. As can be seen by the mechanism, one would want to break this scaling relationship to have the optimum binding energy for each catalyst.

The red star on Fig. 1 represents the binding energies for a thermodynamically ideal catalyst. Rossmeisl concluded that this scaling relation provides a lower limit of the OER overpotential of ca. 0.2–0.4 V overpotential.

Electrolytic water splitting is not only an uphill reaction, as reflected by the positive value of ΔG (Gibbs free energy), but also has to overcome a significant kinetic barrier (Razi et al. 2022). Catalysts play a crucial role in lowering the kinetic barrier (Fig. 2a). The evaluation of the performance of a catalyst for the electrocatalytic water splitting is based on several key parameters for activity,
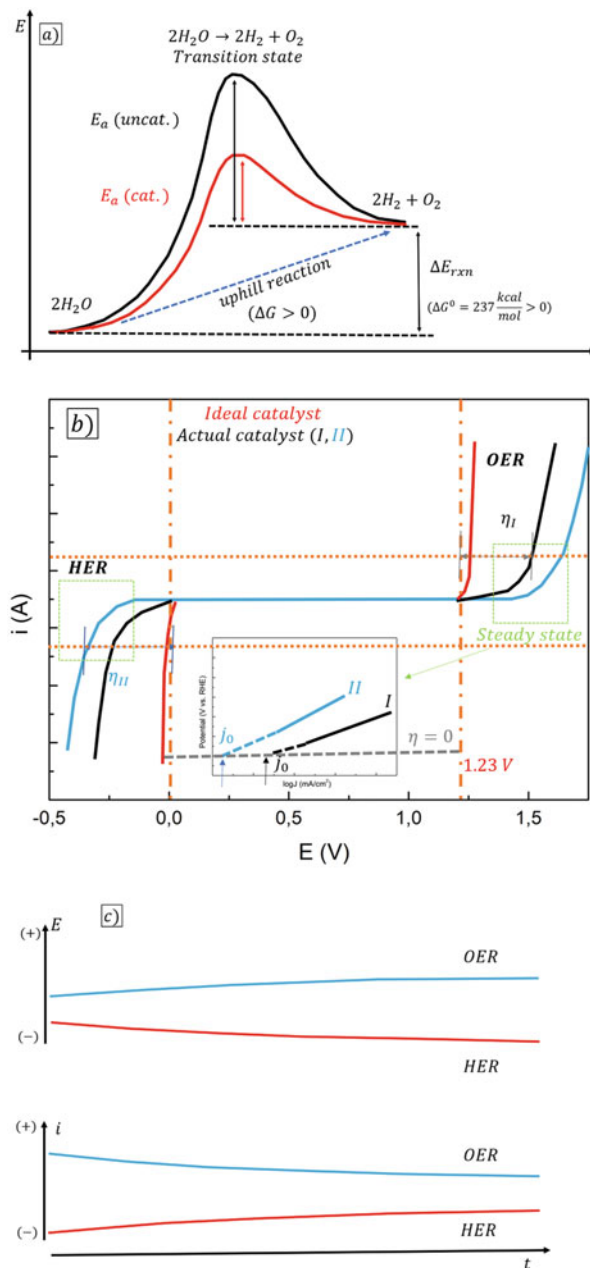
Fig. 2 Schematic illustration of the catalyst's role in lowering the activation energy barrier; (**b–d**) schematic illustrations of the performance evaluation parameters of electrocatalyst, including, (**b**) activity in terms of overpotential, Tafel slope, and exchange current density, (**c**) stability in terms of current- and potential-time curves, and d efficiency in terms of faradaic efficiency and turnover frequency

$$Faradaic\ efficiency = \frac{O_2\ (or\ H_2)\ (experimental)}{O_2\ (or\ H_2)\ (theoretical)}$$

$$Turnover\ frequency\ (TOF) = \frac{jN_A}{nF\Gamma}$$

N_A: Avogadro constant; Γ: Concentration of active sites

Fig. 2 (continued)

stability, and efficiency (Fig. 2). The activity is characterized by overpotential, Tafel slope, and exchange current density, which can be extracted from the polarization curves (Fig. 2b). The stability is characterized by the changes of the overpotential or current over time (Fig. 2c). The efficiency is characterized by the faradaic efficiency and turnover frequency in terms of experimental results vs. theoretical predictions (Fig. 2d).

For electrochemical water splitting reaction, the thermodynamic potential is 1.23 V at 25 °C and 1 atm. However, due to the kinetic barrier for the reaction, water electrolysis requires a higher potential than thermodynamic potential (1.23 V) to overcome the kinetic barrier. The excess potential is also known as overpotential (η) which mainly comes from the intrinsic activation barriers present on both anode and cathode. Overpotential is a very important descriptor to evaluate the activity of the electrocatalysts. Usually, the overpotential value corresponding to the current density of 10 mA cm^{-2} is used to compare the activities among different catalysts.

The Tafel slope and exchange current are two other parameters to assess the activity from the overpotential vs. kinetic current relationship, which is expressed by the equation: $\eta = a + b \log j$, where η is the overpotential, and j is the current density. In the Tafel plot, the linear correlation yields two important kinetic parameters. One is the Tafel slope b, and the other is the exchange current density j_0 which can be obtained by extracting the current at zero overpotential. The Tafel slope b is related to the catalytic reaction mechanism in terms of electron-transfer kinetics. For example, a smaller Tafel slope means that there is a significant current density increment as a function of the overpotential change, or in other words, faster electrocatalytic reaction kinetics. The exchange current density describes the intrinsic charge transfer under equilibrium conditions. A higher exchange current density means a greater charge transfer rate and a lower reaction barrier. A lower Tafel slope and a higher exchange current density are expected for a better electrocatalyst.

Stability is an important parameter to evaluate whether the catalyst has the potential for use in water splitting cells in practical applications. There are two typical methods for characterizing the stability of electrocatalysts. One method is

chronoamperometry (I–t curve) or chronopotentiometry (E–t curve) which measures the current variation with time under a fixed potential or measure the potential change with time at a fixed current. For this measurement, the longer the tested current or potential remains constant, the better the stability of the catalyst. For the comparison with the different research groups, people usually set a current density larger than 10 mA cm^{-2} for at least 10 h test. Another method is cyclic voltammetry (CV) which measures the current by cycling the potential, usually requiring more than 5000 cycles of run at a scan rate (e.g. 50 mV s^{-1}). Linear sweep voltammetry (LSV) is typically applied to examine the overpotential shift before and after CV cycling at a specific current density. The smaller the change of overpotential is, the better the electrocatalyst's stability.

Faradaic efficiency is a quantitative parameter used to describe the efficiency of electrons in the external circuit that is transferred to the electrode surface for the electrochemical reaction. The definition of faradaic efficiency is the ratio of the experimentally detected quantity of H_2 or O_2 to the theoretically calculated quantity of H_2 or O_2. The theoretical values can be calculated from the integration of the chronoamperometric or chronopotentiometric analysis. The experimental values are measured by analyzing the gas production using the water–gas displacement method or gas chromatography method. Turnover frequency (TOF) is a useful parameter to describe the reaction rate in terms of the catalytic sites which is the intrinsic catalytic activity of the catalyst. In general, TOF describes how many reactants can be converted to the desired product per catalytic site per unit time. However, it is usually difficult to calculate the precise TOF value for most heterogeneous electrocatalysts since the precise number of active sites per electrode area is often an estimate. Despite being relatively imprecise, TOF still is a useful way to compare the catalytic activities among different catalysts, especially within a similar system or under a similar condition.

The choice of the techniques for the analysis of activity, stability, and efficiency of the catalysts depends on the specific focus of the research and development. In addition to synthesis and preparation of the electrocatalysts, the current studies of the activity, stability, and efficiency can be grouped in three areas in terms of the specific focus: performance evaluation, structural characterization, and mechanistic determination. While the analysis of the current- or potential-time curves provides information for assessing the catalyst's durability performance, which is very important for practical applications, the determination of the overpotential, Tafel slope, exchange current density, faradaic efficiency, turnover frequency, and provides the basic parameters for assessing the electrocatalytic mechanism. Importantly, coupling of these electrochemical techniques to spectroscopic and microscopic techniques (ex-situ or in-situ) enables the structural characterization, which is crucial for gaining insights into the design of the active and stable catalysts.

In order to try to achieve this minimum possible overpotential, researchers have been investigating catalysts comprised of multiple metals. Among the most active OER catalysts, NiFe-based materials have achieved some of the lowest overpotentials reported for the OER, outperforming Ir and Ru-based electrocatalysts. Additional studies revealed that Fe impurities in Ni would lower the OER

overpotential. A major area of research has been to improve the activity of NiFe-based alkaline OER catalysts. It has been shown that both the morphology and the ratio of nickel-to-iron has been shown to govern OER activity. The optimum elemental ratio has been found to be ca. 80% Ni and ca. 20% Fe where Fe content above ca. 25% results in segregation of the metals, leading to low active site densities.

The kinetics of OER are one factor that restricts the development of efficient water splitting technologies for energy storage. With enormous research efforts devoted to seeking efficient and cost-effective OER catalysts, 3d-orbital transition metal-based catalysts have been identified as promising candidates as alternatives to noble metal catalysts (Tan et al. 2022). Numerous 3d-metal based catalysts with promising OER activity have been reported, including simple and mixed-metal oxides (hydroxides), chalcogenides, phosphates, borates, perovskites, and molecular catalysts (Orfila et al. 2022). Since OER activities are significantly affected by the strength of the M−O bond (where M = 3d-orbital transition metal), previous studies mainly focused on the development of the catalysts with crystalline structures to achieve a M−O bond strength which cannot be too strong or too weak. More importantly, it is recently reported that crystalline catalysts undergo amorphization with highly active metal oxyhydroxide phase evolving on the catalyst surface under the anodic conditions of OER. This finding has attracted research efforts to develop facile methods to fabricate amorphous metal catalysts for OER.

Although detailed mechanisms for OER remain uncertain, these steps provide a framework to describe the OER on metal oxides, and the OER activity correlate to the M-O bond strength. In the OER, the M-O bonds can be envisaged to be formed and broken during the anodic reaction, which can also be viewed as a transition of the metal oxides from a lower to a higher oxidation state. In this context, the enthalpy of the transition plays a vital role in determining the activity. Electrocatalytic activities of an array of metal oxides are shown in Fig. 3.

Fig. 3 Volcano plot showing O_2 production on metal oxide surfaces vs. the enthalpy of transition of the oxide in acidic (■) and basic (□) solution
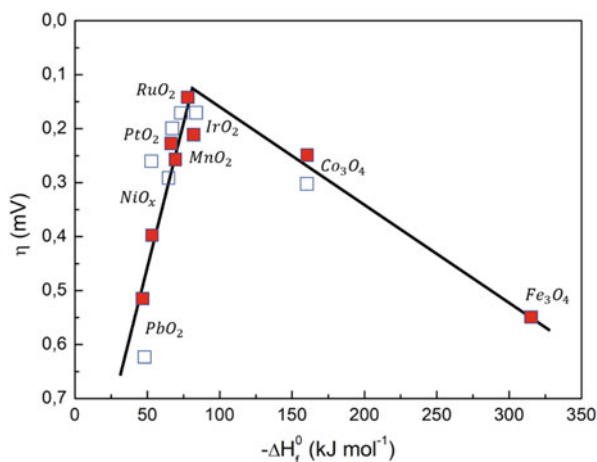
It is revealed that metal oxides with a medium enthalpy of transition from lower to higher oxidation state exhibit better OER activity, as can be attributed to the intermediate adsorption not too strong nor too weak. Therefore, the noble metal oxides RuO_2 and IrO_2 exhibited the best intrinsic OER activities among the mono-metal based catalysts.

HER is the key half-reaction to produce hydrogen at the cathode in water electrolysis which involves a two-electron transfer process. The mechanism of this HER is highly dependent on the environmental condition. For the HER reaction in acidic media, there are three possible reaction steps:

$$H^+ + e^- \leftrightarrow H_{ad}$$

$$H^+ + e^- + H_{ad} \leftrightarrow H_2$$

$$2H_{ad} \leftrightarrow H_2$$
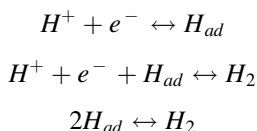
The first step is Volmer step to produce adsorbed hydrogen. Then, the hydrogen evolution reaction can proceed by Heyrovsky step or the Tafel step or both to produce H_2. For the HER reaction in alkaline media, there are two possible reaction steps, i.e., Volmer step and Heyrovsky step, as shown in the following equations, respectively:

$$H_2O + e^- \leftrightarrow OH^- + H_{ad}$$

$$H_2O + e^- + H_{ad} \leftrightarrow OH^- + H_2$$
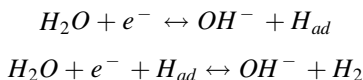
It is vital to trade-off H_{ad}, hydroxy adsorption (OH_{ad}), and water dissociation for HER activity in alkaline media. Theoretical simulations have revealed that HER activity was related to hydrogen adsorption (Had). The free energy of hydrogen adsorption (ΔGH) is widely accepted to be a descriptor for a hydrogen evolution material. A moderate value of hydrogen binding energy will benefit HER process.

The favored condition for HER is typically in acid where there is a single product and no side reactions.

However, with OER constraints it is easier to adapt HER in alkaline than OER in acid. Within an alkaline water electrolyzer, the hydrogen evolution reaction (HER) occurs at the cathode with the predominant reaction being water reduction. This is shown by the following:

$$2H_2O + 2e^- \leftrightarrow H_2 + 2OH^-$$
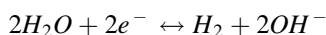
The mechanism for the HER in alkaline media is similar to the mechanism in acidic media and is shown in the following equations:

$$S + H_2O + e^- \leftrightarrow S - H_{ads} + OH^-$$
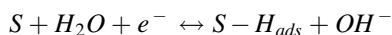
Fig. 4 Volcano plots: an exchange current density vs. the M–H bond energy for each metal surface (for acidic media); (**b**) exchange current density on monometallic surfaces vs. the calculated HBE (for alkaline media)

$$S - H_{ads} + S - H_{ads} \leftrightarrow 2S + H_2$$

or:

$$S - H_{ads} + H_2O + e^- \leftrightarrow S + H_2 + OH^-$$
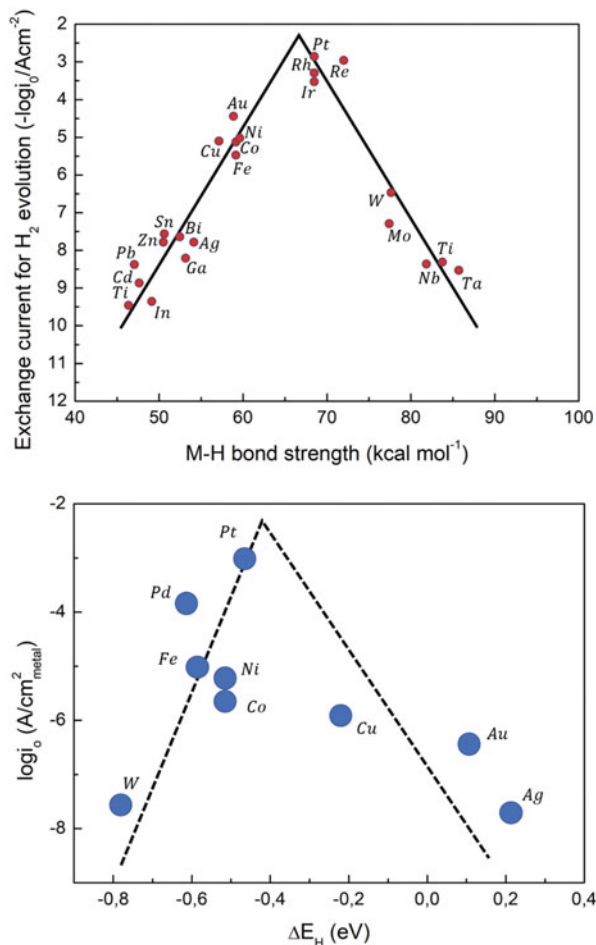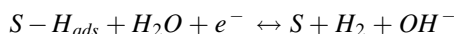
Contrary to the OER mechanism, the HER mechanism mainly depends on the adsorption strength of H on the surface of the catalysts. For the HER, most studies have shown platinum to be the prominent electrocatalyst.

This can be seen in the volcano plot Fig. 4.

In this plot, the HER activity is plotted against the free energy associated with adsorption of the hydrogen atom. At the top of the volcano is where the associated binding energy is optimal, meaning not too strong or weak. Also, an important note

for Fig. 3 is that the elements located closest to the peak of the volcano are all rare and expensive. Recent thought is that by combining certain lower elements in specific quantities could achieve similar results to platinum. Thus, it is important to find new catalysts that can have the same performance as Pt, but are comprised of non-precious metals.

3 Materials for OER

Water electrolysis is a process that decomposes water into oxygen and hydrogen using external electrical energy. Electrochemical water splitting is composed of oxygen evolution reaction (OER) at the anode and hydrogen evolution reaction (HER) at the cathode, while the efficiency of the water splitting can be improved by using efficient electrocatalysts. Water splitting in acid medium needs expensive, scarce, acid insoluble, and stable OER electrocatalysts which could be a crucial bottleneck on the way to the practical applications, while water splitting in alkaline medium can simplify the water electrolyzer system (Huang et al. 2023).

At the cathode, water molecules are reduced by electrons to hydrogen and negatively charged hydroxide ions. At the anode, hydroxide ions are oxidized to oxygen and water while releasing electrons. Overall, a water molecule reacts to hydrogen and oxygen in the ratio of 2:1.

The required cell voltage for this electrochemical reaction can be determined by thermodynamics. The free reaction enthalpy can be calculated with the reaction enthalpy, the temperature, and the reaction entropy.

The reversible cell voltage is determined by the ratio of the free reaction enthalpy to the product of the number of exchanged electrons and the Faraday constant $F = 96, 485 \ Cmol^{-1}$.

At a temperature of 25 °C and an ambient pressure of 1 bar (standard conditions), the free reaction enthalpy for the water splitting reaction is 237 $kJmol^{-1}$, which leads to a reversible cell voltage of -1.23 V. As the free reaction enthalpy is positive at standard conditions, the water splitting is a non-spontaneous reaction. Due to irreversibility, the actual cell voltage needs to be higher than the reversible cell voltage for the water splitting reaction. The thermoneutral voltage depends on the reaction enthalpy, which is composed of the free reaction enthalpy and irreversible thermal losses (de la Calle et al. 2022).

At standard conditions, the reaction enthalpy for water electrolysis is 286 $k \ Jmol^{-1}$. Hence, the thermoneutral voltage is -1.48 V.

The electrolyte is pumped through the electrolysis stack, where the product gases are formed. While natural convection can be a cost-efficient alternative, gas coverage of the electrode surface can raise the required cell voltage and therefore increase the operational costs. Additionally, most alkaline water electrolyzer systems provide a temperature control for the electrolyte to maintain an optimal temperature range.

The two-phase mixtures of liquid electrolyte and product gas leave the electrolysis cell and enter subsequent gas separators. Mostly, the phase separation is realized with a high residence time in large tanks. The product gas is demisted and dried before it is purified to the desired level.

The liquid electrolyte leaves the gas separator and is pumped back to the electrolysis stack. As the product gases are soluble in the electrolyte solution, the mixing of both electrolyte cycles causes losses and higher gas impurities. An alternative can be to use partly separated electrolyte cycles with an equalization line for liquid level balancing of both vessels. With separated electrolyte cycles, the electrolyte concentration will increase on the cathodic side due to water consumption and decrease on the anodic side due to water production. Therefore, the electrolyte requires mixing, on occasion, to maintain an optimal electrolyte conductivity.

After drying and removing oxygen impurities, the hydrogen purity is higher than 99.9%, and the hydrogen can be directly used in the following processes or in the transport sector.

The design of the electrolysis stack depends on the manufacturer; however, some general similarities can be observed.

Earlier alkaline water electrolyzers used a conventional assembly with a defined distance between both electrodes. Later, this concept was replaced by the zero-gap assembly, where the electrodes are directly pressed onto the separator to minimize ohmic losses due to the electrolyte.

Porous materials or dense anion exchange membranes can be used as the separator.

During operation, the required cell voltage is always higher than the reversible cell voltage due to different effects. In addition to the ohmic losses, there are activation overvoltages of the electrodes. The ohmic resistance of the cell design is affected by the electronic conductivity of the electrode material, the specific conductivity of the electrolyte, the ionic conductivity of the separator material, and gas bubble effects.

The zero-gap design tries to eliminate the electrolyte losses by minimizing the electrode distance. There is still a minimal gap between both electrodes, which can increase the cell voltage.

The activation overvoltages are defined by the electrode materials. Whereas nickel is the most used electrode material, it provides very high overvoltages for the oxygen and hydrogen evolution reactions. Hence, electrocatalytic materials are added to the electrodes. Iron is a cost-efficient catalyst for the oxygen evolution reaction. Molybdenum decreases the overvoltage for the evolution of hydrogen at the cathode.

Several authors have proposed correlations for the modeling of cell voltage, some others have proposed physically reasonable models based on actual dimensions and properties of the system rather than on empirical correlations.

The electrolyte resistance is determined by the specific electrolyte conductivity and the cell design. Whereas the electrolyte gap is minimal in zero-gap designs, conventional setups maintain a defined distance between both electrodes. As the specific conductivity of the electrolyte gap is affected by gas bubbles, there is an

optimal electrode distance for conventional designs. If the electrode distance is too small, the gas bubbles accumulate in the gap and lower the conductivity.

With increasing distance, the bubble detachment is enhanced and the specific conductivity increases. It is a trade-off between a small electrolyte gap as the ohmic resistance increases linearly with this parameter and a better conductivity of the space between both electrodes.

In addition to the decreasing electrolyte conductivity with higher amounts of gas bubbles, the active electrode surface can be blocked by gaseous compounds, which leads to additional losses.

As this phenomenon depends on the cell design and operation concept, there are difficulties in describing it properly. Therefore, it is often neglected, or empirical correlations referring to the gas holdup are utilized. Furthermore, the installed separator material also has significant ohmic losses. While a porous separator is often used, anion exchange membranes are promising alternatives.

The most-used electrolyte for alkaline water electrolysis is an aqueous solution of potassium hydroxide (KOH) with 20 to 30 wt.% KOH, as the specific conductivity is optimal at the typical temperature range from 50 to 80 °C. A cheaper alternative would be a diluted sodium hydroxide solution (NaOH), which has a lower conductivity.

While KOH provides a specific conductivity around 95 Sm^{-1} at 50 °C, NaOH reaches a value around 65 Sm^{-1}. At a temperature of 25 °C, a similar effect can be seen. The conductivity of KOH is around 40 to 50% higher than the conductivity of a NaOH solution at the optimal weight percentage. Another aspect is the solubility of the product gases inside the electrolyte, as this influences the resulting product gas purity. In general, the gas solubility decreases with an increasing electrolyte concentration due to the salting-out behavior. NaOH also shows a slightly higher salting-out effect than that of KOH. Hence, the product gas solubility is higher in a KOH solution.

Another approach is to use ionic liquids (ILs) as the electrolyte or as an additive, owing to their remarkable properties.

Ionic liquids are organic substances which are liquid at room temperature and are electrically conductive. A negligible vapor pressure, non-inflammability, and thermal stability are promising arguments for their utilization in water electrolysis. Furthermore, ILs can be used over a wide electrochemical window. The absorption and separation of gases is an additional area of application.

However, the toxicity of ILs is a current field of research, and the viscosity is comparably high, which should be taken into account before any large-scale implementation. In addition to providing high-efficiency water electrolysis at low temperatures, ILs are chemically inert and therefore do not require expensive electrode materials.

3.1 Kinetics of OER

The sluggish kinetics for the OER and HER are among the most serious bottlenecks preventing the mass-adoption of water electrolyzers, but at the same time, alkaline water electrolysis renders it possible to utilize non-precious metal-based electrocatalysts and is thereby widely considered to be the most promising method for large-scale application of water electrolyzes for hydrogen production. In addition, by storing electricity in the form of chemical energy (i.e., hydrogen), water electrolysis helps to mitigate the intermittent issue of renewable energies (e.g., wind, solar).

Presently, noble electrocatalysts such as Ru/Ir-based compounds for OER, and Pt for HER have been utilized as highly active electrocatalysts for water splitting, whereas their high cost and scarcity hinders their usage. Hence, the design of efficient earth-abundant electrocatalysts is imperative.

It is indispensable to develop adequate electrocatalysts with outstanding OER performance to promote the overall energy efficiency. In fact, compared to the HER, the OER process with four-electron transfer endures the more substantial kinetic barrier than thermodynamic equilibrium potential, which demands considerable overpotential to drive the electrochemical reaction, thereby impeding its large-scale applications.

In alkaline environment, the reaction could proceed with the formation of oxygen molecule and water by the oxidation of hydroxyl groups with the involvement of four electrons:

$$4OH^- \rightarrow O_2 + 2H_2O + 4e^-$$
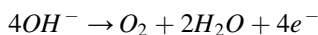
In Fig. 5 it is depicted the basic mechanism for OER.

In the stage 1, a catalyst*OH intermediate and an electron could be formed by the interaction of a hydroxyl group with a catalytic active site:

Fig. 5 OER mechanism for alkaline water electrolyses

$$Catalyst * + OH^- \rightarrow Catalyst * OH + e^-$$
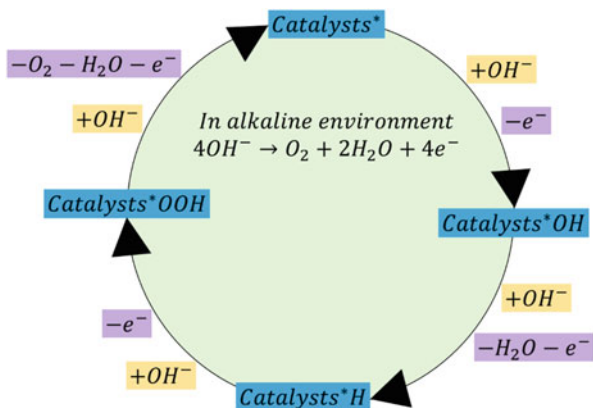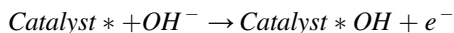
In the stage 2, a catalyst*O intermediate, a water molecule and an electron could be formed by the interaction of a second hydroxyl group with the above catalyst*OH intermediate:

$$Catalyst * OH + OH^- \rightarrow Catalyst * O + H_2O + e^-$$
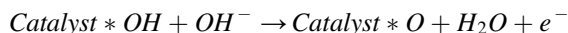
In the stage 3, a catalyst*OOH intermediate and an electron could be formed by the interaction of a third hydroxyl group with the above catalyst*O intermediate:

$$Catalyst * O + OH^- \rightarrow Catalyst * OOH + e^-$$
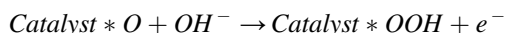
Finally in the stage 4, an oxygen molecule, a water molecule and an electron could be formed, while the catalytic active site could also be retained at this stage by the interaction of a fourth hydroxyl group with the above catalyst*OOH intermediate:

$$Catalyst * OOH + OH^- \rightarrow Catalyst * + O_2 + H_2O + e^-$$
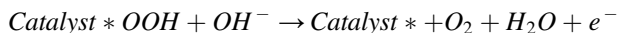
Therefore, developing OER electro-catalysts with efficient, earth abundant, cheap, stable, and operating at low overpotential are essentially important to achieve efficient-cheap hydrogen production even for addressing resource depletion and environmental issues by using renewable solar and wind energy. So now some of the new electrocatalysts are presented.

3.2   NiFe-Based Catalysts for OER

In terms of earth-abundant, Fe and Ni are promising elements for the building of the electrolizers because the former is the 4th most common element in the earth's crust with the abundance of >3%, while the later exhibits >50 ppm of abundance in the earth's crust. The incorporation of Fe in Ni-based catalyst could modify the electronic structure and that could enhance the activity for OER. Here there are presented some of the Ni-Fe electrocatalysts suggesting that could be promising candidates for achieving optimal adsorption for OER intermediates by tuning the electronic structure, and that could enhance the OER activity.

Various promising strategies have been used to achieve high performance electrocatalysts for OER:

1. Gas evolution behavior could significantly influence the activity and stability for OER (Xu et al. 2021), while constructing nanostructured catalyst especially on 3D substrate could be a promising approach to improve the gas evolution behavior (Sumedha et al. 2022). Fabricating nanostructured catalyst could afford superaerophobic surface, which can diminish the bubble size and bubble adhesive

force by forming a discontinuous triple phase contact line (TPCL) rather than continuous TPCL, and that can facilitate the evolution of gas, while it can provide abundant active sites, and that can boost the activity and stability for OER;

2. Theoretical calculations could be potentially useful to design the new catalysts with optimal binding energy for OER intermediates to achieve high activity: Therefore, combining of theoretical calculations with experimental characterization significantly accelerates the development of the high performance OER electrocatalysts;

3. Optimal adsorption for OER intermediates could be achieved by tuning the electronic structure to attain high activity, while the electronic structure can be tuned by constructing nanostructured NiFe LDH with hydroxide interfacial layer, cation/anion doping in NiFe LDH, creating cation/oxygen vacancies in NiFe LDH, integrating graphene with NiFe LDH, integrating graphene with NiFe nitride, constructing heterostructured NiFe LDH/NiFe oxide/NiFe (oxy)-hydroxide/NiFe alloy/NiFe selenide, Fe doping in Ni oxide, heteroatom incorporation in NiFe oxide, borate incorporation in NiFe(oxy)hydroxide, constructing V and Fe co-doped nickel(oxy) hydroxide, constructing NiFe chalcogenide (sulfide and selenide), preparing NiFe nitride, introduction of Fe into metal-organic framework (MOF) structure, and constructing NiFe glycerolate (Adegoke and Maxakato 2022);

4. The in situ formation of thin oxide/oxyhydroxide layer on the catalyst surface with the shrinkage of the metal–oxygen bond length and generation of high valence metal ions, especially high valence Ni ions during OER could also contribute a key role in the enhanced OER performance, while constructing nanostructured NiFe LDH, NiFe chalcogenide (sulfide and selenide), NiFe phosphide, and NiFe alloy integrated with carbon could exhibit the in situ formation of thin oxide/oxyhydroxide layer with the generation of high valence metal ions on their surface during OER (Zhang et al. 2022);

5. Constructing electrocatalysts with metallic character could provide fast electron transfer, which could overcome the Schottky barrier and facilitate the charge transport process, and that could enhance the OER performance, while constructing NiFe pnictide (phosphide and nitride), sulfide, amorphous nickel hydroxide derived from NiFe MOF could exhibit metallic character;

6. Fabricating electrocatalysts with high electrocatalytic active surface area (ECSA) could afford abundant active sites, which could enhance the OER performance, while constructing NiFe based electrocatalysts with different morphologies such as nanomesh, nanocages, holey nanosheet structure, nanoarray, nanowire array, nanoplate array, nanosheet array, nanotube array, nano-cone array, core-shell structure, heterostructure, porous structure, hollow nanocube array, hollow nanochains, hollow nanoparticles, hollow spheres, and microspheres could provide high ECSA.

Now it will be presented a series of the most important NiFe based electrocatalysts in order to improving OER thus improving alkaline water electrolysis performances.

NiFe LDH (LDH: Layered double hydroxide) can be prepared by various synthesis methods such as hydrothermal treatment, alcohothermal method, precipitation method, hydrolysis-promotion-deposition method, electrodeposition followed by oxidation in air, electroless deposition followed by soaking, MgO-mediated strategy, pulsed ultrasonication of monolayer LDH precursors, corrosion engineering method, and dissolution-precipitation process. Hydrothermal treatment is a promising strategy to prepare nanostructured NiFe LDH, where the Fe incorporation into Ni hydroxides can lead to the in-situ formation of highly active NiOOH phase on NiFe LDH during oxygen evolution reaction (OER), while the nanostructure can provide abundant active sites and facilitate the gas evolution, and that can enhance the activity and stability for OER.

In the year 2014, Sun's group has observed that NiFe LDH nano-plate array exhibits enhanced activity and stability for OER. The NiFe LDH nano-plate array possesses nano-plate array morphology, which can afford abundant active sites and facilitate the gas evolution; It is composed of crystalline NiFe LDH with +3 and +2 oxidation states of Fe and Ni, while it contains about 3:1 atomic ratio of Ni and Fe. The NiFe LDH nano-plate array exhibits higher OER activity than $Ni(OH)_2$ and Ir /C.

For OER in 1.0 M KOH, the NiFe LDH nano-plate array exhibits enhanced activity (η of 240 mV at >25 mA cm^{-2}; Tafel slope: 50 mV dec^{-1} (dec: decade)), while it affords high current density of 190 mA cm^{-2} for 10 h with 97.8% retention at η of 270 mV, and it retains its nano-plate array morphology after stability test, which suggests its robust stability. Moreover, in the year 2014, others observed that NiFe LDH prepared by hydrothermal treatment exhibits enhanced activity (η of 240 mV at 10 mA cm^{-2}) for OER in 1.0 M NaOH, while 12.3% efficiency of water photolysis is achieved by the combination of the perovskite tandem cell with NiFe LDH catalysts.

In addition, Xu et al. and Liu et al. have also observed the enhanced OER activity for hydrothermally prepared nanostructured NiFe LDH in alkaline environment. Preparing NiFe LDH with hydroxide interfacial layer could boost the OH intermediate adsorption, and that can enhance the OER performance.

The NiFe LDH nano-array with hydroxide interfacial layer on NiFe foil exhibits higher OER activity, higher TOF (TOF: turnover frequency; TOF of 0.072 s^{-1} at η of 250 mV; and lower charge transfer resistance than NiFe LDH nano array on Ni foil and NiFe LDH nano array on Fe foil. The NiFe LDH nano array with hydroxide interfacial layer is composed of crystalline NiFe LDH with Ni and Fe are in +2 and + 3 oxidation state, respectively, where Ni, Fe, and O are uniformly distributed. It possesses nano sheet array morphology (Thickness: about 15–25 nm; Size: about 400–650 nm).

The NiFe LDH nano-array with hydroxide interfacial layer exhibits enhanced activity (η of 130 mV at 10 mA cm^{-2}) and stability (reasonable stability at η of 270 mV for 10 h) for OER in 0.1 M KOH. Preparing chrysanthemum flower-like NiFe LDH with numerous nano-petal units can afford abundant active sites, which can enhance the activity and stability for OER. It has been observed that NiFe LDH chrysanthemum flower like exhibits enhanced activity and stability for OER.

Preparing NiFe LDH with hierarchical hollow structure can provide abundant active sites and facilitate ion transport kinetics, and that can enhance the activity and stability for OER.

It has been observed that NiFe LDH HS (HS: Hollow spheres) exhibits enhanced activity and stability for OER. The NiFe LDH HS exhibits higher OER activity, TOF (TOF of 0.206 s^{-1} at η of 300 mV), and electrochemically active surface area than that of NiFe LDH nanoparticles. The NiFe LDH HS is crystalline; it possesses hollow spherical structure (shell thickness of LDH: 50 nm), where the LDH spheres (350 nm) is composed of nano-platelets with the thickness of 5 nm and lateral size of 50 nm; it contains Ni and Fe, which are uniformly distributed; it contains Ni^{2+} and Fe^{3+}; it exhibits high specific surface area (155.4 m^2g^{-1}) and mesopores (about 3–5 nm).

The NiFe LDH HS exhibits enhanced activity (η of 239 mV at 10 mA cm^{-2}) and stability (it exhibits negligible decay at η of 300 mV for 11.1111 h, while it retains its morphology after multi-step chronopotentiometric measurement for 2.7777 h) for OER in 1.0 M KOH.

It was observed that NiFe LDH nanomesh exhibits enhanced activity and stability for OER.

The NiFe LDH nanomesh exhibits higher OER activity, TOF (TOF of 1.49 s^{-1} at η of 300 mV), and electrochemically active surface area than that of NiFe LDH nanosheet. The NiFe LDH nanomesh contains Ni, Fe, and O, which are uniformly distributed, while it contains 3.20:1 M ratio of Ni:Fe.

It is composed of single crystalline hexagonal structure of NiFe LDH in the basal xy-plane, where the single crystalline structure can enhance the electrocatalytic process owing to better intralayered conductivity than that of polycrystalline catalysts; It contains abundant nanopores (2.4 nm), which exhibits nanomesh structure; It exhibits high specific surface area of 57.7 m^2g^{-1}.

The NiFe LDH nanomesh exhibits enhanced activity (η of 184 mV at 10 mA cm^{-2}), stability (negligible decay at η of 300 mV for 48 h), and durability (negligible decay at 275 mA cm^{-2} after 3000 cycles of CV) for OER in 1.0 M KOH. The structural investigation on NiFe LDH nanomesh after 100 cycles of CV for OER suggested that the pore region is more electro-active to produce active α-NiOOH phase during repeated redox reactions, which can enhance the OER activity; moreover, enhanced OER stability is observed for NiFe LDH nanomesh, where the structural deformation can be almost inhibited by the abundant nanopores in nanomesh structure, which can afford ample space for buffering the volume change during repeated redox reactions.

It has been observed that NiFe LDH UF (UF: Ultrafine) exhibits enhanced activity and stability for OER. The NiFe LDH UF exhibits higher OER activity and lower charge-transfer resistance than that of NiFe LDH monolayer and NiFe LDH bulk. The NiFe LDH UF is crystalline; it possesses ultrafine structure with small lateral size (≈ 2.3 nm) and monolayer thickness (≈ 0.6 nm); it contains ≈ 2.90: 1.00 M ratio of Ni:Fe.

The NiFe LDH UF exhibits enhanced activity (η of 254 mV at 10 mA cm^{-2}) and stability (reasonable stability at η of 254 mV for 12 h) for OER in 1.0 M KOH. The corrosion rate of the electrode can be altered by the formation of corrosion products on the electrode surface during immersion in electrolyte at different immersion time intervals. The NiFe LDH nanosheet array prepared by corrosion engineering method exhibits higher OER activity and stability than that of NiFe LDH prepared by electrodeposition method. The NiFe LDH nanosheet array is crystalline and it possesses nanosheet array morphology. For OER, the NiFe LDH nanosheet array on 3D Fe foam exhibits enhanced activity (η of 200 mV at 10 mA cm^{-2}) in 1.0 M KOH, while it affords robust stability by exhibiting negligible decay at 1000 mA cm^{-2} for 5000 h in 1 M KOH followed by 1050 h in 10 M KOH (Mathew et al. 2022).

The robust stability and activity could be due to the construction of nanostructured catalyst on 3D substrate, which could facilitate the evolution of gas, while it could alleviate the blocking of abundant active sites, and that could boost the stability and activity.

OER active mixed Ni–Fe oxide has been synthesized by three different methods such as evaporation induced self-assembly, hard templating, and dip-coating. The mixed Ni–Fe oxide with nearly 10 mol % Fe content exhibits highest OER activity, while the mixed Ni–Fe oxide exhibits enhanced OER activity than that of parent metal oxide; Fe predominantly exists in the +3 oxidation state in the Ni–Fe oxide, and Fe_2O_3 phase is formed in >25 mol % Fe content, while mixed $NiO/NiFe_2O_4$ phase is formed at low Fe content. It was observed that under electrochemical oxygen evolution conditions, the average coordination of Fe atoms increases, which could be due to the increase in octahedrally coordinated Fe in $NiFe_2O_4$. This suggests that the enhanced OER activity in Ni–Fe oxide could be attributed to the Fe, while Fe could be in the active site for water oxidation in Ni–Fe oxide.

In the year 2015, it was observed that oxides of Ni and Fe formed after acid etching on NiFe foam exhibits higher OER activity than that of bare NiFe foam. Besides, it was observed that Ni/Fe_3O_4 composite comprising of metallic Ni and Fe_3O_4 along with tiny amount of oxides of Ni exhibits enhanced OER activity than that of NiFe LDH, Fe_3O_4, and Ni, where the composite is prepared by hydrothermal treatment followed by reduction.

It was observed that Ni_2Fe_1–O exhibits enhanced activity and stability for OER. The Ni_2Fe_1–O exhibits higher OER activity, lower charge-transfer resistance, and lower electrochemical activation energy (the OER activity of the Ni_2Fe_1–O increases with increase in temperature) than that of $Ni_{1.5}Fe_{1.5}$-O and Ni_1Fe_2–O, while the Ni_2Fe_1–O loaded at 150 μg cm^{-2} exhibits higher OER activity than that of Ni_2Fe_1–O loaded at 50, 100, and 200 μg cm^{-2}. The Ni_2Fe_1–O is polycrystalline, which contains $NiFe_2O_4$- type of oxide with residual Al; it contains O_2–2/O−, Ni^{2+}, Fe^{3+}, and Al^{3+}. The Ni_2Fe_1–O exhibits enhanced activity (η of 244 mV at 10 mA cm^{-2}) and stability (negligible decay at 10 mA cm^{-2} for 60 h) for OER in 1.0 M KOH. It was observed that $NiFe_2O_4$ QD (QD: Quantum dots) exhibits enhanced activity and stability for OER. The $NiFe_2O_4$ QD exhibits higher OER activity than that of NiFe LDH. The $NiFe_2O_4$ QD exhibits enhanced activity (η of

262 mV at 10 mA cm^{-2}), durability (very slight decay after 2000 cycles of CV) and stability (negligible decay at 10 mA cm^{-2} as well as at η of 260 mV for 100 h) for OER in 1.0 M KOH.

It was observed that Fe doped NiOx nanotubes exhibits enhanced OER activity than that of Fe doped NiOx nanosheets and NiO nanotubes and that NiFeOx nanotube array exhibits enhanced activity and stability for OER. The NiFeOx nanotube array exhibits higher OER activity and kinetics than that of Ni nanotube array. The NiFeOx nanotube array exhibits fringe spacing of 0.254 nm, which corresponds to the (012) lattice plane of NiFe LDH; it contains Ni^{2+}, Ni^{3+}, and Fe^{3+}. It contains Ni, Fe, and O, which are uniformly distributed, and it possesses nanotube array morphology. For OER in 1.0 M KOH, the NiFeOx nanotube array exhibits outstanding activity, which requires only η of 350 mV to deliver huge current density of 1000 mA cm^{-2} and it needs only η of 260 mV to deliver 100 mA cm^{-2}, while it exhibits steady potential from 200 to 2000 mA cm^{-2}, and it exhibits reasonable stability at η of 260 mV for 12 h, and it almost retains its morphology after electrolysis, which indicates its robust stability.

It is observed that NiFeO NC (NC: Nanocubes) exhibits higher OER activity than that of NiFeO nanoparticles, Fe$_2$O$_3$ nanoparticles, and NiO nanoparticles: it possesses 200 nm of side length, while it a composite with 3:2 M ratio of Ni:Fe comprising of NiO, γ-Fe$_2$O$_3$, and α-Fe$_2$O$_3$.

On the other hand, it was observed that heteroatom (P, B, or S) incorporated NiFe–O nanotubes exhibits higher OER activity than that of NiFe–O.

Moreover, it was shown that nanostructured sulfur-incorporated NiFe$_2$O$_4$ exhibits higher OER activity than that of NiFe$_2$O$_4$. Zhang et al. have observed that NiFe$_2$O$_4$–NiOOH nano-array exhibits enhanced activity and stability for OER. The NiFe$_2$O$_4$–NiOOH exhibits higher OER activity and lower charge transfer resistance than that of Fe$_2$O$_3$ and Ni(OH)$_2$. The NiFe$_2$O$_4$–NiOOH nano-array is composed of NiFe$_2$O$_4$ and NiOOH, which can modulate the local electronic structure; it affords high conductivity.

For OER in 1.0 M KOH, the NiFe$_2$O$_4$–NiOOH nano-array exhibits outstanding activity, which requires only η of 410 mV to deliver substantially much high current density of 3000 mA cm^{-2} and it needs only η of 240 mV to deliver 30 mA cm^{-2}, while it exhibits negligible decay in current density for 100 h, and it shows negligible decay at 300 mA cm^{-2} after 1000 cycles of CV, which indicates its robust stability. Besides, it was observed that NiFeOx@CuO nanowire exhibits higher OER activity than that of NiFeOx and CuO, where it could expose abundant active sites and facilitate electron/mass transport, and that could enhance the water oxidation performance. It was shown that FeNi$_3$/NiFeOx exhibits higher OER activity that of NiFeOx, where it could tune the electronic structure and facilitate the electron/mass transport, and that could enhance the water oxidation performance.

The search for especially Fe-based OER electrocatalysts from naturally occurring metallic minerals having unique crystal structure is desirable to achieve efficient water splitting. It was observed that aged-Gibeon-based (Fe-based) electrocatalyst affords much high stability and activity for OER: the Gibeon meteorite is composed of 93.8% of Fe, 5.5% of Ni along with 0.4% of Co, and 0.2% of P, while it exhibits

Kamacite phase with BCC crystal structure with the side length of a unit cell of 2.87 Å. Besides, it was prepared OER active monolithic nanoporous NiFe alloy by dealloying of the laser processed NiFeAl alloy: the NiFe alloy prepared by dealloying exhibits higher OER activity than that of laser processed NiFe alloy; it could expose abundant active sites and facilitate electron/mass transport. Fabricating amorphous NiFe nano-tube array can modulate electronic structure, expose abundant active sites, facilitate the gas evolution, improve electron/mass transport, and that can enhance the water oxidation performance. It was observed that NiFe nanotube array exhibits enhanced activity and stability for OER. The NiFe nanotube array exhibits higher OER activity, higher electrochemical active surface area and lower charge-transfer resistance than that of Fe nanotube array and Ni nanotube array. The NiFe nanotube array is amorphous; it contains about 0.57:0.43 atomic ratio of Ni:Fe. The XPS spectrum of Ni $2p_{1/2}$ for NiFe nanotube array exhibits a positive shift of about 0.2 eV than that of Ni nanotube array suggesting the strong electron interactions between Ni and Fe in the NiFe nanotube array; it exhibits highly hydrophilic and it possesses nanotube array morphology with 300 nm in diameter, 25 nm in wall thickness, and 2.1 μm in length. Thus, amorphous NiFe nanotube array can modulate electronic structure, expose abundant active sites, facilitate the gas evolution, improve electron/mass transport, and that can enhance the performance for OER. The NiFe nanotube array exhibits enhanced activity (η of 216 mV at 50 mA cm^{-2}) and stability (negligible decay at 100 mA cm^{-2}) for OER in 1.0 M KOH.

OER stable and active ternary alloys encapsulated in N doped graphene layers (FeCoNi/N-doped graphene) were fabricated by annealing of metal-organic frameworks, which could increase the degrees of freedom of alloys and modify the electronic structure, and that could enhance the OER performance. Besides, Guo et al. have observed that boronized NiFe sheet exhibits higher OER activity than that of the boronized Ni sheet and boronized Fe sheet, while it retains η of 270 mV at 10 mA cm^{-2} for 3000 h, which indicates its robust stability. Moreover, it was observed that FeNiB exhibits higher OER activity, higher electrochemical active surface area and lower charge transfer resistance than that of bare FeNi foam. In addition, it was observed that amorphous trimetallic boride nanocatalyst (Fe–Co-2.3Ni–B) exhibits higher OER activity than that of Fe–Co–Ni alloy, where the B in amorphous metal boride could alter the electronic structure, which could enhance the water oxidation performance (Yao et al. 2022).

Moreover, it was observed that NiCoFeB exhibits higher OER activity than that of the NiCoB and CoFeB, while it was synthesized by one-step $NaBH_4$ reduction of Co^{2+}, Fe^{2+}, and Ni^{2+} under ambient temperature. Besides, it was observed that $FeNi_3$–B with 30% of rGO exhibits higher OER activity than that of $FeNi_3$–B. Moreover, it was observed that NiFeB/rGO exhibits higher OER activity and lower charge transfer resistance than that of NiFeB. Besides, it was observed that molybdenum oxide decorated NiFe alloy nanosheets exhibits higher OER activity than that of NiFe alloy.

Preparing nanostructured Fe doped Ni phosphide can expose abundant active sites, in-situ form metal(oxy)hydroxide during OER, facilitate the evolution of gas, improve the electron/mass transport, and that can enhance the water oxidation performance. It was, observed that $(Ni_{0.33}Fe_{0.67})_2P$ nanosheet array exhibits enhanced activity and stability for OER. The $(Ni_{0.33}Fe_{0.67})_2P$ nanosheet array exhibits higher OER activity and kinetics than that of Ni_2P and FeP. The $(Ni_{0.33}Fe_{0.67})_2P$ nano sheet array is crystalline, which is composed of Fe-doped Ni_2P, and it exhibits low charge-transfer resistance.

The $(Ni_{0.33}Fe_{0.67})_2P$ nanosheet array exhibits enhanced activity (η of 230 mV at 50 mA cm^{-2}) and stability (98.2% retention at η of 260 mV for 12 h;) for OER in 1.0 M KOH.

It was observed that etched NiFeP exhibits enhanced activity and stability for OER.

The etched NiFeP exhibits higher OER activity and electrochemical active surface area than that of NiFeP. The NiFeP is a free standing electrode, is amorphous, it contains Ni, Fe, and P, which are uniformly distributed, while it contains thin oxide layer on surface (Thickness: 5–7 nm); it contains both metallic Ni/Fe bonds (Ni–Ni: 2.48 Å; Fe–Fe: 2.46 Å) and phosphides bonds (Ni–P: 2.22 Å; Fe–P: 2.30 Å), where the metallic bonds could enhance the electron transport, while the phosphides bonds can afford moderate bonding to the OER intermediates. The etched NiFeP exhibits enhanced activity (η of 219 mV at 10 mA cm^{-2}) and stability (reasonable stability at 10 and 100 mA cm^{-2} for 12 h) for OER in 1.0 M NaOH. Moreover, it was observed that amorphous Ni–Fe–P alloy exhibits higher OER activity and lower charge transfer resistance than that of Ni–Fe alloy, while it is prepared on Cu foil by electrodeposition method. Besides, it was observed that NiFeP nanosheet array with a thin amorphous layer exhibits higher OER activity, lower charge transfer resistance and higher electrochemically active surface area than that of NiFe LDH and NiFe–O, while it is obtained by hydrothermal treatment followed by thermal phosphorization.

Moreover, it was observed that Ni-Fe$_x$P exhibits higher OER activity and lower charge transfer resistance than that of Ni–Fe(OH)$_x$, and Fe$_x$P, while it is prepared by wet chemical process followed by low-temperature phosphidation. In addition, it was fabricated nanoporous $(Ni_{0.67}Fe_{0.33})_4P_5$. Moreover, it was observed that $(Ni_{0.51}Fe_{0.49})_{12}P_5$ exhibits higher OER activity than that of $Ni_{12}P_5$ and Fe_2P, which could afford abundant active sites and facilitate the electron transfer, and that could improve the OER performance.

Besides, it was observed that NiFe-Phosphate/Phosphide exhibits higher OER activity and electrochemically active surface area than that of NiFe-Phosphate and NiFe-Phosphide, while it is prepared on NiFe foam by the CO_2/PH$_3$/H$_2$ plasma treatment followed by PH$_3$/H$_2$ plasma treatment. Moreover, it was observed that $Ni_{40}Fe_{40}P_{20}$ metallic glass exhibits higher OER activity than that of crystallized $Ni_{40}Fe_{40}P_{20}$, glassy $Ni_{40}Pd_{40}P_{20}$, and glassy $Ni_{70}Pd_{10}P_{20}$, while it is prepared by melt spinning method followed by annealing.

Moreover, it was observed that the NiCoFeP hollow nano-cubes exhibits higher OER activity and lower charge transfer resistance than that of NiFeP and CoFeP, while NiCoFeP exhibits higher OER activity than that of NihighCoFeP. The synergistic effect exits from the triad of phosphides (Ni_5P_4, Fe_2P, and CoP) in the optimal porous NiCoFeP hollow nanocubes could expose abundant active sites and facilitate the electron/mass transport, and that could enhance the water oxidation performance. Besides, it was fabricated OER active $Fe_{10}Co_{40}Ni_{40}P$ nanosheet array on Ni foam by electrodeposition followed by low temperature phosphidation, while it could expose abundant active sites, enhance charge transfer, and facilitate the gas evolution, and that could enhance the water oxidation performance. On the other hand, Sial et al. have fabricated OER active NiCoFeP by one step hydrothermal treatment at 150 °C, while it is ultra-thin, porous, and amorphous. Moreover, it was observed that iron-doped nickel cobalt phosphide nanoplate arrays on carbon cloth exhibits higher OER activity and lower charge transfer resistance than that of NiFeP, CoFeP, and NiCoP, while it is obtained by hydrothermal treatment followed by phosphidation (Tang et al. 2023).

Besides, it was observed that $Ni_2P@FePO_x$ exhibits higher OER activity than that of NiFe LDH and $Ni_2P@Ni(OH)_2$, while it exhibits significantly much high stability (reasonable stability at huge current density of 1000 mA cm^{-2} for 25 h).

It was observed that Ni_2P-$(NiFe)_2P(O)$ nano array exhibits enhanced activity and stability for OER. The Ni_2P-$(NiFe)_2P(O)$ nano-array exhibits higher OER activity, higher electrochemical active surface area and lower charge-transfer resistance than that of Ni_2P and $(NiFe)_2P$.

The Ni_2P-$(NiFe)_2P(O)$ nano-array is composed of oxygen-doped nickel iron phosphide; it contains Ni_2P with a fringe spacing of 0.220 nm, which corresponds to the (111) lattice plane, while it contains solid solution of $(NiFe)_2P$ with a fringe spacing of 0.221 nm, which exists between the distance of Ni_2P (0.220 nm) and Fe_2P (0.223 nm); it contains Ni–P and Fe–P and Ni, Fe, P, and O, which are uniformly distributed. For OER in 1.0 M KOH, the Ni_2P-$(NiFe)_2P(O)$ nano-array exhibits enhanced activity (η of 150 mV at 10 mA cm^{-2}). For OER in 1.0 M KOH, the Ni_2P-$(NiFe)_2P(O)$ nano-array exhibits negligible decay at η of 300 mV and 500 mV by delivering 130 mA cm^{-2} and 650 mA cm^{-2}, respectively for 100 h, and it exhibits reasonable stability at η of 650 mV by delivering huge current density of 1000 mA cm^{-2} for 100 h, while, for OER in 7.64 M KOH, it exhibits reasonable stability at η of 570 mV by delivering huge current density of 2000 mA cm^{-2} for 50 h indicating its robust stability. Moreover, Lei et al. have observed that nano-structured NiFe-OH-PO_4 exhibits higher OER activity than that of NiFe–OH, while it is prepared by electrodeposition process. In addition, it was observed that NiFe–OH/NiFeP exhibits higher OER activity and electrochemically active surface area than that of NiFe double hydroxide and NiFeP, while it is obtained by hydrothermal treatment followed by PH_3 plasma treatment followed by electrodeposition. Constructing NiFe-phenylphosphonates with distorted geometry can exhibit the in-situ formation of NiFe hydroxide with distorted geometry and provide synergetic effect between the Ni and Fe metals, and that enhance the water oxidation performance.

It was observed that $Ni_xFe_yO_3PC_6H_5 H_2O$ exhibits enhanced activity and stability for OER. The $Ni_xFe_yO_3PC_6H_5 H_2O$ exhibits higher OER activity, TOF (TOF of $0.100 s^{-1}$ at η of 300 mV) and electrochemically active surface area than that of NiFe LDH and NiFeOx. The $Ni_xFe_yO_3PC_6H_5 H_2O$ is an organic–inorganic compound with layered structures comprising of inorganic layers separated by bilayers of the organic group, where the inorganic layers are composed of strongly distorted corner-shared NiO_6 and FeO_6 octahedra. After OER, the $Ni_xFe_yO_3PC_6H_5 H_2O$ exhibits the in-situ formation of thin NiFe hydroxide nanosheets (Thickness: 3–10 nm) with distorted octahedral coordination.

Thus, the synergetic effect between the Ni and Fe metals, in-situ formation of NiFe hydroxide, and existence of distorted metal sites in $Ni_xFe_yO_3PC_6H_5 H_2O$ can enhance the water oxidation.

Fabricating nanostructured NiFe based sulfide electrocatalysts could modulate the electronic structure, tune the adsorption energies of the OER intermediates, expose abundant active sites, enhance electron transfer, facilitate gas evolution, and exhibit the in-situ formation of the NiFe (oxy)hydroxide, and that could enhance the water oxidation performance.

It was observed that $Fe_{0.1}$ doped NiS_2 nano-array exhibits higher OER activity and electrochemically active surface area than that of NiS_2 and NiFe LDH, while it was obtained by the sulfidation of NiFe LDH precursor, and the precursor was prepared by hydrothermal treatment.

Constructing complex polymetallic sulfides with nano-tube array morphology can expose abundant active sites, exhibit synergistic effects among different metal ions, enhance electron/mass transport, facilitate gas evolution, and that can enhance the water oxidation performance. The MoS_2-$(Co,Fe,Ni)_9S_8$ nanotube array possesses nanotube array morphology with diameter of 150 nm and thickness of about 30–80 nm, which can afford superaerophobic surface. It is comprised of crystalline MoS_2 and $(Co,Fe,Ni)_9S_8$; it contains 1 T0 MoS_2 with 2.79 Å of bond length for Mo–Mo.

The tetragonal symmetry of atomic arrangement for 1 T0 MoS_2 and cubic symmetry of the crystals for $(Co,Fe,Ni)_9S_8$ in MoS_2-$(Co,Fe,Ni)_9S_8$ nanotube array can be seen; it exhibits the coexistence of low and high valence ions (Ni^{2+}, Ni^{3+}, Fe^{2+}, Fe^{3+}, Co^{2+}, and Co^{3+}). Thus, the MoS_2-$(Co,Fe,Ni)_9S_8$ nanotube array can expose abundant active sites, exhibit synergistic effects among Fe, Co, Ni ions, afford excellent conductivity due to metallic 1 T' MoS_2, enhance electron/mass transport, facilitate gas evolution, and that can enhance the performance for OER.

For OER in 1.0 M KOH, the MoS_2-$(Co,Fe,Ni)_9S_8$ nanotube array exhibits enhanced activity (η of 184 mV at 10 mA cm^{-2}), while it affords enhanced stability by exhibiting negligible decay with slight increased initial current density (> 200 mA cm^{-2}) at η of 566 mV for 80 h. In addition, after 1000 OER cycles, it retains its morphology and crystal structures suggesting its robust durability, while the Ni, Fe, and Co 2p of MoS_2-$(Co,Fe,Ni)_9S_8$ nanotube array exhibits slight positive-shifts (0.3 eV), which are ascribed to the in-situ low-level oxidation of Ni, Fe, and Co-based sulfides in the water oxidation.

Moreover, it was observed that MoS_2-$(Co,Fe,Ni)_9S_8$ nano array exhibits higher OER activity than that of MoS_2 and $Fe_5Ni_4S_8$, while it is obtained by chemical vapor deposition using three-temperature-zone furnace.

Besides, it was observed that P–S–NiFe nanocubes exhibits higher OER activity, higher electrochemically active surface area and lower charge transfer resistance than that of S–NiFe, P–NiFe, S–P–NiFe, and NiFe nanocubes, while it was obtained by self-assembly process followed by phosphorization followed by sulfurization. Moreover, it was observed that $(NiFe)PS_3$ nanosheet exhibits higher OER activity and lower charge transfer resistance than that of $(NiFe)S_2$ and $(NiFe)_2P$, while it was obtained by a one-pot phosphorization and sulfurization of NiFe PBA precursor, and the precursor was prepared by modified co-precipitation process.

Constructing Se based NiFe chalcogenide nanostructure could modify electronic structure, afford optimum adsorption energy for OER intermediates, enhance electron transfer, expose abundant active sites, facilitate gas evolution, and exhibit in situ formation of the NiFeOOH on the catalyst surface during OER, and that could boost the performance for water oxidation.

It was observed that $(Ni_{0.75}Fe_{0.25})Se_2$ nanosheets exhibits higher OER activity, higher electrochemically active surface area, and lower charge transfer resistance than that of $NiSe_2$ and NiFe based precursor, while it was obtained on carbon fiber cloth by hydrothermal treatment followed by selenization. Moreover, it was observed that $(Ni_{0.75}Fe_{0.25})Se_2$ hollow nanochains exhibits higher OER activity, higher electrochemically active surface area, and lower charge transfer resistance than that of $NiSe_2$ and Ni_3Fe, while it was obtained by two-step hydrothermal treatment.

On the other hand, it was observed that PVP decorated $(Ni_{0.75}Fe_{0.25})Se_2$ hollow nanoparticles (PVP: polyvinyl-pyrrolidone) exhibits higher OER activity, higher electrochemically active surface area, lower charge transfer resistance and much better surface wettability (15.9°) than that of pristine $(Ni_{0.75}Fe_{0.25})Se_2$, while it was obtained by one-pot hydrothermal treatment. On the other hand, it was observed that Fe doped Ni_3Se_4 ($(Ni,Fe)_3Se_4$) ultrathin nanosheets exhibits higher OER activity, higher electrochemically active surface area, and lower charge transfer resistance than that of Ni_3Se_4, while it was obtained by the topotactic conversion reaction through hydrothermal treatment of the NiFe LDH precursor, and the precursor was prepared by the hydrothermal treatment. It was observed that NiFeSe nanocages exhibits enhanced activity and stability for OER. The NiFeSe nanocages exhibits higher OER activity, higher OER kinetics, higher TOF (TOF of $1.06\ s^{-1}$ at η of 280 mV), higher mass activity ($1000\ Ag^{-1}$ at η of 270 mV), higher electrochemically active surface area, and lower charge-transfer resistance than that of NiFeSe nanodisks and NiFeS nanocubes. The NiFeSe nanocages is composed of cubic pyrite-phase $NiSe_2$ and $FeSe_2$; It contains about 1:0.77 M ratio of $NiSe_2$:$FeSe_2$ and Ni^{2+}, Fe^{2+}, and Fe^{3+}. It possesses cage-like nanostructures and it contains Ni, Fe, and Se, which are uniformly distributed. Thus, the NiFeSe nanocages can expose abundant active sites, enhance electron/mass transport, facilitate gas evolution, and that enhance the water performance for OER. The NiFeSe nanocages exhibits enhanced activity (η of 240 mV at 10 mA cm^{-2}), stability (99.3% retention at

5 mA cm^{-2} for 22 h), and durability (negligible decay at 175 mA cm^{-2} after 500 cycles of CV) for OER in 1.0 M KOH. Moreover, it was observed that Ni–Fe–Se exhibits higher OER activity than that of Ni–Fe–O and Ni–Fe–PBA, while it was obtained by co-precipitation followed by hydrothermal treatment. Constructing porous hierarchical defective NiFeSe can generate copious unsaturated sites, expose abundant active sites and facilitate electron/mass transport and that can enhance the water oxidation performance. Yilmaz et al. have observed that NiFeSe@NiSe|O exhibits enhanced activity and stability for OER.

The NiFeSe@NiSe|O exhibits higher OER activity higher TOF (TOF of 2.88 s^{-1} at η of 350 mV), higher electrochemically active surface area, and lower charge-transfer resistance than that of NiFeSe nanocubes and NiSe|O. The NiFeSe@NiSe|O possesses porous hierarchical heterostructure with pore volume of 0.121 cm^{3}g^{-1}; It possesses high surface area (115.9 m^{2}g^{-1}). It is composed of Ni$_{(0.85-x)}$Fe$_x$Se and NiOx; it contains Ni^{2+}, Ni^{3+}, Fe^{2+}, and Fe^{3+}; it contains Ni, Fe, Se, and O, which are uniformly distributed. It is highly mesoporous comprising of enormous interconnected crystalline nanoparticles of 5–10 nm in size surrounded by pores. Thus, the NiFeSe@NiSe|O can expose abundant active sites and facilitate electron/mass transport and that can enhance the performance for OER. The NiFeSe@NiSe|O exhibits enhanced activity (η of 270 mV at 10 mA cm^{-2}) and stability (negligible decay for 50 h) for OER in 1.0 M KOH. Besides, it was observed that Ni(Fe)-OOH@Ni$_x$Fe$_{1-x}$Se nanostructure exhibits higher OER activity and lower charge transfer resistance than that of NiSe nanowire, while it was obtained by facile ion exchange reaction for 30 s using NiSe as precursor, while the precursor was prepared by solvothermal selenization.

It was observed that Fe$_{0.09}$Co$_{0.13}$-NiSe$_2$ nanosheet exhibits higher OER activity and lower charge transfer resistance than that of NiSe$_2$, Fe$_{0.2}$NiSe$_2$, and Co$_{0.2}$NiSe$_2$, while it was obtained by hydrothermal treatment followed by selenization.

Moreover, it was observed that NiSe$_2$/Fe$_3$Se$_4$/C exhibits higher OER activity than that of Ni/Fe–OH and Ni/Fe@C, while it was obtained by selenization of Ni/Fe MOF precursor, and the precursor was prepared by hydrothermal treatment.

Fabricating nanostructured nickel–iron nitride can expose abundant active sites, enhance electron/mass transport, tune electronic structure, facilitate gas evolution, and that can enhance the water oxidation performance. Jiang et al. have observed that Fe$_2$Ni$_2$N nano-array exhibits enhanced activity and stability for OER. The Fe$_2$Ni$_2$N nano-array exhibits higher OER activity, OER kinetics, and lower charge-transfer resistance than that of Ni–Fe–O and Ni$_3$N. The Fe$_2$Ni$_2$N nano array is composed of crystalline Fe$_2$Ni$_2$N; it possesses nano-array morphology, while it is nanoporous; it contains Ni, Fe, and N, which are homogenously distributed; it contains Ni0, Ni^{2+}, and Fe^{3+}, where the metallic Ni could be obtained by the partial reduction of Ni^{2+} by the thermal treatment of NH$_3$; it exhibits the down-shift for 2p3/2 peaks of both Ni and Fe when compared to that of Ni–Fe–O suggesting the electronic interaction in Fe$_2$Ni$_2$N nano-array, which could be due to the lower electronegativity of nitrogen than that of oxygen and that leads to higher electron density on the metal ions in Fe$_2$Ni$_2$N than that of Ni–Fe–O. Thus, the Fe$_2$Ni$_2$N nano-array can expose abundant active sites, enhance electron/mass transport, tune electronic structure, facilitate gas

evolution, and that can enhance the performance for OER. The Fe_2Ni_2N nano-array exhibits enhanced activity (η of 220 mV at 10 mA cm^{-2}) and stability (91.7% retention at η of 270 mV for 10 h) for OER in 1.0 M KOH. In-situ growth of nanostructured nickel–iron nitride on surface redox etched Ni foam can expose abundant active sites, facilitate electron/mass transport, tune electronic structure, and that can enhance the water oxidation performance. It was observed that $FeNi_3N$ exhibits enhanced activity and stability for OER.

The $FeNi_3N$ exhibits higher OER activity, higher electrochemically active surface area, and lower charge-transfer resistance than that of NiFe(OH)x. The $FeNi_3N$ possesses porous morphology, which is composed of numerous nanorods; It is composed of face-centered cubic $FeNi_3N$, while it contains 3:1 atom ratio of Ni: Fe; it contains Ni, Fe, and N, which are uniformly distributed; it contains Ni0, Ni^{2+}, Fe0, and Fe^{3+}, where the metallic Ni and Fe could be formed by the partial reduction of 2+ and Fe^{3+}, respectively, by the thermal treatment of NH_3. Thus, the porous $FeNi_3N$ can expose abundant active sites, facilitate electron/mass transport, tune electronic structure, and that can enhance the performance for OER. For OER in 1.0 M KOH, the $FeNi_3N$ exhibits enhanced activity (η of 202 mV at 10 mA cm^{-2}), while it affords negligible decay at 400 mA cm^{-2} after 1000 cycles of CV indicating its robust durability. Besides, it was observed that Ni_3FeN nanoparticles exhibits higher OER activity and lower charge transfer resistance than that of Ni_3FeN bulk, Ni_3N, and NiFe mixed metal oxide, while it was obtained by thermal ammonolysis of NiFe LDH precursor, and the precursor was prepared by reverse microemulsion method. Moreover, it was observed that Ni_3FeN exhibits higher OER activity than that of Ni_3Fe alloy, NiFe LDH, and NiFeOx, while it was obtained by thermal ammonolysis of NiFe LDH precursor, and the precursor was prepared by hydrothermal treatment. In addition, it was observed that Ni_3FeN exhibits higher OER activity and lower charge transfer resistance than that of Ni_3N and Fe_2N, while it was obtained on carbon cloth by electrodeposition followed by annealing in NH_3 atmosphere.

Moreover, it was observed that Ni_3FeN exhibits higher OER activity and lower charge transfer resistance than that of NiFe LDH, while it was prepared by nitridation of NiFe LDH precursor, and the precursor was obtained by hydrothermal treatment.

On the other hand, it was observed that porous NiFeMoN nanotube exhibits higher OER activity than that of NiMoN nanotube, while it was obtained by weak alkaline-etching followed by stirring followed by annealing.

Integrating carbon with the NiFe based active material could enhance the electron transfer, facilitate the conductivity, enhance the activity, prevent the aggregation of the active material, improve the stability, and that could enhance the water oxidation performance. It was observed that NiFe-G (G: graphene) exhibits higher OER activity than that of Ni-G and Fe-G, while it was obtained through a laser-induced-graphene-assisted process. Moreover, it was observed that G-Ni4Fe exhibits higher OER activity than that of G-Ni and G-Fe, while it was obtained by solution-processing method. In addition, it was observed that sandwich like NiFe nanoparticles/C exhibits higher OER activity than that of sandwich like Ni/C, while

it was obtained by the hydrothermal treatment of Fe-doped $Ni(OH)_2$. Moreover, it was observed that Ni_2Fe-rGO exhibits higher OER activity than that of Ni-rGO and Fe_3O4-rGO, while it was obtained by hydrothermal approach. Besides, it was observed that NiFeOOH/G exhibits enhanced OER activity, while it was obtained by urea-assisted co-precipitation reaction, and the graphene framework was prepared through MgO-templated CVD method. Moreover, it was observed that NiO–$NiFe_2O_4$-rGO exhibits higher OER activity than that of NiFe LDH-rGO, NiFe LDH, NiO–$NiFe_2O_4$, $NiFe_2O_4$, and NiO, while it was obtained by calcination of NiFe LDH-rGO precursor, and the precursor was prepared by co-precipitation method. It was observed that $NiFeS_2$/S-GO exhibits enhanced activity and stability for OER. The $NiFeS_2$/S-GO exhibits enhanced activity (η of 240 mV at 10 mA cm$^-$^{2}) and stability (>90% retention for 24 h) for OER in 1.0 M KOH. Moreover, it was observed that $(NiFe)S_2$-GN exhibits higher OER activity than that of NiFe LDH-GO and NiS_2-GN, while it was obtained by a sulfidation of the NiFe LDH-GO precursor, and the precursor was prepared by the hydrothermal treatment using GO. Besides, it was observed that G-FeNiP@N-CF (CF: Carbon fiber) exhibits higher OER activity than that of FeNi@N-CF, while it was obtained by pyrolysis reduction of precursor fibers followed by in-situ phosphorization.

It was observed that DR-Ni_3FeN-NG (DR: defect-rich; NG: N-doped graphene) exhibits enhanced activity and stability for OER. The DR-Ni_3FeN-NG exhibits higher OER activity, higher TOF (TOF of 0.46 s^{-1} at η of 350 mV), higher electrochemical active surface area, and lower charge-transfer resistance than that of Ni_3FeN-NG. The DR-Ni_3FeN-NG is composed of cubic phase of Ni_3FeN and N-doped graphene. The DR-Ni_3FeN-NG exhibits enhanced activity (η of 250 mV at 10 mA cm^{-2}) and durability (negligible decay at 100 mA cm^{-2} after 2000 cycles of CV) for OER in 1.0 M KOH. Besides, it was observed that NG-NiFe/NC hollow nanobox exhibits enhanced OER activity, while it was obtained by co-precipitation followed by polymerization at room temperature followed by pyrolysis. In addition, it was fabricated N-doped graphene supported core-shell structured FeNi alloy@N-doped carbon nanocages as OER active and stable catalyst. Moreover, it was prepared rGO supported N-doped porous carbon-coated NiFe alloy composite as OER active catalyst through a facile pyrolysis route. In addition, it was synthesized NiFe carbon composite as OER active catalyst, where the hollow polyhedron is composed of NiFe alloy with a small fraction of its oxides and few-layer N-graphene shell. Moreover, it was observed that NiFe nanoparticles@NC exhibits enhanced OER activity, while it was obtained by calcination of MOF precursor.

It was observed that NiFeOOH-EGH (EGH: partially exfoliated graphite) exhibits enhanced activity and stability for OER. The NiFeOOH-EGH exhibits enhanced activity (η of 214 mV at 10 mA cm^{-2}) and stability (negligible decay at 10 mA cm^{-2} for 100 h) for OER in 1.0 M KOH. Besides, it was observed that NiFeOH-GH (GH: Graphite) exhibits enhanced activity and stability for OER, while it was obtained by pulse mode potentiostatic deposition on graphite paper. More-over, it was observed that sandwiched NiFe/C arrays exhibits higher OER activity than that of Fe-doped $Ni(OH)_2$ nanosheets and NiFe nanoparticles. It was observed that $Fe_{0.5}Ni_{0.5}$@N-GH exhibits enhanced activity and stability for OER. The

$Fe_{0.5}Ni_{0.5}$@N-GH exhibits higher OER activity, higher OER kinetics, higher electrochemical active surface area, and lower charge-transfer resistance than that of $Fe_{0.5}Ni_{0.5}$ and N-GH; the $Fe_{0.5}Ni_{0.5}$@N-GH is composed of NiFe nanoparticles (9.5 nm), which are embedded in N-doped graphite; it exhibits cubic NiFe phase and highly ordered graphitic structure; it exhibits high surface area (106 m^2g^{-1}) and pore volume (0.177 cm^3g^{-1}). Thus, $Fe_{0.5}Ni_{0.5}$@N-GH can expose abundant active sites and facilitate electron/mass transport, and that can improve the performance for OER. For OER in 1.0 M KOH, the $Fe_{0.5}Ni_{0.5}$@N-GH exhibits enhanced activity (η of 210 mV at 10 mA cm^{-2}), while it affords robust durability (negligible decay at 70 mA cm^{-2} after 10,000 cycles of CV), and stability (98% retention at η of 220 mV for 20 h). Besides, it was observed that NiFe@NC exhibits higher OER activity than that of $NiO–NiFe_2O_4$ and Fe-doped NiO, while it was obtained by mixing the precursor with urea followed by annealing in Ar. In addition, it was observed that NiI IFeI I I@NC exhibits enhanced stability and activity for OER, while it was obtained by pyrolysis of the MOF precursor followed by leaching with 0.5 M H_2SO_4 followed by pyrolysis. Moreover, it was observed that NiFe-NC exhibits higher OER activity than that of NiMn-NC and NiCo-NC, while it was prepared by ultrasonic treatment followed by pyrolysis. Besides, it was observed that NiFe-NCx exhibits enhanced OER activity, while it was obtained by annealing the precursor in Ar atmosphere. Moreover, it was observed that S–FeNi@NC exhibits higher OER activity than that of FeNi@NC, S–Ni@NC and S–Fe@NC, while it was obtained by hydrothermal treatment followed by pyrolysis in nitrogen atmosphere. In addition, it was observed that $Ni_{0.75}Fe_{0.25}$-NPSC exhibits higher OER activity than that of Ni-NPSC, Fe-NPSC and NPSC, while it was obtained by pyrolysis of the precursor in nitrogen, where the alfalfa, a natural biomass was used as the carbon source and heteroatom doping precursor. Moreover, it was observed that NC-NiFeOx@NiFe–P exhibits higher OER activity, higher electrochemically active surface area, and lower charge transfer resistance than that of NC-NiFe and NiFeOx@NiFe–P, while it was obtained by co-precipitation followed by phosphorization followed by surface oxidation in air.

Integrating the CNT conductive material with active material could facilitate the electron transfer process and enhance the stability of the active material, and that could improve the performance for OER. Wang et al. have observed that $S–Ni_{6/7}Fe_{1/7}$OH-CNT (CNT: Carbon nano-tube) exhibits enhanced activity and stability for OER. The $S–Ni_{6/7}Fe_{1/7}$OH-CNT exhibits higher OER activity, and lower charge-transfer resistance than that of $S–Ni_{6/7}Fe_{1/7}$OH.

The $S–Ni_{6/7}Fe_{1/7}$OH-CNT is composed of carbon nano-tubes, which are wrapped on the surface of flower-like $S–Ni_{6/7}Fe_{1/7}$OH. The $S–Ni_{6/7}Fe_{1/7}$OH contains mixed phase of hexagonal $\beta Ni(OH)_2$ and jamborite (hybrid of β-$Ni(OH)_2$ and γ-NiOOH); The $S–Ni_{6/7}Fe_{1/7}$OH-CNT exhibits enhanced activity (η of 190 mV at 10 mA cm^{-2}) and stability (negligible decay at 10 mA cm^{-2} for 20 h) for OER in 1.0 M KOH. Besides, it was fabricated OER stable and active FeNi@NCNT by dip-coating followed by pyrolysis. Moreover, it was observed that FeNi@N-CNT exhibits enhanced OER activity, while it was obtained by thermal decomposition of the MOF precursor under Ar flow at 1000 °C for 1 h, and the MOF precursor was

prepared by direct reaction at room temperature. In addition, it was observed that Fe–Ni@NC-CNT exhibits higher OER activity and lower charge transfer resistance than that of Fe–Ni@C, while it was obtained by pyrolysis of the MOF/dicyandiamide composite precursor at 800 °C for 3 h in Ar atmosphere. Moreover, it was observed that NiFe@N-CNT exhibits higher OER activity than that of Ni@N-CNT and Fe@N-CNT, while it was prepared by pyrolysis of the precursor followed by carbonization. In addition, it was observed that $Ni_{0.9}Fe_{0.1}$/N-CNT exhibits higher OER activity than that of Ni/N-CNT, while it was obtained by pyrolysis of precursor. It was observed that Ni@γFe_2O_3/ES-MWCNT (ES: Nitrogen-rich emeraldine salt; MWCNT: Multi-wall carbon nanotubes) exhibits enhanced activity and stability for OER. The Ni@γ-Fe_2O_3/ES-MWCNT is composed of Ni@γFe_2O_3 nanoparticles with core-shell structure, which are decorated on catalyst support comprising of multiwall carbon nanotubes functionalized with nitrogen-rich emeraldine salt.

The Ni@γ-Fe_2O_3/ES-MWCNT exhibits enhanced activity (γ of 260 mV at 10 mA cm^{-2}) and stability (reasonable stability at η of 290 mV for 30 h) for OER in 1.0 M and 0.1 M NaOH, respectively. MOFs (MOFs: Metal–organic frameworks) have emerged as an exclusive kind of crystalline solid-state porous materials due to their tunable structural and functional design including post-synthetic modifications, use of different metals, reticular chemistry, etc. MOFs exhibit wide range of applications however limited MOF materials could be used as electrocatalysts with high performance, where their utilization as electrocatalysts could be hindered by the poor conductivity, active-metal-centers blockage by organic ligands, possible deterioration of 3D framework, and low mass permeability. Constructing bimetallic MOF on conductive substrate can enhance electron/mass transport, afford abundant active centers (in the form of bimetallic clusters), provide high surface area, and facilitate the gas evolution, and that can enhance the water oxidation performance. It was observed that NiFe-MOF nanosheet array exhibits higher OER activity than that of Ni-MOF, Fe-MOF, and powder NiFe-MOF, while it was obtained on Ni foam by facile one-step chemical bath deposition method using aqueous solution in the presence of an organic ligand at 60 °C for 20 h. It was observed that ultrathin NiFe MOF nanosheets exhibits higher OER activity than that of NiCo-MOF nanosheets, while it was obtained by ultrasonic oscillation method. Besides, it was observed that NFN MOF nano-array (NFN: NH2-MIL-88B(Fe2Ni)) exhibits enhanced activity and stability for OER.

The NFN-MOF nano-array on Ni foam exhibits higher OER activity than that of bulk NFN-MOF coated on Ni foam and Ni-MOF. The NFN-MOF nano-array is composed of nanoporous NH2-MIL88B(Fe_2Ni)-metal–organic framework with bimetallic clusters $Fe_2Ni(\mu_3$-O)(COO)$_6$(H2O)$_3$, which are in-situ grown on the surface of a highly conducting 3D macroporous nickel foam. The NFN MOF nano array exhibits enhanced activity (η of 240 mV at 10 mA cm^{-2}) and stability (>90% retention for 30 h) for OER in 1.0 M KOH. Introduction of Fe into MIL-53 MOF structure can increase active sites, enhance electrochemically-active surface area, facilitate electron transport, modulate electronic structure, afford more favorable for foreign atoms adsorption, and provide increased 3d orbital electron density, and that could enhance the water oxidation performance.

It was observed that MIL-53(FeNi)MOF exhibits enhanced activity and stability for OER. The MIL53(FeNi)MOF exhibits higher OER activity, higher mass activity, higher TOF (TOF of 0.4 s^{-1} at η of 252 mV), higher resistance than that of MIL-53 (Ni)MOF, and TPA. The MIL-53(FeNi)MOF is composed of metal–organic framework with Ni and Fe metal centers and TPA as organic ligand molecules.

The MIL-53(FeNi)MOF exhibits enhanced activity (η of 233 mV at 50 mA cm^{-2}), stability (negligible decay for 13.3 h), and durability (negligible decay at 100 mA cm^{-2} after 1000 cycles of CV) for OER in 1.0 M KOH. Moreover, it was observed that Fe_2Ni-BPTCMOF (BPTC: Biphenyl3,4′,5-tricarboxylic acid) exhibits enhanced OER activity, while it was obtained by the reaction between BPTC ligands and Fe_2Ni clusters precursor with acetic acid under solvothermal condition.

It was observed that NiFe-PBA100 cycles (PBA: Prussian blue analogue) exhibits enhanced activity and stability for OER. The NiFe-PBA possesses cubic morphology, while it is crystalline with cubic structure, and it contains Fe, Ni, and C, which are homogeneously distributed, and it contains Ni^{2+} and Fe^{2+}. In contrast, the activated NiFe-PBA (NiFe-PBA100 cycles) is amorphous.

The NiFe-PBA100 cycles exhibits enhanced activity (η of 258 mV at 10 mA cm^{-2}) and stability (negligible decay at 20 mA cm^{-2} for 110 h) for OER in 1.0 M KOH.

3.3 3d Dual Transition Metal Catalysts for OER

Rather than noble metal catalysts with scarcity and expense, first raw 3d dual transition metal non-oxides are promising candidates to achieve superior OER activity and durability in alkaline solution due to their tunable electron structure, high conductivity, and cost-off advantages.

With the development of synthesis and characterization analysis technologies, significant progress has been made in the study of promising low cost and earth-abundant candidates for replacing commercial noble metal catalysts for OER, where first raw 3d dual transition metals-based materials have demonstrated a great potential in this research area due to their tunable physical and chemical properties.

In particular, 3d dual transition metals (Ti, V, Mn, Fe, Co, Ni, Cu, and Zn, etc.) in forms of transition metals sulfides, selenides, phosphides, nitrides, and non-oxides could act as next-generation OER electrocatalysts. Owing to these dual cations with unsaturated coordination and high electrical conductivity, they can be acted as active catalytic centers for adsorption/activation of OER intermediates. To the best of our knowledge, the secondary metal always assists intrinsic active species, like Fe, Co, or Ni, with variable valence electrons in 3d orbitals to improve overall OER performance through several effective strategies.

In comparison to transition metal oxide catalysts, transition metal sulfides have shown superior OER catalytic activity and durability in an alkaline electrolyte due to high conductivity and unique electronic structure features. Especially, first raw 3d dual transition metals sulfides possess a tunable electronic structure for strengthening intrinsic electrocatalytic performance. To be specific, benefitting from secondary

metal served as an electron donor to increase charge carrier concentrations, adsorption free energy of *OOH intermediate on the surface of transition metal sulfides could be decreased, which significantly enhanced intrinsic catalytic activity of 3d dual transition metal sulfides towards OER.

Meanwhile, the band structure of 3d dual transition metal sulfides is consecutive near the Fermi level, indicating a metallic property, which facilitated the efficient electron transport during the OER process. In particular, spinel AB_2S_4 structure with more redox couples are featured with the above-mentioned benefits. Among them, $NiCo_2S_4$ as a representative of well-reported Ni–Co–S catalysts has been comprehensively investigated in term of diverse nanostructures, including nanowire arrays, core-shell nanorods, hollow coaxial nanotubes, nanosheets, hierarchical nanoflakes networks, and nanoparticles.

Compared with other nanostructured samples, the 3D nanocaterpillar-like $NiCo_2S_4$ arrays exhibited the smallest overpotential of 279 mV at 50 mA cm^{-2} with the lowest Tafel slope of 68 mV dec^{-1} in 1.0 M KOH, which was attributed to its 3D interconnected structure, high electrochemical active surface area (ECSA), rapid charge transfer, and high-efficiency oxygen release. Owing to the delicate design of morphology structure reflected by the increased electrochemical double-layer capacitance, the NiCo2S4–4 with optimized Ni/Co ratio delivered an overpotential of 247 mV at a current density of 10 mA cm^{-2} during OER process, surpassing single metal sulfides of Co_3S_4 and Ni_3S_2. With the help of introduced Ni species in NiCo2S4–4 for absorbing more valence electrons, the Co atom in electron deficiency state preferred to form strong Co–S bond and accept electrons from adsorbed O atoms for further establishing M-OOH intermediates. Moreover, the calculated overpotential to enable OER process was smaller on the Co top site of (110) surface than that on Ni top site, S top site, Ni–S bridge site, and Co–S site, revealing the Co top acted as the most active site in theory.

The $Ni_xCo_3-xS_4/Ni_3S_2$ hybrid exhibited compelling OER catalytic activity with 160 mV overpotential at 10 mA cm^{-2}, nearly achieving the best OER performance among all reported 3d dual transition metal sulfides and even the state-of-art RuO_2 catalyst with the same mass loading amount.

The excellent OER activity was benefitted from the synergetic effect of β-Ni/Co (IV)–OOH as active sites and Ni_3S_2 with high conductivity. The NiS_2/CoS_2–O NWs delivered an impressive OER activity with overpotential of 235 mV at 10 mA cm^{-2}, which was better than the NiS_2/CoS_2 NWs hybrid without oxygen vacancies and precursor $NiCo_2O_4$ catalyst. The diminution of the adsorption energy barrier resulted from more oxidative Co and Ni active species caused by abundant oxygen vacancies could explain the reason for efficient oxygen evolution. The porous structure was also vital for accelerating the OER process so that a self-interconnected porous $(Ni_{0.33}Co_{0.67})S_2$ networks hybrid grown on carbon cloth (CC) was fabricated.

Thanks to the large numbers of active sites exposed by mesoporous structure, the porous $(Ni_{0.33}Co_{0.67})S_2$/CC hybrid only required a much smaller overpotential of 216 mV with respect to the 253 mV for NiS/CC and 324 mV for CoS/CC, to reach a current density of 20 mA cm^{-2}. The excellent OER electrocatalytic performance was ascribed to the synergetic effect generated by dual transition metals, porous network

structure, and high conductivity of CC supports. Similar to the Ni reported species in Ni–Co–S catalysts, other secondary 3d transition metals, especially for Mn, Fe, Cu, and Zn, also play a crucial role in enhancing OER performance of Co-based sulfides by virtue of subtly different valent electron structures of 3d orbitals. These transition metals could replace the Ni sites in spinel $NiCo_2S_4$ to form a series of MCo_2S_4 structured catalysts, where M is denoted as secondary transition metals. As an identical spinel, a $CuCo_2S_4$ catalyst where Co (III) occupied octahedral B sites and Cu (II) occupied tetrahedral A sites were prepared. When applied as an OER catalyst in alkaline electrolyte, the $CuCo_2S_4$ nanosheets displayed the higher electrocatalytic activity with a current density of 10 mA cm^{-2} at 310 mV overpotential than Co_3S_4 counterpart without spinel structure (430 mV). The $CuCo_2S_4$ nanosheets with unique structure modified by Cu species exhibited strong adsorption for reactant OH- in aqueous electrolyte, thus boosting the OER performance. Compared with single metal sulfides of Co–S (465 mV) and Zn–S (557 mV), the Co–Zn–S required a lower overpotential of 320 mV at the same 10 mA cm^{-2} current density for efficient OER catalysis. The enhanced OER activity of Co–Zn–S was attributed to not only the small kinetic resistance for fast electron transfer but also the unique nanoporous structure with a high specific area to expose more active sites. It should be noted that most of the OER performance enhancement in the aforementioned MCo_2S_4 catalysts by doped foreign atoms majorly result from the adsorption energy modulation or charge/mass transfer improvement during the OER process. For the optimized sample, the c-$FeCo_2S_y$ /carbon exhibited an overpotential of 247 mV to reach a current density of 10 mA cm^{-2}, smaller than the CoS_y/carbon with 390 mV, c-$FeCoS_y$/carbon with 341 mV, and c-Fe_2CoS_y/carbon with 356 mV at the same current density, respectively.

The development of 3d dual transition metals sulfides based on Ni element with superior OER performance has been broadly investigated. In terms of activity enhancement, the low overpotential of 282 mV at 10 mA cm^{-2} was attributed to the low OER thermodynamic barrier, and strong adsorption ability of H_2O molecular on the surface of Fe–Ni_3S_2/FeNi originated from dopant Fe centers, serving as electron active sites to increase charge carrier concentrations. The Cu1-xNixS/NF only displayed OER performance with an overpotential of 350 mV at 10 mA cm^{-2}.

Compared to Ni_3S_2/NF, the constructed Zn–Ni_3S_2/NF required an overpotential of 330 mV to reach a higher current density of 100 mA cm^{-2}. The significant progress of OER performance could be attributed to the introduced Zn species, which acted as an effective promoter to modify the coordination valence state and chemical environment of active Ni sites. Besides, when the secondary metal V element was added into Ni-based dual metals sulfides, the increment of OER catalytic activity was observed, thanks to electron structure optimization with strong interaction between active sites and intermediates. In this regard, an ingenious structured Ni_3S_2/VS_2 in-situ grown on Ni foam was fabricated. The Ni_3S_2/VS_2 delivered an overpotential of 227 mV to drive a current density of 10 mA cm^{-2} for OER, superior to the noble metal catalyst IrO_2/C with the same mass loading amount. The Ni3S2/VS_2 not only possessed more exposed active sites with empty d

orbitals on Ni sites to enhance binding ability with OH* intermediate but also strengthened mechanical adhesion and increased conductivity for boosting OER performance.

Different from the congeneric S element, the Se element with the larger radius and the lower electronegativity has shown superior electroactivity as well. Notably, in recent years, 3d dual transition metal selenides have attracted considerable attention as highly active catalysts in OER electrocatalysis.

Among various 3d dual transition metal selenides, first raw 3d dual transition metal selenides based on Co element with high intrinsic catalytic activity are considered as promising catalysts for boosting electricity-driven water oxidation. For instance, a $(Ni, Co)Se_2$ nanocage was synthesized.

The in-situ growth of $(Ni, Co)Se_2/GA$ catalyst boosted the OER performance with an overpotential of 250 mV at 10 mA cm^{-2}, much smaller than that of the $(Ni, Co)Se_2$ without GA (320 mV).

Apart from GA support, carbon fiber paper (CFP) was also worked as a useful substrate for enhancing electrical conductivity. Hence a spinel $CoNi_2Se_4$ catalyst was designed. The $CoNi_2Se_4@CFP$ required the smallest overpotential of 160 mV to drive the 10 mA cm^{-2}. The outstanding OER performance was ascribed to the facile donor-acceptor chemisorption for intermediate species on active sites as well as rapid electron and mass transfer caused by the synergetic effect of dual Ni and Co metals. Among all the investigated samples, the $Zn_{0.1}Co_{0.9}Se_2$ with subtle distortion in orthorhombic structure exhibited the highest OER performance with 340 mV overpotential at 10 mA cm^{-2}. It was notable that certain Se defects with flexible electronic structures and gap states were formed in the $Zn_{0.1}Co_{0.9}Se_2$, which significantly declined the transfer resistance and gained the optimal adsorption ability for OER intermediates. In reference to well-known dual-metal chalcogenides derived corresponding transition metal oxides/hydroxides as real active sites for promoting OER catalysis, the selenization treatment could play a special role in altering rate-determining step (RDS). The $Co_{1-x}Fe_xSe_2/Ni$ displayed excellent electrocatalytic activity for OER, as revealed by the lower overpotential of 217 mV at 10 mA cm^{-2} and smaller Tafel slope of 41 mV dec^{-1}, than corresponding CoFe layered double hydroxide (LDH) precursor (277 mV and 82 mV dec^{-1}). The reduced Tafel slope after senelization treatment implied that the RDS of the OER process was transformed from OH$-$ breakage to O–O formation in Co–Fe–Se-derived oxide/hydroxide. The splendid OER performance was ascribed to the subtle lattice distortion caused by Fe introducing and more exposed active sites with the dissolution of Se during the reaction process.

For the 3d dual transition metal selenides based on Co element, other secondary elements, including Fe and Ni, have also been designed together to work as efficient anodic catalysts for boosting OER activity. For instance, a $NiSe_2/FeSe_2$ mixed diselenide with open-cage nanostructure was prepared. The optimized $NiSe_2/FeSe_2$ catalyst performed excellent OER activity with an overpotential of 240 mV at a current density of 10 mA cm^{-2}; the overpotential value was slightly smaller than that of Ni–Fe–Se cubes (270 mV) and Ni–Fe–Se disks (380 mV). The benefits of cage structure for OER catalysis were clarified in the unique 3D architecture, which

possessed more exposed active defects associated with efficient ion exchange for improving the water oxidation process.

In addition to a traditional composite consisting of two kinds of transition metals selenides, dual metals selenide involved with close contact between Ni and Fe species has also been reported.

The $Ni_{0.75}Fe_{0.25}Se_2$ catalyst afforded the smaller overpotential of 286 mV to deliver a current density of 20 mA cm^{-2} for OER for the 356 mV for $NiSe_2$ and 364 mV for Ni_3Fe at the same current density. In comparison to previously discussed $Ni_{0.75}Fe_{0.25}Se_2$ without PVP wrapped, the OER activity of P–$Ni_{0.75}Fe_{0.25}Se_2$ catalyst with the same mass loading amount was relatively improved, featured by a low overpotential of 255 mV to drive the current density of 10 mA cm^{-2}, due to its unique hydrophilic property.

Due to the isotropic structure with more coordinatively unsaturated atoms on the surface and narrow bandgap with high electrical conductivity, transition metal phosphides have been considered to be appropriate candidates for oxygen evolution reaction electrocatalysis. The core shell-structured $MnCo_2O_4$/Mn–Co–P catalyst displayed an OER performance with an overpotential of 269 mV at 10 mA cm^{-2}, which was 93 mV less than that for $MnCo_2O_4$. The enhancement of intrinsic activity for $MnCo_2O_4$/Mn–Co–P could be attributed to the fact that in-situ formed amorphous Mn–Co–P shell ensured high electric conductivity and rapid charge-transfer. The Co_3O_4/$Fe_{0.33}Co_{0.66}$P catalyst acquired a smaller overpotential of 215 mV at 50 mA cm^{-2} for OER catalysis with respect to commercial RuO_2 on NF (259 mV) with the same mass loading amount.

The roles of transition metal sites are varied according to the various constitutions and structures at the interface region. For instance, a Fe–CoP/CoO hybrid was synthesized. The obtained Fe–CoP/CoO hybrid possessed outstanding OER performance with the smaller overpotential of 219 mV at a current density of 10 mA cm^{-2}, than that of CoP/CoO (295 mV) and Fe–CoP (250 mV) under same conditions. Besides, the introduction of Fe species mainly increased the charge carrier density of CoP structure, especially at Co atoms adjacent to Fe sites, which could activate more metal active sites for OER. Also, transition metal phosphides containing Ni and Co elements with unique heterojunction structures could also convey superior OER performance (Zhang et al. 2023). As a typical example, a multi-dimensional Ni/NiCoP heterojunction with a core/shell structure was prepared.

The resulted Ni/NiCoP heterojunction possessed the smaller overpotential of 260 mV to deliver 20 mA cm^{-2} current density for OER. The experimental results showed that the emerging regulation of electronic configuration at interface region donated electron from active transition metals to OH* for forming high valence Ni/Co species, contributing to the accelerated OER process. An alloyed Fe–Co–P hollow sphere was synthesized. In such a Fe–Co–P alloy structure, both Co and Fe species performed metallic nature with a slightly oxidized species on the surface of Fe–Co–P alloy, which was favorable for rapid electron transfer during OER process. As a result, the Fe–Co–P alloy exhibited enhanced OER performance with a smaller overpotential of 252 mV at 10 mA cm^{-2} in comparison to the CoP and FeP with overpotentials of 320 and 361 mV, respectively. Due to the too strong or too weak

adsorption ability on single Fe-based or Co-based materials, the synergetic effect of Fe and Co species modulated the adsorbing energy of intermediates by retaining Co species in low-valent, thus leading to the high OER activity. For instance, a series of $CuxCo_3$-xP/Ndoped carbon (NC) catalysts were prepared. Among all the investigated catalysts with different compositions, the $Cu_{0.3}Co_{2.4}P$/NC with optimized Co^{3+}/Co^{2+} ratio possessed compelling OER performance with an overpotential of 190 mV at 10 mA cm^{-2}, which was attributed to the optimized electron structure caused by inhibition of phosphorylating metallic Co into CoPx species, thus resulting in the formation of more Co^{3+} species with high intrinsic activity for boosting OER catalysis.

Inspired by those mentioned above Co-based dual transition metal phosphides, 3d dual transition metal phosphides based on Ni elements are also in favor of electrochemical water oxidation, thanks to tunable chemical environment and theoretically high electrocatalytic activity.

For instance, a series of NiCuP catalysts with various Ni/Cu molar ratios were synthesized. The $Ni_{59}Cu_{19}P_9$ exhibited the highest OER performance with an overpotential of 318.7 mV at 10 mA cm^{-2} among all investigated samples. Doping of oxygen atoms was another feasible strategy for boosting OER performance of well-designed 3d dual transition metal phosphides. For instance, a series of O–V–Ni_2P catalysts were prepared. The overpotentials required to achieve a current density of 10 mA cm^{-2} were 257 mV, 308 mV, and 333 mV for the optimized O_3–V10–Ni_2P catalyst with 3 min O_2 plasma and 10% V doping amount, V10–Ni_2P, and Ni_2P, respectively. It worth to remember that the development of highly efficient OER catalysts with large current density and long-term stability is still a purpose for large scale application up to now. Following earlier work, a nanotube array (NAs) of O-doped Fe–Ni phosphide $(NiFe)_2P(O)$ grown on Ni_2P nanosheets was fabricated. The rationally designed $Ni_2P/(NiFe)_2P(O)$ NAs required the overpotential of 540 mV to deliver a large current density of 2000 mA cm^{-2} in 30 wt% KOH solution.

A new OER catalyst of Fe-doped Ni_2P supported on stainless steel mesh was synthesized via a mild chemical bath deposition and phosphorization treatments. Benefitting from active sites engineering, the Fe-doped Ni_2P catalyst containing high content of Fe reached an extremely high current density of 500 mA cm^{-2} under low overpotential of 255 mV.

Although the N element possesses similar electronegativity with other non-oxide elements (S, Se, P, etc.), to date, exploring 3d binary transition metal nitrides as efficient electrocatalysts for OER is relatively limited with respect to transition metal sulfides, selenides, and phosphides. As a typical example, a $Co_xFe_{1-x}N_{0.5}$ nanosheet (NSs) was fabricated.

Among the counterparts with various Co/Fe ratios, the $Co_{0.15}Fe_{0.85}N_{0.5}$ NSs delivered the smallest overpotential of 266 mV at 10 mA cm^{-2} and Tafel slope of 30 mV dec^{-1} for OER.

Owing to the tunable valence state and small electrical resistance, the Ni_3FeN materials as efficient OER catalysts have been systematically investigated. For instance, the Ni_3FeN nanoparticles were prepared. The achieved Ni_3FeN catalyst

just needed a low overpotential about 280 mV to gain a current density of 10 mA cm^{-2}, less than the Ni$_3$FeN-bulk (320 mV) and Ni$_3$N (430 mV). The unusual OER activity of the Ni$_3$FeN catalyst could be attributed to high electronic conductivity and optimal electronic structure for adsorbing H$_2$O molecular tightly. Also, the strong interaction among Ni, Fe, and N species, as well as low charge-transfer resistance, further accelerated the OER process. Apart from reports concentrated on transition metals Fe, Co or Ni mixed nitrides, other secondary elements have also been reported as efficient anodic OER catalysts. For instance, a hierarchical TiN@Ni$_3$N nanowire arrays hybrid was synthesized. Compared to single Ni$_3$N nanosheets (about 420 mV), hierarchical TiN@Ni$_3$N catalyst demanded the lower overpotential of 350 mV to ensure water oxidation with a current density of 10 mA cm^{-2} in 0.1 M KOH electrolyte, which was ascribed to the synergetic roles of TiN and Ni$_3$N in providing a conductive network for electron transport and forming NiOOH active sites for promoting OER process.

Besides well-reported transition metal sulfides, selenides, phosphides, and nitrides, there were relatively few reports regarding other first raw 3d dual transition metal non-oxides including transition metal borides, carbides, and tellurides, and their electrochemical applications towards OER.

Since the general synthesis method for borides catalysts was based on chemical reduction with sodium borohydride as both reducing agent and boron source, numerous as prepared transition metal borides existed as an amorphous phase with undercoordinated metal atoms in the lattice, leading to superior catalytic performance. The optimized Co$_2$–Fe–B catalyst achieved the current density of 10 mA cm^{-2} with 298 mV overpotential, and the overpotential value was much smaller than that of the Co–B (340 mV) and Fe–B (372 mV). The synergetic effect of introduced Co and Fe species was the main reason for boosting OER activity, as revealed by the increased extent of high oxidation of Co species with the introduction of Fe, facilitating bonding with OOH* intermediate as well as promoting electrical conductivity. The OER performance of the optimized FeNi@FeNiB-700 catalyst (overpotential of 272 mV at 10 mA cm^{-2}) was much better than that of RuO$_2$ with 301 mV overpotential under the same current density. It was noted that all FeNi borides in the FeNi@FeNiB-700 catalyst were converted into oxy-hydrogenated species of NiOOH and FeOOH phases, which possessed decreased kinetic barrier for hydroxylation reaction, thus accelerating the bonding of OOH* intermediate on superficial active sites. Owing to the synergetic effect of two metals tellurides, the Ni$_3$Te$_2$–CoTe/CC afforded an OER current density of 300 mA cm^{-2} with a low overpotential of 454 mV. However, the Ni$_3$Te$_2$/CC, CoTe/CC, and commercial RuO$_2$ could not achieve such high current density at the same overpotential. The enhanced OER performance could be attributed to the introduced CoTe with high Cdl value for enlarging ECSA and the Ni$_3$Te$_2$ with a unique band structure for possessing high electronic conductivity and easy electron transport. Compared with other 3d dual transition metal non-oxides discussed above, it is rare to report 3d dual transition metal carbides for promoting OER activity. As a typical instance, a Co$_3$ZnC/Co heterojunction encapsulated within N-doped graphene was synthesized by directly annealing PBA precursor. Such Co$_3$ZnC/Co heterojunction

composed of slightly oxidative Co atoms, CoZn bimetallic carbide, and metallic Co could provide sufficient redox couples at the Co_3ZnC/Co interface. As a result, Co_3ZnC/Co catalyst acquired overpotential of 366 mV to drive 10 mA cm^{-2}, as efficient as the state-of-art RuO_2 (377 mV). The impressive OER performance was ascribed to the strong electron coupling effect of Co_3ZnC in a unique structure.

3.4 Perovskite Oxide Electrocatalysts for OER

Among the various non-precious electrocatalysts reported thus far perovskite-type oxides have garnered much attention due to their low cost, earth abundance, and promising activities. To achieve low overpotential, it is essentially important to design electrocatalysts with suitable electronic structure, which could generate active sites with optimal binding energy for OER intermediates, and that could diminish the energy barrier for OER.

In various FDMPOs, cobalt-based perovskite oxides are the most extensively investigated for water electrolysis. One of the most widely investigated Co-based perovskites is $Ba_{0.5}Sr_{0.5}Co_{0.8}Fe_{0.2}O_{3-\delta}$, which has an optimal eg orbital filling close to unity and intrinsic OER activity approximately one order of magnitude higher than that of IrO_2. One particularly interesting phenomenon regarding this material is that $Ba_{0.5}Sr_{0.5}Co_{0.8}Fe_{0.2}O_{3-\delta}$ experiences an in-situ surface transformation into amorphous cobalt oxyhydroxide during the OER, leading to increased OER activity upon electrochemical cycling. Recently, Fabbri and coworkers found that the in-situ surface restructuring of $Ba_{0.5}Sr_{0.5}Co_{0.8}Fe_{0.2}O_{3-\delta}$ was related to the lattice oxygen evolution reaction (LOER) process. It was provided direct evidence for the oxidation of lattice oxygen during the OER using online electrochemical mass spectrometry (OLEMS). In their experiments, the perovskite oxides were isotopically labeled with 18O, and the oxygen gas evolved by perovskite catalysts under normal KOH electrolyte conditions was monitored in-situ using OLEMS. In addition to $32O_2$, $34O_2$ (16O18O) and $36O_2$ (18O18O) were also detected for the highly covalent $SrCoO_{3-\delta}$ catalyst, confirming the LOER process since only the isotopically-labeled perovskite oxide provided 18O. A plausible mechanism explaining the formation of $36O_2$ is proposed, which consists of O-O bond formation, the evolution of oxygen gas, and the generation of oxygen vacancies.

Even though Co-based perovskite oxides have shown promising OER activities, the relatively high price of cobalt is unfavorable for their large-scale application. When compared with Co, many other first d-block transition metals, such as Ni, Mn, and Fe, are significantly cheaper. As a result, they are also frequently investigated for water electrolysis. One popular Ni-based perovskite oxide is $LaNiO_3$, which is a well-known conducting perovskite oxide. Its high electronic conductivity (1000 W^{-1} cm^{-1} at room temperature) is expected to favor the charge transfer kinetics required during electrolysis, eliminating the need for a conductive carbon support, which affects the catalytic activity. Bulk $LaNiO_3$ is superior to Pt in catalyzing the OER, even though its OER activity is still inferior to that observed for more active NiCoOx and RuO_2.

In order to further enhance the catalytic activity of $LaNiO_3$, strategies such as Fe-doping, strain tuning, and oxygen vacancy engineering have been investigated to date. It is worth noting that these strategies can perturb or distort the octahedral geometry of BO_6. Identifying this perturbation and further clarifying its role in water electrolysis are imperative. It was visualized the atomic-scale perturbation of the octahedral oxygen atoms in $LaNiO_3$ thin films using high-resolution scanning transmission electron microscopy (STEM). In contrast to the bulk where four oxygen atoms were placed at the corners of a white rhombus for a Ni octahedron, the surface unit cells denoted by the yellow rhombus were substantially distorted. The strong distortions in the oxygen octahedron were generated by the surface exchange of Ni with Fe, which enhanced the OER activity by several orders of magnitude. Density functional theory (DFT) calculations further demonstrated that this atomic-scale structural perturbation changes the O 2p and Ni/Fe 3d states in particular near the Fermi level (from -2 to 0 eV). Notably, Ni-based perovskite oxides can also undergo a structural transformation during electrolysis.

One representative example is $BaNiO_3$, which has a hexagonal structure with face-shared octahedral NiO_6 oriented toward the chain units. During the OER cycling process, $BaNiO_3$ was transformed into $BaNi_{0.83}O_{2.5}$ ($Ba_6Ni_5O_{15}$), which has mixed valence states of Ni^{2+}, Ni^{3+}, and Ni^{4+} with distorted-prism coordinations. Due to these structural transformations, the OER activity of $BaNiO_3$ was improved substantially, even far beyond the state-of-the-art IrO_2 catalyst. From the DFT calculations, $BaNi_{0.83}O_{2.5}$ requires a smaller overpotential to make all the OER sub-steps downhill when compared to BaNiO3, supporting its higher OER activity.

Considering the abundance of Fe in the earth's crust is far larger than that of Co and Ni, it is appealing to develop Fe-based perovskite electrocatalysts with comparable activity to their Co- and Ni-based counterparts.

Fe is usually incorporated into Co- or Ni-based catalysts to boost the catalytic performance. However, Fe-based perovskites, in which Fe acts as a single active site, have not been investigated as broadly as their Co- and Ni-based counterparts. This is mainly due to the low intrinsic activity of Fe-based perovskite oxides.

Recent efforts have been devoted to improving the catalytic performance of Fe-based perovskite oxides. A series of Fe-based perovskite oxides including $Ca_2Fe_2O_{6-\delta}$, $CaSrFe_2O_{6-\delta}$, and $Sr_2Fe_2O_{6-\delta}$, which have different structures, have been compared in the OER. The tetrahedral chains in each layer of $Ca_2Fe_2O_{6-\delta}$ are oriented in an opposite direction to their neighboring layers, which is in contrast to $CaSrFe_2O_{6-\delta}$ where the tetrahedral chains are orientated in the same direction. $Sr_2Fe_2O_{6-\delta}$ has a different type of defect order with alternating square pyramidal and octahedral coordination. These unique structures render distinct electronic conductivities.

The room temperature conductivities determined using 4-probe measurements followed the order of: $Ca_2Fe_2O_{6-\delta}$ (1.13 10^{-9} Scm^{-1}) $<$ $CaSrFe_2O_{6-\delta}$ (7.78 10^{-3} Scm^{-1}) $<$ $Sr_2Fe_2O_{6-\delta}$ (7.30 Scm^{-1}). With the highest conductivity favorable for the charge transfer process, $Sr_2Fe_2O_{6-\delta}$ exhibited the best OER activity. In addition to optimizing the conductivity, another strategy is to increase the proportion of Fe^{4+} to improve the binding strength with the reaction intermediates.

Even though cationic and anionic dopants have been introduced into the perovskite framework to provoke Fe^{4+}, stabilizing most or even all of the Fe cations in the tetravalent state remains challenging. The intrinsic OER activity (normalized by surface area) of $CaCu_3Fe_4O_{12}$ exceeds that of the state-of-the-art BSCF and RuO_2, demonstrating its great potential for water electrolysis. The tetravalent Fe atoms in $CaCu_3Fe_4O_{12}$ improved the covalency of the transition metal-oxygen bonds and shortened the interatomic distance between the nearest neighboring OH adsorbates, making the formation of O–O bonds possible, which is regarded as the rate-limiting step in the OER.

Anionic dopants have been introduced into the perovskite framework to provoke Fe^{4+}, stabilizing most or even all of the Fe cations in the tetravalent state remains challenging. A quadruple $AA'_3B_4O_{12}$-type perovskite structure ($CaCu_3Fe_4O_{12}$) has been applied to accommodate Fe^{4+}. In this type of perovskite structure, the A-sites are occupied by alkaline/alkaline-earth/rare-earth metal ions, the A8- sites are occupied by Jahn-Teller active ions such as Cu^{2+} or Mn^{3+}, and the B-sites contain d-block transition metal ions. The intrinsic OER activity (normalized by surface area) of $CaCu_3Fe_4O_{12}$ exceeds that of the state-of-the-art BSCF and RuO_2, demonstrating its great potential for water electrolysis. The tetravalent Fe atoms in $CaCu_3Fe_4O_{12}$ improved the covalency of the transition metal-oxygen bonds and shortened the interatomic distance between the nearest neighboring OH adsorbates.

In addition, the oxygen vacancies can also cause structural transformations within Mn-based perovskite oxides and affects water electrolysis performance. In a recent study, it was demonstrated that perovskite oxides with ordered oxygen vacancies can achieve enhanced HER and OER activity in an alkaline electrolyte. In their study, $Nd_{0.5}Ba_{0.5}MnO_{3-\delta}$ (NBM3-δ) was used as the parent material and a series of perovskites with different structures and oxygen vacancy concentrations were easily obtained by extending the reductive annealing time, including $NdBaMn_2O_{5.5+\delta}$ (NBM5.5 + δ, where δ < 0.5), $NdBaMn_2O_{5.5}$ (NBM5.5), and $NdBaMn_2O_{5.5-\delta}$ (NBM5.5-δ, where δ < 0.5). Upon reduction, the partial removal of crystalline oxygen and an increased number of oxygen vacancies forces the A-site cations to be ordered; the layers of Nd-O and Ba-O are alternated along the c-axis, in which the oxygen vacancies were disorderly localized in the Nd-O layer. However, when the oxygen non-stoichiometry reached 0.5, MO_5 square pyramids and MO_6 octahedra were alternated periodically along the b-axis, generating orderly distributed oxygen vacancies.

This unique arrangement of orderly distributed oxygen vacancies endowed NBM5.5 with a half-filled eg orbital, optimized O p-band, and distorted structure, which significantly improves the OER and HER activity. However, it should be noted that Mn-based perovskite oxides exhibit far from satisfactory catalytic performance. The OER and HER activity are still inferior to those observed for their commercial counterparts and future effort are required to further enhance their activity.
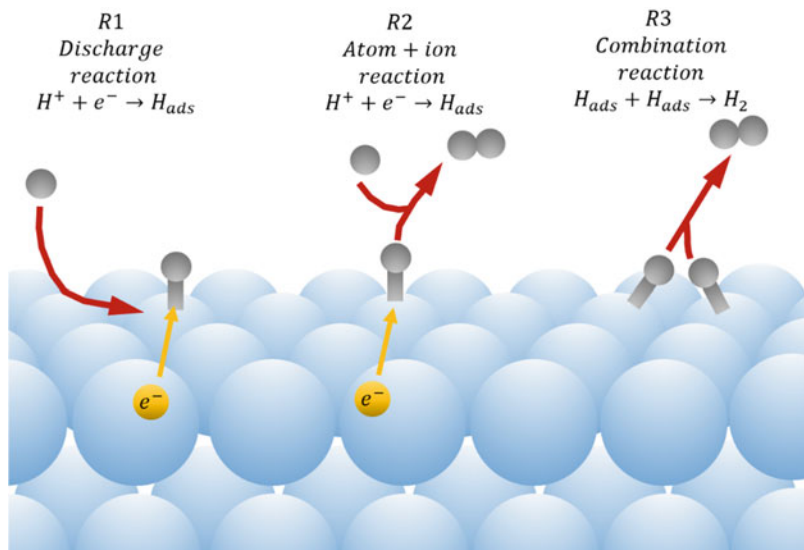
Fig. 6 The reaction pathway for hydrogen evolution reaction. R1–R3 shows the three elementary reaction steps

4 Materials for HER

The HER occur through three main elementary reaction steps, shown in Fig. 6.

The first step in HER is the discharge reaction, also called Volmer reaction, where a hydrogen ion from the electrolyte is adsorbed on the surface of the catalyst while simultaneously gaining an electron from it. Hydrogen gas is thereafter produced, either from an electrochemical or a pure chemical reaction. In the electrochemical desorption, a second hydrogen ion from the electrolyte reacts with the adsorbed hydrogen, gains an electron and immediately desorbs as H_2. This reaction is sometimes called the Heyrovsky or atom+ion reaction. In pure chemical desorption, the adsorbed hydrogen instead combines with a second adsorbed hydrogen atom and desorb as H_2 without any electron transfer, which is usually called the Tafel, or combination reaction. The elementary reactions in HER are given by:

$$SH^+ + e^- \rightarrow H_{ads} + S$$
$$H_{ads} + SH^+ + e^- \rightarrow H_2 + S$$
$$H_{ads} + H_{ads} \rightarrow H_2$$
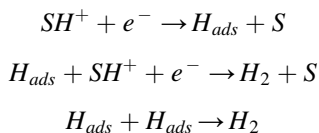
where H_{ads} are adsorbed hydrogens and S is either H_2O in acidic or OH^- in alkaline electrolytes. In HER, the hydrogen ions and gas in the solution are considered to be in equilibrium, meaning that the chemical energies of hydrogen are the same for the

initial and final states, while the adsorption of the intermediate hydrogen is either positive or negative in energy. A catalyst should lower this adsorption energy so that it is as close to zero as possible for the reaction to proceed without any activation barrier. This can also be concluded by the Sabatier principle, that states that a catalyst is considered optimal for HER if the hydrogen binds neither too strongly nor too weakly, and if the binding energy is just right, the H^+ ions are able to adsorb, but also easily desorb as H_2.

In order to compare different electrocatalyst materials, it is important to define quantitative parameters allowing a comparison under more or less identical conditions. Various parameters evaluating and comparing catalytic activities of selected catalysts are turnover frequency, mass and specific activity, Faradaic efficiency, Tafel slope and exchange current density, overpotential at given current density, and stability.

The equilibrium potential for H_2/H^+ is defined as 0 V (vs normal hydrogen electrode). However, HER cannot spontaneously proceed under the equilibrium potential for the activation barrier, slow diffusion of ions as well as the series resistance (Rs) and needs additional energy to drive the polarization current. In other words, an extra potential away from equilibrium is required to be applied on the cathode and the difference between the practical and equilibrium potentials is defined as overpotential.

The overpotential to deliver the current density of 10 mA cm^{-2} is the most frequently used criterion in many studies for evaluating the electrocatalytic activity, with the current density normalized either by the geometric area of the electrode, or the electrochemically active surface area of the electrocatalysts:

$$E_{corrected} = E_{uncorrected} - I \times R_s$$

The value of Tafel slope can be used to evaluate the HER kinetics and determine the HER mechanism. The common way of calculating Tafel slope is to fit the linear portion of Tafel plot (overpotential vs logarithm of current density) converted by the LSV curve (where η, b, j and j_0 represents overpotential, Tafel slope, current density and exchange current density, respectively). The Tafel slope, as an inherent property for a specific electrocatalyst, can be theoretically obtained from the Butler–Volmer equation and used for probing the rate-determining step in HER, with b equals to 29, 39 and 118 mV dec^{-1} at 298 K for Tafel, Heyrovsky and Volmer reaction, respectively. In general, a smaller Tafel slope often indicates a faster HER kinetics and is thereby more favorable for HER electrocatalysts:

$$\eta = b \log \frac{j}{j_0}$$

The exchange current density refers to the current density at equilibrium condition when the cathodic current density equals to the anodic current density. According to the previous Equation, j_0 can be obtained by the intersection at the X-axis when extrapolating the Tafel slope. The exchange current density can be used to evaluate

the charge transfer between the electrode and electrolyte at equilibrium. Therefore, a larger exchange current density often indicates that the reaction can be driven with less overpotential and can be used as a parameter to compare the intrinsic activity of different HER electrocatalysts.

Even though it has been generally accepted that it is sufficient to measure the long-term stability of the catalyst for approx. 12 h, it is strongly recommended to continue the measurements for at least 240 h to obtain stability results that are at least partly industrially relevant. Additionally, short power interruptions/power reductions within an order of minutes should be included in the long-term measurements. Such a procedure will be able to reveal the durability of the material for intermittent water electrolysis.

After dozens or even hundreds of hours' continuous test, a smaller shift on potential/current density indicates the electrocatalyst has a better durability. The surface morphology, internal structure and composition of the electrocatalysts could change during the continuous electrochemical measurements and should be carefully characterized after the durability test.

Although the theoretical principles behind HER mechanisms are relatively easy to understand, the practical implementation of hydrogen production via electrolysis of water often has the drawbacks such as low-efficiency and energy-consuming owing to the low intrinsic activity of the electrodes. Pt-group metals are generally regarded as the most prominent electrocatalysts for HER, while the scarcity and high cost are limiting their scaled applications. As a result, precious-metal-free electrocatalysts are intensively studied as alternatives.

4.1 Precious Metals Catalysts for HER

Platinum-group metals (PGM), being the most active materials towards the HER, can be considered as a benchmark of cathode catalysts over a broad pH range. Although noble metals show the best catalytic activity for the HER, their high price and scarcity make them unsuitable for larger industrial applications. Therefore, optimizing the geometric factors of Pt-based catalysts while maintaining electrocatalytic activity has been studied extensively.

Supporting platinum nanoparticles on a high surface carbon is an inexpensive and easy method to prepare active electrocatalysts.

Commercially, the most used 20 wt% Pt deposited on carbon black (Pt/C) is able to achieve one of the lowest values of overpotential of approx. 46 mV at 10 mA cm^{-2} under alkaline and also neutral conditions. Nevertheless, due to their high activity, the Pt/C catalyst is still commonly used as a comparative material for newly developed catalysts.

Ni–Fe layered double hydroxide (Ni–Fe LDH) support matrix with high crystallinity represents another possibility to tether and support Pt nanoparticles. The Ni–Fe LDH-Pt-ht catalyst exhibited overpotential of approx. 101 mV at 10 mA cm^{-2} which was 20 mV less than 20 wt% Pt/C catalyst tested under the same conditions.
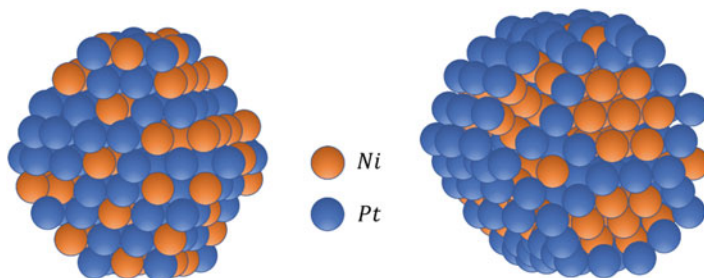
Fig. 7 Scheme of the Pt–Ni alloy and Pt–Ni heterostructure model catalysts

Even though the reduction of Pt particle size to nano-size is a promising method to reduce Pt loadings, it has proved to reach its limits. Due to the high surface energy, nanosized Pt particles tend to agglomerate or leach out during the electrochemical reaction which leads to a reduction in the active surface of the catalyst. Isolating single Pt atoms in a conductive matrix proved able to minimize this issue.

A second approach to reduce precious metal loadings is alloying it with less expensive metals. A preferable technique is to use one or more metals which have an additional positive effect on the catalytic activity of the material. A number of crystalline ultrathin Pt-M (M = Fe, Co, Ru, Cu, Au) alloy nanowires were prepared in order to partially replace Pt with less expensive metals with favorable synergy. They reported two main reasons for the enhanced performance of the above materials compared with commercial Pt nanoparticle-based catalysts.

It has been proved that Pt-Sm and $MoPt_2$ alloys exhibit superior activities compared to the individual metals. The latter material exhibited a Tafel slope of 39 mV dec^{-1} and overpotential at 100 mA cm^{-2} of 210 mV.

Another interesting finding is the importance of the atomic distribution and segregation throughout the catalyst structure. It has been compared plane Pt–Ni alloy and Pt–Ni heterostructure (Fig. 7), with respect to the HER activity. To obtain a current density of 10 mA cm^{-2}, overpotentials of 48, 82 and 61 mV were required for the Pt–Ni heterostructure, Pt–Ni alloy and commercial Pt–C, respectively. The reason for the enhanced activity for the Pt–Ni heterostructure can be attributed to the reduced energy barriers of both water dissociation and H_2 generation caused by atomic segregation of Pt and Ni.

4.2 PGM-Free Metals and their Alloys Catalysts for HER

Materials based on transition metal-based alloys, sulphides, selenides, phosphides, etc. have been investigated. The next paragraphs summarize selected state-of-the-art cathode electrocatalysts based on the most common transition metal groups and present a direct comparison of the individual groups and Pt-based electrocatalysts.

Fe is an inexpensive metal widely used in industrial practice. At the same time, it exhibits relatively high HER activity (overpotential can reach the lowest values around 260 mV at 10 mA cm^{-2}). Pure Fe is occasionally used as a comparative material where it can exhibit diverse results with respect to various preparation methods, morphology or surface area. Regrettably, very little data on pure Fe as a cathode material are available. One possible reason is that Fe alone exhibits worse stability in an alkaline environment at elevated temperature.

From a historical point of view, steel materials were frequently used as bifunctional catalysts in overall water splitting, even though their catalytic activity, especially for the HER, was far inferior to the state-of-the-art catalysts. Surface modification seems to be a feasible strategy to substantially increase the activity of steel-based materials. The modified material exhibited an overpotential of 370 mV at 10 mA cm^{-2}, i.e., almost 100 mV lower compared to pristine stainless steel (466 mV). Moreover, the overpotential was further reduced to 244 mV. Even though great progress has been achieved in this field, to the best of our knowledge, the most active steel-based catalysts still need doping with more active species, such as Ni, Mo or P, in order to reach overpotentials of only 80–120 mV higher than that observed for commercial Pt/C catalysts.

Apart from stainless steel, the most studied Fe-based alloys are Fe–Mo and Fe–Co groups that can either be used as binary alloys or complemented by another metal forming more complex systems. Fe–Mo alloys with high real surface area represent promising materials for the HER.

The addition of Mo increases the surface roughness (formation of micro-cracks) that can consequently lead to an increase in surface area and possibly enhanced activity. Moreover, the corrosion resistance of deposited Fe–Mo can be improved by incorporating a third metal, thus forming a ternary alloy Fe–Mo-M.

Ni represents the most promising choice for the third metal in the alloy.

A novel microwave-assisted electrochemical deposition was reported to allow the formation of Fe–Co alloys with a high Co content up to the Fe:Co ratio close to unity. The high amount of Co, structural defects under fast deposition and thus increased real surface area resulted in a low onset overpotential (145 mV) and Tafel slope (68 mV dec^{-1}) of the HER, and high exchange current density (20 mA cm^{-2}).

Another approach to enhance the activity of Fe-based alloys is the change in their crystalline structure to nano-crystalline or completely amorphous via rapid solidification. An amorphous structure represents a thermodynamically unstable state of the material and is thus characterized by a different oxidation state of the surface atoms compared to the crystalline one. Alloys with an amorphous structure exhibit many attractive properties, such as high corrosion resistance, promising mechanical stability and sufficient electrochemical activity.

Co-based catalysts have attracted much attention for their excellent electrical conductivity and durability in alkaline media. Co–Mo alloys and their modifications belong to the most investigated Co-based catalysts. The content of Mo in Co–Mo alloy strongly influences the catalytic activity and hardness of the material. The Co–Mo catalyst containing 45% of Mo in the alloy exhibited high catalytic activity. The addition of Ni to the binary Co–Mo alloy increased the real surface area, which

resulted in enhanced catalytic activity of the ternary Co–Ni–Mo alloys (overpotential of 110 mV at 10 mA cm^{-2} compared to 145 mV for the Co–Mo alloy).

Apart from alloying with other metals, Co is more commonly used in other compounds (e.g., sulphides and phosphides) where it can provide sufficient activity and stability under different alkalinities of the environment.

Ni alone is one of the most investigated materials for the HER in alkaline media on account of its excellent stability in an alkaline environment and sufficient catalytic activity towards the HER.

However, the activity strongly depends on the Ni morphology and surface area. Ni in the form of foam or mesh exhibited relatively high overpotential of approx. 217 mV and 275 mV at 10 mA cm^{-2}, respectively. However, the overpotential of pure Ni starts to increase after a certain time under cathodic polarization in alkaline media. This can be attributed to the formation of a hydride layer on the active Ni surface.

A very promising and cost-effective approach to increase the activity and, possibly, even the long-term stability of pure Ni is the addition of reduced graphene oxide (rGO). In such a case, the rGO enhances the recombination of H adatoms on the catalyst surface, leading to much higher activity of the prepared materials. The Ni@rGO composite exhibits reduced overpotential of 97 mV at 10 mA cm^{-2}.

Ni can also be used in alloys with different metals and oxide or non-oxide groups. The addition of other metals (such as Co, Mo, Fe) or groups influences various properties of pure Ni, e.g. electronic configuration, H_2O/H_2 adsorption/desorption, kinetics, etc.

Even though the incorporation of Co increases the intrinsic catalytic activity per unit of true surface area, the overall lower surface roughness caused by the change in surface morphology results in higher overpotential and lower exchange current density. The use of a sacrificial stainless-steel counter-electrode affected the composition of the finished coatings (co-deposition of Fe, Cr, Mo and Cu). The obtained material exhibited a higher electrochemical surface area and longer lifetime.

Ni–Mo alloys are the benchmark of non-platinum catalysts. The post-deposition reductive annealing or addition of carbon black can significantly increase the HER activity of Ni–Mo catalysts. On the other hand, the activity decreases at a positive potential due to the dissolution of Mo oxides. This could be a problem, especially during intermittent operation.

One of the most active materials for the HER is $MoNi_4$ supported by MoO_2 cuboids on Ni foam. Its specific surface morphology and synthesis procedure played a major role in the catalytic activity of the material. The $MoNi_4$/MoO_2@Ni catalyst exhibited remarkably low overpotential of 15 mV at 10 mA cm^{-2} and a Tafel slope of 30 mV dec^{-1}. Moreover, the stability test (30 h) proved this material to be fairly stable under alkaline water electrolysis conditions.

The application of nickel-molybdenum coatings on hydrogen storage alloys can significantly improve the endurance of Ni–Mo species to intermittent electrolysis. Whilst the Ni–Mo coating works as the HER catalyst, the hydrogen storage alloys enhance the corrosion resistance by the absorption of hydrogen during electrolysis and subsequent desorption during shutdowns and maintenance.

Besides in an alkaline environment, Ni-based materials have also proven to be applicable in a neutral environment. A nitrogen-modified porous Ni framework exhibited remarkable catalytic activity (overpotential of 64 mV at 10 mA cm^{-2}) as well as robust stability (18 h, 20 mA cm^{-2}, pH 7) under HER conditions. To the best of our knowledge, such activity in a neutral environment is one of the best of the non-precious materials yet reported and can even bear comparison with the commercial Pt/C catalyst (overpotential of approx. 46 mV at 10 mA cm^{-2}).

4.3   Other PGM-Free Material Groups for HER

Recently, the combination of transition metals and non-metal elements (S, Se, N, C, P) has emerged as a promising option to replace noble metals.

Low cost and simple preparation make metal sulphides promising candidates as cathode catalysts. Moreover, representatives of this group can be used in a full range of pH. Molybdenum sulphide (MoS_2) is one of the most investigated and oldest candidates of the sulphide group. In acidic media, metallic MoS_2 exhibited decent catalytic activity (Tafel slopes around 42 mV dec^{-1} and overpotential at 10 mA cm^{-2} around 180 mV).

Ni-based sulphides have also been reported as catalysts for the HER under acidic and alkaline conditions. The combination of Ni with other metals or metal-based materials seems to be one of the promising options. For example, defect-rich heterointerfaces of MoNi-based sulphides on carbon cloth prepared via a hydrothermal process exhibited low overpotential of 68 mV at 10 mA cm^{-2}.

Recently, metal sulphides have also been extensively studied for their possible application at neutral pH. The combination of Ni and Co sulphides outperformed both CoS_2 and NiS_2 at neutral pH, reaching a low overpotential of 72 mV at 10 mA cm^{-2}.

Transition metal selenides exhibit higher catalytic activity compared to metal sulphides. Also, in the case of selenides, the activity of the catalyst is strongly influenced by the number of active sites on its surface, as the reaction proceeds exclusively on the crystal edges. It is, therefore, necessary to optimize the catalyst surface to provide enriched, active edge sites. For instance, nanostructured defect-rich $MoSe_2$ with highly exposed active edge sites exhibited significantly lower overpotential than defect-free $MoSe_2$ (243 mV vs 364 mV at 10 mA cm^{-2}) (Ur Rehman et al. 2023).

Similar to sulphides, the combination of metal selenides and other metals or metal-based materials has also received a great deal of attention in the past decade. Fe-doped NiSe nanosheets on Ni foam exhibited high and stable catalytic activity for both the OER and the HER in alkaline solution. For the HER, the catalyst achieved an overpotential of 163 and 296 mV at 10 and 500 mA cm^{-2}, respectively. Surprisingly, the CoSe/$MoSe_2$ catalyst was stable in the entire range of the electrolyte pH and exhibited better activity in an alkaline environment than in an acidic one (overpotential of 115 mV vs 190 mV at 10 mA cm^{-2}). Recently, self-supported

Ni_2P-decorated $NiSe_2$ nanosheet arrays on carbon cloth have been reported as a very active catalyst for the HER. The catalyst maintained a low overpotential of 66 mV to drive a current density of 10 mA cm^{-2} for 12 h without significant degradation.

Overall, the metal selenides follow similar path to the metal sulphides with respect to their ability to provide an active catalyst for the HER in an alkaline medium.

Transition metal nitrides have recently emerged as efficient HER electrocatalysts due to their unique electronic structure and metal-like electric conductivity.

The conventional method of nitride preparation is direct nitridation. Heating a nickel foam in a NH_3 atmosphere can yield an active Ni_3N/Ni foam catalyst (overpotential of 121 mV at 10 mA cm^{-2}) that is also stable in an alkaline environment. It should be noted that a slight degradation could be observed at a higher temperature. Additionally, the Ni_3N catalyst, in the form of nanosheets prepared by a sintering process, shows interesting activity (overpotential of 112 mV at 10 mA cm^{-2}) and stability (12 h at 90 mA cm^{-2}) even at neutral pH.

Mo and Co doping can significantly improve the performance of metal nitrides towards the HER. Similar to previous groups, elemental doping and surface modification proved to be feasible strategies to design an active nitride-based catalyst. Co- or Mo-containing nitrides are able to achieve Pt-like activity in alkaline media. Another factor that should be considered is the simplicity of the catalyst preparation with respect to the potential industrial application.

Similar to nitrides, metal carbides also exhibited Pt-like properties and HER activity due to the shift in the d-band center. WC is the most commonly studied candidate possessing activity close to Pt in HER electrocatalysis. WC is more commonly used as a substrate for a compact Pt monolayer loading where it can deliver a performance comparable to bulk Pt, but it is at the same time protected from oxidative degradation. The stability of WC without the need of precious metals as well as the HER activity can also be enhanced by Ni doping or by changing its structure.

Alternatively, Mo and Co-based carbides were tested for the HER. Mo_2C-embedded nitrogen-doped porous carbon nanosheet (Mo_2C@2D-NPCs) material was able to achieve catalytic activity comparable to commercial Pt-based catalysts (overpotential of 45 mV at 10 mA cm^{-2}).

On another note, a Co–Mo bimetallic carbide catalyst exhibited comparable HER activity (overpotential of 46 mV at 10 mA cm^{-2} and Tafel slope of 46 mV dec^{-1}) but much higher stability in alkaline solution.

Metal phosphides have been considered as potential HER catalyst candidates for several decades. One of the reasons is that the activity of phosphides is not limited to the sites of crystal edges, but the HER can proceed in the bulk material, too. Nickel- and cobalt-based phosphides are among the most investigated members of this group. One of many examples, the 3D microporous NiFeCoP/NM electrode, exhibited remarkable catalytic activity for the HER and delivered a current density of 10 mA cm^{-2} at an extremely low overpotential (33 mV) with a relatively small Tafel slope.

The catalytic activity of metal-based phosphides can be further enhanced by appropriate doping with other elements. N-doped NiCoP nanowires (NW) on carbon fiber paper (CFP) were synthesized by a hydrothermal reaction followed by a phosphorisation-nitrogenation method (Li et al. 2022).

Amorphous Mo-doped Co–P catalyst synthesised by room temperature electro-deposition is one of the most active Pt-free catalyst yet reported. The addition of Mo positively influenced the energetics of water dissociation and M-H binding energy of the material, resulting in an active (overpotential of 30–35 mV at 10 mA cm^{-2}) and stable (24 h without increasing overvoltage) cathode catalyst.

The high cost and scarcity of precious metals are still the major obstacles to mass expansion in industry. Thus, the most promising approach, especially for large-scale application, is the development of a catalyst based on different and inexpensive materials, where the loading is not a crucial issue compared to the capital expenses of the final unit.

Regarding Fe alloys, they generally do not exhibit comparable catalytic activity to the PGM catalyst, their low cost, high abundance, and sufficient stability make them suitable for practical applications. Fe–Mo–Ni alloy with high activity and stability seems to be a promising and interesting catalyst for further optimization.

As demonstrated, the activity of pure Ni in alkaline media is not yet comparable to that of the PGM catalyst. Instead, Ni in the form of foam or mesh can serve as an excellent support due to its high electric conductivity, surface area and stability, as well as sufficient activity. On the other hand, the combination of Ni and Mo proved to be a promising way for developing an active catalyst, even though the stability during intermittent electrolysis in some cases still remains a problem. Furthermore, research into the use of Ni-based materials at neutral pH could also yield extraordinary results and should be pursued in greater depth.

Regarding PGM-free material, metal sulphides, due to the fact that they request a surface treatment, are not much stable under HER conditions, due to the reconstruction or deterioration of the modified surface.

Low cost, high abundance and the possibility to achieve superb activity make metal carbides ideal candidates for HER catalysts in alkaline media. Surprisingly, to the best of our knowledge, metal carbides do not exhibit favorable activity toward the HER at neutral pH.

Just recently, metal phosphides have yet again attracted much attention due to their interesting properties toward the HER. The Mo-doped Co–P catalyst outperformed the majority of Pt-based catalysts in terms of activity and stability under HER conditions.

4.4   Zero-Dimensional Catalytic Materials for HER

0D nanomaterials possess 3D nanoparticles all in the nanometer scale range (1–100 nm) or are composed of these as basic units. Normally, 0D materials possess more obvious quantum size effects as well as surface and quantum confinement

Fig. 8 IR-corrected
polarization curves of the
samples for hydrogen
evolution reaction (HER)
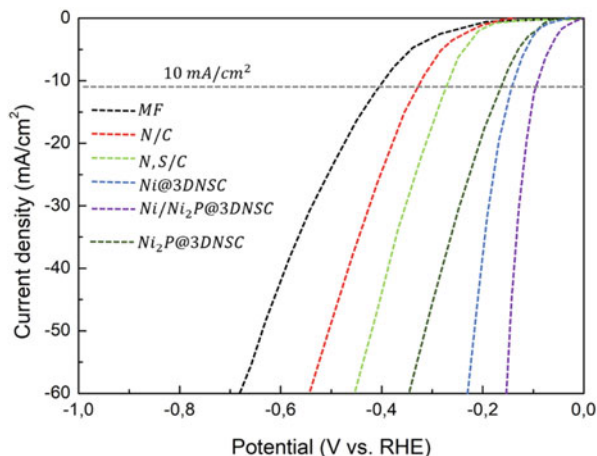
effects and in general, four types of 0D electrocatalytic materials for HER exist, including nanoparticles, quantum dots, atomic clusters and single atoms.

Many non-noble metal-based nanoparticles have been extensively studied for HER, and high energy efficiency per unit mass has been achieved. Using Ni nanoparticles as HER electrocatalysts, for example, it has been synthesized hybrid Ni/Ni_2P nanoparticles through a two-step process involving cleaned melamine foam (MF) being first transferred to a $NiCl_2$ solution to form MF@PSS-Ni^{2+} followed by heat treatment at 800 °C under N_2/H_2 (90/10 mass%) protection and subsequent mixing with NaH_2PO_2 at 350 °C under N_2 to form a Ni_2P/Ni composite electrocatalyst. As a result of the strongly coupled interface of Ni and Ni_2P, the synergistic effect between hybrid Ni/Ni_2P and graphitic carbon, the unique porous structure and the heteroatom-doped effect, the resulting Ni/Ni_2P@3DNSC exhibited highly efficient and durable electrocatalytic HER activities with an overpotential of only 92 mV at 10 mA cm^{-2} (Fig. 8).

More recently, cobalt phosphides have also been reported to possess higher electrocatalytic HER performances than other non-noble transition metal phosphides such as iron, nickel, copper, tungsten, and molybdenum phosphides. Researchers have also shown that P atoms doped into Co crystal lattices, can play a crucial role in promoting HER electrocatalysis. Based on this, it has been reported a one-pot strategy for the synthesis of Co_2P nanoparticles in which the resulting Co_2P@N, P-doped graphene (NPG) electrocatalyst (Fig. 9a) catalyzed HER with low electrode overpotentials of 45, 103, 128 and 220 mV at current densities of 1, 10, 20 and 100 mA cm^{-2}. Here, the linear portions of the plots using the Tafel equation (Fig. 9b) showed Tafel slopes of 58, 76, 118, 132 and 231 mV dec^{-1} for Co_2P@NPG, Co_2P clusters, NPG, NG and PG electrocatalysts, respectively, suggesting that these two catalysts followed the Volmer-Heyrovsky reaction during HER and that the rate-determining step was the slow combination of hydronium ions with hydrogen atoms.
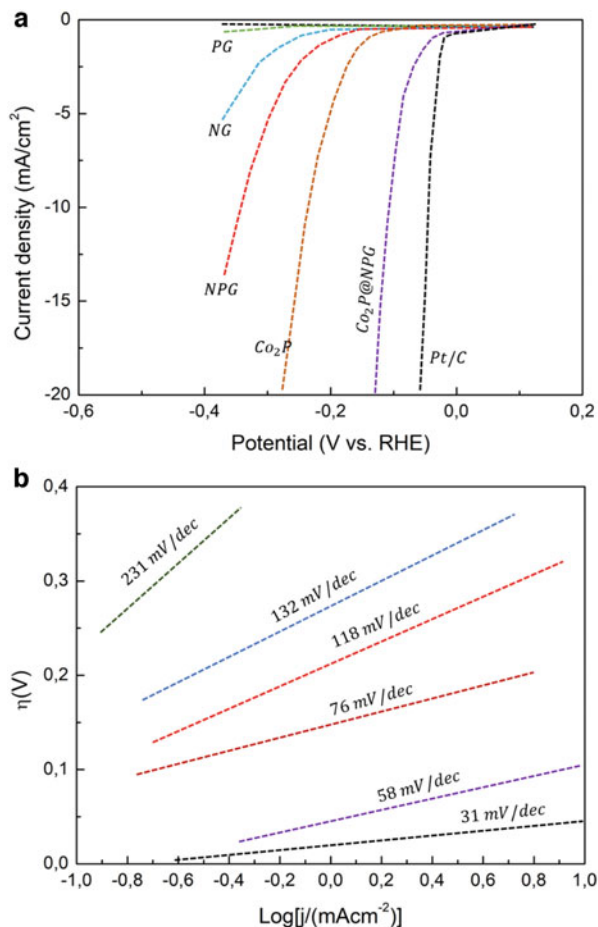
The results in this study further demonstrated that the $Co_2P@NPG$ catalyst possessed similar performances to that of Pt/C.

These researchers also synthesized other transition metal phosphorous compounds supported by carbon materials (TMPs@Carbon nanostructures), including $Fe_2P@NPG$, $Ni_2P@NPG$ and $Pd_5P_2@NPG$ using the one-pot strategy, and reported that based on electrochemical test results, the synthesized materials possessed better catalytic activities as compared with those without the N, P-doped graphene layers. Different Co-doped $Ni_{0.85}Se$ chalcogenides were also synthesized through a one-step hydrothermal method and it was reported that suitable doping can result in synergetic effects toward enhanced catalytic performance in which among the different synthesized catalysts, $Co_{0.1}Ni_{0.75}Se$ showed the highest HER performance.

Overall, non-noble metal nanoparticles are less stable in strong acidic or alkaline media and under high overpotentials and to overcome this issue, non-noble metal nanoparticles can be composited with carbon materials to avoid agglomeration and
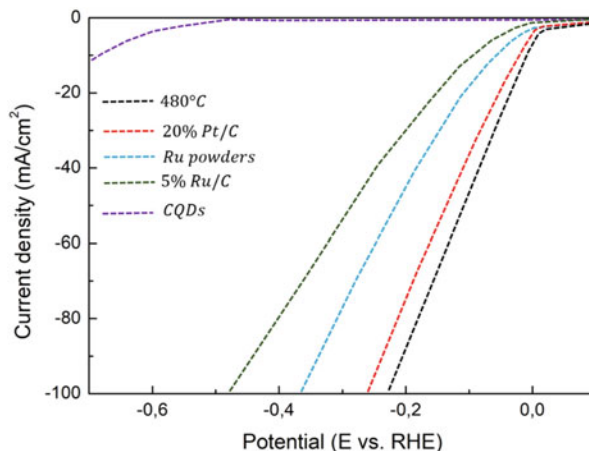
possible corrosion, which will improve electron transfer efficiency and will enhance electrocatalytic HER activity.

Carbon quantum dots (CQDs), which are novel carbon nanomaterials smaller than 10 nm, have attracted significant attention because of their highly adjustable photoluminescence ability, fast electron transfer, large electron storage ability and catalytic activity. As an example, Ru@CQDs electrocatalysts have been synthesized. Ru was selected in this study as the metal to study the function of CQDs in HER catalysis despite not being a non-noble metal.

The onset overpotential of the Ru@CQDs480 catalyst was found to be nearly 0 mV at a current density of 10 mA cm^{-2} without IR correction, which was 20 mV lower than that of 20% commercial Pt/C and was likely the lowest overpotential value reported in the literature (Fig. 10). Based on this, the HER performance of this novel Ru@CQDs480 catalyst was superior to that of even noble metals in alkaline media.

The remarkable catalytic performance of the RuNi/CQDs for HER can mainly be attributed to several synergistic effects, including:

- The key role played by metallic Ru in water dissociation and hydrogen adsorption/desorption in alkaline media in which metallic Ru possesses moderate Ru-H* bonding energy and shows great potential for HER;
- The excellent conductivity of CQDs, which can accelerate electron and ion transport in RuNi/CQDs during HER;
- The regulation of electronic properties in adjacent carbon atoms through intramolecular charge transfer arising from N doping in carbon matrixes, which can enhance electrocatalytic performance;
- The enhanced intrinsic activity of individual active sites and the alteration of the electronic structure of Ru as a result of Ni doping.

As recognized, CQDs, which are abundant, inexpensive and nontoxic, possess unique electron transfer abilities and large specific surface areas, which render
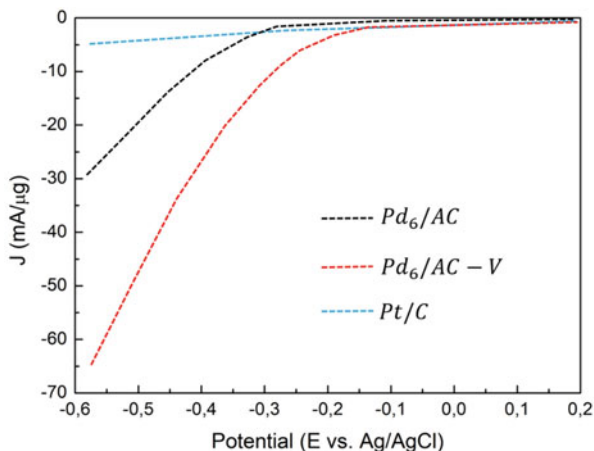
them excellent catalyst compositing materials. Abundant functional groups (OH, COOH, NH$_2$, etc.) on CQD surfaces can further provide favorable sites for the fabrication of multicomponent photo- and electroactive catalysts.

Atomic clusters are groups of atoms (or molecules) bound together. In recent years, this new class of nanoscale materials made up of a few to tens of atoms with sizes less than 2 nm, called nanoclusters or quantum clusters (QCs), has received increasing attention due to unique physical and chemical properties. In general, these materials fall in the nanoparticle-to-atom/molecule transition region and can exhibit molecule-like properties due to the gradual emergence of discrete electronic states.

As a typical example to demonstrate the merits of QCs, Pd-based QCs, despite not being a non-noble metal QC, can demonstrate the characteristics of these advanced materials in which it has been reported that Pd-based QCs can provide high electrocatalytic HER performances. The clear atomic-packed structure of Pd clusters can also help elucidate underlying catalytic HER mechanisms by identifying active sites and structure–property relationships. Based on this, several atomically precise Pd clusters [Pd$_6$(C$_{12}$H$_{25}$S)$_{12}$, Pd$_6$/AC and Pd$_6$/AC-V], supported on activated carbon with and without annealing, have been synthesized.

The synthesized Pd$_6$/AC and Pd$_6$/AC-V exhibited obvious HER currents in 0.5 mol L^{-1} H$_2$SO$_4$ and that as compared with commercial Pt/C, HER on the Pd nanoclusters exhibited much higher mass activities. Moreover, the onset potentials for Pd$_6$/AC and Pd$_6$/AC-V ($-$ 0.073 and $-$0.043 V vs. RHE, respectively) were close to that of commercial Pt/C ($-$0.043 V) (Fig. 11).

All QCs can show higher catalytic activities as compared with commercial Pt/C. This may be due to the favorable characteristics of sub-nanometer-sized metal clusters, such as their dimensions being between metal atoms and nanoparticles as well as their unique physical and chemical properties. Because the unique properties of these materials are strongly dependent on size, however, the development of synthetic strategies that can allow for the precise tuning of cluster cores with high monodispersity and purity is necessary. Furthermore, these materials

are also interesting due to possible application in a wide variety of fields such as environment, energy and biology.

Single-atom catalysts have recently drawn intensive attention in the fields of heterogeneous and electrochemical catalysis due to the virtues of their atomic dispersion, maximized noble metal utilization and unsaturated coordination. In general, non-noble metal single-atom catalysts possess distinct single active sites and unsaturated coordination environments in which strong interactions between supports and individual metal atoms can regulate the electronic structure of metal elements and improve the stability of corresponding catalysts, thereby achieving outstanding reactivity and selectivity.

For example, an electrocatalyst involving single-atom Ni on graphene has been synthesized, using chemical vapor deposition (CVD) in which in the synthesis process, a nanoporous Ni substrate was prepared by dealloying $Ni_{30}Mn_{70}$ alloy sheets with $(NH_4)_2SO_4$ aqueous solution at 50 °C followed by the deposition of graphene onto the porous Ni substrate through CVD and subsequent etching with hydrochloric acid to form a Ni-graphene monatomic catalyst.

The researchers further evaluated the catalytic performance of this Ni-doped graphene in 0.5 mol L^{-1} H_2SO_4 solution using a three-electrode setup and reported that the HER activity of the single Ni atom-doped graphene was strongly dependent on the concentration of the substitutional Ni dopant in which a low Ni concentration (0.38 at.%) led to much lower HER activities (Fig. 12a), demonstrating that Ni dopants play a crucial role in determining HER activity. In addition, the Tafel slope of the Ni-doped graphene (Fig. 12b) showed a low value of circa 45 mV dec^{-1} that was comparable to the low values (41 and 50 mV dec^{-1}) reported for MoS_2-based catalysts. Based on the comparison of Tafel slopes and overpotentials of the Ni-doped graphene with previously reported highly efficient HER catalysts, the Ni-doped graphene showed excellent HER performances with circa 90% retention of initial activity after 120 h of operation at a constant overpotential of 150 mV (Fig. 12c).

Single metal atoms trapped by defect sites in transition metal compounds form a unique class of single-atom catalysts. Since low-coordinated metal atoms often function as catalytically active sites, the specific activity per metal atom usually increases with decreasing metal particle size. However, the surface free energy of metals increases significantly with decreasing particle size to promote the aggregation of small clusters. Here, the use of appropriate support materials that can strongly interact with metal species can prevent this aggregation and create stable, finely dispersed metal clusters with high catalytic activities. Although this support approach has been used in industry for many years, practicable supported metal catalysts are inhomogeneous and usually consist of a mixture of sizes ranging from nanoparticles to sub-nanometer clusters. Such heterogeneity not only reduces metal atom efficiency, but also frequently leads to undesired side reactions.

Fig. 12 (**a**) Polarization curves of Ni-doped graphene samples with different Ni dissolution periods (4, 6 and 9 h) along with those of Pt and the reduced graphene oxide (rGO) electrodes for comparison; (**b**) Tafel plots of Ni-doped graphene (6 h of dissolution) and Pt; (**c**) durability of Ni-doped graphene at a constant overpotential of 150 mV for 120 h (the green line) and cycling stability tests. [The red line: the polarization curve of pristine Ni-doped graphene (6 h of dissolution). The black dashed line: after 1000 cycles]
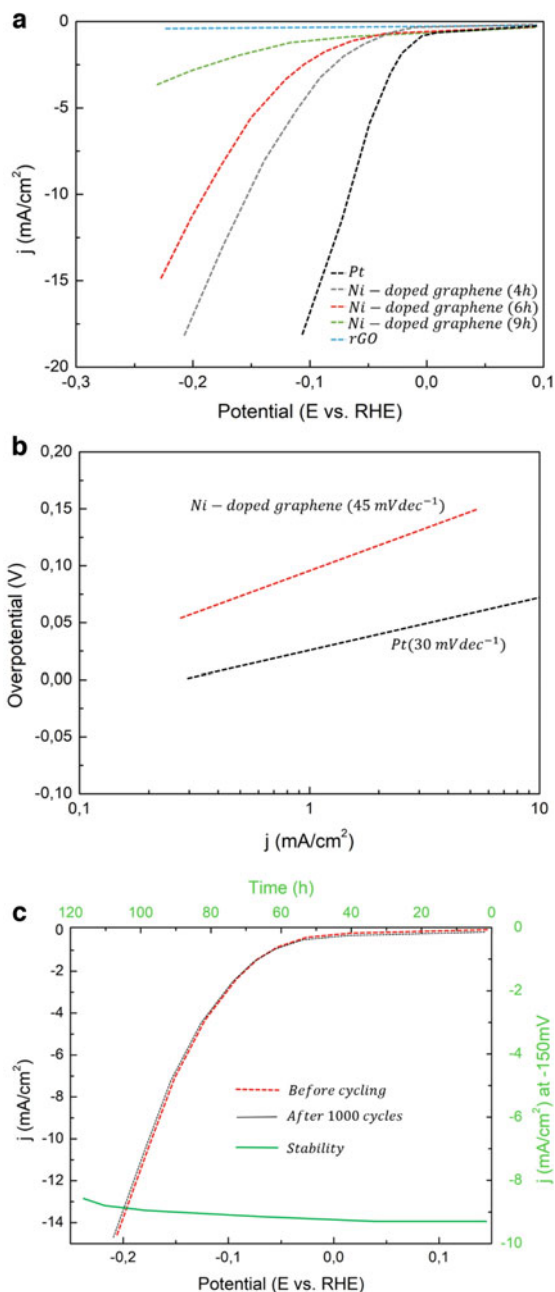
4.5 One-Dimensional Catalytic Materials for HER

1D nanomaterials refer to materials with two dimensions at the nanometer scale with examples including nanowires, nanorods and carbon nanotubes, all of which possess high specific surface areas and aspect ratios.

1D metallic nanowires have received significant attention due to their special physicochemical properties as well as potential applications. For example, Mo-Ni$_2$P nanowire arrays have been synthesized through a two-step method as an efficient HER electrocatalyst in electrolyte solutions with a wide range of pH values. In the corresponding synthesis process, the first step involved a hydrothermal method in which a mixed solution of NiCl$_2$· 6H$_2$O and Na$_2$MoO$_4$· 2H$_2$O was transferred into a Teflon-lined stainless autoclave and reacted at 160 °C for 6 h together with cleaned Ni foam (NF) to form the precursor. The second step of the synthesis process involved calcination in which red phosphorus was placed at the upstream of the tube furnace and the prepared precursor was placed at the downstream. The obtained sample was subsequently heated at 500 °C for 90 min with Ar gas flow to produce the catalyst of NiMoO$_4$ nanowires supported on NF.

The following results shown efficient HER activities with low overpotentials of 47 mV, 67 mV and 84 mV at a current density of 10 mA cm^{-2}, respectively, that were like these of Pt catalysts and better than those of Ni and Mo-based HER electrocatalysts (Fig. 13a–c).

These works above have not only afforded convenient and scalable synthesis methods toward Ni, Mo-based electrocatalysts, but also provided new opportunities in the design of integrated mixed-metal or doped transition metal phosphide nanoarrays with enhanced HER electrocatalysis and robust multifunctional materials.

As discussed above, high-performance electrocatalysts should possess large surface areas to expose active sites and excellent conductivity to facilitate electron transfer. In this regard, the growth of materials such as nanorods directly onto conductive substrates without the use of binders has widely been demonstrated as an efficient method to enhance conductivity and enlarge surface area. For example, a nickel-cobalt-iron-sulfur-phosphorus composite has been synthesized, self-supported tightly on NF as an electrocatalyst for overall water splitting by combining hydrothermal electrodeposition with in-situ electrochemical dealloying followed by a process for P/S co-treatment in which hydrothermal electrodeposition can give rise to much better crystallinity and stronger bonds between catalysts and substrates than films obtained through traditional electrodeposition at normal pressures and temperatures as well as rough surfaces with large surface areas.

The researchers also suggested that the nanorod-like structure of the composite catalyst can be tuned through the in-situ removal of the Zn template to expose more active sites and that P and S can be introduced to the composite to further improve conductivity and tune the electronic structure to boost catalytic performance.

Fig. 13 (**a**) Polarization curves; (**b**) polarization curves in PBS; (**c**) polarization curves in 0.5 mol L^{-1} H$_2$SO$_4$
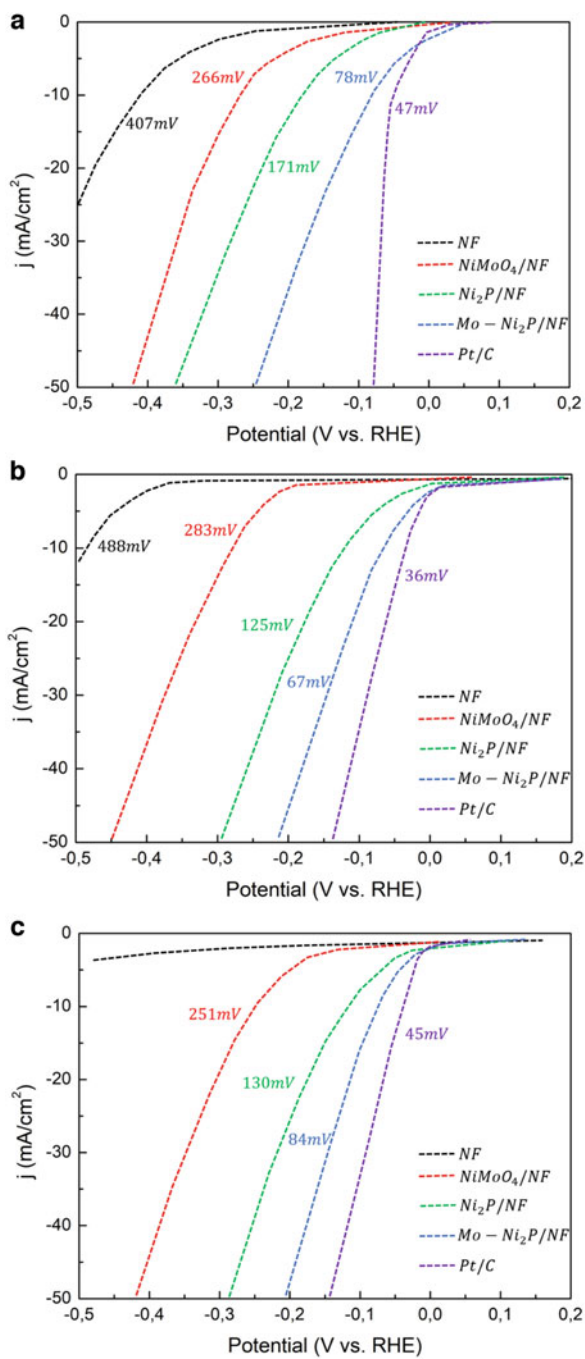
Fig. 14 Polarization curves
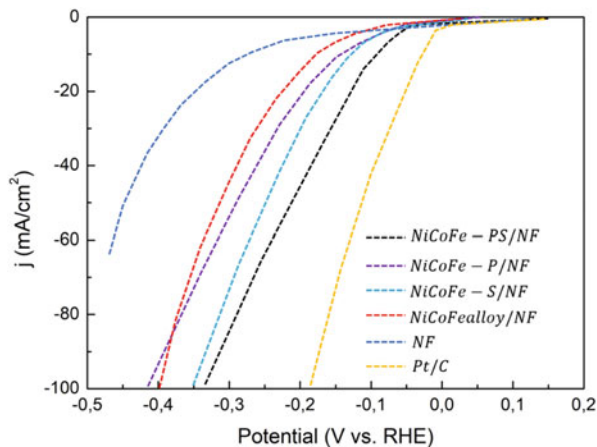
In terms of HER activity (Fig. 14), the as-prepared NiCoFe-PS nanorod/NF electrocatalyst exhibited an overpotential of only 97.8 mV at a current density of 10 mA cm^{-2}, which was smaller than that of the NF substrate but still larger than Pt/C, whereas after P and S doping/codoping, the formed electrocatalysts provided more enhancements to HER catalysis as compared with un-doped electrocatalysts.

Overall, the excellent catalytic performances can be attributed to several factors, including:

- A novel fabrication strategy involving hydrothermal electrodeposition, which enabled electrocatalysts with rough surfaces and superior stability. In addition, the formation of bubbles on electrodes during synthesis as well as the hydrothermal conditions can influence interfaces and allow for the exposure of more efficient active sites on catalyst surfaces. Moreover, high temperatures can give rise to enhanced crystallization to result in improved electrochemical stability and hydrothermal electrodeposition can enhance binding between catalysts and conductive substrates to further enhance stability;
- The construction of a mesoporous morphology through a self-generated sacrificial template, which can enhance surface areas and active sites to facilitate the diffusion of OH$^-$ ions and transmission of electrons. In addition, the highly porous structure can release bubbles faster and therefore prevent the peeling of electrochemically active materials due to bubbling during water splitting;
- The introduction of P and S elements into the catalytic material, which can modify electronic structures and improve conductivity, thus leading to improved catalytic properties.

Nanotubes with 1D structures are one of the most popular materials for electrocatalysis, particularly N, B-doped carbon nanotubes. For example, it has been proposed a bottom-up strategy to encapsulate CoP nanoparticles into B-doped carbon nanotubes (CoP@BCN) through pyrolysis and phosphidation using Co-MOF as the Co precursor, in which phosphidation with phosphorous acid can be effective in synthesizing CoP@BCN nanotubes.

As employed as HER electrocatalysts in acid (0.5 m H_2SO_4, pH $= 0.3$), alkaline (1 mol L^{-1} KOH, pH $= 13.9$) and phosphate buffer solution (PBS) (pH $= 7$), CoP@BCN-2, Co@BCN and CoP@CP showed higher overpotentials than CoP@BCN-1, indicating that CoP@BCN-1 can provide optimal catalytic HER activities in all electrolyte media (Jiang et al. 2022).

Overall, the results in this study demonstrated that the encapsulation of heteroatom-doped carbon caged CoP nanoparticles into BCN nanotubes can effectively prevent agglomeration with neighboring nanoparticles. In addition, the synergism of B and N dopants on graphitic nanotubes and confined CoP nanoparticles can provide CoP@BCN-1 nanotubes with highly active sites for catalytic HER. The co-doping of B and N into graphene nanotube encapsulated metal phosphide nanoparticles can also prevent metal agglomeration and produce additional active sites to enhance HER performance. Moreover, the inner tube spacing can further promote electrokinetics and good electrical conductivity as well as shorten electron diffusion lengths and these interconnected tubes can provide maximum exposure for active sites to achieve better catalytic performance.

4.6   Two-Dimensional Catalytic Materials for HER

2D materials involve nanomaterials in which electrons can move freely in a 2D plane and in general, the connotation of 2D materials can be considered based on the following points (Ashour Kermani and Fathirad 2022):

- Longitudinal structural units cannot be further divided;
- In-plane forces can maintain structural self-support;
- Horizontal and vertical proportions are large enough;
- Properties relative to bulk materials are sufficiently different;
- Ultra-thin 2D materials have a thickness of 2–5 nm.

Here, ultra-thin 2D nanolayers are often accompanied by structural deformations that help reduce surface energy and ensure structural stability and overall, 2D materials can be divided into two categories, including 2D ultra-thin materials and 2D crystal materials.

Of the two types of 2D materials, 2D ultra-thin materials possess nanostructures 2–5 nm in thickness as well as large enough horizontal and vertical ratios in which corresponding atoms in planes are arranged periodically. Examples of 2D ultra-thin materials include multilayered graphene, ultra-thin metal nanosheets and ultra-thin semiconductor nanosheets.

As examples, 2D materials involving nitrided-Ti_2CTx (N-Ti_2CTx) have been synthesized using Ti_2CTx as a starting material from Ti_2AlC as HER electrocatalysts in which the synthesis process involves nitridation to result in a distinct multilayered structure. This free-standing flexible 2D material was subsequently employed as an HER electrocatalyst with an overpotential of -215 mV versus NHE at a current density of 10 mA cm^{-2} (Fig. 15).

Fig. 15 Linear sweep
voltammetry (LSV) curves
without iR correction of
electrocatalysts with a scan
rate of 10 mV s^{-1}
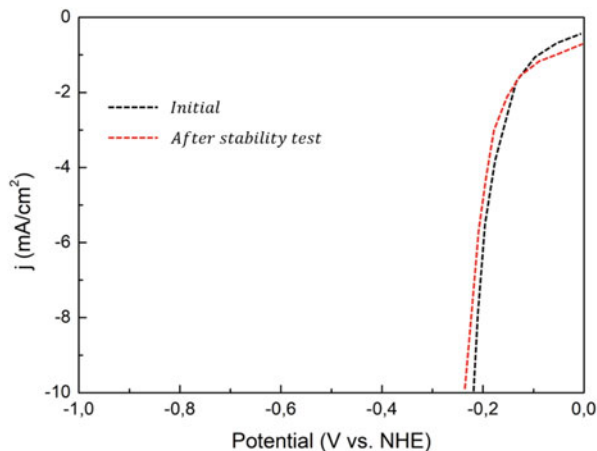
Fig. 16 Polarization curves
after iR compensation
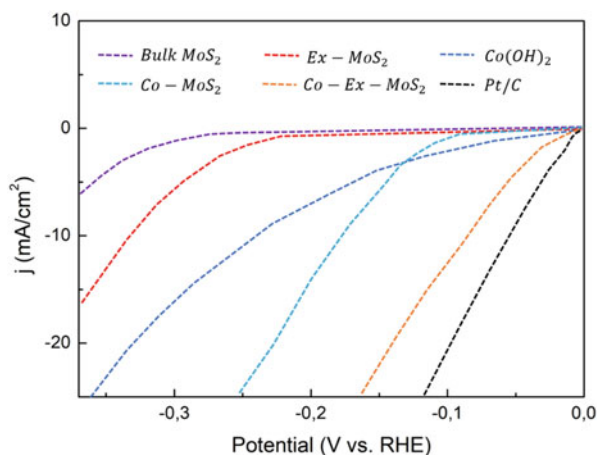
Furthermore, cobalt-phosphorous derived films (Co-P) can act as HER catalysts
for overall water splitting in which their as-prepared Co-P film exhibited remarkable
catalytic HER performances in alkaline media with an overpotential of 94 mV at a
current density of 10 mA cm^{-2} and a Tafel slope of 42 mV dec^{-1}. These researchers
also reported that their catalyst can be employed in both the anode and the cathode
for overall water splitting.

More interestingly, lamellar Ni$_3$FeN nanosheets were composed of stacked
nanoparticles with more active sites exposed for electrocatalytic reactions, which
differed from the Ni$_3$FeN nanoparticles that could not maintain the nanosheet
morphology. With these unique structural advantages, the resulting NSP-Ni$_3$FeN/
NF exhibited excellent HER activities with a low overpotential of 45 mV at
10 mA cm^{-2}, suggesting that ultra-thin 2D metalorganic framework nanosheets
synthesized through simple processes can be widely used in future energy conver-
sion devices.

Fig. 17 Tafel plots of the bulk MoS_2, Ex-MoS_2, Co-MoS_2, Co-Ex-MoS_2 and Pt/C in KOH (1.0 mol L^{-1}) at a scan rate of 5 mV s^{-1}
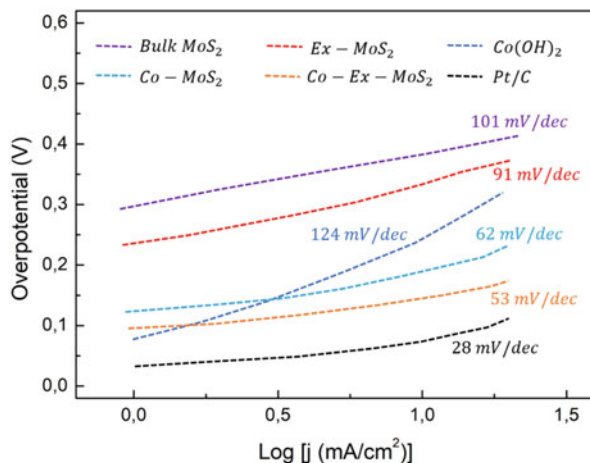
2D crystal materials are the second type of 2D materials and mainly possess atoms arranged periodically in planes with examples including graphene with periodically arranged surface carbon atoms and monolayered MoS_2. For example, it has been proposed a two-step synthesis method for a Co-Ex-MoS_2 HER electrocatalyst based on $Co(OH)_2$ nanoparticles confined by 2D MoS_2 nanosheets.

In terms of electrocatalytic HER measurements, Co-Ex-MoS_2 electrocatalyst showed a much smaller HER onset overpotential of circa -15 mV versus RHE as compared with bulk MoS_2 (-230 mV), which suggested superior catalytic activities (Fig. 16).

To further analyze HER reaction pathways, Tafel plots of the different catalyst samples were obtained (Fig. 17), which indicated that the linear region of the Co-Ex-MoS_2 sample possessed a slope of 53 mV dec^{-1}, which was close to the theoretical value of 40 mV dec^{-1}.

Other 2D Crystal materials that have been developed are MoS_2/NiFe-LDH superlattice, NCNFs-MoS2|P and MOF-derived nickel nitride on NF. Among host materials used to confine catalysts, 2D materials are of particular importance for two reasons in which one is that the layers of 2D materials are held together by weak interactions such as van der Waals forces and layer-layer distances (i.e., Van der Waals gaps) are tunable from tens to several nanometers, which make them excellent hosts for a large variety of small species such as alkali metal ions, metal nanoparticles and water molecules. The other reason is that many 2D materials such as MoS_2 and TaS_2 are intrinsically good HER electrocatalysts, and therefore, the rational design and selection of 2D nanoconfined materials as hosts and intercalants can jointly allow for catalysts with both high efficiency and good stability to address the long-standing need for high-efficiency non-noble HER electrocatalysts.

3D materials can be defined as solid figures, objects or shapes that possess three dimensions of length, width and height. Different from 2D materials, 3D materials possess thickness or depth.

Fig. 18 LSV curves of the prepared materials in 0.1 mol L^{-1} KOH
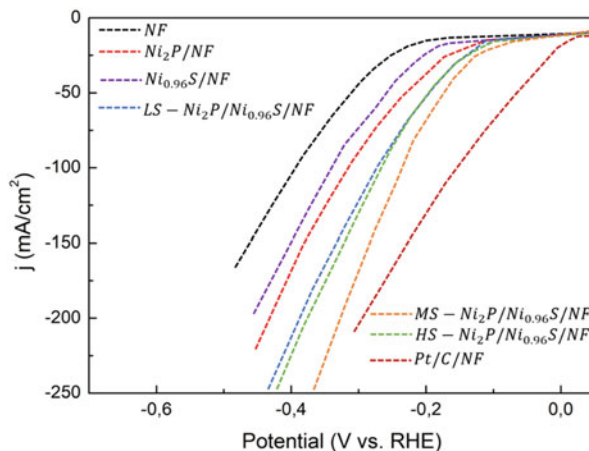
For example, many supported catalyst materials can be considered as 3D materials. Because many catalysts possess both insufficient electrical conductivity and specific surface area, however, the selection of suitable substrates to support catalysts is essential for improved electrical conductivity and specific surface area with maximized active sites from a catalytic point of view. As an example of 3D electrocatalyst supports for HER, NF with a honeycomb 3D network electrode structure and high electric conductivity is widely used as a support to promote the electron transport, electrolyte permeability and electrochemical surface area of supported catalysts. In addition, electrocatalysts combined with NF can allow for the uniform and regular growth of 3D porous nanostructures to promote electrolyte movement without the addition of binders in water-urea electrolysis.

As an example, $Ni_2P/Ni_{0.9}6S/NF$ has been synthesized using a two-step method, with overpotentials of 72 and 239 mV to reach 10 and 100 mA cm^{-2} (Fig. 18), respectively, which were higher than those of the other synthesized catalysts and were close to that of noble metal Pt/C (overpotential of 168 mV to reach 100 mA cm^{-2}).

The optimal catalytic activity and durability of the heterostructured HER catalyst of MS-$Ni_2P/Ni_{0.96}S/NF$ consisting of a medium-level $Ni_{0.96}S$ in the structure can be attributed to:

- Lattice defects that can provide more active sites to greatly improve electron transfer efficiency;
- Uniform heterogeneous interfaces that can reduce phase interface influences;
- The complete diffusion of the electrolyte to the electrode.

Furthermore, the structure of such interwoven clusters can be designed by controlling the non-sulfur content so that MS-$Ni_2P/Ni_{0.96}S/NF$ possesses a higher surface area.

It has been developed method to fabricate a 3D nest-like ternary NiCoP/carbon cloth (CC) electrocatalyst with superior catalytic activity and stability toward HER in which the nest-like NiCoP/CC required HER overpotentials of 44 and 62 mV to reach a current density of 10 mA cm^{-2} in acidic and alkaline media, respectively. Here, the improved performances were attributed to the unique 3D nest-like structure of the NiCoP, which can provide faster charge transfer rates and facile release of evolved H$_2$ to improve activity and stability.

Overall, the results from these studies suggest that the large specific surface areas and conductive networks of 3D materials can provide faster electron conduction and more active sites after catalyst loading for enhanced catalytic HER performance.

5   Conclusions

Taken together, significant progress has been made in the design of electrocatalysts for water splitting to produce hydrogen by advancing the atomic, molecular, and nanoscale materials engineering strategies. Hydrogen is a promising substitute for fossil fuel as its highest gravimetric energy density and zero pollution emission, which provides a clean and renewable energy as an alternative to fossil fuels. The development of water splitting cells as an efficient energy conversion and storage system play an important role in hydrogen production. However, the energy efficiencies of water electrolysis are hindered by the sluggish reaction kinetics of OER and HER due to high overpotentials which lead to only 4% of the word's hydrogen generation from water splitting at present. To facilitate the practical use of water splitting in industries, the design of efficient catalysts plays a major role in both OER and HER to minimize the overpotential and improve the energy efficiencies. In this review, some of the significant advances in the development of nanostructured noble-metal-based and non-noble-metal-based electrocatalysts for HER and OER have been highlighted, which show high performance approaching benchmark catalysts Pt and IrO$_2$/RuO$_2$ for the HER and OER with low cost. Fundamental insights have been gained into the mechanistic details of the synergistic structure, morphology, and composition of the catalysts for HER and OER in different media. The current understanding of the reaction mechanisms for HER and OER, especially the emerging LOM for OER, could lead to new advances in overcoming the limitation of the traditional AEM by providing a new avenue for the design of better OER electrocatalysts.

Despite the significant progress in understanding the electrocatalytic processes of the OER and HER, several challenges remain for the ultimate commercial large-scale production of hydrogen by water splitting electrolysis. First, the development of non-noble metal OER electrocatalysts with high activity and long-term stability performance in acidic media remains a challenging area of research and development. This challenge stems from the increasing use of proton exchange membrane (PEM) electrolysis is promising water electrolysis because of PEM's high energy efficiency and fast hydrogen production rate. PEM electrolysis for water splitting is

operated under acidic conditions. For HER, there is various efficient non-noble metal electrocatalyst available in acid media. However, for OER, most of the efficient OER catalyst is Ir and Ru based electrocatalysts which have higher dissolution resistance in acidic condition. For non-noble metal-based electrocatalysts, most of them, cannot survive under such conditions. Thus, there is a clear need for the development of stable and robust non-noble metal OER electrocatalysts. Recently, it was demonstrated a rational approach for designing non-noble metal based electrocatalysts that exhibit high activity and stability in acidic media by treating activity and stability as a decoupled elements of mixed metal oxides.

For example, manganese is used as a stabilizing structural element which is coupled to the catalytically active Co center in CoMnOx film. Secondly, there is a limited knowledge of the detailed catalytic mechanisms especially for transition-metal-based HER and OER electrocatalysts. The intrinsic active site of electrocatalysts cannot be completely determined based on the descriptor of TOF.

Recently, non-noble-metal-based carbides, phosphides, and chalcogenides have drawn great attention due to their high performance for OER in alkaline media. However, the nanostructured electrocatalysts undergo composition and structural transformations during the reaction under OER conditions. Therefore, understanding the structural transformation is required to determine the real active phases and sites. Gaining insight into the detailed mechanism, structural transformation, real active sites is critical for the rational design of the optimal performance catalysts. Integration of in situ characterization techniques and theoretical modeling is an advanced approach to gain insights into the structural transformation, reaction intermediates, and reaction pathways of the catalysts. Thirdly, it is difficult to directly compare various nanostructured catalyst materials based on the performance descriptors due to the different mass loadings of the catalysts on the electrode and the different materials of substrate which may affect the electron transfer rate by different electrochemical measurement methods. More effective electrocatalysts screening strategies are needed to establish the standard evaluation protocol for effective comparisons of the performances of catalysts from different research groups. Nevertheless, the surge of recent interests in nanostructure and lattice oxygen engineering of catalysts is expected to lead to new advances in the design of active, stable, and low-cost OER and HER electrocatalysts for the mass commercialization of water-splitting based hydrogen production.

References

Adegoke KA, Maxakato NW (2022) Empirical analysis and recent advances in metal-organic framework-derived electrocatalysts for oxygen reduction, hydrogen and oxygen evolution reactions. Mater Chem Phys 289:126438. https://doi.org/10.1016/j.matchemphys.2022.126438

Ashour Kermani R, Fathirad F (2022) Fabrication of 0D/1D/2D ZnS–CuS nanodots/GNRs/g-C3N4 heterojunction photocatalyst for efficient photocatalytic overall water splitting. Int J Hydrogen Energy 47(93):39376–39385. https://doi.org/10.1016/j.ijhydene.2022.09.119

de la Calle A, Ermanoski I, Stechel EB (2022) Towards chemical equilibrium in thermochemical water splitting. Part 1: thermal reduction. Int J Hydrogen Energy 47(19):10474–10482. https://doi.org/10.1016/j.ijhydene.2021.07.167

Huang C-J, Xu H-M, Shuai T-Y (2023) A review of modulation strategies for improving catalytic performance of transition metal phosphides for oxygen evolution reaction. Appl Catalysis B 325:122313. https://doi.org/10.1016/j.apcatb.2022.122313

Jiang R, Li Q, Zheng X (2022) Metal–organic framework-derived Co@NMPC as efficient electrocatalyst for hydrogen evolution reaction: revealing the synergic effect of pyridinic N–Co. Int J Hydrogen Energy 47(64):27374–27382. https://doi.org/10.1016/j.ijhydene.2022.06.096

Jiang Y, Liu H, Jiang Y et al (2023) Adjustable heterointerface-vacancy enhancement effect in RuO2@Co3O4 electrocatalysts for efficient overall water splitting. Appl Catalys A 324:122294. https://doi.org/10.1016/j.apcatb.2022.122294

Li J, Yuan Z, Zhu Y (2022) Engineering multiphasic heterostructure NiCoP@Co0.5Ni0.5Se2 with optimized electronic structure enabling robust hydrogen evolution. Chem Eng J 450:138426. https://doi.org/10.1016/j.cej.2022.138426

Mathew S, Hosseinirad E, Kim KC (2022) Enhanced electrocatalytic water splitting by Sm and Gd-doped ceria electrocatalysts on Ni foam substrate. Electrochim Acta 435:141382. https://doi.org/10.1016/j.electacta.2022.141382

Moradi M, Hasanvandian F, Bahadoran A et al (2022) New high-entropy transition-metal sulfide nanoparticles for electrochemical oxygen evolution reaction. Electrochim Acta 436:141444. https://doi.org/10.1016/j.electacta.2022.141444

Orfila M, Linares M, Pérez A et al (2022) Experimental evaluation and energy analysis of a two-step water splitting thermochemical cycle for solar hydrogen production based on La0.8Sr0.2CoO3-δ perovskite. Int J Hydrogen Energy 47(97):41209–41222. https://doi.org/10.1016/j.ijhydene.2022.03.077

Razi F, Hewage K, Sadiq R (2022) A comparative assessment of thermodynamic and exergoeconomic performances of three thermochemical water-splitting cycles of chlorine family for hydrogen production. Energy Convers Manag 271:116313. https://doi.org/10.1016/j.enconman.2022.116313

Sumedha HN, Shashank M, Teixeira SR (2022) Novel 3D-flower shaped KTaO3 perovskite for highly efficient photocatalytic and H2 generation ability. Sci Rep 12(1):10776. https://doi.org/10.1038/s41598-022-14590-3

Tan D, Xiong H, Zhang T (2022) Recent progress in noble-metal-free electrocatalysts for alkaline oxygen evolution reaction. Front Chem 10:1071274. https://doi.org/10.3389/fchem.2022.1071274

Tang Y, Liu F, Liu W (2023) Multifunctional carbon-armored Ni electrocatalyst for hydrogen evolution under high current density in alkaline electrolyte solution. Appl Catalysis B 321:122081. https://doi.org/10.1016/j.apcatb.2022.122081

Ur Rehman S, Tariq Z, Zou B (2023) Type-I/Type-II Transition of MoSe2/g-GaN van der Waals heterostructures mediated by biaxial strain and electric field for overall water splitting. Mater Sci Eng B 288:116195. https://doi.org/10.1016/j.mseb.2022.116195

Xu Y, Fan K, Zou Y et al (2021) Rational design of metal oxide catalysts for electrocatalytic water splitting. Nanoscale 13(48):20324–20353. https://doi.org/10.1039/d1nr06285a

Yao Y, Zhang Z, Jiao L (2022) Development strategies in transition metal borides for electrochemical water splitting. Energy Environ Mater 5(2):470–485. https://doi.org/10.1002/eem2.12198

Zhang A, Liu H, Wang C (2022) Efficient CoNi-bimetal phosphide embedded carbon matrix derived from a novel phosphonate complex for hydrazine-assisted electrolytic hydrogen production. Electrochim Acta 435:141406. https://doi.org/10.1016/j.electacta.2022.141406

Zhang WX, Xi S, Liang Y (2023) Construction of novel PG/GeP2 and PG/SiP2 vdW heterostructures for high-efficiency photocatalytic water splitting. Appl Surf Sci 608:155106. https://doi.org/10.1016/j.apsusc.2022.155106

Nuclear Hydrogen Production

1 Introduction

Centralized energy production in large quantities favours the use of nuclear plants, which should operate in baseload mode, with conventional plants covering peak load. Nuclear emits virtually no airborne pollutants.

Therefore, it appears to also be an ideal option for large scale centralized hydrogen production (Nadaleti et al. 2022; Kim et al. 2022a).

The future of hydrogen and the potential for nuclear generated H_2 will be driven by major factors such as:

- Production rates of oil and natural gas.
- Societal and governmental decisions concerning global climate change due to GHG emissions.
- The need to save fossil resources for use in environmentally friendly applications (substitution of nuclear for conventional process heat production would allow resource savings of up to 40%).
- If the cost of nuclear heat is sufficiently low, it may help to meet growing rates of energy use, replace expensive electricity generation with fossil fuels and replace old plants.
- Energy security from extended fuel reserves and independence from foreign oil uncertainties.
- Economics of large-scale hydrogen and synthetic fuels production and transmission.

A principal variant of electrolysis considered promising for the future is high temperature steam electrolysis (HTSE). Unlike low temperature water electrolysis, the total energy demand of electrolysis in the vapour phase is reduced by the heat of vaporization, which can be provided much more inexpensively by thermal rather than electric energy. Decreasing electricity input can be seen with increasing
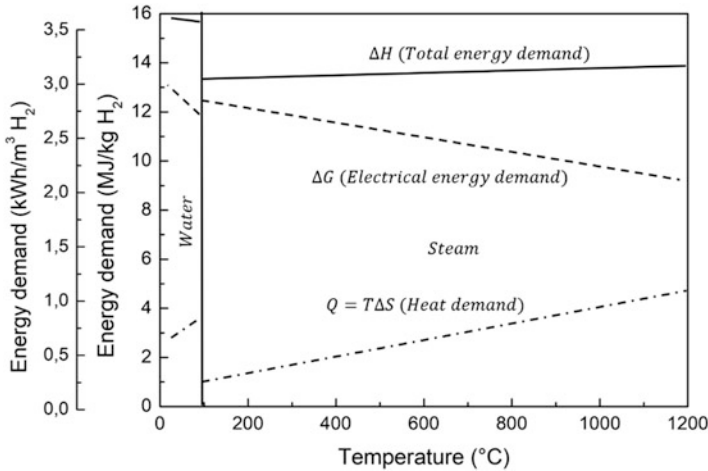
Fig. 1 Energy demand for water/steam electrolysis

temperature from Fig. 1, and is about 35% lower compared to conventional electrolysis in the high temperature range of 800–1000 °C.

The efficiency of electrical generation at this high temperature level is also significantly better.

The HTSE process is advantageous because of its high overall thermal-to-hydrogen efficiency when coupled with high efficiency power cycles (El-Eman et al. 2020). HTSE corresponds to the reverse process of the SOFC; the devices could be operated in both modes. The HTSE development may therefore benefit of ongoing R&D efforts in the SOFC area.

A major difference is that a high temperature electrolyser must be coupled with a heat and power source (Gao et al. 2022a). Nuclear plants, in particular those of the fourth generation, could provide the electricity and, in the case of a VHTR, also deliver relatively high temperatures and high net power cycle efficiencies (Sahin and Sahin 2021).

Essentially the electrolytic cell consists of a solid oxide electrolyte with conducting electrodes deposited on either side.

The electrolyte is an oxygen-conducting ceramic material, typically Y_2O_3 stabilized ZrO_2 (YSZ) and MgO. A mixture of steam to be dissociated and some hydrogen is supplied to the hydrogen electrode at 750–950 °C. At the hydrogen electrode–electrolyte interface, the steam is split into hydrogen and oxygen:

$$2H_2O + 4e^- \leftrightarrow 2H_2 + 2O^{2-}$$
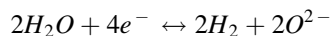
Oxygen ions are drawn through the ceramic electrolyte by the electrical potential of about 1.3 V, until they recombine to oxygen gas at the electrolyte–oxygen electrode interface:

$$2O^{2-} \leftrightarrow O_2 + 4e^-$$
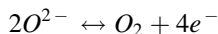
The oxygen then flows along the anode, typically made of a composite of YSZ and Sr-doped lanthanum manganite (LSM)), while the hydrogen–steam mixture passes along the hydrogen electrode (Ni/YSZ cermet with ~30% porosity) on the opposite side of the electrolyte. Preheated air or steam can be used as a sweep gas to remove oxygen from the stack. The purpose of the sweep gas is to dilute the oxygen concentration and thus decrease corrosion of the oxygen-handling components. Pure oxygen can be produced by the stack and would be a valuable commodity if satisfactory materials and/or coatings could be developed for construction of the oxygen-handling components.

At these high temperatures, all reactions proceed very rapidly. The steam–hydrogen mixture exits from the stack and then passes through a separator to separate hydrogen from the residual steam. The feedgas stream to the HTSE cell contains a 10% fraction of hydrogen in order to maintain reducing conditions and avoiding oxidation of the nickel in the hydrogen electrode. HTSE cells can be operated at high current densities, which allow large production capacities in comparatively small volumes. A practical electricity-to-hydrogen efficiency of about 90% appears to be realistically achievable. The main issue that needs further improvement remains the lifetime of the hydrogen electrode, which is limited by degradation.

A large part of the energy demand reduction is related to water vaporization which does not require high temperature heat. Once vaporization is achieved, the extra heat necessary to reach the high temperature required to have high enough ionic conductivity in the electrolyte may also be provided by a combination of nuclear heating, recuperation of the sensible heat of the produced hydrogen and oxygen, and self-heating of the cell due to its inherent electrical resistance.

With respect to the electricity requirements, values of 2.6–3 kWh/Nm^3 of H$_2$ are expected. The heat for steam production to supply the cells, however, must be added. The process with the production of hot steam and cell operation at high temperatures requires a solid oxide membrane electrolyte (Milewski et al. 2021). For example, Y$_2$O$_3$ stabilized ZrO$_2$ acting as both gas separator and electrolyte is used where oxygen ions start migrating when a voltage is applied.

Steam electrolysis at about 800 °C will have an overall efficiency (including the electrical conversion efficiency) in the range of 35–45%. The efficiency will even rise to around 50% at 900 °C. Two main problems to be solved are the improvement of the long-duration performance of the cells and the development of techniques for manufacturing and assembling large area cells in order to reduce the overall cost of the commercial plant (Sorgulu and Dincer 2018).

2   High Temperature Co-electrolysis of Steam and Carbon Dioxide

The principle of high temperature electrolysis is also applicable when steam and carbon dioxide are present simultaneously. In this case, both H_2O and CO_2 can be co-electrolysed to hydrogen and CO. A mixture of CO_2 and steam is electrolytically decomposed at a required cell voltage of 1.48 V (if no external heat source is available), resulting in the production of synthesis gas that may be subsequently used for synthetic fuel production. The quantities produced are dependent on the quantities of H_2O and CO_2 in the feedstream, the electrolysis current applied, and the reverse water gas shift reaction. The net reaction of CO_2 electrolysis is:

$$2CO_2 \leftrightarrow 2CO + O_2$$
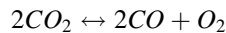
The solid oxide electrolysis cell (SOEC) negative electrode is usually made of a Ni–YSZ composite, where the Ni serves directly as a catalyst (AlZahrani and Dincer 2018). As for the electrolyte, a higher ionic conductivity and a lower ohmic loss are the focus of research, and new materials (ScSZ, LSGM, LSGMC) are being looked into as alternatives to YSZ.

The process taking place is more complex than pure steam electrolysis, since it involves several reactions.

Also, in a co-electrolysis cell (Fig. 2), about 10% of the product (here synthesis gas) is recycled and added to the feed stream to maintain reducing conditions at the steam/H_2 electrode. The mixture then enters the electrolysis cell, where the oxygen is removed electrolytically and the product stream is enriched in synthesis gas.

Two design concepts are possible: planar and tubular. The tubular design pursued in Germany and the USA was first selected for its mechanical stability and because fabrication of thin-walled ceramic parts with large surfaces was not state of the art. The tubes were vertically deployed on support tracks which contained steam input and hydrogen output ducts. Tubular cells have the advantage of achieving a high degree of leak tightness, while planar cells can be fabricated with a larger active area per volume.

3   Nuclear Reactor for Hydrogen Production

The next generation of nuclear reactors (Generation IV) is expected to be introduced in about 20–30 years from now. The concepts of such reactors, however, are being developed today based on requirements leading to further progress of the nuclear technology by addressing the areas of safety and reliability, proliferation resistance and physical protection, economics and sustainability (Gao et al. 2022b).

In the future, nuclear power will require a further enhancement of the safety standards. Safer operation of nuclear reactors can be obtained by designs with a very

$$33\% \, H_2 + 33\% \, H_2O + 34\% CO_2 \qquad 62\% \, H_2 + 5\% \, H_2O + 2\% CO_2 + 31\% \, CO$$

$$H_2O + CO_2$$

Porous cathode,
Nickel − Zirconia cermet

$4e^-$

$H_2 + CO$

$xCO_2 + yH_2O + 4e^- \rightarrow xCO + yH_2 + 2O^-$

Gas − tight electrolyte,
Stabilized Zirconia

$2O^-$

O_2 $2O^- \rightarrow O_2 + 4e^-$ Porous anode, Strontium −
doped Lanthanum Manganite

O_2

Metallic interconnect

$H_2 + H_2O + CO_2 \longrightarrow$

$H_2O + CO_2$

$H_2 + CO$

Porous cathode,
Nickel − Zirconia cermet
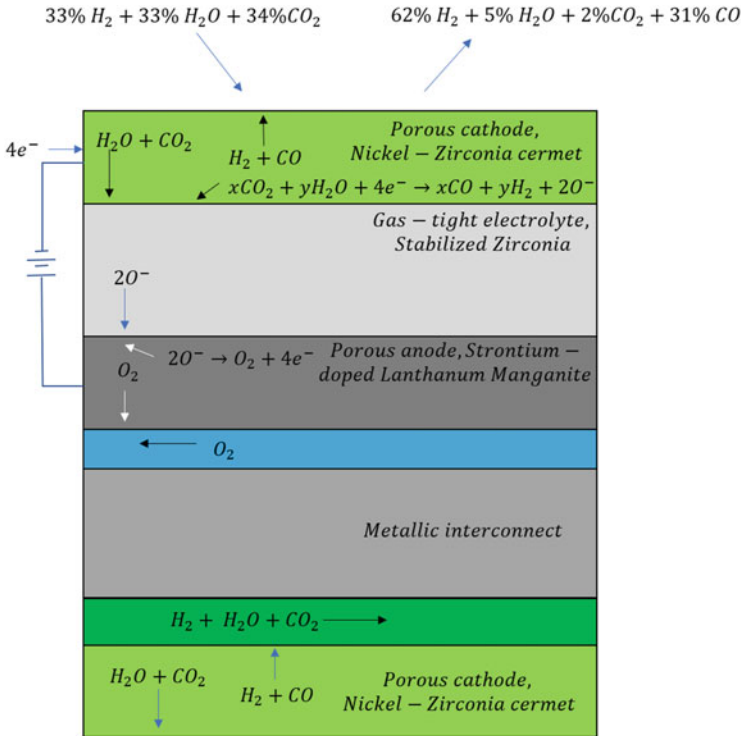
Fig. 2 Solid oxide cell used for the co-electrolysis of CO_2 and steam

low probability and degree of core damage, with minimal consequences even after severe accidents and limitation of effects to the plant site. The accident management will be further improved such that the public will not be affected and off-site emergency response will be almost unnecessary. This can be achieved through a robust design, a high level of inherent safety and transparent safety features, and by sharing experience on an international basis (Kim et al. 2022b). In order to be competitive, reliability and performance must be at a very high level that is achievable by considering both technical improvements and the improvement of individual and organizational performance.

International safeguards must be strengthened against misuse of fissile material by diversion of weapons-usable material during enrichment and reprocessing activities. Controlling and securing nuclear material can be provided for by modified design features or other innovative measures and international policies to make potential diversion or theft or a sabotage act unattractive, and to make dispersion of material more difficult. A robust design is also a means to protect against actions related to war or terrorism.

Sustainability as the ability to meet the needs of both the present and future generations is mainly looked at in terms of nuclear fuel supply over a long period of time and spent fuel management with the requirement of meeting environmental

objectives (Khan 2019). The fuel resources available are essential, as is and reactor deployment for each potential fuel cycle such as the once-through approach, modified open cycle or fuel reprocessing. Prolonged availability of resources can be achieved by breeding new fissile material or by recycling used fuel. Future radioactive waste management must include processes leading to significantly reduced quantities of waste to be safely stored, transported and disposed of. Furthermore, a considerable reduction in toxicity and a lifetime not significantly longer than its natural limits will simplify the requirements of a safe operation of the repositories.

The development toward a simpler reactor design, economical plant sizes and life cycles, and improvement of the plant's efficiency will help in achieving costs competitive with those of other energy options (Lee et al. 2022). The economic risk can be reduced by employing modular reactor designs and using improved or innovative construction techniques.

Future nuclear reactors must also be flexible in meeting the need for energy products other than electricity. The penetration of non-electricity markets by supplying process heat/steam for district heating, seawater desalination or hydrogen generation will enhance efficiencies and thus competitiveness (Bolfo et al. 2021).

4   Hydrogen from Nuclear Energy

Today, we are alarmed by the depletion of fossil energy and the adverse effects of the rapid increase in fossil fuel burning on the environment, such as climate changes and acid rain, because our lives still depend heavily on fossil energy. It is, thus, widely recognized that hydrogen is one of the important future energy carriers because it is used without the emission of carbon dioxide greenhouse gas and atmospheric pollutants and that the demand to it is expected to increase greatly as the fuel cells are developed and applied widely in the near future. However, hydrogen hardly exists naturally. Hydrogen production by direct thermal decomposition of water molecules would require a high-temperature heat of several thousands of Kelvin. By using electrolysis of water or combining high-temperature endothermic chemical reactions and low-temperature exothermic chemical reactions, in which the net chemical change resulting from the sequence of component chemical reactions is water decomposition; it is possible, in principle, to split the water molecule with heat at a considerably lower temperature. A practical answer for protecting the global environment would be to produce hydrogen economically and from energy sources without carbon emission and air pollution.

Hydrogen production from water using nuclear energy offers one of the most attractive zero-emission energy strategies and the only one that is practical on a substantial scale. Recently, strong interest is seen in hydrogen production using heat of a high-temperature gas-cooled reactor (HTGR), a.k.a. very high-temperature reactor (VHTR) in the form of very high-temperature advanced design (Norouzi et al. 2021). The HTGR is particularly attractive because it has unique capability, among potential future generation nuclear power options, to produce high-

temperature heat ideally suited for nuclear-heated hydrogen production, in addition to being inherently and passively safe and near-term deployable. This chapter introduces representative HTGR hydrogen production methods, high-temperature electrolysis of steam (HTE) and thermochemical splitting of water in an iodine–sulfur (IS) process, and coupling these methods to the HTGR to enable economical and safe hydrogen production from nuclear energy (Corgnale et al. 2020).

4.1 High-Temperature Elecrolysis of Steam

The process of the HTE is a reverse reaction of the solid-oxide fuel cell (SOFC): an oxygen ionic conductor is usually used as a solid oxide electrolyte. Steam (H_2O) is dissociated at the cathode with hydrogen molecules (H_2) forming on the cathode surface: $H_2O(g) + 2e - \rightarrow H_2(g) + O_2-$, whereas oxygen ions migrate simultaneously through oxygen vacancies in the lattice of the electrolyte material. Oxygen molecules (O_2) form on the anode surface with the release of electrons: $O_2 - \rightarrow 1/2O_2(g) + 2e-$. The products, hydrogen and oxygen, are separated by the gas-tight electrolyte. Reactions on the two electrodes are summed up as:

$$H_2O_{(g)} \rightarrow H_{2(g)} + \frac{1}{2}O_{2(g)}$$
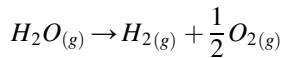
In the previous reaction, theoretical energy demand (ΔH) for water and steam decomposition is the sum of the Gibbs energy (ΔG) and the heat energy ($T\Delta S$). The electrical energy demand, ΔG, decreases with increasing temperature as shown in the figure; the ratio of ΔG to ΔH is about 93% at 100 °C and about 70% at 1000 °C. Thus, the HTE demands less electricity to produce hydrogen than the conventional water electrolysis. This reaction can be expressed as follows:

$$\Delta G = \Delta G_0 + RT ln \left(\frac{a_{H_2} a_{O_2}^{\frac{1}{2}}}{a_{H_2O}} \right)$$

where ΔGo is the standard Gibbs free energy change (per mole) for the reaction 4.1 at a temperature of T, R the gas constant, and aH_2, aO_2, and aH_2O the activities of H_2, O_2, and H_2O in the cell. The Equation can be rewritten using relations of $E = \Delta G/2F$ and $Eo = \Delta Go/2F$ as:

$$E = E_0 + \left(\frac{RT}{2F} \right) \ln \left(\frac{a_{H_2} a_{O_2}^{\frac{1}{2}}}{a_{H_2O}} \right)$$

where F is the Faraday constant and Eo ($= \Delta Go/2F$) the standard electromotive force (EMF) of the following reaction in the quasi-static state:

$$H_{2(g)} + \frac{1}{2}O_{2(g)} \rightarrow H_2O_{(g)}$$
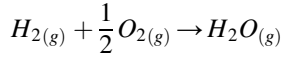
The energy Equation is equivalent to the Nernst equation for EMF of SOFC. Activities of reactants and products can be expressed as partial pressures in the cell because the reaction proceeds in the gas phase regardless of the electrolyte. The applied voltage increases with polarization in the operating cell. The overvoltage, η, is caused mainly by shortage of steam concentration at the cathode (concentration overvoltage) and electrical resistance including electrical leads, interconnections, and others (resistance overvoltage). The energy Equation can be rewritten as:

$$E = E_0 + \left(\frac{RT}{2F}\right) \ln\left(\frac{p_{H_2}p_{O_2}^{\frac{1}{2}}}{p_{H_2O}}\right) + \eta$$

where PH_2, PO_2, and PH_2O are the partial pressures of H_2, O_2, and H_2O, respectively. In the model cell, steam of molar flow rate, fo, and pressure, Po, is reduced to hydrogen gas of flow rate, fo − f, and partial pressure, Po(fo − f)/fo, in the cathode compartment: (fo − f)/fo is a conversion ratio from steam (H_2O) to H_2 (steam conversion ratio). The partial pressure of O_2, PO_2, is assumed to be unity. Using the steam conversion ratio, X = (fo − f)/fo, the previous Equation can be written as follows:

$$E - \eta = E_0 + \left(\frac{RT}{2F}\right) \ln\left\{\frac{X}{1-X}\right\}$$

The value of E − η is called the open-circuit voltage of the cell, which is related to the composition of the product. Note that the steam conversion ratio, X, depends on the open-circuit voltage, and is not affected by the pressure or flow rate of the reactant. Also, the open-circuit voltage decreases with increasing temperature because of the endothermic nature of the reaction. However, due to the temperature dependence of the logarithmic term, this effect decreases with the value of X.

Performance parameters of the electrolysis include the applied voltage, E (V), the applied current, I (A), and the hydrogen production rate, Q (Nl/h) at the reference condition of 0.1 MPa (1 bar) and 273 K (0 °C). The Faraday efficiency, εf, expressed in:

$$\varepsilon_f = \frac{\Delta G}{IE} = \frac{2f(E-\eta)Q}{IE}$$

is the ratio of ΔG to the applied power, I * E, that is, the ratio of the theoretical electric power needed for the electrolysis to the actually applied power of the cell. Thus, the Faraday efficiency is one useful measurement to judge electrolysis performance.

Fig. 3 Applied voltage versus hydrogen production rate
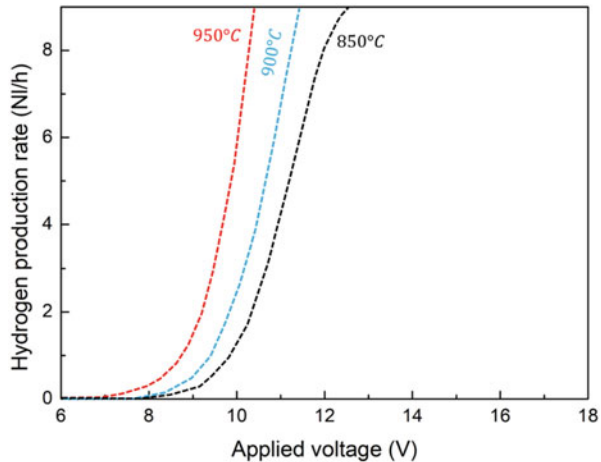
The energy efficiency, εe, is the ratio of the produced hydrogen (H_2) energy and the applied power. Then, the produced H_2 energy is estimated with the combustion heat of produced H_2, by using the lower heating value, ΔH (kJ/mol), provided along the reaction ($H_2(g) + 1/2\ O_2\ (g) \rightarrow H_2O\ (g)$). The energy efficiency is useful for comparing the performances of hydrogen production systems:

$$\varepsilon_e = \frac{\Delta H}{IE}\ \frac{Q}{22.4}$$

where Q/22.4 is the molar rate of produced hydrogen.

Figure 3 shows the relation between the theoretical hydrogen (H_2) production rate and the applied voltage.

H_2 production rate increased with the applied voltage and the electrolysis temperature.

Hundreds of cycles have been studied from the viewpoint of the feasibility of component chemical reactions in terms of conversion ratio or product separation, theoretical thermal efficiency of hydrogen production, etc. Among them, those that utilize thermal decomposition of sulfuric acid, which are categorized as "sulfur cycles," have been considered one of the most promising cycles.

Thermal decomposition of sulfuric acid, proceeds in the following two steps:

$$H_2SO_{4(aq)} = H_2O_{(g)} + SO_{3(g)}\ 300 - 500\,^\circ C$$

$$SO_{3(g)} = SO_{2(g)} + \frac{1}{2}O_{2(g)}\ 800 - 900\,^\circ C$$

$$H_2SO_4 = H_2O + SO_2 + \frac{1}{2}O_2$$
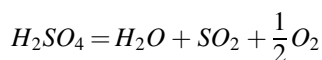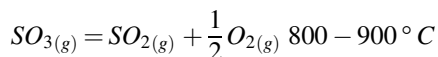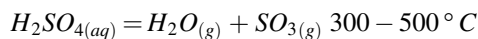
Both steps are highly endothermic and proceed smoothly without side reactions and with a high conversion ratio at the temperature range indicated. The endothermic characteristics match well with the temperature distribution of the heat source— HTGR. The heat of HTGR is transferred to the chemical process through the sensible heat of helium gas, the temperature of which varies from 900 °C to 400 °C. Therefore, the reaction is quite suited as the high-temperature endothermic reaction for the thermochemical water splitting cycle.

IS cycle (or IS process) combines the following chemical reactions with the sulfuric acid decomposition reaction:

$$SO_2 + I_2 + 2H_2O = 2HI + H_2SO_4$$

$$2HI = H_2 + I_2$$
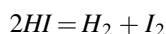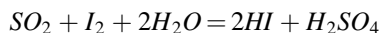
Here, reaction, known as "Bunsen reaction," is the low-temperature exothermic reaction, where the raw material, water, reacts with iodine and gaseous sulfur dioxide producing an aqueous solution of hydriodic acid and sulfuric acid. The acids are then separated and thermally decomposed to produce hydrogen and oxygen. The total reaction scheme is shown in Fig. 4.

There are two main issues concerning the chemistry of the reaction and the separation. One is how to separate the hydriodic acid and sulfuric acid produced by the Bunsen reaction. The other is how to carry out the hydrogen iodide (HI) decomposition section, where the presence of azeotrope in the vapor–liquid equilibrium of the hydriodic acid makes the energy-efficient separation of HI from its aqueous solution difficult, and also, the unfavorable reaction equilibrium limits the attainable conversion ratio of HI to a low level, around 20%.

As for the former problem, the researchers of General Atomic found that the mixed acid solution produced by the Bunsen reaction separates spontaneously into two liquid phases in the presence of excess amount of iodine. The heavier phase is mainly composed of HI, I_2, and H_2O, and is called "HIx" solution. The main components of the lighter phase are H_2SO_4 and H_2O. The phenomenon (liquid– liquid (LL)-phase separation) offered an easy way of separating the hydriodic acid and the sulfuric acid. As for the HI processing, some ideas have been proposed by General Atomic, RWTH Aachen, and JAEA. JAEA studied the utilization of membrane technologies for concentrating the HIx solution to facilitate the HI separation and also for enhancing the one-pass conversion of HI decomposition.

One of the specific and important characteristics of thermochemical water splitting cycles is that the reactants except water are cyclically used in the process. The closed-cycle continuous hydrogen production by the IS process featuring the LL-phase separation has been examined at JAEA. Although the chemistry of sulfuric acid decomposition section and that of hydrogen iodide decomposition section are rather straightforward in terms of reaction and separation, in the Bunsen reaction section, occurrence of side reactions forming sulfur or hydrogen sulfide should be suppressed while maintaining the LL-phase separation. JAEA has devised a basic methodology for the closed-cycle continuous hydrogen production and also for the
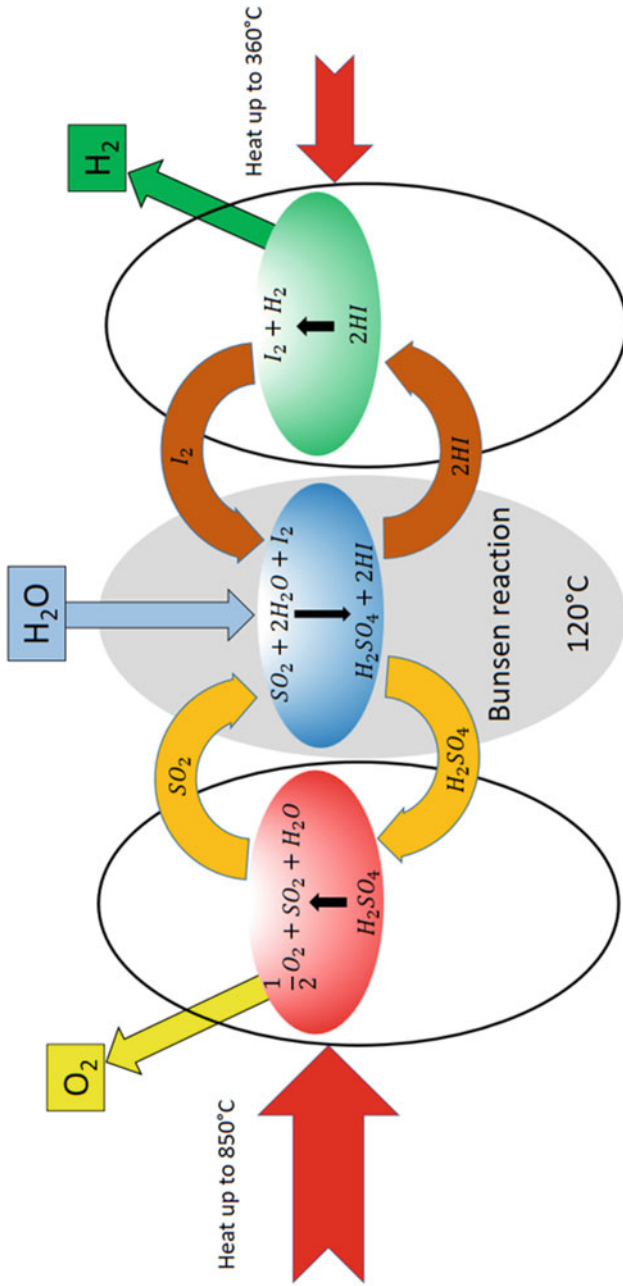
Fig. 4 Sulphur-iodine process schematic

Fig. 5 One week
continuous hydrogen
production with the bench-
scale test apparatus—
relationship between
operation time and integrated
amount of H_2 and O_2
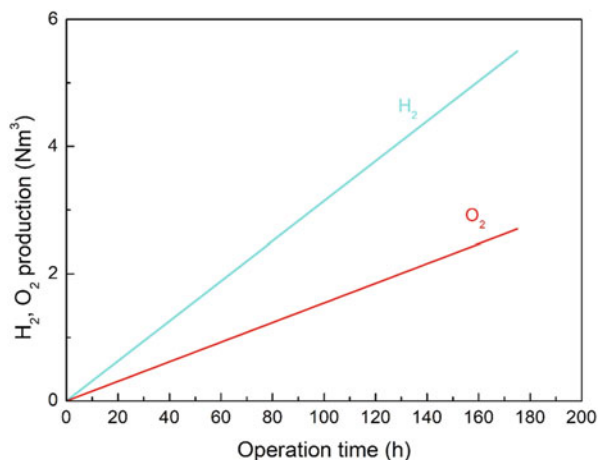
reaction control in the Bunsen reaction step. Feasibility of the methodology was
verified in small-scale continuous hydrogen production experiments of 1 Nl/h (H_2)
in 1997 by using a laboratory-scale experimental apparatus. Continuous hydrogen
production was successfully achieved with a hydrogen production rate of about
31 Nl/h for 1 week. Figure 5 shows the experimental result and the relationship
between the operation time and the integrated amount of H_2 and O_2.

In the experiments, newly developed automatic control system with ultrasonic
detectors, etc. were applied to the control of the Bunsen reaction. These laboratory
and bench-scale tests were carried out under atmospheric pressure (0.1 MPa).

Preliminary flow sheeting studies have been carried out based on the LL-phase
separation for the separation of the Bunsen reaction products. In 1982, General
Atomic published a result of the total flow sheet analysis, where extractive distilla-
tion using phosphoric acid was applied for the hydrogen iodide processing. Assum-
ing intensive heat recovery, a "process thermal efficiency" of 47% was estimated.
Here, the thermal efficiency is defined as the ratio of the higher heating value (HHV)
of hydrogen to the net energy input for the process. Later, a reactive distillation was
proposed by RWTH Aachen for the hydrogen iodide processing, where the separa-
tion of hydrogen iodide from the HIx solution and the decomposition of hydrogen
iodide into hydrogen and iodine were carried out in one column. The concept was
further studied by General Atomic and CEA as well. The reactive distillation is quite
interesting because of its simplicity, although the estimated process thermal effi-
ciency varies from 35 to 50% at present. The application of the membrane systems
for the hydrogen iodide processing proposed by JAEA also gives a similar estima-
tion of the process thermal efficiency. As for the sulfuric acid processing, main
efforts in the flow sheeting study have been on how to recover the heat of concen-
tration. A steam recompression method and a multiple effect evaporator system have
been proposed. The precise thermodynamic data concerning the concentrated pro-
cess solutions is desired for the much more accurate evaluation of the heat/mass
balance.

Fig. 6 Weight loss of base materials in the gas-phase sulfuric acid decomposition environments at 850 °C; (**a**) upstream of catalyst bed and (**b**) downstream of catalyst bed
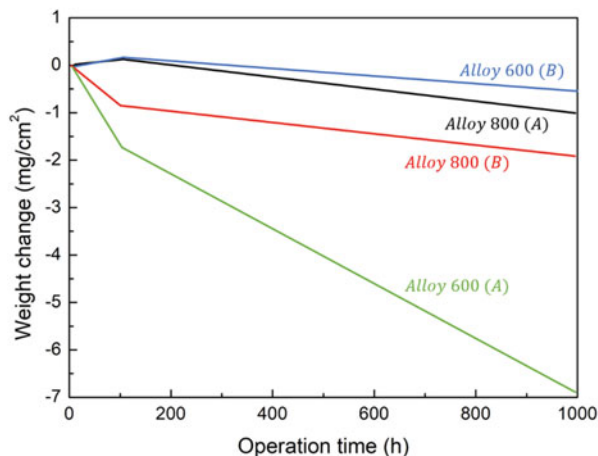
Because sulfuric acid and halogen are very corrosive, selection of the structural materials is an important issue. Screening tests have been carried out using test pieces of commercially available materials at General Atomic, JAEA, etc. As for the gas-phase environment of the H_2SO_4 decomposition step, some refractory alloys that have been used in conventional chemical plants showed good corrosion resistance. Figure 6 shows one of the experimental results of Alloys 800 and − 600 obtained under gas-phase sulfuric acid decomposition environments at 850 °C.

Gas compositions in the upstream and downstream of the catalyst bed are a mixture of H_2O, SO_3, and H_2SO_4, and that of H_2O, SO_2, O_2, SO_3, and H_2SO_4, respectively.

In the gas-phase environment of the HI decomposition step, a Ni–Cr–Mo–Ta alloy was found to show good corrosion resistance under 450 °C. As for the Bunsen reaction step operated at about 100 °C, glass-lining materials, Ta, etc., showed good corrosion resistance. In the environment of the HIx distillation operated at about 230 °C, Ta showed excellent corrosion resistance. The severest environment is the boiling condition of concentrated sulfuric acid under high pressure (e.g., 2 MPa) and temperature up to 400 °C, where ceramic materials containing Si such as Si–SiC, SiC, and Si_3N_4 were the only materials that showed excellent corrosion resistance. For example, SiC has a much better corrosion resistance than the stainless steel.

4.2 Ultra High-Temperature Reactors

The VHTR is well placed to take on the nuclear energy's traditional role of generating electricity. It has many advantages over other types of nuclear reactor, however. The chief advantage is its unique capability of producing a high-temperature heat of about 950 °C, which increases the thermal efficiency of electricity generation to 50% by Brayton cycle from the present 34% in the light water reactor
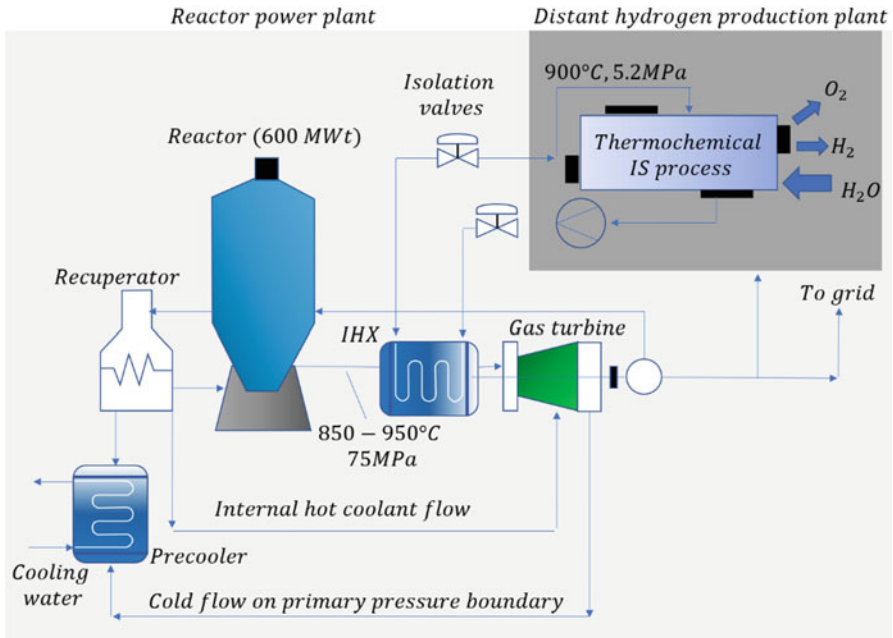
Fig. 7 VHTR-based nuclear electricity and hydrogen generation process

with Rankine cycle and expands the role of nuclear energy to various other fields including mass production of hydrogen to help fuel a sustainable world economical development.

Combination of a VHTR with a recuperated Brayton cycle forms the basic production process. The direct cycle gas turbine generates electricity and circulates the reactor coolant, performing both tasks most efficiently relative to all other forms of process arrangement. Hydrogen cogeneration is enabled by adding an intermediate heat exchanger (IHX) in serial between the reactor and the gas turbine. The particular serial arrangement allows for large logarithmic mean temperature difference (LMTD) between the primary and the secondary fluids, creating a desired condition for a compact IHX. A secondary loop delivers hot helium from the IHX to the hydrogen plant over a sufficient distance that together with the isolation valves located in the secondary loop circuits provides a safe and environ- mental separation between the nuclear plant and the conventional-grade hydrogen plant.

Electricity is generated in a range 45–50% efficiency based on 850 °C and 950 °C reactor coolant temperature, respectively (Fig. 7).

A nominal 170 MWt of the total 600 MWt reactor thermal power is extracted by the IHX as 900 °C process heat supply to the hydrogen process and the balance of reactor thermal power is used for electricity generation at 850 °C gas turbine inlet. A fraction of the 200 MWe electricity generated supplies in-house operations, mainly the hydrogen plant operations, to power electrolyzers, circulators, pumps, and other utilities, while exporting a more significant fraction to grid. The process heat

extracted from the IHX is increased to 371 MWt while electricity is generated at 730 °C gas turbine inlet and 38% efficiency mainly to meet the significant demand of electricity for hydrogen production.

The basic reactor technologies are developed with the test reactor HTTR (Sato et al. 2016). The fuel is in the form of tri-isotropic (TRISO) ceramic-coated particles containing low-enriched UO_2 kernels. The particles secure containment for fission products at 1600 °C or higher. The particles are dispersed in a graphite matrix and then sintered to form a fuel compact. A number of fuel compacts are encaged in a fuel rod for insertion into the graphite fuel block. Helium coolant flows in the annular space provided around the outer surface of a fuel rod. The HTTR's cylindrical active core, measuring 2.9 m in height and 2.3 m in diameter, contains 30 fuel columns, each comprising a stack of five fuel blocks high, and additional seven control rod guide columns. Dowels and mating sockets provided on the fuel block secure vertical alignment of a column. The active core is enclosed by replaceable reflector graphite blocks, which are laterally tightened by a graphite block–lined core restraint mechanism. The core structure is contained in a steel reactor pressure vessel.

The coolant is ducted into and away from the reactor by a concentric double pipe. The HTTR has demonstrated inherent and passive reactor safety.

An annular active core instead of the cylindrical one is required to raise reactor power without exceeding the limit of 1600 °C for fuel during passive conduction cool down in accidents. Fuel burnup is extended to 120 GW day/t from the HTTR's maximum 33 GW day/t mainly by resizing kernel buffer and coating layers. R&D have, thus, been made to extend the technical base for higher burnup fuel. More work is being done in this area. Carbon–carbon composites are being developed to replace the existing alloy cladding of control rods to improve the high-temperature structural integrity.

Helium gas turbine of high aerodynamic efficiency, reliability, and serviceability is required to qualify for nuclear service. The development of a helium gas turbine to meet these goals presents technical challenges, the extent of which depends heavily on design choices to be made.

The baseline design is a single-shaft unit consisting of 6 turbine stages and 20 compressor stages without compressor intercooling. Rated at 300 MWe and 3600 rpm, it drives a synchronous generator from the shaft cold end. The unit is horizontally installed to minimize bearing loads. These design features are aligned with established practice in industrial gas turbines. The design elements unique to the present application include the narrow compressor flowpath, which is the result of working in helium, and the magnetic bearings used to avoid large high-power shaft penetration to the primary pressure boundary or possibility of bearing lubricant contamination to reactor.

Different choices for gas turbines are made by other designers based on specific project requirements. Relative features of the major systems were compared. The gas turbine-modular helium reactor (GT-MHR) selects a bold vertical, asynchronous unit to facilitate a tight plant arrangement and compressor intercooling. The PBMR changes to a new single-shaft and horizontal unit using oil bearings from its earlier choice of a multi-shaft and vertical installation. The global nuclear industry supplier

AREVA-NP prefers an indirect combined cycle of gas and steam turbines using a mixed nitrogen–helium gas to relate to more familiar air gas turbine conditions.

The IHX is a barrier of reactor pressure boundary. A proven nuclear design is the helical tube and shell heat exchanger for services at 950 °C and 4.0 MPa in the HTTR.

Tubing is made of Hastelloy-XR, a corrosion and heat-resistant superalloy. New promising designs have been proposed such as the one under an extensive industrial study on plate IHX to develop fabrication, ISI methods and a design standard for gas reactors, and another plate-type design for the indirect cycle reactor plant. These works demonstrate that a plate IHX would simplify integration in the primary system because of its drastically reduced size.

An available HTE-based plant can be connected to the reactor in the same manner as the IS process plant is connected. The HTE similarly requires a high-temperature process heat, and about 25% of its total energy input is heat and the balance electricity, which are fully and efficiently met in-house by the reactor heat and gas turbine power plant.

Hydrogen plant and gas turbine generator are each a partial load of the nuclear reactor during normal cogeneration operations. Transient or upset conditions in one system may disturb or interrupt the operations of the other system or the reactor.

High-temperature gas isolation valves are safety components located in the secondary gas loop. They protect the IHX from chemicals released from any failed hydrogen plant equipment and act as nuclear reactor confinement barriers to prevent radioactive releases from accidental rupture of the IHX tubing.

5 Conclusions

Nuclear energy can produce hydrogen in several ways: (1) nuclear heated steam reforming of natural gas, (2) electrolysis of water using nuclear power, (3) HTE using minor heat and major electricity from nuclear reactor, and (4) thermochemical splitting of water using major heat and minor electricity from the nuclear reactor. The existing light water reactor is only applicable to electrolysis of water and at <30% efficiency.

The GIF identified six nuclear reactor systems for future development that can be licensed, constructed, and operated to provide economical and reliable energy products while satisfactorily addressing nuclear safety, waste, proliferation, and public acceptance. Of the six technologies, the VHTR is uniquely suited for both electricity and hydrogen production and doing so at the highest potential efficiency of about 50%. It is also considered the nearest-term deployable reactor. Because of these important attributes the U.S. Department of Energy has chosen it to demonstrate the Next Generation Nuclear Plant (NGNP) including nuclear-heated hydrogen cogeneration.

References

AlZahrani AA, Dincer I (2018) Modeling and performance optimization of a solid oxide electrolysis system for hydrogen production. Appl Energy 225:471–485. https://doi.org/10.1016/j.apenergy.2018.04.124

Bolfo L, Devia F, Lomonaco G (2021) Nuclear hydrogen production: modeling and preliminary optimization of a helical tube heat exchanger. Energies 14(11):3113. https://doi.org/10.3390/en14113113

Corgnale C, Gorensek MB, Summers WA (2020) Review of sulfuric acid decomposition processes for sulfur-based thermochemical hydrogen production cycles. PRO 8(11):1383. https://doi.org/10.3390/pr8111383

El-Emam RS, Ozcan H, Zamfirescu C (2020) Updates on promising thermochemical cycles for clean hydrogen production using nuclear energy. J Clean Prod 262:121424. https://doi.org/10.1016/j.jclepro.2020.121424

Gao Q, Wang L, Peng W et al (2022a) Safety analysis of leakage in a nuclear hydrogen production system. Int J Hydrog Energy 47(7):4916–4931. https://doi.org/10.1016/j.ijhydene.2021.11.099

Gao Q, Qu X, Peng W et al (2022b) Influence of obstacle morphology on safety of nuclear hydrogen production system. Int J Hydrog Energy 47(86):36733–36748. https://doi.org/10.1016/j.ijhydene.2022.08.235

Khan SUD (2019) Using next generation nuclear power reactors for development of a techno-economic model for hydrogen production. Int J Energy Res 43(13):6827–6839. https://doi.org/10.1002/er.4683

Kim Y, Kim J-H, Yoo S-H (2022a) South Koreans' acceptance of hydrogen production using nuclear energy. Int J Energy Res 46(4):5350–5361. https://doi.org/10.1002/er.7465

Kim J, El-Hameed AA, Soja RJ et al (2022b) Estimation of the levelized cost of nuclear hydrogen production from light water reactors in the United States. PRO 10(8):1620. https://doi.org/10.3390/pr10081620

Lee JM, Lee S-I, Kye DH et al (2022) Environ-economic analysis of high-temperature steam electrolysis for decentralized hydrogen production. Energy Conv Manag 266:115856. https://doi.org/10.1016/j.enconman.2022.115856

Milewski J, Kupecki J, Szczęśniak A et al (2021) Hydrogen production in solid oxide electrolyzers coupled with nuclear reactors. Int J Hydrog Energy 46(72):35765–35776. https://doi.org/10.1016/j.ijhydene.2020.11.217

Nadaleti WC, Gomes de Souza E, Melegari de Sousa SN (2022) The potential of hydrogen production from high and low-temperature electrolysis methods using solar and nuclear energy sources: the transition to a hydrogen economy in Brazil. Int J Hydrog Energy 47(82):34727–34738. https://doi.org/10.1016/j.ijhydene.2022.08.065

Norouzi N, Talebi S, Fani M et al (2021) Exergy and exergoeconomic analysis of hydrogen and power cogeneration using an HTR plant. Nuclear Eng Technol 53(8):2753–2760. https://doi.org/10.1016/j.net.2021.02.027

Sahin S, Sahin HM (2021) Generation-IV reactors and nuclear hydrogen production. Int J Hydrog Energy 46(57):28936–28948. https://doi.org/10.1016/j.ijhydene.2020.12.182

Sato H, Yan XL, Sumita J (2016) HTTR demonstration program for nuclear cogeneration of hydrogen and electricity. J Nuclear Eng Rad Sci 2(3):031010. https://doi.org/10.1115/1.4032480

Sorgulu F, Dincer I (2018) Cost evaluation of two potential nuclear power plants for hydrogen production. Int J Hydrog Energy 43(23):10522–10529. https://doi.org/10.1016/j.ijhydene.2017.10.165

Hydrogen Separation and Purification

1 Introduction

Realization of the vision of "hydrogen economy" and utilization of hydrogen as an energy carrier will require increasing the hydrogen production by more than an order of magnitude over the current production levels. About 42 million t of hydrogen is currently produced per year worldwide. Most of the hydrogen is used captively on-site in "nonenergy" uses for the production of ammonia, methanol, and other chemicals and for hydroprocessing in petroleum refineries primarily to remove sulfur and upgrade the heavier fractions into more valuable products (Huang et al. 2023). The hydrogen production in the United States is estimated to be about 9 million t/year, 7.5 million of which are consumed on-site. The remaining 1.5 million t/year of hydrogen production may be considered as transportable and available for other applications.

The demand for hydrogen will escalate even more if hydrogen is used as an energy carrier for power generation applications, for example, portable or distributed power. Central as well as distributed hydrogen generation plants will probably be necessary to meet the projected hydrogen demand. For successful transition to hydrogen economy, hydrogen must also be affordable.

Currently, a large number of hydrogen generation plants are located at captive utilization sites, for example, in ammonia and methanol plants to produce an appropriate synthesis gas mixture, and in refineries to generate hydrogen needed for hydrotreating or hydrocracking operations. A large fraction of these hydrogen plants are designed to pro- duce synthesis gas rather than pure hydrogen with a H_2:CO ratio in the synthesis gas suitable for the intended product, for example, for methanol production, a H_2:CO ratio of 2:1 is desirable, whereas for ammonia production, partial oxidation (POX) of hydrocarbon fuels with air is used to produce the N_2:H_2 ratio of 3:1 with no CO (Ishaq and Crawford 2023). Hydrogen separation and purification requirements in the existing plants depend on the intended use of hydrogen, for example, for ammonia production it is customary to convert almost all

of the CO to hydrogen using low-temperature water–gas shift (WGS) reaction followed by CO_2 scrubbing and final methanation step to convert residual CO and CO_2 to methane, whereas CO_2 removal may not even be necessary for the utilization of synthesis gas for producing methanol or liquid fuels.

Increasing the utilization of hydrogen as an energy carrier in transportation and distributed power generation applications based on proton exchange membrane (PEM) fuel cells will create a demand for plants that produce high-purity hydrogen as the primary product (Wang et al. 2022).

In hydrogen generation processes based on natural gas and liquid hydrocarbon fuels, the feedstock is first desulfurized by hydrodesulfurization and H_2S removal to reduce the sulfur levels to below 2 ppm to protect catalysts used in the downstream reforming process (Poser et al. 2023). After desulfurization, SMR is carried out at 800–900 °C temperature and 25–35 atm pressure using an alkali promoted Ni-based catalyst supported on alumina. SMR is a highly endothermic process and heat is supplied by the combustion of a part of the fuel. In some cases, especially when using heavier hydrocarbon feedstocks, a prereformer is used upstream of the primary reformer to first convert the heavy hydrocarbons to methane. A prereformer typically operates at a lower temperature of 400–500 °C and may also convert some of the methane to CO and H_2. SMR produces a synthesis gas constituting primarily hydrogen, carbon monoxide, carbon dioxide, and unreacted methane (Salahi et al. 2023). Alternatively, oxygen or air may be used in addition to steam in POX or ATR processes, which combine heat generation by fuel combustion with the steam reforming process. Typical hydrogen production plants use SMR process, whereas syngas production plants use either ATR or POX, for example, methanol and ammonia plants tend to use ATR.

Solid fuels such as coal and biomass are gasified again using steam, oxygen, or air. A variety of commercial designs are available for the gasification process. The synthesis gas generated by coal or biomass contains much higher $CO:H_2$ ratio due to greater carbon content in the feedstock. The synthesis gas produced by gasification is then cleaned to remove particulates, H_2S, ammonia, HCl, and any other contaminants that may be present depending on the raw material used (e.g., tar when using certain biomass materials) in the gasification process.

The hydrogen content of the synthesis gas produced by using any of the feedstock is further increased by WGS reaction, in which steam reacts with carbon monoxide to produce additional hydrogen and carbon dioxide. Hydrogen is then separated from other gas-phase constituents, primarily carbon dioxide. The separated hydrogen may need to be purified further to meet the requirements of the specific intended application. The level of hydrogen purification depends strongly on the mode of hydrogen utilization, for example, to use in a PEM fuel cell much greater purity hydrogen will be required than for its utilization in a solid oxide fuel cell (SOFC) or in a gas turbine for power generation (Pashchenko 2023).

Hydrogen generation processes based on water electrolysis using electricity generated from renewable solar or wind energy will produce relatively much purer hydrogen with only water vapor as a diluent. Very little hydrogen purification will be needed for such hydrogen generation approaches. This chapter will, therefore, focus

on synthesis gas-based hydrogen generation processes and the pertinent hydrogen separation and purification approaches (Singla et al. 2022).

All processes using carbonaceous feedstocks, including hydrocarbon fuels and biomass to generate pure hydrogen will involve a suitable combination of processes to produce synthesis gas followed by WGS reaction. Subsequent hydrogen separation and purification options will, thus, be similar to all carbonaceous feedstock-based hydrogen production.

2 Hydrogen Separation and Purification

Four technologies have been most commonly used for separating hydrogen, carbon dioxide, and carbon monoxide from synthesis gas:

1. Adsorption of gas species other than hydrogen, which produces pure hydrogen as a product;
2. Absorption (physical or chemical) of CO_2, which produces pure carbon dioxide as a product;
3. Polymeric membranes, which offer bulk separation of hydrogen;
4. Cryogenic separation, which can provide multiple pure products and is especially used for separation of pure carbon monoxide.

Absorption of CO_2 in suitable solvents followed by methanation of residual CO and CO_2 was the technology of choice before 1980 for producing pure hydrogen as a product. For plants built after 1980, pressure swing adsorption (PSA) has been the most commonly used technology for producing high-purity hydrogen as a product by SMR (Wang et al. 2023). Retrofit PSA separation has also replaced CO_2 scrubbing systems in a number of existing installations for hydrogen production. Scrubbing of CO_2 is still primarily used in producing N_2–H_2 synthesis gas for ammonia production and a number of solvents are available for CO_2 absorption, both physical and chemical. Amine absorption processes also remove sulfur compounds that may be present in the synthesis gas. Membrane separation is a relatively new technology for separating hydrogen (Lee et al. 2020). The prism membrane was introduced for hydrogen recovery in 1979 by Monsanto (now available from Air Products and Chemicals, Inc.). Hydrogen separation membranes have also been introduced by several other companies, for example, PolySep by UOP, Inc., and are commonly used for recovering hydrogen from a variety of waste streams containing a high content of hydrogen in refinery and chemical processing operations. Polymeric membrane processes do not produce high-purity hydrogen in a single stage, and multiple stages with a low overall hydrogen recovery are necessary to produce a high-purity hydrogen product (Kim et al. 2021). Polymeric membranes are, however, used for bulk separation of hydrogen and may be combined with another process, for example PSA, in a hybrid configuration for high-purity hydrogen production. Cryogenic separation processes are now largely replaced by PSA systems and are only used for specialized applications to produce multiple pure products, for example, CO (Amin et al. 2023).

The overall processes utilizing SMR with PSA, CO_2 absorption, and membrane-based hydrogen separation systems are shown schematically in Figs. 1, 2, and 3, respectively.

The choice of applicable hydrogen separation technology often depends on the hydrocarbon feedstock used and the resulting synthesis gas composition. PSA has been dominant for hydrogen production plants utilizing natural gas as the feedstock,
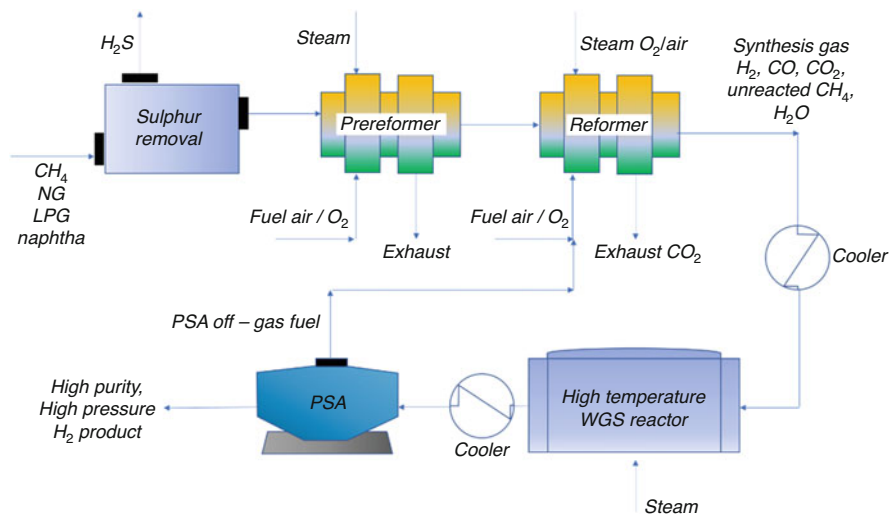
Fig. 1 Steam methane reforming with PSA for hydrogen production
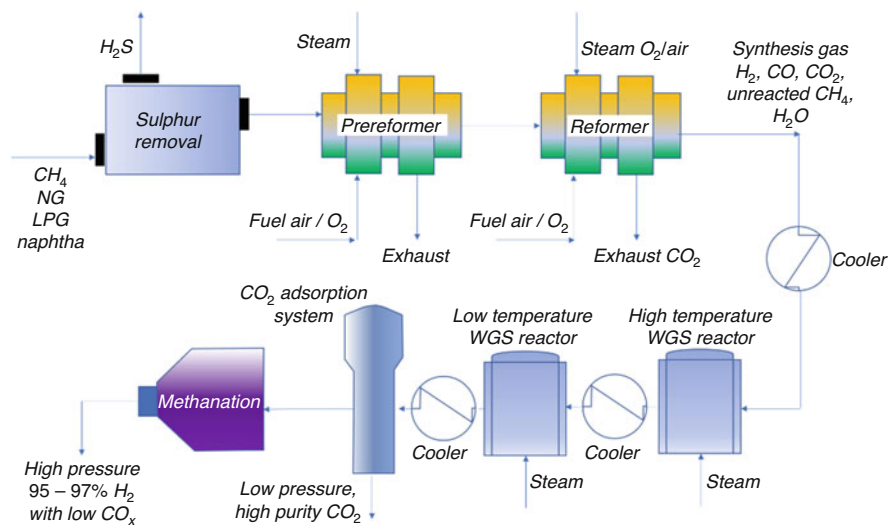
Fig. 2 Steam methane reforming with CO_2 absorption for hydrogen production
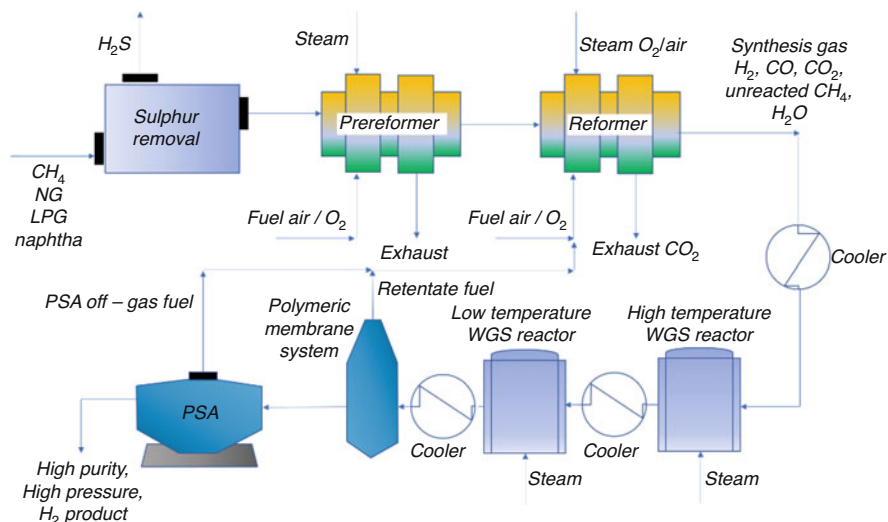
Fig. 3 Steam methane reforming with polymeric membrane for hydrogen production

which is currently often the best option based on the least cost and availability. The synthesis gas produced by SMR contains a high concentration of hydrogen making the economics favorable to a PSA system. For feedstocks containing high carbon to hydrogen ratio, for example, heavy hydrocarbon fuels and coal, other hydrogen separation systems such as CO_2 absorption–based systems or bulk membrane separation systems may become attractive either as stand alone or in hybrid configuration combining two or more approaches. The current emphasis on global climate control will also have a strong impact on the selection of hydrogen separation approaches; hydrogen separation processes that can also capture the CO_2 in a pure form suitable for sequestration are, therefore, likely to become attractive in the new generation of pure hydrogen plants.

Although, in large-scale hydrogen plants, the cost of producing hydrogen is dominated by the cost of feedstock (most often natural gas) used and the cost of fuel used to supply heat for the reforming reaction, the hydrogen separation and purification equipment contributes at least 50%, and sometimes up to 80%, of the capital investment costs. Thus, hydrogen separation and purification component will contribute significantly to the depreciation and investment costs in plant operation. The total in-plant energy consumed in the SMR process for hydrogen production is estimated at about 56,200 Btu/lb of H_2 produced with energy used for separation process accounting for about 12,400 Btu/lb of H_2 produced. The hydrogen separation and purification process, thus, contributes significantly to the operating costs of hydrogen production.

Reducing the energy requirement for the separation and purification of hydrogen and the separation equipment cost will significantly reduce the cost of producing hydrogen. Substantial research efforts are, therefore, underway to investigate new

concepts for hydrogen separation as well as to improve existing proven processes especially PSA.

Since 1980, PSA systems have largely replaced the CO_2 removal systems based on amine absorption followed by methanation as well as cryogenic separation systems as the technology of choice in new plants for producing hydrogen. PSA systems have also replaced CO_2 absorption systems in existing plants producing hydrogen. Advantages of PSA systems over the amine absorption system include lower equipment cost, simpler operation, less operational maintenance, and ability to deliver a high-purity hydrogen product. As seen in Fig. 1, in a PSA-based process, the LTS reactor is generally eliminated along with the final methanation step for hydrogen purification. The PSA system is installed following the HTS reactor and gas cooler in the conventional SMR hydrogen production process. Although PSA systems produce a high-purity hydrogen product, the hydrogen recovery is correspondingly low. The waste residual PSA off-gas, however, has significant fuel value since it contains unreacted methane, unrecovered H_2, as well as unreacted CO remaining after the HTS reactor. The tail gas is, therefore, burned in the reformer to meet almost all heat requirements for the hydrocarbon fuel reforming process.

The PSA units are extensively used not only for hydrogen production by SMR but for hydrogen recovery from a variety of hydrogen-rich off-gas streams containing a wide range of impurities. PSA is well suited for hydrogen separation from hydrogen-rich gas streams since hydrogen is hardly adsorbed on most adsorbents. Thus, high-purity hydrogen may be recovered using almost any adsorbent. For various applications, adsorbents are selected based on the species other than hydrogen that are present in the gas stream for their efficient removal from hydrogen (Kim et al. 2022). The PSA process for hydrogen purification was first commercialized by UOP in 1966. Since then, over 530 units have been installed worldwide, 40% of which were installed for hydrogen production by SMR. Because a PSA process for hydrogen separation adsorbs all gas species except hydrogen, PSA hydrogen separation is attractive when the feed gas contains a high concentration of hydrogen. With a dilute hydrogen stream, PSA may still be effectively used in a hybrid process configuration by employing another process for hydrogen enrichment, for example, CO_2 absorption, to produce a hydrogen-rich high-pressure feed gas for the PSA system.

Solid adsorbents, for example, molecular sieves, 5A zeolite, activated carbon, alumina, and silica gel, adsorb more adsorbates at a higher gas partial pressure than at a lower partial pressure. In addition, some of the compounds are adsorbed more strongly than others allowing the separation of strongly adsorbed compounds from the weakly adsorbed compounds when their mixture is passed over a fixed adsorbent bed. Hydrogen essentially is not adsorbed by the adsorbents used in the PSA process for hydrogen purification. In principle, for purification of hydrogen from SMR product gas, for example, all other gas species besides hydrogen (i.e., CO, CO_2, CH_4, and H_2O) are adsorbed at a high pressure producing high-purity hydrogen product. Using sufficient quantity of the adsorbent material and by regulating gas flow rate and adsorption cycle time, very high purity of hydrogen can be achieved (Omoniyi et al. 2021). After saturation of the fixed bed by the contaminants, the

Vessel
no.

1	Adsorption		E	PD		BD	P		R	
2	R		Adsorption			E	PD		BD	P
3	BD	P	R			Adsorption			E	PD
4	E	PD	BD	P		R			Adsorption	

Cycle time ⟶

E = Equalization and cocurrent depressurization
PD = Purge and cocurrent depressurization
BD = Blowdown and cocurrent depressurization
P = Purge
R = Repressurization
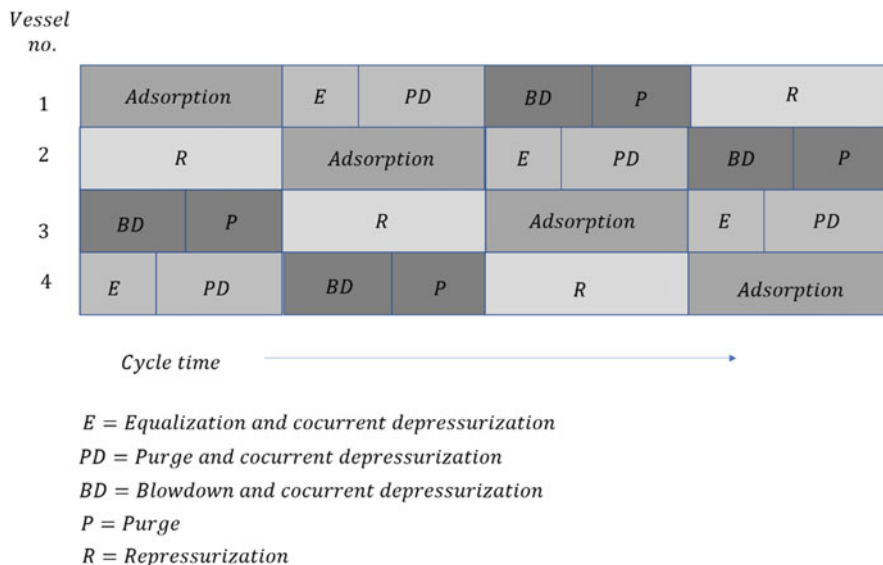
Fig. 4 Pressure swing adsorption cycle sequence for a four-bed system

adsorbent bed is regenerated by removing the contaminants by lowering the pressure (pressure swing) in the bed. The contaminants may also be removed by increasing the temperature of the bed at constant pressure in a thermal swing adsorption (TSA) process; however, the cycle times for TSA are typically much longer due to slow heat transfer to/from a solid bed. Thus, PSA systems are preferred over TSA for hydrogen separation applications.

Although PSA is a batchwise process, by using multiple beds in a sequential manner the overall process is operated in a continuous fashion. Each bed may contain layers of different adsorbent materials selective for specific contaminants in the hydrogen gas stream to be purified. Each bed undergoes a sequence of four basic steps in a PSA cycle: adsorption, depressurization, purge at low pressure, and repressurization. This sequence of cyclic operations for each bed is shown schematically for a four-bed PSA process in Fig. 4.

The feed gas is introduced at the high adsorption pressure in the adsorption step, impurities are adsorbed on the internal surfaces of the adsorbent leaving high-purity hydrogen product gas in the void spaces of the vessel, and high-purity hydrogen is withdrawn continuously as product from the top of the vessel under pressure. The gas flow is normally in the upward direction. When the adsorber bed reaches its adsorption capacity, it is taken off-line and the feed is automatically switched to another fresh adsorber bed.

The pressure in the saturated adsorber is then reduced and the product gas remaining in the void spaces of the vessel is first recovered in a concurrent depressurization, that is, gas is withdrawn in the same direction as that of feed gas flow in

the adsorption cycle. The recovered intermediate product gas stream is used internally for purging and repressurization. The adsorbed impurities are then removed in a countercurrent depressurization step (i.e., the gas is withdrawn in the opposite direction as that of the feed gas flow in the adsorption cycle) as a PSA off-gas. The adsorber vessel is then purged with a small amount of high-purity product gas withdrawn during the concurrent depressurization step to complete the regeneration of the adsorbent bed. Finally, the vessel is repressurized with a part of the product gas and the high-purity hydrogen stream from the concurrent depressurization.

Because each of the cyclic process step is a batch process, at least four beds are needed undergoing the cyclic steps described earlier in a sequential manner to provide a nearly continuous product gas flow. In addition, large surge tanks are used to dampen variations in flows of feed, product, and exhaust streams. To improve product gas yields, more complex PSA cycles can be used with a greater number of adsorbent beds. A polybed PSA process was commercialized by UOP in 1976 with the utilization of up to 12 beds. Increased number of beds leads to shorter cycle time, increased hydrogen recovery and greater hydrogen capacity per unit adsorbent weight, and more operational flexibility. The optimal number of beds is determined by a trade-off with greater product gas yield and recovery efficiency and higher capital cost for additional beds with additional flow switching equipment. To switch gas flows between beds during a typical cycle, a complex network of valves is used along with associated instrumentation, control systems, and process piping. The valves are actuated by solenoids using a logic controller. As the number of beds increase, the number of mechanically operated valves increases significantly. For example, for an eight-bed hydrogen PSA process, 42 valves are needed. The network of valves adds complexity and cost to the PSA system. In addition, the valves and piping also add dead volume to the overall PSA system reducing product yield and process efficiency. The optimal selection of the number of beds is determined by the required hydrogen capacity and percentage recovery. For small capacity systems of <5000 Nm^3/h, four beds are normally used, whereas more than eight beds may be used for capacities exceeding 50,000 Nm^3/h.

Hydrogen PSA units typically operate with a feed gas pressure in the 200–700 psig range and are operated at a pressure slightly greater than the desired hydrogen delivery pressure. The normal operating temperature range is 100–150 °F. Typical hydrogen purity ranges from 99.5% to 99.9999%, depending on the hydrogen recovery. The required hydrogen product purity also has a minor impact on the hydrogen recovery achievable and the amount of adsorbent needed for a given capacity. Hydrogen recovery defined as the ratio of the amount of hydrogen in the product to hydrogen in the feed is not very sensitive to feed gas pressure but is very sensitive to the purge gas pressure. The purge gas pressure is set to be sufficient for feeding the off-gas to the reformer burner directly. With a feed gas pressure of 400–500 psig and purge gas pressure of 5 psig, the hydrogen recovery will be in the 80–90% range. Increasing the purge gas pressure to 50 psig, for example, will reduce the recovery to 65%. The optimum feed gas pressure for maximum hydrogen recovery is typically 300 psig.

Despite PSA's widespread use for hydrogen as well as other separation applications, utilization of beaded sorbent materials and mechanical switching valves do introduce certain limitations. The maximum gas flow through the adsorbent bed is limited by the fluidization velocity for the adsorbent beads used. Increasing the bead size will allow greater flow velocity but will also result in a greater mass transfer resistance for the adsorption process. An optimal adsorbent bead size must be selected to match the throughput rate with the rate of removal of impurities from the hydrogen gas stream. Although the PSA process is simple in operation, the numerous switching valves needed for its operation are the most complicated part of the system and is also the most vulnerable to mechanical failure.

Although the basic principle of PSA operation is simple, there are a number of operational variables due to large number of beds and sequencing steps, and a number of operational improvements have been reported to reduce the cycle time and increase hydrogen throughput capacity per unit of adsorbent weight. For example, by extending the duration of the purge step, the production capacity of a PSA unit was increased exceeding $110 \, Nm^3/h$ with 16 beds. Using storage tanks to collect high-purity hydrogen and reusing it as purge gas during cycle steps was found to increase hydrogen capacity and decrease the number of PSA beds required. Cycle time was also found to be reduced by manipulating pressure equalization steps. Performance of a PSA process and hydrogen throughput may be improved by reducing the cycle time, made possible by process innovation for handling gas flows. Improvements in a PSA system are also sought by modeling and simulation for the optimization of various process parameters.

Using three-dimensionally structured adsorbent with a large number of uniform gas channels, the limitations of mass transfer kinetics and fluidization of the conventional beaded sorbents may be removed. Such structured adsorbents have been described in recent patents. A novel rotary valve design with rotating beds instead of switching valves has been shown to increase the cycle speeds by an order of magnitude to 100 cycles/min. Both of these improvements have been incorporated in a "rapid cycle PSA" claimed to reduce the size of conventional PSA by a factor of 50 and the cost by a factor of 2.

Although PSA systems have largely replaced hydrogen separation based on CO_2 absorption in the SMR process, PSA systems are not well suited for capturing the CO_2 as may be mandated by the need to control greenhouse gas emissions (primarily CO_2) for stemming global warming. As seen in the process schematic for PSA-based hydrogen production of Fig. 1, all of the carbon initially present in the feedstock used for hydrogen generation is accumulated in the PSA off-gas, which is burned for its fuel value to provide heat in the reformer. If carbon capture is desired in processes for hydrogen generation using carbonaceous feedstocks, CO_2 absorption–based systems would be attractive since they allow the production of pure hydrogen and pure CO_2 product streams. For CO_2 absorption–based bulk hydrogen separation systems, a final PSA-based hydrogen purification may be used for utilizing the product hydrogen stream in applications requiring stringent hydrogen product specification (e.g., power generation by PEM fuel cells). The size of such polishing units will, however, be much smaller than the conventional PSA units for bulk

contaminant removal. Methanation process is commonly used to convert any CO or CO_2 present in the product hydrogen leaving CO_2 absorption process to methane, which is often a benign diluent, for example, in ammonia synthesis or for a PEM fuel cell. A PSA polishing bed may be preferred if any other trace contaminants are present in the product gas, for example, sulfur compounds. CO_2 absorption–based systems are currently used for hydrogen and N_2/H_2 synthesis gas generation in ammonia plants, and the technology is considered mature due to its widespread use in pre-1980 hydrogen plants.

Because sulfur present in the carbonaceous feedstocks, including natural gas, is usually removed before their reforming, the hydrogen separation from the product gas primarily needs to focus on CO_2 removal rather than CO_2 and H_2S removal. Liquid sorbents that have been commercially used for CO_2 removal include ethanol amine solutions, ammonia solutions, potassium carbonate solutions, methanol, and water. As seen in Fig. 2 process schematic, CO_2 absorption is preceded by both HTS and LTS to convert almost all of the CO in the synthesis gas to hydrogen and CO_2. A liquid sorbent chosen to remove CO_2 from the product gas after LTS should:

- be highly selective for absorbing CO_2 relative to H_2, CH_4, and CO;
- have a low vapor pressure, which will minimize absorbent losses in the regeneration step;
- not be irreversibly poisoned by other contaminants in the gas stream, for example, COS and HCN;
- be readily regenerated by steam stripping;
- be non-corrosive to mild steel;
- be inexpensive.

The processes use either the chemical interaction between CO_2 and the absorbent (e.g., amine, alkali metal hydroxide or carbonate) or the physical solubility of CO_2 in the absorbent (e.g., methanol and polyethylene glycol). In either case, CO_2 is removed from the gas stream into the sorbent at a lower temperature or higher pressure and is released later at a higher temperature or lower pressure regenerating the sorbent. Although absorption by chemical interaction is more efficient, the process typically requires greater energy for regeneration compared to physical solvents. Thermal regeneration of chemical absorbents may also lead to degradation over a number of cycles due to irreversible reactions with contaminants, for example, sulfur compounds. Physical solvents can also degrade over time and are usually more volatile leading to losses due to evaporation. Therefore, physical solvents, for example, methanol, are typically used at lower temperatures than the amine-based systems and are regenerated by depressurizing and heating.

Absorbents based on a variety of amines are by far the most common. Amines that have been used include monoethanolamine (MEAs), diethanolamine (DEA), triethanolamine (TEA), diisopropanolamine (DIPA), methyl diethanolamine (MDEA), and diglycolamine (DGA). CO_2 is typically absorbed at 80–140 °F temperature and up to 1000 psig pressure by chemically reacting with the basic amine functional group in the absorbent (Kucharska et al. 2018), for example, primary amine, MEA, reacts with CO_2 by the following reaction forming a carbamate salt:

$$2HOC_2H_4NH_2 + CO_2 \leftrightarrow HOC_2H_4NHCOO^- + NH_3C_2H_4OH^+$$
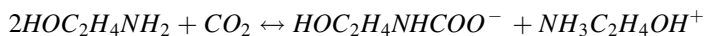
All amines are relatively weak bases, which react with CO_2, H_2S, and COS forming bonds that can easily be broken at elevated temperatures. Primary amines are chemically stronger than secondary, which in turn are stronger than tertiary. Weaker amines have greater selectivity for H_2S, which is especially high for tertiary amines where the nitrogen atom does not have a free hydrogen association to form the carbamate ion by direct reaction with CO_2. CO_2 reacts with secondary amine by forming carbamate ion similar to the reaction with primary amine:

$$2R_2NH + CO_2 \leftrightarrow R_2NCOO^- + H_2NR_2^+$$
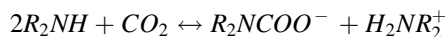
However, reaction of CO_2 with a tertiary amine results in the formation of bicarbonates:

$$R_3N + CO_2 + H_2O \leftrightarrow HCO_3^- + HNR_3^+$$
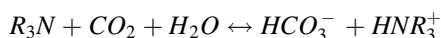
The product salts formed by reactions are thermally unstable and decompose at higher temperatures releasing CO_2 and regenerating the MEA absorbent. The amine regeneration is typically conducted at about 240 °F and at low pressure of 10–15 psig.

Compared to the PSA process, amine-based hydrogen separation encounters more operational issues and are generally more expensive to operate. Some of the disadvantages of the amine-based processes include:

- severe corrosion problems especially with high CO_2 concentration in the feed gas;
- ethanolamines are relatively expensive;
- significant loss of absorbent due to vaporization and irreversible reactions ions of amine with stronger acids such as thiocyanate (SCN–) that may be present in the gas being treated produce irreversible degradation products, which are thermally stable. Degradation products are also formed by the reaction among amines themselves. MEA is currently the most widely used solvent for CO_2 capture and can achieve CO_2 recovery rates of 98% with product purity in excess of 99%. However, absorption processes based on activated MDEA are increasingly used due to higher CO_2 absorption capacity and biodegradability of solvent. BASF (aMDEA), Dow chemical company (UCAR- SOL series), INEOS (Gas/Spec CS 2000), and Shell (ADIP-X), for example, offer commercial accelerated MDEA processes for CO_2 separation from synthesis gas in ammonia plants.

Another successful CO_2 absorbent utilizing chemical interaction has been potassium carbonate used in the "hot carbonate process." The CO_2 absorption and absorbent regeneration occur at about the same temperature of 225 °F in this process. CO_2 absorption occurs at high pressure and the sorbent regeneration occurs due to lowering of pressure with steam stripping. The absorption/regeneration reactions are represented as:

$$K_2CO_3 + CO_2 + H_2O \leftrightarrow 2KHCO_3$$
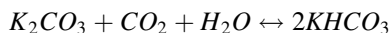
Different variations of the hot carbonate process exist (e.g., Catacarb and Benfield) based on proprietary catalyst used to enhance the rate of reactions, for example, formaldehyde, arsenite, and hypochlorite. The activation by catalysts is apparently necessary to make the process economical compared with the amine-based processes.

Recent developments for reactive CO_2 sorbents include sterically hindered amines such as 2-amino-2-methyl-1-propanol (AMP) and 1,8-p-methanediamine (MDA) and 2-piperidine ethanol (PE), which are claimed to have good reversible CO_2 capacity and low-temperature molten salts called ionic liquids. Ionic liquids are attractive due to their negligible vapor pressure up to their decomposition at >300 ° C, however, the materials currently used, for example, $(CH_3)_4$ NF-, $4H_2O$-, and TSL1- containing imidazolium anion need to be further investigated.

Three prominent commercial processes that use physical sorbents include Selexol by UOP utilizing dimethylether polyethylene glycol, Rectisol process using cold methanol developed by Lurgi, and Purisol using NMP also developed by Lurgi. These processes are based on a higher solubility of CO_2 in these solvents for CO_2 when compared with H_2, CO, and CH_4. Physical absorption processes require much less energy for solvent regeneration and often the solvent can be regenerated just by decreasing the pressure. Physical absorption systems are typically used when the partial pressure of CO_2 is high. Rectisol process is especially suited for removing CO_2 from the synthesis gas mixture used in methanol plants since the solvent is also methanol and the vaporized solvent present in the synthesis gas is not a problem. One advantage of the Selexol process is the low vapor pressure of its solvent permitting its operation at near ambient temperature instead of cryogenic or chilled temperature as used in Rectisol and Purisol systems. The selexol solvent is a mixture of polyethylene glycol/dimethyl ethers $(CH_3O(C_2H_4O)nCH_3)$ with n from 3 to 9.

A combination of Selexol with PSA was demonstrated to be lower in capital and operating cost compared to a conventional Rectisol/liquid N_2 cryogenic system at the Coffeyville Resources Gasification Ammonia Complex in Coffeyville, Kansas, for the production of ammonia and urea granules. Recently, CO_2 absorption by chilled ammonia is being investigated for CO_2 removal from power plant flue gases as a lower cost option compared to the amine absorption process.

Although the preceding processes described for CO_2 separation are based on liquid absorbent solutions operating at low (cold methanol) to moderate temperatures (hot carbonate), CO_2 may also be separated by solid sorbents, typically operating at high temperatures, for example, base metal oxide such as CaO can absorb CO_2 at 600 °C temperatures by reversible carbonation/decarbonation reaction:

$$CaO + CO_2 \leftrightarrow CaCO_3$$
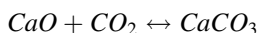
Sorbents such as lithium silicate and lithium zirconate can absorb CO_2 at somewhat lower temperature of 500 °C:

$$Li_4SO_4 + CO_2 \leftrightarrow Li_2CO_3 + Li_2SiO_3$$
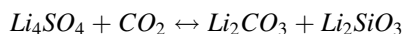
whereas highly active sorbents such as sodium carbonate may be used for removing CO_2 from flue gases at moderate temperatures of 100–150 °C:

$$Na_2CO_3 + CO_2 + H_2O \leftrightarrow 2NaHCO_3$$
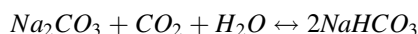
CO_2 is removed and the solid sorbent is regenerated by heating it at a temperature greater than the carbonation temperature reversing the equilibrium.

Pure solid sorbents have lower percentage of utilization, typically about 30%, due to the accumulation of the product on the active surface. The degree of utilization of the active sorbent may be increased by using smaller porous particles or loading the active sorbent onto the surface of suitable nonactive supports such as alumina. The solid sorbents also present operational challenges for moving the solids (e.g., in a transport reactor) or otherwise providing good gas/solid contact for effective mass transfer in fixed/fluidized beds.

The solid sorbent material must also be heated and cooled for regeneration and absorption cycles. Because the solid CO_2 sorbents operate at higher temperatures than the liquid absorption systems, they provide opportunities for simultaneous WGS reaction with CO_2 removal improving the CO conversion in sorbent-enhanced reaction process (SERP).

Some of the polymeric membranes are suitable for bulk separation of hydrogen from impurities to enrich a dilute hydrogen stream (Bernardo et al. 2020). Dense polymers permeate gases by solution diffusion mechanism. The permeation rate of a gas species through a polymer membrane is, therefore, proportional to the solubility of the gas species in the polymer as well as the diffusivity of the dissolved species in the polymer. Hydrogen, being a small molecule usually is much more permeable through a polymer compared to other species present in the reformer gas streams: CO_2, CH_4, and H_2O. However, its solubility is often lower than other condensable and polar species such as CO_2 and water. Glassy polymers are dominated by diffusivity selectivity, and therefore, exhibit greater separation factors for hydrogen, for example, polyimide membranes. Rubbery polymers, however, tend to have lower separation factors for hydrogen. The polymeric membranes are temperature sensitive and are generally operated at ambient or only a slightly elevated temperature. Membrane permeability generally increases with temperature for all species, whereas membrane selectivity often decreases with temperature due to a decrease in solubility selectivity with temperature.

Because polymeric membranes separate hydrogen from other species based on relative permeability, they are not capable of providing high-purity hydrogen or absolute separation of species. Purity of the hydrogen product strongly depends on the hydrogen recovery by the membrane.

Greater the hydrogen recovery by a membrane, lesser would be the purity of the hydrogen product. The performance of a membrane system, that is, its relationship between product purity and product recovery for a given feed, primarily depends on the feed to permeate pressure ratio and is only slightly dependent on the absolute pressure level. The membrane area required for a desired separation, however, is inversely proportional to the partial pressure differential, which depends on the absolute pressure level. Greater the feed side pressure, lesser membrane area will be required for the same feed to permeate pressure ratio used for a desired membrane performance. The hydrogen permeate is produced at a lower pressure, often slightly above the ambient pressure. The product hydrogen may, therefore, need to be recompressed depending on the intended hydrogen application.

Hydrogen permeability of the membrane is inversely proportional to the membrane thickness. Therefore, it is desirable to reduce the thickness of the membrane layer providing the gas separation. Yet, the membrane must have sufficient mechanical strength and chemical/thermal stability. Two types of membrane synthesis are, therefore, used to provide the desired membrane properties: asymmetric and composite membranes. An asymmetric membrane consists of a thin dense layer of the polymer providing gas separation supported on a thicker but microporous layer of the same polymer material that provides the mechanical strength. Such membranes are prepared by a phase inversion technique used in polymer film synthesis. In a composite membrane, two distinct layers, possibly of two different materials, are combined consisting of a thin dense polymer layer providing the gas separation and a thicker microporous substrate polymer layer.

The thinner layer may be coated on to the substrate layer or laminated with it. The composite membrane concept allows using expensive polymers with desired gas separation properties since only a thin layer of this material needs to be fabricated and the support layer can be made of an inexpensive material. Multiple layers of materials are often used in a composite membrane with graded density to obtain high permeability without loss of selectivity and provide the necessary mechanical structural strength.

Polymeric membranes are fabricated as flat sheets or as hollow fibers for the composite and the asymmetric membrane configuration. Flat sheet membranes are typically packaged as spiral wound modules to provide a compact high surface area packaging. Flat membranes are sandwiched between a porous feed spacer and a porous permeate spacer. The membrane assembly sheets are wound around a central permeate tube. All permeate channels are connected to the permeate tube. Feed gas flows axially through the feed spacers, whereas the permeate flow passing through the membrane flows perpendicular to the feed flow toward the central collection tube. Hollow fiber membranes inherently provide high surface area to volume ratio. Hollow fiber modules are similar to a shell and tube heat exchanger. Hollow fibers are arranged in fiber bundles with ends potted in tube sheet at each end. The feed generally flows through the shell side outside the fibers and the permeate is collected in the tubesheet manifolds. The fibers may be wound on porous support tubes for structural strength.

Both types of modules can provide a large membrane surface area in a compact volume. Although polymeric membranes are generally less expensive, they are modular in nature and the scale of economy is not available for larger capacities. Large capacity must be provided by simply adding more membrane modules.

The first commercial "PRISM" hydrogen separation membrane based on polysulfone membrane material was introduced in 1979 by Monsanto and is now available from Air Products and Chemicals, Inc. Other commercially available hydrogen separation membranes include a polyimide-based membrane by Ube, polyaramide and polyimide-based membrane by MEDAL, and PolySep/Separex family of membranes by UOP. These membranes are extensively used to recover hydrogen from high-pressure waste or recycle streams. For the hydrogen generation application, polymeric membranes may be used to provide bulk hydrogen separation (Fig. 3) and in hybrid configuration with PSA or CO_2 absorption system, for example, to recover hydrogen from PSA off-gas stream.

Cryogenic separation uses the difference in boiling points of the components in a feed gas to separate condensable components by partial condensation of the gas stream. This technique is often used for separating hydrogen from C_{2+} hydrocarbons. Cryogenic separation has also been used to separate high-purity CO as a product from the synthesis gas stream. Although cryogenic separation can be used for producing pure hydrogen from synthesis gas along with other fractionated products, primarily CO, earlier cryogenic systems have largely been replaced by PSA systems when pure hydrogen is desired as the primary product.

A realistic possible pathway for the evolution of hydrogen economy starts with the current industry standard process of SMR. Hydrogen produced by SMR at a distributed scale is projected to be cost-effective compared to the cost of hydrogen based on central large-scale production with delivery by compressed gas tube trailers or cryogenic trucks. The cost of distributed hydrogen production by SMR is estimated to be about $5/gasoline gallon equivalent (gge) (U.S.$2003) based on SMR technology available commercially, which utilizes PSA as the hydrogen purification process. Based on production and installation of 500 distributed-scale (forecourt) SMR units/year, the cost of hydrogen as predicted by U.S. DOE's hydrogen analysis model (H2A) is $3/gge, which is significantly greater than the U.S. DOE Year 2010 target of $2.5/gge and the U.S. DOE 2015 target of $2/gge. (One gge is a considered equivalent to 1 kg of hydrogen based on the current performance of a 100 kW PEM fuel cell stack for automotive power.) This analysis assumes the utilization of the SMR and PSA purification technology that is commercially available today. The cost targets are based on producing hydrogen cost competitively compared to the currently available transportation fuel, that is, gasoline. The cost of the currently available SMR technology for hydrogen production must, therefore, be reduced to make the hydrogen cost competitive for the transportation fuel market as envisioned in the transition to the hydrogen economy.

To reduce the cost of hydrogen produced by SMR, approaches are being pursued for improving the reforming process itself as well as to reduce the cost of hydrogen separation. All of the commercially available hydrogen separation approaches described in earlier sections require cooling the product gas to a lower separation

process temperature (e.g., ambient for PSA and amine absorption). If hydrogen separation could be conducted at high temperatures suitable for WGS reaction (e.g., 250–450 °C) or even at a higher temperature suitable for methane reforming (e.g., ~ 600 °C or greater) reaction, hydrogen separation process could be integrated with either the WGS reaction or with methane reforming and WGS reactions together. The WGS reaction as well as methane reforming/methanation reactions are equilibrium limited and hydrogen separation simultaneous with the reaction can provide an additional benefit of increasing reaction conversions by removing one of the products from the reaction environment. Separation of one of the reaction products (H_2) will also allow conducting reaction at lower temperatures and with lower, near stoichiometric, steam to carbon ratios leading to less steam consumption. Separation of CO_2 from the reaction environment also offers similar advantage of increasing reaction conversion. Integrating hydrogen separation (or CO_2 separation) either with the WGS reaction or both the methane reforming and WGS reactions will reduce the number of unit operations involved in hydrogen production and is likely to reduce the capital cost of the hydrogen plant equipment. Therefore, approaches are being investigated for high-temperature separation of hydrogen (or CO_2) and integrating hydrogen separation with the hydrogen generation process, by combining either WGS shift reaction or the methane reforming and WGS reactions together with hydrogen separation.

Membrane reactor processes for conducting WGS reaction and methane reforming reaction with simultaneous hydrogen separation are shown schematically in Figs. 5 and 6.
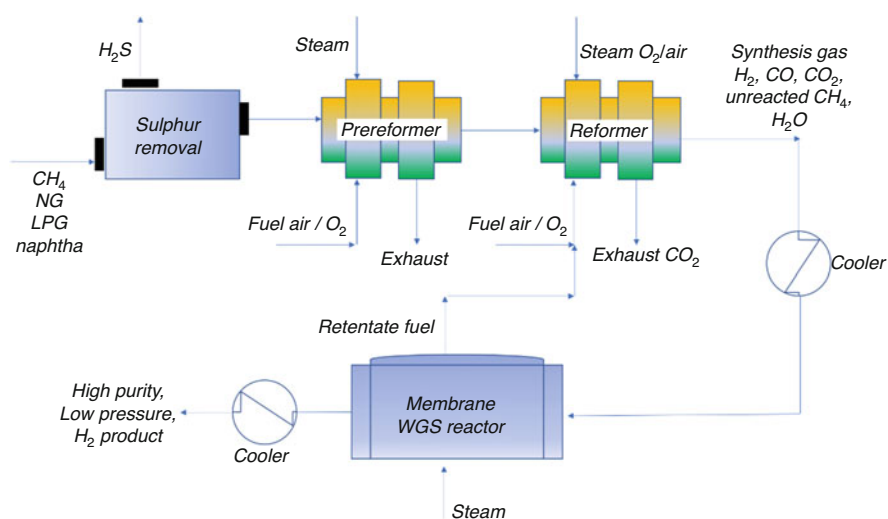
Fig. 5 Steam methane reforming with membrane WGS reactor for hydrogen production
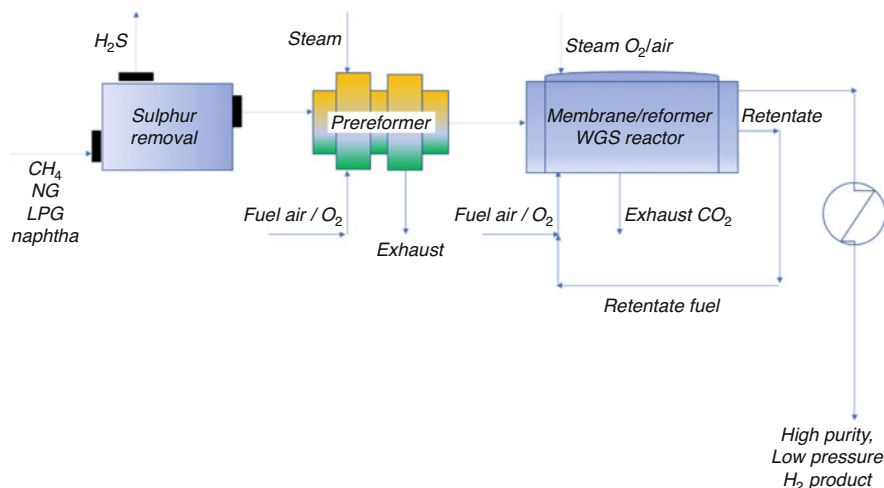
Fig. 6 Steam methane reforming with membrane reformer/WGS reactor for hydrogen production

Reducing the energy requirement for separation and purification of hydrogen and reducing the separation equipment cost will significantly decrease the overall cost of producing hydrogen. Substantial research effort is, therefore, underway to investigate new concepts for hydrogen separation as well as to improve existing proven processes especially the PSA. Hydrogen separation membranes have been shown to have potential to reduce separation costs by over 30% compared to PSA hydrogen purification. Although SMR is expected to be the near-term technology for hydrogen production, gasification of coal and biomass as well as reforming of biomass-derived liquid fuels such as ethanol are the first candidates likely to replace SMR in the future. All of these hydrogen production technologies first produce synthesis gas followed by hydrogen enrichment by WGS reaction and hydrogen separation. The developmental concepts based on improving hydrogen separation process or integration of hydrogen separation with hydrogen gen-eration will, thus, be applicable to all of the various options that are likely to be used for hydrogen production in the foreseeable future.

Several inorganic materials are being pursued as membrane candidates for high-temperature hydrogen separation: (1) dense metallic membranes, (2) dense ceramic ion transport membranes, and (3) porous inorganic membranes including molecular sieve-based carbon and zeolite membranes. Two types of polymer membranes are being investigated: high-temperature polybenzimidazole (PBI) and similar polymer membranes and reverse-selective CO_2 separation membranes. In addition, high-temperature CO_2 sorbents are being investigated for simultaneous reforming/WGS reaction and CO_2 separation in SERP. Among these developmental concepts, palladium-based metallic membranes have received the most attention and may be considered as the most promising candidate for high-temperature hydrogen

separation membrane. Most of these concepts are being demonstrated on a small laboratory or bench-scale systems. Long-term stability and durability of the materials at an industrial scale have not yet been demonstrated for most of these developmental processes including the palladium-based membranes. One disadvantage of all membrane materials preferentially permeating hydrogen is that the hydrogen product stream is produced at a much lower pressure compared to the feed gas pressure. If a high product hydrogen pressure is desired, for example, for transportation and storage, the cost of an additional compressor must be taken into account in determining the cost of hydrogen. Membrane reactor concept using hydrogen separation membranes is, thus, more attractive for applications utilizing hydrogen at a lower pressure, for example, in a distributed power generation using PEM fuel cells with on-site hydrogen generation.

Hydrogen permeates through solid metals in atomic form by solution—diffusion mechanism. Hydrogen molecules first adsorb on the metal surface and are dissociated into atoms, which then diffuse through the bulk metal under a concentration gradient. After passing through the bulk metal, the hydrogen atoms recombine into hydrogen molecules at the opposite metal membrane surface and the molecular hydrogen gas exits from the surface to the gas phase. The diffusive flux of hydrogen through a bulk metal membrane of thickness L is generally described by Sievert's law:

$$J = -\frac{k\left(\sqrt{P_f} - \sqrt{P_p}\right)}{L}$$

where J is diffusive flux, mol/m^2-s, k is the hydrogen permeability of the metal, mol/m-s-Pa$^{0.5}$, L is the membrane thickness, m, Pf and Pp are the hydrogen partial pressures on the feed side and permeate side of the membrane surface, Pa, and "–ve" sign indicates hydrogen flux toward lower concentration.

The square root proportionality of hydrogen flux with respect to the partial pressure driving force is indicative of the bulk-phase diffusion as the rate-limiting step. In practice, for thin membranes, the proportionality can be different with the power law exponent between 0.5 and 1 as other factors such as gas-phase mass transfer and surface dissociation may contribute to the overall permeation. Because hydrogen is transported through a unique dissociated atomic form through the metal, the metal membranes are 100% selective to hydrogen and allow the permeation of other gas species only through pinholes and defects in the metal membrane. Palladium is the most widely researched metal membrane since it is highly permeable to hydrogen, resistant to ambient conditions of air, oxygen, and moisture, and is able to rapidly dissociate hydrogen molecules into atoms on the surface.

Palladium-based dense metallic membranes have been known to be completely selective for hydrogen permeation and are used in commercially available small-scale hydrogen purification units.

These hydrogen purification units typically use palladium-alloy oils 25–30 μm thick or tubes (60–100 μm thick) to produce high-purity hydrogen (e.g., 99.99999%)

for specialized applications using industrial-grade hydrogen. The small-scale hydrogen purifiers are expensive on unit hydrogen flow basis. Because membrane systems are modular in nature, that is, larger capacities are provided by adding more modules or increasing membrane surface area linearly, palladium foil or tube-based hydrogen separation is likely to be cost prohibitive for large-scale hydrogen separation applications. Palladium-alloy foils or tubes have also been incorporated in small hydrocarbon fuel reformers that are being demonstrated. Palladium-alloy membranes are used either to purify the product hydrogen after a fuel reformer (e.g., IdaTech and InnovaTek) or integrated within the fuel reforming process (e.g., MesoGen unit by Intelligent Energy). The hydrogen capacity of such available units is typically designed to support a PEM fuel cell power rating up to a few kilowatts or about 100 standard liters of H_2 per minute or less.

The cost of Pd-alloy membranes used for hydrogen separation may be reduced by depositing a thin Pd-alloy film on a suitable porous substrate to form a composite membrane. Almost all of the Pd-alloy membrane development efforts are, thus, focused on preparing thin yet defect-free Pd-alloy composite membranes.

Pd-alloy composite membranes may be prepared by depositing a thin Pd-alloy film on a suitable porous support. A porous support provides the mechanical and structural strength to the composite membrane allowing the selective gas separation metal film to be thin. Porous ceramic (e.g., alumina and zirconia) and metallic (e.g., stainless steel) supports have been used for the preparation of composite membranes. Porous supports generally have graded pore size structure with a coarse pore size bulk support and finer pore size layers near the surface and are typically used in liquid filtration applications. The thickness of the metal film deposition needed to assure a defect-free composite membrane strongly depends on the porous support characteristics such as the pore size in the top most surface layer. Ceramic supports are generally prepared by depositing a layer of fine ceramic particles prepared by sol–gel technique, producing pores that are small and have a narrow distribution.

The disadvantage of ceramic supports is their fragility and difficulty in providing connections and seals especially in the high-temperature operation. Porous metallic supports are sturdier but are generally coarser in pore size, have a low overall porosity, and generally require much thicker Pd-alloy film deposition to produce high hydrogen selectivity. Another disadvantage of metallic supports is the possibility of intermetallic diffusion, especially at high operating temperatures, between Pd-alloy and the porous metal itself. A diffusion barrier is, thus, needed between the porous metal and the Pd-alloy film for long-term stability. Approaches for introducing a suitable barrier include oxidizing the surface of the porous metal or deposition of a fine pore size ceramic layer on the porous metal surface. The latter approach can combine the advantages of both ceramic (smaller pore size) and metallic (structural strength) supports and is recently being investigated using zirconia/porous stainless-steel composite tubular substrates.

Pure palladium becomes brittle in the presence of hydrogen during thermal cycling due to dimensional changes caused by a transformation between two phases (α and β) of palladium hydride around 300 °C. To avoid metal embrittlement and resulting membrane cracking or distortion, pure palladium membrane should not be

exposed to hydrogen at temperatures below 300 °C. To increase resistance to embrittlement, Pd is alloyed with other metals such as Ag and Cu. The most commonly used alloy in the commercially available membrane modules contains 23% Ag and 77% Pd by weight; this composition is also claimed to maximize the hydrogen permeability of the Pd–Ag alloy. In addition to providing thermal stability, alloying Pd with other metals also increases its resistance to chemical contaminants. Among the contaminant species present in hydrocarbon fuels used for hydrogen production, Pd is especially vulnerable to sulfur (H_2S) present in fuel gases. Alloying of Pd with Cu has been reported to offer significant tolerance to the presence of H_2S in the hydrogen gas stream. Various compositions of Pd–Cu alloys were evaluated in a systematic study at U.S. DOE NETL in which 80% Pd–20% Cu alloy was indicated to be an optimized composition with regard to contaminant tolerance including no significant effect of 1000 ppm H_2S on the hydrogen permeation. Minimal effect of CO or H_2O was observed on the hydrogen permeation by the membrane of the same composition except for CO exposure at about 635 °C, which was attributed to carbon deposition on the surface due to CO reduction. The membrane surfaces, however, were observed to experience pitting and surface roughening during the exposure tests.

The sulfur tolerance of 60% Pd and 40% Cu alloy was found to depend on temperature of operation with marked permeability reduction at temperatures 500 °C or lower in the presence of H_2S. This temperature also corresponds to the transition between face centered cubic (fcc) lattice structure above 500 °C to body centered cubic (bcc) lattice structure below 500 °C. Among all Pd–Cu alloy compositions, the hydrogen permeability is thought to be the highest for the 60% Pd and 40% Cu composition and for this composition, it passes through a maximum at about 450 °C. Several other alloying elements, for example, Au, Y, and Ce have been identified with significant increase in hydrogen permeability with 8% Y and 8% Ce alloys. Ternary alloy compositions (Pd–Cu-transition metal) are also being investigated for maximizing membrane permeability and stability.

Several approaches have been used to produce thin-film Pd-alloy composite membranes: physical vapor deposition (PVD), chemical vapor deposition (CVD), electroplating, compression cladding, sputtering, spray pyrolysis, and electroless plating. Of these methods, CVD and electroless deposition methods are considered as the promising routes for thin composite membrane fabrication. The electroless plating method is generally preferred over CVD for several reasons: electroless deposition provides thin metal and metal-alloy films that have excellent adhesion properties; the deposition rate is high, and it can be easily controlled. Further, this is an autocatalytic process that does not require any expensive equipment. The CVD process requires appropriate stable organometallic precursors, which are expensive. It is also difficult to deposit two metal alloying species simultaneously by CVD for the fabrication of palladium-alloy membranes. Techniques for forming thin free-standing Pd-alloy films by sputtering on smooth, high surface finish substrates, for example, polymers and silicon wafers, are also being investigated.

The film formed on a smooth surface is later separated from the substrate to yield a free-standing dense Pd-alloy film, which is then supported on a suitable porous
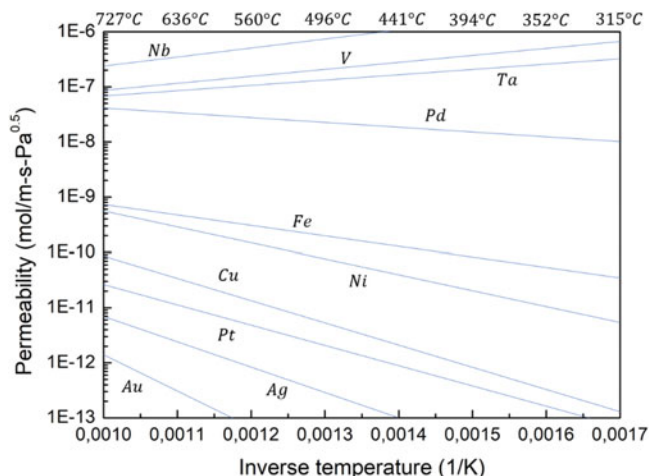
Fig. 7 Hydrogen permeability of various metals

support (e.g., porous stainless steel) to prepare a functional composite membrane. The porous material provides only the mechanical support for the film. The advantage of this technique is that the Pd-alloy film is formed without any influence of the porous support characteristics; however, the thin free-standing film is highly flexible and must be handled appropriately to prevent warping, creases, and stresses.

Because Pd-alloy membranes operate at high temperatures in the range of WGS reaction and on the lower end of methane reforming reaction, they can be used in a membrane reactor configuration for the simultaneous separation of hydrogen.

Although Pd-alloy composite membranes have been studied extensively over the past 20 years, the scale of the membrane used has been very small and the durability and stability of such membranes has not yet been demonstrated on an industrial scale.

Although considerable research has been conducted with Pd-alloy foils, tubes, and thinner composite membranes, long-term durability and stability need to be further demonstrated, especially in the fuel reforming or WGS operating conditions, for acceptance of this technology in a commercial sector. Furthermore, mass-scale and cost-effective production of industrial-scale Pd-alloy thin-film composite membranes need to be demonstrated to be competitive in the hydrogen production and purification market.

Group V elements of niobium, tantalum, and vanadium have over an order of magnitude more permeability for hydrogen than palladium as seen in Fig. 7.

These membranes, termed "superpermeable" in the nuclear industry, have been used successfully to separate isotopes of hydrogen from helium in plasmas. Because hydrogen is transported in its dissociated atomic form through the dense metals, it is necessary to dissociate hydrogen on the metal surface rapidly. In addition, unlike noble metals such as Pd, the reactive metals including Nb, Ta, Ti, V, and Zr readily get oxidized effectively destroying the membrane's hydrogen transport property. It

is, therefore, necessary to cover the surfaces of these metals by a protective as well as a catalytic layer of suitable materials capable of dissociating hydrogen (Xue et al. 2022a, b). The catalytic protective layer must be sufficiently thin for not introducing significant additional resistance to hydrogen permeation and must adequately adhere to the base metal with intimate contact to allow the transfer of dissociated hydrogen. In addition, there needs to be a good match in the thermal expansion property between the catalyst layer material and the base metal to avoid cracking and delamination during thermal cycling. Among the suitable candidates of noble metals such as palladium, platinum, iridium, and rhodium, a thin layer of palladium alloy is most commonly applied, for example, by electroless plating technique, to protect the metal membrane surface as well as to catalyze hydrogen dissociation on the surfaces (Lim and Kim 2022).

The group V elements, Nb, Ta, and V have a very high solubility for hydrogen resulting in a high H/metal ratio during hydrogen permeation, which can lead to embrittlement of the metal that may lead to subsequent cracking of the membrane. Long-term durability of a proprietary membrane/catalyst formulation of this type was recently determined over 300 days in a reformate gas environment at 340 °C containing 41% H_2, 37% H_2O, 18% CO_2, and 3% CO in which the hydrogen permeability was found to decrease by a factor of three over the test duration. Further improvement in membrane/catalyst formulations for durability and stability are ongoing. Small-scale brazable vanadium-alloy membranes are being evaluated for WGS membrane reactor applications. Systematic evaluation of a variety of binary transition metal alloys with protective catalytic coatings is being conducted to develop a dense metallic membrane with superior hydrogen separation properties and long-term durability and resistance to embrittlement.

In dense ceramic membranes, hydrogen permeation occurs in its ionic (protonic) form. Molecular hydrogen first dissociates into protons and electrons on the surface of the membrane. The protons move through the membrane by an ionic transport mechanism under a proton concentration gradient across the membrane to the opposite face. The protons must then recombine with electrons to form molecular hydrogen, which then dissociates from the membrane surface. As a result, the ceramic membrane must also be able to transport electrons through the membrane, that is, should have the protonic and electronic conductivity to be able to permeate hydrogen. Because the membranes are dense, they are 100% selective for hydrogen and allow the permeation of other gas species only through pinholes and defects in the ceramic membrane. The ceramic materials that exhibit such properties are perovskite-based oxides with a general formula ABO_3. For improved permeation properties, dopant elements are often used to replace a small part of either A or B or both elements and create oxygen deficiency represented by $A_{1-x}A'_xB_{1-y}B'_yO_{3-\delta}$, where A' and B' are dopant elements, x and y are fractions of dopants in A and B, respectively, and δ is the number of oxygen vacancies in the material formula. Barium and strontium cerates and zirconates are the most commonly studied perovskite materials with trivalent dopants such as Y, Yb, and Gd, since these materials have the necessary mixed proton/electron conductivity.

The hydrogen flux of the cerate and zirconate perovskite materials increases with temperature and becomes appreciable at high temperatures of 800–900 °C. Hydrogen flux of such materials, however, is limited by low electronic conductivity. A number of studies are ongoing to improve the hydrogen permeability of these materials with different approaches. One promising approach is to mix the ceramic phase with a metallic phase to form "cermet" materials. The metal component in cermet provides a high electronic conductivity, whereby ceramic materials with high protonic conductivity could be used regardless of their electronic conductivity. Alternatively, a hydrogen permeable metal such as palladium may be incorporated in the ceramic matrix to form metal–ceramic composite materials, whereby the hydrogen transport occurs through the metal phase alone with the ceramic material acting only as a support matrix. The hydrogen permeation performance in such metal–ceramic composite membranes essentially depends on the metal used and will be similar to the dense metallic membranes discussed earlier, taking into account the fraction of metal in the composite.

One major concern of perovskite membranes and cermets where the perovskite materials provide the protonic conductivity is their chemical stability in the presence of major syngas components of CO_2 and H_2O as they can form carbonates and oxides. In metal-ceramic composite materials, where the ceramic provides only a structural support, materials with most resistance to the syngas components including H_2S may be chosen. Metal ceramic composites using alumina and yttria-stabilized zirconia were reported to be stable in syngas environments with H_2S. Developments are continuing in dense ceramic membranes to decrease the thickness of metal–ceramic composite as well as cermet membranes and support the thinner membranes on another porous ceramic material to increase overall hydrogen flux rates. There is also a need to reduce the operating temperature below 700 °C while maintaining high hydrogen flux rates for practical hydrogen separation applications. The scale of the development of these types of membranes may be considered as laboratory scale.

Porous ceramic membranes can separate gas components by various mechanisms that depend on the pore size and gas species properties. When the pore size is much smaller than the mean free path of gas molecules, the gas species permeate by Knudsen diffusion where the gas species permeability is inversely proportional to the square root of its molecular weight. Depending on the temperature of operation (mean free path of gas molecules increases with temperature), pore sizes in the range 2–10 nm pore diameter can separate gas species by Knudsen diffusion. Hydrogen, being a low-molecular-weight species compared to the other syngas components, permeates faster through the small pores than other gas species in the Knudsen diffusion regime. However, the separation selectivity offered by Knudsen diffusion is quite low, for example, H_2 to CO_2 selectivity can only reach 4.69, which is not sufficient to achieve a high hydrogen purity in the permeate with high hydrogen recovery in a single stage. Multiple stages of separation would be necessary to increase hydrogen purity in the permeate of each successive stage, however, with considerable cost and low hydrogen recovery. Advantages of porous ceramic membranes, for example, alumina, include chemical stability against contaminants and

high permeation rates. Ceramic porous membranes, however, do not provide high selectivity and, therefore, high purity hydrogen product. Control of pore size distribution or its narrowness is necessary for assuring Knudsen diffusion-based selectivity. Ceramic membranes, especially silica-based membranes and γ-alumina membranes (with an initial nominal pore size of 4 nm), exhibit pore coarsening in the presence of steam, which decrease their selectivity over time.

Porous ceramic membranes with a pore size in the 1–10 nm range are generally prepared by sol–gel technique and have commonly been prepared with alumina, silica, zirconia, and titania materials. To obtain greater gas separation selectivity than that offered by Knudsen diffusion mechanism, the pore size generally needs to be reduced below 3 nm. A number of studies have been undertaken to evaluate permeability and selectivity of microporous (International Union of Pure and Applied Chemistry [IUPAC] defines pores <2 nm as micropores) membranes. These membranes have also been studied for gas/vapor separation and pervaporation applications. High hydrogen selectivity has been reported with silica membranes, however, these membranes have been known to be affected by steam. Porous inorganic membranes, for example, 4 nm pore size γ-alumina, generally undergo pore coarsening in the presence of steam with decrease in selectivity over time. Steam reforming of methane using porous membranes was evaluated theoretically and experimentally with microporous silica membranes. Silica membranes were prepared by the sol–gel technique with a pore size in the 1–2 nm range with H_2/N_2 selectivity in the range 42–87 and H_2/H_2O selectivity in the range 8–10. Methane conversions greater than those predicted for equilibrium at feed conditions were obtained by selectively permeating hydrogen. The selectivity of the silica membrane was, however, observed to decrease over time in the reaction environment due to the presence of steam.

As the pore size is reduced to 1 nm or less, gas permeation may exhibit a thermally activated diffusion phenomena. For example, in studies at Oak Ridge National Laboratory, for a certain proprietary membrane material and configuration, permeation of helium appeared to increase much faster than other gases resulting in an increase in Helium to CO_2 selectivity from ~5 at 25 °C to about 48.3 at 250 °C. Hydrothermal stability of this membrane in the presence of steam, however, was not reported.

At sufficiently low temperatures (e.g., near ambient), certain gas species may adsorb on the pore surfaces or condense in small enough pores by capillary condensation. Strongly adsorbed species or species that are able to condense in the pores can effectively block permeation of other gas species. Membrane surfaces having an affinity for one of the gas species can separate that species by selective surface flow (SSF). SSF membranes utilizing high surface area carbonaceous material with uniform pores in the molecular sieving range allow the adsorption of a heavier adsorbable gas such as CO_2, which decreases the pore size excluding permeation of gas species that would have otherwise permeated. The heavy component then simply diffuses along the surface of the walls. The selectivity of such membranes, however, is not very high (e.g., CO_2/H_2 selectivity ~5 at 20 °C) and decreases with increasing temperature.

When the membrane pore size is reduced further to molecular dimensions, gas species separation can occur by molecular sieving. To separate hydrogen selectively from the other syngas components (CO, CO_2, CH_4, and H_2O), porous membranes need to be able to discriminate molecules in the 0.3–0.4 nm size with 0.1 nm or less in size difference.

With appropriate membrane pore size and a narrow distribution, membrane selectivity for smaller gas molecules can be high but the overall permeability is generally low due to a high flow resistance in fine pores. Several studies are being conducted to develop molecular sieve-type membranes using different inorganic materials, for example, those based on carbon, silica, and zeolites.

Carbon molecular sieve (CMS) membranes are generally prepared by controlled pyrolysis of organic precursors in an inert atmosphere. CMS membranes with pore diameters of 3–5 Å (0.3–0.5 nm) have been prepared for various gas separation applications. Polymeric precursors used include thermosetting polymers that harden during heating (instead of melting), such as polyacrylonitrile, phenolic resins, polyfurfural alcohol, and polyimides. The permeation characteristics of the molecular sieve membranes strongly depend on the pyrolysis conditions of temperature and duration as well as posttreatment. The pore system of CMS membranes consists of relatively wide openings with narrow constrictions. The openings contribute the major part of pore volume and are, thus, responsible for the adsorption capacity, whereas the constrictions of molecular dimensions are responsible for the species selectivity. Accurate control of the pore structure is needed to develop CMS membranes with desired properties. As a pore structure usually has a certain distribution associated with a mean pore size, the separation is not absolute and the selectivity depends on the narrowness of the pore size distribution. Because the membranes are generally several microns thick, the permeability of CMS is low due to the fine pore size and low porosity. Polymer layers may be deposited on porous substrates such as porous carbon before pyrolysis for synthesizing supported CMS membranes. Polymer precursors may be used in their hollow fiber form to produce carbon hollow fiber membranes.

Because carbon has a natural affinity for adsorption of heavy hydrocarbon species and polar molecules, CMS membranes need to be used at a sufficiently high temperature to eliminate contribution/interference of the adsorption. In contrast, strong adsorption of heavier molecules may be used to separate those species by adsorption as discussed earlier by the SSF mechanism. The SSF carbon membranes typically have pore dimensions much greater than those needed for CMS membranes since the separation is based on the adsorbed species effectively blocking permeation of other components. Carbon membranes are resistant to contaminants such as H_2S and are thermally stable and can be used at higher temperatures compared to the polymeric membranes. For the synthesis gas environment, the hydrothermal stability of carbon in the presence of steam will be a concern limiting its operation temperature.

Carbon membranes have been studied since the early 1980s and have been evaluated for hydrocarbon separations based on their adsorption properties and air separation. CMS membranes prepared from polyimide precursor were recently

evaluated for their hydrogen separation potential. When tested at 50 °C, a very high H_2/CO selectivity, over 1000, was observed. The H_2/CO_2 selectivity was relatively lower, which is thought to be due to the greater adsorption of CO_2 compared to CO. Application of CMS membranes for conducting low-temperature WGS reaction at ~200 °C with simultaneous hydrogen separation is being investigated at pilot scale with membranes exhibiting H_2/N_2 selectivity of ~50–100 and hydrogen permeance of 1 m^3/m^2-h-bar at 220 °C.

The CMS membrane was demonstrated to be stable in the presence of H_2S, NH_3 and higher hydrocarbon contaminants. Although the hydrogen selectivity with respect to other gases is not very high, it is considered to be adequate for high hydrogen recovery with sufficient hydrogen product purity. For example, with feed gas containing 44% H_2, typical of reformate gas streams, permeate hydrogen purity of ~90% was obtained with ~80% hydrogen recovery. These membranes also have a high permeability for water, comparable or greater than that of hydrogen, which must be taken into account in designing a membrane reactor system.

Zeolites are crystalline microporous aluminosilicates with well-defined cagelike pore structures of molecular dimensions (<1 nm). Zeolite membranes separate gas molecules by molecular sieving depending on the pore size of their structure. Among various types of zeolite membranes synthesized to date, the 10-member ring MFI structure (silicalite-1 and ZSM-5) is the most extensively studied for gas separation applications. MFI-type membranes have straight, circular channels of 0.54 nm × 0.56 nm running perpendicular to sinusoidal and elliptical channels of 0.51 nm × 0.54 nm and are used for several industrial separations. The kinetic diameters of the synthesis gas components are, however, in the 0.28–0.38 nm range: 0.28 nm for H_2, 0.33 nm for CO_2, 0.37 nm for CO, and 0.38 nm for CH_4. Thus, MFI-type zeolite membranes have too large pores to provide a good separation. To separate hydrogen from the syngas components, the zeolite membranes need to be 0.3–0.4 nm in size with a narrow pore size distribution within 0.1 nm. At the same time, nonzeolite large pores or defects need to be eliminated to improve membrane selectivity. Small pore size zeolite membranes include zeolite A, SAPO-34, ETS-4, SSZ-13, and sodalite membranes. SAPO-34 membranes with an eight-member ring chabazite structure and pore size of 0.38 nm have been synthesized; however, they appear to contain a significant number of bigger nonzeolite defects reducing their gas species selectivity.

Zeolite materials are commonly prepared by precipitation (crystallization) under hydrothermal conditions in the presence of a template that dictates the zeolite structure during crystal growth. A common template is tetrapropyl ammonium hydroxide (TPAOH), which is burned off after zeolite crystal growth resulting in significant lattice contraction and mesoporous defects. In the secondary growth, template-free method, a zeolite seed layer is dip-coated on the support followed by the growth of seeds into a continuous zeolite layer. To make a good quality–supported zeolite membrane, it is necessary to select the synthesis conditions so that the membrane structure nucleates and grows on the surface of the porous support, for example, porous alumina or zirconia, forming an integral zeolite/support composite membrane. Homogeneous nucleation and zeolite crystal growth in the

bulk solution needs to be avoided as it forms detached particles that deposit on the support leading to defects.

Zeolite membranes can be synthesized as a dense layer on a porous support surface (α-alumina, γ-alumina, or stainless steel) or within the pores of a support. The porous support can be thick but with large pores (0.2–0.5 μm), so that mechanical stability is excellent without introducing additional mass transfer resistance. Because of the inorganic nature of zeolite materials, these membranes are robust and usable in high pressure and high temperature (at least up to 750 K) environments and are resistant to chemical contaminants including H_2S. The selectivity depends on the particular zeolite used for the membrane, its chemical composition (e.g., Si/Al ratio in ZSM-5), the crystal orientation, the identity of the charge neutralization ion, and the quality of the membrane, and these properties can be changed by preparation conditions or by posttreatment.

At low temperatures, adsorptive separation becomes important for zeolite membranes as sorption of one species can effectively hinder permeation of other species.

For example, for a ZSM-5 membrane at room temperature the CO_2/H_2 permeation ratio was found to be ~12. At a higher temperature, as CO_2 desorbs the membrane becomes hydrogen selective as hydrogen begins to permeate faster due to its smaller size. Because the most common MFI-type zeolite membranes have larger pore size than needed for effective hydrogen separation, recent research has focused on reducing the crystal pore size by the deposition of precursor materials in the pores by absorption followed by cracking/sintering of the absorbed precursors or by CVD of a cracked/ sintered precursor directly in the pores. For example, methyldiethoxysilane (MDES) was chemisorbed in the MFI membrane at 350 °C followed by its cracking at 550 °C resulting in an increase in H_2/CO_2 selectivity (determined with mixed gas tests at 300 °C) from ~2 before treatment to ~48 after treatment. However, hydrogen permeability decreased by more than an order of magnitude. Alternatively, one-step cracking of MDES over the MFI membrane at 450 °C was found to increase H_2/CO_2 selectivity at 450 °C from ~2 before treatment to ~9 after treatment with a decrease in hydrogen permeability by half. Continued annealing at 450 °C increased selectivity slightly to ~12 with a stable hydrogen flux. The zeolite membrane development is at a laboratory scale. For commercial applications, greater hydrogen flux and selectivity needs to be demonstrated.

Amorphous silica membranes with pore sizes <1 nm may be formed by sol-gel or CVD techniques. Silica polymeric sols are formed by acid-catalyzed hydro-lysis and the polymerization of tetraethylorthosilicate (TEOS) or methyltriethoxysilane under controlled reaction conditions of temperature, pH and duration. In a CVD technique, silica particles may be formed by chemical reactions, for example, gas-phase silane hydrolysis or thermal decomposition of precursors. Although silica membranes have been known to be selective for hydrogen at high temperatures with thermally activated diffusion, it has also been known to be reactive with water with degradation of separation performance over time in the presence of steam at high temperatures. Because silica membranes are porous, the hydrogen selectivity is not very high. Owing to low selectivity and concerns about hydrothermal stability in the synthesis gas environment containing steam, a recent study concluded that porous silica membranes are not suitable for hydrogen separation from the synthesis gas.

Polymeric membranes are commercially used for hydrogen recovery from waste gas streams, for example, an ammonia recycle stream. There are two primary shortcomings of the polymeric membranes when used for hydrogen separation: (1) Polymeric membrane materials are highly temperature sensitive and are typically used at ambient temperature, which requires cooling of the product hydrogen stream from upstream operations before hydrogen can be separated. Low-temperature polymeric membranes cannot, therefore, be used as membrane reactors even for the low-temperature WGS reaction. (2) Because hydrogen preferentially permeates through these membranes, the product hydrogen is produced at a lower pressure, whereas a high pressure may be desirable depending on the intended use and downstream operation. Although there is still some development of new hydrogen selective membrane materials, the primary research effort in polymeric membranes relevant to hydrogen production application is focused on alleviating the preceding two shortcomings: high-temperature polymer membrane with selectivity for hydrogen compared to other synthesis gas components and reverse selective membranes that selectively permeate CO_2 leaving hydrogen in the residue gas at a high feed gas pressure.

Polymer PBI is a thermally stable polymer, reportedly stable up to 450 °C temperature. PBI has been shown to be selective for hydrogen compared to other syngas components at several temperatures up to 400 °C. PBI is also being actively pursued as a material for high-temperature PEM fuel cells by Celanese Ventures GMBH and Plug Power. PBI is a glassy polymer with a glass transition tempera- ture of 450 °C and is claimed to be similar to polyimides with good chemical stability. A recent evaluation of permeation properties of a PBI composite membrane prepared with stainless-steel microporous support indicated a H_2/CO_2 selectivity of about 20 and H_2/CO selectivity of about 35 °C at 300 °C. The hydrogen permeability of the PBI membrane, however, is low and an economic analysis of the composite membrane indicated that the PBI composite membrane prepared with a stainless-steel support will not be able to meet the hydrogen cost targets, and the study recommended an all-polymer asymmetric PBI composite membrane development with thin dense PBI film supported on a porous PBI support. PBI is much more permeable to water vapor compared to hydrogen with water to hydrogen selectivity of ~7. The water vapor permeability must, therefore, be taken into account for utilizing PBI-based membranes for WGS membrane reactor applications where water is one of the active reactant in the feed gas. Other thermally stable polymers that may potentially be useful as high-temperature hydrogen separation membranes include polybenzoxazole and polyimide with glass transition tem- peratures of ~330 °C.

Approaches to make a polymeric membrane selective to CO_2 attempt to enhance the solubility selectivity of the polymer material for CO_2 and reduce the diffusivity selectivity of the polymer that favors smaller hydrogen molecule. The permeability of a polymer membrane for species A, PA, is often expressed as:

$$P_A = D_A \cdot S_A$$

where DA is the diffusion coefficient and SA the solubility coefficient of gas A in the membrane. The ability of a membrane material to separate two components, A and B, is often characterized in terms of the ideal selectivity, αA/B, which is defined as the ratio of their permeabilities:

$$\alpha_{A/B} = \frac{P_A}{P_B} = \left(\frac{D_A}{D_B}\right) \cdot \left(\frac{S_A}{S_B}\right)$$

It follows that αA/B can be expressed as the product of the diffusivity selectivity, DA/DB, and the solubility selectivity, SA/SB. Diffusion (or mobility) selectivity is governed primarily by the size difference between gas molecules and always favors smaller gas molecules. Solubility selectivity is controlled by the relative condensability of the gases in the polymer and their relative affinity for the polymer. Solubility selectivity typically favors larger, more condensable molecules. From Equation, it is seen that the product of gas mobility and solubility selectivity determines the overall membrane selectivity. It is clear that for a membrane to be CO_2 selective, it must have high diffusivity selectivity based on the affinity for CO_2 but it should be flexible enough to permeate larger molecules such as CO_2 as easily as the H_2 molecule, that is, it would be necessary to reduce the diffusivity selectivity for hydrogen to nearly one. Among various organic functional groups, ethylene oxide (EO) has been identified as the best functional group to interact favorably with CO_2 resulting in a high solubility selectivity for CO_2. If polymers containing EO can be made highly flexible leading to weak size-sieving ability, the diffusivity selectivity of the polymer for hydrogen can be reduced considerably. Although pure polyethylene oxide (PEO) has high CO_2 selectivity as expected, it has a very low permeability for CO_2 (~12 Barrer at 35 °C) as a result of high crystallinity levels. To inhibit crystallinity, short non-PEO segments and chain branches of short noncrystallizable EO segments were introduced in the PEO polymer backbone resulting in increased permeability while still preserving CO_2 selectivity in a family of amorphous, high-molecular-weight, cross-linked network copolymers. The family of copolymers contained different composition ratios of poly(ethylene glycol) diacrylate (PEGDA) and poly(ethyleneglycol) methyl ether acrylate (PEGMEA) with 70 wt% PEGMEA/30 wt% PEGDA copolymer, providing CO_2 permeability of ~400 Barrer and CO_2/H_2 selectivity of 10 at 35 °C. Contrary to commonly observed behavior, the CO_2/H_2 selectivity increased to ~30 as the temperature decreased to −20 °C while maintaining nearly the same CO_2 permeability.

Another way of reducing diffusivity selectivity for small molecules is to introduce nanoparticles in the matrix of a polymer that has a high solubility selectivity for CO_2. Intuitively, incorporation of nanoparticles as fillers is expected to reduce gas species permeability due to a reduction in the proportion of polymer through which the gas species diffuses. However, incorporation of 13 nm size fumed silica particles containing trimethylsilyl groups in a high free-volume glassy polymer poly-4-

methyl-2-pentyne (PMP) was found to increase the selectivity of large organic molecules such as n-butane over smaller molecules such as methane. By adding 45 wt% silica in PMP increased n-butane selectivity from 13 to 22 while also increasing n-butane permeability from 7000 to 25,000 Barrers. This concept is being explored for polymer materials with high CO_2 solubility selectivity by decreasing the diffusivity selectivity of the polymer for hydrogen and, thus, increasing overall selectivity. Reverse selective (i.e., polymers selective to larger molecules compared to smaller molecules) rubbery polymer membranes are commercially used for separation of heavier hydrocarbons from natural gas. In principle, such membranes could be used to selectively remove CO_2 from synthesis gas components if the diffusivity selectivity for hydrogen could be reduced either by adding nanoparticles as indicated earlier or simply by adsorptive blockage.

Similar to high-temperature hydrogen separation-based membrane reactors, separation of CO_2 simultaneously with the WGS or methane reforming reaction may also be used to shift the reaction equilibrium toward greater hydrogen production. Separation of CO_2 has an added benefit of keeping the product hydrogen at a high pressure. Separation of CO_2 in a high purity stream will also be helpful for its sequestration if so desired. Sorbent materials that are being developed and evaluated for separating CO_2 at high temperatures may be grouped into two categories based on the mode of sorbent regeneration. Sorbent materials adsorbing CO_2 at high pressures by chemisorption may be regenerated by reducing the CO_2 pressure over the sorbent, that is, by pressure swing. Sorbent materials chemically reacting with CO_2 at high temperatures such as CaO and lithium silicate/zirconate must be regenerated by heating them at a higher temperature, that is, by temperature swing. Hydrotalcites and double salts containing MgO have been shown to exhibit pressure reversible CO_2 capacity at temperatures of 300–500 °C suitable for WGS or methane reforming reaction. Hydrotalcites are divalent and trivalent metal ions and An– is an anion. The value of x is in the range 0.2–0.33. The metal ions and the anions appear in a layered structure. A naturally occurring mineral and the most commonly studied "hydrotalcite". The reversible CO_2 adsorption capacities of potassium carbonate–promoted hydrotalcites range from 0.4 to 0.7 gmol/kg (<3% by weight) at 300–400 °C, even in the presence of steam. Adsorbent materials containing an alkali metal salt and a magnesium salt are referred to as double salts with a general formula: $\{(M_2CO_3)m(2MHCO_3)1–m\}n(MgCO_3)p(MgO)1–pxH_2O$, where M is an alkali metal such as Li, Na, K, Rb, and Cs. Double salts have been shown to have even greater CO_2 adsorption capacities in the range 1–10 gmol/kg at 350–400 °C.

Although double salts appear to have a greater hydrogen capacity, their stability has not been studied in detail and they are also difficult to pelletize for a fixed-bed reactor application. Potassium carbonate–promoted hydrotalcite in a pelletized form has been evaluated at the bench- and pilot-scale system for SERP for conducting methane steam reforming with simultaneous adsorption of CO_2. Commercial SMR catalyst was mixed with the CO_2 sorbent and SMR was conducted at a low temperature of 450 °C and 55 psig pressure with steam to methane ratio of six resulting in 82% conversion of methane and a product stream containing 95% hydrogen, 5% unreacted methane, and <50 ppm of carbon oxides. Utilization of

hydrotalcite adsorbent in the form of a thin film membrane deposited on a porous support for a continuous membrane reactor process is also being investigated, however, such membranes appeared to give low overall methane conversion.

Alkali metal oxides such as CaO and MgO have been known to react with CO_2 at high temperatures. The oxides can be regenerated by calcining respective carbonates at a greater temperature with carbonation/calcination equilibrium depending on the reaction temperature and CO_2 partial pressure. Because CO_2 is absorbed by chemical reaction, the theoretical material weight–based CO_2 absorption capacity as determined by reaction stoichiometry is high. Formation of the carbonate product layer on the active sorbent surface, however, limits the CO_2 absorption capacity typically to 30–40 wt%. The active sorbent weight–based CO_2 capacity may be increased substantially to up to 80% by improving sorbent particle morphology or by loading the active sorbent on a porous support. Because CaO reacts with CO_2 at temperatures suitable for methane reforming, for example, 650 °C, CaO has been investigated for sorbent-enhanced methane reforming with simultaneous CO_2 removal. CaO has also been investigated for sorbent-enhanced WGS reaction at 600 °C. Although greater than equilibrium CO conversion was observed, the effectiveness of the regenerated sorbent in the second cycle was significantly lower than the virgin sorbent. Also, the CO_2 absorption capacity was found to decrease with each regeneration cycle. As the metal oxide-based sorbents are regenerated by thermal decomposition at temperatures of >700 °C, efficient sol- ids heating system must be designed for fixed-bed reactors. Alternatively, fluidized-bed absorption and regeneration reactors may be used with circulation of solids between the two reactors at high temperatures and interstage solids heating and cooling making the overall system more complex. The solid particles must be made attrition-resistant, and heat-resistant alloys must be used for the reactor vessels due to high temperatures involved.

Lithium metal-based reagents such as lithium zirconate and lithium silicate react with CO_2 at lower temperatures than CaO, for example, at 400–500 °C with nearly 30 wt% CO_2 absorption capacity. Alkali carbonates are typically added as promoters. Because CO_2 absorption and sorbent regeneration occur at lower temperatures than those involved with CaO sorbent, lithium-based sorbents would be more attractive for SERPs especially for WGS reaction. The capacity of lithium silicate–based materials was also shown to be reproducible over a number of car- bonation/regeneration cycles and the sorbent may be regenerated by a temperature swing or by inert purge at the absorption temperature. In further developments, attrition resistant and fluidizable sorbent formulations were being prepared to allow the sorbent carbonation and regeneration processes to be carried out in more efficient fluidized beds.

Regenerable CO_2 sorbents capable of removing CO_2 at 300–400 °C have recently been developed. This sodium-based sorbent shows a very high carbon dioxide capture capacity and greater than 99% carbon dioxide removal efficiency at 315 °C. The sorbent can be regenerated at 700 °C. A 10-cycle test conducted at U.S. DOE NETL showed that the capture capacity increased during the cyclic testing. Such sorbents will especially be attractive for conducting LTS reaction with simultaneous CO_2 removal in a sorbent-enhanced reactor process similar to the earlier described sorbent materials suitable for higher temperatures.

Developments of sorbent materials for high-temperature CO_2 removal from synthesis gas and their utilization as SERPs appears attractive, however, the development scale may be considered as laboratory/bench scale.

3   Conclusions

Here are discussed the developmental hydrogen separation processes being investigated. Although a large amount of research effort is ongoing, it is clear that substantial progress still needs to be made for developing commercially viable alternatives to the established hydrogen separation processes of PSA, CO_2 absorption, and currently available polymeric membranes. Among the developmental activities, most effort is being devoted to palladium-alloy composite membrane as being the most promising. Among commercially available processes, PSA is often the most cost-effective option for hydrogen separation and purification, especially for hydrogen production by steam reforming of natural gas. For coal and biomass-based feedstocks for hydrogen generation, CO_2 absorption either alone or in combination with PSA may become attractive due to the greater content of CO_2 in the product hydrogen stream. With increasing emphasis on carbon sequestration, producing pure CO_2 as well as hydrogen will become important, increasing the attractiveness for CO_2 absorption and hybrid CO_2 removal/PSA configurations.

References

Amin M, Butt AS, Ahmad J et al (2023) Issues and challenges in hydrogen separation technologies. Energy Rep 9:894–911. https://doi.org/10.1016/j.egyr.2022.12.014

Bernardo G, Araújo T, da Silva LT et al (2020) Recent advances in membrane technologies for hydrogen purification. Int J Hydrogen Energy 45(12):7313–7338. https://doi.org/10.1016/j.ijhydene.2019.06.162

Huang Z, Rafiq M, Woldu AR et al (2023) Recent progress in electrocatalytic nitrogen reduction to ammonia (NRR). Coord Chem Rev 478:214981. https://doi.org/10.1016/j.ccr.2022.214981

Ishaq H, Crawford C (2023) CO2-based alternative fuel production to support development of CO2 capture, utilization and storage. Fuel 331:125684. https://doi.org/10.1016/j.fuel.2022.125684

Kim S, Nguyen BTD, Ko H (2021) Accurate evaluation of hydrogen crossover in water electrolysis systems for wetted membranes. Int J Hydrogen Energy 46(29):15135–15144. https://doi.org/10.1016/j.ijhydene.2021.02.040

Kim T, Song Y, Kang J (2022) A review of recent advances in hydrogen purification for selective removal of oxygen: deoxo catalysts and reactor systems. Int J Hydrogen Energy 47(59): 24817–24834. https://doi.org/10.1016/j.ijhydene.2022.05.221

Kucharska K, Łukajtis R, Słupek E (2018) Hydrogen production from energy poplar preceded by MEA pre-treatment and enzymatic hydrolysis. Molecules 23(11):3029. https://doi.org/10.3390/molecules23113029

Lee HI, Mehdi M, Kim SK et al (2020) Advanced Zirfon-type porous separator for a high-rate alkaline electrolyser operating in a dynamic mode. J Membrane Sci 616:118541. https://doi.org/10.1016/j.memsci.2020.118541

Lim T, Kim S-K (2022) Non-precious hydrogen evolution reaction catalysts: stepping forward to practical polymer electrolyte membrane-based zero-gap water electrolyzers. Chem Eng J 433: 133681. https://doi.org/10.1016/j.cej.2021.133681

Omoniyi O, Bacquart T, Moore N (2021) Hydrogen gas quality for gas network injection: state of the art of three hydrogen production methods. PRO 9(6):1056. https://doi.org/10.3390/pr9061056

Pashchenko D (2023) Hydrogen-rich gas as a fuel for the gas turbines: a pathway to lower CO_2 emission. Renew Sustain Energy Rev 173:113117. https://doi.org/10.1016/j.rser.2022.113117

Poser M, Duarte E Silva LR, Peu P (2023) Cellular concrete waste: an efficient new way for H2S removal. Sep Purif Technol 309:123014. https://doi.org/10.1016/j.seppur.2022.123014

Salahi F, Zarei-Jelyani F, Meshksar M (2023) Application of hollow promoted Ni-based catalysts in steam methane reforming. Fuel 334:126601. https://doi.org/10.1016/j.fuel.2022.126601

Singla S, Shetti NP, Basu S (2022) Hydrogen production technologies - membrane based separation, storage and challenges. J Environ Manag 302:113963. https://doi.org/10.1016/j.jenvman.2021.113963

Wang T, Cao X, Jiao L (2022) PEM water electrolysis for hydrogen production: fundamentals, advances, and prospects. Carbon Neutrality 1(1):21. https://doi.org/10.1007/s43979-022-00022-8

Wang S, Cheng M, Luo L (2023) High-throughput screening of metal–organic frameworks for hydrogen purification. Chem Eng J 451:138436. https://doi.org/10.1016/j.cej.2022.138436

Xue X, Zhang M, Wei F (2022a) Gold as an efficient hydrogen isotope separation catalyst in proton exchange membrane water electrolysis. Int J Hydrogen Energy 47(63):26842–26849. https://doi.org/10.1016/j.ijhydene.2022.06.052

Xue X, Chu X, Zhang M (2022b) High hydrogen isotope separation efficiency: graphene or catalyst? ACS Appl Mater Interfaces 14(28):32360–32368. https://doi.org/10.1021/acsami.2c06394

Hydrogen Infrastructure

1 Introduction

Of the annual production of 8 EJ or ~ 190 Mtoe of hydrogen, most is in the form of 'captive' hydrogen (consumed at the producer's place). Only an estimated 5% of the total hydrogen production is supplied as 'merchant' hydrogen (produced centrally and transported to the consumer), requiring the appropriate infrastructure for transportation and distribution. Other market types are by-product and stranded hydrogen produced in the chemical industries and either used internally as a raw material or fuel, or simply vented or flared if no marketing infrastructure is available. Only 1% of current hydrogen production is used for direct energy purposes. The hydrogen market in Europe is 64% captive hydrogen, 27% by-product hydrogen and 9% merchant hydrogen (Wappler et al. 2022).

The conversion of existing gas infrastructures to hydrogen operation has the potential to achieve a breakthrough for the hydrogen industry.

Using existing storage and transport capacities, hydrogen, as the main pillar of energy transition, can reliably ensure security of supply during the change to renewable energy sources. In this way, energy transition – and sector integration specifically – can be promoted comparatively quickly and inexpensively along with the expansion of the power grids (Kovač et al. 2021).

At the same time, the long-distance gas networks open up the prospect of a European and global hydrogen market – and therefore the opportunity to consider the expansion of the regenerative energies increasingly globally: linking generation capacities in countries that are rich in renewable energy sources with markets and customers in different regions of the world, reliably and on competitive terms.

The technical challenges of hydrogen technology can largely already be addressed today. The anticipated progress and the use of digital solutions will lead to continuous improvements of the overall system. The utilization and interactions of gas and electricity grids can be increasingly and more effectively controlled to

compensate for discrepancies between the generation of renewable energy and individual needs in national and international operations (Schnettler et al. 2020).

Politics, industry, and the energy industry are widely committed to hydrogen as one of the central energy sources of energy transition. Two things must now follow: the consistent expansion of capacities for renewable electricity generation and the appropriate regulatory framework that shows the route to an efficient hydrogen economy.

According to current estimates, the establishment of a hydrogen infrastructure is possible with limited economic effort. In particular, the use of existing pipeline routes eliminates lengthy and time-consuming planning and approval procedures. The development of new technologies and materials also faces few fundamental challenges and has already been initiated in many areas (Noussan et al. 2020).

Against this backdrop, the costs for retrofitting the lines – including decommissioning, water pressure tests, replacement of fittings and blowers and dismantling of connections, etc. – can be estimated at around 10–15% of a new construction according to current estimates by transmission system operators.

Converting the compressor infrastructure to maximize the flow of energy in hydrogen operation requires approximately three times the compression performance compared to natural gas operation. Accordingly, the compression equipment of a hydrogen pipeline, including the drives, would be approximately three times the cost of a natural gas pipeline.

2   Liquefaction of Hydrogen

There are different pathways for cooling hydrogen gas down to its boiling point, but they all require the same minimum specific exergy. The type of process selected depends on different parameters such as the real energy demand determined by the efficiencies of the single compressing and cooling steps, the amounts of irreversible losses, and the availability of the necessary systems and their costs (Cardella et al. 2017a). The minimum specific work (exergy) required for the liquefaction of hydrogen at ambient conditions is composed of:

– the work for cooling the gas to the boiling point determined by the Carnot cycle;
– the work for condensation of the gas;
– additional work necessary for the temperature dependent ortho–para conversion.

The total minimum (theoretical) energy required for liquefying hydrogen is 3.92 kW·h/kg or 14.1 MJ/kg.

The actual technical work required, however, is a minimum of 11.1 kW·h/kg of LH_2, corresponding to 33.3% of the LHV of hydrogen.

The first step in the liquefaction process is the precooling of the hydrogen, usually done with liquid nitrogen.

Fig. 1 Schematic of Claude process for hydrogen liquefaction
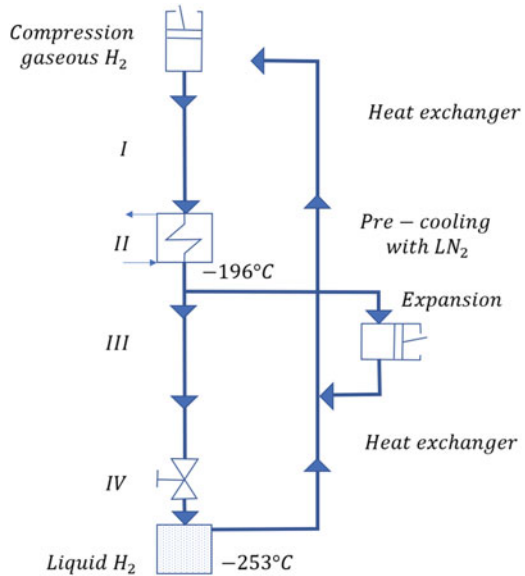
This precooling step is necessary, because if a gas is to cool down upon expansion, its temperature must be below the inversion temperature, which is 193 K for hydrogen at ambient pressure. Ortho–para conversion can be done adiabatically simply using a catalyst bed; however, this is at the expense of a temperature increase of the flowing hydrogen. There is also an isothermal method, placing the catalyst into LN_2 or LH_2 at boiling point with the temperature remaining constant.

Most liquefaction processes in practice use thermodynamic gas cycles with compression, heat exchange and expansion (Ratlamwala et al. 2012). The Linde–Hampson method is the simplest one, using isenthalpic expansion as a single thermodynamic process. Its efficiency, however, is not very high. Under optimized conditions, the liquefaction energy requirement is 13.12 kW·h/kg of LH_2 plus 6.7 kg of LN_2 per kg of LH_2 for precooling. Hampson applied the process in 1896 for the liquefaction of air, using air at ~20 MPa to be expanded to atmospheric pressure and passing the cooled air through a heat exchanger. A power of 3.7 kW was necessary to produce 1 L/h of liquid air.

A major step in the further improvement of the process was suggested by Georges Claude in 1902 with the use of an expansion engine, a cylinder with a moving piston, i.e. applying 'external work', to achieve lower temperatures than the Linde process (Krasae-in et al. 2010). Heat is removed as mechanical energy. Later, expansion engines were replaced with expansion turbines, first introduced by Kapitsa in 1936. The Claude process has since become the commonly applied method in large-scale liquefaction plants. Refrigeration is conducted in four principal steps (Fig. 1):

(1) compression of hydrogen gas at ambient temperature, removal of compression heat;
(2) cooling with liquid nitrogen (~80 K);

(3) expansion of a part of the hydrogen in an expansion turbine resulting in a further cooling of the residual hydrogen (80 → ~30 K);

(4) expansion of residual hydrogen in a Joule–Thomson valve until liquid state is reached.

The final cooling stage from 80 to 30 K represents the most energy intensive step. Possible solutions are either the 'classic' cascade refrigeration, with cycles using different coolants (as was demonstrated by Dewar), or the more economical Brayton cycle, with just one gaseous coolant that is sequentially expanded before it cools down the hydrogen in a countercurrent heat exchanger. Expansion step 3 would already be sufficient for liquefaction. But the Joule–Thomson expansion is applied for the final step to avoid two-phase flow in the expander (Li et al. 2021).

Variations of the dual-pressure Claude process as a large-scale liquefaction method have proven to be the optimal solution. The large-scale plants of today usually operate with six heat exchanging stages, the first of which is the LN_2 stage. The principle of the heat exchanger is to use the adiabatic expansion with smaller temperature drops per expansion step. The cooled gas is taken to precool the incoming gas, which then starts expansion at a lower temperature level ('progressive cooling').

Heat exchangers typically operate at pressures up to 6 MPa. They are compact to minimize heat input from outside and made of aluminium or chromium alloy steels with sufficiently high thermal conductivity and sufficiently low thermal expansion and they are resistant against hydrogen embrittlement. The ortho–para conversion is also done in several stages at different temperature levels achieving a para fraction of >95%. The maximum impurity level in re-gasified hydrogen is in the order of 1 ppm. Efficiencies are in the range of 60%.

A magnetic type of cooling was proposed by Debye and Giauque in 1926. The magnetic refrigeration method takes advantage of the magneto–caloric effect, i.e. the adiabatic temperature increase in the presence of a magnetic field in the working material, and a temperature decrease if the magnetic field is removed. The effect benefits from the isentropic demagnetization of a ferromagnetic material as a cooling process. The materials are slowly magnetized at the higher temperature before they are suddenly demagnetized and return to the initial state. The magnetic refrigeration cycle consists of the following steps:

(1) adiabatic magnetization in an external magnetic field causing alignment of the magnetic dipoles (thus reducing entropy, thus increasing temperature);

(2) transfer of the heat to a fluid (water, helium) at the same magnetic field strength;

(3) adiabatic demagnetization with removal of the magnetic field at constant entropy, i.e. decreasing the temperature;

(4) heat transfer from the gas (to be cooled) to the working material (solid).

The temperature can drop by 10–15 K depending on the strength of the magnetic field. The temperature change is maximal at ±25 K around the material's Curie point where it changes from ferromagnetic to paramagnetic. Various candidate materials with reversible transition and significant adiabatic temperature change are available

covering the total range between 20 and 300 K. The most appropriate materials to show a high magneto–caloric effect are based on gadolinium and some of its alloys, e.g. $Gd_5Si_2Ge_2$.

This method promises a compact cooling system design with a long lifetime, higher efficiencies and lower capital costs, since neither expanders nor compressors are required. The liquefaction work is estimated at the level of 7.3 kW·h/kg. Magnetic refrigeration, however, is still at the R&D level. Within the WE-NET project, a 10 kg/d capacity laboratory scale plant was constructed and operated.

A realistic unit power value for today's large-scale liquefaction plants in the USA comprising the whole process of cooling H_2 from ambient temperature to its liquid state at the boiling point, including all thermal and mechanical losses, is in the order of 12.5–15 kW·h/kg. This corresponds to an exergy efficiency of 26–32%.

The smaller scale facility in Ingolstadt, Germany, requires an energy input of ~15 kW·h/kg of H_2 or up to about 38% (45%) of the higher (lower) heating value of hydrogen. But even for the most recent liquefaction plants, efficiency has only improved slightly.

Of the costs for a typical hydrogen liquefaction plant, capital costs account for about 63%, mainly due to the compressors and brazed aluminium heat exchanger cold boxes. This is followed by power costs (~30%) and O&M (~7%). Further cost reductions are seen in the development of improved expanders and compressors, lower cost insulation and more efficient refrigeration, but also in the construction of larger scale plants with capacities up to 850 t/d and modular type systems with plant repeatability (Cardella et al. 2017b).

Starting with the Apollo space program in the USA in the 1960s, hydrogen liquefaction plants have been designed and constructed on a large-scale. Their concepts were based on the experience gained from the numerous small-scale plants previously developed in laboratories around the world and on the requirement of economically viable production of LH_2. Also, mobile hydrogen liquefaction stations on a small capacity scale have been constructed to meet the temporary demands, e.g. at testing sites. At present, the total global hydrogen liquefaction capacity amounts to approximately 290 t/d.

In Europe, it was the Ariane space program that started the construction of LH_2 production plants in the 1980s. There are now four plants in Europe with a total capacity of ~25 t/d. In the Russian Federation, two hydrogen liquefaction plants are reported to have been commissioned in the late 1960s at NIICHIMMASH in Serguiev Posad (Zagorsk), north of Moscow, to serve the fuel production for rocket and space systems. The capacities of the plants were 4.3 t/d and 7.2 t/d, respectively, for an annual production of up to 5000 t of LH_2. The first plant still seems to be in operation. Liquid hydrogen production in China and in India (since 1996) is only temporary and dedicated to their respective space rocket developments. In India, a 1 t/d capacity plant was constructed for the Indian Space Research Organization in Saggonda and a smaller plant for the Liquid Propulsion System Centre in Mahendragiri. One of the first hydrogen liquefaction facilities in Japan has been operating since 1977 at the Noshiro Test Centre (Akita prefecture) with a production capacity of ~50 kg/d for rocket propulsion experiments.

Recently, in addition to the existing Japanese space programme, smaller scale production of LH_2 started as part of the current national hydrogen and fuel cell programme. There appears to be a growing market for smaller facilities to serve the needs for LH_2 fuelled vehicles.

3   Storage of Hydrogen

Unlike electricity, hydrogen can be conveniently stored. The major storage options are at high pressures, low temperatures, in porous materials or in the form of (complex) metal hydrides. Due to its low volume related energy density, hydrogen requires a comparatively large volume for storage. While its gravimetric density is three times that of gasoline, the volumetric density is only 25% (Broom 2011). What is at first surprising is the fact that even 1 m³ of liquid hydrogen has, at 71 kg, a lower H_2 mass content than other chemical hydrogen storage media, e.g. gasoline (84 kg), ammonia (136 kg) and even water (111 kg) as shown in Table 1.

A proven technology for storage systems for stationary applications is the steel bottle/tube bundle, based on the use of steel as a structural material and involving gas pressures up to 23 MPa. These systems are essentially used at industrial chemical/metallurgical plants and distribution centers. The storage of compressed hydrogen in high pressure cylinders is bulky and rather expensive compared with the small quantity of hydrogen stored.

A significant amount of energy is needed to compress the gas (e.g. 9% of the stored energy for a 70 MPa tank). The compression process may be isothermal or adiabatic. The difference is the final temperature of the compressed medium remaining constant in the former and rising considerably in the latter case. Multistage compressors with intercoolers operate somewhere in between isothermal and adiabatic compression. In the near term, gaseous hydrogen storage might become possible at a mass fraction of up to 9% (Yanxing et al. 2019).

Table 1   Hydrogen density in different forms of storage

Fuel	Formula	Density (kg/m³)	Energy per mass (kJ/kg)	Energy per volume (GJ/m³)	H_2 density (kg H_2/m³)
Hydrogen	H_2	0.09	141,890	0.013	0.09
LH_2	H_2	71	141,890	9.9	71
LNG (Methane)	CH_4	423	55,530	20.5	106
LPG (Propane)	C_3H_8	581	50,400	25.2	106
Gasoline (octane)	C_8H_{18}	745	47,400	30.4–34.8	118
Methanol	CH_3OH	793	22,700	18	99
Ethanol	C_2H_5OH	794	29,900	23.5	104
Methylcyclohexane.	C_7H_{14}	862	42,500	26	9 96
Ammonia	NH_3	771	22,500	17.4	136
Water	H_2O	1000			111

A classification of high pressure tanks for hydrogen storage in vehicles is given in four categories, with Type 1 being the classic heavy, all-metal tanks, Type 2 being metal tanks with a glass fibre wrapping around the cylindrical part, which takes approximately 50% of the pressure load, Type 3 being light-weight tanks made of composite materials (carbon fibre) with a metallic liner inside, and Type 4 being composite tanks with a polymer liner. The weight reduction for Type 3 and 4 tanks is 70% compared with Type 1 tanks.

The principal advantage of composite material is its light weight, reducing total weight by 25–75% compared with a metal tank. For the new generation of pressurized H_2 tanks for vehicle applications designed for 70 MPa, the development of a thermoplastic polymer liner which ensures a maximum loss rate of 1 cm^3 of H_2 per liter of volume per hour and good mechanical strength in the temperature range of − 40 to +85 °C are important tasks.

Compressed gas in Type III and Type IV tanks is currently the preferred method for on-board vehicular storage. The very high gas storage pressure of 70 MPa will be a practical optimum required to contain a sufficient driving range of fuel, whereas 20–25 MPa is the typical pressure level for stationary hydrogen storage, for instance at a hydrogen refueling station. Hydrogen vehicle pressure tanks for pressures of 35 MPa have already reached a commercial stage for fleet vehicles. They are relatively expensive, and the high operating pressures give rise to safety concerns in the event of an accident. The targets set by the Strategic Research Agenda are (vehicle range of 500–600 km): 5 kg of storage at 70 MPa (~12 MPa at 20 °C), with hydrogen delivery temperatures between −40 °C and +85 °C and a lifetime of at least 1500 cycles. Vehicle tanks are fitted with various safety and monitoring related components.

While short term storage of hydrogen takes place in spherical high pressure tanks, long term underground storage in geological formations may represent a low cost technology in the capacity range of 100 GW·h. Very large quantities of hydrogen can be stored as a compressed gas in salt caverns or deep saline aquifers. Typical parameters are 700,000 m^3 of geometrical volume and a maximum operating pressure of 20 MPa. If the roof of the cavern is at a depth of ~1000 m, the net storage capacity will be around 6000 t with a cushion gas, i.e. the gas contents at minimum pressure ensuring easy recovery, to be around 3000 t hydrogen. Maximum withdrawal rates are about 10% of the storage capacity per day. In a natural storage volume, the ceiling structure must be additionally sealed by water in the capillaries. Natural loss of hydrogen from diffusion through rock and operating loss are estimated to amount to ~5% per cycle. Centralized underground bulk storage facilities favor the use of centralized hydrogen production (such as by nuclear energy) rather than hydrogen transportation from dispersed sources (Böttcher et al. 2017).

The safe and economic long-term storage of gases, primarily natural gas, in depleted gas fields and natural aquifer formations has been standard engineering practice for many decades (Kharel and Shabani 2018). There are two existing underground hydrogen storage sites, including an 8000 t capacity cavern in the USA and another one under construction. In Teesside, UK, three smaller caverns with 200–300 t of H_2 each have been in operation for many years. Other examples

are a large aquifer in Beynes, France, with a value of 364×106 Nm^3 of town gas with a 56% share of hydrogen, and an exploited natural gas field in Amarillo, TX, which contains 840×106 Nm^3 of helium. In addition, co-storage of hydrogen with natural gas has been proposed. Commercial hydrogen storage technology will be based on natural gas storage technology. There are 417 locations in the USA where natural gas is stored, with a total storage capacity greater than 2.4×1012 Nm^3. Germany currently has about 170 caverns in use for the storage of natural gas for seasonal load balancing, shutdown and trading reserve. Salt caverns are the ideal and currently the only underground facilities for hydrogen gas storage. Salt rock is highly gastight, does not react with hydrogen (or natural gas), and has low specific construction cost. The research will look at other storage options like aquifers or buried cavern tanks for smaller quantities.

Storage of hydrogen in the liquid phase is highly beneficial due to its high energy storage density and is practicable in many applications. Storage of larger amounts as liquid allows for lower central storage costs and provides greater flexibility (Valenti 2016). More storage capacity leads to a higher utilization rate of a hydrogen consuming plant. Liquid hydrogen is particularly demanded where the hydrogen is needed at a high purity level and where volume and weight are an issue such as in the transportation sector. The disadvantages are special handling requirements, boiloff losses, the need to control temperature stability to avoid overpressure, and most importantly, the liquefaction energy requirement. LH$_2$ storage technology is commercially available in a wide range.

Vessels are manufactured in sizes from 0.1 to several thousands of cubic meters.

Because of its low temperature, liquid hydrogen must be stored in an effectively insulated container, a dewar or 'cryostat'. The principal design of a storage tank is a double-walled, vacuum jacketed fluid container (Fig. 2).

The outer tank serves as a protection for the inner tank against impacts from outside as well as of the neighbourhood if the inner tank fails. The space between the two vessels serves as an insulation layer to minimize heat transfer to the inside. The supporting structure and interconnections have to fix the inner shell, but also ensure that it can freely undergo contraction and expansion due to the numerous temperature cycles (refills) that may occur during the tank's lifetime. Also, heat transfer from the outside must be minimized. For large vessels, even more complex structural design is required. The ideal shape of the vessel is spherical because of the minimum surface to volume ratio and the more uniform distribution of stresses and strains.

A multilayer foil insulation is usually chosen for tank sizes up to 300 m^3 to minimize the transport of radiation heat. It consists of some 60–100 layers of reflective foils fixed on the outside of the inner vessel, with a total thickness of at least 20 mm (the layered type of insulation is usually called superinsulation). The remaining void volume of the intermediate space basically serves as vacuum jacket to avoid air condensation on the cold surfaces and heat transport by convection or residual gas conduction.

Maximum and minimum design temperatures are determined by the loss of strength of the storage walls at the higher end and by loss of ductility (embrittlement) at the lower end. A relief valve should be designed to handle abnormal operating
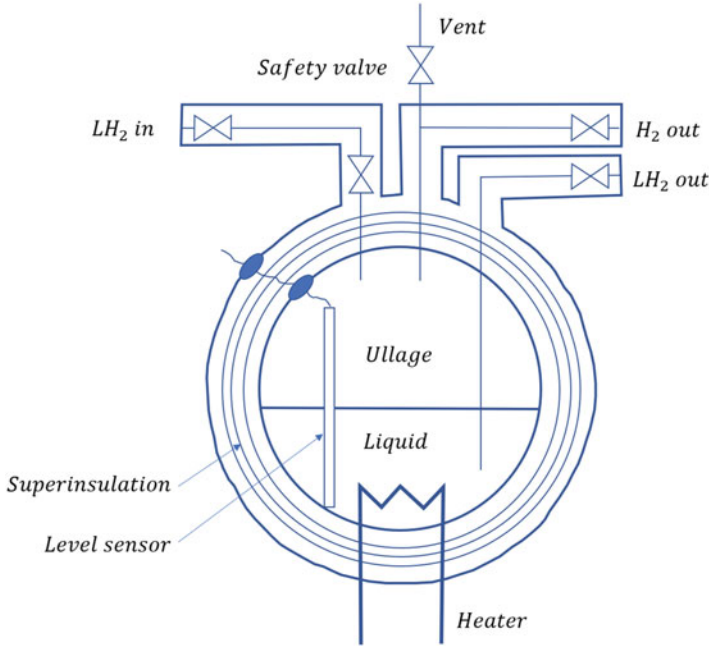
Fig. 2 Principal schematic of LH$_2$ tank

conditions such as overfilling. It should open at pressures less than or equal to the design pressure to allow a relief such that the pressure does not exceed 110% of the design pressure (Okonkwo et al. 2023).

Depending on the quality of the insulation and the surface to volume ratio, a certain fraction of the stored cryogen is an unavoidable boiloff to keep the rest cold. This amount is in the order of a few per cent per day for a passenger car tank and decreases with increasing volume to 0.4%/d for a 50 m^3 cryogenic tank and an estimated 0.06%/d for a 20,000 m^3 LH$_2$ tank. Overpressures exceeding specified limits after a certain time, the so-called lock-up time, are relieved via a boiloff valve and a safety valve.

Liquid hydrogen will be expelled from the container by pressurization. This can be done by either a pressurizing gas from an external source or a vaporizer in the form of a heat exchanger which receives liquid from the container by means of a pump or gravity and sends the gas into the ullage space. Some of the liquefaction work can potentially be recovered when the liquid is vaporized, which is a matter of downstream engineering technology.

The theoretical maximum is 10% of the energy invested. The autonomy of the storage system, i.e. the time without any loss of the contents, is typically 30 days.

Appropriate materials used for a cryogenic tank are carbon steel for the outer vessel and stainless steel or aluminium for the inner vessel. Tubing from the inner vessel to the outside is generally made of stainless steel with vacuum-sealed

transition on the cold side. Concerning further weight reduction, fibre reinforced (composite) materials are being investigated to be used not only for high pressure tanks, but also for cryo-tanks, and with a specific energy storage capacity similar to that of conventional tanks. The advantages would not only be the higher strength compared with steel and the lower weight, but also, due to the lower pressure, the possibility to adjust the shape of the tank to the vehicle structure. On the other hand, composites are prone to enhanced embrittlement and exhibit an anisotropic thermal expansion, almost none in the fiber direction and a high one perpendicular to the fiber direction (Zhang et al. 2019).

Large scale LH_2 tanks at the production site typically have a capacity of more than 100 t (~1400 m^3). The ullage gas carries a large refrigeration potential, which is being recovered for the liquefaction process via a vapor return line whenever practical. Tanks at the utilization sites are usually smaller, with capacities from 110 up to 2500 kg for vertical tanks or up to 5300 kg for horizontal tanks. The vessels usually operate with an overpressure of 1.2 MPa.

Large stationary LH_2 tanks usually have an additional outer wall with the space filled with LN_2 (Abdin et al. 2021). Inner vessel walls are preferably thin due to cost and cooling, whereas the outer walls should be thick for the purpose of stability and stress uptake. Most of the large vessels are of a spherical shape. Lock-up times are in the order of 50 h.

Boiloff losses can also be reduced by making sure that most of the LH_2 to be filled is para-hydrogen.

The world's largest LH_2 tank is reported to be located at the Baykonur Cryogenic Centre in the Russian Federation with a total volume of 5600 m^3. At the NASA Kennedy Space Centre (KSC) in the USA, two identical ball shaped tanks have been constructed which are used within the space shuttle program. The tanks are 3800 m^3 double-walled, vacuum perlite insulated spherical storage vessels. The outer sphere is made of carbon steel with an inside diameter of 21.34 m, and the inner sphere is made of austenitic stainless steel with an inside diameter of 18.75 m. With maximum nominal LH_2 contents of 3218 m^3, the ullage is about 15%. The tank operated at a pressure of 620 kPa has a boiloff rate of 0.025%/d or about 800 L/d.

Other advanced hydrogen storage methods include metallic and chemical hydrides, amides, alanate storage systems and carbon nanotubes. Solid metal and chemical systems offer some unique storage solutions for hydrogen, with the main challenges at the current time being their weight and their slow response time during refuelling. The interstitial storage of hydrogen in carbon nanotubes is another concept with potential for very light weight hydrogen storage, but the R&D is still preliminary (Liu et al. 2010). In addition, several other storage systems and mechanisms may be promising, including the use of sponge iron and glass microspheres.

In rechargeable solid state storage, H_2 is absorbed at interstitial sites in intermetallic compounds or stored via phase transitions in complex hydrides. In both cases, the loading with hydrogen is connected with the release of heat (hydrogenation enthalpy) which must be removed. The heat is the enthalpy (heat of formation) of the reaction and is an indication of the strength of the metal–hydrogen bond in the metal hydride phase. When molecular hydrogen from the hydrogen gas comes into contact

Table 2 Energy capacity

Material	Volumetric capacity (kWh/l)	Gravimetric capacity (% total weight)
MgH_2	3.65	7.6
$FeTiH_2$	3.37	1.89
Mg_2NiH_4	3.31	3.6
$LaNi_5H_6$	3.09	1.37
H_2 liquid at 20 K	2.36	100
H_2 gas at 80 MPa	1.54	100
H_2 gas at 50 MPa	1.11	100

with the surface of a hydrogen storage metal hydride material, it dissociates into atomic hydrogen and distributes compactly throughout the metal lattice (Davoodabadi et al. 2021). For refueling a hydrogen driven vehicle with typically 5 kg within a few minutes, a power in the order of MW is involved.

Heat transfer in this order of magnitude requires large, heavy and expensive equipment. Storage materials with acceptable H_2 density are still slower than what is required for rapid refueling. The hydrogen releasing step takes place in the form of a catalyzed hydrolysis reaction which is achieved by means of excess of water. Characteristics to be considered are solubility, excess water, hydration of by-products, reactivity of the catalyst and lifetime.

The advantages of solid state storage are its safety, since low pressures are involved, and its high volumetric storage capacity. The disadvantages are the low gravimetric absorption capacity (of most hydrides) and the high cost. Volumetric and gravimetric capacities are listed in Table 2 for selected hydrides and are compared with gaseous and liquid hydrogen.

Complex hydrides are also considered promising hydrogen storage materials with capacities of up to 5.5 wt% of H_2 (compared with 1.5 wt% of conventional hydrides). These are low density powdery substances consisting of <10 μm particles, but with a high BET surface in the order of several tens of m^2/g. An example is $NaAlH_4$ which was discovered to exhibit enormous hydrogen discharging and recharging ability if doped with Ti as a catalyst. In terms of safety, hydrides have the advantage that heat is consumed in the hydrogen discharge reaction. A safety issue with complex hydrides containing $NaAlH_4$, $LiNH_2$, $Mg(NH_2)_2$, LiH and $LiBH_4$ is that they were found to be flammable, pyrophoric and water reactive. Additionally, dust cloud explosions may be triggered by spark ignition (Lamb and Webb 2022).

An innovative hydrogen storage system developed by the Austrian Institute of Technology (AIT) uses hollow microspheres for combined high pressure and chemical hydrogen storage. Water carrying the microspheres with a 5–200 μm diameter is injected together with $NaBH_4$ into a reaction chamber where a catalytic reaction takes place to produce hydrogen, $NaBO_2$ and heat. The glass spheres, which are gas-tight at ambient temperature, store hydrogen at high pressures of 14–70 MPa. Such a system can theoretically reach hydrogen storage capacities of up to 10 wt%.

4   Transportation/Distribution of Hydrogen

Centrally produced hydrogen must be transported to markets. The development of a large hydrogen transmission and distribution infrastructure is a key challenge. The main transportation modes are water, road, rail and pipelines which form a distribution system for the products to the final consumer. Storage structures are located within the transportation network to accommodate the capacities of different transportation modes (Ishaq et al. 2022). The delivery methods selected are determined chiefly by the production volume and the delivery distance. Small and medium-sized hydrogen consumers use truck, rail and barge transportation modes for hydrogen in either liquid or gaseous form over longer distances. Chemical and petrochemical industries, which produce/consume large quantities of hydrogen, use pipelines and compressors for transportation of the hydrogen gas over short distances.

The transportation of hydrogen in the liquid state is considered practicable if it is consumed as a liquid, if the distance is sufficiently long, if large quantities need to be stored, or if high purity hydrogen is required. For liquid hydrogen, the costs of the equipment needed at the customer's site (cryogenic storage tank, vaporizer) and installation are much higher than those for handling gaseous hydrogen. On the other hand, customers that need high pressure hydrogen would need the installation of compression and storage equipment if the hydrogen is delivered as a liquid. Such requirements mainly determine the choice of the more cost-effective transportation mode (Reuß et al. 2021).

For sites where no hydrogen production plant is available and only smaller quantities of hydrogen are needed, pipeline delivery methods usually are not competitive. Very small quantities of up to 50 kg of H_2 are mostly sold and distributed via high pressure cylinders. Larger quantities are more likely delivered by tube trailers and liquid tank trucks. A liquid is easier to transport and easier to handle than compressed gas. But compressed gas transportation via tube trailer has lower power requirements and slightly lower capital costs. Distance is the main deciding factor between liquid and gaseous hydrogen (Demir and Dincer 2018).

Most of the hydrogen produced today is transported over short distances only, mainly by pipeline, e.g. on-site in refineries. Pipeline distribution is most effective for large flows and currently amounts to approximately 240 t/d, with pipeline diameters usually ranging between 10 and 300 mm and delivery pressures of up to 10 MPa. Pipelines become competitive when the demand grows to large capacities. The pipeline option may allow carrying much higher capacities of hydrogen at no additional cost. Energy loss during transportation is about 4% of the energy content.

Several networks for the commercial transmission and distribution of hydrogen gas have been developed and are being operated by the industrial gas industry with a good safety record. As of 2006, the US hydrogen pipeline network totalled ~2000 km in length, not considered on-site and in-plant hydrogen piping. This, however, is still small compared with about 475,000 km of natural gas transmission lines in the USA or more than 2 million km worldwide. Because of concerns over potential leakage, the hydrogen pipes tend to be much smaller in diameter.

Special positive displacement compressors are also required to move hydrogen through the pipelines (Tian et al. 2022). The length of hydrogen gas piping tends to be short, because it is usually less expensive to transport the hydrogen feedstock, such as natural gas, through the existing pipeline network than to move the hydrogen itself through new piping systems.

The costs of a centralized hydrogen transmission and distribution system will depend on numerous factors such as distance to the consumer, pipeline diameter, quality and nature of the pipeline materials, operating pressures, rights-of-way, and how the applicable environmental and safety issues in the production, transmission, distribution and dispensing of hydrogen are addressed (Yang et al. 2021). Furthermore, pipelines that carry pure hydrogen will require special construction and materials in order to avoid issues of steel embrittlement and leakage. Alternatives to metallic pipelines are polymer and fiber reinforced polymer pipelines.

Larger grids for gaseous hydrogen connecting industrial producers with industrial consumers are being operated in Europe and the USA. The largest agglomeration of chemical and petrochemical industries in Europe is located in the Netherlands and Belgium where Air Liquide of France is operating a more than 900 km pipeline grid for hydrogen transportation, currently connecting eight hydrogen units. The Ruhr-H2 pipeline, also operated by Air Liquide, connects four large scale production plants and six industrial consumers. The capacity of the pipeline is 40,000 Nm^3/h at pressures up to 2.5 MPa. In the USA, most of the approximately 1200 miles (~1930 km) of hydrogen pipelines are concentrated in the states of Texas and Louisiana, where the majority of the US refinery industry is located.

If the use of hydrogen pipelines were to be expanded, possible embrittlement problems for pipes and fittings would have to be considered. The technology is available to prevent embrittlement, but depending on the configuration being considered, distribution costs may be affected (Laadel et al. 2022).

Pipeline transportation of liquid hydrogen is realized on a small scale and short range. Similar to LH_2 storage tanks, pipelines are of double-wall design and vacuum jacketed. Because of the high costs increasing linearly with distance, LH_2 pipelines are economically attractive only for short distances. The transfer is done by pressure difference rather than by pumps. Major concerns, apart from heat leakage, are the mechanical stress imposed on the inner line due to contraction/expansion, pressure oscillations upon cooldown and two-phase flow. The Kennedy Space Centre uses a LH_2 (and LOX) pipeline of ~600 m length with an inner pipe diameter of 150 mm. The flow rates are up to 250 m^3/min of LH_2 and 100 m^3/min of LOX.

A government funded project in Germany, Integrated Cable Energy for Fuel and Power or icefuel, which began in 2006, aims at a new, highly efficient infrastructure for transport, storage and conversion of energy. A system for energy storage and the transportation of both chemical and electrical energy as part of a decentralized infrastructure will be developed and tested. The goal is to design a flexible, thermally insulated line for the simultaneous transport of cryogenic liquids (LH_2 or LNG), electricity and data through a high temperature superconducting material (Fig. 3).
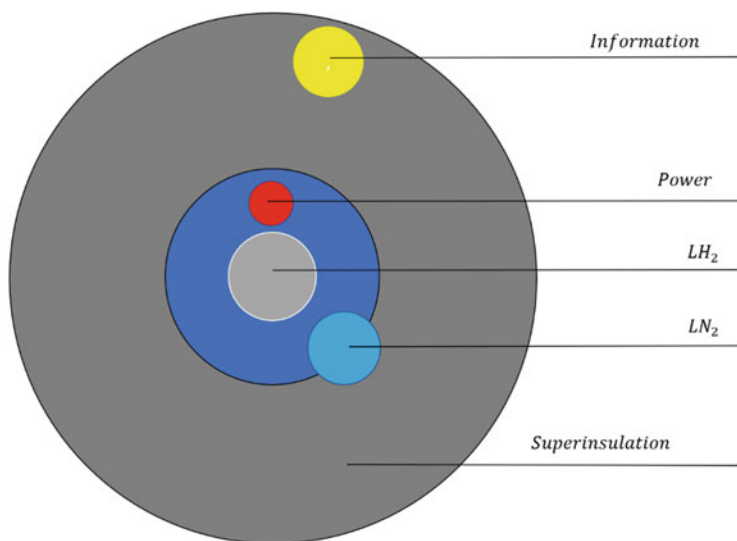
Fig. 3 Schematic of an icefuel cable

Due to the high energy density of LH$_2$, an energy flux of ~10 MW could be realized through a low viscosity pipeline of less than 20 mm diameter over a 10 km distance. Tests up to now on a laboratory scale have comprised cable samples with 40 mm diameter and lengths up to several tens of meters for a transport capacity of 200–400 kW (LHV). The project also includes the development of infrastructure components such as heat exchangers, junctions, sensors and actuators. In a later stage, it is planned to demonstrate the concept on pilot plant scale.

Unlike conventional fuels, the transportation of hydrogen by trucks is limited with regard to volume rather than weight. The amount of gaseous hydrogen transported in pressure tube trailers ranges between 100 kg for short semi-trailers and 300 kg for the larger trailers, equivalent to about 3300 Nm^3. The hydrogen load may even go up to 600 kg with higher volume tubes in carbon fiber composite structures, still light compared to the 40 t gross weight of a tank truck. The distribution of hydrogen as a compressed gas is mainly done for shorter distances (200–300 km) and smaller consumers (<250 Nm^3/h).

Today's modern liquid hydrogen trucks can carry up to 3.5–4.2 t, or more than 50 m^3 of LH$_2$, which is at least ten times more than a tube trailer for gaseous H$_2$. The typical pressure in superinsulated tanks with an additional LN$_2$ shield is 0.15–0.2 MPa (maximum pressure: 1.11 MPa). The potential hazard of stratification in the tank does not really occur in transportation, because the liquid is stirred by the movement and kept in thermal equilibrium.

LH$_2$ trucks will preferably be used to meet the demands of a growing market in the near future. This delivery method is typically limited to small and medium sized quantities and distances of less than 500 km. Replacing conventional gasoline fuel with liquid hydrogen would increase the number of tank truck transports by a factor

of three. Design criteria for a LH_2 container used in transportation are essentially the same as for LH_2 storage containers. The differences involve, for example, the degree of insulation required, which is lower in short term transportation compared with long term storage. Also, in general, geometry and weight are limited.

Barges carrying liquid hydrogen have been used for fuel supply within the US and French space programs.

Storage containers with a capacity of 947 m^3 of LH_2 have been used on the way from Louisiana to Florida since the NASA Apollo project, today serving the space shuttle. The European Ariane project was supplied with LH_2 by maritime transportation from New Orleans to Kourou, French Guiana, in 20 m^3 storage vessels with vapor or LN_2 cooled multilayer insulation. These transports were discontinued with the beginning of the operation of the 5 t/d capacity, on-site liquefaction plant in 1990.

Various ship designs were developed in the 1990s within the Euro–Quebec project for future maritime transportation. Future LH_2 tank ships are designed for a load capacity of 125,000 m^3 to take up 8150 t of LH_2. The proposed hydrogen gas turbine propulsion system will be fueled by the LH_2 as well as the boiloff losses. The system allows regaining a part of the technical work that was introduced during the liquefaction process (Enhanced Cryogen Exergy Recovery System (ECERS)). Flowsheet analysis of the exergy or technically usable energy conducted within the Euro-Quebec project for maritime LH_2 transportation (from Canada to Europe) yielded an overall estimated efficiency of the system of 42%.

A fraction of 10.4% of the primary energy input is needed for the hydrogen fueled propulsion system of the ship.

Other major losses are due to the electrolysis step and subsequent liquefaction of the hydrogen gas (Yin and Ju 2020).

Studies of LH_2 maritime transportation were also conducted in Japan based on their broad experience of LNG ship construction. Within the WE-NET project, ships were conceived at a scale to deliver a 10 d supply of LH_2 as fuel to a 1000 MW (e) gas turbine power plant consuming 1200 t of LH_2 per day. With the additional consumption of H_2 for the 6000 sea mile trip (~11,100 km) every 10 days plus estimated losses, one ship transport was to carry some 200,000 m^3 (or ~ 14,000 t) of LH_2.

Hydrogen also can be transported using hydrogen rich carrier compounds such as ethanol, methanol, gasoline and ammonia. Such carriers offer lower transportation costs, because they are liquids at room temperature and are usually easier to handle than cryogenic hydrogen. But they also require an extra transformation step with costs that must be weighed against the cost savings associated with transporting low pressure liquids.

The key components of a chemical energy transmission system (CETS) or a chemical heat pipe are a primary energy source (fossil, renewable, nuclear) to provide heat to an input catalyst reactor. In this reactor, a mixture of appropriate materials is chosen for the desired endothermic reaction, i.e. for storing energy in the newly created products. After transportation of the product gas mixture at ambient temperatures, the reverse exothermic chemical reaction in an output catalyst

converter helps to extract the stored heat for consumption as high grade or low grade heat or in a turbine. In a closed cycle, product materials are then returned to the heat source.

Unlike liquid hydrogen, chemical compounds with hydrogen provide an economical method of seasonal storage of energy. The reactions must be reversible, rapid, and as complete as possible to avoid unwanted secondary products. They should have a high efficiency and a high reaction enthalpy in order to minimize the masses to be transported, plant and pipe sizes, and operating cost. They must be controllable to allow intermittent storage/retrieval operation. Furthermore, feedstock and products should be inexpensive, non-corrosive, non-toxic, and easy and safe to handle. CETS have to compete against hydrogen pipeline systems or the electricity grid.

Among a wide variety of potential energy carriers, the gas-based system 'synthesis gas/methane' is one of the most promising and has been the subject of research, development and demonstration considering a connection to both nuclear and solar as the primary source of process heat because of the following advantages:

– chemical reactions proceed in one direction under certain conditions and in the reverse direction under other conditions;
– the reaction is heat consuming in the one direction and heat releasing in the other direction;
– the process takes place only in the presence of a catalyst, otherwise the system remains in a stable status without any reactions;
– all (partial) reaction steps are well known and widely applied in conventional technologies;
– the pipelines required correspond to the former town gas and present natural gas systems.

This methane based CETS became known under the acronym EVA/ADAM with a nuclear energy source and has been demonstrated in Germany, the USA and the Russian Federation.

The CO_2 reforming process of methane has been studied as a chemical transportation system since 1980 as an alternative, in order to overcome some of the potential difficulties. In contrast to the CH_4–H_2O system, a third pipe is not required since it is not necessary to clean the water. Thus, an open cycle system could be adopted. At the Weizmann Institute of Science (WIS) in Rehovot, Israel, a 480 kW solar steam/CO_2 methane reformer was designed, constructed and operated intermittently over 2 years as a complete solar heat pipe system. The insulated, pentagon shaped reformer box contained eight tubes (length: 6.4 m, diameter: 51 mm) in two rows made of Inconel 617. The 4.5 m long heated section contained the catalyst. In the case of CO_2 reforming, which is thermodynamically more efficient and easier to operate under changing conditions (as in solar), the catalyst was 1% Ru on alumina. The tubes were directly heated by the solar radiation entering through a 600 mm aperture and reflected from the walls of the enclosure. The heat take-up was found to be quite uniform, with no local overheating tendency. The maximum average surface temperature was ~930 °C and the heat flux was in the range of 80–84 kW/m^2. The

flow rate of the process gas, which could be varied over a wide range of $CO_2/H_2O/CH_4$ feed mixtures, was limited to ~300 kg/h due to higher than expected pressure drop. It entered the reformer tubes at 500 °C and 1.6–1.8 MPa and left at ~800–830 °C.

Another example is the hydrogenation of toluene (C_7H_8) on the supply site and the hydrogen evolution from methylcyclohexane (MCH, C_7H_{14}) on the demand site. This system offers the advantage of safe and easy transportation at ambient temperatures in chemical tank ships or trucks and mild reaction conditions, with a high yield of toluene in the reforming reaction. The gravimetric storage capacity of MCH for hydrogen is 6.1 wt% or 47 kg of H_2 per m^3.

Many candidates for closed loop reversible chemical energy transportation or seasonal storage systems with varying operating temperature ranges and storage capabilities have been identified. Certain limitations of the long distance heat transport are given by its restricted storage capabilities, by the limited temperature ranges and by the complex distribution systems required.

5 Hydrogen Infrastructure Overview

To make renewable energies universally usable with the help of green hydrogen, in addition to sufficient capacity for green electricity and hydrogen generation, a storage and transport network infrastructure is required that can effectively and reliably serve the needs of business and consumers (Hardman and Steinberger-Wilckens 2014).

Regardless of how the hydrogen is generated, if it is not produced directly at the point of use, it must be transported.

There are various technical processes for this: for example, as a gas in high-pressure containers, as liquefied gas in thermally-insulated containers, further processed into methanol or ammonia in liquid form, or chemically dissolved in a carrier medium using the so-called 'Liquid Organic Hydrogen Carrier' ('LOHC').

Transport via pipelines is particularly economical. Due to the high calorific value and the compressibility of the hydrogen, an extraordinarily high energy density can be achieved. In comparison to a 380 kV double system overhead line with 1.5 GW, a gas line (PN 80, DN 1000) can transmit up to ten times the power in natural gas and hydrogen operation, at around a fourteenth of the specific costs.

Pipeline systems at a length of several hundred kilometers each are already in use in pure hydrogen operation worldwide.

The existing pipeline routes represent an extremely valuable element of the transmission system and offer the opportunity to build a climate-neutral hydrogen industry in a manageable time and with little investment (Kim et al. 2022).

As measuring devices, compressors and fittings can be exchanged relatively easily, replacing or building new pipelines would be very expensive. In addition to the technical costs, the necessary spatial planning and planning approval procedures are extremely time- and cost-intensive.

In the best-case scenario, the process takes 5–7 years from initial planning to commissioning. The gas network's pipeline routes, including their rights of way and use, are however available and accepted by the population.

Contrary to popular belief, the transport energy density of hydrogen is only slightly lower than that of natural gas.

Therefore, the switch from natural gas to hydrogen has little impact on the capacity of a pipeline to transport energy.

The upper calorific value of natural gas at around 11 kWh/Nm^3 is about three times higher than that of hydrogen at 3.5 kWh/Nm^3, so that at the same pressure, around three times the volume of hydrogen is required to keep the energy content constant.

When comparing the energy flow of two gases through a pipeline, it is not only the volume that is important, but above all the parameters of density, flow velocity, and pressure. As hydrogen has a density nine times lower and three times the flow rate of natural gas, almost three times the volume of hydrogen can be transported in the pipeline at the same pressure and during the same time.

Relevant studies and previous practical knowledge indicate that it is possible to convert the existing steel pipelines from natural gas to hydrogen operation to the extent required for the ramp-up of a hydrogen industry (Laureys et al. 2022).

A significant reduction in the service life of high-pressure lines due to the influence of hydrogen does not seem likely.

Nevertheless, further examination is needed on whether the operating parameters must be adjusted for certain types of steel and operating conditions. In the case of fittings and control valves, the suitability for hydrogen of the membranes and seals used must also be determined.

In the case of safety shut-off valves and pressure regulators, it must be clarified if the control and regulating functions must be adapted for the flow properties of hydrogen.

The specific conditions of the existing infrastructure should be inspected and assessed and the relevant codes and regulations consulted prior to determining if the pipelines are suitable.

To be fed into the transmission system, the hydrogen must be compressed to the operating pressure of the network.

Compressor stations at certain intervals along the line ensure that the pressure is maintained despite loss of flow in the pipeline. To enable optimal utilization with high transport energy density in hydrogen operation, more and higher-power compressors are required than in natural gas operation.

For the planned pipeline projects with the short and medium-term expected amounts of hydrogen, the necessary compressor technologies are available in the form of 'tried and tested' piston compressors. In the long-term, where a nationwide switch to hydrogen with a transport requirement in the gigawatt range, the turbo-compressor concepts currently used will be optimized for hydrogen. It can be assumed that these will be available in a few years if the market demands them.

The generation of energy from renewable sources, such as wind power and photovoltaics is subject to strong natural fluctuations. In order to be able to use energy efficiently and according to need, large and flexible storage options are required that can compensate for these fluctuations. Electricity cannot provide the necessary large industrial capacities (especially via grid buffers and battery storage) for the foreseeable future at economically viable terms.

Alternatively, hydrogen is well suited as an energy source due to its compressibility and storage capacity in storage facilities and can supplement the electricity grid based on the gas storage facilities.

The operating regime of storage facilities in a gas infrastructure geared towards renewable energies differs fundamentally from previous natural gas operations. While natural gas storage primarily serves long-term security of supply, in hydrogen operation they primarily compensate for the short-term fluctuations in 'green' generation.

Therefore, cavern storage facilities are particularly suitable for storing hydrogen, as their flexible storage and retrieval options make them ideal for the fluctuating availability of renewable energy sources.

The success of a green hydrogen economy essentially depends on whether hydrogen can meet the needs of customers in a competitive way under future market conditions. In addition to technological developments for the efficient production of green hydrogen on an industrial scale, above all this requires uniform and appropriate framework conditions for the hydrogen market.

6   Conclusions

A hydrogen infrastructure is the infrastructure of hydrogen pipeline transport, points of hydrogen production and hydrogen stations (sometimes clustered as a hydrogen highway) for distribution as well as the sale of hydrogen fuel. Hydrogen is being developed as an electrical energy storage medium. Hydrogen is produced, then compressed or liquefied, stored, and then converted back to electrical energy or heat or used as an input to (industrial) processes. Hydrogen can be used as a fuel for portable (vehicles) or stationary energy generation. Compared to pumped water storage, CAES and batteries, hydrogen has the advantage that it is a high energy density fuel that can be fed into the grid, stored or converted in ammonia and then stored. However, the development of production and transport infrastructure, and a functioning market for hydrogen is still in its infancy.

Blending hydrogen into natural gas networks and infrastructure is foreseen for the transition phase. Networks are expected to be based on the conversion of existing natural gas pipelines for cross-border transport. At present, hydrogen is being transported using the existing gas grid or with modifications to the existing gas pipelines, or through dedicated pipelines. Transport cost data indicates that pipelines have a clear cost advantage compared to other transport means, reinforcing the need for regulation.

The infrastructure needed in an economy in which hydrogen is primarily used as a transport fuel is very different from one in which its primary value is as a heating fuel. Today no major hydrogen pipeline networks exist, and no liquified hydrogen ships are in commercial operation.

An ongoing debate is how hydrogen will be delivered to demand centers, or in other words, what will be the preferred energy carrier. One option would be to generate carbon-free power and transmit it to residential, commercial, and industrial users. The electricity would then be used to produce hydrogen directly onsite. This approach eliminates hydrogen transmission costs at the expense of overburdening power grids already constrained by the need to transport increasing shares of renewable energy. Another option would be to pipe hydrogen directly to customers. While not impacting power grids, this approach requires upgrading existing natural gas pipelines to allow for increasing shares of hydrogen or building new hydrogen-dedicated infrastructure.

Admittedly, the use of natural gas infrastructure could significantly lower the overall cost of transporting hydrogen, both in terms of reduced investment in pipeline infrastructure and avoided investment in the expansion of the electricity grid. Still, a careful case-by-case evaluation is needed to determine the technical and economic feasibility of competing options together with the overall value chains implications of a transition from natural gas to hydrogen.

The conversion of existing gas infrastructures to hydrogen operation has the potential to achieve a breakthrough for the hydrogen industry.

Using existing storage and transport capacities, hydrogen, as the main pillar of energy transition, can reliably ensure security of supply during the change to renewable energy sources. In this way, energy transition – and sector integration specifically – can be promoted comparatively quickly and inexpensively along with the expansion of the power grids.

The technical challenges of hydrogen technology can already be largely addressed today. The anticipated progress and the use of digital solutions will lead to continuous improvements of the overall system. The utilization and interactions of gas and electricity grids can be increasingly and more effectively controlled to compensate for discrepancies between the generation of renewable energy and individual needs in national and international operations.

References

Abdin Z, Tang C, Liu Y et al (2021) Large-scale stationary hydrogen storage via liquid organic hydrogen carriers. iScience 24(9):102966. https://doi.org/10.1016/j.isci.2021.102966

Böttcher N, Görke UJ, Kolditz O et al (2017) Thermo-mechanical investigation of salt caverns for short-term hydrogen storage. Environ Earth Sci 76:98. https://doi.org/10.1007/s12665-017-6414-2

Broom DP (2011) Hydrogen storage materials the characterisation of their storage properties. https://doi.org/10.1007/978-0-85729-221-6

Cardella U, Decker L, Sundberg J et al (2017a) Process optimization for large-scale hydrogen liquefaction. Int J Hydrogen Energy 42(17):12339–12354. https://doi.org/10.1016/j.ijhydene.2017.03.167

Cardella U, Decker L, Klein H (2017b) Roadmap to economically viable hydrogen liquefaction. Int J Hydrogen Energy 42(19):13329–13338. https://doi.org/10.1016/j.ijhydene.2017.01.068

Davoodabadi A, Mahmoudi A, Ghasemi H (2021) The potential of hydrogen hydrate as a future hydrogen storage medium. iScience 24(1):101907. https://doi.org/10.1016/j.isci.2020.101907

Demir ME, Dincer I (2018) Cost assessment and evaluation of various hydrogen delivery scenarios. Int J Hydrogen Energy 43(22):10420–10430. https://doi.org/10.1016/j.ijhydene.2017.08.002

Hardman S, Steinberger-Wilckens R (2014) Mobile phone infrastructure development: lessons for the development of a hydrogen infrastructure. Int J Hydrogen Energy 39(16):8185–8193. https://doi.org/10.1016/j.ijhydene.2014.03.156

Ishaq H, Dincer I, Crawford C (2022) A review on hydrogen production and utilization: challenges and opportunities. Int J Hydrogen Energy 47(62):26238–26264. https://doi.org/10.1016/j.ijhydene.2021.11.149

Kharel S, Shabani B (2018) Hydrogen as a long-term large-scale energy storage solution to support renewables. Energies 11(10):2825. https://doi.org/10.3390/en11102825

Kim C, Cho SH, Cho SM et al (2022) Review of hydrogen infrastructure: the current status and roll-out strategy. Int J Hydrogen Energy 48(5):1701–1716. https://doi.org/10.1016/j.ijhydene.2022.10.053

Kovač A, Paranos M, Marciuš D (2021) Hydrogen in energy transition: a review. Int J Hydrogen Energy 46(16):10016–10035. https://doi.org/10.1016/j.ijhydene.2020.11.256

Krasae-in S, Stang JH, Neksa P (2010) Development of large-scale hydrogen liquefaction processes from 1898 to 2009. Int J Hydrogen Energy 35(10):4524–4533. https://doi.org/10.1016/j.ijhydene.2010.02.109

Laadel NE, El Mansori M, Kang N et al (2022) Permeation barriers for hydrogen embrittlement prevention in metals–A review on mechanisms, materials suitability and efficiency. Int J Hydrogen Energy 47(76):32707–32731. https://doi.org/10.1016/j.ijhydene.2022.07.164

Lamb KE, Webb CJ (2022) A quantitative review of slurries for hydrogen storage–Slush hydrogen, and metal and chemical hydrides in carrier liquids. J Alloys Compd 906:164235. https://doi.org/10.1016/j.jallcom.2022.164235

Laureys A, Depraetere R, Cauwels M (2022) Use of existing steel pipeline infrastructure for gaseous hydrogen storage and transport: a review of factors affecting hydrogen induced degradation. J Nat Gas Sci Eng 101:104534. https://doi.org/10.1016/j.jngse.2022.104534

Li J, Su Y, Yu B et al (2021) Influences of hydrogen blending on the Joule–Thomson coefficient of natural gas. ACS Omega 6(26):16722–16735. https://doi.org/10.1021/acsomega.1c00248

Liu C, Chen Y, Wu CZ et al (2010) Hydrogen storage in carbon nanotubes revisited. Carbon 48(2):452–455. https://doi.org/10.1016/j.carbon.2009.09.060

Noussan M, Raimondi PP, Scita R et al (2020) The role of green and blue hydrogen in the energy transition—A technological and geopolitical perspective. Sustainability 13(1):298. https://doi.org/10.3390/su13010298

Okonkwo PC, Belgacem IB, Mansir IB et al (2023) A focused review of the hydrogen storage tank embrittlement mechanism process. Int J Hydrogen Energy 48:12935–12948. https://doi.org/10.1016/j.ijhydene.2022.12.252

Ratlamwala TAH, Dincer I, Gadalla MA et al (2012) Thermodynamic analysis of a new renewable energy based hybrid system for hydrogen liquefaction. Int J Hydrogen Energy 37(23):18108–18117. https://doi.org/10.1016/j.ijhydene.2012.09.036

Reuß M, Dimos P, Léon A et al (2021) Hydrogen road transport analysis in the energy system: a case study for Germany through 2050. Energies 14(11):3166. https://doi.org/10.3390/en14113166

Schnettler A, Heunemann F, von dem Bussche C (2020) Hydrogen infrastructure –the pillar of energy transition The practical conversion of long-distance gas networks to hydrogen operation. Conference of the European Commission of 08.07.2020

Tian Z, Lv H, Zhou W et al (2022) Review on equipment configuration and operation process optimization of hydrogen refueling station. Int J Hydrogen Energy 47(5):3033–3053. https://doi.org/10.1016/j.ijhydene.2021.10.238

Valenti G (2016) Hydrogen liquefaction and liquid hydrogen storage. In: Compendium of hydrogen energy. https://doi.org/10.1016/B978-1-78242-362-1.00002-X

Wappler M, Unguder D, Lu X et al (2022) Building the green hydrogen market–Current state and outlook on green hydrogen demand and electrolyzer manufacturing. Int J Hydrogen Energy 47(79):33551–33570. https://doi.org/10.1016/j.ijhydene.2022.07.253

Yang Y, Ma C, Lian C et al (2021) Optimal power reallocation of large-scale grid-connected photovoltaic power station integrated with hydrogen production. J Clean Prod 298:126830. https://doi.org/10.1016/j.jclepro.2021.126830

Yanxing Z, Maoqiong G, Yuan Z et al (2019) Thermodynamics analysis of hydrogen storage based on compressed gaseous hydrogen, liquid hydrogen and cryo-compressed hydrogen. Int J Hydrogen Energy 44(31):16833–16840. https://doi.org/10.1016/j.ijhydene.2019.04.207

Yin L, Ju Y (2020) Review on the design and optimization of hydrogen liquefaction processes. Front Energy 14:530–544. https://doi.org/10.1007/s11708-019-0657-4

Zhang M, Lv H, Kang H et al (2019) A literature review of failure prediction and analysis methods for composite high-pressure hydrogen storage tanks. Int J Hydrogen Energy 44(47):25777–25799. https://doi.org/10.1016/j.ijhydene.2019.08.001

Hydrogen Storage

1 Introduction

Hydrogen can be stored as a gas, liquid, or as a part of a solid metal, polymer, or liquid hydride. Studies have indicated that large-scale storage could take place with gaseous hydrogen underground in aquifers, depleted petroleum or natural gas reservoirs, or man-made caverns from mining operations. One of the obstacles in using hydrogen as an automotive fuel is storing it safely and efficiently on board vehicles (Graez 2009; Chen and Zhu 2008). Although it is possible to store hydrogen as a high pressure gas in steel containers, there are drawbacks due to the weight of the storage containers and the safety hazard in the event of an accident. Other methods of storage for hydrogen include solid or liquid hydrides, low temperature cryogenic liquids, or a combination of the two.

Hydrogen (H_2) possesses a number of chemical and physical properties that have allowed it to be widely used in the synthesis and processing of materials in research laboratories as well as in industrial manufacturing. These uses are in addition to the emerging use of hydrogen in power generation technology, including transportation, as discussed in chapter "Hydrogen and Energy Transition". Except for situations such as in the petrochemical industry, in which hydrogen is utilized more or less immediately after its production from a hydrocarbon feedstock, most applications require that hydrogen be stored after its production by some method prior to its eventual endpoint usage. Many factors influence the physical state (i.e., gas, liquid, solid, or contained in a chemical substance) in which hydrogen will be stored and how it will be supplied for a specific application in those situations where hydrogen has been a well-established commodity, the physical state is well understood, and storage systems have been developed over the years. For example, hydrogen is often used as a reactant in laboratory research or in manufacturing. In these applications, compressed hydrogen gas is deployed in appropriate size cylinders at pressures up to about 200–300 bar. In addition, when hydrogen is used in a unique and critical capability (e.g., as a rocket propellant for launching spacecraft), then cryogenic
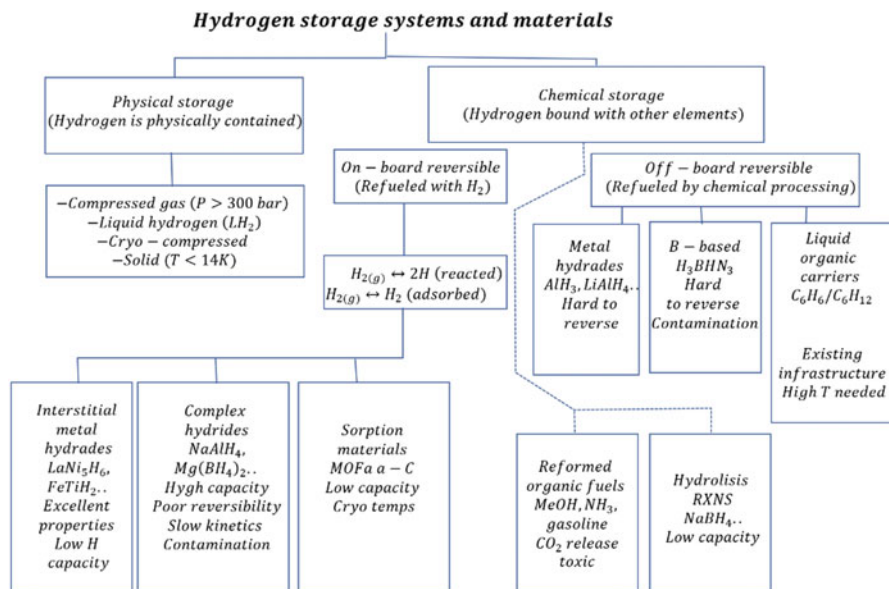
Fig. 1 Overview of hydrogen storage systems and materials

liquid hydrogen (LH_2) is used and stored in cryogenic containment vessels as part of the launch vehicle. On the other hand, whenever hydrogen is to be used in a role that would either replace existing technologies or serve a novel function, the current storage approaches generally must be heavily adapted, or new ones developed, to meet the different operating parameters and constraints (Hardy and Anton 2009).

Figure 1 lists the various physical states of hydrogen (solid, liquid, gas, chemical compound) that can, in principle, be used for hydrogen storage.

In the broadest sense, hydrogen can be contained either as a diatomic molecule (i.e., H_2) via physical constraints (i.e., in some kind of vessel) or as monatomic hydrogen (i.e., H atom) reacted and bonded with other elements in the form of chemical compounds or materials. Ideally, these hydrogen storage materials would be "reversible." By reversible, we mean that hydrogen gas can be directly used to reestablish the original hydrogen storage material after the original (stored) hydrogen has been used. Reversibility typically implies conditions of temperature and pressure such that the material can be regenerated "on-board" the vehicle. These are termed "on-board-reversible" materials. Another set of the chemical compounds in Fig. 1 is "irreversible" in that regeneration of the initial H-containing phase or compound cannot be achieved on-board the vehicle or "in place" for a nonvehicular application. Reversibility of these materials can only be achieved by excessive pressure/temperature conditions requiring removal of the material from the vehicle, followed by processing via an industrial-scale process. Such materials are considered "off-board-reversible" materials. This book discusses recent advancements in both on-board-reversible and off-board-reversible hydrogen storage materials.

There is a long history of the synthesis and characterization of materials with large hydrogen contents that theoretically could act as hydrogen storage media. These investigations have substantially intensified over the past decade as a greater emphasis has been placed on hydrogen-powered vehicles as a way of reducing greenhouse gas (GHG) emissions. The automotive application is a particularly challenging setting for the use of various hydrogen storage approaches due to the volume and weight constraints. A number of chapters in this book give extensive descriptions of the scientific and engineering investigation of materials being explored and considered as hydrogen storage media.

In this chapter, we give a broad overview of the types of hydrogen storage approaches that have been investigated in the past and the interesting applications that have needed hydrogen storage. We cover some of the key generic material properties and characteristics having an impact on the configuration and performance of the various types of hydrogen storage systems discussed and focus on materials that can directly supply molecular hydrogen (i.e., H_2) for immediate usage. This book does not consider those materials requiring additional processing to release molecular H_2. Examples of systems not covered include those that store and release ammonia (NH_3) for downstream decomposition to form H_2 or the reformation of hydrocarbons (e.g., gasoline) to produce hydrogen.

The generation of energy from renewable sources, such as wind power and photovoltaics is subject to strong natural fluctuations. To be able to use the energy efficiently and as required, large and flexible storage options are required that can compensate for these fluctuations.

Electricity cannot provide the necessary large industrial capacities (especially via grid buffers and battery storage) for the foreseeable future at economically viable terms. Alternatively, hydrogen is suitable as an energy source due to its compressibility and storage capacity in storage facilities and can supplement the electricity grid based on the gas storage facilities at short notice and at low cost.

The operating regime of storage facilities in a gas infrastructure geared towards renewable energies differs fundamentally from previous natural gas operations.

While natural gas storage primarily serves long-term security of supply, in hydrogen operation it primarily compensates for the short-term fluctuations in 'green' generation.

Therefore, cavern storage facilities are particularly suitable for storing hydrogen, as their flexible storage and retrieval options make them ideal for the fluctuating availability of renewable energy sources.

To check the hydrogen capability of the storage in individual cases, technical and geological investigations, as well as corresponding adjustments of certain components and materials are necessary.

There are two types of UGS for storing natural gas: pore storage and cavern storage.

Pore storage
- Gas is pressed into porous rock like a sponge;
- mainly extracted natural gas or oil reservoirs.

Advantage:

- receives large volumes.

Disadvantages:

- high pressure required;
- time-consuming storage process;
- saline water in combination with hydrogen attacks rock, steel, and cement;
- bacterial methanation in existing stores.

Cavern storage
- cavities in underground salt domes;
- found predominantly in northern Germany.

Advantages:

- injection and withdrawal process in the cavity possible at short notice;
- volume control through brine pendulum cavern (reduction of cushion gas);
- short link to the above ground facility.

Disadvantages:

- saline water in combination with hydrogen attacks rock, steel, and cement;
- mixing with remaining stocks of methane in used storage facilities.

An examination of the technical and geological integrity is necessary to check the hydrogen capability of the storage facilities:

- corrosion and diffusion resistance of the materials used;
- thermodynamic properties under operating conditions;
- permeability, long-term stability, and barrier effectiveness of casing, cement, and storage rock;
- microbial activities (e.g. methanation processes);
- qualification of materials for the use of components such as fittings, compressors, piping, containers, etc.;
- evaluation of compression ability using compressors in the injection and withdrawal area with a working pressure depending on the filling level at approx. 200 bar. Definition of the materials and the required speed for the compression.

2 Compressed Gas Hydrogen Storage

Hydrogen is a gas at essentially all normal use and storage temperatures. Hydrogen is the lightest of all elements with a very low normal density of 0.09 g/L at 288 K and 1.0 bar. With a lower heating value (LHV) of 120.9 kJ/g, hydrogen has the highest specific energy of any known fuel, making it highly applicable to weight-sensitive

applications such as aircraft and spacecraft. Liquid hydrogen has a normal boiling temperature of about 20 K and a critical temperature of approximately 33 K, above which LH_2 cannot be formed through the application of pressure. To overcome the low volumetric density of normal hydrogen gas, it is usually compressed to high pressures (Barthélémy et al. 2017). Merchant hydrogen gas is typically delivered at 150–300 bar. Hydrogen has been stored and transported as a compressed gas in metal cylinders since the late nineteenth century, when the British used wrought-iron metal cylinders weighing in excess of 500 kg for transporting hydrogen to inflate balloons during military expeditions across Asia and Africa.

Hydrogen exhibits significant deviation from ideal gas law behavior at elevated pressure, and the gas density increases much more slowly than the pressure. At 350 bar, the molar volume of hydrogen is 22% larger than predicted by the ideal behavior due to intermolecular repulsion of the hydrogen molecules. As a result, it takes more pressure-volume work to compress it to a desired density as the pressure increases. Storing gas at high pressures requires robust pressure vessels, which incur significant weight and cost penalties. In addition, repeated cycles from low to high pressure stress the materials used in hydrogen tanks. The design, manufacture, transport, and use of gas cylinders and pressure vessels are typically regulated by government agencies. The regulations often require compliance with specific design, manufacture, or use codes and standards developed by organizations such as the International Organization for Standardization (ISO), the Compressed Gas Association (CGA), and the American Society of Mechanical Engineers (ASME).

Historically, there have been four standard types of cylinders developed and used for the transport and storage of hydrogen: Type I, all-metal cylinders; Type II, hoop-wrapped composite cylinders; Type III, fully wrapped composite cylinders with metallic liners; and Type IV, fully wrapped composite cylinders with non-load-bearing nonmetallic liners. Type I steel or aluminum cylinders are the most common type found in use for merchant hydrogen delivery and storage. Metals selected for these vessels must not permit hydrogen permeation or be subject to hydrogen embrittlement, especially when their use involves extensive pressure or temperature cycling. The cylinders are designed for a maximum working pressure, with the minimum wall thickness determined by the metal's yield and tensile strength. Because the mass of the metal is substantial, the mass of hydrogen stored is typically only about 1% of the cylinder mass and will drop to less than 1% at pressures of 350 bar and higher as the tank walls need to be thicker to hold back the pressure.

For automotive applications, weight and volume constraints make Type I cylinders impractical. However, they are suitable for many stationary applications in laboratory or manufacturing facilities as well as some types of specialty and utility vehicles (such as forklifts), for which excess weight is not a concern. In Type III and IV cylinders, thin, light-weight metal or nonmetallic liners, respectively, are wrapped by a fiber/epoxy matrix. Aluminum metal is commonly used for the liner as it cannot be embrittled by hydrogen. The fiber wrapping supplies the strength to contain the high-pressure gas, while the liner primarily acts as a gas permeation barrier. When high-tensile-strength carbon fiber is used to provide the strength for

350- and 700-bar cylinders, recent analyses indicated that hydrogen system capacities of 5.9% and 4.7% by weight, respectively, are achievable.

Although the carbon fiber wrappings dramatically reduce the weight of the cylinders from the all metal variety, they add significant cost. This cost is currently projected to be nearly three quarters of the storage vessel cost, taking into account high-volume manufacturing methodology (Niaz et al. 2015).

The most severe limitation of compressed gas storage systems (especially for any transportation application) is the overall volume occupied by the tank itself. The density of H_2 gas at room temperature is 23 g/L and 39 g/L at 350 bar and 700 bar, respectively. Thus, to store 5 kg of hydrogen on-board a light-duty hydrogen-powered vehicle, minimum volumes of 217 L and 128 L are required just to accommodate the gas volumes at 350 bar and 700 bar, respectively. In reality, the volume must be even greater since the additional volumes of the cylinders and balance-of-plant components (i.e., supply lines, valves, pressure regulators, sensors, etc.) are required. The 5 kg of hydrogen is the estimated quantity a fuel-cell-powered vehicle needs for a 300-mile driving range.

The use of higher pressures will severely impact weight and cost of the vessel as well as decrease efficiency for filling the tank. Nevertheless, types III and IV storage systems have been extensively used in demonstration assessments of prototype cars due mainly to their commercial availability, manageable cost, and straightforward means of installation into the vehicles and refilling at the test facilities. To fit the compressed H_2 storage systems into these vehicles with minimal impact on the passenger spaces, they are often separated into multiple cylinders located in trunks, under seats, or in spare wheel compartments. Compressed gas tanks have also been used in larger demonstration vehicles, including trucks, buses, and even a switch locomotive. While the compressed gas tanks are put into the beds of pickup trucks, they are often located just below roofs of buses (i.e., above and outside the passenger compartment) as well as in the fuel cell hybrid locomotive. To operate the nominal 250 kW PEM (proton exchange membrane) fuel cell in the locomotive, 70 kg of H_2 gas was stored in 14 carbon-wrapped tanks. During demonstration tests in an urban railyard, the mean time between required refueling of the locomotive was reported to be 11 h.

2.1 Cryogenic Hydrogen Storage Systems

The most obvious first approach to increasing the volumetric storage density of hydrogen is to change the physical state of hydrogen from gas to liquid. James Dewar first liquefied molecular hydrogen in 1898. During the first half of the twentieth century only relatively small quantities of liquid hydrogen (LH$_2$) were produced and stored, mainly to conduct and support fundamental research activities. Commercial-scale production of LH$_2$ was stimulated in the 1950s by the need of very large quantities of liquid hydrogen for the launching of spacecraft. Extensive efforts were implemented to enhance the exothermic conversion rate of ortho-H_2 to

Fig. 2 Schematic of Space
Shuttle spacecraft
highlighting external tank
that contains the liquid
hydrogen and oxygen
storage systems supplying
these propellants to the three
main engines in the Orbiter
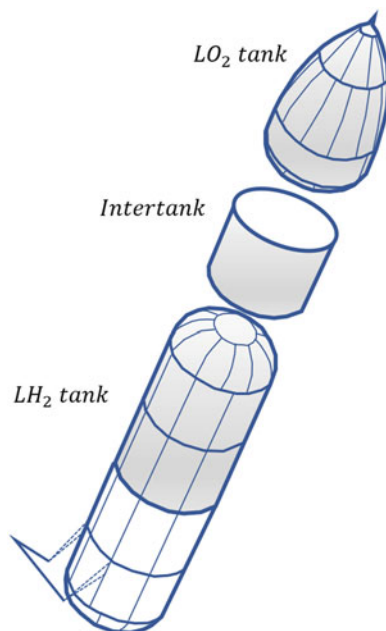
para-H_2 to greater than 95% during the liquefaction process to contain the costs of
hydrogen liquefaction and minimize evaporative losses of this low-boiling temper-
ature (i.e., ~20 K) cryogenic liquid (Aceves et al. 2000).

   The international development of launch vehicles containing one or more LH_2
and liquid oxygen (LO_2) stages has led to the construction of facilities in several
countries to produce, store, and transfer the large quantities of liquid hydrogen
consumed during launches of spacecraft for military, communications, and space
exploration missions. As an example, the three engines on the NASA Space Shuttle
orbiters burned up to 230,000 kg of hydrogen during each launch. Figure 2 shows
the Space Shuttle vehicle with the orbital and the external LH_2/LO_2 storage tank,
which is the only component of the launch system that is not reused.

   The density of liquid hydrogen at its 20 K boiling point is 71 g/L, which is nearly
twice that of 700 bar compressed gas at room temperature. Still, LH_2 is itself a
low-density liquid. For context, the density of water is 1000 g/L, and the mass
density of hydrogen in water is 111 g hydrogen per liter of water. The storage of LH_2
requires highly specialized and sophisticated vessels that can minimize heat transfers
from thermal conduction, thermal convection, and thermal radiation while exhibiting
mechanical robustness throughout their operational life (Baroutaji et al. 2019). The
cryogenic storage vessels must also safely manage the release of the evaporated gas
(i.e., boil-off) due to heating from residual thermal leaks or the ortho-para conver-
sion. Evaporative loss is exacerbated by the very low enthalpy of vaporization
ΔHvap of LH_2. LH_2 has a ΔHvap value of only 0.46 kJ/mole, 17.8 times less than
that of liquid natural gas (LNG), whose ΔHvap = 8.19 kJ/mole. In other words, if
you look at LH_2 cross-eyed, it will evaporate.

Nearly all LH_2 storage vessels use metallic double-walled containers that are evacuated and contain multiple layers of alternating metallic and thermally insulated polymeric or glass films to reduce heat leaks to the cryogenic fluid via convection and radiation. Designs and materials used to construct the containers and all of the components are chosen to minimize thermal conduction. It was stated that most current LH_2 tanks have evaporation losses between 0.3% and 3% per day. An innovative vessel design used circulating liquid air formed when liquid hydrogen is delivered from the inner vessel to cool its wall and can extend storage times by up to a factor of approximately 4. Furthermore, the addition of activated cryocoolers within the LH_2 storage vessel is being developed for zero boil-off (i.e., no H_2 gas venting) for long-duration space flights. This last approach is probably not an economical solution for most terrestrial applications, such as storage for hydrogen-powered vehicles.

The first space-qualified liquid hydrogen and oxygen storage vessels that operated in near-zero gravity environments were developed for the NASA Apollo missions. These vessels held the reactants for the alkaline fuel cells that provided the electrical power in the Apollo Command/Service Modules (CSM) and generated potable water as a by-product. These tanks supplied H_2 and O_2 at 4.1 bar to the fuel cells, which were operated at nominally 483 K, forming extremely pure water saturated with hydrogen gas. There were three separate vessels of each cryogen; the total stored quantity of LH_2 was 36.5 kg at liftoff. During a normal lunar mission, the fuel cells would supply about 650 kWh of energy with a generation rate for potable water of about 0.54 kg/h.

More recently, the Space Shuttle orbiters used liquid hydrogen and oxygen to provide electrical power and potable water during these missions. In this case, the LH_2 and LO_2 were both stored in vacuum-insulated spherical tanks under the payload bay liner of the orbiters. The hydrogen vessels were constructed of aluminum alloy 2219 with an outside diameter of 1.16 m and total volume of 606 L. Each of these tanks has an empty mass of 98 kg and stores about 42 kg hydrogen at an initial temperature of 22 K. H_2 gas is supplied to the alkaline fuel cell power plants at pressures between 13.8 and 15.4 bar.

Liquid H_2 storage has remained the primary option for proposed aviation systems due to its much greater effective storage capacity per volume and mass compared to compressed gas. Aviation interest in hydrogen drove the development of hydrogen-burning gas turbines starting in the 1950s. It is given a detailed description of the potential and issues of hydrogen as an aviation fuel. Included in this review are brief descriptions of flight tests performed in the United States and former Soviet Union on jet engines and aircraft running on hydrogen with LH_2 storage. More recent assessments and conceptual designs are still being explored to incorporate LH_2 storage tanks for hydrogen-fueled aircraft.

Starting in the early 1970s, liquid hydrogen storage was used in several prototype ground vehicles operating with ICEs. Development took place in the United States, Japan, and Germany, where the most sustained efforts were by the BMW Corporation. The designs and configurations of these LH_2 storage vessels were adapted from aerospace technology but had been significantly modified for accommodation in

Fig. 3 Plot of tank mass fraction vs. LH$_2$ capacity for different applications
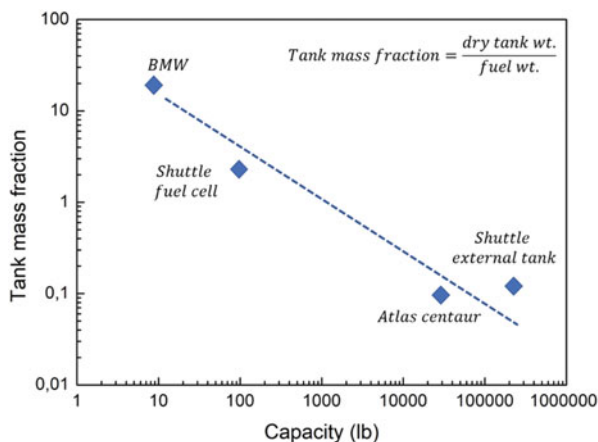
buses and passenger cars. The capacities of these tanks were mostly between 7 and 11 kg of hydrogen, with the maximum pressures usually below 10 bar. Numerous refinements have been incorporated over the years in designs and construction methods to lengthen storage dormancy by reducing liquid boil-off as well as to facilitate safe filling of the tank with minimal loss of the cryogenic hydrogen.

One clear concept emerging from these different historic uses of LH$_2$ is the following: if you are going to store LH$_2$, it is better to store a lot of it. Figure 3 gives a plot of tank mass fraction, defined as (Dry tank weight)/(Fuel mass), for a number of these different applications involving LH$_2$. Ideally, the tank mass fraction would be zero. Since the mass of the spherical tank in an LH$_2$ storage system varies with the square of the radius of the storage tank, whereas the mass of stored fuel varies with the cube of the radius, the weight penalty associated with the storage tank drops significantly with the total stored quantity of LH$_2$ increases. This approximately explains the tank mass fraction variation shown in Fig. 3.

An approach initiated at the Lawrence Livermore National Laboratory (LLNL) combines high pressure and cryogenic storage vessels to increase gravimetric and volumetric capacities while extending storage times before significant venting of the boil-off gas. Over the past several years, LLNL along with BMW has worked to improve the performance of these "cryocompressed" hydrogen storage vessels so that they could be viable for use in passenger cars. Independent systems and cost analyses recently projected that currently configured cryocompressed vessels have the largest storage capacities along with competitive costs when compared to the properties and status of other systems now available for passenger vehicles. The properties of these cryocompressed hydrogen storage systems are examined further in chapter "Water Purification and Desalinization" by Guillaume Petitpas and Salvador Aceves.

Since the density of solid molecular hydrogen exceeds 85 g/L below the 14 K triple point, both solid and slush hydrogen (a two-phase cryogenic fluid) have been considered for propellant storage in space and aviation systems. However, the

numerous technical challenges in producing and thermally isolating solid and slush hydrogen have kept the experimental investigations to the research laboratory up to the present.

On the other hand, hydrogen stored as a solid has been successfully utilized as a cryogen to cool infrared sensors and optics to below 12 K in two space missions. The first use of solid hydrogen as a cryogen was for cooling the long-wavelength infrared (LWIR) sensors in the Spatial Infrared Imaging Telescope III (SPIRIT III) sensor systems of the Mid-Course Space Experiment (MSX). The SPIRIT III cryogen tank contained 80 kg of solid hydrogen at about 9 K in a volume of 944 L that also had a 1.7% dense aluminum foam structure for heat conduction to the tank walls. The MSX instrument was launched in 1996 to test a variety of multispectral imaging technologies. The SPIRIT III instruments were successfully controlled by the solid hydrogen cryogen to 10.5 K for nearly 11 months before all the hydrogen was depleted. In 2009, NASA launched the Wide-Field Infrared Survey Explorer (WISE) satellite to generate a survey of the entire sky in the 3.5- to 23-µm infrared region while in Earth orbit. A two-stage solid hydrogen cryostat cooled the detectors and optics below 15 K for approximately 10 months before losing its solid coolant.

2.2   On Board Reversible Hydrogen Storage Materials and Systems

So far, the discussion has focused on hydrogen storage associated with the physical states of molecular hydrogen, namely gas, liquid, and solid. Another "physical state" is atomic hydrogen bound with other elements in chemical compounds. We alluded to this when we described water as having a hydrogen storage mass density of 111 g hydrogen per liter. Water is actually a good hydrogen storage material, although it is too stable to be used in mobile applications. Fortunately, it turns out that hydrogen forms some remarkable compounds with other elements that do have application for reversible high-capacity hydrogen storage (Pukazhselvan et al. 2012).

Hydrogen is very reactive with numerous metals and alloys as well as forming chemical compounds or complexes with most other elements. A few examples that are potential candidates for hydrogen storage are shown in Fig. 1. Metal hydrides (MHx) can be classified in terms of the hydrogen bonding to the metal (i.e., metallic, ionic, or covalent with complexes being intermediate cases). For most metals, intermetallic compounds, and alloys, hydrogen is bound in the interstitial sites in a metallic state with usually minor distortions of the generally stable H-free alloy lattice. Many practical MH_x materials are denoted as AB_y that involve a combination of elements A that are strongly exothermic hydrogen absorbers (e.g., Mg, Ti, Zr, La, etc.) with elements B that are either endothermic or very weakly exothermic hydrogen absorbers (e.g., Ni, Fe, Co, Mn, etc.), and y is in the range 0–5. There have been many studies on the formation, properties, and applications of these AB_yH_x materials over the past 40+ years, as summarized in several books.

Table 1 Energy storage and conversion applications for metal hydrides

Application	Desired MHx attributes	Candidate metal alloys
Stationary fuel storage	P = 1–10 bar, very low cost, uses waste heat, H capacity >2%, safety	TiFe, V alloys, Mg alloys, AB2 alloys
Portable and mobile fuel storage	P = 1–10 bar, compactness, low cost, uses air cooling or waste heat, fast kinetics, H capacity >2%, safety, durability	AB4, AB2, AB, alanites
Passenger vehicle fuel storage	H capacity >5%, P = 1–10 bar, uses waste heat, fast kinetics, durability during cycling, safety, contamination	AB2, Mg alloys, alanites

Listed in Table 1 are applications for which metal hydrides have been seriously considered or are currently used. Various key properties along with candidate MH_x systems are given in Table 1 for each application along with references where further descriptions of these hydrides and systems as well as the requirements and limitations imposed in specific applications can be found. Nickel metal hydride (Ni-MH) batteries are now well-established commodities in the international marketplace, and several niche devices (i.e., getters, purifiers, portable storage vessels, etc.) using hydrides have been developed and are commercially available.

Prototypes and demonstrations of numerous specialty, utility, and passenger hydrogen-powered vehicles have used hydrides for on-board storage as well as for chemical heat pumps and refrigerators. However, the limited gravimetric capacities (i.e., less than 5 wt%) for all known interstitial and many complex hydrides (e.g., $NaAlH_4$) limit their potential for general-purpose passenger vehicles. There have been successful development and deployment of hydride systems on at least one military application (e.g., storage in fuel-cell-powered submarines), gas gap heat switches, and sorption cryocoolers for space flight missions (Bowman Jr 2019).

Many of the intermetallic compounds and solid-solution alloys can readily absorb and desorb hydrogen gas around room temperature over the pressure range of 1–100 bars. Unfortunately, these hydrides can reversibly store only 1–3 wt% H_2, which is not considered large enough for most passenger vehicles. However, these capacities are fully suitable for stationary storage systems as well as various types of mobile applications, including utility/service vehicles such as forklifts and tow tractors, submarines, canal boats, scooters, and so on.

One significant advantage of interstitial metal hydride storage is the ability to refuel it using readily available low-pressure (~150 bar) sources of bottled merchant hydrogen, eliminating the need for a hydrogen compressor to generate high pressures. Another significant advantage of these "low-temperature" hydrides is the relative simplicity of using the waste heat from an ICE or a proton exchange membrane (PEM) fuel cell to discharge the hydrogen gas from the storage beds via a heat exchange fluid. The transfer of waste heat from a hydrogen energy conversion device to the metal hydride storage medium is an example of the balance of plant thermal management. Any practical engineered hydrogen storage system using metal hydrides must bring these thermal management issues under control,

providing heat to the metal hydride for hydrogen release and removing heat from the engineered system when the spent material is recharged with hydrogen.

Over the past decade, substantial progress has been made with "complex metal hydrides" containing mixed ionic-covalent bonding that can reversibly store more than 4 wt% H_2, often with operating temperatures below about 400 K. Development challenges presented by the complex metal hydrides have included improving the slow reaction kinetics of these materials, as well as decreasing the high heats of desorption, which require desorption temperatures above those available from ICE or PEM fuel cells.

The most common engineering solution to the problem of too high a desorption temperature is to catalytically oxidize (i.e., burn) a portion of the hydrogen stored in the bed. Thermal modeling analyses of alanate storage beds indicated that about 25–40% of the total hydrogen content would be consumed during H_2 discharge, which greatly decreases both the effective gravimetric and volumetric capacities. Hence, the advantages of $NaAlH_4$ and most other complex hydrides are clearly negated when much of the hydrogen must be consumed to provide the heat for desorbing the gas. This motivates the desire to find complex metal hydrides with an enthalpy of hydrogen release that is consistent with the temperature of the fuel cell waste heat, typically about 85 °C.

One possible alternative would be the development and incorporation of fuel cells that operate at higher temperatures (i.e., >400 K) to provide the necessary waste heat for desorption from the complex hydride.

Heat transfer during both hydrogen desorption and absorption involving any metal hydride is a major engineering issue due to their heats of reactions and the low thermal conductivities of the materials stemming from their fine-powder nature.

Many variants of these configurations have been described in the hydrogen storage literature. There have always been major conflicts in designing any hydride storage vessel in an effort to reconcile heat transfer management, minimal mass and volume, mechanical and structural stability, and so on. Some impacts of the performance of a nearly full-scale (i.e., up to 3 kg H_2 capacity) storage system using sodium alanate have been experimentally investigated, revealing that both reaction kinetics and thermal management issues are involved but can be kept under control.

The easily reversible adsorption of H_2 molecules by solids with large surface areas (i.e., usually much greater than 1000 m^2/g) and very highly porous structures offers another type of hydrogen storage method. Most attention has been focused on activated carbons (a-C) and metal organic framework (MOF) compounds, although nanocarbons, zeolites, microporous polymers, and other materials have also been investigated over the past two decades. Since adsorption bonding arises from relatively weak van der Waals attractions of the H_2 molecules to the sorbent surfaces, the binding energies are usually about 2–10 kJ/mole. This limits significant storage capacities at ambient temperatures requiring the sorbent materials to be cooled to cryogenic temperatures (i.e., usually ~100 K or lower). Extensive measurements have established that H_2 adsorption capacities increase approximately linearly with pressure, yielding maximum contents of about 5–6 wt% and about 7–7.5 wt% for a-C and MOFs, respectively, at 77 K and pressures of 50–150 bar. Since these

materials generally have very rapid kinetics for adsorption as well as other potentially attractive properties for hydrogen storage, several systems have been proposed and their thermal performance parameters analyzed for vehicular applications.

The final general hydrogen storage category, identified in Fig. 1, involves materials where hydrogen has formed sufficiently strong chemical bonds such that the material after the release of hydrogen cannot be regenerated on-board the vehicle using H_2 gas at "reasonable" pressures and temperatures. The on-board reformation of hydrocarbons, alcohols, and ammonia creates primarily gaseous by-products (e.g., CO_2, H_2O, N_2), which are inconvenient to collect and reprocess into the original hydrogen-storing molecule. Hence, refueling the storage vessel requires replacement by fresh fuel produced from new outside resources, much like we do currently with gasoline. Since there is also simultaneous release of the detrimental greenhouse gas CO_2 during the creation of hydrogen via the reformation of the carbon-based fuels, there are immediate environmental impacts using this approach to hydrogen storage. Consequently, reformation is not discussed any further in the present review. In contrast, there are several classes of compounds and types of chemical reactions that do produce condensed phase products following hydrogen release. These spent materials are generally available to regenerate the original fuel on the addition of hydrogen, although they typically require considerably complex and energy-intensive treatment that cannot be performed within the storage containers themselves.

There are a number of liquid cyclic hydrocarbons which react reversibly with H_2 gas at pressures of about 100 bar or lower, albeit at rather elevated temperatures of 500–600 K in the presence of suitable catalysts. Examples of these liquid hydrogen carriers include benzene/cyclohexane (7.1 wt%), toluene/methylcyclohexane (6.1 wt %), naphthalene/decalin (7.2 wt%), and several substituted carbazoles. Because these moderately high-capacity liquids can be transported and handled as conventional fuels to fill the storage tanks of vehicles and other storage systems in remote or distance locations, they have often been proposed as attractive options in a hydrogen fuel infrastructure.

The development of practical systems using these liquid organics has been hindered by the need for much more efficient and robust catalysts during both the hydrogenation and the dehydrogenation reactions. This results in burning significant portions of the released hydrogen to maintain the reactor chambers at temperatures high enough to continue the dehydrogenation reaction. Maintenance of an elevated temperature is also required to avoid solidification of the reaction products so that they can be separately stored and removed from the vehicle for regeneration. There have not been any demonstrations of complete hydrogen storage systems using any of the candidate liquid organic hydrogen carriers, although several concepts of stations and distribution systems for fueling vehicles have been published (De Corato et al. 2022).

Diverse approaches for initiating and controlling the highly exothermic reactions with water have been reported in the patent and research literature. While hydrolysis reactions can take place in both acidic and basic media, the importance of including appropriate catalysts and additives has been widely recognized, and they have been

incorporated into nearly all these chemical hydrogen storage/production concepts. The hydrolysis of aluminum powders has been suggested for various systems, including submarines powered by fuel cells; however, since all the hydrogen must come from the water reactant alone, reactions with metal hydrides would provide larger yields since both components contribute hydrogen. A very interesting approach has been proposed that combines thermal and hydrolysis decomposition of alane (AlH_3) with $NaH/NaAlH_4$ mixtures to enhance the yield of gaseous hydrogen. However, the issues of regenerating the extremely stable aluminum oxides/hydroxides remain.

3   Hydrogen Storage in Pressure Vessels: Liquid, Cryogenic, and Compressed Gas

When hydrogen gas is liquefied, it needs to be cooled to −421.6 °F, making liquid hydrogen a cryogenic fuel. Cryogenics is the study of low-temperature physics. A beaker of liquid hydrogen at room temperature will boil as if it was on a hot stove. If the beaker of liquid hydrogen is spilled on the floor, it vaporizes and dissipates in a few seconds. If liquid hydrogen is poured on the hand, it will feel cool to the touch as it slides through the fingers. This is due to the thermal barrier that is provided by the skin. But placing a finger in a vessel containing liquid hydrogen severe injury will occur within seconds due to the extreme cold. This hydrogen fuel on board a vehicle would allow the use of a small, efficient fuel cell Stirling engine cryocooler system to provide air conditioning.

Liquid hydrogen is a fuel option that could be utilized on a large-scale since it most resembles gasoline in terms of space and weight (Wijayanta et al. 2019). Although a liquid hydrogen storage tank for a vehicle could be about five times heavier in dry weight than a 30-lb gasoline tank, in vehicles that carry greater volumes of fuel, such as trucks or trains or aircraft, the difference in tank weight could be more than offset by the difference in fuel weight. Studies by Lockheed Aircraft have shown that a large commercial aircraft could have its overall takeoff weight reduced by as much as 40% if liquid hydrogen were used instead of aviation fuel. Liquid hydrogen has the lowest weight per unit of energy, with relatively simple supply logistics and normal refuel times, and it is generally safer than gasoline in accidents. Cryogenic fuels like liquid hydrogen are more difficult to handle and substantially more difficult to store, compared to hydrocarbon fuels like gasoline or aviation kerosene. Even with highly-insulated, double-walled, vacuum-jacketed storage tanks, liquid hydrogen can evaporate at a rate of almost 9% per day (Zheng et al. 2019).

This evaporation increases the pressure on the tank wall, and the gaseous hydrogen must be vented to the atmosphere to keep the tank from rupturing. During tests at the Los Alamos National Laboratory, a liquid hydrogen-fueled vehicle tank of liquid hydrogen evaporated away in about 10 days.

This venting of the fuel must be done to keep a fuel tank full when refueling. In an enclosed space, the vented hydrogen also presents a risk because of hydrogen's wide flammability limits. Hydrogen explosions are rare, but any combustible gas in an enclosed space can be a safety problem. One solution is to burn off the escaping hydrogen and use this energy for heating or cooling. It can also be used to power a fuel cell. Stationary liquid hydrogen storage tanks used in laboratories are able to keep the hydrogen in a liquid state for several months. It should be possible to build vehicular storage tanks that would maintain hydrogen in a liquid state for several weeks. The small quantity of hydrogen that evaporates from such tanks could also be sent to a fuel cell that would use the hydrogen to generate electricity. It is also possible to vent the vaporized hydrogen gas to an auxiliary hydride system for storage.

The double-walled, vacuum-jacketed storage tanks and piping that are required for liquid hydrogen are expensive compared to conventional fuel storage tanks. A gasoline tank might cost about $150, while a liquid hydrogen storage tank could cost a few thousand dollars. Because of the energy density of liquid hydrogen, a fuel tank 3–4 times larger in volume is required than that used for gasoline or aviation fuel. Liquid hydrogen fuel systems would require changes in the energy infrastructure and end use systems, such as stoves, engines, and fueling systems. While the disadvantages of liquid hydrogen are substantial, they can be minimized. A few thousand dollars for a liquid hydrogen storage tank seems high, but consider that the emissions control equipment required on gasoline fueled engines adds much to the cost of current vehicles.

Unlike other fuels, hydrogen (H_2) can be generated and consumed without producing carbon dioxide (CO_2). This creates both significant engineering challenges and unsurpassed ecological advantages for H_2 as a fuel while enabling an inexhaustible (closed) global fuel cycle based on the cleanest, most abundant, natural, and elementary substances: H_2, O_2, and H_2O. If generated using light, heat, or electrical energy from solar, wind, fission, or (future) fusion power sources, H_2 becomes a versatile, storable, and universal carbonless energy carrier, a necessary element for future global energy systems aimed at being free of air and water pollution, CO_2, and other greenhouse gases. The physical and chemical properties of H_2 make its use superior to fossil fuels. H_2 is a simple nontoxic molecule that generates power cleanly and efficiently, even silently and without combustion if desired. However, widespread use of H_2 has been challenging due to its low density. Whether it is compressed to extreme pressures, cooled to cryogenic temperatures, or bonded to metals or sorbent structures, H_2 stores little energy per unit of volume relative to conventional (hydrocarbon) fuels. Therefore, storing enough H_2 fuel on-board a vehicle to achieve sufficient (500+ km) driving range in a compact, lightweight, rapidly refuelable, and cost-effective system remains the predominant technical barrier limiting widespread use of H_2 automobiles. Other issues (e.g., hydrogen supply) will likely be addressed during the early deployment of hydrogen infrastructure.

Fig. 4 Calculated results for temperature (solid lines) and exergy (dashed lines) as a function of H_2 pressure and density. Exergy does not include ortho-para H_2 conversion, which can be important for H_2 stored more than a few days at temperatures below 60 K. The ideal work of converting normal (75% ortho) LH_2 to pure para-LH_2 is 0.65 kWh/kg
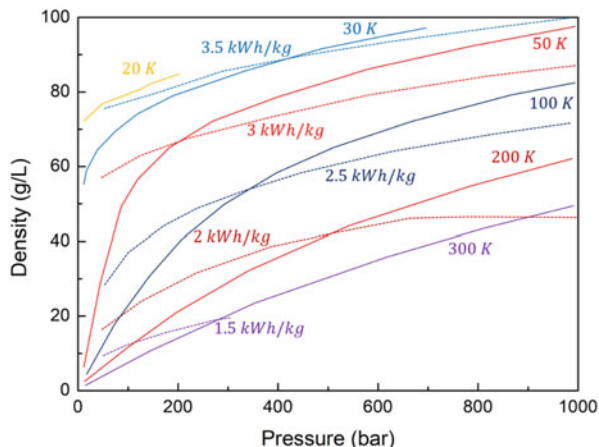

This chapter focuses on H_2 storage in pressure vessels. Depending on pressure and temperature operating regimes, three common approaches exist to H_2 pressure vessel storage (Liu et al. 2012):

1. Compressed gas vessels operating at high pressure (typically 350–700 bar) and near ambient temperature; typically made of carbon fiber composite wound around an aluminum (Type III vessels) or polymer (Type IV vessels) liner;
2. Liquid hydrogen (LH_2) vessels for low pressure (~6 bar) and temperatures below the H_2 critical point (20–30 K); consist of an inner stainless steel vessel surrounded by vacuum insulation and an outer metallic vacuum jacket;
3. Cryogenic pressure vessels, sometimes called "cryocompressed" vessels, compatible with both high pressure (350 bar) and cryogenic temperatures down to LH_2 (20 K) and comprising a Type III aluminum-composite vessel surrounded by a vacuum space and an outer metallic vacuum jacket.

System hydrogen storage density is the most important parameter in H_2 vessels. High storage density enables long-range vehicles necessary for practical carbonless transportation. Increasing the storage density also increases the H_2 weight fraction (kilograms H_2/ kilograms vessel and accessories) and reduces costs (dollars/kilogram H_2) because compact vessels require less material (metal and composite) for manufacture. Compact vessels also fit better within available spaces in the vehicle, leaving more space for passengers or cargo.

Figure 4 shows the gravimetric density of H_2 gas (grams/liter, solid lines) as a function of temperature and pressure. Focusing for a moment on the 300 K line, it can be observed that the density of ambient temperature compressed gas is a relatively low 50 g/L, even when pressurized to 1000 bar. For context, note that the density of saturated LH_2 at 1 bar is 70.7 g/L, and gasoline has the energy equivalent density of 264 g H_2/L. In addition to this, curvature in the 300 K line indicates that gaseous H_2 is not an ideal gas.

Fig. 5 The compression energy need in relation to the components' specific energy content for hydrogen and methane. Calculations based on adiabatic compression
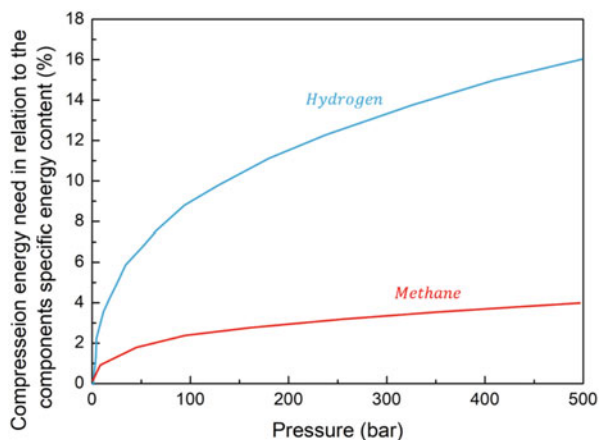
It is less compressible as pressure increases and becomes more so at high pressures. At 350 bar, the molar volume of hydrogen is about 20% larger than that predicted by the ideal gas law due to intermolecular repulsion of the hydrogen molecules. Nonetheless, significant increases in H_2 volumetric density can be achieved via compression.

Another issue with hydrogen is the compression effort before storage. Depending on what type of compression is used, i.e. adiabatic, multistage or isothermal, the energy needed will vary significantly. However, to simplify the matter, the compression effort in this case is described using an adiabatic compressor. Figure 5 compares the difference in specific energy need between hydrogen and methane for an adiabatic compressor and is calculated with the adiabatic compression equation for gases greatly exceeding their boiling temperatures.

For instance, looking at the gases compressed to 200 bar, for hydrogen the compression effort accounts for almost 12% of the energy content of the gas. The corresponding figure for methane is about 3%.

Aside from pressurization, much potential exists to increase storage density by cooling. Very cold gaseous H_2 (also called cryogenic hydrogen) at 100 K reaches a density of 50 g/L at a moderate pressure of 300 bar. The density of LH_2 is 70.7 g/L when saturated at 1 bar at 20.3 K. Densities above 90 g/L (~30% denser than LH_2) can be obtained with very cold pressurized H_2, although refueling at such high density has not been demonstrated at vehicle scale.

Increasing H_2 density is typically a productive effort. While the previous discussion considers only the density associated with the physical state of hydrogen (gas, liquid), it is the system storage density that ultimately matters since thick vessel walls and thermal insulation occupy volume otherwise available for H_2 storage. The strength of practical materials and the performance of thermal insulation therefore limit ultimate vessel storage system density. Beyond the tank itself, other storage system hardware, such as valves and manifolds, contribute to the total system volume.
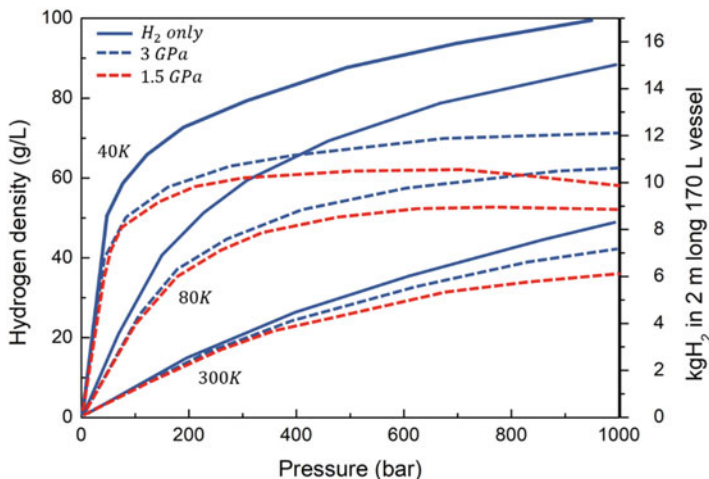
Fig. 6 Predictions for H₂ storage capacity vs. pressure for idealized pressure vessels of varying wall stress at ambient (300 K) and cryogenic (40 and 80 K) temperatures. All vessels shown are cylindrical with ellipsoidal end caps and identical external volumes (170 L) and dimensions (2-m length, 35-cm diameter). Vessel wall thickness calculations include thick-wall effects. Three vessels are shown for each temperature case: 3.0-GPa wall strength, 1.5-GPa wall strength, and H₂ only (amount stored considering zero wall thickness). Safety factor is 2.25. Analysis assumed negligible liner thickness. Cryogenic vessels had 1.5 cm vacuum insulation. Corresponding H₂ storage system densities are shown on the left axis

The net impact of H₂ real gas behavior, vessel wall strength, and thermal insulation is best illustrated by modeling the amount of H₂ that can be stored in a volume of fixed dimensions as shown in Fig. 6.

Consider a long (2 m), slender (35-cm outer diameter) pressure vessel, similar to the dimensions preferred by manufacturers due to efficient packaging along the central tunnel. The fixed total outer cylindrical vessel volume is 170 L, assuming ellipsoidal heads. Internal vessel volume is a function of design pressure since wall thickness increases with increasing pressure to maintain stresses below a maximum (ultimate strength divided by 2.25 safety factor). For cryogenic vessels, the vacuum insulation (assumed 1.5 cm thick from a recent prototype) occupies 29 L, which has to be deducted from the total volume.

We assume two vessels made of materials with two different inherent wall strengths: 1.5 GPa, similar to today's advanced composite materials and 3 GPa, which may be obtained in the future with improved materials. Figure 6 assumes no vessel liner or a thin vessel liner. For any design pressure, a material with higher strength allows vessels with thinner walls, leading to a greater available inner volume. Increasing the inner volume increases the available hydrogen storage volume contained within the fixed external volume, leading to greater volumetric efficiency. We call the ratio of inner volume to external volume the geometric volume efficiency (Purewal et al. 2019).

Compressed H_2 vessels made of high-strength materials (dotted lines in Fig. 6) achieve 90–95% geometric volumetric efficiency at pressures up to 350 bar at ambient temperature. Above 350 bar, as thicker walls become necessary, the inner volume available to store gas goes down, and the geometric volumetric efficiency and hydrogen storage capacity decrease. For example, a 700-bar, 170-L (external volume) pressure vessel made of 1.5-GPa material with a safety factor of 2.25 is predicted to store only 5.3 kg of H_2 instead of the theoretical 6.6 kg H_2 due to the reduced inner volume available. The same 170-L vessel made of materials with twice the strength (3.0 GPa) would have thinner walls and could store 6 kg H_2 at 700 bar.

The disadvantage of low-strength wall materials is made worse by the real-gas nonlinear relationship between pressure and H_2 density. Referring to Fig. 6, let us consider the situation at 700-bar storage at 300 K. For H_2 gas only, with a volume equal to the external volume of 170 L, the calculations show we can store about 7 kg of H_2. If we go to a real storage vessel with wall strength of 3.0 GPa, we take up some inner volume with the tank wall. At 3.0 GPa, we can only store about 6 kg of hydrogen in the reduced inner volume at 300 K and 700 bar. If we want to get back to 7 kg, we would have to increase the pressure to about 900 bar at 300 K for the 3.0 GPa case. Alternatively, if we went with a 1.5 GPa wall material, the vessel wall would be even thicker still, and instead of storing 7 kg of H_2 (gas only) at 700 bar and 300 K, we could now only store about 5 kg of H_2. It is impossible to recover the 7 kg H_2 storage capacity of a 1.5 GPa vessel by raising pressure.

At higher pressures (1000 bar), an ultimate H_2 storage density is reached as H_2 becomes more incompressible and vessel walls must be ever thicker. These two factors ultimately limit maximum H_2 storage density to pressures of approximately 10% of vessel wall material strength and 60% geometric volumetric efficiency, whereas maximum economic compressed H_2 pressures are likely to occur at approximately 5% of vessel wall material strength (Xu et al. 2009).

In summary, system storage density of compressed gas vessels is limited by the nonideal properties of H_2 and the strength of available vessel materials. Although a maximum system density can be reached at a pressure about 10% of the wall strength (e.g., 1500 bar for a 1.5 GPa composite material), it is unlikely that pressure vessels will operate beyond about 5% of ultimate strength because only marginal density gains are obtained at considerable increase in material cost.

Compressed gas and LH_2 vessels operate at (nearly) constant temperature. Cryogenic pressure vessels, sometimes called cryocompressed vessels, do not. They continuously change temperature, depending on how the hydrogen-powered car is driven. The cryo-compressed tanks cool down if the vehicle is driven, and they warm up if the vehicle is parked for a long time. Figure 6 therefore considers two cryogenic temperatures: 40 and 80 K. Hydrogen at these temperatures deviates from ideal gas behavior at very low pressure (~100 bar), where the lines start exhibiting considerable nonlinear behavior. As a result, while cryogenic H_2 density increases to over 100 g/L (at 40 K and 1000 bar), system H_2 density for real vessels with walls reaches its maximum at much lower pressures than for ambient temperature gas: 300–700 bar for 1.5 GPa vessels and slightly over 1000 bar for 3.0 GPa vessels.

While there is little density gain in increasing cryogenic vessel pressure rating beyond 350 bar, there is a dormancy gain that may justify the additional expense.

Alternatives for H_2 delivery and dispensing are similar to those used for vehicle storage: liquefaction and compression. These two paths can be thermodynamically analyzed in terms of exergy. Defined as the minimum theoretical work necessary for compressing and cooling H_2 from a reference state (300 K and 1 bar) to any state (T, p), exergy is therefore an indication of the energy necessary for H_2 densification.

Going back to Fig. 5, the dashed lines show exergy as a function of pressure and density (or temperature). The figure shows that H_2 compression is exergetically inexpensive compared to cooling: any level of densification from 10 to 100 g/L is achieved with minimum possible exergy by maximizing pressurization and minimizing cooling. To better appreciate this, select any density (e.g., 40 g/L) and observe how exergy drops monotonically as we move toward higher temperatures. H_2 liquefaction is especially expensive (3.92–3.27 kWh/kg depending on whether ortho-para H_2 conversion is included or not). This is reflected in reality by the very large liquefaction energy (7–13.4 kWh/kg) vs. compression energy (1.5–2 kWh/kg theoretical and 3–5 kWh/kg in practice). The energetic disadvantage of liquefaction also makes it more expensive and more polluting when using today's average grid electricity.

LH_2 has, however, a virtue that largely mitigates the high cost of liquefaction: high density at low pressure. Being dense, LH_2 can be dispensed in inexpensive low-pressure tanker trucks that carry about 10 times as much H_2 as tube trailers for compressed H_2 (4000 vs. 550 kg), reducing driver and truck costs and therefore reducing delivery cost.

Finally, LH_2 dispensing is less expensive than compressed gas dispensing. Following the 3.5 kWh/kg exergy line in Fig. 5, we can see that 100 g/L H_2 at 1000 bar and 43 K has the same exergy as 70.7 g/L LH_2 at 1 bar and 20 K. It would therefore be theoretically possible to densify LH_2 to 100 g/L without work input. While impractical in practice, this points to the thermodynamic advantage of LH_2 pumps (discussed further in this chapter) vs. pressurizing gaseous H_2. Aside from demanding considerable work input (2 kWh/kg exergy for 1000 bar and 50 g/L), compressed H_2 dispensing is expensive because it demands compressors, a cascade charging system, and, for 700-bar delivery, a booster compressor and a chiller.

Evaporative losses are, however, a key challenge. Operating at cryogenic temperatures, these systems are exposed to continued environmental heat transfer. While high-performance vacuum insulation can go a long way toward reducing heat transfer, even a few watts can result in evaporative losses when a vehicle is not frequently operated. The dormancy (period of inactivity before a vessel releases H_2 to reduce pressure buildup) is an important parameter for cryogenic storage acceptability (Hardy et al. 2018).

Dormancy can be calculated from the first law of thermodynamics and the properties of H_2 and can be illustrated with a diagram of H_2 thermodynamic properties (Fig. 7) to simplify visualization and graphical calculation of H_2 vessel dormancy.
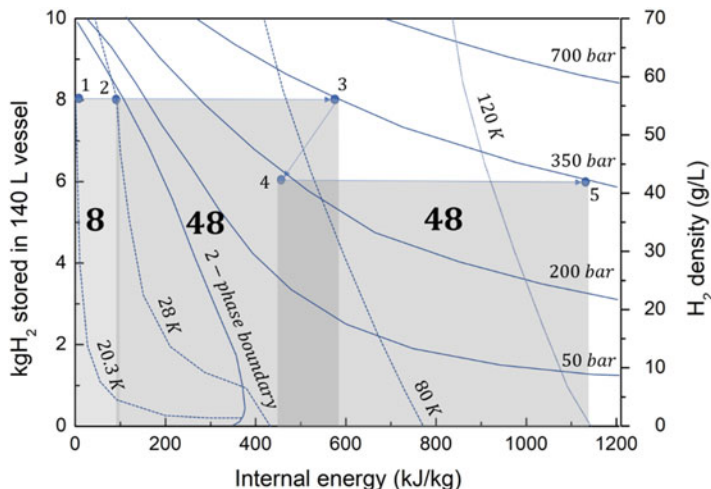
Fig. 7 Phase diagram for H_2 showing density (right vertical axis) and internal energy (horizontal axis), with lines for constant pressure (solid) and temperature (dashed). Curves for entropy are not shown. The left axis shows the mass of H_2 contained in a vessel with 140-L internal volume, which would store 10 kg of LH_2 at 20 K and 1 bar. The figure also shows points to areas representing dormancy (in watt-days) of conventional LH_2 tanks (light gray) and cryogenic pressure vessels (all shadings). Thermodynamic states that are "inside" (to the left of) the 2-phase boundary line consist of two phases, whereas states to the right of this line consist of one supercritical phase

Figure 7 uses axes of specific internal energy and density instead of more traditional temperature and pressure. An appropriate choice of scales in Fig. 7 radically simplifies dormancy calculations. The grid scale in the specific internal energy (horizontal) axis is set at 86.4 kJ/kg H_2, which converts to 1 watt-day/kg H_2 (1 day = 86,400 s). The grid scale in the vertical axis represents 1 kg H_2. Therefore, the area of a grid square represents 1 watt-day of heating. The total change in internal energy (in watt-days) can be easily calculated by counting the squares under the curve representing changing the state of hydrogen from one point to another in Fig. 7. Dormancy (days) is calculated by dividing the internal energy change (in watt-days) by the rate of heat transfer (in watts).

A dormancy calculation begins by identifying the initial thermodynamic state in Fig. 7 of the H_2 contained in the vessel. As an illustration, consider a parked automobile with a LH_2 tank with 140 L internal volume and 6 bar maximum working pressure, which is 80% full with 8 kg LH_2 at 20 K and 1 bar (point 1 in Fig. 7). As the vehicle is parked (not using H_2), heat transfer warms the H_2, increasing both its temperature and pressure. Dormancy ends in this case when the pressure reaches 6 bar (point 2), when H_2 venting or vehicle driving becomes necessary to maintain pressure within the vessel rating. Total heat absorbed during this process from point 1 to point 2 can be calculated by counting the number of squares (8 watt-days) in the area marked by the light gray shaded area under the 1–2 line. Dormancy can then be calculated by dividing 8 watt-days by the heat transfer

Fig. 8 Contour lines of dormancy vs. heat transfer rate (x-axis) and vessel-rated pressure (y-axis) calculated for a 140-L vessel initially full of 10 kg LH$_2$ saturated at 1 bar
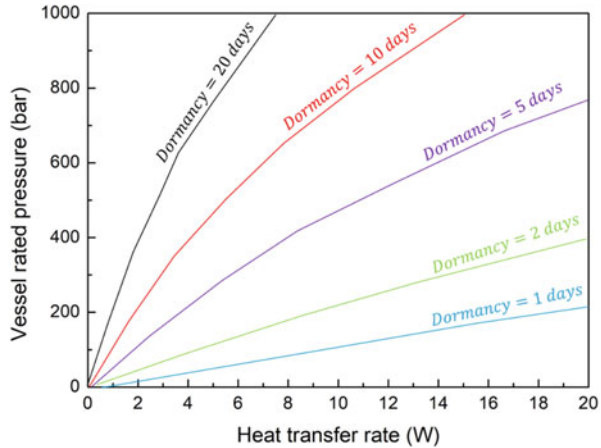
rate. If one has a heat leak rate of 4 W total, then the dormancy would be 2 days before loss of hydrogen.

From Fig. 7, it is clear that insulation performance can be traded off vs. vessel pressure rating: dormancy can be increased by either improving insulation (reducing heat leaks) or strengthening the vessel (raising the vent pressure). This trade-off is better illustrated in the predictions of Fig. 8, which shows contour lines of dormancy vs. heat transfer rate (x-axis) and vessel-rated pressure (y-axis) for an initially full vessel (140 L internal volume and 10 kg LH$_2$ at 1 bar).

The figure shows that a pressure vessel may reach acceptable dormancy (for example, 5 days) through either high-performance insulation (~3 W heat leak rate) of an inexpensive low-pressure (~167 bar) vessel or, alternatively, using low-performance insulation (~17 W heat leak rate) of a high-pressure (700 bar) vessel.

The optimum design point depends on the relative cost of vessel materials and insulation, as well as the particular mission requirements. Even larger heat transfer rates would be allowable in continuously driven vehicles (e.g., taxis, buses) as driving increases dormancy, as shown in Fig. 7, and the allowed dormancy can be as short as 1 day in such fleet vehicles. Strong vessels (>500 bar rated pressure) deliver 1 day of dormancy at heat leak rates under 50 W, possibly allowing use of inexpensive powder or foam insulation (Yatsenko et al. 2022).

It should also be noted that Fig. 8 assumes a completely full vessel at LH$_2$ density, the best case for low-pressure vessels and the worst case for high-pressure vessels. Low-pressure vessels (<10 bar) have maximum dormancy when full because the thermal inertia of the evaporating LH$_2$ slows the pressure rise. On the other hand, cryogenic pressure vessels gain most of their dormancy from containing the H$_2$ as it heats up and therefore have the longest dormancy at low fill levels, at which the vessel can heat up more before reaching the rated pressure. Dormancy is infinite when ambient temperature H$_2$ at rated pressure is denser than the cryogenic H$_2$ stored in the vessel.

Rapid and high-density refueling is key for H_2 storage acceptability. Pressure vessel refueling is also strongly influenced by thermodynamics, which determines ultimate H_2 storage density and therefore vehicle driving range. We discuss the thermodynamics of both compressed gas and LH_2 storage, starting with compressed hydrogen storage.

Typically, before filling an empty compressed hydrogen vessel with H_2, the following should be known: (1) How hot will the hydrogen vessel get as we are compressing hydrogen gas within it?; (2) What will the final pressure be?; (3) How much hydrogen will be in the vessel? Pressure vessel refueling can be modeled with the first law of thermodynamics for open systems. To illustrate the thermodynamic implications of vessel fill processes, we start by considering a simplified case: a large hydrogen station tank storing H_2 at temperature T_i and pressure p_i. This tank fills a relatively small compressed gas storage vessel on-board a vehicle at the station (Ahluwalia et al. 2012).

As a first approximation, we consider an initially empty vehicle vessel with negligible thermal mass and negligible heat transfer to/from the environment. Under these assumptions, the first law of thermodynamics simplifies to $u_f = h_i$, where u_f is the specific internal energy of the hydrogen inside the vehicle vessel, and h_i is the specific enthalpy of the H_2 flowing at the station vessel. The enthalpy h_i is calculated at the hydrogen station's tank conditions (p_i, T_i), assumed constant due to its large relative size. From thermodynamics, $h_i = u_i + p_iv_i$. The term p_iv_i, frequently named flow work, explains the heating that occurs when gases are forced into a vessel.

Figure 9 shows how the density of hydrogen in the vehicle vessel changes during the fill and how the temperature of the gas increases due to the compression. In this modeling study, the large storage tank at the hydrogen filling station is assumed to have an initial pressure p_i of 700 bar, and with varying assumed initial temperatures T_i of 100, 200, and 300 K. Figure 9 shows that compressing hydrogen in the vehicle vessel to the 700 bar limit heats the hydrogen in all cases, but by smaller amounts if the initial station tank temperature T_i is lower. If the station hydrogen is initially at 300 K, the final delivered gas temperature in the vessel is 460 K, an increase of 160 K. This higher temperature limits the density of the delivered hydrogen to only 28 g/L (at 700 bar) in the vehicle's vessel (dashed line at 300 K). Alternatively, if we lower the temperature of hydrogen in the station tank to 200 K, we are able to deliver 38 g/L into the vehicle at a final temperature of 310 K at the 700 bar pressure limit. If we are able to store large quantities of 100 K hydrogen gas at the station, then filling the vehicle vessel leads to a final vessel temperature of 175 K (only a 75 K temperature rise), and the final density of hydrogen in the vehicle's storage vessel is 56 g/L, consistent with the lower gas temperature.

Although there is a jump in temperature from station tank to vehicle vessel, the temperature inside the vehicle vessel, once established, is nearly constant during the filling process, changing only slightly due to H_2's nonideal behavior, especially at lower temperature. It is worth pointing out that H_2 heats up as it flows into the vessel regardless of the value of the Joule-Thomson coefficient (negative at ambient temperature, near zero at 200 K, and positive at 100 K): vessel filling processes
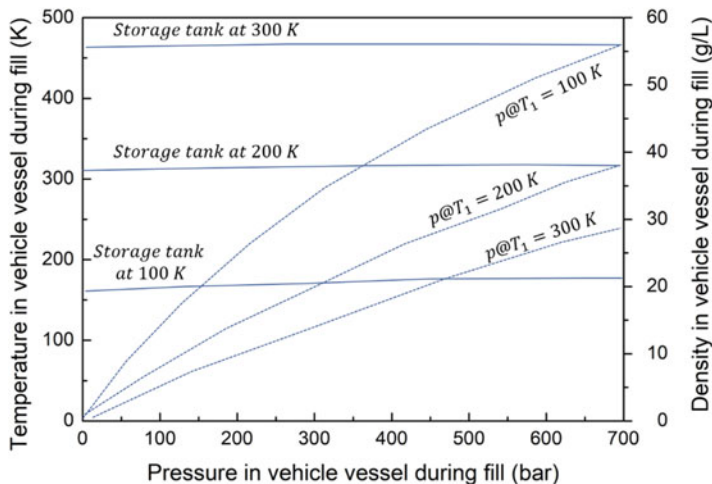
Fig. 9 Model results for automotive vessel temperature and density during the filling process as a function of pressure when filled from a large hydrogen station tank at $p_i = 700$ bar and $T_i = 100$, 200, and 300 K, assuming an initially empty vehicle vessel with negligible thermal mass and no environmental heat transfer

are not isenthalpic and therefore not controlled by the Joule-Thomson coefficient. Flow work plays the key role in describing the process. In addition, heating of the hydrogen gas with compression can lead to degradation of the internal surfaces of the tank if the temperature gets too high.

Results in Fig. 9 can be generalized by varying p_i and T_i over broad ranges. Figure 10 predicts vehicle vessel temperature (labeled in K), and vehicle vessel fill density (solid lines labeled in g/L), at the end of the refueling process, when pressure equilibrium is reached with the hydrogen station tank ($p = p_i$), for an initially empty vehicle vessel with negligible thermal mass, for any combination of H_2 station tank pressure and temperature (p_i, T_i). As an example, assume that the H_2 station tank contains H_2 at $T_i = 100$ K and $p_i = 300$ bar. From the Fig. 10, the vehicle vessel at the end of the fill process (when both vessels equilibrate at 300 bar) would be at 150 K and about 40 g/L.

Figure 10 once again shows the considerable heating that occurs during the filling process. For an ideal gas with constant specific heat, heating is constant ($T = \gamma T_i$, where γ is the specific heat ratio c_p/c_v), and therefore temperature lines are fairly horizontal at low pressures and high temperatures. At higher pressures, heating increases because H_2 becomes increasingly incompressible ($pv > nRT$). Minimum heating occurs at low temperature and pressure, where H_2's compressibility factor drops as H_2 approaches the liquid phase. This is observed by the 50 K blue line reaching a local maximum at about 50 bar.

In particular, looking at $T_i = 300$ K (top of Fig. 10), we can see the substantial heating that occurs during compressed gas filling. H_2 heats up to 440–464 K when
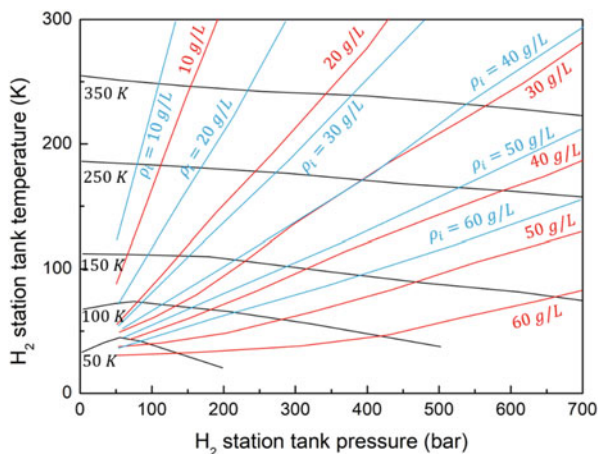
Fig. 10 Model calculations for vehicle vessel temperature (labeled in K) and fill density (solid lines labeled in g/L), at the end of the refueling process, when pressure equilibrium is reached with the H_2 station tank ($p = p_i$), for an initially empty vehicle vessel with negligible thermal mass, for any combination of station tank pressure and temperature (p_i, T_i). The figure also shows (dashed lines) the density of the hydrogen in the station tank at (p_i, T_i). The difference between dashed lines and solid density lines represents the density losses due to flow work

filled to 350–700 bar, reducing storage capacity by 38% and demanding 48–55% overpressurization to recover the density that would be obtained during isothermal filling. Fortunately, in practice, pressure vessels absorb some of this thermal energy, so warming to only about 350 K is observed. This reduces storage capacity by only 14–12% (at 350–700 bar), and the storage capacity can be restored with 17% overpressure. Overpressure effects vary little with filling pressure between 350 and 1000 bar and are lessened because H_2 is easier to compress as it warms.

In addition to the fill density and temperature, Fig. 10 also shows the hydrogen density ρ_i of H_2 station tank at p_i, T_i (dashed lines). This would be the fill density if no flow work existed, or if the vehicle vessel were somehow cooled down to the station tank temperature during filling. Density losses during vessel filling are represented in Fig. 10 by the difference between the dashed and the solid density lines. Flow work therefore has a large impact on delivered density. On average, fill density would be approximately 1.4 times higher without flow work. The fact that this average factor is almost identical to the specific heat ratio γ is no surprise since γ determines fill heating, at least when H_2 behaves ideally and specific heats remain constant.

The results of Fig. 10 characterize fill processes involving compressed hydrogen gas for both a hydrogen station storage tank and the vehicle hydrogen storage vessel being filled. However, cryogenic vessels are more likely to be filled with an LH_2 pump coupled to a large station LH_2 Dewar. Considering that pressurizing LH_2 is exergetically inexpensive, LH_2 pumping enables rapid compression and efficient densification with low evaporation (less than 3%) in commercially available
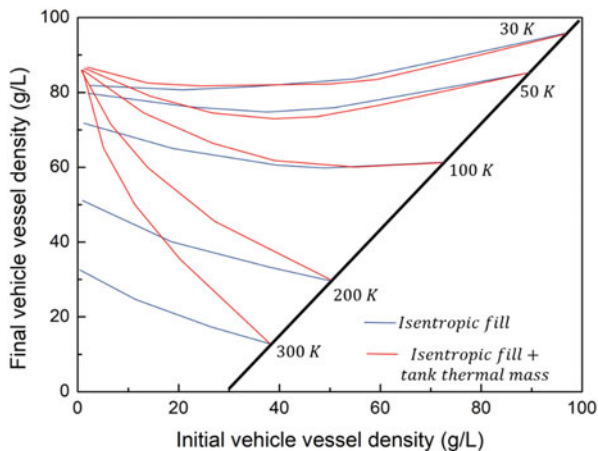
Fig. 11 Model predictions for H_2 density after refueling with an isentropic LH_2 pump as a function of H_2 density before refueling for multiple initial vessel temperatures (30, 50, 100, 200, and 300 K). Two sets of lines are shown: isentropic pump with negligible pressure vessel thermal mass (dashed) and isentropic pump including the vessel thermal mass and assuming thermal equilibrium between vessel and H_2. The black diagonal line in the right of the figure gives the initial vehicle hydrogen density if the vehicle had a full-capacity charge of hydrogen at 700 bar at the temperatures indicated

systems. Evaporated LH_2 is recycled into the Dewar, avoiding losses and repressurizing the Dewar after LH_2 extraction.

Predicting LH_2 pump refueling is similar to predicting compressed gas vessel refueling and the same equations dominate the process. However, delivery conditions are functions of LH_2 pump performance details, and these remain unpublished. We therefore assume, as a first approximation, isentropic LH_2 pumping. While real pumps will not reach this level of performance, final vessel density may be reasonably well approximated due to the low exergetic cost of LH_2 pumping. We assume that the large LH_2 hydrogen station Dewar is saturated at 3 bar and 24.6 K, filling a vehicle pressure vessel to 700 bar at various temperatures.

Modeling results in Fig. 11 show final vehicle H_2 density after refueling (when the vehicle drives away from the fueling station) as a function of vehicle H_2 density before refueling (when the vehicle drives into the fueling station) for multiple initial vehicle vessel temperatures: 30, 50, 100, 200, and 300 K. Two sets of lines are shown: isentropic pump with negligible pressure vessel thermal mass (dashed) and isentropic pump including the vessel thermal mass and assuming thermal equilibrium between vessel and H_2 (solid lines). We assume vessel refueling to 700 bar. Note the ordinate of Fig. 11 begins at 30 g/L.

Looking first at the dashed lines, we see that all fills from empty end at very high density, nearly 90 g/L, because the initial vessel temperature does not matter if the vehicle pressure vessel has negligible thermal mass. Comparing dashed lines vs. solid lines in Fig. 11 shows that nonnegligible vessel thermal mass plays

a large role in fill density for warm (200–300 K), empty vessels, refueling from the LH$_2$ pump at the station. These realistic vessels cool only partially during refueling, driving away pressurized (700 bar) at relatively low density due to their elevated temperature. A few rapid drive-refuel cycles would be necessary to reach low temperature and full density.

At very low starting temperatures (30–50 K), the heat absorbed by the vessel is relatively small because the starting temperature is only 10–30 K different from that of LH$_2$. As a result, the difference between the solid and dashed lines for 30–50 K starting temperatures is much smaller, and high-density refueling is achieved regardless of the initial fill level. In the limit of an initially empty vessel with zero thermal mass, the fill density is 91.45 g/L, obtained from isentropic compression of 3 bar saturated LH$_2$. All dashed lines approach this density for an initially empty vessel. Even higher densities (>95 g/L) are obtained when refueling very cold (30 K), nearly full vessels, for which the pump is essentially compressing low-entropy H$_2$ already in the vessel.

The black diagonal line in the right of Fig. 11 gives the initial vehicle hydrogen density if the vehicle had a full capacity charge of hydrogen at 700 bar at the temperatures indicated. Since Fig. 11 assumes refueling at 700 bar, the black line is a limit where no refueling is possible and density after refueling equals density before refueling. Driving is necessary before refueling to reduce pressure and cool the vessel.

In summary, the low exergetic cost of pumping LH$_2$ may lead to rapid and efficient refueling at high densities (Khosravi et al. 2018). Flow work is also lowest near the liquid phase (Fig. 10), minimizing heating and density losses during vessel filling. Future experiments will reveal how closely the isentropic pump models real pump performance. However, the density of the fueling is reduced by warm tanks with nonzero thermal mass.

Safety, both real and perceived, is an often-raised criticism of pressurized H$_2$ storage. However, the safety risks of storing compressed or cryogenic fluids are not a simple function of pressure. The overall safety of pressure vessels can be counterintuitive, since although vessel wall strength and impact resistance increase directly with storage pressure, the maximum mechanical energy released by sudden expansion (e.g., in a vessel rupture) of the stored gas (H$_2$) does not. Here, we consider some of the thermodynamic aspects of safety associated with compressed gas, LH$_2$, and cryocompressed approaches.

Thermodynamically, the mechanical energy released during a sudden expansion can be calculated as $W = \int p\,dv$, where p is pressure and dv is a differential volume expansion. Considering that sudden expansions are often rapid enough to be adiabatic, the first law of thermodynamics reduces to $\Delta U = W$. Therefore, the mechanical energy equals the adiabatic change in internal energy when the gas expands from storage pressure to ambient pressure while cooling down considerably in the process.
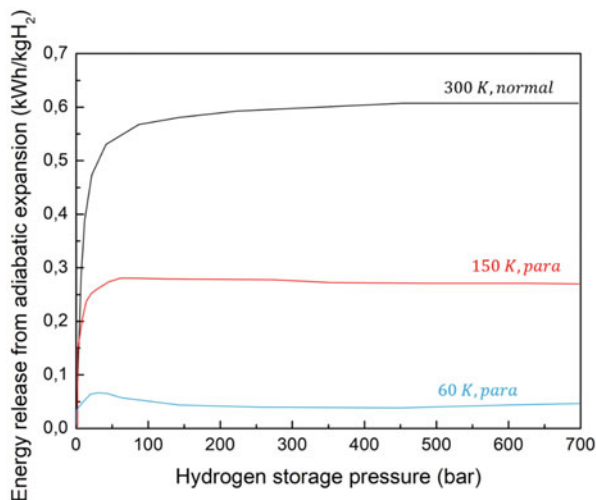
Fig. 12 Calculated results for the maximum mechanical energy (per kilogram of H_2) released on instantaneous expansion of H_2 gas (e.g., from a pressure vessel) as a function of initial storage pressure at 60, 150, and 300 K. For comparison, note that the chemical energy content of H_2 is 33.3 kWh/kg. The figure reports normal-H_2 expansion energy at 300 K and para-H_2 expansion energy at 60 and 150 K. In the last two cases, the real adiabatic expansion energies are slightly lower because the para-H_2 content is less than 100% before expansion (between 99.8% and equilibrium, depending on the previous use of the storage and the actual ortho-to-para H_2 transition rate)

The most dramatic and perhaps counterintuitive result from integrating the expansion energy equation is the radically lower theoretical burst energy of cold H_2. Figure 12 shows the theoretical maximum specific mechanical energy released by a sudden adiabatic expansion to atmospheric pressure (e.g., in a vessel rupture) of high-pressure H_2 gas from three temperatures (60, 150, and 300 K). H_2 stored at 70 bar and 300 K will release a maximum mechanical energy of 0.55 kWh/kg H_2 if suddenly (i.e., adiabatically) expanded to atmospheric pressure (cooling substantially in the process). Counterintuitively, this maximum specific energy release increases only slightly with much higher H_2 pressures. Raising vessel pressure to 700 bar (1000% increase from 70 bar) increases the maximum specific mechanical energy release by only 10%, while shrinking vessel volume and strengthening (thickening) vessel walls many times over. We emphasize here that these numbers are for specific energy release (kilowatt hours/kilograms H_2). To the extent that higher-pressure vessels of equal internal volume hold a larger number of kilograms of hydrogen, more total mechanical energy release can be realized from higher-pressure vessels.

Cooling down the H_2, on the other hand, considerably reduces specific expansion energy (by nearly an order of magnitude between 300 and 60 K). In addition to this, the specific expansion energy of cold H_2 (150–60 K) decreases slightly as the pressure increases between 100 and 700 bar due to nonideal gas behavior. The low burst energy and high H_2 storage density of cryogenic temperatures combine

synergistically, allowing for smaller vessels, which can be better packaged on-board to withstand automobile collisions. The vacuum jacket surrounding a cryogenic pressure vessel offers a second layer of protection, eliminating environmental impacts over the life of the pressure vessel. Vacuum jacketing also provides expansion volume to mitigate shocks from H_2 release.

Cryogenic vessels avoid the fast fill heating and potential overpressures typical of compressed gas storage ambient temperature vessels, consequently operating at higher safety factors, especially as driving the automobile cools the remaining H_2 fuel and reduces average H_2 pressures further over typical driving and refueling cycles. Finally, due to the high storage density of cryogenic H_2 and the potential for relatively low refueling pressure, the number and amplitude of pressure peaks in a cryogenic pressure vessel can be lower than in ambient high-pressure vessels, reducing thermal cycling wear. Of course, hydrogen at ambient pressure is completely harmless if it comes into contact with humans (except for simple asphyxiation, which isn't so simple if you are the one being asphyxiated), while severe frostbite can result from exposure to skin at LH_2. However, reliable and safe procedures have been developed for the handling of LH_2 based on the decades-long experience of NASA.

4 Hydrogen Storage in Interstitial Metal Hydrades

Considering only the hydrogen itself (and ignoring the tankage and balance of plant), one can compress gaseous hydrogen at 300 K to a density of 39 g/L using pressures of 700 bar. If one cools the gas to 100 K, the gas intrinsically becomes denser, and it requires only 300 bar pressure to densify it to 50 g/L. Liquid hydrogen LH_2 at 20 K has a density of 70.7 g/L. Isentropically compressing LH_2 at 3 bar can increase the density into the solid hydrogen range of about 90 g/L. Thus, it can be seen that the low-density nature of hydrogen, in all its pure states, allows storage density of at most 90 g/L and considerably lower when taking into account the required tankage. The cryogenic options offer considerably more density than the room temperature compression of hydrogen gas. However, LH_2 has, until now, been nowhere near as available as hydrogen from compressed gas hydrogen stations and merchant compressed gas cylinders. As a result, there has historically been interest in finding another means of storing hydrogen that combines the near-ambient-temperature character of compressed gas storage with the higher density and lower-pressure attributes of LH_2 and cryocompressed storage.

This third option is storing hydrogen in a chemical compound that ideally releases and reabsorbs hydrogen like a sponge, with little inducement for either process (Rusman and Dahari 2016).

It was noted that the mass density of hydrogen in water (H_2O) is 111 g/L at room temperature and ambient pressure. It turns out that water is a poor sponge for hydrogen because the H-O bond is sufficiently strong (~426 kJ/mol) that water does not readily release H atoms which would eventually form molecular H_2.

However, there are a number of compounds with even higher volumetric hydrogen density than water that act as excellent sponges for hydrogen. Storing hydrogen in the solid-state hydride form not only holds a volumetric advantage over compressed and liquid hydrogen states but also can potentially offer several additional key features. These features include low-pressure operation, compactness, safety, full reversibility, tailorable delivery pressure, excellent absorption/desorption kinetics, modular design for easy scalability and long cycle life. Research on solid-phase hydrogen storage systems has focused on "on-board-reversible materials", by which the spent material remains on-board the vehicle and is refueled with molecular hydrogen, and "off-board-reversible materials," for which the rehydrogenation requires removal of the material from the vehicle followed by industrial processing. The on-board-reversible materials include interstitial metal hydrides, complex hydrides, and sorption materials. The interstitial and complex hydrides involve chemical bonding between the hydrogen and elements in the storage material, whereas "sorption materials" involve hydrogen physically absorbed on materials with high surface densities, such as various forms of carbon and the metal organic frameworks (MOFs) and their derivatives (Langmi et al. 2014).

Activated carbon is a good example of a sorption material in which molecular hydrogen is adsorbed on the carbon surface by the weakly bonded van der Waals force. The storage capacity of physical adsorption is dramatically increased with reduced temperature and increased pressure, a regime called cryoadsorption in which the hydrogen gas forms a condensed form on the substrate at the temperature of liquid nitrogen (77 K).

Metal hydrides, in which atomic hydrogen is chemically bonded to the host elements, is an example of chemical hydrogen storage. Depending on the nature of chemical bonding and its bond strength, the hydride formation process can be either reversible or irreversible. The nature of the metal-hydrogen bonds can be classified into three types: metallic, ionic, and covalent. Listing in order of decreasing level of reversibility, we can order the types of bonding as metallic > ionic > covalent in terms of reversibility of hydride formation. For example, the metallic-bonded $TiFeH_2$, $LaNi_5H_6$, and $TiMn_2H_3$ are all reversible. Similarly, the ionic-bonded lithium, calcium, and magnesium hydrides (LiH, CaH_2, and MgH_2) are also reversible but with more difficulty. However, the covalent bonds formed between hydrogen and metals and metalloids of elements in group IB to VB of the periodic table lead to chemical compounds that are irreversible, such as CH_4 (methane) and C_8H_{18} (octane).

A special class of metal hydrides, called complex metal hydrides, consists of compounds with a mixed ionic and covalent character. For example, the material $LiAlH_4$ consists of Li+ cations bound to (AlH_4)– anions, yet within the (AlH_4)– moiety there is substantial covalency. As a class, these complex metal hydrides often have reversibility problems introduced by their partial covalent nature (Ley et al. 2015).

Metal hydrides are a broad class of materials that undergo a reversible reaction with hydrogen. The reaction is written as:
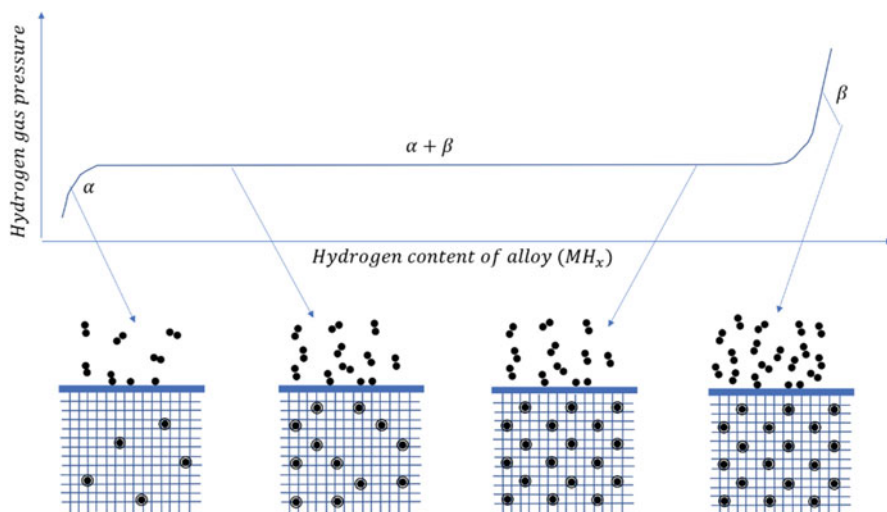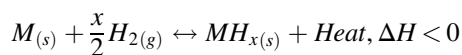
Fig. 13 A PCT curve illustrates the hydride formation mechanism on metal hydride

$$M_{(s)} + \frac{x}{2}H_{2(g)} \leftrightarrow MH_{x(s)} + Heat, \Delta H < 0$$

where M is the metal element or alloy to be hydrogenated, MH_x is the metal hydride, and ΔH is the enthalpy of formation of the metal hydride. The forward charging reaction is exothermic ($\Delta H < 0$), where heat is liberated, whereas the reverse discharge reaction is endothermic ($\Delta H > 0$), requiring the supply of heat to release hydrogen. Without adding heat to metal hydride MH_x during hydrogen release, the temperature at the metal hydride bed would drop as heat was scavenged from the surroundings.

The reaction of gaseous hydrogen with a metal or alloy is illustrated in Fig. 13 by a pressure-composition-temperature curve, commonly referred to as PCT curve. At a given temperature, when gaseous hydrogen is introduced into a vessel containing a pure metal or alloy, molecular hydrogen first dissociates on the material surface into atomic hydrogen. The atomic hydrogen then dissolves in the crystal lattice of the metal alloy or intermetallic compound to form a solute solution prior to reaction with the metal. This is usually designated as the α phase. Further increases in hydrogen pressure above the substrate leads to more dissolved hydrogen, and the pressure in the vessel remains relatively flat. The chemically bonded hydride (MH_x) phase, or the β phase, starts to grow. As more hydrogen is introduced above the sample, the β phase continues to grow and in an ideal scenario, the hydrogen pressure remains at a flat plateau value as more hydrogen is added (Von Colbe et al. 2019).

The β-phase formation is a hydrogen nucleation and growth mechanism resulting in expansion of the lattice. Depending on the absorbed hydrogen content, the volume expansion can be up to 30–40%, a large expansion indeed. The α and β phases coexist in the plateau pressure region. As more hydrogen is added, the β phase will

continue to grow until atomic H reaches its solubility limit, at which point the β phase is completed. After the solubility limit, further additions of hydrogen cannot be absorbed by the sample, and the hydrogen pressure will rise sharply in the test volume.

Reversing the process above, when the applied hydrogen pressure decreases below the equilibrium value for the complete β phase, the metal hydride MH_x starts to release atomic hydrogen, which diffuses to the surface of the metal alloy or intermetallic compound to form molecular hydrogen. The H_2 thus formed desorbs off the material and the lattice begins to contract back toward its original state (Kyoung et al. 2015).

Hydride materials will absorb hydrogen like a sponge and then release it when heated. There are hundreds of hydride materials. The first hydride systems used in automotive vehicles consisted of metal particles of iron and titanium that were developed at Brookhaven National Laboratory. These were tested by Daimler-Benz in Stuttgart, Germany. These early hydride systems were shown to be safe for storing hydrogen in automobiles, but they are almost 5 times heavier than liquid hydrogen storage systems. Other hydride systems have no such weight penalties and include magnesium nickel alloys, non-metallic polymers, or liquid hydride systems that use engine heat to disassociate fuels like methanol into a mixture of hydrogen and carbon monoxide. In an iron titanium hydride system, for a range of 300 miles (480 km), the tank could weigh about 5600 pounds (2520 kg). A liquid hydrogen tank for this range would weigh about 300 pounds (136 kg), a comparable gasoline tank would weigh about 140 pounds (63 kg).

An electric vehicle with a similar range and lead acid batteries would have a battery weight of about 6500 pounds (2925 kg). More efficient battery systems are available, but the most efficient electric vehicles of the future may be energized by fuel cell systems that convert hydrogen and oxygen directly into electricity. These systems would depend on having hydrogen fuel more readily available (Hwang and Varma 2014).

It is really remarkable that the lattice of the metal could expand/contract in this way during the hydrogen absorption/desorption reaction. The hydrogen-metal system can be considered as a gaseous analogy to a water sponge. Metal crystals contain interstices that will absorb and desorb hydrogen atoms just as sponges have pores that will absorb and desorb drops of water. However, unlike the purely physical action of water in the sponge, the hydrogenation and dehydrogenation reactions of interstitial metal hydrides are true reversible chemical reactions.

The thermodynamic aspects of hydride formation from gaseous hydrogen can be derived from the PCT curves, as displayed in Fig. 14.

It consists of a set of PCT curves at three temperatures. The plateau or equilibrium pressure depends strongly on the temperature. The enthalpy of formation ΔH and the entropy of formation ΔS of a metal hydride can be derived from the PCT curves by means of the van't Hoff equation written for the hydrogenation reaction:
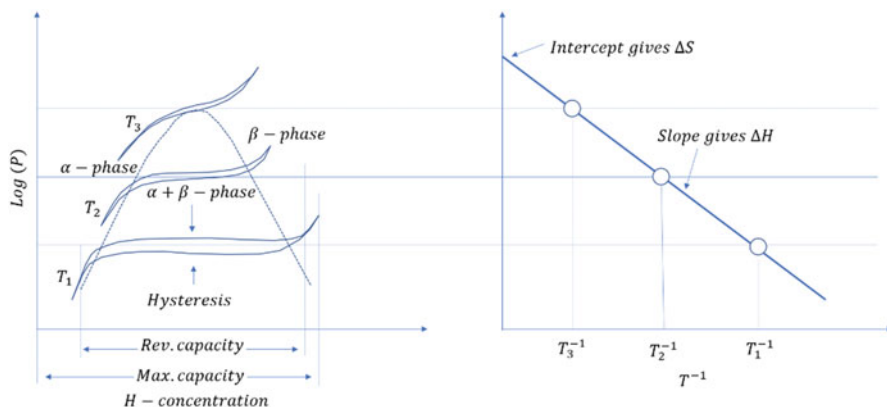
Fig. 14 PCT absorption/desorption curves conducted at three temperatures (left) and the corresponding van't Hoff plot (right)

$$lnP = \frac{\Delta H}{RT} - \frac{\Delta S}{R}$$

Plotting lnP vs. 1/T yields a line with slope $\Delta H/R$ and y-axis intercept of $-\Delta S/R$. Since ΔH is typically negative for hydrogenation, the plot slopes downward with increasing 1/T.

For the interstitial metal hydrides, the entropy of formation ΔS is determined largely by the change in entropy of the hydrogen itself as it transforms from molecular H_2 into dissolved atomic hydrogen. A ΔS value of -120 J/K mol H_2 is typical for many of all metal-hydrogen systems.

We will soon see that many interstitial metal hydrides have enthalpy barriers for hydrogen release on the order of 30 kJ/mol H_2. For context, the bond dissociation energy of molecular hydrogen is 436 kJ/mol H_2, and the H-O bond strength in water is about 426 kJ/mol. So, we can see that it takes about an order of magnitude less energy to release atomic hydrogen (on a molar basis) from the average interstitial metal hydride than it does to release atomic hydrogen from typical covalent chemical bonds (Chao and Klebanoff 2012).

The absorption and desorption reactions of metallic hydrides are surprisingly easy and simple. Since there is no distinct activation energy required in forming metallic hydrides, absorption and desorption reactions readily occur spontaneously. The intrinsic material kinetics do not limit the practical hydride/dehydride cycle times. The main constraints at the storage system level actually lie on (1) how to engineer the heat management and (2) how to prevent the metal hydride surfaces from becoming contaminated.

The majority of the binary metal (single-element) hydrides have large negative enthalpy of formation ΔH values, meaning too stable metal-hydrogen bonds that would require higher heat to break the bonds (>150 °C).

Complex metal hydrides represent a class of compounds composed of metal cations (typically group I and II elements) and "complex" hydrogen-containing anions such as alanates (AlH_4^-), borohydrides (BH_4^-), and amides (NH_2^-). The IUPAC (International Union of Pure and Applied Chemistry) recommended names for the AlH_4^- and BH_4^- salts are tetrahydroaluminates and tetrahydroboronates, although these names are rarely used in the literature (Møller et al. 2017).

Complex metal hydrides are interesting for hydrogen storage applications due to their light weight and high hydrogen content. They release molecular hydro- gen either by heating or by a chemical reaction, such as hydrolysis. In fact, many complex hydrides release hydrogen in the presence of water or aqueous solutions. However, such reactions are quite exothermic and are not easily reversible.

For a hydride with an equilibrium pressure of 1 atm, a 10 kJ/mol H_2 variation in ΔH results in about an 80 K change in the decomposition temperature. In general, higher values of ΔH suggest higher stability of the complex metal hydride, while lower ΔH values suggest lower stability. Most complex metal hydrides required heat to release H_2, but there are also some important exceptions.

It is important to consider the kinetics of hydrogen absorption/desorption for complex metal hydride reactions. Solid-state reactions involving H_2 often suffer from high kinetic barriers required for diffusion. The dependence of the rate constant k on the reaction temperature (in kelvin) and activation energy E_a is given by the Arrhenius equation:

$$k = Ae^{-\left(\frac{E_a}{RT}\right)}$$

where A is the preexponential factor. The activation energy originates from the barrier associated with bond breaking in the transition state of the potential energy surface between the reactants and products of a reaction. Higher temperatures typically result in accelerated H_2 release reaction rates.

Many reactions involving metal hydrides occur in the presence of catalysts. The role of the catalysts is to accelerate a dehydrogenation or rehydrogenation reaction without modifying ΔG (standard Gibbs energy change) of the reaction or being consumed in the process (Chamoun et al. 2015). Catalysts participate in the reaction and lower the activation energy for various processes; however, they are regenerated as the reaction proceeds to completion. Often, the role of the catalysts in reactions involving complex metal hydrides is to form activated species for rapid H_2 release or aid the dissociation of H_2 at the gas/solid interphase and accelerate diffusion of atomic H. To extract values of the E_a, measurements are made of the variation of the rate constant k with temperature, as follows:

$$lnk = -\frac{E_a}{RT} + lnA$$

Plotting lnk vs. 1/T gives a line of slope $-E_a/R$, with the preexponential factor obtainable from the intercept. With R = 8.314 J·mol^{-1}·K^{-1}, the units of activation

energy are joules per mole. The E_a values for hydrogen release from complex metal hydrides are typically ≥ 100 kJ·mol^{-1}, but catalysts can significantly reduce the activation energy (to tens of kilojoules per mole), as discussed in the following sections.

Although many metal hydrides display high volumetric and gravimetric hydrogen densities, for true commercial viability, the complex metal hydrides need to satisfy many performance requirements that are especially stringent for light-duty hydrogen-powered vehicles with fuel cells or internal combustion engines (ICEs). Complex metal hydrides have high gravimetric and volumetric capacities and tunable thermodynamics, which can allow reversible H_2 storage without removing the material from the H_2 tank. On-board reversibility is one of the most challenging requirements driving recent complex hydride materials discovery.

Complex metal hydrides aim to improve on the one deficiency of the interstitial metal hydrides, namely, gravimetric capacity. Therefore, the targets for gravimetric capacity are particularly important. For example, the 2017 system gravimetric target, indicating the mass of hydrogen stored per mass of the entire hydrogen storage system (including hydrogen storage material, tankage, and necessary plumbing), is 5.5 wt%. Assuming a 50% weight penalty arising from the required system hardware, the actual material's hydrogen storage capacity must be about 11 wt% or higher to satisfy the 2017 targets. This is much larger than the 2–3 wt% gravimetric density provided by the interstitial metal hydride materials.

Another critical requirement is that of material reversibility. The requirement for reversibility is implicit in the requirement for cycle lifetime (2017 target: 1500 cycles). This is a challenging requirement from a materials perspective, and experience has shown that reversibility is especially difficult for the higher-capacity complex hydride materials. From a practical perspective, the reversibility would need to be in excess of 99.9% per cycle for a commercial storage system.

A third system consideration involves the thermodynamic requirements. It is desirable to be able to use the waste heat from a fuel cell operating at 70–85 °C to drive off hydrogen from the metal hydride. Beyond the practical engineering issue of collecting and transporting fuel cell waste heat, if the material requires a high temperature to liberate hydrogen, then energy efficiency drops dramatically. In a sense, the hydrogen storage material needs to be "metastable." The material should be stable enough to store hydrogen near room temperature but be sufficiently unstable that only a modest amount of additional heat is required to liberate hydrogen completely and quickly. The high H_2 desorption temperatures of most of the complex metal hydrides arise from thermodynamic limitations. However, even a material with good thermodynamics can require high desorption temperatures if the material has poor kinetics.

A fourth material property considers material stability and volatilization, which is not explicitly called out in the targets but is implicit in the requirements for cycle lifetime and hydrogen purity. Ideally, it is preferred that the hydrogen storage material liberates only hydrogen when heated and does not release volatile and reactive components such as NH_3, BH_3, or other gas-phase components. This requirement serves two purposes: preserving the fuel cell catalysts (which become

poisoned by reactive impurities in the hydrogen gas stream) and maintaining the storage material's physical integrity. If the storage material loses some of its components by volatilization as the material is heated, that is bad.

For fuel cell systems, the contamination target levels are less than 10 ppb sulfur, 1 ppm carbon monoxide, 100 ppm carbon dioxide, 1 ppm ammonia, and less than 100 ppm non-methane hydrocarbons on a C-1 basis. Furthermore, oxygen, nitrogen, and argon must not exceed 2%. A H_2 ICE engine would have less-stringent requirements for the purity of the hydrogen stream.

Finally, material kinetics is critically important and forms the basis of the targets for fuel-dispensing rate and hydrogen discharge. Although the H_2 desorption rates are critical, perhaps even more challenging are the material's kinetics associated with rehydrogenation. In analogy with the current refueling operation of automobiles, a storage material must be able to receive a 5 kg charge of hydrogen in about 3.3 min for a 5 kg hydrogen charge.

5 Engineering Properties of Hydrogen Storage Materials

In general, hydrogen storage materials are high-surface-area materials consisting typically of transition metals, alkali metals, and other light elements such as B, N, or C. Characteristic particle sizes tend to be small. Beds may sinter or decrepitate with thermal or hydrogen cycling. Decrepitation is the systematic disintegration of bulk particles into smaller particles or "fines." The morphology of the bed may vary significantly as a function of hydrogen content. Also, for reversible materials, significant changes can occur during the life cycle of the bed, leading to order-of-magnitude changes in engineering properties (Kojima 2019).

The engineering properties, coupled with the chemical kinetics, define the dimension and engineering characteristics of the storage system. In general, packing density controls the overall volume of the system and is arguably the most influential parameter. Thermal conductivity controls the rate at which heat can be added or removed from the bed and helps define the characteristic thermal path in the bed. Permeability controls the rate at which hydrogen can be added or removed from the bed. Mechanical expansion forces during sorption of hydrogen control packing density and vessel design (e.g., strength).

The packing density of particles and powders has been studied and characterized by industries such as food processing, chemical packaging, oil and gas, and geotechnology. The packing density of a bed depends on a large number of particle characteristics, including size distribution, shape, plasticity, and interparticle friction. A convention for the engineering packing density is referred to as the tap density, which is simply defined as the bulk density resulting from manually compacting the bed with mechanical shock. The process of developing tap density relies on developing the optimal arrangement of close-packed particles in the absence of physical pressure being directly applied to the particles or bed. Although tap densities can vary tremendously, 50% of single-crystal density is common.

Exceeding tap density typically requires the process of continuous mechanical vibration, melting, or hydraulic/mechanical bed packing. Mechanical packing is the most straight forward of packing processes and typically is performed mechanically or hydraulically. Other material specific methods have been considered, including melting the materials to form a bed (heating the materials to a point that a phase transition occurs from solid to liquid). Care must be taken when performing this process as phase segregation or insufficient permeability can result.

Packing density has a significant impact on each of the other engineering properties. Increased packing density has a positive impact on thermal properties by improving solid fraction and decreasing interfacial resistance (Hirscher and Hirose 2010). The resulting thermal properties can then result in less system complexity. Conversely, high packing density decreases permeability by both increasing the tortuosity and restricting the flow area through the bed. This can result in challenges to adding or removing hydrogen. For some materials, such as the AB_2 or AB_5 metal hydrides discussed in chapter "Alkaline Liquid Electrolyte Water Electrolysis", the increased packing density can result in excess mechanical pressures due to swelling and contraction of the matrix during hydrogenation and dehydrogenation, respectively. The presence of this excess pressure can require overdesign to accommodate the added stress to avoid safety impacts such as vessel structural failure.

The thermal properties of hydrogen storage beds directly influence the efficiency, performance, and cost of hydrogen storage systems. Thermal design is perhaps the most challenging aspect of hydride-based automotive hydrogen storage system design due to the thermodynamic characteristics of hydrogen storage materials that can operate in the pressure and temperature regime of conventional proton exchange membrane (PEM) fuel cells. Enthalpies of hydrogenation in the best cases are about -30 to -40 kJ/mol H_2, requiring approximately 200 MJ of heat transfer for each hydrogen fill-and-delivery cycle when considering an automotive-scale system. Hydrogen uptake (refueling) is the most thermally challenging operational state as the reaction is exothermic, and on-board automotive refueling scenarios require rapid refueling rates. During rapid hydrogen uptake of an automotive-scale system, nearly 0.5 MW of cooling can be required to maintain a constant system temperature.

These intensive heat flux conditions demand a detailed understanding and optimization of the thermal transfer properties present within a hydrogen storage system (Visaria et al. 2010). High thermal conductivity of the metal hydride and low thermal resistance at the wall mitigate the effects of thermally limited reactions, enabling the use of larger diameters and a reduction in the number of parts required for efficient operation. Since thermal resistance at the vessel wall can generally be accommodated during absorption with the temperature and flow characteristics of the coolant fluid, the effective thermal conductivity of the storage material is of specific interest as this can limit the rate of the absorption reaction most significantly.

As discussed, hydrogen storage beds generally take the form of packed particles immersed in hydrogen gas. There are three different regimes of effective thermal conductivity within a packed particle bed. The low-pressure regime (typically subatmospheric) is characterized by molecular transport where gas pressure does not influence the thermal conductivity of the bed. The intermediate-pressure regime
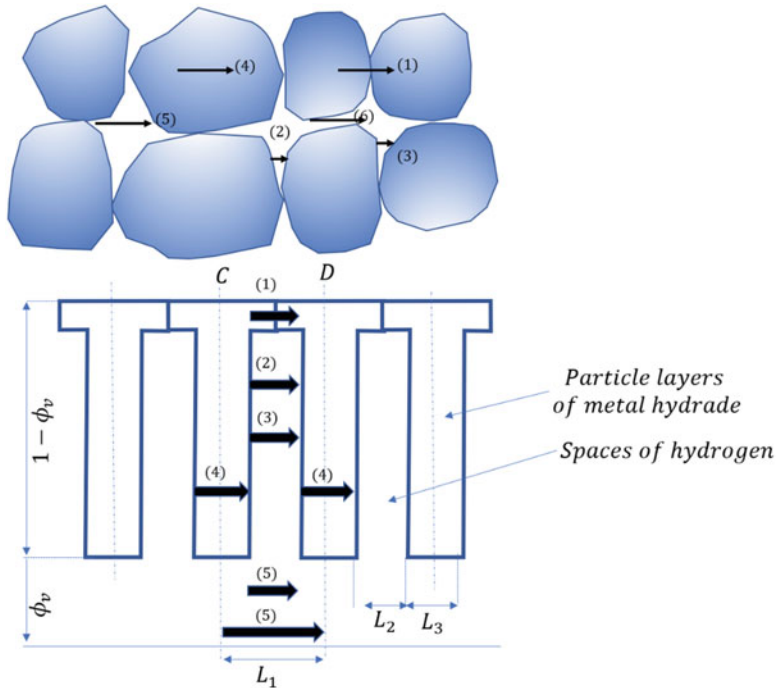
Fig. 15 Schematic and resistance model of six heat transfer modes within a hydrogen storage bed

is characterized by transition between molecular and continuum transport within the void spaces where thermal conductivity is significantly affected by the gas pressure. The high-pressure regime is characterized predominantly by continuum transport within the void spaces, and thus pressure no longer affects the thermal conductivity of the bed. The inflection point between transition and continuum transport is called the critical pressure. The boundaries of each of these regimes depend on the characteristic void space pore size within the bed. The intermediate- and high-pressure regimes are of specific interest for typical hydride-based hydrogen storage systems.

There are a total of six modes of heat transfer within the bulk metal hydride packed particle structure as described in Fig. 15.

The six modes of heat transfer are:

(1) Heat conduction at the particle contacts; (2) Heat conduction through a thin "film" of hydrogen; (3) Heat radiation between the particles; (4) Heat conduction through the particles; (5) Heat conduction through hydrogen in larger void spaces (6) Heat radiation between vacant spaces.

Models have been constructed describing the complete heat transfer mechanisms within the bed. It was developed generalized resistance models for packed beds, which others adapted for application to metal hydride beds. For lower- and
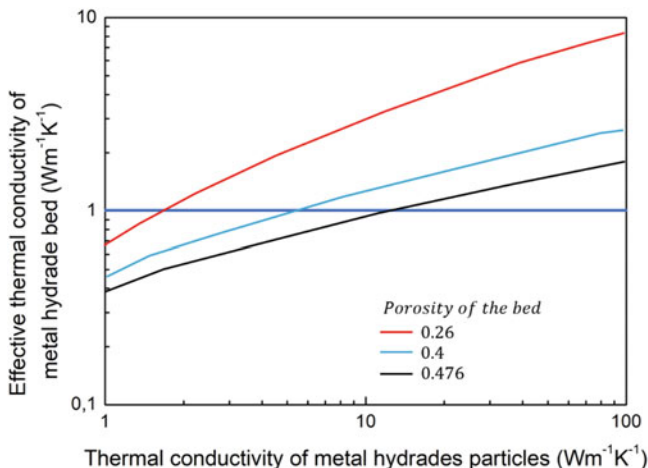
Fig. 16 Resistance model results for effective thermal conductivity of a metal hydride bed as a function of particle thermal conductivity and void fraction

moderate-temperature applications of these models, radiation heat transfer can be neglected. In general, the resistance model of effective thermal conductivity of a packed metal hydride bed can be described as:

$$K_{th} = K_{H_2} \left[\phi_v + \frac{1 - \phi_v}{\gamma + \frac{2}{3} \left(\frac{K_{H_2}}{K_S} \right)} \right]$$

where K_{H2} is the thermal conductivity of the hydrogen gas, K_S is the thermal conductivity of the metal hydride solid, φ_v is the porosity of the bed. The constant γ is defined as the ratio of the effective length of solid relating to conduction and the average hydride particle diameter. This ratio is difficult to quantify and is a function of particle contact angle, shape, and roughness. For metal hydrides, typical values fall between 0.01 and 0.1.

Using this resistance model, it was predicted the thermal conductivity of a typical metal hydride bed as a function of metal hydride particle thermal conductivity for three different porosities, as shown in Fig. 16.

Resistance models are useful for making quick estimations of packed bed effective thermal conductivities, yet are subjective and lack accuracy. Other types of models have been developed, including numeric methods. The most useful and apparently accurate model consists of a unit cell of two particle halves of equivalent shape encased in a cylinder of fluid (hydrogen). The model presented here neglects radiation and assumes spherical particles. The effective thermal conductivity of the bed K_{th} is calculated by:

$$K_{th} = K_g \left\{ \left(1 - \sqrt{1 - \Psi}\right) \Psi \frac{1}{\Psi - 1 + \frac{1}{K_g}} + \sqrt{1 - \Psi \left[\phi K_p + K_{SO}(1 - \phi)\right]} \right\}$$

In this expression, K_g is the thermal conductivity of hydrogen, Ψ is the porosity, ϕ is a flattening coefficient that defines contact quality, K_p is the particle thermal conductivity, and K_{SO} is an expression for the thermal conductivity at the particle-gas-particle interface. The effective thermal conductivity is highly influenced by K_{SO} as it describes the contribution of the fluid to the particle thermal contact quality.

Effective thermal conductivities of sodium alanate (a prototypical complex metal hydride) were calculated as a function of hydrogen pressure, particle thermal conductivity, particle diameter, and void fraction. The results are shown in Fig. 17.

Ranges selected for these variables were chosen based on typical metal hydride packed bed characteristics. Other model inputs include the deformation factor and contact-flattening coefficient of the particle, indicating the area of contact between the particles. These factors are difficult to calculate or predict and are usually estimated from experimental results. Overall, the effective conductivity of the bed is less sensitive to the deformation factor and contact-flattening coefficient compared to the other variables.

Effective thermal conductivity as a function of hydrogen pressure and void fraction is described in Fig. 17a. In general, higher pressures and lower void fractions lead to higher conductivities up to the critical pressure. The critical pressure for these calculated geometries is near 1×10^8 Pa (1000 bar), as observed by a reduction in rate of effective thermal conductivity increase with pressure. The effective thermal conductivity as a function of particle thermal conductivity is shown in Fig. 17b. In general, particle thermal conductivities above 50 W/m-K do not significantly influence bed effective thermal conductivity due to dominance in this regime by porosity and the particle-to-particle thermal contact. The effective thermal conductivity as a function of particle diameter is presented in Fig. 17c. Larger particle diameters lead to higher effective conductivities due to the reduction of particle-to-particle contacts and an increase in continuum regime gas transport relative to transition regime gas transport.

The calculations presented here are consistent with many models and measurements described in the literature. Models and measurements indicate that the effective thermal conductivity of particles loaded in a packed bed is generally limited to values below about 5 W/m-K, even with significant increases in the particle thermal conductivity, as shown in Fig. 17b. More clever methods must be employed to enhance thermal conductivity to levels above 5 W/m-K. In addition, the models discussed have been developed for distinct particles typical of classic/interstitial hydride materials. These beds are generally characterized as unsintered powders, while complex hydrides such as sodium alanate ($NaAlH_4$) can become porous sintered solids. Sintered solids are formed when a powder is heated (but not melted) and made to coalesce into an agglomerated porous mass. Packed particle models have not been directly applied to sintered solid materials.

Fig. 17 Calculated effective thermal conductivity of a packed particle bed as a function of void fraction, hydrogen pressure and particle characteristics
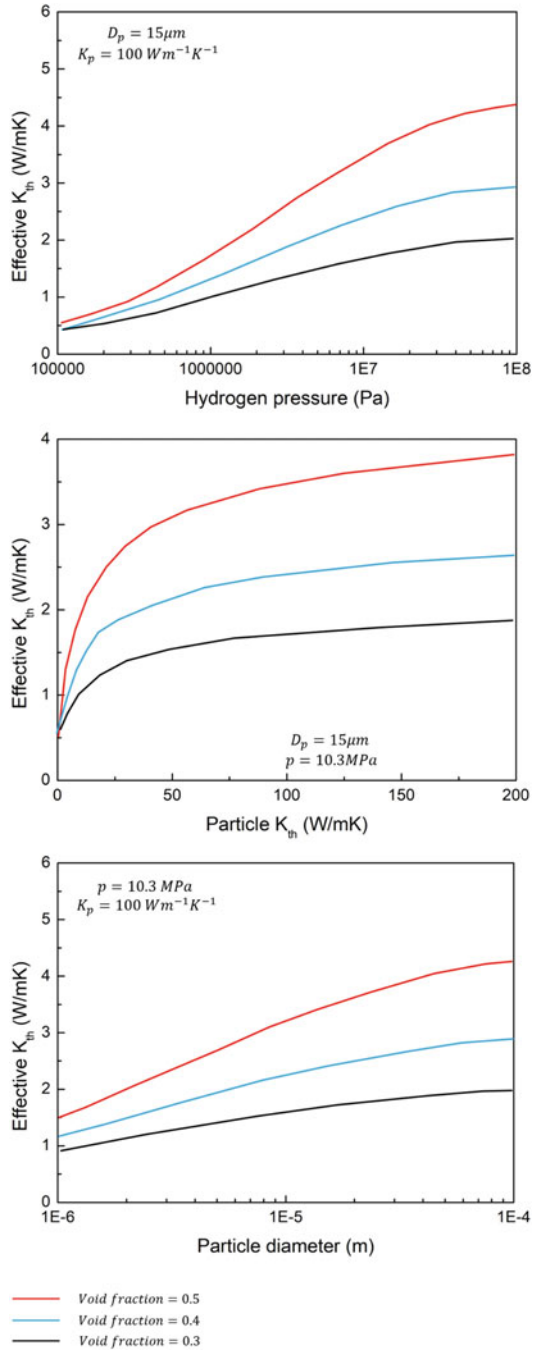
Several authors have described the importance of thermal conductivity enhancement to provide improved performance of metal-hydride-based hydrogen storage systems. Lower thermal resistances enable the use of larger thermal length scales and increased rate of hydrogen uptake. Many methods have been proposed and some tested for enhancing the thermal conductivity of hydrogen storage materials.

Increasing gas pressure of the surrounding hydrogen up to the critical pressure improves the overall effective conductivity of the bed as shown in the previous calculations (Fig. 17a). The critical pressure is defined as the point at which the mean free path of the gas is significantly less than a critical thermal path length within the bed. Further application of gas pressure to thermal property enhancement to sodium alanates is limited as the gas pressures required for absorption are near to or exceed the critical pressure of the bed (note the small increase in effective thermal conductivity of sodium alanates between 50 and 100 atm).

Larger particles or grains will significantly enhance thermal conductivity by reducing the number of particle-to-particle contacts and an increase in continuum-regime gas transport relative to transition regime gas transport (Dornheim et al. 2006). Application of this enhancement mode to complex hydrides is not straightforward as particle size and morphology vary significantly as a function of hydrogen content, and larger grains lead to a reduction of reaction surface area (Ueoka et al. 2007). If the grain size could be controlled with some undefined method, the performance improvement due to thermal conductivity enhancement would need to be balanced with the required reaction surface area.

Densification and reduced porosity improve particle contact and volumetric solid fraction, thus enhancing heat transport within the bed. Upper limits of densification are governed by requirements for gas diffusion within the bed. Experience has proven that further densification may lead to gas-diffusion-limited reactions of metal hydride systems.

Flow through the porous bed enhances the radial effective or apparent thermal conductivity of packed beds. Models and heat transfer coefficients have been developed for packed spherical particle reactors that are invariant with the bed to-particle-diameter ratio. The radial effective thermal conductivity is defined as the sum of the thermal transport of the packed bed K_{bed} and the thermal dispersion caused by fluid flow K_{flow}, or:

$$K_{bed+flow} = K_{bed} + K_{flow} = K_{bed} + X_1 P_{e_0} \frac{u_c}{u_{ave}} f(r) K_{gas}$$

The coefficient X_1 is a correlation function that describes the rate of increase of the effective thermal conductivity with flow velocity, Pe_0 is the Péclet number that describes the contribution of forced convection relative to hydrogen heat conduction, u_c is the velocity at the centerline of the bed, u_{ave} is the average velocity, f (r) describes the radial variation in dispersion, and K_{gas} is the thermal conductivity of the fluid (hydrogen). For our purposes, u_c and u_{ave} are assumed to be near equivalent due to the large vessel-to-particle-diameter ratio. The radial dispersion variation f(r) is assumed to be unity for similar reasons.

Fig. 18 The increase in the effective thermal conductivity of a sodium alanate bed as a function of average flow
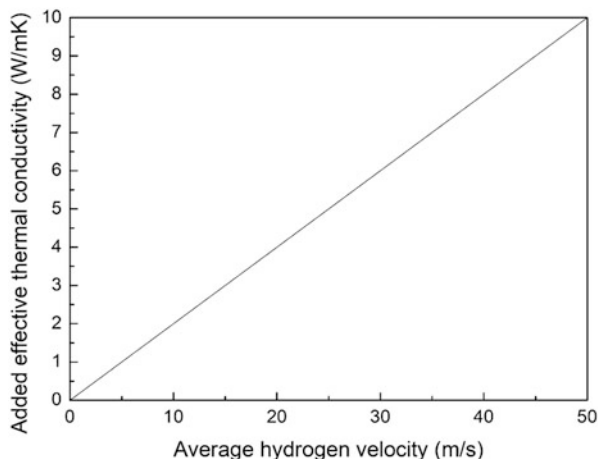
Using the model described, added effective thermal conductivity was calculated for a 2 cm diameter sodium alanate bed. Properties for hydrogen at 100 °C and 120 atm were utilized and the velocity along the centerline was assumed to be equivalent to that of the average. Significant enhancements in thermal conductivity may be experienced at modest flow velocities of 20–30 m/s (this corresponds to Reynolds numbers Re_0 of ~1000 and a volumetric flow rate of ~2 L/s). Figure 18 describes the relationship of increased effective conductivity to hydrogen flow.

Researchers have experimented with enhancing heat transport by coating metal hydride pellets with high-conductivity, high-ductility metals. Copper has been frequently used for this purpose. It was reported conductivities as high as 9 W/m-K for higher packing densities of 25% by weight for copper-coated $LaNi_5$ powders (thermal conductivity of uncoated powders typically less than 1 W/m-K). This corresponds well with results seen in Fig. 19, which describes effective thermal conductivity of $LaNi_5$ as a function of copper mass percentage.

This approach may not be the most favorable method of enhancing the thermal properties of sodium alanate or other high-energy-density metal hydride systems, as significant copper mass is required to attain moderate increases in thermal conductivity. In addition, gas and solid mass transport may be adversely affected when this technology is applied.

Various high-conductivity materials have been alloyed with metal hydrides to form enhanced heat transport composite materials. They were experimented with various alloyed metal additives, including copper, aluminum, lead, and lead-tin. The samples documented in this reference were alloyed at elevated temperature (200–600 °C) and cycled. In many samples, cycling resulted in the separation and fracture of the alloy and thus a reduction in composite thermal conductivity. Sintered aluminum structures of 20% solid fraction have been integrated with $LaNi_5$ hydride materials with success, resulting in effective thermal conductivities of 10–33 W/m-K. Temperatures required for this process and added mass and volume may exclude application to some materials such as complex metal hydrides.

Fig. 19 Thermal
conductivity of LaNi$_5$
powders at approximately
60% packing density as a
function of copper mass
percentage
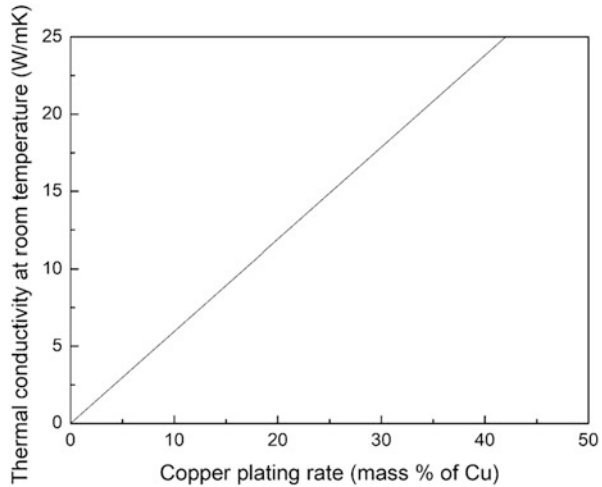
Fig. 20 The relationship
between the effective
conductivity and the volume
fraction of 1.6-mm carbon
fiber plates installed in a
10-cm-diameter metal
hydride bed for two metal
hydride effective
conductivities
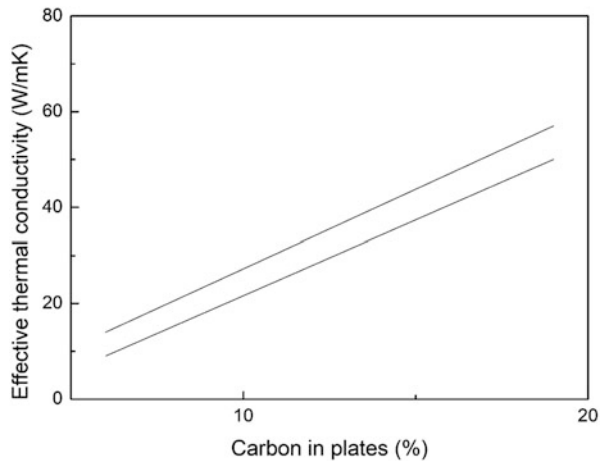
   High-thermal-conductivity structures have been used to enhance thermal conduc-
tivity, including copper wire matrices, periodic plates, nickel foams, and aluminum
foams. It was designed and integrated a 90% porous corrugated copper wire matrix
with a MmMi$_{4.46}$A$_{l0.54}$ hydride bed and improved the overall conductivity by a
modest 15%. Aluminum and nickel foams have been used with some success.
Practically, metal foams tend to be costly and are a significant challenge to load
with metal hydrides in ways that result in low void fractions. Thermal analysis of a
sodium alanate bed with periodic structures indicated that thermal conductivities
near 20 W/m-K may be possible as shown in Fig. 20.
   Work at Sandia has demonstrated the use of excess aluminum powders to
increase the average particle thermal conductivity and enhance the effective con-
ductivity of the bed. Thermal conductivity was enhanced threefold (from 0.5 to

1.5 W/m-K) by adding 12% by mass of 20 μm aluminum to stoichiometric sodium alanates and compacting the bed to approximately 60% of the single-crystal density.

Carbon fibers have also been implemented by Sandia to enhance the thermal conductivity of sodium alanate beds. A total of 9% by mass of woven carbon fibers was found to enhance effective thermal conductivity by at least an order of magnitude.

Expanded natural graphite fibers have been described as appropriate additives due to their characteristic high thermal conductivity, porosity, dispersibility, and low cost. Expanded natural graphite (ENG) fibers are produced from natural graphite that is soaked in sulfuric acid and heated to high temperatures, thereby expanding to very fine flakes. Thermal conductivities of approximately 20 W/m-K are attainable with volumetric fractions as low as 10%. Experimentally, thermal conductivities as high as 10 W/m-K were attained with mass fractions as low as 5%.

The permeability of a packed bed is well understood through many experimental and analytical studies in the twentieth century. Generally, the metal hydride bed consists of high-surface-area close-packed particles. Models used to describe flow through a packed bed generally need to accommodate Knudsen effects due to the small characteristic particle size. The flow properties of a metal hydride bed can be enhanced through the integration of flow channels in the bed.

6 Conclusions

Salt caverns have been used for hydrogen storage by the chemical sector in the United Kingdom since the 1970s and in the United States since the 1980s. They typically cost less than USD 0.6/kgH$_2$, have an efficiency of around 98%, and have a low risk of contaminating the hydrogen that is stored. Their high pressures enable high discharge rates, making them attractive for industrial and power sector applications. Because salt cavern storage is generally operated as a series of separate, adjacent caverns, natural gas storage facilities could be converted to hydrogen stores one at a time as hydrogen use increases, reducing upfront costs. The United States has the largest salt cavern hydrogen storage system currently in operation; it can store around 30 days of hydrogen output from a nearby steam methane reformer (between 10 and 20 thousand tonnes of H$_2$ (ktH$_2$)) to help manage the supply and demand for refining and chemicals. The United Kingdom has three salt caverns that can store 1 ktH$_2$, while a 3.5 ktH$_2$ storage demonstration project in a salt cavern is under preparation in Germany (planned for 2023).

Depleted oil and gas reservoirs are typically larger than salt caverns, but they are also more permeable and contain contaminants that would have to be removed before the hydrogen could be used in fuel cells. Water aquifers are the least mature of the three geological storage options, and there is mixed evidence for their suitability (although they were previously used for years to store town gas with 50–60% hydrogen). As with oil and gas reservoirs, natural barriers trap the vast majority of the hydrogen deep underground. However, reactions with

microorganisms, fluids and rocks can lead to losses of hydrogen. As they have not previously been investigated for commercial use with pure hydrogen, many aquifers would also incur exploration and development costs. The feasibility and cost of storing hydrogen in depleted reservoirs and aquifers have still to be proven. If they could overcome the challenges and establish themselves as viable, both would be options to provide storage on the scale required for seasonal hydrogen storage, especially in locations without access to salt caverns. Although geological storage offers the best prospects for long-term and large-scale storage, the geographical distribution, large size and minimum pressure requirements of sites make them much less suitable for short-term and smaller-scale storage. For these applications, tanks are the most promising option.

Compressed hydrogen (at 700 bar pressure) has only 15% of the energy density of gasoline, so storing the equivalent amount of energy at a vehicle refuelling station would require nearly seven times the space. Ammonia has a greater energy density and so would reduce the need for such large tanks, but these advantages have to be weighed against the energy losses and equipment for conversion and reconversion when end uses require pure hydrogen (see below). When it comes to vehicles rather than filling stations, compressed hydrogen tanks have a higher energy density than lithium-ion batteries, and so enable a greater range in cars or trucks than is possible with battery electric vehicles.

Research is continuing with the aim of finding ways to reduce the size of the tanks, which would be especially useful in densely populated areas. This includes looking at the scope for underground tanks that can tolerate 800 bar pressure and so enable greater compression of hydrogen. Hydrogen storage in solid-state materials such as metal and chemical hydrides is at an early stage of development but could potentially enable even greater densities of hydrogen to be stored at atmospheric pressure.

In general, the engineering properties of metal hydride beds follow the behavior of generic packed beds. This will likely be true for new materials that are developed that have similar physical characteristics, such as high surface area and small particle sizes. As new reversible materials are developed with lower enthalpies of hydrogen desorption and rehydrogenation, thermal properties may become less important due to reduced thermal duty. Conversely, as materials with higher hydrogen capacities are developed, flow properties become more important to enable high fluxes in and out of the metal matrix.

For many applications, life-cycle properties such as capacity durability will become important to understand and manage. Life-cycle durability may be impacted by contamination or morphology changes as experienced during the cyclic loading of the matrix. These properties and characteristics vary entirely depending on the specifics of the material chemistry and physical characteristics of the developed materials.

References

Aceves SM, Martinez-Frias J, Garcia-Villazana O (2000) Analytical and experimental evaluation of insulated pressure vessels for cryogenic hydrogen storage. Int J Hydrogen Energy 25(11): 1075–1085. https://doi.org/10.1016/S0360-3199(00)00016-1

Ahluwalia RK, Hua TQ, Peng JK (2012) On-board and off-board performance of hydrogen storage options for light-duty vehicles. Int J Hydrogen Energy 37(3):2891–2910. https://doi.org/10.1016/j.ijhydene.2011.05.040

Baroutaji A, Wilberforce T, Ramadan M et al (2019) Comprehensive investigation on hydrogen and fuel cell technology in the aviation and aerospace sectors. Renew Sustain Energy Rev 106:31–40. https://doi.org/10.1016/j.rser.2019.02.022

Barthélémy H, Weber M, Barbier F (2017) Hydrogen storage: recent improvements and industrial perspectives. Int J Hydrogen Energy 42(11):7254–7262. https://doi.org/10.1016/j.ijhydene.2016.03.178

Bowman RC Jr (2019) Metal hydride compressors with gas-gap heat switches: concept, development, testing, and space flight operation for the Planck sorption cryocoolers. Inorganics 7(12): 139. https://doi.org/10.3390/inorganics7120139

Chamoun R, Demirci UB, Miele P (2015) Cyclic dehydrogenation–(re) hydrogenation with hydrogen-storage materials: an overview. Energy Technol 3(2):100–117. https://doi.org/10.1002/ente.201402136

Chao B, Klebanoff L (2012) Hydrogen storage in interstitial metal hydrides. ISBN 9780429093715

Chen P, Zhu M (2008) Recent progress in hydrogen storage. Mater Today 11(12):36–43. https://doi.org/10.1016/S1369-7021(08)70251-7

De Corato A, Saedi I, Riaz S et al (2022) Aggregated flexibility from multiple power-to-gas units in integrated electricity-gas-hydrogen distribution systems. Electr Pow Syst Res 212:108409. https://doi.org/10.1016/j.epsr.2022.108409

Dornheim M, Eigen N, Barkhordarian G et al (2006) Tailoring hydrogen storage materials towards application. Adv Eng Mater 8(5):377–385. https://doi.org/10.1002/adem.200600018

Graez J (2009) New approaches to hydrogen storage. Chem Soc Rev 38:73–82. https://doi.org/10.1039/B718842K

Hardy BJ, Anton DL (2009) Hierarchical methodology for modeling hydrogen storage systems. Part I: scoping models. Int J Hydrogen Energy 34(5):2269–2277. https://doi.org/10.1016/j.ijhydene.2008.12.070

Hardy B, Tamburello D, Corgnale C (2018) Hydrogen storage adsorbent systems acceptability envelope. Int J Hydrogen Energy 43(42):19528–19539. https://doi.org/10.1016/j.ijhydene.2018.08.140

Hirscher M, Hirose K (2010) Handbook of hydrogen storage: new materials for future energy storage. ISBN 978-3-527-32273-2

Hwang HT, Varma A (2014) Hydrogen storage for fuel cell vehicles. Curr Opin Chem Eng 5:42–48. https://doi.org/10.1016/j.coche.2014.04.004

Khosravi A, Koury RNN, Machado L et al (2018) Energy, exergy and economic analysis of a hybrid renewable energy with hydrogen storage system. Energy 148:1087–1102. https://doi.org/10.1016/j.energy.2018.02.008

Kojima Y (2019) Hydrogen storage materials for hydrogen and energy carriers. Int J Hydrogen Energy 44(33):18179–18192. https://doi.org/10.1016/j.ijhydene.2019.05.119

Kyoung S, Ferekh S, Gwak G et al (2015) Three-dimensional modeling and simulation of hydrogen desorption in metal hydride hydrogen storage vessels. Int J Hydrogen Energy 40(41): 14322–14330. https://doi.org/10.1016/j.ijhydene.2015.03.114

Langmi HW, Ren J, North B et al (2014) Hydrogen storage in metal-organic frameworks: a review. Electrochim Acta 128:368–392. https://doi.org/10.1016/j.electacta.2013.10.190

Ley MB, Meggouh M, Moury R et al (2015) Development of hydrogen storage tank systems based on complex metal hydrides. Materials (Basels) 8(9):5891–5921. https://doi.org/10.3390/ma8095280

Liu PF, Chu JK, Hou SJ et al (2012) Numerical simulation and optimal design for composite high-pressure hydrogen storage vessel: a review. Renew Sustain Energy Rev 16(4):1817–1827. https://doi.org/10.1016/j.rser.2012.01.006

Møller KT, Sheppard D, Ravnsbæk DB et al (2017) Complex metal hydrides for hydrogen, thermal and electrochemical energy storage. Energies 10(10):1645. https://doi.org/10.3390/en10101645

Niaz S, Manzoor T, Pandith AH (2015) Hydrogen storage: materials, methods and perspectives. Renew Sustain Energy 50:457–469. https://doi.org/10.1016/j.rser.2015.05.011

Pukazhselvan D, Kumar V, Singh SK (2012) High capacity hydrogen storage: basic aspects, new developments and milestones. Nano Energy 1(4):566–589. https://doi.org/10.1016/j.nanoen.2012.05.004

Purewal J, Veenstra M, Tamburello D et al (2019) Estimation of system-level hydrogen storage for metal-organic frameworks with high volumetric storage density. Int J Hydrogen Energy 44(29): 15135–15145. https://doi.org/10.1016/j.ijhydene.2019.04.082

Rusman NAA, Dahari M (2016) A review on the current progress of metal hydrides material for solid-state hydrogen storage applications. Int J Hydrogen Energy 41(28):12108–12126. https://doi.org/10.1016/j.ijhydene.2016.05.244

Ueoka K, Miyauchi S, Asakuma Y et al (2007) An application of a homogenization method to the estimation of effective thermal conductivity of a hydrogen storage alloy bed considering variation of contact conditions between alloy particles. Int J Hydrogen Energy 32(17): 4225–4232. https://doi.org/10.1016/j.ijhydene.2007.06.003

Visaria M, Mudawar I, Pourpoint T et al (2010) Study of heat transfer and kinetics parameters influencing the design of heat exchangers for hydrogen storage in high-pressure metal hydrides. Int J Heat Mass Transf 53(9–10):2229–2239. https://doi.org/10.1016/j.ijheatmasstransfer.2009.12.010

Von Colbe JB, Ares JR, Barale J et al (2019) Application of hydrides in hydrogen storage and compression: achievements, outlook and perspectives. Int J Hydrogen Energy 44(15): 7780–7808. https://doi.org/10.1016/j.ijhydene.2019.01.104

Wijayanta AT, Oda T, Purnomo CW et al (2019) Liquid hydrogen, methylcyclohexane, and ammonia as potential hydrogen storage: comparison review. Int J Hydrogen Energy 44(29): 15026–15044. https://doi.org/10.1016/j.ijhydene.2019.04.112

Xu P, Zheng JY, Liu PF (2009) Finite element analysis of burst pressure of composite hydrogen storage vessels. Mater Des 30(7):2295–2301. https://doi.org/10.1016/j.matdes.2009.03.006

Yatsenko EA, Goltsman BM, Novikov YV et al (2022) Review on modern ways of insulation of reservoirs for liquid hydrogen storage. Int J Hydrogen Energy 47(97):41046–41054. https://doi.org/10.1016/j.ijhydene.2022.09.211

Zheng J, Chen L, Wang J et al (2019) Thermodynamic modelling and optimization of self-evaporation vapor cooled shield for liquid hydrogen storage tank. Energ Conver Manage 184: 74–82. https://doi.org/10.1016/j.enconman.2018.12.053

Hydrogen Transportation

1 Introduction

A central question when converting to renewable energy sources is: how can the energy be effectively stored and made available?

As regenerative energy production is subject to strong natural fluctuations, powerful and needs-based storage and transport solutions are required to compensate for the inevitable energy-market differences. In contrast to the existing gas and electricity infrastructure, new construction of the necessary infrastructure is subject to elaborate and complex planning and approval procedures. The establishment of a hydrogen industry creates comparatively cheap solutions to the above-mentioned challenges that can be implemented in the short term.

Hydrogen as a source of energy by itself is a storage medium. Like natural gas, it can be stored in large underground storage facilities, transported to the end-user by pipeline, and even achieves a similarly high transport energy density due to its material properties (Kuczyński et al. 2019).

Regardless of how the hydrogen is generated, if it is not produced directly at the point of use it must be transported. There are various technical processes for this: for example as a gas in high-pressure containers, as liquefied gas in thermally-insulated containers, further processed into methanol or ammonia in liquid form, or chemically dissolved in a carrier medium using the so-called 'Liquid Organic Hydrogen Carrier' ('LOHC').

Transport via pipelines is particularly economical. Due to the high calorific value and the compressibility of the hydrogen, an extraordinarily high energy density can be achieved.

In comparison to a 380 KV double system overhead line with 1.5 GW, a gas line (PN 80, DN 1000) can transmit up to ten times the power in natural gas and hydrogen operation – at around a fourteenth of the specific costs.

Pipeline systems at a length of several hundred kilometers each are already in use in pure hydrogen operation worldwide (Li et al. 2022).

The existing pipeline routes represent an extremely valuable element of the transmission system and offer the opportunity to build a climate-neutral hydrogen industry in a manageable time and with little investment. As measuring devices, compressors and fittings can be exchanged relatively easily, replacing or building new pipelines would be very expensive. In addition to the technical costs, the necessary spatial planning and planning approval procedures are extremely time- and cost-intensive. In the best-case scenario, the process takes 5–7 years from initial planning to commissioning. The gas network's pipeline routes, including their rights of way and use, are however available and accepted by the population.

Contrary to popular belief, the transport energy density of hydrogen is only slightly lower than that of natural gas. Therefore, the switch from natural gas to hydrogen has little impact on the capacity of a pipeline to transport energy.

The upper calorific value of natural gas at around 11 kWh/Nm^3 is about three times higher than that of hydrogen at 3.5 kWh/Nm^3, so that at the same pressure, around three times the volume of hydrogen is required to keep the energy content constant.

When comparing the energy flow of two gases through a pipeline, it is not only the volume that is important, but above all the parameters of density, flow velocity, and pressure (André et al. 2013). As hydrogen has a density nine times lower and three times the flow rate of natural gas, almost three times the volume of hydrogen can be transported in the pipeline at the same pressure and during the same time.

2   Hydrogen Embrittlement

The damage that hydrogen generates in steel can be manifold. It can reduce toughness, strength, total elongation, and area reduction, produce cracks or blisters in the material, accelerate crack growth, etc. (Álvarez et al. 2019). The term HE is generally used to refer to the degradation of the mechanical properties of steel caused by H. In the study of hydrogen embrittlement phenomena, the entry of hydrogen into metal, the variations in solubility of hydrogen in steel, its high mobility even at room temperature, and its attraction to regions with high triaxial tensile stresses are of fundamental importance. Hydrogen is the lightest of the elements, typically presenting in the molecular form H_2 (hydrogen gas). Molecular hydrogen is too large and is neither absorbed nor diffused into the solid metal. After adsorption on the metal surface and dissociation into atomic H, it is dissolved from the atmosphere according to (Chen et al. 2020):

$$H_{2_{gas}} \leftrightarrow 2H_{dissolved}$$
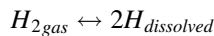
and its concentration is proportional to the square root of the hydrogen pressure in the environment, according to Sieverts' law. Figure 1 shows the solubility of hydrogen in iron as a function of crystal structure and temperature at one atm pressure of hydrogen.

Fig. 1 Hydrogen solubility in iron as a function of temperature. Hydrogen pressure at one atm. The sudden change in solubility with the change of the crystalline structure is evident
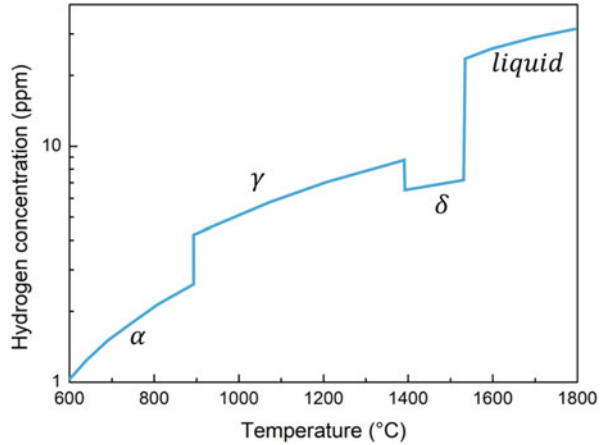
Hydrogen solubility is highest in liquid steel. For this reason, it can easily be absorbed by steel during fabrication or welding. Hydrogen solubility significantly decreases in delta ferrite (δ phase), increases in austenite (γ phase), and decreases again in alpha ferrite (α phase) falling below 1 ppm for temperatures below 600 °C. Although hydrogen solubility in iron is very low at room temperature, the hydrogen content in steel can be significant due to the numerous microstructural traps that hold it back and do not allow it to diffuse and escape as the steel cools. Furthermore, the processing to which the material is subjected generates residual stresses that promote the localization of H.

Figure 2 shows a scheme of trap sites for H. These sites include grain boundaries (including prior-austenite grain boundaries), delamination interfaces, voids, cracks, dislocations, particles, and inclusions (Bhadeshia 2016).

Currently, to bring the hydrogen content to very low concentrations in manufacturing, the steel is vacuum degassed. In very clean steels, the sulfur control is reduced in order to reduce the sulfur inclusions which are strong hydrogen traps. Other manufacturing techniques are sources of H, such as electroplating, acid cleaning, applying protective coatings, pickling, phosphating, paint stripping, etc. The hydrogen absorption can also occur in the service of the component. It is adsorbed by iron oxides and sulfides as a result of the iron-water and iron-H_2S reactions, respectively. The most important reactions that occur during the corrosion of iron in an acid environment are:

$$Fe + 2H^+ \leftrightarrow Fe^{2+} + 2H_{ads}$$

$$2H_{(ads)} \leftrightarrow H_{2(gas)}$$

$$H_{(ads)} \leftrightarrow H_{(dissolved)}$$
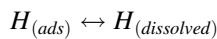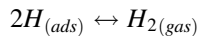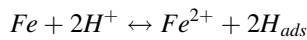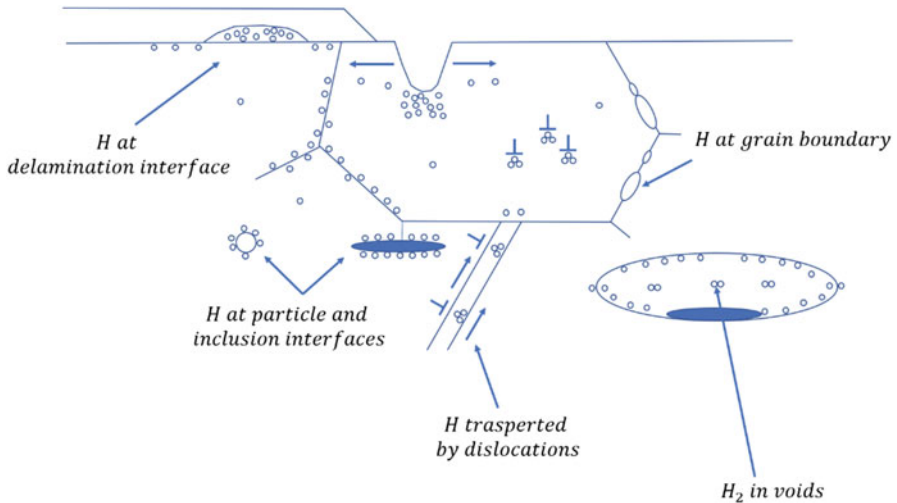
Fig. 2 Scheme of different trap sites

Recently, hydrogen is being promoted as an energy carrier. Many more hydrogen storage and production structures will be exposed to hydrogen. High strength quenched and tempered steels are rather sensitive to HE (Garrison Jr and Moody 2012). It was documented the typical characteristics of the embrittlement produced by hydrogen in high strength quenched and tempered steels. They used electrochemical hydrogen charging samples, which were subsequently plated. They noted that increasing the baking time (at a temperature of 150 °C) increases the stresses and the time required to cause a fracture, due to the decrease in the initial hydrogen content of the specimen. For sufficiently long baking times it was possible to restore the resistance of the loaded samples to that of the unfilled samples. For crack initialization, a certain amount of time is required for hydrogen to diffuse at the tip of a crack. This phenomenon makes high strain rate tests unsuitable for effectively detecting HE. Sustained load or low strain rate tests are more sensitive to detecting the hydrogen susceptibility of a material.

2.1 Hydrogen Embrittlement Mechanisms

Hydrogen weakens and eventually breaks the cohesive bonds of iron atoms, resulting in a loss of overall strength. Characterizing HE has led to several terms used to describe different forms of HE. Some terminologies are used based on the source of hydrogen and the type of damage (Djukic et al. 2015). The Hydrogen Environment Embrittlement (HEE) consists of the subcritical cracking of the material under load in hydrogen or hydrogen sulfide gas. In materials that form hydrides, embrittlement often involves the formation and fracture of brittle hydrides at the

apex of the cracks is termed hydride embrittlement. Internal Hydrogen Embrittlement (IHE) involves the concentration of pre-existing hydrogen in regions of high applied and residual hydrostatic stress and consequent failure at a stress value lower than the yield strength (Dwivedi and Vishwakarma 2018). Other forms of hydrogen damage involve the formation of cracks after weld cooling, blistering caused by the accumulation and formation of hydrogen in the material and hydrogen attack. The latter occurs at high temperatures in steels exposed to high hydrogen partial pressures. Hydrogen reacts with the material and forms gases such as methane and high-pressure steam, which lead to internal voids and cracks. Numerous HE mechanisms have been proposed in the literature. However, the most accredited are the hydrogen-enhanced decohesion (HEDE) and the hydrogen-enhanced localized plasticity (HELP) mechanism (Djukic et al. 2019).

The HEDE mechanism is based on the fact that hydrogen reduces the bond energy between the atoms of the metal, facilitating decohesion. This mechanism was introduced based on the observation of the fragile features of H-charged iron.

It was hypothesized that the weakening of the interatomic bonds of iron was due to the donation of the 1s electron of hydrogen to the 3d shell of the iron atom.

HEDE was used to explain the toughness reduction of the material, observing an increase in the crack tip opening angle with increasing hydrogen content. It states that HE occurs at the crack tip, where the tensile stress exceeds the local maximum atomic cohesive force. Hydrogen trapping sites such as grain boundaries increase the local hydrogen solubility, resulting in a reduction in the local cohesive force between the metal atoms. HEDE was used to explain the brittle intergranular fracture surface in high-strength steels. HEDE is supported by the fact that hydrogen accumulates in areas of high stress, such as at a crack tip. The atomic simulations also validated the hypothesis of the reduction of atomic cohesion as the hydrogen content increases. However, the effect of hydrogen on atomic decohesion cannot be experimentally demonstrated. Continuous HEDE models are often based on the assumption that material failure occurs when the local hydrogen concentration reaches a threshold value. It was proposed a HE model in high-strength martensitic steels in terms of intergranular fracture, relying on the fact that the fracture initiates the decohesion of the carbides and propagates along the grain boundaries. In this model, the rupture process begins at the grain boundary carbide particles and the rupture depends on local stress and hydrogen accumulation associated with a dislocation pile-up at the matrix-carbide interface.

It was suggested that the ductile characteristics present on the surfaces of H-induced fractures were because of hydrogen-enhancing plasticity processes (Martin et al. 2019). It was provided the theoretical explanation of the increased mobility of dislocations. The concept of hydrogen shielding was developed, which laid the foundation for the HELP mechanism of HE. The hydrogen accommodated in the dislocations modifies the stress field around it, increasing it in some directions and reducing it in others, also reducing the interaction energy of the dislocation with the obstacles or other dislocations, that prevent its movement. Atomistic simulations indicate that hydrogen reduces the stress for dislocation movement by lowering the dislocation core energy. Direct observations of the increase in H-induced dislocation

activity were carried out using high voltage TEM on thin sheets subjected to stress in a hydrogen environment. Hydrogen dissociates rapidly under the influence of the electron beam and diffuses into the samples. Dislocations that are initially stationary begin to move, and those in motion increase velocity by one or two orders of magnitude.

A decrease in the spacing between dislocations was also observed. Lower flow stresses were observed during tensile testing for samples loaded with hydrogen or tested in a hydrogen environment compared to H-free samples tested in air. The degree of softening is usually less than 10%. However, the influence of hydrogen on stress-strain curves depends on different variables, and in some circumstances, a hardening was observed.

The Adsorption-Induced Dislocation Emission (AIDE) mechanism was proposed to explain previous HE theories based on adsorbed hydrogen facilitating nucleation of dislocations on surfaces (Lynch 2019). The term dislocation emission refers to either the nucleation of the dislocation, facilitated by the adsorption of hydrogen and the subsequent movement under the applied stress away from the crack tip. Crack growth under stress occurs not only by the emission of dislocations from the crack apex but also by nucleation and growth of microvoids or nanovoids. Void nucleation and growth occur at second phase particles, slip band intersection, since the stresses required for dislocation emission are sufficiently high that some general dislocation activity occurs before the crack. Void formation contributes to crack growth. However, it occurs mainly by the emission of dislocation from the crack tips.

It was proposed a H-enhanced deformation-induced vacation (HESIV) mechanism by stating that hydrogen enhances the deformation-induced vacation leading to premature fracture of the material (Nagumo and Takai 2019). Vacancies result to be stabilized, and their mobility is reduced by H, thus forming clusters that act as vacuum sources by reducing the carrying capacity of the material.

Simultaneously fracture mechanisms can occur. Figure 3 schematically shows two cases in which multiple mechanisms occur together.

Nucleated dislocations at the crack tip (AIDE) can more easily move away due to HELP, thus decreasing the back-stress on the subsequent dislocation issue (Nagao et al. 2016). Figure 3a shows how the nucleation of voids ahead of the crack tip can be favored at the intersections of the slip-bands at the particle-matrix interfaces. Figure 3b shows crack propagation due to the AIDE and HEDE mechanisms. The AIDE occurs as long as the back-stress of the emitted dislocations does not reach a value such as to cause the HEDE to intervene. Once the crack has moved far enough away from the stress field of the dislocations, a new release of dislocations occurs.

2.2   Hydrogen Diffusion and Trapping Models

By diffusion we mean the process by which matter is transported into the material as a result of random molecular motions. During diffusion, hydrogen can occupy normal interstitial lattice sites or atomic and microstructural imperfections such as

Fig. 3 Schematic illustrating multiple hydrogen embrittlement mechanisms acting simultaneously. AIDE with contributions from HELP and HEDE (**a**), AIDE alternating with HEDE (**b**)
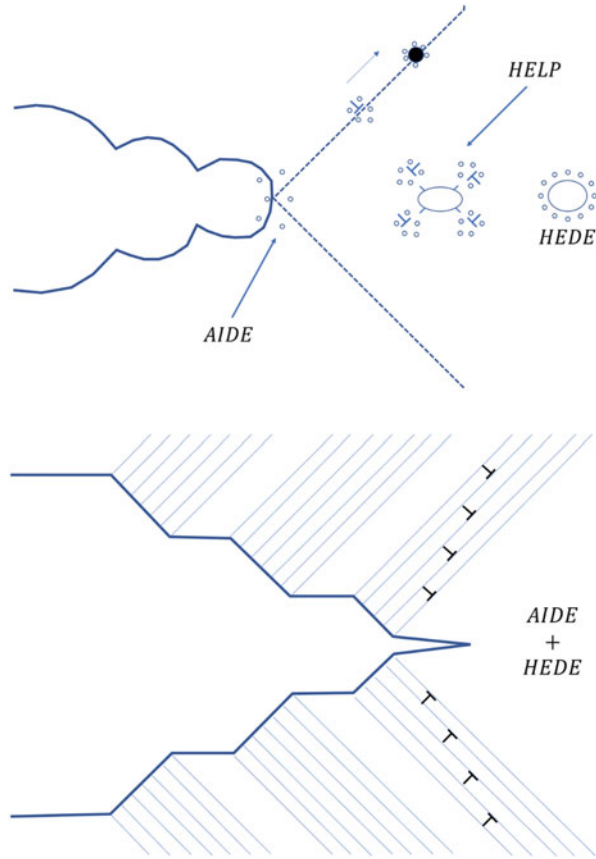
vacancies, grain boundaries, voids, dislocations, crack, etc. These latter sites are referred to as traps. In voids or cracks, the atomic hydrogen can recombine to hydrogen gas. According to Sieverts' law, the increase in gaseous hydrogen increases the hydrogen solubility in the lattice, therefore, these types of traps can accommodate a theoretically infinite number of hydrogen atoms (Jothi et al. 2015).

Traps such as dislocation and grain boundaries can accommodate a finite number of hydrogen atoms. The latter are called saturable traps. Figure 4 shows the potential energy levels for hydrogen diffusion with a single type of trap.

Referring to Fig. 4, E_L is the activation energy to move between two adjacent lattice sites, E_t and E_d are the activation energies for trapping and detrapping, respectively, E_b is the binding energy of trap and represents the change in energy from a normal interstitial lattice site to a trap site. Hydrogen volume concentrations at normal interstitial lattice sites and trap sites are identified with CL and CT, respectively. When there are multiple types of trap sites, the corresponding concentrations can be further divided into the concentrations of each trap type.
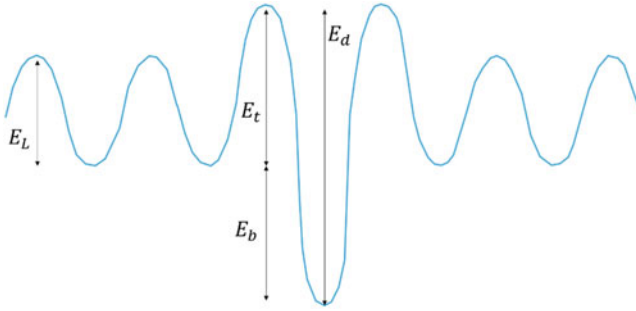
Fig. 4 Potential energy profiles for diffusion with a single type of trap

In formulating a mathematical model that describes the hydrogen diffusion in the presence of traps and in the absence of mechanical stress, it is commonly assumed that hydrogen atoms diffuse through the crystal lattice following Fick's law. Therefore, in an isotropic material, the hydrogen flux vector J~ is proportional to the gradient of CL:

$$\vec{j} = -D_L \nabla C_L$$

where D_L is the hydrogen lattice diffusion coefficient. It is function of temperature according to an Arrhenius-like relationship:

$$D_L = D_{L,0} \exp\left(-\frac{E_L}{RT}\right)$$

where $D_{L,0}$ is the pre-exponential factor, R is the universal gas constant, T is the absolute temperature, and E_L was described in the comment relating to Fig. 4. If the material is stressed, the hydrostatic stress gradient, σH, promotes the diffusion of hydrogen towards regions with a higher value of σH. In this case J~ becomes:

$$\vec{j} = -D_L \nabla C_L + \frac{D_L V_H C_L}{RT} \nabla \sigma_H$$

where V_H is the partial molar volume of H. In the diffusion processes, the number of hydrogen atoms is conserved. Therefore, the continuity equation, is:

$$\frac{\partial}{\partial t}(C_L + C_T) = -\nabla \vec{J}$$

Assuming D_L constant in the material, it is possible to obtain the expression that describes the hydrogen concentration change in normal interstitial lattice site and trap sites by eliminating the hydrogen flux from the previous equation:

$$\frac{\partial}{\partial t} C_L + \frac{\partial}{\partial t} C_T = D_L \nabla^2 C_L$$

or in the presence of mechanical stresses:

$$\frac{\partial}{\partial t} C_L + \frac{\partial}{\partial t} C_T = D_L \nabla^2 C_L + D_L \nabla \left(\frac{V_H C_L}{RT} \nabla \sigma_H \right)$$

This equation coincides with Fick's second law when the material has no traps and therefore, C_T is equal to zero. Generally, it contains two unknown functions, therefore it cannot be solved without introducing a second equation.

Saturable traps can be classified into three different types based on their ability to retain a captured hydrogen atom. In the traps of the first category, the hydrogen atoms are held and released, and the delay effect is negligible. In the traps of the second category, the delay effects are significant, while the third category includes the traps that do not release the captured hydrogen atom. Due to their ability to definitively release or remove hydrogen from the diffusive contribution, the traps of the second and third categories are defined as reversible and irreversible, respectively. It was developed an equation that considers the interchange of atoms between reversibly trapped and diffusing populations. By defining C_T, as the product of the number of trap sites per unit volume, N_T, and the fractional occupancy of traps, θ_T, they obtained the following equation:

$$\frac{\partial}{\partial t} \theta_T = k C_L (1 - \theta_T) - p \theta_T$$

The trapping effects can be described by two parameters k and p. The parameter k and p are related with the hydrogen atoms captured per second and the mean probability that a trap containing a hydrogen atom will release it before 1 second has passed, respectively. Both are functions of temperature according to Arrhenius-type relationships:

$$k = k_0 \exp\left(-\frac{E_t}{RT}\right)$$

$$p = p_0 \exp\left(-\frac{E_d}{RT}\right) = p_0 \exp\left(-\frac{E_b + E_t}{RT}\right)$$

where E_t, E_d and E_b were described in the comment relating to Fig. 4. They were provided analytical expressions of the solution in some particular cases; however, their resolution generally requires the use of a numerical method. It was subsequently formulated a model based on the local equilibrium between the population upon normal interstitial lattice sites and trapped population. The equilibrium between the two populations, occupying a fraction θ_L and θ_T, of the available sites N_L and N_T can be described by the equilibrium constant K. It is defined as the ratio between the activity of the hydrogen upon the trapping sites and upon the normal

interstitial lattice sites, which can be written in terms of the respective fractional occupancy or E_b:

$$K = \frac{1 - \theta_L}{\theta_L} \frac{\theta_T}{1 - \theta_T} = \exp\left(\frac{E_b}{RT}\right)$$

The definition of K allows having an algebraic equation between C_L and C_T, at the steady-state ($\partial\theta_T / \partial t = 0$) and with small value of θ_L. With these hypotheses it is possible to obtain a relationship between K and the parameters k and p:

$$\frac{k}{p} N_L = \frac{1}{\theta_L} \frac{\theta_T}{1 - \theta_T} \approx K$$

By replacing k, p and K with their expressions as a function of temperature:

$$\frac{k_0}{p_0} = \frac{1}{N_L}$$

In some cases, such as in numerical simulations, it may be convenient to reformulate the diffusion equations. When C_T is a function only of C_L, with the use of chain rule for time derivative, as:

$$\frac{\partial}{\partial t} C_L = D_{eff} \nabla^2 C_L$$

$$\frac{\partial}{\partial t} C_L = D_{eff} \nabla^2 C_L \pm D_{eff} \nabla \left(\frac{V_H C_L}{RT} \nabla \sigma_H\right)$$

where D_{eff} is the hydrogen effective diffusion coefficient defined as:

$$D_{eff} = \frac{D_L}{1 + \frac{\partial C_T}{\partial C_L}}$$

It was pointed out how the literature refers to the quantity expressed different denominations, and the same expression of D_{eff} is improperly used in different reformulations of the diffusivity equation. The expression of $\partial C_T / \partial C_L$ depends on the trapping mechanism and is usually a function of C_L making D_{eff} a non-constant quantity. By differentiating the expression of K, it is possible to have the following analytical expression for D_{eff}:

$$D_{eff} = D_L \left\{1 + \frac{K N_L N_T}{[(K-1)C_L + N_L]^2}\right\}^{-1}$$

it can be seen how, in the presence of trap sites, D_{eff} is always less than D_L. One of the prominent effects of trapping is to decrease the apparent diffusivity. In the regime of low trap occupancy this equation is independent of C_L and it becomes:

$$D_{eff} = D_L \frac{1}{1 + \frac{KN_T}{N_L}}$$

3   Transmission Through Pipelines

As the following pressure loss calculation shows, the lower calorific value of hydrogen during transport in pipelines can be largely compensated for:

$$p_2 = p_1 \sqrt{1 - \lambda \frac{L}{D} \frac{\rho_{1,i}}{p_{1,i}} c^2 k_m}$$

where p_1 is the gas pressure, L is the pipe length, c is the flow velocity, λ is the pipe friction coefficient, D is the pipe diameter, ρ_i is the gas density, k_m is the compressibility number.

As the compressibility numbers K_m of hydrogen and natural gas are different, the pressure loss can be calculated as follows, K_m is calculated for methane up to a pressure of 70 bar (simplified) as follows:

$$k_m = 1 - \frac{p_{abs}}{450 bar}$$

A pressure of up to 300 bar can be used for hydrogen:

$$k_m = 1 - \frac{p_{abs}}{1500 bar}$$

As the pressure changes during transport, an average pressure p_m is used to calculate an average compressibility number K_m:

$$p_m = \frac{2}{3} \frac{\rho_1^3 - \rho_2^3}{\rho_1^2 - \rho_2^2}$$

From the previous results, the pressure curve for a pipeline 100 km long and 1000 mm in diameter results as shown in Fig. 5:

If the pressure loss is to be kept the same over the distance, in this case the energy flow of the hydrogen is 83%. Figure 6 shows the ratio of the energy flows when the mean pressure changes.

Fig. 5 Pressure curve when transporting methane and hydrogen with the same energy content in a 100 km long high-pressure pipeline with a diameter of 1000 mm
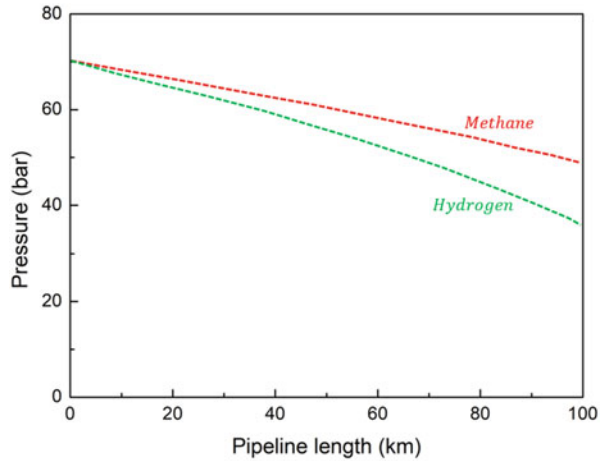
Fig. 6 Ratio of the energy flow as a function of medium pressure
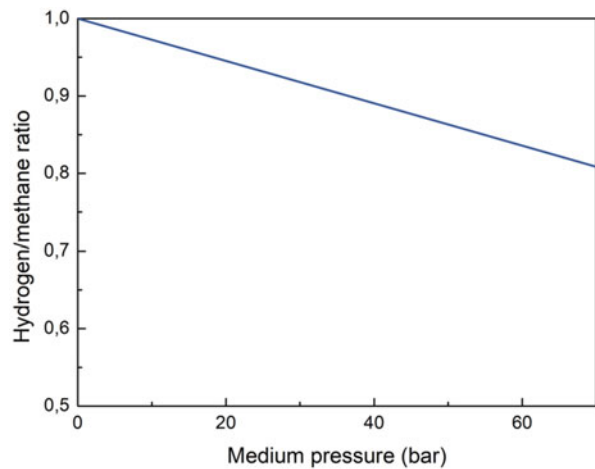
Figure 6 clearly shows that the hydrogen/methane ratio tends toward one when the pressure is reduced (0.997 at normal pressure). The higher the pressure, the greater the influence of the different compressibility numbers of methane and hydrogen. This reduces the inherently good flow properties of hydrogen compared to methane (Witkowski et al. 2018). This negative effect on the energy flow of the lower calorific value is largely compensated for by the higher flow rate. This effect also occurs in transmission line networks, and particularly at high pressures, so that the energy flow hardly decreases in comparison to natural gas operation.

Relevant studies and previous practical knowledge indicate that it is possible to convert the existing steel pipelines from natural gas to hydrogen operation to the extent required for the ramp-up of a hydrogen industry.

A significant reduction in the service life of high-pressure lines due to the influence of hydrogen does not seem likely (Herzler and Naumann 2009). Nevertheless, further examination is needed on whether the operating parameters must be adjusted for certain types of steel and operating conditions. In the case of fittings and control valves, the suitability for hydrogen of the membranes and seals used must also be determined. In the case of safety shut-off valves and pressure regulators, it must be clarified if the control and regulating functions must be adapted for the flow properties of hydrogen. Specific conditions of the existing infrastructure would need to be inspected and assessed and the relevant codes and regulations consulted prior to determining if the pipelines are suitable.

The physical H_2 readiness of the natural gas system essentially depends on the possible influence of hydrogen on the materials used. Especially for pipeline pipes and fittings made of steel, a reduction in material toughness can be measured under the influence of hydrogen ('hydrogen embrittlement'). Depending on the steel grade and the operating conditions of the pipeline, this reduction in toughness can lead to the growth of existing crack-like defects. In these cases, the service life of the line is therefore reduced.

According to current knowledge, the following factors are essential:

- existing crack-like defects, especially on the inside of the pipeline;
- hydrogen in atomic form;
- strong dynamic line pressure changes.

However, these factors are unlikely to coincide, as usually:

- Crack-like defects are uncommon;
- no major pressure load changes occur during regular operation;
- no atomic hydrogen is produced during transport.

Figure 7 shows an example in the case of hydrogen and methane.

Figure 7 shows the crack growth in dependence on load changes and change in fracture toughness under the given operating conditions. The influence on the material properties of the pipeline steel is recognizable, however this effect does not lead to a significant decrease in the service life.

Nevertheless, it cannot be ruled out that the binding energy of the H_2 molecule is broken up by various effects during transport and that atomic hydrogen is generated on the inner wall of the tube. This can diffuse into the steel and, among other things, reduce its fracture toughness. Therefore, a comprehensive and continuous integrity management of the systems is recommended to counteract any risks from hydrogen embrittlement at an early stage. The observation and analysis of the material conditions is carried out by physical internal and external inspection devices and monitoring systems, as well as tests of the pipeline (Nguyen et al. 2020).

Special technologies and inspection devices exist that can detect various changes in the pipeline during operation. An essential means of determining the condition and maintenance of natural gas pipelines today is the so-called 'pigging technique'. Depending on the test technology used, this 'pigging' allows the pipe wall to be checked repeatedly for any anomalies that may already exist. The existing

Fig. 7 Schematic
representation of the growth
of a crack with the initial
depth a_0 depending on the
number of load changes
N. The critical crack depth is
determined here by the
fracture toughness KIC
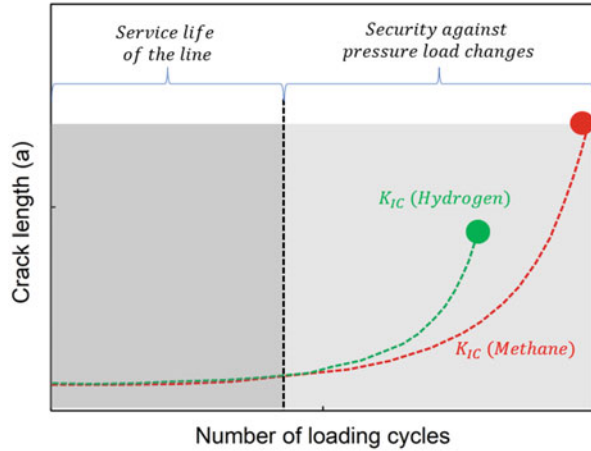
maintenance concepts and tools can be adapted to the requirements of hydrogen
transport with minor adjustments that ensure the safe and reliable long-term opera-
tion of the hydrogen transport lines. In 2017 and 2019, for example, a hydrogen
transport line built in 1996 with correspondingly designed pigs was inspected in the
USA. The required tool components have been adjusted to ensure resistance to
uneven wear. At a pressure of 20 bar and a flow of 13,000 Nm^3/h, the tool was
able to move safely and without damage, and the inspection was completed with a
100% sensor cover.

4 Hydrogen Compression

To be fed into the transmission system, the hydrogen must be compressed to the
operating pressure of the network. Compressor stations at certain intervals along the
line ensure that the pressure is maintained despite loss of flow in the pipeline. To
enable optimal utilization with high transport energy density in hydrogen operation,
more and higher-power compressors are required than in natural gas operation
(Sdanghi et al. 2019).

For the planned pipeline projects with the short and medium-term expected
amounts of hydrogen, the necessary compressor technologies are available in the
form of 'tried and tested' piston compressors. In the long-term, where a nationwide
switch to hydrogen with a transport requirement in the gigawatt range, the turbo-
compressor concepts currently used will be optimized for hydrogen. It can be
assumed that these will be available in a few years if the market demands them.

Natural gas infrastructure mainly uses turbo-compressors with one or two impel-
lers. These compressors are operated with gas turbines or motors with a drive power
of up to 30 MW. Depending on the hydrogen content in the pipeline, this infrastruc-
ture can be maintained or adapted accordingly:

- up to approx. 10% H_2, the compressor can generally continue to be used without major changes;
- the compressor housing can be maintained up to approx. 40% H_2, impellers and feedback stages as well as gears must be adjusted;
- from approx. 40% H_2 the compressor must be replaced.

Due to the intensive development work in this area, it can be assumed that by 2030 the standard compressor drive turbines can be operated with up to 100% hydrogen or can be converted accordingly.

Compressors that are driven by gas turbines draw their drive energy directly from the line and must be adapted accordingly to the hydrogen admixture. Most common gas turbines for pipelines can already burn a significant amount of H_2 in the fuel.

In the pure hydrogen operation of a pipeline, an energy flow of 80–90% of the natural gas capacity can be achieved by roughly tripling the amount of gas extracted. This increase can also be achieved in the existing pipeline network due to the higher flow rate of the hydrogen. However, this requires a higher drive power than is reserved for the transportation of natural gas. To maximize the hydrogen capacity of the gas network, approximately three times the drive power and therefore a correspondingly higher number of turbines and compressors are required than in natural gas operation.

For transport capacities of up to 750,000 Nm^3/h, current state of the art piston compressors are the most economical solution.

For transport capacities above 750,000 Nm^3/h, however, turbo-compressors are required. These should be available within a few years.

In the piston compressor, the gas is compressed with high efficiency in the cylinders.

By increasing the number of cylinders and drive power as well as a parallel arrangement of compressors, an economically viable transport capacity of up to 750,000 Nm^3/h can be achieved.

In the downstream and petrochemical sector, turbo-compressors for hydrogen-rich synthesis gases have been used for many decades. The technology is already available, but its efficiency is currently lower than that of piston compressors. As a result, many impellers are required to achieve an acceptable compression ratio. Therefore, there remains a need for optimization for future large-scale hydrogen applications.

Studies recommend increasing the peripheral speeds of the impellers to over 700 m/s due to the low molar weight of hydrogen to achieve a compression ratio of approximately 1.3 to 1 per impeller. This corresponds approximately to a tripling of the circumferential speed that is common today. This requires new hydrogen-resistant impeller materials that can withstand high centrifugal forces. The necessary developments have already been initiated so that appropriate wheels should become available in the coming years.

5   Refueling Issues

An efficient mode of hydrogen storage has to satisfy a set of criteria based on net energy density, weight, safety, cost, charging-discharging kinetics, cycle life, and other considerations for a particular application. Despite having the largest heat of combustion per unit of mass, hydrogen energy systems suffer from performance issues when volumetric considerations are factored in due to the low density of hydrogen gas at ambient temperature and pressure conditions.

The operating environment of hydrogen storage systems includes primarily the temperature and pressure required for the system to store and deliver hydrogen. These operating conditions, along with the storage material properties, are the primary drivers for the design. For example, system geometry and structural material selection are primarily determined by the operating temperature, hydrogen compatibility, and hydrogen pressure required for refueling, which determines the required material strength (Apostolou and Xydis 2019).

The van't Hoff equation relates the changes in reaction enthalpy ΔH and entropy ΔS to the equilibrium pressure existing above a hydrogen storage material at a given temperature T. These immutable thermodynamic quantities determine the ball field in which engineers play to exploit the hydrogen storage properties of materials in real systems. However, the van't Hoff equilibrium expression may not describe the actual pressure measured if the approach to equilibrium is slow (poor kinetics) and true equilibrium is not achieved. Both thermodynamics and kinetics are very important for the real engineered hydrogen storage systems.

The hydrogen refueling of a "spent material" typically occurs at elevated pressure to provide fast kinetics. The refueling pressure is thus the pressure limit for design since hydrogen desorption takes place at pressures below the material equilibrium pressure at similar temperatures to refueling. The operating environment for refueling is typically set to maximize the capacity while refueling in a reasonable time, 3–10 min perhaps. For some systems, an optimization for pressure and temperature can be performed based on the material kinetics and thermodynamics.

In contrast, the operating conditions for hydrogen delivery are determined by the fuel cell and application requirements.

Many classic interstitial metal hydrides can satisfy these requirements at or near room temperature, while complex metal hydrides typically require elevated (often excessive) temperature due to thermodynamics, kinetics, or both. In this case, the desorption temperature required to release hydrogen at a sufficient rate defines the maximum operational temperature. Some sorption materials will not release their entire capacity at 3 bar unless heated. This will affect system design and overall system delivery efficiency.

While generally an elevated pressure is required for a high capacity, pressures range from tens of bar up to several hundred bar for solid-state hydrogen storage systems. However, each class of storage material has more tightly grouped properties. Several system design considerations are based on the operating environment. For high-pressure compressed hydrogen tanks, expensive carbon fiber composite

Fig. 8 Adsorption isotherms of hydrogen on the activated carbon AX-21
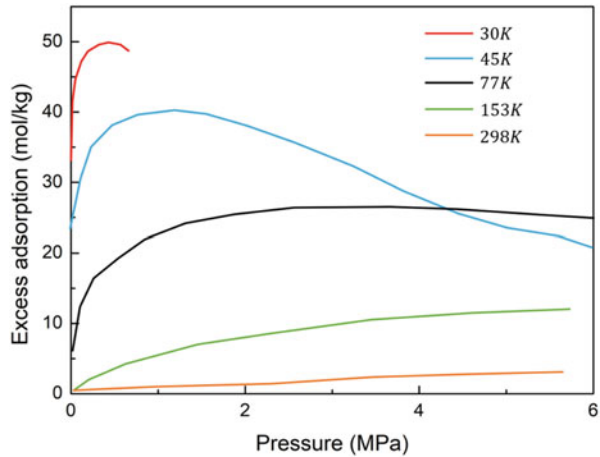
vessels are used for the extremely high specific strength of this material. However, at some lower pressure level the specific strength of carbon fiber is unnecessary because the wall thickness decreases to a level that is impractical to fabricate. For metal hydrides, system design can be optimized by trading refueling pressure against vessel wall thickness. To some limit, increasing the refueling pressure for metal hydrides will increase the absorption rate, assuming that temperature is controlled. However, the greater the refueling pressure, the thicker the vessel walls must be to maintain a sufficient factor of safety against failure. Since thicker walls result in a heavier vessel, increasing the refueling pressure creates competing effects that result in an optimum pressure for system gravimetric efficiency.

Temperature can be a driver for material selection as well. For example, cryogenic temperatures may require different vessel materials than operation at 500 K. Low-temperature embrittlement can be a problem for some steels, for instance, and these materials should not be used for cryogenic service. In addition, sealing materials can be problematic at both high temperatures (>200 °C) and cryogenic temperatures. Many elastomers are not suitable for either of these temperature regimes.

Since sorption materials rely on physisorption, they are typically only effective near cryogenic temperatures. Most storage capacities are listed at 77 K, for instance, although recent work has pushed toward operation at temperatures closer to ambient.

Figure 8 reports the hydrogen adsorption excess isotherms on the activated carbon AX-21 (which is equivalent to the activated carbon MaxSorb) as a function of temperature from 30 to 298 K.

The adsorption isotherms, as shown in Fig. 8, represent the amount of hydrogen adsorbed per unit mass of the adsorbent as a function of pressure and temperature in excess of the amount that would be present in the dead volume of the adsorbent. The isotherms shown in Fig. 8 indicate that significant excess densities (about half the liquid density of hydrogen) can be achieved at pressures on the order of 10–30 bars

for temperatures lower than 77 K, whereas negligible quantities of hydrogen can be found in the porous structure at ambient conditions in excess of the bulk gas density. Although researchers are working to find a sorption material that can function closer to room temperature, such a material has to date remained elusive. The operating environment of the physisorption storage unit thus requires cryogenic conditions, and the storage efficiency is expected to drop rapidly with increasing temperature.

Most sorption studies have considered moderate hydrogen pressures. However, for many materials, increasing pressure has limited positive impact on capacity. In fact, it is release pressure that limits these materials. Many cannot release their entire capacity at the pressure required for delivery to a fuel cell

The recoverable hydrogen is the net storage density of a sorption-based hydrogen storage unit. It corresponds to the amount of hydrogen stored that can be practically recovered from the storage system by reducing the pressure to a minimum set pressure, which could be the operating pressure of a hydrogen fuel cell. The recoverable hydrogen density depends the application (which sets the minimum set pressure required) and the thermodynamic conditions during discharge. Discharge can be isothermal or adiabatic or performed by allowing a temperature swing in which the temperature of the reservoir is allowed to rise during discharge. The residual storage density, which is the density adsorbed in the tank at the minimum pressure, becomes larger as the temperature drops. The residual density can be partially recovered by heating the system using heat from the environment or a heater. In the latter case, the storage system is then considered "active."

From Fig. 9, we see that the recoverable hydrogen is a strong function of storage pressure using either isothermal discharge (Fig. 9a) or by allowing a temperature swing of 50 K (Fig. 9b). The minimum pressure is 8 bars. The storage density in the adsorbent material required to achieve a recoverable system storage density of 36 kg/m^3 is indicated as a constant line (48 kg/m^3).

Refueling can be performed with hydrogen pressure as low as 10–20 bar, provided the material temperature is sufficiently controlled. The main problem with the classic interstitial materials is their poor gravimetric capacity, leading to engineered H$_2$ storage systems that are too heavy and carry too little hydrogen for some applications.

In contrast, interstitial metal hydrides have relatively high volumetric storage capacity due to the high density of the metal alloys.

To take advantage of the high volumetric capacity of metal hydrides and the high gravimetric capacity of high-pressure composite tanks.

Complex metal hydrides generally require high pressure (>100 bar) for refueling along with elevated temperature for both refueling and delivery, due primarily to kinetic limitations. Sodium alanate (NaAlH$_4$), which has been the most studied complex metal hydride, requires pressures of 100–140 bar and temperatures of 120–150 °C for rapid refueling to full capacity. Most other complex hydrides require even more extreme pressures and temperatures.

All hydrogen storage systems must contain an elevated pressure of hydrogen for delivery to a fuel cell or hydrogen internal combustion engine (ICE), whether the pressure is 10 or 700 bar (Zheng et al. 2012). As a practical matter, since bottles

Fig. 9 Recoverable hydrogen as a function of storage pressure using isothermal discharge (up) or by allowing a temperature swing of 50 K (down). The minimum pressure is 8 bars. The storage density in the adsorbent material required to achieve a recoverable system storage density of 36 kg/m^3 is indicated as a constant line (48 kg/m^3)
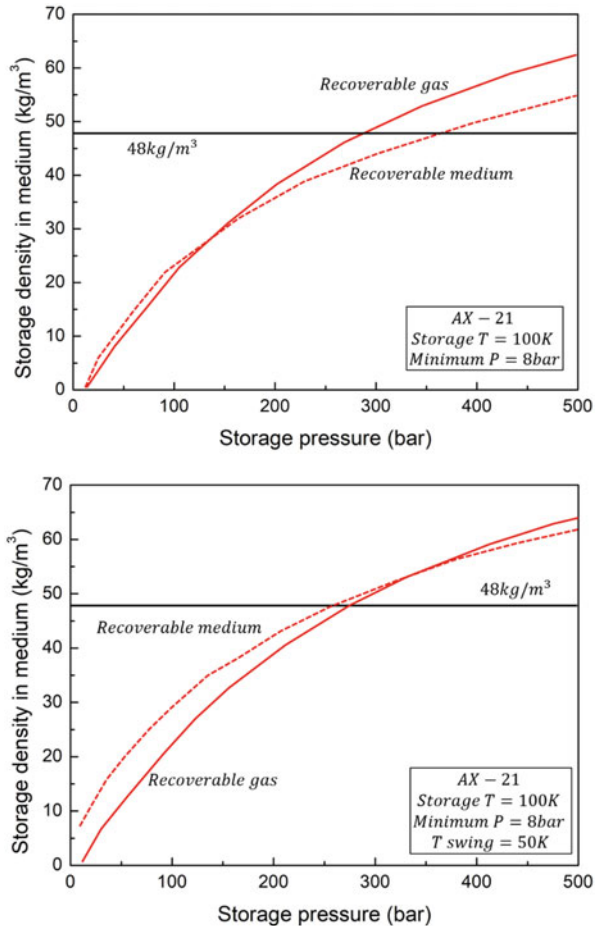
pressurized to 150 bar are the most convenient and widely available form of merchant hydrogen, ambient temperature systems must be able to withstand at least 150 bar if they are to be refueled from compressed gas cylinders. In general, to withstand elevated hydrogen pressure, the hydrogen storage vessel is constrained to either a spherical or a cylindrical shape to provide uniform stress distribution, thus minimizing the wall thickness and the weight of the vessel. Any flat-sided shape would require much thicker walls, resulting in a much more massive vessel. In addition, a cylindrical shape is much more convenient than a sphere with regard to tank packaging, fabrication, and material loading. Thus, most hydrogen storage systems consist of one or more cylindrical vessels.

Some attempts have been made to design conformable or semi-conformable hydrogen storage vessels. Conformability is highly desirable so that the storage tank can fit into spaces between other vehicle components like gasoline tanks do

today. Hydrogen storage tanks can be made in odd or noncylindrical shapes, but it is difficult to do so without greatly increasing the weight for a given pressure rating.

The number and diameter of the cylinders that make up the system are largely determined by the thermal management design. For hydrogen storage solutions that do not require thermal management, such as gaseous storage, a single large cylinder is typically optimal. However, most, if not all, advanced storage materials will require heat removal during hydrogen refueling and heat addition during hydrogen delivery. This heat transfer is governed by the material reaction enthalpy. For example, regenerating $NaAlH_4$ from spent $NaH + Al$ with hydrogen releases 40 kJ/mol H_2. In other words, the enthalpy ΔH of hydrogenation is -40 kJ/mol H_2. So, by absorbing 6 kg of hydrogen in 5 min, 400 kW of heat is produced by the system.

This heat must be removed or the hydrogen storage material will heat to a temperature above the optimum fill temperature, which will slow or even stop the absorption of hydrogen. This is a nice "self-regulating" feature of solid-state hydrogen storage, but care must be taken that the maximum temperature reached does not damage the surrounding tank material. To affect this heat removal or, in the case of hydrogen delivery, heat addition, heat exchange must be designed into the storage system. Broadly, the heat exchangers for hydrogen storage vessels can be lumped into two categories: external or internal. External heat exchange involves circulating a heat transfer fluid over the outside of the storage cylinders. With multiple cylinders, this design takes on the form of a shell-and-tube heat exchanger. Internal heat exchange involves circulating a heat transfer fluid through the inside of the cylinders via cooling tubes. With internal heat exchange, the hydrogen storage cylinders are typically larger in diameter than with external heat exchange. In either case, the thermal conductivity of the hydrogen storage material may require enhancement by some means to achieve a practical or optimal design.

For vessel length, longer is better for mass and volume efficiency since end caps will have a fixed size independent of length. To illustrate this, consider two extremes: (1) a system with a single tube long enough to hold all of the required metal hydride and (2) a system with hundreds of short tubes to hold the same amount of hydride. In the first case, only two end caps are required, while the second case requires hundreds of end caps. Longer tubes are also better for cost since part count is reduced. Actual tube length will be limited based on packaging constraints for the application. For the automotive market, cylinder lengths are probably limited to a meter or less for transverse mounting or 3 m for longitudinal mounting.

Modularity is a concept developed to maximize the energy efficiency and performance of an advanced hydrogen storage system.

The differences between a bulk bed and a modular system are shown in Fig. 10. The same mass of storage media M is used, but it is distributed to n smaller vessels; the exact number of modules depends on the properties of the storage media, the details of the control strategy, and the vehicle size. Each of these smaller vessels is individually controlled, with its own temperature T_n, pressure P_n, and composition.

Fig. 10 Comparison of bulk bed to modular system configurations. Here, Q is heat added to the system and α is the hydrogen concentration in the solid species
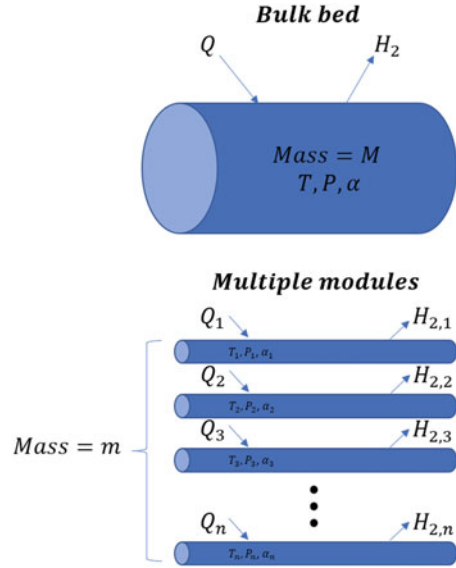
The main benefit of modular systems is an overall increase in storage system energy density due to three enabling aspects: efficiency in thermal management, reducing parasitic heating losses; increased hydrogen flow rate capability at all fill states; and rapid startup (Zhou et al. 2022). During desorption, if only a portion of the system is required for operation, only that segment is heated, reducing parasitic losses. When starting up a cold system, a single module can be rapidly heated to the operating temperature required to deliver hydrogen. Finally, only the modules that have hydrogen left in them are heated. This is especially important in operation over many days because continually heating spent storage media wastes energy. In addition, if certain portions of the system are reacting at different rates (due to composition, temperature, etc.), the capabilities of each module can be coordinated to provide the appropriate flow for the immediate system demands. This can reduce heat use as well as ensure maximum hydrogen flow rate when the storage system is nearly empty. Beyond the efficiency improvement, there are additional system advantages of a modular approach. For one, contamination control and quarantine are made possible. With individual modules, the amount of material exposed to air or water would be minimized if only one module of a 10-module system were damaged. Another advantage is conformability. Many small modules could conform to an odd shape or could be distributed throughout a vehicle. Third, counting modules as they are emptied could be used as a coarse fuel gauge.

To summarize, the basic concept for an advanced hydrogen storage system consists of one or more high aspect ratio cylindrical pressure vessels with external or internal heat exchange. The details of the number and size of the vessels are driven primarily by the operating conditions and properties of the storage material. Tradeoffs between cost and mass and volume efficiency may also shape the design space.

An example of these choices is given further in this chapter when an NaAlH$_4$ storage system is described in detail. For material-based systems that require hydrogen desorption temperatures greater than the waste heat available from a fuel cell (~85 °C for a proton exchange membrane [PEM] fuel cell), another design concept that is required is an on-board heater. The heating method that is most practical for a fuel cell vehicle is hydrogen combustion since hydrogen is stored on-board and can be converted to heat much more efficiently than electrical energy. Heat can be produced and distributed to the hydrogen storage system using a hydrogen burner coupled to a heat exchanger or with a catalytic heater. A catalytic heater produces heat using low-temperature catalytic reaction of hydrogen and oxygen. Concepts for burners and catalytic heaters have been developed for sodium alanate systems.

Thermal management is the most challenging aspect of the design of advanced hydrogen storage systems. For these material-based systems, the movement of hydrogen to and from the storage system is often accompanied by the movement of significant amounts of heat. The challenge is transferring heat efficiently to and from solid storage materials, which are generally characterized by poor thermal transport properties due to either the inherent material properties or the morphology of a packed powder or highly porous solid.

The reaction enthalpy of the storage material coupled with the material thermal conductivity determines the degree of the challenge. For materials with high reaction enthalpy and low thermal conductivity, such as most complex metal hydrides, the challenge is greatest. During hydrogen absorption, the high reaction enthalpy results in a large amount of heat generation. Low thermal conductivity prevents this heat from moving easily through the material to be coupled to the tank cooling loop. This combination results in high peak temperatures, large temperature gradients, and poor thermal control, all of which are undesirable. Peak temperatures that are too high will prevent hydrogen absorption and actually promote hydrogen desorption from the material. The ideal material from a thermal management perspective would have a low reaction enthalpy and high thermal conductivity. This material would produce little heat during absorption and require little heat to desorb hydrogen. High thermal conductivity would result in uniform temperatures that could easily be maintained at the optimum value.

For most advanced hydrogen storage systems, the thermal management design will be driven by requirements for hydrogen refueling rather than delivery. This is because the rate of hydrogen sorption is typically much higher for refueling where the entire storage capacity must be replaced in a few minutes. High hydrogen absorption rates equate to high heating rates.

Taking absorption as the limiting case, the hydrogen storage vessels must be cooled to control the storage material temperature for the maximum refueling rate. With external heat exchange, a heat transfer fluid is circulated over the outer surface of the storage vessel or vessels. With internal heat exchange, a heat transfer fluid is circulated through one or more cooling tubes inside the vessel(s). In either case, to design the heat exchanger requires analyzing the conduction heat transfer through the storage material and the coupled convective heat transfer to the heat transfer

Fig. 11 Externally cooled cylindrical storage vessel
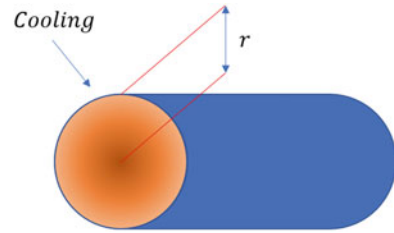
fluid. The goal of the design is to minimize the added mass and volume of the heat exchanger while achieving the desired temperature distribution in the storage vessel.

Heat conduction within the hydrogen storage material is governed by Fourier's law, which states that heat flux q (watts per square meter) is proportional to the negative of the local temperature gradient:

$$q = k\frac{dT}{dx}$$

The proportionality constant k is the thermal conductivity in watts per meter per degree Kelvin (W/mK) of the material.

Here, the various contributions to heat transfer are lumped together into an effective thermal conductivity of the material and the effect of this material property on the design of the storage vessel is considered. Fourier's law defines a relationship between the effective thermal conductivity, heat flux, and the temperature difference over a unit length of material. Assuming that a maximum temperature difference can be defined, this relationship can be used to determine a characteristic length for the design. This length is the maximum allowable distance to a temperature-controlled surface whether it is the radius of a vessel with external cooling or the distance between cooling tubes in an internally cooled system (Cao et al. 2022).

As an example, consider an externally cooled cylindrical storage vessel as shown in Fig. 11. The material in the center of the cylinder is hottest, while the material next to the cooled cylinder wall is coolest.

For this simple geometry and with some simplifying assumptions, the maximum vessel radius can be defined. The primary assumption is that there is constant and uniform volumetric heat generation due to the hydrogen absorption reaction. The volumetric heat generation Q (watts per cubic meter) is equal to the hydrogen absorption rate per unit volume multiplied by the absorption enthalpy ΔH. Typically, $\Delta H < 0$ for absorption. The hydrogen absorption rate per unit volume can be defined as the gravimetric capacity w divided by the time to reach that capacity t multiplied by the hydride packing density ρ_p divided by the molecular weight of hydrogen M. Thus, Q can be defined as:

$$Q = -\frac{w\rho_p H}{Mt}$$

If it is then assumed that the thermal conductivity is not a strong function of temperature, an analytical solution to the one-dimensional, steady-state heat transfer equation exists as:

$$T_i - T_0 = \frac{Q}{4k}r_0^2$$

Here, T_i is the temperature at the centerline, and T_o is the temperature at the cooled outer radius.

The vessel radius can be calculated as:

$$r_0 = \sqrt{(T_i - T_0)\frac{4k}{Q}}$$

The temperature difference is chosen based on the sensitivity of the hydrating kinetics to temperature. A gradient in temperature can affect the kinetics of the absorption reaction and thus the effective capacity. So, the temperature gradient must be correlated with the effective capacity. Ideally, the temperature difference would be zero and the entire volume of the material would be at the optimum refueling temperature. However, a zero-temperature difference is impractical for a real material, and a temperature difference must be found that results in an acceptable reduction in the absorption rate.

The characteristic length determines much about the heat exchanger geometry and is essentially fixed by the packing density, enthalpy, and thermal conductivity of the storage material and the desired refueling rate. However, rather than be limited by this intrinsic characteristic length, in some cases it is desirable to increase the characteristic length through thermal conductivity enhancement. Thermal conductivity enhancement is the addition of another material or structure to the hydrogen storage material that results in an increased effective thermal conductivity of the mixture.

Heat exchange is required for most, if not all, materials-based hydrogen storage systems. The enthalpy of reaction and rate of absorption or desorption determine the required heat removal or heat addition rates, respectively. To transfer heat to and from the storage vessel or vessels, these systems need an internal or external heat exchanger and a circulating heat transfer fluid. Some sorption systems may be the exception.

For sorption materials, low reaction enthalpy may allow for thermal management schemes that only include the flow of precooled or liquid hydrogen during refueling.

Numerous examples of internal heat exchangers can be found in the literature. Internal heat exchangers consist of one or more coolant tubes that provide fluid flow straight through the vessel or more commonly are looped so that the inlet and outlet are at the same end of the vessel. Recently, some researchers have suggested the use

of spiral or helical cooling tubes as the best way to provide an even distribution of heat transfer. Often, the tubes are finned to provide more heat transfer surface area. The fins can be either radial or longitudinal. In all cases, there is a trade-off between minimizing the mass and volume of the heat exchanger and maximizing the temperature uniformity of the bed.

For internal heat exchangers, the convective heat transfer coefficient can be calculated using a correlation for coolant flow in a round tube. These can be found in any heat transfer textbook. Since the heat transfer coefficient for laminar flow is quite low (50–200 W/m^{2}K) and independent of flow velocity, turbulent flow may be required to achieve the required cooling rate. With a Reynolds number in the 5000–10,000 range (turbulent flow), a factor of 10 increase in the heat transfer coefficient can be achieved over the laminar case. However, the increased heat transfer rate comes at a cost. The higher coolant flow rate will require more pump work. The pressure drop through the heat exchanger can be calculated with correlations as well and must be taken into account in the overall design.

The other option for thermal management for hydrogen storage systems is to perform convective heat transfer on the outside of the storage vessel using an external heat exchanger. For a single vessel, the heat exchanger could be an annular shell in which heat transfer fluid flows around the vessel. More commonly, an external heat exchanger configuration takes the form of a shell-and-tube heat exchanger where multiple hydrogen storage vessels make up the tube bank and fluid flows within a surrounding shell. The fluid flow can be along the vessel axes or baffles can be used to create multiple cross-flow passes over the bank of tubes. The latter case produces higher heat transfer rates for a given fluid flow rate but also results in higher pressure drop.

For hydrogen storage systems that operate at temperatures significantly higher or lower than the ambient environment, insulation can be an important design aspect. As previously discussed, complex metal hydrides typically are operated at temperatures much higher than ambient. These systems must be insulated to maintain their operating temperature without significant heat input. Adsorption systems typically are operated at temperatures much lower than ambient and must be insulated to minimize heating from the environment.

Cryogenic storage systems are invariably subject to heat leaks from the environment, the degree of which is set by the quality of the insulation of the storage system (Zou et al. 2019). The heat leaks result in heating the storage unit, which causes a release of hydrogen from the dense phase (either liquid or adsorbed) of the stored hydrogen, resulting in the gradual increase of the pressure of the gaseous hydrogen in thermodynamic equilibrium with the stored phase. In the case of a cryocompressed storage unit, heat leaks will result in an increase of temperature inside the reservoir and an increase in pressure. When the level of pressure reaches the maximum storage pressure, the gas must be vented to prevent the pressure to build up to unsafe levels. The time required to reach this point is defined as the dormancy of the storage system. The dormancy depends linearly on the intensity of the heat leak.
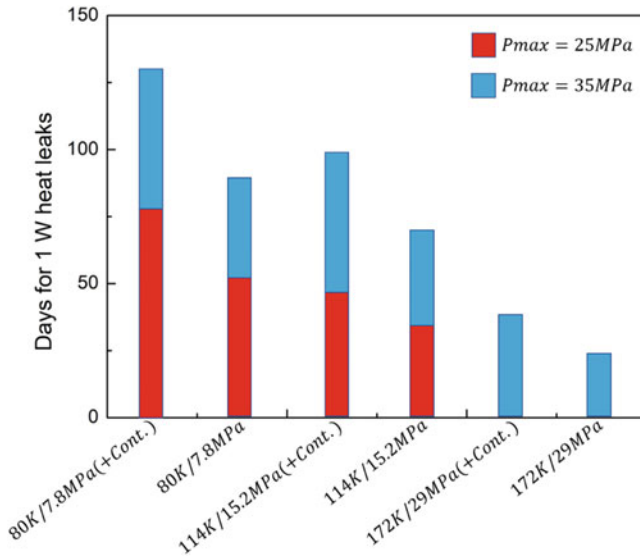
Fig. 12 Predicted dormancy for a 150-L adsorption storage unit filled with AX-21 as a function of storage conditions and maximum pressure settings. A 1-W heat leak is assumed

For a sorption-material hydrogen storage tank operating near 77 K, the dormancy depends highly on the tank design. Figure 12 shows the dormancy for a 1-W heat leak for the AX-21 sorption storage unit.

Figure 12 shows the results for a 150-L storage unit filled with 5 kg of hydrogen with maximum tank pressures set to 25 MPa (250 bar) and 35 MPa (350 bar). Due to linear dependence of the dormancy with the heat leaks, the dormancy can be estimated by dividing the dormancy with the thermal power of the heat leak. If the heat leaks can be limited to 1 W, the dormancy can reach several weeks.

Heat leaks from the environment must be minimized through proper insulation to maximize dormancy and maintain the temperature as close as possible to the optimal operating temperature of the storage unit, which for hydrogen is on the order of 100 K. This is typically done through superinsulation (also known as multilayer vacuum insulation), which consists of a vacuum space between the cryogenic vessel containing the adsorbent and the environment. The presence of the vacuum reduces heat transfer by gaseous conduction and convection. Radiative heat transfer between the inner vessel and the external shell is minimized by multilayer insulation, which consists of layers of low-emittance radiation shields supported by spacers with low thermal conductivity. Experimental test beds generally use a liquid nitrogen bed to maintain the temperature close to 77 K.

High-temperature hydrogen storage systems (i.e., complex metal hydride systems) experience a challenge similar to dormancy. These systems must be maintained at an elevated temperature to overcome thermodynamic or kinetic limitations to rapidly absorb and release hydrogen. The energy required to heat

and maintain these systems at elevated temperature is a parasitic loss to the hydrogen storage capacity. For example, if a hydrogen burner or catalytic heater is used to provide heat to the system, a fraction of the stored hydrogen must be used for this purpose rather than for fuel. To minimize this parasitic loss, these systems should be well insulated.

Multilayer vacuum insulation can be used for these systems, just as for adsorption systems. However, it can be costly and bulky, and in some cases lower-performance alternatives may be acceptable. One such alternative is the use of vacuum insulation panels (VIPs).

We have previously discussed that heat exchange for hydrogen storage systems may take place in internal or external heat exchangers. For internal heat exchangers, coolant flows within tubes inside the storage vessels and for external heat exchangers, coolant flows on the outside of the vessels. In either case, heat transfer calculations for flow in tubes or for shell-and-tube heat exchangers can be made using empirical correlations, which can be found in standard heat transfer textbooks. The correlations are used to compute an average heat transfer coefficient based on geometry and fluid properties. Pressure drop can also be estimated. However, for more accurate predictions or cases of complex geometry, a higher-fidelity model may be required. In these cases, fluid dynamics models must be developed and coupled to conjugate heat transfer models to more accurately predict local heat transfer rates, temperature variations, and fluid pressure drop.

For complex heat exchanger manifolds, flow uniformity and pressure drop are calculated using computational fluid dynamics (CFD) models that solve the Navier-Stokes equations for momentum and mass transport of the heat transfer fluid, including turbulent kinetic energy and dissipation rate (k-e model), when appropriate. For complex heat exchanger designs, the energy transport equation is also solved for the conjugate heat transfer problem. These heat transfer solutions can then be directly or indirectly coupled to heat transfer calculations within the storage vessels to provide the overall storage system thermal management solution. Heat transfer calculations within the storage vessels are covered in the following discussion.

If heat and mass transport processes are not understood, the local temperature and pressure environment of each particle is unknown and subject to averaging uncertainties. The result of this uncertainty is poor prediction of hydriding and dehydriding rates. In the case of rapid hydriding in packed-bed reactors, as reactants are consumed, the intrinsic porous nature of the bed limits the rate of hydrogen replenishment, and the effective rate of reaction is limited not by local kinetics, but rather by the depletion of available reactants. In the case of dehydriding processes, an inability to remove low-pressure hydrogen rapidly from the solid matrix results in rate limitations.

Predicting the state (temperature, pressure, and species concentrations) of these hydrogen storage vessels during hydrogen absorption and desorption requires the simultaneous solution to the conservation equations for mass, momentum, energy, and species. Each of these conservation equations in turn requires material property models for closure.

For all material-based hydrogen storage systems, hydrogen will be either physically or chemically bound to the solid. Thus, all such systems require a mass balance for hydrogen to account for the conversion from gas phase to solid. A general form of mass conservation is:

$$\frac{\partial}{\partial t}\rho + \nabla(\rho v) = R$$

where ρ and v are the hydrogen density and velocity, respectively. The right-hand side of the mass conservation equation is nonzero to account for absorption or desorption of hydrogen to and from the solid phase. This source term R is calculated from an equation or set of equations that describes the sorption kinetics for the material.

Solid storage materials are typically packed powders or porous solids. Thus, momentum conservation is expressed for gas flow through a porous medium. A number of different expressions for gas flow through porous media have been developed and reported in the literature.

The Ergun model, shown in:

$$\frac{P}{L} = A\mu v + B\rho v^2$$

treats the porous medium as a series of capillary flow channels that induce viscous and inertial pressure losses similar to those resulting from porous media.

Here, the gradient of pressure P is related to the velocity v, where μ is dynamic viscosity and ρ is the fluid density. Ergun also went on to derive the values of the A and B coefficients for beds of packed spheres as follows:

$$A = 150\frac{(1-\phi)^2}{\phi^3 d_p^2}$$

$$B = 1.75\frac{1-\phi}{\phi^3 d_p}$$

Here, φ is the porosity and d_p is the diameter of the spheres. Darcy's law describes a linear relationship between flow through porous media and the pressure gradient. The constant of proportionality is the material permeability K divided by the fluid dynamic viscosity μ. The Darcy-Brinkman equation combines Darcy's law with the Stokes equation to produce the following relationship.

$$\mu_e \nabla^2 v - \nabla p - \frac{\mu}{K}v = 0$$

This relationship allows for modeling of gas flow through multidimensional porous media using finite element analysis. It does, however, require knowledge of the

permeability of the porous media and the effective viscosity μ_e. It has been shown experimentally that the effective viscosity term is required to reconcile experimental data with the model. However, often it is assumed that the effective viscosity is equal to the "real" viscosity μ.

For a transient analysis, Brinkman's equation results in the following momentum equation:

$$\frac{\rho}{\phi} \frac{\partial}{\partial t} v + \frac{\rho}{\phi} v \nabla u = -\nabla p + \nabla \left[\frac{\mu}{\phi} \left(\nabla v + \nabla v^T \right) - \frac{\mu}{K} v \right]$$

The hydrogen superficial velocity v is equal to the seepage velocity u multiplied by the porosity. Similar equations for momentum conservation have been used in the literature for flow through hydrogen storage materials. For high-flow rates, an additional viscous drag term is sometimes included on the right-hand side. This Forchheimer term is proportional to the square of the fluid velocity.

One form of the energy equation for hydrogen storage materials is:

$$\left(\rho c_p \right)_m \frac{\partial}{\partial t} T + \left(\rho c_p \right)_g v \Delta T = \nabla \left(k_m \Delta T \right) + R \Delta H$$

In addition to the variables defined previously, c_p is specific heat capacity of the storage material m and the hydrogen gas g. In most cases, the hydride material temperature T is assumed to be in thermal equilibrium with the gas temperature. The term k_m is the thermal conductivity of the solid.

The first term in Equation is the rate of change of temperature of the solid, while the second term is the hydrogen advection term. Note that the advection term uses the density and specific heat of the advecting phase (i.e., hydrogen), while the thermal inertia term uses the density and specific heat of the solid phase, which is the dominant source of inertia. The first term on the right-hand side accounts for heat conduction through the solid, where an effective conductivity of the hydride bed is used. The second term on the right accounts for the chemical reaction rate R between the hydride and gas phase, which can be either exothermic (hydrogenation) or endothermic (dehydrogenation), where ΔH is the enthalpy of reaction. Note that terms accounting for pressure variation work and viscous dissipation are neglected here because they are much smaller (by three or more orders of magnitude) than the other terms.

For all materials-based hydrogen storage systems, a detailed analysis must keep track of the free hydrogen, typically gaseous, and the hydrogen bound by the solid storage material. In chemically reacting systems such as complex metal hydrides, several solid species must be accounted for as well. Thus, species conservation equations are a necessary part of the analysis. Here, we consider the most complicated case of a multispecies complex metal hydride.

In this general case, species conservation for each solid, immobile species is given by:

$$\frac{\partial}{\partial t}c_j = \dot{R}_j$$

where j stands for the reacting species. For sodium alanates, for instance, this would include NaH, Na_3AlH_6, $NaAlH_4$, and Al. The solid species production rates $\dot{R}_j$ are given by combinations of the reaction rates according to the stoichiometry of the reactions.

The conservation equations rely on the solution to the chemical rate equations to determine mass source terms for hydrogen. To this end, chemical kinetics models must be used, many of which have been developed for a number of hydrogen storage materials. For instance, a number of kinetic models of sodium alanate have been developed. These models primarily take the following form:

$$\dot{R}_j = Ae^{\frac{Q}{RT}}f(P)f(c_j)$$

where there is an Arrhenius temperature dependence multiplied by a function of the hydrogen pressure and a function of the hydrogen concentration in the solid phase. The functions of pressure vary but always contain a reference to the equilibrium pressure of the storage material. This guarantees that the sign of the rate is in agreement with the thermodynamics; that is, hydrogen is absorbed when the pressure is greater than the equilibrium pressure and desorbed when the reverse is true. Often, the equilibrium pressures are modeled as an Arrhenius expression themselves based on the van't Hoff equation. Functions of solid-phase concentration also vary but enforce that the rate approaches zero when the solid is saturated.

In addition to the chemical kinetics model, several other properties are required to solve the system of equations. To solve the momentum equation, hydrogen transport through the porous media must be described. This solution requires a permeability model for the material. One such model captures the dependence on porosity φ, the particle diameter d_p, the tortuosity τ, and the Knudsen number K_n:

$$K = \frac{\phi d_p^2}{\tau^2}\left(\frac{1}{32} + \frac{5}{12}K_n\right)$$

This model spans both continuum (viscous) and free molecular flow regimes (Knudsen flow). The porosity K can be determined from measurements of the storage material mass loading, volume of the vessel, and knowledge of the single-crystal density of the storage material. The pore size and tortuosity can be determined from microscopy or, as is more likely, fit using experiments carried out on samples of the material. These experiments involve flowing gas through the samples while measuring the mass flow rate and pressure drop across the sample.

To solve the energy equation, the thermal properties of the storage material are needed. In particular, the thermal conductivity of the porous solid is required. Ideally, this property will be measured for the storage material in the form and

density that it will take within the hydrogen storage system since bulk properties do not apply for small particles at packing densities below the solid density.

If physical measurements cannot be made, models exist that can predict the thermal conductivity of porous materials. Since thermal conductivities of packed particle beds are inherently low, one might try to enhance the thermal conductivity of these materials with additives. In addition to thermal conductivity, the specific heat capacity of the storage material must be known. A simple combination of the weighted bulk specific heats is often used.

All advanced hydrogen storage systems must be designed as hydrogen pressure vessels due to the fact that at some point in the refueling or delivery of hydrogen an elevated pressure of hydrogen must be contained. As previously discussed, this constrains most storage vessels to a cylindrical geometry. To design the vessels for safe operation, a structural analysis is required to determine the thickness of the vessel walls. This includes the cylinder wall thickness t_w and the thickness of the cylinder ends t_e, which may be different. For simple geometries, these thicknesses can be estimated using equations for thin-walled pressure vessels:

$$t_w = \frac{P \cdot r_0}{\sigma - 0.6P}$$

$$t_e = \sqrt{\frac{3P \cdot r_0^2 \cdot \sqrt{v^2 - v + 1}}{4\sigma}}$$

The quantities t_w and t_e both depend on the applied hydrogen pressure P, the vessel material allowable stress σ, and Poisson's ratio v. For more complex geometries, as with a detailed final design, finite element models may be required. Also, these equations assume isotropic material properties. Composite vessels, even if simple cylinders, may require more complex design calculations due to anisotropic material properties inherent in these structures.

The hydrogen pressure used in these calculations should be the highest pressure to which the vessel will be subjected, which is likely to be the refueling pressure. In most cases, higher pressure improves hydriding kinetics but also requires thicker-walled pressure vessels. Since the system gravimetric efficiency includes the weight of the vessel as well as the storage material, an optimum pressure can be found that maximizes the gravimetric efficiency of the system for a given refueling time. At a hydrogen refueling pressure lower than the optimum, slower refueling is dominant over the reduced weight of the vessel. At a hydrogen refueling pressure higher than the optimum, the increased vessel weight dominates the improvement in refueling rate. The optimum refueling pressure is thus a function of the pressure dependence of the storage material chemical kinetics.

In addition to the maximum operating pressure, the structural design of some hydrogen storage systems must take into account density changes of the storage material during hydrogen uptake and release. Some materials, notably interstitial and complex metal hydrides, undergo significant density changes during hydrogen absorption.

In addition to material expansion, decrepitation, which is the breakdown of metal hydrides into smaller particles due to hydrogenation cycles, can pose structural design challenges. Decrepitation can lead to density gradients in a storage vessel due to the movement of smaller particles due to gravity. With a large density gradient, the local expansion of the material in the high-density region due to hydrogen absorption can cause such extreme pressures that vessel failure can result.

The allowable stress σ used in design calculations may be based on material property data or code requirements, depending on the application.

If finite element analysis is required to determine the pressure vessel geometry, the allowable stress for the material is normally compared to the calculated maximum von Mises stress under the maximum pressure load. The geometry is then adjusted until the maximum von Mises stress is everywhere lower than the allowable stress.

Hydrogen storage vessels must be designed to meet the requirements of safety codes and standards for each application.

In addition to the pressure vessels, the heat exchanger may require a structural analysis for design. In the case of external heat exchange, the shell must contain the heat transfer fluid and withstand the operating pressure as the fluid is circulated through the heat exchanger. So, a structural analysis is required to define the shell thickness and design any reinforcement that may be required. In this case, the shell material does not have the requirement of hydrogen compatibility, so the material space is significantly expanded. A low-cost, high-strength material should be used. A finite element structural model may be required to evaluate the minimum thickness to withstand the force, including a factor of safety from the yield strength.

With an internal heat exchanger, the heat transfer fluid is circulated through the hydro- gen storage vessel through tubing. This tubing must withstand the internal fluid pressure along with the external hydrogen pressure. In addition, the tubing must be made of a hydrogen-compatible material, limiting material choice. The thin-walled pressure vessel equation shown previously can be used for sizing this tubing.

A key part in the design of hydrogen storage systems is structural material selection.

Current compressed H_2 vessels for vehicle applications are Type III or Type IV pressure vessels that rely on high-strength carbon fiber composite outer layers for strength. Type III vessels have aluminum inner liners, while Type IV have plastic liners, typically high-density polyethylene (HDPE). The liners are fairly thin, a few millimeters thick, and serve only to prevent hydrogen permeation. The material choices for these vessels are based on hydrogen compatibility and low weight. Aluminum and HDPE are essentially inert in hydrogen, and carbon fiber composites can obtain extremely high specific strength. However, this specific strength comes at a high cost, which is one of the primary limitations of current compressed H_2 systems.

The materials used in compressed H_2 systems may be appropriate for some advanced hydrogen storage systems, but operating environments must be taken into account. The 700-bar compressed H_2 tanks require the high specific strength of composites to minimize weight, but many materials-based systems operate at

much lower pressures. For low-pressure systems, a lower-strength material may provide a low-cost alternative. In addition, compressed H_2 tanks operate over a range of temperatures from -40 to $85\,°C$.

Adsorption systems that operate much colder or metal hydride systems that operate much hotter may require different materials. For instance, many composites may not withstand temperatures greater than $150\,°C$, where some complex metal hydrides operate. Thus, each material operating environment must be considered when choosing the best structural materials.

That being said, one of the primary drivers in the choice of structural materials for hydrogen storage systems is hydrogen compatibility. Many structural metals are embrittled by hydrogen. So, while titanium alloys may have good specific strength, they are mostly a poor choice for a hydrogen storage vessel due to the high permeability of hydrogen in titanium and subsequent formation of titanium hydride. Hydrogen compatibility coupled with high specific strength and ductility leads to a fairly narrow choice of materials that should be used for hydrogen storage vessels. The pipeline steels and pressure vessel steels offer the possibility of greatly reduced cost with little loss in specific strength since higher-strength pipeline steels are being developed. Pipeline steels have been successfully utilized for hydrogen service in the past, so there is considerable engineering experience with them. However, this experience is primarily with low-strength materials (yield strengths of 35–52 ksi) used in applications with high safety factors. These applications are also at ambient temperature, so there is not much experience at elevated temperature. At higher temperature, hydrogen precipitation at hydrogen trapping sites during cooling might occur. There is limited knowledge of properties in hydrogen gas and potentially susceptible microstructures are not known. Also, resistance to fatigue in pipeline steels is not well established. For joining pipeline steels, welds can be more sensitive to environmental effects than base materials. Also, postweld heat treating is required. All of these facts suggest that while a pipeline steel could be a good hydrogen storage vessel candidate, more information is needed to be certain.

A similar statement can be made for pressure vessel steels. These are quenched and tempered low-alloy steels that, in addition to the issues with pipeline steels, can be susceptible to hydrogen-assisted fracture, especially at higher strengths and higher operating stress.

Figure 13 shows the effect of hydrogen on a number of materials, including some carbon and low-alloy steels. Note that compared to these materials, 316L and A286 are nearly impervious to hydrogen. Coupled with cost and weldability, this is why 316L is the most common structural material used for high-pressure hydrogen components such as tubing, fittings, valves, regulators, and so on (Ye et al. 2022).

Hydrogen storage systems require a number of ancillary components in addition to the primary storage vessel itself. These balance-of-plant (BOP) components will almost universally include the following: tubing, valves, pressure regulators, pressure relief devices, and pressure transducers. In addition, many advanced storage systems will require temperature sensors for operation and control.

Fig. 13 Effect of hydrogen
on strength and ductility of
structural metals, relative to
a control measurement using
helium
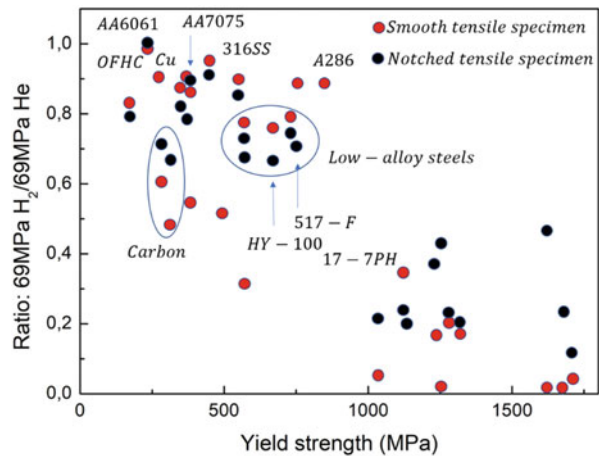
Components that are "wetted" by pressurized hydrogen will have the same compatibility requirements as the structural materials of the storage vessels. Most BOP components used in H_2 storage systems today are made of 316L stainless steel for reasons previously discussed. In fact, the Japanese government currently only allows H_2 storage system components to be constructed from 316L stainless steel. However, as with vessel structural materials, research is ongoing to find or develop alternative materials for these components that will meet or exceed the performance of stainless steel to lower system costs.

In addition to the gas system components, advanced H_2 storage systems are likely to include some form of heat exchanger. Typically, the heat exchanger is an integral part of the storage vessel and is not considered separately here. However, additional BOP components will be required for heat exchange. For refueling, a common assumption is that the cooling fluid that is used for heat removal from the storage system is supplied and circulated by the refueling station. Thus, the only additional BOP components required for refueling are the coolant lines that connect the heat exchanger to the refueling interface. However, for those systems that require heat for H_2 delivery to the conversion device, the heat exchange must take place while the system is in use. For these systems, heat of sufficient quality (temperature) must be generated and distributed to the H_2 storage vessel.

With regard to safety, there are a number of hazards associated with a materials-based hydrogen storage system. Along with the hazards of a pressurized combustible gas, these systems may include pyrophoric or water-reactive material and either high-temperature or cryogenic thermal hazards. From a practical standpoint, these hazards must be able to be managed safely for such a technology to be commercialized. From the system engineering perspective, it would be required not only to be able to handle the materials safely but also to do so economically in a production manufacturing environment. For some of the more hazardous materials, that could pose a significant challenge.

From the perspective of qualification, an advanced hydrogen storage system would need to meet the codes and standards requirements that govern the application in which it would be used. For vehicular applications, codes and standards are currently being developed for hydrogen storage systems and their refueling (see chapter "Hydrogen Applications").

6   Conclusions

Hydrogen value chains can follow many different paths. Demand for low-carbon hydrogen can come from a variety of sectors, and there are many permutations of hydrogen supply and handling that could meet it. The most cost-competitive outcome will, moreover, be different in various regions and applications. For each possible value chain, investments and policies need to be synchronised in scale and time if hydrogen is to be produced and delivered to end users that are ready to use it. Building trust throughout the value chain so that investments are coordinated takes time and may require new contractual relationships. In some cases, governments and companies will need to think and act cross-sectorally in new ways to take full advantage of hydrogen's flexibility.

Infrastructure such as pipeline and delivery networks are of particular importance for a new energy carrier such as hydrogen. While hydrogen can be produced locally, its storage and distribution benefit from economies of scale. When produced from fossil fuels in particular, its supply is cheaper when centralised. In the case of hydrogen use for road transport, where a network of refuelling stations will be a precondition for widespread adoption of FCEVs, the current pace of infrastructure development is a brake on adoption. The ability of governments to commit to large (and necessary) infrastructure investments is limited in many countries and regions: public–private investment models can help, but may add further complexity. In some cases, these investments will also need to be co-ordinated across borders, requiring international collaboration at a level not yet seen for hydrogen.

Hydrogen has low energy density, which makes it more challenging to store and transport than fossil fuels. However, it can be converted into hydrogen-based fuels and feedstocks, such as synthetic methane, synthetic liquid fuels and ammonia, which can make use of existing infrastructure for their transport, storage and distribution. This can reduce the costs of reaching final users. Some of the synthetic hydrocarbons produced from hydrogen can be direct substitutes for their fossil equivalents. Ammonia is already used today as a feedstock in the chemical industry and could be a hydrogen carrier for the long-distance transport of hydrogen in the future, or itself be used as fuel in the shipping sector.

The potential benefits and opportunities of these hydrogen-based fuels and feedstocks have to be weighed, however, against the costs of converting hydrogen into these products. Many of the technology pathways to produce these fuels and feedstocks are at an early demonstration stage, resulting in high costs. Producing ammonia requires the separation of nitrogen from the air, while the production of

synthetic hydrocarbons requires carbon as an input, which has implications for the cost of production, while the origin of the carbon also affects the environmental impact and the carbon intensity of the synthetic hydrocarbon.

Various pathways exist to convert hydrogen into fuels and feedstocks that can be more easily handled, transported and used. Ammonia can be produced by combining hydrogen and nitrogen, and synthetic hydrocarbons, such as methane, methanol, diesel or jet fuel, can be produced by combining hydrogen with carbon in the form of CO_2. However, for pathways based on electrolytic hydrogen, much of the electricity used to convert hydrogen into fuels and feedstocks is lost during the process of conversion.

Developing a new hydrogen value chain would be contingent upon successfully completing and connecting production, transmission, distribution, storage and end-use infrastructure. This would require co-ordinated investment by many different market participants, which could be challenging for them to implement. Blending hydrogen into the natural gas infrastructure that already exists would, however, avoid the significant capital costs involved in developing new transmission and distribution infrastructure. Further, if blending were to be carried out at low levels, while it might increase the cost of natural gas delivery to consumers, it would also provide reductions in CO_2 emissions. Blending would be considerably easier to implement if steps were taken to clarify existing national regulations on hydrogen in natural gas and to harmonise regulations across borders.

There are almost three million kilometres (km) of natural gas transmission pipelines around the world and almost 400 billion cubic metres (bcm) of underground storage capacity; there is also an established infrastructure for international liquefied natural gas (LNG) shipping. If some of this infrastructure could be used to transport and use hydrogen, it could provide a major boost to the development of hydrogen. For example, a blend of 3% hydrogen in natural gas demand globally (around 3900 bcm in 2018) would require close to 12 MtH_2. If the majority of this hydrogen came from electrolysers, then this by itself would require around 100 gigawatts (GW) of installed electrolyser capacity (at a 50% load factor), a level that could deliver around a 50% reduction in the capital cost of electrolysers. However, hydrogen blending faces a number of challenges:

– the energy density of hydrogen is around a third of that of natural gas and so a blend reduces the energy content of the delivered gas: a 3% hydrogen blend in a natural gas transmission pipeline would reduce the energy that the pipeline transports by around 2%. End users would need to use greater gas volumes to a given energy need. Similarly, industrial sectors that rely on the carbon contained in natural gas (e.g. for treating metal) would have to use greater volumes of gas;
– hydrogen burns much faster than methane. This increases the risk of flames spreading. A hydrogen flame is also not very bright when burning. New flame detectors would probably be needed for high-blending ratios;
– variability in the volume of hydrogen blended into the natural gas stream would have an adverse impact on the operation of equipment designed to accommodate only a narrow range of gas mixtures. It could also affect the product quality of some industrial processes;

– the upper limit for hydrogen blending in the grid depends on the equipment connected to it, and this would need to be evaluated on a case-by-case basis. The component with the lowest tolerance will define the tolerance of the overall network.

Making an LOHC involves "loading" a "carrier" molecule with hydrogen, transporting it, and then extracting pure hydrogen again at its destination. LOHCs have similar properties to crude oil and oil products, and their key advantage is that they can be transported as liquids without the need for cooling. However, as with ammonia, there are costs associated with the conversion and reconversion processes involved. These processes would require energy equivalent of between 35% and 40% of the hydrogen itself. In addition, the carrier molecules in an LOHC are often expensive and are not used up when hydrogen is created again at the end of the process, so need to be shipped back to their place of origin.

Several different LOHC molecules are under consideration, each with various benefits and drawbacks. In this chapter LOHCs refers to methylcyclohexane (MCH), a relatively low-cost option with toluene as the carrier molecule. Around 22 Mt of toluene is currently produced annually (for commercial products), a quantity that could carry 1.4 MtH$_2$ if it were to be used as an LOHC. It costs around USD 400–900 per tonne. However, toluene is toxic and would require careful handling. A non-toxic alternative LOHC is dibenzyltoluene. Although this is much more expensive than toluene today, scaling up could make it a more attractive option in the long run, especially given its non-toxic nature. Methanol and formic acid are other options, but they lead to greenhouse gas emissions if used directly (unless produced with non-fossil sources of carbon).

For both ammonia and LOHCs, effective utilisation of the heat released in the conversion process could increase the efficiency of the value chain and reduce overall costs. Transmission of hydrogen as a gas by pipeline is generally the cheapest option if the hydrogen needs be transported for distances of less than about 1500 km. For longer distances, transmission as ammonia or LOHC may well be a more cost-effective option, especially if the hydrogen needs to be moved overseas, even taking into account the costs of converting hydrogen into ammonia or LOHC and back again. For local distribution, pipelines are cost-effective for distributing high volumes of hydrogen over longer distances; in other cases trucks are likely to be the cheaper option.

References

Álvarez G, Peral LB, Rodríguez C et al (2019) Hydrogen embrittlement of structural steels: effect of the displacement rate on the fracture toughness of high-pressure hydrogen pre-charged samples. Int J Hydrogen Energy 44(29):15634–15643. https://doi.org/10.1016/j.ijhydene.2019.03.279

André J, Auray S, Brac J et al (2013) Design and dimensioning of hydrogen transmission pipeline networks. Eur J Oper Res 229:239–251. https://doi.org/10.1016/j.ejor.2013.02.036

Apostolou D, Xydis G (2019) A literature review on hydrogen refuelling stations and infrastructure. Current status and future prospects. Renew Sustain Energy Rev 113:109292. https://doi.org/10.1016/j.rser.2019.109292

Bhadeshia HKDH (2016) Prevention of hydrogen embrittlement in steels. ISIJ Int 56:24–36. https://doi.org/10.2355/isijinternational.ISIJINT-2015-430

Cao Y, Dhahad HA, Mansir IB et al (2022) Development of a combined system based on a PEMFC and hydrogen storage under different conditions equipped with an ejector cooling system. Int J Hydrogen Energy 47(62):26687–26700. https://doi.org/10.1016/j.ijhydene.2021.10.195

Chen L, Xiong X, Tao X et al (2020) Effect of dislocation cell walls on hydrogen adsorption, hydrogen trapping and hydrogen embrittlement resistance. Corros Sci 166:108428. https://doi.org/10.1016/j.corsci.2020.108428

Djukic MB, Zeravcic VS, Bakic GM et al (2015) Hydrogen damage of steels: a case study and hydrogen embrittlement model. Eng Fail Anal 58(2):485–498. https://doi.org/10.1016/j.engfailanal.2015.05.017

Djukic MB, Bakic GM, Zeravcic VS et al (2019) The synergistic action and interplay of hydrogen embrittlement mechanisms in steels and iron: localized plasticity and decohesion. Eng Fract Mech 216:106528. https://doi.org/10.1016/j.engfracmech.2019.106528

Dwivedi SK, Vishwakarma M (2018) Hydrogen embrittlement in different materials: a review. Int J Hydrogen Energy 43(46):21603–21616. https://doi.org/10.1016/j.ijhydene.2018.09.201

Garrison WM Jr, Moody NR (2012) Hydrogen embrittlement of high strength steels. In: Gaseous hydrogen embrittlement of materials in energy technologies. https://doi.org/10.1533/9780857093899.3.421

Herzler J, Naumann C (2009) Shock-tube study of the ignition of methane/ethane/hydrogen mixtures with hydrogen contents from 0% to 100% at different pressures. Proc Combust Inst 32(1):213–220. https://doi.org/10.1016/j.proci.2008.07.034

Jothi S, Croft TN, Wright L et al (2015) Multi-phase modelling of intergranular hydrogen segregation/trapping for hydrogen embrittlement. Int J Hydrogen Energy 40(43):15105–15123. https://doi.org/10.1016/j.ijhydene.2015.08.093

Kuczyński S, Łaciak M, Olijnyk A et al (2019) Thermodynamic and technical issues of hydrogen and methane-hydrogen mixtures pipeline transmission. Energies 12(3):569. https://doi.org/10.3390/en12030569

Li H, Niu R, Li W et al (2022) Hydrogen in pipeline steels: recent advances in characterization and embrittlement mitigation. J Nat Gas Sci Eng 105:104709. https://doi.org/10.1016/j.jngse.2022.104709

Lynch S (2019) Discussion of some recent literature on hydrogen-embrittlement mechanisms: addressing common misunderstandings. Corrosion Rev 37(5):377–395. https://doi.org/10.1515/corrrev-2019-0017

Martin ML, Dadfarnia M, Nagao A et al (2019) Enumeration of the hydrogen-enhanced localized plasticity mechanism for hydrogen embrittlement in structural materials. Acta Mater 165:734–750. https://doi.org/10.1016/j.actamat.2018.12.014

Nagao A, Dadfarnia M, Sofronis P et al (2016) Hydrogen embrittlement: mechanisms. In: Encyclopedia of iron, steel, and their alloys. isbn:978-1-351-25450-2

Nagumo M, Takai K (2019) The predominant role of strain-induced vacancies in hydrogen embrittlement of steels: overview. Acta Mater 165:722–733. https://doi.org/10.1016/j.actamat.2018.12.013

Nguyen TT, Park J, Kim WS et al (2020) Effect of low partial hydrogen in a mixture with methane on the mechanical properties of X70 pipeline steel. Int J Hydrogen Energy 45(3):2368–2381. https://doi.org/10.1016/j.ijhydene.2019.11.013

Sdanghi G, Maranzana G, Celzard A et al (2019) Review of the current technologies and performances of hydrogen compression for stationary and automotive applications. Renew Sustain Energy Rev 102:150–170. https://doi.org/10.1016/j.rser.2018.11.028

Witkowski A, Rusin A, Majkut M et al (2018) Analysis of compression and transport of the methane/hydrogen mixture in existing natural gas pipelines. Int J Press Vessel Pip 166:24–34. https://doi.org/10.1016/j.ijpvp.2018.08.002

Ye J, Zhao Z, Cui J et al (2022) Transient flow behaviors of the check valve with different spool-head angle in high-pressure hydrogen storage systems. J Energy Stor 46:103761. https://doi.org/10.1016/j.est.2021.103761

Zheng J, Liu X, Xu P et al (2012) Development of high pressure gaseous hydrogen storage technologies. Int J Hydrogen Energy 37(1):1048–1057. https://doi.org/10.1016/j.ijhydene.2011.02.125

Zhou J, Li S, Zhou X et al (2022) Operation optimization for gas-electric integrated energy system with hydrogen storage module. Int J Hydrogen Energy 47(86):36622–36639. https://doi.org/10.1016/j.ijhydene.2022.08.224

Zou Q, Tian Y, Han F (2019) Prediction of state property during hydrogen leaks from high-pressure hydrogen storage systems. Int J Hydrogen Energy 44(39):22394–22404. https://doi.org/10.1016/j.ijhydene.2019.06.126

Hydrogen Applications

1 Introduction

While small amounts of energy can temporarily be stored in batteries, flywheels or supercapacitors, chemical storage in the form of hydrogen or methane is particularly suitable for the long-term storage of large amounts of energy. For the emission-free production of hydrogen, the power-to-gas (PtG) concept is discussed, which involves the utilization of surplus renewable energy for the operation of water electrolysis (Buttler and Spliethoff 2018). In a consequent step this hydrogen can then be converted to methane (synthetic natural gas, SNG) by using an external CO or CO_2 source. The produced SNG is applicable for the injection into the gas grid or usable as motor fuel (Pan et al. 2019). Alternatively, the direct feeding of hydrogen into the gas grid is also conceivable.

Figure 1 shows a general overview of the PtG concept with possible mass and energy flows. In addition to the possible uses shown in the figure, it is also imaginable to use the hydrogen for fuelling vehicles, for the production of hydrocarbons via Fischer-Tropsch synthesis or other chemicals such as methanol or ammonia.

As mentioned before, water electrolysis represents the key technology for a successful realization of the PtG concept.

The global hydrogen demand in 2012 was approximately 600 billion Nm3 ($\approx$ 54 million tonnes). It is especially needed in the chemical industry for ammonia production via Haber-Bosch process or petroleum refining, which each demand about 45% of the total production capacity. Today hydrogen is primarily produced by the reformation of natural gas or liquid hydrocarbons (Boretti 2021). Here, particularly three reforming methods are distinguished: Catalytic steam reforming (CSR), partial oxidation (POX) and autothermal reforming (ATR). Until now, steam reforming of natural gas represents the most economical and established industrial technology for hydrogen production. However, the main downside of this
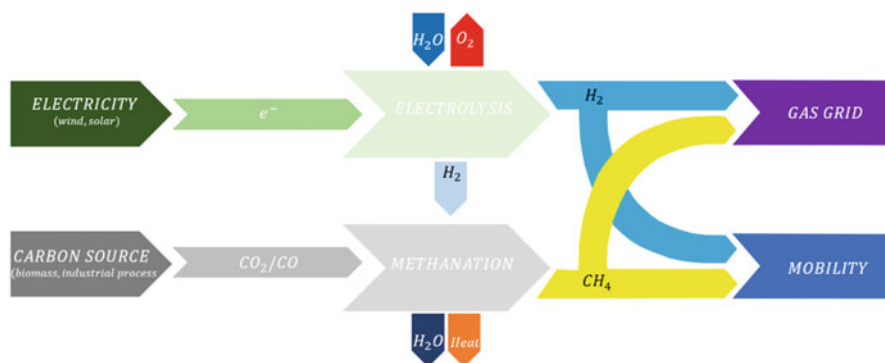
Fig. 1 Power-to-gas concept with possible mass and energy flows

production technology is that depending on the feedstock 9 t to 12 t of CO_2 are produced per tonne of H2.

Gasification of coal or biomass represents a further hydrogen production alternative (Midilli et al. 2021).

Using biomass can reduce CO_2 emissions into the atmosphere, since the CO_2 released during gasification has previously been absorbed from the atmosphere and converted by photosynthesis (Cao et al. 2020). Furthermore, hydrogen can be produced in a purely biological way by fermentation of biomass or by photobiological processes. However, biological processes are still at an early stage of development and therefore unlikely to become commercially available in the next years.

2   Current Uses of Hydrogen

The first industrial applications of hydrogen were in the early nineteenth century as a fuel gas for lighting and heating. The hydrogen was mainly produced from the anaerobic reaction of hot coal and water vapour. It was used for many years in commercial and residential applications until it was eventually replaced with natural gas.

Of the annual production of 8 EJ or ~ 190 Mtoe of hydrogen, most is in the form of 'captive' hydrogen (consumed at the producer's place). Only an estimated 5% of the total hydrogen production is supplied as 'merchant' hydrogen (produced centrally und transported to the consumer), requiring the appropriate infrastructure for transportation and distribution. Other market types are by-product and stranded hydrogen produced in the chemical industries and either used internally as a raw material or fuel, or simply vented or flared if no marketing infrastructure is available. Only 1% of current hydrogen production is used for direct energy purposes. The hydrogen market in Europe is 64% captive hydrogen, 27% by-product hydrogen and 9% merchant hydrogen.

Fig. 2 Global hydrogen production and use (in million t)

Ammonia
Refining
Methanol
Other

Captive production

North America   Western Europe   Japan   Rest of world   Total
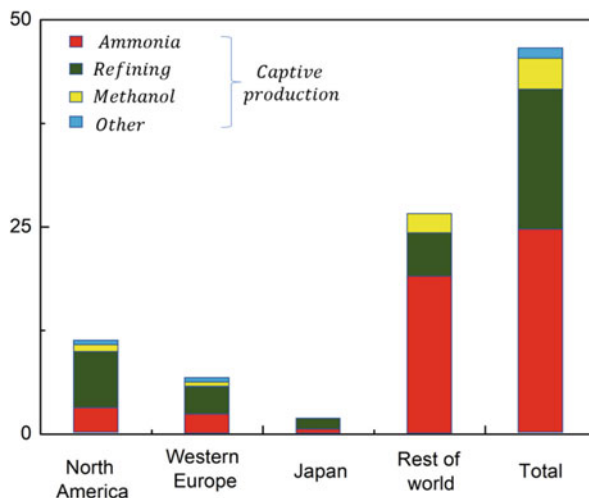
Fig. 3 Hydrogen consumption in the US refineries between 1985 and 2005
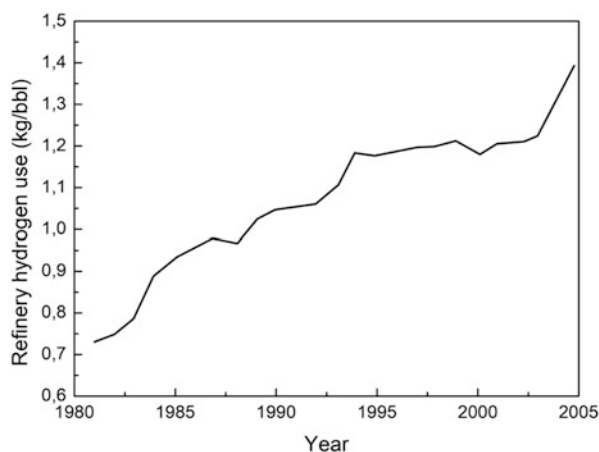
There is a wide variety of industrial customers for hydrogen which require, depending on the application area, different quantities and purities of hydrogen. The largest consumer of hydrogen is the chemical industry, with a demand for hydrogen growing at an annual rate of 7–10% (Ausfelder and Bazzanella 2016). As is shown in Fig. 2, about half the total hydrogen is used for producing ammonia (fertilizer), 35% is used in petroleum refining processes (tendency increasing due to heavier crude oils), 8% is used in methanol production, 1% is used as a fuel in space programmes, and the residual amount is used for other purposes (Dalena et al. 2018).

The most important processes for producing hydrogen in refineries are steam reforming of natural gas (59%) followed by off-gas purification (35%). The merchant suppliers may operate a hydrogen plant or a hydrogen supply pipeline. Figure 3 shows the specific demand for hydrogen in refineries in the USA over the past 25 years,

revealing a strong increase in recent years due to the increased processing of lower quality, heavy crude oils and other unconventional fossil resources. For a present throughput of 20 Mbbl/d, this translates into a hydrogen demand of 28,000 t/d.

Indirect energetic use of hydrogen occurs in refineries where the H2 is used in catalytic cracking operations or hydro-treating to upgrade heavy and unsaturated compounds into lighter and more stable species (Speight 2016). It is also used in the production of synthetic fuels via Fischer–Tropsch synthesis, of methanol, or of SNG. Furthermore, it is used in the hydrogenation of coal and heavy crude oil. Hydrogen is also used to remove sulphur from crude oil and gasoline, and to purify gases, e.g. by capture of oxygen traces in argon. Other H2 consuming processes are welding and glass production. In the glass production process, the hydrogen is used as an oxygen scavenging atmosphere (~6% H2 and ~ 94% N2), and to prevent oxidation of the large tin bath in the float glass process. Polishing and melting of high quality optical glass is done by means of a soot free hydrogen flame. In the food industry, the properties of fats and oils are changed through hydrogenation of organic intermediate products like amines and fatty acids, making food less susceptible to oxidation and spoilage.

Specific applications for liquid hydrogen are in the metal industries, where LH2 is used in the metal production process directly (e.g. tungsten, tungsten carbide, molybdenum metal powder), and, if mixed with inert gases, in secondary processes to act as a reducing atmosphere in heat treating, sintering and copper brazing. In the electronics industry, highly pure hydrogen is mainly needed as a carrier gas for active elements such as arsine and phosphine in the manufacture of integrated circuits, polycrystalline silicon for semiconductors, optical fibres for communication, or fused quartz. The pure water vapour required is generated from mixing oxygen with vaporized LH2. The hydrogen is either used as atmosphere or as a clean burning fuel. In power plants, LH2 can be used for the cooling of large electric turbogenerators and to protect piping in nuclear reactors.

The following is a list of non-energy and indirect energy applications of hydrogen:

– Heavy oil hydrogenation for the production of preprocessed crude oil;
– Hydro-cracking of heavy distillates, which are difficult to reform, by using hydrogen and catalysts to convert into lighter fractions (kerosene, light and heavy gas oil, fuel oil ('naphtha'); cracking by heating or catalytic reforming to obtain various fuel qualities;
– Hydro-treating, i.e. a process that reduces sulphur or nitrogen content of the feed;
– Hydro-processing, i.e. a process used for desulphurization and substantial removal of most other impurities (nitrogen, oxygen, heavy metals) from the products of distillation processes; for example, desulphurization of heating oil grade S by 80% requires approximately 146 Nm3 of H2 per toe;
– Fischer–Tropsch synthesis for the production of synthetic liquid fuels;
– Methanol synthesis, also for the production of base materials for plastics;
– Coal hydrogenation for the production of synthetic oil;

- Methanation for SNG production;
- Chemical processing to manufacture chlorine, caustic soda, and hydrogenated non-edible oils for soaps, insulation, plastics, ointments and other chemicals;
- Hydrogenation of organic interim products for the production of polyamides, cyclohexane, fat alcohols, fat hardening;
- Synthesis of ammonia (NH_3) for the production of fertilizer and synthetic materials (acrylic fibres);
- Oxo-synthesis for alcohol production;
- Pharmaceuticals to produce sorbitol, which is used in cosmetics, adhesives, surfactants and vitamins;
- Direct reduction of iron ore for sponge iron production, raw iron in the metal industries;
- Metallurgy to use pure hydrogen/oxygen flames in cutting, welding, brazing, annealing;
- Food processing to hydrogenate plant fats and oils, such as soybean, fish, cottonseed, and corn oil, for hardening;
- Electronics to create a special atmosphere for the production of semiconductor circuits;
- Reduction gas, protection gas in high temperature operations, such as glass manufacturing to use high-purity flames for cutting and welding, artificial gemstone/diamond production, to create high-purity atmospheres in furnaces or protective atmospheres for float glass production, sintering processes, silicon chemistry;
- Generator cooling in power industry.

Hydrogen was first used at a large scale in balloons and large airships (Zeppelin) toward the end of the nineteenth century, although here the hydrogen was not used directly as a fuel, but rather as a lighter-than-air gas to provide positive buoyancy. The idea of using liquefied hydrogen as aircraft and rocket fuel was considered as early as 1918, stressing that hydrogen had a larger heat content than any other fuel. A strong increase in the demand for hydrogen was given with the developing space aviation programme in the USA (Dincer and Acar 2016). The first systematic experimental investigations in the USA to investigate its use as a fuel for aircraft and to study the properties of LH2 and the low temperature impact on materials started in the 1940s. But it was not until the 1950s that the attractiveness of LH2gradually became evident, despite its low availability and handling hazards. This was due to incentives for the development of airplanes for use at very high altitudes, advances in LH2 technology, and experiments indicating that hydrogen could combust readily at low pressures. The first (of three) successful in-flight tests of an experimental hydrogen-propelled aircraft were made in the USA in 1957 with the 'Project Bee', a B-57B twin-engine aircraft. The one engine operated on hydrogen fuel for about 20 min at a speed of Mach 0.72 before the fuel tank ran empty.

In 1958–1959, it was decided in the USA to use LH2 and LOX in the rocket engines of the upper stages of Centaur and Saturn, successful programmes of unmanned space missions and manned moon voyages, respectively, marking the

first time that this high energy propellant combination was used in practical applications. The subsequent NASA programmes Apollo and Space Shuttle then applied LH2 at a large scale. A total of 12,000 m3 of LH2 was necessary to fill up the tanks of the Saturn V carrier rockets. For a space shuttle launch, the required quantity of LH2 is 2380 m3, of which 1454 m3 is for loading the external tank, with the remainder mainly used for pre-chilling of fuel lines or lost as boiloff.

Some 40 years ago, almost all produced LH2 was consumed in the various space programmes. Although this share has decreased to about 25% today, the space industry still is one of the main customers for liquid hydrogen (Cecere et al. 2014).

3   Uses of Hydrogen as Raw Material

The refining of crude oil is a well established technology. The type of crude oil discovered and produced, however, is changing, with the average crude oil becoming gradually heavier connected with higher CO_2 emissions. From the processing, a tendency which is expected to continue. Industrial processes such as oil refining, shale oil production and tertiary oil recovery require massive quantities of hydrogen and high temperature heat/steam (Elsherif et al. 2015).

Temperatures required for petroleum refining processes are mainly in the range of 500–600 °C, but may sometimes reach 950 °C. From a typical refinery capacity of 180,000 bbl/d or 10.55 million t/a, approximately ten million t/a of refinery products are being generated. This corresponds to an energy consumption of about 5.5% of the energy content of the oil processed mainly in the form of high temperature heat for distillation columns and thermal crackers for distillation, desulphurization and many other processes. The corresponding CO_2 emissions amount to about 1.73 million t/a.

A refinery consists of a complex system of units with highly optimized energy and mass flow structures. The heat and power demand of a refinery depends on its size, but also on its distillation capacity and the type and amount of downstream processing, as well as on the product balance.

Petroleum refineries convert petroleum from its natural state to a range of commercial products. About 90% of petroleum products are fuels such as gasoline, aviation fuel, distillate and residual oil (diesel oil, heating oils, industrial oils), liquefied petroleum gas, coke and kerosene. The remaining 10% goes to non-fuel products such as ethylene, propylene and benzene.

Most industrial heat is consumed in the 400–600 °C temperature range. The energy is typically supplied by firing produced process gases. Additional natural gas firing is needed for high temperature processes. Standard practice is to use steam in equipment considered 'critical units' such as turbo-machines. Non-critical equipment usually relies on off-site electricity supply, with redundant equipment powered by steam in the case of maintenance or accidental shutdowns. To become totally independent of external energy providers, refineries are operating cogeneration plants which provide 'secure' electricity for their own needs, the surplus electricity being consumed in other facilities or sold to the grid.

More than 80% of the world's production of ammonia and ammonium compound derivatives is used as fertilizer (Chai et al. 2021). Of the remaining 20%, 5% is used in chemical manufacturing (explosives, fibres and plastics, pharmaceuticals), and the remainder is used for refrigerants and in the pulp and paper industry. The total demand of hydrogen is currently 250×10^9 Nm3 per year or about 50% of the world H2 production. Demand in the EU is 33×10^9 Nm3/a or ~ 55% of the European production. The synthesis reaction runs as an exothermic catalytic reaction according to the Haber–Bosch process which was developed between 1905 and 1913:

$$N_2 + 3\_H_2 \leftrightarrow 2NH_3$$
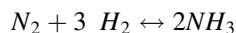
Operating conditions are low temperatures (~400–500 °C) and high pressures (up to ~50 MPa) to favor the equilibrium toward ammonia. The catalyst is a mixture of iron oxide and aluminum oxide. Still, not more than 15% of the feedstock is converted to ammonia, while the remaining unconverted gases are recycled. The most energy consuming part of an ammonia plant is the air liquefaction process and the compression steps. With high operation temperatures and atmospheric pressure, the above reaction is shifted toward ammonia decomposition. The separation step requires ~3.5 MJ of heat per Nm3 of H2.

The ammonia compound can also easily be utilized as a chemical energy carrier for long distance energy transportation (Klerke et al. 2008). The big advantage is the densification factor for the hydrogen of 1333. Ammonia is liquid at ambient temperature and easily transportable in pipes and storable in containers.

Among the largest consumers of hydrogen is the steel industry, where the hydrogen is used to upgrade raw iron to steel. The direct reduction iron (DRI) process is applied for the production of iron and steel from iron ore (Cavaliere 2019, 2022).

DRI is performed with either coal or synthesis gas in fixed or fluidized beds of iron ore to reduce the ore to sponge iron, which can be smelted directly to steel in an electric arc furnace. The major chemical reaction is:

$$Fe_2O_3 + 3CO \leftrightarrow 2Fe + 3CO_2$$
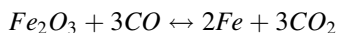
The chemical reduction process can also be conducted with hydrogen to replace the coal, thus reducing CO_2 emissions, assuming the H2 is from a nuclear or renewable source:

$$Fe_2O_3 + 3H_2 \leftrightarrow 2Fe + 3H_2O$$
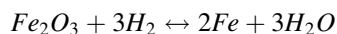
While the latter process takes place at ~500 °C and 3–4 MPa, the former process operates at 800 °C and 0.3 MPa.

Steel production has risen sharply from 200 million t in the 1950s to about 1300 million t in 2007 and is responsible for the release of 2106 million t of CO_2 into the air. The traditional primary blast furnace is a countercurrent gas–solid reactor where

the iron oxide is reduced with coke and limestone. With a typical input of 80% ore and 20% scrap metal plus fossil energy, the iron is melted and the liquid metal separated from the slag and converted into steel by oxidation of impurities and controlled addition of alloying elements.

According to the World Steel Association, the estimated energy consumption is in the order of ~30 GJ/t of steel for primary steel production methods and ~ 11 GJ/t for secondary steel production (recycling). Assuming a nuclear assisted process with cogeneration of hydrogen and electricity, and based on a 1000 t/d production rate, the feed required for the production of one million t of steel has been estimated to be about 1.43 million t of Fe2O3 plus ~65,800 t of hydrogen to obtain the iron at 900 ° C, plus ~8.4 MW(e) to heat the iron up to 1600 °C.

A large blast furnace plant at a power level of ~1600 MW(th) produces a tonne of iron every 10 seconds. The overall iron yield is very high at ~99.5%. Blast furnaces are used for about 65% of all steel making, but account for 90% of worldwide steel industry emissions. Purified iron is needed for the production of high quality steels with electric arc furnaces, which are more environmentally benign than the traditional blast furnaces. The heat needed to melt the metal is produced by electricity. This process requires inexpensive sources of hydrogen if the old production methods are to be replaced with electric arc furnaces.

Coal liquefaction processes were developed in the first half of the twentieth century. Coal has the potential to provide almost every product that can be produced from oil. Bergius or Pott/Broche used a direct method to convert coal by a hydrogenation process. The conversion to a liquid is done in a single step by dissolution in a solvent at elevated temperatures and pressures followed by hydro-cracking with hydrogen:

$$C + H_2 \leftrightarrow -CH_2^-$$
$$CH + 0.5H_2 \leftrightarrow -CH_2^-$$
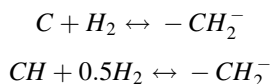
Pulverized coal is mixed with oil and catalyst to produce an oily, medium sized interim slurry which is either reprocessed to a coal oil or, in a subsequent step, after mixing with hydrogen, passes through a series of hydrogenation reactors at 450–490 °C and 20 MPa, and in the presence of an iron oxide powder as catalyst to a coal oil. Here the coal having a molecular weight of over 5000 splits into smaller pieces with the concomitant accretion of hydrogen. Thermodynamic conditions determine the quantity and type of products, and they can be adjusted to the feedstock. Coal to liquids (CTL) processes require about 5–8 kg of H2 per bbl to produce transportation fuels. The coal demand for 1 t of 'coal oil' is 1.25 t to be hydrogenated plus 1.36 t for the hydrogen plus 1 t for the process heat.

Overall thermal efficiencies for the direct method are generally in the range of 60–70% in modern processes. Different kinds of pyrolysis (high temperature, mild, rapid) with different liquid yields have been developed and tested in pilot plants, however, no demonstration plant has been operated so far.

Direct coal liquefaction puts stringent requirements on the type and quality of the coal, and its products need further upgrading before being used as transportation fuel. On the other hand, it achieves favourable efficiencies.

Brought to large technical maturity by Pier, Germany operated 12 coal hydrogenation plants from 1940 to 1944 to produce four million t/a of coal gasoline. British Coal developed a two stage direct coal liquefaction process called 'liquid solvent extraction' where two reactors in series are applied. Coal dissolution with little or no catalyst is done in the first stage, while hydro-treatment of the heavy coal liquids takes place in the second stage. The thermal efficiency for a conceptual coal liquefaction plant based on this process was estimated to be >60%.

In contrast to the direct process, Fischer and Tropsch started from synthesis gas. In their indirect liquefaction process, developed between 1922 and 1926, coal is gasified in a first step to synthesis gas followed by a catalytic hydrogenation of the CO where synthesis gas is reacted at relatively low temperatures and pressures (220–340 °C, 2–2.5 MPa) to high quality clean fuels:

$$2nH_2 + nCO \leftrightarrow -CH_2^- + nH_2O$$
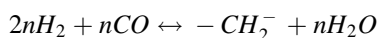
or, if the production of long carbon chain alkanes is favored:

$$\left(\frac{n}{2} + m\right)H_2 + mCO \leftrightarrow C_mH_n + mH_2O.$$
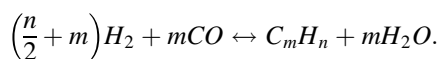
After the volatiles have been cleaned out of the gas stream, the water gas shift reaction is applied in order to adjust the H2:CO ratio and match requirements for the hydrocarbon synthesis and produce CO_2 as the main byproduct. In CTL processes, more than 40% of the synthesis gas is shifted to make the required hydrogen. Catalysts are selected depending on the product spectrum requirements. Special catalysts are used to rebuild the molecules into liquid hydrocarbons and remove by-products.

The product spectrum depends on the operating conditions applied with the higher temperatures/pressures to yield synthetic gasoline and chemicals, whereas the low temperature process leads to the production of synthetic naphtha, kerosene or high quality diesel fuel. Gasifier product gases with a H2:CO ratio of around 0.5 to 0.7 are recommended as a feed to the Fischer–Tropsch process when using an iron catalyst. A high H2, low CO_2, low CH4 content is required for chemical and fuel production. In general, liquid products are of lower quality compared with those from direct liquefaction processes.

The generation of 1 kg of Fischer–Tropsch product requires an input of 4.5 kg of coal and 7.2 kg of water, and it produces 9.3 kg of CO_2 plus 0.4 kg of solid waste. The tremendous CO_2 emissions of CTL fuels made from coal are a major disadvantage, being more than double of those for crude oil derived fuels.

The Fischer–Tropsch process is a preferred liquefaction process because it has a large experience basis and yields high quality fuel (diesel) containing only very little sulphur. The drawback is that coal liquefaction is comparatively expensive,
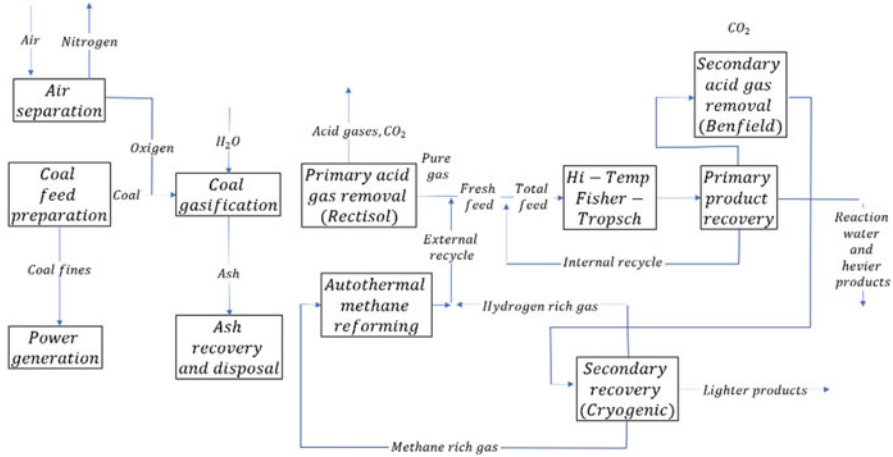
Fig. 4 Schematic of conventional CTL process

particularly at the front end where all contaminants have to be removed before processing to a gas or liquid. The indirect process is superior to the direct one because of the lower operational pressures necessary and thus a higher reliability of the plant, and a higher grade product spectrum. Efficiencies are around 40%, being lower than for the direct process, and in modern plants up to about 55%. Economics demand large scale plants with a massive demand for hydrogen and oxygen.

Figure 4 shows a schematic of the conventional CTL process.

Technical plants use solid bed (Arge process) or flue stream reactors (Synthol process). In the Arge process, apart from gasoline, preferably solid paraffins are produced, whereas gaseous hydrocarbons are produced in the Synthol process. The Fischer–Tropsch synthesis yields a gasoline with low octane number, but a higher value diesel fuel compared with coal hydrogenation (Aziz et al. 2017).

A major disadvantage is the significant quantity of CO_2 that is emitted during the synthesis gas production. If an independent source of H2 and O2 were available, e.g. from a water splitting process by nuclear or renewable energies, processes like air separation, steam generation and shift reaction would no longer be required and process related CO_2 release would be significantly reduced.

Starting as early as around 1840, both direct and indirect methods of coal liquefaction were developed in Germany to industrial maturity in the 1940s applying brown coal and stone coal. Coal liquefaction in Germany, however, eventually became uneconomic and was later abandoned. Significant R&D work was initiated during the oil crisis in the 1970s in the USA, the UK, Japan, and other countries. Activities in Germany resulted in the operation of a pilot plant with a production rate of 200 kg/d. Since then, only a few joint international projects, e.g. with South Africa, have remained, the only country to apply this technology still today at a large scale.

Recent trends have revived interest in coal liquefaction technologies as an alternative means of generating transportation fuels and other oil products used in a number of countries as insurance against crude oil supply problems. Primarily, high oil prices, increasing demand from China and India, US refining capacity limitations, and increasing reserve replacement costs as well as a growing desire for energy independence from foreign sources create the political will to explore more domestic energy resources. Lignite is considered an ideal feedstock for coal liquefaction because of its low relative cost and high hydrogen content. Newer processes convert the syngas to methanol before transforming it to other liquid fuels. An alternative option is use of outside (allothermal) production of hydrogen and oxygen, like from a (nuclear) water splitting process. Engineering studies are required to optimize the modified flowsheets for a nuclear assisted hydrogen coal liquefaction plant and to assess the economics (Lewis 2008).

The Mobil Oil process is principally based on a new catalyst which allows easy production of liquid fuels from methanol. Gas to liquid (GTL) capacity, however, is expected to grow slowly due to the huge and risky investment. By 2050, an estimated 5–10% of the transportation fuel demand may be covered by GTL fuels.

China, with its abundant coal reserves, is experiencing a strong growth in coal liquefaction. Fischer–Tropsch fuels are considered feasible and practical options to replace petroleum based fuels in China in both the short and medium terms, and thus reduce its dependence on oil imports. Commercial scale plants are already in the design and construction phase. A coal liquefaction plant has been constructed in Shenhua, China, with a throughput of 9.7 million t/a of coal to be converted into five million t of gasoline, kerosene, diesel and other fuels. For the next few years, China is planning the construction of 27 coal liquefaction plants. More liquefaction plants based on the direct process are planned, with a total capacity of 60 million t/a of oil. China will soon become the worldwide volume leader in CTL fuel production. In cooperation with SASOL, China is currently involved in two plants planned for Inner Mongolia to deliver an annual capacity of 60 Mt of oil. The first plant, with a one million t/a capacity, is expected to produce gasoline and diesel by 2007. Also a plant able to produce 50,000 bbl of ethanol per day is planned. Further coal to chemicals (CTC) plants are planned in regions with proven coal reserves for ammonia and methanol production.

In Japan, the liquefaction of bituminous coal was promoted under the Sunshine project which started in 1974. The so-called 'NEDOL' liquefaction technology (Fig. 5) has been developed where the three processes of direct hydrogenation, solvent extraction and solvolysis were merged to one.

The result is a light-distillate rich oil produced under mild reaction conditions. But also the liquefaction of low-rank coal is being investigated in Japan.

The so-called brown coal liquefaction (BCL) technology is currently being tested on pilot scale in a 50 t/d plant in Australia.

A 150 t/d pilot plant for bituminous coal was operated between 1996 and 1998 and provided engineering data for a commercial plant to follow. Japan is currently the only country active in large scale process development.

High − performance catalyst (Fe)

Coal

Liquefation
reaction

Separation   Coal oil

Solvent

450°C, 170 atm   ▸solvent

Hydrogen

Ni − Mo catalyst

Solvent
hydrogen   Heavy

Hydrogen
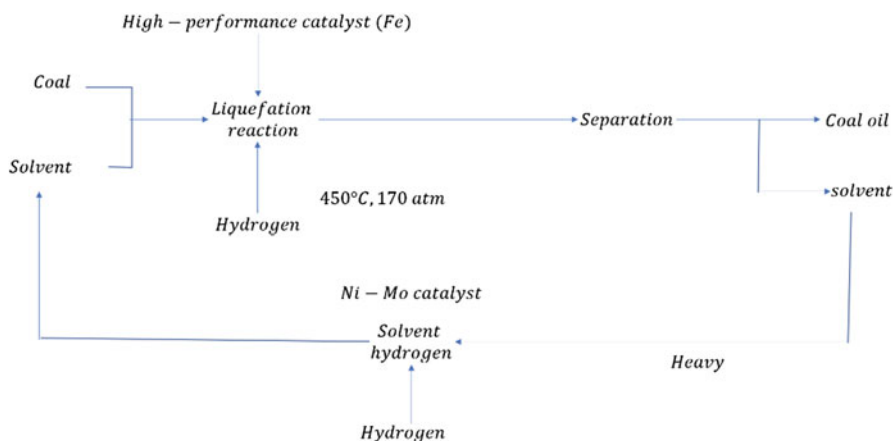
Fig. 5 Schematic of the Japanese NEDOL bituminous coal liquefaction process

The South African corporation SASOL Limited is a fuels and chemicals manufacturing company and the largest gasification centre in the world. Since 1955, SASOL has been producing higher value oil products from low grade coal, today at an output of 150,000 bbl/d of fuels and petrochemicals, supplying about 40% of the domestic demand for liquid fuels. The SASOL complex in South Africa consists of three facilities at two sites. Sasol Two and Sasol Three located in Sasolburg comprise the world's two largest gasification facilities. Within the USDOE's Clean Coal Technology Demonstration Program, a liquefaction plant with a capacity of 1000 t/d was commissioned based on the 'mild pyrolysis' process. North Dakota has received recent attention regarding coal liquefaction with the proposal of a 10,000 bbl/d facility with expansion opportunities to 50,000 bbl/d. If diesel is included in the fuel mix at the proposed coal liquefaction plant, coal based diesel could be blended with biodiesel. Also, the KIER in the Republic of Korea is currently testing CTL in a 15 bbl./d pilot plant.

The methanol industry is the third most important user of hydrogen. Methanol is a high octane alcohol, a colourless liquid with a boiling point of 65 °C that is easily ignitable, with a flammability range between 6.7 and 36.5 vol% in air. Commercial methanol synthesis involves reacting CO, H2 and steam over a copper–zinc oxide catalyst in the presence of a small amount of CO_2. Methanol is produced, e.g. through synthesis gas from coal by clean coal technologies with CO_2 from the reverse water shift reaction and the hydrogenation of carbon dioxide at 250–300 °C and 5–20 MPa by:

$$CO_2 + 3H_2 \leftrightarrow CH_3OH$$

$$CO_2 + 3H_2 \leftrightarrow CH_3OH + H_2O$$
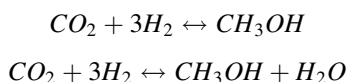
Other feedstocks like natural gas or heavy oils are also possible. The product gas from coal gasification is not appropriate for methanol production owing to its high

fraction of CO_2 and methane. The preceding POX step could reduce the methane fraction. To best use the raw product syngas in methanol synthesis and limit the extent of further syngas treatment and steam reforming, it is essential to maintain the following conditions:

- A H_2:CO ratio of at least 2;
- A CO_2:CO ratio of about 0.6 to prevent catalyst deactivation and keep the catalyst in an active reduced state;
- Low concentrations of N_2, CH_4, C_2+, etc., to prevent the buildup of inert gases within the methanol synthesis loop;
- Low concentrations of CH_4 and C_2+ to limit the need for further steam reforming.

Alternative methanol production occurs via direct hydrogenation of carbon monoxide:

$$CO + 2H_2 \leftrightarrow CH_3OH$$
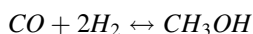
This second reaction demands more energy, is slow and incomplete. Therefore the product gas should contain only small amounts of CO_2 and have an H_2:CO ratio of ~2.2. The methanol synthesis reaction is equilibrium controlled, and excess reactants (CO and H_2) must be recycled to obtain economic yields.

Methanol is a classic basic material for chemical production chains, e.g. the production of chemicals such as propylene, poly-propylene, phenol or acetone. The methanol to gasoline (MTG) process is an effective route for CTL processing where methanol is directly converted to gasoline:

$$nCH_3OH \leftrightarrow \left(- CH_2^- \right)_n + H_2O$$
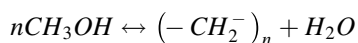
The process is simple and robust in design and operation and promises high plant availabilities. It was demonstrated in New Zealand, but has not been conducted so far at a large scale. Still, MTG plants are currently foreseen in China and the USA. A new MTG plant with coal based methanol production in Jincheng, China, started operation in 2009. It has a 100,000 t/a of gasoline capacity which may be extended to one million t/a later.

Commercial application of methanol as a fuel, however, is limited due to its high toxicity and relatively low energy density (~65% of that of gasoline).

Methanol can be used in direct methanol fuel cells and also in higher temperature fuel cells for electricity production or even in PEFC after a reforming stage. Methanol is also used for the production of alternative automotive fuels such as DME. A route to transport fuels is hydro-treating/hydro-cracking to a naphtha-like product with upgrading to diesel. But the high pressure and high hydrogen requirement of hydrotreating routes makes this route much too expensive. A major issue is the catalyst stability and lifetime. The coproduction of chemicals and fuels undoubtedly offers the most interesting opportunities.

The world market for methanol was 40 million t/a in 2007 which is expected to increase to 80 million t/a by 2020. Most methanol is currently produced from coal and natural gas. It is used as feedstock for fuel addition and chemical materials such as formaldehyde and acetic acid. Emerging markets are seen in the transportation sector. At present, the largest plants with a capacity of ~5500 t/d are operational in the Islamic Republic of Iran and Trinidad.

The transportation sector and stationary power applications are widely viewed as the two critical sectors where there may be an opportunity to greatly expand the future use of hydrogen. Most of today's transportation fuels are being generated from refining crude petroleum oil. Petroleum fuels which are well qualified for widespread use and offer a number of benefits which make it likely that they will continue to dominate the overall fuel mix:

– High energy density;
– Strong demand from the current stock of vehicles and a widely established infrastructure for delivery to users;
– Relatively low cost;
– Easy, low-cost handling and transport at atmospheric temperature and pressure;
– Extensive experience and knowledge of fuel systems, coupled with considerable progress in optimization;
– Ease of long term storage.

But petroleum fuels also have at least two major drawbacks: potential supply limitations, including significant geopolitical dependencies for many countries, and high CO_2 emissions. For both of these reasons, there are strong incentives to develop and secure acceptable substitutes.

Figure 6 and Table 1 list various transportation fuels for both ICE and FCVs, and some of their characteristics.

Not only is hydrogen considered a transport fuel which may be applied in the future on a large scale, it is also a basic building block with increasing significance (and market potential) for the production of conventional liquid fuels, but also — partially — for other alternative fuels or synthetic fuels. Diversification of fuel supply is the driving force to move away from crude oil and gradually displace conventional petroleum products, meeting the challenges of air pollution, CO_2 emissions and supply security. If captured CO_2 is used for their production, they would even represent CO_2 neutral alternatives.

Production of synthetic liquid fuels requires the input of carbon, hydrogen and energy. All three can be taken from fossil fuels or biomass. An IEA analysis suggests that the least expensive alternative to oil based fuels is large CTL plants, which are cost effective at oil prices above US$60/bbl. GTL and hydrogen produced from natural gas are strongly influencing fuel production cost. Biomass to liquid (BTL) fuel is cost competitive only if low cost biomass is available.

SNG is the starting point for many industrial chemical processes. The exothermic methanation reactions are:
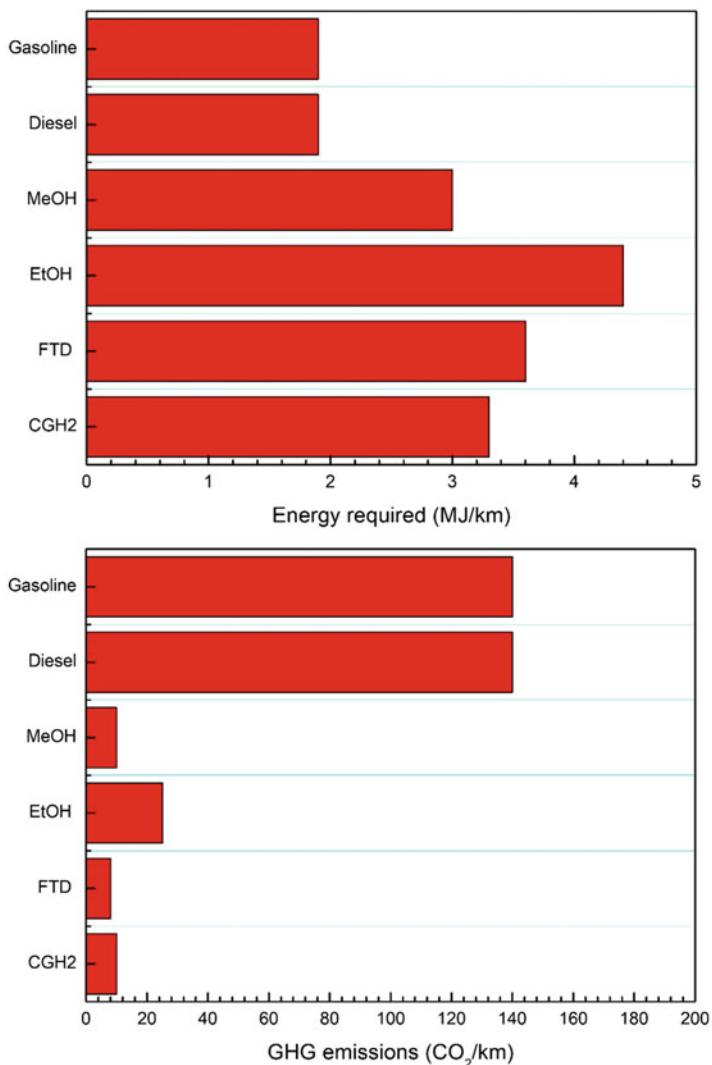
Fig. 6 Comparison of today's petroleum fuels with alternative non-fossil derived fuels

$$CO + 3H_2 \leftrightarrow CH_4 + H_2O$$

$$CO_2 + 4H_2 \leftrightarrow CH_4 + 2H_2O$$
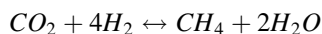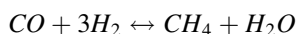
The second reaction (Sabatier reaction) is slow and incomplete. Therefore, the product gas should contain only small amounts of CO_2 and have an H2 to CO ratio of ~3.2, conditions that are achievable in non-catalytic steam–coal gasification, but under stringent operating conditions not possible for the catalytic process. The

Table 1 Comparison of transport fuels

Fuel	Main source	Molecular weight	Density (kg/m3)	HHV (MJ/kg)	Energy per volume (GJ/m3)
Hydrogen	NG, oil, coal, methanol	2.02	0.08988	141.9	2.6 at 20 MPa 10.3 at 80 MPa
LH2	Hydrogen	2.02	70.8	141.9	9.9
NG (methane)	Fossil resource	16.04	0.7175	55.5	8.1 at 20 MPa 32.1 at 80 MPa
LNG	NG	16.04	422.6	55.5	20.5
LPG (propane)	Refining of petro-leum, NG	44.1	581	50.4	25.2
Methanol	NG, cola, biomass	32.04	793	22.7	18
Ethanol	Biomass, grain, corn	46.07	794	29.9	23.5
Gasoline	Crude oil	100–105	745	47.4	30.4–34.8
Diesel	Crude oil	200	832	45.8	35.7–36.2
Biodiesel	Biological oil, ani-mal fat	120–320	830–850	39.8	32.6–33.4
DME	NG, cola, organic material	46	670	31.7	21.1
MTBE	Isobutylene	88.15	741	7.8	28.1
Toluene	Crude oil, tolu tree	112	862	42.5	26.9
Ammonia	NG, heavy oil	17	771	22.5	17.4
Jet A	Crude oil	144–226	775–830	46.5	34.2

use of coal gasification raw gas is less economic for on-purpose methanol or hydrogen production compared with the gas from autothermal processes. The conversion of coal to SNG offers the option of transporting the energy content of coal via pipeline.

Besides storage, there is also the option of using CO_2 as a raw material, i.e. taking it directly as a C1 building block to be used as reaction partner in chemical and biotechnological processes and built into products. Storage time would correspond to the product's lifetime, ranging between decades for long lived polymers and practically zero for synthetic fuels.

As of 2005, the worldwide anthropogenic CO_2 emissions from using fossil fuels amounted to 28 Gt/a. The main (large, stationary) sources are the energy sector with 10.5 Gt or 46%, the transportation sector with 5.6 Gt or 24%, steel production with 1.5 Gt or 6%, refineries and the chemical industry with 1.2 Gt or 5%, and others. The CO_2 sources in the transportation sector are small and numerous and therefore not appropriate for sequestration and further use. The same holds for the firing of fossil fuels for heating purposes.

Different from the storage option where CO_2 is taken out of the CO_2 cycle, no CO_2 is usually saved in the case of using it as a carbon source. It would only be saved if the energy required for the reduction of CO_2 as the reverse process of combustion is from a CO_2 emission free energy source. CO_2 as a raw material is obviously

available in large amounts, but only a small quantity can be utilized and only in a few industrial processes. The industry uses approximately 120 million t of CO_2 per year. Although most of it will be consumed again (urea synthesis), at least ten million t/a would be available for chemical conversions. Other applications are in the beverage industry, for enhanced oil recovery, and in its supercritical state as a technological fluid. As an inert and safe gas, it is also used as a protective gas and in its solid state for refrigeration.

For products of the chemical industries, the estimated substitution potential amounts to 178 million t of CO_2 per year, which is not more than 0.6% of the total annual anthropogenic CO_2 emissions worldwide. The use of carbon for synthetic fuel production would increase the potential by a factor of 10, but it would not change the atmospheric CO_2 concentrations, since subsequent combustion of the fuels will immediately recycle the CO_2 back to the atmosphere. The purity of CO_2 is an important prerequisite that eliminates the CO_2 emitted from fossil power plants as source candidates. Their use would require an extensive purification as a preceding step. Exceptions are the emissions from IGCC plants (Giuliano et al. 2018).

The most common method of recovering atmospheric CO_2 is by absorption using aqueous potassium carbonate. The external energy source to be used (mainly for hydrogen production) can be, for example, in the form of electricity. The use of nuclear primary energy would provide the option of unlimited liquid fuel production without any greenhouse impact.

The CO_2 or dry reforming process can be applied for the production of synthesis gas, which is then converted by means of Fischer–Tropsch synthesis to gasoline or diesel fuels. In GTL technologies, atmospheric CO_2 can be used as a carbon source for the conversion with hydrogen to synthetic liquid fuels, such as methanol or its derivates methyl T-butyl ether (MTBE), dimethylcarbonate, or dimethylether. Furthermore, it allows the direct production of DME from CO_2 and H2. Methanol and dimethyl-carbonate (DMC) are considered alternatives to the currently used gasoline; DME may replace diesel fuel. The above processes, however, are only reasonable if there is a source of (inexpensive and) 'clean' hydrogen feedstock. Technological challenges for the development of energetically efficient processes are seen in the areas of catalysis and reaction kinetics.

KIST developed and demonstrated a direct methanol production process using hydrogen and captured CO_2 (CAMERE-I process) with an integrated steam reformer for hydrogen production (CAMERE-II process). The concept of nuclear methanol is now to introduce nuclear energy into the steam reforming process using an advanced HTGR. A 450 MW(th) plant would be able to produce one million t/a of methanol and recycle at the same time 0.35 million t/a of CO_2.

Hythane is a blend of natural gas and hydrogen with a fraction of 8–30% of hydrogen. Since methane emits NOx and has a relatively narrow flammability range that limits the fuel efficiency, the addition of a small amount of hydrogen extends the lean flammability range significantly. Hythane is more buoyant and more diffusive than methane. Methane has a slow flame speed, especially in lean air–fuel mixtures, while hydrogen has a flame speed about eight times faster and is much more easily ignited (Mahant et al. 2021).

Hydrogen is a powerful combustion stimulant for accelerating the methane combustion within an engine, and it is also a powerful reducing agent for efficient catalysis at lower exhaust temperatures. In the case of explosive combustion, a hythane explosion is expected to be stronger than a methane explosion, but exhibits significantly lower pressures than do pure hydrogen explosions.

Hythane could represent an interim step on the way to a hydrogen based economy. A big advantage is the fact that hythane can benefit from the existing infrastructure for natural gas without major changes. The same holds for hythane combustion in a natural gas driven internal combustion engine. Test vehicles in public transportation running on hythane are being operated at various places in the world.

4   Prospective Uses of Hydrogen

For future large scale applications of hydrogen, it should be kept in mind that electricity and hydrogen can form a symbiosis, allowing an optimization of electricity generating systems with regard to the substitution of fossil energy carriers currently being used for load following and peak demands. This is due to the fact that electricity and hydrogen are principally interchangeable, i.e. the production of hydrogen (e.g. via electrolysis) and the re-conversion of hydrogen into electricity (and heat) (e.g. by fuel cells). This fundamental interconnection is being addressed as 'hydricity' (Hoffmann 2012).

With increasing production of electricity from renewable energies instead of fossil fuels, novel energy storage systems are needed to compensate for the strong variations of supply and demand. Hydrogen may here play an important role as a storage element for energy that can easily be retrieved upon demand. In addition to the industrial hydrogen demand as a chemical product, commercial growth of hydrogen production is expected, most probably starting in the coming decades in road transport and in the residential and service sector to expand the application as a fuel in fuel cell vehicles and stationary power generation (Tsujimura and Suzuki 2019).

Niche market applications such as hydrogen powered consumer electronics may play a role, specifically in the area of public acceptance, in the introduction of hydrogen in the energy system. All these potential applications may contribute in the medium term to an increased need for clean hydrogen production routes. The further future beyond 2030 may see a significant increase in hydrogen consumption due to cost reductions in the production technologies and a stronger demand from the transport sector.

Crude oil is a finite resource. Conventional oil production will peak at some point and then gradually decline, increasing the share for unconventional oil production. Therefore, there will be an increasing demand for more capacity to refine heavier grades of oil, including other non-conventional liquids such as condensates, natural gas liquids, tar sands, bitumen, extra heavy oil and oil shales, but also synthetic fuels

from anything to liquid (XTL) processes to contribute to global petroleum supply. While the economics of heavy oil might be promising, the harnessing of non-conventional resources is handicapped by high development costs, consumption of large quantities of water and natural gas, and severe environmental impacts.

Heavy oil is a dense and viscous kind of oil with high contents of sulphur and metals. Extra-heavy oil resources are mainly located in Venezuela. Large reserves of oil exist in the form of highly viscous crude oils inaccessible by methods available at present.

Thermal methods are the most developed technology, where steam injection plays the overwhelming role. The type of steam required depends on, e.g. the depth of the resources, porosity of the rock matrix or oil viscosity. For improved recovery methods, high pressures of 12 MPa and more are necessary. Oil yield increases significantly with the steam temperature and pressure. Oil recovery steam generators currently on the markets are in the power range of 1.5–15 MW(th), providing steam at pressures up to 17 MPa and temperatures up to 350 °C, and at rates of up to 110 t/h (250 000 lb/h). Dry saturated steam of high temperature to be injected into deep oil wells could be produced by an HTGR.

But besides steam, large quantities of hydrogen will also be required for tertiary oil recovery (upgrading to synthetic crude), which requires a significant increase of the present power capacity to allow for efficient large scale hydrogen production in the future.

Most of the world's oil shale resources (estimated at 75%) are located in the Green River Formation in the USA, with estimated resources of 1.5–1.8 trillion bbl of oil. The largest oil shale producer and consumer country, however, is Estonia, with peak production of 31 million t in 1980 (today ~15 million t/a). Shale is a fine-grained rock of sedimentary origin containing, but varying widely in content and composition (quality) of, high-molecular organic substances (kerogen) embedded in its inorganic matrix. Criteria of oil shale reserves are energy rating, location, depth and thickness of seams, mining technology, world price and transportation costs compared to alternatives, and protection of the environment.

Oil and gas can be extracted by destructive distillation. Only some of these organic compounds (the natural bitumen) are soluble. Depending on the site, the rock contains an average of 10–20% insoluble organic matter and bitumen — in some cases the organic content can be as high as 60%. At temperatures of 350–400 °C, the yield can be 20–200 L of oil per tonne of shale. The negative aspects are the immense toxic waste which is left by the oil shale chemical industry, the large CO_2 emissions from oil shale power stations and the deterioration of water quality.

The high temperature heat required to heat the oil shale could be provided by nuclear energy. The direct use of high temperature heat avoids the conversion of electricity to heat. Another advantage of the nuclear system is a significant reduction of CO_2 compared with other methods of synthetic crude oil production. The distances from reactor to well are sufficiently short that heat transport is practicable. About 12 GW(th) of high temperature heat would be required to produce a million barrels of oil per day. In practice, the required temperatures would be near 700 °C.

Tar sands are a mixture of sand, clay, water and bitumen (viscous heavy oil), from which the bitumen is extracted. They represent a major energy resource that increases in importance as world supplies of crude oil become limited; on the other hand, they are the dirtiest fuel on Earth. The hydrogen to carbon ratio of tar sand is ~1, which must be raised to 1.5–2 for conversion to gasoline. Oil sands are mainly located in Canada in the state of Alberta, the regions of Athabasca, Cold Lake River and Peace River, with proven reserves of 174 billion bbl of oil, representing about 80% of the world's technically recoverable resources and 95% of Canadian oil reserves.

Oil sands feature an intermediate density and viscosity. The methods involve the in situ steam assisted gravity drainage (SAGD) technology, since ~80% of the deposits in Canada are not accessible for surface mining. The product recovered from the sands is a heavy, sour bitumen. Upgrading with hydrogen is required to transform it into a lighter product (with lower density and viscosity) that can be transported to refineries via pipelines. The products are synthetic crude (refinable by current technology) and petroleum coke. The Athabasca oil sands are estimated to require 3–4 kg of H2 per barrel as well as steam (14 MPa, 340 °C) and electric power for the recovery and upgrading processes. Current production from oil sands amounts to 1300 bbl/d, which is expected to increase to six million bbl/d by 2030.

Producing fuels from oil sands requires large amounts of natural gas and water, and produces large quantities of waste material and carbon dioxide. The shale can be distilled autothermically after open pit mining. This method requires hot water of ~70 °C and process steam at around 1–2 MPa and has a yield of less than 50% of the organic matter. A second in situ method for high-permeability shales is SAGD, in which two horizontal wells of 0.5–1 km length and at least 50 m below surface are drilled with one about 5 m below the other one. Steam at high pressure and temperature (10 MPa and 540 °C) is continuously injected into the upper well, where the bitumen heats up and flows downwards. The formed emulsion of bitumen, steam and water is drained through the lower well and recovered. A pair of wells is able to recover in the range of 2000 bbl/d of synthetic crude oil.

Other methods are cyclic steam stimulation (CSS) or pressure cyclic steam drive (PCSD) requiring steam of more 300 °C and pressures of 8–16 MPa. Novel technologies replace the steam with either solvents, e.g. a liquid salt, or in situ combustion. The possible yield also represents 50% of the in-place reserve. Oil shale contribution is marginal so far, as no industrial scale recovery has yet been envisaged due to the high production costs.

Furthermore, the processing is presumed to produce five times more CO_2 emissions than conventional refining. But oil shale would roughly add another 300 billion bbl of oil to the global reserves.

Various fuel cell types have been developed, usually classified according to the electrolyte used. In Table 2, fuel cell types (Fig. 7) are listed along with their operating temperatures and anode/cathode reactions (Staffell et al. 2019).

Certain constraints to the fuel cell do apply depending on the type of fuel cell. In low temperature fuel cells, noble metal (Pt) electrodes are necessary to increase the reactivity. Poisoning of electrodes can be minimized by purification of the feed

Table 2 Different types of fuel cells

	Electrolyte	Temperature (°C)	Fuel	Oxidant	Efficiency (% LHV)
Low temperature					
AFC	Alkaline	80–200	H2	O2	50–60
PEFC	Polymer	80–100	H2	O2, air	40–45
HT-PEFC	Polymer	120–180	H2, CO	O2, air	40–50
DMFC	Polymer	80–100	MeOH	O2, air	25–30
PAFC	Phosphoric acid	200	H2	O2, air	40–45
High temperature					
MCFC	Molten carbonate	650	H2, CO, CO2, CH4	O2, air	50–55
SOFC	Ceramic	750–1000	H2, CO, CH4	O2, air	50–55
LT-SOFC	Ceramic	550–650	H2, CO, CH4	O2, air	50–55
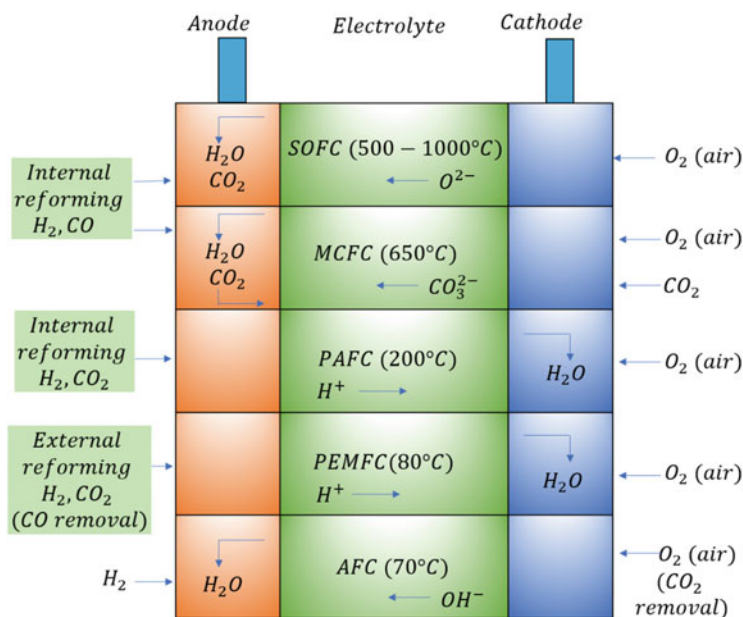
Fig. 7 Fuel cells schematic

stream. Various methods have been developed to remove sulphur, which is a poison to many oxygen electrode catalysts. High temperature fuel cell designs avoid expensive noble metal catalysts. Thermal activation is insensible to pollutants. Drawbacks are performance degradation limiting lifetime and expensive plant components. To avoid dilution of the electrolyte by the product water, it must be

removed by evaporation or vaporization. In high temperature fuel cell systems, the water is steamed off anyway.

If carbon containing fuel gases are used instead of pure hydrogen, oxidation must be realized first in a reforming reaction. Internal reforming has the advantage that there is no requirement for hydrogen storage (Sengodan et al. 2018).

Incomplete reaction at lower temperatures results in the presence of carbon monoxide, which is a catalyst poison and must be removed, at the expense of efficiency. CO causes no trouble at high operating temperatures since reforming can take place internally. Attempts at a direct conversion of coal or oil in an integrated gasification fuel cell system are currently at an early R&D stage, but they are considered potential primary fuels in the long run.

The alkaline fuel cell (AFC) is a highly efficient low temperature fuel cell ($<100\,^\circ$C) with a very high power density, and therefore ideally appropriate for mobile applications. The AFC, however, requires a demanding process control that is complicated because of the corrosive liquid electrolyte, a 30% potash lye, and the need for extremely pure fuel (no CO_2), leading to high cost. Efficiencies of 60% and more have been achieved with clean hydrogen and oxygen and noble electrode materials (Haseli 2018). The AFC was demonstrated to also work with a hydrogen–air system. What remains unsatisfactory is its observed power decrease with operating time.

The polymer electrolyte fuel cell (PEFC), or proton exchange membrane fuel cell (PEM-FC), is an efficient, compact, robust and quiet method of generating electricity. It has a 0.1 mm thick proton conducting foil as a solid electrolyte which is coated on either side with the electrodes representing the so-called membrane electrolyte assembly (MEA). It has the highest power density of all cell types, a relatively low operating temperature and thus long cell lifetime, good load change behaviour and good efficiency at partial load, and good standby performance, thus being appropriate for mobile applications. A problem in PEFCs is the need to keep the polymer electrolyte membrane in a wet state and at higher operating temperatures to prevent a dry-out by means of external wetting. Applicable fuels are hydrogen, reformed methanol or methane with purity requirements of less than 10 ppm of CO, less than 1 ppm of NH3 and less than 0.1 ppm of H2S. The development is concentrating on improvement of catalysts and reduction of CO poisoning effects. The electricity output from the fuel cell depends on the availability of oxygen. It is maximal when pure O2 is used, but can be reduced by a factor of 2–4 in the case of air.

The first complete PEM fuel cell system was developed in 1963 and utilized during the Gemini space flights.

The 1 kW cell stack employed sulfonated polystyrene membranes as an electrolyte, which was later replaced by the polymer Nafion. Today, PEFCs constitute the main pillar of fuel cell technology in both transport and stationary applications, with an emphasis being placed on system integration and demonstration programmes. The market is generally seen in smaller scale applications, whereas those on a larger scale have mainly disappeared.

Another low temperature fuel cell, the direct methanol fuel cell (DMFC), runs on either liquid or, with better performance but higher system complexity, on gaseous methanol and is normally based on a solid polymer electrolyte. The operating temperature for DMFCs is in the range of 60–130 °C, typically around 120 °C, producing an efficiency of about 40%. Due to the low temperature conversion of methanol to hydrogen and carbon dioxide, the DMFC system requires a noble metal catalyst. Pt–Ru catalysts were found to produce the best oxidation results at the oxygen electrode. Because of the still ten times higher loading with catalysts compared with PEFCs and the relatively low efficiency and power density due to internal fuel leakage through the membrane, the DMFC is not suitable for large units. Typical areas for DMFCs are in small units from a few Watts up to approximately 2 kW for portable applications. An advantage in mobile applications is the use of the methanol in liquid form at low pressures. But detailed development is still necessary, with major improvements to be seen in a further reduction of degradation rates, simplification and compaction of the system, and further increase of system efficiencies.

Most practical experience has been gained in the operation of phosphoric acid fuel cells (PAFCs). Because of the higher operating temperature, PAFCs have a minor CO poisoning problem, plus they offer operation in the CHP mode providing good quality steam of approximately 200 °C. The fuel is hydrogen or reformed methane plus CO converter. The principal poison for the Pt catalyst is sulphur carried in the reformate stream as H2S. The PAFC has successfully played a pioneering role in the introduction of fuel cell systems. Several hundred ONSI-delivered PAFC stations were tested and have proven technical maturity with 8000 operating hours per year and an availability of more than 90%. Most demonstration tests, however, were terminated after sufficient data were collected. Investment costs are still too high to be competitive.

A molten carbonate fuel cell (MCFC) is being operated in the 500–700 °C temperature range with porous Ni catalysts and a molten binary carbonate made of Li_2CO_3/K_2CO_3 or Li_2CO_3/Na_2CO_3 immobilized in a porous matrix of $LiAlO_2$ as an electrolyte. Carbon dioxide yielded at the anode needs to be fed back to the cathode, where it is consumed by conversion to carbonate ions which provide the means of ion transfer. Due to the high operating temperature, there is no need to employ noble metals as a catalyst. A key advantage over low temperature fuel cells is the fuel flexibility. Besides hydrogen, the MCFC can be operated with methanol or methane or coal gas, with external or with partial or full internal reformation; the possibility of internal naphtha reforming is also being examined. In the future, synthesis gas from (internal) coal gasification systems may be linked to MCFC electricity generation, inducing a further increase of coal conversion efficiencies. Recently, the applicability of biomass derived gases has also been investigated.

A number of MCFC installations with the 'HotModule' manufactured by the German company MTU are being operated successfully in Germany, Italy and Spain, and have achieved an a accumulated operating time (by 2007) of more than 170,000 h, and the industrial development is expanding. The drawbacks of this fuel cell type are its low current and power densities. A problem often observed in

MCFCs is the strong corrosivity of the electrolyte and its leakage through gaskets. Long term experimental operation is still required to demonstrate that ageing of the stack is acceptable. Also, the high serial resistance of the hot carbonate electrolyte limits the efficiency to 40%.

The solid oxide fuel cell (SOFC) has a solid ceramic as the electrolyte, e.g. zirconium oxide stabilized with yttrium oxide, in which oxygen ions migrate from the cathode to the anode. Heat and CO_2 are also generated at the anode. The SOFC is attractive because of its very high operating temperature range of 800–1000 °C, which allows fast chemical reactions. The high temperatures, on the other hand, imply stringent requirements for materials and construction. Two different stack designs are currently pursued using tubular or flat cell geometry. Typical dimensions of the tubular design are: support (cathode) with an inner diameter of 12–22 mm, 2.2 mm wall thickness, and a length up to 1500 mm, an electrolyte layer of 20–40 μm, and outside the anode with 100 μm thickness. For a flat cell, the typical data are: a gas-tight electrolyte of 150–200 μm thickness, electrodes with 50 μm thickness and 30–50% porosity. Most research efforts are currently conducted on planar SOFCs. With only slight modifications, the SOFC can be operated either in the electrolysis or in the fuel cell mode.

Due to the high operation temperatures, SOFCs convert gaseous hydrocarbons either directly or after internal reforming with a very low emission level. Utilization of the high temperature waste heat raises the overall efficiency to a maximum. Furthermore, the waste gas at the anode, consisting of CO_2, H_2O, CO and residual H_2, could be utilized in other chemical processes. The time needed to heat up or cool down the system limits the use of SOFCs in applications with rapid temperature changes. Heat release during internal reforming, creating sharp temperature gradients, is difficult to control. Also, high temperature corrosion can sometimes be a problem and requires the use of expensive materials and protective layers within the cell. Problems related to sealing have also been observed.

SOFC systems are generally thought to be best suited to the generation of electricity and heat in industrial applications, especially in combination with gas turbines. Recent SOFC development shows potential for high electricity efficiencies of ~60%. The main SOFC applications are seen in larger scale stationary power generation and in smaller scale residential power generation (<10 kW) and auxiliary power units (APUs) for mobile applications. Most of the SOFC power units currently being tested have a power capacity of 1 and 5 kW, respectively. A 100 kW SOFC power plant is being operated in Italy. A 10 kW(e) SOFC stack with 60 planar cells has been constructed at the Research Centre Jülich and operated for 1500 h. Both hydrogen and methane fuels were tested. The next step will be a 20 kW (e) SOFC system demonstration. Goals of the future development are the reduction of the operating temperature and the extension to larger power units.

5   Hydrogen Vehicles

Hydrogen is being considered as a potential energy vector in the transport sector both for internal combustion engine (ICE) and FCV applications, basically with on-board storage of the hydrogen. In recent years, car producers have manufactured a range of prototype ICE and PEM fuel cell passenger cars using hydrogen as the fuel (Jones et al. 2020).

Numerous demonstration programmes for hydrogen powered vehicles with PEM fuel cell drive trains and — to a lesser extent — with ICE have been initiated, mainly in Europe, Japan and the USA, comprising a broad spectrum of vehicle classes for small and medium range requirements. The development of hydrogen fueled vehicles is mainly driven by the market, i.e. they have to compete against other technologies such as gasoline–electric hybrid vehicles, which have already achieved a high level of efficiency.

For a broad application of hydrogen as a vehicle fuel, however, further R&D work needs to be done, e.g. to develop a hydrogen storage medium allowing hydrogen fueled PEM fuel cell cars to have range capabilities comparable with those of current baseline gasoline and diesel vehicles. Also, the infrastructure and logistics for distribution and supply must be established, which in turn will be strongly dependent on the demand for hydrogen in the transportation sector. Therefore, before hydrogen is broadly introduced as a fuel in the traffic sector, it may appear in niche applications characterized by special boundary conditions such as a locally high environmental benefit. The main niche markets for the commercial use of hydrogen as transportation fuel are seen in city buses, passenger car fleets and light duty vehicles. Public transportation buses may represent an ideal entry point. Heavy duty trucks may switch to other alternatives such as biofuels (Onarheim et al. 2020).

Hydrogen can be directly used as a fuel in ICEs where the hydrogen burning engine mechanically drives the vehicle. The positive features for such a hydrogen application are the low spark energy requirement, wide flammability range, high auto-ignition temperature and high flame speed. A disadvantage is the low volumetric density which limits the power output of the engine. BMW and Mazda have been the only two mainstream manufacturers to seriously pursue internal combustion hydrogen technology, with most others preferring to use it to supply a fuel cell and produce electricity. Further advancements to internal combustion hydrogen units appear to be limited in the future.

Electricity is expected to play an increasingly important role in the transport sector. PEM fuel cells can be used for on-board supply with electricity (APUs), for uninterrupted electricity supply in decentralized applications, and in light transport systems. The use of pure hydrogen with fuel cells in vehicle propulsion systems offers the benefit that it produces electricity at high efficiency without combustion and, except for water vapor, with zero emissions. It shows reliable startup and can be sized in small and large power packages.

Fuel cell technology has arrived at an advanced technological state. But a gap is apparent between the impressive success of technologies and the development of market opportunities, especially with vehicles. A major market introduction is hampered by the high costs and limited demonstration of reliability and longevity. According to today's fuel cell technology, about 60 g of platinum is necessary for a PEFC for automotive application, whose worth is more than 30% of the current engine costs. Progress is expected from a further development of the membrane electrolyte assembly with higher operation temperatures (>120 °C), more freezing tolerance, more impurity tolerance and reduced catalyst need (~0.2 mg/cm2 of Pt). Resulting from a USDOE field evaluation of fuel cell vehicle from several automobile manufacturers, an average fuel efficiency for future fuel cell car production of 60 miles (~100 km) per kg was deemed a reasonable goal. About 120 fuel cell buses under various demonstration support programmes have been or are currently being tested worldwide, along with more than 1000 prototype, concept and demonstration cars, refueled at approximately 100 refueling stations. But costs for FCVs are still far too high. The current cost of a fuel cell bus averages US$1.5 million, and passenger cars cost more than US$100000. Extrapolating the current development status of a fuel cell stack to the production of 500,000 cars per year, the USDOE reports a value of US$61 per kW and compares this value with the target of US$30 per kW for 2015.

Research is a basis for solving many of the outstanding problems, including lifetime extension to practical levels, cost reduction to acceptable levels in specialized markets, battery replacement, fuel supply and distribution, and advanced fuel conversion technologies (biomass and waste). However, with increasing pressure for higher efficiency and lower emissions, fuel cells can expect a bright future.

Fuel cell technology has also been considered in connection with a chemical processing unit for the use of widely available liquid hydrocarbons as feedstock to extract the hydrogen by on-board autothermal reforming (ATR) and operate the electric propulsion system of a vehicle (Rau et al. 2017). It appears, however, that potential users have moved away from on-board fuel processing and are concentrating instead on on-board storage of hydrogen. This tendency became obvious with the decision of the USDOE in 2004 to discontinue funding of R&D activities. The "no go" decision was based on the expectation that decisive technical criteria such as startup time (less than 1 min at 20 °C) and startup energy (less than 2 MJ for a 50 kW fuel processor) would not be met within a reasonable time frame and thus there was no economic advantage over the rapidly emerging gasoline/battery hybrid vehicles.

On-board reforming has since been concentrating on small scale fuel processors in combination with a fuel cell for 'power on demand' applications. With the increasing demand for on-board electricity from about 0.8 kW(e) in today's cars to several kW(e) in future vehicles, it is considered to provide this electricity (plus heat) by means of a fuel cell-based APU. Combined with a small fuel cell stack in the order of 5 kW(e), APUs may generate all non-propulsion power in future cars to substitute for the conventional battery. They are advantageous because of their high efficiency and low noise, vibrations, and emissions. In addition, they extend the lifetime of the main engine. If sufficiently dynamic and stable to follow all potential states of the system and if reaction by-products and other contaminants can be kept at

tolerable levels, APUs may represent the first step for fuel cells to penetrate the transportation market at a larger scale, with the prime candidates being energy consuming trucks or recreational vehicles (Doucet et al. 2009).

Today there are numerous vehicles being tested with electricity supply from PEFC based APUs to gradually substitute for conventional batteries. In cooperation with Delphi Automotive Systems, BMW is considering an SOFC based APU for their future vehicles. Its feasibility was demonstrated in 2001 with a proof-of-concept unit. BMW has already achieved some experience with low-temperature fuel cell based APUs, where among the 15 hydrogen fueled vehicles of the fifth generation, a few cars were equipped with a PEM fuel cell.

Marine transport worldwide currently contributes 14% of the global nitrogen oxide emissions and 7% of sulphur emissions. Therefore, fuel cells are also envisaged for use in marine applications if the specific maritime requirements can be fulfilled. Small demonstration projects are testing fuel cells in passenger boats and submarines. An example is the European Fuel Cell Systems for Zero Emission Ships (ZEMSHIPS) project demonstrating a 48 kW(e) fuel cell propulsion system for a ship in Hamburg. Hydrogen fueled fuel cells may be used in ships that do not need long ranges and can be filled up frequently, whereas ships that need longer ranges would need to use fuel cells based on fuels with higher energy densities, such as liquid natural gas, methanol or ethanol. In particular, the molten carbonate fuel cell (MCFC) with LNG as the fuel currently offers the largest potential as a power system for maritime applications (de-Troya et al. 2016). In the EU's MethAPU project (Validation of a Renewable Methanol Based Auxiliary Power System for Commercial Vessels), methanol fueled SOFCs in the power range of 250 kW have been investigated, including on-board testing of a 20 kW SOFC. For larger sea-going ships, fuel cell application currently would be limited to auxiliary supply of power in the 500 kW range.

A major driver for using fuel cells in ships is the possibility of reducing emissions drastically. Although, as a rule, gas applications on ships are not permitted, discussions have started on the on-board use of natural gas. The European project FCSHIP (Fuel Cell Technologies for Ships — Environmental Impacts and Costs of Hydrogen, Natural Gas and Conventional Fuels for Fuel Cell Ships) indicates possible future concepts and prepares regulations for the design and operation of fuel cell technology in the marine market.

Aviation is another energy consuming sector growing at a rate of ~5%/a that is required to reduce emissions in the future. Currently contributing a relatively low 2.6% of global CO_2 emissions, this is expected to increase to 3.2% by 2020, since synthetic hydrocarbons or hydrogen may play a significant role in the future.

Aviation fuels are characterized by special technical requirements in terms of energy density, flow characteristics (freeze, viscosity) and thermal stability at higher temperatures (carbon deposition). Alternative products to kerosene, at present the standard aviation fuel, have started either to be blended with or to even substitute for the kerosene. The mixture of traditional Jet A-1 fuel with GTL fuel is in the testing phase. The first commercial flight with a 1:1 mixture was in 2008. A first flight test with a 1:1 mixture of Jet-1 and BTL fuel took place in 2009. In this regard, hydrogen

may play a role in the long term. Another role that H2 may play in aviation is as a fuel in PEFCs or SOFCs for ground or on-board power supply. The water at a high quality resulting from fuel cell operation could be further used on-board. The preferred storage options are liquid hydrogen for short range missions and JET A-1/ BTL reforming for long range missions. Further development here needs to concentrate on extreme reliability and availability.

The direct use of liquid hydrogen as a substitute for kerosene in an airplane propulsion system was investigated in the CRYOPLANE project. This project was launched in 1990 by a joint German–Russian consortium (DASA as the lead, with the main partners being MBB, MTU, Tupulev and Kuznetsov), and later continued as an EU activity with 35 partners from 11 countries and coordinated by EADS Airbus GmbH. Its objective was to study the feasibility of an aircraft propelled by cryogenic fuels. The aim was to find out whether the use of liquefied natural gas (mainly on the Russian side) or liquid hydrogen (on both sides) as an aircraft fuel was technically possible and reasonable in terms of ecology and economy. Topics covered by the project were scenarios for the transition to an alternative aviation fuel, infrastructure, aircraft design, fuel system layout, engine modifications and ecological issues (e.g. water vapor and NOx emissions). The transition of short/medium range aircraft serving routes between leading industrial nations was seen as an introduction phase, followed by the development of the appropriate infrastructure and the operation of a demonstrator airplane (Hoelzen et al. 2022).

An Airbus A310–300 was selected as the baseline aircraft to be converted to LH2 propulsion. For the new fuel tank concept, the most favorable design was seen in the top-mounted tank configuration with four tanks, two active ones with 40 m3 each for either engine, and two passive ones with 80 m3 each to refill the active tanks. Total fuel weight for the Airbus cryoplane was estimated to be 15.6 t of LH2 (compared with 27 t of kerosene for the same flight range). Due to the environmental impact on the stratosphere from the formation of long-lived ice cloud condensation trails, the typical cruising height of ~12 km would be lowered to ~10 km. The cruising range of the cryoplane was estimated to be 2700 nautical miles (5000 km). At a later stage in the project, a smaller airplane was chosen to precede the Airbus as the LH2 demonstrator — a 30 passenger Fairchild-Dornier 328 regional airplane with one of the two engines to be converted to hydrogen fuel. The fuel capacity is 420 kg (6 m3) of LH2 stored in two cylindrical tanks underneath the wings (plus 1150 kg of kerosene for the second engine). The advantages of this intermediate step are the availability of the hydrogen engine, the lower investment in infrastructure and the earlier introduction of a series aircraft.

A technological development programme for the fuel system components began in 1993, including the selection of materials for tanks and piping, control system and sensors for hydrogen leak detection, fuel pumps, LH2 gasifier and combustion chamber. The first generation of LH2 aviation was foreseen to require a fleet of 400–500 airplanes and the modification of ~70 European airports. The fuel consumption was assessed to be about two million t/a of LH2 or ~170 t/d for an average size airport.

6   Stationary Applications

Stationary applications refer to decentralized power generation by fuel cells, combustion engines or gas turbines, including residential (1–10 kW) and community (5–50 kW) applications, public and commercial buildings, and industrial (50–500 kW) and large scale (1 MW and above) applications (Felseghi et al. 2019). Moreover:

– Large cogeneration (combined heat and power) systems are being manufactured for large commercial buildings or industrial sites that require significant amounts of electricity, water heating, space heating and/or process heat. Fuel cells combined with a heat recovery system can meet some or all of these needs, as well as providing a source of purified water.
– Uninterruptible power supply systems, in which fuel cells are used as backup power supplies if the primary power system fails, are one of the fastest growth areas for stationary fuel cell technologies.
– Niche and power premium applications such as uninterruptible power supply and other backup systems which require short or even instantaneous response, load flexibility, high degree of safety, reliability and availability.

For applications in power and in CHP production, fuel cells have to compete with technologies that have already been established, such as gas and steam turbine plants. Fuel cells promise higher efficiencies at comparable unit sizes. They offer the chance to reduce the pollution level in urban areas with high population density. Fuel cells also allow for small CHP units for residential use. Many fuel cell power units may be combined to large virtual power plants. In connection with energy storage, the hydrogen and fuel cell system may compensate for the mismatch between renewable energy sources and energy demand.

The general design of a fuel cell power system forms an assembly of integrated systems including:

– Fuel cell module — assembly of one or more fuel cell stacks and electrical connections;
– Fuel cell stack — assembly of cells, separators, cooling plates, manifolds and supporting structure;
– Fuel and oxidant processing system — to prepare the fuel for utilization by means of catalytic or chemical processing equipment;
– Thermal management system — to provide cooling and heat rejection, and recovery of excess heat, and to assist in heating the power train during startup;
– Water treatment system — to treat and purify recovered or added water;
– Power conditioning system — to adapt the produced electrical energy to the manufacturer's requirements;
– Automatic control system — to maintain the system parameters within the specified limits by means of an assembly of sensors, actuators, valves, switches and logic components;
– Ventilation system — to provide air.

Unlike the use of hydrogen in mobile applications, stationary power applications with hydrogen or natural gas or coal derived gas as a fuel have advanced and have reached market penetration status already. A near term area of demand for H2 fuel cells includes backup power units, power for remote locations, and distributed generation for hospitals, industrial buildings and small towns (Oldenbroek et al. 2017).

Stationary fuel cell power systems are currently being tested in field experiments in several countries (e.g. Germany and Norway) to show the feasibility of a combined electrical power and heat supply for households utilizing, for example, PEM fuel cells or SOFCs. They are already commercially viable in remote areas, where they can be installed independent of the grid and where fossil fuel transportation costs are prohibitive. By 2008, the cumulative power capacity had reached 180 MW (e), with an average of 50 units per year installed and an average size of 1 MW. The potential flexibility of SOFCs is what is especially is important for a future strategy of decentralized electrical power supply, as this will help stabilize the demand of electrical power.

The energy used for small scale combustion installations is mainly used for the heating of buildings (residential and corporate), hot water and boilers for small industrial applications, including agriculture. A significant amount of this heat could be replaced with hydrogen or electricity. Both could be provided by nuclear power.

Different types of fuel cell systems are currently being demonstrated and introduced commercially in sizes ranging from a few kW up to MW sizes, often as small, standalone cogeneration systems combining local production of electricity with the use of waste heat for producing hot water and residential heating. For example, 1.2 kW PEM fuel cells are currently being introduced in Japan in limited volume by Ballard Power Systems, and the company Vaillant is currently installing a number of PEM fuel cells in Europe. SOFCs can also be made available for small scale CHP in the future.

For large generators today's fuel cell systems do not offer higher electrical efficiencies than other technologies that are already on the market such as gas turbines. At the utility scale, hybrid systems integrating fuel cell systems and gas turbines could bring about systems using natural gas with electric efficiencies greater than 65%, and such systems are expected to become cost competitive with competing generating technologies within the next decades. By comparison, current state of the art power plants using combined-cycle technology combining gas turbines and steam turbines have electrical efficiencies of around 55–60% and are currently less expensive (400–500 €/kW) than fuel cell systems (2500–8000 €/kW).

Technologies available for distributed power generation, with electrical capacities of less than 60 MW, include gas turbines, reciprocating engines, microturbines, wind turbines, biomass based generators, solar photovoltaic systems and fuel cells. Some studies foresee that fuel cells might initially emerge as distributed generators in applications where users are willing to pay an extra margin for reliable energy generators. In the USA, 10.7 million distributed generators are in place, of which 99% are small emergency/standby reciprocating engines that are not connected to

the grid. The market for distributed generation is typically in the commercial sector in applications where reliable energy is needed or in remote locations where grid power is not available.

The oxy-hydrogen steam cycle represents the direct production of high pressure, high temperature (~1500 °C) steam and is applicable for peak electricity production. It is a system with low capital cost promising a high efficiency of ~70%.

In a cooperative effort between the DLR (today the Deutsches Zentrum für Luft- und Raumfahrt) and other German companies from 1989 to 1993, the concept of a hydrogen and oxygen fueled steam generator was developed. This component is actually the re-configuration of an H2/O2 rocket engine which allows the instantaneous provision of steam of any desired quality. H2 and O2 are compressed and injected into a combustion chamber.

A stoichiometric mixture is necessary to generate superheated steam of high quality without any side products. The combustion gas with a temperature of 3000 °C can be cooled by adding water to achieve exactly the desired steam condition for injection into the power plant process. The startup time of such a steam generator is in the order of 1–2 s with a combustion efficiency of greater than 99%. The steam generator can act as a backup system for fast power-up of steam generation plants to serve as a cold standby spinning reserve in decentralized power production.

In a first experimental series, a total of 285 combustion tests were conducted in 1991–1992 with a prototype operated in the power output range of between 25 and 70 MW. The second step was the construction of the demonstration facility for H2/O2 instant reserve, HYDROSS, consisting of a modified H2/O2 steam generator of 2 m length and 0.4 m outer diameter plus a storage and supply system. Full power was obtained after 1 s, and after 3–5 s, there was stable steam production. The experimental version produced steam of 560–950 °C at 4–9 MPa. This compact, soot free and low-cost component is largely ready for the market.

7 Potential Industrial Uses of Hydrogen

Hydrogen use today is dominated by industrial applications. The top four single uses of hydrogen today (in both pure and mixed forms) are: oil refining (33%), ammonia production (27%), methanol production (11%) and steel production via the direct reduction of iron ore (3%).

Virtually all of this hydrogen is supplied using fossil fuels. These existing uses of hydrogen underpin many aspects of the global economy and our daily lives. Their future growth depends on the evolution of demand for downstream products, notably refined fuels for transport, fertilizers for food production, and construction materials for buildings.

More than 60% of hydrogen used in refineries today is produced using natural gas. Tougher air pollutant standards could increase the use of hydrogen in refining by 7% to 41 MtH2/yr by 2030, although further policy changes to curb increases in

oil demand could dampen the pace of growth. Current global refining capacity is generally thought sufficient to meet rising oil demand, which implies that the majority of future hydrogen demand is likely to arise from existing facilities already equipped with hydrogen production units. This suggests an opportunity for retrofitting CCUS as a suitable option to reduce related emissions.

Demand for ammonia and methanol is expected to increase over the short to medium term, with new capacity additions offering an important opportunity to scale up low-emissions hydrogen pathways. Greater efficiency can reduce overall levels of demand, but this will only partially offset demand growth. Whether via natural gas with CCUS or electrolysis, the technology is available to provide the additional hydrogen demand growth projected for ammonia and methanol (up 14 MtH2/yr by 2030) in a low-carbon manner. As a priority, substituting low-emissions pathways for any further coal-based production without CCUS would significantly help cut emissions.

In the longer term, steel and high-temperature heat production offer vast potential for low-emissions hydrogen demand growth. If the technological challenges that currently inhibit the widespread adoption of hydrogen in these areas can be overcome, the key challenges will be reducing costs and scaling up. In the long term it should be technically possible to produce all primary steel with hydrogen, but this would require vast amounts of low-carbon electricity (around 2500 TWh/yr, or around 10% of global electricity generation today) and would only be economic without policy support at very low electricity prices.

7.1   Hydrogen in Oil Refining

Oil refining – turning crude oil into various end-user products such as transport fuels and petrochemical feedstock – is one of the largest users of hydrogen today. Some 38 MtH2/yr, or 33% of the total global demand for hydrogen (in both pure and mixed forms), is consumed by refineries as feedstock, reagent, and energy source. Around two-thirds of this hydrogen is produced in dedicated facilities at refineries or acquired from merchant suppliers (together called "on-purpose" supply). Hydrogen use is responsible for around 20% of total refinery emissions, and produces around 230 MtCO2/yr. Refineries' existing large-scale demand for hydrogen is set to grow as regulations for sulphur content of oil products tighten. This provides a potential early market for hydrogen from cleaner pathways, which could lower the emissions intensity of transport fuels (Abdin et al. 2020).

Hydrotreatment and hydrocracking are the main hydrogen-consuming processes in the refinery. Hydrotreatment is used to remove impurities, especially sulphur (it is often simply referred to as desulphurisation) and accounts for a large share of refinery hydrogen use globally. Today refineries remove around 70% of naturally incurring sulphur from crude oils.
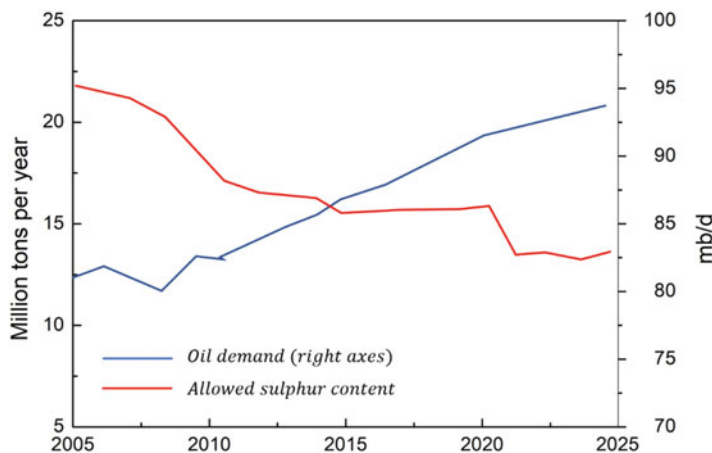
Fig. 8 Allowed sulphur content in oil products

With concerns about air quality increasing, there is growing regulatory pressure to further lower the sulphur content in final products. By 2020 40% less sulphur will be allowed in refined products than in 2005 despite the continued growth in demand (Fig. 8).

Hydrocracking is a process that uses hydrogen to upgrade heavy residual oils into higher-value oil products. Demand for light and middle distillate products is growing and demand for heavy residual oil is declining, leading to an increase in the use of hydrocracking. In addition to hydrotreatment and hydrocracking, some hydrogen that is used or produced by refineries cannot be economically recovered and is burned as fuel as part of a mixture of waste gases (Felix et al. 2017).

The United States, the People's Republic of China ("China") and Europe are the largest consumers of hydrogen in refineries. The three regions represent around half of total refinery hydrogen consumption, reflecting the volume of crude oil they process and the stringency of their product quality standards.

Hydrogen is also used for upgrading oil sands and hydrotreating biofuels. For oil sands, the amount of hydrogen needed to remove sulphur from the raw bitumen varies considerably depending on the upgrading technology and the quality of the synthetic crude oil produced.

Overall around 10 kg of hydrogen is used per tonne of bitumen processed.24 The resulting synthetic crude oil still needs to be refined at a refinery, using hydrogen. For biofuels, hydrotreatment removes oxygen and improves the fuel quality of vegetable oils and animal fats processed into diesel substitutes. This process requires around 38 kg of hydrogen per tonne of biodiesel produced, but no further hydrogen is needed in subsequent refining steps.

Globally, refinery hydrogen demand is met through the use of on-site by-products, dedicated on-site production, or merchant supply.

On-site by-product hydrogen comes largely from catalytic naphtha reforming, a process that produces high-octane gasoline blending components and generates

hydrogen at the same time. Refineries with integrated petrochemical operations also derive by-product hydrogen from steam cracking. However, on-site by-product hydrogen is unable to fully cover refinery hydrogen demand, except in small refineries running on very low sulphur crude oils and with relatively low yields of road transport fuels. On average, on-site by-product hydrogen meets one-third of refinery hydrogen demand. The gap needs to be met, either by dedicated on-site production (about 40% globally) or procurement from merchant suppliers (around a quarter).

Most dedicated on-site production uses natural gas feedstock, but light fractions of oil distillation and heavier feedstocks – petroleum coke, vacuum residues and coal – are also used in some regions. Use of heavier feedstocks is mostly restricted to India and China, where gas needs to be imported. Coal gasification is routinely included in new refinery setups in China as a main or auxiliary hydrogen production unit.

Merchant supply of hydrogen is an option in densely industrialised areas where developed hydrogen pipeline infrastructure exists, such as the US Gulf Coast and Europe's Amsterdam-Rotterdam-Antwerp hub. As with dedicated on-site production, merchant hydrogen is mostlyproduced from natural gas, although a certain amount also comes from chemical processes, where it is a by-product of operations such as steam cracking and chlorine production. In regions such as the US Gulf Coast, merchant hydrogen can meet over a third of total hydrogen demand.

Hydrogen production costs vary widely, largely reflecting differences in natural gas prices. US production costs are among the world's lowest, while costs are substantially higher in Europe and Asia. In the United States, hydrogen costs amount to around USD 1.1/kgH2 or USD 0.7 per barrel of oil refined. This may seem a relatively small cost component for refineries overall, for example in comparison with crude costs, but even a small cost advantage in hydrogen costs can have a notable impact on refining margins, which are generally thin in what is a very competitive market.

In recent decades, refinery hydrogen demand has grown substantially as a result of growing refining activity and rising requirements for hydrotreating and hydrocracking. This trend is set to continue as fuel specifications globally further reduce acceptable levels of sulphur content.

Many countries, including China, have already reduced sulphur content requirements in road transport fuels such as gasoline or diesel to under 0.0015%, and others may introduce similar standards. The International Maritime Organization has also introduced new bunker fuel regulations that limit the sulphur content of marine fuels to no more than 0.5% from 2020, and this is likely to lead to a significant increase in hydrogen requirements for marine fuel production. However, hydrogen demand is also a function of inherent sulphur content in crude oils. The average quality of crude oil supply has been getting lighter and sweeter in recent years, due primarily to surging US tight oil output, and this is likely to moderate the need for hydrogen to some degree. Under current trends, overall hydrogen demand in refineries is set to grow by 7% to 41 MtH2/yr in 2030.

Beyond 2030 current trends and policies suggest the pace of hydrogen demand growth to slow down, as the scope to tighten product quality standards decreases and as oil demand for transport fuels is affected by a combination of efficiency improvements and electrification (Gjorgievski et al. 2021).

Refiners are also likely to increase the efficiency of hydrogen recovery from waste refinery gases, lowering requirements for additional hydrogen production. Refinery hydrogen demand would decline in a scenario compatible with the objectives of the Paris Agreement, with the impact of declining oil demand more than offsetting that of higher hydrogen intensity.

Irrespective of the future trajectory of global energy demand, one common aspect is the dominant share of existing refineries in projected hydrogen demand. There is already sufficient refining capacity globally to fulfil the expected need for oil products. Together with the long lifetime of refineries, this limits the scope for substantial addition of new refining capacity. As a result, some 80–90% of cumulative on-purpose hydrogen supply (including both dedicated on-site production and merchant procurement) between today and 2030 would come from existing refineries in both scenarios (Fig. 9).

Hydrogen production – unless supplied as a by-product of refining operations – currently results in considerable CO_2 emissions. Globally the production of hydrogen for use in refineries contributes some 230 MtCO2/yr emissions, which is around 20% of total refinery emissions.

Demand and emissions are all set to rise in future. If future demand growth is met using coal, which is widely used without CCUS to produce hydrogen in countries such as China, the level of CO_2 emissions would further increase.

Producing hydrogen in a cleaner way is therefore vital to achieving a significant reduction in emissions from refining operations. Other key measures – such as energy efficiency and fuel switching away from emission-intensive fuels – have already been widely adopted in many refineries, limiting opportunities for further emissions reduction. Against this background, together with sizeable demand already existing today, the refining industry offers a potential early market for low-carbon hydrogen.

There are two main cleaner pathways to hydrogen production for refineries: equipping coal- or natural gas-based hydrogen production facilities with CCUS; and using electrolytic hydrogen from low-carbon electricity. Given that the bulk of future hydrogen demand comes from existing refineries and that most refineries are already equipped with SMR units, natural gas with CCUS offers a more obvious route to low-carbon hydrogen than does renewables-based electrolysis. The incremental costs for the production of low-carbon hydrogen are limited to CCUS facilities, which makes natural gas with CCUS more competitive than electricity-based options, and capturing CO_2 emissions from an SMR unit represents one of the lowest-cost opportunities to apply CCUS in a refinery because much of this CO_2 is emitted in a highly concentrated stream.

However, despite the continued decline of technology costs for CCUS, the large-scale adoption of CCUS at hydrogen production units in refineries needs a helping hand from policy makers, especially given the tight margins and highly competitive

Fig. 9 Future hydrogen
demand in oil refining under
two different pathways
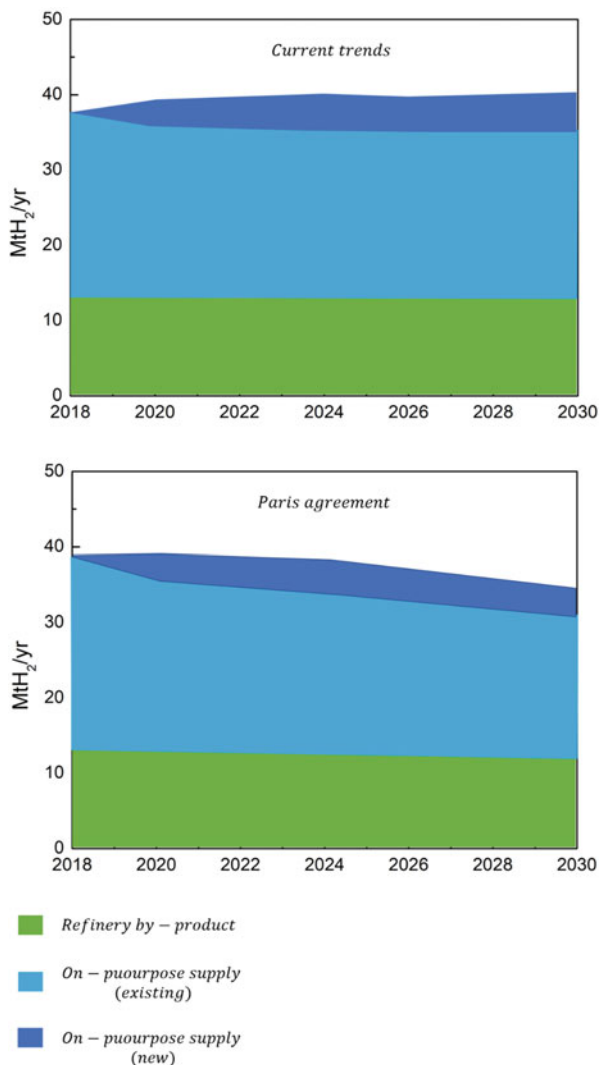
nature of the refining industry. Introducing CCUS would add an incremental cost of
some USD 0.25–0.5/barrel, which is higher than today's carbon price levels (zero to
USD 0.1/barrel).25 This implies that refiners are likely to be inclined to pay CO_2
prices rather than to direct effort to capturing and storing CO_2. Higher carbon prices,
or equivalent policy incentives, would change the picture.

A carbon price higher than USD 50/tCO_2, for example, would make natural gas
with CCUS economically attractive in most regions and could trigger a wider
deployment of CCUS at SMR facilities (Fig. 10).

In the United States a tax incentive known as "45Q" is worth up to USD 50/tCO_2
for CCUS operations online by 2026. The case for investment would be further

Fig. 10 Hydrogen production costs from natural gas with and without CCUS by region under different carbon prices, 2030
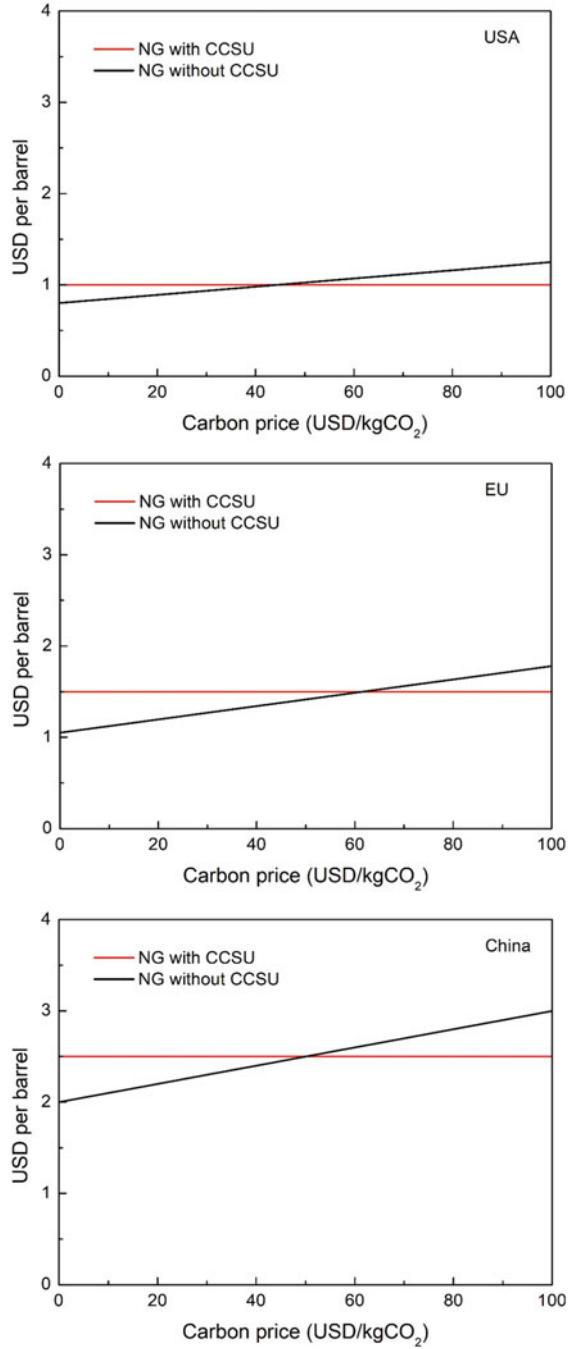
strengthened if captured CO_2 could be sold to industrial users or upstream oil companies for enhanced oil recovery (EOR). Low-carbon fuel standards could also help spur CCUS: standards of this kind have already been introduced in Canada, Europe and some US states, including California.

The costs of introducing CCUS also depend on the costs of CO_2 storage, which means that the successful introduction of CCUS is contingent on CO_2 storage being available and accessible with known and manageable costs and risks. Cost reduction efforts therefore need to be complemented by policy measures to bring about the building of CO_2 storage infrastructure and the development of operating businesses in the appropriate locations. This would also have the benefit of laying the ground for the adoption of CCUS in other industries (Goel et al. 2018).

Several refineries have already installed CCUS facilities for hydrogen production. Some of the emissions from the 400 thousand barrels per day (kb/d) Pernis refinery in Rotterdam are captured, transported and used in nearby greenhouses. In 2017 Air Product's Port Arthur project in Texas completed its demonstration phase; it captures CO_2 for EOR operations at the West.

Hastings oil field. In France, Air Liquide's Port Jerome project captures and sells CO_2, and Hokkaido Refinery in Japan has put in place pilot CCUS facilities. There is also one bitumen upgrader equipped with CCUS in operation today – the Quest project in Canada – which captures around 20% of the emissions from the 255 kb/d upgrader. In total, the four CCUS plants which are now in operation in refineries have the capacity to produce over 150 ktH2/yr of low-carbon hydrogen.

Potential also exists at refineries for electrolytic hydrogen to replace dedicated hydrogen production from natural gas or coal. For the moment no refineries are using electrolytic hydrogen, but Shell's 200 kb/d Rheinland refinery in Germany has announced a 10 MW electrolyzer project for 2020 that will supply around 1 ktH2, or 1% of the refinery's hydrogen needs. Heide, a small refinery near Hamburg, Germany, has announced a 30 MW electrolyzer paired with offshore wind power to replace purchases of up to 3 ktH2/yr. BP, Nouryon and the Port of Rotterdam Authority are also jointly assessing the feasibility of a 250 MW electrolysis plant for the production of 45 ktH2/yr for the BP refinery in Rotterdam. Despite this progress, policy support is going to be needed if electrolysis is to take off at scale.

In certain instances, there is also scope to avoid some current hydrogen-related emissions through "outside-gate collaboration". Petrochemical steam crackers tend to generate a surplus of hydrogen that could be used in refineries; conversely, the low-value fuel gases produced by refineries can be used in steam crackers. Incentivizing the development of the necessary infrastructure to exchange these products within industrial clusters would help to reduce overall emissions.

7.2   Chemical Sector

The chemical sector accounts for the second- and third-largest sources of demand for hydrogen today: ammonia at 31 MtH2/yr and methanol at 12 MtH2/yr. Other

comparatively minor applications take its overall demand to 46 MtH2/yr, or 40% of total hydrogen demand in both pure and mixed forms. It is also a large producer of by-product hydrogen, which is both consumed within the sector itself and distributed for use elsewhere. Most of the hydrogen that the chemical sector consumes is produced using fossil fuels, and this generates considerable quantities of greenhouse gas emissions. Reducing the level of emissions represents an important challenge for the sustainability of the sector's energy use, and a significant opportunity to make use of low-carbon hydrogen (Rambhujun et al. 2020).

The chemical sector produces a complex array of outputs, from plastics and fertilizers to solvents and explosives. This section focuses primarily on ammonia and methanol, and to a lesser extent on ethylene, propylene, benzene, toluene and mixed xylenes. These seven "primary chemicals" account for around two-thirds of the chemical sector's energy consumption, and much of its demand for energy products as raw material inputs (so-called "feedstocks").

Hydrogen is part of the molecular structure of almost all industrial chemicals, but only some primary chemicals require large quantities of dedicated hydrogen production for use as feedstock, notably ammonia and methanol.

More than 31 MtH2/yr of hydrogen are used as feedstock to produce ammonia, and more than 12 MtH2/yr to produce methanol. A further 2 MtH2/yr are consumed in comparatively small-volume processes (for example in hydrogen peroxide and cyclohexane production), but most of this is supplied from by-product hydrogen generated within the sector.

Fossil fuels have long been a convenient and cost-effective source of both the hydrogen and carbon for ammonia and methanol production. In 2018 around 270 Mtoe/yr of fossil fuels were used to produce the hydrogen for these two products, 27 roughly equivalent to the combined oil demand of Brazil and the Russian Federation. Because production via natural gas (reforming) is more efficient than via coal (gasification), the former accounts for 65% of hydrogen production, but less than 55% of the energy inputs required to produce it. The differing regional prices of gas and coal are also a key determining factor in the choice of process route. Almost all hydrogen from coal for use in the chemical sector is produced and used in China.

Ammonia is mostly used in the manufacture of fertilizers such as urea and ammonium nitrate (around 80%). The remainder is used for industrial applications such as explosives, synthetic fibers and other specialty materials, which are an increasingly important source of demand.

Methanol is used for a diverse range of industrial applications, including the manufacture of formaldehyde, methyl methacrylate and various solvents. Methanol is also used in the production of several other industrial chemicals, and for the methanol-to-gasoline process that produces gasoline from both natural gas and coal, which has proven attractive in regions with abundant coal or gas reserves but with little or no domestic oil production. This is one of the fuel applications of methanol, whether blended in pure form or used after further conversion (e.g. to methyl-tert butlyl ether), that account for around a third of the chemical's use globally.

The development of methanol-to-olefins and methanol-to-aromatics technology has opened up an indirect route from methanol to high-value chemicals (HVCs), and thus to plastics. Methanol-to-olefins technology is currently deployed at commercial scale in China, accounting for nine million tons per year (Mt/yr) or 18% of domestic HVC production in 2018. Methanol-to-aromatics, which is used to produce more complex HVC molecules, is currently still in the demonstration phase.

Unlike ammonia and methanol, HVCs – the precursors of most plastics – are produced mostly from oil products such as ethane, liquefied petroleum gas and naphtha. HVCs produced directly from oil products do not require hydrogen feedstock, but their production generates by-product hydrogen that can be used in oil refining and other chemical sector operations, such as the upgrading of other cracker by-products. Steam cracking and propane dehydrogenation processes for HVC manufacture produce around 18 MtH2/yr as a by-product globally. HVC demand is growing at a faster rate than refined oil product demand, which means that an increasing quantity of this by-product hydrogen could be available for use in other industries.

Chlor-alkali processes are another source of by-product hydrogen in the chemical sector, supplying around 2 MtH2/yr. While by-product hydrogen generated in the steam cracking process stems from oil products (mainly ethane and naphtha), the chlor-alkali process is a form of electrolysis (of brine) and is powered by electricity. Smaller volumes of by-product hydrogen are also produced from other processes such as styrene production.

Demand for hydrogen for primary chemical production is set to increase from 44 Mt/yr today to 57 Mt/yr by 2030 as demand for ammonia and methanol grows.

Demand for ammonia for existing applications is set to increase by 1.7% per year between 2018 and 2030 and to continue to rise thereafter. The share represented by demand for industrial applications grows more quickly during this period; that for nitrogen-based fertilizers is likely to start to plateau or even decline in many regions after 2030.

Demand for methanol for existing applications is set to grow at 3.6% per year between 2018 and 2030. The methanol-to-olefins/methanol-to-aromatics demand segment grows more quickly than the total, at 4.1% per year over the same period, with nearly all this growth coming from China. This rate of growth would require 19 MtH2/yr for methanol production for these existing applications by 2030, compared with 12 MtH2/yr today.

Together with energy efficiency measures, materials efficiency strategies are an important way of reducing emissions in IEA decarbonization scenarios and could reduce these increases in demand. Recycling and reusing plastics and other materials could reduce the amount of future primary chemical production required, although this would be likely to have a less pronounced impact on ammonia and methanol demand than on demand for other primary chemicals such as ethylene. Improving the efficiency with which fertilizer is used could also reduce future demand for chemicals. Specific policies have been announced in some countries to limit fertilizer use, such as the target for zero growth from current levels in China.

Conversely, demand for ammonia and methanol could rise further if these chemicals were to become established as energy carriers for the transmission, distribution and storage of hydrogen, facilitating its use in new applications, or if they were to be used as fuels in their own right. If these new applications were to become widespread, the chemical sector could evolve to share the role that refineries play today in providing energy to downstream users.

Without any change in the current economics or regulation of production, current growth trajectories for chemical products are likely to lead to a growth in hydrogen production from natural gas and coal without the application of CCUS. Projecting forward current trends, this growth would cause total direct CO_2 emissions from ammonia and methanol production to rise by around 20% between 2018 and 2030.

The global production of ammonia and methanol currently generates CO_2 emissions of around 630 $MtCO_2$/yr. The global average direct emissions intensity of ammonia production is 2.4 tons of CO_2 per ton (tCO_2/t), with average intensities for major regions in the range of 1.6–2.7 tCO_2/t. New gas-based plants in the Asia Pacific region tend to be at the lower end of this range, whereas pure coal-based production (around 4 tCO_2/t), widespread in China, constitutes the most CO_2-intensive production route. For methanol the global average figure is 2.3 tCO_2/t, with average intensities for major regions in the range of 0.8–3.1 tCO_2/t. As for ammonia, production based purely on coal is the most emissions-intensive pathway.

The production of HVCs is responsible for a further 250 $MtCO_2$/yr of CO_2 emissions. However, the key mitigation options currently under development (including the direct application of CCUS to existing process units, dry methane reforming and steam cracker electrification) do not involve additional dedicated hydrogen production. HVCs could also be produced from methanol, but this would similarly not involve additional hydrogen production beyond that required for the methanol. The focus in this section is therefore on ammonia and methanol.

Alternative process technologies and feedstocks could meet growing demand for large quantities of dedicated hydrogen feedstock in the chemical sector for ammonia and methanol while reducing CO_2 emissions. The three main cleaner process technology options are: using CCUS to reduce fossil fuel-related emissions (assuming sufficient CO_2 transport and storage infrastructure is in place); using electrolysis-derived hydrogen (assuming a renewable electricity supply); and using biomass feedstocks (assuming a sustainable supply of bioenergy). Today all these options are more costly than using fossil fuels without CCUS.

Using biomass for ammonia and methanol production looks significantly less cost-competitive than the other options.

Meeting future ammonia and methanol demand entirely from these cleaner pathways would considerably increase demand for energy inputs to the chemical sector (Fig. 11).

If future demand in a Paris-compatible pathway were to be met entirely with hydrogen produced from natural gas with CCUS, around 320 bcm of natural gas would be required by 2030, nearly half of which would be used as feedstock. This is around 10% of global natural gas demand today.
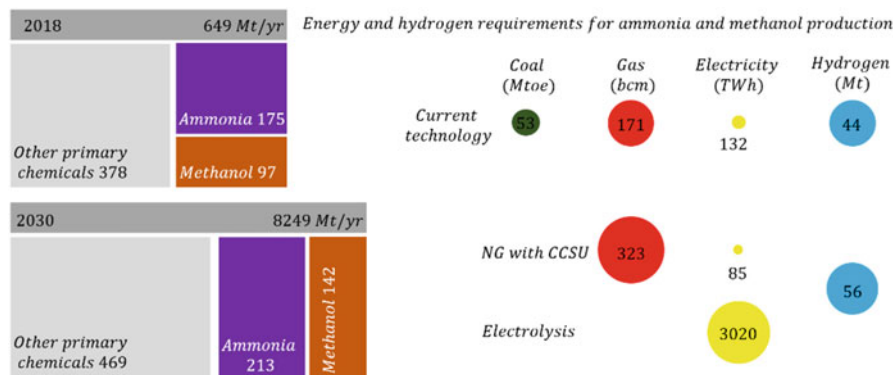
Fig. 11 The implications of cleaner process routes for methanol and ammonia production

Around 450 MtCO$_2$/yr would need to be captured, although around one-third of this could be used to produce urea. The largest carbon capture installations today are in the region of 1 MtCO$_2$/yr. Capturing 450 MtCO$_2$/yr by 2030 would require around 450 new projects of this size to be operational by this date, with a build rate of around 4 new projects per month between now and 2030.

If future demand were to be met entirely from low-carbon electrolytic hydrogen, this would require around 3020 terawatt hours per year (TWh/yr) of additional electricity by 2030, equivalent to around 11% of today's global electricity generation. It would also require 350–450 GW of electrolyzer capacity, depending on efficiency levels and capacity factors. The largest individual electrolyzers currently under development are at the 100+ MW scale, meaning that 3500–4000 such installations would need to be constructed by 2030, or 6–7 per week between 2018 and 2030. Around 0.6 billion cubic meters per year (bcm/yr) of water would also be needed as feedstock for the electrolyzers, which is around 1% of total water consumption in the energy sector today. Some 0.5 gigatons per year (Gt/yr) of oxygen would be produced as a by-product, which could be used in other industrial processes.

The electrolysis pathway would use some CO$_2$ for the manufacture of urea (CH4N2O) and methanol (CH3OH).30 To avoid fossil fuel use in methanol synthesis altogether in 2030, 200 MtCO2/yr (or the equivalent amount of carbon monoxide, if available) would need to be sourced and captured from biogenic (e.g. biomass gasification) or atmospheric (e.g. direct air capture) sources. A further 170 MtCO2/yr or equivalent would be required for urea.

In the absence of an economic source of biogenic or atmospheric CO$_2$, it would still be beneficial to capture and utilize CO$_2$ streams from unabated stationary point sources of CO$_2$ (e.g. steel and cement production). These are likely to remain much cheaper in the short to medium term. However, the total emissions avoided would be much lower unless that CO$_2$ would otherwise unavoidably have been emitted. Geographically matching locations of low-cost renewable electricity, water availability and persistent CO$_2$ sources that are not prohibitively expensive presents a significant challenge.

Cleaner ways of producing ammonia and methanol have higher costs than those that are commercially available today. Production costs vary widely, however, between regions, depending on the costs of in each region of natural gas, coal, biomass and electricity.

In locations with the lowest cost renewable electricity (for example in Chile, Morocco and China), electrolytic hydrogen would be close to being competitive in cost terms with natural gas and coal for ammonia and methanol production, even if they did not use CCUS.

Transporting renewable electricity to the main demand centers is another option, but would also involve additional costs.

Much of the technology and equipment required for the cleaner pathways in the chemical sector is already in widespread use across the industry, including the pumps, compressors and separation units required for CO_2 capture. Electrolyzers have been constructed at scales above 100 MW in the past, and significant efforts are being made to bring down their costs further. The key variables affecting the economics of production via electrolysis and natural gas with CCUS are natural gas and electricity prices.

Electrolysis becomes competitive with natural gas with CCUS at electricity prices in the range of USD 15–50/MWh for ammonia and in the range of USD 10–65/MWh for methanol, on the assumption of gas prices of USD 3–10/MBtu.31 In order to compete with natural gas without CCUS at these gas prices, however, electricity prices would need to drop to USD 10–40/MWh for ammonia and USD 5–50/MWh for methanol.

While the upper end of these cost-competitive electricity price ranges show promise for alternative pathways, the economics in most regions are such that policy support is likely to be required in the short to medium term if low-carbon forms of production are to take off. Policy measures could stimulate demand for low-carbon hydrogen in the chemical sector and thus stimulate investment in a cleaner supply of hydrogen. These measures could include the use of certificates, public procurement, or portfolio standards to create market value for chemicals produced via low-carbon process routes. In the case of methanol produced as a fuel or fuel additive, this could include the use of fuel specifications or fuel standards. Governments could also use standards to support ammonia produced with lower CO_2 intensity. In the near term, initial projects that take on value chain and market risks to invest in CCUS or electrolysis hydrogen for chemical production are likely to need some direct government support. The support should be aimed at managing these risks and extending the benefits of cost sharing to other facilities in industrial clusters.

7.3   Iron and Steel Sector

DRI is a method for producing steel from iron ore. This process constitutes the fourth-largest single source of hydrogen demand today (4 MtH2/yr, or around 3% of total hydrogen used in both pure and mixed forms), after oil refining, ammonia and
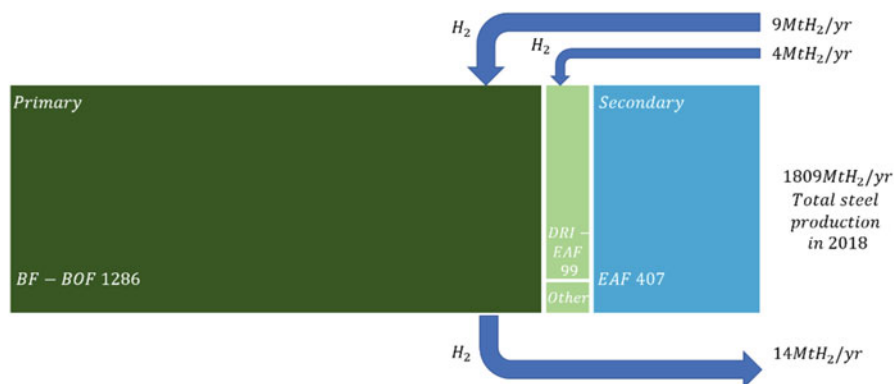
Fig. 12 Hydrogen consumption and production in the iron and steel sector today

methanol. Based on current trends, global steel demand is set to increase by around 6% by 2030, with demand for infrastructure and a growing population in developing regions compensating for declines elsewhere.

Like the chemical sector, the iron and steel sector produce a large quantity of hydrogen mixed with other gases as a by-product (e.g. coke oven gas), some of which is consumed within the sector and some of which is distributed for use elsewhere. Virtually all this hydrogen is generated from coal and other fossil fuels. To reduce emissions, efforts are underway to test steel production using hydrogen as the key reduction agent (as opposed to carbon monoxide derived from fossil fuels), with the first commercial-scale designs expected in the 2030s. In the meantime, low-carbon hydrogen could be blended into existing processes that are currently based on natural gas and coal to lower their overall CO_2 intensity.

More than three-quarters of global steel demand today is met using primary production methods that convert iron ore to steel, as opposed to the secondary production route, which utilizes limited supplies of recycled scrap steel (Fig. 12).

The two main primary production routes already involve some production and consumption of hydrogen (Cavaliere 2019).

The blast furnace-basic oxygen furnace (BF-BOF) route accounts for about 90% of primary steel production globally. It produces hydrogen as a by-product of coal use. This hydrogen, contained in so-called "works-arising gases" (WAG), is produced in a mixture with other gases such as carbon monoxide.33 WAG is used for various purposes on site, but also transferred for use in other sectors including power generation and, in China, methanol production. The portion utilized within the iron and steel sector is estimated at 9 MtH2/yr today, or around 20% of the global use of hydrogen in mixed forms (i.e. not as pure hydrogen).

The direct reduction of iron-electric arc furnace (DRI-EAF) route accounts for 7% of primary steel production globally. It uses a mixture of hydrogen and carbon monoxide as a reducing agent. The hydrogen is produced in dedicated facilities, not

as a by-product. Around three-quarters of it is produced using natural gas (reforming) and the rest using coal (gasification). It accounts for around 4 MtH2/yr in 2018, or 10% of the use of hydrogen consumed in mixed forms globally.

Without policy intervention, demand for dedicated hydrogen production in steel-making is expected to grow from the current level of 4 MtH2/yr roughly in line with the gas-based DRI-EAF route.

While the gas-based DRI-EAF can be more energy-intensive than the BF-BOF route, it uses simpler and slightly less capital-intensive equipment. It tends to bedeployed in regions with low natural gas prices (e.g. the Middle East) or low coal prices (e.g. India).

The two main factors to influence future dedicated hydrogen demand for steel production are: the share of the DRI-EAF route in primary steel making, and the split between primary and secondary steel production in overall output. Considering the dynamics of steel stocks in the built environment, on current trends the share of scrap-based production in total steel production is projected to grow from around 23% today to 25% in 2030. In this case, the commercial gas-based DRI-EAF route could supply 14% of primary steel demand. This would require 8 MtH2/yr as a reducing agent, doubling the use of hydrogen for DRI-EAF production from today's levels. In the same case, if the share of secondary steel production continued to rise (to 29% by 2050) and the gas-based DRI-EAF route was used to satisfy 100% of primary steel demand, hydrogen demand in the sector could theoretically reach 62 MtH2/yr.

If, instead of following current trends, an alternative pathway was to be followed that aligns the future development of the energy sector with the goals of the Paris Agreement, the outlook for hydrogen demand and production in the sector could be very different. In such a pathway, the share of scrap recycling in total steel production is projected to grow more rapidly, from 23% today to 29% in 2030 and 47% in 2050, limited only by the availability of steel scrap. Our analysis suggests a slightly larger share of the gas-based DRI-EAF in primary steel production by 2030 (16%) in this case, and that progress on materials efficiency strategies would also be accelerated, leading to a reduction in the overall level of output.

Two parallel technological developments relating to DRI-EAF are also assumed to take place in this case. First, 30% of the natural gas consumed in DRI-EAF production would be replaced by 2030 by externally sourced pure hydrogen from electrolysis, which could be done without major equipment changes. Second, progress on developing the HYBRIT concept would be sufficient to demonstrate the first commercial-scale 100% hydrogen-based DRI-EAF plant by 2030, supplying 1.5 Mt/yr of crude steel, or 0.1% of total steel demand.

If these ambitious developments were to take place, hydrogen demand for iron and steel production would be 9–11 MtH2/yr by 2030, like the level of 8 MtH2/yr expected on the basis of current trends. However, only around 4.5 MtH2/yr would be sourced from renewable electricity, with the remainder coming from natural gas. By comparison, under current trends all of the additional hydrogen demand would be met by natural gas without CCUS. This would require 230 TWh/yr of electricity, approximately equivalent to the total electricity consumption of Turkey today (Fig. 13).
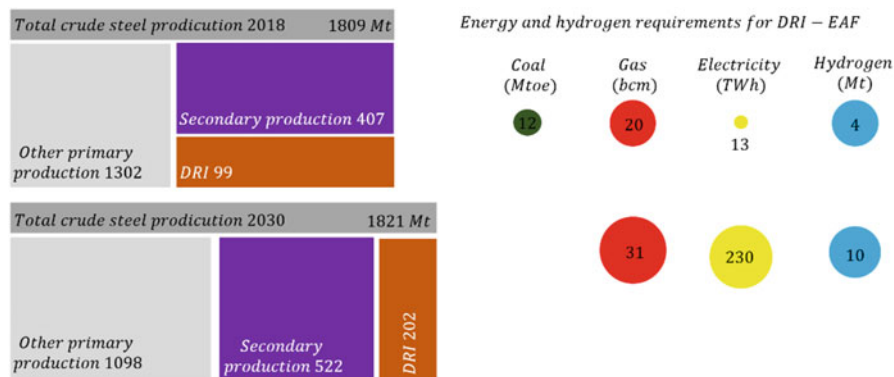
Fig. 13 Energy implications of fulfilling hydrogen demand via the DRI-EAF route

Natural gas would nonetheless still play an important role in supplying the remaining hydrogen in 2030, resulting in 31 bcm/yr of natural gas demand, which is approximately equal to the natural gas consumption of Spain today. Coal-based DRI-EAF production would disappear by 2030 in this scenario, eliminating 12 Mtoe/yr, roughly the annual coal consumption of Mexico today.

In the long term a Paris-compatible pathway would seek to drastically reduce CO_2 emissions from primary steel production.38 Using the 100% hydrogen DRI-EAF route for all primary steel production would largely eliminate CO_2 emissions, provided the electricity was sourced from renewables. This would require 47–67 MtH2/yr.

More than 2500 TWh/yr of electricity would be needed to produce this much hydrogen, or roughly the combined electricity consumption of India, Japan and Korea today. A substantial but manageable amount of water would also be required as feedstock for electrolyzers: around 0.6 bcm/yr, which is about 1% of total water consumption in the energy sector today. Some 500 Mt/yr of oxygen would be produced as a by-product; this could be put to use elsewhere in industry.

7.4 High Temperature Heating

Industrial high-temperature heat is a potential source of hydrogen demand growth in the future, but virtually no dedicated hydrogen is produced for this application today. Industry uses heat for a variety of different purposes, including melting, gasifying, drying, and mobilizing a wide array of chemical reactions. Heat can be used both directly, for example in a furnace, or indirectly, for example by first raising steam and then transferring it for heating needs. There are three main temperature ranges for industrial heat: low temperature (<100 °C), medium temperature (100–400 °C) and high temperature (>400 °C).

Global demand for high-temperature heat in industry was around 1280 Mtoe/yr in 2018, of which just 370 Mtoe/yr was outside the chemical and iron and steel sectors covered in the previous sections. More than half of this remainder was consumed in cement manufacture. This level of demand is set to rise gradually on current trends to just over 400 Mtoe/yr in 2030. This demand trajectory would not change significantly even if strong climate change mitigation measures were pursued, although some small differences would arise from increases in energy and materials efficiency.

Fossil fuels are the primary source of high-temperature heat today (around 65% from coal, 20% natural gas and 10% from oil), although small amounts of biomass and waste are used in certain sectors. Electricity is also used extensively to generate high-temperature heat in specific applications, either directly (e.g. electric arc and induction furnaces in the steel industry) or indirectly (e.g. to drive electro-chemical reactions in aluminum smelting). Resistance heaters are used in the production of carbon fiber, reaching temperatures of 1800 °C, and there are ways to utilize electromagnetic heating technologies (e.g. microwave and infrared) to achieve similar temperatures for other specific heating applications.

However, several large-scale processes, such as steam crackers and cement kilns, remain challenging to electrify although demonstration and feasibility studies are being conducted in both of these areas.

Excluding the chemical and iron and steel sectors, industrial high-temperature heat is responsible for approximately 1.1 $GtCO_2$/yr of direct emissions today, or around 3% of global energy-sector CO_2 emissions. Combustion of sustainable bioenergy or hydrogen (or direct use of hydrogen-based fuels such as ammonia) offer ways of reducing emissions that are proven at scale. However, negligible quantities of hydrogen are currently used for this purpose today.

Despite having the potential to eliminate emissions from high-temperature heat for industry, hydrogen remains an expensive alternative to fossil fuels in the context of a low-carbon pathway for the energy system, even when CO_2 prices reach USD 100/tCO_2.

Bioenergy tends to be more cost-competitive in this context, assuming a bioenergy price range of USD 8–12/GJ in 2030.

Bioenergy is set to become cost-competitive with natural gas as a source of high-temperature heat in 2030 in India, China and Japan, even at the higher end of the bioenergy price range explored (USD 12/GJ). This is due to relatively high natural gas prices in these regions in the context of a Paris-compatible pathway for the energy system (USD 3.8–10.6/MBtu). A CO_2 price of around USD 200/tCO_2 would be needed before the cheapest hydrogen-based fuels (at a delivered cost of USD 2.3–2.7/kgH_2) become competitive with coal and natural gas.

Hydrogen does, however, offer some advantages for decarbonizing elements of this diverse segment of energy demand, despite its relatively high costs and the need for it to overcome certain practical difficulties. For example, low-carbon hydrogen has the potential to help decarbonize the more geographically fragmented portions of industrial high-temperature heat demand where direct application of CCUS may prove impractical. Hydrogen, either via pipeline or using small-scale on-site

electrolysis, could form a low-carbon energy supply to these "hard-to-reach" segments of industry. Its potential role may also grow if the supply of sustainable bioenergy is limited in the future; bioenergy is also likely to be in demand in other end-use sectors such as aviation.

8   Potential Uses of Hydrogen in Transport

Hydrogen holds long-term promise in many sectors beyond existing industrial applications.

The transport, buildings and power sectors all have potential to use hydrogen if the costs of reduction and utilization develop favorably relative to other options. The complex processes involved in developing and deploying hydrogen, however, mean that carefully crafted policy support will be critical.

The competitiveness of hydrogen FCEVs in transport depends on fuel cell costs and on the building and utilization of refueling stations. For cars the priority is to bring down the cost of fuel cells and on-board hydrogen storage. This could make them competitive with battery electric vehicles at driving ranges of 400–500 km and make them potentially attractive for consumers that prioritize range. For trucks the priority is to reduce the delivered price of hydrogen. In early stages of deployment, building hydrogen stations that serve captive fleets on hub-and-spoke missions could help to secure high refueling station utilization and thus could be a way to get infrastructure construction off the ground (Hienuki et al. 2021).

Shipping and aviation have limited low-carbon fuel options available and represent an opportunity for hydrogen-based fuels. Ammonia and hydrogen have the potential to address environmental targets in shipping, but their cost of production is high relative to oil-based fuels. Hydrogen-based liquid fuels provide a potentially attractive option for aviation at the expense of higher energy consumption and potentially higher costs. Policy support in the form of low-carbon targets or other approaches is critical to their prospects.

The largest near-term opportunity in buildings is blending hydrogen into existing natural gas networks. In 2030 up to 4 Mt of potential hydrogen use for heating buildings could come from low-concentration blending which, if low-carbon, could help to reduce emissions. The potential is highest in multifamily and commercial buildings, particularly in dense cities, where conversion to heat pumps is more challenging than elsewhere. Longer-term prospects in heating could include the direct use of hydrogen in hydrogen boilers or fuel cells, but both of these would depend on infrastructure upgrades and on measures to address safety concerns and provide public reassurance.

Power generation offers many opportunities for hydrogen and hydrogen-based fuels. In the near-term ammonia could be co-fired in coal-fired power plants to reduce CO_2 emissions.

Hydrogen and ammonia can be flexible generation options when used in gas turbines or fuel cells. At the low-capacity factors typical of flexible power plants, hydrogen costing under USD 2.5/kg has good potential to compete. Key low-carbon competitors for such services include natural gas with CCUS and biogas. In the longer term, hydrogen can play a role in largescale and long-term storage to balance seasonal variation.

Maximizing the potential long-term promise of hydrogen depends on moving beyond the existing industrial uses of hydrogen described in chapter "Hydrogen in the Chemical Industry", and on the development of a strong case for its use as a versatile fuel in various new sectors. This case rests largely on its ability to help diversify the fuel mix and, if produced from low-carbon sources, support the transition to a cleaner energy system. Numerous opportunities exist to use hydrogen outside industrial applications: practically all modes of transport could potentially be run on hydrogen or hydrogen-based fuels; building heating, cooling and electricity needs could be supplied through hydrogen; and the power sector could use hydrogen or hydrogen-rich fuels such as ammonia for the production of electricity.

Given this versatility, it may be tempting to envisage an all-encompassing low-carbon hydrogen economy in the future. However, other clean energy technology opportunities have greatly improved recently, most importantly solutions that directly use electricity, which means that the future for hydrogen may be much more one of integration into diverse and complementary energy networks. This is especially so since the use of hydrogen in certain end-use sectors faces technical and economic challenges compared with other (low-carbon) competitors. There is also an element of path dependency; for example, rail transport is already widely electrified in many countries.

8.1 Hydrogen as a Clean Transport Fuel

Hydrogen gas has long been heralded as a potential transport fuel. It is seen as offering a low-carbon alternative to refined oil products and natural gas, and complementing other alternatives like electricity and advanced biofuels. Hydrogen fuel cell electric vehicles (FCEVs) would reduce local air pollution because – like battery electric vehicles (BEVs) – they have zero tailpipe emissions. Hydrogen can be converted to hydrogen-based fuels, including synthetic methane, methanol and ammonia, and synthetic liquid fuels, which have a range of potential transport uses. Synthetic liquid fuels produced from electrolytic hydrogen are often referred to as "power-to-liquid" (Blanco et al. 2018).

Hydrogen-based fuels could take advantage of existing infrastructure with limited changes in the value chain, but at the expense of efficiency losses. Hydrogen-based fuels offer particular advantages for aviation (in the form of synthetic jet fuel) and for shipping (as ammonia), sectors where it is more difficult to use either hydrogen or electricity.

Fig. 14 Fuel cell electric cars in circulation
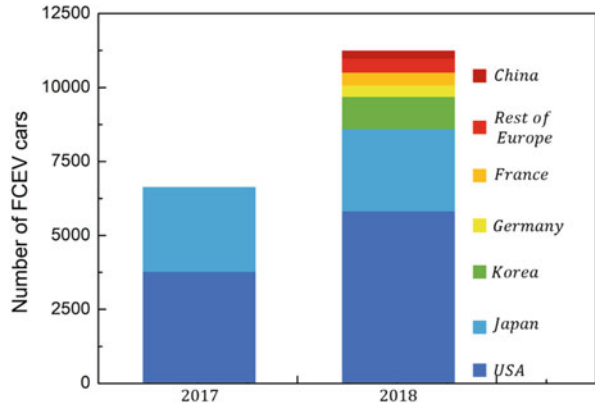
Light-duty FCEVs receive most public attention when it comes to the direct use of hydrogen in mobility applications today. FCEVs have, however, also been deployed for material handling applications (mainly forklifts), buses, trains and trucks.

Cars account for the vast majority of fuel cell power deployed in road transport. About 4000 fuel cell electric cars were sold in 2018 to reach a total stock of 11,200 units (Fig. 14), an increase of 56% over the previous year.

This is still a small number compared with the 2018 BEV stock of 5.1 million or the global car stock of more than one billion. The United States accounts for about half of registered FCEVs, followed by Japan (about a quarter), the European Union (11%, primarily in Germany and France) and Korea (8%).

Almost all passenger car FCEVs are made by Toyota, Honda and Hyundai, although Mercedes-Benz has recently begun leasing and selling limited volumes of a plug-in hybrid electric vehicle with a fuel cell.

Hydrogen fuel cell electric forklifts are already commercially viable as replacements for existing battery electric forklifts, and it is estimated that 25,000 forklifts have fuel cells globally. In the case of buses, the People's Republic of China ("China") has reported the largest deployment, with more than 400 registered by the end of 2018 for demonstration projects. An estimated 50 fuel cell electric buses were also in operation in Europe in 2017, 25 in California and about 30 in other US states. Other demonstration projects have rolled out fuel cell electric buses in Korea and Japan. Volumes are scaling up rapidly and thousands are expected to be in operation by the end of 2020 (mostly in China).

Globally at least 11 companies currently manufacture fuel cell electric buses. Because their long range means that there is generally no need to recharge during the day, they are in general well suited to: higher daily mileage (above 200 km per day); larger bus fleets, where refueling can be simpler than recharging battery electric buses; and flexible routing and operations, for example extending a given route at certain periods of the year.

Fig. 15 Hydrogen
refuelling stations and
utilisation, 2018
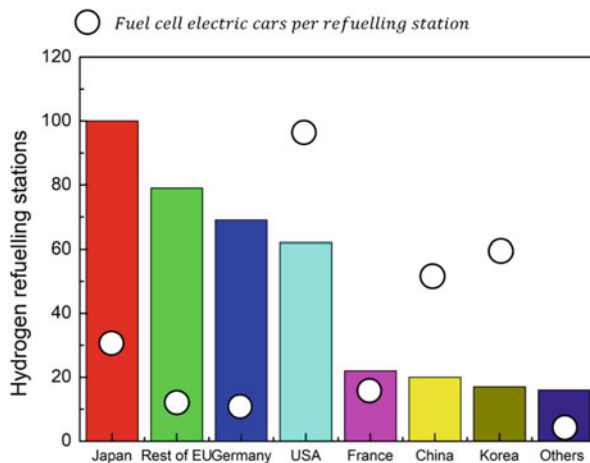
New models of battery electric trucks and buses have recently been produced, purchased and put into operation. The market growth has been fastest in fleets that have access to daily charging opportunities and limited daily ranges (up to 350 km per day), notably urban buses and delivery fleets. Certain operations in these fleets are intensively used and require long ranges, and some fleet owners and operators have found it cost-effective in regions where hydrogen stations exist to install fuel cell range extenders on light- and medium-duty trucks and buses.

Intercity buses in particular are likely to be a promising and competitive application for fuel cell electric powertrains.

As regards trucks, China leads the global deployment of fuel cell electric trucks and accounts for the majority of demonstration projects. Country-level statistics in 2018 refer to 412 units registered in China, supplemented by 100 vans. Separately 500 hydrogen fuel cell delivery vehicles are reported as operating in the city of Rugao alone and well over 100 are in full daily operation in and around Shanghai. Outside China, FedEx and UPS, two delivery companies, are trialing fuel cell range-extender Class 6 delivery vehicles in the United States, and the h2Share project is planning to test a 27-tonne heavy-duty truck in Europe. The French postal service and other logistics companies in France have also installed small fuel cells as range extenders onto 300 battery electric vehicles in their fleet, and other companies have brought to market fuel cell range extenders for electric vans in France.

The installation of hydrogen refueling infrastructure, while relatively limited to date, has picked up momentum in the past few years. Hydrogen refueling stations for road transport vehicles, including both publicly accessible and private refueling points, reached a worldwide total of 381 in 2018 (Fig. 15).

Japan (100), Germany (69) and the United States (63) are the three countries with the highest numbers of publicly available hydrogen refueling stations. These are, however, still small numbers compared with those for BEVs: there are almost 144,000 public fast chargers in the world for light-duty vehicles, 395,000 public slow chargers and 4.7 million private chargers.

These numbers mean that there are around 10 BEVs for every public charger and one for every private charger; the average number of FCEVs for every hydrogen refueling station in most regions where they have been deployed is currently much higher. For a fully developed infrastructure, 2500–3500 FCEVs per station are expected.

Delivered hydrogen prices are highly sensitive to hydrogen refueling station utilization. For example, a ratio close to 10 cars per station (as is the case in Europe) implies that pumps operate less than 10% of the time if the refueling stations were as small as 50 kgH2 per day.

This translates to a high price of around USD 15–25/kgH2 if the costs of building and operating refueling stations are repaid by fuel sales over the lifetime of a station.44 A higher ratio of cars to refueling stations implies better co-ordination between vehicle and infrastructure deployment and should lead to lower hydrogen prices. However, some countries with high ratios today have FCEVs that are mostly used as fleet vehicles, with fixed routes and refueling patterns that are not representative of the needs of more widespread deployment. This is the case in China and France, for example.

The variability of this ratio among countries indicates different approaches to the risks associated with refueling infrastructure development. Refueling stations can take as little as six months to bring into operation in China, but generally take up to two years.

Approaches that try to mitigate the co-ordination problem and time lag related to infrastructure development include using refueling stations at or near hydrogen production sites (for instance at industrial sites, intermodal interchange hubs or ports) to serve dedicated fleets (such as industrial operations or, potentially, public buses or taxis).

Together with BEVs, FCEVs are the only vehicles with no exhaust emissions and thus offer the potential to drastically reduce local air pollution, especially in cities. They can also dramatically reduce CO_2 emissions when low-carbon hydrogen is used. The driving range and pattern of refueling for FCEVs is similar to internal combustion engine vehicles. Furthermore, hydrogen has some attractive attributes compared to biofuels as it does not generally face resource constraints or competition for land use. FCEVs have nevertheless been slow to take off.

Technical challenges and high prices have delayed their market introduction. While the Hyundai Tucson-ix 35 was introduced in 2013 and the Toyota Mirai in 2014, there is a need to further reduce costs and build up refuelling station networks concurrently with vehicle uptake if more automakers are to be attracted to the market.

The theoretical potential for future use of hydrogen in road transport is very large. Any road transport mode can technically be powered using hydrogen, either directly using fuel cells or via hydrogen-based fuels in internal combustion engines. As an indication of the size of this market, if all the one billion cars, 190 million trucks and 25 million buses currently on the road globally were replaced by FCEVs, hydrogen demand would be as high as 300 MtH2/yr, more than four times current global demand for pure hydrogen.

The theoretical potential future demand is even larger. Over the next 10 years to 2030, oil demand from road transport is set to grow by 10% without strong action to meet the goals of the Paris Agreement. In particular, this would be driven by demand for trucks in emerging economies, but also rising car ownership. Car ownership in countries like India and even China is well below that of industrialized countries such as the European Union and the United States. US per-capita car ownership is 25 times higher than India's.

While the theoretical potential is very large, actual deployment will depend very strongly on the interactions between vehicle costs, fuel costs and policies, as well as the cost of alternatives and evolving driving habits in different countries.

The fuel cell has seen considerable cost reductions over the past decade, but costs remain high and production volumes are still low. The current commercial cost of a typical fuel cell is estimated to be USD 230/kW, although the use of state-of-the-art technologies is soon likely to bring this cost down to USD 180/kW.

Costs could be further reduced in the future through research-driven advances in technology. It may be possible to increase catalyst activity and thus reduce the platinum content, which is one of the expensive components of the fuel cell. It may also be possible to develop a platinum-free catalyst. Research is also needed to optimize the design and integration of fuel cell components in the membrane electrode assembly and to decrease the costs of the bipolar plates (which are expected to account for an increasing share of the future costs) and balance of plant components (e.g. compressors and humidifiers).

Costs could also be reduced in the future through economies of scale: increasing the number of units fabricated in a single manufacturing plant reduces the specific cost of each component.

About half of the system cost is in the bipolar plates, membranes, catalyst and gas diffusion layers. The combined cost of these components could be reduced by 65% by increasing plant scale from 1000 to 100,000 units per year, bringing system costs down to USD 50/kW.

Increasing the scale further to 500,000 units per year would be likely to decrease the cost by only an additional 10%, taking it down to USD 45/kW. These cost reduction estimates must, however, be balanced against the challenge of simultaneously improving fuel cell performance and durability. Higher durability requirements could translate into higher fuel cell cost and limit the cost reductions achieved through economies of scale. Recent US Department of Energy (DOE) data take into account these trade-offs and provide a preliminary durability-adjusted cost target of USD 75/kW. However, automakers are working to increase durability, such as via constructing fuel cell operation maps to mitigate performance degradation.

Economies of scale in manufacturing could be achieved quickly. Global truck sales stood at around 1.6 million medium-duty and 1.8 million heavy-duty vehicles in 2017. A medium-duty truck requires about twice as much power as a car, and a heavy-duty truck needs about four times as much. These requirements could, however, be met by installing fuel cell stacks next to each other; the most cost-effective way of proceeding might be to equip a medium-duty fuel cell electric truck with two fuel cell stacks, and a heavy-duty truck with four. To reach a 5% global

market share in trucks would require five fuel cell system plants producing 100,000 units (stacks) a year. China would need 10 plants producing 100,000 units annually to satisfy just a quarter of its current annual sales for domestic medium- and heavy-duty trucks. The passenger vehicle sector has a market size much larger than trucks, with annual new car sales of around 85 million and light commercial truck sales of ten million in 2017. These light-duty vehicles

require a system consisting of a single fuel cell stack, with a peak power of 80–100 kW per vehicle. Achieving a market share of 5% of the global car market would require 40 fuel cell manufacturing plants, each with an average output of 100,000 units a year.

On-board storage tank costs are determined by expensive composite materials and are expected to fall at a slower pace than fuel cells. On-board storage of hydrogen requires it to be compressed at 350–700 bar for cars and trucks, and this uses the equivalent of 6–15% of the hydrogen energy content.45 The costs of current on-board storage systems (including fittings, valves and regulators) are estimated at USD 23/kWh of useable hydrogen storage at a scale of 10,000 units per year, decreasing to USD 14–18/kWh at a scale of 500,000 units per year. The US DOE has an ultimate target of USD 8/kWh. For a car with a range of 600 km, this implies costs of around USD 3400 today and USD 1800 in the long term for a tank of 225 kWh. For a heavy-duty truck with a range of 700 km, it implies costs of USD 27700 today and a potential reduction to USD 16700 for a tank of 1800 kWh, compared with USD 100000–150,000 for the full cost of a conventional diesel truck tractor.

The roll-out of hydrogen refueling infrastructure is a key requirement for FCEVs. Hydrogen refueling takes almost as little time as refueling conventional liquid transport fuels.

Supplying refueling stations with hydrogen, however, may require more time and labor than is the case for conventional transport fuels. Validation of cost estimates is difficult because there are fewer than 400 hydrogen refueling stations around the world and because their data are usually not disclosed. However, investment costs for hydrogen refueling stations are estimated to be in the range of USD 0.6–2 million for hydrogen at a pressure of 700 bar, and USD 0.15–1.6 million at 350 bar. The lower end of these ranges is for stations with a capacity of 50 kgH$_2$/day while the upper is for 1300 kgH$_2$/day.

The two largest cost components are the compressor (which can be up to 60% of the total cost when the delivery pressure is 700 bar) to achieve the delivery pressure, and the storage tanks (which are relatively large due to lower hydrogen density). The actual cost of building a station varies considerably across countries, mainly as a result of different safety and permitting requirements. There are strong economies of scale. Increasing the capacity from 50 to 500 kgH2/day would be likely to reduce the specific cost (i.e. the capital cost per kg of hydrogen dispensed) by 75%. Larger capacity stations of up to a few 1000 kgH2/day are being planned, especially for heavy-duty applications, and these offer potential for further economies of scale. There is also potential for costs to be reduced through a shift to more advanced supply options (such as very high pressure or liquid hydrogen) and through scale-up

in the manufacturing of refueling station products (via mass production of components, such as the compressors).

Risks related to the tension between refueling station size, the cost of hydrogen and hydrogen demand are among the barriers to rapid hydrogen uptake for transport. Small stations make more economic sense in the initial deployment phase as they are more likely to secure higher capacity utilization rates when demand for hydrogen from transport vehicles is limited, but they come at higher cost per unit of hydrogen delivered. Once sufficient demand volumes have been established, larger stations become more economic and can help reduce the cost of hydrogen for the end users. The cost of delivered hydrogen will also depend on whether the hydrogen is produced locally or delivered from centralized production facilities. The cost advantages of centralized production may be outweighed by the cost of distribution to the refueling station by truck or pipeline. The cheapest option will be determined case by case.

Despite higher initial costs than BEV charging infrastructure, hydrogen refueling stations can offer significant advantages when deployed at scale, such as faster refueling and space requirements around 15 times lower, as well as potentially lower final investment costs. In the longer term over 400 refueling stations would be needed to service a fleet of one million hydrogen FCEVs if the ratio of refueling stations to cars were similar to that for today's oil-powered car fleet. This compares to almost one million private charging stations and at least 10,000 fast-charging public stations that would be needed for a fleet of one million BEVs.

To meet the needs of a growing FCEV fleet, policy makers will need to ensure investment flows at the right times. Most fueling stations serving non-captive fleets in the early stages of FCEV deployment will be small (< 200 kgH2/day), and the total investment needed to build these 400 stations is likely to be on the order of USD 0.5–0.6 billion. This would rapidly increase, however, and for a mature market with larger stations (>1000 kg/d) an investment of USD 35–45 billion would be required to serve just 5% of the global car fleet (around 60 million vehicles).

As well as collaborating with industrial stakeholders on roadmaps for building refueling stations in the initial phases, before their revenue can sustain investment in expansion, policy makers could incentivize owners of captive fleet stations to open them for public use, thus allowing general users to access more stations.

Energy consumption per kilometer tends to be greatest on large vehicles used over long distances. This means that fuel costs generally make up a greater share of total costs for heavier vehicles, and for vehicles with high utilization (such as long-haul trucks, intercity buses and commercial car fleets). As the capital cost of a car ranges from 70% to 95% of the total cost of ownership, depending on the vehicle, it will be imperative to bring down the cost of fuel cell systems and hydrogen storage tanks to achieve cost competitiveness with other options. The case is somewhat different for trucks, for which the capital cost ranges from 40% to 70% of the total ownership cost, meaning that cost reductions for delivered hydrogen are just as important.

Car buyers typically consider the total cost of ownership as one among several decision criteria.
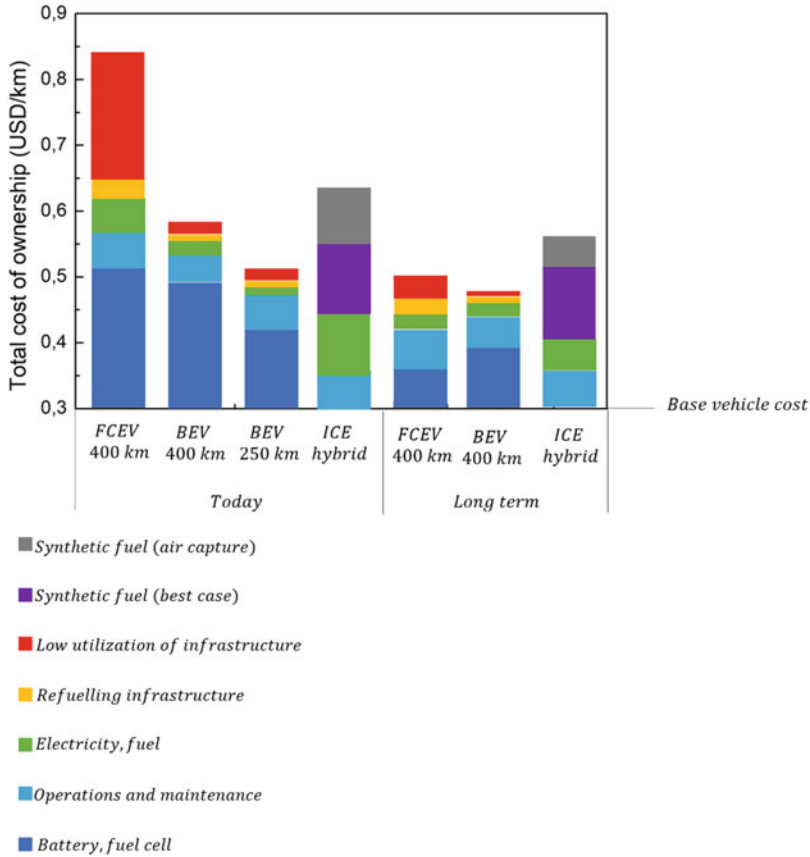
Fig. 16 Total cost of car ownership by powertrain, range and fuel

For example, the range of a car can be important to some buyers. The global average BEV sold today has a range of around 250 km; this is sufficient for most daily trips. FCEVs sold today offer a longer range: the Toyota Mirai offers some 400 km and the Hyundai Nexo even more. This makes them attractive for consumers who prioritize range. To illustrate the relevance, assuming hydrogen refueling facilities are located along desired routes, FCEVs could drive from Paris to Marseille (about 750 km) with a single short refueling stop. The same trip in a BEV with a range of 250 km would require stopping to charge at least twice, with fast charging depending on the availability of stations. This extra range offered by FCEVs, however, comes at a price in terms of the cost of the vehicle. Different consumers will weigh the considerations differently, according to their individual priorities and preferences.

Currently hydrogen fuel cell cars are generally more expensive than battery electric cars, owing to the high cost of the fuel cell and fuel tanks and to the fact that they are generally designed to have a longer range (Fig. 16).

Fig. 17 Break-even fuel cell cost to be competitive with BEV in the long term
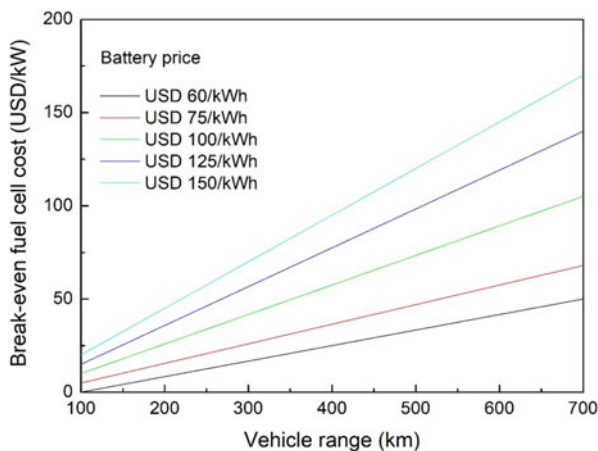
The competitiveness improves if one assumes the same range for FCEVs and BEVs, although such range would be only possible today for a limited number of BEV models. If cost reductions through economies of scale were to bring down fuel cell costs to USD 50/kW and those of batteries fall to USD 100/kWh, then FCEVs become competitive with BEVs at a range of 400 km. If fuel cell costs were only to fall to USD 75/kW, for example because of the need for durability requirements as discussed earlier in this chapter, then FCEVs would become competitive with BEVs at a range of 500 km (Fig. 17). This underscores the fact that FCEVs can be economically attractive for consumers who prioritize driving range.

Utilization of refueling infrastructure is another determinant of the future competitiveness of FCEVs. In the initial roll-out phase, the cost of hydrogen fuel can be expected to range from 12% (at USD 9/kgH2) to 22% (at USD 18/kgH2) of the total cost of ownership. As discussed above, the additional cost accounted for by the hydrogen refueling station depends on size and utilization: stations with a capacity of 200 kgH2 per day that dispense fuel at 10–33% of capacity add a margin of USD 4–13/kgH2, and that margin declines with station size and higher capacity utilization. The risk of underutilized hydrogen refueling stations highlights the importance of securing high utilization to bring down costs in the initial stages of FCEV deployment, even in cars, the mode where fuel costs are least determinant.

It is worth noting that in California it took around two years to increase the average utilization of the network from 5% to 40%; the average station size is now around 200 kgH$_2$/d and some stations are still operating at below 10% utilization. The high cost of synthetic fuel, however, suggests that transitioning to alternative powertrains – whether battery or fuel cell electric – is likely to be a lower-cost strategy for reducing CO_2 and local pollutant emissions from cars and trucks, also considering the significant energy consumption and need for biogenic CO_2 this route would require.

The above analysis suggests that BEVs and FCEVs could complement each other as alternative options satisfying different consumers, with FCEVs offering the best opportunities for vehicles driven at long ranges, with fast refueling requirements and in regions with access to cheap hydrogen. Furthermore, it suggests that once a hydrogen refueling infrastructure has been built out, light-duty FCEVs with different configurations (e.g. fuel cell range extenders) could take advantage of cost and performance improvements in both fuel cells and batteries.

The heavy-duty long-haul segment, including trucks and intercity buses (or "coaches"), offers strong prospects for hydrogen FCEVs because it calls for long range and high-power requirements. As a result, heavy-duty FCEVs tend to be more immediately competitive against BEVs than in the case of cars. The direct electrification of regional bus operations and heavy-duty trucking for long-distance freight both face major challenges with larger battery capacity, long charging times and high-power requirements that translate into payload loss and additional recharging infrastructure costs. Fuel cell electric trucks overcome some of these challenges.

In the case of heavy-duty long-haul trucks, fuel cell costs are higher than light-duty vehicle applications, mainly as a result of high durability requirements. This currently necessitates increased catalyst loading, translating into higher costs. Future fuel cell system costs for heavy-duty trucks are estimated at USD 95/kW (for a production volume of 100,000 units per year). Even with current fuel cell costs, FCEVs could in general be competitive against BEVs in heavy-duty applications at ranges of more than 600 km if hydrogen could be delivered at less than USD 7/kgH2, although the exact hydrogen price at which they become competitive depends on overall annual mileage and other operational characteristics.

Powertrain and fuel options for decarbonizing heavy-duty long-haul trucking include FCEVs, battery electric trucks, dynamic charging (catenaries are the most commercially advanced and lowest-cost option on existing roads) and conventional diesel hybrids using synthetic fuels (or advanced biofuels).

A range of low-carbon powertrain options could conceivably co-exist: plug-in hybrid electric vehicles, BEVs with or without fuel cell range extenders and FCEVs of different configurations could be designed and ordered to cater to different mission profiles.

Bringing down fuel cell costs to USD 95/kW could make hydrogen fuel cell trucks in the heavy-duty segment competitive with diesel hybrid trucks at a hydrogen price of around USD 7/kgH$_2$, compared with the price of USD 5/kg currently needed to make them competitive with an ICE truck running on diesel. For fuel cell electric trucks to be competitive with electric road systems or battery electric trucks at a range of less than 500 km, however, the hydrogen price would need to be less than USD 5/kg H2. Because of the limited size of the truck market, reaching this fuel cell cost target may not be feasible by deployment of fuel cells in trucks alone and will most likely rely on substantial deployment of fuel cells in cars.

Fuel cell production for small mobile equipment, such as forklifts, may also help to bring down costs, but since the power requirements of this equipment is typically

less than one-third that of a car, high production volumes of roughly 3000 units per year would be needed to achieve cost reductions below USD 80/kW.

In the case of trucks (and also buses), the cost contribution from the infrastructure could be reduced by the operation of a "hub-and-spoke" model: a dedicated fleet operating on fixed routes could refuel at a single centralized hydrogen refueling station. Since refineries and industrial clusters are often co-located at ports, port operations (and handling equipment) offer further attractive initial markets. The efficiency of these strategies has been demonstrated by the rapid adoption of hydrogen fuel cell electric buses and trucks in China, where the business case for intensive medium- and heavy-duty operations has been strengthened considerably by success in accessing low-cost hydrogen and achieving high utilization rates of refueling stations.

8.2 Hydrogen in Maritime Sector

The maritime sector is an important consumer of oil products, accounting for around 5% of global oil demand. This section of the report focuses on international shipping, which is the cheapest way to move long-distance freight. By volume around 90% of global physical trade in goods is by sea, of which one-third is energy products, in particular oil products.

About 80% of fuel use in the maritime sector is in international shipping, of which 90% is used for maritime freight. As a result, international shipping is an important contributor to climate change: it is responsible for around 2.5% of global energy-related CO_2 emissions. As it uses heavy fuel oil, it also has large detrimental effects on air quality, notably around ports. Hydrogen, mostly in the form of hydrogen-based fuels, is a leading option for tackling these challenges in international shipping. One advantage of these applications is that they offer the opportunity to address not only emissions during sea transport, but also those arising from port operations, making use of synergies with forklifts, trucks and goods movement in and around ports. Opportunities also exist to use hydrogen and fuel cells for shorter routes within national jurisdictions, especially those operated by ferries (Temiz and Dincer 2021).

Oil products currently dominate the shipping sector, and the use of hydrogen-based fuels in shipping is accordingly very limited. There is, however, one project in Belgium for co-firing hydrogen with diesel in maritime internal combustion engines, and more than 20 projects for fuel cells of up to 300 kW, mostly for auxiliary power units. Projects using fuel cells, often in combination with batteries, are planned in California, Ireland, Norway and for some Europe-wide operations.

Ships do not use ammonia as fuel today, but ammonia containing the equivalent of around 3.5 MtH_2/yr is traded in ships. Several research and demonstration projects are looking at the firing of ammonia as fuel for ships. Satisfactory combustion of ammonia in existing engines would generally require ignition promotors (to overcome its lower ignition energy) and engine modifications.

The volume of international shipping is expected to more than triple by 2050 under current trends. In the absence of climate change mitigation policies, this could lead to a 50% increase in demand for oil products in the sector, to around 6 mb/d. Action to reduce the emissions associated with this oil use could open a pathway to the use of hydrogen-based fuels. The International Maritime Organization (IMO) has put in place strategies for reducing both sulphur and greenhouse gas emissions.

Possible measures to address the challenge of reducing sulphur emissions are the installation of scrubbers, fuel switching to LNG and the use of very low sulphur fuel oil (VLSFO), although these measures will only make a partial contribution to the 50% greenhouse gas reduction target by 2050 compared to 1990. As described in chapter "Hydrogen in the Chemical Industry", limitations on sulphur emissions are likely to stimulate demand for hydrogen at refineries rather than as shipping fuel. To achieve the greenhouse gas emissions target, advanced biofuels, hydrogen and ammonia are all options, as well as hydrogen-based synthetic liquid fuels. The choice of fuel switching relies on infrastructure deployment outside the direct control of ship owners. LNG, hydrogen and ammonia would require the development of bunkering facilities, while both LNG and ammonia could build upon the existing distribution network. Availability and costs of advanced biofuels are uncertain as there is demand competition from other sectors for a limited supply of sustainable biomass.

Targets are also in place in some countries for low-carbon alternatives in domestic shipping. Sweden and Norway are two examples of this, while the European Commission is developing a strategy to set CO_2 reduction targets for maritime transport based on monitoring, reporting and verification of CO_2 emissions from large ships. Shipping may be incorporated into the European Emission Trading System from 2023.

Among businesses, Maersk, the world's largest maritime company, announced in 2018 that it aims to become carbon neutral by 2050. To achieve this, it recognizes that low-carbon vessels will need to be commercially viable by 2030. Industry leaders have also drafted an action plan to decarbonize the shipping sector, which includes demonstration projects, technology adoption, transparency and knowledge sharing.

Ships have high per-kilometer energy intensity and large power needs (up to 130 MW for the largest container ships), and therefore pose demanding fuel requirements. The main cost components for ships are the same as for road transport: infrastructure (bunkering facilities), on-board equipment (fuel cell/engine and storage) and fuel.

Information on the costs of using liquid hydrogen for international shipping is uncertain. One estimate for the additional cost of bunkering facilities suggests that liquid hydrogen infrastructure could be 30% more expensive than LNG. However, this estimate is likely to omit the upfront costs associated with developing a new infrastructure for hydrogen that does not currently exist. The main cost components are the storage and bunker vessels, which would need to be scaled in parallel with the number of ships serviced.

On-site or nearby hydrogen would be needed for small ports given the smaller flows and the high cost of dedicated hydrogen pipelines. Conversely, ship and infrastructure costs are a relatively small component of total shipping costs over a 15-year lifetime, with fuel costs being a much larger factor.

Among hydrogen-based fuels, ammonia is already globally traded and some of the infrastructure that would be needed to use it as a fuel already exists (distribution to ports and storage tanks). However, new bunkering facilities would need to be built; massive scale-up of ammonia production, port and distribution facilities and storage tanks would also be needed.

As an indication, satisfying shipping demand in the long term would require 500 Mt of ammonia, almost three times the level of current global production and around thirty times the volume of ammonia currently traded.

A switch to low-carbon fuels seems unlikely to occur in the absence of policy, whether mandates, direct carbon pricing, and/or more flexible and potentially more palatable measures such as low-carbon fuel standards (LCFS). Charterers, who currently oversee more than half of container fleet operations and who hire vessels from ship owners on a lump-sum or per-ton basis, are likely to operate much shorter payback periods.

Ships serving long-distance maritime trade routes may offer the best potential scope for hydrogen, ammonia and other hydrogen-based fuels. This is because fuel cell system and hydrogen storage costs have a comparatively lower impact when compared to fuel costs.

In addition, the space requirements of fuel cells could be an issue, especially for smaller ships (< 2 MW), as they need almost double the space of an ICE.

Storage of liquid hydrogen requires at least five times more volume than conventional oil-based fuels, and ammonia requires three times more volume. In the longer term this could require the redesign of ships, shorter distance trips and more frequent refueling, reduced cargo volumes, or a mix of these operational factors, depending on ship and cargo types and routes.

Low-carbon fuels are expensive today compared with fuel oil and LNG. Fuel prices are the key to cost competitiveness; the share of total cost that comes from infrastructure is much lower for ships than for other transport modes, currently accounting for about 3% of the total cost of using hydrogen in shipping on the basis of a hydrogen price of USD 10/kgH2.

This would rise to 17% if hydrogen prices were to decrease to USD 2/kgH2, and could be significantly higher (up to 40%) if bunkering facilities were oversized or underutilized. As for road transport, risks of underutilization of bunkering facilities can be hedged by: rolling out smaller vessels; using smaller storage tanks (which can be expanded as the capacity grows); using tank trucks to fuel ships; and using a smaller refueling station. However, to lower fuel costs, larger facilities would be needed for more widespread deployment.

In a 15-year first-owner lifetime calculation, a CO_2 price of USD 40–230/tCO_2 would be required to make ammonia cost-competitive with fossil-based fuels, depending on the delivered cost of ammonia, which will vary by region (Fig. 18).

Fig. 18 Break-even carbon price for ammonia to be competitive with fossil fuels
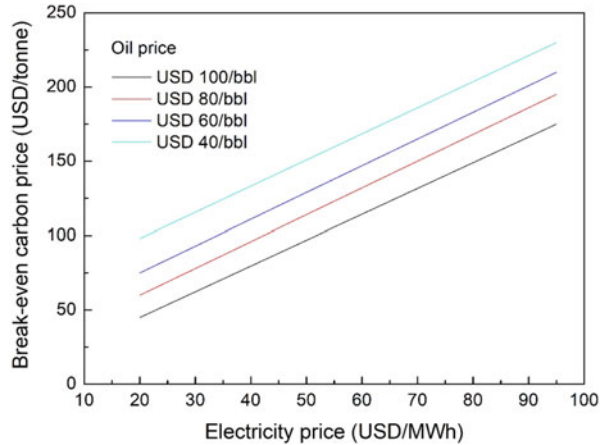
The break-even carbon prices for hydrogen are USD 35–45/tCO$_2$ higher than ammonia, mainly due to the higher storage cost resulting from its lower energy density. It would represent a substantial cost increase for the ship owner and the switch would require policies that have an effect equivalent to these CO$_2$ prices across competing fleets, for example mandates or low-carbon fuel standards. However, the impact of passing these costs on to the final consumer would be limited because transport costs represent a small share (often less than 1%) of the total price of shipped goods.

8.3 Hydrogen in Rail

Rail is already the most electrified mode of transport. Although the percentage share of electrified tracks is still expanding in most countries, further electrification of rail networks is likely to come up against diminishing returns on investment, since highly utilized lines are the first to be electrified.

In France and Germany, for example, electrified lines now carry over 80% of traffic, even though less than half of the railway network has been electrified. Beyond bi-mode diesel-electric options, several technologies offer zero tailpipe emissions on non-electrified tracks and the industry seems set to move towards these in the coming decades. The most innovative of such technologies are battery electric trains and hydrogen fuel cell trains. Battery electric trains with smaller batteries can also be used on partially electrified lines, enabling electrification costs to be sharply reduced by missing out those portions of track that are most difficult to electrify (such as bridges or tunnels).

Plans involving hydrogen trains already exist in a number of countries, with at least three companies working to supply them (Böhm et al. 2022). Germany intends to expand the fleet of hydrogen trains to 14 by 2021 and 5 federal states have signed a letter of intent to purchase 60 trains from Alstom, with 27 ordered as of May 2019.

Two hydrogen trains that can travel almost 800 km a day on a single refueling already operate in Lower Saxony in Germany. Austria's Zillertalbahn plans to deploy five hydrogen trains by 2022 for a total investment of almost USD 175 million. The UK government is supporting development of the first hydrogen trains by 2022. The French government is similarly considering 2022 as the target for the first hydrogen train to be on the rails. Japan Rail East also has a project underway, in partnership with Toyota.

Under optimistic assumptions about fuel cell cost reductions, hydrogen trains could become competitive against other passenger services options with low frequency of utilization. Hydrogen fuel cell technology is most competitive for services requiring long-distance movement of large trains with low-frequency network utilisation, a common set of conditions in rail freight. The use of hydrogen in rail could be combined with its use for forklifts, trucks and other railyard and logistics hub machinery to decrease costs and improve flexibility.

8.4 Hydrogen in Aviation

Aviation accounted for almost 2.8% of global energy-related CO_2 emissions in 2017, and air passenger traffic is expected to more than double to almost 16,000 billion km/yr by mid-century under current trends. Efficiency improvements should reduce energy consumption and slow the increase in energy demand, but alternative fuels will eventually be needed to avoid increases in emissions from the sector. Advanced biofuels and hydrogen-based fuels are leading options.

While there have been feasibility studies and demonstration projects testing the scope for using hydrogen in small planes, the use of pure hydrogen as an aviation fuel requires significant further R&D. Hydrogen's low energy density and the need for cryogenic storage would require changes in aircraft design, as well as new refueling and storage infrastructure at airports. More projects – 130 in total in 2018 – are in development for the direct use of electricity than for pure hydrogen, mostly for urban air taxis (Ahluwalia et al. 2021).

However, direct electrification also faces challenges, specifically relating to battery weight and costs.

In contrast, hydrogen-based liquid fuels would require no changes to design or refueling infrastructure at airports. Synthetic fuels based on electrolytic hydrogen (so-called power-to-liquid) are estimated to be four to six times more expensive than conventional jet fuel currently.

Fuel represents a large share of the total costs of operating aircraft so this would significantly increase the operating costs and, presumably, ticket prices. This would be the case regardless of the cost of conventional jet fuel, which could itself become

more expensive due to carbon pricing or other policies to reduce emissions. Estimates of the CO_2 price that would be needed to encourage a shift to power-to-liquids in aviation in the long term vary widely, from USD 115/tCO_2 to USD 660/tCO_2, with the lower value accounting for the possible value provided to the wider energy system via the electricity grid. Given the lack of other alternatives, most estimates place these costs among the higher abatement costs to complete the transition to a low-carbon energy system.

As with biofuels, the use of hydrogen-based fuels in aviation could be promoted through a target for blend shares. Even a modest target could help to demonstrate feasibility and support the scaling up of production. The standards development organization, ASTM, currently sets blending limits for alternative fuels that vary by fuel from as low as 10% to up to 90%. These might provide a helpful reference point for public and private decision makers to set upper bounds and could be updated as new engine technology emerges.

Besides on-board use of hydrogen in aviation, hydrogen is already used today in a few auxiliary power units that generate electricity when the jet engine is not running. Such units, which usually run on natural gas, can account for up to 20% of ground aircraft emissions.

9 Hydrogen for Power Generation and Electricity Storage

Hydrogen plays a negligible role in the power sector today: it accounts for less than 0.2% of electricity generation. This is linked mostly to the use of gases from the steel industry, petrochemical plants, and refineries. But there is potential for this to change in the future. Co-firing of ammonia could reduce the carbon intensity of existing conventional coal power plants, and hydrogen-fired gas turbines and combined-cycle gas turbines could be a source of flexibility in electricity systems with increasing shares of variable renewables. In the form of compressed gas, ammonia or synthetic methane, hydrogen could also become a long-term storage option to balance seasonal variations in electricity demand or generation from renewables (Elberry et al. 2021).

Although pure hydrogen does not generally feature as a fuel in power generation today, there are small-scale exceptions. For example, a 12 MW hydrogen-fired combined-cycle gas turbine in Italy uses hydrogen from a nearby petrochemical complex, while in Kobe, Japan, a hydrogen-fired gas turbine is providing heat (2.8 watts thermal) and electricity (1.1 MWe) to a local community. Somewhat more common is the use of hydrogen-rich gases from steel mills, petrochemical plants and refineries. Reciprocating gas engines today can handle gases with a hydrogen content of up to 70% (on a volumetric basis), 53 while in the future gas engines should be able to operate on even 100% hydrogen. Gas turbines also have the capability to run on hydrogen-rich gases. In Korea a 40 MW gas turbine at a refinery has run on gases with a hydrogen content of up to 95% for 20 years.
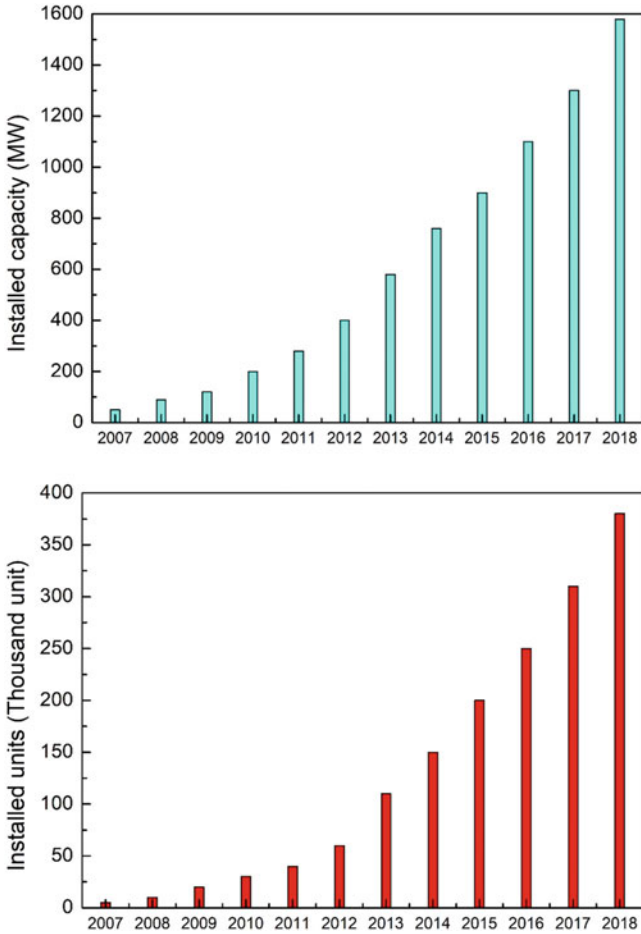
Fig. 19 Development of global stationary fuel cell capacity, 2007–18

Fuel cells are a further option to convert hydrogen into electricity and heat, producing water and no direct emissions. They can achieve high electric efficiencies of over 60% and reveal a higher efficiency in part load than full load, which makes them particularly attractive for flexible operations such as load balancing.

Global installed stationary fuel cell capacity has been rapidly growing over the last ten years, reaching almost 1.6 GW in 2018 (Fig. 19), although only around 70 MW uses hydrogen as fuel; most of the existing fuel cells today run on natural gas.

The number of globally installed fuel cell units is around 363,000, largely dominated by micro co-generation systems. The Japanese ENE-FARM initiative accounts for the majority, with around 276,000 micro co-generation systems, but represents only 12% of the installed capacity at 193 MW. Outside Japan, the

residential fuel cell market is also growing in Germany, driven by the KfW433 support program with around 1900 funding approvals by November 2018. Larger fuel cell systems above 100 kW to 2.4 MW are still almost exclusively deployed in Korea and the United States, with installed capacities of 300 MW and 150 MW, respectively. A further growing market for fuel cells is the provision of back-up power and off-grid electricity.

Very few countries have stated explicit targets for the use of hydrogen or hydrogen-based fuels in the power sector. Japan is one of the few exceptions: it aims to reach 1 GW of power capacity based on hydrogen by 2030, corresponding to an annual hydrogen consumption of 0.3 MtH2, rising to 15–30 GW in the longer term, corresponding to annual hydrogen use of 15–30 MtH2. Korea is another exception: its hydrogen roadmap sets a target of 1.5 GW installed fuel cell capacity in the power sector by 2022, and 15 GW by 2040. A number of countries have, however, recognized the potential of hydrogen as a low-carbon option for power and heat generation.

Research and pilot projects to introduce hydrogen and ammonia as fuel for gas turbines and coal power plants are being pursued in Japan. An existing 440 MW combined-cycle gas turbine (CCGT) plant is being converted from natural gas to hydrogen in the Netherlands, and ammonia is being considered for long-term storage there; it would be reconverted into hydrogen and nitrogen before combustion of the hydrogen in the gas turbine. The Port Lincoln Green Hydrogen Project under construction in Australia includes a 30 MW electrolyzer plant and an ammonia production facility, as well as a 10 MW hydrogen-fired gas turbine and a 5 MW hydrogen fuel cell, which will supply balancing services to the grid and the ammonia plant. The facility will also support to two new solar farms, as well as a nearby micro-grid which will be utilized by local aqua agriculturists who have been affected by ageing back-up power generation.

Hydrogen and hydrogen-based fuels such as ammonia and synthetic natural gas can be fuels for power generation. Ammonia can be co-fired in coal-fired power plants to reduce coal usage and reduce the carbon footprint of these plants; if low carbon, it would also reduce overall emissions. Hydrogen and ammonia can also be used as fuels in gas turbines, CCGTs or fuel cells, thus providing a flexible and potentially low-carbon generation option. Hydrogen-based fuels are also options for large-scale and long-term energy storage to balance seasonal variations in electricity demand or variable renewable power generation.

In 2017 the Japanese Chugoku Electric Power Corporation successfully demonstrated the co-firing of ammonia and coal, with a 1% share of ammonia (in terms of total energy content) at one of their commercial coal power stations (120 MW). Using ammonia as fuel raises concerns about an increase in NOx emissions, but the demonstration managed to keep them within the usual limits and to avoid any ammonia slip into exhaust gas. Higher blending shares of up to 20% ammonia in energy terms might be feasible with only minor adjustments to a coal power plant. In smaller furnaces with a capacity of 10 MW thermal, blending shares of 20% ammonia have been achieved without problems, and in particular without any slippage of ammonia into exhaust gas.

The economics of substituting coal with ammonia depend on the availability of low-cost ammonia, but ammonia could help to reduce emissions if produced from low-carbon hydrogen. By 2030 around 1250 GW of coal power plants worldwide that are currently in operation or under construction could not only still be in service but could also still have a remaining lifetime of at least 20 years. Co-firing with a 20% share of ammonia could reduce the 6 $GtCO_2$/yr annual emissions of these coal plants by 1.2 $GtCO_2$, provided that the ammonia was produced from low-carbon hydrogen. Reaching a 20% blending share would result in an annual ammonia demand of 670 Mt, more than three times today's global ammonia production, which in turn would require 120 MtH_2.

Hydrogen can be used as a fuel in gas turbines and CCGTs. Most existing gas turbine designs can already handle a hydrogen share of 3–5% and some can handle shares of 30% or higher.

The industry is confident that it will be able to provide standard turbines that are able to run entirely on hydrogen by 2030.

Ammonia is another potential fuel for gas turbines. The direct use of ammonia has been successfully demonstrated in micro gas turbines with a power capacity of up to 300 kW. In larger gas turbines above 2 MW, the slow reaction kinetics of ammonia with air, the flame stability and the NOx emissions are issues still being investigated by researchers. Instead of directly burning ammonia, an alternative approach is to reconvert the ammonia first into hydrogen and nitrogen, to burn hydrogen in the combustor of the gas turbine. The heat required for decomposing (or cracking) the ammonia at temperature levels of 600–1000 °C (the temperature depends on the catalyst) can be supplied by the gas turbine, though this slightly reduces the electricity generation efficiency of the overall process.

Fuel cells can also be used as a flexible power generation technology. With electric efficiencies of 50–60% (lower range today, upper future potential) being in a similar range to those of CCGTs, the choice between fuel cells and CCGTs in economic terms largely depends on their capital costs. It is, however, worth noting that fuel cell stacks today still suffer from a shorter technical lifetime than gas turbines (10,000 to 40,000 hours of operation), and that stationary fuel cells today typically have a smaller power output (up to 50 MW for the largest fuel cell power plants), which makes them most suitable for distributed generation. For comparison, CCGT units can reach capacities of 400 MW. The heat produced by the fuel cell while generating power can be used to provide an additional revenue stream. Future cost reductions for fuel cells will depend on future deployment levels and the learning effects and economies of scale that follow from this. On optimistic assumptions, CAPEX for hydrogen fuel cells may fall to USD 425/kW by 2030 compared to USD 1600/kW for a 1 MW PEMFC unit today or USD 1000/kW for a CCGT today.

Hydrogen and ammonia could offer low-carbon flexibility for electricity systems with increasing shares of VRE. Alternative low-carbon flexible generation options are natural gas-fired power plants equipped with CCUS and biogas power plants. Both alternatives are characterized by higher capital costs per unit of power than needed for a hydrogen-fired CCGT power plant, due to the additional capture equipment needed for CCUS and the typically smaller scale of biogas power plants.

Fig. 20 Break even for
hydrogen CCGT against
other flexible power
generation options
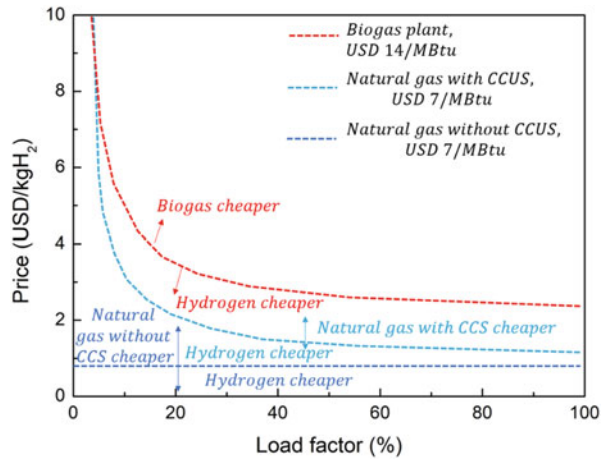
The capital cost advantage of the hydrogen option is more pronounced when the load
factor is low (Fig. 20), and it often is low in systems with high shares of VRE. At a
capacity factor of 15%, low-carbon hydrogen would become competitive with
electricity generation from natural gas with CCS at hydrogen prices of USD 2.5/
kgH_2, if the gas price is USD 7/MBtu.

The competitiveness of hydrogen-fired power plants with natural gas-fired power
generation for load balancing and peak load generation depends on the gas price and
the potential level of carbon prices. Looking, for example, at a load factor of 15%
and a natural gas price of USD 7/MBtu, the CO_2 price would have to be USD
100/tCO_2 to make hydrogen-fired power generation at a hydrogen price of USD 1.5/
kgH_2 competitive with natural gas. If the hydrogen price was USD 2/kg H2, the CO_2
price would have to be USD 175/tCO_2 to make electricity from hydrogen compet-
itive against natural gas.

For illustrative purposes, if 1% of the globally installed gas-fired power capacity
(or 25 GW) was fired by hydrogen (or ammonia) in 2030, this would result in annual
electricity generation of around 90 TWh (40% load factor) and hydrogen demand of
4.5 MtH_2 (or 30 Mt. of ammonia). This would help to scale up demand and the
supply infrastructure for hydrogen, since the annual hydrogen demand of 25 GW of
hydrogen power plants would correspond to the annual consumption of around
23 million fuel cell vehicles. Even a single 500 MW power plant would create a
hydrogen demand equivalent to 455,000 fuel cell vehicles or the heat demand of
221,000 homes in the United Kingdom and might therefore provide an opportunity
to create a hub for other potential hydrogen users, such as transport or buildings.

The integration of increasing shares of VRE sources in the electricity system
requires a more flexible electricity system. High shares of renewables can create a
need for long-term and seasonal storage, for example to provide electricity during
periods of several days with very little wind and or sunshine.

Hydrogen and hydrogen-based fuels (such as methane, liquid organic hydrogen
carriers [LOHCs] and ammonia produced from electricity via electrolysis) are

potential options for long-term and large-scale storage of energy. Salt caverns are the best choice for the underground storage of pure hydrogen because of their tightness and low risk of contamination. Alternative underground hydrogen storage options such as pore storage and storage in depleted oil and gas fields are also being investigated. Converting electricity into methane via power-to-gas is a further long-term storage option, and one which could take advantage of the existing transport and storage infrastructure for natural gas. Around 70 power-to-gas projects to produce methane are in operation today, most of them in Europe. Storing electricity in the form of ammonia is another long-term and large-scale storage option. Large steel tanks are already commonly used in the fertilizer industry for storing ammonia.

Hydrogen-based storage options suffer from low round-trip efficiency: in the process of converting electricity through electrolysis into hydrogen and then hydrogen back into electricity, around 60% of the original electricity is lost, whereas for a lithium-ion battery the losses of a storage cycle are around 15% (Fig. 21).

Pumped-hydro storage facilities offer one alternative: they have been used for more than a century to store electricity for relatively long periods. Batteries offer another alternative, although they are unlikely to be used for long-term and large-scale storage because they suffer from self-discharge and because of the immense number of batteries that would be needed for large-scale storage. A single large, refrigerated liquid ammonia tank with a diameter of 50 meters and a height of 30 meters, as typically used in the fertilizer industry, can store energy amounting to 150 GWh, comparable to the annual electricity consumption of a city with a population of 100,000. To store the same amount of electricity with batteries would require around 1150 times the installation of the Australian

Hornsdale Battery Reserve, the largest lithium-ion battery storage today in the world with a capacity of 129 MWh.

All the alternatives have advantages and disadvantages. For shorter discharge durations below a few hours, hydrogen and ammonia are much more expensive than pumped-hydro storage or battery storage. With longer discharge durations, compressed hydrogen and ammonia become more attractive, benefitting from their relative low capital costs for energy storage volumes (the investment costs to develop underground salt caverns or storage tanks). Among the different storage technologies considered here, compressed hydrogen becomes the most economic option for discharge durations beyond 20–45 hours.

Hydrogen as an electricity storage option could also be combined with other uses of hydrogen in the interests of competitiveness. In the United States, for example, the Three-State Generation and Transmission utility is considering producing ammonia from electricity for the domestic fertilizer market. Situated in an area with low-cost electricity from wind, solar and hydropower, the project would use a reversible solid oxide electrolyzer cell (rSOEC) to produce hydrogen when the cost of electricity is less than USD 25/MWh (which is 85% of the time), turning it into ammonia for sale on the market, while storing some of it for electricity generation in the rSOEC during peak hours, thus improving its overall utilization rate. This approach may be an

Fig. 21 Levelised costs of
storage as a function of
discharge duration

Ammonia
Compressed hydrogen
CAES
PHES
Li − ion
CCGT with CCUS
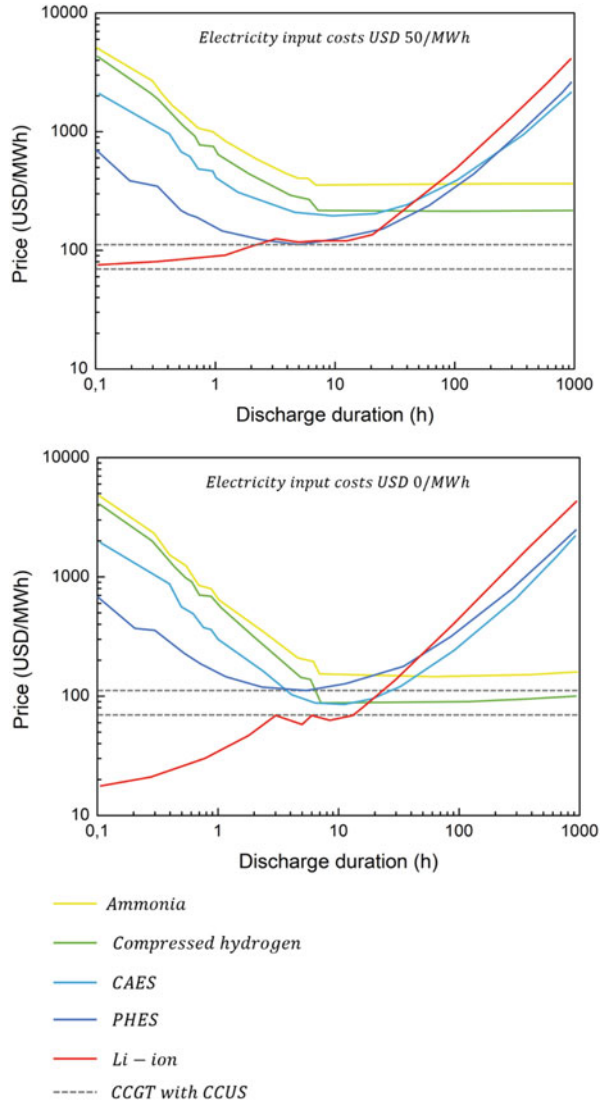
alternative to installing new electric generation resources that are expected only to be
needed during peak load times.

It may not be necessary to use large-scale storage of hydrogen-based fuels to
cover the full storage cycle, i.e. taking electricity as input and converting it in the end
back into electricity.

Instead of filling long-term storage with hydrogen from domestic electricity,
hydrogen-based fuels can also be imported from other parts of the world with
seasonal surpluses of renewable electricity generation at that time, taking advantage
of complementary seasonal patterns of renewable electricity supply and electricity

demand. Depending on the frequency and scale of the imports, this could reduce the storage volumes needed in the importing region. The conversion back to electricity may also not always be needed. Stored methane, ammonia or hydrogen could be directly used as fuel to cover seasonal demands, such as for space heating.

10 Conclusions

The increased focus on reducing emissions to near zero by mid-century has brought into sharp relief the challenge of tackling hard-to-abate emissions sources. These emissions are in sectors and applications for which electricity is not currently the form of energy at the point of end use, and for which direct electricity-based solutions come with high costs or technical drawbacks.

Four-fifths of total final energy demand by end users today is for carbon-containing fuels, not electricity. In addition, much of the raw material for chemicals and other products contains carbon today and generate CO_2 emissions during their processing.

Hard-to-abate emissions sources include aviation, shipping, iron and steel production, chemicals manufacture, high-temperature industrial heat, long-distance and long-haul road transport and, especially in dense urban environments or off-grid, heat for buildings. Rapid technological transformations in these sectors have made limited progress in the face of the costs of low-carbon options, their infrastructure needs, the challenges they pose to established supply chains, and ingrained habits. While significant financial and political commitments will be necessary to realise deep emissions cuts, there is an increasing sense of urgency on the part of governments and companies about the need to start developing appropriate solutions. As a low-carbon chemical energy carrier, hydrogen is a leading option for reducing these hard-to-abate emissions because it can be stored, combusted and combined in chemical reactions in ways that are similar to natural gas, oil and coal. Hydrogen can also technically be converted to "drop-in" low-carbon replacements for today's fuels, which is particularly attractive for sectors with hard-to abate emissions, especially if there are limits to the direct use of biomass and CCUS.

While interest in hydrogen continues to be strongly linked with climate change ambition, there has been a noticeable broadening of the policy objectives to which hydrogen can contribute.

The benefits of hydrogen for energy security, local air pollution, economic development and energy access are now routinely cited.

Hydrogen can support energy security in several ways. When hydrogen is deployed alongside electricity infrastructure, electricity can be converted to hydrogen and back, or further converted to other fuels, making end users less dependent on specific energy resources and increasing the resilience of energy supplies. Hydrogen produced from fossil fuels with CCUS or from biomass can also increase the diversity of energy sources, especially in a low-carbon economy. If the right infrastructure is developed, it could be attractive in the future for countries to

diversify their economies by exporting low-carbon energy in the form of hydrogen and hydrogen-based fuels, or importing hydrogen to benefit from competition that restrains prices. Countries with high-quality resources for hydrogen production are widely dispersed around the globe, and many current energy exporting countries are also endowed with renewable resources that could produce hydrogen. In an ambitious low-carbon context, such hydrogen trade would effectively enable trade and storage of wind and sunshine between different regions to overcome seasonal differences. Lastly, hydrogen could provide an additional way for countries to store reserves of energy strategically in a highly electrified low-carbon world.

Using hydrogen instead of carbon-containing fuels in energy end uses could also reduce local air pollution, improving environmental and health outcomes. Urban air pollution concerns and its related health impacts are now major drivers of energy policy decisions, and governments are keenly interested in ways of reducing air pollution and improving air quality. When used in vehicles and heating appliances, hydrogen does not produce particulates or sulphur oxides or raise ground-level ozone. When used in a fuel cell, hydrogen does not produce nitrogen oxides.

Because hydrogen can be stored or used in a variety of sectors, converting electricity to hydrogen can help with the matching of variable energy supply and demand, both temporally and geographically, alongside alternatives such as pumped-storage hydropower, batteries and grid upgrades. If renewable power generation becomes sufficiently cheap and widespread, it can be used not only to provide low-carbon electricity, but also to create low-carbon hydrogen that can displace fossil fuels in transport, heating and industrial raw materials, and indeed almost any application not susceptible to electrification. All this makes hydrogen one of a suite of technologies that work well together to support the growth of low-carbon energy at the level of the overall energy system.

The question of cost is of course very important in this context. The cost of electricity is the single most significant factor in the cost of electrolytic hydrogen production, and recent sharp declines in solar and wind power costs have therefore reduced the real and expected prices of renewable hydrogen. For example, utility-scale solar photovoltaic (PV) capital costs are 75% lower than in 2010, and electricity from onshore wind is around one quarter cheaper today than it was ten years ago. This has led more potential end users to look closely at whether renewable hydrogen is becoming a competitive way to meet their needs and reduce their environmental impact. Recent investments include a project to use electrolysers for the generation of low-carbon hydrogen to displace a share of fossil fuel-based hydrogen in oil refining and fertiliser production.

References

Abdin Z, Zafaranloo A, Rafiee A et al (2020) Hydrogen as an energy vector. Renew Sustain Energy Rev 120:109620. https://doi.org/10.1016/j.rser.2019.109620

Ahluwalia RK, Peng JK, Wang X et al (2021) Performance and cost of fuel cells for urban air mobility. Int J Hydrog Energy 46(74):36917–36929. https://doi.org/10.1016/j.ijhydene.2021.08.211

Ausfelder F, Bazzanella A (2016) Hydrogen in the chemical industry. https://doi.org/10.1002/9783527674268.ch02

Aziz M, Zaini IN, Oda T et al (2017) Energy conservative brown coal conversion to hydrogen and power based on enhanced process integration: Integrated drying, coal direct chemical looping, combined cycle and hydrogenation. Int J Hydrog Energy 42(5):2904–2913. https://doi.org/10.1016/j.ijhydene.2016.10.060

Blanco H, Nijs W, Ruf J et al (2018) Potential for hydrogen and Power-to-Liquid in a low-carbon EU energy system using cost optimization. Appl Energy 232:617–639. https://doi.org/10.1016/j.apenergy.2018.09.216

Böhm M, Del Rey AF, Pagenkopf J et al (2022) Review and comparison of worldwide hydrogen activities in the rail sector with special focus on on-board storage and refueling technologies. Int J Hydrog Energy 47(89):38003–38017. https://doi.org/10.1016/j.ijhydene.2022.08.279

Boretti A (2021) There are hydrogen production pathways with better than green hydrogen economic and environmental costs. Int J Hydrog Energy 46(46):23988–23995. https://doi.org/10.1016/j.ijhydene.2021.04.182

Buttler A, Spliethoff H (2018) Current status of water electrolysis for energy storage, grid balancing and sector coupling via power-to-gas and power-to-liquids: a review. Renew Sustain Energy Rev 82(3):2440–2454. https://doi.org/10.1016/j.rser.2017.09.003

Cao L, Iris KM, Xiong X (2020) Biorenewable hydrogen production through biomass gasification: a review and future prospects. Environ Res 186:109547. https://doi.org/10.1016/j.envres.2020.109547

Cavaliere P (2019) Clean ironmaking and steelmaking processes. https://doi.org/10.1007/978-3-030-21209-4

Cavaliere P (2022) Hydrogen assisted direct reduction of iron oxides. Springer, Cham. https://doi.org/10.1007/978-3-030-98056-6

Cecere D, Giacomazzi E, Ingenito A (2014) A review on hydrogen industrial aerospace applications. Int J Hydrog Energy 39(20):10731–10747. https://doi.org/10.1016/j.ijhydene.2014.04.126

Chai WS, Bao Y, Jin P et al (2021) A review on ammonia, ammonia-hydrogen and ammonia-methane fuels. Renew Sustain Energy Rev 147:111254. https://doi.org/10.1016/j.rser.2021.111254

Dalena F, Senatore A, Marino A et al (2018) Methanol production and applications: an overview. https://doi.org/10.1016/B978-0-444-63903-5.00001-7

de-Troya JJ, Alvarez C, Fernández-Garrido C et al (2016) Analysing the possibilities of using fuel cells in ships. Int J Hydrog Energy 41(4):2853–2866. https://doi.org/10.1016/j.ijhydene.2015.11.145

Dincer I, Acar C (2016) A review on potential use of hydrogen in aviation applications. Int J Sustain Aviat 2(1):74–100. https://doi.org/10.1504/IJSA.2016.076077

Doucet G, Etievant C, Puyenchet C et al (2009) Hydrogen-based PEM auxiliary power unit. Int J Hydrog Energy 34(11):4983–4989. https://doi.org/10.1016/j.ijhydene.2008.12.029

Elberry AM, Thakur J, Santasalo-Aarnio A et al (2021) Large-scale compressed hydrogen storage as part of renewable electricity storage systems. Int J Hydrog Energy 46(29):15671–15690. https://doi.org/10.1016/j.ijhydene.2021.02.080

Elsherif M, Manan ZA, Kamsah MZ (2015) State-of-the-art of hydrogen management in refinery and industrial process plants. J Nat Gas Sci Eng 24:346–356. https://doi.org/10.1016/j.jngse.2015.03.046

Félix G, Quitian A, Rodríguez E et al (2017) Methods to calculate hydrogen consumption during hydrocracking experiments in batch reactors. Energy Fuels 11:11690–11697. https://doi.org/10.1021/acs.energyfuels.7b01878

Felseghi RA, Carcadea E, Raboaca MS et al (2019) Hydrogen fuel cell technology for the sustainable future of stationary applications. Energies 12(23):4593. https://doi.org/10.3390/en12234593

Giuliano A, Poletto M, Barletta D (2018) Pure hydrogen co-production by membrane technology in an IGCC power plant with carbon capture. Int J Hydrog Energy 43(41):19279–19292. https://doi.org/10.1016/j.ijhydene.2018.08.112

Gjorgievski VZ, Markovska N, Pukšec T et al (2021) Supporting the 2030 agenda for sustainable development: special issue dedicated to the conference on sustainable development of energy, water and environment systems 2019. Renew Sustain Energy Rev 143:110920. https://doi.org/10.1016/j.rser.2021.110920

Goel M, Sudhakar M, Shahi RV (2018) Carbon capture, storage and utilization-A possible climate change solution for energy industry. ISBN 9780367179083

Haseli Y (2018) Maximum conversion efficiency of hydrogen fuel cells. Int J Hydrog Energy 43(18):9015–9021. https://doi.org/10.1016/j.ijhydene.2018.03.076

Hienuki S, Hirayama M, Hirayama Y et al (2021) Public acceptance for the implementation of hydrogen self-refueling stations. Int J Hydrog Energy 46(72):35739–35749. https://doi.org/10.1016/j.ijhydene.2021.08.115

Hoelzen J, Silberhorn D, Zill T et al (2022) Hydrogen-powered aviation and its reliance on green hydrogen infrastructure–review and research gaps. Int J Hydrog Energy 47(5):3108–3130. https://doi.org/10.1016/j.ijhydene.2021.10.239

Hoffmann P (2012) Tomorrow's energy: hydrogen, fuel cells, and the prospects for a cleaner planet. https://www.jstor.org/stable/j.ctt5vjpvs

Jones J, Genovese A, Tob-Ogu A (2020) Hydrogen vehicles in urban logistics: a total cost of ownership analysis and some policy implications. Renew Sustain Energy Rev 119:109595. https://doi.org/10.1016/j.rser.2019.109595

Klerke A, Christensen CH, Nørskov JK et al (2008) Ammonia for hydrogen storage: challenges and opportunities. J Mater Chem 18:2304–2310. https://doi.org/10.1039/B720020J

Lewis D (2008) Hydrogen and its relationship with nuclear energy. Prog Nucl Energy 50(2–6):394–401. https://doi.org/10.1016/j.pnucene.2007.11.072

Mahant B, Linga P, Kumar R (2021) Hydrogen economy and role of Hythane as a bridging solution: a perspective review. Energy Fuels 19:15424–15454. https://doi.org/10.1021/acs.energyfuels.1c02404

Midilli A, Kucuk H, Topal ME (2021) A comprehensive review on hydrogen production from coal gasification: challenges and opportunities. Int J Hydrog Energy 46(5):25385–25412. https://doi.org/10.1016/j.ijhydene.2021.05.088

Oldenbroek V, Verhoef LA, Van Wijk AJM (2017) Fuel cell electric vehicle as a power plant: Fully renewable integrated transport and energy system design and analysis for smart city areas. Int J Hydrog Energy 42(12):8166–8196. https://doi.org/10.1016/j.ijhydene.2017.01.155

Onarheim K, Hannula I, Solantausta Y (2020) Hydrogen enhanced biofuels for transport via fast pyrolysis of biomass: a conceptual assessment. Energy 199:117337. https://doi.org/10.1016/j.energy.2020.117337

Pan Z, Chan WP, Veksha A et al (2019) Thermodynamic analyses of synthetic natural gas production via municipal solid waste gasification, high-temperature water electrolysis and methanation. Energy Conv Manag 202:112160. https://doi.org/10.1016/j.enconman.2019.112160

Rambhujun N, Salman MS, Wang T et al (2020) Renewable hydrogen for the chemical industry. MRS Energy Sustain 7:E33. https://doi.org/10.1557/mre.2020.33

Rau F, Herrmann A, Krause H et al (2017) Production of hydrogen by autothermal reforming of biogas. Energy Proc 120:294–301. https://doi.org/10.1016/j.egypro.2017.07.218

Sengodan S, Lan R, Humphreys J et al (2018) Advances in reforming and partial oxidation of hydrocarbons for hydrogen production and fuel cell applications. Renew Sustain Energy Rev 82(1):761–780. https://doi.org/10.1016/j.rser.2017.09.071

Speight JG (2016) Hydrogen in refineries. https://doi.org/10.1002/9783527674268.ch01

Staffell I, Scamman D, Abad AV et al (2019) The role of hydrogen and fuel cells in the global energy system. Energy Environ Sci 12:463–491. https://doi.org/10.1039/C8EE01157E

Temiz M, Dincer I (2021) Techno-economic analysis of green hydrogen ferries with a floating photovoltaic based marine fueling station. Energy Convers Manag 247:114760. https://doi.org/10.1016/j.enconman.2021.114760

Tsujimura T, Suzuki Y (2019) Development of a large-sized direct injection hydrogen engine for a stationary power generator. Int J Hydrog Energy 44(22):11355–11369. https://doi.org/10.1016/j.ijhydene.2018.09.178

Safety Issues and Regulations

1 Introduction

Many believe that hydrogen is particularly dangerous. There are some that think hydrogen energy is related to the hydrogen bomb. But hydrogen used as a fuel involves a simple chemical reaction involving the transfer of electrons to produce an electric current, while a hydrogen bomb requires a high temperature nuclear fusion reaction similar to that which occurs in our sun and other stars (Najjar 2013).

It is true that hydrogen has a wider range of flammability when compared to gasoline (Yang et al. 2021). A mixture as low as 4% hydrogen (or as high as 74%) will burn in air, while the fuel to air ratios for gasoline only range 1–7.6%. It also takes very little energy to ignite a hydrogen flame, about 20 micro-joules, compared to gasoline which requires 240 micro-joules. However, these hazardous characteristics are reduced by the fact that, as the lightest of all elements, hydrogen has a very small specific gravity.

Since the diffusion rate of a gas is inversely proportional to the square root of its specific gravity, the period of time in which hydrogen and oxygen are in a combustible mixture is much shorter than with other hydrocarbon fuels. The lighter the element, the more rapidly it disperses when it is released into the atmosphere. In a crash or accident where hydrogen is released, it rapidly disperses up and away from the ground and any combustible material within the area. Gasoline and other hydrocarbon fuels are heavier since the hydrogen is bonded to carbon, a much heavier element. When hydrocarbon fuels vaporize, their gases tend to sink rather than rise in the atmosphere. This allows burning gasoline to cover objects and burn them. In most accidents, hydrogen would be a more desirable fuel.

Hydrogen can be produced with multiple processes and energy sources; a color code nomenclature is becoming commonly used to facilitate discussion (Fig. 1).

GREY HYDROGEN is produced with fossil fuels (i.e. hydrogen produced from methane using steam methane reforming (SMR) or coal gasification). The use of

Fig. 1 Selected shades of hydrogen

grey hydrogen entails substantial CO_2 emissions, which makes these hydrogen technologies unsuitable for a route toward net-zero emissions (Hermesmann and Müller 2022).

During early stages of the energy transition, the use of BLUE HYDROGEN (i.e. grey hydrogen with carbon capture and storage [CCS]) could facilitate the growth of a hydrogen market. Around three-quarters of hydrogen is currently produced from natural gas. Retrofitting with CCS would allow the continued use of existing assets while still achieving lower GHG emissions. This is an option is to produce hydrogen with lower GHG emissions while reducing pressure on the renewable energy capacity installation rate to produce green hydrogen. Notably, industrial processes like steel production may require a continuous flow of hydrogen; blue hydrogen could be an initial solution while green hydrogen ramps up production and storage capacity to meet the continuous flow requirement.

However, blue hydrogen has limitations that have so far restricted its deployment: it uses finite resources, is exposed to fossil fuel price fluctuations, and does not support the goals of energy security.

Moreover, blue hydrogen faces social acceptance issues, as it is associated with additional costs for CO_2 transport and storage and requires monitoring of stored CO_2. In addition, CCS capture efficiencies are expected to reach 85–95% at best, which means that 5–15% of the CO_2 will still be emitted. And these high capture rates have yet to be achieved.

In sum, the carbon emissions from hydrogen generation could be reduced by CCS but not eliminated (Quarton and Samsatli 2020).

Moreover, these processes use methane, which brings leakages upstream, and methane is a much more potent GHG per molecule than CO_2. This means that while blue hydrogen could reduce CO_2 emissions, it does not meet the requirements of a net-zero future. For these reasons, blue hydrogen should be seen only as a short-term transition to facilitate the uptake of green hydrogen on the path to net-zero emissions.

TURQUOISE HYDROGEN combines the use of natural gas as feedstock with no CO_2 production.

Through the process of pyrolysis, the carbon in the methane becomes solid carbon black. A market for carbon black already exists, which provides an additional revenue stream. Carbon black can be more easily stored than gaseous CO_2. At the moment, turquoise hydrogen is still at the pilot stage.

Among the different shades of hydrogen, GREEN HYDROGEN – meaning hydrogen produced from renewable energy – is the most suitable one for a fully sustainable energy transition. The most established technology options for producing green hydrogen are water electrolysis fueled by renewable electricity. This technology is the focus of this report. Other renewables-based solutions to produce hydrogen exist.

However, except for SMR with biogases, these are not mature technologies at commercial scale yet. Green hydrogen production through electrolysis is consistent with the net-zero route, allows the exploitation of synergies from sector coupling, thus decreasing technology costs and providing flexibility to the power system. Low VRE costs and technological improvement are decreasing the cost of production of green hydrogen. For these reasons, green hydrogen from water electrolysis has been gaining increased interest.

But policy makers should design policy using an objective measure of impact based on life-cycle greenhouse gas (GHG) emissions, especially since there might be cases that do not fully fall under one color (e.g. mixed hydrogen sources, electrolysis with grid electricity).

1.1 Drivers for Hydrogen Penetration

There have been several waves of interest in hydrogen in the past. These were mostly driven by oil price shocks, concerns about peak oil demand or air pollution, and research on alternative fuels. Hydrogen can contribute to energy security by providing another energy carrier with different supply chains, producers and markets; this can diversify the energy mix and improve the resilience of the system. Hydrogen can also reduce air pollution when used in fuel cells, with no emissions other than water. It can promote economic growth and job creation given the large investment needed to develop it as an energy carrier from an industrial feedstock.

As a result, more and more energy scenarios are giving green hydrogen a prominent role, albeit with significantly different volumes of penetration (Quarton et al. 2020). The new wave of interest is focused on delivering low-carbon solutions and additional benefits that only green hydrogen can provide. The drivers for green hydrogen include:

– Low variable renewable energy (VRE) electricity costs. The major cost driver for green hydrogen is the cost of electricity. The price of electricity procured from solar PV and onshore wind plants has decreased substantially in the last decade. In 2018, solar energy was contracted at a global average price of 56 USD/MWh, compared with 250 in 2018. Onshore wind prices also fell during

that period, from 75 USD/MWh in 2010 to 48 in 2018. New record-low prices were marked in 2019 and 2020 around the world: solar PV was contracted at USD 13.12/MWh in Portugal and USD 13.5/MWh in the United Arab Emirates (Abu Dhabi); onshore wind was contracted at USD 21.3/MWh in Saudi Arabia while in Brazil, prices ranged between USD 20.5 and 21.5/MWh. With the continuously decreasing costs of solar photovoltaic and wind electricity, the production of green hydrogen is increasingly economically attractive.

– Technologies ready to scale up. Many of the components in the hydrogen value chain have already been deployed on a small scale and are ready for commercialization, now requiring investment to scale up. The capital cost of electrolysis has fallen by 60% since 2010, resulting in a decrease of hydrogen cost from a range of USD 10–15/kg to as low as USD 4–6/kg in that period. Many strategies exist to bring down costs further and support a wider adoption of hydrogen. The cost of fuel cells for vehicles has decreased by at least 70% since 2006. While some technologies have not been demonstrated at scale yet (such as ammonia-fueled ships), scaling up green hydrogen could make those pathways more attractive as production costs decrease.

– Benefits for the power system. As the share of VRE rapidly increases in various markets around the world, the power system will need more flexibility. The electrolyzers used to produce green hydrogen can be designed as flexible resources that can quickly ramp up or down to compensate for fluctuations in VRE production, by reacting to electricity prices. Green hydrogen can be stored for long periods and can be used in periods when VRE is not available for power generation with stationary fuel cells or hydrogen-ready gas turbines. Flexible resources can reduce VRE curtailment, stabilize wholesale market prices and reduce the hours with zero or below zero electricity prices (or negative price), which increases the investment recovery for renewable generators and facilitates their expansion. Finally, hydrogen is suitable for long-term, seasonal energy storage, complementing pumped-storage hydropower plants. Green hydrogen thus supports the integration of higher shares of VRE into the grid, increasing system efficiency and cost-effectiveness.

– Government objectives for net-zero energy systems. By mid-2020, seven countries had already adopted net-zero GHG emission targets in legislation, and 15 others had proposed similar legislation or policy documents. In total, more than 120 countries have announced net-zero emissions goals. Among them is the People's Republic of China (hereafter "China"), the largest GHG emitter, which recently pledged to cut its net carbon emissions to zero within 40 years. While these net-zero commitments have still to be transformed into practical actions, they will require cutting emissions in the "hard-to-abate" sectors where green hydrogen can play an important role.

– Broader use of hydrogen. Previous waves of interest in hydrogen were focused mainly on expanding its use in fuel cell electric vehicles (FCEVs). In contrast, the new interest covers many possible green hydrogens uses across the entire economy, including the additional conversion of hydrogen to other energy carriers and products, such as ammonia, methanol and synthetic liquids. These uses can

increase the future demand for hydrogen and can take advantage of possible synergies to decrease costs in the green hydrogen value chain. Green hydrogen can, in fact, improve industrial competitiveness, not only for the countries that establish technology leadership in its deployment, but also by providing an opportunity for existing industries to have a role in a low-carbon future.

Countries with large renewable resources could derive major economic benefits by becoming net exporters of green hydrogen in a global green hydrogen economy.

– Interest of multiple stakeholders. As a result of all the above points, interest in hydrogen is now widespread in both public and private institutions.

These include energy utilities, steel makers, chemical companies, port authorities, car and aircraft manufacturers, shipowners and airlines, multiple jurisdictions and countries aiming to use their renewable resources for export or to use hydrogen to improve their own energy security.

These many players have also created partnerships and ongoing initiatives to foster collaboration and coordination of efforts.

However, green hydrogen still faces barriers.

2   Barriers to the Penetration

Green hydrogen faces barriers that prevent its full contribution to the energy transformation. Barriers include those that apply to all shades of hydrogen, such as the lack of dedicated infrastructure (e.g. transport and storage infrastructure), and those mainly related to the production stage of electrolysis, faced only by green hydrogen (e.g. energy losses, lack of value recognition, challenges ensuring sustainability and high production costs).

– HIGH PRODUCTION COSTS Green hydrogen produced using electricity from an average VRE plant in 2019 would be two to three times more expensive than grey hydrogen. In addition, adopting green hydrogen technologies for end uses can be expensive. Vehicles with fuel cells and hydrogen tanks cost at least 1.5 to 2 times more than their fossil fuel counterparts. Similarly, synthetic fuels for aviation are today, even at the best sites in the world, up to eight times more expensive than fossil jet fuel (Lemus and Duart 2010).
– LACK OF DEDICATED INFRASTRUCTURE. Hydrogen has to date been produced close to where it is used, with limited dedicated transport infrastructure. There are only about 5000 kilometers (km) of hydrogen transmission pipelines around the world, compared with more than three million km for natural gas. There are 470 hydrogen refueling stations around the world, compared with more than 200,000 gasoline and diesel refueling stations in the United States and the European Union. Natural gas infrastructure could be repurposed for hydrogen, but not all regions of the world have existing infrastructure. Conversely, synthetic fuels made from green hydrogen may be able to use existing infrastructure, though it might need to be expanded (Kurtz et al. 2019).

– ENERGY LOSSES. Green hydrogen incurs significant energy losses at each stage of the value chain. About 30–35% of the energy used to produce hydrogen through electrolysis is lost. In addition, the conversion of hydrogen to other carriers (such as ammonia) can result in 13–25% energy loss, and transporting hydrogen requires additional energy inputs, which are typically equivalent to 10–12% of the energy of the hydrogen itself. Using hydrogen in fuel cells can lead to an additional 40–50% energy loss. The total energy loss will depend on the final use of hydrogen. The higher the energy losses, the more renewable electricity capacity is needed to produce green hydrogen (Kovac et al. 2019).

The key issue, however, is not the total capacity needed, since global renewable potential is in orders of magnitude higher than the hydrogen demand, and green hydrogen developers are likely to first select areas with abundant renewable energy resources. The key issue is whether the annual pace of development of the solar and wind potential will be fast enough to meet the needs for both the electrification of end-uses and the development of a global supply chain in green hydrogen, and the cost that this additional capacity will entail.

– LACK OF VALUE RECOGNITION. There is no green hydrogen market, no green steel, no green shipping fuel and basically no valuation of the lower GHG emissions that green hydrogen can deliver. Hydrogen is not even counted in official energy statistics of total final energy consumption, and there are no internationally recognised ways of differentiating green from grey hydrogen. At the same time, the lack of targets or incentives to promote the use of green products inhibits many of the possible downstream uses for green hydrogen. This limits the demand for green hydrogen.
– NEED TO ENSURE SUSTAINABILITY. Electricity can be supplied from a renewable energy plant directly connected to the electrolyzer, from the grid, or from a mix of the two. Using only electricity from a renewable energy plant ensures that the hydrogen is "green" in any given moment (Dincer and Acar 2015).

Grid-connected electrolyzers can produce for more hours, reducing the cost of hydrogen. However, grid electricity may include electricity produced from fossil fuel plants, so any CO_2 emissions associated with that electricity will have to be considered when evaluating the sustainability of hydrogen. As a result, for producers of hydrogen from electrolysis, the amount of fossil fuel-generated electricity can become a barrier, in particular if the relative carbon emissions are measured based on national emission factors.

For hydrogen from electrolysis to have lower overall emissions than grey hydrogen, CO_2 emissions per unit of electricity need to be lower than 190 grams of CO_2 per kilowatt hour (gCO_2/kWh). Only a few countries (mostly benefiting from hydropower) have average CO_2 emissions per kWh below that threshold and thus can ensure the sustainability of electrolytic hydrogen. Most other countries are currently above that threshold.

However, electrolyzers can be designed to be flexible demand-side resources and can be ramped down or turned off when the national power mix is above a certain threshold of CO_2 emissions, if tracked, and then turned back on when renewable production is higher, and in particular when VRE production would otherwise be curtailed. In general, low electricity prices are a proxy for high renewable energy production, so electricity prices may be naturally the signal for electrolyzer activities. Moreover, when electricity prices are too high to produce competitive hydrogen, the electrolyzer would shut down anyway. The significant (for some countries) and increasing renewable energy share of electricity production will also decrease the carbon footprint of electrolytic hydrogen production.

A hybrid model can also be used, where off-grid VRE generation is the main source of electricity, but grid electricity can top up production to decrease the impact of initial investment costs while causing only a small increase in the carbon footprint of the electrolysis plant.

Power purchase agreements with grid connected VRE plants may also ensure the sustainability of electricity consumption and at the same time make green hydrogen an additional driver for the decarbonization of the power grid.

3   Safety Issues

Hydrogen explosions can be powerful when they occur, but they are rare. Hydrogen must be in a confined space for an explosion to occur. In the open, it is difficult to cause a hydrogen explosion without using heavy blasting caps (Tanaka et al. 2007).

While hydrogen safety issues depend on the application, they can be classified into two main categories: material properties-related issues and handling-related issues. For example, the primary hazards include hydrogen release and subsequent ignition. Immediate ignition of hydrogen usually causes hydrogen jet fires, whereas delayed ignition of hydrogen leads to the explosion, which is the result of deflagration and/or detonation. There are direct and indirect impacts on humans, the environment, structures, and properties due to these accidents and their consequences, including jet fire heat flux, thermal radiation, explosion, overpressure, asphyxiation due to oxygen replacement, projectile damage due to high-pressure hydrogen from a ruptured containment vessel (Abohamzeh et al. 2021).

Understanding the safety aspects of hydrogen is essential to achieve reliable, safe, and effective use of hydrogen as a clean energy source. Numerous projects have worked on hydrogen safety issues, and a summary of these projects is given by the International Association for Hydrogen Safety (IA HySAFE).

While combustion properties of hydrogen, such as its wide range of flammability, low minimum ignition energy, and high burning velocity, make it an excellent alternative fuel, due to these properties, there are various safety aspects in hydrogen utilization and storage. As shown in Table 1, hydrogen has a very low boiling point, and density, and a relatively low ignition temperature of 585 °C, whereas its diffusion coefficient in the air is high. Furthermore, hydrogen has low ignition

Table 1 Physical properties of hydrogen

Property	Liquid	Gaseous
Density (gas)	708 (kg/m^3 @-273 °C))	0.0899 (kg/m^3 @ 0 °C))
Molecular weight		2.01594 (g/Mol)
Boiling temperature	-252.76 °C	–
Diffusion coefficient	–	0.61 cm^2/s
Flammable range	–	4–75% concentration in air
Heat of combustion	–	142 kJ/g
Heat of vaporization	447 (kJ/g @-273 °C)	–
Thermal conductivity	–	0.019 (kJ/kg @ 25 °C)
Minimum ignition energy	–	0.017 MJ
Ignition temperature	–	585 °C
Heat capacity	14.3 (kJ/kg °C @25 °C)	8.1 (kJ/kg °C @-256 °C)

energy of 0.017 MJ and high latent heat of combustion of 141.6 MJ/kg. The detonation of hydrogen can occur at a volumetric concentration ratio of hydrogen to air as low as 4% and as high as 75%. On the other hand, hydrogen has a high permeability through many materials. These properties make safety measures to be very important for hydrogen. Accurate hydrogen detection techniques are critical to measuring hydrogen concentration, particularly in accidental leakage events, since hydrogen is a colorless, odorless, and tasteless, flammable gas that cannot be noticed by human senses.

As schematically shown in Fig. 2, the hazardous issues encountered in hydrogen applications and facilities can be classified as (i) material properties-related issues and (ii) hydrogen handling-related issues.

3.1 Material Properties-Related Safety Aspects

Hydrogen embrittlement (HE) happens when metals are exposed to hydrogen, leading to degradation of metals' mechanical properties, failure, and leaks (Dwivedi and Vishwakarma 2018). The process commonly gains importance when it results in cracking, particularly for hydrogen storage and transmission pipelines. This occurs by applying sufficient stress on the object, which is embrittled with hydrogen. Both applied service and residual stresses generated during fabrication operations can cause such sufficient stress states. Embrittlement is a complicated phenomenon and dependent on metal purity, surface conditions, exposure time to H$_2$, and environmental pressure and temperature. With enhancing hydrogen purity, the vulnerability of steel to embrittlement increases. The influence of partial pressure of hydrogen on embrittlement was investigated. They were conducted tests of disk rapture on AISI 321 steel and observed that the highest embrittlement happens in the partial pressure range of 20–100 bar. Furthermore, the investigation of X100, X65, and X52 steel behaviour under a high-pressure hydrogen gas environment revealed that increasing
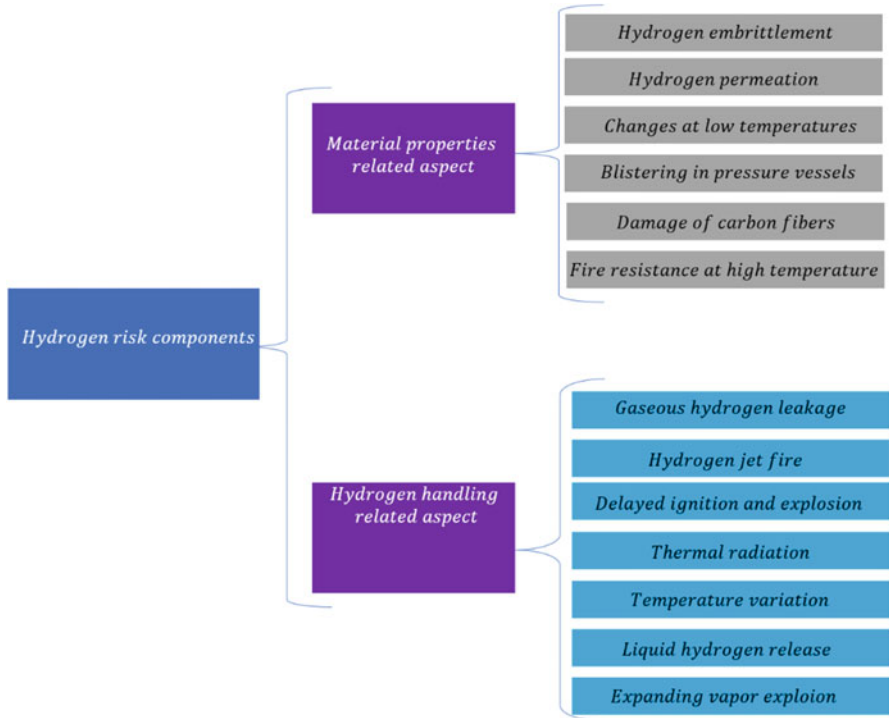
Fig. 2 Safety issues concerning the application of hydrogen

alloy strength and hydrogen pressure results in larger embrittlement. The stress concentration in crack and notch roots decreases when yield strength is lower. A key issue regarding hydrogen embrittlement is the dependency of this phenomenon on the exposure time which should be considered in the test procedures.

Permeability is one of the material considerations within the usage of hydrogen. Due to the small size of hydrogen molecules, hydrogen can migrate through permeable materials or embrittle them over time. Within the framework of compressed gaseous hydrogen storage systems, permeation can be determined as the rate of hydrogen flux passing through the walls or gaps of tanks, interface materials, or piping. It is a current safety issue in standardization and regulatory activities. Permeation increases with increasing material ageing, temperature, and storage pressure. The permeation rate in the pressure vessels of Type I, II, and III is insignificant. Losses of hydrogen might happen within several years, and it does not cause any safety matter for daily applications. Nevertheless, it is a safety issue for pressure vessels with non-metallic (polymer) liners (pressure vessels of Type IV), which have higher rates of hydrogen permeation. Approaches were developed to calculate an upper limit for hydrogen permeation in automotive applications by investigating the hydrogen behavior during the release. Several issues such as level of safety, environmental scenarios, vehicle scenarios, and hydrogen dispersion

Table 2 Allowable hydrogen permeation rate from different sources

Source	Justification reference	New or simulated end of life container	Minimum testing temperature (°C)	Maximum allowable rate for hydrogen permeation (Nml/h/ L water capacity-except where indicated)
SAE J2579: 012009	–	Simulated end of life	55	150 NmL/min per standard vehicle
ACEA for EC hydrogen regulation	LLNL	New	20 +/− 10	10
JARI for UN ECE HFCV GTR	–	–	15	5
ISO/ TS15869: 2009 Option ii) Test E5	–	Simulated end of life	20	75 NmL/container
ISO/ TS15869: 2009 Option i) Test B16	JARI	New	Ambient	20@350 bar & 2.8@700 bar
HySafe Proposal	–	New	15	4.6
			20	6

behavior should be considered to estimate the allowable rate. The permeation rate is considerably restricted in new containers by the carbon fiber overwrap, while in the containers that are reaching the end of their lives, the substantial micro-cracking affects the resin/carbon fiber matrix, allowing the rise in the permeation of hydrogen (Okonkwo et al. 2023). The allowable hydrogen permeation rates presented in some standards and regulations are given in Table 2.

The most important considerations for materials behaviour at low temperatures are the transition from ductile to brittle, certain unusual modes of plastic deformation, and the effect of phase transformations in the crystalline structure on the elastic and mechanical properties of materials. Materials used in liquid hydrogen services are exposed to cryogenic temperatures, so in particular, for selecting the materials to be used in these services, these changes in the material properties should be considered (Qiu et al. 2021). The most important thermal characteristics for hydrogen services at cryogenic temperatures are low-temperature thermal contraction and low-temperature embrittlement. Various materials show the transition from ductile to brittle at low temperatures, which might result in the storage tank or pipe failure, leading to an accident. Such an accident due to low-temperature embrittlement took place in 1994 for a tank containing liquid natural gas in Cleveland, U.S. state of Ohio where a nearby tank collapsed that caused 200 to 400 injuries, 128 deaths, and huge property damage. Generally, most metals have room-temperature to liquefaction temperature of H_2, showing less than 1% contraction, while this value is between 1% and 2.5% for the most common structural plastic.

Pressure vessels of Type VI consist of carbon fibre composites overwrap, a polymer as the liner for sealing purposes, and at least one boss. Under high pressures, hydrogen gas is absorbed by a plastic liner, and if the depressurisation rate becomes higher than the rate of escaping the absorbed gas by diffusion, plastic liner blistering occurs. A model for the prediction of blistering in the hydrogen storage tank of Type IV has been developed. Their study provided showed a good agreement with the experimental data, so the prediction of the blistering as a function of depressurisation rate and liner thickness was presented through performing a parametric investigation. The required number of experiments can be decreased by the presented pre-selection approach for liner materials and designs in this model, resulting in reducing the expenses for developing hydrogen storage systems. A test rig was built to replicate liner blistering that allowed the detection of the liner failure. Both liner deformation and composite cracks were observed with the tomographic monitoring on collapsed samples. Based on their observations, the collapses happen at the interface of liner/composite in regions that are not efficiently bonded. It was found blistering in the hydrogen tank of Type IV depends on working conditions such as including dwell time at residual pressure level before emptying initial filling pressure, the emptying rate, and initial filling pressure. The main collapse after the decompression test resulted in a void of 1.54 mm high. After seven days, this amount decreased to 0.51 mm.

Pressured hydrogen vessels are equipped with a thermally activated pressure relief device (TPRD) that empties the vessels in case of elevated temperatures to reduce the chance of burst/explosion. The opening diameter in the case of TPRD activation has a significant impact on the safety release of hydrogen and, consequently, the hydrogen flame length. Although the installation of TPRD is necessary for preventing the catastrophic rupture of vehicular high-pressure hydrogen vessels, there is a risk of fire hazards for drivers as a result of the intended release of hydrogen from TPRD. The mitigation measures for the reduction of hydrogen fire risks caused by TPRD have been developed. The new design of TPRD, which was rotatable, provided the opportunity of adjusting the release direction of H_2 for the system, leading to minimising the hydrogen fire risks.

Regarding safety issues, verifying the activation of TPRD to release H_2 from the cylinder is required. A method for TPRD activation was developed. For the development of an uncomplicated approach to verify the activation of TPRD at post-fire accident sites, they performed an investigation on a verifying method based on measuring the concentration of hydrogen at the gas release port of TPRD, utilising an H_2 densitometer. They reported that in the case of using a catalytic combustion H_2 densitometer, it is possible to continuously measure the concentrations of hydrogen above 3000 ppm for approximately 24 h for cylinders of Type IV and approximately a month for cylinders of Type III.

The structures of composite pressure vessels are complicated, and their characteristics are dependent on several parameters. Designing a reliable pressure vessel that meets the safety considerations requires comprehensive knowledge on the physical basis of matrix cracking, delamination, fibre breaks, the influence of dome geometry on the composite vessel burst pressure, and the resistance

mechanism against various kinds of impact. They were numerically and experimentally analysed the damage mechanisms of carbon fibre. Further studies focused on the influence of repetitive and single impacts on burst pressure of glass fibre reinforced vessels, reporting a 47% reduction in burst pressure. However, the properties of composite materials change remarkably by fibre density, stacking procedure, and so forth. Thus, probabilistic approaches for the prediction of fibre failures can be an acceptable path forward.

Polymers and resins are considerably more susceptible to high temperatures compared to metallic materials. Thus, the maximum operating temperature is a safety concern for their use. Consequently, evaluation of the composite behaviour in fire and the fire protection mechanism is extremely important, in particular, for onboard applications. A bone-fire test was conducted on fully composite vessels, showing the pressure increase before leakage or bursting was small (up to 12.7%), and the bursting delay was between 6 and 12 min, which was not acceptable.

A further study applied a three-dimensional CFD model to evaluate the characteristics of heat transfer in 700 bar hydrogen composite vessels exposed to localised fire. They observed that during 600 s exposure to the localised fire, the rise in pressure and temperature is slow. The intensity of convective heat transfer in the internal hydrogen is higher than conductive heat transfer in the walls of vessels when the area of flame impingement is far from the pressure relief device (PRD). Furthermore, the heat transfer in Type III vessels is faster compared to Type IV vessels. In another study, a Type III vessel was experimentally and numerically studied to understand the air and hydrogen effect in the filling media. They developed a three-dimensional model of the whole process of localised fire test and observed that with extending the time of exposure to the localised fire, the activation time of PRD increases.

3.2   Hydrogen Handling-Related Safety Aspects

The major handling hazards issues that can happen to liquid hydrogen and compressed hydrogen storage tanks during operations, often result in a loss of containment (LOC). A LOC is an uncontrolled or unplanned release of materials from primary containment (Skjold et al. 2017). Therefore, LOCs involve both spills and leakages. Table 3 presents a summary of the possible accident scenarios upon loss of containment for gaseous and liquid hydrogen.

Hydrogen's small molecular weight causes a high tendency leaking issue through pipelines or storage, which is a key safety issue. The hydrogen release may be due to damaged piping, loose-fitting, or a valve on the system. Hence, any small cracks or deformities within the vessel result in the rapid ejection of hydrogen gas. As a result, mixtures of hydrogen gas with atmospheric oxygen are formed over a wide range of concentrations in the range 4.0–75% v/v, resulting in the combustible mixture and 18–59% v/v causing explosive mixtures. Hydrogen release is followed by immediate ignition causing jet fires or a delayed ignition resulting in the explosion. The

Table 3 Accident scenarios upon loss of containment

	Consequences
Compressed H$_2$ storage	Fireball
	Overpressure generation
	Missile ejection
	Jet fire
	Flashfire
	Vapour cloud explosion (VCE)
	Gas puff (ignited)
	Gas dispersion
	Gas jet (ignited)
	Fire
Liquid hydrogen (LH$_2$)	Fireball
	Overpressure generation
	Missile ejection
	Jet fire
	Flashfire
	Vapour cloud explosion (VCE)
	Gas puff (ignited)
	Gas dispersion
	Gas jet (ignited)
	Fire
	Aerosol puff ignited
	Aerosol puff
	Two-phase jet
	Pool dispersion
	Pool ignited
	Pool formation

consequences of these events have a direct or indirect impact on humans, the environment, structures, and properties.

The hydrogen release without fire accidents is still a hazard issue, particularly in confined spaces, since it causes asphyxiation. This is because H$_2$, which is a non-toxic gas, replaces O$_2$, and hence oxygen concentration reduces below 19.5% by volume. The accumulation of hydrogen into closed spaces adjacent to the source then poses an asphyxiation hazard for the people being there. Recently, the CFD modelling of hydrogen dispersion within closed facilities was conducted to simulate the accumulation of helium (as a surrogate for H$_2$) within an enclosure representing a garage with real scale under a low rate of release. Because of the studied flow nature, different turbulence modelling methods (LES and RANS), as well as the laminar one, were investigated. Despite the gas release in low Reynolds, the formation of turbulent flow was observed. The results confirmed that the LES and RANS methods were able to provide the most accurate data for the distribution of gas within the facility, whereas more increased stratification was predicted by the laminar method at the phase of release.

It was applied CFD simulation to study the release and dispersion of un-ignited hydrogen from onboard storage with the pressure of 700 bar within a closed car park, which is ventilated naturally. The effect of leak direction angle and leak diameter on forming flammable clouds and the consequences for car park ventilation, first

responders, and vehicle passengers are discussed. The study considered a parking space with two opposing vents. The comparison between the release from three TPRD having different diameters of 0.50, 2.00, and 3.34 mm was conducted to understand the dispersion of gas, particularly the envelope formation dynamics for 4%, 2%, and 1% hydrogen volume. Based on their results, the TPRD release angle was revealed to possess consequences for the egress of passengers, showing the TPRD with a diameter of 0.5 mm was safer for 700 bar storage.

A possible scenario that happens after the release of hydrogen is immediate ignition that leads to a jet fire. A jet fire is a high-velocity turbulent flame that results from the combustion of fuel releasing in a certain direction with substantial momentum. For stored gaseous hydrogen in pressurised vessels, the pressure difference between the ambient environment and conditions within the vessel causes the high momentum of released fuel that quickly mixes with the turbulent ambient air. The ignition can be initiated by several sources such as sparks from electrical equipment and/or rapidly closing valves, electrostatic discharges, etc. Gaseous hydrogen store tanks for hydrogen fuel cell vehicles are pressurised between 350 and 700 bar, whereas other fuels such as Liquefied petroleum gas (LPG) store tanks in similar gas-powered vehicles are pressurised between 2.5 and 21 bar. Therefore, the risk of an accident or collision involving a hydrogen fuel cell vehicle may be catastrophic. This risk is further ameliorated in hydrogen fuel cell buses, which can carry up to 50 kg of hydrogen on board, as opposed to a hydrogen fuel cell car, which can carry up to 4 kg of hydrogen.

It is worth noting that a hydrogen fire burns clean with minimal smoke and soot yield, and hence a hydrogen flame may not be detectable or visible to the naked eye. Considering hydrogen flames have high velocity and high heat release rate, this presents an increased risk of fire growth and exposure to occupants as humans. Hence, the North American National Fire Protection Association (NFPA) has awarded hydrogen with a flammability rating of 4, the highest rating on the NFPA 704 flammability scale.

It was modelled hydrogen jet fire with high pressure applying a laminar flame let technique and LES approach and compared the results with the experimental test of large-scale vertical jet fire. The LES sensitivity analysis imposing at the nozzle exit showed that for 0–20% turbulence intensity, a restricted influence on the width and length of the flame was observed. Above 20%, increasing in turbulence intensity resulted in a reduction in the length of the flame and increasing the width of the flame. The most accurate results compared to experimental tests were obtained for a turbulence length scale of 7% equivalent diameter and a turbulence intensity equal to 25% for a finer grid.

It was performed a CFD study to determine the outcomes of hydrogen jet fires produced at pipelines of high-pressure hydrogen at a pipe rack structure in a processing plant. Using the Kameleon FireEx(KFX) code, they computed radiant heat, jet fire temperature, and heat flux distribution upon the complicated pipe rack structure configuration. They also analysed the consequence of thermal damages and presented the fire damages from large-scale jet fires at pipe rack structures. They were performed CFD numerical studies on the hydrogen jet fire from a hydrogen-

powered car within a tunnel. Various parameters, including the leakage location, the tunnel volume, transverse ventilation, longitudinal ventilation, leakage area, and the rate of hydrogen leakage, were studied. With increasing the rate of H_2 release, the rate of hydrogen diffusion and temperature rise increased within the tunnel. On the other hand, further hydrogen diffusion within the tunnel was inhibited with the excessive rate of leakage. With increasing the cross-sectional tunnel area, the rate of hydrogen diffusion decreased. The overall temperature in the tunnel can be efficiently reduced by longitudinal ventilation. However, the layer with a high temperature would be lowered under the safe height. Enough transverse and longitudinal ventilation is required within the tunnel for controlling hazards and avoiding the consequent disaster of the H_2 jet fire.

Another possible scenario after the release of hydrogen is a delay between release and ignition, which may cause an explosion. In this case, the hydrogen has sufficient time to be mixed with air before being ignited, and the consequence would be a flash fire or a vapour cloud explosion (VCE). The delayed ignition probability significantly differs from the release conditions. The hazardous effects of the continuous and instantaneous release of liquid hydrogen were studied. They concluded that for both cases, VCE has the highest harmful effects and can be considered as a basis for the determination of the safety distances from liquid hydrogen vessels since it is more destructive than jet fire and flash fire. In another study for the nozzle diameter of 12 mm and the pressure of 36 bar, the ignition of the flammable cloud was on the centreline of the jet at a position downstream of the releasing point where the mixture of air/hydrogen having a 30% volume of H_2. They measured the explosion overpressure at different positions and concluded that the highest overpressure was defined at a distance of 2.5 m and perpendicular to the point of ignition, which was equal to 0.08 bar. It was performed a numerical study to determine the worst-case ignition position of hydrogen jets with high pressure; 260 g/s at 36 bar, and 1000 and 8000 g/s at a pressure of 70 bar. They conducted a parametric investigation for identifying the position of ignition in proportion to the case with the highest overpressure (the worst scenario), leading to the development of a new methodology for the prediction of explosion strength from delayed ignition releases of high-pressure hydrogen.

There are risks of damage for equipment and structures exposed to thermal radiation and direct flames. A summary of the types of damage for different thermal radiation intensities is presented in Table 4. Thermal radiation from hydrogen has no significant effect on equipment and structures. However, exposure to thermal radiation from hydrogen fires can be extremely destructive. Hydrogen is flammable, and hence there is a risk of fire. Escaping hydrogen gas from the leak can lead to creating a jet flame, and thermal radiation from this flame might be substantial. Based on reports, several hydrogen failures in the delivery phase caused injuries, damage the neighbourhood's properties, and led to negative effects on human life.

As previously mentioned, the storage of hydrogen is in the liquid state at moderate pressure and low temperature or in the gaseous state at normal temperature and high pressure. In both cases, a substantial possible risk exists for the explosion of vessels containing hydrogen in the case of their exposure to thermal radiation or high

Table 4 Possible damages for structure exposed to thermal radiation

Thermal Radiation Intensity (kW/m^2)	Type of damage
4	Glass breakage (30 min exposure)
12.5–15	Piloted ignition of wood, melting of plastics (>30 min exposure)
18–20	Cable insulation degrades (>30 min exposure)
10 or 20	Ignition of fuel oil (120 or 40 s, respectively)
25–32	Unpiloted ignition of wood, steel deformation (>30 min exposure)
35–37.5	Process equipment and structural damage (including storage tanks) (>30 min exposure)
100	Steel structure collapse (>30 min exposure)

temperature. The exposure of hydrogen vessels to high thermal radiation may result in a considerable hazard potential for mechanical explosion. Commonly, the main sources of ignition can be neighbouring fires or electrostatic sparks caused by discharging of the content. These circumstances are recognised as domino effects because a primary coincidence creates other accidents making an accident's chain with intensified effects on the surroundings, leading to increasing temperature in the shell of the vessel and its content. As a result, the vessel explodes, and its content commonly ignited and burns in the fireball or jet fire form. Unlike storage tanks of gaseous hydrogen with high pressure, the operation of the ones containing liquid hydrogen is at low to moderate pressures lower than 20 bar. Consequently, the design of the wall is sensible to be based on less pressure resistance compared with the design for gaseous hydrogen. The engulfing of the container in the fire resulted in heating the metal and losing mechanical strength.

Compared with the liquid phases, which absorb considerable quantities of heat, the specific heat capacity of vapours is much lower, leading to the rise of the local temperature of the wall in the container part with vapour phase as a result of supplied heat, which makes its metal to weaken. The overheating of vessels in the case of the storage of liquid hydrogen cause interior temperatures to become more than the content boiling point, leading to the superheating of the liquid. The occurrence is noticed in the case of the existence of a nucleation site shortage in the liquid bulk. Nevertheless, above a specified temperature limit, the remaining fluid in the liquid phase is not possible any longer (superheat limit temperature or homogeneous nucleation limit). The fluctuations of random molecular density at that limit in the liquid bulk generate hole-like areas with molecular dimensions that might perform as bubbles. This finally results in the liquid explosive flash in the company of a severe shock wave propagating across the fluid and rupturing the vessel and the spill of the content. The travel of ruptured walls' missiles up to a hundred meters is probable, while a sphere (fireball) is formed by the flammable content to burn from the outer to inner layers.

A fast filling is required in the compressed gas filling process to achieve a satisfactory refuelling duration, close to that of conventional vehicles, which results in high gas temperature due to compressor work on gas for increasing its pressure.

On the other hand, for fueling the gas inside the vessel, the process of discharging is a cooling process. The mechanical characteristics of carbon fibres and epoxy resin would be seriously affected by temperature variations. At low temperatures, the fracture toughness of the epoxy resin matrices reduces dramatically, whereas, at high temperatures, composites interlaminar shear strength reduces seriously. Moreover, considerable thermal stresses are created in the composite layer and aluminium liner of the vessel. The structural integrity of the storage system might be jeopardised due to high temperatures, and in the long term, temperature variations of gas and tank have negative effects on the storage vessel's lifetime. Three thermodynamic phenomena attribute to this issue. The first phenomenon is transforming the hydrogen kinetic energy generated by a higher pressured tank into internal energy. The second phenomenon is increasing gas temperature due to passing the hydrogen through the dispenser throttling device, and the third phenomenon is continuous gas compression within the cylinder throughout the filling process when the gas with higher pressure enters from the fuelling station. Although some parts of the heat inside the cylinder transfer to the ambient, some amount of this heat is stored in the cylinder material.

Temperature rise in the filling process has been investigated in previous studies, showing both properties of tanks and filling conditions can affect the temperature increase. Type III pressure vessels reach lower temperatures during the refuelling process compared to Type IV and when the diameter of the hydrogen dispenser or nozzle is smaller, the maximum temperature is lower, and gas temperatures distribute more uniformly within the tank. Moreover, the increase in gas temperatures within the tank decreases by reducing the length to diameter ratio of the vessel. Regarding the filling conditions parameters, if the starting pressure in the refuelling process increases, the maximum temperature of the gas in the vessel decreases. Various studies showed that lower flow rate, ambient temperature, and inlet gas temperature result in a lower maximum temperature of the gas. There are still some doubts regarding the heat exchange between the tank solid components and the inside gas in the process of hydrogen vessels' on-road services (refuelling and holding under pressure). Furthermore, locations of temperature measurement points in onboard vessels have not still been specified in the available regulations and standards for hydrogen-fuelled cars.

Storage and transportation of hydrogen as a cryogenic liquid (or LH_2) is common since it enhances the volumetric density and hence requires significantly less volume for the same mass of hydrogen fuel compared to gaseous hydrogen. The LH_2 can be achieved under extremely low temperature (-251.35 C) and low pressure (a few bars above atmospheric) that can be used in ICE, particularly ship engines. One of the main concerns is the accidental release of LH_2 from pressurised and non-pressurised tanks. The LH_2 release involves two-phase flow jet dispersion with the subsequent spreading of the LH_2 on the ground or water surface, followed by vaporisation and formation of a potentially dense hazardous gas cloud that may cause damage to equipment and structure and/or harm to people. The main physical phenomena involved in an accidental LH_2 leak can be classified as (i) flash evaporation, (ii) partial or full vaporisation, (iii) cryogenic boiling pool formation, and

(iv) air components condensation and freezing. The pressure change from the storage to the atmospheric pressure results in instantaneous vaporisation of saturated liquid hydrogen at the orifice that causes the occurrence of flash inside the tank or pipelines. Due to the temperate difference between LH_2 and atmospheric temperature, the released fuel evaporates and mixes with the air. However, in the case of partial vaporisation, the cryogenic pool forms on the ground surface that absorbs heat from the atmosphere and the ground, creating a boiling film while causing freezing of the solid ground. Finally, due to the extremely low prevailing temperatures, the nitrogen, oxygen of the air, and ambient humidity may condense and or freeze, creating liquid or solid particles. During air and humidity phase change, the mixture density increases due to the formation of liquid and solid phase that enhances the cloud's dense behaviour, which has negative buoyancy effects. On the other hand, the heat release from the phase change results in a positive buoyancy effect. These conflicting phenomena affect the formation and dispersion of the flammable cloud. The standards related to LH_2 safety are presented in Table 5.

CFD models have been extensively applied to study the release and spread of LH_2. It was used CFD modelling for the simulation of LH_2 dispersion based on experimental tests performed by the Health Safety Laboratory (HSL). Modelling air components (oxygen and nitrogen), ambient humidity condensation, and impose of transient wind profile were investigated in this study. The numerical studies that modelled the wind variability, the slip impacts among phases, and the humidity and oxygen and nitrogen phase change provided more accurate results with a satisfactory agreement.

They have simulated two experiments, Test-06 and Test-07 that consider a vertical downward jet with a distance of 0.1 m above the ground and a horizontal release of liquid hydrogen with a distance of 860 mm above the ground. For defining the source term impacts on the flow field, a sensitivity study was carried out. An upward velocity is generated by nitrogen and oxygen condensation through energy release, leading to bringing cold hydrogen gas to upper heights in comparison with when there is no air condensation. The temperature time series showed that the incapability of the CFD model for predicting the hydrogen presence at different sensor locations in both tests.

In another study, the CFD code, ADREA-HF, was adopted to model three experimental studies on the LH_2 spill experiments performed by HSL in 2010. It was found that the humidity existence in the atmosphere and fluctuating wind direction had important influences on the vapour dispersion. Both hydrodynamic and non-hydrodynamic equilibrium models were considered. Similar to the hydrodynamic equilibrium model, the non-hydrodynamic equilibrium model (slip model) assumed that there is thermodynamic equilibrium between two phases, but it allows that the phases to achieve dissimilar speeds utilising additional slip terms in the equation of conservation. They found the slip effect and humidity greatly influenced the cloud buoyancy, where the model used the slip model (humid slip) provided more accurate data.

Table 5 The standards related to liquid hydrogen

Standard	Title	Notes
CGA H-5-2014	Installation Standard for Bulk Hydrogen Supply Systems	This standard covers requirements for gaseous and liquid hydrogen bulk supply systems
CGA P-12-2017	Safe handling of cryogenic liquids	This standard presents information on the characteristics, transport, storing, safe handling, and utilization of the cryogenic liquids commonly utilized in institutions and industry.
CGA PS-17-2004	CGA position statement on the underground installation of liquid hydrogen storage tanks	This standard presents information on minimum criteria and the design of underground installation of LH_2 storage vessels.
CGA H-3-2019	Standard for cryogenic Hydrogen Storage	This standard includes the proposed minimum design and performance requirements of vacuum-insulated, shop-fabricated cryogenic tanks intended for above-ground storage of liquid hydrogen.
ISO 13985:2006	Liquid hydrogen – Land vehicle fuel tanks	This standard defines the construction criteria for liquid hydrogen fuel vessels used in land vehicles and also testing procedures needed for ensuring an acceptable degree of safety against loss of life and property due to explosion and fire.
NFPA-2-2020	Hydrogen Technologies Code	This standard presents safety requirements for the production, piping, storage, installation, utilization, and handling of hydrogen in all cryogenic liquid or compressed gas forms.
ISO 13984:1999	Liquid hydrogen – Land vehicle fueling system interface	This standard defines the features of liquid hydrogen dispensing and refueling systems for all types of land vehicles for reducing risks of explosion and fire during the refueling process and thereby providing an acceptable degree of protection against loss of property and life.
CGA G-5.4-2019	Standard for hydrogen piping systems at user locations	This standard provides the recommendations of general principles and specifications for piping systems for liquid or gaseous hydrogen.
NFPA 55	Compressed gases and cryogenic fluids code	It presents standards for the handling, use, and storage of cryogenic fluids and compressed gases in portable and stationary tanks, cylinders, and containers
NFPA 50B	Liquefied Hydrogen Systems at Consumer Sites	This standard covers the standards recommended for the use of liquid hydrogen for consumer use.

A possible event scenario for the LH$_2$ technology is boiling liquid expanding vapour explosion (BLEVE). This accident scenario is an explosion caused by the rupture of tanks containing LH$_2$.

at atmospheric pressure and under temperatures above the boiling point because of the expansion of both the liquid and vapour phases. BLEVE is caused by quick phase change and expansion, not by chemical reactions, so it can be considered a physical explosion. Pressure waves, a fireball in case of flammable materials and presence of ignition sources, and fragment projection are the consequences of BLEVE. The generation of pressure waves as a result of the explosion is the first consequence of BLEVE. Depending on the intensity of the blast wave, overpressure, injury and death of humans, and various forms of structural damages can be caused.

Fragments (also referred to as projectiles or missiles) are a consequence of BLEVE involving the tear of the vessel and throwing away its debris and is caused by part of the mechanical energy released by the explosion. In the case of the flammability of the stored material and the presence of an ignition source, the occurrence of a fireball is probable. An actual fireball does not occur in some cases. Instead, following the loss of containment, a fire initiates on the ground, which can represent the third type of consequence for BLEVE. These event circumstances were studied. They defined the rocket propellant's critical mass above which the fireball is formed and lift off. They were evaluated all the consequence typologies (fireball, fragments, and pressure wave) for LH$_2$ BLEVEs, for both mid-scale and small-scale tests applying analytical and theoretical models. The experimental data from BMW safety tests were used to validate the models, and then the most appropriate approaches were chosen for conducting the blind prediction study of the forthcoming liquid hydrogen BLEVE experimental studies of the Safe Hydrogen fuel handling and Use for Efficient Implementation (SH2IFT) project. They also highlighted the shortcomings of the models, as well as the uncertainties and information gap in liquid hydrogen physical explosions.

They were estimated the consequences of both supercritical and subcritical LH$_2$ BLEVE applying real and ideal gas behavior models. At a fixed distance from the tank, they calculated the blast wave overpressure and the generated mechanical energy by the explosion. To perform comparative hazard assessments, similar estimations were performed for methane and liquefied propane tanks. However, there is still a lack of knowledge in the literature for the LH$_2$ BLEVE phenomenon, and further experimental tests and studies are required.

4 Hydrogen Risk Assessment

Hydrogen risk analysis creates a reliable connection between scientific knowledge from numerical analysis, experimental data, theoretical models, and industry practices (Pasman 2011). Identification of key risk drivers, the establishment of mitigation strategies, and the prevention of potential accidents are some of the outcomes of hydrogen risk assessment. Risk assessment has been performed to form the basis of

regulations, codes, and standards (RCS). Measures of a preventive and protective nature based on this RCS are applied to limit the quantity of hydrogen release, reducing its frequency of occurrence, and reducing the intensity of the impact and the probability of exposure of the subsequent hazard to different targets, including people and structures. The outcomes of hydrogen risk assessment can be used as a reference for hydrogen system operation and system failure analysis (Groth and Hecht 2017).

When the hydrogen system is comprehensively described, identification of the condition that has the potential for causing damage to target and characterization of the occurrence that result in an accident is straightforward. Decisions making on whether to build, operate, or modify a hydrogen application system is easier once the total risk is determined and the subsequent risk acceptance procedure is performed. With the total risk determined, the risk acceptance procedure is applied, facilitating in decisions making on whether to build, operate, or modify the hydrogen application system.

As the hydrogen industry grows, various data-driven approach methods have been studied to risk inform on operational and design requirements of hydrogen systems, providing a baseline for the guidelines for the hydrogen systems design and operational parameters. The CFD simulations of different accidental scenarios provide a comprehensive understanding of hydrogen physics, which is required for the development of RCS. These codes are based on the hazards such as the dispersion of hydrogen and understanding the consequences of events like the heat-flux of hydrogen flame.

The safe performance of hydrogen-related technologies can be evaluated by a promising approach which is analyzing the embedded hazards using the inherent safety guidewords of "simplification", "moderation", "substitution", and "minimization". Inherent safety assessment has been identified as an appropriate indicator for the evaluation of the possible effects on health during the design of the energy systems since the selection of process conditions and conversion technologies can be classified based on their intrinsic characteristics. It was developed a new quantitative methodology for assessing the inherent safety of process flow diagrams in the early stages of design. Based on a series of key performance indicators (KPIs), a metric is presented as the output for quantifying the process scheme's inherent safety fingerprint (Tugnoli et al. 2009). The objective of each KPI is the assessment of a particular aspect of the inherent safety fingerprint of the system. The suggested KPIs make it possible to score the inherent safety values of limitation, simplification, attenuation, substitution, and minimization of effects. For quantifying the hazards associated with process conditions, materials, and equipment characteristics, they used physical parameters. The analysis focuses on identifying and modelling possible incidence consequences for equipment and humans. A clear and accurate image from the inherent safety performance can be provided by adopting tangible factors based on consequence modelling.

The anticipated inherent safety performance for technologies of hydrogen storage was investigated. They considered different sizes for storage, associated with several industrial applications. According to the results of the comparative analysis, the

novel hydrogen storage technologies always have lower potential hazards. This is mostly due to the employment of concepts underlying the inherent safety guideword "substitution" because hydrogen was stored as a hydride with fewer hazards in these replacement technologies. Furthermore, compared to conventional technologies, the operative conditions for storage systems of complex hydrides and metal hydrides containment structures are less severe, underlying the inherent safety "substitution" guideword. However, in the case of considering credit parameters of loss of containment (LOC) incidents, lower safety performances are exhibited by novel technologies, especially by metal hydrides storage in comparison with conventional storage processes, according to the standard equipment reliability data. They also developed an innovative consequence-based methodology for assessing the inherent safety of the envisaged hydrogen production, transport, and application systems for vehicle purposes. They assessed different scenarios for the hydrogen system chain from production on a large scale to end utilization. In their analysis, the transport and delivery of hydrogen were also considered. A set of KPIs was used to quantify the inherent safety fingerprint of every system. They also conducted comparisons with proposed technologies for the utilization of other fuels like natural gas and LPG. The hazards of compressed hydrogen-powered cars were similar, but reference new hydrogen technologies showed a possibly greater level of safety. As a result, moving toward inherently safer technologies can have a significant effect on the safety improvement of hydrogen cars, leading to a considerable increase in the entire hydrogen system safety performance (Foorginezhad et al. 2021).

The conceptual design of distributed energy systems was investigated using a multi-objective optimization strategy for addressing the social, environmental, and economic aspects in the design of energy systems. They first considered and evaluated the inherent safety indicators and the water consumption with two single-objective optimization problems for enhancing the evaluation of the social and environmental dimensions of sustainability. To conduct the multi-objective analysis, they utilized a framework containing inherent safety index, grid dependence, water consumption, CO_2 emissions annualized cost. They suggested four optimization cases involving various sustainability indicator combinations for conducting a comprehensive and thorough analysis. They identified a compromise between the objective functions and explored the obtained Based on the results, values between 27.8 and 70.2 m^3 H_2O/GWh for water consumption, 10.6 and 68.5 $kgCO_2$/MWh for the CO_2 emissions, 0.37 and 0.63 €/kWh for the energy cost were obtained.

5   Safety Issues for Hydrogen Storage

Hydrogen has been used commercially for decades (e.g., agriculture, refining, scientific laboratories, and hospitals). It is transported over roadways in trucks and moves through pipelines to refineries. Industry codes and standards and government regulations for the transport and use of gaseous and liquid hydrogen are well established (Dadashzadeh et al. 2018).

International vehicle standards have been under development primarily at the Society of Automotive Engineers International (SAE) and the International Organization for Standardization (ISO). A global technical regulation (GTR) is under development at the United Nations as a voluntary basis for global harmonization of national regulations for the safety of hydrogen-fueled passenger vehicles.

Industry standards for fuel cell vehicles have been developed before the vehicles have been commercialized by retail sales in the marketplace, but are in the advanced precommercialization phase, during which fleets of prototype vehicles are in evaluation in on-road service. The development of industry safety standards and government regulations for fuel cell vehicles well before commercialization has been driven by interest in achieving global harmonization of regulatory requirements to enable vehicles to be deployed internationally. With global harmonization higher initial volumes can be realized, and, thereby, the environmental benefits of these vehicles can be achieved more rapidly on a global scale (San Marchi et al. 2017).

Industry codes and standards are being established for the following:

1. Installation/operation of vehicle fueling stations (National Fire Protection Association [NFPA]
2. Station fueling nozzle and vehicle fuel receptacle (SAE J2600)
3. Fueling station protocol for fuel transfer (e.g., flow rate and pressure cutoff) (SAE J2601)
4. Vehicle fuel system leak tightness (on road and in crash) (SAE J2578)
5. Hydrogen fuel storage on-board vehicles (SAE J2579).

The safety standards for the hydrogen storage systems in vehicles contain best-practice guidelines for their design and installation. They also specify the performance-based test procedures that are used to formally qualify storage systems for on-road service. At present, compressed gaseous hydrogen is the type of storage system receiving the primary focus because of its wide use by vehicle manufacturers of fuel cell prototype vehicles and because the rupture risk from the high pressure of compressed gaseous storage merits specific attention. From a safety perspective, high-pressure on-board hydrogen storage is the feature that most distinguishes fuel cell vehicles from battery-powered electric vehicles. Battery and fuel-cell powered vehicles use similar high-voltage electric power trains; their safety is ensured by requirements like those that apply to hybrid electric vehicles.

Hydrogen-fueled vehicles are required to pass crash safety tests with leakage limits equivalent (on an energy basis) to gasoline-fueled vehicles (Rodionov et al. 2011).

In recent years, the development of industry standards has focused on performance-based requirements instead of prescriptive requirements that focus on known failures of previous technologies. There are two key reasons for the focus on performance-based standards. First, on-road safety is a high priority. Therefore, requirements must be developed comprehensively and in anticipation of extremes of on-road service learned from decades of experience to avert adverse on-road experiences. Second, they provide stringent requirements to verify safe performance of new technologies with environmental benefits under broad conditions of on-road

Fig. 3 Typical storage
system
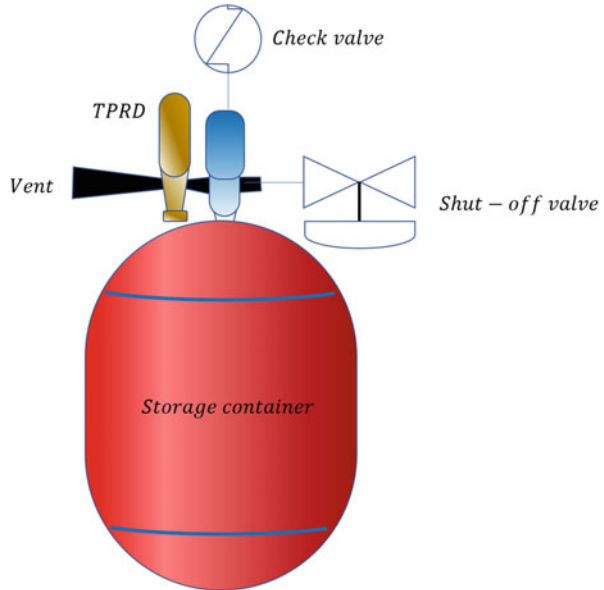
use. Vehicle crash tests are an example of performance-based requirements—the
crash conditions relate to statistics for on-road crash conditions. They are applied
uniformly to all vehicles without differentiation for the materials used in a vehicle's
structure, for its structural design, or for the techniques used in its manufacture, that
is, without pre-knowledge of specific failure modes. Vehicles must pass crash tests
to qualify for on-road service. Likewise, hydrogen storage systems must pass
additional performance-based tests based on extreme conditions of on-road usage
to qualify for on-road service (Gye et al. 2019).

A typical hydrogen storage system is illustrated in Fig. 3.

It consists of a high-pressure containment vessel equipped with three compo-
nents: a check valve, a temperature- activated pressure relief device (TPRD), and an
automatic shutoff valve (Shen et al. 2018). The check valve is installed on the
containment vessel at the connection to the fuel line from the fueling receptacle. It
prevents backflow of hydrogen gas. The TPRD opens when activated by fire. It
releases hydrogen gas in a controlled manner (hydrogen gas then dissipates rapidly
due to its high buoyancy). The automatic shutoff valve is installed in the fuel line to
the power system (e.g., the fuel cell system). It is equipped to close automatically in
the event of an accident, when the vehicle is not operating, or other specified
conditions. It is important to note that the high-pressure part of the hydrogen storage
system shown in Fig. 3 does not incorporate a pressure-activated pressure relief
device (PRD). As described further in this chapter, the responsibility to prevent over
pressurization during refueling lies with the hydrogen fueling station. Hydrogen
storage systems are generally pressurized to either 350 or 700 bar when fully filled.
Leak-tight performance (leak less than 3.6 normal cubic centimeters per minute
(Ncc/min)) is required throughout service life.

Compressed natural gas (CNG) vehicles provide a useful historical reference for compressed gaseous fuel storage up to 300 bar. Perhaps surprisingly, storage standards for natural gas vehicles are not sufficiently general to handle all safety issues specific to hydrogen storage. Four aspects lead to unique safety considerations: (1) chemical and physical properties of hydrogen (e.g., Joule Thompson temperature effect, rates of permeability and dispersion, and hydrogen embrittlement); (2) higher pressures (greater than 300 bar); (3) broader operating conditions; and (4) fuel quality constraints.

Many of the previous historical requirements for the storage of natural gas in vehicles can be seen as a list of tests that screen for on-road failures that have occurred in CNG tanks operating at less than 300 bar made with materials and structures developed prior to 1990. Recorded failures (rupture) of CNG tanks in vehicles have been traced to fire, to abuse/damage, to chemical exposure, or to the durability of metal and glass-fiber-composite tanks after extended static and cycling pressure. Each circumstance was addressed in historical standards with a test replicating the extremity of conditions causing the failure. In several cases, the resulting requirements are prescriptive, rather than performance based, in that tests are applied differently for systems with different materials or construction design. Such tests target the specific failure mechanisms that have occurred with CNG tanks with historical materials/constructions operating at pressures under 300 bar. Hence, the prescriptive requirements are reactive (reflecting past failures) rather than proactive (screening for future failures that may occur under different combinations of on-road conditions, new materials, and new constructions).

Performance-based standards do not assume failure mechanisms are known or that materials and constructions can be fully anticipated but instead seek to identify comprehensively worst-case, stressful on-road conditions to be managed by a roadworthy system. The breadth of conditions under which CNG metal and glass-fiber tanks failed when operated at pressures below 300 bar is not necessarily sufficient to encompass risk conditions for hydrogen systems made with new materials and constructions or operating at different working pressures and fueling conditions.

Another difference from the CNG history has been the involvement of a broader community of experts early in the process of developing safety requirements for hydrogen storage. The early CNG community drew primarily on the expertise of pressure vessel and component manufacturers and aftermarket converters of gasoline vehicles into CNG vehicles. The broader community engaged in development of hydrogen requirements for vehicles includes vehicle designers and manufacturers, who bring broader experience with on-road vehicle safety and have experience with management of risk when a product is in use by a diverse population and in highly variable on-road conditions. In addition, experts from the emerging fueling and repair/service infrastructures were engaged to coordinate requirements for fueling and defueling. Component manufacturers were engaged to specifically coordinate requirements for component reliability, durability, and performance so that those features would be consistent with the expected performance of safety for the storage systems into which they would be incorporated. And finally, independent test
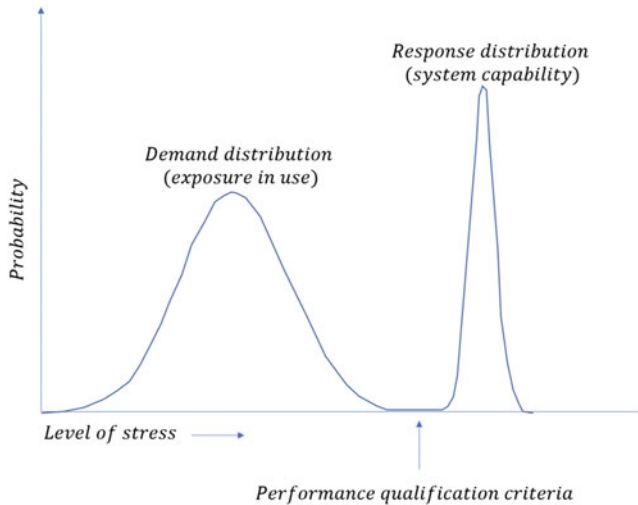
Fig. 4 Management of risk

laboratories (including national laboratories) have evaluated material properties and developed test procedures.

The development of qualification tests for on-road service and other specifications for hydrogen storage systems have been based on systematic risk management. Risk = (Probability of an adverse event occurring) × (Severity of an adverse event). Risk is managed by reducing the probability or severity of adverse events. The unintended releases of fuel by leakage or rupture are the primary adverse events of concern with high-pressure hydrogen storage systems in fuel cell vehicles (López-Arquillos et al. 2015).

Figure 4 illustrates the approach used in SAE J2579.

The probability of an adverse event is given by the overlap of two probability distribution functions: the probability distribution for stressful conditions that occur in varying severities during service life and the probability distribution for storage systems to leak/rupture when subjected to various stressful on-road conditions. If the overlap is insignificant, then the risk is minimal (Hadef et al. 2020).

The severity of stresses applied in qualification testing is represented by the "performance qualification criteria", which correspond to severe stress conditions at or beyond the extreme for on-road lifetime service. Setting these criteria correctly—at worst-case extremes of on-road conditions—is the key to establishing robust design qualification tests.

Design qualification testing is designed to manage both leak and rupture risk. The risk associated with leakage is primarily a fire risk; that risk is mitigated by the rapid dispersion of hydrogen away from a vehicle and by vehicle controls that shut down the vehicle well before hydrogen leakage can reach its lower flammability limit (LFL). The probability of vessel leakage or rupture is specifically managed with requirements for durability, residual structural strength, and stability at the end of service (Liu and Zhang 2014).

It is not enough for qualified (tested) prototype storage system units to demonstrate their ability to sustain comprehensive on-road stresses. In addition, the production units must demonstrate tight correspondence to the capabilities of the validated tested units to ensure that production units have the required performance capability.

Three features make qualification tests established in this manner more demanding than historical CNG vessel tests: (1). Compounded stresses, (2). Full-system performance, and (3). Comprehensive on-road stress conditions.

Compound stresses refer to the application of on-road stresses simultaneously or in sequence to a single storage system unit. For example, in real-world on-road use, a vessel that is subjected to chemical exposures may also have been dropped during installation and could be in service for decades and thereby experience a lifetime of fueling pressure cycles. So, to verify on-road performance, these stresses must be applied to a single vessel, each in its worst-case extreme. This compounded test criterion is more severe than historical requirements, for which each stress is applied to a separate vessel. And, it corresponds more closely to the extreme of real-world potential risk. In another example, internal temperature stresses exacerbated by the presence of hydrogen gas and extreme ambient temperatures during fueling/ defueling are produced by the simultaneous application of these factors during testing.

Full-system performance refers to the requirement that the full storage system (defined as all surfaces in direct contact with high-pressure hydrogen in the storage vessel) must demonstrate reliable containment of hydrogen without rupture or unacceptable leak. The key feature is that interfaces between components (e.g., shutoff valves, check valves, TPRDs, and connecting O-rings) and the storage tanks are validated as leak tight and not susceptible to blowout during extremes of vehicle service. In addition, components responsible for enclosure of high-pressure hydrogen (shutoff valves, check valves, and TPRDs) are expected to be individually qualified for reliable and durable operation with high-pressure hydrogen.

And finally, comprehensive on-road stress conditions refer to a comprehensive evaluation of all anticipated sources of stress during service life, not just those that have been linked to failures of earlier tank designs or materials. Therefore, if new designs/materials/ manufacturing processes are subject to failure mechanisms that differ from those seen in the past, the qualification testing is designed to assess performance under extreme conditions where those failure mechanisms might occur in on-road service.

Performance standards designed to verify safety in on-road vehicle service need two elements:

- Qualification test protocols that produce worst-case stress conditions of service life
- Acceptance criteria

n setting test conditions, awareness of historical failure mechanisms is helpful but not sufficient. Instead, a comprehensive approach to defining extreme conditions of on-road vehicle service is required. Storage systems must function under stresses of

1. baseline performance,
2. expected (normal) vehicle operation,
3. extreme service conditions (externally imposed stresses and conditions of extreme usage), and
4. fire.

Verification testing for normal, or expected, vehicle operation and performance in fire (items 2 and 4) are performed pneumatically with hydrogen gas to replicate real-world factors potentially leading to leakage/permeation as well as rupture. Verification testing for baseline and extreme conditions (items 1 and 3) requires the application of physical stresses potentially leading to structural failure and rupture; these pressure forces can be applied hydraulically.

Baseline performance metrics provide reference points for subsequent design qualification testing and for comparison of production units with the prototypes that undergo formal design qualification testing. They also establish that design prototypes are sufficiently similar to one another to be representative of design properties and are sufficiently capable to merit further testing.

For example, SAE J2579 requires three types of baseline system performance tests. The first are material tests that establish reference points for comparison of production units with the formally qualified (tested) design prototypes and establish that metals in contact with hydrogen are not subject to embrittlement. The second are initial burst pressure (BP0) tests that establish that three randomly selected design prototype units are similar to one another (within ±10%) and that the BP0 of each exceeds 200% nominal working pressure (NWP). NWP is the maximum (full-fill) pressure at 15 °C, the rated pressure for fueling station fills, and is equivalent to the service pressure of gas cylinders.

The third verifies minimal pressure cycle life (number of full-fill pressure cycles until failure) of three vessels and assesses the variability in their pressure cycle life. If variability in pressure cycle life is greater than ±25%, then more than one vessel must be subjected to the item 3 extreme service testing.

SAE J2579 provides an example of robust performance requirements that comprehensively address expected (normal) vehicle operations. The Expected Service (Pneumatic) Performance Test is illustrated in Fig. 5.

Storage systems are subjected to a high incidence of expected worst-case conditions and are required to perform without rupture or unacceptable leak/permeation. In addition, they must demonstrate residual strength after lifetime-equivalent durations of exposure to extreme stresses of vehicle service.

Expected vehicle operations for storage systems include fueling, parking, and driving (defueling). In each case, stress is applied internally by high-pressure hydrogen. Performance must be demonstrated with hydrogen gas because the unique properties of hydrogen can create additional internally imposed stresses. For example, because hydrogen is a small molecule, pressure changes may drive greater infusion-into/withdrawal- from interstices within materials and sealing interfaces than would occur with larger molecules, like natural gas. The combination of stress factors that occur in normal operation could promote previously unrecognized
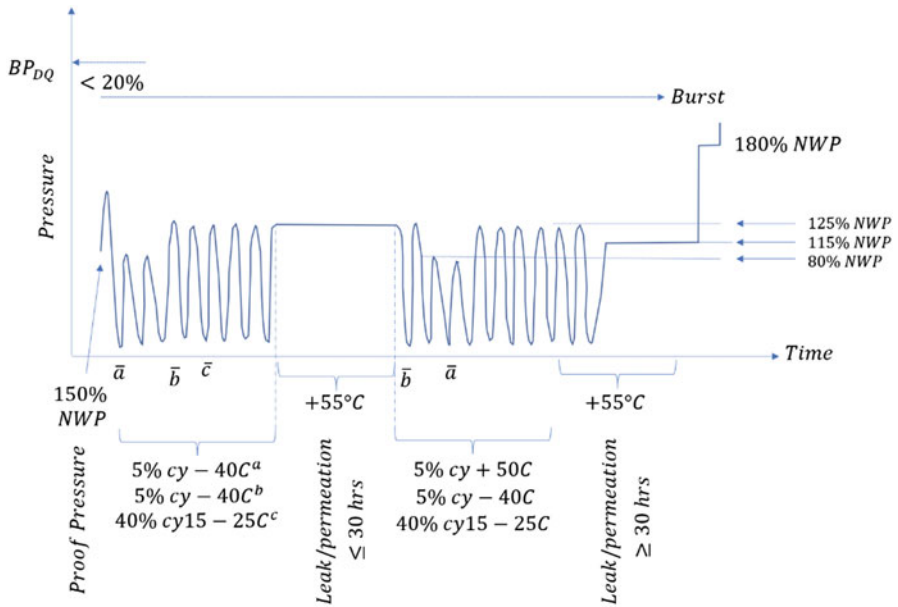
Fig. 5 Expected service performance test. (**a**) Fuel/defuel cycles @ –40 °C with initial system equilibration @ –40 °C, 5 cycles with +20 °C fuel; 5 cycles with <−35 °C fuel. (**b**) Fuel/defuel cycles @ +50 °C with initial system equilibration @ +50 °C, 5 cycles with <−35 °C fuel. (**c**) Fuel/defuel cycles @ 15–25 °C with service (maintenance) defuel rate, 50 cycles

failure mechanisms (e.g., temperature- amplified, hydrogen-induced embrittlement of metals or contraction and rigidity in sealing materials) that should be elicited in qualification testing rather than on-road service. Therefore, qualification testing must include compounded and realistic extreme conditions of fueling, parking, and defueling (driving) with hydrogen.

The following features are key to achieving comprehensiveness with regard to the stressful fueling/defueling conditions that are tested:

- Rate of internal pressure change. Maximum temperature and pressure shock occur with rapid fueling and defueling, so rapid 3-min fuelings to 125% NWP (using a constant-pressure ramp rate according to SAE J2601) are required, as are defuelings at the maximum rate (maximum vehicle fuel consumption rate) to 20 bar. If the defueling rate used for vehicle maintenance/service is higher, then systems must demonstrate at least 50 of the more rapid defuelings in addition to normal defuelings associated with driving.
- Peak fueling pressure. Maximum stress is applied with fueling from 20 bar to 125% NWP at ambient (20 °C) and high (+50 °C) external temperatures, and fueling to 80% NWP at cold (−40 °C) external temperatures. Fueling protocols (e.g., SAE J2601) do not permit fueling above 80% NWP at −40 °C to ensure that systems are not over-pressured if subsequently exposed to warmer temperatures

(e.g., moving inside or in diurnal warming). A precision of ± 10 bar on pressure cycle extremes ensures correspondence with vehicle usage and that appropriate pressure controls are used in the testing facility.

- Tank internal temperature and pressure at onset of fueling. Maximum thermal shock is produced using both cold-soak and hot-soak test conditions. A $-40\ °C$-cold-soaked, fully filled system is subjected to rapid defueling (to create the coldest possible interior temperature conditions) followed by rapid heating from fueling with 25 °C fuel (indoor fueling without temperature control) and also with fuel at $-35\ °C$ or less (expected at public fueling stations). In addition, a $+50\ °C$ hot-soaked, empty (20-bar) system is subjected to the impact of $-40\ °C$ fuel under fueling.

- External temperature. Fueling/defueling cycles are conducted under both $-40\ °C$ and $+50\ °C$ extremes of environmental (external) temperature. The percentage of extreme temperature pressure cycles corresponds to twice the percentage of occurrence in populated extreme latitudes. The remaining pressure cycles are conducted at nominal 20 °C ambient temperature. umber of expected fueling/defueling pressure cycles. The maximum number of high-stress full fueling/defueling cycles has been determined from (Lifetime vehicle range)/(Driving range per full tank) = L/R. Under no circumstances is this expected service qualification test cycle number allowed to be less than 500 empty-to-full fuelings with hydrogen gas (500 = 150,000 lifetime miles of driving/300 miles per fueling). The extremity of this number derives from the low probability that all vehicle fuelings through a vehicle's life would be under the maximum stress condition of an empty-to-full fill. In addition, potential buildup of impurities or charge from multiple fuelings is managed by fuel quality requirements (SAE J2719 and ISO 14687-2).

- Interaction between fueling/defueling pressure/temperature cycles and the static stress associated with parking. Sensitivity to fatigue mechanisms induced by the interplay and cumulative impact of cyclic and static pressure is elicited by sequential exposure to cyclic and static high pressure.

In SAE J2579, qualification for lifetime service requires a robust test of the durability of vessels to survive exposure to externally imposed stresses and thereafter to perform reliably through a service lifetime of extreme usage.

Storage systems used in on-road vehicles can be expected to encounter four types of externally imposed stresses: impact (drop during installation, road wear, and crash damage), fire, fueling station malfunction (over-pressurization), and environmental exposures. Crash performance is evaluated in government-required vehicle crash testing, for which fuel integrity requirements are established to manage fire risk due to leakage (e.g., SAE J2578). For exposure to external fire sources, the probability of rupture is reduced by the requirement to demonstrate release without rupture (discussed in the following section on fire). The remaining external factors—drop, road wear, and environmental exposure (chemicals combined with temperature/humidity exposure),and fueling station malfunction (over-pressurization)—can be aggressive assaults on the vessel structure and hence present rupture risks. SAE
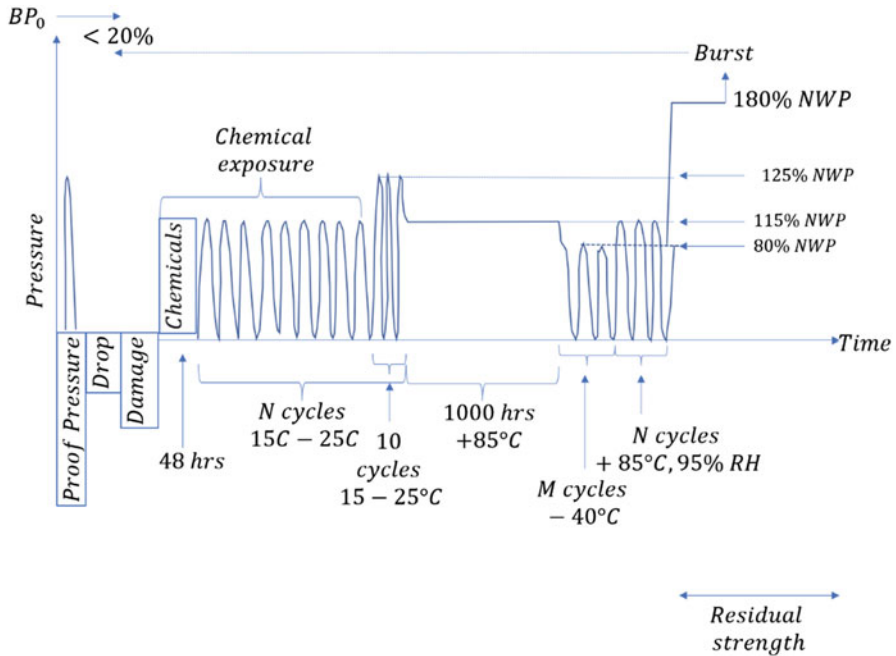
Fig. 6 Durability performance test. N cycles • 3500 cycles passenger light-duty • 7000 cycles commercial, heavy-duty, M cycles • 1000 cycles passenger light-duty • 2000 cycles commercial, heavy-duty

J2579 provides an example of robust performance requirements that comprehensively address these externally imposed stresses. The Durability (Hydraulic) Performance Test: Extreme Conditions and Extended Usage requirement is illustrated in Fig. 6.

Since a vessel dropped during installation would thereafter be exposed to road wear (e.g., stone chips and abrasion from vessel bindings) and to environmental factors, the application of these stresses in series is required. The worst-case factors to be applied include drop (e.g., from a forklift), expected in-service wear, and concentrated application of chemicals to punctures through external coatings with refreshed exposure throughout 48 h of high humidity with the system at full pressure, followed by a demonstration of the capability to sustain extreme usage in vehicle operations that include fueling, parking, and driving (defueling). Stresses exerted during fueling and driving (defueling) are replicated by hydraulic pressure cycles. Stresses exerted during parking are replicated by sustained hydraulic pressure.

Surveys of gasoline passenger vehicles (not buses) showed the extreme lifetime in miles has been about 360,000. Since vehicles currently exceed 200 miles of travel with a full fuel tank, 360,000/200 = 1800 exceeds the number of full fuelings in current vehicles. As the driving range per full fueling rises, the maximum number of full fuelings decreases. As an added assurance of residual strength for rupture

prevention, consideration of additional numbers of fuelings in the likelihood of partial fillings is accommodated in the qualification testing by considering a lifetime of fuelings at only one-third capacity, thereby requiring $3 \times 1830 = 5500$ pressure cycles to 125% NWP; this is beyond worst case since partial fuelings have been shown to cause considerably less fatigue than full fuelings. As a corroboration, it has been shown that a six-sigma projection (~10–9 probability) from the distribution of recorded lifetime vehicle miles traveled would also support about 5500 pressure cycles as the statistically extreme worst case. These pressure cycles, which serve to accelerate the fatigue of vessel wrap material, can be applied either pneumatically or hydraulically. For commercial heavy-duty vehicles, such as buses, 15,000 pressure cycles are required to accommodate higher lifetime usage.

Requirements for fueling stations have been established (CSA and ISO have standards under development; the NFPA has established requirements) that limit the fueling pressure to 125% NWP and require monitoring/intervention to limit a potential over-pressurization to less than 150% NWP. Thus, it is the responsibility of the hydrogen fueling station to prevent dangerous overpressure events, hence the requirement for the fueling stations to install PRDs to manage pressure. As a worst case, exposure to over-pressurization due to fueling station failure is assumed to occur 10 times during service life prior to extreme parking (static pressure) and extreme temperature refuelings. In the absence of reports of over-pressurization at CNG fueling stations, this frequency is expected to be extreme. In addition, a final end-of-service over-pressurization is applied.

Parking is associated with prolonged exposures to high pressure, which could cause fatigue and stress rupture. Parking cannot be directly replicated in qualification testing because the relevant cumulative time period is years to decades, which is too long for a practical qualification test. Therefore, a performance verification test that amplifies the physical stress to accelerate resulting stress fatigue is needed. The amplified stress should not, however, induce failure modes that could not occur in on-road service (Lv et al. 2023).

The worst-case exposure to static high pressure (full-fill parking) has been selected as 25 years under full-fill conditions (100% NWP). Vessel strength derives from properties of the structures, which have been metal in past portable applications and have been composite (resin-impregnated fiber) in modern vehicle applications. A robust approach for accelerating the effects of prolonged high-pressure exposure is to set requirements appropriate to verifiable properties.

Experimental findings on tensile stress failure of representative strands used in composite wraps of pressure vessels are shown in Fig. 7a and b. (Strands are fibers [10,000–15,000 filaments] coated in resin and cured.)

In each case, failures were shown to be well represented by Weibull distributions, which have the characteristic that failures that occur with the same probability fall on a straight line in log-log plots of the load fraction (load as a fraction of the median initial strength) plotted against time to failure when held under that load. The plots show the median (0.5 probability), and the shaded area indicates the region of data used for the Weibull fit. By looking at the slopes, it is clear that the time to failure increased when the load was reduced. Carbon strands showed greater resistance to
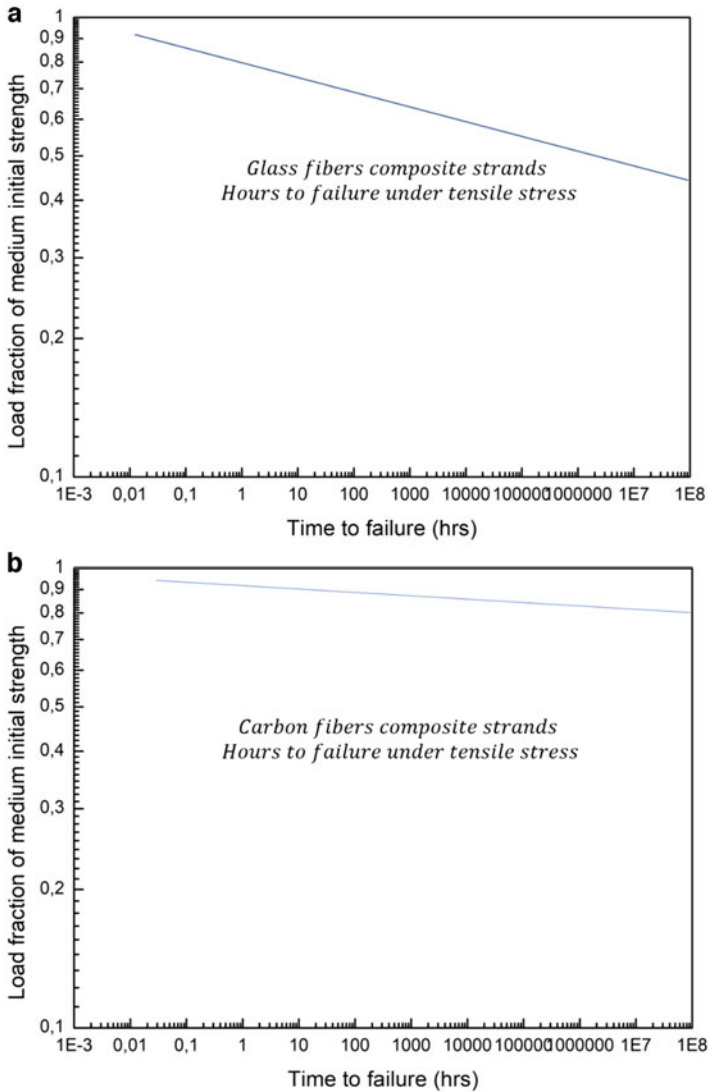
Fig. 7 Composite strand experimental data: hours to failure under sustained tensile stress. (**a**) glass fiber composite strands; (**b**) carbon fiber composite strands

stress rupture than glass strands in that a small reduction in the applied load resulted in a greater increase in time to failure for the carbon strands than for the glass strands. Carbon strands appeared highly resistant to stress rupture. In contrast, glass strands fatigued more rapidly (failure at a much lower load fraction for a specific time to failure, or stated another way, much shorter time to failure for a given load fraction).

For carbon strands, a reduction in load of just 3% resulted in a lengthening time to failure by a factor of 100; for glass strands, a reduction in load of 18% was required for the same improvement in time to failure.

It is important to note that the failure probability shown in Fig. 7 is not the probability for vessel failure; it is the estimated probability for a single-point strand failure. Vessel fiber-wrap patterns and resin adhesion accommodate individual strand segment failures through load sharing. This is consistent with the observation that multiple adjacent strand failures transferring large load-sharing burdens are needed for a broader failure. Vessel measurements have shown longer times to failure for a given load fraction than strand data.

The slopes of the lines in Fig. 7 have relevance to vessels, however, since the fatigue response of strands to load stress is the main underlying source of vessel fatigue. Using the slope of lines in Fig. 7a one can conclude that for vessels with glass-fiber-composite strand wraps, the probability of failure for 25 years under tensile stress imparted by 100% NWP was equivalent to 1000 h under tensile stress imparted by 122% NWP. Consequently, a glass-composite vessel would have the same probability of failing (or passing) a performance test where it is subjected to 100% NWP for 25 years as for a performance test where it is subjected to 122% NWP for 1000 h. Given the difference in the practicality of the different test times, the 1000-h test has been selected. From a test facility perspective, a shorter test conducted at a higher pressure would be even more convenient, but since even short-term parking pressures cannot exceed the fueling maximum pressure, 125% NWP, that could potentially drive failure modes that would not occur in real-world vehicle service.

Figure 6 shows that SAE J2579 includes 1000 h of exposure to 125% NWP as the performance test for survival of parking stresses. An elevated temperature of 85 °C, which is an extreme recorded under-hood temperature for a parked vehicle, is applied to account for systems subject to heat-accelerated deterioration. Exposure to ultraviolet light is not included as SAE J2579 explicitly requires ultraviolet shielding of vehicle storage systems.

The parking performance test verifies sufficient resistance to stress rupture for full-fill parking lasting 25 years for a worst-case (such as glass-fiber-reinforced composite) where (for a given failure probability) the time to failure shortens times 10–2 when the sustained pressure increases by 18%. To ensure that this is the worst-case condition for future fiber technologies, SAE considered adding the requirement that vessels demonstrate capability beyond this expected worst case by requiring that vessels be held at 75% BP0 for 1000 h without rupture. In addition to verifying that the qualification testing applies for 25 years of parking at 100% NWP, it also ensures capability to sustain 115% NWP for 10 years, which is a lifetime of overnight parking after full fills. Experiments on vehicles fueled and parked overnight at temperatures over 20 °C showed internal pressures within carbon fiber tanks with insulating plastic liners dropped by 10% within 5 h, so a criterion to demonstrate capability equivalent to holding 115% NWP for 10 years (12 h per day over 20 year of service) would be conservative. And it would ensure that fibers with higher sensitivity to stress rupture than glass fibers would not be qualified for on-road service.

More recently, SAE has undertaken consideration of an alternative criterion that vessels have capability to sustain parking at 150% NWP for 25 years (Hao et al. 2020). This would be intended to correspond to the even more conservative extreme of a tank subjected to maximum overpressurization due to service station malfunction followed by a lifetime of exposure to an ultra-extreme elevated temperature of 85 °C. If this criterion is adopted, then tanks would be required to demonstrate the capability to sustain pressures above 175% NWP for 1000 h without failure, and fiber-reinforced composite tanks would be limited in construction to carbon or glass fiber. In that case, it would be expected that generic performance-based requirements for vessel qualification would be developed in the future that would allow the qualification of future vessels using novel fibers.

In either case, because extensive experimental data and records of established on-road service are available for glass-fiber and carbon-fiber reinforced composite vessels, they would be allowed to be qualified more simply by demonstrating 330% NWP and 200% NWP initial burst pressures, BP0, respectively.

Reliable rupture-free performance is the paramount requirement for on-road service. In the event of a vehicle fire, rupture could be caused by fire damage of a storage vessel or by increased pressure of the contained gas. Therefore, storage systems are required to vent hydrogen in a controlled manner through a TPRD when exposed to fire. To verify this capability, storage systems are exposed to fire conditions that replicate worst-case conditions (temperature and timing) determined from studies of vehicle fires. An assortment of localized vehicle fires has been examined; the duration and temperature are considered to be relevant only when the localized fire makes contact with the storage system above 300 °C (the temperature at which resin reaction is noted). The test protocol in SAE J2579, which is illustrated in Fig. 8, remains under discussion and hence subject to revision.

It begins with a localized fire exposure that progresses to an engulfing fire condition. The localized fire is applied at 600 °C, an extremely damaging condition not expected to remain localized as long in an on-road vehicle fire as in the test before transitioning to an engulfing fire; therefore, it is considered to be an extreme-case condition. A storage system may be tested with vehicle componentry designed to reduce localized fire intrusions; in which case the storage system alone is also tested with exposure to an immediately engulfing bonfire to ensure basic capability for the isolated storage system.

The performance metrics for storage are the absence of rupture or unacceptable leak throughout service life. So, both must be evaluated during testing and at the end of test sequences to verify the performance capability is retained at end of life.

In the pneumatic test, permeation (including leakage) is evaluated. The permeation limit is set at 150 Ncc/min, so that the flammability within a tight space cannot exceed 25% LFL (LFL of hydrogen in air is 4%). Consistent with defining worst-case requirements, tight means 30.4 m^3 (close to nominal car dimensions) and having the minimum air exchange per hour (ACH) recorded for a garage (0.03 ACH). For vehicles of unconventional size, the permeation limit is apportioned to the minimum size of garage where it will fit. Hence, even at the end of a worst-case stressful service life, the system could be parked safely in confined spaces.
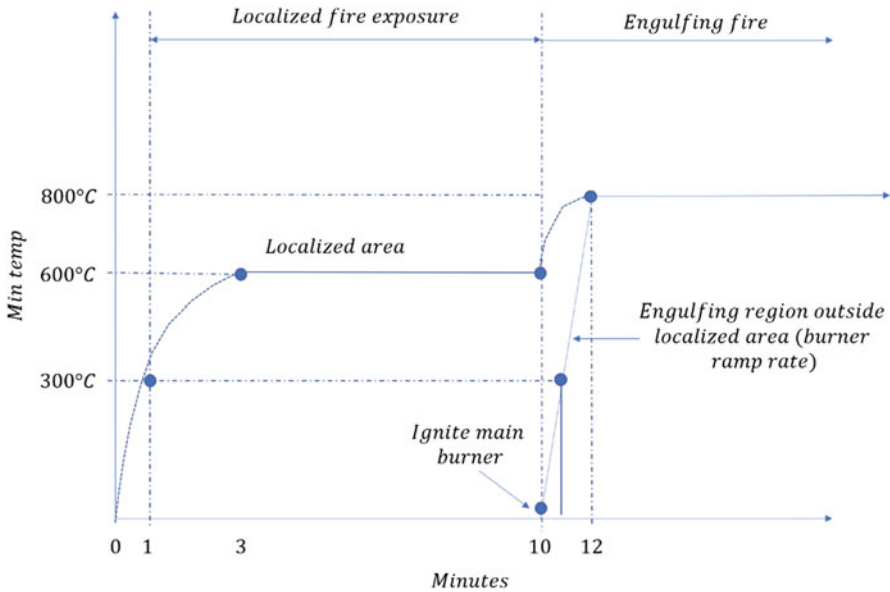
Fig. 8 Fire performance test

The maximum allowable discharge due to leakage and permeation from a hydrogen storage system was originally established at 150 Ncc/min for standard passenger vehicles to prevent a buildup to 25% LFL in a "very tight" 30.4-m^3 garage with the lowest recorded 0.03 air changes per hour. The value is obtained from:

$$C_\% = 100\,\frac{Q_{H_2}}{Q_{Air} + Q_{H_2}}$$

where $C_\%$ is the steady-state hydrogen concentration (percentage in air), Q_{air} is the airflow rate, and Q_{H2} is the hydrogen permeation rate. Consideration of tight garage volumes for vehicles of unconventional size led to the requirement that the maximum allowable permeation/leakage discharge for systems be A·150 Ncc/min, where

$$A = (V_{width} + 1)\,\frac{(V_{height} + 0.5)(V_{length} + 1)}{30.4}\,m^3$$

and V_{width}, V_{height}, and V_{length} are the vehicle width, height, length (m), respectively. Equivalently, if the total water capacity of the storage system is less than 330 L, then the system may qualify to 46 mL/L/h at 55 °C and 115% NWP. The temperature for the leak/permeation test was selected to be at least 55 °C as an extreme condition for long-term parking in a tight garage. The full-fill pressure at 55 °C is 115% NWP.

In addition to the permeation requirement, localized leakage is evaluated by bubble testing and is limited to 3.6 Ncc/min. This is the smallest leakage that could support a pinhole flame. Thus, a localized hydrogen leak cannot sustain a flame that could subsequently degrade surface material and cause a loss of containment. Per SAE 2008-01-0726, "Flame Quenching Limits of Hydrogen Leaks," the lowest flow of H_2 that can support a flame is 20 Ncc/min from a typical compression fitting, and the lowest leak possible from a miniature burner configuration is 3.6 Ncc/min. Since the miniature burner configuration is considered a conservative worst case, the maximum leakage criterion was selected as 3.6 Ncc/min. It is expected that visual detection of unacceptable leakage should be feasible. When using standard leak test fluid, the bubble size is expected to be approximately 1.5 mm in diameter. For a localized rate of 3.6 Ncc/min, the resultant allowable rate of bubble generation is about 2030 bubbles per minute. Even if much larger bubbles are formed, the leak should be readily detectable. For example, the allowable bubble rate for 6-mm bubbles would be approximately 32 bubbles per minute.

End-of-Life strength, as used here, refers to residual strength to resist rupture after having survived compounded worst-cast extremes of service life. The robustness of the test sequences (expected operation and extreme service durability) has been quantified. For example, extremes of environmental temperature are taken from climate data. Also, the number of stressful fueling-induced pressure cycles was linked to 10–9 probability of occurrence from broad surveys of vehicle lifetime mileage. Further, worst-case parking stress was linked through stress rupture data for composite strands to 25 years of parking under full-fill conditions. However, given the severe consequences of rupture, two additional quantifiable metrics for residual, or end-of-life, strength have been developed:

1. Residual strength: end-of-life capability
2. Residual strength: stability

Vessels are required to demonstrate the capability to sustain a 150% NWP over-pressurization from fueling station failure at the very end of simulated extreme service life and have the capability to sustain the over-pressurization for 10 h. This requirement is linked through strand data to the test criterion of 180% NWP for more than 4 min without rupture (Casamirra et al. 2009).

The vessel BP measured at the end of life must be within 20% of the median BP of fresh vessels. Therefore, the mean virgin burst pressure BP0 must be verified as part of design qualification.

This requirement is consistent with the expectation that the vessel has not reached a condition for which the primary failure mechanism has advanced sufficiently to produce pronounced loss of strength. This expectation is consistent with traditional vehicle safety assurance, which precludes use of materials whose properties change substantially over vehicle life, even if excess capacity were built into newly manufactured units.

Temperature specifications in performance tests designed to confirm function during expected service are linked to worst-case on-road requirements as follows:

- Temperatures of −40 °C and +50 °C during pressure cycling correspond to nominal extremes in global ambient temperature records that could be encountered repeatedly during vehicle service.
- Temperatures of 55 °C or greater during permeation testing correspond closely to the global maximum recorded temperature. Since temperature stabilization of a storage system requires many hours, a peak temperature below the global short-term high would be an extreme condition for garage parking.
- A temperature of 85 °C during 1000hat125% NWP has three elements of justification:

  (a) The maximum temperatures known to have occurred within vehicles parked in direct sunlight on dark asphalt are in the range 80–85 °C.
  (b) Full-fill fuelings (SAE J2601 when completed) may commonly result in interior tank temperatures of 85 °C. For 150,000-mile lifetime mileage and 200 miles/ fueling, a vehicle would experience 750 lifetime fuelings. Allowing time for cool down, 500–1000 h of exposure of the interior liner to 85 °C is a possibility. Time spent in the test is intended to show that the materials can withstand the maximum expected temperatures without degrading or creeping under load.
  (c) Elevated temperatures have been used to accelerate stress rupture testing, although a test of a single cylinder or limited number of cylinders may not have the statistical significance that has been associated with planned studies involving a larger number of cylinders. The acceleration of testing is associated with the Arrhenius rate equation, in which rate of reaction varies with temperature. It has been observed that for many composites, the rate of reaction doubles with a 10 °C increase in temperature. To this extent, 85 °C represents a 27-fold time acceleration of these factors (1000 h × 27 > 14 years) and can thereby emulate stress rupture in an accelerated manner.

There are two ways to validate qualification requirements for on-road service. One is retroactive: If mass-produced storage systems qualified using the requirements provide safe performance over 15 years or more of vehicle service, then the requirements have been sufficient (and possibly, but not necessarily, overly conservative). The other is proactive: (1) The requirements must be capable of execution by qualified test facilities; (2) they must screen out vessels known to fail in on-road service; (3) they must address known extremes of on-road service; and (4) they must only fail vessels having good on-road service if a previously unrecognized vulnerability to failure is revealed.

6 Engineering Issues Related to Condensed Phase Storage

The development of efficient and safe hydrogen storage systems includes the design and fabrication of containment and auxiliary components (i.e., the so-called engineering issues). Whether hydrogen storage is via physical or chemical means, this hardware must address initial and long-term performance requirements for the desired application (Moradi and Groth 2019). Furthermore, the engineering process will impact overall cost and system-level performances. Since H_2 gas is highly flammable, all storage systems need to be configured and constructed to minimize its leakage into any confined spaces, such as engine or passenger compartments within vehicles or the structures where the hydrogen-powered devices are kept or operated. The chemical reactivity of candidate chemical storage media with the atmosphere and common environmental materials (e.g., water, alcohols, lubrication oils, etc.) should be investigated and addressed via appropriate engineered safeguards for normal operation and plausible accident scenarios. To optimize the weight and volume storage densities of condensed-phase chemical storage media, these materials are often highly compacted powders. Vessel designs for these compacts must accommodate the expansion/contraction cycles during the hydrogen absorption/ desorption process without generating excessive stresses on their structural walls. Substantial engineering efforts are necessary to meet these often-conflicting requirements.

Probably the most commonly used (and frequently misrepresented) parameter in hydrogen storage technology is gravimetric capacity, which is the ratio of hydrogen (H_2) mass stored to either the mass of the hydrogenated sorbent material itself or to the mass of the complete storage system. Researchers and proponents for improved or "advanced" condensed- phase storage media often assign gravimetric capacity to the theoretical (or idealized) total hydrogen content of a chemical system rather than the actual amount available during its discharge from a storage container under realistic operational conditions. Hence, their performance claims can be greatly exaggerated or outright misleading.

While using the materials-based criteria can be useful for screening candidates, only system-level capacities that include the storage media as well as initially stored hydrogen along with all vessel and auxiliary components are meaningful for representing the performance level for the complete storage system in any specific application. Furthermore, the contributions from the storage vessel and components will exceed the weight of the condensed-phase storage media (i.e., combination of hydrogen and host materials themselves) by at least 50–60% even for the most aggressive (i.e., minimal weight/volumes and highly integrated components) designs and under the most favorable operating scenarios. The actual weights and volumes of past and current hydrogen storage systems built and demonstrated under laboratory or field conditions have weighed more than the storage media by factors greater than two and sometimes as much as an order of magnitude. These increases reflect use of commercially available hardware components, efforts to minimize manufacturing and fabrication costs, and high safety factors to account for high

pressure and temperature during testing. Significant refinements in engineering designs and analyses are needed to permit meeting all performance and safety targets with minimal weight and volume for the hydrogen storage systems.

Conventional interstitial metal hydrides and complex metal hydrides are chemically similar from the storage system view- point and are considered together here. These materials are rechargeable inside their container with only the addition of hydrogen gas and the removal of heat. These materials typically have enthalpies of hydrogen absorption of -30 to -60 kJ/mol H_2. Thus, during charging, the system will need to dissipate this amount of heat during the charging time. In addition, as hydrogen is delivered, the same amount of heat will need to be supplied to system.

For a compound with re-hydrogenation enthalpy of -40 kJ/ mol H_2, this requires a heat dissipation of 100 MJ in 2.5 min or 40 MJ/min. This typical thermal transfer requirement necessitates the use of substantial heat exchange equipment within the storage vessel. A number of recent studies have been published to determine the required heat exchanger characteristics as a function of media-specific heat, thermal conductivity, enthalpy, and absorption kinetics. A very important study has developed a simple relationship between the technical target, the media characteristics, and the heat exchanger design. This relationship is given as:

$$\left(\frac{1}{L^2}\right)\left(\frac{kM_{Hyd-eff}\Delta T}{-\Delta H_{overall}\rho_{Hydride}}\right) = \frac{1}{mM_{H_2}}\frac{m_{H_2}}{\Delta t}$$

where L is the characteristic length between heat transfer components, k is the media thermal conductivity, M_{hyd_eff} is the mass of hydride required to meet the system capacity target, ΔT is the temperature difference allowable in the media to meet the absorption target, $\Delta H_{overall}$ is the total enthalpy of hydrogen absorption, $\rho_{Hydride}$ is the density of hydride media, m is a geometric constant, MH_2 is the molar mass of hydrogen, and $\Delta mH_2/\Delta t$ is the charging rate. This equation can be broken down into a system design component $1/L2$, media characteristics, and a critical system design target as the filling time $\Delta mH_2/\Delta t$.

The implications of this relationship are discussed in greater detail in, but it is immediately apparent that the critical system design element (in this case the cooling element spacing) and a set of media-specific characteristics can be expressed as a given technical target Equation shows the fundamental relationship between technical target of hydrogen charging, the media characteristics, and fundamental heat exchanger spacing. This relationship illustrates the importance of modifying specific media characteristics to increase heat exchanger spacing. This is illustrated by the necessity of increasing thermal conductivity. To minimize the heat exchanger mass and cost, thermal conductivity enhancements may be added to the storage media. This addition will allow for increased heat exchanger surface spacing. In addition to the tank and internal heat exchanger, one needs to supply heat to aid in the hydrogen discharge. This heat supply is more than an order of magnitude slower, however, since driving a vehicle takes significantly longer than refueling.

Many conventional interstitial metal hydrides considered for storage applications have very rapid hydrogen adsorption and desorption characteristics. Thus, they are not kinetically limited. They are, however, thermally limited in that during charging the evolved heat needs to be removed at a fast enough rate to allow for further charging. Complex hydrides, however, are usually kinetically limited. The slow kinetics is a major technical hurdle for complex hydrides that needs to be overcome in their potential implementation.

Complex and metal hydride storage systems are comprised of a storage tank, which is typically a pressure vessel (Khalil 2015). The utilization of a pressure vessel is important in meeting both the volumetric target as well as the charging target. The free space within the storage tank not filled with media can be used to store compressed hydrogen gas. This compressed gas also serves as a buffer, supplying hydrogen under high-demand circumstances but prior to the delivery of heat to the system. Since heat needs to be added to the system continuously to release hydrogen as noted, a heat source is needed. This can be accomplished by either burning some of the discharged hydrogen or supplying heat from a waste heat source or electrical resistive heating. Hydrogen combustion is the most efficient when used in conjunction with a waste heat source. The amount of hydrogen combusted depends on the quality of the waste heat stream and the ability to deliver this heat into the storage system.

For many conventional metal hydrides, water can be used as the heat transfer medium since these materials are benign to potential water exposure from an inadvertent leak. In using complex hydrides, one must first understand the risk of inadvertent water contact and assess the risk of using this material as a heat transfer fluid. For a number of the complex hydrides under consideration, such as NaAlH4 and $LiNH_2$, water contact could potentially liberate significant hydrogen in an exothermic reaction. Thus, prudent system design would use a nonreacting heat transfer fluid such as any number of heat transfer oils as was implemented in the GM/Sandia NaAlH4 storage system. The use of any heat transfer fluid will necessitate the inclusion of a pump and external heat exchanger.

Chemical hydrides differ from metal and complex hydrides in that after hydrogen release the storage media must be removed from the system and regenerated at a separate offboard chemical processing facility (Nakayama et al. 2016). The most significant technical hurdle involved in the development of chemical hydride material is the efficiency by which the spent material can be regenerated.

The chemical hydrides can be either exothermic or endothermic discharge materials. A prototypical exothermic material is ammonia borane (AB), which has a 20 wt % hydrogen density if fully discharged but with an exothermic -20 kJ/mol H_2 discharge enthalpy. This large enthalpy works to both decrease the overall well-to-wheels efficiency since this is nominally wasted energy and to increase the system mass since heat exchange BOP must be added to the system to remove the heat released during hydrogen desorption. Aluminum hydride (AlH3), on the other hand, is a typical endothermic chemical hydride having an enthalpy of 10 kJ/mol H_2. Endothermic media will require continuous feed of heat to maintain the discharge reaction, reducing its wells-to-wheels efficiency.

The chemicals themselves can be either liquid or solid materials at ambient conditions both before and after dehydrogenation. It is preferred that they maintain their original form throughout the reaction to minimize BOP complexity. Liquids are most attractive since they are easily pumped, and heat transfer is facilitated. A hybrid approach is to use the solids mixed with a nonreactive liquid into pumpable slurry. Slurries are often problematic, tending to separate over time, and they can be quite abrasive. In addition, the carrier liquid needs to maintain chemical inactivity and maintain a low vapor pressure at the dehydrogenation temperatures in the reactor. Either liquids or slurries will need to maintain a viscosity, at all operational temperatures, below 1500 centipoise to maintain pumpability with minimal impact on efficiency. Significant work yet needs to be performed to ensure slurry stability.

Solid materials are generally difficult to transport both on and off the vehicle during filling and through the reactor during discharge. For this reason, for the current analysis, solid transport was not considered.

The baseline material used in this engineering assessment was liquid ammonia borane composed of pure $NH3BH3$ dissolved in $b_{mim}Cl$ to a mass fraction of 10% AB.

Adsorbent materials, similar to metal and complex hydrides, are in situ rechargeable materials.

The significant difference is that the enthalpy of adsorption of these materials, which is also known as the isosteric heat of adsorption, is typically -4 to -10 kJ/mol H_2. This requires maintenance of the adsorbent at cryogenic temperatures, typically 77 K or below. Both super-activated carbon and framework materials have been considered for automotive storage applications. These materials typically hold 6–8 wt% hydrogen at 77 K. They are high-surface-area materials, holding hydrogen on the surface through induced dipole interactions. These high surface areas, measured at about 3000 m^2/g, result in rather voluminous powders, somewhat hindering volumetric capacity.

Figure 9 shows the approximate ranges in hydrogen capacity that storage systems may find initial acceptance.

The total capacity range spans from 1 g to 100,000 kg of hydrogen and is divided into roughly three segments: portable, transportable, and stationary. For use in this discussion, portable is defined as being carried easily by one human, such as would be the case for using small electronic equipment of less than 1 kW. Transportable is meant to cover mobile applications such as small through heavy-duty vehicles for which energy consumption is 1–200 kW. Stationary storage is defined as greater than 100 kg of hydrogen is envisioned for distributed and centralized energy storage with generating capacity greater than 500 kW or launching spacecraft. These definitions are arbitrary and may be revised or adapted as new technologies become available, but they should serve as a helpful guide.

Gaseous compressed hydrogen is bound at the lower limit of about 1 kg by the mass of the conventional Type I (i.e., all-metal) tank required to meet government-mandated safety conditions. More exotic tanks incorporating graphite reinforcement have been estimated to be expensive for most commercial light-duty vehicles. Replacement of graphite fibers with glass or aramid fibers could be useful in driving
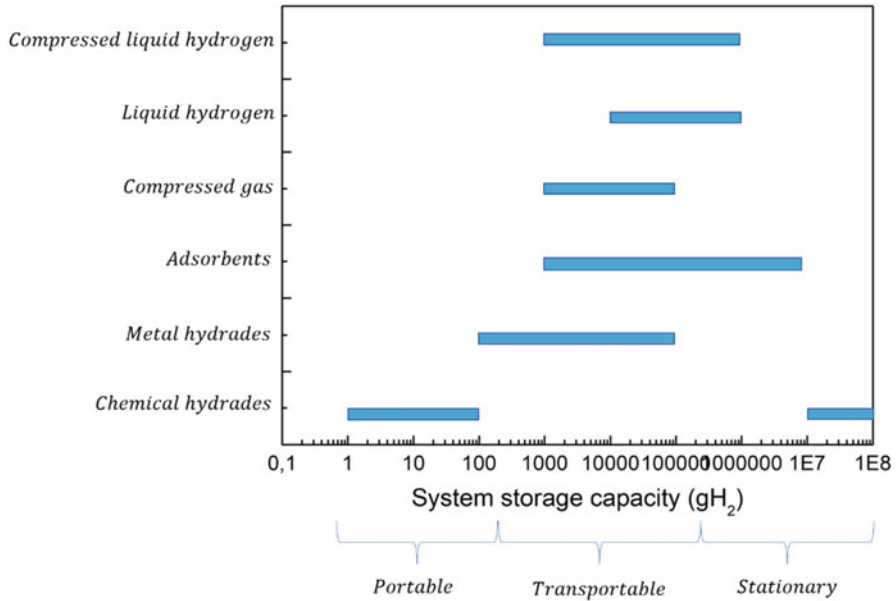
Fig. 9 Approximate range of storage system hydrogen content for the various system types

down this cost and thus lower limits for compressed gas acceptability in this and other applications. The upper bound on compressed hydrogen is about 100 kg and is primarily governed by the size of the tanks. Gaseous hydrogen is not volumetrically efficient, and large storage capacities will require large tanks and high expense. Some stationary applications may be able to take advantage of relatively cheap storage, such as underground reservoirs either naturally occurring or made specifically for gas storage.

Cryogenic liquid and compressed liquid hydrogen storage vessels are anticipated to be viable above 1 but less than 1000 kg of storage hydrogen for most power applications (Correa-Jullian and Groth 2022). Conventional liquid hydrogen storage systems have limited dormancy time and are thus unsuitable for most stationary applications except for when usage will be in relatively short times such as rocket fuel. Compressed liquid storage is foreseen for use at larger transportable applications, including aviation and small stationary applications where larger size and resultant lower surface area to volume will reduce the heat loss of the cryogenic systems.

Adsorbents, similarly, limited to cryogenic temperature operation, will probably retain many of the same disadvantages as compressed liquid hydrogen. This behavior may limit their storage capacity range to 1 to 1000 kg.

The chemical hydrides are different from most of the other media. Regeneration at a central facility will affect the storage capacity of these systems. At small capacities, ranging from 1 g to 1 kg, these materials provide viable options for high-value functions, including military systems. The chemical storage media can be

saved for recycling or discarded as economics dictates. Large-scale uses of chemical hydrides for light-duty transportation systems will require development of an efficient and cost-effective infrastructure to handle interchangeable tanks with hydrogen capacities of 1–10 kg along with central reprocessing/refilling. Requiring a large stationary facility for regeneration would allow chemical hydrides to also find application in large storage systems, greater than 10,000 kg, where the reprocessing facility can be custom built specifically for that storage system's needs.

7   Hydrogen Engineering Safety

Hydrogen is considered as one of the most promising fuels for generalized use in the future, mainly because it is an energy-efficient, low-polluting, and renewable fuel. Hydrogen is versatile and clean, and aiming at environmental benefits, the production of hydrogen from renewable energy sources and nuclear is under consideration. Yet, discussion of potential problems that widespread use of hydrogen might bring, such as whale oil and petroleum before it, is missing. The identification and control of potential adverse consequences is an ethical requirement whenever any new technology is introduced, and certainly in the hydrogen case with such world-influencing potential.

Hydrogen has been, for more than a century, produced and used with a high safety record for commercial and industrial purposes such as refinery and chemical processes and rocket propulsion. Industry has significant experience in safe handling of hazardous materials in chemical plants, where only well-trained personnel come in contact with hydrogen. Nevertheless, the wide use of hydrogen as an energy carrier will result in its use by laypersons necessitating different safety regulations and technologies that are now under development.

One of the major issues affecting the acceptance of hydrogen for public use is the safety of hydrogen installations (production and storage units) as well as its applications (i.e., as vehicle fuel or home use). The hazards associated with the use of hydrogen can be characterized as physiological (frostbite and asphyxiation), physical (embrittlement and component failures), and chemical (burning or explosion), the primary hazard being inadvertently producing a flammable or explosive mixture with air. As far as European countries are concerned, hazardous chemicals installations come under the so-called SEVESO II Directive (96/82/EC) for the control of major-accident hazards involving dangerous substances. Hydrogen is included in this directive, indeed with stricter minimal quantity for the Directive's implementation than any other ordinary fuel.

In recent theoretical and computational works, safety comparisons between hydrogen and other fuels do not allow a clear viewpoint for the safest one. Indeed, in the past, certain hydrogen applications gave rise to severe accidents with significant economic and societal cost, affirming the need of augmented safety measures wherever hydrogen is handled. Undoubtedly, the need for safety measures should be

pointed out when loss prevention and public safety are concerned. This demands the knowledge of potential hazards of storing, transporting, and using hydrogen.

In the previous decades, severe accidents have happened involving hydrogen utilized in industrial and other applications. The determinant causes for a catastrophic event may be classified into the following:

- Mechanical or material failure
- Corrosion attack
- Over-pressurization
- Enhanced embrittlement of storage tanks at low temperatures
- Boiling liquid expanding vapor explosion (BLEVE)
- Rupture due to impact by shock waves and missiles from adjacent explosions
- Human error.

Hydrogen gas is colorless, odorless, and not detectable in any concentration by human senses in atmospheric conditions. Therefore, inability of detection renders hydrogen a potential asphyxiant and a latent fuel, ready to ignite. With regard to its buoyancy, hydrogen gas is about 14 times lighter than air in normal conditions and this is why any leak moves fast upward, thus reducing ignition hazards. Nevertheless, the cold dense fuel vapors produced by liquid hydrogen (LH_2) spills will initially remain close to the ground and then rise more slowly than standard temperature and pressure fuel gases.

The limiting oxygen index is the minimum concentration of oxygen that will support flame propagation in a mixture of fuel vapors and air. For hydrogen, no flame propagation is observed at normal temperature and pressure (NTP) conditions if the mixture contains <5% by volume oxygen. Burning velocity (subsonic) in NTP air for hydrogen depends on pressure, temperature, and mixture composition. This high burning velocity of hydrogen indicates the difficulty of confining or arresting hydrogen flames. Explosion confinement is much more difficult to achieve in detonations where velocities are three orders of magnitude faster.

Hazards in addition to those taken for hydrogen gas should be taken when handling or storing LH_2. Therefore, any LH_2 splashed onto the skin or into the eyes can cause frostbite burns or hypothermia. Vents and valves in storage vessels and dewars may be blocked by accumulation of ice formed from moisture in the air. Excessive pressure may then result in mechanical failure with jet release of hydrogen and potentially in BLEVE.

Moreover, storage vessels should be kept under positive pressure to prevent air from entering and producing flammable mixtures. Liquefied hydrogen may be contaminated with air condensed and solidified from the atmosphere. The quantity of solidified air can increase during repeated refilling or pressurization of storage vessels producing explosive mixtures with hydrogen.

Liquefied hydrogen confined, for instance, in a pipe between two valves will eventually warm to ambient temperature resulting in a significant pressure rise. Standard storage system designs usually assume a heat leak equivalent to 0.5% per day of the liquid contents.

The high density of the saturated vapor resulting immediately after release from a liquefied hydrogen storage leaking vessel causes the hydrogen cloud to move horizontally or downward for some time.

Since electrical conductivity of liquefied hydrogen is about 1019 W cm at 25 V, the electric current–carrying capacity is small and more or less independent of the imposed voltage. Investigation has shown that electric charge buildup in flowing liquefied hydrogen is not a great concern.

Personnel present during leaks, fires, or explosions of hydrogen mixtures with air can incur several types of injury. Asphyxiation may occur when entering a region where hydrogen or another nontoxic gas has displaced the air, lowering the oxygen concentration below 19.5% by volume.

Blast waves from explosions may cause overpressure injury as a result of a combination of overpressure and duration at a given distance. For instance, the threshold of lung rupture may be 70 kPa (0.7 atm) overpressure for 50 ms or 140–210 kPa (1.4–2.0 atm) overpressure for 3 ms.

Thermal burns result from the radiant heat emitted by a hydrogen fire and absorbed by a person, which is directly proportional to many factors including exposure time, burning rate, heat of combustion, size of the burning surface, and atmospheric conditions (mainly wind and humidity). For instance, thermal radiation flux exposure level of 0.95 W/cm^2 may cause skin burns in 30 s. Cryogenic burns may result from contact with cold fluids or cold vessel surfaces. Exposure to large liquefied hydrogen spills could result in hypothermia, if proper precautions are not taken.

Owing to hydrogen embrittlement, the mechanical properties of metallic and nonmetallic materials of containment systems may degrade and fail resulting in leaks. Hydrogen embrittlement depends on many factors such as environmental temperature and pressure, purity of metal, concentration and exposure time to hydrogen, stress state, physical and mechanical properties, microstructure, surface conditions, and the nature of the crack front of material.

The types of hydrogen embrittlement are environmental hydrogen embrittlement of metals and alloys resulting in increased surface cracks, internal hydrogen embrittlement caused by absorbed hydrogen resulting in premature failures with internally starting cracks, and hydrogen reaction embrittlement caused by the chemical reaction of the absorbed hydrogen with one or more of the constituents of the metal to form a brittle metal hydride or methane with the carbon in steels.

Studies of the deterioration of mechanical properties observed in hydrogen cracking have shown that the susceptibility of a metal (or alloy) due to hydrogen increases with the strength of the metal. The internal and the environmental hydrogen embrittlement maximizes in the range 200–300 K (-73 °C to 27 °C), whereas hydrogen reaction embrittlement occurs at temperatures above room temperature. In addition, the susceptibility to embrittlement generally increases with the tensile stress.

The main factors governing hydrogen embrittlement are the metal surface films that can restrict hydrogen absorption, the effect of electrical discharge machining that may insert hydrogen (produced by the decomposition of a dielectric fluid) into a

machined component, and the effect of trapping sites within the structure of the metal.

Control of hydrogen embrittlement can be obtained by oxide coatings, elimination of stress concentrations, additives to hydrogen, proper grain size, and careful alloy selection. Additional measures may be the use of aluminum as construction material or medium strength steel (for hydrogen gas) and stainless steel (for LH_2), the design of metal components assuming an up to fivefold safety factor, and the consideration of the fact that environmental and internal hydrogen embrittlement increases in the temperature range 200–300 K (-73 °C to 27 °C).

The main considerations of mechanical properties of metals and alloys at low temperatures taken into account for safety reasons are the transition from ductile-to-brittle behavior, certain unconventional modes of plastic deformation, and mechanical and elastic properties changes due to phase transformations in the crystalline structure.

With regard to low temperature embrittlement, this change may lead to an accidental failure of a hydrogen storage vessel or pipe and cause an accident. Such an accident occurred in Cleveland in 1944 due to low-temperature embrittlement of a liquefied natural gas (LNG) storage vessel made of 3.5% nickel steel with a capacity of 4248 m^3. The vessel ruptured and released 4163 m^3 of LNG, which ignited after having spread into nearby storm sewers. As a domino effect, a nearby storage vessel collapsed from the fire and spilled its contents, which also burned with flames up to about 850 m height. The accident resulted in 128 deaths and 200–400 injuries and an estimated U.S.$6,800,000 (1944 dollars) in property damage.

Different structural materials have different thermal contraction coefficients, meaning that accommodations should be made for their different dimensions at cryogenic temperatures. If not, problems associated with safety (e.g., leaks) may arise. Generally, the contraction of most metals from room temperature (300 K) to a temperature close to the liquefaction temperature of hydrogen (20 K) is <1%, whereas the contraction for most common structural plastics is from 1% to 2.5%.

Safety measures in installations handling hydrogen include the elimination of all likely sources of ignition. An investigation of industrial accidents has shown that 53% of them occurred because of leaks, off-gassing, and equipment ruptures.

The flammability limits of mixtures of hydrogen with air, oxygen, or other oxidizers depend on the ignition energy; temperature; pressure; presence of diluents; and size and configuration of the equipment, facility, or apparatus. Such a mixture may be diluted with either of its constituents until its concentration shifts below the lower flammability limit (LFL) or above the upper flammability limit (UFL). The flammability limits of hydrogen mixtures with either air or oxygen widen for upward flame propagation and narrow for downward flame propagation. Mixtures of LH_2 and liquid oxygen (LOX) or solid oxygen as oxidizer are not hypergolic. In accidental fires of these mixtures during the mixing process, the system caught fire because the required ignition energy is very small. However, LH_2 and liquid or solid oxygen can detonate when initiated by a shock wave. Flammability limits move closer to one another when pressure reduces below 101.3 kPa (1 atm).

Hydrogen–air mixture. The lowest pressure for which a low-energy ignition source ignites a hydrogen–air mixture is approximately 6.9 kPa (0.07 atm) at a hydrogen concentration between 20% and 30% by volume. Hydrogen–air mixtures ignited by a 45 mJ spark ignition source at 311 K (38 °C) have an LFL equal to 4.5% by volume over the pressure range 34.5–101.3 kPa (0.34–1 atm). An increasingly higher LFL was required to obtain combustion below 34.5 kPa (0.34 atm). The lowest pressure for which a low-energy ignition source could inflame the mixture was 6.2 kPa (0.06 atm) at a hydrogen–air mixture of between 20% and 30% by volume hydrogen. Yet, using a strong ignition source, the lowest pressure for which ignition can occur is 0.117 kPa (0.0012 atm). For downward propagation, the LFL of hydrogen– air decreases from 9.0% to 6.3% by volume hydrogen and the UFL increases from 75% to 81.5% by volume hydrogen when the temperature is increased from 290 to 673 K (17–400 °C) at a pressure of 101.3 kPa (1 atm).

Hydrogen–oxygen mixtures. The flammability limits for hydrogen–oxygen mixtures at 101.3 kPa (1 atm) range from 4% to 94% by volume hydrogen for upward propagation in tubes. Reduced pressures increase the LFL. The lowest pressure observed for ignition is 57 Pa (0.56 atm) at a hydrogen concentration of 50% by volume when a high-energy ignition source was used. At elevated pressures, the LFL does not change with pressure up to 12.4 MPa (122 atm), whereas at 1.52 MPa (15 atm) UFL is 95.7% by volume hydrogen. The LFL decreases from 9.6% to 9.1% by volume hydrogen and the UFL increases from 90% to 94% by volume hydrogen, when the temperature rises from 288 to 573 K (15–300 °C).

Effects of diluents and halocarbon inhibitors. The effect of equal concentrations of added diluents in wide tubes on flammability limits for hydrogen in air increases in the order: $CO_2 < N_2 < He < Ar$. Thus, argon is the least effective in reducing the flammable range of hydrogen in air. Measurements performed for the water vapor at 422 K (149 °C) have shown that water is the most effective of all these diluents in reducing the flammability range of hydrogen in air. The effect of the flame inhibitors N_2, CH_3Br, and $CBrF_3$ required to extinguish hydrogen diffusion flames in air has been compared. The chlorinated inhibitors were more effective when added to the air stream, whereas nitrogen was more effective when added to the fuel stream.

Autoignition temperature. The autoignition temperature of hydrogen in air differs only slightly than that in oxygen. It is interesting to note that autoignition temperatures in both cases depend not only on GH_2 concentration and pressure, but also on the surface treatment of containers as well. Therefore, the autoignition temperatures found in the literature are very dependent on the system and values should be applied only to similar systems. At 101.3 kPa (1 atm), the range of reported autoignition temperatures for stoichiometric hydrogen in air is from 773 to 850 K (500–577 °C), whereas for stoichiometric oxygen it is from 773 to 833 K (500–560 °C). At pressures from 20 to 50 kPa (0.20–0.49 atm), GH_2–air ignitions have occurred at 620 K (347 °C).

Quenching gap in air. Quenching distance is the passage gap dimension required to prevent the propagation of an open flame through a flammable fuel–air mixture that fills the passage. In parallel-plate configuration, the quenching gap is defined as the spark gap between two flat electrodes at which ignition of combustible fuel– air

mixtures is suppressed. The quenching gap for hydrogen is 0.6 mm at NTP air. Nevertheless, this value depends on the temperature, pressure, and composition of the combustible gas mixture and the electrode configuration. Generally, faster burning gases have smaller quenching gaps. Consequently, flame arresters for faster burning gases require smaller apertures. The lowest quenching distance found in the literature for hydrogen is 0.076 mm. There are three major factors that determine the quenching distance for a gaseous fuel such as hydrogen: ignition energy, mixture composition, and pressure. Quenching gap depends on the ignition energy. For instance, low ignition energy of the order 0.001 mJ corresponds to a small gap of the order 0.01 cm. In contrast, high ignition energy of the order 10 mJ corresponds to a larger gap of the order 1 cm. Pressure and composition also affect the quenching distance, the quenching distance increasing rapidly at very low pressures. Since specific values for hydrogen–air mixtures are not available, the effect of pressure as a function of tube diameter for deflagration and detonation of acetylene–air mixtures can be used as a guideline.

All ignition sources, such as open flames, electrical equipment, or heating equipment, should be eliminated or safely isolated in buildings or special rooms containing hydrogen systems, and operations should be conducted as if unforeseen ignition sources could occur. The ignition of GH_2–air mixtures usually result in deflagration, whose explosive consequences are significantly less severe than if detonation results. Potential ignition sources ranked according to frequency of occurrence is as follows: open flames > hot works > electrical (short circuits, sparks, and arcs) > hot surfaces > personnel smoking > friction > spontaneous ignition > autoignition > hot particles > static discharge > others (e.g., lightning).

Electrical sparks can be the result of electrical discharges between objects having different electrical potentials, such as breaking electrical circuits or discharges of static electricity. Static electricity sparks can ignite hydrogen–air or hydrogen–oxygen mixtures. Static electricity is caused by many common articles such as hair or fur when combed or stroked or an operating conveyor belt. People can generate high-voltage charges of static electricity on themselves when walking on a synthetic carpet or dry ground, moving while wearing synthetic clothing, sliding on automobile seats, or combing their hair. The flow of GH_2 or LH_2 in ducts or turbulence in containers can generate charges of static electricity, as any other nonconductive liquid or gas. In addition, static charges may be induced during electrical storms.

Hard objects coming into shearing contact with one another can cause friction sparks, as in the cases of metal striking metal, metal striking stone, or stone striking stone. Friction sparks are particles of burning material, initially heated by the mechanical energy of friction and impact that have been sheared off as a result of contact. Sparks from hand tools have normally low energy, whereas mechanical tools, such as drills and pneumatic chisels, can generate high-energy sparks.

Hard objects striking one another can also produce impact sparks. Impact sparks are usually produced by impact on a quarzitic rock, such as the sand in concrete, and then small particles of the impacted material are thrown off.

Minimum spark energy for ignition is defined as the minimum spark energy required to ignite the most easily ignitable concentration of fuel in air and oxygen. The minimum spark energies of hydrogen in air are 0.017 mJ at 101.3 kPa (1 atm), 0.09 mJ at 5.1 kPa (0.05 atm), and 0.56 mJ at 2.03 kPa (0.02 atm). The minimum spark energy required for ignition of hydrogen in air is considerably less than that for methane (0.29 mJ) or gasoline (0.24 mJ). Nevertheless, the ignition energy for all the three fuels is sufficiently low that ignition in air is relatively certain in the presence of any weak ignition source such as, sparks, matches, hot surfaces, open flames, or even a weak spark caused by the discharge of static electricity from a human body.

Hot objects and flames. Objects at temperatures from 773 to 854 K (500–581 °C) can ignite hydrogen–air or hydrogen–oxygen mixtures at atmospheric pressure. Substantially cooler objects, about 590 K (317 °C), can also ignite these mixtures after prolonged contact at less than atmospheric pressure. In cases that ignition sources are a required part of hydrogen use, provisions should be made to acceptably contain any resulting deflagration or detonation. For instance, a combustor or engine should not be operated in atmospheres containing hydrogen without well-dispersed water sprays in its exhaust. Experience has shown that multiple bank sprays will partially suppress the detonation pressures and reduce the number and temperature of ignition sources in an exhaust system. Water sprays should not be relied on as a means of avoiding detonations. Carbon dioxide may be used with the water spray to further reduce hazards.

The general term explosion corresponds to a rapid energy release and pressure rise and can occur in both reactive and nonreactive systems. Pressurized gas vessel failures are typical examples of nonreactive explosions, whereas premixed gases of fuel and oxidizer permit a rapid energy release by chemical reactions in reactive systems. Gas explosions do not necessarily require the transmission of a wave through the explosion source medium, although explosions in most cases involve some kind of wave such as a deflagration or detonation wave. Deflagration is the phenomenon in which the flame front moves through a flammable mixture in the form of a subsonic wave with respect to the unburned mixture. The terms deflagration, combustion, flame, and burn are found in the literature to be used interchangeably as synonymous. Detonation is the phenomenon in which the flame front coupled to a shock wave propagates through a detonable mixture in the form of a supersonic wave with respect to the unburned mixture. Generally, detonation propagates a thousand times faster than deflagration resulting in pressures at the detonation front 15–20 times higher than the initial ones. This explains why detonation has much greater potential for causing personnel injury or equipment damage than deflagration.

Especially, for gaseous mixtures exploding in the open the term unconfined vapor cloud explosion (UVCE) is used, whereas when it explodes in confined spaces the term confined vapor cloud explosion (CVCE) is used. In a very poor or very rich fuel mixture, but still within flammability limits, the flame front travels in the cloud at low velocity and insignificant pressure increase a phenomenon known as flash fire.

Another explosion phenomenon encountered in the storage of liquefied hydrogen under pressure is the BLEVE, which occurs from the sudden release of a large mass of pressurized liquid into the atmosphere. The content of the vessel released into the atmosphere, if flammable, ignites forming a nearly spherical burning cloud, the so-called fireball.

The maximum and minimum concentrations of a gas, vapor, mist, spray, or dust in the air or other gaseous oxidant for a stable detonation to occur are the so-called upper and lower detonation limits. These limits depend on the size and geometry of the surroundings as well as other factors. Therefore, detonation limits found in the literature should be used with caution. Detonation limits are sometimes confused with deflagration limits and the term explosive limits is then used inconsiderately.

Detonable concentrations are narrower than flammable concentrations for hydrogen as well as for all other gases. The worst case during an accidental release is reaching around stoichiometric concentration of a flammable gas for a detonation to occur provided an ignition source is present. These detonable concentrations are quite infrequent to occur in an enclosed area and rather unlikely in the open air for most gases possessing lower and higher detonation limits very close to one another. Unfortunately, in some gases, among which is hydrogen, this concentration span is quite broad and the detonability range is easily attained leading to much more serious accidents than those of the narrow-spanned gases.

The higher diffusion coefficient of GH_2 compared to other gases means that any release will quickly mix with the surrounding air, reach the dangerous range, and then come down to the safe region below the LFL. In an LH_2 leak, fast vaporization occurs first and molecular diffusion in the air follows. However, the positive buoyancy of GH_2 can move a release to higher floors in a building endangering these areas or to safe heights in the open air.

Detonation limits for any fuel–oxidizer mixture depend on the nature and degree of confinement among other factors.

Minimum ignition energy depends on hydrogen concentration in the detonable mixture. This is about 1 g of tetryl for hydrogen–air mixtures at the stoichiometric composition (possessing the highest sensitivity) increasing to several tenths of grams for very rich or very poor mixtures (near the detonation limits). Stable detonation parameters such as detonation temperature and pressure can be calculated by the Chapman–Jouguet approach using the Gordon–McBride computer code. The dependence of detonation temperature and pressure on hydrogen concentration for hydrogen–air mixtures and hydrogen–oxygen mixtures are shown in Figs. 10 and 11, respectively. Maximum values of approximately 3000 K and 1600 kPa for hydrogen–air mixtures near stoichiometric composition are observed, whereas these maxima rise to about 3800 K and 2000 kPa for stoichiometric hydrogen–oxygen mixtures.

With regard to the catastrophic effects of an accidental release and subsequent explosion, the energy of explosion is often taken into consideration. Calculations such as 1 g stoichiometric hydrogen in NTP air is equivalent to 24 g of TNT are usually found in the literature, but they are misleading since they do not take into account the weight of the oxidant (air in this case). By including air in the

Fig. 10 Detonation
pressure and temperature of
hydrogen–air mixtures
starting from 101.3 kPa
(1 atm) and 298 K (25 °C).
Chapman–Jouguet
calculations using the
Gordon–McBride code
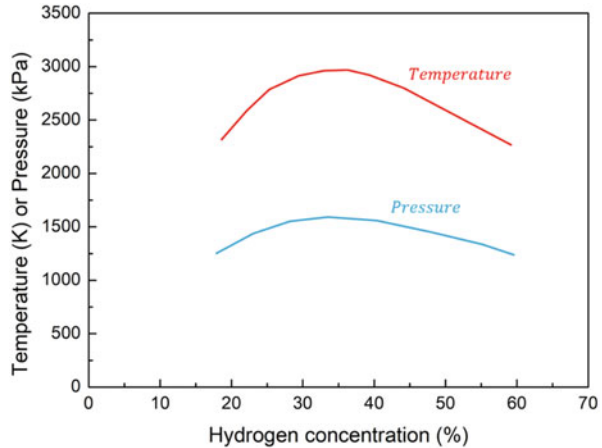
Fig. 11 Detonation
pressure and temperature of
hydrogen–oxygen mixtures
starting from 101.3 kPa
(1 atm) and 298 K (25 °C).
Chapman–Jouguet
calculations using the
Gordon–McBride code
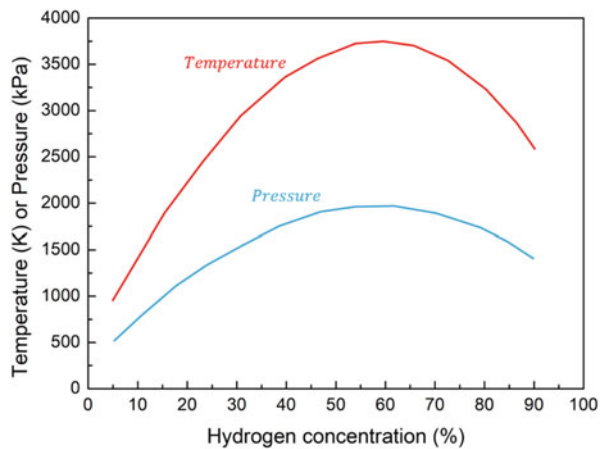
calculations, it becomes clear that the stoichiometric hydrogen–air mixture produces only two-thirds of the explosion energy of TNT. This difference can be easily explained by the dilution effect of nitrogen in the air. In addition, it should be noted that in an accidental release mixing of hydrogen with air is not perfect; therefore, only a small fraction of the theoretical energy will be produced.

Other factors that determine the catastrophic effects of an explosion are the initial density of the explosive (which is more than three orders of magnitude higher for TNT than for hydrogen–air mixture) and detonation velocity (which is three to five times higher in TNT). Therefore, the resulting pressure wave from a hydrogen explosion is considerably flatter (longer duration and lower maximum overpressure) than TNT, and destruction effects are mainly caused by impulse rather than overpressure.

The oxidation (combustion) of hydrogen in the air or other oxidant (e.g., pure oxygen) can be subsonic (deflagration) or supersonic (detonation) depending on the strength of the ignition source. A high energetic source such as a shock wave can initiate a detonation, whereas a low-strength energy source such as a flame or a spark can initiate a deflagration. However, there is a possibility that a deflagration transits to a detonation after the flame has traveled for some time and distance when factors such as sufficient degree of confinement and the presence of obstacles inducing turbulence in the flame front, limit energy losses, and suitably mix the ingredients, thus triggering a detonation. This phenomenon, which is not a continuous process but rather a stepwise change, is known as deflagration-to-detonation transition (DDT).

Generally, the composition range in which a detonation can take place is narrower than that of deflagration. The range for detonation limits for a hydrogen–air mixture is from 18.3% to 59% hydrogen. However, with sufficiently strong ignition sources, these limits can be extended and, in addition, an overdriven detonation can be obtained possessing a higher detonation velocity that gradually declines to a stable detonation at a thermodynamically determined lower velocity.

In contrast to high-pressure GH_2 storage vessels, liquefied hydrogen vessels operate in moderate to low pressures that normally do not exceed 20 bars. As a result, it is reasonable for the walls to be designed with lower pressure resistance than that of hydrogen gas (whose operation pressure may be over than 400 bars) being liable to increased risk of failure. In case that the container is engulfed in a fire, its metal is heated and loses mechanical strength. While the liquid phase absorbs significant amounts of heat, vapors possess far lower specific heat capacity. Therefore, the heat supplied to that part of the container where the vapor phase exists will raise much more the local wall temperature thus weakening its strength.

Concerning liquefied gas storage, vessel overheating may result in internal temperatures higher than the boiling point of the content, indeed without vaporization initiation of the liquid phase, and then the liquid is superheated. The phenomenon is observed when there is a shortage of nucleation sites (i.e., impurities, crystals, or ions) in the bulk of the liquid. However, there is a temperature limit above which the fluid cannot remain in the liquid state anymore (homogeneous nucleation limit or superheat limit temperature). In this limit, random molecular density fluctuations within the bulk of a liquid produce hole like regions of such molecular dimensions that may act as bubbles. The end result is the explosive flash of the liquid accompanied by a strong shock wave that propagates through the fluid and ruptures the container spilling the content into the atmosphere (BLEVE). Missiles of the ruptured walls may travel hundreds of meters, whereas the flammable content ignites forming a sphere that burns from the outer to inner layers (fireball).

At hydrogen refilling stations and vehicles, hydrogen has to be compressed at high pressures (typical value: 400 bars) due to the low energy content per unit volume.

Nevertheless, in some applications, hydrogen needs to be stored in the liquid state at very low temperatures for volume restriction. These temperatures are often lower than −73 °C so that storage conditions are characterized as cryogenic distinguished

from the refrigerated ones. These conditions are preferred, for example, in uses such as rocket propulsion as well as in warehousing for convenience and economy. A crucial factor for the liquefaction implementation is the critical temperature above which the gas cannot be liquefied by pressure application only. In practice, hydrogen is kept liquefied at extremely low temperatures below -240.2 °C and moderate pressures (20–30 bars). Major hazards related to cryogenic storage stem from

- Embrittlement of service materials. The low temperatures inside storage tanks and transmission pipelines may cause significant susceptibleness of the structural material in vibrations and shocks. Mild steel and most iron alloys, at LH_2 temperatures, lose their ductility being liable to increased risk of mechanical failure.
- LH_2 spills. Liquefied hydrogen releases yield dramatically larger volumes of combustible clouds (1 L of liquid produces 851 L of gas on evaporation). Therefore, the consequences of a fire or explosion are more extensive than that of a pressurized hydrogen release.
- Extremely low temperature. It can cause severe tissue frostbite if the material comes into contact with human body. Flesh may stick fast to cold insufficiently insulated pipes or vessels and tear on attempting to withdraw it.
- Hydrogen cloud dispersion. As discussed hereinafter, hydrogen spill originated from cryogenic storage resulting in cloud formation that disperses with a way similar to a heavier-than-air gas increasing the risk of accidental fires and explosions.

Hazard evaluation in hydrogen storage facilities deals with the determination of all credible accidental scenarios. To do this, a variety of methods (event tree, failure mode and effect analysis, what-if, fault tree) can be found in the relevant literature. Of them, event tree analysis (ETA) is a formal technique and one of the standard approaches used for industrial incidents investigations. ETA is a logic model that graphically portrays the combination of events and circumstances in an accident sequence. It is an inductive method, which begins with an initiating undesirable event and works toward a final result (outcome). The general procedure for ETA involves the following steps:

1. Determination of the initiating events that can result in certain types of accident
2. Identification of the critical factors that may affect the initiating event evolution
3. Construction of the event tree taking into account the interaction between the critical factors and the initiating event
4. Designation and evaluation of resulting accidental events

Applying ETA in fuel gas releases, the critical factors that may affect substantially the final outcome are the time of ignition of the resulting cloud and the confinement provided by the surroundings. The former is related to the mixing of escaping fuel gas with air. When immediate ignition occurs, gas cloud mixing with atmospheric oxygen is still limited; thus, the ignition takes place on the outer layer that is between the flammable limits, whereas the inner core of the cloud is too rich in fuel to ignite.
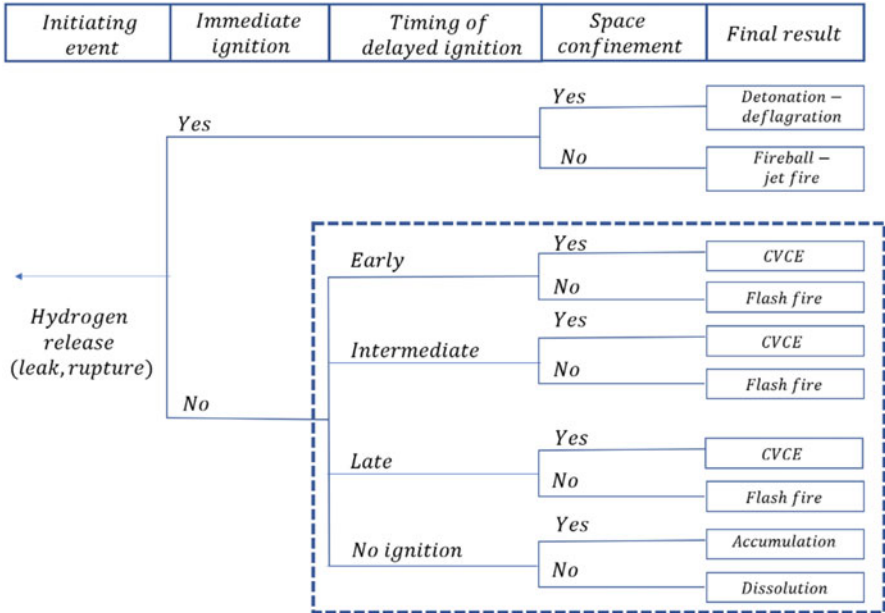
Fig. 12 Event tree analysis adapted to accidental hydrogen releases

As buoyancy forces of the hot gases begin to dominate, the burning cloud rises and becomes more spherical in shape forming a ball into flames. This elevation gradually causes further mixing of the gas with oxygen, which brings new volumes of gas into flammable limits sustaining the fire. In contrast, when delayed ignition occurs, the fuel cloud may have been adequately mixed with air, so that after ignition it flashes back. It differs from fireball since it proceeds faster and can burn from inner to outer flammable layers provided a proper ignition source is found there.

The application of ETA regarding accidental hydrogen release is displayed in Fig. 12.

It is obvious that, unless an immediate ignition takes place, there is some time of dispersion that intervenes between release and ignition. Generally, if hydrogen flammability zones were known, it would be possible to take preventive measures and to prepare emergency response planning against fires and explosions. Consequently, a major issue arises regarding the computation of the dispersion succeeding an accidental hydrogen release.

Furthermore, even if no ignition takes place, escaping hydrogen may accumulate into closed spaces adjacent to the source posing asphyxiation hazard for the people being there. Hydrogen dispersion may be considered safe only when no ignition occurs, and no space confinement exists.

Event tree analysis adapted to accidental hydrogen releases. The selection of the appropriate dispersion model in an accidental release scenario requires the behavior of dispersing gas to be known since each model is specialized on one kind of release (buoyancy or gravity driven).

Hydrogen preserves the property of light gas behavior even when releases from highpressure storage systems occur. But, once hydrogen escapes while stored in the liquid state, its dispersion behavior turns to that of a heavy rather than a light gas. The different way in which a gas disperses according to the storage conditions has been observed in field-scale trials with another light gas (natural gas) that was left to escape and disperse while stored in the liquid state. In this case, instead of elevation the vapor cloud moved along the ground being under the LFL limit for several tenths of meters.

Gasoline is certainly the easiest and perhaps the safest fuel to store because of its higher boiling point, lower volatility, and narrower flammability and detonability limits. This generalized assumption is based on previous discussion concerning fire and explosion hazards. Nevertheless, hydrogen and methane (the principal ingredient of natural gas) can also be safely stored using current technology.

Despite its volumetric energy density, hydrogen has the highest energy-to-weight ratio of any fuel. Unfortunately, this weight advantage is usually overshadowed by the high weight of the hydrogen storage tanks and associated equipment. Thus, most hydrogen storage systems made for transport applications are considerably bulkier or heavier than those used for liquid fuels such as gasoline or diesel fuels. Attempting a comparison with regard to the hazards posed by hydrogen, methane, and gasoline, the following remarks can be made:

- Size of molecules. Since the hydrogen molecule is smallest of all it will leak through permeable materials where methane and gasoline will not.
- Fuel spills. In the event of a fuel spill, it is expected that a fire hazard develops most rapidly in the descending order: hydrogen, methane, and gasoline. With regard to fire duration, gasoline fires last the longest and hydrogen fires are the shortest ones, while all the three fuels burn at nearly the same flame temperature. In fact, for spillage of identical liquid fuel volumes, hydrocarbon fires will endure 5–10 times longer than hydrogen fires.
- Odorization. Natural gas is odorized so that leaks can be detected, whereas gasoline is normally smelly. Odorization of natural gas is a prudent although not entirely effective safety measure. Hydrogen as an industrial gas or fuel cell vehicle fuel is not odorized because sulfur-containing substances (mercaptans) contaminate the catalysts of a fuel cell.
- Buoyancy. Hydrogen is 14.5 times lighter than air at NTP, whereas methane is 1.8 times lighter and gasoline vapor is heavier than air. Thus, hydrogen will rise much more quickly causing greater turbulent diffusion, which reduces its concentration below the LFL more rapidly. Moreover, hydrogen diffuses into air approximately 4 times faster than methane and 12 times faster than gasoline, thus causing rapid concentration decrease in safe levels.
- Energy of explosion. The energy of explosion values should be considered as the theoretical maxima, and yield factors of 10% are considered reasonable for fuel–air explosions. For equivalent volume storage, hydrogen has the least theoretical explosive potential of the three fuels considered, albeit it has the highest heat of combustion and explosive potential on a mass basis.

- Flammability and detonability limits. The broader flammability and detonability limits of hydrogen coupled with its rapid burning velocity renders hydrogen a greater explosive threat than methane or gasoline.
- Ignition energy. The ignition energy of hydrogen is about 1/14 and 1/12 of that for methane and gasoline, respectively. However, the energy levels required for the ignition of these fuels are so low that common ignition sources such as static electricity discharge from a human body will ignite any of these fuels in air.
- Autoignition temperature. Hydrogen and methane possess unusually high autoignition temperatures (585 °C and 540 °C, respectively), whereas gasoline with autoignition temperature ranging from 227 °C to 477 °C appears more hazardous.
- Deflagrations. A confined deflagration of hydrogen–air or methane–air will produce a static pressure rise ratio of less than 8:1. Explosion pressures for confined deflagrations of gasoline–air is about 70–80% of those for hydrogen–air. Unconfined deflagration overpressures are usually <7 kPa. However, a pressure of 3–4 kPa is sufficient to cause structural damage to buildings; therefore, unconfined large-volume gasphase explosions can be destructive. Thus, it is apparent that confined deflagrations with up to 8 atm (811 kPa) of explosion pressure can be devastating and even unconfined deflagrations can cause slight-to-moderate structural damage, and injure people via fire and window-glass shrapnel.
- Detonations. Pressure rises ratios of ∼15:1 for hydrogen–air or methane–air detonations and a ratio of ∼12:1 for a gasoline–air detonation are normally expected. The impulse created by explosion pressure profile should be taken into account in evaluating explosion damage and in the design of barricades or structures to mitigate explosion consequences.
- Shrapnel hazards depend on explosion over pressures, and with ordinary enclosures (L/D < 30) are about the same for hydrogen–air and methane–air and somewhat less severe for gasoline–air mixtures. Nevertheless, in long structures, such as tunnels or pipes, hydrogen poses a greater explosion risk than the other two fuels due to its greater tendency for a DDT. Thus, hydrogen presents the greatest hazard to shrapnel damage.
- Radiant heat. Owing to the heat-absorbing water vapor created during hydrogen combustion and the absence of a carbon combustion reaction, the radiant heat from a hydrogen fire is significantly less than a hydrocarbon fire, and this reduces the risk of secondary fires. The reduced radiant heat entails reduced heating of adjacent equipment in case of a major fire and hence reduced probability for a domino effect that leads to escalating damage and losses.
- Hazardous smoke. The potential for smoke inhalation damage is judged to be most severe in the descending order: gasoline, methane, and hydrogen fires.
- Flame visibility. Unlike visible methane and gasoline flames, hydrogen burns with a near-invisible flame in daylight, but contaminants in air generally add some visibility. Hydrogen flames are visible at night and modern detection equipment can detect them even in daylight.

- Firefighting. Normally, hydrogen and methane fires should be allowed to burn until gas flow is stopped or until liquid spills are consumed because of the potential explosive hazard resulting from extinguishing these fires. However, the fire should be controlled by cooling the storage tanks with water in all situations. Dry chemicals and high-expansion foams can be used to extinguish methane and gasoline fires.

Conclusively, hydrogen has been used and stored safely in the industry for quite a long time as compressed gas or liquefied hydrogen, and it seems that metal hydride storage will be equally safe or even safer. Consideration of future hydrogen applications reveals no safety problems in the industrial and commercial markets. Although hydrogen safety problems have been efficiently controlled in the industry, additional safety analyses are needed in the transportation and residential fuel markets.

The following are general guidelines to ensure safety in the hydrogen storage and transfer areas. Good illumination, lightning protection, alarm systems, and gas detection and sampling systems should be provided in such a facility. More detailed safety guidelines concerning safety policy; safety in construction, operation, maintenance, and final disposition of a hydrogen facility; as well as safety measures in buildings and test chambers used in hydrogen service and emergency procedures can be found in Safety Standard for Hydrogen and Hydrogen Systems from which some synoptic information is given in this section enriched with other references.

- Electrical considerations. Areas where flammable hydrogen mixtures are expected to occur or areas where hydrogen is stored, transferred, or used and where the hydrogen normally is contained are classified as highly hazardous zones according to internationally accepted regulations. All electrical sources of ignition should be prohibited in these areas, using approved explosion-proof equipment or selecting nonarcing approved equipment. Explosion-proof equipment has an enclosure strong enough to contain the pressure produced by igniting a flammable mixture inside the enclosure. Since it is not gas tight, the joints and threads must be tight enough and long enough to prevent issuance of flames or gases that would be hot enough to ignite a surrounding flammable mixture. Another method to prevent a gas explosion is to locate the equipment in an enclosure purged and maintained above ambient pressure with an inert gas. Intrinsically safe installations used in the facility should be approved for hydrogen service.
- Hydrogen transmission lines carrying hydrogen from trailers and storage vessels must be aboveground installations. Hydrogen lines crossing roadways should be installed in concrete channels covered with an open grating and should not be located beneath electric power lines. Area surfaces located below liquefied hydrogen lines from which condensed liquid air may drop must be constructed of noncombustible materials such as concrete. A hydrogen leak, due to its very low density, can easily find the way to upper floors in a building traveling through connecting ducts and other openings and cause secondary explosions in other rooms.

- Elimination of ignition sources. Installations using hydrogen should be protected from lightning-by-lightning rods, aerial cable, and ground rods suitably connected. Lightning strikes may cause inducing sparks; therefore, all equipment in a building should be bonded and grounded to prevent sparks. Static electricity may be generated in moving machinery belts or in flowing fluids containing solid or liquid particles. The measures taken to limit electrostatic charge generation and accumulation include bonding and grounding of all metal parts within a system, use of conductive machinery belts, personnel clothes made of antistatic fibers, and conductive and non-sparking floors. Sparks may also be generated by other mechanisms such as friction and impact. Even spark-proof tools can cause ignitions because the energy required for ignition of flammable hydrogen–air mixtures is extremely small.
- Hot objects, flames, and flame arrestors. The measures taken to eliminate ignition by flames and hot objects and prevent proliferation of a fire to other areas (domino effect) include prohibition to use a flame, welding or cutting within the exclusion area around a hydrogen facility, equipment of internal combustion systems with exhaust system spark arrestors, and carburetor flame arrestors. Only flame arrestors specifically designed for hydrogen applications must be used taking into account the oxidant present. Flame arrestors can quench a flame on the basis of sufficient heat removal from the gas mixture. It is quite difficult to develop flame arrestors and explosion-proof equipment for hydrogen due to its small quenching distance (0.6 mm). Sintered-bronze flame arrestors may be effective in stopping hydrogen flames, whereas sintered stainless steel is not so effective.
- Design and construction of buildings. Buildings in which hydrogen is used must be constructed of light and noncombustible materials on a sufficiently strong frame. Windowpanes must be made of shatterproof glass or plastic. Floors, walls, and ceilings should be designed and installed to limit the generation and accumulation of static electricity and shall have a fire resistance rating of at least 2 h. Explosion venting must be provided only in the exterior walls or the roof. The venting area should be not <0.11 m^2/m^3 of room volume. Vents, designed to relieve at a maximum internal pressure of 1.2 kPa, may consist of one or a combination of walls of light material, lightly fastened hatch covers or outward-opening swinging doors in exterior walls or roof. Doors should be hinged to swing outward in an explosion and must be readily accessible to personnel. Walls or partitions must be continuous from floor to ceiling and securely anchored. At least one wall must be an exterior wall, and the room must not be open to other parts of the building. Only indirect means, such as steam and hot water, should be used for heating in rooms containing hydrogen.
- Barricades. These are constructed to protect uncontrolled areas from the effects of a hydrogen system failure and to protect a hydrogen system from the hazards of adjacent or nearby operations. Barricades have been shown to be most effective against arguments and only marginally effective in reducing overpressures. The housing of equipment provides partial protection in many cases. Shrapnel protection can be achieved by blast curtains or blast mats placed adjacent to the equipment to be protected. Barricades are commonly constructed as mounds and

single-revetted barricades. A mound (earthworks) is an elevation of sloped dirt with a crest at least 0.91 m wide, whereas single-revetted barricades are mounds supported on a retaining wall on the side facing the hazard source. Simulations and experimental works have shown that:

- Barricades should be designed to block the line of sight between equipment from which fragments can originate and protect items.
- Barricades should be placed adjacent to the fragment source for maximum protection.
- The efficiency of barricades depends on the height aboveground and barricade location, dimensions, and configuration.
- Barricades can reduce peak overpressures and impulses behind the barricades, but reflections on obstacles may amplify blast waves behind barricades.
- Single-revetted barricades are more efficient than mounds.

- Liquid spills and vapor cloud dispersion. An LH_2 spill from a storage vessel will result in a brief period of ground-level flammable cloud travel. The quick evaporation of the liquid causes the hydrogen vapors to mix quickly with air, dilute to nonflammable concentrations, warm up, and become positively buoyant. If barricades are chosen, these should not confine excessively the vapor cloud formed because it may lead to detonation rather than simple burning of escaped hydrogen. LH_2 spill tests in an open-ended (U-shaped) bunker may produce detonation of the hydrogen–air mixture even without a roof. The use of dikes and barricades around storage tanks is not recommended for LH_2, although this is required for LNG because it may prolong evaporation and ground-level travel of the flammable cloud. Hydrogen detectors should be positioned to indicate the possible groundlevel travel of flammable mixtures. No sewer drains must be located in an area in which a liquefied hydrogen spill could occur.
- Shields and impoundment areas. Impoundment areas and shields to control the extent of liquid and vapor travel caused by spills should be included in the design of a facility using hydrogen. The terrain below the transfer piping should be directed to a sump or impoundment area. Crushed stone should be used in the impoundment area to provide added surface area for liquefied hydrogen dissipation. Careful design of installations should eliminate possible confinement developed by the equipment or buildings because initial combustion or deflagration of hydrogen– air mixtures may evolve to DDT.

8   Conclusions

Around the world, the state of existing regulations and standards currently limits hydrogen uptake. Certain regulations are unclear or not written with new uses of hydrogen in mind and do not allow exploitation of the full benefits hydrogen can provide. They deal with a range of technical but important questions such as how and where pressurized or liquefied hydrogen can be used, who can handle hydrogen,

where hydrogen vehicles can go, tax regimes for conversion between energy carriers, whether CO_2 can be stored, and how much hydrogen can be present in natural gas pipelines. They need to be updated if hydrogen is to have the opportunity to fulfil its potential.

Some important standards have yet to be agreed, including standards dealing with hydrogen vehicle refueling, gas composition for cross-border sales, safety measures, permitting, materials and how to measure lifecycle environmental impacts. The issue of lifecycle impacts poses a particular challenge in the case of hydrogen because identical hydrogen molecules can be produced and combined from sources with very different CO_2 intensities. Unlike electricity, hydrogen and hydrogen-based fuels can be blended with fossil fuels in mixtures that end-users cannot identify. Accounting standards for different sources of hydrogen along the supply chain may be fundamental to creating a market for low-carbon hydrogen and need to be developed on an internationally agreed basis.

Hydrogen comes with safety risks, high upfront infrastructure costs and some of the industrial dynamics of fossil fuel supply and distribution, especially when paired with CCUS. It is not yet clear how citizens will react to these aspects of hydrogen, or how they will weigh them alongside the convenience and environmental benefits of some hydrogen applications, as well as the potential importance of hydrogen to long-term sustainability.

The recent efforts to develop requirements for vehicle hydrogen storage have drawn on the rich history with CNG vehicle storage and from the broad community of experts. That community has included pressure vessel and component manufacturers, experts from the emerging fueling and repair/service infrastructures, and the vehicle designers/ manufacturers, who bring broad experience with on-road vehicle safety and management of risk when a product is used by a diverse population in uncontrolled conditions.

The more fundamental shifts in perspective that have occurred during these recent efforts have pertained to the data-driven approach to developing performance-based requirements that clearly address simultaneous exposures to different stresses and stress rupture susceptibility that could develop over vehicle life. The end-of-life requirements for residual strength (resistance to rupture and stability of ultimate burst strength) focus on verifying actual characteristics of storage systems after severe exposures to on-road stresses.

The resultant shift to performance-based requirements for compressed storage of hydrogen on vehicles provides a proactive, rather than reactive, approach to preventing on-road failures. It focuses on the breadth and severity of on-road service conditions that all storage systems must survive with full performance. Comprehensive on-road worst-case conditions encompass circumstances of past failures, while they apply more generally to future technologies. The requirements are linked to the severity of on-road stresses that can be experimentally measured to substantiate the specification of performance requirements with data. By these means, the requirements are designed to provide a higher level of safety assurance.

References

Abohamzeh E, Salehi F, Sheikholeslami M, Abbassi R, Khan F (2021) Review of hydrogen safety during storage, transmission, and applications processes. J Loss Prev Process Ind 72:104569. https://doi.org/10.1016/j.jlp.2021.104569

Casamirra M, Castiglia F, Giardina M et al (2009) Safety studies of a hydrogen refuelling station: determination of the occurrence frequency of the accidental scenarios. Int J Hydrog Energy 34(14):5846–5854. https://doi.org/10.1016/j.ijhydene.2009.01.096

Correa-Jullian C, Groth KM (2022) Data requirements for improving the quantitative risk assessment of liquid hydrogen storage systems. Int J Hydrog Energy 47(6):4222–4235. https://doi.org/10.1016/j.ijhydene.2021.10.266

Dadashzadeh M, Kashkarov S, Makarov D et al (2018) Risk assessment methodology for onboard hydrogen storage. Int J Hydrog Energy 43(12):6462–6475. https://doi.org/10.1016/j.ijhydene.2018.01.195

Dincer I, Acar C (2015) Review and evaluation of hydrogen production methods for better sustainability. Int J Hydrog Energy 40(34):11094–11111. https://doi.org/10.1016/j.ijhydene.2014.12.035

Dwivedi SK, Vishwakarma M (2018) Hydrogen embrittlement in different materials: a review. Int J Hydrog Energy 43(46):21603–21616. https://doi.org/10.1016/j.ijhydene.2018.09.201

Foorginezhad S, Mohseni-Dargah M, Falahati Z et al (2021) Sensing advancement towards safety assessment of hydrogen fuel cell vehicles. J Power Sources 489:229450. https://doi.org/10.1016/j.jpowsour.2021.229450

Groth KM, Hecht ES (2017) HyRAM: a methodology and toolkit for quantitative risk assessment of hydrogen systems. Int J Hydrog Energy 42(11):7485–7493. https://doi.org/10.1016/j.ijhydene.2016.07.002

Gye HR, Seo SK, Bach QV et al (2019) Quantitative risk assessment of an urban hydrogen refueling station. Int J Hydrog Energy 44(2):1288–1298. https://doi.org/10.1016/j.ijhydene.2018.11.035

Hadef H, Negrou B, Ayuso TG et al (2020) Preliminary hazard identification for risk assessment on a complex system for hydrogen production. Int J Hydrog Energy 45(20):11855–11865. https://doi.org/10.1016/j.ijhydene.2019.10.162

Hao D, Wang X, Zhang Y et al (2020) Experimental study on hydrogen leakage and emission of fuel cell vehicles in confined spaces. Automot Innov 3:111–122. https://doi.org/10.1007/s42154-020-00096-z

Hermesmann M, Müller TE (2022) Green, turquoise, blue, or grey? Environmentally friendly hydrogen production in transforming energy systems. Prog Energy Combust Sci 90:100996. https://doi.org/10.1016/j.pecs.2022.100996

Khalil YF (2015) Risk quantification framework of hydride-based hydrogen storage systems for light-duty vehicles. J Loss Prev Process Ind 38:187–198. https://doi.org/10.1016/j.jlp.2015.09.008

Kovač A, Paranos M, Marciuš D (2019) Hydrogen in energy transition: a review. Int J Hydrog Energy 46(16):10016–10035. https://doi.org/10.1016/j.ijhydene.2020.11.256

Kurtz J, Sprik S, Bradley TH (2019) Review of transportation hydrogen infrastructure performance and reliability. Int J Hydrog Energy 44(23):12010–12023. https://doi.org/10.1016/j.ijhydene.2019.03.027

Lemus RG, Duart JMM (2010) Updated hydrogen production costs and parities for conventional and renewable technologies. Int J Hydrog Energy 35(9):3929–3936. https://doi.org/10.1016/j.ijhydene.2010.02.034

Liu X, Zhang Q (2014) Influence of initial pressure and temperature on flammability limits of hydrogen–air. Int J Hydrog Energy 39(12):6774–6782. https://doi.org/10.1016/j.ijhydene.2014.02.001

López-Arquillos A, Rubio-Romero JC, Súarez-Cebador M (2015) Comparative risk assessment of vehicle maintenance activities: hybrid, battery electric, and hydrogen fuel cell cars. Int J Ind Ergon 47:53–60. https://doi.org/10.1016/j.ergon.2015.02.005

Lv H, Shen Y, Zheng T et al (2023) Numerical study of hydrogen leakage, diffusion, and combustion in an outdoor parking space under different parking configurations. Renew Sustain Energy Rev 173:113093. https://doi.org/10.1016/j.rser.2022.113093

Moradi R, Groth KM (2019) Hydrogen storage and delivery: review of the state of the art technologies and risk and reliability analysis. Int J Hydrog Energy 44(23):12254–12269. https://doi.org/10.1016/j.ijhydene.2019.03.041

Najjar YSH (2013) Hydrogen safety: the road toward green technology. Int J Hydrog Energy 38(25):10716–10728. https://doi.org/10.1016/j.ijhydene.2013.05.126

Nakayama J, Sakamoto J, Kasa N et al (2016) Preliminary hazard identification for qualitative risk assessment on a hybrid gasoline-hydrogen fueling station with an on-site hydrogen production system using organic chemical hydride. Int J Hydrog Energy 41(18):7518–7525. https://doi.org/10.1016/j.ijhydene.2016.03.143

Pasman HJ (2011) Challenges to improve confidence level of risk assessment of hydrogen technologies. Int J Hydrog Energy 36(3):2407–2413. https://doi.org/10.1016/j.ijhydene.2010.05.019

Okonkwo PC, Belgacem IB, Mansir IB et al (2023) A focused review of the hydrogen storage tank embrittlement mechanism process. Int J Hydrog Energy. https://doi.org/10.1016/j.ijhydene.2022.12.252

Quarton CJ, Samsatli S (2020) The value of hydrogen and carbon capture, storage and utilisation in decarbonising energy: insights from integrated value chain optimisation. Appl Energy 257:113936. https://doi.org/10.1016/j.apenergy.2019.113936

Quarton CJ, Tlili O, Welder L et al (2020) The curious case of the conflicting roles of hydrogen in global energy scenarios. Sustainable Energy Fuels 4:80–95. https://doi.org/10.1039/C9SE00833K

Qiu Y, Yang H, Tong L et al (2021) Research progress of cryogenic materials for storage and transportation of liquid hydrogen. Metals 11(7):1101. https://doi.org/10.3390/met11071101

Rodionov A, Wilkening H, Moretto P (2011) Risk assessment of hydrogen explosion for private car with hydrogen-driven engine. Int J Hydrog Energy 36(3):2398–2406. https://doi.org/10.1016/j.ijhydene.2010.04.089

San Marchi C, Hecht ES, Ekoto IW et al (2017) Overview of the DOE hydrogen safety, codes and standards program, part 3: advances in research and development to enhance the scientific basis for hydrogen regulations, codes and standards. Int J Hydrog Energy 42(11):7263–7274. https://doi.org/10.1016/j.ijhydene.2016.07.014

Shen C, Ma L, Huang G et al (2018) Consequence assessment of high-pressure hydrogen storage tank rupture during fire test. J Loss Prev Process Ind 55:223–231. https://doi.org/10.1016/j.jlp.2018.06.016

Skjold T, Siccama D, Hisken H et al (2017) 3D risk management for hydrogen installations. Int J Hydrog Energy 42(11):7721–7730. https://doi.org/10.1016/j.ijhydene.2016.07.006

Tanaka T, Azuma T, Evans JA et al (2007) Experimental study on hydrogen explosions in a full-scale hydrogen filling station model. Int J Hydrog Energy 32(13):2162–2170. https://doi.org/10.1016/j.ijhydene.2007.04.019

Tugnoli A, Landucci G, Cozzani V (2009) Key performance indicators for inherent safety: application to the hydrogen supply chain. Process Saf Prog 28(2):156–170. https://doi.org/10.1002/prs.10303

Yang F, Wang T, Deng X (2021) Review on hydrogen safety issues: incident statistics, hydrogen diffusion, and detonation process. Int J Hydrog Energy 46(61):31467–31488. https://doi.org/10.1016/j.ijhydene.2021.07.005

Electrolysis Economy

1 Introduction

Hydrogen could become a major energy source, reducing dependence on imported petroleum while diversifying energy sources and reducing pollution and greenhouse gas emissions. It could be produced in large refineries in industrial areas, power parks, and fueling stations in communities and distributed by facilities in rural areas with processes using fossil fuels, biomass, or water as feedstocks, releasing little or no carbon dioxide into the atmosphere.

There are several benefits to be expected from a hydrogen economy (Bockris 2013; Tseng et al. 2005). The expanded use of hydrogen as an energy source should help to address concerns over energy security, climate change, and air quality. Hydrogen can be provided by a variety of domestically produced primary sources, including fossil fuels, renewables, and nuclear power to allow a reduction of the dependence on foreign sources of energy. The byproducts of hydrogen conversion are generally agreeable to human health and the environment (Marbán and Valdés-Solís 2007).

Hydrogen is different than other energy options like oil, coal, nu-clear, or solar. Solar technology is renewable, modular, and generally pollution free, but it has some disadvantages, such as not always being available at the right time. Hydrogen is a primary chemical feedstock in the production of fuels, including gasoline, lubricants, fertilizers, plastics, paints, detergents, electronics, and pharmaceutical products. It is also an excellent metallurgical refining agent and an important food preservative (Falcone et al. 2021). Hydrogen can be extracted from a range of sources since it is in al-most everything, from biological tissue and DNA to petroleum, gasoline, paper, human waste, and water. It can be generated from nuclear plants, solar plants, wind plants, ocean thermal power plants, or green plants. Hydrogen and electricity are complementary, and one can be converted into the other. Hydrogen can be viewed as a type of energy currency that does not vary in quality with origin or location. A

molecule of hydrogen made by the electrolysis of water is the same as hydrogen manufactured from green plant biomass, paper, coal gasification, or natural gas (Armaroli and Balzani 2011).

Hydrogen is often called a secondary energy carrier instead of a primary energy source. This is because energy must be used to extract the hydrogen from water, natural gas, or other compound that contains the hydrogen (Oliveira et al. 2021). This classification is not exact since it assumes solar, coal, oil, or nuclear are primary energy sources, meaning that energy is not needed to obtain them. However, finding, extracting, and delivering these so-called primary energy sources requires energy and major investments before they can be utilized. Coal and natural gas come closer to true primary energy sources since they can be burned directly with little or no refining, but energy is still needed to extract these resources and deliver them to where the energy is needed. Even when extensive drilling for oil is not required from shallow wells or pools, energy must still be used for pumping and refining. Many environmental problems can result from finding, transporting, and burning fossil fuels; however, when hydrogen is used as a fuel, its byproduct is essentially water vapor. When hydrogen is burned in air, which contains nitrogen, nitrogen oxides can be formed as they are in gasoline engines. These oxides can almost be eliminated in hydrogen engines by lowering the combustion temperature of the engine (Nowotny and Veziroglu 2011).

Despite their market availability and maturity, PEM and alkaline water electrolyzers are still considered highly expensive from both CAPEX and OPEX perspectives, compared to fossil fuel-based hydrogen production. PEM water electrolyzers are 50%–60% more expensive than alkaline, representing an additional barrier to market penetration (Proost 2019). Both are still considered to have untapped potential for cost decrease when considering economies of scale, automation, an increase in availability of components from various OEMs, massive market demand and deployment for energy storage (coupling electrolyzers with underground storage or tanks).

For AEM and solid oxide electrolyzers, these cost considerations are much more challenging, as there are only a few companies responsible for their commercialization (Yang et al. 2023). Moreover, many of their components are still lab-scale based, with no OEM responsible for their manufacturing and commercialization. These are small stacks, and system sizes are only up to a few kilowatts. While these two technologies can still contribute to a low production cost of green hydrogen, they have a longer way to go compared to alkaline or PEM. For these reasons, only the cost breakdown for these two technologies is explored in more detail below. Significantly, AEM can use less-expensive materials (in particular titanium, which can represent around half the stack cost for PEM) and therefore AEM has an advantage over PEM in cost-reduction potential (Macedo and Peyerl 2022).

There are two main problems with cost estimates for electrolyzers. First, the availability of data, given its confidential nature and the retention of competitive advantage. Second, the boundaries for the cost estimates are not consistent (e.g. stack, balance of plant, full system) and, in many cases, not even specified, which makes the comparison across studies more difficult. To deal with these
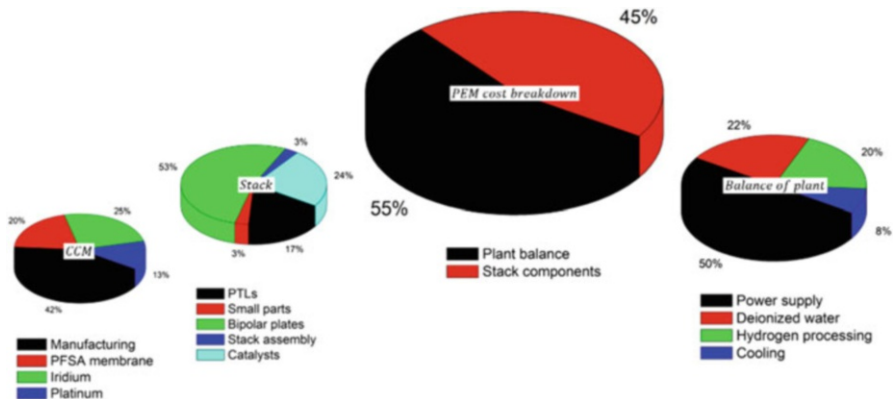
Fig. 1 Cost breakdown for a 1 MW PEM electrolyzer, moving from full system, to stack, to CCM
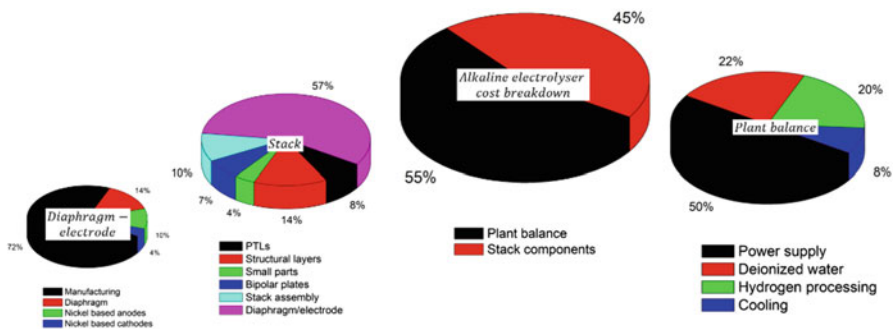
Fig. 2 Cost breakdown for 1 MW alkaline electrolyzer, moving from full system, to stack, to membrane electrode assembly (MEA)

challenges, this report performed a thorough literature review validated by consultations and a peer review with various leading manufacturers, which informed the cost breakdowns shown in Figs. 1 and 2.

For the second barrier (boundaries), different system scopes are analyzed for the cost estimates in this report:

- The first level is a single cell unit. This is the core of the electrolyzer where the main electrochemical process takes place. This includes the catalyst coated membrane where the catalyst layers are coated directly as electrodes onto the membrane for the PEM type and the electrodes and diaphragms for the alkaline type, plus the manufacturing of these components which can represent a large share of the costs (Esposito 2017).
- The second level within stack costs includes the cells plus the PTLs, bipolar plates, end plates and other small parts such as spacers, seals, frames, bolts and
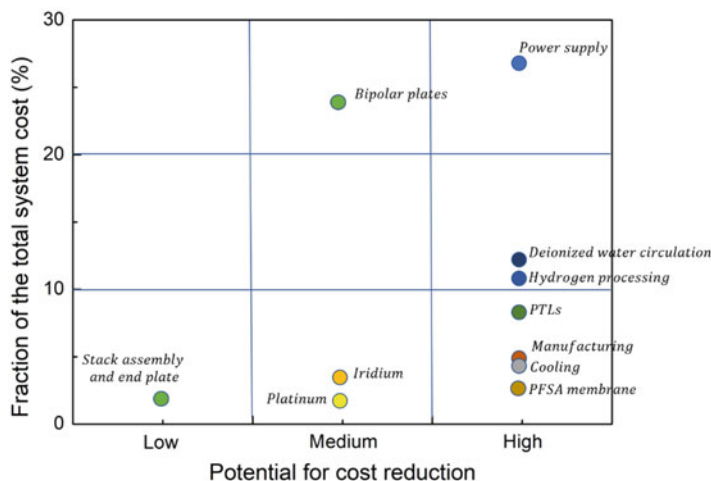
Fig. 3 System components for a 1 MW PEM electrolyzer classified based on contribution to total system cost and potential for cost reduction

others. This level usually represents about 40%–50% of the total (Rojas et al. 2021).

- The third level is the system costs. The scope is all the balance of plant components and peripherals responsible for operating the electrolyzer but excluding any component responsible for further gas compression and storage. The major components for the balance of plant cost models typically include rectifier, water purification unit, hydrogen gas processing (compression and storage) and cooling components. These items can constitute 50–60% of the total cost. Today, the main contributor to system costs is still the stack, which represents 40%–50% of the total, for both alkaline and PEM electrolyzers. This share greatly depends on design, manufacturing strategy, business case, and customer specifications. Cost breakdowns for AEMs and solid oxide systems are still not available, due to the limited number of systems that have been deployed commercially (Nami et al. 2022).

A study showed there had been significant cost reductions over the period for both PEM and alkaline systems, but this reduction was more pronounced for PEM.

It is depicted a significantly large spread in the costs of PEM systems, ranging from USD 306/kW up to USD 4 748/kW, demonstrating the challenge of finding representative numbers for the current system costs.

Figures 1 and 2 show a breakdown of cost components for both PEM and alkaline electrolyzers, while Figs. 3 and 4 combine this information with the potential for cost reduction of the various items in order to identify priority areas for innovation and deployment.

First scalingup initiatives into systems larger than 1 MW will allow quick cost reduction of balance of plant components, as discussed above. Beyond this point,
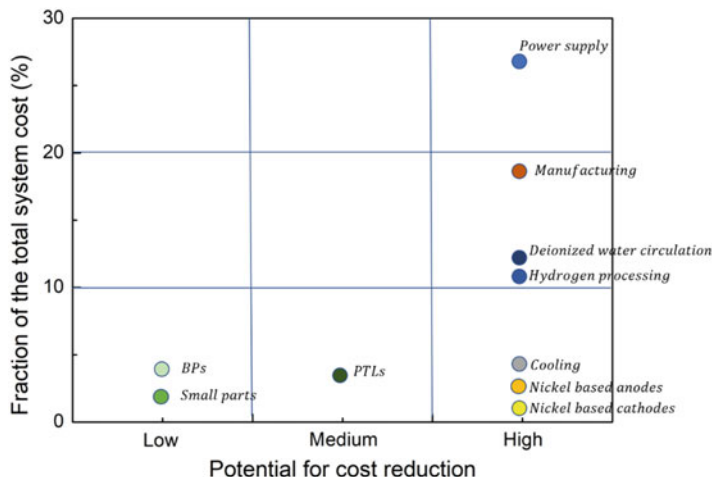
Fig. 4 System components for a 1-MW alkaline electrolyzer classified based on contribution to total system cost and potential for cost reduction

innovation becomes key for any further significant cost reduction. Most of the stack components are still over designed, and significant potential for cost reduction can be found for PTLs, bipolar plates and the highly expensive protective coatings on these.

Figure 1 shows that for PEM electrolyzers the stack represents slightly less than half of the electrolysis system cost. For the balance of plant, power supply represents a very significant cost component.

For PEM stacks, bipolar plates are a significant cost component, as they are often built to provide multiple functions and require advanced materials such as gold or platinum coated titanium. This is one of the areas where innovation can play an important role in both performance and durability enhancement, as well as cost reduction. Research is ongoing to replace titanium with cheaper materials, relying on the coating for its functional characteristics to remain unaffected, while reducing cost.

For the core of the stack, the catalyst coated membrane (CCM), rare metals represent an important part of the cost (Xie et al. 2021). Put into context, however, they represent less than 10% of the cost of a full PEM electrolysis system. Yet, for iridium in particular, they might represent a bottleneck for scaling up manufacturing of PEM electrolyzers, in the absence of a significant scale-up of iridium supply.

When the dimension of potential for cost reduction is combined with the current share of total system cost of each component, some clear priority areas for innovation emerge. Power supply is the single largest area where cost reduction could be achieved (see Fig. 3). Bipolar plates, although with a lower cost reduction potential, also represent almost a quarter of the total PEM electrolysis system cost and should be a priority area. Other balance of plant components, like water circulation and hydrogen processing, also represent important areas where cost reduction can be achieved (Weidner et al. 2018).

For alkaline electrolyzers, the same reasoning in reducing the costs of the balance of plant components applies. As illustrated in Fig. 2, within the stack, over 50% of the costs relate to electrodes and diaphragms, as opposed to 25% of the cost in the CCM for PEM. Significant cost is associated with manufacturing of the electrodes where learning-by-doing, automatization of the manufacturing process and economies of scale can play an important role in cost reduction. Bipolar plates for alkaline, however, account for only a small part of stack costs, as opposed to over 50% in the case of PEM, due to a simpler design, simple manufacturing and cheaper materials (nickel-coated steel) for bipolar plates in alkaline stacks.

Similar to what happens with PEM, some clear priority areas arise for alkaline electrolyzers when the potential for cost reduction is combined with the current share of total system cost of each component (see Fig. 4): power supply is the single largest area where cost reduction could be achieved, followed by the manufacturing of the electrodes and diaphragms. The strategy can be to completely reengineer them, demonstrating CCM concepts similar to the PEM type, where a single component comprised of membranes, electrodes, and eventually PTLs, is fabricated. Balance of plant items, such as lye circulation and hydrogen processing remain important for alkaline too, although no significant potential for reduction in the cost for materials has been observed.

Government support for research programmes is needed to continue improving commercially available technologies and make potential breakthroughs in emerging technologies (Penner 2006). The key areas of focus for this research are identified in this section.

Given the difference in design and maturity for the different technologies, the use of comparable performance indicators seems to be a suitable approach to guide innovation efforts. These performance indicators, including the long-term targets defined in this section, can be used by governments to benchmark performance of funded projects and to set research program goals.

To prevent critical materials from becoming a barrier to scaling up, alkaline systems need to transition to platinum and cobalt free designs. This is already commercially available from some manufacturers today; yet, it has to become a prerequisite for policy support before scaling up manufacturing capacity. For PEM electrolyzers, further efforts are needed to reduce the platinum and iridium content by at least one order of magnitude and, if possible, in the future, replace these with more common materials (Majumdar et al. 2021). Titanium is also a significant cost component that should be reduced in use. Although less scarce than other materials, it is still required in significant quantities for current PEM designs.

Increasing the facility size can have the largest cost reduction effect on the balance of plant. Yet, facility size is not defined based on cost only, but is also based on the application (e.g. the residential or transport sectors use smaller sizes than industrial applications). Higher cost due to smaller scale can partly be offset by savings in the delivery of the hydrogen, due to on-site production.

2   Stack Design

At the stack level, there are mainly two strategies to achieve a lower cost:

- Stack design and cell composition: This includes using less critical materials, redesigning the stack to achieve a higher efficiency (i.e. lower electricity cost), higher durability (longer lifetime to distribute the investment) and increase the current density (higher production rate).
- Increase the module size: This can bring economies of scale to some of the balance of plant components. This strategy should consider a trade-off between a small module size that enables mass-manufacturing, standardization and replication, and a large module size that achieves larger cost reduction in balance of plant components at the expense of fewer units deployed and less learning by deployment (Kim and Kim 2016).

Concerning stacks for alkaline electrolyzers, the key areas to focus on are the electrodes and the diaphragms. Bipolar plates and PTLs have less priority, since they are based on stainless steel plates coated with nickel, which are already significant, cost-effective components. Strategies to integrate PTLs into electrodes and consequently diaphragms can also be of key importance in reducing costs, as outlined below:

Increase current densities: The current densities of the stacks can be increased, from the current, 0.5 A/cm^2 to more advanced units of 2–3 A/cm^2. This current density increase cannot be made, however, at the penalty of lower efficiency. Higher current densities have already been accomplished by some manufacturers, too, with electrode-separator packages that can deliver a performance range as high as 1.2 A/cm^2 at 2 volts (V) now available. Power densities of 2–3 W/cm^2 could be achieved by demonstrating thinner diaphragms or membranes for alkaline electrolyzers. As with PEM, alkaline electrolyzers also need to improve their voltage efficiency levels, reducing ohmic losses and increasing electrode kinetics (Santos et al. 2021).

Reducing diaphragm thickness: This could improve efficiency and reduce electricity consumption. The thinner the diaphragms, the lower the resistance to transporting the OH-species from the cathode to the anode. Eventually, however, this comes at a cost of higher gas permeation, which contributes to higher safety concerns. The other downside is the lower durability, given the higher chance of pinhole formation in the diaphragm and less mechanical robustness. Overall, the diaphragm thickness should reach values that approach those of PEM and AEM. State-of-the-art membranes for PEM are about 125–175 micrometers (µm) with a potential decrease to 20 µm or lower. Below this point (for PEM), there are limited efficiency benefits. For alkaline electrolyzers, the current diaphragm thickness is about 460 µm. Decreasing this to 50 µm would contribute to improving the efficiency from 53% to 75% at 1 A/cm^2 (see Fig. 5).

Re-designing catalyst compositions and electrode architectures into electrodes with a high specific surface area: Despite using cheap and widely available Nickel-based catalysts for their electrodes, alkaline electrolyzers have traditionally

Fig. 5 Relationship
between voltage (the higher,
the lower the efficiency) and
current density (the higher,
the higher the production
volume) for various
diaphragm thickness of
alkaline electrolyzers
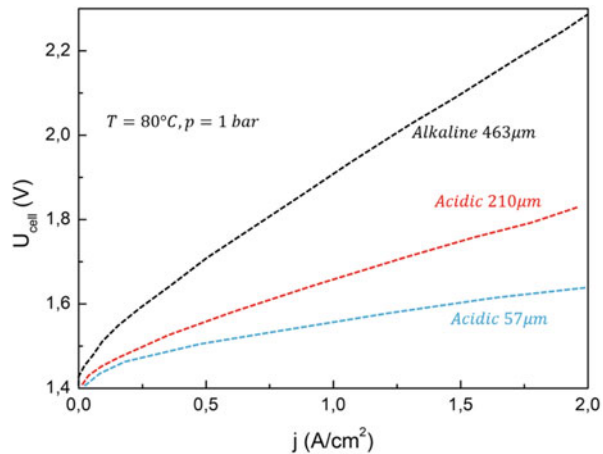
encountered many challenges in moving away from rudimentary, or archaic elec-
trode designs and reaching much higher efficiencies for both hydrogen and oxygen
evolution reactions. Efficiency differences with other technologies are small and
best-in-class designs result in even higher efficiencies.

Apart from increasing surface area, which was traditionally and simply achieved
with Raney-Ni catalysts (nickel-aluminum [Ni-Al], or nickel-zinc [Ni-Zn]), the other
points are considered moderate and difficult challenges. In addition, any novel
concept still needs to keep long-term durability, comparable to those presented by
current nickel coated stainless steel perforated sheets. That is the reason why Raney-
Ni electrodes have not been commercially deployed, at least not in large-scale
electrodes, since they have presented some critical durability aspects for long-term
operation (low mechanical robustness) and much higher costs, due to the use of
expensive manufacturing techniques. Novel PTL concepts: Alkaline electrolyzers
are also not well developed in the use of efficient PTLs, potentially based on nickel.
This is especially so in regard to optimizing these for reduction of mass transport
limitations (e.g. gas bubble resistance, trapped inside alkaline PTLs), and optimal
protective coating alternatives to decrease interface resistances on the anode side.

2.1 PEM Electrolyzers

For PEM stacks, the focus areas are bipolar plates and PTLs, given their large cost
contribution and large potential for reduction. Based on these two criteria (cost share
and potential), the catalyst-coated membrane is the next priority.

Re-designing the stacks can achieve large cost reductions, since it enables the
reaching of higher power densities, up from the current (conservative) 2 A/cm^2 to
6 A/cm^2 or more in the next few decades. Next, electrodes should be scaled up from

the current 1 500–2 000 cm^2, up to 5 000 cm^2 and eventually 10 000 cm^2. The larger area should go in tandem with more mechanically robust membranes that can use the same thickness (Reksten et al. 2022).

Such a strategy would allow an increase in the size of the PEM stacks, from the current 1 MW/unit to next generation stacks of 5 MW or even 10 MW per stack. These need to run at much lower levels of cell voltage to allow for an increase in efficiency and the simplification of waste heat management.

Reducing membrane thickness: This enables an increase in efficiency, which in turn enables a reduction in electricity consumption. Thick membranes (Nafion N117 with approximately 180 μm thickness, for example) are still state-of-the-art and are responsible for efficiency losses of about 25% (at 2 A/cm^2). There are much thinner membranes that are commercially available, with thicknesses as low as 20 μm, yet these are not designed for electrolysis requirements. This thickness reduction would allow a reduction in efficiency losses to about 6% (at 2 A/cm^2).

Further reduction of membrane thickness, down to 5.0 μm or lower (membranelles electrolysis), is not encouraged, since a decrease of no more than 0.5 kWh/Kg H2 can be extrapolated. In this case, R&D is therefore not justified.

Looking at the experience in PEM fuel cells (reverse process of electrolysis), commercial stacks are already equipped with membranes that are 810 μm thick, as gas permeation is not a concern, since they operate a much lower pressures (36 bar) on the air side.

The two challenges that arise with thinner membranes are: their lower durability, given their potentially lower mechanical strength and being more prone to defects and pinhole failures; and the manufacturing of such membranes. During manufacturing, the process of enlarging the catalyst coated membranes and porous transport layers into large electrodes is challenging and therefore of high R&D risk. The thin membrane and electrodes need to be mechanically stabilized over the full area to avoid undesired mechanical stresses that can tear these films and delaminate thin electrodes. This is especially critical at differential pressure operations, where one side is subjected to much higher pressures coming from the other electrode. Re-designing PTLs will be crucial – i.e. with finer structures at the catalyst interface that can better support a thinner membrane and prevent creep failure, thereby enabling lower membrane thickness (Dang et al. 2022).

Removing expensive coatings and redesigning the PTLs and bipolar plates: On the anode side, commercial stacks demand the use of platinum-coated titanium porous sintered PTLs, which is not possible with non-PGMs at this stage.

Platinum loadings on the anodic PTL vary from 1–5 milligrams per square centimetre (mg/cm^2) or 1 2.5 g/kW. Platinum has a dual purpose: to protect the titanium against passivation17 and provide an optimal interface resistance. This is needed because titanium is prone to severe quick and detrimental passivation. Studies have shown that interface resistance at the PTL is responsible for an electricity consumption as high as 1.35 kWh/Kg H2 (4% of hydrogen LHV). The bipolar plates made of titanium also possess protective layers of platinum on the anode side, and gold on the cathode. Alternatives are needed for titanium plates,

based on such materials as niobium, tantalum and eventually stainless-steel approaches, but using protective coatings that are stable and also free from platinum or gold.

Re-designing catalyst-coated membranes: For catalyst coated membranes (electrodes), the strategy can be divided into different timescale scenarios. An initial approach could be to tackle Re-designing catalyst-coated membranes: For catalyst coated membranes (electrodes), the strategy can be divided into different timescale scenarios. An initial approach could be to tackle the economies of scale for CCM fabrication via automation over manufacturing, establishing more reliable and less expensive supply-chains for catalysts and membranes, and implementing quality control. If possible, parallel work can be done to reduce the amount of electrocatalysts by re-engineering the electrodes over the membrane.

Supply chain for PFSA membranes: For PFSA membranes, various suppliers (e.g. Chemours, Solvay, Asahi-Kasei, 3 M and Gore) are available. This is also one of the most solid supply chains for PEM components. Moreover, these membranes have been traditionally supplied at scale for chloroalkali electrolyzers, with membranes reaching areas as high as 3 m^2. Therefore, significant cost reduction is expected as soon as PEM water electrolyzers reach high market volumes.

2.2   AEM Electrolyzers

In terms of components, the AEM membrane and ionomer are the main and most challenging. In terms of performance, the most critical item is durability, but also conductivity. Research efforts are targeted to finding AEM membranes with desirable properties (high mechanical, thermal, and chemical stability, ionic conductivity, and lower permeability with respect to electrons and gases). The polymer backbone is responsible for mechanical and thermal stability. The functional group that transports the OH-anion is accountable for the ion exchange capacity, ionic conductivity, and transport number.

The trade-off for AEM is between mechanical stability, ionic conductivity and cost. For instance, the production of commercial AEM that achieves a high mechanical stability and high ionic conductivity is challenging and therefore expensive. There are known chemical strategies to increase the AEM ionic conductivity, but it leads to loss of mechanical strength due to excessive water uptake. The AEM then becomes chemically unstable, which leads to poor ionic conductivity.

Another major limitation of an AEM is degradation of the polymer due to KOH attack, which quickly reduces the conductivity of the membrane and ionomer within the catalyst layer. The ionic conductivity of an AEM plays a significant role in the performance of the AEM. Higher levels of ion conductivity allow much higher current densities to be achieved. Tasks to increase efficiency and durability of electrodes and PTLs are analogous to those related to alkaline electrolyzers.

2.3 Solid Oxide Electrolyzers

The potential for this technology lies in its higher efficiency, while its main challenge is durability. Some of the areas to focus on are: the improvement of electrolyte conductivity, optimization of chemical and mechanical stability, matching the thermal expansion coefficient to both electrodes, and ensuring minimal reactant crossover (Ba et al. 2022). State-of-the-art electrolytes used in these cells have already exhibited remarkable conductivity for stack operation for thousands of hours, but the degradation of the electrolyte (which translates into a reduction in performance) is still of high importance for research. Structural changes within the electrolyte accelerate the formation of voids within its structure, increasing electrolyte resistance. Moreover, electrolyte also reacts with vaporized water and forms volatile products such as nickel hydroxide ($Ni(OH)_2$) that also deactivates it.

As for the other electrolysis technologies, electrodes used for solid oxide stacks are key components, and many key properties are required to provide high efficiency and durability.

3 Materials

Critical materials are mostly a limitation for PEM. The anode side is subject to a high potential for oxidizing (>1.4 V) and not many materials can provide long-term operation under these conditions.

Because of this, iridium – a scarce material – is used and the PTL requires significant amounts of titanium-based (i.e. expensive) materials, coated with platinum. Although other options are available, platinum is used for the cathode, although tantalum seems to be a promising alternative for the coating.

Titanium components are also responsible for the high costs of PEM, but this is mostly related to the expense of manufacturing titanium components, and less related to the raw cost of titanium.

Alkaline electrolyzers mostly use nickel to resist the highly caustic environment. Some designs derived from the chlor-alkali industry include platinum and cobalt. For alkaline water electrolysis designs optimized for green hydrogen production, however, we have commercial examples available today that do not use these materials. Platinum and iridium, used in PEM, are two of the scarcest, most energy-intensive and emission-intensive metals (see Fig. 6).

Platinum use is currently about 1 g/kW. At the same time, primary platinum production is in the order of 200 tons per year (t/year) with about 20% more coming from the recycling of catalytic reformers in cars and electronic equipment. Two factors that further increase this number are the potential recycling of the platinum used by the industry and the expected decrease in platinum content, over time. These two factors are discussed further below. In the hypothetical case of using the entire production of platinum for electrolyzers, this would support the deployment of 200GW per year (GW/year).
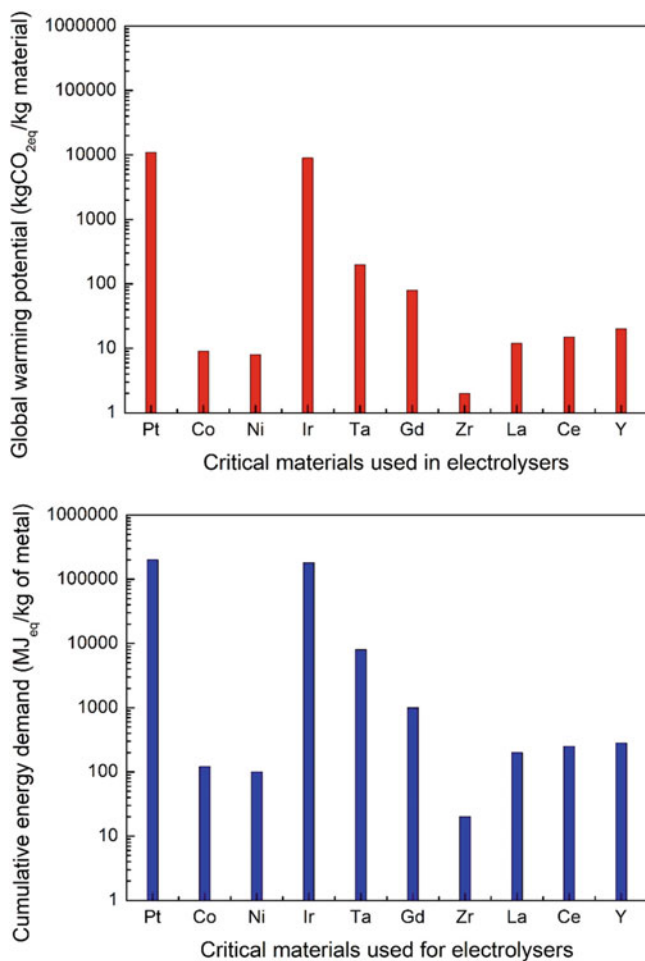
Fig. 6 Global warming potential and cumulative energy demand for critical materials used in electrolyzers

Considering a lifetime of at least ten years and full recycling of platinum from decommissioned stacks, this pace of deployment would support the deployment of 2 000 GW in the next decade and 4 000 GW by the 2030s. Combined with the planned reduction of platinum requirements in

PEM electrolyzers, this will further reduce the risk of material supply bottlenecks.

Iridium use is currently about 1–2.5 g/kW. Global iridium production is about 7–7.5 t/year, which would support the deployment of 3–7.5 GW/year or 30–75GW of electrolyzer capacity in the next decade, reflecting the criticality of reducing iridium content rapidly and significantly (Moliner et al. 2016).

Additionally, platinum and iridium are two of the most carbon and energy intensive materials in the electrolyzers (see Fig. 6). Platinum production emits

about 12.5 tons of carbon dioxide (tCO_2 -eq) per kilo of metal. This translates into about 0.01 kg CO_2 -eq /kg H2, which is relatively small compared to the electricity input (only 10 grammes of CO_2 -eq /kWh would be equivalent to 0.5 kg CO_2-eq /kg H2). Similarly, platinum production is the most energy intensive among the critical materials in electrolyzers with 243 gigajoules per kilo (GJ/kg). Given the high energy consumption of the electrolyzer, however, the share of total electricity consumption in the system taken by producing these metals upstream is less than 0.01%. The supply of critical materials in electrolyzers is mostly dominated by a few countries.

South Africa supplies over 70% of global platinum and over 85% of global iridium. This would strongly link PEM electrolyzer deployment to supply from a few (mainly one) countries, with limited short-term alternatives in sight for replacing these materials for PEM.

Solid oxide electrolyzers, which have the potential for much higher efficiencies, would also suffer from a similar risk, since almost 95% of the supply for all their critical materials currently comes almost exclusively from China.

Alkaline electrolyzers do use some platinum and cobalt, but there are already commercial designs that do not include these materials and the supply of nickel is more diversified when compared to the other metals.

The same applies to AEM, which does not use scarce materials and mostly requires steel and nickel.

In terms of cost, the market for iridium is relatively small (7–7.5 t/year), illiquid and subject to high price volatility.

The ratio between the highest and lowest price over the last 20 years is approximately 15 times.

The highest price was in 2019, with USD 1 480 per troy ounce, which is equivalent to about USD 46/kW (considering an iridium content of 1 g/kW). Furthermore, in the 2016–2018 period, the market was undersupplied, which created an upward pressure on price, with this potentially boosted further by a step demand increase coming from electrolyzers. For platinum, the market is larger than iridium, but the price volatility is still high, with a ratio of five times between the highest and lowest price over the last 20 years. The peak price in that period was just before the 2008 financial crisis, when it was USD 2 000 per troy ounce, which would be equivalent to almost USD 60/kW (with an iridium content of 1 g/kW), while more recently the price has stayed in the USD 800–1 000 per troy ounce range.

There are three main strategies to reduce dependence on critical materials:

• Prevention or reduction of use: This covers substitution of the materials, reducing their amount per unit of installed capacity, or varying the technology mix to achieve a lower use overall (e.g. more alkaline instead of PEM that uses iridium). There are various options being investigated:

  – Use of high surface area supported catalysts – for example, titanium or tin oxide supports.
  – Increase the catalyst surface area through improved catalyst manufacturing techniques, for example using nanostructured thin film catalysts.

- Use a thinner layer of coating material, for example through atomic layer deposition.
- Reengineer the electrode concept. For example, support nanoparticles of iridium on high conductive semi-conductor oxides, alloy iridium to other transition metals, change the morphology of the electrode and shape the nanoparticle of iridium.
- Extension of the use of equipment, or increasing its efficiency: This includes achieving a higher productivity of the stack, which translates into a smaller area (and less material per kilo of hydrogen) or extend the lifetime of the electrolyzer (i.e. the same amount of material allocated over greater production).

- Recycling: There are various methods available for recovering noble metals from electrochemical devices such as fuel cells and electrolyzers. These include: hydrometallurgical treatment, transient dissolution, acid process and selective electrochemical dissolution. All of these can be used for platinum in PEM. Further research is needed to estimate the potential benefit of recycling, which could have an impact on large-scale applications. It could also have an impact in creating a parallel recycling industry to recover these materials and would be fundamental in preventing potential materials bottlenecks, as we rapidly scale-up manufacturing (Parra et al. 2019).

Reducing platinum use is not only beneficial from the perspective of scaling up electrolyzers and reducing reliance on critical materials, but also from the perspective of reducing environmental impact. Platinum production dominates in almost all environmental impact categories (e.g. acidification, eutrophication, photochemical oxidation) and its lower use will also result in lower overall impact.

Implementing these strategies, in combination with the improved electrolyzer performance, can ultimately reduce the specific iridium content by 96% and the platinum content by 97.5%. Parallel to this development, the electrode area is expected to increase almost fourfold and the current density by 2.5 times. This means the loading per unit of capacity will not decrease as drastically, but it can still achieve reductions of 70% and 80%, respectively, for iridium and platinum. The electrolyzer will also be developed in terms of delivering higher current densities (higher hydrogen production) for the same stack unit, which consequently means less catalyst needed per unit produced.

This is an area where the role for innovation will be increasingly important. Large players from the tech scene are getting involved in the context of leveraging their expertise to fight climate change.

For instance, Facebook recently started a project focused on using artificial intelligence to find new catalysts to improve the transformation of renewable electricity into hydrogen.

4 Modules Size

The largest cost share is the balance of plant and not the stack itself. Increasing the module size can lead to some benefits in economies of scale, with these greater for the balance of plant. The stack has limited economies of scale since it cannot be greatly increased in size but will most likely be increased in number. This is due to problems that include, for example, leakage, limitations in the manufacturing of large-scale components, mechanical instability issues for large-scale components, the maximum area of the cell, and others. The balance of plant, however, can have strong economies of scale. For instance, a compressor that is ten times larger (e.g. going from 1 MW to 10 MW) is not ten times more expensive, but only about four times (Gallardo et al. 2022). This would reduce the cost that such a compressor has on the overall cost, since the stack would be 9–10 times more expensive for the same capacity increase.

This leads to the stack having a larger contribution to the total cost, as module size increases (see Fig. 7).

Some studies have looked into the potential cost decrease for increasing the module size and reaping these economies of scale a literature review was conducted to evaluate the published data on investment costs and learning rates for PEM and alkaline electrolyzers from the 1990s until 2017 and the years beyond. The collected data are adjusted for inflation and specified in €2017 per kW-output using the higher
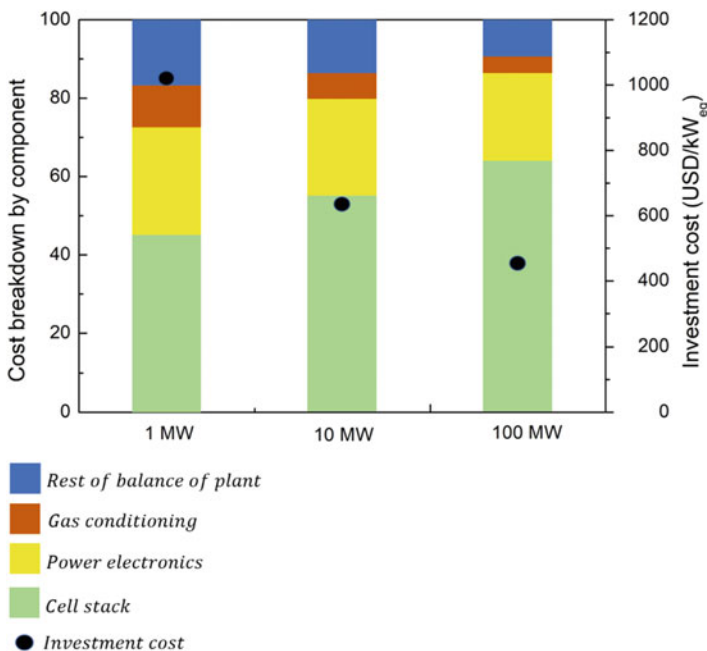
Fig. 7 Cost breakdown by major component for alkaline electrolyzers based on current costs
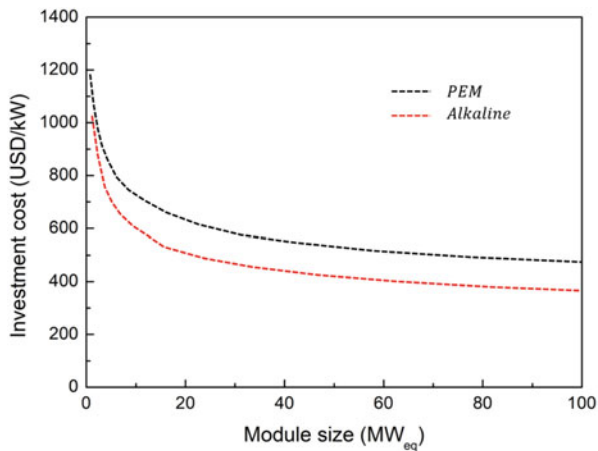
heating value (HHV. It was estimated the cost exponent to be 0.60.75 for the balance
of plant. This would lead to a cost increase of 4–5.6 times when increasing the
capacity by ten times. They were used data from NEL (one of the main electrolyzer
manufacturing companies) and also include the cost penalty for increasing the
operating pressure . It was identified 3–4 MW module size as a tipping point to go
from a single stack to a multi-stack and achieve a significant change in the cost
increase for every additional MW of capacity. This is highly dependent on stack
design, however, and will vary from one manufacturer to another. Figure 8 shows a
comparison.

The largest economies of scale are reaped around the 1 020 MW module size.
Beyond this point, the marginal cost decrease for increasing the capacity is much
lower than for module sizes in the 12 MW range. The "PlanDelyKad" study in
Germany performed a bottom-up design and cost assessment finding close to 50%
cost reduction for a 100 MW alkaline electrolyzer (EUR2014 520/kWinput) vs a
5 MW electrolyzer (EUR2014 1 070/kWinput). One of the manufacturers,
Thyssenkrupp, claims significant cost benefits can still be achieved by going to
100 MW.

Today, the largest electrolyzer installed is a 10 MW facility in Fukushima, Japan,
which is a single stack. Thyssenkrupp and NEL already offer designs up to 20 MW,
achieved with multiple stacks without degradation in the efficiency or response
capability of the electrolyzer. The largest module from McPhy is 4 MW, while the
Sylizer 300 from Siemens is designed for 17.5 MW, constituted by 24 modules
(of less than 1 MW each). Cummins (Hydrogenics) is building a 20 MW PEM water
electrolyzer in Becancour-Canada, based on stack platforms of 2.5 MW.

Another approach applied by some AEM manufactures is a strategy that focuses
on design, achieving cost reduction by mass-manufacturing, standardization, and
supply efforts on a single stack offering. Larger capacities are achieved by using
multiple stacks of this single size. Advantages include: the different flexibility

response (i.e. a set of smaller electrolyzers can react more quickly than a single, large stack); a reduction in the impact of failure by a single unit; and a higher utilization of the manufacturing equipment (Grimm et al. 2020).

5 System Level

The largest benefits for economies of scale for electrolyzer manufacturing seem to be reached around the 1 GW/year level. Several industrial players claim to have reached this scale or are working towards expansion. One measure government could take is to set manufacturing capacity targets, manufacturing tax benefits, grants and loans for capacity expansion and work in close collaboration with industry. The Netherlands and the UK are examples of where this is happening. A predictable 5–10-year pipeline of electrolysis projects – driven by green hydrogen demand – will be key for manufacturers to invest in new, larger and automated production facilities. Uncertainties about the demand for green hydrogen versus fossil-fuels based hydrogen is a key obstacle to the scaling up of electrolyzer manufacturing: policy makers should carefully assess the balance, as learning from investments in green hydrogen versus blue hydrogen production are not interchangeable (Dou et al. 2017).

Water electrolysis deployment for green hydrogen has been limited so far, which introduces uncertainty around the cost reduction that can be achieved by scaling up. From this limited experience, it seems electrolyzers have a similar relationship between cost decrease and global capacity as solar PV does – which could lead to 40% cost reduction, given the capacity targets governments have already announced. One action government could take is to ensure cost is communicated transparently, in order to be able to track progress and identify potential.

Cost decrease is greatest during the current early stage of deployment, when cumulative capacity deployed is still small and the market is relatively concentrated in a few companies. Current costs suffer from lack of transparency, due to the nascent stage of the industry, which will likely be resolved as large-scale manufacturing facilities come online and large projects get commissioned. This, in turn, will facilitate price discovery and improve cost reduction forecasts.

Looking beyond the stack to include the balance of plant, there are two main strategies to reduce the cost:

- Increasing the manufacturing scale of the plant. This allows reducing the cost contribution of each component by performing a high throughput, automated manufacturing operation. This includes, for example, roll to roll manufacturing of the catalyst coated membrane (for PEM) and advanced coating processes for metal plates.
- Learning-by-doing. This relates to standardization, applying lessons learned from deployment and optimizing the installation of equipment through the execution of multiple projects.

These two effects are not independent, since increasing the global cumulative deployment is expected to be linked to an increase in global manufacturing capacity. Nevertheless, applying both concepts separately allow us to draw different insights into the drivers of lower production costs.

5.1 Manufacturing Scale

Increasing the manufacturing scale of the electrolyzer plants can have a positive impact on their specific cost. Large manufacturing volumes can decrease the cost contribution of buildings, improve the utilization of equipment (i.e. increasing the volume produced from each unit and reducing the cost contribution) and improve the process yield (reducing losses). Furthermore, for low volumes, manual assembly might be necessary, while higher volumes make automatic assembly attractive. These economies of scale during manufacturing have been assessed in the past for PEM. Two aspects to note are: the annual production rate where most of the cost benefits have been achieved; the cost categories that do not change significantly with the production rate and dominate the cost, even at high volumes (Schnuelle et al. 2020).

Focusing on the stack first, Table 1 shows that the point where most of the components are dominated by the costs of material (and labor in the case of the assembly) is about 1 000 units per year (i.e. 1 GW/year).

Going from a 10 MW/year scale to 1 GW/year allows a 70% reduction in the stack cost, to about USD 70–80/kW. The largest benefit is for the stack assembly, which can experience a 90% cost reduction by going from a manual to a semi-automated assembly at a volume of about 1 GW/year, with a subsequent change to fully automated at 2GW/year. This automation needs to happen at two levels: the cell and the stack, to have the highest cost impact. The cost saving is not only from automation of the process, but also from using advanced coating technologies, such

Table 1 Economies of scale for PEM stack manufacturing

Stack component	Capacity to reap most of the economies of scale	Dominant costs at high production rates	Cost penalty for low production rates	Cost achieved at 1000 units/year
Catalysts coated membrane	1000 units/year	Platinum, iridium, Nafion membrane	75–80%	46 USD/kW
Porous transport layer	20–100 units/year	Titanium powder, gold	110%	26 USD/kW
Frame	1000 units/year	Materials (95%)	800–900%	1.8 USD/kW
Membrane electrode assembly	1000 units/year	Materials (90%)	350%	11 USD/kW
Assembly	1000 units/year	Labor (50%)	1000%	2 USD/kW

Fig. 9 Cost breakdown for PEM electrolyzers for a (**a**) 10 MW/year; (**b**) 1 GW/year production scale
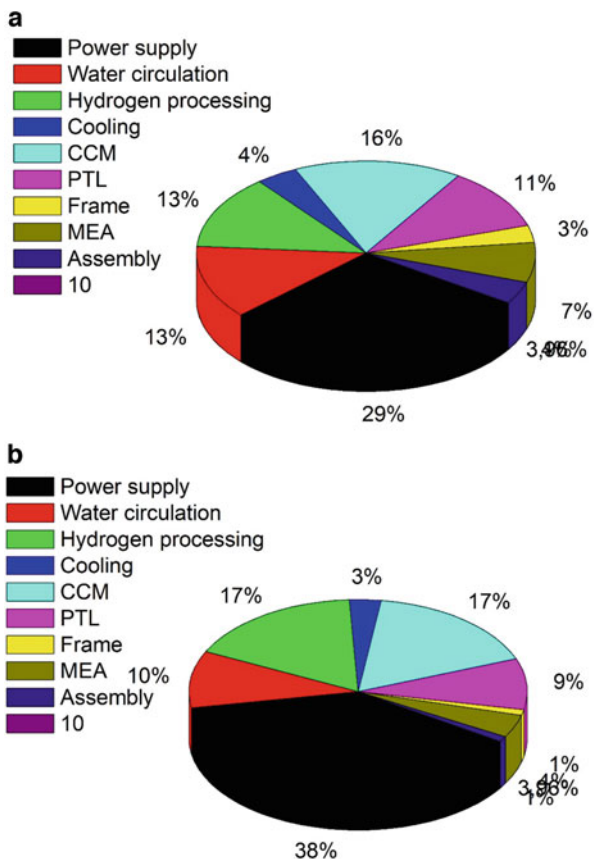
as roll-to-roll and replacing reflects assumptions of 7 g/m^2 for platinum loading in the anode, 4 g/m^2 for the anode (platinum-iridium), a platinum price of USD 1 500 per troy ounce, a Nafion 117 (membrane) and titanium plates coated with 100 nanometers (nm) of gold. One unit requires about 50 MEA, assuming a 1 MW system, so 1 000 units is equivalent to 500 000 MEA/year, which is assumed to trigger the shift from manual to semi-automated assembly.

This allows for a faster, higher throughput process capable of producing thicker uniform catalyst layers material handling equipment. Frame manufacturing achieves a similar (85–90%) cost reduction at the same scale (i.e. 1 GW/year). The cost reduction for components that contain rare materials is less pronounced, with the CCM and PTL only being able to achieve between 45–55% cost reduction at the 1 GW/year scale. This results in stack cost being dominated by the platinum, iridium, membrane, titanium and gold costs, for large production volumes.

For the balance of plant, however, the cost reduction is smaller than for the stack. The same increase in production rate, from 10 MW/year to 1 GW/year, leads to a cost reduction of about 40% in the balance of plant. This means the balance of plant goes from about 55% of the total cost to almost 75% on a 1 GW/year scale (see Fig. 9).

The largest cost reductions – of 50–60% – can be achieved in the deionized water circulation and the cooling systems. These, however, are relatively small and the dominant costs of the power supply and hydrogen processing only reduce by about 30%.

Two years ago, the electrolyzer market was about 135 MW/year, with the largest manufacturers in the order of 10–20 MW/yr. As shown in the figures above, this is where the cost contribution of fixed costs is the largest. Today, various estimates and announcements point towards a higher manufacturing capacity. The World Bank estimates the capacity to be 2.1 GW/year with announcements on capacity expansion adding up to 4.5 GW/year. The IEA estimates a capacity of 1.2 GW/year just in Europe. Looking at claims and announcements from manufacturers:

- Thyssenkrupp has a manufacturing capacity of 1 GW/year that could be expanded.
- NEL is expanding the capacity of their facility at Herøya Industrial Park (Norway) from 40 MW/year to 360 MW/year, with future expansion plans of up to 1 GW/year.
- ITM is part of the Gigastack project, that aims to ramp up production capacity to 60 stacks per year (300 MW/year) by 2023 and 200 stacks (1 GW/year) by 2025. This is to be done with a simultaneous increase in the system size to 20 MW to achieve a specific investment cost of GBP 400/kW with a module size of 100 MW. The ramping up is 60 stacks per year (300 MW/year) by 2023 and 200 stacks (1 GW/year) by 2025.

  The project is currently in the frontend engineering and design (FEED) phase (Phase II), with the design of the 100 MW facility, which is 5 × 20 MW.
- While Siemens does not have an explicit manufacturing target, it is also involved in various 100 MW+ projects around the globe, putting them in a good position to expand capacity. One of these projects is the Murchison Renewable Hydrogen Project in Australia, which has scope for up to 5 GW of renewable capacity and is initially expected to produce hydrogen for transport fuels, followed by blending with natural gas and exports.

6 Electricity

The major cost component for green hydrogen is the electricity supply. Cost decline in this is already underway through the competitive deployment of renewables.

There is a need to focus on reducing the procurement and construction cost and increasing the performance and durability of electrolyzers, to achieve further cost reductions in green hydrogen production.

Green hydrogen can achieve cost-competitiveness with fossil-based hydrogen today in ideal locations with the lowest renewable electricity costs. Cost reductions in renewable electricity and electrolyzers will continue to increase the number of sites where green hydrogen can be produced competitively, however.

Policy supports in recently unveiled hydrogen strategies in many countries is mostly in the form of explicit electrolyzer capacity targets and, to a more limited extent, cost targets. These have yet to translate into specific regulatory instruments. So far, these explicit targets are not enough to be in line with 1.5 °C decarbonization pathways.

The world is undergoing a dramatic change in the way energy is produced, transformed, stored and used in its various forms. People are becoming increasingly conscious of the need to move towards a society where energy stops contributing to climate change and local pollution, replacing fossil fuels with renewable energy.

As the deployment of renewable energy sources increases all over the globe in the power sector, solutions that leverage renewable electricity to decarbonize end-use sectors using power-to-gas strategies, or to convert electricity into high-value chemicals or fuels, need to be quickly introduced. In addition, as electricity needs to increase from around 20% of final energy consumption to around 50% by 2050, there is still a need to decarbonize applications for which direct electrification is more challenging (the so called "hard-to-abate" sectors).

Hydrogen is only one option in decarbonizing hard-to-abate sectors. Energy efficiency is key to reducing the energy supply and renewable capacity upstream, while bioenergy might be suitable, not only in the form of biofuels for those transport sectors that have limited fuel alternatives (especially aviation), but also as a source of carbon for synthetic fuels. Direct electrification is more efficient from a systems perspective, leading to lower cost, with this already commercially deployed in many areas (e.g. heating or passenger vehicles). Carbon capture and storage (CCS) might be attractive for existing assets that are still in early stages of their lifetime (the case for many assets in Asia) and process emissions (e.g. from cement production). Even for the most ambitious scenarios, these technological choices might not be enough, however, and behavioral changes might be needed to push energy demand even lower. Thus, for energy transition, hydrogen is one solution amongst others and should be tackled in parallel. Hydrogen is part of a wider technology portfolio to be adapted to domestic conditions in each country, with this report further exploring this pathway.

Green hydrogen (i.e. hydrogen produced from renewable electricity) links renewable electricity with a range of end-use applications acting as a complement of electrification, bioenergy and direct renewable energy use. The potential for green hydrogen is much higher than fossil fuels, since it is linked to solar and wind potential, which far exceeds global energy demand today and in any future scenario. Most importantly, in the context of decarbonization, green hydrogen is the only zero-carbon option for hydrogen production, as carbon capture in CCS is 85–95% at best and significantly lower to date.

Once produced at scale and competitive cost, green hydrogen can also be further converted into other energy carriers, such as ammonia, methanol, methane and liquid hydrocarbons. As a fuel, hydrogen can be used in fuel cells (i.e. an electrochemical device that combines hydrogen with oxygen from the air and produces electricity), but also combusted in engines and turbines. Fuel cells can be used for stationary applications in large-scale power plants, microgrid or backup generation (e.g. in data

centers), or for a wide range of transport applications – as is already done in fuel cell electric vehicles (FCEV), trucks, light-duty vehicles, forklifts, buses, ferries and ships. As a chemical, green hydrogen can reduce greenhouse gas (GHG) emissions from sectors where hydrogen from fossil fuel is widely used today, including oil refining, methanol and ammonia production.

Green hydrogen is only one of the production pathways. Hydrogen can also be produced from bioenergy, methane, coal or even directly from solar energy. Most of the production today is based on methane and coal (about 95%) and could be made low carbon with the use of CCS. CCS might be suitable for regions with low-cost natural gas and suitable underground reservoirs. In the short term, CCS might also be a good fit for large-scale applications in industry, given the relatively small scale of deployment for electrolysis.

Low-carbon hydrogen can also be produced from methane pyrolysis, where the carbon ends up as solid rather than as CO_2, with 4–5 times lower electricity consumption than electrolysis and potentially lower hydrogen production cost. Each pathway has its own limitations. Bioenergy might be best suited for other applications, considering its limited nature and the low inherent hydrogen yield. CCS does not lead to zero emissions, requires significant infrastructure for the CO_2, does not enable sector coupling, is still exposed to the price fluctuations characteristic of fossil fuels, and could face social acceptance issues. In addition, methane leakages associated with production and transportation of the gas have been increasingly under scrutiny as significant contributors to the acceleration of climate change. Methane has 86 times higher global warming potential compared to CO_2 over a 20-year time horizon. Pyrolysis is still at the pilot scale stage and would require high-temperature renewable or low-carbon heat. Hence, considering the sector, green hydrogen is one of the most attractive options, given its nature and renewable character, and as such, it is the focus of this report.

Green hydrogen, similar to other production pathways, also has its challenges, however. These include: its current high cost across the entire value chain, from electrolysis to transport and fuel cells; the lack of existing infrastructure for transport and storage; the high energy losses (which in turn require higher wind/solar deployment rates); and the lack of value for the main benefit (e.g. lower GHG emissions) that green hydrogen can have.

Renewables are becoming the cheapest source of electricity around the world, with significant potential for further cost reductions. This opens up the opportunity, in the long-term, to trade globally low-cost green hydrogen from the best renewable resources to regions with limited land or renewable potential. This trade can be done directly with liquid hydrogen, in the form of hydrogen carriers that increase the energy density for transport, or in the form of commodities (e.g. reduced iron and chemicals).

The missing element in this equation is the key facility to convert renewable power into green hydrogen: the electrolyzer. Electrolyzers are the technology necessary to produce hydrogen using electricity and water as inputs. Electrolysis is a well-established technology that is deployed mostly in the chemical industry. While scale-up is needed to bring costs down, technological innovation is also needed to further improve the performance of the technology (i.e. its efficiency and lifetime).

This can be done via new catalysts and configurations, the standardization of designs and a move to mass production of the equipment.

Green hydrogen is already close to being competitive today in regions where all the favorable conditions align, but these are usually far from demand centers. For example, in Patagonia, wind energy could have a capacity factor of almost 50%, with an electricity cost of USD 25–30/MWh. This would be enough to achieve a green hydrogen production cost of about USD 2.5/kg, which is close to the blue hydrogen cost range.

In most locations, however, green hydrogen is still 2–3 times more expensive than blue hydrogen.

The cost of the former is defined by electricity costs, investment cost, fixed operating costs and the number of operating hours of the electrolyzer facilities (see Fig. 10).

Fig. 10 Hydrogen production cost as a function of investment, electricity price and operating hours
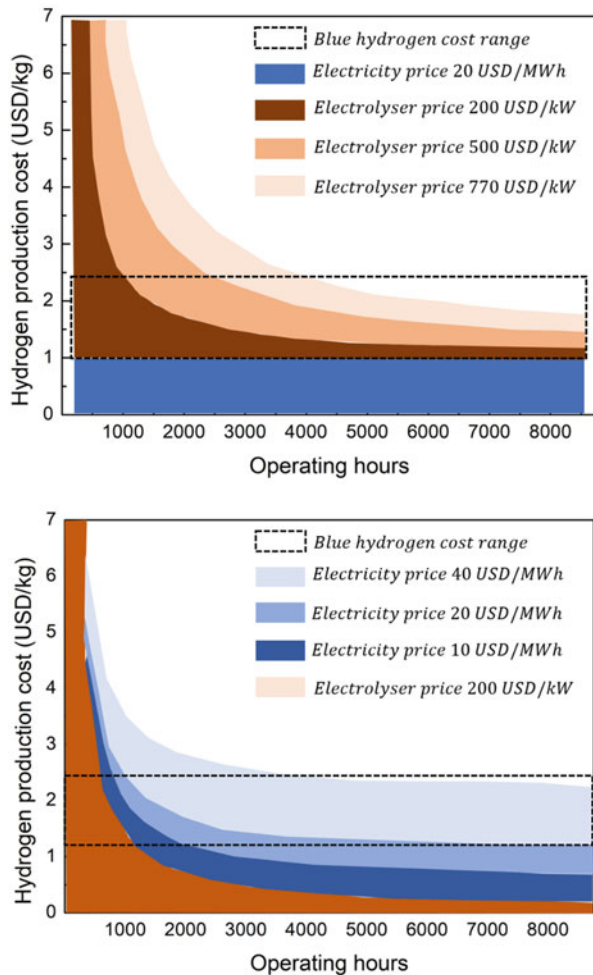
With low operating hours, the investment cost dominates, as it is spread over a smaller amount of hydrogen. This could happen when using only curtailed electricity, or coupling with PV without any storage or backup. The electricity cost becomes dominant as the number of operating hours increases. Solar projects in countries such as Brazil, Portugal, the United Arab Emirates and the United States have been deployed with costs of electricity as low as USD 13.5–20/MWh due to supportive policy instruments, such as auctions, to guarantee a stable payment and reduce the investment risk.

Due to the efficiency of the current process, any power cost that goes into the process translates into roughly 1.5 times this value in final production costs. This means that a power cost of USD 20/MWh results in around USD 31/MWh in the final cost of the hydrogen, or a figure slightly above USD 1/kg H2 Under the optimal conditions of low-cost renewable electricity, low investment cost and a high number of operating hours, green hydrogen could achieve cost competitiveness with fossil-based hydrogen, noting that only about 3000–4000 hours per year may be enough to achieve the largest reduction in the contribution of the investment. This can be achieved by, for instance, large scale hybrid PV wind plants, which, at the best locations in the world, can achieve capacity factors above 5000 hours.

Currently, green hydrogen production is limited to demonstration projects. By September 2020, there were almost 320 of these, adding up to around 200 MW of electrolyzer capacity (IEA TCP). Green hydrogen (through water electrolysis) contributed to less than 0.02% of present day global pure hydrogen production. Projects are mostly in the single-digit MW scale with the largest project in operation currently a 10 MW alkaline electrolyzer in Japan. A 20 MW PEM electrolyzer in Becancour (Canada) by Air Liquide is expected to be operational before the end of 2020. In spite of this small scale, the technology is already commercial and ready to scale up, with projects announced between 2020 and 2025 adding up to more than 25 GW and new projects being announced on almost a weekly basis.

To ensure that green hydrogen supply cost is as low as possible, a holistic approach needs to be applied to system design and operations. System design can be optimized to minimize cost and increase flexibility as necessary, depending on a variety of factors. These can include: the variability of electricity supply (i.e. constant consumption of grid electricity, or direct feed from variable solar or wind farms); the technology used for the stack (e.g. alkaline, PEM and AEM being more flexible than solid oxide); and the flexibility of hydrogen demand (e.g. constant demand for chemical processes, general annual demand for export without hourly or daily constraints). Storage can significantly help to decouple variable supply from hydrogen demand. This can come in the form of electrochemical storage for short-term fluctuations (before the electrolyzer stack), or in the form of hydrogen storage for long-term fluctuations (after the stack, before the downstream off taker).

Similarly, hydrogen storage in tanks, caverns and pipelines can help decouple variable hydrogen production from inflexible hydrogen demand (e.g. to produce ammonia). No single blueprint exists, however, the type of electricity supply and hydrogen demand will drive system design, where no single electrolyzer technology

is better than any other, as the combination with electricity and hydrogen storage can effectively provide any level of flexibility.

Both alkaline and PEM electrolyzer systems have been certified to provide primary reserves (i.e. the most rapid, short term grid service), therefore highlighting how flexibility is more of a design issue related to balance of plant components and sizing. Many small modular stacks, for example, each one with its own rectifier, make a significantly more flexible electrolyzer plant than a single large stack with single rectifier, regardless of stack technology.

In terms of hydrogen storage, hydrogen in a gaseous form can be stored in two favored approaches: pressurized steel tanks and underground reservoirs.

Hydrogen can also be liquefied. This would deliver about 75% higher energy density than gaseous hydrogen stored at 700 bar, while requiring the equivalent of 25%–30% of the energy contained in the hydrogen. Promising developments in large scale facilities show energy consumption as low as 6 kWh/kg of hydrogen.

Underground storage of hydrogen using, for instance, salt caverns is considered to be the most appropriate solution to store hydrogen on a large scale. This method comprises some interesting storage characteristics, such as low investment costs, high sealing potential, and low cushion gas requirement. Salt caverns typically allow storing hydrogen from 100 bar up to 275 bar.

Hydrogen storage at output pressure from the electrolyzer is useful, if the objective is to maximize flexibility, as mechanical compression can limit the speed at which electrolyzer output can change. The use of pressurized electrolyzers (e.g. 30 bar, achievable with both alkaline and PEM technologies today), in combination with a buffer to decouple the electrolyzer operating regime from the compressor operating regime, helps to prevent the compressor from becoming the bottleneck for the flexibility of the electrolysis facility as a whole.

As far as the ability of electrolyzers to provide flexibility to the power system, this can be achieved at multiple time scales.

Except for the provision of inertia, electrolyzer facilities can provide all system services, if designed with this in mind. While PEM might eventually be more effective than alkaline for fast frequency response (FFR), batteries are clearly more efficient and effective in providing fast response to system operator's signals and can quickly saturate such a market, which makes any additional cost incurred for designing electrolyzer facilities capable of providing FFR questionable in terms of potential return. For the remaining services, all electrolyzer technologies can provide them effectively without technical challenges, provided they are designed with grid service provision in mind.

Where hydrogen has a significant role to play in terms of flexibility provision in future decarbonized power systems is in long duration storage and system adequacy. The seasonality of solar, wind and hydropower resources can provide challenges in terms of adequacy – if not every year, at least in unusual weather years (e.g. dry years, or years with extended periods of low wind). Hydrogen from renewable power can be stored cost effectively – for example, in salt caverns – and can be used for power generation in these periods.

Notably, if hydrogen-to-power is performed using gas turbines or internal combustion engines, hydrogen can then also contribute to the provision of system inertia (unlike fuel cells).

The key message is that hydrogen production from electrolyzers can be uniquely positioned to provide seasonal flexibility to the power system – something that no other resource can effectively provide.

This can play a significant role in balancing a power system with high shares of solar and wind, not only instantaneously and intra-day, but also across seasons. To be able to provide such services, electrolyzers must be designed not to operate at full capacity the entire year, but rather to purchase electricity when green and affordable. This is only possible if they are sufficiently oversized to avoid purchasing non-renewable electricity, or prohibitively expensive electricity, just to be able to meet hydrogen demand.

7 Transmission Costs

Transporting energy over long distances is easier when the energy is a chemical fuel rather than electricity. Chemical fuels tend to have high energy densities, do not suffer losses while being transported, benefit from economies of scale, and allow point-to-point trading or transmission across widespread networks. Most natural gas and oil are moved around the world in large-scale pipelines and ships, and both these options can also be used for hydrogen and hydrogen carriers. Moving hydrogen using trains could also be an inland option for some regions, although this would in general be a more expensive option than moving the hydrogen by pipeline (Moreno-Benito et al. 2017).

There are close to 5 000 km of hydrogen pipelines around the world today, compared with around 3 million km of natural gas transmission pipelines. These existing hydrogen pipelines are operated by industrial hydrogen producers and are mainly used to deliver hydrogen to chemical and refinery facilities. The United States has 2 600 km, Belgium 600 km and Germany just under 400 km.

Pipelines have low operational costs and lifetimes of between 40 and 80 years. Their two main drawbacks are the high capital costs entailed and the need to acquire rights of way. These mean that certainty of future hydrogen demand and government support are essential if new pipelines are to be built. Existing high-pressure natural gas transmission pipes could be converted to deliver pure hydrogen in the future if they are no longer used for natural gas, but their suitability must be assessed on a case-by-case basis and will depend on the type of steel used in the pipeline and the purity of hydrogen being transported. Recent studies in the Netherlands have suggested that the existing natural gas network could be used to transmit hydrogen with small modifications.

The main challenge is that three times more volume is needed to supply the same amount of energy as natural gas. Additional transmission and storage capacity across the network might therefore be required, depending on the extent of the growth of hydrogen.

Ammonia is often transported by pipeline, and new pipelines for ammonia would be cheaper than new pipelines for pure hydrogen. Ammonia pipelines in the United States currently feed hundreds of retail points and total 4 830 km in length. In Eastern Europe the 2 400 km Odessa line pumps ammonia from Russia to fertiliser and chemical plants as far as Ukraine.

LOHCs are similar to crude oil and diesel, and so could use existing oil pipelines. However, the need to transfer the hydrogen carrier back to its place of origin to be re-loaded with hydrogen, either by truck or a parallel pipeline operating in the opposite direction, makes this a complicated and expensive method of transport (Preuster et al. 2017).

Imported hydrogen offers scope for countries to diversify their energy imports, and one result of this is significant interest in using ships to transport hydrogen.

There are currently no ships that can transport pure hydrogen. Such ships would be broadly similar to LNG ships and would require the hydrogen to be liquefied prior to transport. While both the ships and the liquefaction process would entail significant cost, a number of projects are actively looking to develop suitable ships. The expectation is that these ships will be powered by hydrogen that boils off during the journey (around 0.2% of the cargo would likely be consumed per day, similar to the amount of natural gas consumed in LNG carriers). Unless a high-value liquid can be transported in the opposite direction in the same vessel, ships would need to return empty.

Among hydrogen carriers, the most developed in terms of intercontinental transmission is ammonia, which relies on chemical and semi-refrigerated liquefied petroleum gas (LPG) tankers. Trade routes today include transport from the Arabian Gulf and Trinidad and Tobago to Europe and North America. LOHCs would be the easiest form in which to transport hydrogen by ship, because oil product tankers could be used, although the cost of conversion and then reconversion back to hydrogen before use would also need to be taken into consideration. Ships would also need to return with the original carrier, adding to the complexity of supply routes.

In all cases, shipping supply chains require the necessary infrastructure, including storage tanks, liquefaction and regasification plants, and conversion and reconversion plants, to be built at the loading and receiving terminals as appropriate.

For pipelines, taking into account all capital and operating costs, the IEA estimates that it would cost around USD 1/kgH2 to transport hydrogen as a gas for around 1 500 km (Fig. 11).

The cost of converting the hydrogen to ammonia is around USD 1/kgH2 (with some variation between different regions). While it is cheaper to move ammonia by pipeline then hydrogen, these conversion costs mean that the total cost of transmitting ammonia for around 1 500 km is about USD 1.5/kgH2. As the transmission distance increases, the cost of transporting hydrogen by pipeline escalates faster than

Fig. 11 Cost of hydrogen
storage and transmission by
pipeline and ship, and cost
of hydrogen liquefaction
and conversion
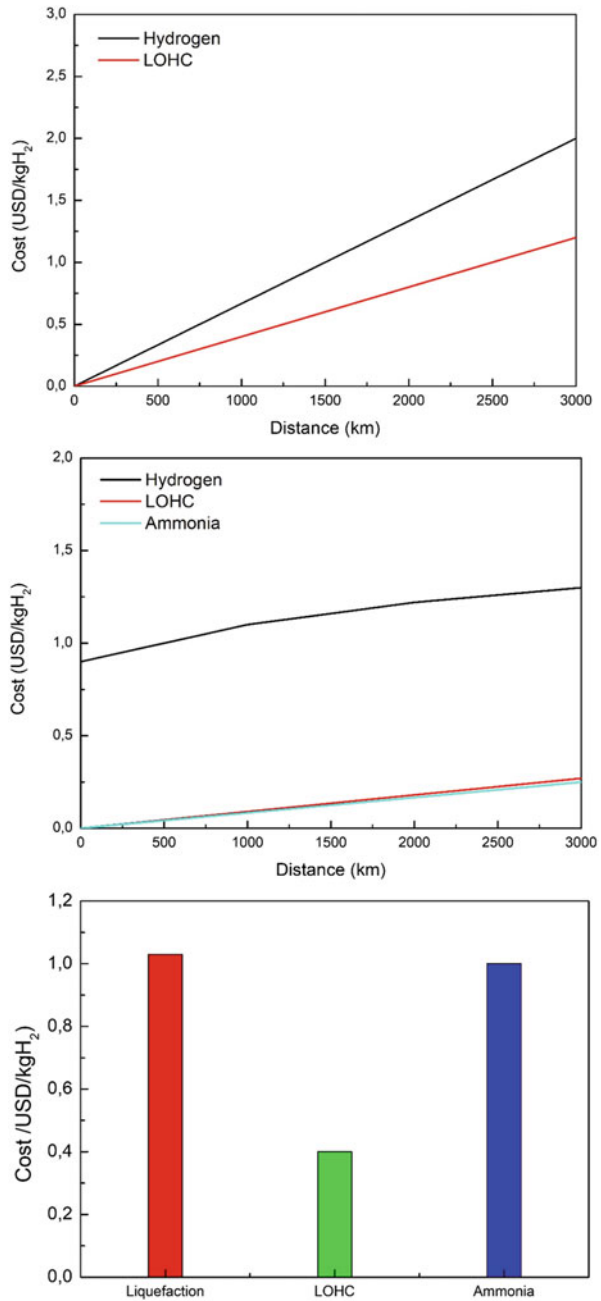
the cost for ammonia since a greater number of compressor stations are required. If the transmission distance is 2 500 km the cost of transporting ammonia by pipeline, including the conversion cost, becomes broadly similar to the cost of transporting hydrogen as a gas (around USD 2/kgH2).

For ships, hydrogen gas must be liquefied or converted prior to transmission. This entails an additional cost to be added to the cost of moving and storing the hydrogen, LOHC or ammonia.

For liquid hydrogen, storing the hydrogen at import and export terminals is also relatively expensive. The cost of conversion and moving hydrogen 1 500 km by ship as an LOHC is USD 0.6/kgH2, as ammonia is USD 1.2/kgH2 and as liquid hydrogen is USD 2/kgH2. The cost of shipping increases as the transmission distance increases given the need for a greater number of ships, longer voyage distances and additional storage, but not by a significant degree compared to the costs of conversion. The increase in costs at greater distances is also much smaller than is the case for pipelines. As noted above, these costs relate solely to hydrogen transmission; a full cost comparison of the different modes needs to take into account the costs of local distribution and reconversion to hydrogen.

Once the hydrogen has reached the import terminal or transmission hub, local distribution is necessary to deliver it to final users. As with transmission, the best options for doing this for hydrogen, ammonia and LOHCs will depend on volume, distance and end-user needs.

Today hydrogen distribution mostly relies on compressed gas trailer trucks for distances less than 300 km. Liquid hydrogen tanker trucks are often used instead where there is reliable demand, and the liquefaction costs can be offset by the lower unit costs of hydrogen transport.

In both cases, the hydrogen is distributed in tubes that are loaded onto trailers. Trucks can be used to distribute ammonia or LOHCs in a broadly similar way.

In theory a single trailer transporting compressed hydrogen gas can hold up to 1 100 kgH2 in lightweight composite cylinders (at 500 bar). This weight is rarely achieved in practice, however, as regulations around the world limit the allowable pressure, height, width and weight of tubes that can be transported. In the United States, for example, the pressure limit for steel tubes means that a trailer has a maximum load of 280 kgH2 (although the US Department of Transport recently approved the manufacture and use of higher-pressure composite storage vessels).

Highly insulated cryogenic tanker trucks can carry up to 4 000 kg of liquefied hydrogen, and are commonly used today for long journeys of up to 4 000 km. These trucks are not suitable for transport above this distance as the hydrogen heats up and causes a rise in pressure.

Around 5 000 kgH2 in the form of ammonia or 1 700 kgH2 in the form of LOHC could be moved in a road tanker. In the case of LOHC, a truck would also be needed to transport the carrier molecules back to the original destination after the hydrogen has been extracted from them.

Many modern low-pressure gas distribution pipes are made of polyethylene or fiber-reinforced polymer and would generally be suitable to transport hydrogen with some minor upgrades. In the United Kingdom almost the entire distribution pipe

network, which is about 14 times the length of the country's gas transmission grid, is being replaced with plastic pipes as part of a gas infrastructure upgrade program. Distribution pipelines for natural gas are extensive in areas with high heating demand, such as northern Europe, the People's Republic of China and North America, reaching into urban areas as well as industrial clusters.

New dedicated hydrogen distribution pipelines would represent a more significant capital cost, especially on the scale required for supplying hydrogen to heat buildings. Distributing ammonia by pipe over long distances would be less costly but is likely to be attractive only if there is a large demand for ammonia given the costs of converting ammonia back into hydrogen before use. As with transmission, distribution of LOHCs by pipeline is likely to be impractical given the need to return the carrier molecules to their place of origin at the end of the process.

While trucks carrying hydrogen gas distribute the majority of hydrogen today, this is a relatively high-cost option (Fig. 12).

Fig. 12 Cost of hydrogen distribution to a large centralised facility and cost of reconversion to gaseous hydrogen
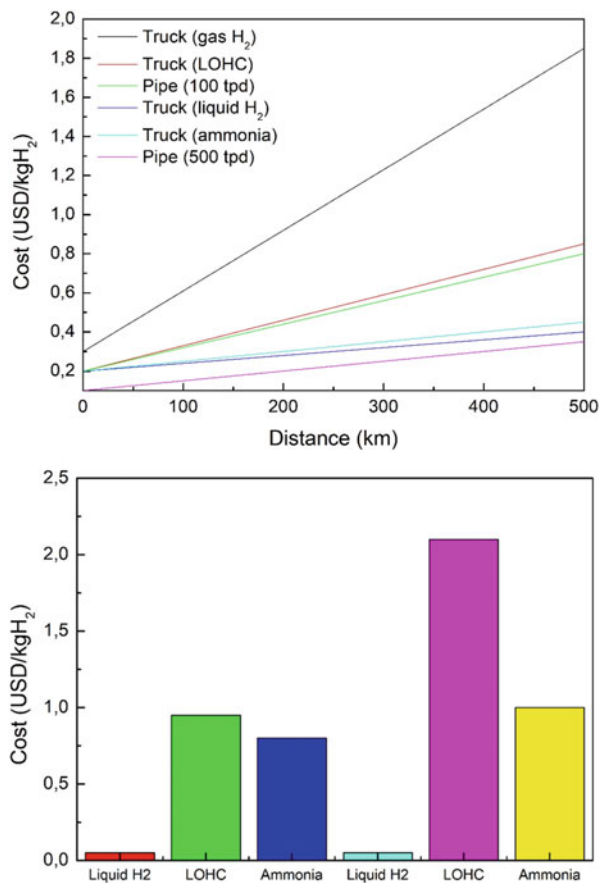
As the distribution distance increases, pipelines become increasingly cost-competitive with trucks. A critical consideration for distribution is how much hydrogen is required by the end user. If large volumes are needed then larger pipes can be used, which reduces the cost of delivery. For example, if 100 tons per day (tpd), roughly the amount of hydrogen that would be required by a single 200 MW hydrogen power plant, are required at a location 500 km away from the point of import, then the use of trucks would be cheaper than constructing a pipeline; if 500 tpd are required, then a pipeline would have lower unit costs.

Nevertheless, it is reasonable to expect that, over the next decade, compressed gas tube trailers and liquid hydrogen tanks will remain the main distribution modes, just as distribution of gasoline and diesel to geographically dispersed refueling stations is mostly carried out using trucks today.

Costs also depend strongly on the required end use of the hydrogen. If pure hydrogen is required, then the additional cost of extracting hydrogen from ammonia or an LOHC must be included. The cost of this reconversion depends on the purity of the hydrogen required: if the hydrogen is to be used in fuel cells rather than combusted, then reconversion is more expensive.

Furthermore, reconversion costs at the point of end use (for example at a hydrogen refueling station) is higher than for centralized reconversion (for example at a transmission import terminal).

The IEA estimates that the cost of distributing LOHC by truck for a distance 500 km would be USD 0.8/kgH2 and the cost of extracting and purifying the hydrogen at the point of end use would be USD 2.1/kgH2. The total cost of local distribution would therefore be USD 2.9/kgH2.

For ammonia the equivalent cost would be USD 1.5/kgH2; however, if the ammonia could be used by the final customer without the need for reconversion back to hydrogen, the cost of distribution would considerably lower, at USD 0.4/kgH2.

8   Costs of Delivering and Storing Hydrogen

The full cost of hydrogen delivery to end users must take into account all possible stages of the supply chain. The different hydrogen carriers and modes of transport have very different conversion, transmission, distribution, storage and reconversion costs. While one option may be cheaper for a specific part of the value chain, this may be offset by higher costs in another part of the chain. The various technologies involved are also at different degrees of maturity and so have very different future cost reduction potentials. There may be scope for synergies between energy, heat and storage requirements. For example, if the specific value chain in question has higher energy requirements at the export terminal than at the import terminal (e.g. liquid hydrogen), this could improve the relative cost and emission dynamics compared with the reverse case (e.g. LOHCs).

Fig. 13 Full cost of hydrogen delivery to the industrial sector by pipeline or by ship in 2030 for different transmission distances
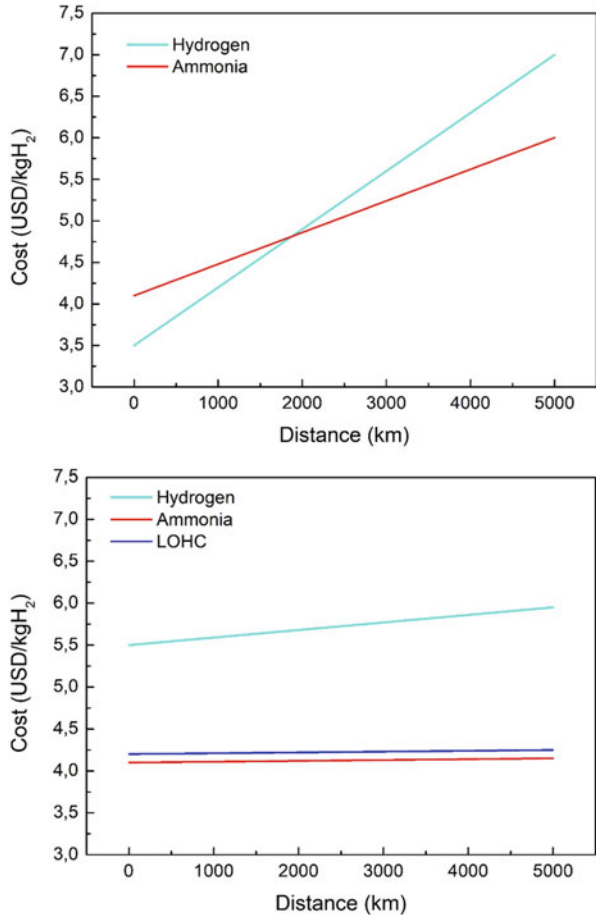
The overall cost of delivering hydrogen will vary according to the infrastructure available in the exporting and importing countries, transmission and distribution distances, the method of transport, and end-use demand. Despite the many uncertainties around most of these cost components, IEA analysis suggests that for inland transmission and distribution, hydrogen gas is the cheaper option for distances below around 3 500 km (Fig. 13).

Above this distance, ammonia pipelines would be the cheaper option. Comparing transport using pipelines and ships, transmission and distribution of hydrogen gas by pipeline is cheaper for distances below around 1 500 km. Above this distance, LOHC and ammonia transport by ship, which are broadly similar in terms of their full costs, become the cheaper delivery options. The transport and use of ammonia or some LOHCs may, however, give rise to potential safety and public acceptance issues, which could limit their application in some situations.

IEA analysis indicates that in the future it may be cheaper in a number of instances to import hydrogen than to produce it domestically. For example, Japan currently imports around 90% of its energy needs and, as its Basic Hydrogen Strategy shows, it views hydrogen as a source of energy diversification, emissions reduction and industrial leadership. IEA estimates that, for Japan's industrial sector in 2030, importing electrolytic hydrogen from Australia (around USD 5.5/kgH2) will be cheaper than domestic production (USD 6.5/kgH2).

This assumes the production of hydrogen in Australia using combined installations of electrolyzers, solar plants and wind farms in a region with high solar and wind resources and the subsequent export of this hydrogen to the point of use in Japan as ammonia or LOHC. The total cost of transporting the hydrogen from Australia to Japan (including conversion and reconversion) would be just over USD 1.5/kgH2, equivalent to USD 45 per MWh. Ammonia would be even more attractive if it could be used directly by the end consumer, thereby avoiding the additional costs of reconverting it back into hydrogen.

The cheapest source of hydrogen would, however, still be substantially more expensive than natural gas. In 2030 the imported natural gas price in Japan is projected to be USD 10/MBtu, equivalent to around USD 1.2/kgH2. Although the actual cost differential may be slightly smaller than it looks because some hydrogen end-use devices may have a higher efficiency than natural gas devices, further cost reductions would be needed to improve the competitiveness of hydrogen against natural gas systems.

For many other possible trade routes, the relatively high cost of hydrogen transmission and distribution means that it will generally be cheaper to produce hydrogen domestically rather than import it. This is because the cost of transport will outweigh differences in the cost of electricity production from renewable sources, or differences in natural gas prices and the cost of CCUS. In Europe, for example, domestic production of low-carbon hydrogen from natural gas equipped with CCUS is likely to be cheaper for industry and power applications than importing low-carbon hydrogen from Russia. Even so, some countries with constrained CO_2 storage or limited untapped renewable resources may still see low-carbon hydrogen imports as worthwhile because of the contribution they make to diversifying their energy systems and reducing their CO_2 emissions.

In the transport sector, centralized reconversion of LOHC or ammonia to produce hydrogen, for example at an import terminal, is generally much cheaper than reconversion at the point of final use, for example at a filling station. However, this needs to be balanced against the higher cost of distributing hydrogen as a liquid or gas.

For hydrogen produced in North Africa and transported to Europe, it is likely to be cheapest to ship the hydrogen as ammonia or LOHC, with the cheapest option for subsequent distribution to a 1 tpd refueling station22 depending on the distances involved. For ammonia, if the distribution distance is below 100 km, then the cheapest option is likely to be to reconvert the ammonia as soon as it has been imported and to distribute the resultant hydrogen using compressed hydrogen gas trucks. If the distribution distance is greater than 100 km, then it is likely to be

cheaper to distribute the ammonia in trucks and reconvert them to produce hydrogen at the refueling station. For LOHC, centralized reconversion is cheaper for distribution distances up to 500 km.

A distribution distance of 100 km would result in a delivered hydrogen price (before tax and margins) between USD 7.5/kgH2 and USD 9/kgH2. Taking into account the higher conversion efficiency of fuel cells compared to internal combustion engines, this would be equivalent to between USD 1.1 and 1.3 per liter of gasoline; this is under current prices at the pump in Europe of around USD 1.4 per liter, although these are prices after taxes.

If existing pipeline infrastructure can be used for hydrogen, the cost of transmission and distribution would be much lower. For example, it is estimated that the cost to convert the gas network of the United Kingdom to supply pure hydrogen to buildings would be around USD $0.6/kgH_2$ (CCC, 2018). Given the lower energy density of hydrogen, additional storage capacity would also be required to meet heat demand, which would add a further USD $0.5/kgH_2$.

In this case, the total cost of hydrogen imported from North Africa and delivered to buildings in the European Union would be around USD 4.5/kgH2 (USD 135/MWh) for hydrogen produced from natural gas with CCUS, or USD $6/kgH_2$ (USD 180/MWh) for electrolytic hydrogen.

9   Conclusions

Today, green hydrogen represents only a limited share of global supply. The transition to a future where green hydrogen has not only displaced fossil-based hydrogen, but also gone beyond the industrial sector to become a fuel and energy carrier, will therefore not happen overnight. It will also not happen without the participation of multiple stakeholders. Coordination is key, across four dimensions at least:

- Across the value chain: Hydrogen supply (as covered in this report) has to be done in parallel with infrastructure development and, more importantly, demand. At least during the early stages, when a market has not yet developed, production projects need to be codeveloped with an off taker, since there is no grid or ubiquitous established sink that can absorb all the production. While blending in the gas grid, if combined with tracing and financial compensation, can provide an alternative, it is only an alternative for early stages of development.
- Across borders: All sectors, from electrolyzers to fuel cells, direct reduction of steel to ammonia ships and synthetic fuels, will benefit from global collaboration. This applies to the deployment level – enabling learning from projects to drive costs down – and at the research level, enabling the coordination of national programs.
- Across sectors: The green hydrogen covered in this report will benefit from combining different applications to aggregate demand, justifying larger projects

and achieving economies of scale that benefit production and, perhaps, infrastructure.

- Across stakeholders: Green hydrogen will not scale up without support from multiple stakeholders. Fortunately, there is already widespread interest in hydrogen from energy utilities, steel makers, chemical companies, port authorities, car and airplane manufacturers, shipowners and airlines, amongst others, but their actions need to be in the same direction.
- Long-term signals and commitments: These are necessary to attract private capital, which will be needed for scaling up. For conventional technologies, investors already have long-term horizons, covering the lifetime of assets, aiming to recover the cost and make a profit. For hydrogen production with water electrolysis – a nascent industry – additional certainty from governments is needed to justify the additional risk and investment. This can come in the form of commitment to net zero emissions targets, since hydrogen is the most useful for hard to abate sectors that are required to achieve these targets, or in the form of strategies that set the direction for hydrogen deployment. This commitment to develop hydrogen should ultimately be reflected in the long-term strategies and nationally determined contributions of each country.
- Market creation: This will drive demand for green hydrogen. One measure in this is public procurement (e.g. a percentage of green steel for public infrastructure). Blending mandates or quotas are also an attractive alternative. Examples include requiring a percentage of industrial hydrogen to shift to green, as already covered in French and Portuguese strategies; requiring a percentage of gas demand to be met by green hydrogen, or requiring a percentage of shipping or aviation fuel to be sustainable. Phase-out mandates, similar to those implemented in fossil fuel or nuclear power, or to internal combustion engines in transport, could be used to promote demand by setting a timeline to phase out blast furnaces for steel or fossil fuel-based ships.
- Standards and certifications: Uptake for green hydrogen requires that the customer is able to know what the source of the hydrogen is to be able to link it to an additional premium or quota target, while the producer is able to validate lower CO_2 emissions and be remunerated accordingly. This needs to be transparent to be able to communicate the emissions that have been accounted for (upstream, production, transport, and re-conversion). It also needs to be robust, potentially including more than CO2 only, to ensure high sustainability standards that are internationally accepted, compatible with other schemes (e.g. electricity and gas) and with an adaptable framework to be adjusted based on lessons learned, once it is deployed.
- Capacity targets: This is the most used measure so far in hydrogen strategies. These should be deployed in tandem with an increase in renewable capacity targets (if any) to make sure renewable electricity use for hydrogen does not displace more efficient uses (such as increasing the renewable share of the grid).
- Financial support: This can be in the form of grants or concessional loans that decrease the investment risk for industry and close part of the cost differential with fossil-based hydrogen. One example is Australia, where hydrogen is one of

the technologies supported under the AUD 1.9 billion investment package for new energy technologies. The Clean Energy Finance Corporation will make AUD 300 million available to support the hydrogen industry and there is also some funding through the Australian Renewable Energy Agency (ARENA), which has a AUD 70 million grant program aimed at demonstrating the technical and commercial viability of hydrogen production.

- Blending quotas: These could be used by either specifying a share of green hydrogen in existing uses, or shares of green hydrogen in final energy demand for specific applications (e.g. similar to the renewable share in transport in the EU). France has already used this approach, specifying 10% of low-carbon hydrogen (potentially from nuclear as well) in industry by 2023 and 20–40% by 2028. Portugal has also specified blending shares for most end use sectors from 2020 to 2050, including 2–5% of green hydrogen in industry by 2030, 10–15% by 2040 and 20–25% by 2050.
- Manufacturing capacity targets: Some regions are aiming for technology leadership in electrolysis and could use incentives to promote domestic production. For instance, the UK government awarded USD 9.8million (GBP 7.5 million) for a feasibility study to scale up the electrolyzer size to 100 MW and the manufacturing capacity to 300 MW/year by 2023 and to 1 GW/year by 2025.
- Tax incentives: These could decrease the impact of the high capital cost on project profitability. Alternatives are lower income or sales taxes, or lower tax on the investment. One example is from the Netherlands, where investments resulting in the displacement of fossil fuels are tax deductible (the tax rate is up to 41.5%). The incoming US administration is considering the introduction of a production tax credit of USD 0.42/kg for clean hydrogen and hydrogen carriers – based on emissions intensity – and a manufacturers production tax credit of USD 500/kW. Similar incentives were fundamental for the deployment of wind and battery electric vehicles respectively.
- Green hydrogen premium: This could be through feed-in tariffs or contracts for difference. An example where this is already applied is the SDE++ program in the Netherlands, which is set to provide subsidies for the production of hydrogen from electrolysis.

References

Armaroli N, Balzani V (2011) The hydrogen issue. ChemSusChem 4:21–36. https://doi.org/10.1002/cssc.201000182

Ba L, Xiong X, Lei Z et al (2022) A study on solid oxide electrolyzer stack and system performance based on alternative mapping models. Int J Hydrogen Energy 47(25):12469–12486. https://doi.org/10.1016/j.ijhydene.2022.01.253

Bockris JOM (2013) The hydrogen economy: its history. Int J Hydrogen Energy 38(6):2579–2588. https://doi.org/10.1016/j.ijhydene.2012.12.026

Dang J, Li Y, Liu B et al (2022) Design and economic analysis of high-pressure proton exchange membrane electrolysis for renewable energy storage. Int J Hydrogen Energy 48:10377–10393. https://doi.org/10.1016/j.ijhydene.2022.11.250

Dou Y, Sun L, Ren J et al (2017) Opportunities and future challenges in hydrogen economy for sustainable development. In: Hydrogen economy-supply chain, life cycle analysis and energy transition for sustainability. https://doi.org/10.1016/B978-0-12-811132-1.00010-9

Esposito DV (2017) Membraneless electrolyzers for low-cost hydrogen production in a renewable energy future. Joule 1(4):651–658. https://doi.org/10.1016/j.joule.2017.07.003

Falcone PM, Hiete M, Sapio A (2021) Hydrogen economy and sustainable development goals: review and policy insights. Curr Opin Green Sustain Chem 31:100506. https://doi.org/10.1016/j.cogsc.2021.100506

Gallardo F, García J, Ferrario AM et al (2022) Assessing sizing optimality of OFF-GRID AC-linked solar PV-PEM systems for hydrogen production. Int J Hydrogen Energy 47(64):27303–27325. https://doi.org/10.1016/j.ijhydene.2022.06.098

Grimm A, de Jong WA, Kramer GJ et al (2020) Renewable hydrogen production: a techno-economic comparison of photoelectrochemical cells and photovoltaic-electrolysis. Int J Hydrogen Energy 45(43):22545–22555. https://doi.org/10.1016/j.ijhydene.2020.06.092

Kim M, Kim J (2016) Optimization model for the design and analysis of an integrated renewable hydrogen supply (IRHS) system: application to Korea's hydrogen economy. Int J Hydrogen Energy 41(38):16613–16626. https://doi.org/10.1016/j.ijhydene.2016.07.079

Macedo SF, Peyerl D (2022) Prospects and economic feasibility analysis of wind and solar photovoltaic hybrid systems for hydrogen production and storage: a case study of the Brazilian electric power sector. Int J Hydrogen Energy 47(19):10460–10473. https://doi.org/10.1016/j.ijhydene.2022.01.133

Majumdar A, Deutch JM, Prasher RS et al (2021) A framework for a hydrogen economy. Joule 5(8):1905–1908. https://doi.org/10.1016/j.joule.2021.07.007

Marbán G, Valdés-Solís T (2007) Towards the hydrogen economy? Int J Hydrogen Energy 32(12):1625–1637. https://doi.org/10.1016/j.ijhydene.2006.12.017

Moliner R, Lázaro MJ, Suelves I (2016) Analysis of the strategies for bridging the gap towards the Hydrogen Economy. Int J Hydrogen Energy 41(43):19500–19508. https://doi.org/10.1016/j.ijhydene.2016.06.202

Moreno-Benito M, Agnolucci P, Papageorgiou LG (2017) Towards a sustainable hydrogen economy: optimisation-based framework for hydrogen infrastructure development. Comput Chem Eng 102:110–127. https://doi.org/10.1016/j.compchemeng.2016.08.005

Nami H, Rizvandi OB, Chatzichristodoulou C et al (2022) Techno-economic analysis of current and emerging electrolysis technologies for green hydrogen production. Energy Convers Manag 269:116162. https://doi.org/10.1016/j.enconman.2022.116162

Nowotny J, Veziroglu TN (2011) Impact of hydrogen on the environment. Int J Hydrogen Energy 36(20):13218–13224. https://doi.org/10.1016/j.ijhydene.2011.07.071

Oliveira AM, Beswick RR, Yan Y (2021) A green hydrogen economy for a renewable energy society. Curr Opin Chem Eng 33:100701. https://doi.org/10.1016/j.coche.2021.100701

Parra D, Valverde L, Pino FJ et al (2019) A review on the role, cost and value of hydrogen energy systems for deep decarbonisation. Renew Sustain Energy Rev 101:279–294. https://doi.org/10.1016/j.rser.2018.11.010

Penner SS (2006) Steps toward the hydrogen economy. Energy 31(1):33–43. https://doi.org/10.1016/j.energy.2004.04.060

Preuster P, Papp C, Wasserscheid P (2017) Liquid organic hydrogen carriers (LOHCs): toward a hydrogen-free hydrogen economy. Acc Chem Res 50(1):74–85. https://doi.org/10.1021/acs.accounts.6b00474

Proost J (2019) State-of-the art CAPEX data for water electrolyzers, and their impact on renewable hydrogen price settings. Int J Hydrogen Energy 44(9):4406–4413. https://doi.org/10.1016/j.ijhydene.2018.07.164

Reksten AH, Thomassen MS, Møller-Holst S et al (2022) Projecting the future cost of PEM and alkaline water electrolyzers; a CAPEX model including electrolyzer plant size and technology development. Int J Hydrogen Energy 47(90):38106–38113. https://doi.org/10.1016/j.ijhydene.2022.08.306

Rojas N, Sanchez-Molina M, Sevilla G et al (2021) Coated stainless steels evaluation for bipolar plates in PEM water electrolysis conditions. Int J Hydrogen Energy 46(51):25929–25943. https://doi.org/10.1016/j.ijhydene.2021.03.100

Santos AL, Cebola MJ, Santos DMF (2021) Towards the hydrogen economy—a review of the parameters that influence the efficiency of alkaline water electrolyzers. Energies 14(11):3193. https://doi.org/10.3390/en14113193

Schnuelle C, Wassermann T, Fuhrlaender D et al (2020) Dynamic hydrogen production from PV & wind direct electricity supply–modeling and techno-economic assessment. Int J Hydrogen Energy 45(55):29938–29952. https://doi.org/10.1016/j.ijhydene.2020.08.044

Tseng P, Lee J, Friley P (2005) A hydrogen economy: opportunities and challenges. Energy 30(14):2703–2720. https://doi.org/10.1016/j.energy.2004.07.015

Weidner S, Faltenbacher M, François I et al (2018) Feasibility study of large scale hydrogen power-to-gas applications and cost of the systems evolving with scaling up in Germany, Belgium and Iceland. Int J Hydrogen Energy 43(33):15625–15638. https://doi.org/10.1016/j.ijhydene.2018.06.167

Xie Z, Yu S, Yang G et al (2021) Optimization of catalyst-coated membranes for enhancing performance in proton exchange membrane electrolyzer cells. Int J Hydrogen Energy 46(1):1155–1162. https://doi.org/10.1016/j.ijhydene.2020.09.239

Yang B, Zhang R, Shao Z et al (2023) The economic analysis for hydrogen production cost towards electrolyzer technologies: current and future competitiveness. Int J Hydrogen Energy 48:13767–13779. https://doi.org/10.1016/j.ijhydene.2022.12.204

Index